Advances in Unsaturated Soils

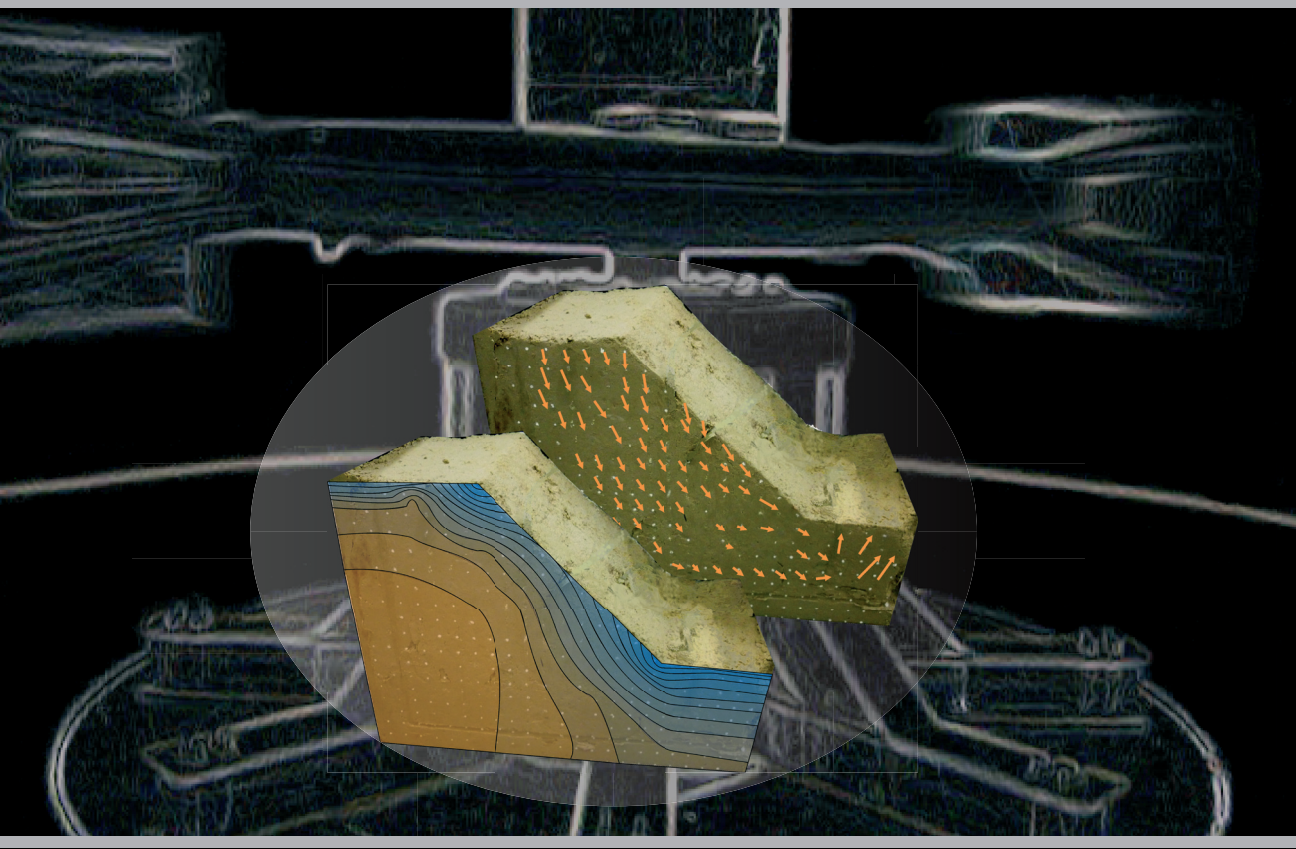

Editor:
Bernardo Caicedo

Co-editors:
Carol Murillo, Laureano Hoyos, Julio E. Colmenares & Iván R. Berdugo

CRC Press
Taylor & Francis Group
A BALKEMA BOOK

ADVANCES IN UNSATURATED SOILS

This page intentionally left blank

PROCEEDINGS OF THE FIRST PAN-AMERICAN CONFERENCE ON UNSATURATED SOILS, CARTAGENA DE INDIAS, COLOMBIA, 20–22 FEBRUARY 2013

Advances in Unsaturated Soils

Editor

Bernardo Caicedo
Department of Civil and Environmental Engineering, Universidad de Los Andes, Bogotá, Colombia

Co-editors

Carol Murillo
Department of Civil and Agricultural Engineering, Universidad Nacional de Colombia, Bogotá, Colombia

Laureano Hoyos
Department of Civil Engineering, The University of Texas at Arlington, USA

Julio Esteban Colmenares
Department of Civil and Agricultural Engineering, Universidad Nacional de Colombia, Bogotá, Colombia

Iván Rafael Berdugo
Department of Civil and Environmental Engineering, Universidad del Norte, Barranquilla, Colombia

CRC Press
Taylor & Francis Group
Boca Raton London New York Leiden

CRC Press is an imprint of the
Taylor & Francis Group, an **informa** business

A BALKEMA BOOK

CRC Press
Taylor & Francis Group
6000 Broken Sound Parkway NW, Suite 300
Boca Raton, FL 33487-2742

Version Date: 20130411

International Standard Book Number-13: 978-0-203-77107-5 (eBook - PDF)

Advances in Unsaturated Soils – Caicedo et al. (eds)
© 2013 Taylor & Francis Group, London, ISBN 978-0-415-62095-6

Table of contents

Numerical modelling

Geotechnical problems and soil atmosphere interaction

This page intentionally left blank

Advances in Unsaturated Soils – Caicedo et al. (eds)
© 2013 Taylor & Francis Group, London, ISBN 978-0-415-62095-6

Preface

There are two main factors explaining the increased interest for Unsaturated Soils in recent years. The first factor is the enhancement of the domain of application of the new theories developed for Unsaturated Soils, which nowadays includes materials like rocks, rock fills, frozen soils and domiciliary solid wastes; and, the efficient applicability of these theories to study new energy-related problems like CO_2 sequestration and nuclear waste disposal, among others. The second factor is the appearance of new experimental techniques that has permitted the analysis of several traditional problems from a new perspective (e.g., swelling or collapsible soils and compacted soils or pavements materials, among others).

In the Americas, the study of unsaturated soils has received particular attention since the apparition of the first theories explaining the behavior of expansive soils. Besides, the recently developed theories constitute effective tools to study the complexity of soils present in the continent, such as residual soils, expansive and collapsing soils and mud rocks, and its interaction with extreme climatic variations.

Advances in Unsaturated Soils is the result of the 1st Pan-American Conference on Unsaturated Soils organized in Cartagena de Indias, Colombia, in February 2013 by Los Andes University and the Colombian National University (Bogotá). The book contains a compendium of the works presented in the conference, and it represents a stimulating sample of every aspect included in the study of unsaturated soils up to 2013. Besides, it links together fundamental knowledge, testing techniques, computational procedures and prediction methodologies. The volume includes 76 research papers coming for all over the world, as well as 7 keynotes papers from international researchers.

I am grateful for the keynote papers prepared by professors Eduardo Alonso, Geoffrey Blight, Delwyn Fredlund, Antonio Gens, Sandra Houston, Serge Leroueil, Robert Lytton, Luciano Oldecop and Sai Vanapalli, and their co-authors. Certainly, these keynotes will become reference papers for researchers and practitioners interested in the area of unsaturated soils.

I would also like to express our gratitude to the international committee TC106 of the International Society for Soil Mechanics and Geotechnical Engineering, who supported this conference, as well as to our co-sponsors: the University of Texas at Arlington, and the Geo Institute.

Finally, thanks are due to all the authors who submitted papers to the conference, to the reviewers who offered an essential part of their time to enhance the quality of these contributions, and to the local organizing committee and the international advisory board for their continuous support.

I hope that this volume will inspire future generations involved in geotechnical engineering of unsaturated soils.

Bernardo Caicedo
Chair, First Pan-American Conference on Unsaturated Soils

This page intentionally left blank

Advances in Unsaturated Soils – Caicedo et al. (eds)
© 2013 Taylor & Francis Group, London, ISBN 978-0-415-62095-6

Organization committees

LOCAL ORGANIZING COMMITTEE

Bernardo Caicedo, *Los Andes University, Colombia*
Manuel García, *National University of Colombia, Bogotá*
Silvia Caro, *Los Andes University, Colombia*
Iván Rafael Berdugo, *Universidad del Norte, Barranquilla*
Julio Esteban Colmenares, *National University of Colombia, Bogotá*
Nicolás Estrada, *Los Andes University, Colombia*
Laureano Hoyos, *University of Texas, Arlington, USA*
Arcesio Lizcano, *Los Andes University, Colombia*
Carol Murillo, *National University of Colombia, Bogotá*

ORGANIZER COORDINATOR

Diana Bolena Sánchez

INTERNATIONAL ADVISORY BOARD

E. Alonso (Spain)
J.L. Briaud (USA)
P. Delage (France)
D. Gallipoli (United Kingdom)
G. Gitirana (Brazil)
S. Houston (USA)
C. Jommi (Italy)
L. Laloui (Switzerland)
W. Likos (USA)
N. Lu (USA)
D. Marcial (Venezuela)
J.S. McCartney (USA)
L. Oldecop (Argentina)
M. Pérez (Mexico)
E. Rojas (México)
M. Sánchez (USA)
A. Tarantino (United Kingdom)
S. Vanapalli (Canada)
A. Zepeda (Mexico)
K. Bicalho (Brazil)
T.M. Pereira de Campos (Brazil)
D. Fredlund (Canada)
A. Gens (Spain)
L. Guimaraes (Brazil)
D. Hurtado (Mexico)
J.F. Thomé Jucá (Brazil)
S. Leroueil (Canada)
T. López (Mexico)
R. Lytton (USA)
F. Marinho (Brazil)
F. Masrouri (France)
A. Pérez (Mexico)
A. Puppala (USA)
E. Romero (Spain)
S. Springman (Switzerland)
L. Vallejo (USA)
O. Monje (Brazil)

This page intentionally left blank

Advances in Unsaturated Soils – Caicedo et al. (eds)
© 2013 Taylor & Francis Group, London, ISBN 978-0-415-62095-6

Acknowledgements

MANUSCRIPT REVIEWERS

The editors are grateful to the following people who helped to review the manuscripts and hence assisted in improving the overall technical standard and presentation of the papers in these proceedings:

J.P. Alvarado
K. Bicalho
D. Cantor
D. Castillo
D. Gallipoli
L. Garzón
G. Gitirana
D. Gómez
L. Guimaraes
D. Marcial
F. Marinho
F. Masrouri
J.S. McCartney
J. Miller
J. Muñoz
F. Lopez
C. Lozada
N. Lu
M. Ocampo
L. Oldecop
T.M Pereira de Campos
L. Ramirez
D. Rojas
E. Rueda
D.B. Sánchez
M. Sánchez
A. Tarantino
J.F. Thomé
L. Thorel
D. Toll
L. Vallejo
S. Vanapalli
L.F. Vesga
C.E. Zapata

This page intentionally left blank

Advances in Unsaturated Soils – Caicedo et al. (eds)
© 2013 Taylor & Francis Group, London, ISBN 978-0-415-62095-6

Sponsors

First Pan-American Conference on
Unsaturated Soils

HOSTING ORGANIZATIONS

Universidad de los Andes

UNIVERSIDAD NACIONAL DE COLOMBIA
SEDE BOGOTÁ
FACULTAD DE INGENIERÍA

CO-SPONSORS

UNIVERSITY OF TEXAS ARLINGTON

ISSMGE

G-I GEO-INSTITUTE
ASCE

ceiBA

This page intentionally left blank

Keynotes lectures

This page intentionally left blank

Advances in Unsaturated Soils – Caicedo et al. (eds)
© 2013 Taylor & Francis Group, London, ISBN 978-0-415-62095-6

Interactions between atmosphere and geosphere—difficulties in measuring evaporation

Geoffrey Blight
University of the Witwatersrand, Johannesburg, South Africa

ABSTRACT: The solar energy balance method and semi-empirical derivatives of this approach are widely used to estimate evaporation (or evapotranspiration) from the soil-covered or soil-like surfaces of waste storage facilities, in order to evaluate the water balances for the facilities. A number of difficulties and uncertainties regarding evaluation of the solar energy balance have been experienced. This paper gives six examples of these, with the purpose of warning against the incautious use of the method.

1 INTRODUCTION

Assessment of the water balance is an essential step in the design of any municipal solid, industrial or mine waste storage facility. The water balance calculation enables the designer to estimate the quantities of water entering, retained within and exiting the waste body (e.g., Fenn, et al., 1975, Blight, 2010 and others). The inputs to the landfill or other waste storage facility usually consist of the water content of the incoming waste and the rainfall infiltration for the site, and the outputs are evaporation from the surface and leachate or seepage exiting from the base of the deposit. Estimation of the inputs and the output evaporation enables the quantity of leachate or seepage to be predicted. This in turn allows the need for an impervious underliner, to prevent ground-water contamination, to be assessed as well as the quantities of leachate or seepage for which the drainage or seepage effluent treatment system need to be designed. Fluctuating water storage within the waste body bridges between inputs and outputs and completes the water balance. At closure of the storage facility, the water balance needs to be reassessed for post-closure conditions to decide on the need for ongoing leachate collection, storage and treatment and to design the post-closure facilities. Recently, Henken-Mellies and Schweizer, (2011) have emphasized the ongoing importance of water balance estimation in all phases of the life-cycles of waste storage facilities.

Evaporation almost always represents a major term in the water balance equation and is also one of the most difficult to quantify. During the 1960s to 1990s, the fields of plant physiology, forestry and agriculture formalized a means of estimating evaporation from soil and water surfaces, based on the solar energy balance (Penman, 1956, Monteith, 1980, Calder, 1990).

However, there are several difficulties in applying the solar energy method to the calculation of water balances in the field of waste storage. Some of these were enumerated and analysed by Blight (2009, 2010). The purpose of this paper is to describe these problems, in order to warn of their existence. Their solution is not clear, as yet, but forewarned is forearmed, and knowing of their existence can prevent the geotechnical engineer working in the waste storage field from making incorrect decisions based on inadequate information.

2 ESTIMATING EVAPOTRANSPIRATION BY SOLAR ENERGY BALANCE

According to established and generally accepted theory, the daily quantity of evaporation or evapotranspiration can be determined by measuring the components of the solar energy balance equation (e.g., Penman, 1963, Monteith, 1980, Calder, 1990) written as:

$$LE = R_n + WE - (G + H + p) \quad (1)$$

The terms are usually expressed in energy units of kJ/m^2, and LE is the latent heat consumed in evaporation or evapotranspiration, R_n is the net incoming short wave solar energy (gross incoming—reflected) at the soil surface, WE is the wind energy (which will not be considered here), G is the energy absorbed by heating the near-surface soil and soil-water (the soil heat), H is the energy absorbed by heating the near-surface air (the sensible heat) and p is the energy used in plant photosynthesis (usually less than 2% of R_n).

LE (in kJ/m^2) is used to calculate the quantity of daily evapotranspiration by dividing the daily total LE by the latent heat for vaporization of water, λ in kJ/kg. That is, evapotranspiration E = LE/λ in kg/m^2. (1 kg/m^2 is equivalent to 1 mm depth of water.) For reasons of lack of space, the reader is referred to Blight (2009 & 2010) for numerical constants and methods of calculating the various terms in equation (1).

In terms of equation (1), G, H and p are heat losses or sinks that subtract from LE and therefore reduce evaporation. One of the problems associated with equation (1) is that it includes only the net incoming short wave-length solar radiation R_n, but omits the outgoing long wave-length Earth heat radiation R_o. This could be subtracted as a proportion (about 25%) of R_n, but because the rate of outgoing heat energy varies throughout the day and night and can be affected by local weather conditions, short-term fluctuations will arise (energy deficits or surpluses) that need to be represented by an energy storage term S, which may be positive or negative (Oke, 1978). With these additions, equation (1) becomes

$$LE = (R_n - R_o) + WE - (G + H + p) + S \qquad (1a)$$

The value of H is negligible in comparison with G and p is also small. The equation lacks a term representing inefficiencies or losses in energy conversion (L). With this addition, equation (1a) can be replaced by

$$LE = (R_n - R_o) + WE - (G + L) + S \qquad (1b)$$

Penman (1956) introduced a semi-empirical equation for calculating evaporation that does not use the energy balance directly, but is based on energy balance principles. His equation is

$$E_p = (\Delta R_n/\lambda + \gamma E_a)/(\Delta + \gamma) \qquad (2)$$

in which E_p is the potential evaporation, Δ is the slope of the temperature versus saturated water vapour pressure curve at the prevailing air temperature, R_n is the net incoming solar radiation, λ is the latent heat for vaporization of water, γ is the psychrometric constant (66 Pa/^{o}C), $E_a = 0.165\,(e_{sat} - e_a)\,(0.8 + u_2/100)$ mm/day, e_{sat} is the saturated vapour pressure of air (mbar), e_a is the actual vapour pressure of air (mbar) and u_2 is the wind speed at a height of 2 m (km/day). Note that E_a (a linear function of u_2) increases E_p, and that no energy storage term appears. As Δ and γ both have units of Pa/^{o}C, if R_n has units of J/m^2 per day and λ has units of J/kg, the units of E_p are kg/m^2, the equivalent of mm/day of water.

Priestly & Taylor (1972) suggested a modified Penman equation that appeared to fit measured evaporation more closely. Their equation is:

$$E_p = 1.26\Delta/\lambda.(R_n - S)/\Delta + \gamma) \qquad (2a)$$

The effect of wind is ignored, and the heat stored in the water or soil being considered is represented by S, regarded as an energy loss. Various others (e.g., de Bruin & Keijman, 1979), have also suggested slight modifications to fit their local climatic conditions.

The original Penman equation (2) is probably the most frequently used method of calculating evaporation from water or soil surfaces. Penman called E_p the potential evaporation, recognizing that actual evaporation could be more or less than this, depending on local circumstances. As evaporation is very often routinely measured by the standard American 'A' evaporation pan, many attempts have also been made to find modification factors that will convert the easily determined A-pan evaporation (E_A) to actual evaporation from soil or water surfaces. Penman (1956) suggested ratios of E_p/E_A for cropped fields varying from 0.8 for summer to 0.6 for winter in Western Europe. Others (quoted by Fenn, et al., 1975) found values for E_p/E_A varying in the range 0.5–0.9. A recent study of the ratio E_B/E_A made at six landfill sites in South Africa (Blight, 2006), gave a large range of seasonal values varying from 0.1 to 0.75 and average annual values from 0.34 to 0.46 with an overall mean of 0.39. E_B is the evapotranspiration measured by energy balance (equation (1), usually with WE, H and p set to zero). The necessity of adopting these correction factors is recognition that both the A-pan and other evaporation pan methods of measuring evaporation as well as the use of equations (1a) and (2) are problematic.

These so-called "crop" or "lake" factors may seem to be a neat solution to the problem, but as shown by Figure 1, can be wildly inaccurate. Figure 1 (Benli, et al., 2010) shows a correlation between A-pan evaporation and evaporation from cropped soil measured directly by means of large-scale lysimeters. No engineer would be happy to apply a correlation like this in work on which his reputation might depend.

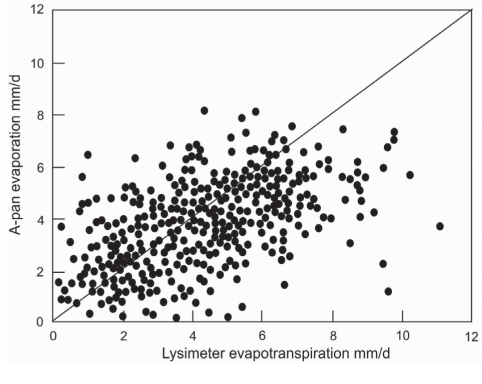

Figure 1. Comparison of two methods of measuring evapotranspiration. (Benli, et al., 2010).

3 DIFFICULTIES IN APPLYING THE ENERGY BALANCE TO ESTIMATING EVAPORATION

3.1 *Field experiments using a large cylindrical pan set into the ground surface (Blight, 2009a)*

Some of the difficulties associated with applying equation (1) are illustrated by Figures 2 and 3. Because similar principles must govern evaporation from both water and soil surfaces, it was decided to pair experiments on water and soil, both to increase understanding of the processes and to act as a series of ongoing checks on the experimental results. A 500 mm diameter by 100 mm deep circular stainless steel pan was let into the surface of a short-mown grassed area so that its rim was level with the soil surface (i.e. slightly below the grass surface). The pan was filled with water and left overnight to reach temperature equilibrium with its surroundings. In the accepted conventional way, the vertical components of the incoming and reflected solar power (in W/m^2) were measured throughout the day, as well as water temperatures. The experiment was then repeated, as a check, a week later. The week thereafter the experiment was carried out with the pan filled with a uniform compacted moist sand. An impervious containing vessel was used so that the depth of water or soil from which water was evaporating could be precisely defined, and at the same time, the sides and base of the soil or water specimen would be insulated by the surrounding soil. The results of the measurements are shown in Figure 2. In the upper diagram, the roughly parabolic curves represent the vertical component of the net incoming solar power $\delta/\delta t R_n(V)$ recorded through the first of each of two test days in W/m^2. The ogive-like curves represent the time-integrated values of $R_n(V)$, in kJ/m^2. The soil heat G is also shown in this diagram. Sunrise was at 07.00 and sunset at 17.00. The lower diagram shows the measured water and soil temperatures, relative to the temperature at sunrise, throughout the day, as well as the residual value at 07.00 the next morning.

The first difficulty that is apparent from Figure 2 is that the maximum soil heat G (5410 kJ/m^2) and water heat WH (8380 kJ/m^2) calculated from the maximum soil and water temperatures exceeded the net cumulative vertical component of solar

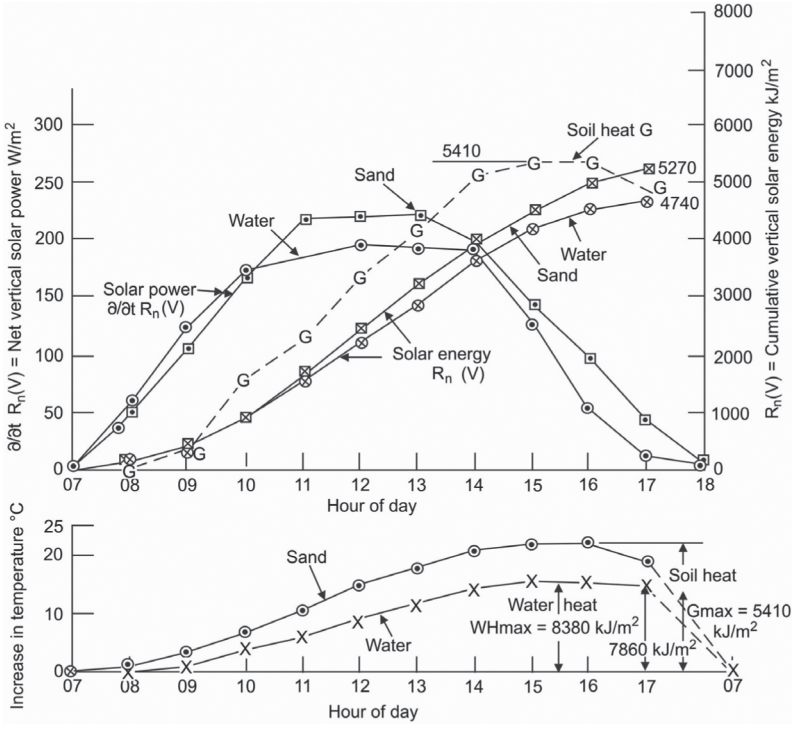

Figure 2. Results of twin experiments made on stainless steel pan set level with ground surface. Pan filled firstly with water, secondly with sand. Measured evaporation (averaged over 5 consecutive days): Water: 3.2 mm/day, Sand: 1.6 mm/day.

energy for the day (of 5270 kJ/m^2 for the sand and 4255 kJ/m^2 for the water). Obviously, more energy was being absorbed by the soil and water than was represented by $R_n(V)$. When the experiment was made with the pan filled with sand, the maximum (R_{max}), the vertical (R_v) and net vertical $R_n(V)$ components of the solar power were measured separately, with the result shown in Figure 3. This shows that the gross incoming solar energy R_{max}, may be 3 times the net value of $R_n(V)$ for the water, which, in conjunction with the completely independently measured G and WH values in Figure 2, must mean that not only the vertical component of solar energy is absorbed at a soil or water surface (as conventionally assumed), but also additional oblique components.

The second difficulty also relates to the values of G. In Figure 2, G exceeded $R_n(V)$ from 09.00 until nearly 16.00. If G is interpreted as a loss and as subtractive from $R_n(V)$, equation (1) would predict negligible evaporation for the day, whereas the actual evaporation measured over 5 days by means of the water contents of cores of sand taken from the pan averaged 1.6 mm/day. Similar results were observed for the evaporation of water (3.2 mm/day).

These tests were repeated several times, varying the colour of the pan's interior surface for tests on water and the water content of the sand and with the pan set into the ground and raised above the surface with insulated sides and base. The results

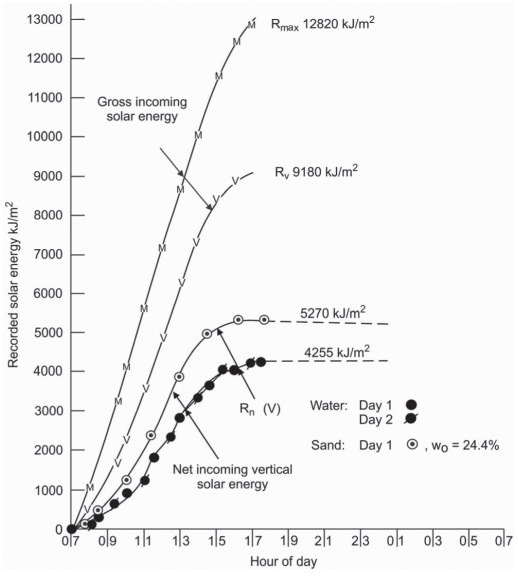

Figure 3. Comparison of gross maximum, vertical and net vertical solar energies. Differences between water and sand for net energies is caused by differences in albedo (reflectance) of surfaces.

were similar in every case. It seemed very likely from the considerations above, that the stored soil and water heat are the opposite of heat losses that decrease evaporation, they are actually the sources and drivers of evaporation.

3.2 *Field measurement of the water balance for a landfill*

Figure 4 shows the water balance, measured over a five year period, for an experimental raising of a landfill in Cape Town, South Africa. (Blight, 2005). In Figure 4, the precipitation, P and the leachate L were measured directly on the landfill, while the evaporation from the landfill surface E_B, was calculated by means of the solar energy balance (eqn. 1). It will be noted from Figure 4 that E_B was by far the largest quantity in the water balance, with an average value of 620 mm/y. The broken line marked E(av) = 400 mm/y shows that there was considerable doubt as to whether the value of 620 mm/y could be correct, as it far exceeded the average annual precipitation of about 400 mm/y, over the 5 year period. Evaporation as large as this would have severely depleted the water stored in the waste, as shown by the solid line labeled ΔS_w. As the landfill continued to emit leachate at an approximately constant rate (L in Figure 4) throughout the 5 years of the experiment, this was unlikely to have happened and cast doubt on the accuracy of assessing E_B. It appears that in this case, eqn. 1 led to a 50% over-estimate of the actual evaporation from the landfill.

3.3 *Evaporation from experimental landfill capping layers*

Figure 5 shows water balance data for a series of experimental landfill covers (or capping layers) constructed in Johannesburg, South Africa to test the infiltrate, stabilize, evapotranspire concept for landfill capping layers (Blight & Fourie, 2005). In Figure 5, evaporation estimated by solar energy balance (E_B) is also the largest component of the water balance and far exceeded rainfall P. The experimental caps were constructed over geomembrane-lined basins, so that all evaporation must have originated in the soil cover, above the geomembrane. As the inset above the main diagram shows, average evaporation rates measured by changes of water content in the soil cover-layers during dry periods were considerably less than rates established by solar energy balance, again throwing doubt on the reliability of the energy balance method, and resulting in up to a seven-fold (2.1/0.3) over-estimate of actual evaporation from the cover-layers. Similar tests carried out at the same time in Cape Town, indicated similar over-estimates of soil evaporation by applying equation (1).

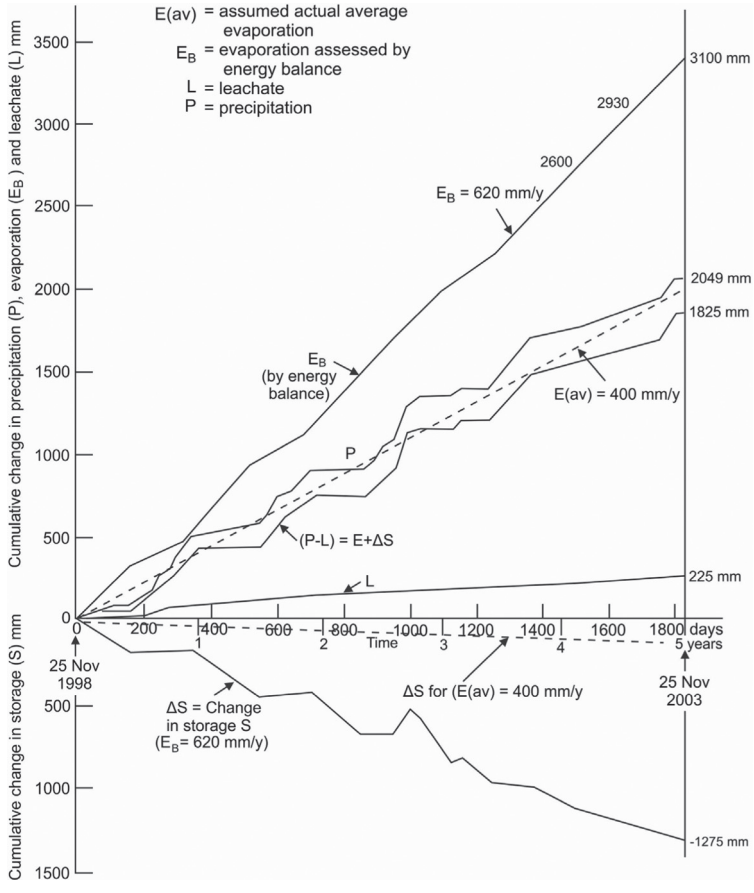

Figure 4. Water balance for raised part of landfill at Cape Town during experiment: changes in water storage as a result of precipitation infiltration, leachate flow and evaporative losses. (November 1998–2003).

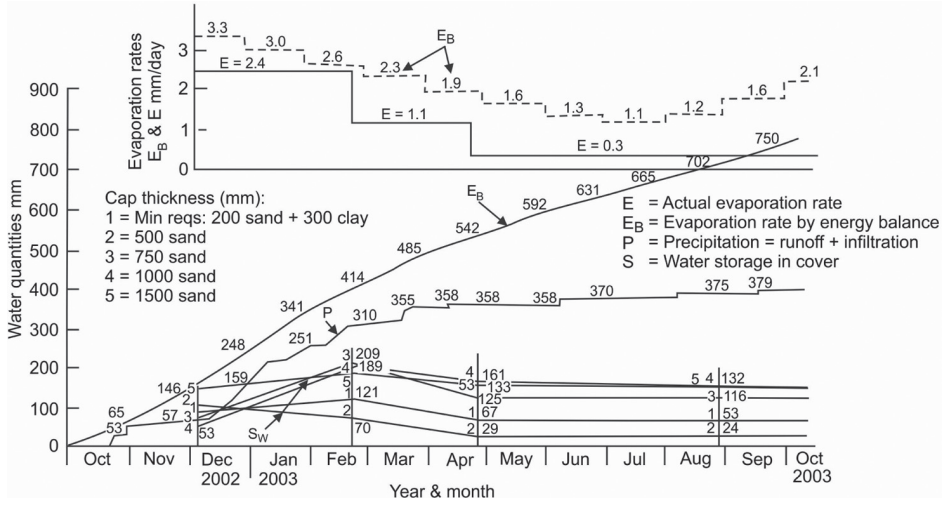

Figure 5. Water balance data for Johannesburg experimental landfill caps: October 2002 to October 2003.

3.4 *Evaporation from a grassed, fissured clay surface*

In the two examples illustrated by Figures 4 and 5, application of equation (1) showed that E_B over-estimated the true evaporation E. In both of these cases, the cover soil was sandy, and apart from any faults with the interpretation of the terms of equation (1), the over-estimate may have been the result of inherent inefficiency in the conversion of stored soil and soil-water heat into evaporation. This has been demonstrated by Blight (2010), pp. 445–446. However, the result of applying equation (1) may in other cases appear accurate or may be an apparent under-estimate of E. Figures 6a and 6b illustrate such cases (Blight, 2006b, 2008a). The soil at the site under consideration consists of 0.5 to 2 m of a stiff fissured clayey silt underlain by sandstone, with the water table at 5 m and a grass-covered surface. Separate studies (Blight, 2009b) had shown that even in rain-storms of as much as 50 mm in 4 hours, run-off from the fissured clay surface was negligible. The measurements for Figure 6a were made under the grassed surface near a lone willow tree. Figure 6a shows the rainfall precipitation (P) and evapotranspiration (EB) for the site from 01 October 2003 to 20 December 2004, with the precipitation measured daily by rain gauge on site, and the evapotranspiration, assessed by equation (1). The water balance for the area adjacent to the lone willow was started in October because it is the end of the dry season and a month in which temperatures are moderate and evapotranspiration low. As Figure 6a shows, in addition to E_B and P, the water stored in the soil profile (S) was measured by means of soil samples taken by hand augering, at 100 mm depth intervals, on six occasions from April to December, 2004. In the case that no water exits the shallow soil profile, to seep down to the water table and no water rises from the water table under a capillary gradient, the following equation should hold:

$$S + E_B = P$$

The inset graph of $(S + E_B)$ against P shows that this was close to true for the data shown on Figure 6a.

The measurements for Figure 6b were made at right angles to a line of evergreen bushes (Leucosidia) and deciduous trees (Populus). Figure 6b shows water balances for the years May 2004 to April 2005 and May 2005 to April 2006, with May to October 2006. The water stored in the soil along two lines at right angles to the line of bushes and trees was measured on two occasions each by hand-augering holes at the positions indicated and measuring water content profiles from surface at intervals of 100 mm down to a depth of 500 mm.

The water stored in the soil remote from the bushes was very similar in quantity on both occasions on which it was sampled and amounted to between 175 and 202 mm. Water stored in the soil remote from the trees amounted to between 152 and 211 mm, i.e. similar to the "bush profiles". By the same argument used above, $(S + E_B)$ should equal P. The experimental points for the assessments of $(S + E_B)$ and P have also been plotted on the graph inset on Figure 6a. These show that as the water stored in the soil decreases, it approaches a constant value as P decreases. This is probably again due to a decreasing efficiency of conversion of soil heat into evaporation, as the surface dries out and surface fissures multiply in number and depth.

An alternate way of looking at the results in Figures 6a and 6b in terms of eqn. (1) is that when the soil is relatively wet, as it was in the measurements in Figure 6a, incoming radiation R_n is almost entirely converted to G, which is then relatively efficiently converted to E. In other words, for a wet soil, eqn. (1b) could be written:

$$LE = R_n + WE = G + WE \qquad (1c)$$

As the soil dries out and the energy conversion becomes less efficient, eqn. (1c) would change to

$$LE < G + WE = \eta G + WE \qquad (1d)$$

where η is an efficiency factor accounting for inefficiency in conversion of heat energy to evaporation.

This reasoning is illustrated by Figure 7 which shows the results of solar heated evaporation tests similar to those described in Figure 2, but performed on smaller insulated containers so that evaporation could be accurately measured by weighing. The two experimental containers each holding water or a saturated sandy silt, were exposed to the weather at sunset on the day before the tests so that they could equilibrate with ambient conditions. Temperatures of the water and soil were measured by means of thermocouples, and the containers were weighed at intervals throughout the day and the following night.

Figure 7 shows the results plotted in terms of evaporation and stored heat energy (see Blight, 2009). The curves show that as the water or soil heat is absorbed, conversion of heat to evaporation occurred simultaneously. The maximum of stored WH or G occurred at about 15.00, whereafter incident solar radiation decreased rapidly, but conversion of soil heat to evaporation continued. In the early hours of the next morning the heat energy

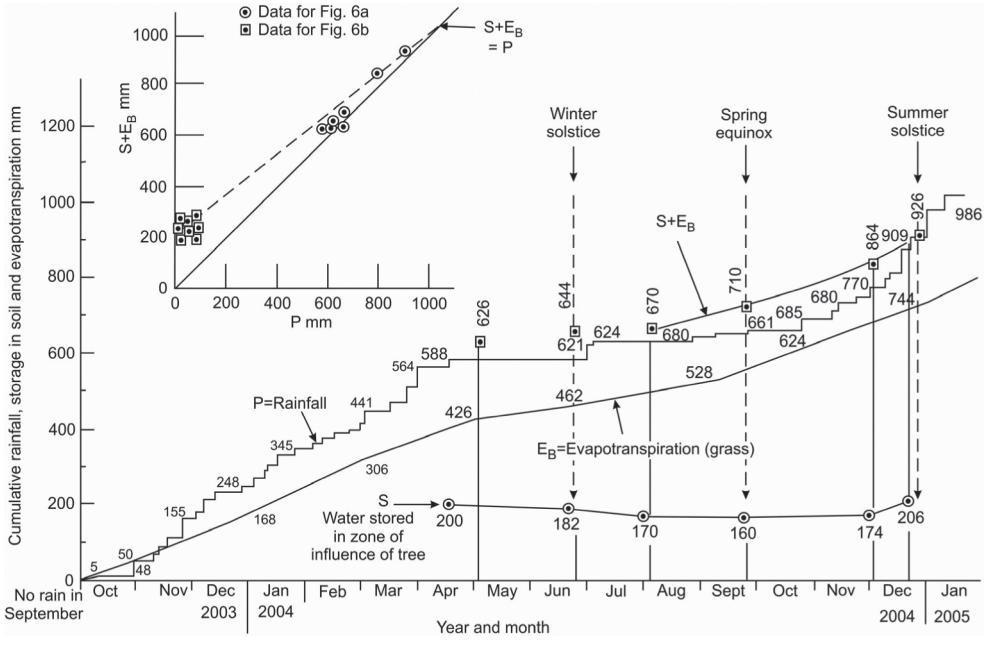

Figure 6a. Water balance data for a grass-covered site adjacent to a single tree where the soil consists of a stiff fissured silty clay of limited thickness, overlying sandstone.

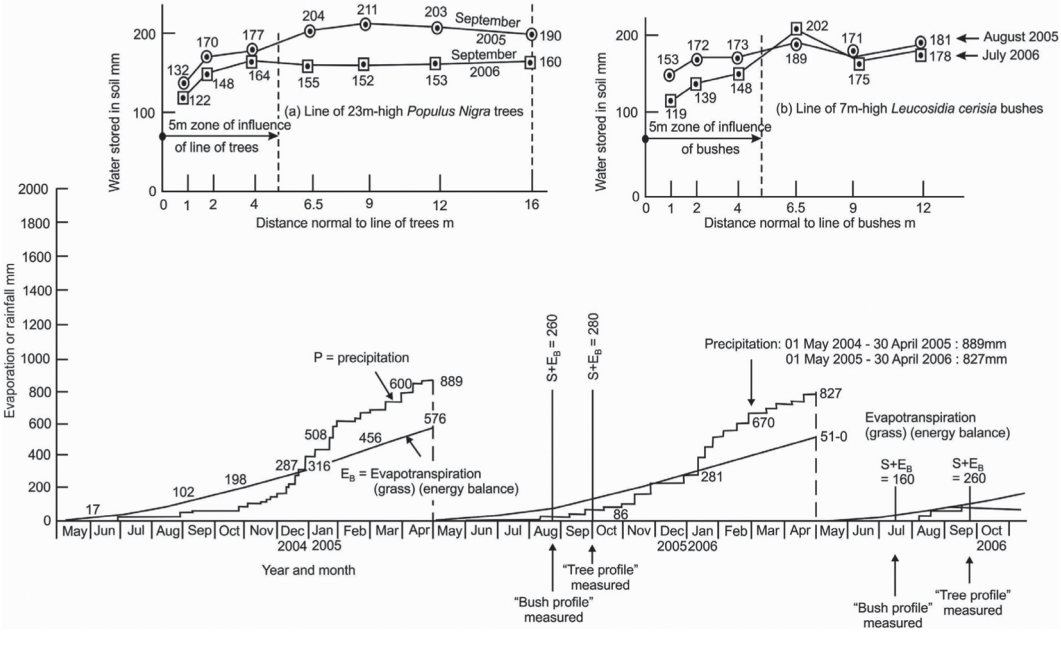

Figure 6b. Water balance for a grass-covered site adjacent to lines of trees and bushes where the soil consists of a stiff fissured silt clay of limited thickness, overlying sandstone.

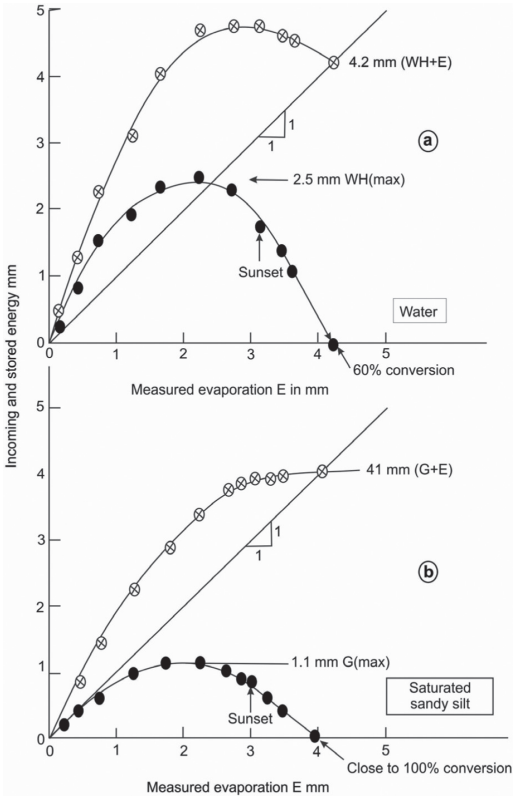

Figure 7. Variation of (a) water and (b) soil heat with evaporation over 24-hour day.

had been exhausted. At this point, evaporation ceased and the sum of the total water or soil heat equaled the evaporation, i.e. in terms of eqn. (1c)

$$LE = WH \text{ or } LE = G$$

3.5 *Near-surface movement of water during evapotranspiration*

The experience described in section 3.4 led to a detailed study of near surface water movement during evapotranspiration (Blight, 2008b). Calibrated glass-fibre mat moisture sensors and gypsum blocks were set and observed in a clayey silt soil beneath a mown grass surface. The observations took place in June, a period with no rain or cloud cover.

Figure 8a shows the decline of water content as evaporation occurred over a period of 16 days at depths of 15, 45 and 75 mm. The gypsum blocks gave very similar results. Figure 8b shows detailed water content profiles measured on days 1 and 8.

While the loss of water over the 8 days from depths 0–75 mm amounted to 0.6 mm/day, that over 0–200 mm amounted to 1.1 mm/day. The latter figure more accurately represents the evapotranspiration from the soil, but the figure is actually larger, as water losses from deeper than 200 mm were not measured. This shows that even direct measurement of evaporation from water content profiles by means of water contents may under-estimate actual evaporation losses.

If it is assumed that the soil heat G at sunset is equivalent to the nocturnal evaporation, a total of 1.6 mm, 0.2 mm/day or roughly 20% of total evaporation took place nocturnally.

3.6 *Drying of tailings beaches*

Apparently anomalous results were observed when studying the rate of drying of 400 mm deep test depositions of platinum tailings on a tailings deposition facility or TSF (Blight, et al., 2012).

To aid in understanding the process of drying of the tailings beaches, a small-scale experiment was set up. A sample of tailings was placed in a small plastic bucket. The bucket was contained in a cardboard box, the base and sides of the bucket being insulated with a minimum of 25 mm of dry wood shavings. The specimen represented a 120 mm thick surface layer of tailings, isolated from interchange of pore water with the tailings around or below it and with the insulation preventing any gain or loss of heat by the tailings specimen, except through the top surface. Changes of mass of the tailings could be measured by weighing to 0.5 g which represented a water loss or gain of 0.03 mm. To record the development of pore water suction in the tailings, two calibrated gypsum block sensors were set into the tailings, one centred 20 mm from the surface and the other at 100 mm below the surface. The bucket of tailings and an identical insulated bucket of water were exposed to the weather, supported 1 m above the ground on a small wooden table, in an area receiving sun from sunrise to sunset. The test was carried out in cool weather during May/June when there was no rain or cloud.

The results of the experiment are shown in Figure 9. Referring to the left diagram, starting at a value of 38.6% the water content declined to 27% after 7 days of exposure before the gypsum blocks registered any suction. As the water content continued to decline, the suction rose by the day, reaching 300 kPa after another 7 days. The important point to note is that suction was only generated once the water content fell below a threshold value (i.e. its field capacity), in this case 27%. Until this threshold was reached, the near-surface pore water was unstressed, and therefore free either to seep downwards into the tailings below, under the gravity pressure gradient, or to be evaporated. The proportions in which these two possible movements occur appears unpredictable.

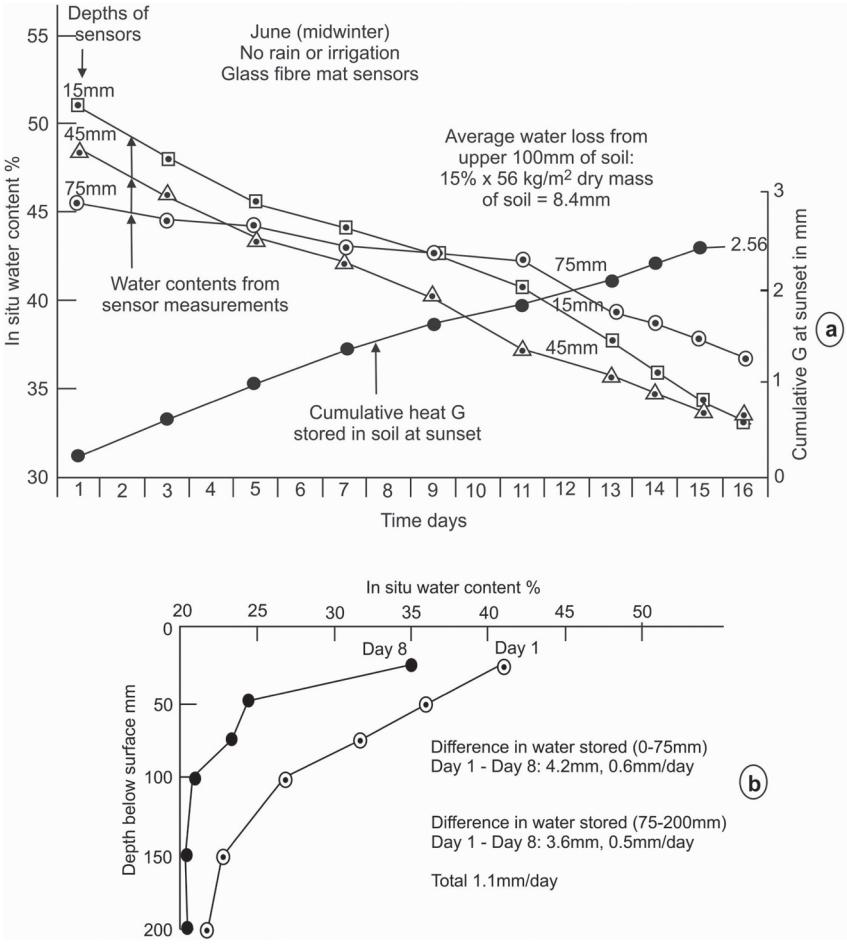

Figure 8. Results of study of near-surface movement of water caused by evaporation.

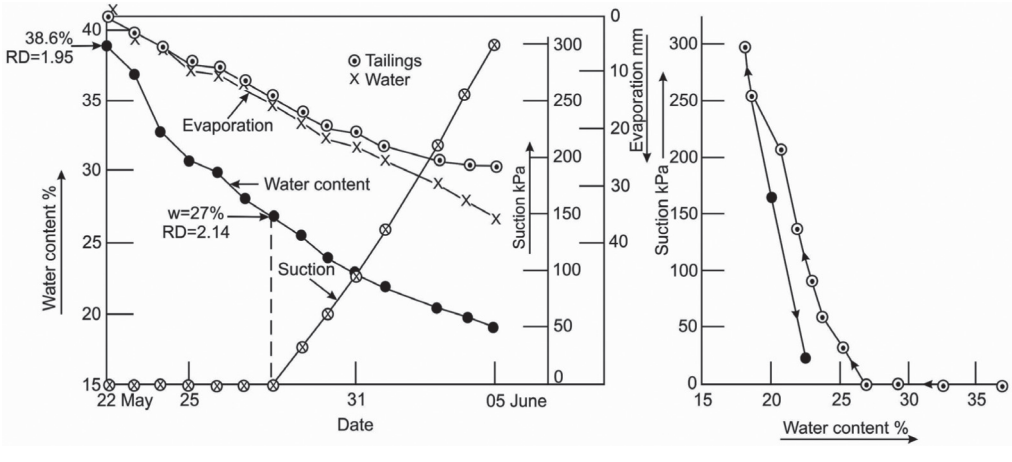

Figure 9. Drying characteristics of platinum tailings.

A suction of 300 kPa represents 30 m of negative water head which is sufficient to draw water up to the tailings surface from a depth of 30 m. It must also be noted that the whole mass of tailings retained by the TSF is consolidating under its own weight. The TSF is built on a highly impervious black clay stratum, for which the permeability, measured in the laboratory, is 0.03 m/y compared with 2 to 3 m/y for the tailings. Although originally desiccated and highly fissured, the clay was presently swollen with seepage water and compressed by the 30 m of overburden imposed by the tailings. Hence, water expelled by consolidation was much more likely to be moving towards the surface of the tailings than towards the impervious foundation stratum.

Calculations based on the consolidation characteristics of the tailings showed that the tailings mass is 90% consolidated and the surface of the tailings is settling at between 1 and 0.1 mm per day depending on the assumptions made. As the porosity of the tailings is about 0.6, 0.6 to 0.06 mm/day of consolidation water is being liberated at the surface. This is enough to partly supply the evaporation during hot weather, and to keep the near-surface tailings damp during cool weather.

The left diagram in Figure 9 shows the cumulative amounts of evaporation of water from both the tailings and water surfaces. Initially, there was very little difference in evaporation losses from the water and tailings surfaces, but once the suction threshold had been passed, evaporation from the tailings slowed, while that from the water surface continued at an almost constant rate. This is mainly because the efficiency of evaporation from the tailings surface reduced considerably as the tailings progressively de-saturated.

The right diagram in Figure 9 shows the suction-water content curve (or SWCC) for the tailings. After the suction reached 300 kPa, the tailings were re-wetted in two stages so as to develop the re-wetting branch of the SWCC. Note that the re-wetting branch is both considerably steeper and, within the suction range of 0–300 kPa, almost completely reversible.

Figure 10 shows typical water content profiles at various times after deposition for two test depositions: (a) and (b). Considering (a), a depth of 400 mm represents the surface of the previous layer, where on 22 March there was evidence that the surface had dried to less than 20% water content.

The water content at this depth did not increase much above this value, because the tailings would now have been on the re-wetting branch of the SWCC (Figure 9, right). It will also be seen that it took 13 to 14 days for the water content at the surface to decrease below 30%, and 28 days after deposition had ceased, the surface water content had only decreased by 6% to 24%, roughly 0.21% per day. Comparing with Figure 9, where the water content reduced by roughly 1.4% per day, in the first 14 days, the drying appears to have been very slow. This is because the surface water content was being augmented continually by water, both evaporation and consolidation water rising from below. This could not happen in the small-scale test, but

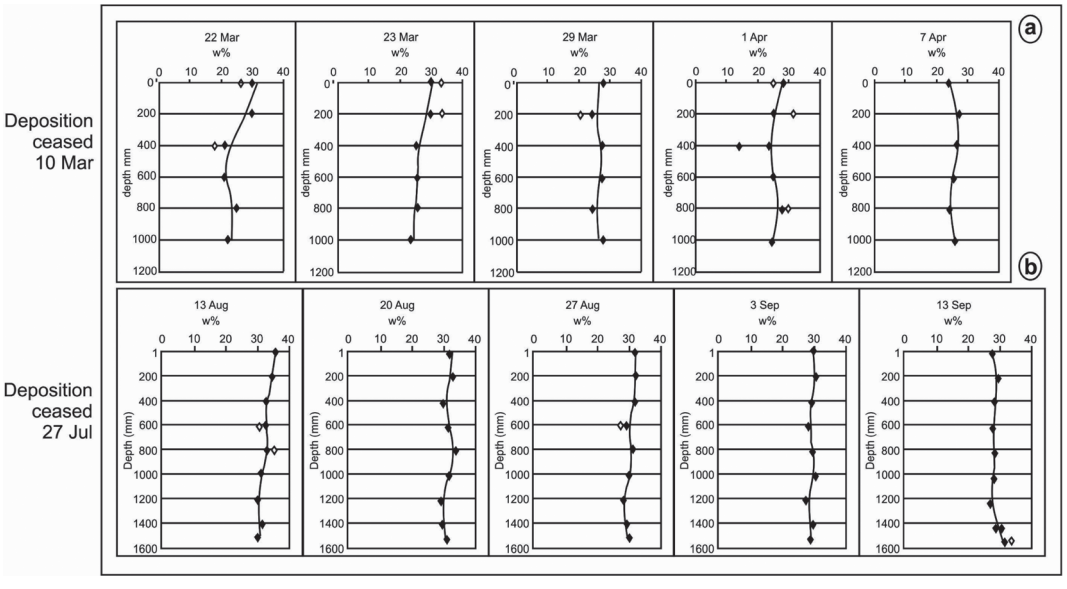

Figure 10. Water content profiles measured at various times in two layers of recently deposited platinum tailings.

the mechanism becomes apparent when the full scale beach is compared with the small-scale test.

Considering Figure 10b, it took 21 days for the surface water content to reduce from 36% to 30%, i.e. 0.29% per day. It is again likely that surface water contents were being augmented continually by water, drawn up by evaporation and rising consolidation water.

4 DISCUSSION AND CONCLUSIONS

Current methods of calculating evaporation from soil surfaces are mostly based on the solar energy balance principle or on a form of Penman's equation in which the major input energy is the net incoming vertical component of solar energy and the major output is the latent heat of vaporization, LE, from which the evaporation is calculated. Current methods either ignore heating of the soil or assume that solar energy converted to soil heat detracts from LE.

Studies over the past decade have highlighted a number of difficulties with currently accepted methods of applying the solar energy balance calculation. These are:

1. The sun's rays strike the Earth's surface at an angle that varies throughout the day. Some of the energy is reflected and some heats the surface. However, the extent of the component that heats the surface is uncertain. Measurements of soil heat G and water heat WH show that the net vertical component is too small, but, because some reflection of energy does occur, the direct or maximum radiation must be too large (Figures 2 and 3).
2. In soils that are unsaturated or desiccated, the energy balance method over-estimates evaporation losses when compared with evaporation established by measured changes of water content (see Figures 4 and 5).
3. In sub-equatorial latitudes, the soil heat G and water heat WH may be as large, or larger than the measured net incoming vertical component of the solar energy, for much of the day. On the basis of equations (1c) and (1d), this suggests that in windless conditions, no evaporation will take place during this time (Figure 3). Measurements show that this is not so.
4. The present approach (equations (1c) and (1d)) leads to the conclusion that no evaporation occurs between sunset and sunrise because the incoming solar radiation is zero during this period. Common experience is that drying and therefore evaporation does occur at night, and this is shown by measurements reported in this paper (Figures 7 and 8).
5. Sections 3.5 and 3.6 illustrate the most difficult aspect of measuring evaporation from a soil surface—it is very difficult, in field measurements, to allow for the effects of water moving upwards under a suction or consolidation-induced flow gradient, or downwards under a gravity gradient.
6. The way ahead is by no means clear, but the difficulties associated with applying equation (1) and its derivatives should be noted, and if used, be used with caution. The substitution of R_n by G multiplied by a conversion efficiency η (eqn. 1d) is a route that warrants further examination.
7. Winter, et al. (1995), Rosenberry, et al. (2004, 2007) and Yao (2009) working in the closely related area of assessing evaporation from wetlands, reservoirs and lakes conclude that although application of the solar energy balance is, in theory, the best way to assess evaporation, it is difficult to apply in practice, mainly, in their case, because of time lags that occur between energy components entering storage and being transformed to evaporation. Similar time lags, such as the conversion of heat into evaporation after sunset, are evident even in the short term tests described in this paper.

REFERENCES

Benli, B., Bruggeman, A., Oweis, T. & Üstün, H. 2010. "Performance of Penman-Monteith FA056 in a Semi-arid Highland Environment." *Journal of Irrigation and Drainage Engineering*, ASCE, 136(11), 757–765.

Blight, G.E. 2005. Consequences of raising the height of a landfill in a water-deficient climate. *Waste Management*, 25, 1021–1036.

Blight, G.E. 2006a. Graded landfill requirements in South Africa: the climatic water balance classification. *Waste Management and Research,* 24(5), 482–490.

Blight, G.E. 2006b. Measuring evaporation from grassed surfaces and trees by energy balance. In: *Unsaturated Soils,* Miller, G.A., et al. (eds). Special Technical Publication No. 147, ASCE, Virginia, USA, 895–904.

Blight, G.E. 2008a. The repeatability of soil water balances at the same site from year to year. In: Unsaturated Soils: *Advances in Geo-Engineering.* Toll, D.G., et al. (eds), Taylor and Francis, London, UK, 889−894.

Blight, G.E. 2008b. Near-surface movement of water in unsaturated soil during evapotranspiration. In: Unsaturated Soils*: Advances* in *Geo-Engineering.* Toll, D.G., et al. (eds), Taylor and Francis, London, U.K. 895–900.

Blight, G.E. 2009a. Solar heating of the soil and evaporation from a soil surface. *Geotechnique*, 59(4), 355–363.

Blight, G.E. 2009b. Desiccation of soil by vegetation and potential interaction with buildings—a field study. *Jour. South African Institution of Civil Engineering,* 51(2), 20–29.

Blight, G.E. 2010. Geotechnical Engineering for Mine Waste Storage Facilities. CRC Press/Balkema, Leiden, Netherlands.

Blight, G.E. & Fourie, A.B. 2005. Experimental landfill caps for semi-arid and arid climates. *Waste Management and Research*, 23, 113–125.

Blight, G., Copeland, A., Jardine, P. & MacRobert, C. 2012. Measurements on freshly-deposited surfaces of two platinum tailings dams. *Paste* 2012, Jewell, R.J., et al. (eds). Australian Centre for Geomechanics, Perth, Australia, 11–24.

Calder, I.R. 1990. Evaporation in the uplands. Wiley, Chichester, UK.

de Bruin, H.A.R. & Keijman, 1979. The Priestley-Taylor evaporation model applied to a large, shallow lake in the Netherlands. *Journal of Applied Meteorology*, 18, 898–903.

Fenn, D.G., Hanley, K.J. & de Geare, T.Y. 1975. Use of the water balance method for predicting leachate generation from solid waste disposal sites. Report EPA/530/SW168. U.S. Environmental Protection Agency, Washington, USA.

Henken-Mellies, W.-U. & Schweizer, A. 2011. Long-term performance of landfill covers—results of lysimeter test fields in Bavaria (Germany). *Waste Management and Research*, 29(1), 59–68.

Monteith, J.L. 1980. The development and extension of Penman's evaporation formula. Applications of Soil Physics, Hillel D. (ed.). Academic Press, New York, USA, 265–275.

Oke, T.R. 1978. Boundary layer climates. Methuen, London, UK.

Penman, H.L. 1956. Estimating evaporation. Transactions, American Geophysical Union, 37, 43–50.

Penman, H.L. 1963. Vegetation and hydrology, Technical Communication No.53. Commonwealth Bureau of Soils, Commonwealth Agricultural Bureaux, Harpenden, UK.

Priestley, C.H.B. & Taylor, R.J. 1972. On the assessment of surface heat flux and evaporation using large-scale parameters. *Monthly Weather Review,* 100(2), 81–92.

Advances in Unsaturated Soils – Caicedo et al. (eds)
© 2013 Taylor & Francis Group, London, ISBN 978-0-415-62095-6

Interpretation of soil-water characteristic curves when volume change occurs as soil suction is changed

D.G. Fredlund
Golder Associates Ltd., Saskatoon, SK, Canada

S.L. Houston
School of Sustainable Engineering and the Built Environment, Arizona State University, Tempe, AZ, USA

ABSTRACT: The soil-water characteristic curve, SWCC, has become a valuable tool for the estimation of unsaturated soil property functions, USPF, in geotechnical engineering practice. At the same time, indiscriminate usage of the estimation techniques for unsaturated soils can lead to erroneous analytical results and poor engineering judgment. Soils that undergo significant volume changes as soil suction is changed constitute one situation where erroneous estimations can occur. In particular, it is the evaluation of the correct air-entry value for the soil that has a significant effect on the estimation of subsequent USPFs. This paper defines the characteristics of a high volume change material and then proceeds to describe how the SWCC laboratory results can be properly interpreted with the assistance of a shrinkage curve. Two laboratory data sets are presented and used to illustrate how the test data should be interpreted in the case of high volume change soils. There have also been developments in the design of SWCC laboratory equipment with the result that both overall volume change and water content change can be monitored when measuring SWCCs. As a result, all volume-mass properties can be calculated. One such apparatus is described along with a description of its benefits and limitations.

1 INTRODUCTION

The soil-water characteristic curve, SWCC, has become an important relationship to determine when applying unsaturated soil mechanics in engineering practice. The technologies related to the SWCC were originally developed in soil physics and agriculture-related disciplines. These technologies have slowly been embraced, with some modifications, in the application of unsaturated soil mechanics (Fredlund, 2002; Fredlund and Rahardjo, 1993).

Soil physics has primarily promoted the use of the SWCC within agriculture for the estimation of the water storage characteristics of soils near the ground surface. Unsaturated soil mechanics has primarily utilized the SWCC for the estimation of unsaturated soil property functions which are subsequently used in numerical modelling solutions of geotechnical engineering problems (Fredlund, 2010). It has long been recognized that there are independent drying and wetting branches for the SWCC, as well as an infinite number of scanning curves between the drying and wetting branches. However, the SWCC has often been treated in both agriculture and geotechnical engineering as though it were a single approximate relationship between the amount of water in a soil and soil suction. Within unsaturated soil mechanics, the drying (or desorption) SWCC branch has received the most attention. Disturbance of the soil samples has historically been of limited concern, or at least neglected, in both agriculture and geotechnical engineering, with disturbed and remolded soil samples often being used for laboratory testing.

Some of the concepts and measurement procedures for determining the relationship between the amount of water in a soil and soil suction (i.e., SWCC) are now receiving increased research interest as unsaturated soil mechanics is increasingly being used in geotechnical engineering applications. It was prudent and appropriate that consideration be given in geotechnical engineering to the wealth of knowledge that has accumulated within soil physics and agriculture. Along with the wealth of accumulated knowledge and experience, however, there are serious differences between the goals to be achieved in agriculture-related disciplines and the goals of geotechnical engineering. Unfortunately, many of these limitations have often been overlooked in the eagerness to make use of the SWCC. Unfortunately, the laboratory test procedures from soil physics and the application

of the SWCC theory in geotechnical engineering have not been fully researched prior to usage in geotechnical engineering. As a consequence, geotechnical engineers are now faced with the need to reconsider various aspects of the application of the SWCC. Some of the areas requiring further research for geotechnical engineering applications are highlighted in this paper.

2 THE PATH FORWARD

There are two approaches that could be taken with regard to further refinement in the application of the SWCC in unsaturated soil mechanics (Figure 1). First, it is possible that modified laboratory test procedures be developed and used for the measurement of the amount of water in the soil versus soil suction relationships in geotechnical engineering. It is also possible that new laboratory test equipment be designed to more realistically simulate field conditions. Second, it is possible that an additional, independent test be performed that would assist with the interpretation of a conventional gravimetric water content SWCC. An independent laboratory test that can be performed is a "shrinkage curve" test. The shrinkage curve test provides a fixed relationship between the gravimetric water content and the instantaneous void ratio of the soil. The authors would suggest that both of the above-mentioned approaches be given consideration. A review of the research literature shows that modified apparatuses for geotechnical applications have already become a trend for measuring the SWCC. Alternate testing procedures have also been proposed in the research literature. In particular, the need for a modification to the determination of an appropriate SWCC has arisen in situations where the soil changes volume as soil suction is changed.

The development of testing apparatuses that measure the SWCC under controlled suction and net normal stress, along with volume change measurements, is appealing for many geotechnical engineering problems (i.e., left branch in Figure 1). The approach that suggests adding a shrinkage test to assist in the interpretation of the SWCC (i.e., right branch in Figure 1), blends in well with the procedures that have already been used in engineering practice as well as agriculture-related disciplines. In other words, the existing laboratory test procedures associated with the SWCC would continue to be used; or available data sets used, however, greater care needs to be taken in the interpretation and application of the results in engineering practice. This approach may be particularly appealing when net normal stress is relatively low in the field application.

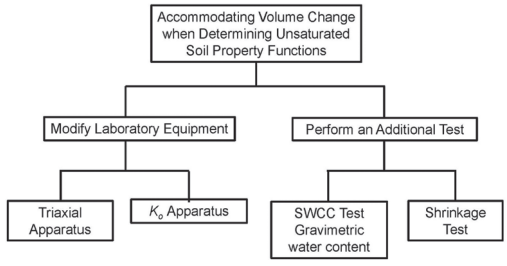

Figure 1. Approaches that can be taken to accommodate volume changes associated with soil suction changes.

This paper presents information on both of the above-suggested options for accommodating volume change that occurs as a result of soil suction changes. The paper also describes the procedures related to the determination of appropriate SWCCs for geotechnical engineering practice. The scope of the paper embraces consideration of sand, silt and clay textured soils and the differences involved in the interpretation of the laboratory results. Differences in interpretation primarily depend upon the amount of volume change experienced during the application of soil suction at a given net normal stress. Another objective is to illustrate the importance of the shrinkage curve in interpreting the SWCC laboratory test results. Laboratory test results are presented for highly plastic soils that are initially prepared in a slurry condition. These materials undergo significant volume change as soil suction is increased. Data is obtained using modified K_o equipment to determine the SWCC curve, with volume change, on a compacted expansive soil.

3 EXAMPLES OF VOLUME CHANGE AS SOIL SUCTION IS CHANGED

The conventional application of the SWCC for the estimation of unsaturated soil property functions commences with the assumption that the soil does not significantly change volume as soil suction is increased. This assumption may be reasonable for low compressibility sands, silts and dense coarse-grained soils. However, there are other situations where the geotechnical engineer must determine unsaturated soil property functions when the soil undergoes considerable volume change with changes in soil suction. Such applications include wetting and drying of expansive clays, wetting of collapsible soils, and drying of slurry materials.

A common situation where extreme volume change occurs in the soil as soil suction is increased, involves the drying of initially wet or slurry materials. Sludge material and slurry material (e.g., Mature Fine Tailings, MFT, from the Oil

Sands operation), are deposited at water contents well above the liquid limit of the material (e.g., w = 100%). The material is deposited in ponds and allowed to dry in order to increase its shear strength. The geotechnical engineer is called upon to undertake numerical modelling simulations of the drying process. Volume changes in excess of 100% are common, and failure to take volume change into consideration yields erroneous results during the drying simulation.

Almost any situation where a soil starts under very wet conditions and is subjected to drying will result in significant volume change. The material may be initially saturated and may remain near saturation, as soil suction increases during the drying process. Estimation procedures that have historically been proposed for the calculation of unsaturated soil property functions assume that a decrease in water content corresponds to a decrease in the degree of saturation of the soil. This may not always be the case and consequently the estimation procedures will give erroneous results when either gravimetric water content or volumetric water content SWCCs are used to calculate unsaturated soil properties such as the permeability functions.

Expansive soils problems are often associated with the soil taking on water as a result of infiltration. This is an adsorption process that involves the wetting SWCC. The effect of hysteresis needs to be taken into consideration as well as the effect of volume changes that occur as the soil dries or goes towards saturation.

Collapsible soils follow a different drying stress path than wetting stress path. The collapsible soil may initially be in a relatively dry state with substantial soil suction. As the soil imbibes water the volume of the soil decreases (or collapses). This has been a difficult stress path to simulate through numerical modelling. Volume change as soil suction is decreased has an effect on the determination of suitable unsaturated soil property functions.

This paper mainly focuses on the estimation of suitable SWCCs for soils that have high initial water content. At the same time it is recognized that there may be other stress paths that might need to be simulated in geotechnical engineering practice. This paper also discusses the benefits that can be accrued through use of modified pressure plate apparatuses for the measurement of the SWCC.

4 DESCRIPTION OF SWCC TEST PROCEDURES COMMONLY USED IN SOIL PHYSICS

Historically, soil specimens have been initially saturated, placed on a pressure plate apparatus under very light confining stress and subjected to increasing matric suction values while equilibrium water contents were measured. The equilibrium water content (for each applied matric suction), was generally established in one to three days depending upon the soil type. Applied air pressures were applied to the soil specimen(s) and the matric suction was established through use of the axis-translation technique. Pressure plate apparatuses were developed that either tested one or multiple soil specimens simultaneously.

Matric suction values were increased on a logarithm scale (i.e., doubling the applied air pressure), until the air-entry value of the ceramic pressure plate was reached. The ceramic pressure plates generally had air-entry values ranging from 100 kPa to 1,500 kPa. The high range of soil suctions (i.e., beyond 1,500 kPa), were generally applied using vapour pressure equalization of small soil samples placed above saturated salt solutions in a vacuum desiccator.

Changes in the amount of water in the soil were either determined through measurement of changes in the overall mass of the soil specimens or the change in the volume of water expelled from the soil under each applied matric suction. In either case, the laboratory results were generally presented as a graph of volumetric water content on the ordinate versus the logarithm of soil suction. The assumption was made that the initial soil specimen was initially saturated. A second assumption was also made in presenting the laboratory results; namely, that the overall volume of the soil specimens did not change as the applied soil suction were increased. This assumption allowed measurements of changes in the mass of water in the soil to be used to back-calculate volumetric water contents for all applied soil suction values.

The above-mentioned testing procedure has served the agriculture-related disciplines quite well where the primary objective was to quantify the water storage in the soil under various applied suction conditions. It should be noted that while the SWCC used in agriculture is usually plotted as a graph of volumetric water content versus soil suction, the plot is only rigorously correct provided there is no volume change as soil suction is increased. All changes in the mass or volume of water removed as soil suction is changed are referenced back to the original volume of the soil specimen. It should be noted that volumetric water content is rigorously defined as the volume of water in the soil referenced to the instantaneous overall volume. Consequently, volumetric water content is correctly defined from gravimetric water content change alone only when no overall volume change occurs.

5 DESCRIPTION OF SWCC TEST PROCEDURES COMMONLY USED IN GEOTECHNICAL ENGINEERING

The purpose for which the SWCC laboratory results are used in geotechnical engineering is quite different from that of the agriculture disciplines and as a result, questions arise as to whether it is necessary to change the SWCC test procedure, the interpretation procedure or both. This paper shows that application of the SWCC in geotechnical engineering is somewhat different from applications in agriculture, primarily because soil volume change in response to wetting and loading for many geotechnical engineering applications can be substantial.

Test procedures that had been used in agriculture for several decades began to be used in geotechnical engineering subsequent to 1960 (Fredlund, 1964). The need to measure the SWCC became apparent when it was realized that changes in the suction of a soil produced an independent effect on soil behavior from changes in total stress. Engineering problems associated with expansive soils provided the initial impetus for understanding swelling soil behavior in terms of changes in soil suction. In most cases, the expansive soils had substantial clay content and underwent considerable volume change during the swelling process associated with wetting. In addition, subsequent applications of matric suction resulted in a decrease in the volume of the soil specimens. There are other applications of unsaturated soil mechanics in geotechnical engineering that involve soil volume change due to change in soil suction. Examples involve the drying of initially slurry materials and the wetting of collapsible soils. For drying of initially slurried soils there can be extremely large volume changes associated with the application of soil suction.

The primary application of SWCCs in geotechnical engineering has been for the estimation of unsaturated soil properties such as permeability function (i.e., hydraulic conductivity versus soil suction) (e.g., Fredlund et al., 1994; van Genutchen, 1980), and the shear strength function, (i.e., shear strength versus soil suction) (e.g., Vanapalli et al., 1996; Fredlund et al., 1996). The estimation of realistic hydraulic conductivity functions depends on the separation of volume changes that might occur while the soil remains saturated from volume changes that occur as the soil desaturates.

Conventional testing procedures adopted within soil physics have not made a clear distinction between these two volume change mechanisms. Direct acceptance and adoption of soil physics SWCC testing procedures can result in serious deficiencies when testing materials that undergo volume change as soil suction is increased. Stated another way, it is not sufficient to measure changes in the mass or volume of water removed from the soil between various applied soil suctions. Rather, it is necessary to quantify the amount of volume change that occurs and to separate the volume changes that occur while the soil remains saturated from the volume changes (and water content changes) that occur as the soil desaturates. The estimation procedures for unsaturated soil property functions is different when the soil is undergoing volume change from the situation where there is no volume change as soil suction is changed.

The differences in physical processes associated with the two types of volume change give rise to the need to be able to measure both changes in the volume of water mass as well as actual (or instantaneous) volume changes of the soil specimen. Two approaches to addressing this need for volume change measurements are considered in this paper. The first approach considers modifying the laboratory SWCC apparatuses such that the volume of the soil specimens is measured during the test. Devices that have been developed to meet this need are discussed later in this paper. The second approach suggests using an independent test to measure the relationship between gravimetric water content and void ratio. The required laboratory test is referred to as a shrinkage test and details related to this procedure are subsequently outlined in this paper.

6 USE OF SIGMOIDAL EQUATIONS FOR SWCCS

There are several sigmoidal type equations that have been proposed to mathematically describe the water content versus soil suction relationship (e.g., van Genuchten, 1980; Fredlund and Xing, 1994). The sigmoidal equations are S-shaped and have the appearance of being able to fit SWCC data regardless of the measure that is used to represent the amount of water in the soil (e.g., gravimetric water content, volumetric water content, or degree of saturation). The sigmoidal equations have a limitation in the extremely low suction range and the extremely high suction range as shown in Figure 2. In spite of the shortcomings of the sigmoidal equations their usage has become prevalent in unsaturated soil mechanics.

The Fredlund and Xing (1994) SWCC equation will be used to illustrate the character and usage of a sigmoidal equation for various designations of water content. The Fredlund and Xing (1994) equation makes use of a correction factor that allows all SWCCs to go to zero water content as soil suction goes to 1,000,000 kPa. Laboratory measured SWCC data can be plotted as a relationship between gravimetric water content and soil suction. The Fredlund and Xing (1994) equation (Equation 1) can then be used to best-fit the SWCC.

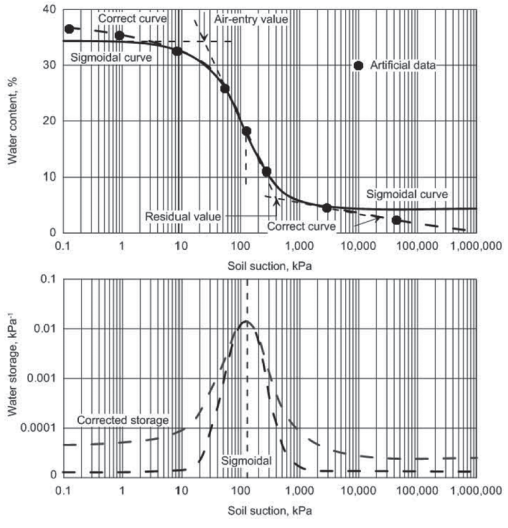

Figure 2. Limitations in the fitting of a sigmoidal equation to SWCC data.

$$w(\psi) = w_s \left[1 - \frac{\ln\left(1 + \frac{\psi}{h_r}\right)}{\ln\left(1 + \frac{10^6}{h_r}\right)} \right] \times \left[\frac{1}{\left[\ln\left[\exp(1) + \left(\frac{\psi}{a_f} \right)^{n_f} \right] \right]^{m_f}} \right] \quad (1)$$

where: $w(\psi)$ = gravimetric water content at any specified suction, ψ; w_s = saturated gravimetric water content; h_r = residual soil suction; a_f, n_f, and m_f = the fitting parameters for the Fredlund and Xing (1994) SWCC equation. Equation 1 is written for the gravimetric water content designation; however, the equation could also be best-fit to any of the designations of water content (e.g., volumetric water content or degree of saturation) versus soil suction. The gravimetric water content SWCC will be used in conjunction with the shrinkage curve to interpret the parameters required for the estimation of unsaturated soil property functions.

It is possible to compute and best-fit the degree of saturation versus soil suction as well as any other designation for the amount of water in the soil by combining Equation 1 with the volume-mass relations for an unsaturated soil. The shrinkage curve for a soil provides information on changes in overall volume as soil suction is changed.

The volumetric water content versus soil suction SWCC must be differentiated with respect to soil suction to obtain the water storage coefficient for the soil. The volumetric water content must be related to the instantaneous overall volume of the soil mass in order to obtain the correct value for numerical modelling purposes. Volume change of the overall soil specimen can be taken into consideration if the relationship between gravimetric water content, w, and void ratio, e, is known. This relationship can be referred to as the "shrinkage curve" when the net normal stress is zero.

7 NEED FOR A SHRINKAGE CURVE

A graphical representation of void ratio versus gravimetric water content can be used to illustrate a variety of volume-mass pathways that might be followed for a particular geotechnical engineering problem involving unsaturated soils. Figure 3 shows typical volume-mass paths for: (a) an initially slurried, high plasticity soil that is dried from a high water content; (b) a swelling soil that is allowed to wet from an initially dry condition; (c) a silt or sand soil that does not undergo volume change as the soil is either dried or wetted; and (d) a collapsible soil that is wetted from a relatively dry initial state. The scope of this paper is limited to consideration of the drying of soils that are initially in a slurry state. Other volume-mass paths should be the focus of further research since the overall volume change of a soil as suction is changed, influences the estimation of unsaturated soil property functions.

The shrinkage limit of a soil has been one of the classification properties in soil mechanics (ASTM D427). Mercury immersion was originally used for the measurement of the volume of a soil specimen. The technique is no longer considered acceptable in most countries. The shrinkage limit is defined as the water content corresponding to a saturated specimen at the void ratio achieved (minimum volume) upon drying to zero water content. It is the entire shrinkage curve, the plot of total volume (or void ratio) versus gravimetric water content, from an initially saturated soil condition to completely oven-dry conditions that is significant for the interpretation of SWCC data.

As saturated clay soil dries, a point is reached where the soil starts to desaturate. This point is called the air-entry value and is generally near the plastic limit of the soil. Upon further drying, another point is reached where the soil dries without significant further change in overall volume. The corresponding gravimetric water content appears to be close to that corresponding to the residual soil suction.

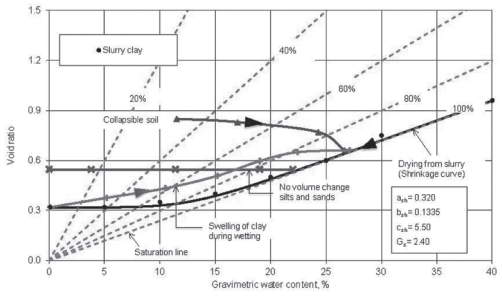

Figure 3. Volume-mass pathways for a variety of possible geotechnical engineering situations.

Figure 4. Digital micrometer used for the measurement of the diameter and thickness of shrinkage specimens.

The shrinkage curve can be experimentally measured from initial high water content conditions to completely dry conditions. A digital micrometer can be used for the measurement of the volume at various stages of drying as shown in Figure 4. Brass rings can be machined to contain the soil specimens (i.e., the rings have no bottom). The rings with the soil can be placed onto wax paper and can be dried through evaporation to the atmosphere. The dimensions of the soil specimens are appropriately selected such that cracking of the soil is unlikely to occur during the drying process. The initial dimensions selected for the shrinkage curve specimens used in this study were a diameter of 3.7 cm and a thickness of 1.2 cm.

The mass and volume of each soil specimen can be measured once or twice per day. Four to six measurements of the diameter and thickness of the specimen were made at differing locations on the specimens. It has been observed that as the specimen diameter began to decrease, with the specimen pulling away from the brass ring, the rate of evaporation increased significantly (i.e., about twice as fast).

The increase in the evaporation rate is related to the increased surface area from which evaporation occurs. Consequently, it is recommended that the measurements of mass and volume be increased to once every two to three hours once the material shows signs of pulling away from the sides of the ring.

The "shrinkage curve" can be best-fit using the hyperbolic curve proposed by Fredlund et al., (1996, 2002). The equation has parameters with physical meaning and is of the following form:

$$e(w) = a_{sh}\left[\frac{w^{c_{sh}}}{b_{sh}^{c_{sh}}} + 1\right]^{\left(\frac{1}{c_{sh}}\right)} \qquad (2)$$

where: a_{sh} = the minimum void ratio (e_{min}), b_{sh} = slope of the line of tangency, (e.g., = e / w when drying from saturated conditions), c_{sh} = curvature of the shrinkage curve, and w = gravimetric water content. The ratio, $\frac{a_{sh}}{b_{sh}} = \frac{G_s}{S_r}$ is a constant for a specific soil; G_s is the specific gravity and S is the degree of saturation.

Once the minimum void ratio of the soil is known, it is possible to estimate the remaining parameters required for the designation of the shrinkage curve. The minimum void ratio the soil can attain is defined by the variable, a_{sh}. The b_{sh} parameter provides the remaining shape of the shrinkage curve. The curvature of the shrinkage curve around the point of desaturation is controlled by the c_{sh} parameter.

8 DIFFERENT DESIGNATIONS FOR THE AMOUNT OF WATER IN THE SOIL

There are three primary ways to designate the amount of water in the soil; namely, gravimetric water content, volumetric water content and degree of saturation. Each designation has a role to play in understanding the physical behaviour of unsaturated soils.

8.1 *Gravimetric water content*

The measurement of water content in the laboratory is generally first measured in terms of gravimetric water content, w, because the mass of water is the easiest variable to measure. Other designations are then computed based on the volume-mass relations. The gravimetric water content SWCC was presented in Equation 1.

8.2 *Volumetric water content (instantaneous volume)*

Volumetric water content can be written as a function of the instantaneous overall volume of the soil

specimen, $(1 + e)$, and gravimetric water content, w. Since gravimetric water content can be expressed as a function of soil suction, it is likewise possible to write volumetric water content as a function of soil suction.

$$\theta(w) = \frac{w(\psi)G_s}{1 + e(w)} \tag{3}$$

The equation for the void ratio can be substituted into Equation 3 to yield the volumetric water content equation in terms of gravimetric water content along with several soil parameters.

$$\theta(w) = \frac{w(\psi)G_s}{1 + a_{sh}\left[\frac{w(\psi)}{b_{sh}{}^{c_{sh}}} + 1\right]^{1/c_{sh}}} \tag{4}$$

8.3 *Degree of saturation*

The degree of saturation of the soil can be written as a function of gravimetric water content (as a function of suction) and void ratio (as a function of gravimetric water content).

$$S(w) = \frac{w(\psi)G_s}{e(w)} \tag{5}$$

The degree of saturation can be further written as a function of gravimetric water content and the equation for the shrinkage curve, both which are functions of soil suction.

$$S(\psi) = \frac{w(\psi)G_s}{a_{sh}\left[\frac{w(\psi)}{b_{sh}{}^{c_{sh}}} + 1\right]^{1/c_{sh}}} \tag{6}$$

The degree of saturation SWCC can also be written as a function of soil suction and the fitting parameters for the gravimetric water content SWCC and the shrinkage curve.

$$S(\psi) = \frac{w_s G_s C_r(\psi_r)}{\left[\ln\left[\exp(1) + (\psi/a_f)^{n_f}\right]^{m_f} \times a_{sh}\left[\frac{w_s G_s C_r(\psi_r) b_{sh}{}^{c_{sh}}}{\ln\left[\exp(1) + (\psi/a_f)^{n_f}\right]^{m_f}}\right] + 1\right]^{1/c_{sh}}} \tag{7}$$

8.4 *Volumetric water content (initial volume)*

It is possible to write the volumetric water content referenced to the initial volume of the soil; however, it should be noted that this designation has little or no value in unsaturated soil mechanics. Only under conditions of no volume change during suction change does the equation become equal to the instantaneous volumetric water content SWCC.

$$\theta(w) = \frac{w(\psi)G_s}{1 + e_o} \tag{8}$$

8.5 *Void ratio*

The void ratio versus soil suction is of value in some situations. One such situation occurs when attempting to describe volume changes while the soil remains saturated under an applied suction. The void ratio can be written as a function of gravimetric water content which is a function of soil suction (i.e., shrinkage curve designated by Equation 2).

8.6 *Experimental and parametric study program on the effect of volume changes on the interpretation of the SWCC*

The effect of volume change on the interpretation of SWCCs was studied using the results from two experimental studies. For both soils, the laboratory SWCCs and shrinkage curve measured on initially slurried soils. The two materials were: (1) Oil Sands Tailings referred to as MFT (Mature Fine Tailings), and (2) Regina clay. The laboratory test results are first presented followed by a parametric study that focuses on the significance of overall volume change as soil suction is increased.

A parametric study was also undertaken for each of the two materials. The parametric study involved changing two of the fitting parameters in the gravimetric water content SWCC. For the Oil Sands Tailings, the first break in curvature along the gravimetric water content SWCC, (referred to as *w Break*), was maintained constant. For the Regina clay soil, the air-entry value, AEV, determined from the degree of saturation SWCC was kept constant. In each case, an empirical construction procedure involving the intersection of two straight lines on a semi-log plot was used to determine a single number for the break in curvature (Vanapalli et al., 1999).

8.7 *Oil sands tailings*

The laboratory program on the Oil Sands tailings involved the measurement of the gravimetric water

content SWCC and the shrinkage curve. The Oil Sands Tailings were prepared with sand to fines ratio, SFR, of 0.1. The liquid limit was 55%, plastic limit 22%, and specific gravity, G_s, was 2.40. Approximately 60% of the material classifies as clay size particles.

The analysis of the test results assumed that the initial starting (saturated) gravimetric water content was increased while the remaining curve-fitting parameters were kept constant. In other words, the first break in curvature along the gravimetric water content SWCC, (*w Break*), was kept constant. Changes in the air-entry values from the degree of saturation SWCC, (i.e., AEV or air-entry value) were then determined.

If the soil did not undergo any volume change, then the "*w Break*" and the AEV would be equal, or the ratio of AEV to *w Break* would be equal to 1.0. Consequently, the ratio of AEV to *w Break* can be used as a measure of the effect of volume change on the interpretation of the correct air-entry value for the soil.

8.8 *Regina clay*

The Regina clay had a liquid limit of 75%, a plastic limit of 25% and contained 50% clay size particles. The material was prepared as slurry and then subjected to various consolidation pressures under one-dimensional loading. After the applied load was removed, the soil specimens were subjected to various applied matric suction values. High suction values were applied through equalization in a constant relative humidity environment. The parametric study then assumed that the air-entry value determined from the degree of saturation SWCC remained at a constant value. (This was confirmed by the experimental results). The "*w Break*" on the gravimetric water content SWCCs were then compared to the air-entry value for the soil. The ratio of AEV to *w Break* was used as a measure of the effect of volume change on the interpretation of the correct air-entry value for the soil.

8.9 *Presentation of the laboratory measurements on oil sands tailings*

Shrinkage curves and soil-water characteristic curves were measured on Oil Sands tailings samples prepared with 10% sand added (i.e., SFR = 0.1). The slurry material has a gravimetric water content of about 100%. The shrinkage curve results are presented in Figure 5. The volume of the Oil Sands tailings decreases as water is removed through evaporation. The material begins to desaturate near the plastic limit.

Figure 6 shows the gravimetric water content, *w*, plotted versus soil suction for the Oil Sands

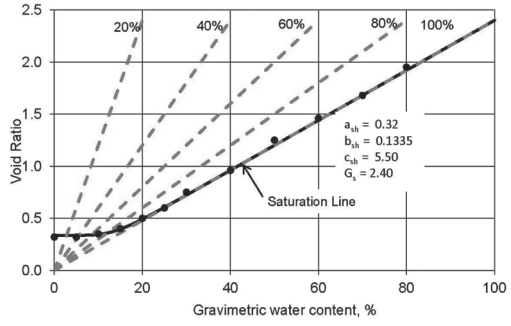

Figure 5. Average laboratory shrinkage curves for the Oil Sands Tailings samples tested (SFR = 0.1).

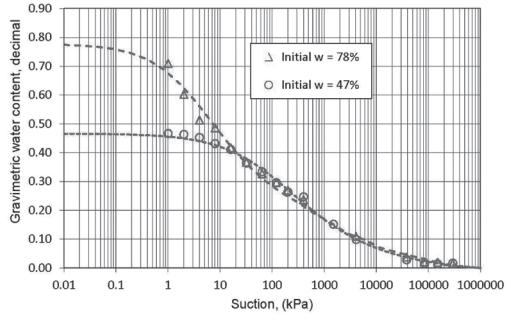

Figure 6. Gravimetric water content SWCC's measured on the Oil Sands tailings (SFR = 0.1).

tailings. One specimen was tested with the initial gravimetric water content near 78% and a second specimen was dried to a water content of 47% and then tested.

The initially high water content specimen showed a break in the curvature in the region around 1 kPa. The lower water content specimen (i.e., 47%) showed a break in curvature around 10 kPa. However, the curvature is not distinct and does not represent the true air-entry value of the material. It is necessary to use the shrinkage curve results in order to properly interpret the SWCC results.

A best-fit shrinkage curve equation can be combined with the equation for the Fredlund and Xing (1994) equation for the SWCC. The resulting plot of degree of saturation, *S*, versus soil suction is shown in Figure 7. The results show that there is a distinct air-entry value for the Oil Sands tailings at about 1,000 kPa. The true air-entry value is the same for the material with initial water contents of 78% and 47%. The results would indicate that it is more correct to use the degree of saturation SWCCs for the estimation of the unsaturated hydraulic conductivity function once the material

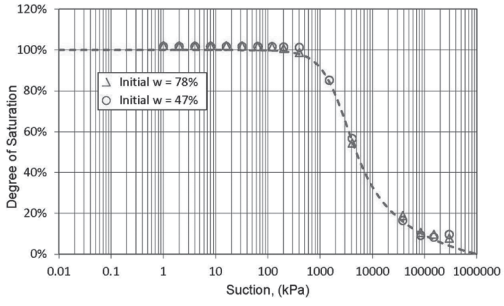

Figure 7. SWCC's plotted as the degree as saturation versus suction for the Oil Sands tailings (SFR = 0.1).

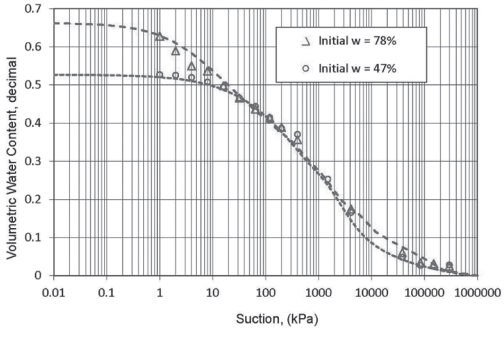

Figure 8. Volumetric water content versus suction for the Oil Sands tailings (SFR = 0.1).

began to desaturate. The degree of saturation plot also indicates that residual condition can be identified at a suction of about 15,000 kPa and a residual degree of saturation of about 20%.

Figure 8 shows the volumetric water content versus soil suction plots for the Oil Sands tailings. These curves appear to be similar in shape to the gravimetric water content plots. The volumetric water content curves are required when quantifying the water storage function for the material.

The basic volume-mass relationship, (i.e., $Se = wG_s$) also makes it possible to plot void ratio, e, versus soil suction as shown in Figure 9. The curves show that there is essentially no volume change at soil suctions higher than the residual suctions.

9 PARAMETRIC STUDY AND INTERPRETATION OF THE OIL SANDS TAILINGS RESULTS

A parametric analysis was performed to quantify the effect of various amounts of volume change on the determination of the correct air-entry value.

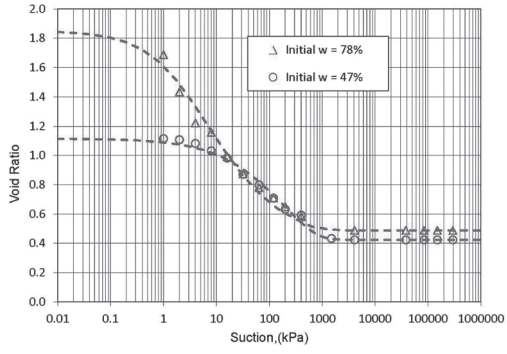

Figure 9. Void ratio versus suction plot for the Oil Sands tailings (SFR = 0.1).

The volume change is assumed to occur as a result of increases in soil suction as the material dries. The degree of saturation SWCC was assumed to remain the same for all soils tested. The initial condition of each soil tested was saturated. The best-fit parameters for the gravimetric water content SWCC were determined for the material tested at 78% initial water content and maintained constant for all other initial saturated water content conditions.

The initial saturated water content of the specimen controlled the amount of volume change that would occur as the soil specimen was subjected to increased suction. The amount of volume change that occurred between the initial low suction value and the residual suction conditions was computed as the change in void ratio, Δe, divided by $(1 + e_o)$ where e_o is the residual void ratio. All void ratio values were determined from the measured shrinkage curve.

Figure 10 shows the difference between the break in curvature on the gravimetric water content SWCC and the true AEV obtained from the degree of saturation SWCC plotted versus percent volume change experienced by the soil. A starting water content equal to the residual water content meant that no volume change occurred and the ratio of the break in the gravimetric water content SWCC was equal to the break in the true AEV observed on the degree of saturation SWCC.

When the starting water content was such that 10% volume change took place during the gravimetric water content SWCC test, the break in the degree of saturation curve was 6 times larger than the break in curvature from the gravimetric water content SWCC. Likewise, when the starting water content was such that 20% volume change took place during the gravimetric water content SWCC test, the break in the degree of saturation curve was 16 times larger than the break in curvature from the gravimetric water content SWCC. Forty percent volume change was also quite feasible and in this case, the break in the degree of saturation

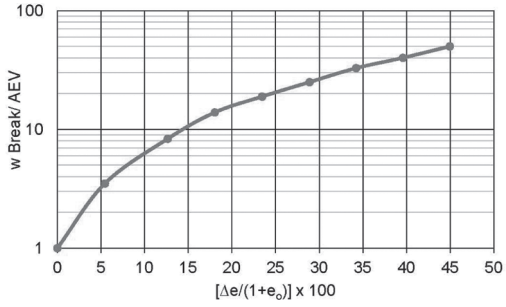

Figure 10. Ratio of the break in the gravimetric water content plot to the true Air-Entry Value for the Oil Sands tailings.

curve was 40 times larger than the break in curvature from the gravimetric water content SWCC. Needless to say, volume changes during suction increases in clayey soils can significantly change the interpretation of SWCC test results.

There are a number of estimation procedures that make use of the SWCC for calculating the permeability function of the soil. Each of these estimation procedures calculate the possible decrease in hydraulic conductivity as the material desaturates. Consequently, it is necessary to separate the changes in hydraulic conductivity that are related to void ratio change (under saturated conditions) from changes in degree of saturation.

10 PRESENTATION OF THE LABORATORY MEASUREMENTS ON REGINA CLAY

Shrinkage curves and soil-water characteristic curves were measured on Regina clay. Slurry Regina clay was prepared at a gravimetric water content slightly above its liquid limit. The shrinkage curve results are presented in Figure 11. The void ratio of Regina clay decreases as water evaporates from the soil surface. The clay begins to desaturate near its plastic limit. The best-fit parameters for the shrinkage curve are $a_{sh} = 0.48$, $b_{sh} = 0.17$, and $c_{sh} = 3.30$. The specific gravity of the soil was 2.73.

Figure 12 shows the gravimetric water content, w, plotted versus soil suction for Regina clay was preloaded at 196 kPa. Its initial water content was 53.5%. The initially high water content specimen showed that a gradual break or change in curvature occurred around 50 kPa. The curvature is not distinct and does not represent the true air-entry value of the material. The gravimetric water content SWCC was best-fit with the Fredlund and Xing (1994) equation and yielded the following

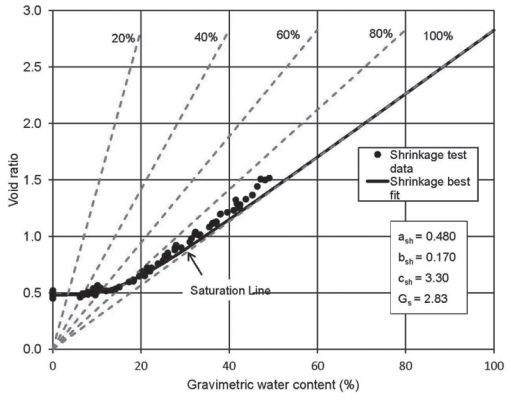

Figure 11. Shrinkage curve for several samples of Regina clay.

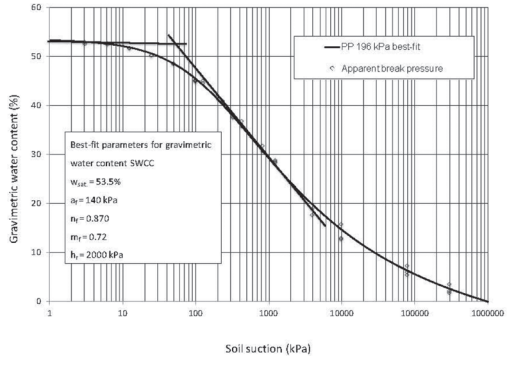

Figure 12. Gravimetric water content versus soil suction for Regina clay preconsolidated to 196 kPa.

parameters; that is, a_f = 140 kPa, n_f = 0.87, and m_f = 0.72. Residual suction was estimated to be around 200,000 kPa. It is necessary to use the shrinkage curve to calculate other volume-mass soil properties and properly interpret the SWCC results for the true AEV.

The best-fit shrinkage curve equation can be combined with the equation for the Fredlund and Xing (1994) equation for the SWCC. The resulting plot of degree of saturation, S, versus soil suction is shown in Figure 13. The results show that there is a distinct air-entry value for Regina clay is about 2,500 kPa. The true air-entry value was also found to be the same for all Regina clay samples preconsolidated at differing pressure values. It is more correct to use the degree of saturation SWCCs for the estimation of the AEV of the soil and subsequently the unsaturated hydraulic conductivity function. The degree of saturation also indicates that residual condition can be more clearly identified as being at a suction of about

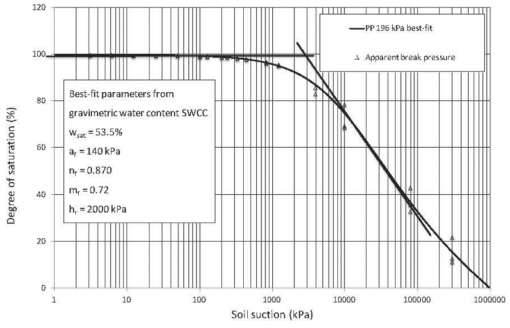

Figure 13. Degree of saturation versus soil suction for Regina clay preconsolidated to 196 kPa.

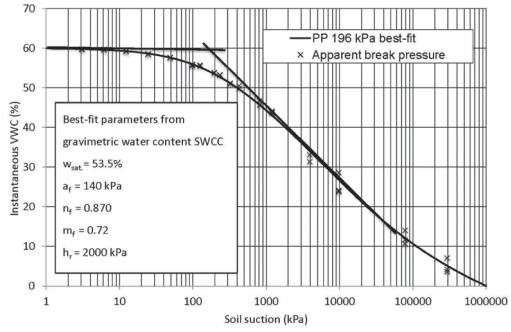

Figure 14. Instantaneous volumetric water content, VWC, versus soil suction for Regina clay preconsolidated to 196 kPa.

200,000 kPa and a residual degree of saturation of about 20 percent.

Figure 14 presents a plot of instantaneous volumetric water content, VWC, versus soil suction for the Regina clay preconsolidated at 196 kPa. The break in curvature is similar to that observed when using the gravimetric water content. While the VWC plot does not reveal the true AEV, it is the volumetric water content plot that must be differentiated with respect to soil suction in order to compute the water storage under any soil suction.

Figure 15 shows still another plot of water content versus soil suction conditions. In this case, gravimetric water content is non-dimensionalized by dividing by the saturated gravimetric water content. The break in curvature occurs around a value of about 46 kPa; a number similar to that observed on the gravimetric water content plot. The water content conditions are plotted in a dimensionless manner but this does not assist with the interpretation of meaningful characteristics on the SWCC.

Figure 16 shows a plot of void ratio versus soil suction conditions. There is a break in the curvature of the graph around 45 kPa; however, it should be noted that the true AEV determined from the degree of saturation graph showed that the value was about 2,500 kPa. This means that the soil did not start to desaturate until the void ratio was about 0.7 (or the water content was about 25% which is near the plastic limit of the soil). The minimum void ratio achieved upon complete shrinkage was 0.48.

Several other SWCC tests were performed on the Regina clay; each test starting with soil that had been preconsolidated from slurry to differing applied pressures. Figure 17 shows the gravimetric water content versus soil suction plot for a soil preconsolidated to 6.125 kPa. The Fredlund and Xing (1994) fitting parameters are a_f = 18.0 kPa,

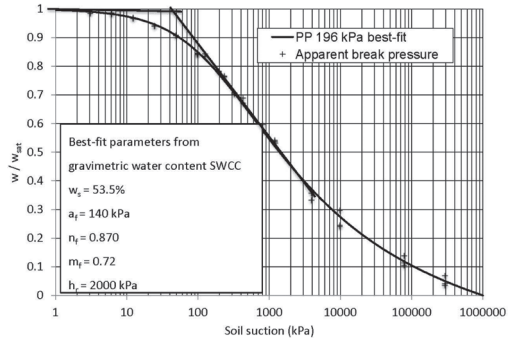

Figure 15. w/w_{sat} versus soil suction for Regina clay preconsolidated to 196 kPa.

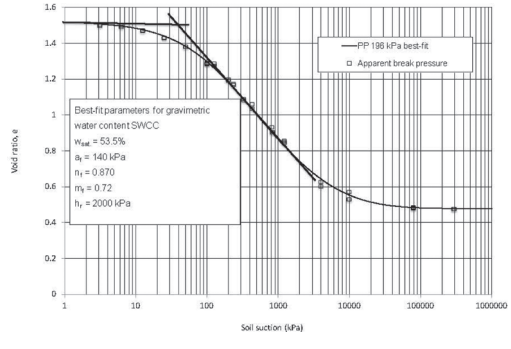

Figure 16. Void ratio versus soil suction for Regina clay preconsolidated to 196 kPa.

n_f = 0.88, m_f = 0.76 and h_r = 800 kPa. The degree of saturation SWCC is the same as shown in Figure 13.

Figure 18 shows the gravimetric water content versus soil suction plot for a soil preconsolidated to 12.25 kPa. The Fredlund and Xing (1994) fitting

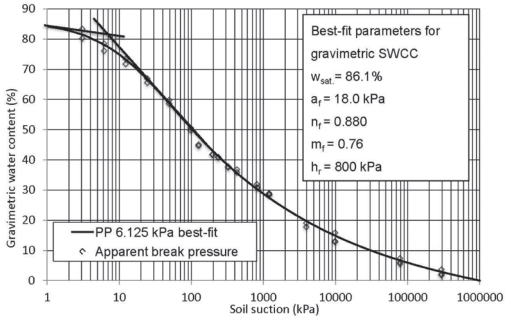

Figure 17. Gravimetric water content versus soil suction for Regina clay preconsolidated to 6.125 kPa.

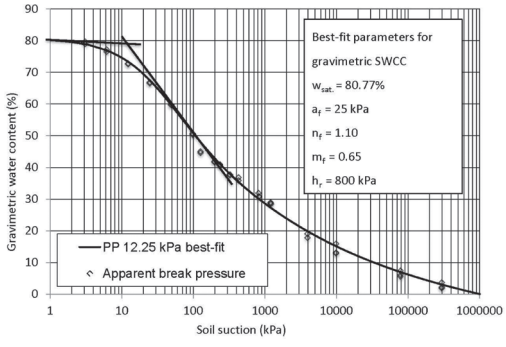

Figure 18. Gravimetric water content versus soil suction for Regina clay preconsolidated to 12.25 kPa.

parameters are $a_f = 25.0$ kPa, $n_f = 1.10$, $m_f = 0.65$ and $h_r = 800$ kPa. The best-fit parameters can readily describe the shape of the entire gravimetric water content SWCC. However, an understanding of the physical behavior of the Regina clay must be carefully gleaned through interpretation of several SWCCs using different water content representations when there is volume change as soil suction is increased.

Figure 19 shows the gravimetric water content versus soil suction plot for a soil preconsolidated to 24.5 kPa. The Fredlund and Xing (1994) fitting parameters are $a_f = 40.0$ kPa, $n_f = 1.30$, $m_f = 0.58$ and $h_r = 1000$ kPa. Figure 20 shows the gravimetric water content versus soil suction plot for a soil preconsolidated to 49.0 kPa. The Fredlund and Xing (1994) fitting parameters are $a_f = 90.0$ kPa, $n_f = 1.10$, $m_f = 0.70$ and $h_r = 2000$ kPa. Figure 21 shows the gravimetric water content versus soil suction plot for Regina clay preconsolidated to the highest pressure of 392 kPa. The Fredlund and Xing (1994) fitting parameters are $a_f = 120.0$ kPa, $n_f = 0.84$, $m_f = 0.70$ and $h_r = 2000$ kPa.

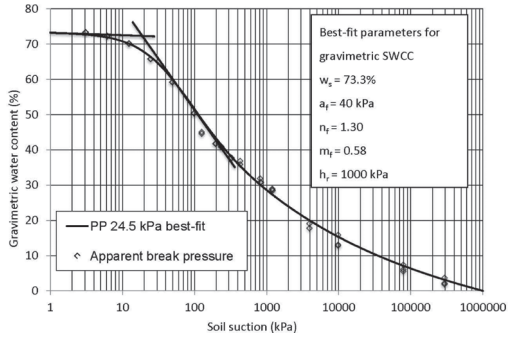

Figure 19. Gravimetric water content versus soil suction for Regina clay preconsolidated to 24.5 kPa.

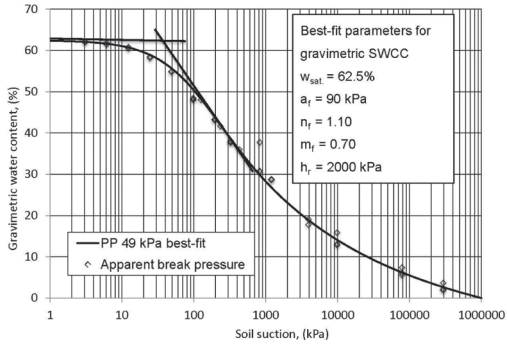

Figure 20. Gravimetric water content versus soil suction for Regina clay preconsolidated to 49 kPa.

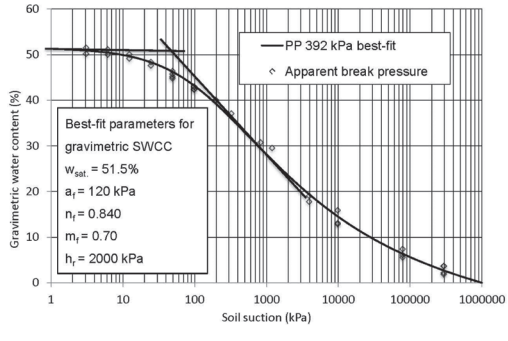

Figure 21. Gravimetric water content versus soil suction for Regina clay preconsolidated to 392 kPa.

The measured SWCCs for Regina clay show that the measurement of the gravimetric water content SWCC and the shrinkage curve for a soil are all that is required to obtain an approximation of the volume-mass versus soil suction relationships when the applied net normal stress is zero. The procedure that should be used for the interpretation of the laboratory data has also been described.

11 INTERPRETATION OF THE RESULTS ON REGINA CLAY

A similar procedure to that used for interpreting the Oil Sands tailings can be used to explain the significance of the measurements on Regina clay (See Figure 22). However, this time the difference between the break in the gravimetric water content SWCC and the true AEV will be expressed in an inverse manner (i.e., AEV/(Break in curvature on w SWCC)). The volume change of the soil is once again expressed as the change in void ratio, Δe, divided by $(1 + e)$ and all void ratio values are determined from the shrinkage curve.

The horizontal axis of Figure 22 shows that the Regina clay soil specimens changed in volume by 65% to 150% as soil suction was increased to residual suction conditions. At 70% volume change, the true AEV is 60 times larger than the break in curvature indicated by the gravimetric water content SWCC. Also at 120% volume change, the true AEV is 129 times larger than the break in curvature indicated by the gravimetric water content SWCC. The laboratory test results clearly indicate the significant influence that volume change as soil suction increases has on the interpretation of the data.

Further research should be undertaken to verify that the unsaturated soil property functions can indeed be estimated by using the interpretations suggested in this paper.

12 EQUIPMENT MODIFICATIONS TO MEASURE OVERALL VOLUME CHANGE

Equipment in common use for measuring this soil-water characteristic (Tempe cell, pressure membrane, pressure plate), often lacks some features that are important to the study of unsaturated soil behavior for geotechnical applications. These features involve a means to apply field-appropriate net normal stress, the determination of volume change as well as water content change (during drying and wetting), and the use of a single specimen for determination of the relationship of soil suction to the volume-mass soil properties. Several research groups have recently developed modified pressure plate-type devices. One such apparatus that allows for testing of the complete SWCC on a single specimen is the modified oedometer (K_o) device (Padilla et al., 2005; Pham et al., 2004). Soil suction is controlled using the axis-translational method, on a pressure plate cell. A K_o SWCC device manufactured by GCTS, Tempe, AZ, is shown in Figures 23 and 24.

Some of the features of the GCTS K_o cell include the simulation of field net normal

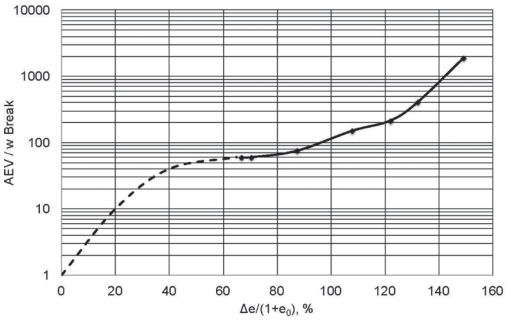

Figure 22. Difference between the break in the gravimetric water content SWCC and the Air-Entry Value for Regina clay.

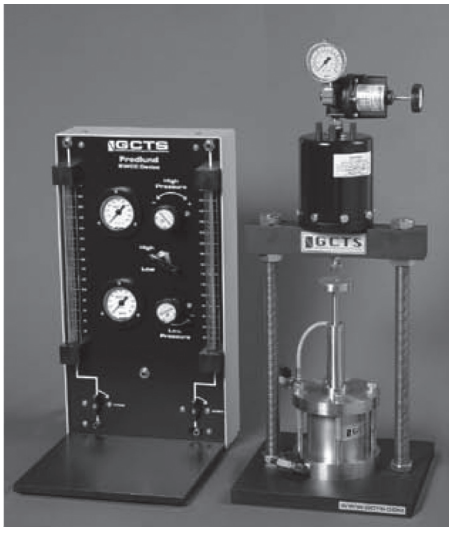

Figure 23. GCTS Pressure plate device.

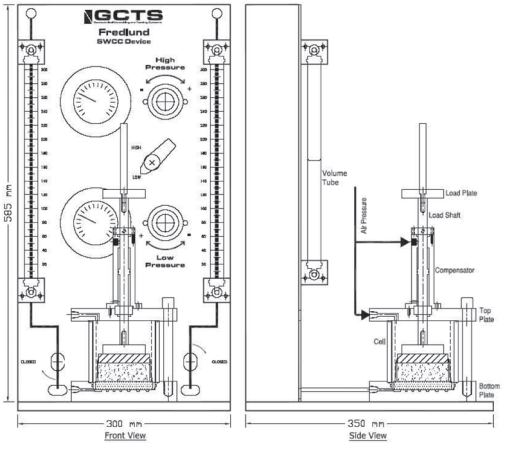

Figure 24. GCTS Pressure plate device.

stress (e.g., overburden plus structural loads), measurement of water released or absorbed from the specimen during the test, capability of tracking the vertical deformation of the soil specimen, and the capability of obtaining several points along the soil-water characteristic curve without dismantling the cell (Perez-Garcia et al., 2008). The ceramic high-air-entry disk, HAED, used in this apparatus is epoxied into a ring that is fitted into a recess on the bottom base plate. The disk has a grooved water compartment to keep the disk saturated and to facilitate the flushing of diffused air. The base has two external ports that connect the water compartment to the drainage system consisting of two graduated volumetric tubes. Each tube has a graduated scale with 1 mm marks. The volume tube measurements can be read to the nearest mm, which translates to accuracy in volume measurements of 0.07 cc. The application of the net normal stress is accomplished with a loading rod inserted from the top of the device and dead weights placed on top of the loading plate. Alternatively, a loading frame can be used to apply loads directly to the loading rod. The application of a vertical load also ensures close contact between the sail specimen and the ceramic disk in addition to more closely simulating field conditions.

A stiff, stainless steel specimen ring is used to constrain the specimen laterally. Compacted or undisturbed specimens with diameters from 50 to 75 mm and 25 mm high can be tested in this device. The platen and the loading rod move up or down with the sample as the sample expands or compresses, and this measurement is tracked with a dial gage or LVDT. A pressure compensator is also provided to null the uplift loads generated when applying pressures inside the cell. The same air pressure applied to the cell is also applied to a piston which has a net area equal to the cross-sectional area of the loading rod.

The axis-translational technique allows the control of negative pore water pressures less than zero-absolute, and consists of elevating the pore-air pressure such that the desired matric suction, $(u_a - u_w)$, is achieved. The saturated HAED used in the axis-translational technique, when saturated, allows the passage of water yet prevents the flow of air up to a value of air pressure corresponding to the air-entry-value of the ceramic disk.

One of the main problems associated with high-air-entry ceramic disk is the diffusion of air that accumulates over time in the water compartment beneath the HAED. For this reason, the device has been designed to allow for flushing air from beneath the HAED. Accumulation of air results in the apparent volume of water coming out of the specimen being larger than actual. If water is going into the sample, diffused air will prevent the water

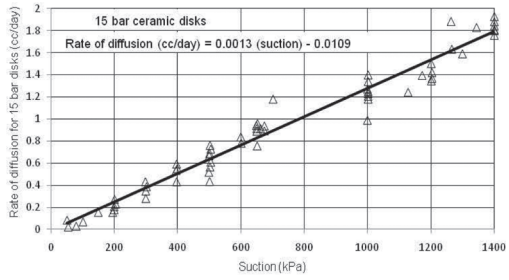

Figure 25. Diffused air through 15 bar high air entry ceramic disks (Padilla et al., 2006).

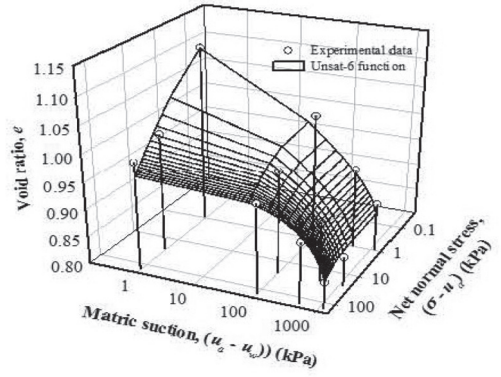

Figure 26. Example of Void Ratio Constitutive Surface for an Expansive Soils Obtained using the GCTS SWCC Device (Singhal, 2010).

from flowing into the specimen if the amount of air is sufficient to retard the water conductivity through the high air entry disk (Padilla et al., 2006). Measured rates of air diffusion as a function of suction for several 15 bar stones are shown in Figure 25. For 15 bar ceramic disks, the diffusion of air at 700 kPa is about 0.9 cc/day and 1.8 cc/day at 1,400 kPa. The amount of diffused air is relatively small when applying low suctions but the rate of air diffusion increases more or less linearly as the air-entry-value of the HAED is approached (Perez, 2006; Perez-Garcia et al., 2008).

An example of the void ratio constitutive surface obtained using the GCTS SWCC device is shown in Figure 26. This surface was obtained along a wetting path, and vertical swell of the specimen was monitored as suction was decreased. The soil classified as a CH, with LL of 82 and PI of 52, and exhibited a medium degree of expansion based on its expansion index (ASTM D 5890–06). Points along the SWCC were obtained for three different net normal stress values, allowing the determination of the constitutive surface. The data

Table 1. Data for Wetting Path for CH soil tested in GCTS SWCC device (Singhal, 2010).

$(u_a - u_w)$ (kPa)	$(\sigma_y - u_a)$ (kPa)	w(%)	S_r(%)	e
1200	1	24.2	76.6	0.890
500	1	26.4	78.6	0.947
100	1	30.3	82.4	1.034
0	1	35.5	88.8	1.126
1200	25	24.8	81.7	0.855
500	25	26.9	83.2	0.910
100	25	30.7	87.6	0.987
0	25	34.5	95.4	1.017
1200	150	25.2	83.5	0.848
500	150	27.1	83.8	0.910
100	150	30.5	89.2	0.963
0	150	32.9	92.7	0.997

points obtained are shown along with the fitted constitutive surface. The fit was obtained using the Unsat-6 function proposed by Vu and Fredlund, 2006. A summary of the data plotted in Figure 26, including degree of saturation data, is provided in Table 1.

It is also possible to obtain the drying SWCC, with volume change determination, using the K_o SWCC device (Singhal, 2010). However, if the confining stress is low, and if the test is begun at a high water content, specimen shrinkage during drying may result in the specimen pulling away from the side walls of the confining ring. There are two effects of specimen shrinkage. One effect is the loss of confinement in the radial direction (K_o conditions no longer apply). Additionally, the SWCC cell must be disassembled and caliper measurements used to obtain radial strains due to shrinkage.

13 BENEFITS AND LIMITATIONS ASSOCIATED WITH ONE-DIMENSIONAL TESTING FOR THE SWCC

An oedometer-type pressure plate apparatus allows for testing of the full SWCC on a single specimen, and does not require cell disassembly at each level of suction considered. Mid-point weighing of the specimen, as required in most pressure plate devices, is not ideal because evaporation of water from the specimen can introduce error. The oedometer-type SWCC cell provides measurements of moisture content change throughout the test without removal of the soil specimen by use of graduated volume tubes, provided evaporation from the graduated tubes in presented or at least accounted for through calibration. It is also helpful for obtaining accurate water content measurements if the SWCC device is kept at relatively stable temperature during testing, as this avoids the development of condensation droplets within the cell that arise from temperature fluctuations. Small differences in water content between direct measurement and volumetric outflow computations at the end of the full SWCC determination, and upon device disassembly, can be adjusted using a correction factor applied to points along the soil-water characteristic curve.

The K_o SWCC device represents an improvement over existing pressure plate devices for geotechnical applications. Net normal stress can be controlled and measurements of volume change can be made during testing to track changes in void ratio and degree of saturation using this device. This is particularly important for geotechnical problems of expansive and collapsible soils.

Void ratio and degree of saturation are not tracked when using conventional pressure plate devices. The general procedure used with the conventional pressure plate device is to have several "duplicate" specimens, and one specimen is removed and weighed to determine water content at each suction value of interest. It is difficult to produce identical specimens unless a compacted soil or a reconstituted soil is being tested. The oedometer apparatus allows the preservation of soil structure in addition to the determination of the SWCC on one specimen. It is likely that sample variability is a greater problem than the potential errors associated with use of "duplicate" specimens and errors associated with mid-point disassembly for obtaining water content measurements.

There are some issues to be addressed and corrections to be made when determining the SWCC relationship using an oedometer-type pressure plate device. The challenges include avoidance of evaporation from water outflow/inflow tubes for long-equilibration time tests, temperature control to minimize or avoid condensation of water inside of the SWCC cell, and determination of volume change during drying if the specimen shrinks from the sidewall of the specimen ring. However, the advantage of the oedometer-type pressure plate device for geotechnical applications are significant. It is important for geotechnical applications to test under appropriate net normal stress and to be able track volume change as soil suction is increased or decreased. It is also important to be able to test specimens for which soil structure is preserved, and this can be done in the K_o pressure plate device. Finally, it is an advantage to be able to develop the full SWCC on one test specimen to avoid variability in the soil specimens.

14 CONCLUSIONS AND RECOMMENDATIONS

Changes in the volume of the soil specimens as soil suction is increased can significantly affect the interpretation of soil-water characteristic curve information. This paper has presented information on the procedures that can be used to properly account for the effects of volume change when interpreting the SWCC for volume change materials. The effects of volume change are shown to be significant, resulting in erroneous calculations of the unsaturated soil property functions.

Laboratory apparatuses have also been described for the measurement of both water volume change as well as overall volume changes. The one-dimensional loading devices may still have the limitation of not being able to measure overall volume change for conditions where the soil specimen separates from the walls of the ring during drying. However, the device can be disassembled after equilibration to each suction to obtain volume change due to shrinkage using micrometer measurements. Studies are needed to determine the effect of net normal stress on radial specimen shrinkage, but it is likely that for many geotechnical applications that sidewall shrinkage may be prevented by the application of net normal (vertical) stress indicative of field conditions.

Following is a summary of the main conclusions from this study.

1. Volume changes associated with an increase in soil suction can significantly affect the determination of the true AEV of the soil.
2. Errors in the determination of the true AEV of an initially slurried clay soil can be several orders of magnitude if volume changes during suction changes are not taken into account.
3. Errors in the determination of the true AEV of a soil can have a significant effect on the estimation of USPFs.
4. The measurement of the shrinkage curve for a soil can be used in conjunction with the gravimetric water content SWCC to determine the true air-entry value for a soil.
5. The true AEV of a soil must be determined from the degree of saturation SWCC.
6. The water storage function can be obtained by differentiating the instantaneous volumetric water content SWCC with respect to soil suction. This is true for suction values less than and greater than the air-entry value of the soil.
7. One-dimensional oedometer apparatuses that can apply controlled soil suctions can provide further insight into the volume-mass behaviour of unsaturated soils.
8. One-dimensional oedometer apparatuses have a limitation in that the soil specimen may pull-away from the confining ring at high soil suctions, particularly when confining stress is low.

The authors would recommend that similar laboratory and parametric type studies be conducted for other volume-mass pathways. Consideration should be given to obtaining the most accurate interpretation of SWCC data for collapsible soils, compacted soils as well as swelling soils.

ACKNOWLEDGEMENTS

The authors desire to acknowledge the equipment development contributions of GCTS, Tempe, AZ, and express our thanks to TOTAL E & P (Canada), for the opportunity to undertake laboratory test results on high volume change Oil Sands tailings.

The authors also wish to acknowledge the assistance of two graduate students in preparing this paper; namely, Elham Bani Hashem, School of Sustainable Engineering and the Built Environment, Arizona State University, Tempe, AZ, supported by the National Science Foundation under Grant No. 1031214. and Fexia Zhang, Department of Civil & Environmental Engineering, University of Alberta, Edmonton, AB, sponsored under NSERC funding. Any opinions, findings, and conclusions or recommendations expressed in this material are those of the authors and do not necessarily reflect the views of the National Science Foundation or NSERC.

REFERENCES

Fredlund, D.G. 1964. Comparison of soil suction and one-dimensional consolidation characteristics of a highly plastic clay. *National Research Council of Canada, Division of Building Research, Technical Report No. 245*, Ottawa, Ontario, Canada.

Fredlund, D.G. 2002. Use of soil-water characteristic curve in the implementation of unsaturated soil mechanics. *UNSAT 2002, Proceedings of the Third International Conference on Unsaturated Soils*, Recife, Brazil, March 10–13, pp. 887–904.

Fredlund, M.D., Wilson, G.W., and Fredlund, D.G. 2002. Representation and estimation of the shrinkage curve. *UNSAT 2002, Proceedings of the Third International Conference on Unsaturated Soils*, Recife, Brazil, March 10–13, pp. 145–149.

Fredlund, D.G. and Rahardjo, H. 1993. *Soil mechanics for unsaturated soils*. John Wiley and Sons New York, N.Y.

Fredlund, D.G. and Xing, A. 1994. Equations for the soil-water characteristic curve. *Canadian Geotechnical Journal*, Vol. 31, No. 3, 521–532.

Fredlund, D.G., Xing, A., and Huang, S.Y. 1994. Predicting the permeability function for unsaturated soils using the soil-water characteristic curve, *Canadian Geotechnical Journal*, Vol. 31, No. 4, pp. 533–546.

Fredlund, D.G., Xing, A., Fredlund, M.D., and Barbour, S. L. 1996. The relationship of the unsaturated soil shear strength to the soil-water characteristic curve, Canadian Geotechnical Journal, Vol. 33, pp. 440–448.

Fredlund, M.D. 2010. User's Manual for SVFlux, Saturated-Unsaturated Numerical Modeling. SoilVision Systems, Saskatoon, Canada.

Padilla, J.M., Perera, Y.Y., Houston, W.N., and Fredlund, D.G. 2005. A new soil-water characteristic curve device. Proceedings of Advanced Experimental Unsaturated Soil Mechanics, An International Symposium, EXPERUS 2005, Trento, Italy, June 27–29, pp. 15–22.

Padilla, J.M., Perera, Y.Y., Houston, W.N., Perez, N., and Fredlund, D.G. 2006. Quantification of air diffusion through high air entry ceramic disks. *Proceedings of the Fourth International Conference on Unsaturated Soils*. Arizona, 1852–1863

Perez, N. 2006. Development of a protocol for the assessment of unsaturated soil properties. *PhD dissertation*. Arizona State University.

Perez-Garcia, N., Houston, S. Houston, W., and Padilla, M., 2008. An odedometer-type pressure plate SWCC apparatus, ASTM Geotechnical Testing Journal, Vol 31, No. 2, pp 115–123.

Pham, H., Fredlund, D.G., and Padilla, J.M. 2004. Use of the GCTS apparatus for the measurement of soil-water characteristic curves. Proceedings of the 57th Canadian Geotechnical Conference, Quebec City, Quebec, Oct. 24–27, pp. 1–6.

Singhal, S. 2010. Expansive Soil Behavior: Property Measurement Techniques and Heave Predction Methods. Ph.D. Disseration, Arizona State University, Tempe, AZ, USA.

Van Genuchten, M.T. 1980. A closed-form equation for predicting the hydraulic conductivity of unsaturated soils. Soil Science Society of America Journal, Vol. 44, pp. 892–898.

Vanapalli, S.K., D.G., and Pufahl, D.E. 1996. The relationship between the soil-water characteristic curve and the unsaturated shear strength of a compacted glacial till, *Geotechnical Testing Journal, ASTM*, Vol. 19, No.2, pp. 259–268.

Vu, H.Q. and Fredlund, D.G. 2006. Challenges to modeling heave in expansive soil, *Canadian Geotechnical Journal*, Vol. 43, pp. 1249–1272.

This page intentionally left blank

Advances in Unsaturated Soils – Caicedo et al. (eds)
© 2013 Taylor & Francis Group, London, ISBN 978-0-415-62095-6

Ventilation effects in an argillaceous rock tunnel examined via unsaturated soil mechanics

A. Gens
Universitat Politècnica de Catalunya (Barcelona Tech), Barcelona, Spain

B. Garitte
CIMNE—Universitat Politècnica de Catalunya (Barcelona Tech), Barcelona, Spain

ABSTRACT: The paper presents the observations, analysis and interpretation of a long-term ventilation test performed in the Mont Terri underground laboratory. An unlined 1.3 m diameter tunnel excavated in Opalinus clay has been subjected to two controlled ventilation periods. Extensive instrumentation has provided observations concerning relative humidity, pore pressures and displacements in the rock. In addition, boreholes have been drilled at several times during the experiment to obtain independent measurements of water content and degree of saturation of the rock. It has been found that an unsaturated zone surrounding the tunnel, though small in extent, largely controls the progress of drying and other effects associated with ventilation. The interpretation of the test has been based on a coupled multi-phase hydromechanical numerical model in which unsaturated soil mechanics concepts such as vapour diffusion, relative permeability and retention curve play a paramount role.

1 INTRODUCTION

All tunnels are subjected to ventilation to a greater and lesser extent, both during construction and during operation. Argillaceous hard soils and soft rocks are potentially sensitive to ventilation effects; ventilation may cause some degree of damage leading to cracking and permeability increases and may also trigger chemical processes such as pyrite oxidation and gypsum precipitation that, in turn, can also have hydromechanical effects.

Those potential effects are quite important in the context of using argillaceous materials as host rocks for geological disposal of radioactive waste. In particular, damage and hydromechanical variations in the zone adjacent to the tunnel is directly relevant to the safety of the repository as it may provide a preferential pathway for the migration of radionuclides. It is therefore necessary to examine those potential effects in detail, preferably under realistic conditions.

In this paper, the observations gathered during a field-scale ventilation test carried out in the Mont Terri underground laboratory are examined and interpreted assisted by the performance of coupled hydromechanical numerical analyses. Because of the nature of a ventilation test (that may lead to desaturation of the host material), the numerical computations must be based on a formulation firmly grounded in the concepts and approaches of unsaturated soil mechanics.

2 DESCRIPTION OF THE TEST

The Ventilation Test (VE) has been performed in a 10 m section of a 1.3 m diameter unlined microtunnel excavated in the Mont Terri underground laboratory (Figure 1).

The Mont Terri laboratory (Thury & Bossart 1999) has been excavated in Opalinus clay, a stiff overconsolidated clay of Lower Aalenian age (Middle Jurassic) found in the Jura mountains of Northern Switzerland. There are three slightly different facies containing different mineral proportions: a shaly facies in the lower part of the deposit, a 15 m thick sandy-silty facies in the centre and a sandy facies interstratified with shaly facies in the upper part. The content of clay minerals may range from 40% to 80%, depending on the facies. The clay was sedimented in marine conditions, it is very strongly bedded and its total thickness is about 160 m. In the location of the Mont Terri laboratory, overburden varies between 250 and 320 m. The laboratory is situated in an asymmetrical anticline formed during the folding of the Jura Mountains. As a result, the rock strata dip with an angle of 25°–45° to the southeast. Information on the properties of Opalinus clay has been reported in Bock (2001), Wileveau (2005), Gens (2012).

The microtunnel was excavated in 1999 in the shaly facies, parallel to the New Gallery, using the raise-boring technique. This direction is perpendicular

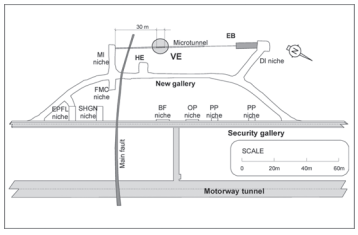

Figure 1. Location of the microtunnel where the VE experiment was performed. Mont Terri underground laboratory.

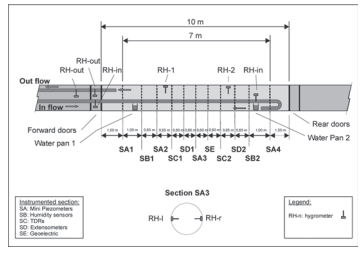

Figure 2. Lay out of the Ventilation test (VE).

to the bedding trace that dips at an angle of 25° towards the SE at this location.

The layout of the VE test is shown in Figure 2. The 10 m section was sealed off by means of two double doors made of exotic wood insensitive to relative humidity (RH) variations (Figure 3). The controlled ventilation during the test was achieved using a system consisting of a blowing device, located outside the test section. It included a compressor, a drier and a bubbler, as well as inflow and outflow pipes equipped with flowmeters, hygrometers and thermometers. Measurement of airflow mass and relative humidity of ingoing and outgoing air allowed establishing the global water mass balance of the test section, as reported below. More details are given in Mayor & Velasco (2008).

Several phases in the history of the test can be distinguished (Figure 4):

- Phase 0 in which the VE tunnel was excavated and left open without controlled ventilation conditions from February 1999 to July 2002. This phase lasted 41 months.
- Phase 1 in which the VE tunnel was subjected to controlled ventilation conditions. During the first stage (from July 8, 2002 to May 28, 2003), the RH in the tunnel was allowed to be close to 100% causing some resaturation of the rock. In the second stage (from May 28, 2003 to January 29, 2004) ventilation with controlled RH was applied. Three RH steps were applied: 80%, 30% and 2%. This Phase lasted about 19 months (11 months for the first stage and 8 months for the second).
- Phase 2 consisted also of two stages. In the first stage (from January 29, 2004 to July 11, 2005), RH was again allowed to be close to 100% causing some resaturation of the host rock. Afterwards, a controlled ventilation stage was performed (from July 11, 2005 to September 24, 2006). In this stage the RH of the incoming air was kept at the low value of 2% to ensure the strongest possible ventilation effects over the time available for the test. In total, this phase lasted 32 months, 12 months for the first stage and 21 months for the final strong ventilation stage.

Figure 3. Ventilation test section.

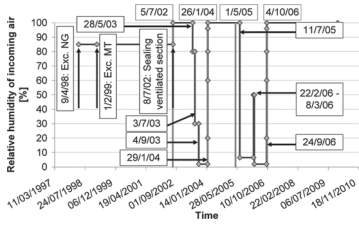

Figure 4. Timeline of the Ventilation test (VE) tunnel section.

The relative humidity values before the start of measurements is an estimation based on the backanalysis of the pore water pressures in the rock when monitoring started. During the test, the nominal relative humidity values of Figure 4 were not exactly achieved; the relative humidity values actually measured inside the tunnel and in a sensor 2 cm inside the rock are shown in Figure 5.

Between May to July 2002, a 2 m radius around the test section was instrumented with hygrometers for the measurement of relative humidity (RH), piezometers and extensometers. Some additional hygrometers and piezometers were installed before the desaturation stage of Phase 2. In addition, several drilling campaigns were also carried out at several stages of the experiment to determine the water content around the microtunnel. The times of the drilling campaigns are indicated by vertical dotted lines in Figure 5.

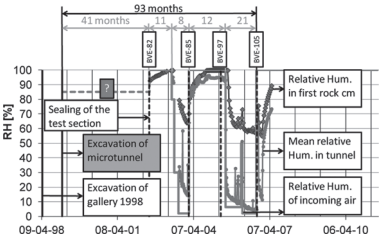

Figure 5. History of the relative humidity in the incoming air, inside the tunnel (mean) and measured in a sensor 2 cm inside the rock. Vertical dotted lines indicate the times of the various drilling campaigns.

3 HYDROMECHANICAL FORMULATION

The hydromechanical (HM) formulation used is a particular case of the general THM formulation developed in Olivella et al. (1994). The key equation in this particular case is the water mass balance (Garitte et al., 2010) expressed as:

$$\frac{\partial}{\partial t}(\theta_l^w S_l \phi + \theta_g^w S_g \phi) + \nabla \cdot (\mathbf{j}_l^w + \mathbf{j}_g^w) = f^w \tag{1}$$

where the first terms reflects the change of water mass with time in a generic representative volume and the second term represents the divergence of water flow. The right hand side term is a sink/source term that is equal to 0 in the present case. θ_l^w and θ_g^w are the volumetric masses of water in the liquid and the gas phase, respectively. $\theta_l^w = \omega_l^w \cdot \rho_l$, where $\omega_l^w = m_w/m_l$ is the mass fraction of water in the liquid. The same nomenclature is used for the gas phase. S_l and S_g are the degrees of saturation of liquid and gas phases, respectively. j_l^w and j_g^w are the fluxes of water (with respect to a fixed reference) in the liquid and gas phases, respectively.

The advective flow of water in the liquid phase j_l^w [kg/m^2/s] is:

$$j_l^w = \theta_l^w \cdot \mathbf{q}_l \tag{2}$$

where q_l [m/s] is the Darcy velocity that is proportional, to the water potential gradient:

$$\mathbf{q}_l = -\frac{\mathbf{k} k_{rl}}{\mu_l}(\nabla P_l - \rho_l \mathbf{g}) \tag{3}$$

where $\boldsymbol{k}$ is the intrinsic permeability [m^2], μ_l is the dynamic viscosity [Pa.s], k_{rl} is a coefficient depending on the degree of saturation (or suction), P_l is the liquid pressure, ρ_l is the liquid density [kg/m^3] and $\mathbf{g}$ is the gravity acceleration [m/s^2].

A critical relationship is the dependence of the permeability on the degree of saturation. It is introduced through the expression:

$$k_{rl} = \sqrt{S_l}(1-(1-S_l^{1/\lambda})^{\lambda})^2 \tag{4}$$

known as Van Genuchten law, where λ is a shape parameter.

The transport of water in the gas phase can be decomposed in:

$$j_g^w = (i_g^w)_{advection} + (i_g^w)_{diffusion} + (i_g^w)_{dispersion} \tag{5}$$

in which the first term represents the flux of water by motion of the gas phase and the second term the flux of water by diffusion of water vapour inside the gas phase (non-advective flow). Dispersion has been neglected.

Vapour diffusion is expressed by Fick's law:

$$(i_g^w)_{diffusion} = -(\phi \rho_g S_g D_g^w \mathbf{I}) \nabla \omega_g^w \tag{6}$$

where D_g^w [m^2/s] is the vapour diffusion coefficient and $\nabla \omega_g^w$ is the gradient of vapour concentration. Although gas motion was found to be negligible, vapour diffusion turned out to have a significant influence on the results.

The relationship between suction ($p_g - p_l$) and the liquid degree of saturation is modelled by the Van Genuchten retention curve:

$$S = \frac{S_l - S_{rl}}{S_{ls} - S_{rl}} = \left(1 + \left(\frac{p_g - p_l}{P}\right)^{\frac{1}{1-\lambda^*}}\right)^{-\lambda^*} \tag{7}$$

where λ^* is a shape parameter, S_{rl} is the residual saturation, S_{ls} is the maximum saturation. P is the air entry value.

Finally, Kelvin's law relates vapour concentration in the gas phase to water potential (suction):

$$\theta_g^w = \omega_g^w \cdot \rho_g = (\theta_g^w)^0 \cdot \exp\left[\frac{\psi \cdot M_w}{R \cdot (273.15 + T) \cdot \rho_l}\right] \tag{8}$$

M_w is the molecular mass of water, R the universal gas constant and ψ is the total potential of the water that in this case coincides with the matric suction (gas pressure is assumed atmospheric and osmotic suction is not considered). The relative humidity (RH) is defined as the ratio of the partial pressure of water vapour in the mixture to the saturated vapour pressure of water at a given temperature. It can be related to θ_g^w through:

$$RH = \frac{p_v}{(p_v)_0} \cdot 100 = \frac{\theta_g^w}{(\theta_g^w)_0} \cdot 100 \tag{9}$$

where p_v is the vapour pressure and subscript $()^0$ stands for the saturated state.

4 MODEL FEATURES AND PARAMETERS

4.1 *Model features*

A plane strain domain representative of the central section of the ventilation test length was adopted for performing the coupled hydromechanical analyses required for the interpretation of the test (Figure 6). Both the ventilation test and the parallel New Gallery are present in the mesh. Initial pore water pressure distribution was taken as hydrostatic, reaching a value of 1.85 MPa at the microtunnel level (Bossart et al., 2004, Croisé et al., 2004). The stress state is isotropic and its initial distribution is geostatic and equal to 4.9 MPa at the microtunnel level, the mean value suggested by Martin and Lanyon (2003). Because the microtunnel is perpendicular to the bedding trace and bedding dip angle is small (25°), it is reasonable to assume anisotropy of permeability in the conceptual model using a higher permeability value in the horizontal plane that corresponds approximately to the bedding plan. Water flow due to osmotic gradients was found to have a negligible effect on results (Garitte & Gens 2007) and it is not considered in this paper. The hydromechanical history prior to the start of the Ventilation test (excavation of the New Gallery, excavation of the microtunnel and the subsequent Phase 0 period) was simulated to provide realistic initial conditions.

The key boundary condition, however, is the hydraulic condition at the tunnel surface boundary. It is known that the average value of RH of the air is different from the RH of the rock close to the interface because of a complex set of phenomena often grouped under the name of skin effect. In the analyses, the concentration of vapour is prescribed at the tunnel wall via the following expression:

$$j_g^w = \beta_g \left(\left(\rho_g \omega_g^w \right)^0 - \left(\rho_g \omega_g^w \right) \right) \tag{10}$$

where j_g^w [kg/s/m^2] is the flux of water in the gas phase, the subscript $()_0$ stands for the prescribed values, ρ_g [kg/m^3] is the gas density, ω_g^w is the mass fraction of water and gas and β_g [m/s] is a coefficient that controls the velocity at which the boundary values tend towards the prescribed values. For low β_g values, equilibrium is not reached instantaneously and water is extracted more slowly. Note that, in accordance with equation (9), applying vapour concentration is equivalent to prescribing relative humidity. In the analyses, the values of β_g have been selected in order to obtain a good agreement with the RH values measured in a sensor in the rock located at 2 cm from the tunnel wall during Phase 1. The values used have been 1E-3 for desaturation phases and 6E-3 in the resaturation phases. The same values have been retained for the analysis of Phase 2. The calculations have been performed using the CODE_BRIGHT simulator (Olivella et al., 1996).

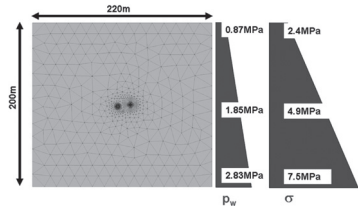

Figure 6. Model domain used in analysis showing initial conditions.

4.2 *Parameters*

The parameters adopted for the analysis are based on some reference works (Bock 2001, Gens et al., 2007) and on some additional information specific to the VE project (Mayor and Velasco 2008). The main ones are listed in Table 1.

Moreover, a laboratory drying experiment was set up before the start of the in situ VE (Floria et al., 2002). Three Opalinus Clay samples were placed on balances in a drying chamber. All sample walls, except the top, were isolated in order to create conditions as close as possible to 1D flow. The measured water losses in the three samples are presented in Figure 7. After 142 days, sample A had lost about 150 gr from the initial 300 gr of water. Simulations were run to calibrate some parameters and to validate the formulation. These simulations showed the importance of i) the value of water permeability and its dependency on degree of saturation and ii) water transport through vapour diffusion. The first step of the calibration consisted in fitting the first days of the experiment to obtain the saturated permeability. The remaining time of the experiment is then used to calibrate the dependency of permeability on degree of saturation (equation 4), a key aspect of the formulation. The influence of the saturation dependency of permeability is illustrated in Figure 7, where λ is the shape parameter of the permeability—saturation relationship. For a value of one, permeability is constant and equal to the saturated value. For lower values of λ, permeability decreases with degree of saturation, the reduction being faster the lower the λ value is. As indicated by Figure 7, a value close to $\lambda = 0.5$ provides a good representation of the drying results. An additional simulation was run in which vapour diffusion was neglected. In this case, an unrealistic increase of the permeability by a factor of three was necessary to keep a good fit of the water loss, demonstrating the importance of water transport in vapour form.

Table 1. Main Opalinus clay parameters.

Parameter	Value
Porosity	0.162
Intrinsic permeability (parallel and perpendicular)	$7 \cdot 10^{-20}$ m^2 $1.4 \cdot 10^{-20}$ m^2
Liquid relative permeability, λ	0.52
Vapour diffusion coefficient	$2.7 \cdot 10^{-5}$ m^2/s
Young modulus	7000 MPa
Poisson coefficient	0.2
Friction angle	19.3°
Cohesion	1.2 MPa
Biot coefficient	0.6
Air entry value*	11 MPa
Surface tension*	$7.2 \cdot 10^{-2}$ N/m
Shape parameter*	0.29

* Retention curve parameters.

As it is often the case in unsaturated soil mechanics, the retention curve was also shown to have a significant influence on the results. Its parameters (Table 1) were determined based on the results of several experimental investigations (Gens 2000, Muñoz et al., 2003, Zhang & Rothfuchs 2005, Villar, 2007). Figure 8 shows the retention curve adopted. Porosity was chosen such that the water content of the saturated material is equal to 7.14% corresponding with the undisturbed water content of saturated Opalinus clay in the vicinity of the microtunnel (averaged from the different drilling campaigns). Permeability was taken anisotropic, with a lower value perpendicular to the bedding plane as suggested by the pattern of pore water pressure observations. Mohr-Coulomb strength parameters were determined using triaxial laboratory tests performed by Schnier (2005).

5 INTERPRETATION OF THE RESULTS

5.1 *Boundary condition and global water balance*

As stated above, there are significant differences between the relative humidity of the incoming air (prescribed) and the relative humidity measured in the tunnel and even larger differences with the relative humidity measured in a sensor placed 2 cm inside the rock. Hence, the value of the parameter β_g of the hydraulic boundary condition was adjusted to account for this difference using the measurements of phase 1. As shown in Figure 9, it has been possible in this way to reproduce satisfactorily the evolution of the relative humidity close to the surface of the tunnel, an essential requirement for a subsequent successful representation of the test results. It should be noted that the results obtained for Phase 2 are purely predictive.

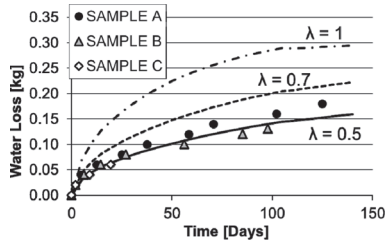

Figure 7. Water extracted in the laboratory drying test (three specimens).

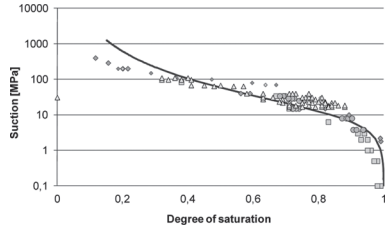

Figure 8. Retention curve used in the analyses.

The ventilation system includes an air blowing device, with monitored air flow, temperature and air relative humidity on entry and exit. This allows the calculation of the water mass balance of the test section. Using the rock parameters and the hydraulic boundary condition determined as described before, an excellent simulation of the amount of water extracted from the test section is achieved (Figure 10). A parametric study of the in situ case also showed the important influence of the permeability value and its dependency on saturation. Vapour diffusion was found to be somewhat less significant than in the laboratory drying experiment but certainly not negligible. The reason probably lies in the fact that, in the tunnel, water from the rock mass is available to partially replace the evaporation water losses causes by ventilation.

5.2 *Evolution of relative humidity in the rock*

In phase 1, the relative humidity in the rock mass was monitored by hygrometers placed between 30 cm and 2.15 m from the tunnel wall. Before the experiment the likely position of the saturation limit was assumed to be in that range, but it turned out to be an overestimation. Indeed, in that range, all hygrometers provided readings above 95% which is outside the confidence limit of these devices. As a result, before phase 2, new hygrometers were installed in the 30 cm adjacent to the tunnel wall allowing a much better characterization of the evolution and distribution of relative humidity of the rock in response to ventilation.

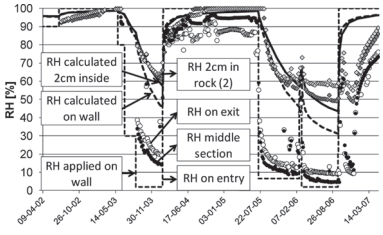

Figure 9. Evolution of the relative humidity in the incoming air, inside the tunnel and in a sensor 1 cm inside the rock. Observed and computed results.

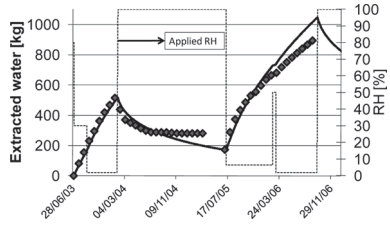

Figure 10. Water extracted from the test section. Observed and computed results.

Figure 11 shows the observed and the computed results of the evolution of relative humidity for the sensors emplaced before the desaturation stage of Phase 2. It can be seen that the measured evolution of relative humidity is closely matched by the numerical model with the exception of the overestimation of the drying in the rock in the sensor placed 7 cm distance from the wall (r = 0.72 m).

5.3 *Distributions of relative humidity, water content and degree of saturation in the rock*

The distributions of the relative humidity with distance to the tunnel wall are shown in Figures 12a for the end of Phase 1 desaturation and in Figure 12b for the end of the stronger Phase 2 desaturation. It can be noted that relative humidity is clearly below 100% only in the 40–50 cm close to the tunnel. It is also apparent that the model closely reproduces the measured distribution. It can be noted that two model results have been plotted corresponding to different line orientations. They are slightly different because of the assumed anisotropy in permeability. Examination of the precise distribution of relative humidity close to the tunnel surface was only possible in Phase 2 where more hygrometers had been added at short distances from the tunnel wall. A close-up of Figure 12b is presented in Figure 13, confirming the good representation of the relative humidity distribution by the numerical model.

In Figure 12, the measured pore pressures in the various piezometers placed in the rock are

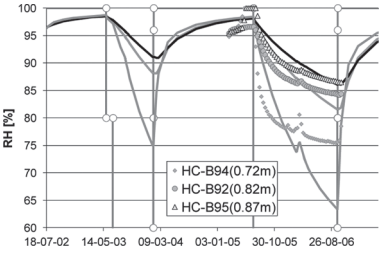

Figure 11. Evolution of relative humidity in the rock at 7 cm (r = 0.72 m), 17 cm (r = 0.82 m) and 22 cm (r = 0.87 m) distance from the tunnel wall.

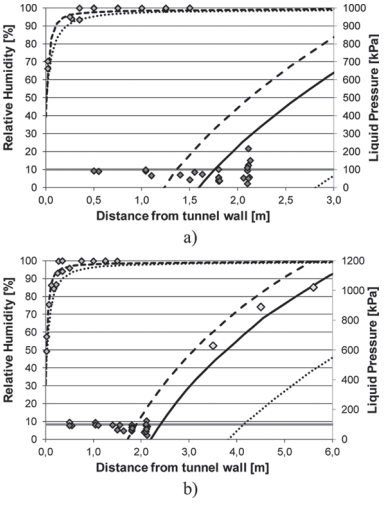

Figure 12. Distribution of relative humidity and pore pressures in the rock. Observations and model results (dashed lines: vertical direction, dotted lines: horizontal direction, full line: 45° direction). a) At the end of Phase 1 desaturation period. b) At the end of Phase 2 desaturation period.

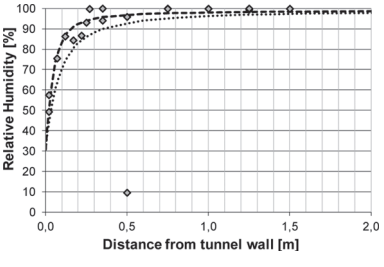

Figure 13. Distribution of relative humidity in the rock close to the tunnel wall. Observations and model results (dashed lines: vertical direction, dotted lines: horizontal direction).

also shown together with the model computations again along different line orientations. It is apparent that for distances below 2–2.5 m the rock

is under suction; this is why all piezometers read atmospheric pressure. However, the piezometers at longer distances from the tunnel, installed after Phase 1, record positive values of pore pressures that are in fact in quite good agreement with model results (Figure 12b).

As mentioned above, boreholes were drilled at different times during the Ventilation Test in order to obtain direct measurements of water content at different distances from the tunnel. Figure 14a shows the water contents obtained at the end of Phase 2 desaturation stage. The average initial water content of the rock (7.14%) is also indicated in the Figure. It should be noted that drilling was accomplished about 10 days after finishing ventilation, but only very slight water content changes have taken place in such a short period that, in any case, has been taken into account in the modelling. It is apparent that this totally independent data confirm the fact that desaturation has only taken place in the 40–50 cm adjacent to the tunnel wall. Figure 14b presents the same data in terms of degree of saturation showing that in the rock adjacent to the tunnel degree of saturation fall down to values of 50%–60%. It is also noteworthy, that the numerical model provides a good representation of the test results in terms of water content and degree of saturation.

Taking into account all those results, it is useful to distinguish two different zones around the tunnel for characterizing the effects of ventilation.

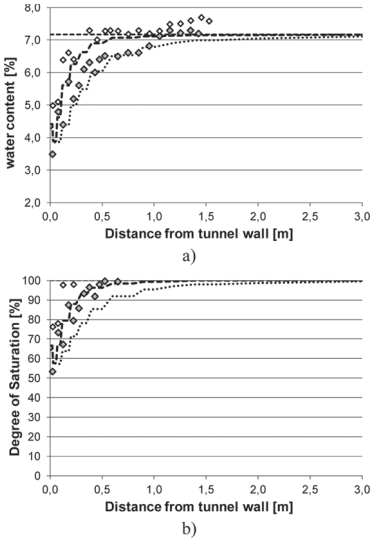

Figure 14. Distribution of water content and degree of saturation in the rock at the end of Phase 2 desaturation. Observations and model results (dashed lines: vertical direction, dotted lines: horizontal direction).

There is a limited zone (maximum thickness about 50 cm) where the material becomes unsaturated and a larger zone (extending to about 2.5–3 m from the tunnel wall) where the material is under suction but still saturated. Naturally, Opalinus clay, being a fine-grained material, can sustain significant suction values without becoming unsaturated. It is interesting to note (Garitte and Gens, 2012) that the suction zone already extended to about 2 m before the start of the ventilation test; so it has been extended only moderately by strong ventilation.

5.4 *Displacements*

Although it is expected that ventilation will generate small displacements only (especially if compared with excavation movements), extensometers were installed in the test section. Figure 15 shows the measured relative displacements between the tunnel wall and an anchor point 2 m inside the rock mass. The relative humidity of the incoming air is also plotted for reference. A clear pattern emerges: each wetting period induces an expansion of the rock mass around the tunnel whereas drying causes compression. The simulation represents quite well this tendency that is basically due to the changes in suction during the drying-wetting cycles. In any case, the magnitude of the displacements induced by the wetting—drying cycles is, as anticipated, small.

6 CONCLUSIONS

The long-term controlled ventilation test performed at the Mont Terri underground laboratory has provided abundant data to examine the potential effects of ventilation in tunnels constructed in argillaceous rock. The field test results have been interpreted using a numerical model capable of simulating the relevant processes and the significant features involved in the test.

Two different zones around the tunnel have been identified: a desaturation zone and a larger zone in which the argillaceous rock is under suction. The desaturation zone reaches only about 50 cm inside the rock in spite of the very low relative humidity applied during ventilation. The suction zone extends to 2.5–3 m away from the tunnel wall but it appears that it has only been moderately enlarged by ventilation.

A coupled hydromechanical numerical model, based on a multi-phase formulation, has been able to reproduce successfully the pattern of observations of the test, both qualitatively and quantitatively. Critical features of the model are a realistic representation of vapour movement and the adoption of a hydraulic boundary condition on the tunnel wall capable of accounting for skin effects.

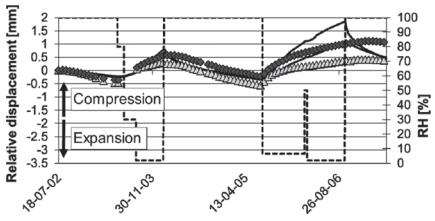

Figure 15. Relative displacement between the tunnel wall and an anchor point 2 m inside the rock mass. Observed and computed results.

It is important to realize that, although the unsaturated zone is small in extent, it largely controls the progress of drying and other effects associated with ventilation. Therefore, features such as the relationship of relative permeability with suction, the retention curve or vapour diffusion play a key role in a proper study of the test. Consequently, unsaturated soil mechanics concepts are essential for a satisfactory interpretation and understanding of the test and, more generally, of ventilation effects in tunnels excavated in argillaceous media.

ACKNOWLEDGEMENTS

This work was supported by the European Commission through NF-PRO project (Contract F16 W-CT-2003-02389). The authors are also grateful for the support of ENRESA and the Mont Terri Project and for the useful discussions with Juan Carlos Mayor and Manuel Velasco. The contribution of the Ministry of Science and Innovation of Spain through grant BIA2011-27217 is gratefully acknowledged too.

REFERENCES

Bock, H. 2001. RA Experiment. Rock Mechanics analyses and synthesis: Data Report on Rock Mechanics. Technical Report 2000–02. Mont Terri Project.

Bossart, P., Meier, P.M., Moeri. A., Trick, T. & Mayor, J.-C. 2004. Structural and hydrogeological characterisation of the excavation-disturbed zone in the Opalinus Clay (Mont Terri Project, Switzerland). *Applied Clay Science* 26: 429–448.

Croisé, J., Schlickenrieder, L., Marschall, P., Boisson, J.-Y., Vogel, P. & Yamamoto, S. 2004. Hydrogeological investigations in a low permeability claystone formation: the Mont-Terri Rock Laboratory. *Physics and Chemistry of the Earth* 29: 3–15.

Floría, E., Sanz, F.J. & García-Siñeriz, J.L. 2002. Drying test: evaporation rate from core samples of "Opalinus clay" under controlled environmental conditions. Deliverable D6, VE project (FIKW-CT2001–00126).

Garitte, B. & Gens, A. 2007. Modelling and Interpretation of the Ventilation Experiment: HM-C mechanisms in Opalinus clay. Final Activity Report. NF-PRO Project, Deliverable D 4.3.23 (F16 W-CT-2003–02389).

Garitte, B. & Gens, A. 2012. The response of an argillaceous rock to ventilation: process identification and analysis of an in situ experiment. In Qian & Zou (eds): *Harmonizing Rock Engineering and the Environment*: 634–639. London: Taylor & Francis Group.

Garitte, B., Gens, A., Liu, Q., Liu, X., Millard, A., Bond, A., McDermott, C., Fujita T. & Nakama, S.. 2010. Modelling benchmark of a laboratory drying test in Opalinus Clay. In Zhao, Labiouse, Dudt & Mathier (eds), *Rock Mechanics in Civil and Environmental Engineering*: 767–770, Taylor & Francis Group.

Gens, A., 2000. *HE Experiment: complementary rock laboratory tests*. Technical Note TN 2000-47. Mont Terri Project.

Gens, A. 2012. On the hydromechanical behaviour of argillaceous hard soils-weak rocks. In A. Anagnostopoulos et al. (Eds.), *Proceedings of the 15th European Conference on Soil Mechanics and Geotechnical Engineering, Athens.* IOS Press.

Gens, A., Vaunat, J., Garitte, B. & Wileveau, Y. 2007. In situ behaviour of a stiff layered clay subject to thermal loading: observations and interpretation. *Géotechnique* 57: 207–228.

Martin, C.D. & Lanyon, G.W. 2003. Measurement of in-situ stress in weak rocks at Mont Terri Rock Laboratory, Switzerland. *International Journal of Rock Mechanics & Mining Science* 40: 1077–1088.

Mayor, J.C. & Velasco, M. 2008. *The Ventilation Experiment Phase II (Synthesis report)*. NF-PRO Project, Deliverable D 4.3.18 (F16 W-CT-2003-02389).

Muñoz, J.J., Lloret, A. & Alonso, E. 2003. Laboratory Report: Characterization of hydraulic properties under saturated and non saturated conditions, Project Deliverable D4, VE project (FIKW-CT2001-00126).

Olivella, S., Carrera, J., Gens, A. & Alonso, E.E. 1994. Non-isothermal Multiphase Flow of Brine and Gas through Saline media. *Transport in porous media* 15: 271–293.

Olivella, S., Gens, A., Carrera, J. & Alonso, E.E. 1996. Numerical formulation for a simulator (CODE-BRIGHT) for the coupled analysis of saline media. *Engineering Computations* 13: 87–112.

Schnier, H. 2005. LT experiment: Strength tests on cylindrical specimens, documentation and evaluation, (Phases 6 and 7). Mont Terri Project: Technical Note, TN 2002–50.

Thury, M. & Bossart, P. 1999. The Mont Terri rock laboratory, a new international research project in a Mesozoic shale formation, in Switzerland. *Engineering Geology* 52 (3–4): 347–359.

Villar, M.V. 2007. Retention curves determined on samples taken before the second drying phase. Technical report M2144/5/07. Madrid: CIEMAT.

Wileveau, Y. 2005. *THM behaviour of host rock (HE-D) experiment: Progress report. Part 1*. Technical Report TR 2005-03. Mont Terri Project.

Zhang, C.L. & Rothfuchs, T. 2005. *Report on instrument layout and pre-testing of large lab VE-tests*. NF-PRO Project, Deliverable 4.3.11 (F16 W-CT-2003-02389).

Advances in Unsaturated Soils – Caicedo et al. (eds)
© 2013 Taylor & Francis Group, London, ISBN 978-0-415-62095-6

Compacted soils: From physics to hydraulic and mechanical behaviour

S. Leroueil
Department of Civil and Water Engineering, Université Laval, Québec, QC, Canada

D.W. Hight
Geotechnical Consulting Group, London, UK

ABSTRACT: Due to the improvements in our knowledge of unsaturated soil mechanics and in the measurement of soil suction, our understanding of compacted soils has improved considerably. The paper describes the physics that underlies the behaviour of compacted soils and its implications in terms of the hydraulic and mechanical behaviour of compacted soils. A resulting conceptual model is presented. Reference is made to practical implications.

1 INTRODUCTION

Compaction of soils is one of the most common activities in geotechnical engineering. However, it is generally recognised that the behaviour of compacted soils is complex and, when it comes time to specifying compaction conditions for earthworks or to predict the behaviour of compacted soils, the geotechnical engineer is often perplexed. In recent years, however, the development of unsaturated soil mechanics and of technologies allowing for testing of unsaturated soils and measurement of suction have significantly improved our understanding of the behaviour of compacted soils. This paper aims to explain the physics that underlies the behaviour of compacted soils and to assess its implications in terms of hydraulic and mechanical behaviour when the soil is as-compacted, submerged and saturated. Aspects related to drying are not considered. Reference is made to some practical implications.

2 PHYSICS OF COMPACTED SOILS

Compaction is the densification of soils by application of mechanical energy to expel air. In the laboratory, compaction can be performed statically, dynamically (by impacts) or by kneading. If a soil is compacted at different water contents with a given type and amount of compaction effort, a compaction curve relating the soil's dry density to its compaction water content can be drawn. As illustrated in Figure 1, the dry density (or dry unit weight) increases to a maximum value and then decreases as the compaction water content increases. The water content at which the maximum dry density is reached is the optimum water content w_{opt}. On the same diagram, lines of equal degree of saturation can also be drawn as they depend only on soil particle density ρ_s. For the examples shown in Figure 1, the optimums correspond to a degree of saturation of about 72%. It can also be noted that the compaction curves never reach the 100% degree of saturation curve, which means that some air remains trapped in the soil.

The bases of the compaction test were established by Proctor (1933) who expressed the relationship between compaction energy, water content and the resulting dry density in the form of the so-called compaction diagram. It is generally recognised that the compaction curve depends on the soil, the mode of

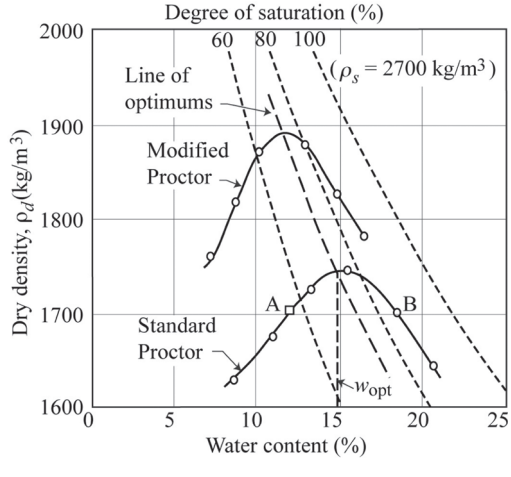

Figure 1. Compaction curves obtained in Standard proctor and Modified Proctor compaction tests performed on the same soil (fictitious data).

compaction and the energy provided. As for the shape of the compaction curve, it has been attributed to the lubricating effect of water that facilitates the arrangement of soil particles as water content increases, and explains the initial increase in dry density towards the maximum. However, as water content increases beyond the optimum, the relative volume of water increases and the dry density decreases. As will be shown later, an important factor influencing the dry density and fabric created by compaction is suction.

The most common compaction test is the Standard Proctor compaction test (ASTM D698-12) corresponding to an energy of 600 kN.m/m^3. The Modified Proctor compaction test (ASTM D1557-12) involves an energy that is 4.5 times larger. As indicated in Figure 1, this results in a higher maximum dry density at a lower optimum water content. However, the degree of saturation at the optimum is not very different and the "line of optimums" is essentially a line of constant degree of saturation $S_{r\text{-}opt}$, of about 72% on the figure. A soil compacted to a degree of saturation larger than that at the optimum is said to be compacted "wet of optimum" whereas a soil compacted to a lower degree of saturation is said to be compacted "dry of optimum". As indicated in Figure 2, the Standard Proctor optimum water content of clayey soils is often close to their plastic limit, but the scatter is important. Fleureau et al. (2002) propose relationships between w_{opt} and the liquid limit of clayey soils, w_L; for the Standard Proctor optimum, the relationship is the following:

$$W_{opt} = 1.99 + 0.46\, w_L - 0.0012 w_L^2 \qquad (1)$$

Figure 3 compares the values of dry density and water content of clayey soils obtained at the optimum with the Standard and Modified Proctor tests.

The fabric of compacted soils has been widely studied, most often by mercury intrusion porosimetry. It has generally been observed that soils compacted on the dry side of optimum have a bimodal pore-size distribution whereas soils compacted on the wet side of optimum have a single family of pores (e.g., Ahmed et al., 1974; Delage et al., 1996; Vanapalli et al., 1999; Watabe et al., 2000). When prepared on the dry side, aggregates of particles are formed and, as indicated, for example, by the test results obtained by Delage et al. (1996) on Jossigny silt (Fig. 4), there are two families of pores: intra-aggregate pores or micropores (entrance pore radii of about 0.3 µm) and inter-aggregate pores or macropores (about 4 µm). On the wet side, the soil fabric appears more homogeneous with a single family of pores: micropores (about 0.5 µm for the Jossigny silt). The optimum thus forms a transition and can appear with one or two families of pores. The soil fabric is directly reflected in the Water Retention

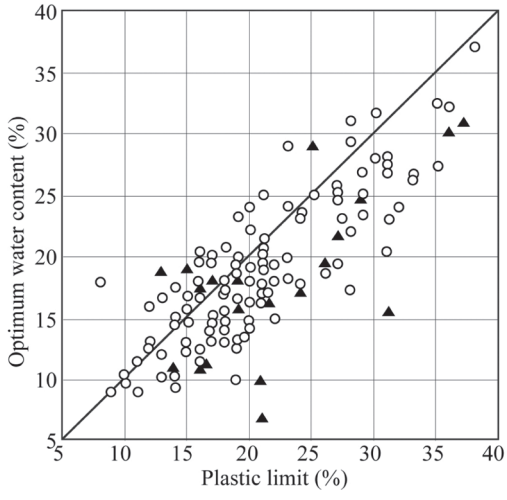

Figure 2. Correlation between Standard Proctor optimum water content and plastic limit. The black triangles correspond to the data used to produce Figure 8 (after Marinho & Olivera, 2012).

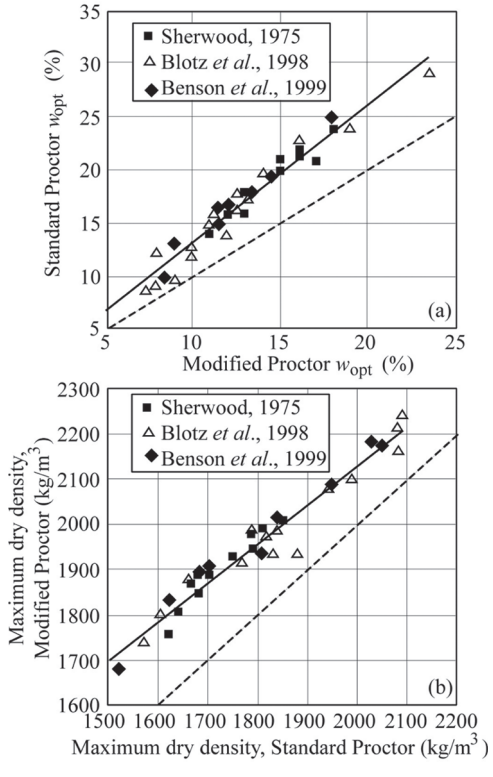

Figure 3. Correlations between the optimum water contents (a) and the maximum dry densities (b) of the Standard and Modified proctor compaction tests on clayey soils (after Chapuis, 2002).

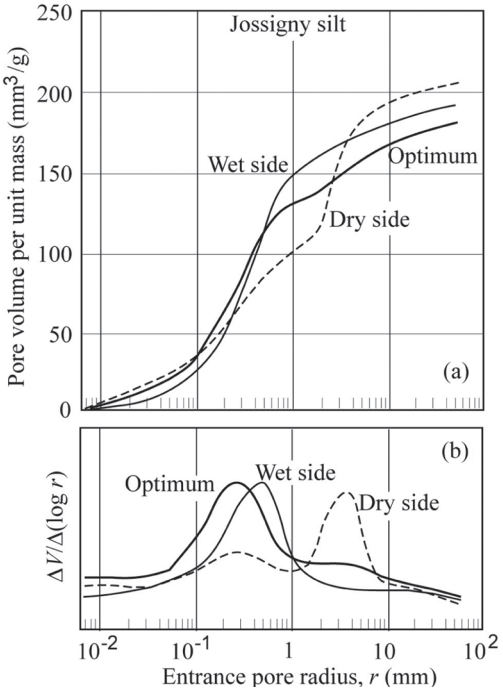

Figure 4. Pore volume distributions (a) and density functions (b) for compacted specimens of Jossigny silt (after Delage et al., 1996).

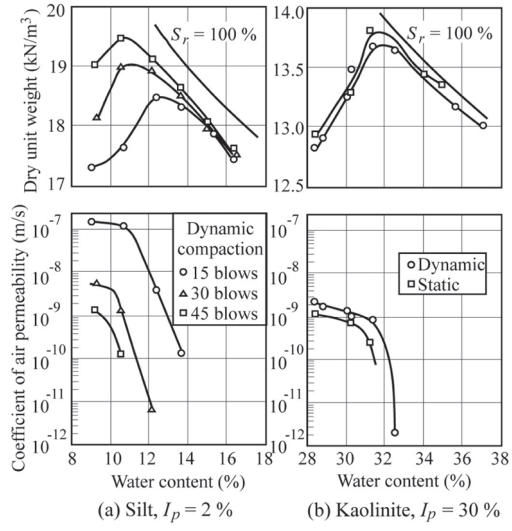

Figure 5. Air permeability of a silt (a) and a plastic clay (b) compacted at different water content (after Langfelder et al., 1968).

Curve (WRC) or Soil Water Characteristic Curve (SWCC). At a given void ratio, the air entry pressure (which directly reflects the size of the largest pores in the soil) is higher for specimens compacted on the wet side than for specimens compacted on the dry side (e.g., Vanapalli et al., 1999; Watabe et al., 2000). This is further discussed and exemplified in Section 4.1 and Figures 18 and 19. These observations also mean that although specimens A and B in Figure 1 are at the same dry density (and thus at the same void ratio), they have different particle arrangements and may exhibit different behaviours given that they are on different sides of the optimum. It should also be noted that the aggregates formed by compaction dry of optimum generally have small pores (and thus a high air-entry value) and remain saturated for most practical applications.

Experience has also shown that the air phase is continuous on the dry side of optimum whereas air is occluded on the wet side of optimum, i.e. the air is in the form of bubbles and so discontinuous. This can be verified by air permeability tests. Langfelder et al. (1968) tested five different soils with plasticity indices between 2 and 30%, and observed an abrupt decrease in air permeability when the water content approached the optimum water content (Fig. 5). Langfelder et al. (1968) showed that these observations are essentially independent of the compaction method. This may confirm the hypothesis suggested by Olson (1963) that the maximum dry density is reached when the air permeability becomes so small that the remaining air cannot be expelled and the dry density cannot increase.

Fleureau et al. (2002), Ridley & Pérez-Romero (1998) and Sawangsuriya et al. (2008) reported suction measurements in compacted soils along compaction curves. Figure 6 presents compaction water content as a function of the logarithm of matric suction for 5 different clayey soils. These relationships are linear and the slopes show a tendency to increase with the liquid limit. Test results obtained for La Verne clay (Fleureau et al., 2002) also show a linear relationship (Fig. 7). For some other soils, Fleureau et al. (2002) observed a change in slope of the relationship at the optimum. In all cases, however, the relationship was continuous at the passage of the optimum. In general, high values of matric suction are consistent with the aggregated fabric observed on the dry side of optimum. On the wet side, the lower values of suction result in weaker deformable aggregates and homogeneous particle arrangements.

The triangular and square symbols in Figure 8 are the measured values of suction at the Standard Proctor optimum water content for a variety of soils. There is a tendency for suction to increase with the optimum water content, and indirectly with plasticity (Fig. 2), but the scatter is large. For

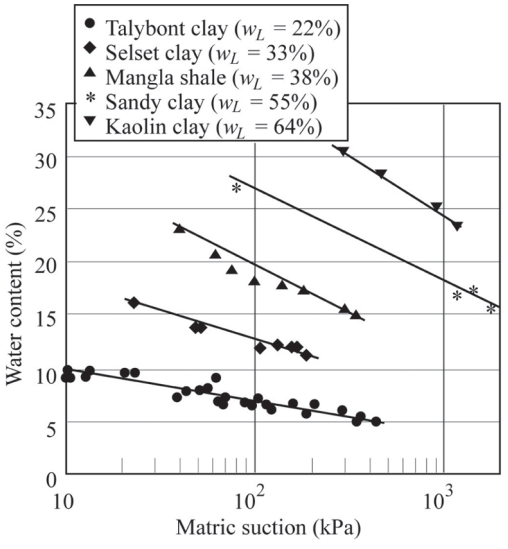

Figure 6. Water content—matric suction relationships for compacted soils (after Ridley & Pérez-Romero, 1998).

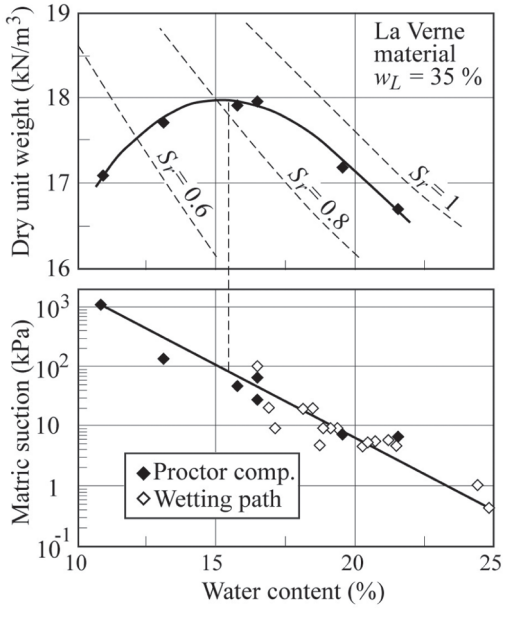

Figure 7. Compaction curve and changes in suction with water content for La Verne material (after Fleureau et al., 2002).

their own data, Fleureau et al. (2002) observed a smaller scatter and proposed the relationships shown by the dashed lines for Standard and Modified Proctor energies.

Results obtained by Gens et al. (1995), (Fig. 9), Marinho & Stuermer (1999) and others show that

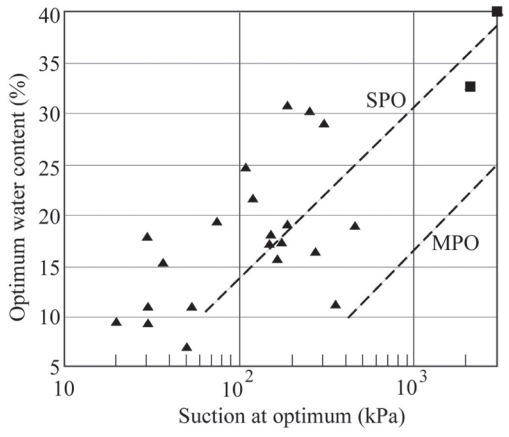

Figure 8. Correlation between optimum water content and suction at optimum water content. Data points for Standard Proctor tests. Dashed lines were proposed by Fleureau et al. (2002) for Standard Proctor Optimum (SPO) and Modified Proctor Optimum (MPO) (after Fleureau et al., 2002 and Marinho & Olivera, 2012).

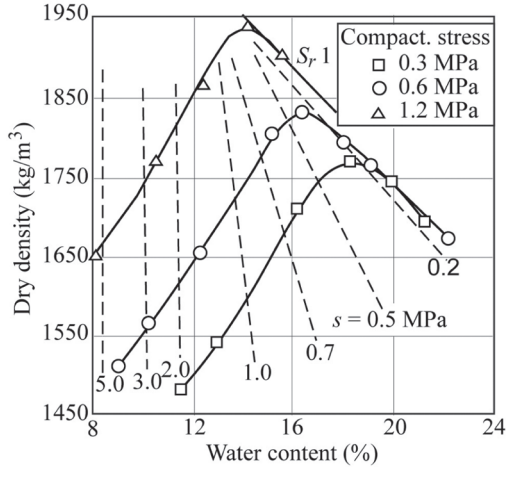

Figure 9. Compaction curves of a low plasticity silt for three values of static compaction stress with contours of equal suction (after Gens et al., 1995).

the post-compaction iso-suction curves are close to vertical in the compaction diagram when the soil is compacted to degrees of saturation significantly lower than that at the optimum and closer to the constant degree of saturation lines when compacted at higher water contents. It should also be noted again that suction is relatively small on the wet side of the optimum whereas it is much larger on the dry side, where it increases with decreasing water content.

Tarantino & De Col (2008) and Caicedo et al. (2013) examined soil behaviour during

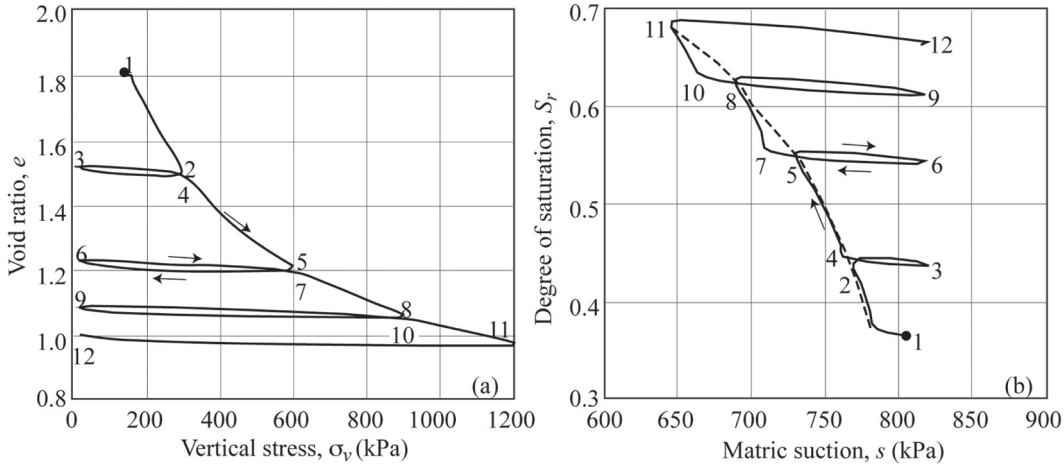

Figure 10. Compaction tests for specimen of Speswhite kaolin at $w = 25.4\%$: (a) void ratio versus vertical stress; (b) degree of saturation versus matric suction (after Tarantino & De Col, 2008).

one-dimensional static compaction. In both studies, Speswhite kaolin was used with w_p equal to 32% and 30%, and w_L equal to 64% and 55% in the respective studies. Tarantino & De Col (2008) prepared 7 samples at water contents varying from 21.5% to 31.1%, on the dry side of optimum, and statically compacted them by applying loading-unloading cycles of 300, 600, 900 and 1200 kPa with unloading to 14 kPa. The unloaded conditions were referred to as "post-compaction" by Tarantino & De Col (2008). The fact that the compaction conditions were on the dry side of optimum was confirmed by the bimodal pore-size distributions, even if at a water content of 31%, the inter-aggregate pores had almost disappeared. As no drainage was provided during the tests, water content remained constant. Figure 10 presents the results obtained at a water content of 25.4%. Figure 10a shows the void ratio against the vertical applied stress. It clearly defines a virgin compression curve (1–2–5–8–11) and essentially reversible unloading-reloading paths (e.g., 5–6–7). It also confirms that compaction is a preloading process of the soil by air expulsion. Figure 10b shows the measured matric suctions, s, against the degree of saturation S_r. The suction decreases as the soil is compressed along the virgin compression curve from 780 kPa to 640 kPa while the degree of saturation increases from 0.37 to 0.69. However, after unloading to 14 kPa (3–6–9–12), the "post-compaction" suction is essentially constant at about 820 kPa. The S_r versus s paths followed for different compaction water contents are presented in Figure 11a. While suction measured along the virgin compression lines decreases as the degree of saturation increases, the "post-compaction" suction (dashed lines) varies only slightly when the applied load increases. This latter aspect is discussed by Vaunat et al. (2000), Tarantino & Tombolato (2005) and Tarantino & De Col (2008). Tarantino & De Col (2008) also present the void ratio as a function of the "average skeleton stress σ_v'' ($\sigma_v'' = \sigma_v + sS_r$)" (Fig. 11b). It can be seen that at a given void ratio the smaller the water content (thus the higher the suction, Fig. 11a), the larger is the "average skeleton stress σ_v''".

It is worth noting that the order of the compression curves is the same when the total vertical stress σ_v (or $\sigma_v - u_a$) is used in place of σ_v''. Caicedo et al. (2013) observe similar behaviour. This is consistent with the results presented by Barbosa & Leroueil (1998) showing that the larger the suction, the larger the total vertical stress at a given void ratio on the virgin compression curves.

Caicedo et al. (2013) performed static compaction tests on Speswhite kaolin in a special oedometer cell equipped for measuring axial and radial stresses, water content and suction. The specimens were subjected to loading-unloading cycles under controlled rate of strain up to total axial stress of 1500 kPa. Unloading was performed to a minimum axial stress of 20 kPa. After the last unloading, the specimens were subjected to wetting. On one additional compaction test performed at a water content of 10%, wetting was performed before unloading, under an axial load stress of 1500 kPa. Several remarks can be made:

– Figures 12a and b show the compression curves for the samples compacted at a water content of 10%. The suction measured at the end of compaction was about 1000 kPa. The changes in void ratio associated with wetting under a vertical

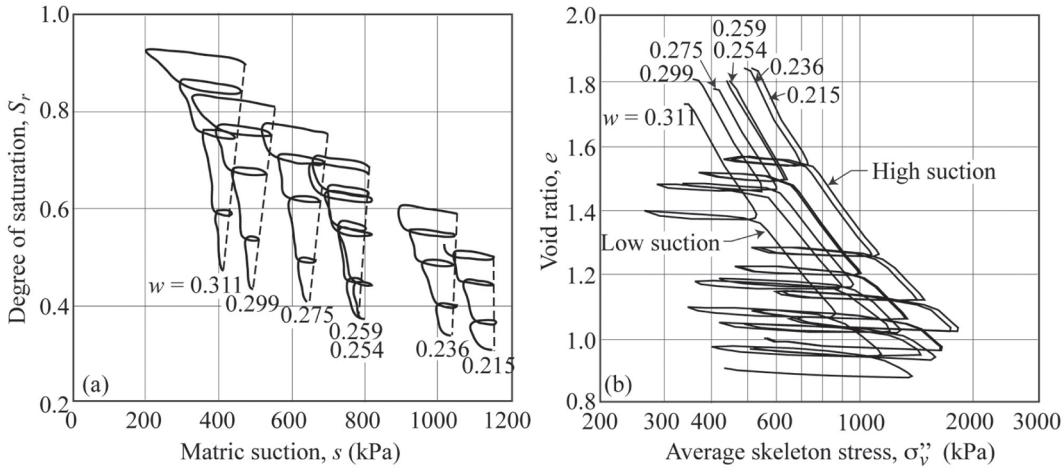

Figure 11. Compaction tests on Speswhite kaolin at different water contents: (a) degree of saturation versus matric suction; (b) void ratio versus average skeleton stress (after Tarantino & De Col, 2008).

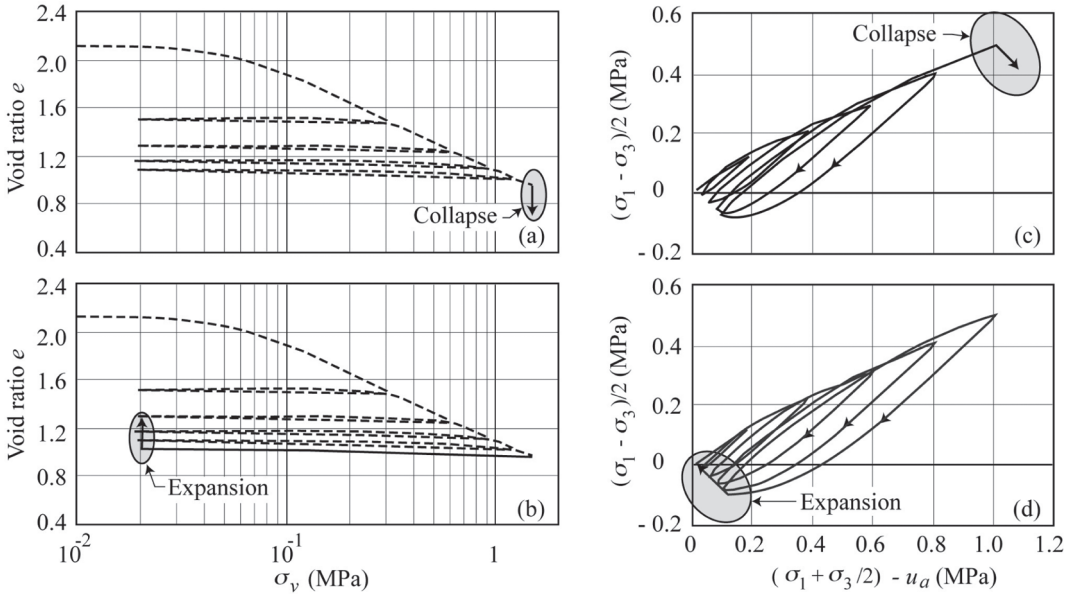

Figure 12. Compression curves obtained during compaction of Speswhite kaolin at water content of 10% and wetted under a vertical stress of 1500 kPa (a) and 20 kPa(b). Figures (c) and (d) present the corresponding stress paths (after Caicedo et al., 2013).

stress of 1500 kPa for one sample (Fig. 12a) and under 20 kPa for the other sample (Fig. 12b) correspond to a collapse for the first one and to a swelling for the second corresponding to a change in void ratio of about 0.20.

– Figures 12c and d show the corresponding stress paths for the tests performed at w = 10%. Each cycle extends the vertical yield stress and consequently the limit state of the soil. The stress ratio σ_h/σ_v, that is about 0.33 when unsaturated under σ_v = 1500 kPa increases to about 0.43 during wetting.

Sridharan et al. (1971) provide an interesting insight into the evolution of soil fabric during the compaction process for a kaolinite with w_p = 36% and w_L = 62%, thus close to the corresponding

values of the kaolinite used by Tarantino & De Col (2008). Sridharan et al. (1971) mixed water with kaolin at a water content of 21% and then statically compacted the soil to void ratios between 0.85 and 0.56 (0.85, 0.74, 0.69, 0.59 and 0.56) corresponding to degrees of saturation of 64, 74, 80, 93 and 100% respectively (values indicated by Delage, 2009). They then determined the pore-size distribution of the soil specimens by mercury intrusion porosimetry. Delage (2009) expressed Sridharan et al.'s data in a pore volume vs entrance pore diameter diagram (Fig. 13). These results can be interpreted as follows: in the early stages of the compaction process, the soil is made of aggregates and shows a bimodal pore size distribution with intra-aggregate pores and inter-aggregate pores. The soil is then at degrees of saturation smaller than the degree of saturation S_{r-opt}, thus on the dry side. With an increase of the compaction effort, the degree of saturation increases to values that may exceed S_{r-opt} (S_r = 93 and 100%) and the aggregates progressively deform to close the inter-aggregate pores that become almost non-existent whereas the intra-aggregate pore space remains constant. The soil then has a homogeneous fabric characteristic of the wet side. Thom et al. (2007) observed similar results.

The results obtained on glacial tills (Vanapalli et al., 1999; Watabe et al., 2000), Speswhite kaolin (Thom et al., 2007) and Barcelona silty clay (Alonso et al., 2012) indicate that soils compacted on the dry side of optimum preserve their bimodal pore-size distribution under wetting. Further evidence for this is provided in Section 4 on hydraulic characteristics. However, results presented by Monroy et al. (2010) show limitations to the previous statement. Monroy et al. (2010) examined the evolution of the pore-size distribution of compacted weathered London clay (I_p = 54%) under wetting. Specimens were statically compacted on the dry side of optimum. After compaction, the matric suction was of about 1 MPa and the soil showed a clear bimodal pore size distribution with inter-aggregate pores with an average entrance pore diameter of about 17 μm and intra-aggregate pores with an average entrance pore diameter of about 0.11 μm (Fig. 14). Some specimens were wetted to matric suctions of 470, 150, 40 and 0 kPa before being subjected to mercury intrusion porosimetry tests (Fig. 14). The results show that when the matric suction decreases: (a) there is an increase in void ratio; (b) there is an increase of the intra-aggregate pore space and of the corresponding entrance pore diameter; (c) from 1 MPa to 40 kPa of matric suction, the soil keeps a bimodal pore size distribution with an almost unchanged inter-aggregate pore space; and (d) it is only when suction drops from 40 kPa to 0 kPa that the inter-aggregate pore space collapses and that the soil then presents a single pore size centered around an average entrance pore diameter of about 1.7 μm.

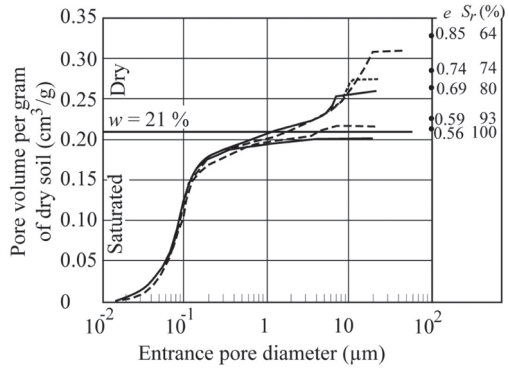

Figure 13. Pore size distribution curves of kaolin samples compacted at various densities with the same water content of 21% (after Sridharan et al. (1971) and Delage (2009)).

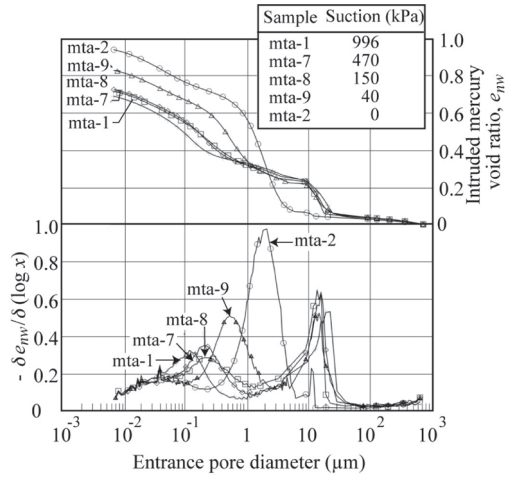

Figure 14. Pore size distribution and density function for samples of weathered London clay compacted to a void ratio of 0.961 and then wetted under different suctions (after Monroy et al., 2010).

3 GENERAL QUALITATIVE MODEL FOR COMPACTED SOILS

From the observations reported in Section 2 and others, it is possible to define a general qualitative model for compacted soils. This model is depicted in Figure 15. It divides compacted soils into two main classes, those compacted on the dry side of optimum (to $S_r < S_{r-opt}$) and those compacted on

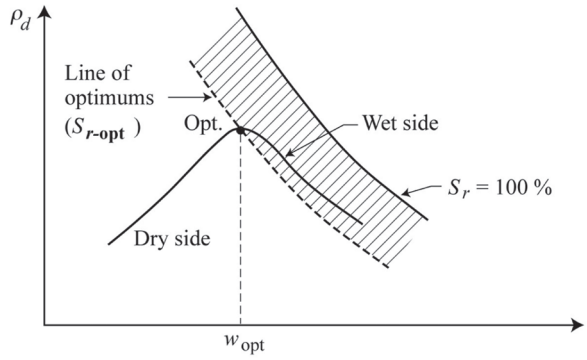

Dry side ($S_r < S_{r\text{-opt}}$)	Wet side ($S_r > S_{r\text{-opt}}$)
(a) After compaction	
• Relatively high suction • Aggregated fabric with large inter-aggregate pores • Continuous air phase • High values of air permeability • Mechanical behaviour controlled by unsaturated soil mechanics, i.e. by, inter alia, net stress ($\sigma - u_a$) and suction ($u_a - u_w$)	• Relatively low suction • Homogeneous fabric with small pores • Occluded air • Very low air permeability • Mechanical behaviour controlled by effective stresses ($\sigma - u_w$) and a compressible pore fluid
(b) During wetting or submergence	
• Some air is displaced by the water front • Volume changes due to the decrease in suction	• Most of air remains trapped • Relatively small volume changes
(c) After wetting or submergence: $S_{r\text{-sub}}$	
• The degree of saturation is larger than that after compaction ($S_{r\text{-sub}} > S_{ro}$ with $S_{r\text{-sub}}$ often close to the degree of saturation at the optimum) • Remaining air is occluded • Mechanical behaviour controlled by effective stresses ($\sigma - u_w$) and a compressible pore fluid	• The degree of saturation is close to that after compaction ($S_{r\text{-sub}} \sim S_{ro}$) • Air remains occluded • Mechanical behaviour controlled by effective stresses ($\sigma - u_w$) and a compressible pore fluid
(d) After saturation: $k_{w\text{-sat}}$	
• $k_{w\text{-sat}}$ relatively high • Mechanical behaviour controlled by effective stresses and an incompressible pore fluid	• $k_{w\text{-sat}}$ relatively low • Mechanical behaviour controlled by effective stresses and an incompressible pore fluid

Figure 15. Synthesis of the behaviour of compacted soils, from just after compaction to saturated conditions.

the wet side (to $S_r > S_{r-opt}$). The line of optimums is a transition line. This model may have limitations in the case of expansive clays in which the aggregates formed by compaction on the dry side swell upon wetting, become more deformable and may fill the space between aggregates, as demonstrated by Monroy et al. (2010) on compacted London clay. The proposed model is thus thought to apply mostly to low plasticity soils. Also, there are aspects of the behaviour of compacted soils that are not considered herein, for example, drying of compacted soils just after compaction or after saturation.

3.1 *After compaction (Fig. 15a)*

The as-compacted material is subjected to relatively high suctions on the dry side of optimum whereas on the wet side, suction is lower and consequently, the soil more deformable. As a result, the soil compacted on the dry side has an aggregated fabric with intra-aggregate pores (or micropores) and larger inter-aggregate pores whereas the soil compacted on the wet side is much more homogeneous with micropores only. The air phase is continuous on the dry side whereas air is occluded on the wet side. An important consequence is that the mechanical behaviour is controlled by unsaturated soil mechanics (i.e. $(\sigma - u_a)$, $(u_a - u_w)$ and possibly S_r) on the dry side whereas on the wet side, menisci have no or little influence on the mechanical behaviour that should then be controlled by effective stresses $(\sigma - u_w)$ and a compressible pore fluid (see Section 5.1).

3.2 *During wetting or submergence (Fig. 15b)*

Le Bihan & Leroueil (2001) compacted non plastic LG2 till specimens (7% clay; S_{r-opt} = 75%) to degrees of saturation varying between 0 and 84% and then percolated water through the specimens from bottom to top. As indicated by the setup A on Figure 16b, the specimen was covered by a cap with a small hole, providing a limited access to the atmosphere. After percolating water through the specimen, the cap was removed and the degree of saturation was determined. The so-called submergence degrees of saturation, S_{r-sub}, are shown on Figure 16a against the as-compacted degree of saturation. It can be seen that for initial degrees of saturation smaller than the optimum, S_{r-opt}, the degree of saturation has increased to a value that is close to that at the optimum, i.e. about 80%. This means that about 20% of the pore volume of the LG2 till is filled with trapped air after submergence. For initial degrees of saturation equal to or larger than that at the optimum, the degree of saturation remains essentially unchanged after submergence, meaning that in these cases too, about 20% of the pore volume is filled with trapped air. Wetting results of Porterville clay (Fig. 17) also show that the final conditions (dark triangles) are not at a degree of saturation of 100% but rather at a degree of saturation close to that at the optimum.

The trapped air is in the form of bubbles at pressures larger than atmospheric pressure. Consequently, and according to Fick's law, the air will move by diffusion from the bubbles towards the atmosphere, progressively increasing the degree of saturation of the soil. This has been demonstrated

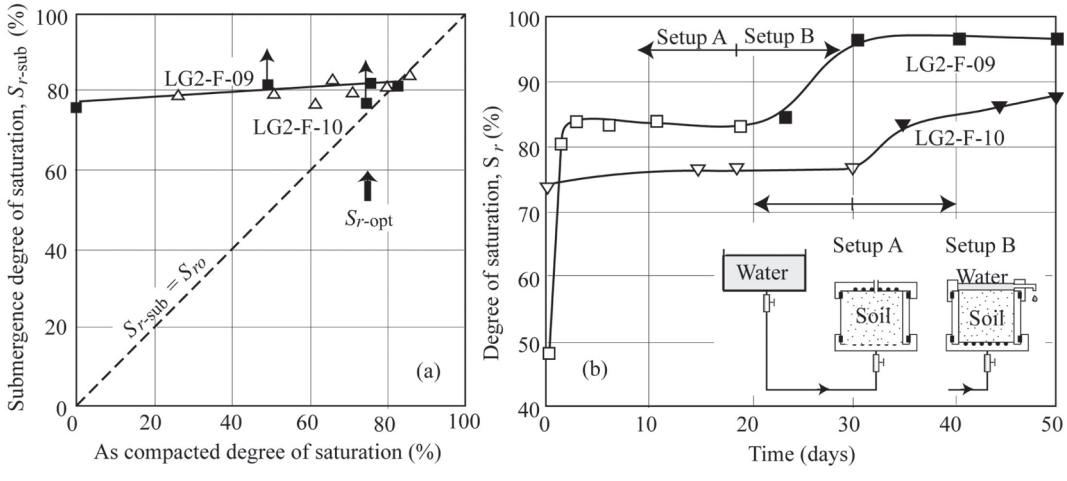

Figure 16. (a) Degree of saturation at submergence versus the compaction degree of saturation for LG2 glacial till; (b) Evolution of the degree of saturation after starting water flow into two samples of LG2 till (after Le Bihan & Leroueil, 2001).

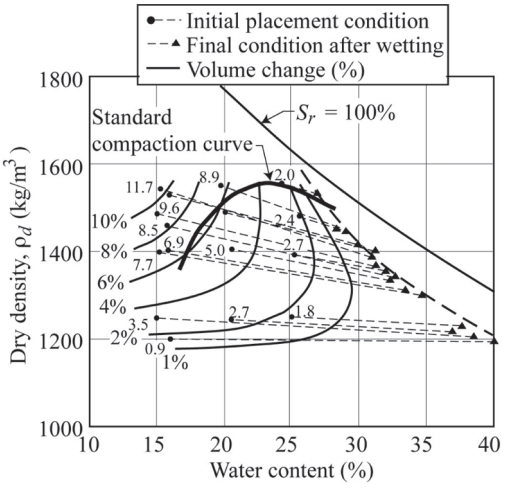

Figure 17. Expansion of Porterville clay under an applied load of 7 kPa for various placement conditions (after Holtz & Gibbs, 1956).

on specimens LG2-F-09 and LG2-F-10 when the cap of setup A has been removed and only a thin layer of water was covering the soil (setup B). As access to atmosphere was then facilitated, diffusion of the occluded air towards the atmosphere became easier and, as shown in Figure 16b, the degree of saturation increased more rapidly with time towards 100%.

During wetting or submergence, water becomes available and this has several consequences: on the wet side, suction decreases in a swelling process controlled by the coefficient of consolidation/swelling, c_{vs}, of the soil along a decreasing effective stress path; on the dry side, as the air phase is continuous, the reduction in suction is associated with a double process: invasion of the macropores with water and swelling of the aggregates (see Gens & Alonso, 1992; Alonso et al., 2001; Ferber, 2006). Since the macropores may collapse during the wetting process, due to the disappearance of the menisci, the final result can be a global swelling or global collapse of the compacted soil. Figure 17 shows volume changes associated with wetting of compacted Porterville clay specimens. Under the small applied stress of 7 kPa, all the volume changes are an expansion.

3.3 *After wetting or submergence (Fig. 15c)*

Some occluded air is generally trapped in the soil whatever the initial degree of saturation. As a consequence, the mechanical behaviour of the soil should be controlled by effective stresses ($\sigma - u_w$) and compressible pore fluid.

3.4 *After saturation (Fig. 15d)*

Because of the presence of macropores on the dry side of optimum, and as discussed in more detail in Section 4, the saturated hydraulic conductivity of compacted soils is larger when the soil has been compacted on the dry side than on the wet side. However, as previously indicated, that could be different in high plasticity clays.

As for the mechanical behaviour, the soil being saturated, it is obviously controlled by effective stresses whether the soil has been compacted on the dry side or the wet side of optimum.

4 HYDRAULIC BEHAVIOUR OF COMPACTED SOILS AND IMPLICATIONS

4.1 *Water retention curves*

The soil-water characteristic curve (SWCC) or water retention curve (WRC) is the relationship between the amount of water in the soil (gravimetric or volumetric water content or degree of saturation) and matric suction ($u_a - u_w$); it is obtained by progressive drying of an initially saturated soil (primary drying curve ABC in Fig. 18); the suction value at which air penetrates into the soil is the air-entry pressure or air-entry value (AEV on Fig. 18). Upon wetting, there is a hydraulic hysteresis (primary wetting curve C to D to A or E in Fig. 18). If wetting is relatively rapid, and as shown in Figure 16, some air is trapped, the wetting curve apparently goes towards a degree of saturation at submergence, $S_{r\text{-}sub}$, that is smaller than 1.0. The word "apparently" is used as, in fact, some air ($1 - S_{r\text{-}sub}$) is in the form of bubbles at a pressure u_a larger than the pressure of the surrounding water. It is only with time and diffusion of air through water that the degree of saturation can progressively increase to 1.0.

Practical implications. The fact that after submergence some air remains trapped has practical implications: in the modelling of infiltration, the wetting curve with a submergence degree of saturation should be considered; in the evolution of pore water pressure in earth dams with time, the trapped air temporarily gives higher pore water pressures than indicated by steady-state conditions with, in particular, a larger downstream gradient (Le Bihan & Leroueil, 2002).

Figure 19 shows SWCC curves obtained on a non-plastic glacial till compacted to degrees of saturation smaller or larger than that at the optimum. It can be seen that the compaction conditions have an important effect on the SWCCs. The air-entry pressure is about 7 times smaller on the dry side of the optimum than on the wet side, directly reflecting the size of the largest pores in the soil, macropores

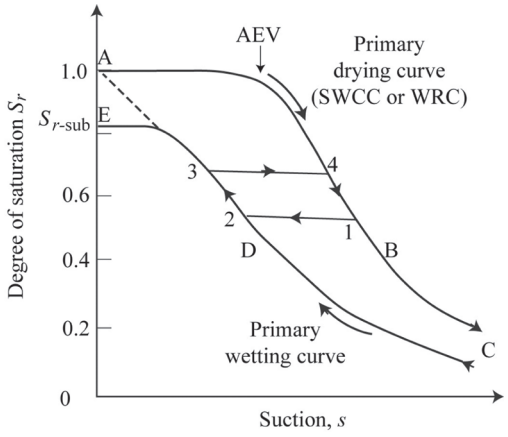

Figure 18. Retention of water in soils (schematic figure).

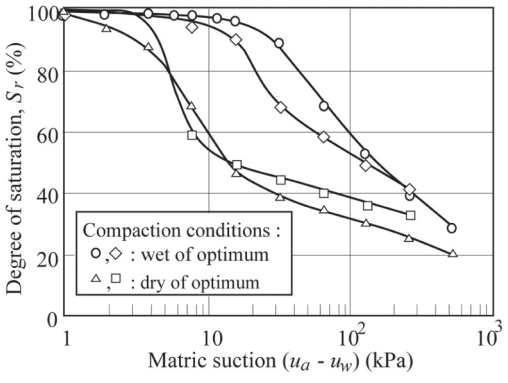

Figure 19. Soil-water characteristic curves of LG2 till compacted to different conditions (after Watabe et al., 2000).

on the dry side and micropores on the wet side. Vanapalli et al. (1999) found similar results on Indian Head till (I_p = 19%). As shown on Figure 20, the air-entry pressure decreases from 100 to 80 kPa as the void ratio increases on the wet side of optimum whereas it is between 35 and 4 kPa on the dry side. As for the conditions at the optimum, it is a transition between the dry and wet sides, which means that the soil at the optimum can have either a bimodal pore size distribution (with macropores and micropores: dry side) or a unimodal pore-size distribution (micropores only: wet side).

4.2 *Hydraulic conductivity of the soil unsaturated*

For the unsaturated as-compacted material, the hydraulic conductivity k_{unsat} is lower than the saturated hydraulic conductivity k_{sat}. The ratio k_{unsat}/k_{sat} is defined as the relative conductivity k_{wr}.

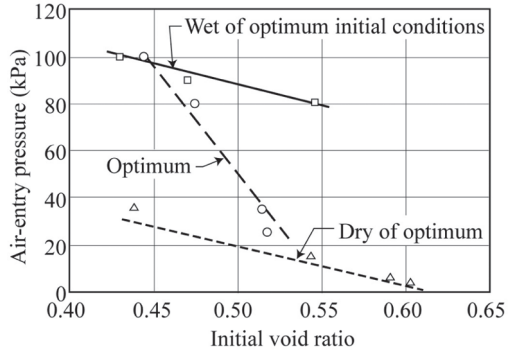

Figure 20. Air-entry pressure versus initial void ratio from the soil-water characteristics obtained on Indian Head till (after Vanapalli et al., 1999).

This latter parameter is generally estimated from more easily measured water retention data (Burdine, 1953; Brooks & Corey, 1964; Van Genuchten, 1980; Fredlund et al., 1994; Watabe et al., 2006). According to Brooks & Corey (1964), it can be estimated as follows:

$$k_{wr} = k_{unsat}/k_{sat} = S_{re}^{\alpha} \quad (2)$$

where $S_{re} = (S_r - S_{rr})/(1 - S_{rr})$ is the effective degree of saturation. S_{rr} is the residual degree of saturation. α is a soil parameter. In general α increases from a value of about 3 for uniform soils to larger values in well graded soils, between 5 and 7 in eastern Canada tills (Le Bihan & Leroueil, 2001).

4.3 *Saturated hydraulic conductivity*

Approximately, the hydraulic conductivity of saturated soils varies with the square of the size of the pores and is thus mostly influenced by the size of the largest pores. Consequently, the variation in hydraulic conductivity with compaction water content amplifies the differences in pore size. As an example, for the glacial till tested by Watabe et al. (2000), the largest pores are typically 8 times larger on the dry side than on the wet side (Fig. 19) and the saturated hydraulic conductivity is, as shown on Figure 21d, about two orders of magnitude larger. Such a change in saturated hydraulic conductivity from the dry side to the wet side of optimum has been observed for a large variety of compacted soils (Fig. 21): glacial tills (Watabe et al., 2000; Leroueil et al., 2002); silty clays (Mitchell et al., 1965; Alberro et al., 1985; Daniel & Benson, 1990); loess (Rinaldi et al., 2006); sandy clay (Lambe & Whitman, 1969); sand and clay mixtures (authors' files). The phenomenon is thus very common, at least for low or medium plasticity soils that keep their bimodal pore-size distribution when

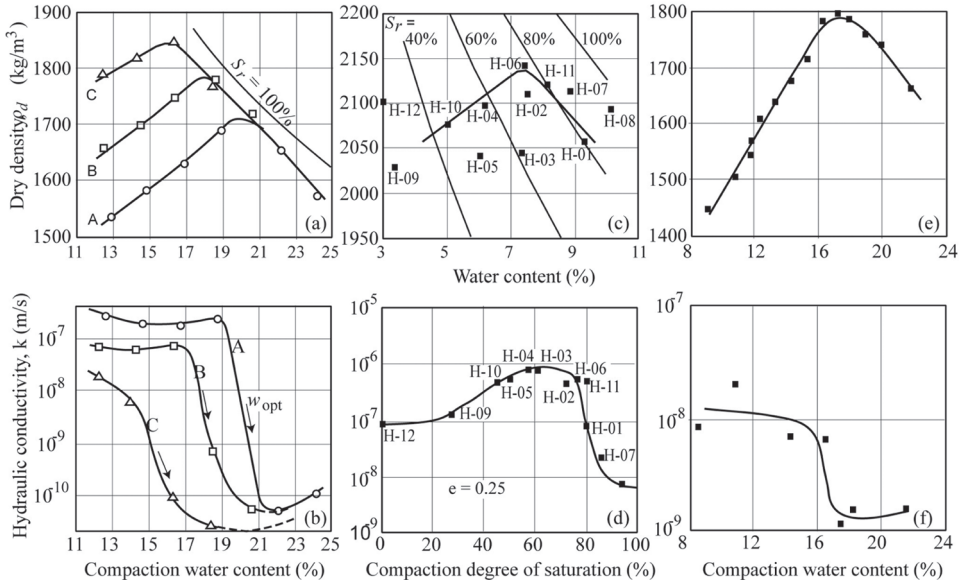

Figure 21. Variation of the saturated hydraulic conductivity of three soils as a function of compaction conditions: (a) and (b) silty clay (Mitchell et al., 1965); (c) and (d) non plastic till (Watebe et al., 2000); (e) and (f) loess (Rinaldi et al., 2006).

they become saturated. It is also very important as the hydraulic conductivity at a given dry density or void ratio may vary by several orders of magnitude in some soils (Fig. 21).

Practical implication. A practical implication of the influence of compaction conditions is the in situ behaviour of clay liners. In order to have the lowest possible hydraulic conductivity, the clays used as hydraulic barriers should be compacted on the wet side of optimum (Daniel & Benson, 1990; Leroueil et al., 1992). Examining the behaviour of 85 clay liners in the United States, Benson et al. (1999) noted that 26% did not satisfy the requirement of $k \leq 10^{-9}$ m/s and that in most cases, the primary cause was compaction on the dry side of the optimum.

Practical implication: Although the authors do not have the evidence, because inter-aggregate pores existing in soils compacted on the dry side are larger than the pores on the wet side, a given soil should be more prone to internal erosion if compacted on the dry side of optimum.

5 MECHANICAL BEHAVIOUR OF COMPACTED SOILS AND IMPLICATIONS

5.1 *After compaction*

Undrained shear strength. The undrained shear strength S_u of the as compacted soil decreases as the compaction water content increases. An example is given in Figure 22 for kaolinite (Seed & Chan, 1959). In addition, it can be seen that specimens compacted dry of optimum have brittle stress-strain behaviour whereas the stress-strain behaviour is ductile with the maximum deviatoric stress reached at large strain for specimens compacted on the wet side. The strength of unsaturated soils can generally be expressed as follows:

$$\tau_f = c' + (\sigma - u_a)\ tg\ \phi' + f(u_a - u_w). \quad (3a)$$

It can also be written as the sum of the strength in saturated conditions and of a component depending on matric suction:

$$\tau_f = \tau_{f\text{-}sat} + f(u_a - u_w). \quad (3b)$$

The decrease in strength when water content increases can then be mostly explained by the decrease in suction (refer to Figs. 6 and 7); for the results in Figure 22, it can also be partly explained by the higher void ratios of the samples compacted on the wet side of optimum. Equation 3 explains why specimen (2) on Figure 22 has an undrained shear strength that is more than four times larger than the strength of specimen (6) at essentially the same dry density and void ratio.

Figure 23 shows S_u plotted as a function of $(w - w_{opt})/I_p$ (with w_{opt} being the optimum water content

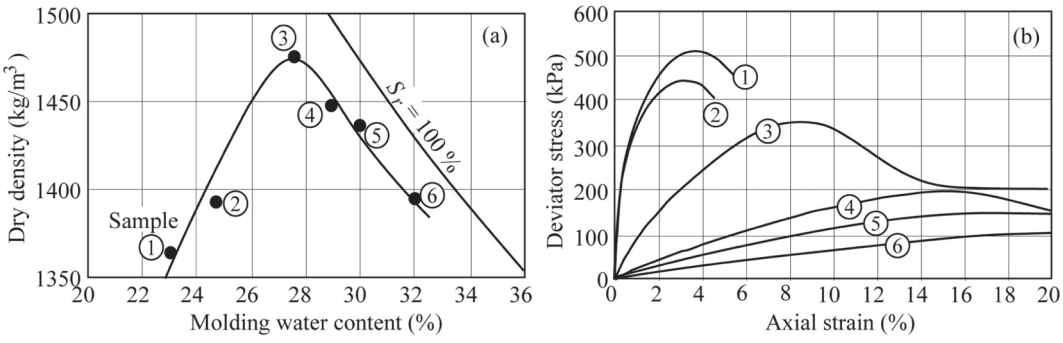

Figure 22. (a) Influence of molding water content on the dry density; and (b) stress-strain relationships for compacted samples of kaolinite subjected to unconsolidated-undrained triaxial compression tests (after Seed & Chan, 1959).

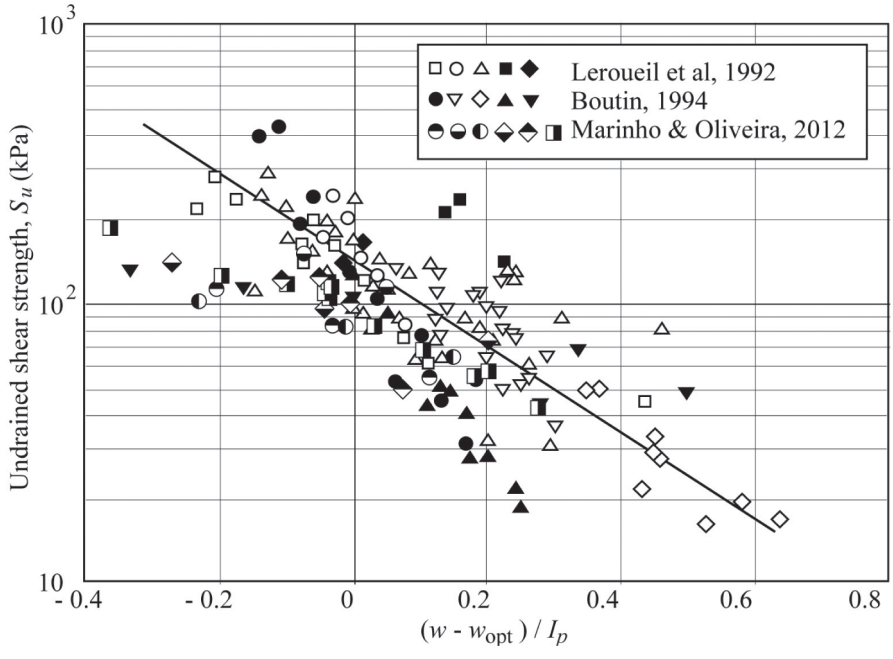

Figure 23. Undrained shear strength against $(w - w_{opt})/I_p$, w_{opt} being the water content at the Standard Proctor Optimum.

obtained in Standard Proctor compaction tests) for a large variety of clayey soils. There is a strong tendency for S_u to decrease as $(w - w_{opt})/I_p$ increases. There is however a large scatter that probably reflects the variations of suction at the optimum water content (refer to Fig. 8). At the optimum, $((w - w_{opt})/I_p = 0)$, the undrained shear strength varies between 80 and 200 kPa with an average of 140 kPa.

This is consistent with the observations that w_{opt} obtained from Standard Proctor compaction tests is close to w_p (Figure 2) and that the undrained shear strength at the plastic limit has often been reported close to that value. On Figure 23, the undrained shear strength seems to continuously increase as water content decreases, but this is not always the case in non-plastic or low plasticity soils (Escario & Juca, 1989; Fredlund et al., 1996; Santucci de Magistris & Tatsuoka, 2004).

In a silty clay (Ip = 14%), Seed & Chan (1959) showed that the compaction method has little influence on the undrained shear strength and shrinkage characteristics for specimens compacted on the dry

side of optimum. On the other hand, the compaction method has an important effect on the measured stiffness and shrinkage for specimens compacted on the wet side of optimum. The strength at 5% strain increases up to four times in the following order: kneading, impact, vibratory and static; shrinkage increases in the following order of compaction methods: static, vibratory and kneading.

Practical implication. S_u vs $(w - w_{opt})/I_p$ relationships can be used to relate the in situ compaction water content to the bearing capacity under compaction and earthmoving equipments.

Limit state curves. The limit state curve defines the domain in which the soil is essentially elastic. It also provides the isotropic yield stress, the one-dimensional yield stress and the strength of the soil. Camapum de Carvalho (1985) was one of the first to study the limit state curve of a compacted soil, the Leyrac marl. The marl was compacted under two conditions, Optimum Standard Proctor (Soil A: γ_d = 19 kN/m^3) and slightly denser than optimum conditions (Soil B: γ_d = 20 kN/m^3), and were tested as-compacted. The results showed: that the limit statecurve of Soil B is larger than that of Soil A; and that the two limit state curves reflect the anisotropy of the compacted soil. It has been shown since that time that the size of limit state curves increases with suction, as shown for example in Figure 24 for compacted Jossigny silt (Cui & Delage, 1996). These results confirm the anisotropy induced by the compaction process. Jotisankasa et al. (2009) found similar results. Also, as indicated by Alonso & Pinyol (2008), the yield stress under saturated conditions increases with dry density.

Practical implication. Anisotropy and the corresponding shape of the limit state curve of compacted soils imply that under isotropic or horizontal loading, the yield stress is much lower than the vertical yield stress.

Small strain shear modulus. Sawangsuriya et al. (2008) examined the small strain shear modulus of three different soils (lean clay, I_p = 24; silt, I_p = 11 and clayey sand, I_p = 14) compacted using Standard Proctor effort. The clayey sand was also compacted under reduced and enhanced Proctor efforts. The results showed that the small strain shear modulus depends primarily on matric suction and to a lesser extent on molding water content and dry unit weight. Sawangsuriya et al. (2008) compiled data obtained by several authors and plotted a normalised small strain shear modulus G_{max} value against a normalised water content, $w/w_{opt.std}$ (Figure 25). There is some dispersion of the data. However, there is a clear tendency for G_{max} to decrease when w increases, from a typical ratio of 1.4 at a normalised water content of 0.7, to 0.4 at a normalised water content of 1.3. This is mostly due to the change in suction. As for strength, the small strain shear modulus of some soils may decrease as the compaction water content becomes low.

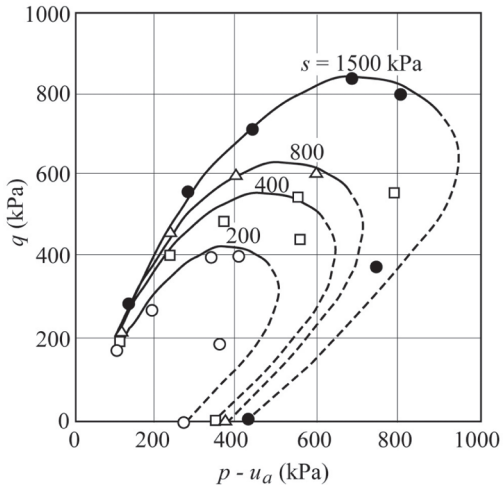

Figure 24. Limit state curves of the compacted Jossigny silt at various suctions (from Cui & Delage, 1996).

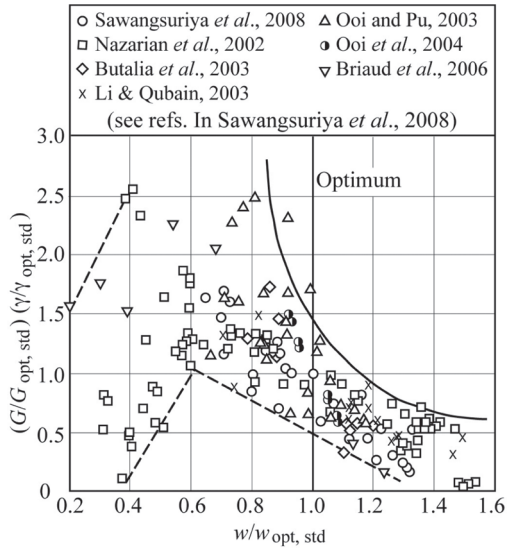

Figure 25. Normalised small strain shear modulus versus normalised water content relationship for a variety of compacted soils (after Sawangsuriya et al., 2008).

G_{max} of compacted soils has also been measured by numerous authors at different matric suctions or degrees of saturation, and under different applied stresses (Wu et al., 1984; Pintado, 1993; Vinale et al., 2001). Figure 26 presents typical results obtained by Vinale et al. (2001) on Metrano

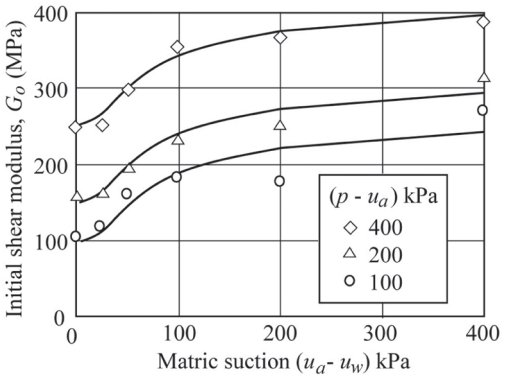

Figure 26. Initial shear modulus versus matric suction in suction controlled torsion shear tests on Metramo silty sand compacted at the optimum (after Vinale et al., 2001). Note that curves have been redrawn.

silty sand compacted at the optimum. Analysis of the results (Leroueil & Hight, 2002) shows that all the results can be written in the form of the following equation, similar to Eq. 3b:

$$G_{max} = G_{max.sat} + g(u_a - u_w) \quad (4)$$

General mechanical behaviour. As mentioned above, the air phase is continuous for specimens compacted on the dry side whereas air is occluded for specimens compacted on the wet side. This has a major influence on models controlling the mechanical behaviour of compacted soils. When the air phase is continuous, the behaviour is to a large extent controlled by the air-water menisci. As indicated by Tarantino (2011), two generations of constitutive models have been formulated for these conditions: the first one has been formulated in terms of net stress ($\sigma - u_a$) and suction ($u_a - u_w$) (e.g., Alonso et al., 1990; Wheeler & Sivakumar, 1995; Cui & Delage, 1996); the second has included the degree of saturation as a generalised stress variable (e.g., Wheeler et al., 2003; Gallipoli et al., 2003; Tamagnini, 2004).

Romero & Vaunat (2000), Tarantino & Tombolato (2005) and Alonso et al. (2010, 2012) suggested that, for a soil made up of aggregates, the mechanical behaviour of the unsaturated soil is controlled by the water partially filling the inter-aggregate pores or macropores. They thus defined a degree of saturation of the macropores, S_{r-M} as follows:

$$S_{r-M} = \frac{e_w - e_{wm}}{e - e_{wm}} \quad (5)$$

where e is the void ratio, e_w is the water ratio (volume of water/volume of solids) and e_{wm} is the water ratio of the intra-aggregate pores or micropores. Equation 5 can also be written in terms of the corresponding degrees of saturation:

$$S_{r-M} = \frac{S_r - S_{rm}}{1 - S_{rm}} \quad (6)$$

Alonso et al. (2010 and 2012) then proposed a so-called "constitutive stress", $\bar{\sigma}$, controlling soil behaviour as follows:

$$\bar{\sigma} = \sigma - u_a + S_{r-M}(u_a - u_w) \quad (7)$$

with $S_{r-M} = 0$ when $S_r \leq S_{rm}$ (condition 7–1).

Equations 5 to 7 imply that the effective stress $\sigma' = \sigma - u_w$ applies only when $S_{r-M} = 1.0$, i.e. when the soil is saturated and $S_r = 1.0$. It is thought, and as indicated above, that the concept of effective stress applies as soon as the degree of saturation is such that gas becomes occluded. In the context of compacted soils, that means that the concept of effective stress applies when $S_r \geq S_{r-sub}$ or S_{r-opt}. So, the possibility of replacing 1 by S_{r-opt} in Equation 6 should be considered. To the above condition 7–1, should then be added the condition 7–2: $S_{r-M} = 1$ when $S_r \geq S_{r-opt}$ in order to ensure continuity in the mechanical behaviour of the soil.

When soils are compacted wet of their optimum, air is trapped in the form of occluded bubbles, resulting in the soil having a compressible pore fluid, which, in turn, means that the compacted soil is compressible under undrained conditions, Skempton's pore pressure parameter B is then less than 1.0, compressional wave velocities are drastically reduced (Rebata-Landal & Santamarina, 2012), and consolidation and swelling are slower than for the same soil when saturated (Vaughan 1978). The pore air pressure in occluded bubbles has little influence on effective stress so that the strength of the soil compacted wet of optimum is controlled by the conventional effective stress, $\sigma - u_w$, and its effective stress strength parameters are the same as for the same soil when saturated (Vaughan, 2003).

5.2 *During wetting or submergence*

During wetting or submergence, the matric suction and the strength of the soil decrease (Eq. 3). For soils compacted on the wet side, the behaviour being controlled by effective stresses, wetting is associated with a decrease in effective stresses and thus with some swelling (controlled by the swelling index of the material). For soils compacted on the dry side and made up of aggregates, the reduction of suction has two effects: swelling of the aggregates and change in volume

of the macropores. The amount of swelling of the aggregates depends on the as-compacted suction and on their swelling index. Given that the as-compacted suction increases when the compaction water content decreases, the smaller the compaction water content and the larger the dry density, the larger is the swelling strain. This is illustrated in Figure 17. The change in volume of the macropores results from the fact that with the reduction in suction, the aggregates soften and their inter-aggregate forces decrease. The aggregates may then move, deform, and partially close the inter-aggregate pores.

The schematic representation shown in Figure 27 can help in understanding the volume changes of compacted soils under wetting. Consider a soil with the compaction curve shown on Figure 27a and its compression curve, when soaked (s = 0), as shown on Figure 27b (This compression curve is assumed to be independent of compaction conditions, which may not always be the case, as indicated by Alonso et al., 2012). Soil specimen (a) compacted on the wet side of optimum is at a low suction, say 50 kPa. Its compression curve is thus the 50 kPa curve shown on Figure 27b. For specimen (b), at the same dry density and void ratio but compacted on the dry side, the suction is higher, say 1000 kPa, and the corresponding compression curve is as shown on Figure 27b.

If both specimens (a) and (b) on figure 27 are loaded up to σ_{vf2} before being soaked, their behaviour will typically be as follows:

- For (b), from b to b_1, the soil is in its pre-yield domain and the change in void ratio is small; from b_1 to b_2 (at σ_{vf2}), the soil is on its compression curve. When soaked, the specimen moves to the 0 kPa compression curve, at point b_3, and shows a large change in void ratio.
- For (a), the soil will be in its pre-yield domain until a_1 and on its compression curve from a_1 to a_2 (at σ_{vf2}). When soaked, the specimen will move to a_3, on the 0 kPa compression curve, showing a much smaller change in void ratio than specimen b.

Consider now specimens such as (c) and (d) compacted on the dry side of optimum that are first loaded to σ_{vf1} and then soaked. As indicated in Figure 27b, at d_1, the soil is in a loose condition and above the 0 kPa compression curve; it will thus collapse to d_2 under soaking. On the other hand, c_1 is below the 0 kPa compression curve and will thus swell under soaking.

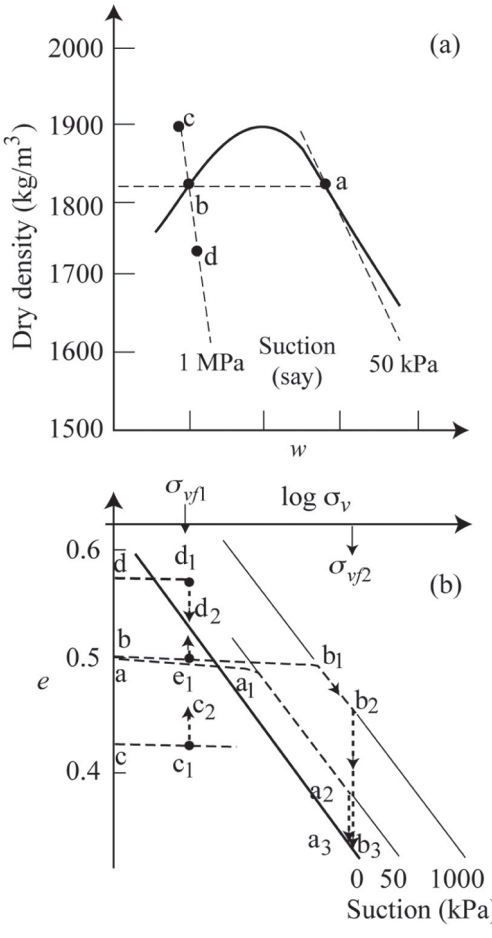

Figure 27. One dimensional behaviour of compacted soils subjected to loading and to wetting (schematic figure).

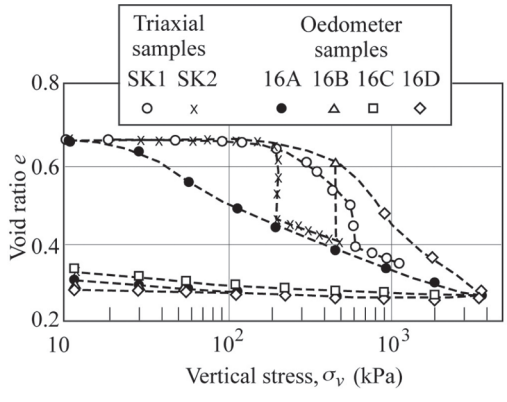

Figure 28. Compression curves for K_0 triaxial and oedometer tests performed on Lower Cromer Till specimens loaded in soaked condition, unsaturated condition and soaked after loading to some stress (after Maswoswe et al., 1992).

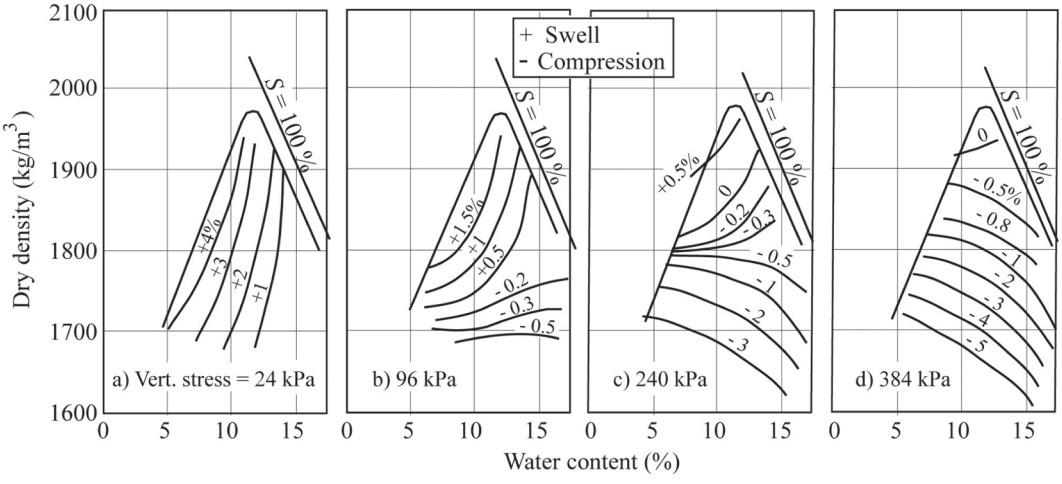

Figure 29. Contours of equal swell and equal compression for Villa Trinidad fill (after Noorany & Stanley, 1994).

The situation of specimens such as (b) can be illustrated by results presented by Maswoswe et al. (1992). These authors one dimensionally and statically compacted specimens of low plasticity Lower Cromer till. The water content was 11.0% and the soil was compacted to a loose condition at an average void ratio of 0.66. Compression test results are shown in Figure 28. Specimen 16 A was soaked and loaded; specimen 16D was compressed without soaking; and specimens SK1, SK2 and 16B were compressed to different vertical stresses before being soaked. It can be seen that these latter specimens follow the unsoaked compression curve and collapse to reach the soaked compression curve when wetted. Alonso et al. (2012) report similar results. Charles (2008) also shows the collapse of several poorly compacted fills that collapse under wetting.

The results obtained by Noorany & Stanley (1994) and presented in Figure 29 illustrate the influence that an applied load may have on the behaviour of a compacted soil when soaked. In Figure 29a, the applied load is of 24 kPa and the soil swells under wetting, a situation similar to that of specimen b on Fig. 27b when loaded to σ_{vf1}, at e_1, before being soaked. In Figure 29d, the soil loaded to 384 kPa collapses, a situation similar to that of specimen b on Fig. 27b when loaded to σ_{vf2}, at b_2 before being soaked.

Practical implication. Changes in volume upon wetting are generally more important for soils compacted on the dry side of optimum and depend critically on the level of compaction and the stress level at which wetting takes place.

6 CONCLUSION

After reviewing observations of the characteristics and behaviour of compacted soils, a general qualitative model for compacted soils is presented. The main features are: the pore-size distribution is bimodal, with micro—and macro-pores, when the soil is compacted dry of the optimum whereas it is unimodal with micro-pores when compacted wet of the optimum; when compacted on the wet side of optimum or compacted on the dry side and then submerged, some air is trapped in the form of bubbles. It is recognised that this model is approximate, incomplete and possibly not applicable to high plasticity clays, but it is thought to explain the main hydraulic and mechanical behaviour of most compacted soils and to be useful to geotechnical engineers, in particular those in practice. Reference is made to some practical implications.

ACKNOWLEDGEMENT

The authors thank Jean-Marie Konrad and Marc Lebeau for commenting a first draft of the paper.

REFERENCES

Ahmed, S., Lovell, C.W. & Diamond, S. 1974. Pore sizes and strength of compacted clay. *ASCE J. of Geotechnical Engng. Division*, 100(GT4): 407–425.

Alberro, J., Marsal, R.J. & Mendoza, M.J. 1985. Comportamiento de suelos cohesivos compactados. No. 493, *Series del Instituto de Ingenieria*, UNAM, Mexico City, Mexico.

Alonso, E.E. 1998. Suction and moisture regimes in roadway bases and subgrades. *Proc. Int. Symp. on Subdrainage in Roadway Pavement and Subgrades*, Grenade, 57–104.

Alonso, E.E., Gens, A. & Josa, A. 1990. A constitutive model for partially saturated soils. *Géotechnique*, 40(3): 405–430.

Alonso, E.E., Vaunat, J. & Gens, A. 2001. Modelling the mechanical behaviour of expansive clays. *Engng. Geology*, 54(1–2): 173–183.

Alonso, E.E. & Pinyol, N.M. 2008. Unsaturated soil mechanics in earth and rockfill dam engineering. *Proc. 1st European Conf. on Unsaturated Soils*, Durham Vol. 1: 3–32.

Alonso, E.E., Pereira, J.-M., Vaunat, J. & Olivella, S. 2010. A microstructurally based effective stress for unsaturated soils. *Géotechnique*, 60(12): 913–925.

Alonso, E.E., Pinyol, N.M. & Gens, A. 2012. Compacted soil behaviour: initial state, structure and constitutive modelling. *Géotechnique*, in press.

ASTM D698–12. Standard test methods for laboratory compaction characteristics of soils using standard effort (600 kN.m/m^3).

ASTM D1557-12. Standard test methods for laboratory compaction characteristics of soils using modified effort (2700 kN.m/m^3).

Barbosa, P.S. & Leroueil, S. 1998. Strength and compressibility of a reconstituted and slightly cemented saprolitic soil. *Proc. 2nd Int. Conf. on Unsaturated Soils*, Beijing, Vol. 1: 1–6.

Benson, C.H., Daniel, D.E. & Boutwell, G.P. 1999. Field performance of compacted clay liners. *ASCE J. of Geotechnical and Geoenvironmental Engng.*, 125(5): 390–403.

Boutin, S. 1994. Comportement mécanique des argiles compactées le long de la ligne de saturation naturelle. M.Sc. Thesis, Laval University, Quebec.

Brooks, H. & Corey, A.T. 1964. *Hydraulic properties of porous media*. Colorado State University, Hydrology Paper 3.

Burdine, N.T. 1953. Relative permeability calculations from pore size distribution data. *Transactions of the American Institute of Mining, Metallurgical, and Petroleum Engineers* 198, 71–78.

Caicedo, B., Tristancho, J., Thorel, L. & Leroueil, S. 2013. Modelling soil compaction using a new oedometer apparatus. In preparation.

Camapum de Carvalho, J. 1985. *Étude du comportement mécanique d'une marne compactée*. Thesis, Institut National des Sciences Appliquées de Toulouse, France. 181 p.

Chapuis, R.P. 2002. The 2000 R.M. hardy Lecture: Full-scale hydraulic performance of soil-bentonite and compacted clay liners. *Canadian Geotech, J.*, 39(2): 417–439.

Charles, J.A. 2008. The engineering behaviour of fill materials: the use, misuse and disuse of case histories. *Géotechnique*, 58(7): 541–570.

Cui, Y.J. & Delage, P. 1996. Yielding and plastic behaviour of an unsaturated compacted silt. *Géotechnique*, 46(2): 291–311.

Daniel, D.E. & Benson, C.H. 1990. Water content—density criteria for compacted soil liners. *ASCE J. of Geotechnical Engng.*, 116: 1811–1830.

Delage, P. 2009. Discussion to Compaction behaviour of clay by Tarantino and De Col. *Géotechnique*, 59(1): 75–76.

Delage, P., Audiger, M., Cui, Y.J. & Howat, M. 1996. Microstructure of compacted silt. *Canadian Geotechn. J.*, 33(1): 150–158.

Escario, V. & Juca, J.F.T. 1989. Strength and deformation of partly saturated soils. *Proc. 12th Int. Conf. on Soil Mech. and Found. Engng.*, Rio de Janeiro, Vol. 1: 43–46.

Ferber, V. 2006. Déformations induites par l'humidification de sols fins compactés—Apport d'un modèle de microstructure. Ph. D. Thesis, École Centrale de Nantes.

Fleureau, J.-M., Verbrugge, J.C., Huergo, P.J., Correia, A.G. & Kheirbek-Saoud, S. 2002. Aspects of the behaviour of compacted clayey soils on drying and wetting paths. *Canadian Geotech. J.*, 39(6): 1341–1357.

Fredlund, D.G., Xing, A. & Huang, S. 1994. Predicting the permeability function for unsaturated soils using the soil-water characteristic curve. *Canadian Geotech. J.* 31, 533–546.

Fredlund, D.G., Xing, A., Fredlund, M.D. & Barbour, S.L. 1996. The relationship of the unsaturated soil shear strength to the soil-water characteristic curve. *Canadian Geotech. J.*, 33(3): 440–448.

Gallipoli, D., Gens, A., Sharma, R. & Vaunat, J. 2003. An elasto-plastic model for unsaturated soil incorporating the effects of suction and degree of saturation on mechanical behaviour. *Géotechnique*, 53(1): 123–136.

Gens, A. & Alonso, E.E. 1992. A framework for the behaviour of unsaturated expansive clays. *Canadian Geotech. J.*, 29(6): 1013–1032.

Gens, A., Alonso, E.E., Suriol, J. & Lloret, A. 1995. Effect of structure on the volumetric behaviour of a compacted soil. *Proc. 1st Int. Conf. on Unsaturated Soils*, Paris, Vol. 1: 83–88.

Holtz, W.G. & Gibbs, H.J. 1956. Engineering properties of expansive clays. *Transactions, American Society of Civil Engineers*, Paper No. 2814, pp. 641–663.

Jotisankasa, A., Coop, M. & Ridley, A. 2009. The mechanical behaviour of an unsaturated compacted silty clay. *Géotechnique*, 59(5): 415–428.

Lambe, T.W. & Whitman, R.V. 1969. *Soil Mechanics*. John Wiley et al.

Langfelder, L.J., Chen, C.F. & Justice, J.A. 1968. Air permeability of compacted cohesive soils. *ASCE J. of Soil Mechanics and Foundation Div.*, 94(SM4): 981–1001.

Le Bihan, J.-P. & Leroueil, S. 2001. Simulation d'écoulement en milieu non saturé – Application au Barrage CD-00 de LG–2. Report GCT-01-11 prepared for Hydro-Quebec.

Le Bihan, J.P. & Leroueil, S. 2002. A theoretical model for gas and water flow through the core of earth dams. *Canadian Geotech. J.*, 39(1): 90–102.

Leroueil, S. & Hight, D.W. 2002. Behaviour and properties of natural soils and soft rocks. *Int. Workshop on Characterisation and Engineering Properties of Natural Soils*, Singapore, Vol. 1: 29–254.

Leroueil, S., Le Bihan, J.-P. & Bouchard, R. 1992. Remarks on the design of clay liners used in lagoons as hydraulic barriers. *Canadian Geotech. J.,* 29(3): 512–515.

Leroueil, S., Le Bihan, J.-P., Sebaihi, S. & Alicescu, V. 2002. Hydraulic conductivity of compacted tills from northern Quebec. *Canadian Geotech. J.*, 39(5): 1039–1049.

Marinho, F.A.M. & Oliveira, O.M. 2012. Unconfined shear strength of compacted unsaturated plastic soils. *Geotechnical Engineering*, 165(GE2): 97–106.

Marinho, F.A.M. & Stuermer, M.M. 1999. The influence of the compaction energy on the SWCC of a residual soil. ASCE *Geotechnical Special Publication 99 Advances in Unsaturated Geotechnics*, pp. 125–141.

Maswoswe, J.J.G., Burland, J.B. & Vaughan, P.R. 1992. Stress path method of predicting compacted soil collapse. *Expansive '92, the Proc. of the 7th Int. Conf. on Expansive Soils*, Dallas, Texas Tech University Press, Lubbock, Vol. 1: 61–66.

Mitchell, J.K., Hooper, D.R. & Campanella, R.G. 1965. Permeability of compacted clay. *ASCE J. of the Soil Mechanics and Foundations Div.*, 91(4): 41–65.

Monroy, R., Zdravkovic, L. & Ridley, A. 2010. Evolution of microstructure in compacted London clay during wetting and loading. *Géotechnique*, 60(2): 105–119.

Noorany, I. & Stanley, J.V. 1994. Settlement of compacted fills caused by wetting. *Proc. Settlement'94, ASCE Geotechnical Special Publication* No. 40: 1516–1530.

Olson, R.E. 1963. Effective stress theory of soil compaction. *ASCE J. of Soil Mechanics and Foundations Div.*, 89(2): 27–45.

Pintado, X. 1993 *Estudi experimental de la relacio entre el modul de tall i la succio en un sol compactat*. Tesina de Especialidad ETS Ing. Caminos, Canales y Puertos de Barcelona, UPC (ref. by Alonso, 1998).

Proctor, R.R. 1933. Fundamental principles of soil compaction. *Engineering News Record*, VII, No. 9, 148–156.

Rebata-Landa1, V. & Santamarina, J.C. 2012. Mechanical effects of biogenic nitrogen gas bubbles in soils. ASCE *J. of Geotechnical and Geoenvironmental Engng*, Vol. 138(2): 128–137.

Ridley, A.M. & Pérez-Romero, J. 1998. Suction-water content relationships for a range of compacted soils. *Proc. 2nd Int. Conf. on Unsaturated Soils*, Beijing, Vol. 1: 114–118.

Rinaldi, V.A., Rocca, R.J. & Zeballos, M.R. 2006. Geotechnical characterization and behaviour of Argentinean collapsible loess. *Int. Workshop on Characterisation and engineering Properties of Natural Soils*, Singapore, Vol. 4: 2259–2286.

Romero, E. & Vaunat, J. 2000. Retention curves in deformable clays. In *Experimental Evidence and Theoretical Approaches in Unsaturated Soils*, Balkema, pp. 91–106.

Santuccci de Magistris, F. & Tatsuoka, F. 2004. Effects of moulding water content on the stress-strain behaviour of a compacted silty sand. *Soils & Foundations*, 44(2): 85–101.

Sawangsuriya, A., Edil, T.B. & Bosscher, P.J. 2008. Modulus-suction-moisture relationship for compacted soils. *Canadian Geotech. J.*, 45(7): 973–983.

Seed, H.B. & Chan, C.K. 1959. Structure and strength characteristics of compacted clays. *ASCE J. of Soil Mechanics and Foundations Div.*, 85(SM5): 87–128.

Sridharan, A., Altschaeffl, A.G. & Diamond, S. 1971. Pore size distribution studies. *ASCE J. of Soil Mechanics and Foundations Div.*, 97(SM5): 771–787.

Tamagnini, R, 2004. An extended Cam-clay model for unsaturated soils with hydraulic hysteresis. *Géotechnique*, 54(3): 223–228.

Tarantino, A. 2011. Unsaturated soils: Compacted versus reconstituted states. Proc. 5th Int. Conf. on Unsaturated Soils, Barcelona, Vol. 1: 113–136.

Tarantino, A. & De Col, S. 2008. Compaction behaviour of clay. *Géotechnique*, 58(3): 199–213.

Tarantino, A. & Tombolato, S. 2005. Coupling of hydraulic and mechanical behaviour in unsaturated compacted clay. *Géotechnique*, 55(4): 307–317.

Thom, R., Sivakumar, R., Sivakumar, V., Murray, E.J. & MacKinnon, P. 2007. Pore size distribution of unsaturated compacted kaolin: the initial states and final states following saturation. *Géotechnique*, 57(5): 469–474.

Vanapalli, S.K., Fredlund, D.G. & Pufahl, D.E. 1999. The influence of soil structure and stress history on the soil-water characteristics of a compacted till. *Géotechnique*, 49(2): 143–159.

van Genuchten, M. Th. 1980. A closed-form equation for predicting the hydraulic conductivity of unsaturated soils. *Soil Science Society of America Journal.*, 44, 892–898.

Vaughan, P.R. 1978. General Report: Engineering properties of clay fills. *Proc. Conf. on Clay Fills*. Institution of Civil Engineers, London, pp. 283–295.

Vaughan, P.R. 2003. Observations on the behaviour of clay fill containing occluded air bubbles. *Géotechnique*, Vol. 53(2): 265–272.

Vaunat, J., Romero, E. & Jommi, C. 2000. An elastoplastic hydromechanical model for unsaturated soils. In *Experimental Evidence and Theoretical Approaches in Unsaturated Soils*, Balkema, pp. 121–138.

Vinale, F., d'Onofrio, A., Mancuso, C. & Santucci de Magistris, F. 2001. The pre-failure behaviour of soils as construction materials. *Proc. 2nd Int. Symp. on Pre-Failure Deformation Characteristices of Geomaterials*, Torino, Vol. 2: 955–1007.

Watabe, Y., Leroueil, S. & Le Bihan, J.-P. 2000. Influence of compaction conditions on pore-size distribution and saturated hydraulic conductivity of a glacial till. *Canadian Geotech. J.*, 37(6): 1184–1194.

Watabe, Y., Le Bihan, J.-P. & Leroueil, S. 2006. Probabilistic modelling of saturated/unsaturated hydraulic conductivity for compacted glacial tills. *Géotechnique*, 56(4): 273–284.

Wheeler, S.J. & Sivakumar, V. 1995. An elasto-plastic critical state framework for unsaturated soil. *Géotechnique*, 45(1): 35–53.

Wheeler, S.J., Sharma, R.S. & Buisson, M.S.R. 2003. Coupling of hydraulic hysteresis and stress-strain behaviour in unsaturated soils. *Géotechnique*, 53(1): 41–54.

Wu, S., Gray, D.H. & Richart, F.E. 1984. Capillary effects on dynamic modulus of sands and silts. *ASCE J. of Geotechnical Engng*, 110(9): 1188–1203.

This page intentionally left blank

Advances in Unsaturated Soils – Caicedo et al. (eds)
© 2013 Taylor & Francis Group, London, ISBN 978-0-415-62095-6

Rockfill mechanics

L.A. Oldecop
Instituto de Investigaciones Antisísmicas "Ing. Aldo Bruschi", Universidad Nacional de San Juan, Argentina

E.E. Alonso
Department of Geotechnical Engineering and Geosciences, Universitat Politècnica de Catalunya, Barcelona, Spain

ABSTRACT: The paper examines several aspects of rockfill behaviour, which are relevant to interpret and analyze the field response of dams and embankments. Experimental observations on rockfill compressibility, time-dependent deformation and deviatoric stress-strain behaviour are presented. Special attention is given to the role of relative humidity. The physics of rockfill deformation, explained by particle breakage are described. Particle breakage is explained by crack propagation, a phenomenon discussed within the framework of fracture mechanics. A macroscopic elastoplastic constitutive model is outlined. Rockfill mechanics are also approached by a Distinct Element modelling of grain assemblages experiencing grain breakage. Finally, rockfill mechanics are discussed from the wider perspective offered by unsaturated soil mechanics.

1 INTRODUCTION

The occurrence of rockfill in civil engineering works steadily increased in number and frequency along the last century. From the first small dams with timber face, built by the mid of the 19th century in California during the gold rush, to the present 200 m tall concrete faced rockfill dams, the building technology evolved and also the knowledge regarding the behaviour of this material. Today's interest in rockfill arises not only from the dam building sector, but also from transportation, maritime and mining works. Mining heap leach pads and waste-rock heaps are examples of 'non-engineered rockfills', very different from typical civil engineering materials, which require a good understanding of their behaviour in order to ensure safety and long term stability.

Perhaps, the most persistent pitfall in the study of rockfill mechanical behaviour was, and continues to be, our inability to test real size rockfill samples ei-ther in the laboratory, or in the field. The research efforts done in the sixties and early seventies using large scale testing apparatuses (Sowers *et al.*, 1965; Fumagalli, 1969; Marachi *et al.*, 1969; Marsal, 1973; Penman & Charles, 1976), allowed gathering a large amount of experimental information. However it is necessary to face the fact that, even taking the huge effort of operating large testing devices (Fig. 1), real size rockfill probes (including 'particles' of, say, 1 m in diameter) are impossible to test. In fact, in the following decades, the use of many of those facilities was abandoned, suggesting that very large testing equipment was an unfeasible approach.

Therefore, the primary source of information about rock-fill behaviour was the observation of real rockfill structures. The dam building industry, with his well-established monitoring tradition, gathered most of the currently available field information. Other recent works using rockfill, like high speed railways, produced new interesting data. Anyway, despite the referred limitations imposed by size, laboratory research works allowed gaining much of the understanding, at least in a qualitative way, about the physical and chemical phenomena involved in rockfill mechanics.

The fact that rockfill is an inherently 'free draining' material, means that in many situations it will remain in an unsaturated or partially saturated condition. This condition may arise from rain, or, more generally, from the interaction with the atmosphere. In some particular cases, in mining heap leach pads for example, partial saturation is the normal operation condition, being the liquid phase the lixiviation solution continuously sprinkled over the top of the heap. Early approaches (based on the point of view of the effective stress principle) assumed that, as a coarse material, rockfill would not be influenced by water as long as saturation is not attained. Later, gathered field data and laboratory and theoretical research, led to a different working hypothesis. In the unsaturated condition, water or other liquids, have indeed a significant influence in

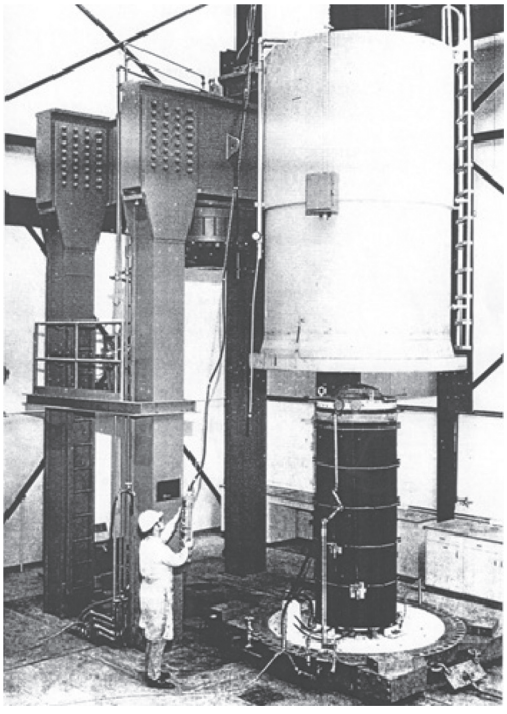

Figure 1. Berkeley giant triaxial cell (Marachi *et al.*, 1969).

the mechanical behaviour of rockfill, although of a different nature of the effects observed in unsaturated soils. Such influence, which is not of mechanical nature but physicochemical, will be addressed in detail later in this paper.

2 BEHAVIOUR OF ROCKFILL AS OBSERVED IN THE FIELD AND LABORATORY TESTS

Regarding the mechanical behaviour of rockfill, two distinct features can be pointed out: time dependent deformations and collapse deformations. Early experimental observations (Sowers *et al.*, 1965; Marsal *et al.*, 1976) clearly showed that rockfill undergoes significant amounts particle breakage during straining. So, the idea that some link should exist between the rockfill singular behaviour and the breakage of the rock particles underlies many of the research efforts since the 70's. As explained in the following sections, both of the observed phenomena share a common origin, *i.e.* the gradual propagation of cracks which lead to a succession of breakages of the rockfill particles, each producing a small strain increment. Macroscopically, this is perceived as a time dependent deformation process.

2.1 *Time dependent strains*

The bulk of field settlement records in dams and embankments suggests that time dependent straining process of rockfill follows a linear relationship with the logarithm of time of the type (Sowers *et al.*, 1965; Charles, 1989):

$$s = \alpha\, H\, Log_{10}\left(\frac{t}{t^r}\right) \tag{1}$$

where s is accumulated the settlement between instants t^r and t, H is the height of the fill and α is a parameter. The origin of time for Eq. (1) has no physical meaning. Sowers *et al.* (1965) suggested adopting as initial time, the moment of completion of half the height of the embankment, while Charles (1989) used the end of construction date. Sowers *et al.* (1965) fitted Eq. (1) to the crest settlement records of fourteen non-compacted rockfill dams, getting values of α between 0.002 and 0.007, exceptionally going up to 0.01.

Charles (1989) determined α–values from cross-arm settlement records at different heights within the downstream shoulder of two UK rockfill dams, plotting them against vertical stress (Fig. 2). Scammonden dam was built with sandstone rockfill and Llyn Brianne dam with mudstone rockfill, both placed with heavy compaction. This explains the lower range of α-values than the dumped rockfill dams analysed by Sowers *et al.* (1965). Figure 2 also displays the case of other two dams: El Infiernillo in Mexico and Lechago in Spain. El Infiernillo rockfill was made of diorite and silicified conglomerate, moderately compacted. Lechago dam was made of a slate rockfill with highly crushable particles, placed with heavy compaction. In any case, it is apparent from Figure 2 that α increases with stress, although it shows a considerable scatter, even within the set of points of each single dam.

Oldecop & Alonso (2002) described the observed behaviour in rockfill oedometer tests under constant vertical stress, by means of an expression analogous to Eq. (1):

$$\varepsilon = \lambda^t\, Ln\left(\frac{t}{t^r}\right) + \varepsilon^r \tag{2}$$

where ε is the vertical strain, λ^t is the time-dependent compressibility index and ε^r is the strain at the reference time t^r. If the laboratory tests are assumed to be representative of field behaviour, Eq. (1) should be related to Eq. (2) by integration in the height of the fill and α and λ^t become related by:

$$\alpha = \frac{2.303}{H}\int_0^H \lambda^t\, dh \tag{3}$$

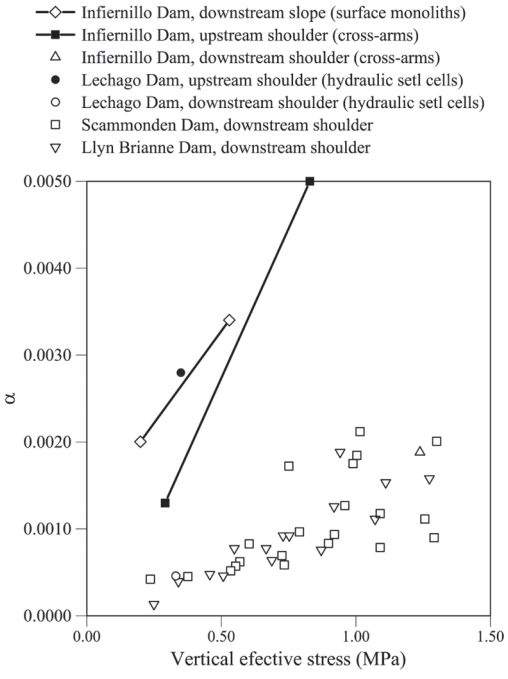

Figure 2. α-values derived from cross-arm settlement records at different heights within the downstream shoulder of Scammonden and Llyn Brianne Dams (Charles, 1989). Similar data from El Infiernillo (Marsal *et al.*, 1976) and Lechago dams.

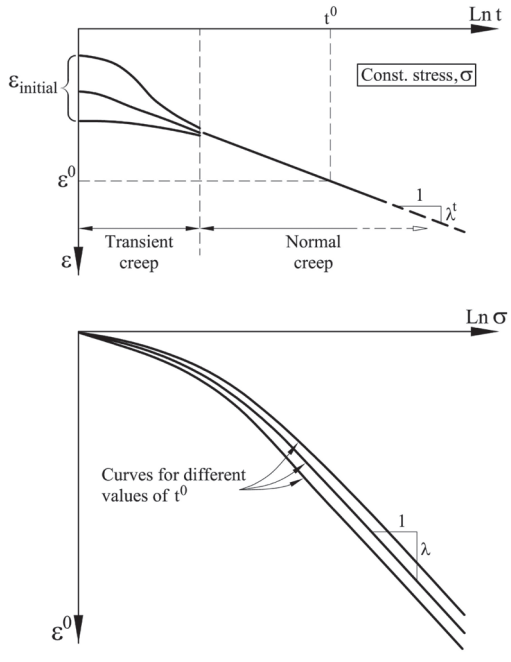

Figure 3. a) Schematic drawing of typical strain records obtained in oedometer tests under constant vertical stress. b) Stress-strain curves built with the data of Figure 3.a using a constant reference time t^0.

The origin of time for Eq. (2) was taken at the instant of each load increment application. However, it was observed that, during the initial stage of deformation, immediately after the load increment application, the behaviour was different than described by Eq. (2). It was only after a certain time (generally less than a couple of hours) that the deformation record approached the logarithmic law. Oldecop & Alonso (2002) called the first stage *transient creep* and the second *normal creep*. The scheme in Figure 3.a explains the typical behaviour observed in these stages.

A logarithmic deformation process implies that strain increments would continue indefinitely. It seems difficult to accept this fact from a physical point of view, but this is indeed what the settlement records of many rockfill dams are suggesting, showing continuing settlements during four decades or more (Oldecop & Alonso, 2007).

During the normal creep stage, the index λ^t depends both on stress and total suction. Moreover experimental evidence suggests that the normal creep line (*i.e.* ε–*Ln t* in the normal creep stage) seems to be unique for each pair of stress-suction values, *i.e.* non-dependent of the material history (Oldecop & Alonso, 2002). The experimental data, gathered in oedometer tests with controlled relative humidity shows that λ^t increases with stress, but the slope of this relationship greatly changes with total suction (Fig. 4). The lower the suction, the faster increases λ^t with stress. A limiting top value seems to exist for λ^t.

On the other hand, in the transient creep stage, the behaviour depends also on the applied stress and suction, but also on the history of the material. Such history is condensed in the accumulated strain by the time of application of the current load step ($\varepsilon_{initial}$). The transient creep strain develops in such a way that it links the state of $\varepsilon_{initial}$ with the normal creep line (Fig. 3.a).

By setting a constant conventional reference time, t^r, and plotting the corresponding ε^r (Fig. 3.a) for each value of vertical stress, σ, a classical stress-strain curve is obtained (Fig. 3.b). Evidently, these compression curves vary with the chosen t^r value (Oldecop & Alonso, 2007). However, it is important to note that, in order to get consistent stress-strain curves, the instant t^r must pertain to the normal creep stage. Along any of the stress-strain curves in Figure 3 the compressibility index, λ, can be computed. Along the initial curved part of the compression curves of Lechago slate rockfill,

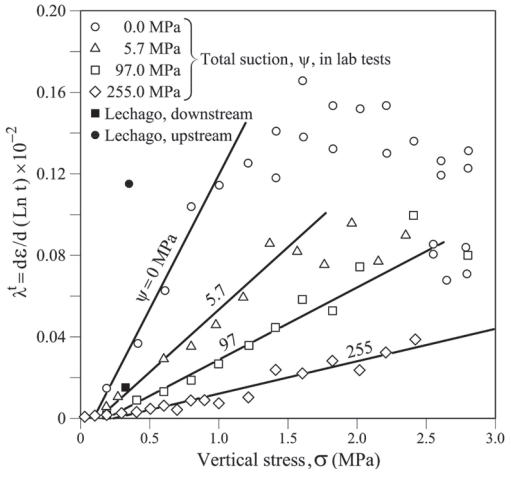

Figure 4. Time-dependent compressibility index, λ^t, measured in one-dimensional compression tests of Lechago slate rockfill, under various stress-total suction conditions (Oldecop & Alonso, 2002).

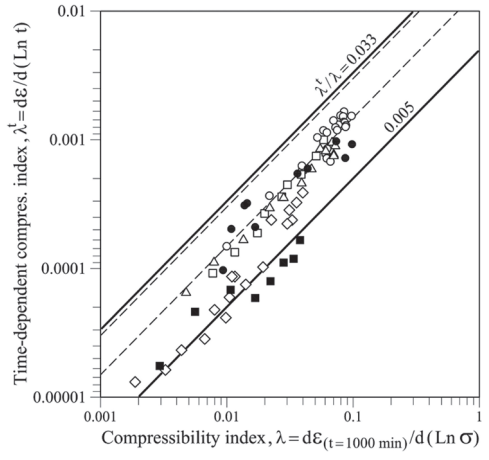

Figure 5. Time-dependent compressibility index, λ^t, plotted against compressibility index, λ, measured in one-dimensional compression tests of Lechago slate and Garraf Limestone, with same grain size distribution. (data from Oldecop & Alonso, 2007; Ortega, 2008).

the compressibility index increases almost linearly with stress, which implies a linear stress-strain relationship. Under higher strain levels, λ becomes constant. Many other granular materials display a similar behaviour (Nobari & Duncan, 1972; Marsal, 1973; Clements, 1981; Pestana & Whittle, 1995; Yamamuro and Lade, 1996).

The data points corresponding to Lechago Dam in Figure 2, were also included in Figure 4 (as 2.303 times α). It is likely that the downstream shoulder point was in a dryer state than the upstream point. Although reservoir filling was still not accomplished at the time of measurements, the phreatic level in the upstream side was close to the instrumented level. Field data suggest that the material is quite sensitive to moisture, a behaviour also observed in the laboratory tests.

Another interesting feature to observe is the behaviour of the ratio λ^t/λ. Mesri *et al.* (1990) found out that, for a variety of geotechnical materials, this ratio fits in a remarkably narrow range of values. In spite of the complex distribution of λ^t shown in Figure 4, this feature also applies for the Lechago slate, as shown in Figure 5. Another rockfill material, with identical grain size distribution as the Lechago slate, but made of limestone, was tested by Ortega (2008). In this case, the rockfill particles are much harder to break. Analogous experiments yielded the set of λ^t values also included in Figure 5. Both tested materials show similar trends. Also, in both cases the driest specimens have a λ^t/λ ratio which departs from the bulk of data, being significantly lower than the obtained with the material at lower suction values.

As proposed by early researchers (Sowers *et al.*, 1965) all these observations are consistent with the idea that some link should exist between time—dependent deformations and the particle breakage phenomenon.

2.2 *Collase strains*

The collapse phenomenon is long known in dam building. In almost every case when, during reservoir filling, the upstream shell of a central core rockfill dam is flooded, sudden deformations take place. Less evident was that the same phenomenon can occur by partial wetting. Detailed analysis of some settlement records showed that this is indeed the case. Relatively intense rainfall periods can be correlated with increase in the settlement rate of: Cogswell Dam (Bauman, 1960), El Infiernillo Dam (Marsal *et al.*, 1976) and Beliche Dam (Naylor *et al.*, 1986, 1997) and also of a high speed railway embankment in the south of Spain (Soriano and Sánchez, 1999).

In fact, the case of El Infernillo Dam displays, in a consecutive manner, the two types of collapse events referred above. Figure 6 presents the vertical and horizontal movements records of surface markers installed in the crest and downstream berms of El Infiernillo Dam. Measurements started immediately after building completion. The flooding collapse event took place in a rather sudden manner with reservoir filling. As typically found in these cases, the crest movement involved strong settlements and upstream horizontal movements, which later changed its sense towards downstream.

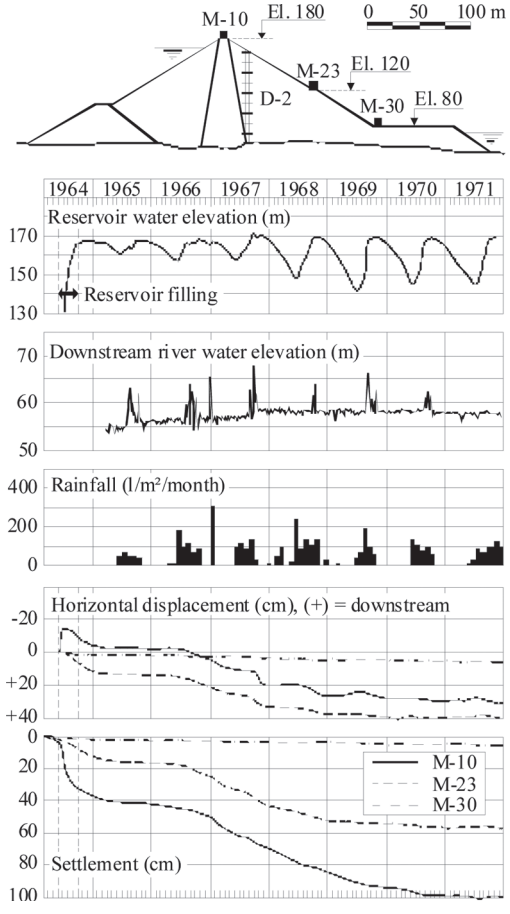

Figure 6. Post-construction behaviour of El Infiernillo Dam, Mexico (data after Marsal *et al.*, 1976).

The deformation process continued afterwards for a year, with a decreasing-rate trend. During the second year after reservoir filling, a new deformation process started, increasing again the movement rates. This second deformation event lasted almost four and a half years, involving displacements of at least the same order of that from the first event.

It is interesting to note that the downstream shell was never flooded, but only the lowest part during periods of spillway operation. However, settlement measurements with cross-arm D–2 show that the deformation process affected the whole fill up to el 120 (Marsal *et al.*, 1976). So, the only remaining explanation for this behaviour is to accept that collapse develops under progressive wetting by rainfall. Such hypothesis is consistent with the fact that 1965 was a relatively dry year, while the following years had more intense rainfall seasons.

Figure 7 shows a collection of flooding collapse strain measurements, for different rockfill materials

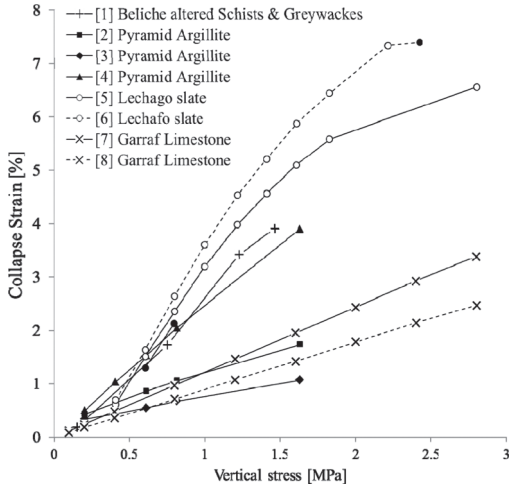

Figure 7. Collapse strains following flooding of rockfill specimens tested in oedometer. Filled symbols correspond to values really measured while open symbols to collapse amounts derived by difference between compression curves of dry and flooded specimens. Properties of the materials referred are given in Table 1.

tested in oedometric devices, under various vertical stresses, in the range of engineering interest. The features of those rockfill specimens are given in Table 1. Collapse strain increases with stress almost linearly for most rockfill materials. The collapse phenomenon does not tend to vanish under high stresses, as observed in soils (Alonso *et al.*, 1990). However, linearity is lost for specimens of weak rock undergoing high strain levels. By comparing the features of the different materials included in Figure 7, some conclusions can be derived about the factors affecting the collapse phenomenon in rockfill. The collapse deformations increases for: 1) weaker rock particles, 2) larger particle size 3) grain size uniformity, 4) less compaction, 5) lower initial moisture. All these observations are consistent with the hypothesis relating collapse with particle breakage.

The case of El Infiernillo (Fig. 6) calls attention on another aspect of rockfill behaviour which differs from that of unsaturated soils. In soils, full collapse deformation is attained when saturation occurs, a situation which is never attained in the case of rockfill subjected to rainfall. Rainfall water percolates through rockfill causing a downwards progressing wetting front. But, due to large voids and high permeability of the material, it is very unlikely that a saturated condition develops due to rainfall. So, field observations suggest that the nature of collapse strains in rockfill is different from the mechanisms observed in soils.

Table 1. Material properties of rockfills tested in oedometer devices referred in Figure 7.

Mat	Max. Part Size [mm]	Cu	Spec. Compact.	Initial moisture cond.	Data source
[1]	50.00	2.5	100%RD	Air dry	Veiga Pinto (1983)
[2]	4.75	14.0	70%RD	Air dry 1.5%wc	Nobari and Duncan (1972)
[3]	4.75	14.0	93%RD	Air dry 1.5%wc	Nobari and Duncan (1972)
[4]	4.75	1.4	95%RD	Air dry 1.5%wc	Nobari and Duncan (1972)
[5]	40.00	2.9	100%StPr	50%RH 0.8%wc	Oldecop and Alonso (2001)
[6]	40.00	2.9	100%StPr	15%RH 0.4%wc	Oldecop and Alonso (2001)
[7]	40.00	1.1	100%StPr	10%RH 0.1%wc	Ortega (2008)
[8]	25.00	1.1	100%StPr	10%RH 0.1%wc	Ortega (2008)

In the oedometer tests of Lechago slate rockfill, Oldecop & Alonso (2001; 2004) found that the range of water content values in which the collapse of rockfill occurs is only a small fraction of the full range up to saturation. Figure 8 depicts this behaviour for specimens subjected to gradual wetting under constant vertical stress. This was achieved by introducing water vapour in the specimen by means of a closed air flow circuit, and controlling the relative humidity of air with chemical solutions. Collapse strains develop from the very beginning of the wetting path, even under extremely dry conditions. As the wetting process goes, strain accumulates at an appreciable rate until a certain point when the deformation process spontaneously halts although water continued to be introduced in the specimen. From the hygrometer readings it was estimated that this point corresponds to 100% RH, which means nil total suction. Such a state would mean that the particles have their internal porosity fully filled with liquid water. The appearance of a specimen under 100% RH is similar to rock particles soaked through with water, covered by a thin water film, but with no "free" water running in the rockfill *macrovoids* (Fig. 14.a).

2.3 *Rockfll behaviour under shear*

The effects of shear deformation on rockfill are seldom observed in engineered fills, since shear

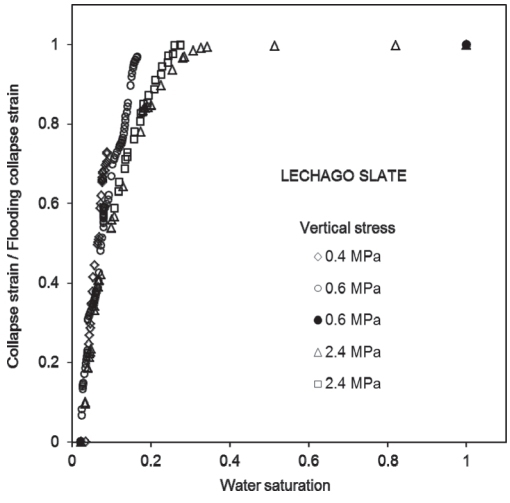

Figure 8. Development of collapse strain under gradual wetting, in oedometer tests of slate rockfill, with RH control.

strains are not expected to occur under design conditions. Some large slope failures have occurred in mining waste-rock and heap leach piles. However these are not rockfills in a strict sense, since they are built by dumping with no compaction and contain significant amounts of fines. Most of these failures are associated to the non-homogeneity of the fill which includes strong segregation, layers of fines, oblique stratification and perched phreatic levels (Dawson *et al*., 1998, Thiel & Smith, 2003).

Laboratory experiments with rockfill in large size triaxial cells were performed by Marsal (1973), Fumagalli (1969), Marachi *et al.* (1969), Nobari & Duncan (1972), Parkin & Adikari (1981), Veiga Pinto (1983), Wilson & Evans (1990), Rein *et al.* (1992), Indraratna *et al.* (1993), Yasuda & Matsumoto (1994), Yasuda *et al.* (1997). Plane strain tests were performed by Marachi *et al.* (1969) and Marsal (1973).

The bulk of experimental data shows that the strength envelopes of rockfill are curved. At low stresses rockfill exhibits quite high friction angles, generally over 40°, commonly reaching 55°. Under increasing confining stress the friction angle decreases to values between 30 and 40°. Increasing the confining stress also causes a marked decrease in the material dilatancy. Extensive particle breakage was observed in triaxial and plain strain tests, much more intense than in oedometer or isotropic compression tests. A correlation was found to exist between the peak friction angle developed by the specimen and the amount of particle breakage (Marachi, 1969; Marsal *et al.*, 1976). Charles & Watts (1980) provided data on the nonlinearity of

the strength envelope of rockfill. De Mello (1977) proposed a nonlinear strength envelope:

$$\tau = A(\sigma)^b \tag{4}$$

where A and b are empirical parameters.

The non-linearity of the envelope was attributed to particle breakage during the compression stages prior to shearing and during the shearing itself. The larger the amount of breakage, the smaller is the friction angle.

At the UPC Laboratory, triaxial tests programs with controlled RH, were carried out with the Lechago slate rockfill (Chávez, 2004) and Garraf Limestone (Ortega, 2008). The aim was to study the influence of water in the mechanical behaviour. The grain size distribution of the specimens was identical in both materials and equal also to the grain size distribution used in oedometer tests (Figs. 4 and 5). All tests performed were of the type consolidated/drained with internal measurement of axial and volumetric strains. The axial strain was imposed at a rate of 1×10^{-4} s^{-1}. Some test results are shown in Figure 9 as deviator stress vs. axial strain and volumetric strain vs. axial strain. It is apparent for both materials that increasing relative humidity, *i.e.* decreasing suction, implies both a reduction of strength and higher deformability. The volumetric behaviour displays a strong reduction of dilatancy for increasing RH. These effects are more evident in the Lechago slate rockfill than in the tougher Garraf Limestone.

A gradual wetting path under constant stress was tested with the Lechago slate rockfill (Chávez, 2004), by means of a RH control system similar to the system used in oedometric tests. RH was increased up to 100% and the sample was finally flooded. The effect of wetting was a gradual increase of axial and volumetric strain (both in compression). The resulting strains exceeded in a significant amount, those developed by a similar specimen previously water-saturated and subjected to the same stress state. It has to be noted that the experimental conditions determined that this test was significantly longer than the rest. In normal tests the deviator application phase lasted no more than 30 min while, in this case, the sole wetting process lasted the same time. So, a possible explanation for the additional strains is the overlap of collapse and time-dependent deformation mechanisms.

The time-dependent behaviour of rockfill in triaxial tests was also showed by Ortega (2008) by applying two different axial strain rates to Garraf limestone rockfill specimens (Fig. 10). The higher rate specimens display lower deformability and higher shear strength. The volumetric behaviour is also affected by the axial strain rate. The specimens deformed at higher rate are initially more compressible, but show higher dilatancy at failure. The effect of the strain rate is less apparent in dryer specimens.

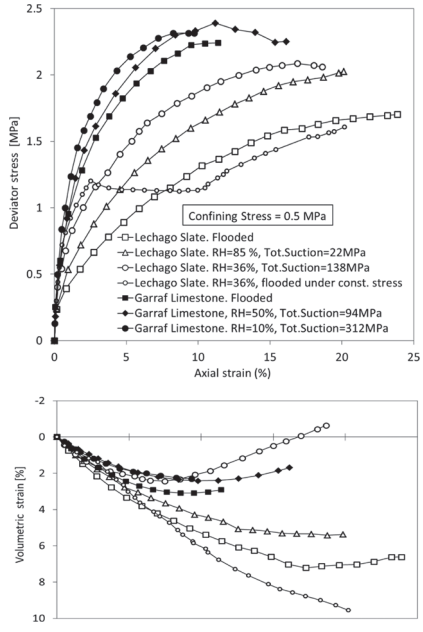

Figure 9. Triaxial tests of rockfill with RH control. Data of Lechago slate obtained by Chávez (2004) and from Garraf Limestone obtained by Ortega (2008).

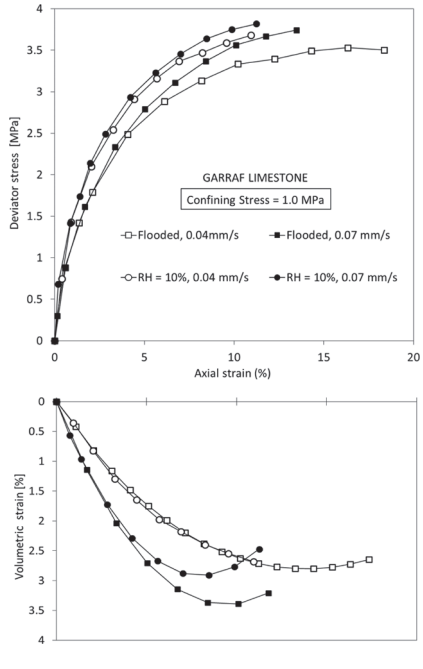

Figure 10. Triaxial tests on Garraf Limestone rockfill showing the dependency of the beahaviour on the axial strain rate applied, under different moisture conditions (data from Ortega, 2008).

Probing tests were designed, in the experiments reported by Chávez (2004), to investigate the shape of the yield surface in the triaxial deviatoric plane. Figure 11 indicates the shape of the yield surface of compacted Lechago slate isotropically loaded to a confining stress p_0.

The geometry of the yield surface may be simplified as the combination of a cap surface and a deviatoric Mohr-Coulomb type of yielding. Plotted plastic strain vectors show a non-associated flow rule, dominated by shear strains during shear loading. In this material, reducing the relative humidity to 42% did not result in a significant change of the shape of the yield locus, as shown in Figure 12.

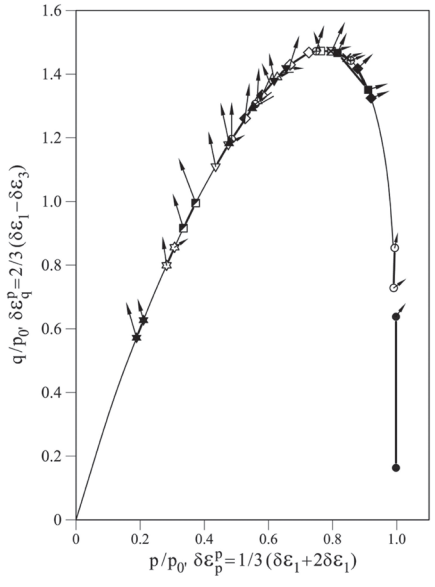

Figure 11. Yield locus of compacted Lechago rockfill (Chávez, 2004).

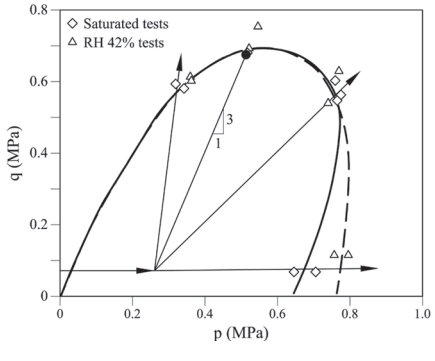

Figure 12. Yield locus of compacted Pancrudo gravel for two relative humidities (Chávez, 2004).

3 PARTICLE BREAKAGE

It was evident from the early experimental observations by Sowers *et al.* (1965), Fumagalli (1969), Marachi *et al.* (1969) and Marsal (1973), among others, that rockfill mechanical behaviour is somehow linked with particle breakage, since most rockfill tests showed an unusually high amount of crushed particles after the end of the test. Some of these authors explored this phenomenon by testing in the laboratory isolated rock particles. Two types of tests were performed: compression of irregular rock particles between two steel plates (Marsal, 1973; Lee, 1992) and irregular or regularly shaped rock points pressed against a flat steel or rock surface (Sowers *et al.*, 1965; Clements, 1981). In both cases, load and displacement were recorded. Lee (1992) reported the results reproduced in Figures 13 and 15.

Along the failure process three stages were observed. In the first stage, the material at the loading points is crushed, causing the contact area with the plates, to increase gradually. Next, spalling and propagation of local cracks occurs in the vicinity of the contact zones. Finally, splitting

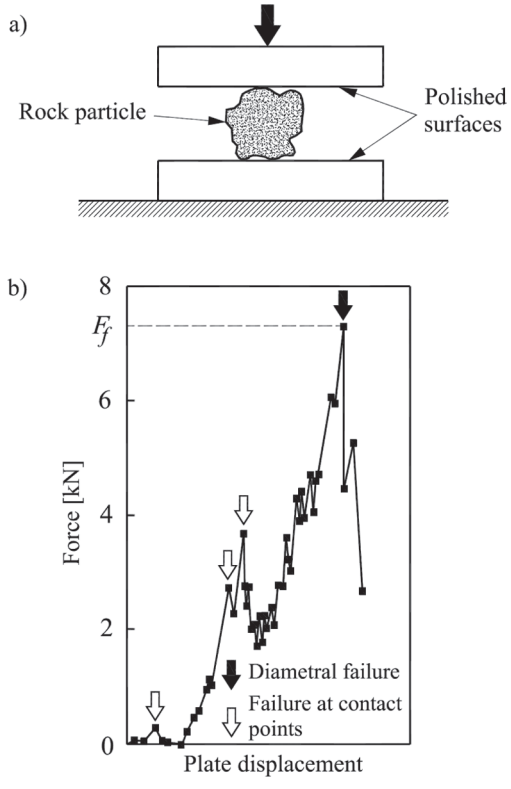

Figure 13. Tests on rock particles reported by Lee, 1992: a) Scheme of the tensile strength test on rock particles b) Typical load-displacement plot.

of the particle is attained involving one or more planes containing the direction of load. This pattern of breakage is also observed in laboratory rockfill specimens (Fig. 14).

Lee (1992) defined the particle failure stress, σ_f, as the load causing the splitting of the particle divided by the square of the average particle size, d. It was found that σ_f decreases with increasing the size of the particle (Fig. 15). The following expression was found to fit the experimental data:

$$\sigma_f \propto d^{\alpha} \tag{5}$$

Exponent α in Lee (1992) data varies between –0.34 and –0.42. In the set of data plotted in Figure 15 the exponent α has negative values ranging between –0.3 and –0.8.

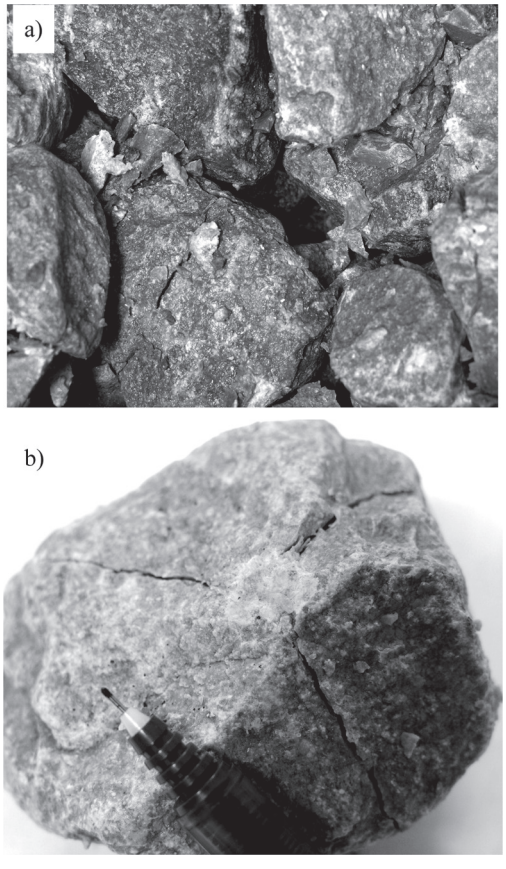

Figure 14. a) Oedometer rockfill specimen of Grainstone (carbonated rock) at 100% RH after test end. b) Crushed contact point and splitting pattern of a Grainstone rockfill particle. Particle recovered from oedometer specimen tested under 2.8 MPa vertical stress and 100% RH.

Fracture mechanics also provide an interpretation for these experimental results. The rock particle is assumed to host defects of varying size and orientation, which are ready to propagate under stress. Under a mode I type of fracture propagation (cracks propagate in a uniform tensile stress field, of intensity σ), cracks propagate at a high speed when the stress intensity factor K reaches the rock fracture toughness, K_c. The failure condition is expressed:

$$K = \sigma \beta \sqrt{\pi a} = K_c \tag{6}$$

where β is a geometric factor and a is the size (length) of the crack or defect. This expression is examined in more detail below.

Therefore, the failure strength is proportional to the inverse of the square root of the defect size:

$$\sigma_f \propto a^{-0.5} \tag{7}$$

In statistical terms, particle size and defect size are equivalent and the size of the particle defines the size of the critical defect size. Therefore, it is expected that:

$$\sigma_f \propto d^{0.5} \tag{8}$$

This relationship is indicated by the dotted line in Figure 15 (b is the slope in the log σ_f – log d plot).

Rockfill deformation involves not only the diametral breakage of particles but also the local crushing at contacts and the subsequent rearrangement

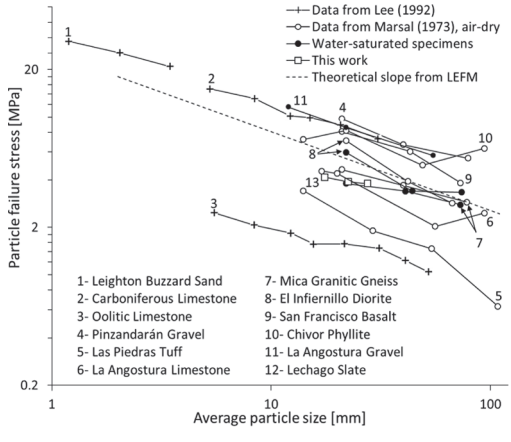

Figure 15. Variation of particle crushing strength with particle size of different rockfill materials and gravels. Each data point was obtained by averaging the results of several tests (10 or more).

of the entire granular structure, which will evolve during testing. Scale effects are therefore unavoidable and, on the other hand, large sample sizes are extremely expensive and unpractical. Even if some trade-off between particle size and cell diameter is adopted (say maximum particle size is a fraction (1/5) of cell diameter) some relevant deformation phenomena such as strain localization cannot develop. In fact, shear band localization in granular assemblage requires a band thickness that involves 10–20 particles. This criterion is an additional drawback to examining experimentally the strength of coarse granular aggregates. It is expected that grain rupture will also be dominant within the highly strained shear band.

Clements (1981) tested conically shaped points of rock pressed against a flat surface. The same breakage sequence as in the tests of particles between plates was observed to occur in this case. The angle of the points tested varied between 60° and 160° and it was observed that the loads at which the different stages of breakage are attained (*i.e.*, crushing, spalling, splitting) increase with increasing point angles. This suggests that angular particles are more prone to breakage than rounded particles. Under a constant load, rock points developed time dependent displacements and, moreover, when these points are wetted or submerged in water, additional displacements take place in a sudden manner, resembling collapse episodes observed in rockfill specimens (Sowers *et al.*, 1965; Clements, 1981).

The time dependent behaviour of rock particles can be also observed in the experimental data shown in Figure 16. Irregular rock particles were pressed between flat steel plates under three different displacements rates (0.001, 0.01 and 0.1 mm/seg). However, since it is expected that the relevant parameter for the phenomenon is the load (or stress) increase rate, this was individually measured from the recorded load history of each particle. The plot of the particle failure stress against the stress increase rate shows a slight but clear increase of the particle strength with increasing loading rate.

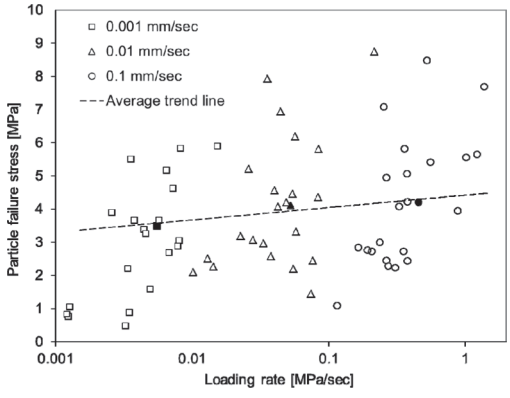

Figure 16. Variation of the particle failure stress with the loading rate (stress increase rate). Material tested: Lechago slate at 40% RH. Size of tested particles: Mean = 20.63 mm, St Dev = 3.37 mm.

4 SIZE EFFECTS

Rockfill particles in embankments and dams reach often sizes in the range 0.30–1.00 m. Laboratory cells able to handle such a range of sizes are out of a reasonable proposal. Grain size may be scaled down in an attempt to preserve the behaviour of the prototype dimensions. This approach has been reported in some testing programs (Fumagalli, 1969; Marachi *et al.*, 1969), but scale effects remain as an unsolved issue.

Let us consider the relationship between the "external" stress (σ_{ext}) and the tensile stress in a given particle (σ_t). For a given applied stress state, this relationship is a consequence of the granular geometry. But under some simplifications an approximate relationship (σ_{ext} vs. σ_t) may be established. For instance, if the particle is loaded along a diameter, the applied concentrated load P is proportional to the square of the diameter and the tensile stress developed on the diametral plane:

$$P \propto \sigma_t d^2 \tag{9}$$

And, in view of Eq. (8), the load causing the breakage of the particle is:

$$(P)_f \propto d^{-0.5} d^2 \propto d^{3/2} \tag{10}$$

For a very simple arrangement of spherical particles (Fig. 17) in a planar view, equilibrium implies:

$$\sigma_{ext} \cdot 1^2 = \sum P = P \frac{1}{d} \frac{1}{d} = \frac{P}{d^2} \tag{11}$$

and therefore:

$$P = d^2 \sigma_{ext} \tag{12}$$

Comparing Eqs. (10) and (12) it turns out that:

$$(\sigma_{ext})_f \propto d^{-0.5} \tag{13}$$

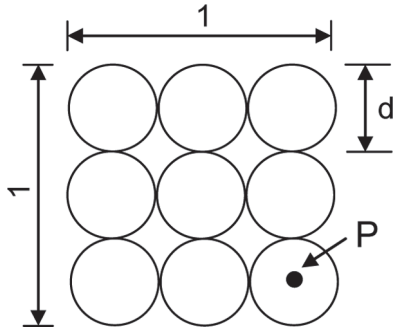

Figure 17. Simple arrangement of spheres. Planar view.

The external stress capable of breaking in tension particles of diameter d is inversely proportional to the square root of particle diameter. Given a stress intensity, the larger the particles, the easier its breakage. If experimental data relating tensile strength and particle diameter is the starting point, Eq. (13) becomes:

$$(\sigma_{ext})_f \propto d^{-\alpha} \tag{14}$$

where α varies between 0.3 and 0.5.

Eq. (14) is useful to analyze scale effects. Take, for instance, rockfill compressibility. If a linear stress-strain relationship is accepted, the compressibility coefficient $\underline{\lambda}$ is proportional to $\Delta\varepsilon / \Delta\sigma$. Therefore:

$$\underline{\lambda} \propto d^{\alpha} \tag{15}$$

If gravels of diameters d and d_0 are compared:

$$\underline{\lambda}^{d} = \underline{\lambda}^{d_0} \left(\frac{d}{d_0} \right)^{\alpha} \tag{16}$$

which provides a scaling law.

Figure 18.a shows some results of gravel compressibility. They were obtained in a 30 cm diameter oedometer for samples of uniform particle size (40–30 mm; 30–20 mm; 25–20 mm and 20–10 mm).

The linear compressibility coefficient (Fig. 18) depends on the particle size and, also, on the aggregate void ratio, either a loose sample ($e_0 = 0.947$) or a dense arrangement ($e_0 = 0.502$). If λ is scaled, following Eq. (16), taking d_0 as the minimum particle diameter tested, the size effect disappears, provided $\alpha = 0.5$ for the loose gravel and $\alpha = 0.33$ for the dense aggregate. Interestingly, the α coefficient and, therefore, the intensity of scale effects, depend on aggregate density.

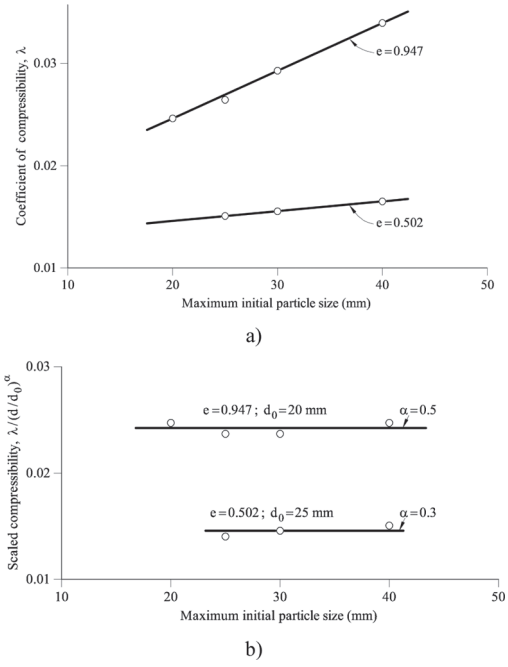

Figure 18. (a) Compressibility coefficient of limestone uniform gravels in terms of particle size (Ortega, 2008); (b) Corrected compressibility to include scale effects.

Frossard (2012) discusses scale effects in a similar manner. When strength is considered (Eq. 4) the scaling law (Eq. 16) is applied to both the shear stress and the confining stress. Therefore,

and

$$\frac{\tau_f}{(d/d_0)^{-\alpha}} = A_0 \left[\frac{\sigma}{(d/d_0)^{-\alpha}} \right]^{b} \tag{17}$$

$$\tau_f = A_0 \sigma^{b} \left(\frac{d}{d_0} \right)^{-\alpha(1-b)} \tag{18}$$

This relationship provides the strength of rockfill of particle size d if the strength envelope of a rockfill for a particle size d_0 ($\tau_{f_0} = A_0 \sigma^{b}$) is known. Frossard (2012) provides examples showing the accuracy of Eq. (18).

The discussion on scale effects becomes more complex if grain size distributions are not uniform. The simple relations previously mentioned will not hold. On the other hand, a full characterization of the rockfill would require a constitutive model developed in terms of few material parameters (and not only the rockfill compressibility or strength).

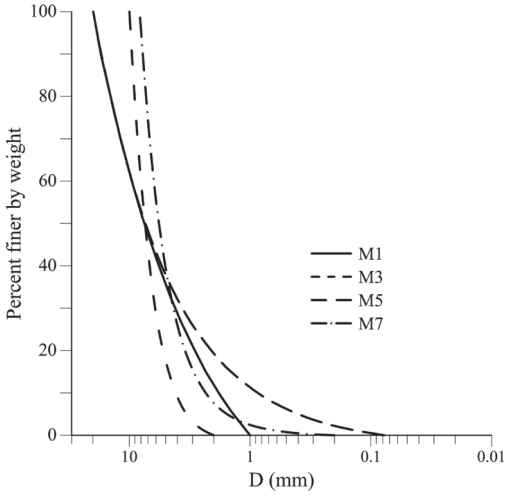

Figure 19. Grain size distributions tested by Ramon *et al.* (2008).

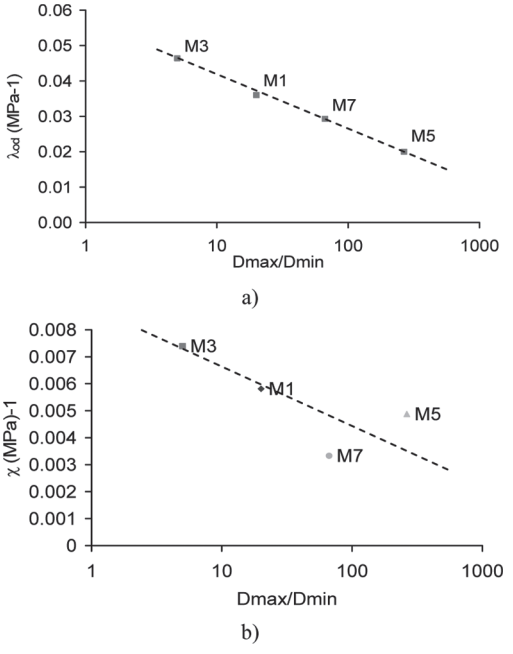

Figure 20. (a) Compressibility parameter λ^d_0 for oedometer tests; (b) Parameter χ Results plotted in terms of D_{max}/D_{min} (Ramon *et al.*, 2008).

However, if a suitable constitutive model is accepted, testing samples of different grain size distributions would provide relationships of constitutive parameter and some indices describing grain size distribution. This was the approach followed by Ramon *et al.* (2008). They report tests on Lechago gravel for the grain size distributions given in Figure 19. The distributions are characterized by a common D_{50} value and a variable fine's content. The constitutive model described in Alonso *et al.* (2005) was used for the analysis of test results. In this model, as explained in detail in a following section, the compressibility index is suction-dependent. Ramon *et al.* (2008) found that the parameters of the function which describes such dependency, λ^d_0 and χ, vary with the grain size distribution.

It was found that the best parameter to identify the influence of grain size distribution in this case was the index D_{max}/D_{min}. Tests were performed under suction control and collapse strains were also measured.

The compressibility parameter, λ^d_0 decreases continuously as D_{max}/D_{min} increases (Fig. 20.a). However, the elastic compressibility was not much affected by the same index. The delayed compressibility, λ^t, maintained in all cases a constant ratio with λ^d_0 and this condition defines the scale for the long term compressibility. The model parameter, χ, which describes the collapse intensity, decreased with the D_{max}/D_{min} coefficient in the manner indicated in Figure 20.b.

5 CONCEPTUAL MODEL BASED IN FRACTURE MECHANICS

5.1 *Basicconceptual model*

From the investigations at the UPC a conceptual model gradually evolved, which explains some of the observed features.

An elementary volume of rockfill contains a number of rock particles forming an arrangement. Studies with photoelastic discs first (De Josselin de Jong & Verruijt, 1969) and, later, with the distinct element method (Cundall & Strack, 1979), show that such particle arrangements transmit the external loads by chains of particles forming a sort of truss. Each individual particle receives forces at its contacts with the neighbouring particles. The magnitude and direction of those forces depends on the size of the particle, shape, number of contacts, relative position in the arrangement and, obviously, on the *macroscopic* stress state. Some particles carry large forces, while others remain idle. So the intensity of loads applied to particles varies in a wide range. This distribution of forces changes with the deformation of the rockfill element since the geometry of the truss is changed. Figure 21 sketches the idea. An isotropic macroscopic stress state is considered for simplicity.

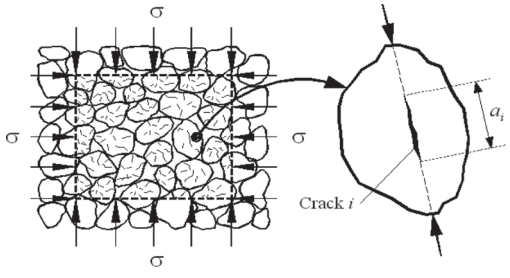

Figure 21. Sketch of elementary volume of rockfill and rockfill particles containing a crack which eventually propagates producing the breakage of the particle.

As stated in a previous section, each rockfill particle contains a (large) number of flaws, microcracks or cracks. Since, at the levels of stress and temperature bearing interest in civil engineering works, the behaviour of most rocks is nearly perfectly brittle, it is reasonable to expect that particles fail by propagation of one or more of those flaws. The particle body, away from the crack tips, remains elastic and hence, linear elastic fracture mechanics (LEFM) applies for the analysis of the propagation of those cracks. The stress at the crack tips of a particular crack can be described by means of the stress intensity factor, computed with Eq. (6).

The whole particle arrangement, with its particular geometry at a certain moment of the material history, can be considered as a single elastic body. With this idea in mind the stress across the crack plane can be thought to be proportional to the macroscopic stress. So, σ in Eq. (6) can be also viewed as the macroscopic stress if the corresponding proportionality constant is included in the factor, β.

The conceptual model for rockfill proposed by Oldecop & Alonso (2001), assumes that under an increasing macroscopic stress state, the rockfill element first deforms by particle rearrangement, involving slip and rotation of the particles in relation to their neighbours. At this stage, the external work is fully consumed in overcoming friction at particle contacts.

At some point of the deformation process, the granular arrangement becomes blocked, *i.e.* no further deformations can occur unless one or several particles undergo breakage. It was also hypothesised that, from there on, any further strain increment implies the breakage of a crack. So, strain increments occur in a stepwise fashion, although, since the number of cracks involved is large, the straining process is perceived as continuous.

5.2 *Conceptual model for time and suction dependent behaviour*

A fracture phenomenon called *stress corrosion* (Wiederhorn *et al.*, 1980; Freiman, 1984) is well suited to explain many of the observed features of rockfill behaviour. It pertains to a group of phenomena known with the generic name of *subcritical crack growth*, which makes reference to the fact that cracks may also propagate with stress intensity factor values lower than the fracture toughness. The difference in this case is that, instead of a sudden failure, propagation occurs in a gradual manner. The best known effect of subcritical crack growth mechanism is the fatigue due to repetition of small loading cycles.

In stress corrosion, a corrosive agent interacts with the stress state at the crack tip. It is the combined action of both factors that produces the propagation of the crack. Cracks are stress concentrators. At the crack tip, the strongly strained molecules of the substances composing the rock (being minerals or not) are more readily attacked by the corrosive agent than the rest of the material. At some stage of the corrosion reaction the newly formed compounds are weaker than the original substance. Hence they break under a stress state that that it is not enough make the crack to propagate in the original material. The crack growth exposes a new fresh tip and the process starts again.

The most ubiquitous corrosion agent in nature is water. Figure 22 illustrates a chemical model and the stoichiometry of the stress corrosion of amorphous silica by water. The *availability* of water for such chemical reaction can be measured (under some simplifying assumptions) by its chemical potential. Chemical potential is proportional to total suction (the proportionality factor being the molar volume) which in turn, under thermodynamic equilibrium, is univocally linked to relative humidity by the psicrometric relationship (Coussy, 1995).

In fact, the typical results of stress corrosion experiments show that the crack propagation velocity increases with a) the value of the stress intensity factor (*i.e.*, mechanical load) and b) the relative humidity in the environment surrounding the tested specimen or, alternatively, the *water concentration* if specimens are tested submerged in a liquid medium. In the latter case the medium is, typically, a mix of water and alcohol, being water the active corrosive agent and the alcohol the inert *solvent*. The typical results of stress corrosion experiments are illustrated in Figure 23.

Assuming it was possible to calculate the stress intensity factor for each crack contained in the rockfill elementary volume (by using Eq. 19), they could be ranked, along the horizontal axis of Figure 23.a. According to their value of K, they

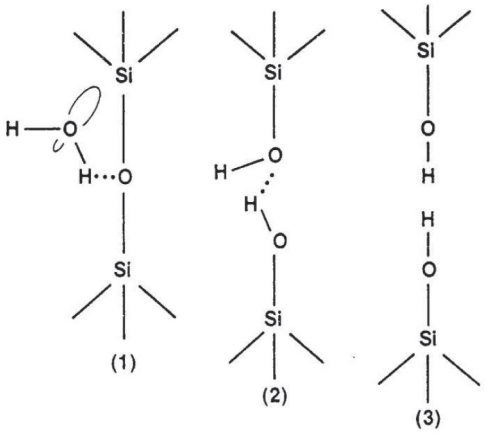

Figure 22. Chemical model and stoichiometry for stress corrosion reaction of amorphous silica (Michalse & Freiman, 1982). (1) Water reacts with the strained Si–O–Si bonds at the crack tip. (2) The reaction yields the activated complex $\chi^{\ddagger}$ which has weaker bonds than the original material. (3) Bonds are broken under the applied loads and the reaction products are Si–OH groups remaining on each crack surface.

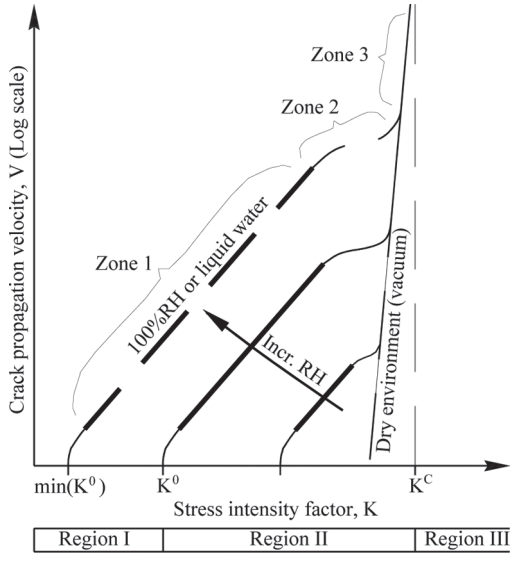

Figure 23. a) Scheme showing the typical shape of stress corrosion curves (Oldecop & Alonso, 2007).

would occupy one of the three regions indicated beneath horizontal axis. The boundaries of these regions are determined by the fracture toughness, K^C, and by the stress corrosion limit, K^0, a singular value of K under which the crack propagation velocity drops to cero.

Upon the application of a load (stress) increment the whole rank of cracks are shifted towards higher values of K. Those cracks which fall in region III cannot survive. They break immediately in a catastrophic manner, being its propagation velocity close to the sound velocity in the rock. As proposed in the model described in the previous section, each breakage is linked to a macroscopic strain increment of rockfill. Hence, cracks reaching region III are responsible for the instantaneous strain increment after load application. Once broken, these cracks disappear from the rank (and obviously from the material too), so in order to produce further strain increments more cracks have to be brought to region III.

In the other end, cracks in region I do not grow at all. Cracks lying in region II grow with a finite propagation velocity whose magnitude depends simultaneously on the stress intensity factor and the relative humidity or total suction. Looking at Eq. (19) it is evident that, under sustained loads, the growth of a crack (*i.e.*, the increase of parameter a) implies an increase in the stress intensity factor. Hence cracks in region II will tend to *travel* to the right, gradually increasing their propagation velocity until they reach the threshold of fracture toughness and break. The resulting succession of breakages is the basic mechanism producing the time-dependent strains observed in rockfill, its rate depending simultaneously on the stress level and water action (measured by total suction or relative humidity).

On the other hand, an increase in moisture under constant loads would cause the cracks of region II to increase their propagation rate, according to the new value of total suction attained. Macroscopically, this would be perceived as increase in the rate of macroscopic strain not linked to any stress change, *i.e.*, a collapse episode.

5.3 *Conceptual model for advanced features*

Atkinson (1984) gives a comprehensive compilation of stress corrosion data from minerals and rocks (Fig. 24). Among the mathematical models available for this phenomenon, Charles (1958) proposed the following simple equation:

$$V = V_0 \left(\frac{K}{K^C} \right)^n \tag{19}$$

In which V_0 and n are model parameters obtained from data fitting, usually done in a double-logarithmic plot. The slope n takes high values, typically in the range 20–200 (Fig. 24).

In order to explore the implications of the proposed conceptual model, Oldecop & Alonso (2007) developed a simplified numerical model of

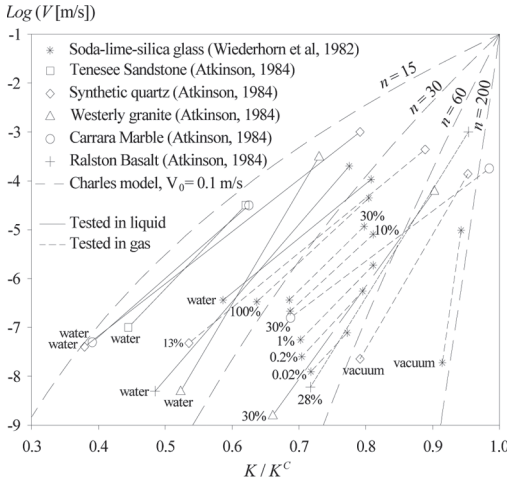

Figure 24. Stress corrosion curves of various rocks, quartz and glass. Testing condition indicated next to each curve: submerged in liquid water, air with controlled relative humidity (in%) or vacuum. Plots of Charles model for different *n*-values (Oldecop & Alonso, 2007).

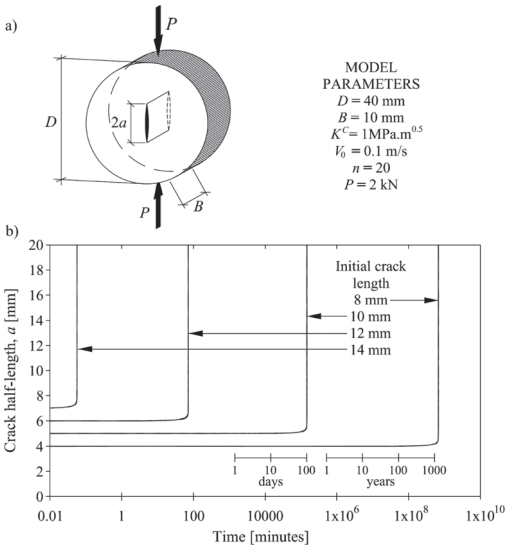

Figure 25. a) Scheme of numerical disc model. b) Model results.

a rockfill particle. The particle was simulated as a disc of rock, containing a crack going-through the thickness of the disc. The disc is loaded by two opposite forces and the crack is aligned with the loading direction (Fig. 25.a). The failure mode of the disc consists in the propagation of the crack by the tensile stresses produced by the external loads.

The simple geometry of the model allows computing the factor β by means of an analytical expression:

$$\beta = \frac{2}{\pi(1-\alpha)^2}(1-0.4964\alpha+1.5582\alpha^2 - 3.1818\alpha^3+10.0962\alpha^4 - 20.7782\alpha^5+20.1342\alpha^6 - 7.5067\alpha^7) \quad (20)$$

with $\alpha = 2a/D$. Hence the stress intensity factor can be computed by means of Eq. (6), for a given load and crack length. Knowing the stress intensity factor at any time of the failure process, it is possible to compute the instantaneous value of the crack propagation velocity with Eq. (19) provided that the material parameters K^C, V_0 and n are known for the disc material. By incremental integration, the crack growth history was computed for different crack lengths and constant load. The results are shown in Figure 25.b for a disc 40 mm in diameter, 10 mm wide under a constant 2 kN force, using average values of the material parameters.

The failure process involves two stages, a first one in which crack growth is remarkably slow and a second stage in which the propagation speeds up and failure is completed in a relatively short time. It was found (Oldecop & Alonso, 2007) that the survival time of a crack is nearly inversely proportional to its initial propagation rate and hence, through Eq. (19), also to its initial stress intensity factor raised to exponent n and, also, to the initial crack length raised to the power $n/2$ (through Eq. 6):

$$t \propto \frac{1}{V} \propto \frac{1}{K^n} \propto \frac{1}{a^{n/2}} \quad (21)$$

At first sight, a surprising fact arises from the previous expression. It appears that the survival time does not to depend on the size of the particle. The reason can be found in the two stage failure process. Along the first stage, the crack size remains small in relation to the particle dimensions. Its behaviour is close to a crack embedded in an infinite body, and the relative position of the body edges and the crack does not influence the stress intensity factor neither the propagation velocity. This means that factor β remains constant along the first stage of propagation. Under this hypothesis, Eq. (21) can be also obtained analytically (Oldecop & Alonso, 2007). The validity of Eq. (21), although it is approximate in nature, is owed to the fact that, for the range of survival times bearing interest for engineering applications (say 1 minute to 1000 years) the first stage of propagation always takes a major fraction of the whole failure process. The second stage, involving the approach of crack

tips to the particles edges, the rapid increase of factor β and, consequently, the relatively sudden development of failure, takes a minor fraction of the survival time.

Some additional interesting features arise from the disc numerical model. It is apparent from the results of the numerical model in Figure 25 that a relatively narrow range of initial crack sizes, namely 4 to 7 mm, give rise to an enormously wide range of survival times, namely 1 minute to 1000 years. This range widely covers the range of interest for civil engineering application. Moreover this feature can explain the fact of the apparently unbounded deformation process of rockfill, extending over decades with no apparent end.

Another interesting feature arises when considering smaller size particles, sand grains for instance. Since, obviously, they cannot contain cracks longer than the particle diameter; the survival time of the cracks existing in those smaller particles is such that it would appear that no particle breakage occurs under normal stress levels. It is only under very high stress levels (10–100 MPa) that particle breakage can be observed in sands (Yamamuro *et al.*, 1996).

Considering a rockfill oedometer specimen subjected to a certain vertical stress value, σ, a vertical strain increment can be obtained by two ways (Fig. 26.a). According to the experimental observations described before, if a stress increment $\Delta\sigma$ is applied, a strain increment $\Delta\varepsilon$ is obtained after a reference time t^r. As previously explained, the value of t^r is conventionally selected. The strain increment can be computed with:

$$\Delta\varepsilon = \varepsilon - \varepsilon^r = \int_{\sigma_0}^{\sigma_0+\Delta\sigma} \lambda(\sigma,\psi,t^r)\frac{d\sigma}{\sigma} \tag{22}$$

where the compressibility index depends on the stress and total suction applied and on the reference time chosen. For the straight portion of the compression curve (Fig. 3.b), the solution of Eq. (22) is:

$$\Delta\varepsilon = \varepsilon - \varepsilon^r = \lambda\, Ln\frac{\sigma+\Delta\sigma}{\sigma} \tag{23}$$

On the other hand, the same strain increment $\Delta\varepsilon$ can be achieved by holding the stress value σ and waiting an additional time $\Delta t = t - t^r$. Since we assume that each strain value attained is tied to the breakage of a particular crack r in the particle assemble (Fig. 26.b), a relationship between its initial stress intensity factor and its survival time can be established by means of Eq (21). Moreover, the

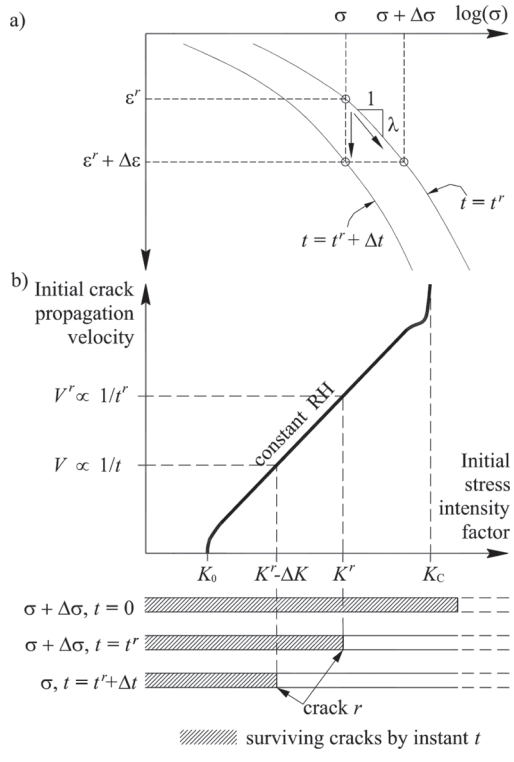

Figure 26. Conceptual link between time dependent compression and crack propagation. a) Stress-strain-time behavior. b) Survival times of cracks according to stress corrosion model.

stress intensity factor is proportional to the external stress. Hence:

$$\left(\frac{t}{t^r}\right)^{1/n} \cong \frac{K^r}{K^r - \Delta K} = \frac{\sigma+\Delta\sigma}{\sigma} \tag{24}$$

Combining Eqs. (21) and (24):

$$\varepsilon \cong \frac{\lambda}{n}\, Ln\frac{t}{t^r} + \varepsilon^r \tag{25}$$

Comparing Eq. (25) with Eq. (2), the constant ratio between the time-dependent compressibility index and

$$\frac{\lambda^t}{\lambda} = \frac{C_\alpha}{C_C} \cong \frac{1}{n} = ctn. = \frac{1}{(20 \div 200)} \tag{26}$$

Oldecop & Alonso (2007) also demonstrated that the same relationship approximately holds for the initial curved part of the compression curve.

This derivation provides an explanation for the experimental behaviour shown in Figure 5. As shown in Figure 24, the range of typical values of n for different rocks is 20 ÷ 200 (Atkinson, 1984). Forty five degrees sloping lines were drawn in Figure 5, marking the boundaries of this range. The experimental data from oedometer tests of Lechago Slate and Garraf Limestone rockfill specimens fit reasonably well within this range, which also encompass the experimental data published by Mesri *et al*. (1990).

It is also worth noting in Figure 5 the case of specimens in a very dry state. Tested materials, when subjected to high suction values (250–300 MPa) depart significantly from the bulk of data. This feature can also be explained within the theoretical framework developed. In a very dry state, water is no longer able to reach the propagating tip of the crack and hence the phenomenon turns to be non-dependent of water presence. This fact can be deduced from the scheme in Figure 23. Stress corrosion experiments in vacuum, which is in fact a very dry environment, result in n-values close to the upper boundary of the typical range (Fig. 24). A value of $n = 200$ seems quite consistent with the oedometer data reported in Figure 5.

6 CONSTITUTIVE MODELS FOR ROCKFILL

Oldecop & Alonso (2001) developed an elastoplastic constitutive model for rockfill taking into account the influence of water in its mechanical behaviour. The model was limited to compression stress states, *i.e.* oedometric or isotropic compression, seizing some features of the BBM (Alonso *et al*., 1990). However, it was realized that the influence of suction is of a completely different nature in rockfill if compared with soils. In fact, the relevant variables in rockfill are stress and total suction (instead of matric suction), the later serving as a measure of the chemical potential of water which, in turn, controls the rate of the stress corrosion reaction.

Figure 27 displays the basic features of the model. Under moderate strain levels (up to 8% in oedometric compression of Lechago Slate rockfill), the stress-strain relationship of many granular materials is observed to be nearly linear. Hence, as shown in Figure 27b, a linear compressibility index was defined as $\underline{\lambda} = d\varepsilon/d\sigma$ (unlike the usual $\underline{\lambda} = \sigma d\varepsilon/d\sigma$).

The compressibility index was split in two components:

$$\underline{\lambda} = \underline{\lambda}^i + \underline{\lambda}^d(\psi) \tag{27}$$

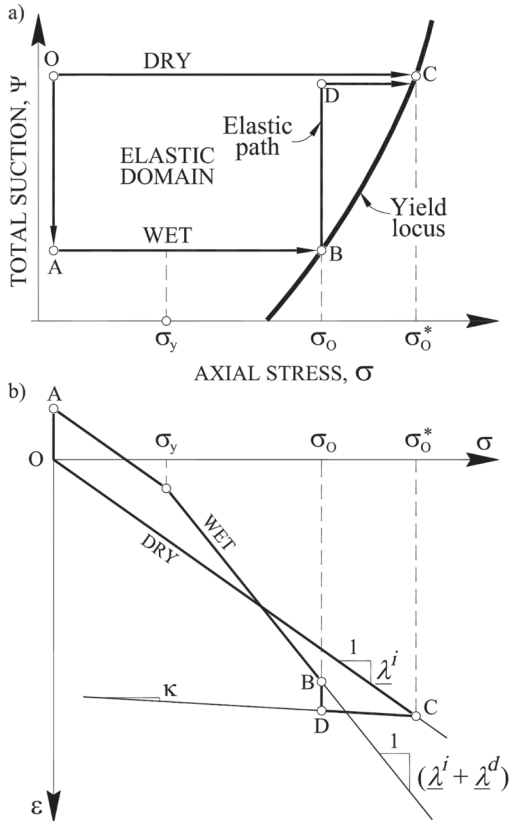

Figure 27. Basic features of the elastoplastic model for rockfill subjected to isotropic or oedometric compression (Oldecop & Alonso, 2001). a) Yield surface formulated in the stress-total suction space. b) Total suction—dependent stress-strain behaviour.

$\underline{\lambda}^i$ is constant (a model parameter) and serves as a low limit under very dry states in which no water influence is expected. $\underline{\lambda}^d$ is the suction-dependent component given by:

$$\underline{\lambda}^d(\psi) = \underline{\lambda}_0^d - \alpha_\psi \, Ln\left(\frac{\psi + p_{atm}}{p_{atm}}\right); \quad \underline{\lambda}^d(\psi) \geq 0 \tag{28}$$

$\underline{\lambda}^i + \underline{\lambda}_0^d$ is the compressibility index measured for saturated specimens. α_ψ is given by:

$$\alpha_\psi = \frac{\chi_\psi + \kappa_\psi}{\sigma_0 - \sigma_y} \tag{29}$$

The parameter χ_ψ is rate of increment of collapse strain with the logarithm of suction decrement. It can be measured along a wetting path under a constant stress value σ_0, as shown in Figure 28.

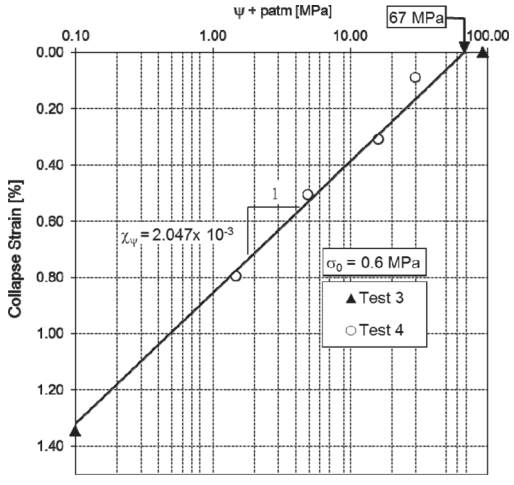

Figure 28. Collapse strains measured in Lechago slate rockfill specimens along a wetting path under constant stress (Oldecop & Alonso, 2001).

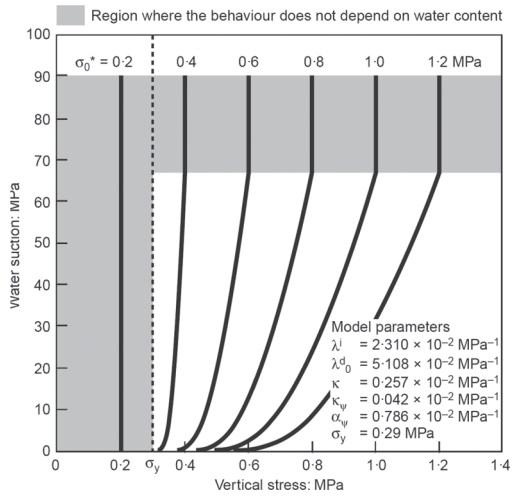

Figure 29. Yield surface of the compression model, plotted for different values of the hardening parameter σ_0^* (Oldecop & Alonso, 2001).

The stress σ_y is a threshold value under which no suction dependency is perceived (Fig. 27b). Moreover, under low stress levels, a moderate heave due to wetting was systematically measured in Lechago slate specimens It was always of minor influence and moreover it was not detected in other materials such as Garraf Limestone. However a recoverable ("elastic") heave component was included in the model by means of the index $\kappa_\psi = \psi\, d\varepsilon/d\psi$. A elastic strain component due to stress changes is also considered through the index $\kappa = d\varepsilon/d\sigma$.

The equation of the yield surface is obtained by equating the strain increments computed along the alternative paths OC and OABDC, depicted in the scheme of Figure 27.a:

$$F(\sigma,\psi) = \sigma_0[\lambda^i + \lambda^d(\psi) - \kappa] - \sigma_y \lambda^d(\psi) - \sigma_0^*(\lambda^i - \kappa) = 0 \qquad (30)$$

where σ_0^* is the hardening parameter. Figure 29 shows the shape of the yield surface for a given set of model parameters fitted to the experimental results obtained with Lechago slate. Yield curves in Figure 29 serve to explain the intimate relation between loading at a given total suction and collapse. Therefore, isotropic yield stress in rockfill is also described by an "LC" type of yield curves, as in unsaturated soils.

The hardening law is based on the increment of the plastic volumetric strain, $d\varepsilon^p$:

$$d\sigma_0^* = \frac{d\varepsilon^p}{(\lambda^i - \kappa)} \qquad (31)$$

By introducing minor changes Oldecop & Alonso (2003) extended the model described to the high strain stage, were the compression curves are no longer linear (but a linear strain-log stress holds). Figure 30 compares the model performance with experimental results.

Chávez & Alonso (2003) describe a complete elastoplastic model for triaxial stress states. It includes particle breakage and relative humidity effects, Yielding is described by an isotropic surface and a deviatoric one. The model adopts, as a starting point, the formulation proposed by Wood *et al.* (1994), which is able to describe in a simple manner a strain softening behaviour. The model introduces a state parameter, namely an effective plastic work accumulated by the sample. The effective plastic work is defined as the difference between total plastic work and the work dissipated in particle rearrangements. It was found that the effective plastic work could be related to particle breakage and also to some material parameters. Figure 31 shows the good agreement between model calculations and some triaxial tests performed on a compacted sample of Lechago slate and tested at RH = 36%, RH = 92%, and RH = 100% (sample flooded). Peak strength envelopes (Fig. 32) follow a nonlinear law, controlled by relative humidity.

Particle breakage was measured in the RH-controlled triaxial tests performed by Chávez (2004). The plot in Figure 33 shows the evolution of the Hardin and Marsal breakage parameters in triaxial tests performed under RH = 36% and RH = 100%. In the figure, breakage parameters are

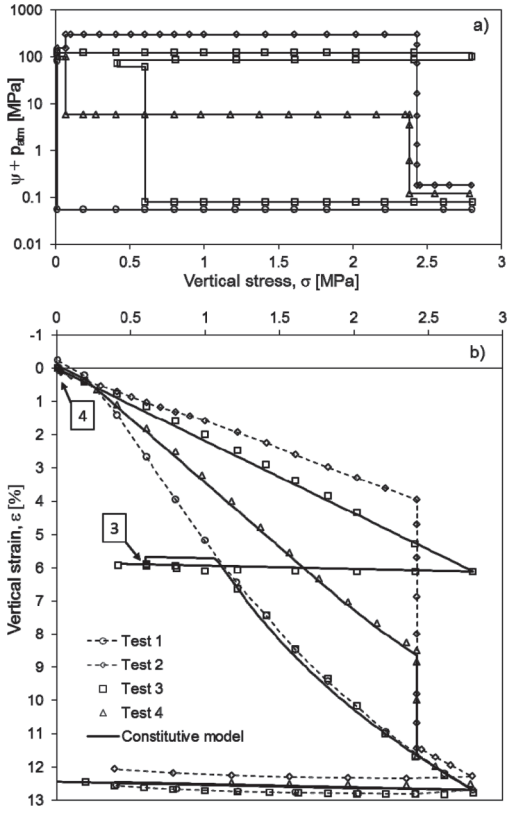

Figure 30. Oedometer tests of Lechago Slate rockfill (Oldecop & Alonso, 2003) (a) Loading paths in the stress–suction space. (b) Vertical stress against measured vertical strain. Square-enclosed numbers indicate flooding of the corresponding specimen. Constitutive model parameters obtained from Tests 1 and 2. Constitutive model performance is capered to the experimental data for tests 3 and 4.

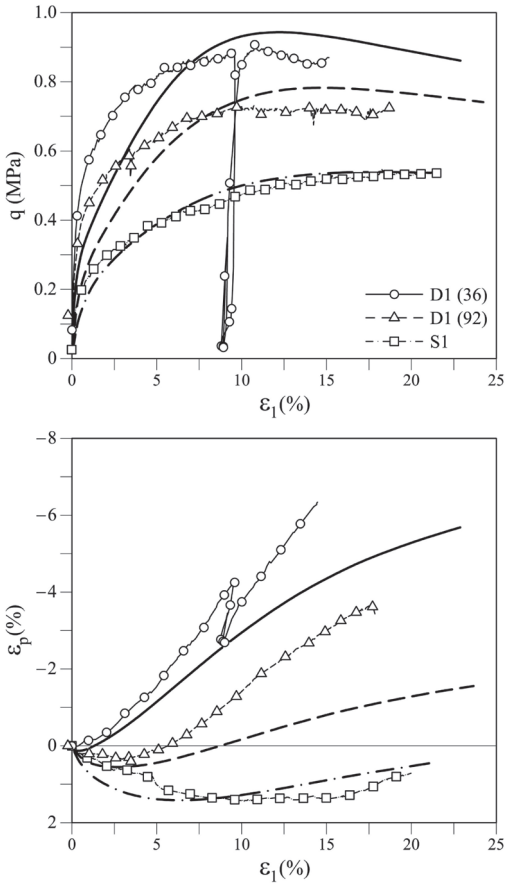

Figure 31. Triaxial test results of samples Pancrudo gravel for two relative humidities and for saturated conditions. Confining stress: 0.1 MPa. Comparison with model predictions (smooth lines) (Chávez & Alonso, 2003).

plotted against the confining stress of the triaxial test. The value measured for $\sigma_3 = 0$ indicates the effect of compaction on particle breakage (samples were compacted to an energy equivalent to standard Proctor).

Dilatancy and its modelling have been found to be a difficult task. One reason is the difficulty to find a critical state in most of the tests performed. Samples exhibit a positive dilatancy rate at the end of the test, when vertical deformations reach high values (around 20%). As in "regular" soils, suction contributes to maintain higher void ratios and stress ratios for a given confining stress. In the tests reported by Chávez *et al.* (2009) on the crushable Lechago slate a reasonable critical state could be found for the sample volume at the end of the applied shearing stage (Fig. 34). However, in the tougher limestone gravel tested by Ortega (2008) critical state conditions were far from being reached at the end of tests.

Alonso *et al.* (2007) provide a discussion of the dilatancy observed in those tests and develop a dilatancy rule, which seems to capture observations. It was concluded that dilatancy rules of the type:

$$d = f\left(\eta, \frac{W^p}{p}, s\right) \tag{32}$$

in which $d = d\varepsilon_v^p / d\varepsilon_s^p$; η is the stress ratio (q/p), W^p is the plastic work, and s the suction provides a satisfactory simulation of measured dilatancy records.

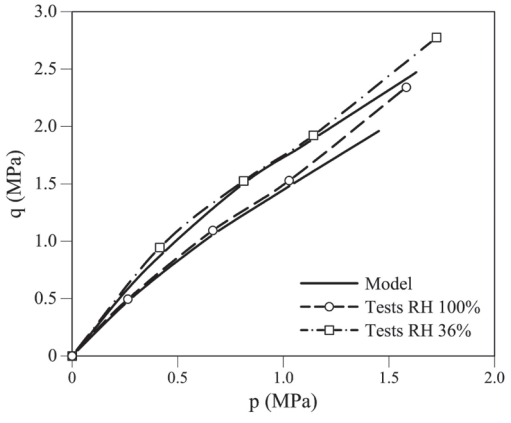

Figure 32. Triaxial strength of samples Pancrudo gravel for two relative humidities (36% and 100%). Comparison with model predictions (smooth lines) (Chávez & Alonso, 2003).

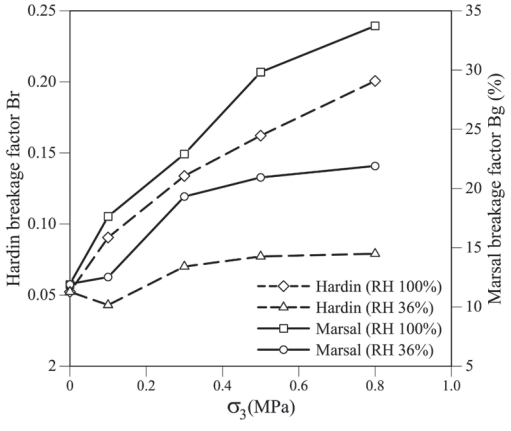

Figure 33. Evolution of Hardin and Marsal breakage parameters in suction controlled triaxial tests of compacted Pancrudo slate. (Chávez & Alonso, 2003).

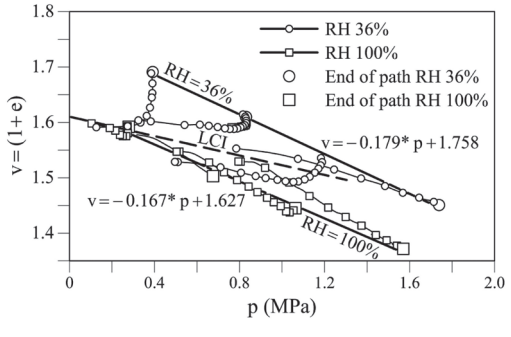

Figure 34. Evolution of void ratio on drained triaxial tests on compacted Pancrudo slate. Straight lines are approximate locus for Critical State conditions at two values of Relative Humidity (36% and 100%) (Chávez & Alonso, 2003).

7 DEM MODELLING

An alternative approach to phenomenological modelling is to develop a numerical analysis following the Distinct Element Method (DEM) (Cundall & Strack, 1979). To be accurate, the model should:

– Approximate realistically the shape of particles
– Simulate particle breakage following a criterion consistent with observations
– Include Relative Humidity and time effects

In the remaining of this section an account of some developments concerning the application of DEM to rockfill modelling will be given. The reported results are part of an ongoing research whose ultimate objective is the development of a virtual laboratory for the investigation of the constitutive behaviour of rockfill. Eventually, the model may be directly used in the analysis of some geotechnical structures.

The computer code PFC3D (Itasca, 2008) offers the possibility of programming the kernel code to simulate a variety of phenomena. The "clump" logic, built into the program, was used to create (macro) particle shapes by aggregating spherical (micro) particles.

This is illustrated in Figure 35. Pyramidal particle shapes integrated by 14 spheres were adopted as the starting geometry of the numerical tests described below.

Once rupture conditions are met, the particles divide following the "logic":

$$14 \rightarrow 8+6;\ 8 \rightarrow 4+4;\ 6 \rightarrow 3+3;\ 4 \rightarrow 2+2;\ 2 \rightarrow 1+1 \quad (33)$$

Note that this logic simulates a "major" breakage and excludes contact crushing.

Oedometer and triaxial tests on groups of particles, randomly oriented, having a given critical porosity have been performed. Figure 36 shows the triaxial sample (height: 50 cm; diameter: 25 cm; initial uniform particle size: 3 cm). The model requires the specification of the normal and shear stiffness of particle contacts and its friction coefficient (values of 0.93, 0.5 and 0.3 were investigated).

7.1 *Partile breakage criteria*

The procedure to simulate particle breakage requires solving the following issues:

– Stress calculations in macro particles
– Failure criteria for macro particles
– Division of macro particles

Stresses are defined for a representative elementary volume (REV). The REV in our case is the macro particle. The expression derived by

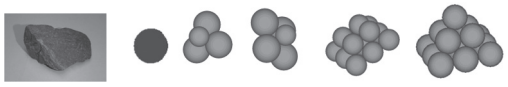

Figure 35. Rockfill macroparticle. Real and clump models of 1, 4, 5, 13 and 14 microparticles.

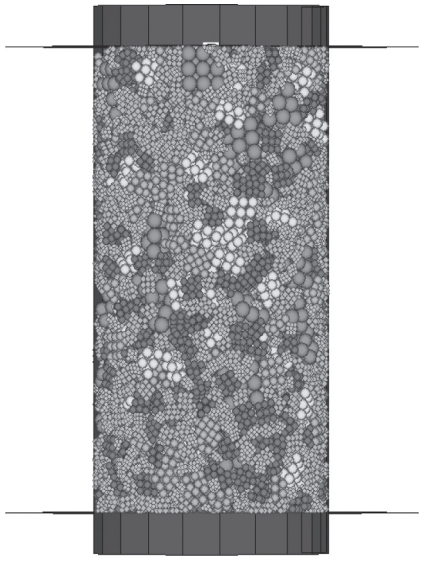

Figure 36. Sample for the simulated triaxial test (Alonso *et al*., 2011).

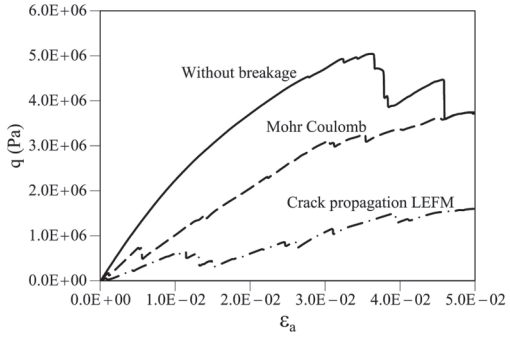

Figure 37. Breakage criteria effect on deviatoric behaviour. Comparison among different criteria: No breakage; crack propagation based on LEFM and Mohr Coulomb. Sample of 100 macroparticles using clumps of 13 microparticles. Confining stress: 0.5 MPa (Alonso *et al*., 2011).

Alonso-Marroquin & Herrman (2005) was used to calculate the stress tensor. Then, principal stresses are derived.

The adopted failure criterion follows fracture mechanic concepts. A defect (crack) of random size is assigned to each macro particle. Different Probability Density Functions (PDF) of defect size were tested. The PDF is related to particle size by limiting the maximum defect size to half the equivalent diameter of each macro particle.

The calculation, which is essentially of a dynamic nature, develops in time. For every time the calculated stress intensity factor is compared with rock toughness. K is calculated for the minor principal stress, provided it is a tensile stress. When $K \geq K_c$, the fissure propagates catastrophically and the particle breaks.

However, subcritical crack propagation is also possible. Atkinson (1984) and Oldecop & Alonso (2001; 2007) describe the fundamentals: subcritical propagation includes the effects of suction and time.

7.2 *Simulated triaxial behaviour*

The capabilities of the outlined model are illustrated by a few examples that explore several effects:

a) Breakage criteria
b) Particle shape
c) Porosity
d) Toughness
e) Friction coefficient
f) Relative humidity

a) The effect of breakage criteria (no breakage, a Mohr-Coulomb criterion and the criterion based on crack propagation) are shown in Figure. 37. It is clear that breakage was a major effect on stress-strain behaviour. Particle breakage leads to a reduction of peak strength and sample stiffness.
b) Particle shape is illustrated in Figure 38. The pyramidal 14 particle shape leads to the highest great strength. Planar or spherical shapes result in significant reductions in strength.
c) Two porosities were tested (n = 51%; n = 61%) (Fig. 39). Peak strength was found similar probably a consequence of particle breakage but there was a clear effect on stiffness.
d) Four toughness values were compared in Figure 40. In all cases n = 51% and σ_3 = 1 MPa. Toughness controls the peak strength and has a more limited effect on residual strength. Dilatancy changes also with particle toughness. The lower K_c, the larger the number of particles broken during the test and the lower the calculated dilatancy.
e) Friction between particles has a very distinct effect on the deviatoric behaviour (Fig. 41). Three friction angles (43°, 27° and 17°) were tested. The two higher contact friction angles led to a "peak" strength followed by residual conditions for vertical deformations in excess of 15%. The low friction material resulted in a ductile behaviour.

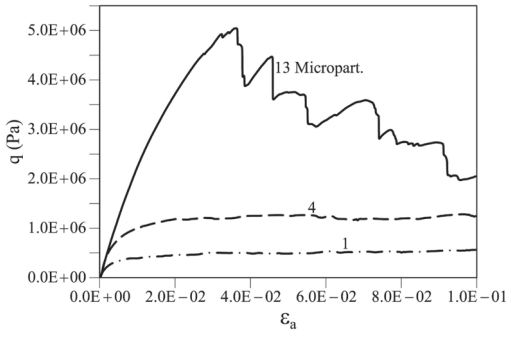

Figure 38. Shape effects. Results of numerical simulation of triaxial test using macroparticles of 1, 4, and 13 microparticles. Confining stress 0.5 MPa (Alonso *et al.*, 2011).

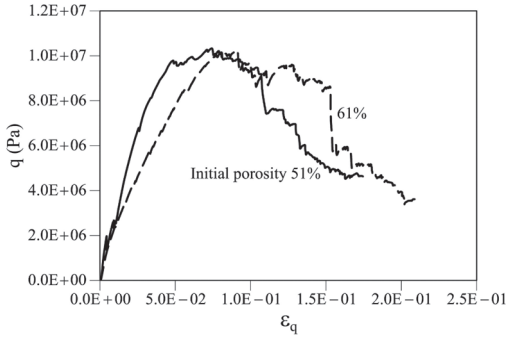

Figure 39. Initial porosity effect. Comparison between two different initial porosities, 51% y 61%. Confining stress 1.0 MPa. Sample of 1000 clumps of 14 microparticles (Alonso *et al.*, 2011).

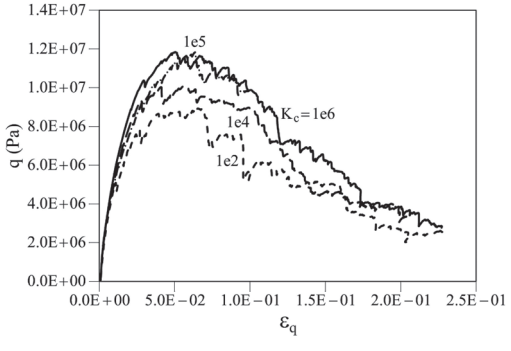

Figure 40. Effect of macroparticle toughness on deviatoric behaviour. Comparison among four different macro-thougness (1e6, 1e5, 1e4, 1e2 Pa√m). Sample of 1000 macroparticles using clumps of 14 microparticles . Confining stress: 1.0 MPa. Initial porosity: 51% (Alonso *et al.*, 2011).

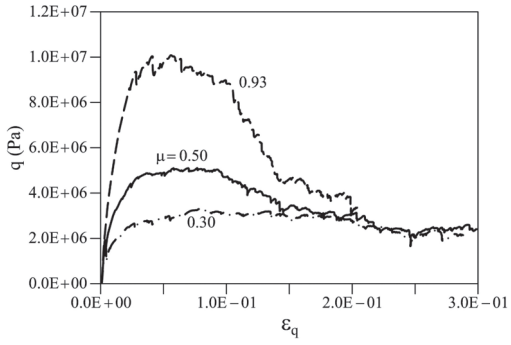

Figure 41. Friction coefficient effect on deviatoric behaviour. Comparison among three friction coefficients (0.93, 0.50, 0.30). Sample of 1000 macroparticles using clumps of 14 microparticles. Confining stress: 1.0 MPa. Initial porosity: 51% (Alonso *et al.*, 2011).

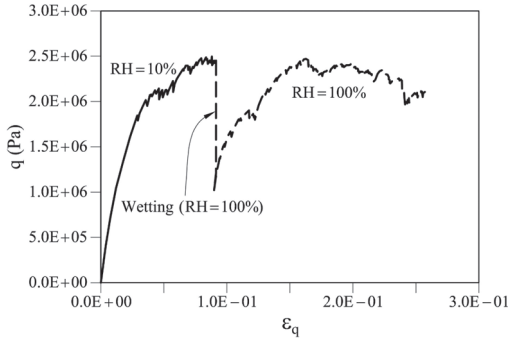

Figure 42. Effect of full wetting of a sample initially loaded ata constant Relative Humidity of 10%.

f) Relative humidity effects were introduced by simulating the crack propagation velocity, which depends on relative humidity. Crack propagation velocity is described by means of a modified Charles law (Eq. 19), in which parameter V_0 is a reference velocity and n is an exponent that depends on relative humidity. A plot of experimental results relating crack propagation velocity against (K/K_c) for different humidity conditions allowed the derivation of an approximate linear relationship:

$$n = 200 - 175(RH) \tag{34}$$

between the exponent n and relative humidity (in a 0–1 scale). The calculation proceeds as follows: For a given time increment Δt, the calculated velocity (Eq. A.5) allows the determination of the incremented crack length $(a + da)$. A particle is assumed to be broken when the updated a value reaches the average particle dimension.

The test simulated in Figure 42 reproduces one of the triaxial tests on hard limestone gravel reported by Ortega (2008). The specimen loaded at a constant axial strain rate and flooded at a particular strain, experiences a collapse of the structure due to the breakage of some particles. The deviatoric stress drops to a new equilibrium state. Upon further straining the sample reacts with an increasing deviatoric stress and it will eventually reach a strength associated with the condition $RH = 100\%$. The sudden wetting results in a sudden breakage of grains and in a sudden decrease in porosity.

The examples shown provide an overview of the model performance. In a paper submitted to the conference, Tapias *et al.* (2013) investigate the scale effects in short and long term compressibility. The model, to be useful in practice, requires a calibration against actual experimental results.

8 CONCLUDING REMARKS

The behaviour of coarse granular materials and rockfill requires, for a proper understanding, a wider framework: the framework offered by Unsaturated Soil Mechanics. In this way a more equilibrated and comprehensible view of the developments described in this paper may emerge.

In this regard, it is useful to recall the recent history of development. After a long period dominated by empiricism, a systematic research into the mechanics of unsaturated soil started in the 80's of 20th century. It could be interpreted, when reading some of the papers published, that a unique theory could be found to solve and explain, in a satisfactory and complete manner, the effect of lack of saturation. Research centered in the pursuit of a theoretical paradigm for understanding the effect of the simultaneous presence of air and water in soil pores.

However, the scenario which progressively unfolded turned out to be more complex and rich in nuances than originally suspected. In the 90's increasing attention was given to the microstructure of soils, typically through the investigation of the pore size distribution. If air and water occupies the pores it was a logical step, thinking in terms of capillary forces, to pay special attention to the distribution of water and to the role of pore families in explaining the overall effect of suction. The attention to microstructure is currently one of the active lines of research in unsaturated soils.

Laboratory research has often been directed to a limited class of soils: low plasticity clays and silts. These are materials where capillary concepts seem to apply and their permeability is high enough to allow reasonable times in suction controlled drained tests. These soils are often artificially manufactured by mixing dry powder with water and statically compacting the mixture at a high void ratio to ensure a measurable and consistent response of the soil to stress and suction changes. This trend left outside the mainstream of research the natural soils and the compacted materials used in practice, including gravelly materials and rockfill, as well as compacted "soils" derived from soft rocks, such as marls.

The sensitivity of coarse granular soils to water action was known well before theories explaining the mechanisms were available. Particle breakage was soon identified as a relevant mechanism. Interestingly the concept of water energy or suction was the link between these two observations.

The fundamental mechanisms of deformation of an extremely wide range of materials ranging from high plasticity expansive clays, natural or compacted, to rockfill make it very unlikely that a unique constitutive framework could be devised, just focusing in the condition of lack of saturation. Attention should be given to the physical deformation mechanisms at the pore of particle scale even if the ultimate objective is to find "large scale" or macroscopic stress-strain laws applicable in engineering practice.

Consider in Figure 43 a list of soils arranged in terms of particle size:

- The particle size of gravels and rockfill varies approximately between two extreme sizes: 1 cm and 1 m. Their deformation is dominated by particle breakage and also by the re-arrangement of the granular structure. Particle breakage is explained by fracture propagation within the grains or rock fragments. Breakage is possible because the grain size results in a low number of contacts per unit area or per unit volume. The weight of these granular aggregates depends on their density and on their total porosity, magnitudes which are largely independent of grain size. As a result contact forces among grains of an accumulation of grains (*i.e.*, an embankment) increase with the size of grains. Contact forces are high enough to let the stress intensity factor inside the grains to approach the rock or grain mineral toughness. This facilitates the propagation of fissures, whose rate of growth is proportional to the relative humidity. Therefore total suction is controlling particle breakage and its associated manifestations, namely collapse behaviour and "creep" deformation.
- Sands span the particle size range $10^{1} - 10^{-1}$ mm. The number of contacts per unit volume now increases substantially, for a given reference total stress. Conceptually, this is a scaled material if compared with rockfill but their behaviour is different because the stress intensity factor of their

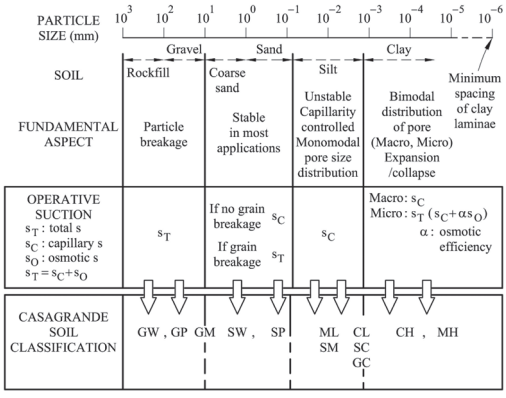

Figure 43. Operative suction in unsaturated soils.

particles is now far from approaching the grain mineral toughness. Particle breakage becomes irrelevant in typical engineering applications. RH of the atmosphere in pores becomes also irrelevant. However, if grain size decrease to the smaller size (say, fine sands) capillary forces between grains may approach the (small) contact forces between grains associated with self weight or external loading. Then capillary forces, linked to capillary suction, become progressively relevant. In silts (particle sizes varying between 8.10^{-2} and 2.10^{-3} mm), capillary forces become more relevant because contact forces induced by external stresses or weight decrease continuously with decreasing particle size. Microstructure continues to be simple (monomodal pore size distributions) and capillary suction remains as the operative suction.

– The transit to clay soils implies a fundamental change. Bi-modal pore size distributions are common. The two dominant pore sizes (in short, "macro" and "micro") are separated by several orders of magnitude. Capillary suction is useful to understand the macro response but the central role of surface tension in capillary suction loses its relevance when examining the physico-chemical phenomena explaining the adsorption of water by the clay crystal surfaces. However, the reduced space between clay particles, stacked together in aggregates, suggests that clay aggregates may act as semi-permeable membranes in contact with the "free" water occupying the macroporosity. This explanation and some experimental results suggest that total suction controls the clay aggregate deformations. Having in mind the imperfect nature of the semipermeable "membranes" bounding the aggregates, only part of the osmotic suction will contribute to the total suction explaining the clay mechanical behaviour. We may introduce the concept of efficiency of the osmotic component. Then a more complex situation comes out: capillary suction will control the deformations of the macrostructure and total suction, with a reduced osmotic component, will explain the deformations of aggregates (micro deformations). RH is again relevant in clayey soils.

Particle size is far of giving precise information of real soils. Soil classification is an alternative. Figure 43 includes a proposal to relate operative suction with soils defined by means of the Casagrande classification. Some soils are easily placed in the plot. Others occupy transition positions. Among them, the clays of low to medium plasticity and the silt-clay or even clay-gravel mixtures often found as natural or compacted soils. Figure 43 does not cover all soils of interest in geotechnical applications. Cemented soils are widely distributed. This is the case of loess and alluvial soils in arid environments, residual soils and tropical soils. They are often unsaturated. Soft clayey rocks are also common in practice. Before quarrying them they are low porosity materials of varying cementation. Degradation in the presence of atmospheric actions may be approached with the tools offered by unsaturated soil mechanics. When compacted, they exhibit properties similar to the described behaviour of rockfill, when the prevailing suction is high, but they become a "true" plastic soil when suction is low (Cardoso *et al*., 2012).

The soil groups identified previously require specific constitutive models because of the identified deformation mechanisms but, also, because of the nature and role of the water suction. The link among all of the mentioned soil classes may perhaps be found in the concept of the "Loading Collapse" or LC yield locus. This idea, whose origin is traced to the simple BBM model, is also present in the models described here for rockfill. Even if the underlying mechanisms (particle breakage or capillary contact forces) are widely different, the fact is that loading and collapse phenomena are directly linked in both cases.

ACKNOWLEDGEMENTS

Authors gratefully acknowledge the sponsorship received from the European Community through the Programme 'People' as part of the International Research Staff Exchange Scheme Project Geo-Excel (PIRSES-GA-2008-230860).

REFERENCES

Alonso, E.E., Gens A., and Josa, A. (1990). A constitutive model for partially saturated soils. Géotechnique, 40(3): 405–30.

Alonso, E.E., Olivella, S., and Pinyol, N. (2005). A review of Beliche Dam. Géotechnique, 55(4): 267–285.

Alonso, E.E., Ortega, E.F., and Romero, E. (2007). Dilatancy of Coarse Granular Aggregates, Experimental Unsaturated Soil Mechanics, T. Schanz ed., Springer, Berlin, pp. 119–135.

Alonso, E.E., Tapias, M., and Gili, J. (2011). Simulating particle breakage and relative humidity effects in rockfill behaviour. Proc. 2nd International Symposium on Computational Geomechanics (ComGeo II). Dubrovnik (Croatia), 27-29/04/2011.

Alonso-Marroquín, F., and Herrmann, H.J. (2005). "The incremental response of soils. An investigation using a discrete-element model". Journal of Engineering Mathematics, Vol. 52, 11–34.

Atkinson, B.K. (1984). Subcritical crack growth in geological materials. J. Geophysical Research 89, No. B6, 4077–4114.

Bauman, P. (1960). Rockfill dams: Cogswell and San Gabriel Dams. Transactions of the ASCE, 125 part 2, 29–57.

Cardoso, R, Maranha das Neves, E., and Alonso, E.E. (2012). Experimental behaviour of compacted marls. Géotechnique, 62, In print.

Charles, R.J. (1958). Static fatigue of glass. Journal of Applied Physics, 29: 1549–1560.

Charles, J.A. (1989). Geotechnical properties of coarse grained soils. Proc. of the 12th Int Conf on Soil Mechanics and Foundation Engineering, General Report, Discussion Session 8, 2495–2519.

Charles, J.A. (1991). Laboratory compression tests and the deformation of rockfill structures. Advances in Rockfill Structures. NATO ASI Series E, 200: 73–95.

Charles J.A. and Watts K.S. (1980). "The influence of confining pressure on the shear strength of compacted rockfill". Géotechnique, 4(3): 353–398.

Chávez, C. and Alonso, E.E. (2003). "A constitutive model for crushed granular aggregates which includes suction effects". Soils and Foundations, Vol. 43, No. 4: 215–227.

Chávez, C. (2004). "Estudio del Comportamiento Triaxial de Materiales Granulares de Tamaño Medio con Énfasis en la Influenciade la Succión" PhD Thesis, Universitat Politècnica de Catalunya, Spain.

Chávez, C., Romero, E. and Alonso, E.E. (2009). A Rockfill Triaxial Cell with Suction Control. Geotechnical Testing Journal, Vol. 32, No. 3.

Clements, R.P. (1981). The deformation of rockfill: interparticle behaviour, bulk properties and behaviour in dams. PhD. Thesis, Faculty of Engineering, King's College, London University.

Coussy, O. (1995). Mechanics of porous continua. John Wiley & Sons Ltd., Chichester.

Cundall, P.A. and Strack, O.D.L. (1979). A discrete numerical model for granular assemblies. Géotechnique, 29(1): 47–65.

Dawson, R.F., Morgenstern, N.R. and Stokes, A.W. (1998). Liquefaction flowsides in rock mountain coal mine waste dumps. Canadian Journal of Geotechnical Engineering, 35: 328–343.

De Josselin de Jong, G. and Verruijt, A. (1969). Etude photo-elastique d'un empilement de disques. Cah. Grpe fr.Etud. RhPol., 2: 73−86.

De Mello, V.F.B. (1977). "Seventh Rankine Lecture: Reflections on design decisions of practical significance to embankment dams". Géotechnique, 27(3): 279–356.

Freiman, S.W. (1984). Effects of chemical environments on slow crack growth in glasses and ceramics. Journal of Geophysical Research 89, No. B6, 4072–4076.

Frossard, E., Hu, W., Dano, C. and Hicher, P.-Y. (2012). Rockfill shear strength evaluation: a rational method based on size effects. Géotechnique, 62(5): 415–427.

Fumagalli, E. (1969). Tests on cohesionless materials for rockfill dams. J. Soil Mech. Found. Engng Div., ASCE, 95(SM1): 313−330.

Indraratna, I., Wijewardena, L.S. S. and Balasubramaniam, A.S. (1993). Large-Scale Triaxial Testing of Greywacke Rockfill, Géotechnique, Vol. 43, No. 1, pp. 37–51.

Itasca, (2008). Manuals of PFC3D v.4.0: Theory and Background, Fourth Edition, Itasca Consulting Group Inc, US.

Lee, D.M. (1992). The angles of friction of granular fills. Ph.D. dissertation, University of Cambridge.

Marachi, N.D., Chan, C.K., Seed, H.B. and Duncan, J.M. (1969). Strength and deformation characteristics of rockfill mater*ials*, *Department of Civil Engineering, Report No. TE-69-5*. University of California.

Marsal, R.J. (1973). Mechanical properties of rockfill. Embankment Dam Engineering. Casagrande Volume. Hirschfeld, R.C. & Poulos, S.J., eds., John Wiley & Sons.

Marsal, R.J., Arellano, L.R., Guzmán, M.A. and Adame, H. (1976). *El Infiernillo. Behavior of dams built in Mexico*. Mexico: Instituto de Ingeniería, UNAM.

Michalske, T.A. and Freiman, S.W. (1982). A molecular interpretation of stress corrosion in silica. *Nature*, 295: 511−512.

Naylor, D.J., Maranha das Neves, E. and Veiga Pinto, A.A. (1997). "A back-analysis of Beliche Dam", Géotechnique 47, No. 2, 221–233.

Naylor, D.J., Maranha das Neves, E., Mattar, Jr., D. and Veiga Pinto, A.A. (1986). "Prediction of construction performance of Beliche Dam", Géotechnique 36, No. 3: 359–376.

Nobari, E.S. and Duncan, J.M. (1972). Effect of reservoir filling on stresses and movements in earth and rockfill dams, Department of Civil Engineering, Report No. TE-72-1. University of California.

Oldecop, L. and Alonso, E.E. (2001). "A model for rockfill compressibility". *Géotechnique* 51, No. 2, 127–139.

Oldecop, L. and Alonso, E.E. (2002). "Fundamentals of rockfill time-dependent behaviour". *Proc. 3rd International Conference on Unsaturated Soils*. Recife (Brazil) 2: 793–798.

Oldecop, L. and Alonso, E.E. (2003). "Suction effects on rockfill compressibility". *Géotechnique*. 53(2): 289–292.

Oldecop, L.A. and Alonso, E.E. (2004). Testing Rockfill Under Relative Humidity Control. *Geotechnical Testing Journal*, Vol. 27, No. 3.

Oldecop, L. and Alonso, E.E. (2007). "Theoretical investigation of the time-dependent behaviour of rockfill". Géotechnique, (57): 289–301.

Ortega, E. (2008). "Comportamiento de materiales granulares gruesos. Efecto de la succión". Tesis Doctoral. Universitat Politècnica de Catalunya, Barcelona, España.

Parkin, A.K. and Adikari, G.S.N. (1981). Rockfill deformation from large-scale tests. Proc. X ICSMFE, Estocolmo.

Penman, A.D.M. and Charles, J.A. (1976). The quality and suitability of rockfill used in dam construction.

Dams and embankments, *Practical Studies from the BRE*. London: The Construction Press, 6: 72−85.
Pestana, J.M. and Whittle, A.J. (1995). Compression model for cohesionless soils. *Géotechnique* 45, No. 4, 611–631.
Ramon, A., Alonso, E.E. and Romero, E.E. (2008). "Grain size effects on rockfill constitutive behaviour". Proc. of the 1st Europ. Conf. on Unsaturated Soils. Taylor and Francis. 341–347.
Rein, J.A., Soriano, A., and Pradera E. (1992). Estabilidad de los terraplenes del ferrocarril de alta velocidad del NAFA. III Simposio Nacional sobre Taludes y Laderas Inestables, La Coruña, España, 509–520.
Soriano, A. and Sánchez, F.J. (1999). Settlements of railroad high embankments. Proc. XII European Conf. on Soil Mech. and Geotech. Eng., Netherlands.
Sowers, G.F., Williams, R.C. and Wallace, T.S. (1965). Compressibility of broken rock and settlement of rockills. *Proc. 6th ICSMFE*. Montreal, 2: 561−565.
Tapias, M, Alonso, E.E. and Gili, J.A. (2013). DEM modelling of unsaturated rockfill. Scale effects. First Panamerican Conference on Unsaturated Soils. Cartagena de Indias. Colombia.
Thiel, R. and Smith, M.E. (2003). State of the practice review of heap leach pad design issues. *Bi-anual meeting of the Geosynthetics Research Institute*, Las Vegas, Nevada, USA.
Veiga Pinto, A.A. (1983). *Previsao do comportamento estrutural de barragens de enrocamento*. PhD thesis, Laboratório Nacional de Engenharia Civil, Lisbon.
Wiederhorn, S.M., Fuller, E.R. and Thomson, R. (1980). Micro-mechanisms of crack growth in ceramics and glasses in corrosive environments. Met. Sci., 14: 450–458.
Wilson, A.C. and J.D. Evans. (1990). The use of low grade rockfill at Roadford Dam. The embankment dam. The British Dam Society VI Conference.
Wood, D.M., Belkheir, K. and Liu, D.F. (1994). Strain softening and state parameter for sand modeling, Géotechnique, 44(2): 335–339
Yamamuro, J.A. and Lade, P.V. (1996). Drained sand behaviour in axisymmetric tests at high pressures. J. of Geotech. Engng., ASCE, 122(2): 109–119
Yasuda, N. and Matsumoto, N. (1994). Comparisons of deformation characteristics of rockfill materials using monotonic and cyclic loading laboratory tests and in situ tests. Can. Geotech. J., 31: 162–174.
Yasuda, N., Matsumoto, N., Yoshioka, R., and Takahashi, M. (1997). Undrained monotonic and cyclic strength of compacted rockfill material from triaxial and torsional simple shear tests. Can. Geotech. J., 34: 357–367.

Advances in Unsaturated Soils – Caicedo et al. (eds)
© 2013 Taylor & Francis Group, London, ISBN 978-0-415-62095-6

Unsaturated soil mechanics in the design and performance of pavements

H. Sahin, F. Gu & Y. Tong
Texas Transportation Institute, Texas A&M University, USA

R. Luo
Texas Transportation Institute, Texas A&M University, USA

R.L. Lytton
Texas A&M University, College Station, Texas, USA

ABSTRACT: Pavements are designed using assumed moduli of the layers and permanent deformation properties of the base course in order to account for the effects of traffic and the weather on the long term performance of the pavement. Performance includes the rate of development of roughness, rutting, and various forms of cracking. However, when the pavement is constructed, acceptance of the project rarely includes verifying that the as-built pavement has the properties that were assumed when it was designed. This paper shows how the use of the principles of unsaturated soil mechanics brings us closer to being able to both design and verify the design assumptions as part of the construction quality control and quality assurance process. The Soil Water Characteristic Curve (SWCC) and a new characteristic, the Soil Dielectric Characteristic Curve (SDCC) are of central importance to these processes and can be easily constructed using simple laboratory equipment that is robust enough to take into the field and on to a construction site. The importance of suction in controlling the important performance related properties of pavement layers is illustrated with several examples relating to different forms of pavement distress in which suction plays an important role.

1 INTRODUCTION

1.1 *Design of pavements*

Pavements are designed to carry traffic loads by arranging the layers to have a modulus and thickness that will carry the traffic loads well for several decades. In both asphalt and concrete pavements, the base course provides a major load-bearing component of the pavement. In addition to assuming the modulus of the base course, the designer also assumes the permanent deformation properties of the base course and uses these assumed values in predicting the development of rutting and roughness with time. The assumed values are usually based on laboratory or field nondestructive testing measurements to which the designer has access.

1.2 *Construction of pavements*

When the pavement is constructed, the compaction of the base course is verified by various means but the modulus or permanent deformation properties that were assumed when the pavement was designed are not determined as a general rule. This is perplexing since several studies have shown that there is only a slight relationship between the dry density of a base course layer and its modulus. Recent developments in the construction quality control and quality assurance processes have been experimenting with ways of measuring the base course modulus in the field but their full implementation lies well into the future.

1.3 *Performance of pavements*

Well designed and built pavements must resist various types of distress due both to traffic and weather and maintain an acceptably smooth and quiet riding quality for an extended period of time. The modulus and permanent deformation properties of the base course play an important role in how well a pavement serves this intended purpose It is even more important for performance that a base course can be evaluated at the time of construction for its ability to resist the changes that will be imposed on it by moisture, freezing and thawing and traffic stresses. In addition, the distortions to

the pavement surface by volumetrically active subgrade soils such as expansive soils and frost heaving soils need to be anticipated and, as far as is cost-effective, neutralized. If the surface layer is asphalt, it too, may deteriorate prematurely due to moisture damage. In all of this, the physical quantity that is central to making realistic evaluations of these pavement properties is the suction. This paper presents a novel process that has been developed making use of the principles of unsaturated soil mechanics to make these evaluations of pavement properties practical making use of the controlling role that is played by suction.

The process makes use of models of the relevant properties of base courses and subgrade soils and makes use of these models for design, construction quality control and assurance and performance prediction.

2 DESIGN OF PAVEMENTS

The model of the resilient modulus of a base course is stress-dependent, including its dependence upon suction.

$$E_y = k_1 P_a \left[\frac{I_1 - 3\theta f\left(h_m + \beta \frac{I_1}{3} + \alpha \tau_{oct}\right)}{P_a} \right]^{k_2} \left(\frac{\tau_{oct}}{P_a} \right)^{k_3} \quad (1)$$

where I_1 = the first invariant of the stress tensor; P_a = the atmospheric pressure; θ = the volumetric water content; h_m = the initial matric suction in the aggregate matrix; f = saturation factor, $1 \le f \le \frac{1}{\theta}$; τ_{oct} = the octahedral shear stress; α and β = Henkel pore water pressure parameters; and k_1, k_2 and k_3 = material parameters that are dependent on material properties dry unit weight, water content, Methylene Blue Value, pfc, and aggregate gradation, angularity, and shape (Ashtiani, 2009 and Ashtiani, et al., 2010).

During the modeling process, θ and f were firstly calculated based on the dry density (γ_d) and water content (ω). Then the Solver Function in the software Excel was used to search for h_m, α, β and k values while minimizing the fitting error. The modeling results show that the average R-squared value of all data sets was 0.943, which demonstrates the goodness of the model fit.

The predicted k values are material properties that depend on the properties of aggregate particles and aggregate matrix. Statistical analysis was performed to investigate the correlation between the k values and the aggregate properties, such as the dry density, water content, Methylene Blue Value (MBV), pfc, and aggregate gradation, angularity, shape and texture in terms of Weibull distribution parameters.. Equations (2) through (4) present the statistical models of k_1, k_2 and k_3.

$$k_1 = 0.1242 + 0.02370 \cdot pfc - 0.2968 \cdot a_S \quad (2)$$

$$\ln k_2 = 5.2963 - 0.001246\gamma_d - 0.5846 \ln \omega - 0.000721\lambda_A \quad (3)$$

$$k_3 = -36.84 + 4.849 \ln \gamma_d + 1.173 \ln \omega + 0.03024 \cdot pfc - 0.000915\lambda_A \quad (4)$$

Typical values of the Henkel pore water pressure coefficients range between –0.003 to 0.380 for α and between 0.787 and 6.661 for β (Henkel, 1960; Holtz & Kovacs, 1981).

The permanent deformation model needs to be established to predict the long-term performance of granular materials accurately. The vast majority of permanent deformation models found in literature were developed based on using the laboratory test results. In this study, the VESYS model and MEPDG model were used to evaluate the permanent deformation behavior of aggregate materials (Tseng & Lytton 1989).

2.1 *VESYS model*

The VESYS model assumes that the relationship between permanent deformation and number of load applications is linear in a logarithm scale (Lai, 1977; Kenis, 1977), which is expressed in Equation (5).

$$\varepsilon^p(N) = IN^S \quad (5)$$

By assuming the resilient strain is constant for each loading application, Equation (6) can be expressed as:

$$\frac{1}{\varepsilon_r}\left(\frac{\partial \varepsilon^p(N)}{\partial N}\right) = \left(\frac{IS}{\varepsilon_r}\right) N^{S-1} \quad (6)$$

Assuming ε_r and α = 1-S, Equation (7) can be rewritten as:

$$\frac{1}{\varepsilon_r}\left[\frac{\partial \varepsilon^P(N)}{\partial N}\right] = \mu N^{-\alpha} \quad (7)$$

where ε_r = the resilient strain of the granular aggregate; ε^p = the permanent strain of the granular aggregate; N = the number of load cycles; μ = the parameter representing the constant of proportionality between permanent and resilient strain; and α = the parameter indicating the rate of

decrease in permanent strain with the number of load applications.

2.2 *MEPDG Model*

Tseng & Lytton (1989) developed a three-parameter model to predict the relationship between permanent strain and number of loading cycles for a granular material, which is expressed in Equation (8):

$$\varepsilon_p = \varepsilon_0^p e^{-\left(\frac{\rho}{N}\right)^\beta} \tag{8}$$

where ε_p = permanent strain of granular material; ε^0 = the maximum permanent strain; ρ = the scale factor; and β = the shape factor.

In the MEPDG manual, this equation was modified to predict the permanent deformation of aggregate layers with thickness h, using Equation (9):

$$\varepsilon_p = \left(\frac{\varepsilon_0}{\varepsilon_r}\right) e^{-\left(\frac{\rho}{N}\right)^\beta} \varepsilon_v h \tag{9}$$

where ε_v = the vertical strain in the granular aggregate layer; and h = the thickness of the aggregate layer.

2.3 *Models of the VESYS permanent deformation properties*

The μ and α properties of the base courses that were modeled by regression analysis to determine which of the indicator tests can reliably predict these properties. The μ-value is an estimate of the permanent strain that will develop in the base course on the first load application. A larger value of the μ-value denotes a base course that is more prone to permanent deformation. The equation that predicts it is in Equation (10):

$$\mu = -247.47 + 33.53 \text{ Log } (\gamma_d) + 5.258 \text{ Log } (\omega) + 0.1942 \ (pfc) - 0.007848 \ (\lambda_A) \tag{10}$$

The α-value is an inverse measure of the rate at which permanent deformation develops in the base course. A larger value of the α-value means a slower rate of development of permanent deformation development in the base course. The equation that predicts it is in Equation (11):

$$\alpha = -25.14 + 3.594 \text{ Log}(\gamma_d) - 0.000913 \ (\lambda_A) + 0.473 \ (\alpha\text{G}) - 0.1699 \ (\alpha\text{A}) + 0.1001(\alpha\text{S}) \tag{11}$$

2.4 *Models of the MEPDG permanent deformation properties*

The three MEPDG properties are the ε_o, ρ, and β. The first of these, ε_o, is the maximum permanent strain that will develop in the base course. The second symbol, ρ, is a measure of how many load applications that will cause 36.8% of this strain level, and the third symbol, β, is an inverse measure of the initial rate of rise of the permanent deformation. The equation for ε_o is in Equation (12):

$$\varepsilon_o = -13.796 + 0.1936 \ (pfc) - 0.0157 \ (\lambda_T) + 4.316 \text{ Log } (\omega) + 1.579 \ (\alpha\text{A}) \tag{12}$$

A larger ρ-value indicates a longer service life under traffic. The equation for the ρ-value is in Equation (13):

$$\rho = 33.07 - 3.348 \text{ Log } (\gamma_d) + 0.0258 \ (pfc) - 0.7954 \ (\alpha\text{G}) \tag{13}$$

The β-value was practically constant for all of the base courses that were tested. A very good value of the β-value is its mean as is given in Equation (14):

$$\beta = 0.304 \tag{14}$$

The indicators of these permanent deformation properties are a mixture of those that can only be measured in the laboratory and others that can also be measured in the field. In the laboratory, the permanent deformation indicators that can be measured are the dry unit weight, the gradation and the Weibull measures of shape, angularity and texture. In the field, the permanent deformation indicators that can be measured are the Methylene Blue Value, the percent fines content (*pfc*) and the water content. Even though the dry unit weight can also be measured in the field, it is not a very sensitive variable in these equations and can be assumed with sufficient accuracy for these purposes from the laboratory compaction curve for a known water content.

These equations can be used to predict the resilient modulus and permanent deformation properties of base courses. The properties that enter into the equations can be divided into two categories: those that can be measured in the laboratory prior to construction and those that can be measured both in the lab and in the field. The field measurements should be capable of determining the most sensitive variables in the field which when combined with the less sensitive variables measured in the lab alone allow an accurate determination of the resilient modulus and permanent deformation properties of the base course in the field.

The laboratory properties are the aggregate gradation (G), shape (S), angularity (A), and texture (T) Wiebull shape and scale parameters, α and λ and the compaction curve. The properties that can be measured both in the laboratory and the field are the Methylene Blue Value (MBV), the percent fines content (*pfc*), the matric suction, h_m, the dry unit weight, γ_d, and the water content, ω. Of these, the suction, dry unit weight and water content are highly variable in the field.

The process that has been developed makes use of one other measurement that can be made both in the laboratory and the field: the dielectric constant of the base course using a hand-held device which is capable of measuring both the permittivity (the complex dielectric value) and the electrical conductivity of a material with which it is in contact. The first letters of the two measurements it makes have been combined to give the device its name: the Percometer:

These equations may be used in estimating the properties of the base course while the pavement is being designed. They can also be used in the field to verify that the in-place, as compacted base course has the resilient modulus and permanent deformation properties that were assumed in the design. Furthermore, these properties may be used in making the same performance predictions in the field that were used originally as a basis for the pavement design. The question remains: how can the highly variable inputs to these equations such as percent fines content, water content, dry unit weight, and matric suction be measured in the field at the time of construction? The answer to that question is summarized in the next section of this paper.

3 CONSTRUCTION OF PAVEMENTS

The process of measuring the highly variable inputs to the resilient modulus and permanent deformation property equations starts with the Methylene Blue test using a new process developed by the W. R. Grace Corporation. Figure 1 shows a picture of this device.

Methylene blue is a large organic polar molecule which is absorbed onto the negatively charged surface of a clay mineral. The concentration of negatively charged particle locations on the clay surface controls the amount of methylene blue absorbed by a given mass of soil. Therefore the relative surface areas of clay particles are determined by using a methylene blue solution of a known concentration (Phelps & Harris, 1967).

Since methylene blue molecules are absorbed at negatively charged clay locations, the absorbed methylene blue may give a measurement of the

Figure 1. A picture of the Grace methylene blue test apparatus.

cation exchange capacity (CEC) of clay samples (Fairbairn & Robertson, 1957).

A number of researchers have assessed that the cation exchange capacity (CEC) is an indicator of methylene blue dye adsorption (Wang & Wand 1993). This conclusion provides recent empirical implementation in field testing. The methylene blue method is simple, rapid and reproducible. The methylene blue test was considered to be appropriate for industrial uses. A methylene blue test procedure was developed to determine the active clay content. This method is included in the European Standards to assess deleterious clay in concretes (Yool et al., 1998).

ASTM C 837 is a standard test method for a methylene blue test index of clay to assess the active fine particles in a mixture. The purpose of this test is to measure the adsorbed methylene blue dye by clay. AASHTO T 330-07 is also a standard test method measuring the qualitative detection of harmful clays in the smectite group in an aggregate mix. This method determines the surface activity of the aggregate through identifying the smectite group material which is considered to be harmful clay. The Grace methylene blue test method is a more time effective test method compared to both ASTM and AASHTO standards.

The next part of the answer comes from the determination the size distribution and mineralogical character of the fines in a base course. It is a well known fact that the fines are very important to the performance of a base course, a fact that is borne out by the models of both the resilient modulus and permanent deformation properties.

The Horiba Laser Scattering Particle Size Distribution Analyzer is a device to determine particle size fraction distribution of a soil mixture. A viscous solution, composed of soil and water, flows through a beam of light to detect particle sizes. The light scattering device analyzes various particle dimensions in the viscous solution passing through the light beam. The data analysis runs through the Horiba software and produces a distribution of

size fractions from the smallest to largest particle dimension.

The soil mixtures are analyzed in the laboratory with the particle size distribution analyzer version LA-910, which is produced by Horiba Instruments, Inc. The sample passing the No. 40 sieve size is then sieved through the No. 200 sieve, which represents the desired largest sieve number that is used to analyze the soil sample for this project. The percent fines contents (*pfc*) represents the particle size fraction passing the No. 200 (0.0075 mm) sieve size. Thus, to achieve this purpose, the largest sieve size that must be used is the No. 200, and the fines content of that size must be analyzed.

3.1 *Relationship between MBV and pfc*

The methylene blue test evaluates the fine fraction of an aggregate system in an aggregate mix. The methylene blue test is considered to be a more suitable test method compared to other standard methods to determine the deleterious fine particles in a mixture.

In addition to the traditional methylene blue test, the Grace methylene blue test is a significantly more rapid, reproducible and simple method to estimate the percent fines amount. This new test method is improved to assess a relation between the adsorbed methylene blue and the percent fines fraction especially in aggregate mixes. This improvement warrants the assessment of the methylene blue value for the smaller than *No. 4* sieve size fraction rather than the size smaller than 2 mm. Additionally, the test method is applicable both in the laboratory and in field applications because the test method requires fewer experimental tools.

Various aggregate samples were compiled throughout Texas to identify the percent fines content. Nine-(9) aggregate quarries provided samples within a three-(3) month time period. The portion passing the *No. 4* sieve was employed to assess the percent fines content. The Grace methylene blue test and Horiba Particle Size Distribution Analyzer were performed on more than a hundred (100) aggregate samples. Based on the test outcomes a general mathematical relation was generated between the methylene blue value and the percent clay content. This relation shows a general form of methylene blue value and fine content for nine quarries in Texas. The relation between methylene blue value (MBV) and percent fines content (*pfc*) is given in Figure 2.

The curve relating the methylene blue value (MBV) and the percent fines content (*pfc*) is a "C" shaped curve. This curve is divided into two zones in Figure 2 based on the methylene blue value. Zone-II is where the methylene blue value is greater than 7 (mg/g), and Zone-I is where the

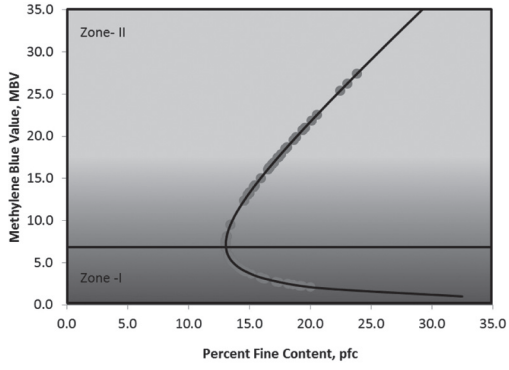

Figure 2. Characteristic curve of methylene blue value versus percent fines content.

methylene blue value is smaller than 7 (mg/g). The MBV value reading at 7 (mg/g) is considered as the critical methylene blue value (MBVc). There is an inverse ratio between the MBV and *pfc* when the MBV is below the critical MBV. As the MB value increases until 7 (mg/g), the pfc values decrease. There is a direct proportion in Zone-II where the MBV is above the critical MBV. If the MB value is above the critical MBV, then as the MB value increases, the pfc values increase. Furthermore, test results showed that if a sample is above the critical MBV point, they have higher liquid limit values. In other words samples above located in Zone-II are more active than samples located in Zone-I. Typically, more "active" means having a higher surface area of the particles per unit weight.

The form of the equation for this "C" shaped curve is in Equation (15).

$$pfc = \frac{a}{(MBV)^n} + b(MBV) \tag{15}$$

where a,b,n = coefficient parameters depend on soil type; MBV = methylene blue value; and pfc = percent fines content.

Each quarry has its unique set of coefficients a, b, and n. After running a minimum of 6 Methylene Blue tests and the particle size analyzer, it is possible to draw the curve and its 90 percent confidence limits. Two examples of the MBV-vs-pfc curves of such quarries are shown in Figures 3a and 3b. The quarry in Figure 3a is known to produce a very high quality base course material.

The base course from the quarry in Figure 3b is known to be a poor base course material because of its high clayey fines content.

The next part of the process is in developing the dependence of the soil water characteristic curve (SWCC) on the percent fines content.

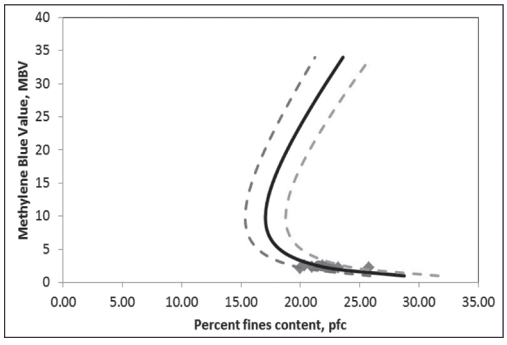

Figure 3a. MBV versus pfc for a quality base course.

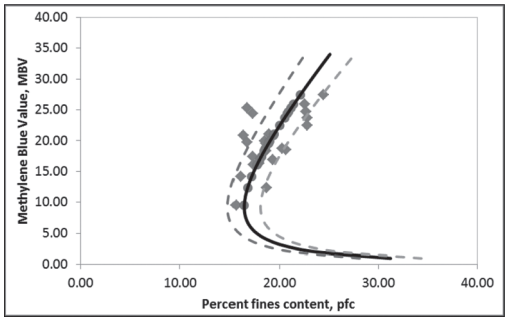

Figure 3b. MBV versus pfc for a poor quality base course.

3.2 *Suction-Water Characteristic Curves (SWCC)*

The soil water characteristic curve is a relation between soil suction and moisture content. The SWCC curve depends on the type of soil and aggregates. All of the measured test data have been used to generate a SWCC for each of the various aggregate sources.

The experimental study found that the methylene blue test and percent fines content (pfc) value have relations that fit well with several important aggregate characteristics. The pfc is an input parameter to generate the suction water characteristic curve (SWCC) and the suction dielectric characteristic curve (SDCC). These curves are generated by using four parameters, all of which are functions of the pfc. Consequently, the pfc is a vital parameter to be determined in order to generate the entire curve of both the SWCC and SDCC.

The four SWCC curve parameters depend upon two experimental parameters that come from the gradation curve and the Methylene Blue test. These parameters are the percent of soil weight smaller than 75 μm (#200 sieve) and 2 μm. The second parameter is the percent of fines content which is the amount of the sample that is smaller than 2 microns (2 μm). Both sizes are determined by the particle size distribution curve. This percent value is denoted percent fines content (pfc) to represent the clay content which passes the No. 200 Sieve (Sahin 2011). The mathematical formulation of the pfc is shown in Equation (16).

$$pfc = \frac{-2\mu m}{-No.200} \times 100 \tag{16}$$

where $-2\mu m$ = sample weight smaller than 2 micrometers in percent; and $-No.$ 200 = sample weight smaller than 75 micrometers in percent.

The methylene blue test is performed to determine the pfc for an aggregate mixture as explained previously.

The relation between the soil moisture content and suction is represented with the soil water characteristic curve (SWCC). The form of the SWCC which is based on the volumetric water content and suction is by Fredlund & Xing (1994). The proposed SWCC curve relation is given in Equations (17) and (18).

$$\theta_w = C(h) \times \left[\frac{\theta_s}{\left[\ln\left[\exp(1) + \left(\frac{h}{a} \right)^b \right] \right]^c} \right] \tag{17}$$

$$C(h) = \left[1 - \frac{\ln\left(1 + \frac{h}{h_r} \right)}{\ln\left(1 + \frac{10^6}{h_r} \right)} \right] \tag{18}$$

where a_f = a soil parameter which is primarily a function of the air entry value of the soil in kPa; b_f = a soil parameter which is primarily a function of the rate of water extraction from the soil, once the air entry value has been exceeded; c_f = a soil parameter which is primarily a function of the residual water content; h_r = a soil parameter which is primarily a function of the suction at which residual water content occurs in kPa; θ_s = Saturated volumetric water content; and θ_s = Volumetric water content.

To be able to generate the SWCC curve, the four parameters in the Fredlund & Xing (1994) equation need to be calculated. The SWCC is generated with these four parameters: a_f, b_f, c_f and h_r and provides the full range of suction and water content values. A recent study showed that all of these four parameters depend upon the pfc value and a relation between each of the four parameters and pfc was proposed by Sahin (2011). This study found that each parameter has a unique function based on the pfc.

The four parameters in the Fredlund & Xing (1994) formulation are estimated by using the SOLVER function in MS Excel. Based on the SOLVER data mathematical equations are developed for each parameter. Each parameter is a function of Percent Fines Content (*pfc*).

The air entry value of soil, a_f, is formulated based on the soil *pfc* value and given in Equation (19). The rate of water extraction of the soil after exceeding the air entry value, b_f, is formulated in Equation (20). The value of b_f decreases as the *pfc* value increases. The mathematical formulation for the residual water content of the soil of c_f is given in Equation (21).The mathematical formulation for the suction value at which the residual water content occurs, h_r is given in Equation (22).

$$a_f(psi) = 0.6384e^{0.0369\,pfc} \tag{19}$$

$$b_f = 11.748e^{-0.037\,pfc} \tag{20}$$

$$c_f = 0.126e^{0.0211\,pfc} \tag{21}$$

$$h_r(psi) = -0.0018\,pfc^2 + 0.5206\,pfc + 2.4305 \tag{22}$$

The suctions were measured using the filter paper method. Both total and matric suction can be determined by means of the filter paper method (ASTM D 5298). In matric suction measurement the filter paper is placed between two samples. When the samples reach equilibrium, the suction in the sample and filter papers will be equal. An illustration of the test sample setup is shown in Figure 4.

The standard filter paper suction testwas used to measure the matric suction of the passing No. 4 sieve size fraction. Two compacted aggregate samples are prepared by using standard compaction method used in ASTM D 698. The size of the compacted samples is 38 mm. high and 76 mm. in diameter. The compacted soil samples are kept in 100 percent humidity room to reach 2 percent moisture content. When the samples have reached the desired moisture content, they are taken from the environmental room, and immediately placed with the filter paper in closed containers.

The SWCC shown in Figure 4 is an example of a typical base course sample. The suction value of 4.86 pF corresponds to a volumetric moisture content of 3.70 in Figure 5. The point shown on the graph is the separately measured filter paper suction and water content.

The accuracy of the SWCC curve to reproduce the measured value of the matric suction is important to the process of determining the performance-related properties of a base course in the field. A direct measurement that is directly related to the water content is the dielectric constant of

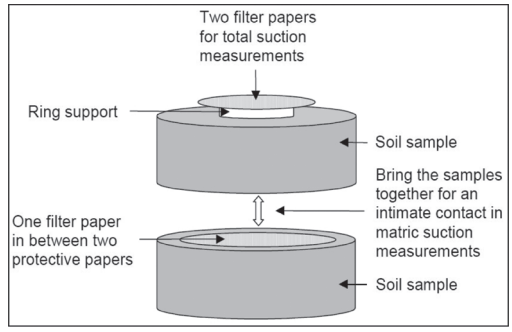

Figure 4. Test setup for measuring total and matric suction in compacted base course samples.

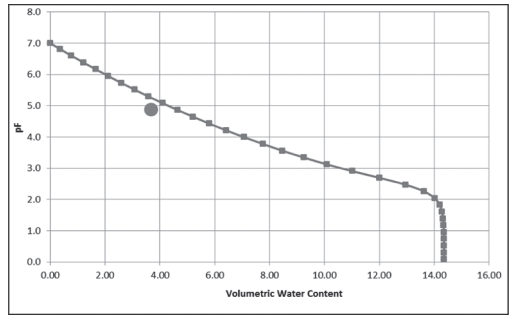

Figure 5. Typical soil water characteristic curve (SWCC) for a compacted base course.

the soil using the percometer. The percometer is commonly used to measure soil dielectric permittivity and conductivity in soil studies (Yeo and et al., 2012). The percometer is a non-destructive test instrument which can be used both in the laboratory and for in-situ testing, while providing quick (15 seconds) and accurate readings. A percometer monitor and a surface probe is shown in Figure 6. The percometer is a frequency domain device which measures at a frequency of 50 kHz. The accurate definition of dielectric constant (ε_r) is the real part of the relative complex electric permittivity which is directly related to the moisture content in the material (Saue & et al., 2008).

The dielectric value (ε_r) of a base course is a composite of the dielectric values of the components of the base course: solids, water, and air. Theoretical developments supported by laboratory and field measurements have shown that the composite dielectric is weighted by the volume concentration of the components as in the following Equation (23).

$$\varepsilon_r^n = \sum_{i=1}^{n} \varepsilon_{ri}^n c_i \tag{23}$$

Figure 6. Photograph of a percometer with surface probe.

where c_i = volume concentration of the ith component of a mixture; ε_r = the dielectric constant of the ith component; n = an exponent which may range between ¼ and 1.

The most commonly used value of the exponent, n = 1/2 produces the Complex Refraction Index Model (CRIM).

The Complex Refraction Index Model (CRIM) is used to determine the dielectric value in the aggregate mix. The CRIM model is used to determine the dielectric constant of the solids ε_s value for the mix. The dielectric value (ε_r) of the base course is measured by using the Percometer. The relative dielectric value of the water in Equation (24) is a known parameter, 81. The only unknown parameter is the dielectric value of solid, ε_s and it is calculated because the two other parameters are known in Equation (23). The saturated dielectric value of the material needs to be determined in Equation (25). The saturated dielectric value ε_r can be calculated by using both θ_{sat} and θ_{solid} in Equation (25). The saturated dielectric value of the base course is calculated in Equation (25). The CRIM dielectric value equation is given as follows:

$$\sqrt{\varepsilon_r} = \left[\left(\sqrt{\varepsilon_s} - 1\right)\theta_{solid} + \left(\sqrt{\varepsilon_w} - 1\right)\theta_w + 1\right] \tag{24}$$

The saturated dielectric value is calculated in Equation (25):

$$\left(\sqrt{\varepsilon_r}\right)_{sat} = \left[\left(\sqrt{\varepsilon_s} - 1\right)\theta_{solid} + \left(\sqrt{\varepsilon_w} - 1\right)\theta_{sat} + 1\right] \tag{25}$$

where ε_r = dielectric value; ε_s = dielectric value of solid; ε_w = dielectric value of water; θ_{solid} = volumetric solid. ε_r = dielectric value; ε_s = dielectric value of solid; ε_w = dielectric value of water; θ_{solid} = volumetric solid. θ_w = volumetric water content; θ_{sat} = saturated volumetric water content

The relation between the base course material suction and the dielectric value was investigated by using a percometer and filter paper measurements of suction. A large number of these measurements were performed on various materials that are compiled from nine-(9) different quarries. All of these measurements were used to develop a unique suction-dielectric constant relationship which gives the whole range of suction change with the material dielectric constant. This model is denoted as Soil Dielectric Characteristic Curve (SDCC). A typical SDCC curve is shown in Figure 7.

The matric suction that was measured with filter paper for this base course material is shown superimposed on the SDCC curve generated using the same Fredlund & Xing (1994) forms of equation as shown in Equations (26) and (27):

$$\varepsilon_r = C(h) \times \left[\frac{\varepsilon_{sat}}{\left[\ln\left[\exp(1) + \left(\frac{h}{a} \right)^b \right] \right]^c} \right] \tag{26}$$

$$C(h) = \left[1 - \frac{\ln\left(1 + \frac{h}{h_r} \right)}{\ln\left(1 + \frac{10^6}{h_r} \right)} \right] \tag{27}$$

where: a_f = a soil parameter which is primarily a function of the air entry value of the soil in kPa; b_f = a soil parameter which is primarily a function of the rate of water extraction from the soil, once the air entry value has been exceeded; c_f = a soil parameter which is primarily a function of the residual water content; h_r = a soil parameter which is primarily a function of the suction at which the residual water content occurs in kPa; ε_{sat} = saturated dielectric value; and ε_r = dielectric value.

The SDCC equation consists of four similar parameters that allow the entire curve to be generated using the same methodology as the SWCC. These a_f, b_f, c_f and h_r four parameters also depend entirely on the pfc value of the mix. There are two sets of equations: one for those base courses with MBV values smaller than the critical value of 7.0 mg/g and the other for those base courses with MBV-values greater than 7.0 mg/g. the equations for the base courses with MBV less than 7.0 mg/g are as follows:

$$a_f = 3.976x(pfcxMBV)^{0.0015} \tag{28}$$

$$b_f = -4x10^{-8}(pfcxMBV)^2 + 4x10^{-7}x(pfcxMBV) + 0.0301 \tag{29}$$

$$c_f = -10^{-7}(pfcxMBV)^2 + 3x10^{-6}x(pfcxMBV) + 0.0113 \tag{30}$$

$$h_r = 0.0023x(pfcxMBV)^{2.0183} \tag{31}$$

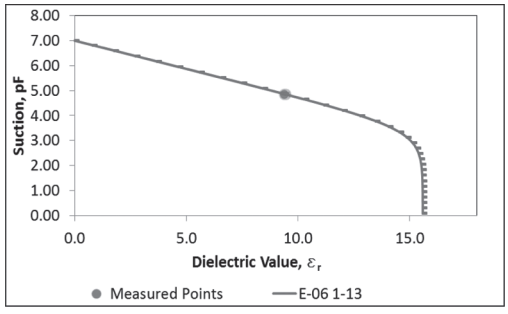

Figure 7. Typical soil dielectric constant curve (SDCC) of a compacted base course sample.

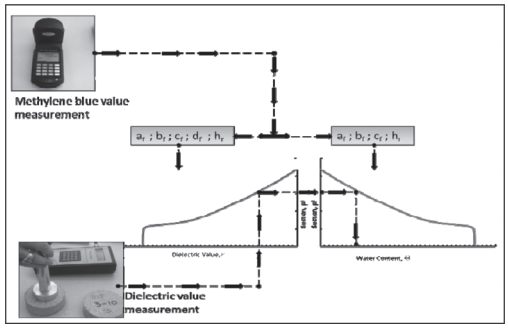

Figure 8. Measurement of matric suction and water content of a base course using the methylene blue test and the percometer.

The equations for the coefficients of the SDCC curve for MBV-values greater than 7.0 mg/g are as follows.

$$a_f = 3.9649x(MBV)^{0.0054} \tag{32}$$

$$b_f = 0.0683x(MBV)^{-0.102} \tag{33}$$

$$c_f = 0.0095x(MBV)^{-0.461} \tag{34}$$

$$h_r = 2.9833x(MBV)^2 - 50.845x(MBV) + 254.75 \tag{35}$$

Having constructed the SWCC curve and the SDCC curve for the base course material from a given quarry, it is now possible to determine in the field in sequence: the Methylene Blue Value, the percent fines content, the SWCC coefficients and curve, the SDCC coefficients and curve, and the dielectric constant is measured with the percometer. Knowing the dielectric constant, the matric suction can be determined the SDCC curve. Knowing the matric suction, and the SWCC curve, the water content can be calculated. The process is illustrated in Figure 8.

Of all of the highly variable factors in the models of the resilient modulus and permanent deformation properties of a base course, the only missing property is the dry unit weight. This, too, can be estimated very accurately once the water content is known using the compaction curve model that has also been developed.

The model consists of three parameters (a,b,n) and three material properties; degree of saturation, specific gravity and unit weight of water. The three parameters vary with aggregate sources and characteristics.

The mathematical formulation of the improved dry unit weight model is given in Equation (36):

$$\left(\frac{\gamma d}{\gamma w}\right) = \left[\frac{a}{\left(\frac{w}{S}+\frac{1}{Gs}\right)} - \frac{b}{\left(\frac{w}{S}+\frac{1}{Gs}\right)^n}\right] \tag{36}$$

where a, b and n are the three parameters which change with aggregate source; γ_d = dry unit weight of base course material (kN/m^3 or lb/ft^3); γ_w = unit weight of water (kN/m^3 or lb/ft^3); w = water content (%); S = degree of saturation (%); and Gs = specific gravity of the solids.

The parameters a, b and n were found to depend upon optimum moisture content as in the following mathematical forms.

$$a = 1.4291(wc)^{0.0343} \tag{37}$$

$$b = -0.6456(wc)^2 + 0.0325(wc) + 0.4507 \tag{38}$$

$$n = 0.4955(wc)^{-0.003} \tag{39}$$

A typical compaction curve generated with this compaction curve model is shown in Figure 9 together with the original data from which the curve was derived. The values of the coefficients a, b and n for each base course are known from laboratory compaction and once the water content is known from the SWCC curve, the corresponding dry unit weight can be computed from this compaction model. Typical values a,b and n are 1.30, 0.45 and 0.50.

At this point, all of the relevant inputs to the resilient modulus and permanent deformation models are known and those properties can be computed on the site. The fact that an onsite value of the dielectric constant of the base course has been measured and is the key to being able to generate the matric suction, water content and dry unit weight suggests that this can be the calibration location for the use of Ground Penetrating Radar

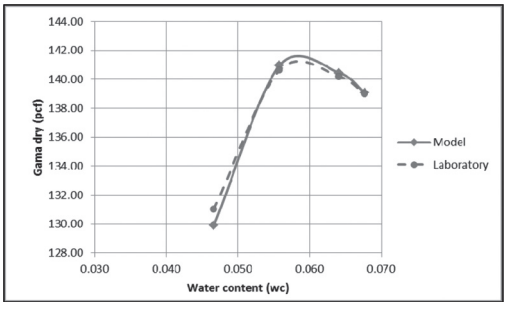

Figure 9. Typical compaction curve as tested in the laboratory and as modeled.

to generate a strip map of measurements of dielectric constants down the length of the compaction project which can be immediately turned into a strip map of resilient moduli and permanent deformation properties of the in-place base course as compacted.

Measurements of the Methylene Blue Value and the inferred percent fines content can be made at the quarry, at the stockpile and on the construction site to determine to what extent the percent fines content has increased because of the handling of the base course material with construction excavation, hauling and compaction equipment. Measurements of the Methylene Blue Value and the dielectric constant at random locations along the length of a pavement project will give an indication of the range of fines in the in-place base course materials and of the clayey or non-clayey character of the minerals in those fines. Each such location then becomes a calibration site for mobile Ground Penetrating Radar runs to determine the dielectric constant at closely spaced intervals to produce a strip map of the base course resilient modulus and permanent deformation properties and their variabilities. Realistic predictions of the performance of pavements requires means and variances of these values in order to anticipate the risk and reliability of the pavement performing as expected when it was being designed.

Performance of the base course depends not only upon the water content and matric suction at the time of construction but also upon the future values of the important variables as they are exposed to the weather and to contact with the existing supporting natural soils and their moisture regimes. Is it possible to anticipate the rate at which the base course and, in fact, the surface course above it changes moisture with time and exposure? The answer is yes as is explained in the following section.

4 PERFORMANCE OF PAVEMENTS

The performance of pavements is the record of how it deteriorates with time and traffic, developing both load-related and non-load-related distress. Load related distress includes fatigue cracking in both concrete and asphalt pavements, rutting and stripping in asphalt pavements, joint faulting and spalling in concrete pavements, and base course erosion and pumping in both types of pavements, among others. Non-load related distress includes roughness due to expansive soils and frost heaving soils, thermal cracking, transverse cracking due to the thermal shrinkage of base course materials and longitudinal cracking due to shrinkage of supporting subgrade soils among others. In all of these types of distress, the distress is accelerated by the effect of the moisture that either enters or is drawn out of the base course material. The influx or efflux of water from the base course is an unsaturated diffusion process which is governed by the parabolic partial differential equation proposed by Mitchell (1979); Lytton, et al., (2004):

$$\frac{\partial u}{\partial t} = \alpha \frac{\partial^2 u}{\partial z^2} \tag{40}$$

where u = the pF of the base course; α = the unsaturated diffusivity of the base course material (typical units cm^2/sec).

The soil diffusion rate, α, for the base course from each quarry was determined based on the water weight loss test data. The test results have shown that there is a relation between percent fines content and diffusion rate. To determine soil diffusion two pieces of soil sample are compacted at the optimum moisture content and placed in a 100 percent relative humidity environment room at 23°C temperature and daily moisture loss was recorded.

The aggregate samples are compacted as two pieces for the diffusion test. The portion of aggregates smaller than Sieve *No. 4* is used to prepare an aggregate mixture. The mixture is compacted at optimum moisture content by using the standard compaction method in ASTM D 698. The compacted sample is a cylinder with a radius of 50 mm and height of 38 mm. Two cylindrical soil samples are obtained by compaction and their shapes are shown in Figure 10.

Daily monitored data was evaluated to determine the diffusion rate. A mathematical function was derived from using Equation (41). The final form of the diffusion equation is given in Equation (43).

Figure 10. Two compacted base course samples in an environmental room for diffusivity measurements.

$$W(t) = W_o\left(1 - e^{\frac{-12Dt}{d^2}}\right) \tag{41}$$

$$\frac{dW(t)}{dt} = \left(-W_o e^{\left(\frac{-12Dt}{d^2}\right)}\right)\left(-\frac{12Dt}{d^2}\right) = \frac{12W_o}{d^2} e^{\left(\frac{-12Dt}{d^2}\right)} \tag{42}$$

$$\ln\left[\frac{dW(t)}{dt}\right] = \ln\left(\frac{12W_o D}{d^2}\right) - \left(\frac{12D}{d^2}\right)t \tag{43}$$

where D = diffusion rate of soil in (cm^2/sec); t = passed time between two weight measurement in seconds; W_o = maximum weight lost in grams; W(t) = weight of sample with time as water is lost in grams; and d = the thickness of the sample.

The diffusion value of the base course from each quarry was determined for selected samples during the three months production period. The percent fines content was also determined by using the Horiba particle size distribution analyzer device for the selected soil samples.

The test results illustrate the trends between the diffusion values and the percent fines content and these relations are formulated as power equations. The results have shown that the diffusion relations changed with the soil methylene blue value. Thus the results were divided into two groups as the MBV is greater than 7.0 and smaller than 7.0. The MBV value of 7.0 is the critical MBV. The forms of the diffusion equations based on the MBV levels are given in Equations (44) and (45).

for MBV is greater than 7.0

$$D = 5.63E^{-0.4}(pfc)^{-2.00} \tag{44}$$

for MBV is smaller than 7.0

$$D = 8.88E^{-0.4}(pfc)^{-2.28} \tag{45}$$

A graph of the diffusivity of these base course materials plotted against the percent fines content for the fines above and below the critical Methylene Blue Value of 7.0 mg/g is shown in Figure 11.

This figure demonstrates a critical characteristic of base course materials: those with high amounts of clayey fines will retain more water and diffuse pore water pressure more slowly, thus allowing excess pore water pressure to build up in the base course between passes of heavy tire loads. This weakens the base course and promotes rutting in asphalt pavements and the formation of voids beneath joints and cracks in concrete pavements. It also promotes and accelerates pumping and erosion of the base course with repeated load applications on both types of pavements.

In addition, no matter how wet or dry the base course is at the time of construction, once the base course is covered with the pavement surface, the base course quickly comes into an equilibrium with the suction of the subgrade beneath it. The speed with which it arrives at the equilibrium condition is governed by the diffusivity of the base course and, as shown in Figure 11, that depends heavily upon the percent fines content and whether those fines have Methylene Blue Values above or below the critical value of 7.0 mg/g. Those base courses with higher than critical MBV values have clayey fines which retain more moisture, accumulate excess pore water pressure more rapidly and perform poorly relative to those base courses that have MBV values below the critical.

These observations on the expected base course performance were surprisingly confirmed with the discovery that this same judgment had been encoded in the AASHTO Specification T 330-07 for the use of the older method of making methylene blue measurements using filter paper. Reproduced below in Figure 12 is the Methylene Blue Value Scale that is found in the AASHTO Specification relating the MBV to the expected performance of the base course with MBV values ranging from 0.0 to 24.0. Also reproduced for comparison is the corresponding Grace Methylene Blue Value Scale ranging from 0.0 to 28.0 and supported by the data that is presented here.

Many more examples could be presented of how the performance of a pavement depends importantly upon the unsaturated properties of the materials in those layers. This paper illustrates only a few of the relations that demonstrate the dependence of pavement performance on the unsaturated properties of the supporting layers. Chief among these is the matric suction which controls the resilient modulus, permanent deformation and diffusivity properties of the base course and the subgrade on which it rests.

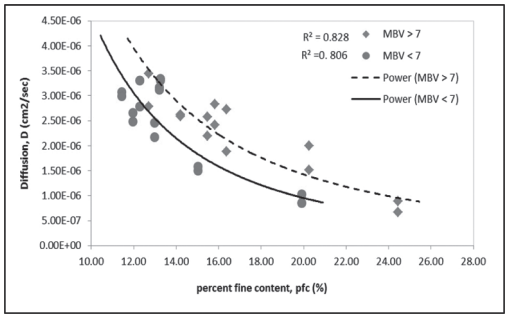

Figure 11. Diffusivity of base course materials dependent upon percent fines content and level of methylene blue value.

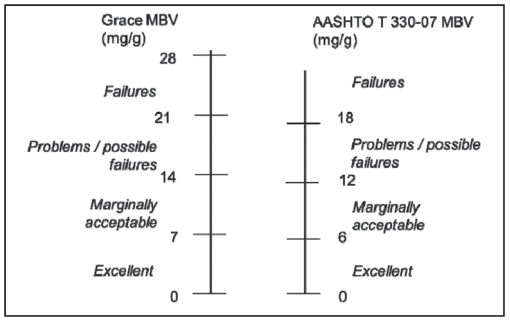

Figure 12. Methylene blue value scale from the AASHTO specification T 330-07 compared with the MBV from the Grace methylene blue test.

5 SUMMARY

Mechanics-based models were developed for the stress-dependent resilient moduli and permanent deformation properties of each base course. Three coefficients are needed with the resilient modulus model: k_1, k_2, and k_3. Regression models of these coefficients were developed showing the relations of these coefficients to the indicator tests. Water content and pfc are significant predictors of these k-values as well as measures of aggregate shape and angularity. The aggregate shape and angularity can be measured in the laboratory while determining the quality characteristics of each pit. However, the water content and pfc need to be measured quickly and accurately in field to assure that the modulus used in design and needed for performance is what has been compacted in the field. The tests also showed that the suction in the base course is a very significant variable that controls the magnitude of the resilient modulus. There is a need to measure this important variable quickly and accurately in the field, also.

Two sets of permanent deformation properties were determined from the measured data: the VESYS and the MEPDG properties. The VESYS properties require the water content and the pfc to predict the amount of rutting and require measures of gradation, shape, and angularity to predict the rate at which rutting develops. The MEPDG properties require the pfc, water content and measures of angularity and texture to predict the maximum amount of rutting that will occur. It requires the pfc and a measure of the gradation to predict the amount of traffic required for the rutting to develop.

Reviewing the properties that are necessary to measure in the field shows that the water content, suction, and percent fines content as determined by the MBV relation are necessary. A field method was developed to measure all of these rapidly and accurately. The method requires the development of suction-vs-water content (SWCC) and suction-vs-dielectric constant (SDCC) curves for each source of base course in the laboratory prior to construction. The labor involved in doing this is less than what is required for compaction curves.

In the field, two measurements can be made on a sampling basis: a Grace MBV to determine the percent fines content and a Percometer test to determine the dielectric constant of the compacted base course. The percent fines content and MBV can be used to construct the suction-vs-water content (SWCC) and suction-vs-dielectric (SDCC) curves. The measured dielectric constant can be used with the suction-vs-dielectric curve to determine the suction. The suction can be used with the suction-vs-water content curve to determine the water content. The two tests, the MBV and dielectric constant test can be done in about ten minutes in the field. Both measurements are accurate and repeatable as well as rapid. A laptop computer can do the calculations to determine the pfc, suction, water content and resilient modulus of the base course and a matter of seconds. Furthermore, the permanent deformation properties which also depend significantly on the water content and pfc can also be calculated and the expected rutting and its variance can be calculated on the spot.

The fact that the Grace Methylene Blue test is so rapid and repeatable and that it has proven to be so reliable in determining the distribution of the fines content of a base course suggests that it can be used to track the amount by which the base course powders as it is handled from the pit to the stockpile to the job site and in the compaction process.

The net result is a quick, accurate and simple process for determining reliable values of the in-place as compacted base course modulus and permanent deformation properties. In addition, the measurements that are made should also contribute to the assurance of the quality of the process of

taking the base course from its quarry, transfer it to a stockpile and then haul it to a job site and compact it in place. In all of this process, from design to construction to quality control and assurance and ultimately to performance, all of it depends principally upon the principles and properties of unsaturated soil mechanics.

REFERENCES

AASHTO, T. 330-07. "The Qualitative Detection of Harmful Clays of the Smectite Group in Aggregates Using Methylene Blue".

ASTM C837-09. Standard Test Method for Methylene Blue Index of Clay.

ASTM D5298-10. Standard Test Method for Measurement of Soil Potential (Suction) Using Filter Paper.

Ashtiani, R.S. 2009. "Anisotropic characterization and performance prediction of chemically and hydraulically bounded pavement foundations." Ph.D. Dissertation, Texas A&M University, College Station, Texas.

Ashtiani, R.S., Luo, R. & Lytton, R.L. 2010. "Performance Prediction and Moisture Susceptibility of Anisotropic Pavement Foundations." ASCE Geotechnical Special Publication No. 203, Paving Materials and Pavement Analysis, American Society of Civil Engineers (ASCE), pp. 327–334.

Fairbairn, P.E. & Robertson, R.H. 1957. "Liquid limit and dye adsorption," Clay Minerals Bulletin. 3, 129–136.

Fredlund, D.G. & Xing, A. 1994. "Equations for the soil-water characteristic curve", Canadian Geotechnical Journal, Vol. 31, pp. 521–532.

Henkel, D.J. 1960. "The Shear Strength of Saturated Remoulded Clays," Proceedings of the ASCE Research Conference on Shear Strength of Cohesive Soils, Boulder, Colorado, pp. 533–554.

Holtz, R.D. & Kovacs, W.D. 1981. An Introduction to Geotechnical Engineering. Prentice-Hall, Englewood Cliffs, New Jersey.

Humboldt, 2010. Testing equipment for construction materials for H-4112 Percometer manual. Web page: www.humboldtmfg.com 3801 North 25th Avenue Schiller Park, Illinois 60176 U.S.A.

Kenis, W.J. 1977. "Predictive Design Procedures, a Design Method for Flexible Pavements Using the VESYS Structural Subsystem," Proceedings, 4th International Conference on Structural Design of Asphalt Pavements, Vol. 1, pp. 101–147.

Lai, J.S. 1977. VESYS-G, A Computer Program for Analysis of N-Layered Flexible Pavement, Report No FHWA-77-117, Federal Highway Administration.

Lytton, R.L., Aubeny, C.P. & Bulut, R. 2004. "Design Procedure for Pavements on Expansive Soils," Volume 1, Technical Report 0-4518-1, Texas Transportation Institute, Texas A&M University, College Station, Texas.

Mitchell, P.W. 1979. "The Structural Analysis of Footings on Expansive Soil," Kenneth W.G. Smith and Associates Research Report No.1, (1st Edition), Newton, South Australia.

Phelps, G.W. & Harris, D.L. 1967. "Specific surface and dry strength by methylene blue adsorption." American Ceramic Society Bulletin, Vol. 47, pp. 1146–1150.

Sahin, H. 2011. Characterization of expansive soil for retaining wall design. MS Thesis, Texas A&M University, College Station, Texas, USA.

Saue, T., Kadaja, J. & Plakk, T. 2008. "Measurement of soil water content by percometer," in Workshop Program and Papers: 1st Global Workshop on High Resolution Digital Soil Sensing and Mapping, Sydney, 2008, pp. 184–192.

Tseng, K.H. & Lytton, R.L. 1989. "Prediction of permanent deformation in flexible pavements materials, implication of aggregates in the design, construction, and performance of flexible pavements." ASTM STP 1016, American Society for Testing and Materials (ASTM), pp. 154–172, West Conshohocken, Pennsylvania.

Wang, M., Wang, S. & Wang, W. 1993. "Rapid estimation of cation exchange capacities of soils and clays with methylene blue exchange". Soil Science American Journal, Vol. 60, pp. 138–141.

Yeo, Y.S., Nikraz, H. & Jitsangiam, P. 2012. Tube Suction Test to Measure Moisture Susceptibility of Australian Pavements. Engineering Journal, 16(4).

Yool, A.I.G., Lees, T.P. & Fried, A. 1998. "Improvements to the Methylene blue dye test for harmful clay in aggregates for concrete and mortar". Cement and Concrete Research, Vol. 28, pp. 1417–1428.

This page intentionally left blank

Advances in Unsaturated Soils – Caicedo et al. (eds)
© 2013 Taylor & Francis Group, London, ISBN 978-0-415-62095-6

Estimation of the *1-D* heave of a natural expansive soil deposit with a light structure using the modulus of elasticity based method

S.K. Vanapalli & H.H. Adem
University of Ottawa, Ottawa, Ontario, Canada

ABSTRACT: Many studies are reported in the literature for estimating the maximum potential heave of expansive soils; however, limited efforts have been directed towards estimating the heave with respect to time. In this paper, a Modulus of Elasticity Based Method (MEBM) proposed by Adem & Vanapalli (2013) is used for estimation of the *1-D* heave over time of a light industrial building constructed on an expansive soil in Regina, Saskatchewan, Canada. This case study results were originally reported by Yoshida et al. (1983). The MEBM approach involves integrating semi-empirical and numerical techniques into a unified approach to estimate heave with time in response to the net changes in soil suction within the active zone depth of an expansive soil deposit. The variation of modulus of elasticity with respect to suction required for this approach is estimated using the semi-empirical model proposed by Oh et al. (2009) and introduced into the soil structure constitutive equation proposed by Fredlund & Morgenstern (1976) to estimate the soil heave over time. The net changes in the soil suction required for this approach was estimated using the commercial software VADOSE/W, a product of Geo-Studio. There is a good comparison between the results of the MEBM and the published data of measurements and estimations of heave over time. The encouraging results of the study presented in this paper suggest that the MEBM is simple and promising approach for use in engineering practice by geotechnical engineers for estimation of the *1-D* heave of expansive soils.

1 INTRODUCTION

Lightly loaded structures constructed on unsaturated expansive soils are often subjected to severe distress as a result of soil movement due to changes in their natural water content conditions. Water movement into an unsaturated expansive soil which is typically associated with natural rainfall infiltration or due to other activities such as garden watering/water pipe leaks leads to a decrease in suction contributing to soil heave predominantly in the vertical direction (i.e., *1-D* heave). In many cases, heave is also likely when the natural expansive soil deposit is covered with a pavement or due to the construction of a structure which contributes to an increase in water content and decrease in suction. Damage costs associated with expansive soil movements (heave/shrink) has been estimated to be around several billions of dollars annually.

Table 1 summarizes the annual costs associated with the damages to structures constructed on/with expansive soils for various regions of the world. A typical year losses due to structures constructed on or with expansive soils is greater than earthquakes, floods, hurricanes and tornadoes in USA (Nelson & Miller, 1992).

Table 1. The annual cost of damage to structures constructed on/with expansive soils for regions of the world (Adem and Vanapalli, 2013).

Region	Cost of damage/ year	Reference
USA	$13 billion	Puppala & Cerato (2009)
UK	£ 400 million	Driscoll & Crilly (2000)
France	€ 3.3 billion	Johnson (1973)
Saudi Arabia	$ 300 million	Ruwaih (1987)
China	¥ 100 million	Ng et al. (2003)
Victoria, Australia	$ 150 million	Osman et al. (2005)

Several methods have been proposed in the literature for the determination, prediction or estimation of the volume change behaviour of expansive soils. A comprehensive review of these methods is available in Vanapalli & Lu (2012). The focus of most of the methods has been towards estimating or predicting the maximum potential heave which occurs when the soil attains saturation condition.

Limited studies were reported in the literature (Ching & Fredlund 1984, Allman et al., 1998,

Ng et al. 2003, Fityus et al. 2004) to measure the soil heave with respect to time. Such studies are useful to propose reliable design procedures for structures with or in expansive soils. However, such studies are expensive and cumbersome and hence cannot be undertaken for routine engineering practice applications. Several investigators in recent years proposed prediction procedures (Sattler & Fredlund 1991, Briaud et al. 2003, Vu & Fredlund 2004, Chao 2007; Nelson et al. 2011, 2012a&b) for estimating the heave over time. The proposed methods however have been validated with field measurements using one or limited number of case studies to date.

It is well-known that the amount of expansive soil heave due to water migration depends on the stiffness of the soil, which is equivalent to the soil modulus of elasticity (Jones & Jefferson 2012). In other words, the modulus of elasticity varies with the change in water content and associated soil suction within the active zone depth. The information related to the variation of the modulus of elasticity due to soil water migration is a valuable tool for estimating the soil movements. The modulus of elasticity is not only a sensitive parameter but also comparatively an easier parameter to measure its value reliably in-situ using pressuremeter tests or estimate from conventional cone penetration tests.

A modulus of elasticity based method (hereafter referred to as MEBM) is proposed recently by Adem & Vanapalli (2013) to estimate the variation of *1-D* heave in terms of soil suction changes over time. In the MEBM, Fredlund & Morgenstern (1976) constitutive equation for soil structure (that includes the modulus of elasticity) is integrated along with the soil-atmosphere model VADOSE/W (GeoSlope, 2007) (hereafter referred to as software).

An example problem of volume change of expansive soil investigated by Vu & Fredlund (2006) was tested in Adem & Vanapalli (2013) to validate the MEBM. The MEBM has been found to be relatively simple which can be used for estimating the *1-D* heave of expansive soils with respect to time. An overview of this example analysis has been succinctly presented in the present paper. However, the volume change behaviour of natural in-situ expansive soils in the active zone depth is much more complex due to the influence environmental factors such as precipitation, evaporation and transpiration. In addition, other parameters such as the soil history including its geology, macro and microstructure, cracks associated with the desiccation, clay mineralogy and over burden pressure influence the heave.

In this paper, case history of a light industrial building in north-central Regina, Saskatchewan is investigated using the MEBM. History of the site and details of testing and monitoring programs are available in Yoshida et al. (1983). Heave analyses of the case history using laboratory oedometer data and various assumptions concerning the final pore water pressures are presented in Vu & Fredlund (2004). The proposed MEBM is evaluated by comparing heave estimates with the field measurements beneath the industrial building.

2 LITERATURE REVIEW

2.1 *Heave prediction methods*

The expansive soils heave behaviour has a significant influence on the design of the structures constructed on/with unsaturated expansive soils. Various attempts have been made by several investigators to propose different methods for predicting the heave of expansive soils during the last six decades (Vanapalli & Lu, 2012). The methods developed to date can be classified into three main categories: empirical methods; oedometer methods; and suction methods. The available heave prediction methods in the literature are succinctly summarized. In addition, their shortcomings for use in engineering practice are briefly discussed.

2.1.1 *Empirical methods*

Empirical methods are encouraging to the practicing engineers as they are based on physical and index properties of soils. In other words, they are simple and economical. The swelling behavior of expansive soils (which includes key characteristics such as the volume change, swell percent, and swelling pressure) is represented by using empirical equations relating to physical and index properties of expansive soils (liquid limit, plasticity index, initial water content, dry density, and clay content). A large number of such equations or relationships available in the literature have been originally derived from testing limited number of expansive soils (e.g., Seed et al., 1962, Van der Merwe 1964, Nayak & Christensen 1971, Vijayavergiya & Ghazzaly 1973, Brackley 1975, Weston 1980, Dhowian et al., 1985).

Soil heave can be estimated using these methods by dividing the soil profile into layers, multiplying the appropriate swell percent by the layer thickness and then sum up the heaves of various layers of the expansive soil profile. The comparative studies undertaken by Noble (1966) and Zein (1987) clearly show that the empirical heave prediction equations, while seemingly adequate for known conditions in the regions where they were developed, have severe limitations when they have been used for other regions. These limitations can be attributed to not considering many parameters that influence the swell behaviour such as the soil structure, clay mineralogy, and environmental factors to list a few. In addition, the procedures for

collection of data from different regions may vary based on the local site stratigraphy and the recommended procedures for regional codes. Furthermore, clay property variation over the same site or sites makes it a challenge to obtain representative soil samples and determine reliable data from laboratory tests.

Recently, Vanapalli et al. (2010) proposed an empirical method that can be used to estimate the maximum potential *1-D* heave of natural expansive soils occurring as a response to the water content variations. The empirical equations required for using the method were developed from the published data of various regions of the world. The required information for these empirical equations can be obtained from simple laboratory tests. The proposed relationships eliminate the need for difficult and time consuming laboratory/in-situ tests. This method was tested on 7 case studies published in the literature. The method appears to be promising for providing reasonable estimates of the soil heave. However, this method can be only used to estimate the maximum potential heave.

2.1.2 *Oedometer methods*

Considerable research has been conducted to predict the soil heave based on the results of oedometer tests (e.g., Jennings & Knight 1957, Salas & Serratosa 1957, Lambe & Whitman 1959, Clisby 1963, Aitchison & Woodburn 1969, Sullivan & McClelland 1969, Aitchison et al., 1973). The oedometer based methods require representative undisturbed samples collected from active zone depth typically in a dry season. The samples are then placed in oedometers and allowed to swell to saturation under a vertical applied pressure equivalent to their in-situ overburden pressures. The swelling pressure and heave index obtained from the results of oedometer test are used to estimate the soil heave of each layer. Total heave is then estimated by summation of individual layers heaves. Researchers have focused on improving and predicting heave using different types of odeometer test results suggesting various corrections including taking account of the compressibility of the apparatus (e.g., Fredlund et al., 1980, Fredlund 1983, Nelson & Miller 1992, Fredlund & Rahardjo 1993, Feng et al., 1998, Nelson et al., 1998, Bonner 1998, Nelson et al., 2003 & 2006).

Two different oedometer test procedures have been used commonly for estimating the soil heave, namely (i) consolidation-swell test, and (ii) controlled strain (i.e., constant volume swell, CVS) test. Figures 1 and 2 show idealized plots of consolidation swell test data and constant volume test data, respectively. A detailed description of these test methods are available in Nelson & Miller (1992) and ASTM Test Method D4546.

The oedometer test results are widely used in practice for estimating the expansive soil heave; however, environmental factors such as drainage conditions similar to in-situ conditions and effects of lateral pressures cannot be simulated well in the oedometer tests. Another disadvantage of oedometer methods is that the extremely long time periods required for achieving equilibration conditions which makes these methods both costly and tedious to use (Holland & Cameron, 1981). In addition, different oedometer methods provide significantly different swell pressure values; for example, Fredlund and Rahardjo (1993) report that the swelling pressure taking account compressibility corrections of the apparatus can be twice as much as the uncorrected swelling pressure.

The oedometer methods use simplified assumptions to evaluate the matric suction variations by assuming that the soil will change from current unsaturated conditions to saturation condition (Fredlund & Rahardjo, 1993). Research studies show that the predicted soil heave by using an assumption of saturation condition as a limiting condition is much higher than the measured values. Simple yet reliable methods are necessary to estimate the suction or water content fluctuations through the soil profile to estimate the in-situ expansive soil heave (Zhang & Briaud 2010).

2.1.3 *Suction methods*

Several investigators have proposed soil suction methods in the literature for predicting the amount of volume change of expansive soils (e.g., Johnson 1977, Johnson & Snethen 1978, Fredlund 1983, Snethen, 1980, McKeen 1981 &1992, Lytton 1994 &1997). These methods involve the measurement of soil suction and associated volume change over the moisture content range between shrinkage limit and plastic limit (Hamberg 1985,

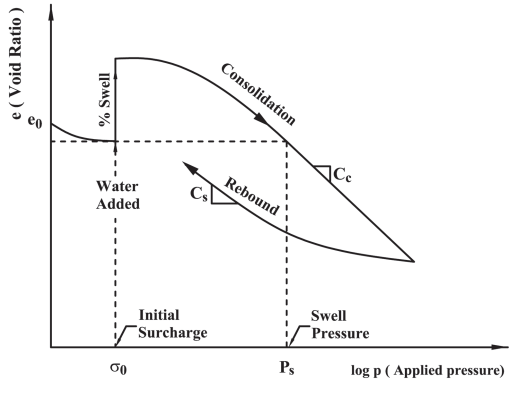

Figure 1. Typical consolidation-swell test results (modified after Hamberg, 1985).

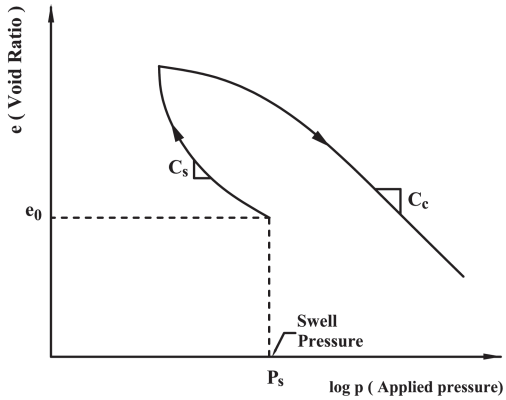

Figure 2. Typical constant volume test results (modified after Nelson & Miller, 1992).

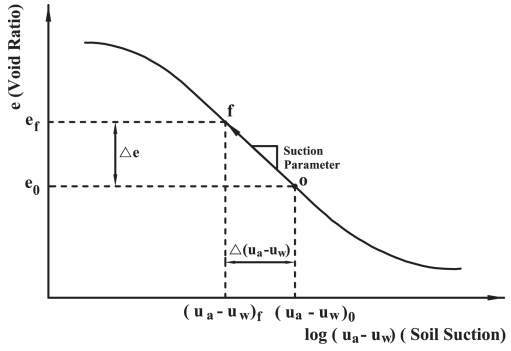

Figure 3. Idealized void ratio versus logarithm of suction relationship for a representative sample (modified after Hamberg, 1985).

Johnson & Snethen 1978, Mitchell & Avalle 1984). Figure 3 shows an idealized relationship between void ratio and log suction for a representative soil sample. The soil suction parameter, which represents the slope of a void ratio versus soil suction plot, has been determined differently for each method (e.g., soil suction index (Johnson 1977, Snethen 1980), suction index ratio (Hamberg & Nelson 1984, Hamberg 1985), instability index (Aitchison 1973, Mitchell & Avalle 1984), or suction compression index (McKeen & Nielsen 1978, McKeen 1980 & 1981, Wray 1997). The different names for the soil suction parameter arise from the concept that unit volume change (i.e., void ratio changes) is related linearly to either soil suction change or moisture content change within the range of field conditions. The initial soil suction profile, the assumed final soil suction profile and the suction parameter are the commonly used parameters in soil suction methods. The initial suction can be measured by thermocouple psychrometer, thermal conductivity sensors, filter paper, or other suitable methods. However, assumptions can also be used for the final soil suction profile (Fredlund et al. 1980, Fredlund 1983, and Snethen 1980). Three different scenarios suggested by Fredlund et al. (1980) can be used for estimating the final matric suction: (i) assuming the groundwater table at the soil surface; (ii) the pore water pressure approaches zero throughout its depth; and (iii) the pore-water pressure will remain slightly negative under long-term equilibrium conditions. These assumptions are simple and reasonable; however, they do not provide details of how unsaturated expansive soils volume changes with respect to time.

Suction methods are considered to be reliable and capable of simulating field conditions. However, several possible limitations summarized below are likely when they are extended in practice:

(i) suction parameter is not a constant value but is a function of stress state (i.e., loading condition including the overburden pressure);
(ii) the relationship of the soil suction on log scale versus volume change is linear only over a certain range of suction; this range is not known or well defined in most cases.
(iii) matric suction values have to be measured or estimated for each site. However, it is a challenge to reliably measure field matric suction values especially in expansive soils; and
(iv) A fixed depth of active zone (the depth of suction variations) cannot be assumed as it varies with site and depends on the environmental changes such as the extent of wetting, the duration of wetting, and the pattern of moisture migration. (Snethen & Huang, 1992).

2.2 *Rate of heave*

The amount of soil heave that occurs in the field is function of time. As water migrates through the soil profile due to environmental or other factors, expansive soil heave increases with time. Nevertheless, most of existing heave prediction methods estimates the maximum potential heave by assuming the saturation conditions throughout the active zone of the expansive soil profile. The results of heave estimation considering saturated soil profile conditions are not always practical or economical in engineering practice. In an attempt to develop both reliable and economical procedures of analysis, few methods were proposed during the last decade for computing heave

considering partial wetting conditions (heave variations over time).

2.2.1 *Briaud et al. (2003) method*

Briaud et al. (2003) developed a shrink test-water content method for estimating the vertical movement of the ground surface due to variations in water content over time. Figure 4 shows the typical relationship of the water content versus the volumetric strain obtained from a shrink test. The shrink–swell modulus (i.e., the slope of the water content versus the volumetric strain line), and the shrinkage ratio (i.e., the ratio of the vertical strain to the volumetric strain) are the key parameters that are calculated from a shrink test. This method is based on the information of water content which is more reliable and simpler to measure using various methods in comparison to the soil suction. However, it is uncoupled analysis of unsaturated soils where only the influence of moisture variation on the volume change of expansive soils is considered. In addition, when the soil is highly fractured, a shrink test is difficult to perform.

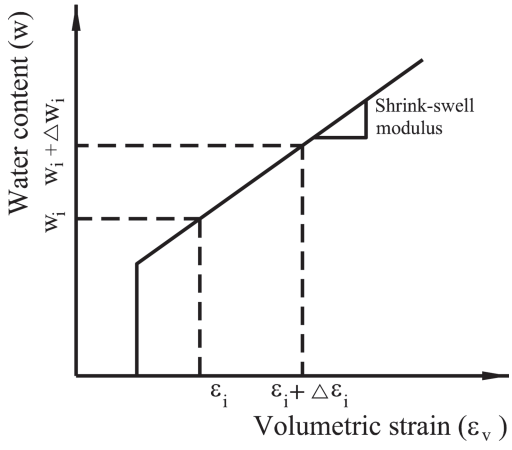

Figure 4. The water content versus the volumetric strain obtained from the shrink test (modified after Briaud et al., 2003).

2.2.2 *Vu & Fredlund (2004) method*

Vu & Fredlund (2004) proposed a method for the prediction of one-, two-, or three-dimensional heave of expansive soils over time using the general theory of unsaturated soils. It is suggested that changes in matric suction (or pore-water pressure) in the soil mass can be estimated through a saturated–unsaturated seepage analysis. The results of the seepage analysis are then used as input for the prediction of displacements due to loading and changes in matric suction in a stress–deformation analysis. The governing equation for the seepage analysis can be obtained by substituting the time derivative of water phase constitutive equation (Fredlund & Rahardjo, 1993) and Darcy's law into the water phase continuity equation (Freeze & Cherry, 1979). However, for the stress-deformation analysis, the governing equation can be obtained by substituting the strain-displacement relationship and the soil structure constitutive relationship (Fredlund & Rahardjo, 1993) into the soil structure equilibrium equation. The governing equations for both seepage analysis and stress-deformation analysis can be numerically solved using finite element computer programs. Some numerical modelling problems associated with the solutions of the partial differential equations have been encountered in this method: i) unstable and unreasonable numerical solution (i.e., extremely low elastic moduli associated with unreasonably large soil movements) at low stresses and (or) low suction, and (ii) the difficulty to obtain the solution of coupled equations with several nonlinear unsaturated soil property functions. In this method, conventional oedometer tests are used to determine the elasticity parameter functions required for a stress–deformation analysis. One disadvantage associated with the oedometer tests is the difficulty in measuring a unique swelling pressure, since it is sensitive to the testing procedure. In addition, this single value may not be representative value over the entire depth of the active zone and for the area considered for expansive soils heave.

2.2.3 *Nelson et al. method*

Recently, Nelson et al. (2011, 2012a & b) developed a finite element method of analysis to compute pier movement in expansive soils having variable soil profiles, complex wetting profiles, large length-to-diameter ratios, and complex pier configurations and materials. In Nelson et al. method, the depth of wetting and corresponding degree of saturation is calculated using commercial software VADOSE/W. The free-field heave (i.e., the heave that will occur at the surface of a soil profile if no stress is applied) is the fundamental parameter required in this method for estimating the pier movement. Methods for calculating free-field heave have been developed that use either oedometer tests or soil suction tests. Using the results of these analyses, the amount of heave with respect to time that is expected to occur in the partially wetted zone can be calculated. The results show the versatility of this method with regard to variable soil profiles and wetting zones. Experimental determination of the free-field heave using oedometer tests or soil suction test is both time consuming and difficult to develop. Other limitations of the oedometer methods were discussed in greater detail in earlier sections and are not repeated here.

3 MODULUS OF ELASTICITY BASED METHOD (MEBM) PROPOSED BY ADEM & VANAPALLI (2013)

The variation of expansive soil heave over time is estimated using the MEBM proposed by Adem and Vanapalli (2013) based on the following information: (i) the active zone depth (considering the fluctuations of soil suction); (ii) the range of soil suction fluctuations as a function of time within the active zone; and (iii) the constitutive equation that links the governing parameter (soil suction) to the heave of expansive soil.

The finite element software VADOSE/W has been used as a tool to estimate the matric suction changes in the active zone depth due to environmental changes. The constitutive equation of Fredlund & Morgenstern (1976) for soil structure has been simplified to relate the *1-D* heave of expansive soil with the matric suction changes using soil compressibility index with respect to the matric suction. More details of the MEBM are available in Adem & Vanapalli (2013). The key procedural steps are succinctly summarized in the following sections.

3.1 *Simulation of the changes in soil suction over time*

The simulation of matric suction changes over time can be performed using the commercial software VADOSE/W. The software has features to predict suction and temperature changes in the soil profile in response to variations in environmental data (i.e., air temperature, relative humidity, solar radiation, wind speed and precipitation). The software can be used as a simplified *1-D* finite element model or a *2-D* model with complex geometry. It accounts for the physical processes of evaporation and infiltration in unsaturated soils, using the Penman–Wilson method (Wilson 1990) and a modified form of the Darcy equation (Richard 1931, Milly 1982, Wilson 1990, Adu-Wusu et al., 2007). The initial condition (i.e., initial matric suction or initial water content profile), the boundary conditions (i.e., climate, hydraulic and thermal boundaries), and the soil properties (SWCC, coefficient of permeability function, thermal conductivity function, and volumetric heat capacity) are the required input parameters into the model.

3.2 *Prediction of the 1-D heave of the expansive soil*

The constitutive equation proposed by Fredlund & Morgenstern (1976) extending continuum mechanics principles to rationally interpret the volume change behaviour of unsaturated soils using two stress state variables; namely, net normal stress, $(\sigma - u_a)$ and matric suction, $(u_a - u_w)$, (where, σ = the total stress, u_a = the pore-air pressure, and u_w = the pore-water pressure). Fredlund et al. (1980) suggested that the volume change behaviour of unsaturated expansive soils can be expressed in terms of vertical strain estimated by extending the assumption of K_0-loading (one-dimensional case). Strains in the *x*- and *z*- directions are zero while their changes in total stress are equal. The strain in the *y*- direction can be calculated using Equation 1.

$$\varepsilon_y = m_1^s \, d(\sigma_y - u_a) + m_2^s \, d(u_a - u_w) \tag{1}$$

where ε_y = linear strain in *y*-direction, $m_1^s = 2(1+\mu)/(E(1-\mu))$ = soil structure compressibility modulus associated with a change in net normal stress $(\sigma_y - u_a)$, and $m_2^s = (1+\mu)/(H(1-\mu))$ = soil structure compressibility modulus associated with a change in matric suction $(u_a - u_w)$.

Equation 1 can be visualized as a *3-D* surface (Fig. 5). This surface is not unique and differs for loading and unloading conditions, and for increasing and decreasing matric suction values (Fredlund et al., 1980).

Fredlund et al. (1980) computed the maximum potential heave by dividing soil profile for a given site into several layers; the maximum potential *1-D* heave for each layer (Δh_i) is computed by multiplying the vertical strain of a soil layer (ε_y) occurring when the soil attains saturation condition (Eq. 1) by the layer thickness (h_i). The total maximum heave for the soil profile is the summation of the heave of all layers within the active zone.

$$\begin{aligned} \Delta h &= \sum_{i=1}^{n} \Delta h_i \\ &= \sum_{i=1}^{n} \left(h_i \left[m_1^s \, d(\sigma_y - u_a) + m_2^s \, d(u_a - u_w) \right]_i \right) \end{aligned} \tag{2}$$

For pavements and lightly loaded structures, the changes in the total mechanical stress are not significant. The cumulative soil heave hence can be computed considering only the change in matric suction using the expression below.

$$\Delta h = \sum_{i=1}^{n} \left(h_i \left[m_2^s \, d(u_a - u_w) \right]_i \right) \tag{3}$$

In the MEBM, Equation (3) is used to estimate the *1-D* heave of soil associated with change in matric suction for each day. The in-situ fluctuation of soil suction for each day predicted using VADOSE/W is multiplied by the thickness of soil layer and the compressibility modulus associated with the soil suction value to estimate the heave of

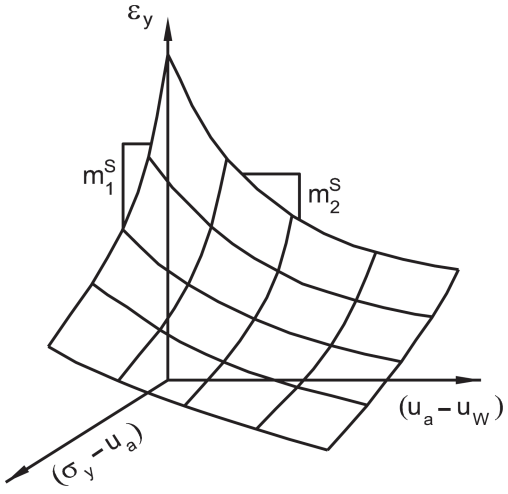

Figure 5. Constitutive surface for soil structure (modified after Fredlund et al. 1980).

the layer per each day. The soil-water characteristic curve (hereafter referred to as SWCC) and daily climate data for a given site is required to estimate the variations of matric suction in the active zone depth with respect to time. The heave of each layer at a given time is the cumulative value of heave for all days prior to that period. The total heave at any point in the soil profile is the summation of the heave of all layers below it.

The compressibility modulus associated with change in matric suction (m_2^s) is a function of the modulus of soil elasticity (E). The modulus of elasticity however varies significantly with soil water content (or soil suction) (Oh et al., 2009, Nelson et al., 2011). A semi-empirical model introduced by Vanapalli & Oh (2010) to estimate the modulus of elasticity with respect to suction for both coarse and fine-grained soils has been extended for expansive soils.

$$E_{unsat} = E_{sat}\left[1 + \alpha\frac{(u_a - u_w)}{(P_a/101.3)}(S)^{\beta}\right] \quad (4)$$

Where E_{unsat}, E_{sat} = the moduli of elasticity under unsaturated and saturated conditions, respectively, P_a = atmospheric pressure (i.e., 101.3 kPa), S = degree of saturation, and α, β = the fitting parameters.

The value of E at saturated conditions can be determined using triaxial or oedometer tests results for saturated soil samples. The saturated modulus of elasticity (E_{sat}) value required for the present analyses has been calculated using Equation 5 introduced by Zhang (2004) based on the results of oedometer tests (the relation between the soil void ratio and the mechanical stress at saturated condition).

$$E_{sat} = \frac{3(1-2\mu)(1+e_0)}{(\partial e/\partial(\sigma - u_a))} \quad (5)$$

where e_0 = the initial void ratio.

4 VALIDATION OF THE MEBM

4.1 *Example problem (Vu & Fredlund 2006)*

This section provides a succinct summary of the simulation of the example problem elaborated in Adem & Vanapalli (2013). The example problem was originally modeled by Vu & Fredlund (2006), considering 5 m thick deposit of Regina expansive clay partially covered with a slab of lightly loaded structure. An infiltration of 2×10^{-8} m/s (i.e., 1.73 mm/day) was imposed at the ground surface around the structure over a period of 175 days (Fig. 6). The coefficient of permeability function of the soil for this example was estimated using the software, based on the input information of saturated coefficient of permeability and the SWCC given by Vu (2003). Figure 7 shows the SWCC and the permeability function used in the study analysis. Soil properties for Regina expansive clay is presented in Table 2. Soil properties for the example problem analysis was assumed by Vu & Fredlund (2006) as shown in Table 3.

The simulation of matric suction was implemented using the software to model over the period of 175 days. The example was modeled as *2-D* problem considering transient isothermal analysis. The boundary conditions and the initial condition for the suction simulation are illustrated in Figure 6.

Vu & Fredlund (2006) estimated heaves at three points A, B and C at depths of 0 m, 1.5 m and 3.5 m, respectively (see Figure 6). The same points were investigated in Adem & Vanapalli (2013) using the MEBM. Figure 8 shows the changes of matric suction values with time at A, B, and C. Figure 8 shows that the initial matric suction of 400 kPa decreases with respect to time. The matric suction at the ground surface (at A) has a lower value compared to the other two locations (B & C) due to influence of infiltration. Figure 9 shows the variations of matric suction profiles at the right of the outer edge of the slab in response to the infiltration through the period of simulation. This figure highlights the effect of the infiltration on the soil suction as discussed before.

Based on the estimated changes in matric suction within the soil profile over time, the total *1-D* heave was calculated at any depth over time.

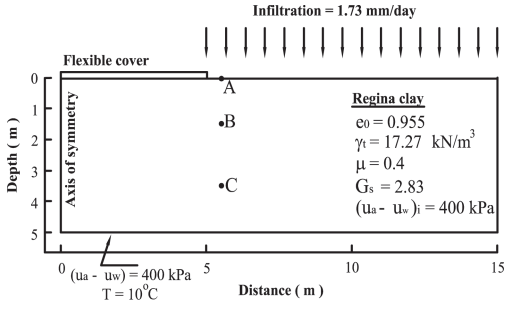

Figure 6. Geometry, key soil properties, and boundary conditions for the example problem (modified after Vu & Fredlund 2006).

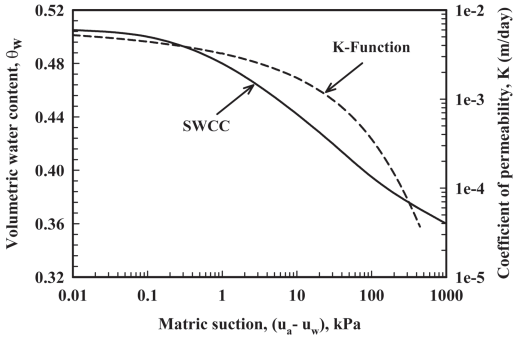

Figure 7. Hydraulic characteristics of Regina expansive clay used for the example problem (Adem & Vanapalli 2013).

Table 2. Soil properties for Regina expansive clay (Shuai 1996).

Soil properties	Values
Atterberg limits	$w_l = 69.9\%$; $w_p = 31.9\%$; $I_p = 38\%$
Unified Soil Classification System	CH, Inorganic clay of high plasticity
Specific gravity	$G_s = 2.80$
Maximum dry density	$\gamma_{dmax} = 14.01$ kN/m^3
Optimum water content	$w_{optm} = 28.5\%$
Swelling index	$C_s = 0.09$
Corrected swelling pressure	$P_s = 300$ kPa

Figure 10 shows a good agreement between the *1-D* heave that was estimated using the MEBM and those from Vu & Fredlund (2006) studies. The excellent agreement for the results of Vu & Fredlund (2006) for a slab-on-ground constructed on Regina expansive clay are encouraging for the use of the MEBM in estimating the variations of actual *1-D* heave with time.

Table 3. Soil properties used for the simulation of the example problem (Vu & Fredlund 2006).

Soil properties	Values
Total unit weight	$\gamma_t = 17.27$ kN/m^3
Initial void ratio	$e_0 = 0.955$
Poisson's ratio	$\mu = 0.4$
Saturated modulus of elasticity	$E_{sat} = 1071$ kPa
Saturated coefficient of permeability	$K_{sat} = 0.00523$ m/day
Saturated volumetric water content	$\theta_s = 0.5015$
Initial matric suction	$(u_a - u_w)_i = 400$ kPa
Fitting parameters used in Eq. 4	$\beta = 2$, $\alpha = 0.1$

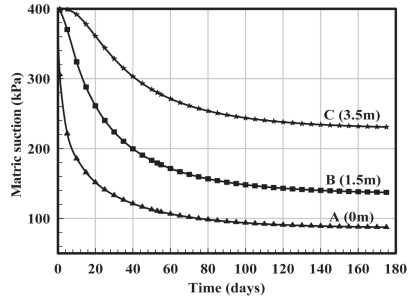

Figure 8. Matric suction changes with time.

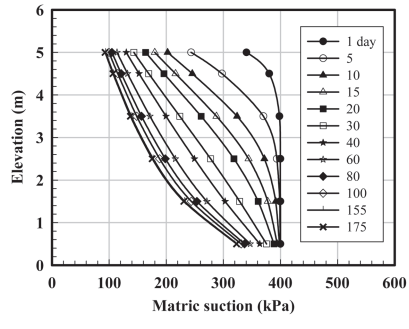

Figure 9. Matric suction profiles for the 5 m depth over a period of 175 days.

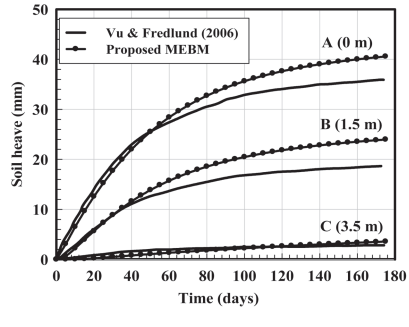

Figure 10. Predicted heaves using the proposed MEBM and Vu & Fredlund (2006) method.

4.2 *Case history (Yoshida et al., 1983, Vu & Fredlund 2004)*

The case history used in this paper for validation of the MEBM for *1-D* heave prediction is a light industrial building constructed on an expansive soil deposit in Regina, Saskatchewan. The building was constructed by the Division of Building Research, National Research Council in 1961. One year after construction, heaving and cracking of floor slab was noticed by the building owner. The owner also noticed unexpected loss of 35 m^3 of water. This amount of water loss was traced to a leak, in a hot-water line beneath the floor slab (Yoshida et al., 1983). The maximum heave observed on the slab was found to be 106 mm. Figure 11 shows the geometry and the boundary conditions for the case history analysis. A 2.3 m thick deposit of Regina expansive clay was considered for the estimation of *1-D* heave. This depth was considered to be equivalent to the active zone depth beyond which there will be no tendency for swelling. It was assumed that water leaked from the pipe line along a 2 m length (Yoshida et al., 1983) (Figure 11). The matric suction was relatively high close to the surface and decreased with depth. The values of matric suction through the soil profile dissipated with time and reached steady state condition which was equal to 20 kPa in about 150 days (Figure 14). More details are discussed in later sections of the paper.

For comparison purposes, the initial and the boundary conditions assumed by Vu & Fredlund (2004) were used in the present simulation. Figure 12 presents the SWCC and the permeability function given by Vu & Fredlund (2004) and used in the current analysis. The SWCC was estimated using the Fredlund and Xing (1994) equation and the coefficient of permeability function was described using the Leong and Rahardjo (1997) equation.

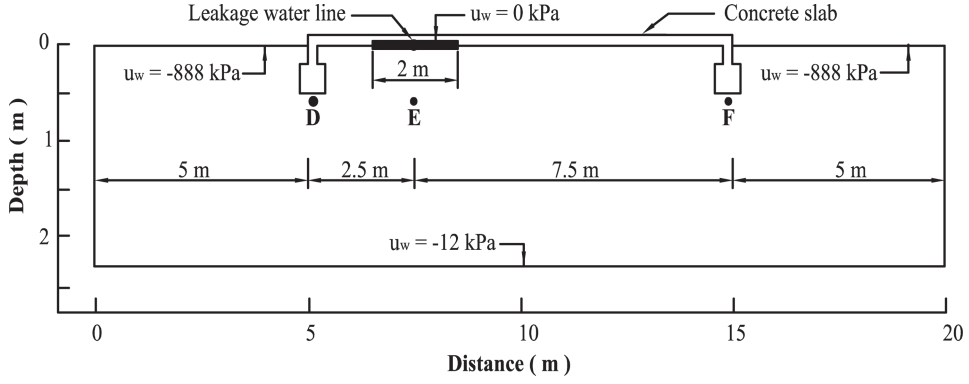

Figure 11. Geometry and boundary conditions (modified after Vu & Fredlund 2004).

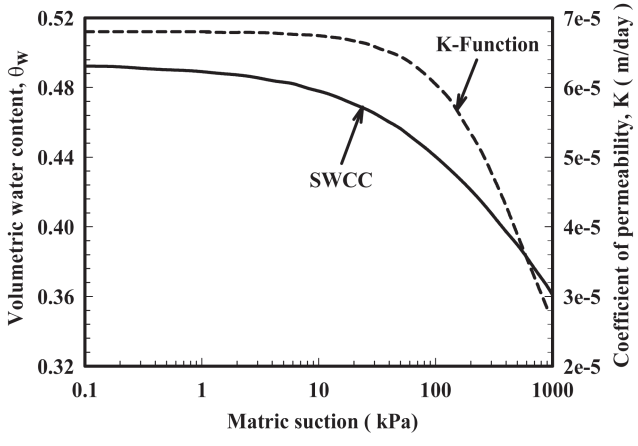

Figure 12. Hydraulic characteristics of unsaturated Regina expansive clay for the case history. (modified after Vu & Fredlund 2004).

The soil properties for Regina expansive clay are summarized in Table 4. The two steps, namely matric suction simulation and soil heave prediction of the MEBM are applied on the case history for various elapsed times (i.e., 5, 20, 50, 100 days, and at the steady state condition).

4.2.1 *Matric suction simulation*

The simulation of matric suction over time was carried out using the software. The case history was modeled as a *2-D* problem considering transient isothermal analysis to solve the system of equations for the surface water and energy balances, subsurface heat transport, and variably saturated flow. The boundary conditions for the suction simulation following Vu & Fredlund (2004) are presented in Figure 11. A suction of 12 kPa was maintained along the bottom boundary during the period of simulation. This was achieved by specifying a pressure head of –1.223 m (i.e., –12/9.807) at the bottom boundary. A suction of 888 kPa (i.e., –90.52 m pressure head) was maintained along the top boundary around the slab. The temperature in the soil was assumed to be constant (T = 10 °C); in other words, the temperature effects were omitted in the model (transient isothermal analysis was assumed). The initial matric suction as a function of depth given by Vu & Fredlund (2004) is used to represent the initial condition.

Vu & Fredlund (2004) predicted the changes of matric suction with time at three locations (D, E, and F) at 1.3 m depth as shown in Figure 11. The same locations are investigated using the MEBM. Figure 13 shows the comparison of the predicted matric suction values at D, E, and F versus time using the MEBM with the numerical modeling results published in Vu & Fredlund (2004). Figure 14 presents the comparison of the predicted and the published pore-water pressure profiles under the center of the slab for various elapsed times (i.e., 5, 20, 50, 100 days, and at the steady state condition).

4.2.2 *Soil heave prediction*

The leakage from the water line below the floor slab of the building leads to an increase in pore-water pressure (i.e., decrease in matric suction), which contributes to soil heave. Once the changes in soil suction over time are estimated within the soil profile, the total heave with respect to time can be calculated at any location. The day to day changes of the matric suction values estimated using the software were substituted into the reduced constitutive relationship (Eq. 3) to calculate the *1-D* heave with respect to time. The semi-empirical model proposed by Vanapalli & Oh (2010) (Eq. 4) was solved for the soil properties summarized in Table 4 and based on the SWCC to estimate the modulus of elasticity of the soil in terms of the matric suction. The average modulus of elasticity of the soil under saturated condition given in Table 4 (E_{sat} = 800 kPa) was calculated using Equation 5. The change in the void ratio with respect to the net normal stress was obtained using the constitutive relationships

Table 4. Soil properties used for the case history analysis (Vu & Fredlund 2004).

Soil properties	Values
Total unit weight	$\gamma_t = 18.88$ kN/m^3
Specific gravity	$G_s = 2.80$
Initial void ratio	$e_0 = 0.962$
Poisson's ratio	$\mu = 0.4$
Saturated modulus of elasticity	$E_{sat} = 800$ kPa
Saturated coefficient of permeability	$K_{sat} = 6.8$e-5 m/day
Saturated volumetric water content	$\theta_s = 0.493$
Fitting parameters used in Eq. 4	$\beta = 2$, $\alpha = 0.05$

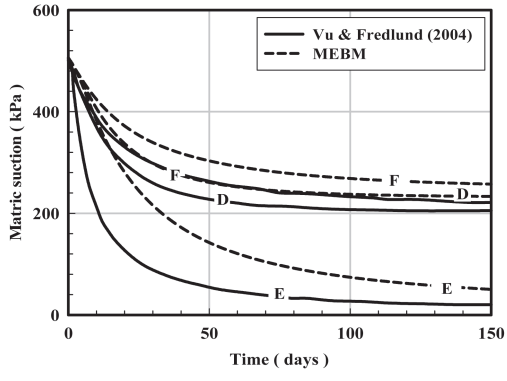

Figure 13. Matric suction changes with time for the three locations (D, E, and F).

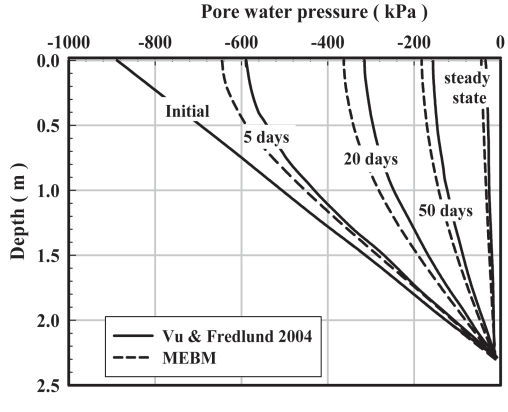

Figure 14. Pore-water pressure profiles for various elapsed times under the center of the slab.

provided in Vu (2003). To evaluate the *1-D* heave at the ground surface for each time interval, the 2.3 m depth of soil (depth of suction variations) was divided into six equal layers of 0.3 m thickness and a 0.5 m thick bottom layer. The total heave for a certain time was computed by adding the heave associated with that time for all layers below the considered point (Eq. 3). Figures 15 and 16 show the comparison of predicted soil heave using the MEBM with both the measurements and the numerical modeling results published in Vu & Fredlund (2004) under the center of the slab and along the surface of the slab, respectively.

4.2.3 *Analysis and discussion*

The matric suction variations with respect to time are evaluated at the three locations (D, E, and F) using the software. Review of Figure 13 shows that the initial matric suction significantly decreases with time and approaches a steady state condition in about 150 days. A good agreement is obtained between the soil suction that is estimated using the proposed MEBM and Vu & Fredlund (2004) method. However, the predicted matric suction at E (below the leakage position) using the MEBM is slightly higher compared to the predicted suction values of Vu & Fredlund (2004) at the same point. The reason for this difference may be attributed to the effect of the boundary condition that is used to represent the leakage (i.e., $u_w = 0$). Also, the differences may be due to the use of different software to simulate the matric suction variations. VADOSE/W was used in the analysis presented in this paper while FlexPDE2 (the general-purpose partial differential equation solver) was used in Vu & Fredlund (2004). Review of Figure 13 also shows that the matric suction at E has a lower value compared to the other two locations (D and F). This reflects the effect of the wetting which is accompanied by a reduction in negative water pressures or suctions. Figure 14 shows the variations of the negative pore-water pressure (matric suction) profiles at the center of the slab in response to the wetting over the period of simulation. There is a reasonably good comparison between the soil suction variations estimated using the MEBM and the Vu & Fredlund (2004) method. The wetting primarily influences in the upper soil layers near the ground surface, which contributes to significant changes of the soil suction within the surface zone.

Based on the estimated changes in soil suction over time, the total *1-D* heave with respect to time can be calculated at any depth. Figure 15 shows a good agreement between the *1-D* heave under the centre of the slab estimated using the proposed MEBM and published in Vu & Fredlund (2004). The total heave increases with a decrease in matric suction, with most of the heave occurring in upper soil layers near the ground surface in which the changes of soil suctions are relatively high. The heaves measured by Yoshida et al. (1983) are also plotted on the same graph (Fig. 15). Some differences between the predicted and the measured heave can be observed. The heave values measured at depths of 0.58 and 0.85 m correspond to the predicted heave at 100 days. Figure 16 compares the predicted soil heaves obtained from the present analysis and Vu & Fredlund (2004) analysis with the measured total heave at the surface of the slab. The total heave predicted using the MEBM agrees well with the heave predicted by Vu & Fredlund (2004).

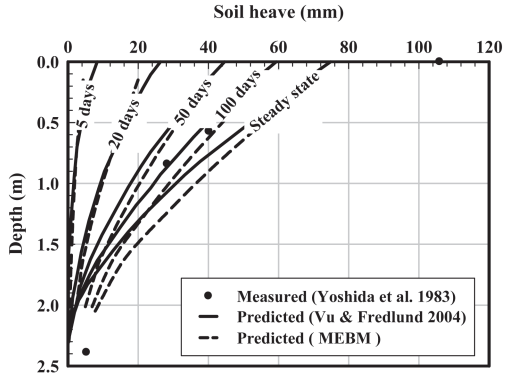

Figure 15. Measured and predicted soil heave profiles under the center of the slab.

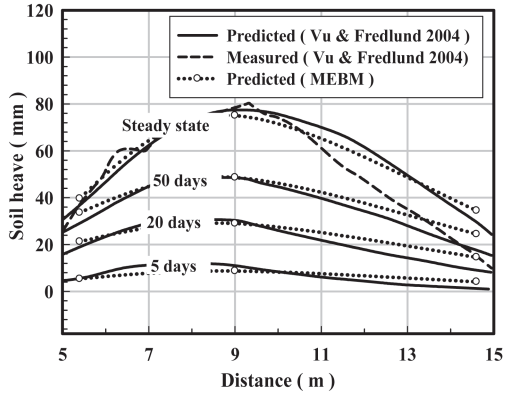

Figure 16. Measured and predicted soil heave values along the surface of the slab.

5 SUMMARY AND CONCLUSIONS

The Modulus of Elasticity Based Method (MEBM) proposed by Adem and Vanapalli (2013) is evaluated in this paper to predict the *1-D* heave

of unsaturated expansive soils. This method is based on the theoretical concepts of unsaturated soils and involves integrating the numerical modeling results of the VADOSE/W model (i.e., matric suction distribution) and the constitutive equation for soil structure proposed by Fredlund & Morgenstern (1976). The semi-empirical model developed by Vanapalli & Oh (2010) is used to estimate the variations of the modulus of elasticity with respect to suction. The strength of the MEBM lies in its use of conventional soil properties (i.e., the modulus of elasticity of soil under saturated condition, the Poisson's ratio, the saturated coefficient of permeability and the SWCC).

The validity of the proposed MEBM has been accomplished using simple example and a case study of light loaded structures constructed on Regina expansive clay. Good comparisons have been observed between the results of the MEBM and the published data (measurements/estimates). The MEBM has also been validated using other case studies (see Vanapalli & Adem 2012). The findings of the proposed study to date suggest that the MEBM is based on a relatively simple procedure and is useful to estimate the *1-D* heave of expansive soils with respect to time.

REFERENCES

Adem, H.H. & Vanapalli, S.K. 2013. Constitutive modeling approach for estimating the *1-D* heave with respect to time for expansive soils. *Int. J. Geotech. Eng.,* Accepted for publication (to be published in April 2013 issue).

Adu-Wusu, C., Yanful, E.K., Lanteigne, L. & O'Kane, M. 2007. Prediction of the water balance of two soil cover systems. *Geotech. Geol. Eng.* 25(2): 215–237.

Aitchison, G.D. 1973. The quantitative description of the stress-deformation behavior of expansive soils—preface to set of Papers. *Proc. 3rd Int. Conf. on Expansive Soils* 2: 79–82.

Aitchison, G.D. & Woodburn. J.A. 1969. Soil suction in foundation design. *Proc. 7th Int. Conf. of Soil Mech. and Foundation Eng., Mexico* 2: 1–9.

Aitchison, G.D., Peter, P. & Martin, R. 1973. The quantitative description of the stress deformation behaviour of expansive soils. *CSIRO Division of Applied Geomechanincs, Research Paper, 204*.

Allman, M.A., Delaney, M.D. & Smith, D.W. 1998. A field study of seasonal ground movements in expansive soils. *Proc. 2nd Int. Conf. on Unsaturated Soils*. *International Academic Publishers, Beijing*: 309–314.

ASTM Standards (D4546–96). 1997. Standard test methods for one-dimensional swell or settlement properties of cohesive soil. ASTM standards annual book, 04.08.

Bonner, J.P. 1998. *Comparison of Predicted Heave Using Oedometer Test Data to Actual Heave*. M.S. Thesis, Colorado State University, Fort Collins, Colorado.

Brackley, L.J. 1975. A model of unsaturated clay structure and its application to swell behavior. *Proc. 6th Afr. Conf. Soil Mech. & Foundation Eng., Durban. Balkema, Rotterdam*: 65–70.

Briaud, J.L., Zhang, X. & Moon, S. 2003. The shrink test – Water content method for shrink and swell prediction. *J. Geotech. Geoenviron. Eng., ASCE* 129(7): 590–600.

Chao, K.C. 2007. *Design principles for foundations on expansive soils*. Ph.D. thesis, Colorado State University, Fort Collins, Colorado.

Ching, R.K.H. & Fredlund, D.G. 1984. A small Saskatchewan town copes with swelling clay problems. *Proc. 5th Int. Conf. on Expansive Soils, Adelaide, Australia*, 306–310.

Clisby, M.B. 1963. Predicting the movement of clays. Annual Meeting of the Highway Research Board, Mississippi State University, State College.

Dhowian, A.W., Erol, A.O & Youssef, A. 1985. Evaluation of expansive soils and foundation methodology in the kingdom of Saudi Arabia. *6th Progress Report*, SANCST AT-5–88.

Driscoll R. & Crilly, M. 2000. Subsidence damage to domestic buildings. Lessons learned and questions asked. Building Research Establishment, London.

Feng, M., Gan, K.M. & Fredlund, D.G. 1998. A laboratory study of swelling pressure using various test methods. *Proc. 2nd Int. Conf. on Unsaturated Soils, Beijing, China* 1:350–355.

Fityus, S.G., Smith, D.W. & Allman, M.A. 2004. An expansive soil test site near Newcastle. *J. Geotech. Geoenviron. Eng., ASCE* 130(7): 686–695.

Fredlund, D.G. 1983. Prediction of ground movements in swelling clays. 31st Ann. Soil Mech. and Foundation Eng. Conf. University of Minnesota, Minneapolis.

Fredlund, D.G. & Morgenstern, N.R. 1976. Constitutive relations for volume change in unsaturated soils. *Can. Geotech. J.* 13(3): 261–276.

Fredlund, D.G. & Rahardjo, H. 1993. *Soil Mechanics for Unsaturated Soil*. John Wiley & Son, Inc., New York, NY.

Fredlund, D.G., & Xing, A. 1994. Equations for the soil-water characteristic curve. *Can. Geotech. J.* 31(4): 521–532.

Fredlund, D.G., Hassan, J.U. & Filson, H.L. 1980. The prediction of total heave. *Proc. 4th Int. Conf. on Expansive Soils, Denver, Colorado, USA*: 1–17.

Freeze, R.A. & Cherry, J.A. 1979. *Groundwater*. Prentice-Hall Inc., Englewood Cliffs, NJ.

Geo-Slope. 2007. Vadose zone modeling with VADOSE/W 2007: An engineering methodology. 3rd edition. Geo-Slope, Calgary, Canada.

Hamberg, D.J. 1985. *A Simplified Method for Predicting Heave in Expansive Soils*. M.S. thesis, Colorado State University, Fort Collins, Colorado.

Hamberg, D.J. & Nelson, J.D. 1984. Prediction of floor slab heave. *Proc. 5th Int. Conf. on Expansive Soils, Adelaide, Australia*: 137–140.

Holland, J.E. & Cameron, D.A. 1981. Seasonal heave of clay soils. *Institution of Engineers (Australia) Civ. Eng. Trans.* CE23(1): 55–67.

Jennings, J.E. & Knight, K., 1957. The prediction of total heave from the double oedometer test. *Proc. a*

symposium on expansive clays. S Afr. Instn Civ. Engnrs, Johannesburg, 7 (9): 13–19.

Johnson, L.D. 1973. Influence of suction on heave of expansive soils. Miscellaneous Paper S-73–17, US Army Engnrs Waterways Exp. Station, Vicksburg, MS.

Johnson, L.D. 1977. Evaluation of laboratory suction tests for prediction of heave in foundation soils. *Rep. WES-TR-S-77–7, August. US Army Engnrs. Waterways Exp. Station, Vicksburg, MS.*

Johnson, L.D. & Snethen, D.R. 1978. Prediction of potential heave of swelling soils. *Geotech. Test. J.* 1(3): 117–124.

Jones, L.D. & Jefferson, I. 2012. ICE Manual of Geotechnical Engineering Volume 1: Geotechnical Engineering Principles, Problematic Soils and Site Investigation, Chapter 33 Expansive soils: 413–441.

Lambe, T.W. & Whitman, R.V., 1959. The role of effective stress in the behavior of expansive soils. *Quarterly of the Colorado School of Mines* 54(4): 33–66.

Leong, E.C. & Rahardjo, H. 1997. Permeability functions for unsaturated soils. *J. Geotech. Geoenviron. Eng., ASCE* 123(12): 1118–1126.

Lytton, R.L. 1994. Prediction of movement in expansive clays. *Proc. settlement '94 Conf. Geotechnical Special Publication. Reston, Virginia, ASCE* 2(40): 1827–1845.

Lytton, R.L. 1997. Foundations in expansive soils. In: C.S. Desai and J.T. Christian, eds. *Numerical methods in geotechnical engineering.* Chapter 13. McGraw-Hill. New York: 427–458.

McKeen, R.G. 1980. Field study of airport pavements on expansive clay. *Proc. 4th Int. Conf. on Expansive Soils, Denver, Colorado*: 242–261.

McKeen, R.G. 1981. Design of airport pavements for expansive soils. *Federal Aviation Agency, US Department of Transportation, Washington, D.C.*

McKeen, R.G. 1992. A model for predicting expansive soil behavior. *Proc. 7th Int. Conf. on Expansive Soils, Dallas, Texas*. 1: 1–6.

McKeen, R.G. & Nielsen, J.P. 1978. Characterization of expansive soils for airport pavement design. *US Department of Transportation, Federal Aviation Administration, FFA Rep. FAA-RD-78–59*.

Milly, P. 1982. Moisture and heat transport in hysteretic, inhomogeneous porous media: A matric head-based formulation and a numerical model. *Water Resources Res.* 18: 489–498.

Mitchell, P.W. & Avalle, D.L. 1984. A technique to predict expansive soils movement. *Proc. 5th Int. Conf. on Expansive Soils, Adelaide, Australia*: 124–130.

Nayak, N.V. & Christensen, R.W. (1971). Swell characteristics of compacted expansive soils. Clay Clay Miner. 19(4): 251–261.

Nelson, J.D. & Miller, D.J. 1992. *Expansive soils: problems and practice in foundation and pavement engineering*. John Wiley & Sons, Inc. New York.

Nelson, J.D., Durkee, D.B. & Bonner, J.P. 1998. Prediction of free-field heave using oedometer test data. *Proc. 46th Ann. Geotech. Eng. Conf., University of Minnesota, St. Paul, Minnesota*.

Nelson, J.D., Overton, D.O., & Chao, K.C. 2003. Design of foundations for light structures on expansive soils. *California Geotech. Engineers Assoc. Ann. Conf., Carmel, California*.

Nelson, J.D., Reichler, D.K., & Cumbers, J.M. 2006. Parameters for heave prediction by oedometer tests." *Proc. 4th Int. Conf. on Unsaturated Soils. Carefree, Arizona*: 951–961.

Nelson, J.D., Chao, K.C., Overton, D.D. & Schaut, R.W. 2011. Calculation of heave of deep pier foundations. *Proc.Unsaturated Soils: Theory and Practice 2011. Kasetsart University, Thailand*: 59–74.

Nelson, J.D., Thompson, E.G., Schaut, R.W., Chao, K.C., Overton, D.D. & Dunham-Friel, J.S. 2012a. Design procedure and considerations for piers in expansive soils. *J. Geotech. Geoenviron. Eng., ASCE*. 138(8):945–956.

Nelson, J.D., Chao, K.C., Overton, D.D. & Schaut, R.W. 2012b. Calculation of heave of deep pier foundations. *Geotech. Eng. J. SEAGS & AGSSEA* 43(1):12–25.

Ng, C.W.W., Zhan, L.T., Bao, C.G., Fredlund, D.G. & Gong, B.W. 2003. Performance of an unsaturated expansive soil slope subjected to artificial rainfall infiltration. *Géotechnique* 53(2): 143–157.

Noble, C.A. 1966. Swelling measurements and prediction of heave for a lacustrine clay. *Can. Geotech. J*. 3(1): 32–41.

Oh, W.T., Vanapalli, S.K. & Puppala, A.J. 2009. Semi-empirical model for the prediction of modulus of elasticity for unsaturated soils. *Can. Geotech. J.*, 46(8): 903–914.

Osman, N.Y., McManus, K. & Ng, A.W.M. 2005. Management & analysis of data for damage of light structures on expansive soils In Victoria, Australia. *Proc. 1st Int. conf. Structural condition assessment, monitoring and improvement, Perth, Australia, 12–14th December, CI-Premier, Singapore*: 283–290.

Puppala, A.J. & Cerato, A. 2009. Heave distress problems in chemically-treated sulfate-laden materials. *GeoStrata*, 10(2): 28–30, 32.

Richard, L.A. 1931. Capillary conduction of liquids through porous mediums. *J. Appl. Phys.* 1(5): 318–333.

Ruwaih, I.A., 1987. Experiences with expansive soils in Saudi Arabia. *Proc. 6th Int. Conf. on Expansive Soils*. New Delhi, India: 317–322.

Salas, J.A.J. & Serratosa, J.M. 1957. Foundations on swelling clays. *Proc. 4th Int. Conf. Of Soil Mech. and Foundation Eng. 1, London, England*: 424–428.

Sattler, P. & Fredlund, D.G. 1991. Numerical modelling of vertical ground movements in expansive soils. *Can. Geotech. J.* 28(2): 189–199.

Seed, H.B., Woodward, R.J., Jr & Lundgren, R. 1962. Prediction of swelling potential for compacted clays. *J. Soil Mech. and Foundation Eng. Div., ASCE* 88(I): 53–87.

Shuai, F. 1996. *Simulation of swelling pressure measurements on expansive soils*. Ph.D. thesis. Department of Civil Engineering, University of Saskatchewan, Saskatoon, Sask.

Snethen, D.R. 1980. Characterization of expansive soils using soil suction data. *Proc. 4th Int. Conf. on Expansive Soils, Denver, Colorado*: 54–75.

Snethen, D.R. & Huang, G. 1992. Evaluation of soil suction-heave prediction methods, *Proc. 7th Int. Conf. on Expansive Soils, Dallas* 1: 12–17.

Sullivan, R.A. & McClelland, B. 1969. Predicting heave of buildings on unsaturated clay. *Proc. 2nd Int. Res. Eng. Conf. Expansive Soils, Texas A & M Univ. Press, College Station, TX*: 404–420.

Van der Merwe, D.H. 1964. The prediction of heave from the plasticity index and the percentage clay fraction of soils. *Trans. S Afr. Instn Civ. Engnrs.* 6(6): 103–107.

Vanapalli, S.K. & Adem, H.H. 2012. Estimation of the *1-D* heave in expansive soils using the stress state variables approach for unsaturated soils. Keynote paper. *Proc. 4th Int. Conf. Problematic Soils, Wuhan, China.*

Vanapalli, S.K. & Oh, W.T. 2010. A model for predicting the modulus of elasticity of unsaturated soils using the soil-water characteristic curve. *Int. J. Geotech. Eng.,* 4(4): 425–433.

Vanapalli, S.K. & Lu, L. 2012. A state-of-the art review of *1-D* heave prediction methods for expansive soils. *Int. J. Geotech. Eng.,* 6(1): 15–41.

Vanapalli, S.K., Lu, L. & Oh, W.T. 2010. Estimation of swelling pressure and *1-D* heave in expansive soils. *Proc. 5th Int. Conf. on Unsaturated Soils, Barcelona, Spain* 2: 1201–1207.

Vijayavergiya, V.N. & Ghazzaly, O.I. 1973. Prediction of swelling potential for natural clays. *Proc. 3rd Int. Conf. on Expansive Soils*, *Haifa*: 227–236.

Vu, H.Q. 2003. *Uncoupled and Coupled Solutions of Volume Change Problems in Expansive Soils*. Ph.D. thesis. Department of Civil Engineering, University of Saskatchewan, Saskatoon, Sask.

Vu, H.Q. & Fredlund, D.G. 2004. The prediction of one-, two-, and three-dimensional heave in expansive soils. *Can. Geotech. J.* 41(4): 713–737.

Vu, H.Q. & Fredlund, D.G. 2006. Challenges to modelling heave in expansive soils. *Can. Geotech. J.* 43(12): 1249–1272.

Weston, D.J. 1980. Expansive roadbed, treatment for Southern Africa. *Proc. 4th Int. Conf. on Expansive Soils, Denver, Colorado*: 339–360.

Wilson, G.W. 1990. *Soil evaporative fluxes for geotechnical engineering problems*. Ph.D. thesis. Department of Civil Engineering, University of Saskatchewan, Saskatoon, Sask.

Wray, W.K. 1997. Using soil suction to estimate differential soil shrink or heave. *In Unsaturated Soil Engineering Practice. Geotechnical Special Publication no. 68, ASCE*: 66–87.

Yoshida, R.T., Fredlund, D.G. & Hamilton, J.J. 1983. The prediction of total heave of a slab-on-grade floor on Regina clay. *Can. Geotech. J.* 20(1): 69–81.

Zein, A.K. 1987. Comparsion of measured and predicted swelling behaviour of a compacted Black Cotton Soil. *Proc. 6th Int. Conf. on Expansive Soils. New Delhi, India*: 121–126.

Zhang, X. 2004. *Consolidation theories for saturated-unsaturated soils and numerical simulations of residential buildings on expansive soils*. Ph.D. Thesis, Department of Civil Engineering, Texas A&M University, College Station, TX.

Zhang, X. & Briaud, J.L. 2010. Coupled water content method for shrink and swell predictions. *Int. J. Pavement Eng.* 11(1):13–23.

Advances in testing techniques

This page intentionally left blank

Advances in Unsaturated Soils – Caicedo et al. (eds)
© 2013 Taylor & Francis Group, London, ISBN 978-0-415-62095-6

Physical modelling of the effect of partial saturation on the stability of geocell walls

D. Gómez
Department of Civil and Environmental Engineering, Universidad de Los Andes, Bogotá D.C., Colombia

ABSTRACT: Reduced scale centrifuge model tests are performed on geocell retaining structures with the aim to examine their structural capacity and failure mechanism under two different saturation conditions, fully and partially saturated. A critical load condition is imposed to the walls, including incremental surcharge at the top backfill. The effect of partially saturated soil in a geocell retaining wall is analyzed in terms of the load capacity of the backfill and its deformation. The results showed an increase in load capacity of 27% to the geocell retaining wall provided by the unsaturated soil and a characteristic failure mode based in an intern failure surface in the geocell wall.

1 INTRODUCTION

Cellular confinement systems, generally known as geocells, are a type of three-dimensional geosynthetics that consist basically in a network of interconnected cells. They are formed by several high-tensile resistance strips welded together into strong cells to produce a special arrangement when they are expanded in order to contain soil. Several authors have studied the mechanical behavior of the geocell-soil composite systems with the aim to understand its real operation. Bathurst & Karpurapu (1993) performed several large-scale triaxial tests on isolated geocell-soil specimens concluding a stiffening effect and strength increase in the soil due a rise in its confinement. Karpurapu et al. (1999) also performed triaxial tests but this time including multiple geocells. The results indicated that the soil develops a considerable quantity of apparent cohesive strength due the geocell confinement. More current research on investigating the stress-strain behavior of soil reinforced with geocells was executed by Wesseloo et al. (2009).

Nowadays, one of the most important applications of geocells deals with earth retaining structures. In fact during the last decades, there has been an increasing utilization of geocells for the construction of retaining walls, either gravity wall or reinforced soil wall. The walls are built with several geocell layers filled with compacted granular soil and stacked one over other forming a specific face slope. Furthermore, some researchers have studied their principal characteristics finding outstanding results about their mechanical behavior, for static and dynamic solicitations. The first study known that introduced the utilization of geocells in retaining walls highlighted the advantage of these structures when constructed over weak or compressive foundations, due to their flexibility that allow them to withstand differential settlements (Bathurst & Crowe, 1994).

Subsequent studies about the subject tested a pair of reduced scale geocell retaining walls with two different materials in order to investigate their mechanical response at 1 g (Racana et al., 2001).

Chen & Chiu (2008) carried out a more complex research where they executed 9 models test of geocell retaining structures with the aim to analyze their failure mechanism and their behavior under surcharge. This time more variables were included like the height, facing angle and type of the wall. According to this research, the gravity-type walls failed by interlayer sliding and overturning, and besides the maximum lateral displacements occurred at the top of the walls. The reinforced-soil walls developed more displacement and settlement than the gravity types due to a lack of sturdiness in their structures. It is also remarked that the reinforcements reduce considerably the deformation of the walls. Finally, it is given some recommendations for the design of geocell retaining walls. In their study, Chen & Chiu (2008) employed a similarity and dimension analysis in order to be able to compare the behavior of the model with the prototype. However, only strength characteristics of the geocell were considered in the analysis due complicated similitude requirements. Moreover, it is well knownthat reduced-scale physical models tested at 1 g generate stresses in the soil much smaller than the corresponding stresses in the real or prototype structure, therefore altering the similitude of soil characteristics and the capacity to compare adequately the model and prototype (Zornberg et al., 1997). A recognized technique to generate

approximately the same stresses in the scaled model and the prototype structure is the physical modelling using geotechnical centrifuges. For this reason, this study developed centrifuge tests at 20 g in two geocell retaining walls with the aim to evaluate and verify the impact of partially saturated soil in the mechanical behavior and failure mode of geocell walls. Therefore, direct comparison between a saturated model and an unsaturated model is performed and analyzed.

2 MODEL GEOCELL DESIGN

In order to model successfully a geocell retaining wall, it is needed to characterize correctly the proto-type geocell in mechanical terms and then scale its properties in the model of geocells.

2.1 *Prototype geocell characterization*

An essential aspect about centrifuge scaling is sizing and geometr, Table 1 presents the nominal general dimensions of the prototype geocell.

Other principal feature that needs to be scaled is the global strenght of the geocells with respect the mechanical solicitations required. There are four recognized resistance test for geocells performance. These are the tensile strength test, the junction shear test, the junction peel strength and the junction split test (Cancelli et al., 1993; Chen & Chiu, 2008).

Concerning the junction strength tests, each one assesses a potential failure mode of the geocell seam. Thus, it was executed several resistance test in the prototype geocell for each strength required. For the tensile strength there were tested two different specimens, three times each, one of a strip with perforations and another without perforations (Fig. 1).

For the junction strength tests, there were executed three trials for each failure mode (Fig. 2.).

All the tests were based in the ASTM D4595 and ASTM D5035standards. The load velocity was 50 mm/min. The average results of the strength tests are shown in Table 2.

The junction shear strength was defined equal to the tensile strength (non-perforated) because in the shear strength tests the samples did not fail by the seam because at first failed the pure material in tension.

Table 1. Prototype geocell nominal dimensions.

Prototype geocell properties	Description
Cell wall height (mm)	200
Distance between seals (mm)	445 (±2.5%)
Dimensions open cell (mm)	340 × 290 (±3%)

2.2 *Prototype geocell scaling*

First of all, the most important linear dimensions were scaled by its length scale factor ($1/n$). Therefore, having $n = 20$ g, the height of the model geocell becomes 10 mm and the space between seams is 22.3 mm. Regarding the strenght properties, the scale factor corresponded also to $1/n$ since strength in geosynthetics is expressed in force per unit length. Thus, it is required a material with 20 times less strength than the prototype material, regardless its modulus because the scaling was done only in terms of strength. Several tensile strength tests were carried out in four different materials: industrial acetate, acetate, plastic greenhouse and vinyl. According to the test results, the material that best approximated the prototype geocell behavior was the industrial acetate (Table 3). Respecting the junction strength scaling, two adhesives were

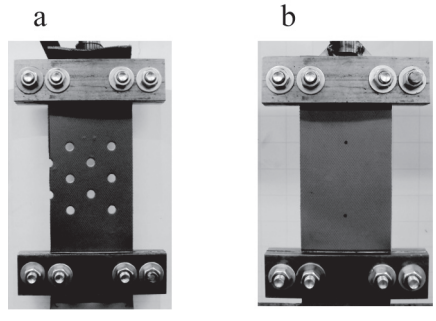

Figure 1. Tensile strength tests in specimens: a) with perfora-tions b) without perforations.

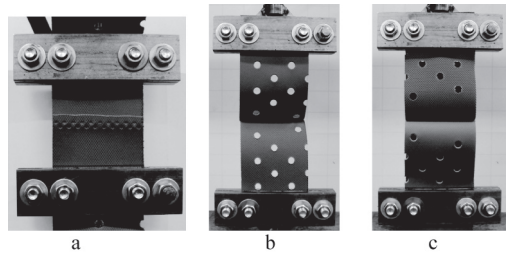

Figure 2. Junction strength tests: a) Shear failure. b) Peel failure. c) Split failure.

Table 2. Prototype geocell global strength.

Prototype geocell strength	Average value
Tensile strength Perforated (kN/m)	12.78
Tensile strength Non-Perforated (kN/m)	20.08
Junction shear strength (kN/m)	20.08
Junction peel strength (kN/m)	5.48
Junction split strength (kN/m)	7.62

Table 3. Strength properties of model geocell.

Model geocell strength	Scaled value	Test results
Tensile strength (Perforated) (kN/m)	0.64	1.05
Tensile strength (Non-Perforated) (kN/m)	1.00	1.11
Junction shear strength (kN/m)	1.0	1.11
Junction peel strength (kN/m)	0.27	0.46
Junction split strength (kN/m)	0.38	1.41

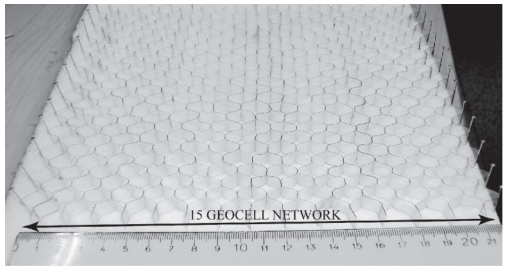

Figure 3. Model geocell network constructed.

tested for each junction solicitation: polyvinyl ester and cyanoacrylate. The adhesive more suitable for modelling the seam strength with its solicitations was the cyanoacrylate. The strenght properties of the selected model geocell materials are shown in Table 3.

Even though the perforated tensile strength and the junction split strength are slightly higher than the scaled resistance value, this is an acceptable approximation to model the real geocell material behavior.

30 model geocell networks were constructed having different quantity of cells in the wall load direction, from 7 cells to 15 cells (Fig. 3). Afterwards perforations of 1 mm diameter were perforated in the geocell models to reproduce the holes of the prototype geocell.

3 PROTOTYPE RETAINING WALL DESIGN AND SCALING

The prototype geocell retaining wall is selected as a slender gravity retaining wall in order to evidence considerable settlement and displacement of the wall. A preliminary design is performed using the classical Rankine theory of earth pressures for a gravity retaining wall. The height of the prototype wall is 6 meters and its face slope angle is 70º. Afterwards, all the dimensions of the prototype wall were reduced to yield the corresponding geometry of the model geocell retaining wall. Thus, the

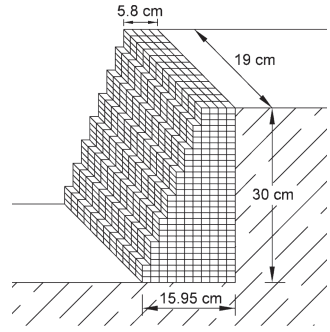

Figure 4. Geometry of model geocell retaining wall.

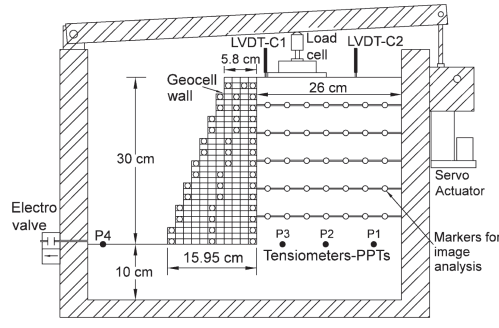

Figure 5. Cross-section and plan view of the model with instrumentation.

height of the model retaining wall is 30 cm and its base is 15.95 cm (Fig. 4). The depth of the model wall is restricted by the strongbox, which is 19 cm width (Fig. 5).

The geometry of both model geocell retaining walls are presented in Figure 4. To highlight the effect of partial saturation on the load capacity of the walls two tests were performed: one test saturated with a total inundation of the model during loading and the other one with the backfill under partially saturated conditions.

4 MODEL INSTRUMENTATION

With regard to the instrumentation in the model wall, a set of tensiometers with pore pressure transducers (PPTs); LVDTs; a servo actuator; a load cell and a digital camera were used to measure the loading-settlement behavior (Fig. 5). Three tensiometers with their transducers are located behind the wall at its base to measure pore water pressure in the backfill (P1, P2 and P3) and another is located in front the wall to control water outflow (P4). For the unsaturated model, the water is evacuated in-flight through an electrovalve and stored in an adjacent tank. Two vertical LVDTs are located at the top backfill of the model geocell wall in order

to register the settlement induced by the surcharge in both models at 2 cm (C1) and 12 cm (C2) from the wall (Fig. 5). The surcharge is executed in-flight at the wall top backfill with a nominal 1-ton servo actuator and a lever system to increase the actuator load capacity. The load applied is measured with a load cell located over the surcharge plate. Several markers are placed all over the wall and its backfill in lines with the purpose of identify their displacement vectors and record the failure mechanism with a digital camera assembled in front of the sidewall acrylic with a special frame.

5 MODEL CONSTRUCTION

The two-dimensional model geocell walls are constructed inside a 56.2 cm × 19 cm × 45 cm strongbox that included a 12 cm thick acrylic sidewall to observe the wall deformation. Furthermore, in the construction of the model there are used two kinds of soils: a coarse sand for the proper model geocell wall and a silty sand for the backfill of the wall and its foundation.

5.1 *Backfill and foundation soil*

Regarding the backfill and foundation soil, it is selected a intermediate soil made by a mixture of 80% sand with a grain diameter less than 2 mm and 20% kaolin clay (Fig. 7). The behavior of this mixture of soils is similar to a natural in-situ soil and is selected to simulate a more realistic approach to the issue.

Regarding the compaction of this intermediate soil, a Proctor standard test was performed on the soil, finding a maximum dry unit weight (γ_d max) equal to 19.16 kN/m^3 and optimal moisture content (w_{opt}) equal to 9.6%. Thus, the backfill and foundation are compacted according the Proctor results by tamping the soil in a controlled volume. The measured soil coefficient of permeability is 1.72×10^{-7} m/s and the hysteretic soil-water characteristic curve for this material is presented in Figure 6.

5.2 *Geocell wall soil*

The geocell wall uses sand with a high permeability allowing easy drain characteristics of the wall. This issue is in agreement with past studies indicating the advantages of using granular material in the geocells infill (Bathrust et al., 1993, 1994; Chen & Chiu, 2008). Consequently, it is employed a coarse Guamo sand whose grain size properties are well known and its grain size distribution is presented in Figure 7. A constant head permeability test is performed and a coefficient of permeability of 5.48×10^{-4} m/s is obtained for this material. In order to preserve the model geocell networks, it was decided to compact the Guamo sand by pluviation

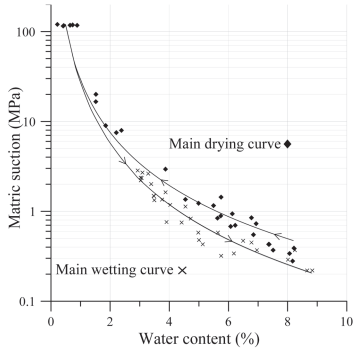

Figure 6. Backfill and foundation soil water retention curve.

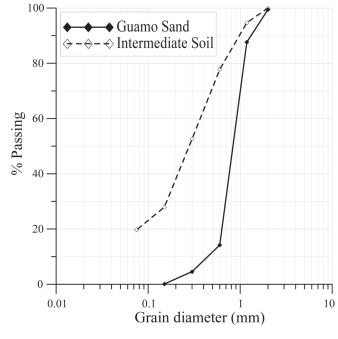

Figure 7. Grain size distribution of the Guamo sand and the intermediate soil.

of the dry sand over each geocell network. Hence, the sand compaction is done in terms of maximum dry density ($\rho_d$max) and the optimal falling height of pluviation is found by the maximum relative density (Dr) achieved in the compacted sand for each different height. The maximum relative density obtained was 53% at 30 cm pluviation falling height. This optimal falling height is employed in the construction of the geocell walls.

5.3 *Construction procedure and model constructed*

The construction began with the compaction of the foundation of the wall according with the proctor results. When the foundation reached 10 cm height, it is assembled a wood frame in one side of the strong-box in order to contain the backfill soil while it is compacted adequately. Afterwards, the three tensiometers and their PPTs are located in the base of the wall, and then the backfill soil is compacted in six different layers, 5 cm thick each. For all layers, at its base are located markers and colored sand interface for image analysis and failure identification. Afterwards, the wood

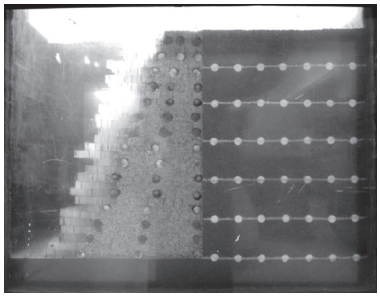

Figure 8. Model geocell retaining wall constructed.

frame is removed and each model geocell network is expanded properly. Because the model geocell networks were initially constructed for a different geometry of the wall, it was necessary to block some cells during pluviation in order to avoid their compaction and obtain the correct geometry of the scaled wall (Fig. 8). These remaining cells in the model do not affect the wall behavior and its strenght because they are not confining any soil material. All model geocell net-works are pluviated with the correct falling height. The complete model geocell wall is shown in Figure 8.

6 TEST PROCEDURE AND RESULTS

The objective of the centrifuge test is to impose a critical charge condition in two model geocell retaining walls, one totally saturated and another partially saturated, in order to compare their mechanical behaviors and failure modes.

There is a main procedure for the saturated model: the inundated model wall is centrifuged at 20 g and then, with the electrovalve closed, it is surcharged in-flight at its top backfill in multiple load steps. Settlements and deformation are measured with LVDTs and digital video.

On the other hand there are two sequences for the unsaturated model:

1. the initially inundated model wall is centrifuged to 20 g and then the water table is lowered in-flight, leading water flowing throughout the model.
2. after water outflow, the unsaturated geocell wall is surcharged at its top backfill in multiple load steps and the corresponding settlements are registered.

6.1 *Saturated case*

At the beginning of the test, it is executed a 5 g centrifuge cycle to the saturated model in order to verify that all the instrumentation is working properly. Afterwards, the model is centrifuged again until the correct test acceleration (20 g) and then the surcharge in load steps begins with the model inundated. Unexpected technical problems with the servo actuator leaded to only two load steps, an initial one of 0.49 kN and a second maximum load of 5.93 kN. The load-settlement (C1) diagram of this wall is presented in order to compare it with the unsaturated wall case (Fig. 11). The maximum settlement generated at C1 is 29.3 mm and at C2 it is registered a displacement of 1.3 mm. The PPTs performed correctly and register in average 50 kPa of pore water pressure during test. The image analysis of the geocell wall gives its failure mode and the failure surface. The displacement vectors show the direction of movement of specific points and their respective magnitudes (Fig. 9).

6.2 *Unsaturated case*

In this case, the procedure is repeated until the inundated model is centrifuged at 20 g. At this point, the electrovalve is opened in-flight and water outflow toward adjacent tank starts, generating a seepage force in the model soil and lowering water table. Besides, the hydraulic potential is also modified in the model, varying the pore pressure throughout the model soil and producing negative pore pressure or suction at certain points of the retaining structure and its backfill. The measured values of pore water pressure obtained by the PPTs reached 50 kPa again and decreased gradually until 10 kPa as the model was drained.

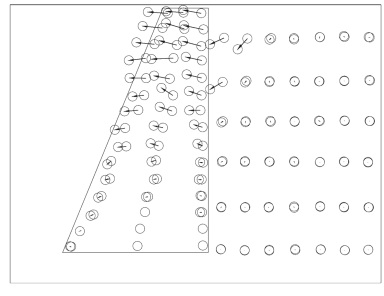

Figure 9. Displacement vectors for saturated model wall.

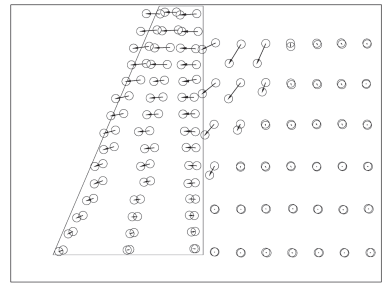

Figure 10. Displacement vectors for unsaturated model.

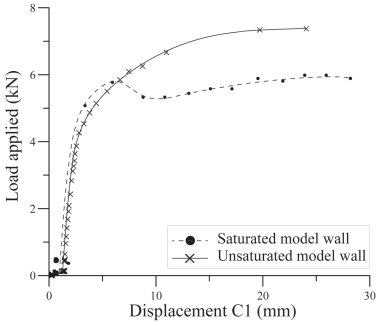

Figure 11. Load-Settlement (C1) results for both models.

After water outflow is completed and the soil is partially saturated, it is waited until LVDTs generate a constant value and then surcharge in load steps is started. This time the loading system performed correctly and several small step loads are applied until a maximum load of 7.53 kN. Again, the load-settlement (C1) diagram for this case is presented (Fig. 11). Vertical LVDT (C1) measured a maximum settlement of 23.7 mm and C2 registered a maximum of 0.85 mm.

Respecting vector displacement due water table lowering, no significant movement was noticed by image analysis. However, regarding loading steps the image analysis produced the displacement vectors displayed in Figure 10.

7 DISCUSSION

According to the load-settlement results from the two models tested (Fig. 11), it was observed that the unsaturated geocell model wall was the model that withstand more surcharge until failure, as expected.

As the walls backfill were initially surcharged, both model walls followed nearly the same load-settlement path in an elastic zone where the soil backfill was resisting the load, until approximately 3 mm settlement. From this point forth, the geocell walls started their actual performance. In the case of the saturated model wall there was a small discharge at 5.85 kN and subsequent plastic deformation. However, it continued resisting until reach a maximum resistance load of 5.93 kN at its top backfill with a settlement of 29.3 mm. Conversely, the partially saturated model wall continued bearing the incremental surcharge until a flat plastic zone with a load of approximately 7.53 kN, and then failed with a settlement of 23.7 mm at its backfill.

Considering the fact that the unsaturated model wall resisted 27% more surcharge than the saturated model wall, it is clear that the soil tested in the partially saturated model developed more shear strength due to a matrix suction or negative pore pressure created in the soil when it was drained and the pore water pressure decreases throughout the model. Furthermore, the walls evidenced a characteristic failure mode in which a failure wedge at the backfill plastically deforms the wall and creates an intern failure surface on it, identified as a sliding between geocell networks. This mobilization of the layers is greater at the upper part of the wall than at its base.

8 CONCLUSIONS

Two properly reduced scale geocell retaining wall models are designed, constructed and tested until failure in a geotechnical centrifuge at 20 g. Certainly, the effect of the partially saturated soil in the geocell model wall is reflected in a greater surcharge endured by the wall in 27% more than in the saturated soil model wall. The suction generated in the unsaturated soil provided higher load capacity to the model wall. It is found a failure mode in which an internal failure surface is developed into the geocell wall. Subsequent effects analysis will be performed in the model walls based in the shear strength theory of unsaturated soils.

REFERENCES

Bathurst, R.J. & Crowe, R.E. 1994. Recent case histories of flexible geocell retaining walls in North America. In Tatsuoka, F., Leshchinsky, D. (eds), Recent case histories of permanent geosynthetic-reinforced soil retaining walls. Japan. Rotterdam: Balkema.

Bathurst, R.J. & Karpurapu, R. 1993. Large-scale triaxial compression testing of geocell-reinforced granular soils. Geotechnical Testing Journal. Vol. 16, No. 3, pp. 296–303.

Cancelli, A., Rimoldi, P. & Montanelli, F. 1993. Index and performance test for geocells in different applications. In Cheng, J. (ed.), Geosynthetic soil reinforcement testing procedures, ASTM Publications.

Chen, R.H. & Chiu, Y.M. 2008. Model tests of geocell retaining structures. Geotextiles and Geomembranes. Vol. 26, 56–70.

Karpurapu, R., Krishnaswamy, N.R. & Madhavi, L.G. 1999. Behaviour of sand confined with single and multiple geocells. Geotextiles and Geomembranes. Vol. 17(3): 171–184.

Racana, N., Gourvès, R. & Grédiac, M. 2001. Mechanical behavior of soil reinforced by geocells. In Ochiai, H. (eds), Proc. Intern. Symp., on Earth Reinforcement. Japan. Rotterdam: Balkema.

Wesseloo, J., Visser, A.T. & Rust, E. 2009. The stress-strain behaviour of multiple cell geocell packs. Geotextiles and Geomembranes, Vol. 27, 31–38.

Zornberg, J.G., Mitchell, J.K. & Sitar, N. 1997. Testing of reinforced slopes in a geotechnical centrifuge. Geotechnical Testing Journal. Vol. 20(4): 470–480.

Advances in Unsaturated Soils – Caicedo et al. (eds)
© 2013 Taylor & Francis Group, London, ISBN 978-0-415-62095-6

Calibration in the laboratory of capacitance sensors for water content monitoring

F. Avanzi, M. Caruso & C. Jommi
Politecnico di Milano, Milano, Italy

ABSTRACT: The influence of water salinity and of heterogeneity of the dielectric properties of the access tube on the performance of capacitance sensors for soil water content monitoring is discussed. These sensors operate through measurement of the resonant frequency of an oscillating electrical circuit, which includes a representative volume of the soil as the dielectric part of the capacitor. Resonant frequency changes with soil water content, but water salinity and the properties of the access tube affect the electric response of the whole circuit, and the calibration relationships adopted to infer water content. An experimental investigation was performed in the laboratory to analyse the influence of these factors on the calibration curves and on the error associated to the use of literature relationships in the determination of water content. A calibration curve is proposed accounting for water salinity, based on the experimental data collected.

1 INTRODUCTION

Prediction of water exchanges with the atmosphere is one of the most important goals when dealing with unsaturated soil layers above the water table, both for hydrological and for geotechnical reasons. Predictive capabilities of theoretical and numerical models for hydrologic balance may increase to a great extent if calibration is performed by comparison with measured data.

The hydraulic state of the soil is completely known if independent measurements of suction and water content are performed. Different suction and water content probes have been developed to this aim, which still present some limitations depending on the soil to be monitored. In fine grained soils, direct suction measurement may not be feasible, due to limited air entry value; hence water content determination appears to be mandatory to follow the hydraulic state of the soil.

Most current equipment and techniques for monitoring soil-water status rely on indirect methods in which other properties of the soil depending on water content are measured (Scanlon et al., 2002, Charlesworth 2005, Cui et al., 2007).

The soil dielectric constant of soils, at frequencies between 1 MHz and 1 GHz, is strongly dependent on volumetric water content (Topp et al., 1980), due to dielectric constant of water being much higher than that of the other soil constituents. This observation promoted the development of non-destructive techniques which infer the amount of water in the soil from measurements of electrical permittivity. With time domain reflectometry (TDR) water content is deduced from measurement of the propagation velocity of a high-frequency electromagnetic pulse signal (Noborio 2001). Soil electrical conductivity and salinity problems may complicate the interpretation of probe readings (Mojid et al., 2003). However, the main issue in the use of TDR is its installation procedure, which requires manual probe insertion into the soil, with direct access at the depth were the probe is installed.

The dielectric constant of soils can also be derived based on capacitance. This method includes the soil as part of the capacitor in which the permanent dipoles of water in the dielectric medium are aligned by the electric field and become polarized. The capacitor is arranged to be part of an oscillator circuit, the resonant frequency of which allows inferring capacitance, hence soil water content (Gardner et al., 1991, Robinson et al., 1998). Capacitance probes are fast, safe and relatively cheap. Monitoring depth can reach 5 meters below the ground level, by means of appropriate installing procedures (Caruso, 2007). Response time of the probes, less than 1 second, is one of the most attractive features of capacitance probes. Influence of soil salinity and soil temperature is also reported, but literature works (Kelleners et al., 2004, Schwank et al., 2006, Schwank & Green 2007) suggest that these effects can be accounted for through adequate calibration.

2 THE ENVIROSCAN CAPACITANCE PROBES

The EnviroSCAN® capacitance probes consist of two brass rings (50.5 mm outer diameter and 25 mm height) mounted on a plastic sensor body.

The probes are inserted inside a PVC access tube, strictly in contact with the rings and the surrounding soil. Up to 16 probes can be mounted on a plastic guide at different depths. Minimum relative distance between probes is 10 cm.

The resonant frequency of the inductive-capacitive circuit, in which the probe is inserted, F_r, is linked to the inductive L and capacitive C elements by the following relationship

$$F_r = \left[2\pi \sqrt{(LC)} \right]^{-1} \tag{1}$$

where L is the circuit inductance and $C = C_s + C_p$ is the total capacitance, including the soil component, C_s, together with probe constants, C_p (Kelleners et al., 2004). L and C_p are constant for each probe, but they may vary from one probe to the other due to the construction process. Since the sensors output primarily varies with the air/water ratio, the resonant frequency is scaled to the maximum measurement range, and the scaled frequency is used for calibration purposes (Paltineanu & Starr 1999).

The normalised scaled frequency, SF, is defined as

$$SF = \left(F_a - F_r\right)\left(F_a - F_w\right)^{-1} \tag{2}$$

where F_r is the reading in the soil, and F_a and F_w are the frequency readings when the access tube is surrounded by air and water, respectively. After scaling, unique relationships between the scaled frequency SF and the soil volumetric water content, θ, are established, which are independent of the characteristics of the specific probe. These relationships play the role of calibration curves for water content.

Typical relationships for the silty soils used in this investigation read (Paltineanu & Starr 1999)

$$\theta = 0.49\, SF^{2.1764} \tag{3}$$

or (Sentek 2001)

$$\theta = 0.01\left(\frac{SF - 0.02852}{0.1957} \right)^{1/0.404} \tag{4}$$

Therefore, the calibration procedure for this kind of probes requires a two steps procedure. The first step is the evaluation of the resonant frequencies in air and in water. The second step gives the relationship between the scaled frequency in the soil and its water content.

Paltineanu & Starr (1999) provide detailed description of the probes working principle, and they show that 99% of the sensor response is influenced by a cylindrical soil volume having a diameter of about 20 cm. They state that these sensors have been designed to oscillate in excess of 100 MHz so that the effects of water salinity and fertilizers, typically found in agricultural soil, can be disregarded.

An experimental activity was developed at the Politecnico di Milano to further investigate the influence of water salinity on the probe response for typical silty soils of geotechnical interest.

3 DIELECTRIC PROPERTIES OF THE ACCESS TUBE

The effect of the local dielectric properties of the access tube on probes readings was investigated by placing a sensor in different positions along a prototype access tube (Fig. 1). Resonant frequencies were measured on the system surrounded by air or by water. A first access tube was placed in air far enough from any possible interference. A second one was sealed inside a PVC container (38 cm × 53.5 cm × 29 cm), ensuring a minimum distance of 12 cm from its base. The container was filled with water up to another 12 cm above the tube. Probe readings vary only as a function of the local properties of the access tube provided minimum distance from the lateral boundaries is respected.

The results with access tube surrounded by water are reported in Figure 2 for $5 \le s \le 40$ cm, where the effects of the boundaries of the container can be disregarded. The test was repeated three times with the same sensor. In the same figure results are reported of two runs with the same sensor in air, spanning the same length covered in water.

The experimental results in water and air show that the resonant frequency of the circuit depends on the position of the sensor itself inside the access tube. The mean resonant frequency in water is 100.8 MHz, with a standard deviation of ± 0.3 MHz. The corresponding mean resonant frequency in air is 149.4 MHz, with a standard deviation of ± 0.08 MHz. Oscillations in water are more marked than in air, since air has a lower dielectric constant than water. These effects are almost repeatable, as Figure 2 shows.

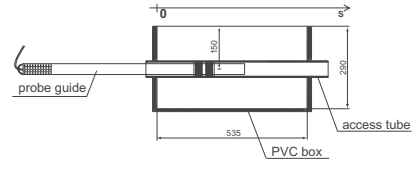

Figure 1. Geometry of the calibration arrangement in water. Coordinate s describes the distance between the inward lateral boundary and the sensor plates.

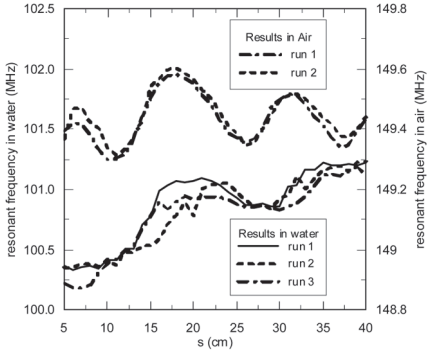

Figure 2. Experimental results in water (3 tests run) and in air (2 tests run). The resonant frequency of the sensor is plotted as a function of its position inside the access tube.

In terms of the maximum expected error in evaluating water content, the local differences in the dielectric properties of the access tube cause an uncertainty in estimating the actual water content of a soil, which increases with water content itself. The maximum error on the estimated water content is relatively small, and it keeps always below 2.5% of the actual water content.

4 EFFECTS OF WATER SALINITY

Water in soils may contain different salts, which have either a natural or an anthropic origin. It is well known that ions from dissociated salts modify the electrical conductivity and the dielectric constant of water (Nörtemann et al., 1997). Therefore, they will influence the resonant frequency of capacitance sensors, since they weaken the dielectric properties of the medium. A few tests were conducted to quantify this effect on the volumetric water content-scaled frequency relationship.

4.1 *Conductivity of water as a function of molarity*

The theoretical conductivity, σ, of a water solution reads:

$$\sigma = F \sum_i M_i u_i |z_i| \tag{5}$$

where M_i is the molarity of ion i, z_i is the valence of the ion, u_i is its ionic mobility, and F is the Faraday constant ($9.6487 \cdot 10^4$ C/mol). For NaCl in distilled water, with $z = \pm 1$, u equal to $5.19 \cdot 10^{-4}$ cm^2/Vs for Na^+ and $7.91 \cdot 10^{-4}$ cm^2/Vs for Cl^-, at 20°C, equation (5) gives

$$\sigma = 126\, M_{\mathrm{NaCl}} \tag{6}$$

where M_{NaCl} is the molarity of NaCl.

To verify the conductivity of the actual solution used in the following experimental tests, known molarities of NaCl were added to distilled water, and the electrical conductivity was measured by means of a conductimeter. A linear trend was found

$$\sigma = 110.4\, M_{\mathrm{NaCl}} \tag{7}$$

with a correlation coefficient $R^2 = 0.99$. The difference between the theoretical equation (6) and the experimental relationship (7) is mostly due to impurities in the commercial NaCl used in tests, besides the effects of temperature.

4.2 *Resonant frequency as a function of conductivity*

To verify the effects of water conductivity on the capacitance sensors reading, hence on its resonant frequency, the PVC container in Figure 1 was initially filled with distilled water fixing the water table 27 cm above the base. An increasing amount of NaCl was progressively added and mixed to the solution. The corresponding conductivities were measured, together with the resonant frequencies of a fixed probe, placed in the middle of the access tube. Results are reported in Figure 3. The data show that the resonant frequency changes with electrical conductivity, ranging from a value of roughly 101 MHz with distilled water to a value of 97.8 MHz with saline water having conductivity of σ = 25 mS/cm.

The experimental results were compared to model simulations. For each value of measured

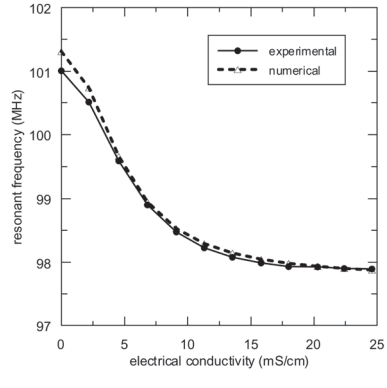

Figure 3. Comparison between measured and modelled values of the relation between the resonant frequency of a sensor and the electrical conductivity of a water solution.

conductivity, the theoretical resonant frequency of the LC circuit was computed, according to Kelleners et al. (2004).

The simulation results reported in Figure 3 show very good match with the measured values. The difference between simulated and measured values is equal to 0.2% at most, for distilled water. The values of σ were chosen so as to cover all the possible range for soils, up to marine ones.

5 CALIBRATION OF CAPACITANCE PROBES ACCOUNTING FOR INTERSTITIAL WATER CONDUCTIVITY

To evaluate the effects of water salinity on the calibration relations, eight soil samples of sandy silt (D_{50} = 0.04 mm) were prepared by moist tamping. Three of them were tamped with distilled water, at increasing degrees of saturation (*Sr*) of roughly 0.1, 0.5 and 0.9 (the measured water contents slightly varied from sample to sample because of non-perfect repeatability of the preparation procedure). Three of them were prepared at roughly the same degree of saturation *Sr*, with water having an electrical conductivity of 0.5 mS/cm. Two samples were prepared at $Sr = 0.5$ and $Sr = 0.9$, with water having the electrical conductivity of marine water, σ = 25 mS/cm. NaCl was used to reach the desired conductivities. The porosity was fixed to 0.45 for all the samples. The samples were prepared inside a metacrylate cylinder, with internal diameter of 19 cm and 20 cm height, after positioning the access tube at the centre of the cylinder.

At the middle of the access tube, at suitable distance from any external interference, four different sensors (indicated as 1, 2, 3 and 4) were placed, and their resonant frequencies were measured. Each sensor had been previously calibrated both in air and in water. Water resonant frequencies had been registered both in distilled water and in water having the same conductivity of that used to prepare the samples. The scaled frequency *SF* could be calculated, with respect to the relevant frequency range, and compared to the measured water content, θ, of the sample.

At the end of each test, the actual soil volumetric water content was verified by oven-drying samples trimmed from the soil in the container.

5.1 *Samples prepared with distilled water*

The scaled frequencies computed from resonance frequencies measured with sensor number 1, and the corresponding soil volumetric water contents, are compared to some literature calibration relations in Figure 4.

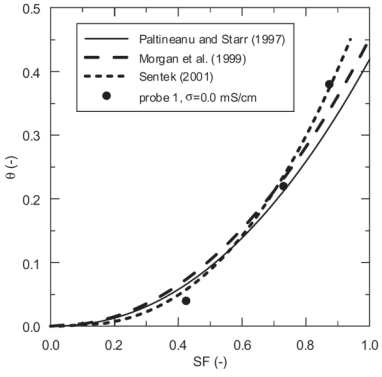

Figure 4. Comparison between some literature calibration curves and measured data (probe 1) obtained for soil moist-tamped with distilled pore water.

The comparison shows that literature calibration relations almost succeed in correctly estimating the actual volumetric water content data when the soil water has low conductivity. The conclusion was also verified on the measurements performed with the other sensors.

5.2 *Samples prepared with saline water*

Results for soil samples prepared with saline water are reported in Figure 5, with reference to sensor 1. Similar results were found on the other sensors.

Data refer to measured frequencies scaled both in the range given by resonant frequency in air and resonant frequency in distilled water ($F_{\sigma_w=0}$), henceforth indicated as uncorrected *SF*, and in the range bounded by the resonant frequency registered in water with the same conductivity used in the preparation of the soil samples ($F_{w_\sigma_w=0.5}$for σ = 0.5 mS/cm and $F_{w\_\sigma_w=25}$ for σ = 25 mS/cm), indicated as corrected *SF*.

For low conductivity (0.5 mS/cm), experimental data do not differ significantly from the data of the samples prepared with distilled water. As a consequence, at low salinity, literature relations succeed in predicting water content with sufficient accuracy, starting from the measured value for resonant frequency. This is verified referring both to corrected and uncorrected *SF,* whose numerical difference is small.

For higher conductivities (25 mS/cm) the correct water content is more difficult to infer from standard calibration curves, as the resonant frequency is strongly influenced by salinity effects. The error between the actual water content obtained by direct measurement (θ) and the one inferred from probe readings by means of standard calibration curves (θ_{probes}) is reported in Figure 6, as a function

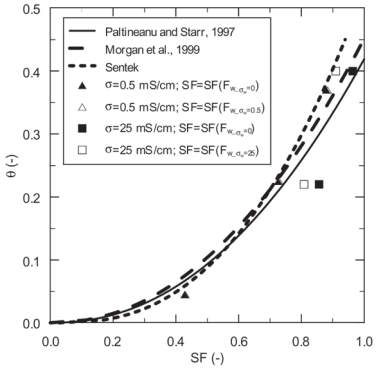

Figure 5. Comparison between some literature calibration curves and measured data (probe 1) obtained for soil moist-tamped with water at different conductivities. Each probe reading has been converted adopting both distilled and non-distilled water resonant frequencies.

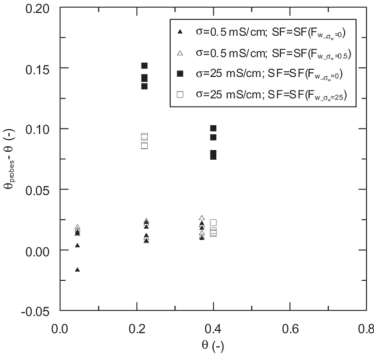

Figure 6. Error in estimating volumetric water content from probe readings as a function of actual water content, θ, and salinity, σ, of the interstitial water and adopted bounding water resonant frequency.

of the measured water content of the samples, of the salinity of the samples water, and of the actual scaling law adopted for *SF*.

In the range analysed, the difference $\left(\theta_{probes} - \theta\right)$ reaches 0.15, corresponding to 70% overestimation of the actual value of θ, if salinity effects are disregarded (adopting $F_{\sigma_w=0}$). The error can be halved if scaling is performed on the range bounded by the value obtained by previous calibration of the sensors in water with the same salinity as the one of the soil.

5.3 *Calibration curves accounting for salinity*

Firstly, each recorded resonant frequency F_r was scaled on the range bounded by the frequency measured in water with the same salinity.

Afterwards, interpolating calibration curves in the general form

$$\theta = a\,SF^b \tag{8}$$

were adopted and calibrated. The results are reported in Figure 7, and the values of the parameters *a* and *b* are summarised in Table 1.

These results were exploited to propose a new calibration curve which may account for salinity of water, at least as a first tentative.

The values of the parameters *a* and *b* are reported in Figure 8 as a function of normalised water conductivity σ/σ_{ref}, where σ_{ref} = 11.04 mS/cm

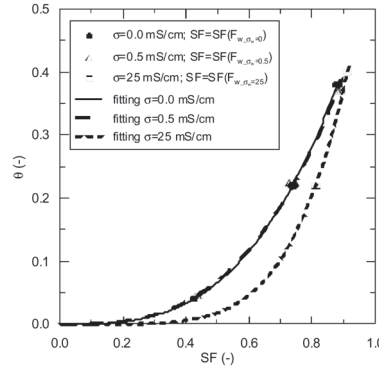

Figure 7. Calibration curves in the plane (scaled frequency: water content), as a function of water conductivity.

Table 1. Parameters a and b for the calibration curves (8).

Parameter	a	b
Distilled water	0.574	3.1
Water at 0.5 mS/cm	0.614	3.0
Water at 25 mS/cm	0.643	5.1

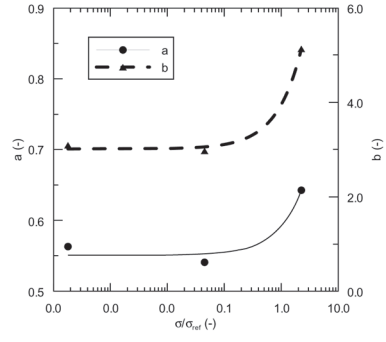

Figure 8. Dependence of the calibration curves parameters on normalised electrical conductivity.

is the conductivity of a 0.1 M solution of NaCl in distilled water.

A suitable interpolation of the results in Figure 7 allows a calibration curve accounting for water salinity to be proposed in the form:

$$\theta = \left[0.04\left(\frac{\sigma}{\sigma_{ref}} \right) + 0.55 \right] SF^{\left[0.93\left(\frac{\sigma}{\sigma_{ref}} \right) + 3.02 \right]} \quad (9)$$

It is worth noting that the previous expression should be considered only a preliminary proposal at this stage, and it should be verified against larger amount of experimental data.

6 CONCLUSIONS

Results have been presented of an experimental investigation focused on the influence of access tube heterogeneity and of water salinity on the performance of capacitance sensors for water content measurement.

The results presented show that a small error may be associated to the heterogeneity of the dielectric properties of the access tube. The latter in turn gives an error in the estimation of water content, which keeps under 2.5% of the actual value of water content, in the most unfavourable case.

Water salinity should be taken into account when calibrating the scaled frequency/water content relationship. The difference between the response of the sensor at varying water salinity is relatively small for low and high saturation scaled frequencies, but it may become relevant for intermediate values of scaled frequencies, hence for intermediate values of soil saturation.

The error in the estimated water content may reach 70% of the actual value, if the effects of salinity are disregarded. Nonetheless, it was observed that significant errors are associated only to very high salinity of water, typical of marine saltwater. For usual groundwater conditions, the effects of salinity are not dominant on the sensors response, and they may be hardly appreciated.

A calibration relation based on the data collected has been proposed. The relationship may be used for preliminary purposes to infer water content when the salinity of water is known, although it should be verified on a larger body of experimental data.

REFERENCES

Caruso, M. (2007). A theoretical, experimental and numerical approach to predict the hydrologic balance in the upper unsaturated soil layers (in Italian). Doctorate Thesis, Università di Parma.

Charlesworth, P. (2005). Soil water monitoring. An information package. 2nd ed. *Irrigation Insight* No 1.

Cui, Y.-J., Tang, A.-M., Mantho, A.T., De Laure, E. Monitoring field soil suction using a miniature tensiometer. *Geotechnical Testing Journal* 31(1): 95–100.

Gardner, C.M.K., Bell, J.P., Cooper, J.D., Dean, T.J., Hodnett, M.G. & Gardner, N. (1991). Soil Water Content. In Smith R.A., Mullings C.E., (eds) *Soil analysis—Physical methods*. Marcel Dekker, New York.

Kelleners, T.J., Soppe, R.W.O., Robinson, D.A., Schaap, M.G., Ayars, J.E. & Skaggs, T.H., (2004). Calibration of capacitance probe sensors using electric circuit theory. *Soil Science Society of America Journal*. 68: 430–439.

Mojid, M.A., Wyseure, G.C.L. & Rose, D.A. (2003). Electrical conductivity problems associated with time-domain reflectometry (TDR) measurement in geotechnical engineering. *Geotechnical and Geological Engineering* 21: 243–258.

Nichol, C., Smith, L. & Beckie, R. (2003). Long-term measurement of matric suction using thermal conductivity sensors. *Canadian Geotechnical Journal*, 40: 587–597.

Noborio, K. (2001). Measurement of soil water content and electrical conductivity by time domain reflectometry: a review. *Comp and Elec in Agric* 31: 213–237.

Nörtemann, K., Hilland, J. & Kaatze, U. (1997). Dielectric properties of aqueous NaCl solutions at microwave frequencies. *J. Phys. Chem.* 101: 6864–6869.

Paltineanu, I.C. & Starr, J.L. (1997). Real time soil water dynamics using multisensors capacitance probes. *Soil Science Society of America Journal* 61: 1576–1585.

Robinson, D.A., Gardner, C.M.K., Evans, J., Cooper, J.D., Hodnett, M.G. & Bell, J.P. (1998). The dielectric calibration of capacitance probes for soil hydrology using an oscillation frequency response model. *Hydrology and Earth System Sciences* 2(1): 111–120.

Scanlon, B.R, Andraski, B.J. & Bilskie, J. (2002). Miscellaneous methods for measuring matric or water potential, in Dane, J.H. & Topp, G.C. (eds), *Methods of soil analysis, part 4, physical methods*. Soil Sci Soc. of Am., Inc., 643–670.

Schwank, M. & Green, T.R. (2007). Simulated effects of Soil Temperature and Salinity on Capacitance Sensor Measurements. *Sensors*, 7(4): 548–577.

Schwank, M., Green, T.R., Mätzler, C., Benedickter, H. & Flürer, H. (2006). Laboratory characterization of a commercial capacitance sensor for estimating permittivity and inferring soil water content. *Vadose Zone Journal*. 5: 1048–1064.

Sentek. (2001). Calibration of Sentek Pty Ltd Soil Moisture Sensors. Sentek Pty Ltd, Stepney, South Australia.

Topp, G.C., Davis, J.L. & Annan, A.P. (1980). Electromagnetic determination in soil-water content: measurement in coaxial transmission lines. *Water Resources Research.* 16: 574–582.

Advances in Unsaturated Soils – Caicedo et al. (eds)
© 2013 Taylor & Francis Group, London, ISBN 978-0-415-62095-6

Unsaturated soil response under plane strain conditions via true triaxial testing

L.R. Hoyos
University of Texas at Arlington, Arlington, Texas, USA

J.A. Cruz
Universidad de los Andes, Bogotá, Colombia

A. Lizcano
SRK Consulting, Vancouver, British Columbia, Canada

ABSTRACT: Results from a series of servo/suction-controlled true triaxial tests, conducted on consolidated specimens of silty sand under plane strain conditions (restrained intermediate principal strain), are presented. The experiments were accomplished in a true triaxial apparatus suitable for testing cubical, 7.62 cm (3 in) side, specimens of unsaturated soil under controlled-suction states. The apparatus is a mixed-boundary type of device, with the soil specimen seating on top of a high-air-entry ceramic disk and between five flexible membranes on the remaining sides of the cube. The cell features two independent pore-air and pore-water pressure control systems and a fully automated principal stress application-control system. Suction states are induced in the specimens via the axis translation technique. Specimens are prepared by uniaxial consolidation of a slurry mixture, made of 75% silty sand and 25% kaolin, into a custom-made cubical acrylic mold. The induced range of matric suctions, 50–100 kPa, is shown to have a key influence on unsaturated soil response under suction-controlled plane strain conditions.

1 INTRODUCTION

The stress-strain-strength response of soils in many geotechnical systems, such as earth dams, slopes and highway embankments, may be best modeled using plane strain analyses. The assumption of plane strain condition is justified by virtually negligible deformations experienced by the soil along one of three principal axes of reference. Plane strain devices have been introduced to investigate the response of soils under these conditions and varying saturation states: Wood (1958), Vardoulakis & Goldscheider (1981), Vardoulakis & Graf (1985), Dresher et al. (1990), Alshibli et al. (2004), Schanz & Alabdullah (2007), Fauziah & Nikraz (2008), Cruz et al. (2011, 2012). Few attempts, however, have been made to study the engineering response of soils under plane strain conditions using more reliable and sophisticated true triaxial devices, including Desrues et al. (1985), testing dry dense sands; and Matsuoka et al. (2002), testing compacted silty soils under constant negative pore water pressure of –59 kPa.

In the present work, results from a short series of servo/suction-controlled true triaxial tests, conducted on consolidated specimens of silty sand under plane strain conditions, i.e. restrained intermediate principal strain, are presented. The experiments were accomplished in a true triaxial cell that is suitable for testing cubical, 7.62 cm (3 in) per side, specimens of unsaturated soil under controlled-suction states. The apparatus is a mixed-boundary type of device, with the soil specimen seating on top of a high-air-entry (5-bar) ceramic disk and between five flexible membranes on the remaining sides of the cube. The cell features two independent pore-air and pore-water pressure control systems and a fully automated principal stress application-control system. Target matric suctions are induced in the soil specimens by means of axis-translation technique (Hilf, 1956). All specimens were identically prepared by uniaxial consolidation of a slurry mixture, 75% silty sand and 25% kaolin, into a custom-made cubical acrylic mold.

2 TRUE TRIAXIAL CELL: BASIC FEATURES

The true triaxial cell used in this investigation can be classified as a mixed-boundary type of cell (Arthur, 1988), with features similar to those

used by Reedy et al. (1992), and by Hoyos and Macari (2001). A detailed description of its main components is given by Pérez-Ruiz (2009), and Hoyos et al. (2012). Figure 1 shows a panoramic view of the entire servo/suction-controlled true triaxial setup, including its core cell, PCP-5000-UNSAT and PVC-100-UNSAT pressure panels, and DA/PCS.

The core frame features six pressure cavities to accommodate one top and four lateral membranes, a cubical base piece at the bottom assembly to house a 5-bar ceramic, and four symmetrically spaced coarse porous stones, as shown in Figure 2. A grooved water compartment underneath the ceramic disk allows for application of pore-water pressure u_w and flushing of diffused air during testing. Small cavities were machined on each corner of the cubical base piece to accommodate four porous stones, allowing for application of constant pore-air pressure u_a during testing.

Cubical membranes are prepared using a Silastic J-RTV type of silicon rubber (Dow Corning), which renders membranes with high tear strength and relatively low stiffness. Each membrane forms a pressure seal between the wall assembly and the reaction frame, acting as the actual fluid barrier for the water pressurizing the top and lateral faces of the cubical specimen: Figure 2. Each wall assembly consists of a cover plate, pressure inlet/outlets, and optional housings for up to three LVDTs. (The cell, however, does not require the use of LVDTs, in direct contact with the membranes, for monitoring of soil deformation.)

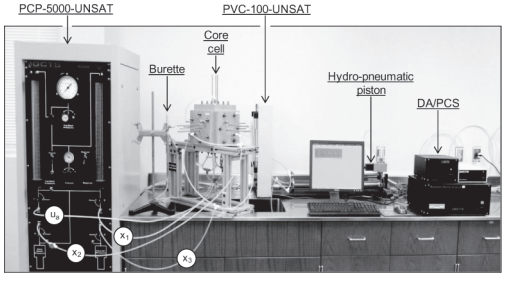

Figure 1. Panoramic view of complete servo/suction-controlled true triaxial testing system.

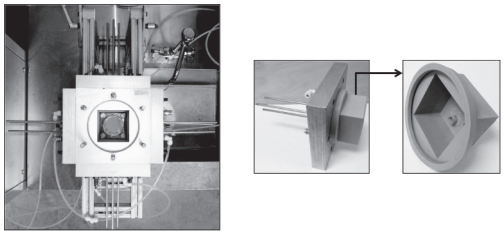

Figure 2. Top view of partly assembled cell, including 5-bar ceramic; and typical lateral wall assembly, including membrane.

The PCP-5000-UNSAT panel is used to control the major, intermediate, and minor principal stresses along the vertical (X_1) and horizontal (X_2 and X_3) directions, respectively. The panel features a full set of independent servo valves to control the displacement of an equal number of hydraulic pistons, therefore controlling the external pressure being applied to the soil in any principal direction. Any principal stress combination path in the first octant can be achieved by simultaneous and independent control over these three servo valves. The output line from each servo valve splits into two lines to supply the same pressure to the positive and negative faces of the cube.

In the present work, axis-translation technique is implemented via the $s = u_a$ testing approach ($u_w = 0$). Air pressure is supplied to the bottom assembly from a spare air-pressure outlet in the PCP-5000-UNSAT panel: Figure 1. The output line splits into two separate T fittings, hence simultaneously supplying same pore-air pressure through all four stones into the soil. During suction-controlled testing, the PCP-5000 unit automatically adjusts the supply of air to ensure constant pore-air pressure u_a throughout the test.

A flush-in line, made of flexible nylon tubing, is directly connected to a spare water-pressure outlet in the PVC-100-UNSAT panel, which is seen right behind the assembled cell in Figure 1. A flush-out line releases the entrapped air from underneath the 5-bar ceramic disk to the atmosphere. Prior to testing, the flushing lines and the water compartment underneath the ceramic are thoroughly saturated by generating a constant flow of water from the PVC-100 unit. Finally, the external pressure applied in all three principal directions, and the resulting soil deformations, are recorded and/or processed in real time by a fully automated DA/PCS.

3 TEST SOIL AND SPECIMEN PREPARATION

The test soil used in this investigation is an artificially mixed soil made of 75% silty sand (SM) and 25% kaolin (CH). Both soils were sampled from a locality near to the city of Bogotá, Colombia, then shipped overseas to the University of Texas at Arlington. The silty sand yields specific gravity, $G_s = 2.63$; the kaolin clay yields specific gravity, $G_s = 2.58$. Atterberg limits tests on kaolin clay yielded liquid limit, LL = 57.1%, and plastic limit, PL = 45.8%. The soil-water characteristic curve is given by Cruz et al. (2012).

The specimen is prepared by uniaxial consolidation of a slurry mixture (75% silty sand and 25% kaolin) into a custom-made cubical acrylic mold of 80 mm × 80 mm × 200 mm dimensions: Figure 3. The dry soils (1 kg each) are thoroughly mixed with deionized water to a target moisture about twice the liquid limit of the slurry mixture (LL = 25.3%). The slurry is then mixed for 15–20 min with an electrical mixer and carefully poured into the cubical mold.

An incremental vertical load is applied to the slurry mixture through a squared acrylic plate featuring an affixed coarse porous stone at its bottom surface. The loads are applied via a pneumatic actuator. During uniaxial consolidation, the vertical deformations are measured with a dial gauge while the expelled water, from within the slurry, is collected in a graduated cylinder: Figure 3. The initial height of the slurry mixture is about 140 mm, and it is consolidated to final target dimensions of 80 × 80 × 100 mm. Load increments of 12.5, 25, 50, 100, 200, and 400 kPa are typically applied, with each load increment acting on the slurry until no further vertical deformation or expelled water is observed (normally after 90% of primary consolidation, t_{90}). The consolidation yields an average water content of 25.5% and average saturated unit weight of 19.8 kN/m^3.

The compacted 80 × 80 × 100 mm sample is then gently removed from the consolidation mold, from which one solid specimen is trimmed for true triaxial testing: Figure 4. The specimen is trimmed to final dimensions, d_{10} = 76 mm, d_{20} = 76 mm and d_{30} = 76 mm, as shown in Fig. 5, with a final average mass of about 890.3 g. Finally, the specimen is gently slid in through one of the lateral cavities of the core frame, after which the remaining wall assemblies are set into place and the DA/PCS system readied for testing.

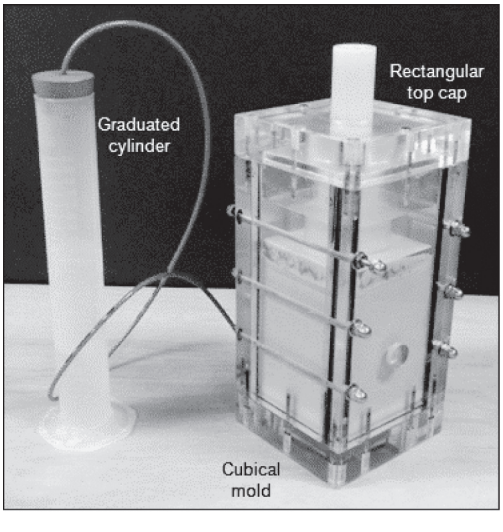

Figure 3. Uniaxial consolidation of cubical specimen via an 80 × 80 × 200 mm acrylic custom-made mold.

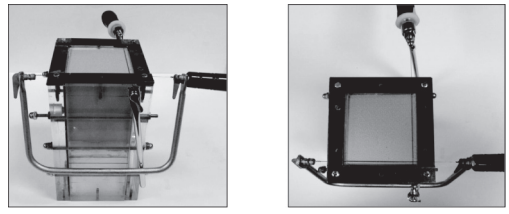

Figure 4. Trimming of cubical specimen after consolidation.

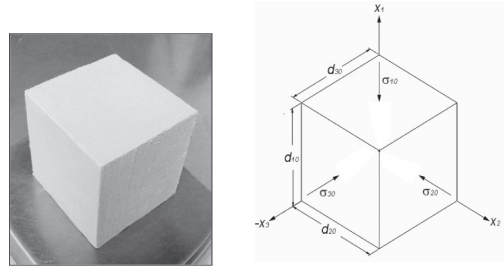

Figure 5. Trimmed specimen and reference coordinate system.

4 SOIL RESPONSE UNDER PLANE STRAIN

In this work, three identically prepared specimens of compacted SM soil were tested at constant-suction plane strain conditions in the true triaxial apparatus. The soil is first hydrostatically compressed to a target mean stress, $p = (1/3)(\sigma_1 + \sigma_2 + \sigma_3)$. The pore-air pressure u_a is then gradually increased (soil drying) to the pre-established values of suction and net mean stress in all three principal directions. Pore-air pressure u_a is maintained constant until no further change in expelled water (less than 0.035 ml/day) or specific volume (less than 0.01/day) was observed, at which point the pore-fluid equalization stage is considered complete. The suitable pore-fluid equalization time ranged from 144–244 hrs (6–11 days) for matric suction values ranging from 50–100 kPa.

The soil is finally sheared by following a mixed-controlled testing scheme until it is readily apparent that the soil has reached peak strength. During shearing, a constant strain rate of 0.004 mm/min

is programmed in the major principal direction X_1—strain controlled; a constant strain rate of 0.000 mm/min is programmed in the intermediate principal direction X_2—strain controlled; and, finally, the net principal stress is kept constant in the minor principal direction X_3—stress controlled.

A typical principal-strain response of compacted SM soil during suction-controlled plane strain shearing is shown in Figure 6. The results are presented in terms of deviatoric stress vs. major, intermediate and minor principal strains for a specimen tested under initial net mean stress, $p = (\sigma_c - u_a) = 100$ kPa, and constant matric suction, $s = 50$ kPa. (σ_c = isotropic confining pressure). It can be readily noticed that the true triaxial system reproduces plane strain condition with reasonable efficiency, as evidenced by all of the following: 1) Significant increase in major principal strain (compressive); 2) Virtually negligible intermediate principal strain; 3) Decrease in minor principal strain (extensive); and 4) Virtually no change in deviatoric stress in the minor principal direction X_3 (constant σ_3). A coefficient of earth pressure for plane strain condition K_{PS} can be assessed as the ratio of the intermediate net principal stress, $(\sigma_{2c} - u_a)$, to the major net principal stress, $(\sigma_{1c} - u_a)$; i.e. $K_{PS} = (\sigma_{2c} - u_a)/(\sigma_{1c} - u_a)$, as shown in section 5.

Figure 7 shows the stress-strain response, during suction-controlled plane strain shearing, of two identically prepared specimens of SM soil. Both specimens were sheared at initial net confinements, $p = 50$ kPa (Test 1) and 100 kPa (Test 2), respectively; and same suction, $s = 50$ kPa. Apparent peak stress values of 328 kPa and 535 kPa, corresponding to final axial strain values of 0.092 mm/mm (9.2%) and 0.106 mm/mm (10.6%), were attained, respectively; with the larger stress observed under

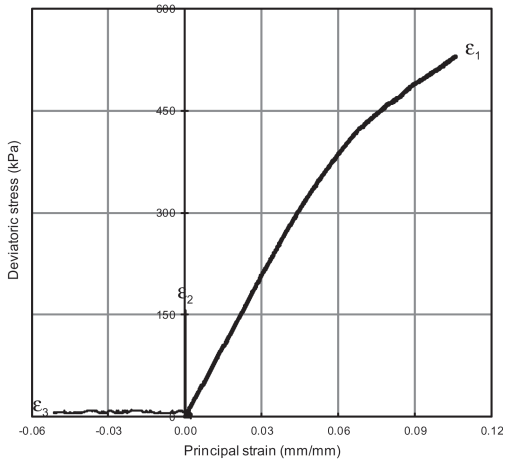

Figure 6. Strain response of SM soil: p = 100 kPa, s = 50 kPa.

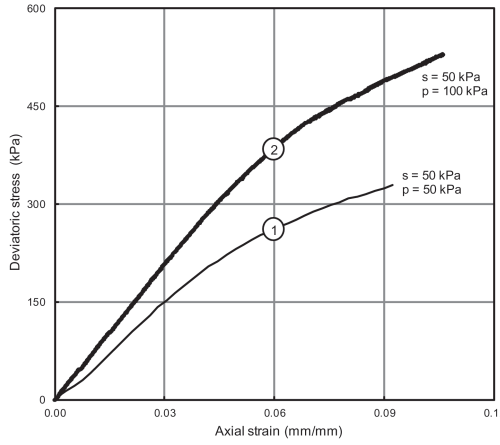

Figure 7. Stress-strain response of SM soil: suction-controlled plane strain shearing.

greater initial net confinement. In this preliminary investigation, all tests were programmed to be stopped when an axial strain of about 9–10% had been reached; therefore, a thorough assessment of a definitive peak stress value was not necessarily feasible in all cases, as illustrated by the stress-strain curves in Figure 7.

5 COEFFICIENT OF EARTH PRESSURE—K_{PS}

As previously mentioned, a coefficient of earth pressure for the plane strain condition can be readily assessed as: $K_{PS} = (\sigma_{2c} - u_a)/(\sigma_{1c} - u_a)$. Figure 8 shows an schematic of the typical suction-controlled stress path induced on compacted specimens of SM soil in net principal stress space $(\sigma_1 - u_a):(\sigma_2 - u_a):(\sigma_3 - u_a)$. The specimen is first isotropically consolidated to an initial stress state, represented by point A: net mean stress, $p = (\sigma_c - u_a)$; constant matric suction, $s = u_a$. The specimen is then sheared by following a mixed-controlled testing scheme until it is readily apparent that it has reached peak strength at point B. The soil is sheared with constant strain rate of 0.004 mm/min in the major principal direction X_1, constant strain rate of 0.000 mm/min in the intermediate principal direction X_2, and constant intermediate net principal stress, $(\sigma_{3c} - u_a)$, in the minor principal direction X_3—stress controlled.

The line OB in Figure 8, with slope $1/K_{PS}$, represents the locus of critical state condition from a series of plane strain tests conducted on several identically prepared samples, each tested under a different initial stress state (point A). Line OB is

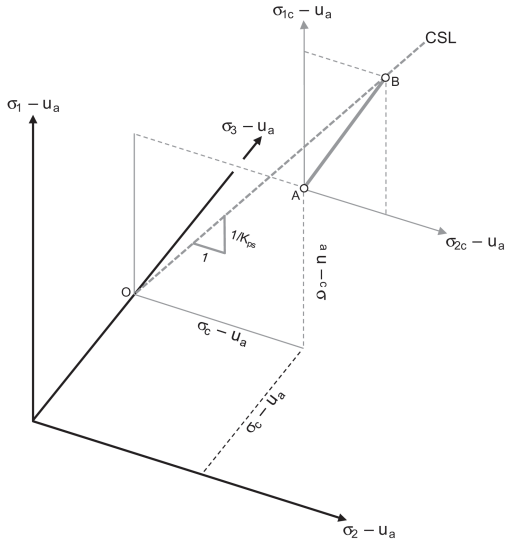

Figure 8. Suction-controlled stress paths in net principal stress space $(\sigma_1 - u_a):(\sigma_2 - u_a):(\sigma_3 - u_a)$.

expected to be asymptotic with respect to the stress paths AB at the end of shearing. Wood (1958) observed that the behavior of the intermediate stress under plane strain condition can be approximately as $\sigma'_2 \approx K_o\sigma'_1$ at the point of failure, where K_o = coefficient of earth pressure at rest under zero lateral strain.

Figure 9 shows the stress paths induced on three identically prepared specimens of SM soil in the net principal stress plane $(\sigma_1 - u_a):(\sigma_2 - u_a)$. The first specimen was brought to an initial stress state A(50, 50) under constant matric suction, s = 50 kPa, prior to shearing. The second specimen was brought to an initial stress state A(100, 100) under constant matric suction, s = 50 kPa. The third specimen was brought to an initial stress state A(100, 100) under constant matric suction, s = 75 kPa. In all cases, the initial intermediate net principal stress value, $(\sigma_{3c} - u_a)$, was kept constant during plane strain shearing. Figure 9 appears to confirm the asymptotic nature of the critical state line, with respect to all three stress paths, at the end of shearing. The CSL yields a mean value of the coefficient of earth pressure for plane strain condition, $K_{PS} = 0.395$.

Figure 10 shows a series of actual photographs of the specimens failed under plane strain shearing. Lower deformation is observed in the specimen tested under higher matric suction, s = 75 kPa. Since the deformation in all specimens was limited to 9–10%, no apparent shear band formation is observed. Stress concentrations at the corners of either specimen also appeared to be minimal.

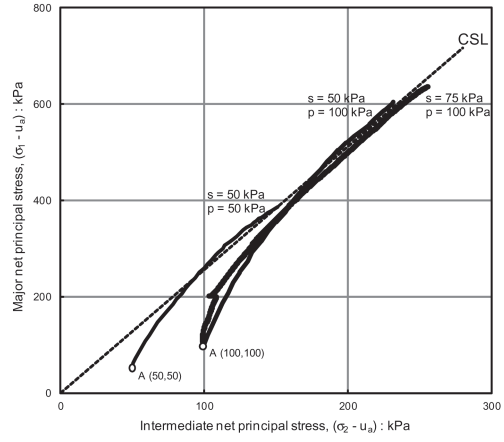

Figure 9. Suction-controlled stress paths in net principal stress plane $(\sigma_1 - u_a):(\sigma_2 - u_a)$.

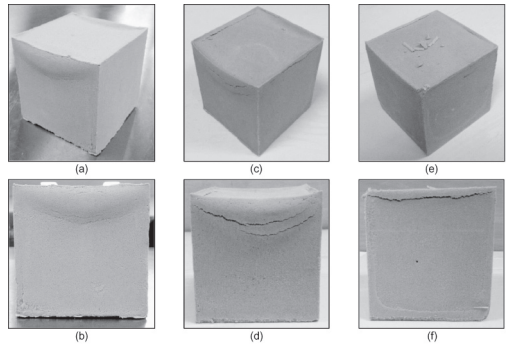

Figure 10. Photographs of failed specimens under plane strain conditions: (a)–(b) p = 50 kPa, s = 50 kPa; (c)–(d) p = 100 kPa, s = 50 kPa; (e)–(f) p = 100 kPa, s = 75 kPa.

6 CONCLUDING REMARKS

The true triaxial system used in this work reproduces plane strain condition with reasonable accuracy and efficiency. Test results from a short series of suction-controlled plane strain tests appear to corroborate the asymptotic nature of critical state line CSL, with respect to plane strain stress paths, at the end of shearing; yielding a mean value of the coefficient of earth pressure for plane strain condition, $K_{PS} = 0.395$, for compacted SM soil. Less deformation was observed in the specimen tested under higher matric suctions. Deformation in the specimens was limited to 9–10%, hence no apparent shear band formation was noticed. A thorough experimental program is currently being undertaken by the same authors in order to compare results from suction-controlled plane strain tests using both true triaxial and biaxial systems.

ACKNOWLEDGEMENTS

The research work is being developed under the auspices of COLCIENCIAS ("Departamento Administrativo de Ciencia, Tecnología e Innovación"), Bogotá, Colombia; and the CEIBA ("Centro de Estudios Interdisciplinarios Básicos y Aplicados en Complejidad"), University of the Andes, Bogotá, Colombia. This support is gratefully acknowledged.

REFERENCES

Alshibli, K.A., Godbold, D.L., and Hoffman, K. (2004). "The Louisiana plane strain apparatus for soil testing." Geotechnical Testing Journal, ASTM, 27(4), 337–346.

Arthur, J.R.F. (1988). "Cubical devices: versatility and constraints." *Advanced Triaxial Testing of Soil and Rock*, R.T. Donaghe, R.C. Chaney and M.L. Silver, eds., STP 977, ASTM, Philadelphia, 743–765.

Cruz, J.A., Hoyos, L.R., and Lizcano, A. (2011). "A novel suction-controlled biaxial apparatus for unsaturated soils." *Unsaturated Soils: Theory and Practice 2011*, Proc., 5th Asia-Pacific Conference on Unsaturated Soils, November 14–16, 2011, Pattaya, Thailand, Eds: A. Jotisankasa, A. Sawangsuriya, S. Soralump, and W. Mairaing, vol. 1, pp. 233–237.

Cruz, J.A., Hoyos, L.R., and Lizcano, A. (2012). "Unsaturated soil response under plane strain conditions using a servo/suction-controlled biaxial apparatus." *Unsaturated Soils: Research and Applications*, Springer, Proc., Second European Conference on Unsaturated Soils, June 20–22, 2012, Naples, Italy, Eds: C. Mancuso, C. Jommi, and F. D'Onza, vol. 1, pp. 31–38.

Desrues, J., Lanier, J., and Stutz, P. (1985). "Localization of the deformation in tests on sand sample." Engineering Fracture Mechanics, 21(4), 909–921.

Drescher, A., Vardoulakis, I., and Han, C. (1990). "A biaxial apparatus for testing soils." Geotechnical Testing Journal, ASTM, 13, 226–234.

Fauziah, M., and Nikraz, H.R. (2008). "The behaviour of unsaturated compacted clay under plane strain condition." *Geo-Environment and Landscape Evolution III*, Proc., 3rd International Conference on Evolution, Monitoring, Simulation, Management and Remediation of the Geological Environment and Landscape, June 2008, New Forest, UK, 77–85.

Hilf, J.W. (1956). "An investigation of pore water pressure in compacted cohesive soils." Technical Memorandum No. 654, United States Department of Interior, Bureau of Reclamation, Design and Construction Division, Denver, CO.

Hoyos, L.R., and Macari, E.J. (2001). "Development of a stress/suction-controlled true triaxial testing device for unsaturated soils." Geotechnical Testing Journal, 24(1), 5–13.

Hoyos, L.R., Pérez-Ruiz, D.D., and Puppala, A.J. (2012). "Refined true triaxial apparatus for testing unsaturated soils under suction-controlled stress paths." International Journal of Geomechanics, ASCE, 12(3), 281–291.

Matsuoka, H., Sun, D.A., Kogane, A., Fukuzawa, N., and Ichihara, W. (2002). "Stress-strain behaviour of unsaturated soil in true triaxial tests." Canadian Geotechnical Journal, 39, 608–619.

Pérez-Ruiz, D.D. (2009). "A refined true triaxial apparatus for testing unsaturated soils under suction-controlled stress paths." Ph.D. dissertation, University of Texas at Arlington, 320 p.

Reddy, K.R., Saxena, S.K., and Budiman, J.S. (1992). "Development of a true triaxial testing apparatus." Geotechnical Testing Journal, 15(2), 89–105.

Schanz, T., and Alabdullah, J. (2007). "Testing unsaturated soil for plane strain conditions: A new double wall biaxial device." *Experimental Unsaturated Soil Mechanics*, Springer, 169–178.

Vardoulakis, I., and Goldscheider, M. (1981). "Biaxial apparatus for testing shear bands in soils." Proc., 10th Int. Conf. on Soil Mechanics and Foundation Engineering, Stockolm, Sweden, vol. 4, 819–824.

Vardoulakis, I., and Graf, B. (1985). "Calibration of constitutive models for granular materials using data from biaxial experiments." Géotechnique, 35(3), 299–317.

Wood, C.C. (1958). "Shear strength and volume change characteristics of compacted soil under conditions of plane strain." Ph.D. dissertation, University of London, UK.

Advances in Unsaturated Soils – Caicedo et al. (eds)
© 2013 Taylor & Francis Group, London, ISBN 978-0-415-62095-6

Measuring water retention properties of a series of bentonite clays in a wide range of suctions

D. Marcial
Universidad Central de Venezuela, Caracas, Distrito Capital, Venezuela

ABSTRACT: High plasticity clays have sensitivity to a wide range of suctions, varying from very low to very high suction values, thus various methods must be combined to obtain the water retention curve WRC in the whole range of suctions. In this work, the osmotic method and the vapour phase method were combined to obtain the WRC of a series of bentonite clays to be used as engineered barriers. Different details of the experimental set up, to improve the vapour phase method are presented. To enlarge the use of vapour phase method to medium low suction, a relative humidity generator was employed. Concerning the osmotic method, difficulties were observed when the suction values exceed about 2 MPa. Results obtained in a range of suction from a few kPa up to 113 MPa are presented, and a good agreement between osmotic method and vapour method is observed.

1 INTRODUCTION

1.1 *The problem*

Engineered barriers for nuclear waste disposal at great depth are conceived to be built with heavily compacted unsaturated bentonite blocks. After Pusch (1982), these blocks are characterized by a very complex behaviour due to the swelling properties and double porosity microstructure of bentonite based materials. Because of the concept of these repository structures, large voids can be initially present between compacted blocks and the underground galleries, as indicated by Marcial et al. (2006). Thus, as bentonite blocks hydrate with available underground water, free swelling of clay aggregates to these large voids may occur to be temporary filled-up with a bentonite gel. As the hydration of bentonite blocks goes on, new formed gel will gradually consolidate and, at the long term, the bentonite barriers will turn to a saturated state with a more stable microstructure. This scenario leads us to study the water retention properties of bentonite clays from a slurry state in a wide range of suctions.

1.2 *Some recent improvements on water retention experimental methods*

Since high plasticity clays have sensitivity to a wide range of suctions, varying from very low to very high suction values, there is not a unique method to obtain the water retention curve WRC of these soils. Often at least two methods are combined to cover from a few kPa to several MPa suction values. This work only concerns the vapour phase method and the osmotic method. The vapour phase method has been currently used to control total suction from medium to very high values. The classical experimental setup, consisting in a close system to reach equilibrium with saturated o diluted chemical solutions in a simple desiccator, is quite slow. However, some improvements are shown further to be useful to obtain significant reductions on equilibrium times. A few tests with different bentonite clays are presented in this work to illustrate this aspect. Concerning the lower range of suctions, a recent work from Delage & Cui (2008) shows important advantages of the osmotic method, including an extension of the method beyond the classical range of 1500 kPa. They also deal with some disadvantages of the osmotic method, related to the resistance of the semi-permeable membrane such as the resistance to shear stresses. A series of tests, presented in this work, shows that difficulties beyond the classical range of 1500 kPa may be observed. This basically concerns an increasing pollution of soil specimens, with the osmotic solution, as suction increase beyond the classical range.

2 MATERIALS AND METHODS

2.1 *Experimental set-ups*

The principles of the osmotic method to control soil suction in geotechnical testing have been widely explained since the early 1970s, and a deep review is resented by Delage & Cui (2008). Thus, no deep descriptions of the method are presented here.

The osmotic device for the determination of the water retention curve is a very simple one. The soil sample is introduced in semi-permeable membrane tubing, and then plunged in a container with a polyethylene glycol (PEG) solution and placed on a magnetic stirrer. After equilibrium time is reached, the soil sample is withdrawn to measure its water content. The corresponding osmotic suction value depends on the final concentration of the PEG solution. To avoid water evaporation in the solution, the container is covered with a plastic film. In this work, PEG 6000solutions were used with 3500 molecular weight cut off semi-permeable membranes. The classical experimental set up was simply improved by placing the solution container in a thermostatic bath (see Figure 1). As will be seen further, the use of a fine temperature control system is desirable.

Concerning the vapour phase method, as indicated above, the classical experimental setup, consisting in a close system to reach equilibrium with a saturated o diluted chemical solution in a single desiccator, is quite slow. Schneider (1960) presents a huge selection of salts to control suction in a wide range of values by using saturated solutions. Temperature changes appear also as a main aspect to be considered. The classical experimental set up can be improved as presented in Figure 2. A pneumatic pump is incorporated to increase the mobility of water molecules in a relative humidity controlled closed system. Thus, water exchanges between soil samles and humid air are accelerated. The close system consists of two glass bottles, a desiccator and a pneumatic pump. All components are interconnected with silicon thick wall tubing. To minimize temperature changes, the system is installed in a thermostatic water bath. If bottles or desiccators are to light, some gravel may be placed inside to prevent flotation in the bath. The capacity of the pneumatic pump should be of a few litres per minute. The first glass bottle contains a saturated solution corresponding to a target suction; the tubing coming from the pump is immerged in the solution to continuously mix it with the salt crystals. The air passes through the saturated solution and goes to the second glass bottle that works as a transient reservoir where air mixture is more homogeneous in terms of relative humidity and temperature. Then, the stable air mixture is injected to the bottom of the desiccator where the soil samples are exposed to an ascending air flow. The air mixture is finally taken again by the pump and so on. It is important to check the system to be free of leaks. To do so, the system is pressurized by strangulating the tubing while the pump is running. A soap solution is used to check that no air bubble appears at any connection. As done with the osmotic method, after equilibrium time is reached, the soil sample is withdrawn to measure its water content.

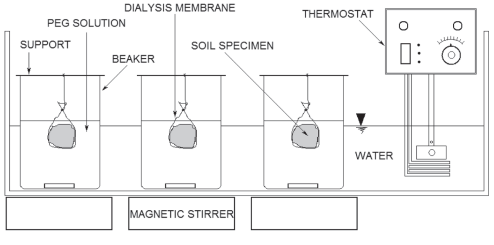

Figure 1. The osmotic method in a thermostatic bath.

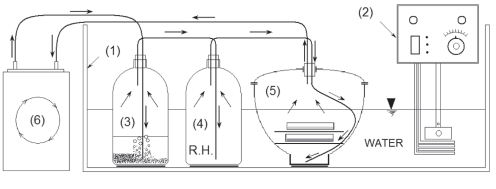

Figure 2. The vapour phase method with air circulation, transient flow in a storage bottle and thermostatic bath.

2.2 *Bentonite clays index properties*

The water retention properties of three reference bentonite clays were investigated. The index properties of these clays are summarized in Table 1. The FoCa7 is a French calcium bentonite, the Kunigel VI is a Japanese sodium bentonite considered in the Japanese concept of nuclear waste disposal and the Wyoming bentonite, so called MX80, have been the reference swelling clay in geotechnical

Table 1. Index properties of referenced bentonite clays.

	Clay name		
Properties	FoCa7	Kunigel VI	MX80
Mineralogy	80% Ca-Smectite	65% Na-Smectite	82% (Na/Ca = 5,5) Smectite
C.E.C, meq/100 g	69.1	76	69.6
Liquid limit, %	120	474	520
Plastic limit, %	50	27	42
Specific gravity	2.67	2.79	2.65
Skempton activity	0.78	6.9	5.8
Specific surface, m^2/g	515	687	800

engineering. Thus, there are important reference research works about these clays: Bolt (1956), Pusch (1982), Dixon et al. (1996), Komine & Ogata (1994), Saiyouri et al. (2000), among others.

As indicated above, the water retention properties of these clays were studied from slurry state in a wide range of suctions. To do so, all tests were carried out in drying paths. The initial state of soil samples was defined to be beyond the liquid id limit. For Foca7 nd Kunigel VI the initial water conent was equal to 1.1 times liguid limit, but with MX80 samples, it was fixed to 1,5 times liquid limit. The soil—distilled water mixture was carefully prepared and left to be homogenised in a hermetic container for at least 48 hours before testing.

3 RESULTS AND DISCUSSIONS

3.1 *The osmotic method*

The first aspect to be established was the equilibrium time between osmotic suction and water content of slurry soil samples. To do so, 6 slurry samples of different bentonite clays were plunged in a PEG solution corresponding to a 7 MPa osmotic suction. Each sample permits to determine the water content a different time, from 48 to 362 hours.

The samples consisted to 10 ml of slurry, placed into de semi-permeable membrane with an open end syringe. The membrane is provided in form of tube rolls that must be cut in pieces to hold each sample. Each piece of membrane is first plunged in distilled water during some minutes to allow the membrane soften to be opened. Then, the syringe open end is carefully introduced into de piece of membrane to place the 10 ml slurry sample. Both ends of the piece of membrane are then tightened together and fixed to a support to avoid the ends to be submerged into de solution. See Figure 1.

After each immersion time is reached, samples are withdrawn from de membrane, weighed and oven dried to measure the corresponding water content. Changes of water content with time are presented in Figure 3 for FoCa7 and Kunigel VI bentonites. Note that most water exchanges occur during the first 100 hours (about 4 days). However, the equilibrium time was fixed equal to 14 days for the whole suction range.

To investigate the sensitivity of osmotic tests to temperature control, a series of test were carried out at a controlled room temperature of 20 °C with and without immersion in the thermostatic bath. Important variations of the equilibrium water content were observed with different bentonites clays. However, the most relevant differences were obtained with the Kungel VI bentonites. These results are presented in Figure 4.

After oven drying the MX80 samples it was observed a colour change of samples, from clear grey to dark grey depending on the applied suction level. The samples submitted to lower suctions, below about 1 MPa, conserved their clear grey colour that characterises this benonite at the dry state. However, as applied suction values are beyond about 2 MPa, the colour after oven drying the samples becomes darker. The higher the suction, the darker the colour becomes when the samples are oven dried. This is explained by the presence of a PEG film around the sample that is burned when the sample is dried. This PEG film is thicker as higher is the suction. The pollution of samples with PEG may be due to the presence in PEG 6000 of molecules of molecular size lower than the membrane molecular cut off of 3500. Because de PEG concentration increases with suction, the presence of lower size molecules increases also, giving rise to a thicker PEG film. Elsewhere, Delage & Cui (2008)

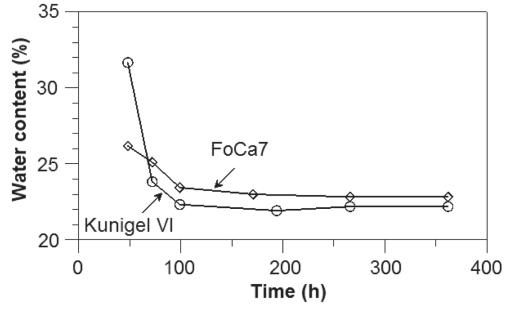

Figure 3. Water content changes with time for a 7 Mpa suction.

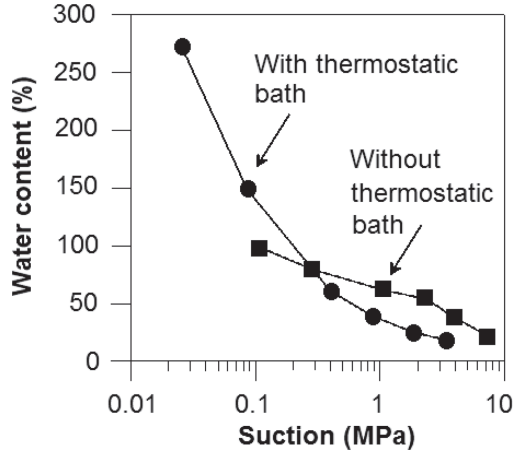

Figure 4. WRCs of Kuigel VI bentonite obtained with and without the thermo static bath by the osmotic method.

highlight the fragility of cellulotic membranes to stresses.

The changes of colour of oven dried samples submitted to different suctions can be observed in Figure 5.

To somewhat limit this problem, PEG 20000 molecules were combined with 3500 molecular weight cut off semi-permeable membranes. Because the viscosity of the osmotic solution increases with the molecular weight of PEG, the maximal suction applied with PEG 20000 molecules was limited to 3.5 MPa. For this series of tests the same pollution problem with PEG was observed as it was with PEG 6000 molecules when suction values are beyond the classical range of 1.5 MPa.

The results obtained with the 3 different bentonites, with thermo static bath and PEG 20000 molecules are plotted together in Figure 6.

Notice that all curves obtained within the thermo static bath are smooth and regular typical curves. Comparing the position WRCs of all bentonites, one observes that MX80 bentonite retains more water than Kunigel VI bentonite and FoCa7

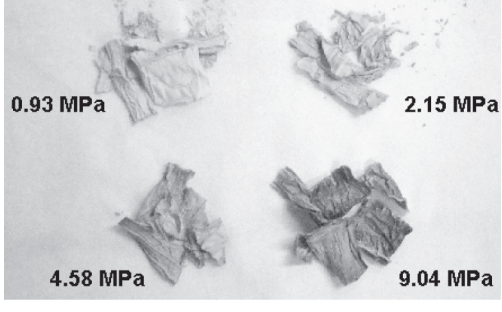

Figure 5. Aspect of oven dried bentonite samples after testing.

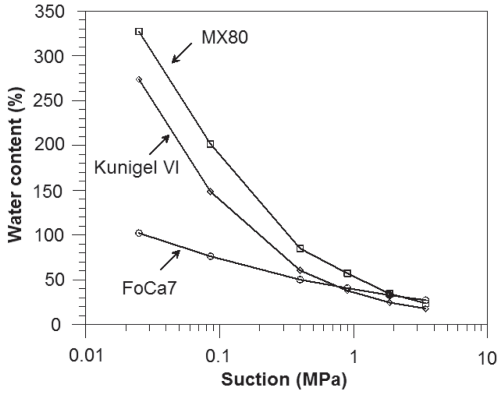

Figure 6. WRCs obtained with the osmotic method for 3 different bentonites up to 3.5 MPa.

bentonite respectively. This is good agreement with the mineralogical activity of the clay samples. Both, MX80 and Kunige VI are sodium bentonites, thus their water potential is higher and well differentiated from FoCa7 that is calcium bentonite that retains less water in the low suction range. This difference of behaviour is due to the double layer effects observed in bentonites when sodium is the main exchangeable cation. These double layer effects are quite well known since the work of Bolt (1956) with homoionic Wyoming bentonites.

3.2 *The vapour phase method*

Concerning the vapour phase method, it is typically employed to obtain water retention properties in the high range of suctions. As indicated above, the classical set up consists of a simple desiccator containing both a diluted of saturated chemical solution, and the soil sample. In this work, only saturated solutions were used with both, the classical and the improved set up (see Figure 2). The selected salts and corresponding suction of the saturated solution are summarized in Table 2.

Some tests, corresponding to higher suction values were done with the classical set up. Thus, samples were placed inside a desiccator with the saturated solution and left to equilibrate with time in a controlled 20 °C temperature room inside a water thermo static bath. The samples were placed in capsules inside the desiccators and periodically weighed to monitor water content changes with time. Some of drying curves obtained with FoCa7 bentonite are presented in Figure 7. Notice that a time of about 200 days is necessary to reach equilibrium with a 24,9 suction value. Also, a typical trend is to have faster water exchanges with increasing suction values. However, the equilibrium time depends not only on the suction value but also on the composition of the salt. In the case of NaCl, equilibrium times are lower than with other salts that give rise to higher suctions.

The use of an improved set up, as shown in Figure 2, permits to considerably shorten equilibrium times. This is illustrated in Figure 8 where

Table 2. Salts and corresponding suctions.

Salt	Suction (MPa)
K_2SO_4	4.2
KNO_3	9
$Z_nSO_47H_2O$	12.6
$(NH_4)_2SO_4$	24.9
NaCl	38
$NaNO_2$	57
$Mg(NO_3)_2$	82
K_2CO_3	113

drying curves of MX80 bentonite are presented. Notice that equilibrium times are just a few days, one order of magnitude less than equilibrium times obtained with the classic set up and similar suction range (as compared with results of Figure 7).

In the case of lower suctions values imposed with saturated solutions, even with the improved method equilibrium times are quite low. The drying curves of 3 different bentonites, submitted to a 4.2 MPa suction with a saturated solution of K_2SO_4 are presented in Figure 9. One can see that equilibrium times are of about 60 days in the case of sodium bentonites (MX80 and Kunigel VI) and about 15 days in the case of calcium bentonites (FoCa7). Since lower suction values require the use of diluted solutions, difficult to control at a constant value, a relative humidity regulator was employed to compare the equivalence of both osmotic and vapour phase method 7. The relative humidity generator consists in two sources of air to be mixed by a dew point controller system. One of the sources is a dry air source, and the other one is a saturated air source. The quantity of air taken from each source is automatically controlled to maintain a fixed relative humidity value.

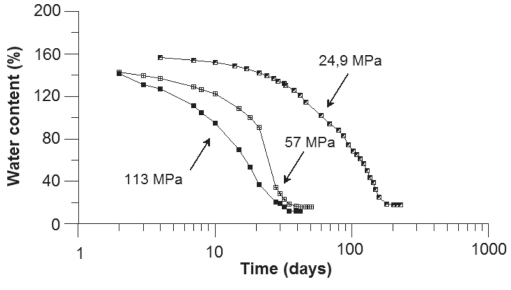

Figure 7. Water content changes with time of FoCa7 samples submitted to different suctions by classic vapour phase method.

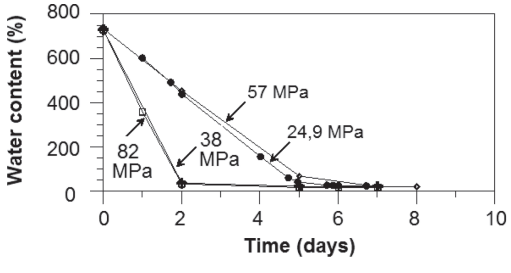

Figure 8. Water content changes with time of MX80 samples submitted to different suctions by the improved vapour phase method.

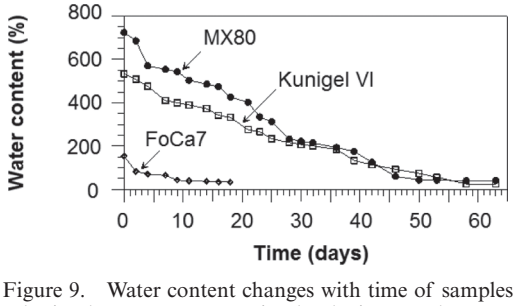

Figure 9. Water content changes with time of samples submitted to a 4.2 MPa suction by the improved vapour phase method.

Because of the very high relative humidity, necessary to obtain low suction values by the vapour phase method, water exchanges are very low in drying path and equilibrium time very long, even with an improved method. Thus, only one low suction point is presented in this work with the vapour phase method. The drying curve of a MX80 bentonite sample, submitted to a suction value of 0,271 MPa (relative humidity of 98,8% and T = 20 °C) is plotted in Figure 10. Note that equilibrium time is of about 180 days to reach a water content of 123.61%.

To compare osmotic and vapour phase methods, the results obtained with both methods for MX80 bentonite are plotted in Figure 11. It is interesting to note that the vapour phase point obtained at a low suction value (0.271 MPa) fits quit well with points obtained with the osmotic method. However, there is not good agreement with the osmotic method when suction is beyond 1.5 MPa. Two points, corresponding to suction values of 1.85 and 3.45 MPa are placed quite below the general trend. These points correspond to samples polluted with PEG. Thus, when computing water content, the mass of the PEG film covering the samples increases the weight of solids and water content is computed lower than the real value. Thus only the points obtained below the classic range of 1.5 MPa are considered in the WRC with the osmotic method.

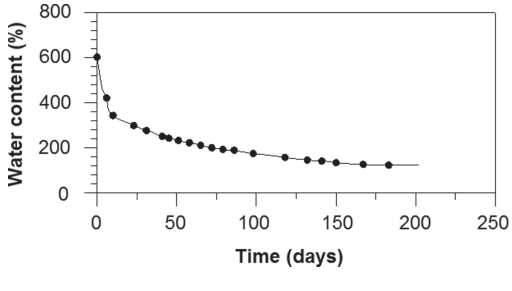

Figure 10. Water content changes with time of a MX80 samples submitted to a 0.271 MPa suction with a relative humidity generator.

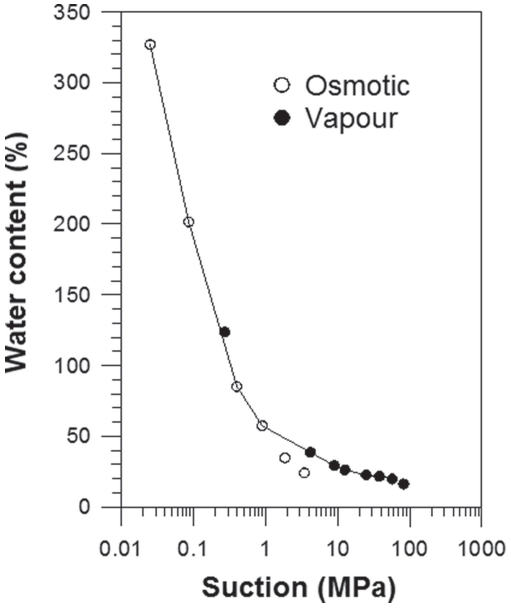

Figure 11. Results obtained with MX80 bentonite with both the osmotic and vapour phase method.

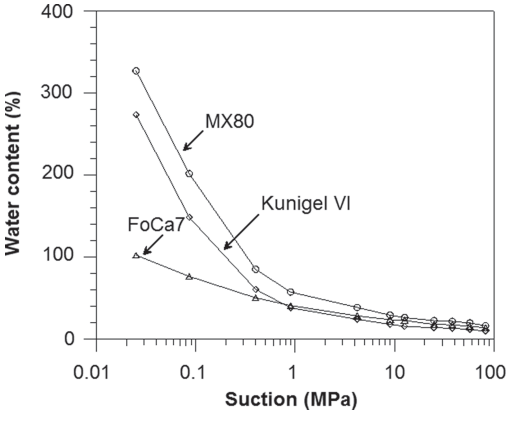

Figure 12. Results obtained with MX80 bentonite with both the osmotic and vapour phase method.

The complete set of results is presented in Figure 12; note that for high to very high suction values, all WRCs are quite close and parallel. At this stage, Sposito & Prost (1992) indicate that water exchanges are only controlled at the hydrophilic sites of the clay (exchangeable cations and the mineral surface) by a different phenomenon: the extraction layer by layer of adsorbed water molecules.

4 CONCLUSIONS

WRCs of 3 reference bentonites clays were obtained with only two methods in a wide range of suctions. A good agreement and a continuous trend is observed between both the osmotic and the vapour phase method in the range of low to medium suction values.

It was found systematically that pollution of soil samples submitted to osmotic suctions beyond 1.5 MPa. Thus it suggests that the extension of the osmotic method is difficult to be applied.

In the light of the results obtained here with the improved vapour phase method, researchers are encouraged to enlarge its application to lower suctions by using relative humidity air generators.

REFERENCES

Bolt, G.H. 1956. Physico-chemical analysis of the compressibility of pure clays. *Geotechnique* 6: 86–93.

Delage, P. & Cui, Y.J. 2008. An evaluation of the osmotic method of controlling suction. *Geomechanics and Geoengineering: An International Journal* 3: 1–11.

Dixon, D.A. Gray, M.N. & Graham, J. 1996. Swelling and hydraulic properties of bentonites from Japan, Canada and the USA. *Environmental Geotechnics* 1, 43–48.

Komine, H. & Ogata, N. 1994. Experimental study on swelling characteristics of compacted bentonite. *Canadian Geotechnical Journal* 31, 478–490.

Marcial, D., Delage, P. & Cui, Y.J. 2006. A laboratory study of the self sealing behaviour of a compacted sand bentonites mixture. *Geomechanics and Geoengineering: An International Journal* 1, 73–85.

Pusch, R. 1982. Mineral-water interactions and their influence on the physical behavior of highly compacted Na bentonite. *Canadian Geotechnical Journal* 19, 381–387.

Saiyouri, N., Hicher, P.Y. & Tessier, D. 2000. Microstructural approach and transfer water modelling in highly compacted unsaturated swelling clays. *Journal of Mechanics of Cohesive and Frictional Materials* 5: 41–60.

Schneider, A. 1960. Neue Diagramme zur Bestimmung der relativen Luftfeuchtigkeit über gesättigten wässerigen Salzlösungen und wässerigen Schwefelsäurelösungen bei verschiedenen Temperaturen. Munchen: Holz als Roh- und Werkstoff 18, 269–272.

Sposito, G. & Prost, R. 1982. Structure of water adsorbed on smectites. *Chemical Reviews, USA* 82: 552–573.

Advances in Unsaturated Soils – Caicedo et al. (eds)
© 2013 Taylor & Francis Group, London, ISBN 978-0-415-62095-6

Physical modeling of the mechanical improvement of unsaturated silt through heating

C.J.R. Coccia, A. Casady & J.S. McCartney
Department of Civil, Environmental and Architectural Engineering, University of Colorado Boulder, Boulder, Colorado, USA

ABSTRACT: A potential method of improving the performance of geotechnical systems involving unsaturated soils is to induce water flow away from heat exchangers embedded in the soil, with the goal of maintaining unsaturated conditions. The mechanical response of an unsaturated, compacted silt layer with a heat exchanger embedded at mid-height is investigated in this study using a plate load test. Plate load tests after different stages of heating indicate an increase in stiffness of the soil layer with increasing temperature. Further, the soil layer was observed to exhibit irreversible contraction during heating which led to a greater stiffness upon subsequent cooling. The results from this preliminary study indicate the potential for using embedded heat exchangers for the mechanical improvement of geotechnical systems incorporating unsaturated soils.

1 INTRODUCTION

Because the performance of near-surface geotechnical systems can be adversely affected by water flow arising from environmental interactions, most geotechnical design guides for fill-type systems require the use of free-draining backfill soils (Sabatini et al., 1997). Soils with low permeability are avoided because their strength and stiffness may decrease with increasing water content (or decreasing suction), leading to undesirable deformations. However, by maintaining poorly-draining backfill soils in unsaturated conditions, it may be possible to minimize deformations during environmental interaction.

It is well known that suction is directly related to the effective stress in unsaturated soils (Khalili & Khabbaz 1998, Lu & Likos 2006). An increase in effective stress can lead to significant improvements in shear strength and stiffness. This paper investigates a novel approach to maintain unsaturated conditions in poorly-draining backfills by employing heat exchangers embedded in the soil to drive water from the soil through thermally induced water flow. Further, heating of unsaturated soils may lead to thermal consolidation, which may lead to additional improvement in mechanical properties (Uchaipichat and Khalili 2009). Because of these features, heating of soils may be a feasible approach to enable use of a broader class of backfill soils than currently accepted, especially in the case where spurious heat from buildings and industry is readily available.

Although a substantial amount of research has been performed on the influence of temperature on the engineering properties of saturated soils, there have only been a limited amount of studies on the thermal impact of unsaturated soils. The objective of this paper is to present the preliminary results of a laboratory study designed to investigate the impact of heat exchange on the mechanical behavior of an unsaturated, compacted silt layer.

2 BACKGROUND

2.1 *Thermally induced water flow*

In the presence of a temperature gradient, water will move through soils from regions of high to low temperature in both liquid and vapor phases. Vapor transport is primarily a diffusive process resulting from the development of a vapor pressure gradient corresponding to a thermal gradient. Liquid water flows from areas of warm to cold due to a surface tension gradient, as the air-water surface tension increases with decreasing temperature (Cary 1966). Thermally induced water flow in soils depends on the initial saturation, hydraulic conductivity, thermal conductivity, and porosity. A greater zone of influence is expected for silts or clays of low plasticity with a higher initial degree of saturation.

2.2 *Thermal effects on volume change*

In addition to thermally induced water flow in response to a thermal gradient, heating of a soil element in drained conditions can also lead to both recoverable (elastic) and irrecoverable (plastic) volume change. During drained heating tests on normally consolidated and lightly overconsolidated saturated soils, differential expansion between the water and soil particles leads to the generation of excess pore water pressure, which dissipates with time resulting in a time-dependent, irrecoverable volumetric contraction of the soil (Sultan et al., 2002, Abuel-Naga et al., 2007). Saturated soils with overconsolidation ratios (OCRs) greater than 1.5 to 3 tend to expand elastically during heating (Towhata et al., 1993, Cekerevac & Laloui 2004).

There have been fewer studies on the thermal volume change behavior of non-swelling unsaturated clays. Saix et al., (2000) performed heating tests on a low plasticity clayey silt specimen at a constant suction of 4.9 kPa and observed plastic contraction upon heating. Uchaipichat and Khalili (2009) performed heating tests on compacted silt under various suctions and observed larger thermal contraction with increasing effective confining pressure.

2.3 *Thermal effects on strength and stiffness*

Temperature is not generally observed to have a significant impact on the material properties of a saturated or unsaturated soil. Studies on the influence of temperature on the compression behavior of soils have found the compression index to be independent of temperature for saturated soils (Campanella & Mitchell 1968, Graham et al., 2001) and unsaturated soils (Saix et al., 2000, Uchaipichat & Khalili 2009). Further, Cekerevac & Laloui (2004) observed that temperature does not have a significant impact on the critical state friction angle. Temperature can influence the shear strength and stiffness of soils through volume change and changes in the shape of the plastic yield surface. For saturated normally consolidated clays, thermal volumetric contraction has been found to correspond to an increase in shear strength and stiffness (Abuel-Naga et al., 2009), likely due to an apparent overconsolidation effect (Tidfors & Sällfors 1989, Eriksson 1989). Conversely, overconsolidated soils show a decrease in shear strength after heating due a decrease in the apparent preconsolidation stress. Although unsaturated soils may show thermal contraction during heating, the peak shear strength may decrease with increasing temperature (Uchaipichat and Khalili 2009).

3 TESTING APPARATUS

To assess the impact of heat exchange on the mechanical improvement of unsaturated soils, a new physical modeling setup was developed. This setup incorporates a strongbox containing a soil layer with an embedded heat exchanger at mid-height, a loading system to apply a distributed load to the soil surface, and instrumentation to measure soil deformations. Dielectric sensors (model 5TE) obtained from Decagon Devices were used to track changes in water content and temperature in the soil layer. The experimental setup is shown in Figure 1.

3.1 *Soil container*

A soil container with interior dimensions of 30.5 cm-depth by 76.2 cm-width by 40.6 cm-height was used in this study. The container includes a 12.5 cm-thick aluminum base and three 1.25 cm-thick aluminum plates forming the left, rear, and right sides of container. The front of the container is a 3.8 cm-thick acrylic plate which permits visual observation of the soil layer. 6 mm-thick insulation sheets were placed around the container walls to reduce heat flux into or from the soil container. The installed insulation has a thermal resistivity of 4 m^2 K/W.

3.2 *Temperature control system*

Heat is applied to the mid-height of the soil layer by circulating ethylene glycol through a heat exchange loop embedded within the compacted soil specimen. The heat exchange loops are made from polyethylene tubing with an outer diameter of 6.35 mm, arranged in an overlapping circular orientation (Figures 1a and 1b). The temperature of the heat exchange fluid is controlled using a heat pump (F25-ME refrigerated/heated circulator from Julabo, Inc.) which also circulates the fluid. Two pipe-plug thermocouples, TC1 and TC2 (Figure 1a), are used to measure the inlet and outlet temperatures of the heat exchange fluid, respectively. The soil temperature and volumetric water content (VWC) profiles during testing are measured using ten 5TE soil sensors from Decagon Devices, spaced evenly with height in the soil layer (Figure 1a). Ambient temperature is measured with a K-type thermocouple.

3.3 *Mechanical loading system*

Distributed loads are applied to the compacted soil layer using a 10 mm-thick, 16.5 cm by 8.5 cm aluminum loading plate. A double-acting pneumatic air cylinder manufactured by Bellofram Precision Controls is used to generate loads applied to the plate. The axial force is measured using a

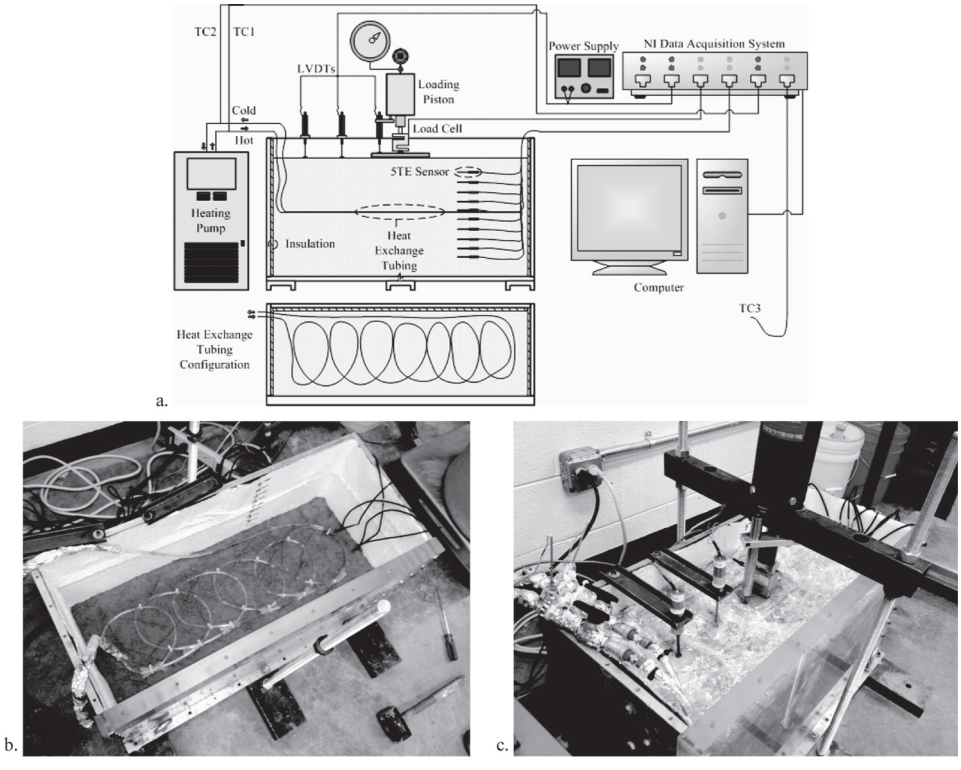

Figure 1. Experimental setup: a. Schematic of container with instrumentation locations; b. Photo of heat exchange tubing at mid-height of the soil layer; c. Photo of LVDTs and loading system on the soil surface with plastic to avoid excess drying.

Futek S-type load cell, Model LSB530, mounted between the bottom of the air cylinder rod and the top of the aluminum loading plate (Figure 1a/c). The settlements of the soil and plate are monitored using three linearly variable differential transformers (LVDTs) (Model HR-DC 500). Settlements are assumed to be symmetrical so LVDTs were only placed on side of the plate (Figure 1a/c). In addition to the LVDT on the plate to track deformation during heating or mechanical loading of the plate, two LVDTs are mounted at 14 cm and 24.1 cm from the center of the plate.

4 MATERIAL & PREPARATION

Tests were performed on a layer of compacted Bonny silt. Bonny silt is an ML silt with liquid and plastic limits of 25 and 21, respectively, and a fines content of 83.9%. An activity of 0.29 indicates that Bonny silt does not contain clay minerals whose behavior may be affected by temperature. The thermal conductivity of saturated Bonny silt was measured using a KD2Pro thermal needle from Decagon Devices, and ranged from 1.40 to 1.55 W/(m °C) for void ratios ranging from 0.60 to 0.46, respectively.

The silt layer evaluated in this study was prepared in 12 equal lifts using dynamic compaction to reach a dry density of 1.5 g/cm^3. The gravimetric water content was 19.5%, which is 5.9% wet of the standard Proctor optimum water content. Each lift was scarified to minimize weak planes. A 5TE sensor was placed upon a mound of loose silt prior to compaction of the next lift. Plastic wrap was placed above the top of the soil surface (except around the plate and LVDTs). This approach was used to impose a no-flux boundary at the soil surface and reduces atmospheric effects during testing.

5 EXPERIMENTAL PROGRAM

Following compaction of the unsaturated silt specimen, the instrumentation was assembled and a seating load of 15 N was applied to the loading plate in order to ensure contact between the plate and soil surface. To quantify the impact of heat exchange on

the mechanical improvement of the compacted silt, six load-settlement tests were performed at varying temperatures. A typical loading scheme is shown in Figure 2a. The plate load was slowly increased until the soil reached virgin compression (Load 1) after which the plate load was decreased to half the previous maximum load to measure the recompression stiffness (defined load required to deflect the soil by 1 mm). To ensure accuracy in recompression stiffness measurements, two to three unloading curves were measured per temperature increment. To do so, the soil would be reloaded to a new maximum load (Load 2—roughly 130% of the previous maximum load) and then unloaded (Figure 2a).

A load-settlement test was performed at ambient temperature (≈20 °C) to provide a baseline measurement. Additional load-settlement tests were performed after reaching input heat pump temperatures of 35, 50, 65 and 80 °C, and a cooling temperature of 40 °C (Figure 2b). The goal of these tests was to quantify irreversible effects on the loading-unloading plate load stiffness which may have occurred after heating. These heat pump temperature settings correspond to soil temperatures at the heat exchanger level of 20.0, 29.6, 39.4, 50.6, 61.3, and 31.4 °C, measured using thermocouple TC1. Heat was applied to the specimen following each previous load-settlement test at a rate of 0.5 °C/hr as inferred from the temperature

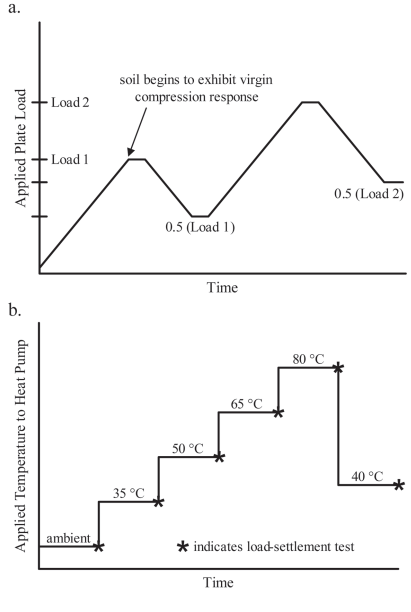

Figure 2. Experimental procedures: a. Mechanical loading scheme; b. Applied temperature and load-settlement test schedule; c. Applied and measured soil temperatures.

readings within the specimen. During each heating increment, the applied temperature was maintained until the soil surrounding the heat exchange reached a uniform temperature and volumetric water content. Approximately 1 week was required for the compacted silt layer to reach steady state conditions. All thermally induced settlements and soil volumetric water content and temperature profiles were recorded at increments of 15 seconds and 1 minutes during heating/cooling, respectively.

6 TESTING RESULTS

Typical volumetric water content profiles, temperature profiles, and load-settlement results for the compacted specimen (in the case of heating and loading at 52.5 °C) are shown in Figure 3. The temperature profiles in Figure 3a are observed to increase dramatically and reach steady state within 10 hours after initial heating with the largest increase at the location of the heat exchange tubing. The theory of thermally induced water flow is reflected in Figure 3b. Initially, the volumetric water content increases along the entirety of the soil specimen, with the largest increase occurring at the location of the heat exchanger. This is most likely due to the pore water expanding under increased temperatures and filling the remaining pore space. Following this initial increase, the volumetric water content is observed to decrease nearest the heat exchanger as water begins to flow toward zones of lower temperature. These results illustrate the two phases of thermal response of water in unsaturated soils.

The plate settlements during loading/unloading are shown in Figures 3c and 3d. The soil layer exhibits an elastic response to loading prior to reaching the virgin compression curve, with less settlement occurring further away from the point of loading (Figure 3c). A coupled elasto-plastic soil response is observed in Figure 3d once the soil is placed under loads greater than the previous maximum load. Both recompression curves exhibit the same slope.

7 ANALYSIS

The results for the six temperature intervals applied to the compacted silt specimen are summarized in Figure 4. The temperature profiles for each of the six intervals are plotted in Figure 4a. As expected, the temperature was highest at points closest to the heat exchange tubing, with decreasing temperature towards the boundaries of the soil layer. During all heating increments up to 52.5 °C, the volumetric water content was observed to increase with increasing temperature with the largest magnitude increase occurring near the heat exchange tubing

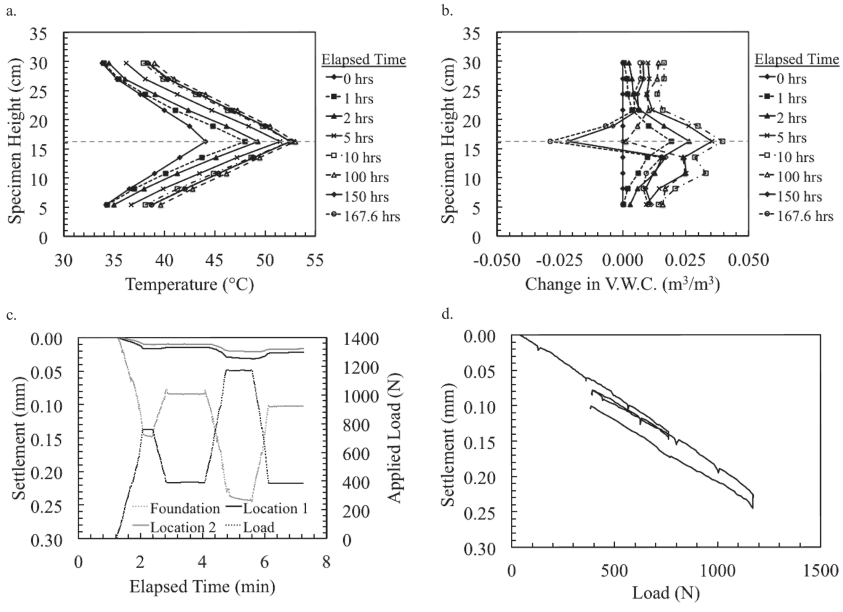

Figure 3. Results from test at 80 °C: a. Temperature profile with time; b. Volumetric water content profile with time; c. Soil surface settlements during loading; d. Load-settlement curve.

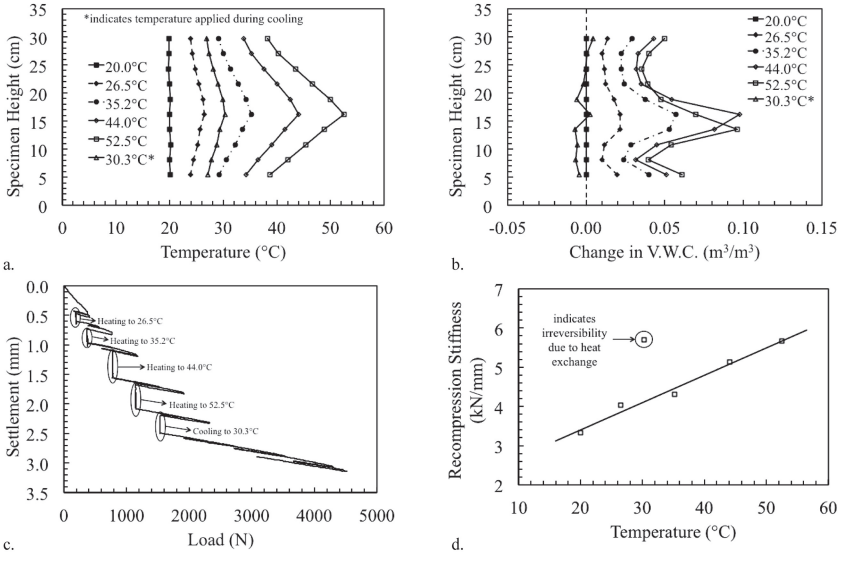

Figure 4. Summary of results: a. Temperature profile for each temperature increment; b. Volumetric water content profile for each temperature increment; c. Load-settlement results from all six temperature increments; d. Unloading stiffness versus temperature.

and also along the top and bottom soil boundaries (Figure 4b). The measured increase in volumetric water content nearest the heat exchange tubing is mostly due to the thermal expansion of the pore water during heating. However, assuming thermal expansion to be the only cause for increased volumetric water content would suggest a decreasing water content profile towards the soil boundaries, which is not observed in the data. The increase in volumetric water content along the soil

boundaries is most likely due to the accumulation of pore water as a result of thermally induced water flow away from the heat exchangers.

This behaviour is further indicated by the volumetric water content profile measured following cooling to 30.3 °C. A slightly drier profile seen during the cooling stage suggests an overall movement of water due to heating as volumetric water content changes due to the thermal expansion of water is considered a reversible process which would place the cooling volumetric water content profile somewhere between the measured profiles at 26.5 and 35.2 °C. Additionally, dry zones were observed near the heat exchange tubing upon excavation of the compacted specimen.

The load-settlement results from all six temperature increments are presented in Figure 4c. Thermal settlements were observed during heating and cooling as expected for a normally consolidated to lightly overconsolidated soil (Cekerevac & Laloui 2004). As the soil was heated, larger loads were required to reach the apparent preconsolidation stress, indicating an overconsolidation effect as a result of heating. Further, the recompression stiffness was observed to increase with increasing temperature as shown in Figure 4d. This increase in stiffness is due to the development of a drier soil zone located around the heat source and an apparent increase in soil density resulting from settlement of the soil layer during heating.

During cooling, the recompression stiffness remained unchanged from the previous stiffness measured at 52.5 °C, indicating that a partially irreversible process occurred during the preceding heating increments. As water is driven away from a heat source, an apparent reduction in thermal conductivity and hydraulic conductivity occurs within the zone of influence of the heat exchanger (defined as the zone of water content change within a soil layer where flow takes place) due to the decrease in water content. Therefore, cooling will not result in complete recovery of the change in water content. Because of this, the zone of influence surrounding the heat exchanger will remain slightly drier than measured prior to heating. Additionally, the increase in density of the soil layer due to thermal settlement will result in an additional irreversible increase in soil stiffness.

8 CONCLUSION

Tests were performed in this study to evaluate the impact of heating on the mechanical properties of a compacted, unsaturated layer of silt. An irreversible increase in the plate load stiffness was observed after application of heat in increments using a heat exchanger at mid-height. This is attributed to the movement of pore water away from the heat source, leading to an increase in the effective stress in the unsaturated soil layer. This increase in stiffness also is caused by an increase in density of the soil layer due to thermal settlement. Further research is needed to quantify the individual influence of both phenomena on the soil stiffness. The results indicate that heat exchangers can be integrated into earthen embankments as a means of soil improvement.

REFERENCES

Abuel-Naga, H.M., Bergado, D.T. & Bouazza, A. 2007. Thermally induced volume change and excess pore pressure of soft Bangkok clay. Eng. Geo. 89: 144–154.

Abuel-Naga, H.M., Bergado, D.T., Bouazza, A. & Pender, M. 2009. Thermomechanical model for saturated clays. Géotechnique. 59(3): 273–278.

Alonso, E.E., Gens, A. & Josa, A. 1990. A constitutive model for partially saturated soils. Géotechnique. 40: 405–430.

Campanella, R.G. & Mitchell, J.K. 1968. Influence of temperature variations on soil behavior. J. of the Soil Mech. and Found. Eng. Div. 94(3): 709–734.

Cary, J.W. 1966. Soil moisture transport due to thermal gradients: Practical aspects. SSSA. 30(4): 428–433.

Cekerevac, C. & Laloui, L. 2004. Experimental study of thermal effects on the mechanical behaviour of a clay. Int. J. for Num. Anal. Meth. Geomech. 28: 209–228.

Eriksson, L.G. 1989. Temperature effects on consolidation properties of sulphide clays. Proc. of the 12th Int. Conf. on Soil Mech. and Found. Eng. Rio de Janeiro. 3: 2087–2090.

Ewen, J. & Thomas, H.R. 1989. Heating unsaturated medium sand. Géotechnique. 39(3): 455–470.

Graham, J., Tanaka, N., Crilly, T. & Alfaro, M. 2001. Modified cam-clay modeling of temperature effects in clays. Can. Geotech. J. 38(3): 608–621.

Khalili, N. & Khabbaz, M.H. 1998. A unique relationship for the determination of shear strength of unsaturated soils. Géotechnique. 48(5): 681–688.

Lu, N. & Likos, W.J. 2006. Suction stress characteristic curve for unsaturated soils. J. of Geotech. And Geoenv. Eng. 132(2): 131–142.

Sabatini, P.J., Elias, V., Schmertmann, G.R. & Bonaparte, R. 1997. Geotechnical Engineering Circular Number 2: Earth Retaining Systems. Washington, D.C: FHWA.

Saix, C., Devillers, P. & El Youssoufi, M.S. 2000. Element de couplage thermomechanique dans la consolidation de sols non satures. Can. Geotech. J. 37: 308–317.

Sultan, N., Delage, P. & Cui, Y.J. 2002. Temperature effects on the volume change behaviour of Boom clay. Eng. Geo. 64: 135–145.

Tidfors, M. & Sällfors, G. 1989. Temperature effect on preconsolidation pressure. Geot. Test. J. 12(1): 93–97.

Uchaipichat, A. & Khalili, N. 2009. Experimental investigation of thermo-hydro-mechanical behaviour of an unsaturated silt. Géotechnique. 59(4): 339–353.

Yong, R.N. & Mohamed, A.-M. 1996. Evaluation of coupled heat and moisture flow patterns in a bentonite-sand buffer material. Eng. Geo. 41: 269–286.

Advances in Unsaturated Soils – Caicedo et al. (eds)
© 2013 Taylor & Francis Group, London, ISBN 978-0-415-62095-6

Triaxial cell for nonisothermal shear strength of compacted silt under high suction magnitudes

N.A. Alsherif & J.S. McCartney
Department of Civil, Environmental and Architectural Engineering, University of Colorado Boulder, Boulder, Colorado, USA

ABSTRACT: This study introduces a new triaxial cell which was developed to measure the shear strength of unsaturated soils under elevated temperatures and high suction magnitudes. Suction control is implemented by circulating vapor through a soil specimen having an initially low degree of saturation. The relative humidity in the vapor is controlled using an automated humidity system which uses a probe in the bottom platen of the triaxial cell to partition wet and dry Nitrogen gas through the specimen. The temperature of the soil specimen is controlled using heating elements in the cell fluid. This paper also presents the experimental procedures used to calibrate the temperature effects on the deformation response of the cell and the suction control system under elevated temperatures. The results from this study indicate the versatility of this new device in measuring the shear strength and volume change of soils under high temperature and suction magnitudes.

1 INTRODUCTION

An improved understanding of the relative impacts of the coupled thermo-hydro-mechanical behavior of unsaturated soils during application of elevated temperatures and high suction magnitudes is needed to interpret the behavior of thermally active geotechnical systems. These include ground-coupled heat exchangers (Brandl 2006), containment systems for nuclear waste (Gens et al., 1998) and buried electrical cables (Abdel-Hadi & Mitchell 1981). An improved understanding of the roles of temperature and suction may also be needed to understand the impact of using spurious heat from industry or cooling of buildings to improve the mechanical behavior of soils (McCartney 2012).

The objective of this paper is to understand the nonisothermal shear strength and deformation behavior of unsaturated silt under high suction magnitudes. Specifically, this study involves an investigation of the effects of temperature changes on the soil-water retention curve (SWRC), volume change parameters, and the shear-stress strain curve parameters for unsaturated soils. Although some studies have evaluated the impact of high suction magnitudes on these variables (Blatz & Graham 2000, Nishimura & Fredlund 2000, Lloret et al., 2003) and others have evaluated the impact of elevated temperatures on these variables (Uchaipichat & Khalili 2009), the combined effects of these variables have not been investigated. An understanding of the inter-relationships between these variables will also help improve our understanding of the effective stress in unsaturated soils under different conditions, and will help to develop nonisothermal elasto-plastic constitutive relations for unsaturated soils. Although a range of constitutive relationships have been developed for saturated soils (Huekel & Baldi 1990, Cui et al., 2000, Laloui & Cekerevac 2003, Abuel-Naga et al., 2009, Huekel et al., 2009), the behavior of unsaturated soils in nonisothermal conditions has not been thoroughly investigated (Saix et al., 2000), especially under high suctions.

To achieve the objective of this study, a new triaxial cell was designed which incorporates the vapor equilibrium technique to control high suction magnitudes, and a temperature control system to apply elevated temperatures. The suction control system proposed by Likos & Lu (2003) is particularly suited for this application. They developed a mass flow control system with relative humidity feedback to mix water-saturated and dry air to a known proportion and pass it through the soil specimen. Further, the triaxial system developed by Uchaipichat & Khalili (2009), which incorporated a resistance heater, cell fluid circulation, a glass cell, and digital image analysis to track changes in volume of specimens under various temperature and suction ranges. This paper presents the unique calibration issues involved in the cell deformation response and the suction control system.

2 BACKGROUND

2.1 *Vapor equilibrium technique for control of high suction magnitudes*

The vapor equilibrium technique has been used in several studies, including those by Tessier (1984), Delage et al., (1998), Romero (1999), Delage & Cui (2000), Villar (2000), and Blatz et al., (2008). This technique involves the use of saturated salt solutions to control the relative humidity of the air within a closed chamber. If a soil specimen is suspended above the air within the chamber, the relative humidity within the chamber will cause evaporation or condensation of water from the soil pores. The basis of the vapor equilibrium technique is Kelvin's law, which relates the total suction in the soil with the relative humidity of the air in closed environmental chamber containing saturated salt solutions (Fredlund & Rahardjo 1993). The suction was calculated using equation 1as follows:

$$\psi = \frac{\rho_w RT}{M_w} \ln(R_h) \quad (1)$$

where ψ = the total soil suction (kPa), R = the universal (molar) gas constant, equal to 8.31432 J/molK, T = the absolute temperature in Kelvin, M_W = the molecular mass of water vapor equal to 18.016 g/mol, ρ_w = the density of water (kg/m^3), and R_h = the relative humidity of the pore air in decimal form. The relative humidity is related to the total suction in the soil, not the matric suction. The matric suction is related to capillarity while the total suction incorporates both capillarity and osmotic suction effects.

Several studies have incorporated the vapor equilibrium technique into triaxial cells for application of high suctions (Blatz & Graham 2000, Nishimura & Fredlund 2003), but none have evaluated the coupled role of high temperatures on the shear strength of unsaturated soils using the same technique. However, due to the sensitivity of this technique to air temperature, Tang & Cui (2005) performed a calibration tests for several saturated salt solutions to account for the effect of temperature on the relative humidity and consequently on the suction applied. They found that changes in temperature from 20 to 80˚C can lead to changes in suction from 82 to 184 MPa for a saturated solution of $Mg(NO_3)_2$. This increase in suction due to temperature and the coupled effect on the shear strength of unsaturated silt was also investigated by Alsherif & McCartney (2012).

Although the vapor equilibrium technique using the saturated salt solutions is a simple approach to control the total suction, it may be time consuming due to the slow rates of evaporation and condensation. In addition, the change in the salt solution concentration and the solubility of the salt due to temperature increase over time would change the target suction applied to the soil specimen. To speed up the rate of evaporation, circulation system was used to force the air to flow through the soil specimens using an air flow pump (Cunningham et al., 2003, Nishimura & Fredlund 2003, Blatz & Graham 2003). The effect of using the circulation system on the target suction applied was assessed by Pintado et al., (2009) using the same odometer apparatus that used by Lloret et al., (2003). Their test results indicate that the time needed to reach equilibrium can be shortened from weeks to days by using air circulation. They also stated that necessary precautions should be taken because equilibrium suction could differ from the applied suction due to the gas pressure difference between the boundaries. They suggested some precautions such as keeping the air pressure difference smaller than 10 kPa between boundaries to improve the accuracy of results and using soils with high air permeability to help reducing this differential pressure. High air permeability for compacted soils can be achieved by by lowering the initial degree of saturation at compaction or drying the specimen before placement in the device.

Due to the issues noted with the use of saturated salt solutions to independently control the temperature and suction in soils, an alternative approach involving vapour control may be more appropriate. The suction control system proposed by Likos & Lu (2003) is particularly suited for this application. They developed a system to control the relative humidity of pore air flowing through a soil specimen by using mass flow controllers to mix water-saturated and dry air to a known proportion. The advantages of the new system over existing suction measurement techniques are that it is fully automated, has a much broader measurement range and is capable of determining both wetting and drying characteristics in significantly less time.

2.2 *Effects of suction on the shear strength of unsaturated soils*

Many studies have evaluated the shear strength of unsaturated soils. Most of the testing has been performed under isothermal conditions with low suction magnitudes controlled using the axis translation technique. Blight (1967) conducted consolidated-drained (CD) triaxial tests for specimens of unsaturated silt and found that the shear strength of the soil increases with increasing the suction applied and increasing the net normal stress. Escario (1980) performed suction-controlled direct shear tests on unsaturated soil and found that the slope of the failure envelope (the tangent of the drained friction angle) is independent of suction. This implies that the slope of the failure envelope defined under saturated conditions should be the same as at different suction magnitudes.

Many other studies have focused on evaluating the shear strength of unsaturated soils under high suction magnitudes. Nishimura & Fredlund (2000) conducted isothermal triaxial compression tests on silty soil under high suction magnitudes. They found constant values of shear strength with increasing suction after the soil reached residual saturation, and that the rate of increase in peak shear strength with net normal stress was similar to the effective internal friction angle for saturated conditions. Blatz (2002) examined the effect of high suction and high confining pressure on the behavior of a compacted sand-bentonite by performing a series of undrained triaxial tests. Their test results show a nonlinear increase in the strength and stiffness with increasing suction. They also suggested that the gains in strength were probably connected to the corresponding increases in density more than the effect of shear resistance due to suction forces. A ring shear apparatus adapted with suction control using the vapor equilibrium technique was used by Vaunant et al., (2007) and Merchan et al. (2008) to investigate the effect of high magnitudes of total suction on the residual shear strength of low plasticity clay, and an increase in strength was noted with increasing suction.

2.3 *Effects of elevated temperature on the shear strength of unsaturated soils*

Recently, Uchaipichat & Khalili (2009) evaluated the shear strength and volume change of unsaturated soils under non-isothermal conditions. They performed an evaluation of compacted silt behavior for suction magnitudes less than 300 kPa. For a given suction magnitude, they observed a decrease in peak shear strength with increasing temperature, although the shear strength at critical state conditions was unaffected. The peak and critical state shear strengths were more sensitive to suction than temperature.

Although interesting lessons were learned from these tests on low suctions, there has not been a thorough study on the impact of temperature on the strength of unsaturated soils under higher suction magnitudes. Most research on the impact of high suction magnitudes has focused on the impact of suction on the shear strength of soils, and the impact of temperature has not been thoroughly investigated. Alsherif & McCartney (2012) performed a preliminary set of tests to assess the roles of suction and temperature on the effective stress and shear strength of unsaturated compacted silt. They found that the peak shear strength increases slightly for compacted silt under high suction magnitudes with increasing temperature, which is contradictory to the observations of Uchaipichat & Khalili (2009) for low suction magnitudes, which confirms the importance of further investigation into the impacts of temperature on the shear strength of compacted silts under high suction magnitudes.

3 TESTING APPARATUS

A triaxial cell was designed to accommodate the application of high temperatures and high suction magnitudes using the vapor equilibrium technique. A drawing of the complete system including the modified triaxial cell is shown in Figure 1(a), while a picture of the system is shown in Figure 1(b). Duran Borosilicate tubing with a 180 mm outer diameter, a 9 mm wall thickness and a 381 mm length is used as the pressure vessel. This material is resistant to thermal shock, has low thermal expansion and high chemical resistance. Internal pressures of up to 630 kPa (90 psi) can be applied, making this a suitable cell for triaxial testing at elevated temperatures.

3.1 *Suction control system*

The upper and lower platens were designed to allow the application of high suctions using the vapor equilibrium technique. Specifically, N_2 gas was forced through the bottom of the specimen using an air flow circulation system and vented from the top of the specimen. The air circulation system consists of a computer-automated humidity-control system developed previously by Likos & Lu (2001) which permits control of the relative humidity of the pore air and consequently the suction applied to

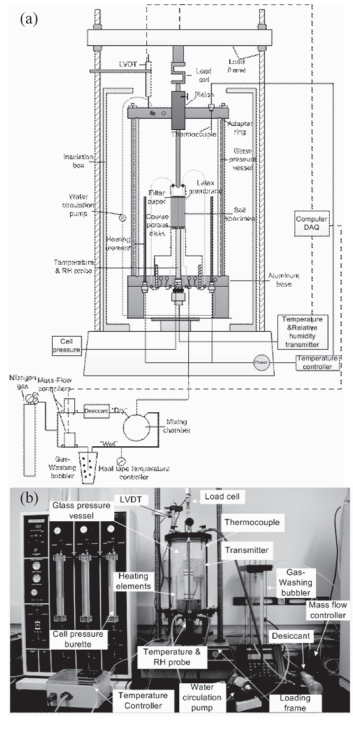

Figure 1. Thermo-hydro-mechanical triaxial setup: (a) Schematic; (b) Picture.

the soil specimen. This system also insures that the temperature of the gas stream is the same as that of the specimen. The relative humidity is controlled using mass-flow valves (MKS Instruments, Type 1179 A) which mix different proportions of vapor-saturated, or 'wet', N_2 gas and desiccated, or 'dry', N_2 gas (e.g., Chipera et al., 1997).

Specifically, N_2 gas is passed from a pressure regulated tank through 6.35 mm-diameter PFA (perfluoroalkoxy) tubing, which is split into two separate gas streams through the mass-flow valves. These valves can regulate the flow of each gas stream between zero and 200 cm^3/min based on a signal from LabView. The first gas stream is vapor-saturated by passing it through a tank filled with distilled water resting on a heat plate maintained at the same temperature as the soil specimen. The PFA tubing coming out of the bottle was covered with aluminum foil to reduce temperature losses. The second gas stream is routed through a Hammond cylinder filled with color-indicating drierite desiccant media (calcium sulfate, >98% $CaS0_4$, >2% $CaCl_2$). The two gas streams (wet and dry) are then introduced into a mixing chamber at a combined flow rate of 200 cm^3/min. The combined gas stream with a relative humidity that is a function of the 'wet' to 'dry' gas flow ratio (w/d) was forced through the bottom of the soil specimen.

Assessment of applied suction was made using a relative humidity and temperature probe obtained from Vaisala, Inc. of HMT330. The bottom platen has a port through which the probe can be installed to monitor the relative humidity at the bottom of the specimen. The probe can function under pressures up to 407 kPa and can measure the full range of relative humidity over temperatures ranging from –70 °C to +180 °C. A rigid porous disk separates the bottom of the specimen from the head of the probe so that the probe does not impact the mechanical performance of the specimen. Signals from the humidity probe are used in a LabView feedback loop to regulate the 'wet' to 'dry' gas flow ratio (w/d).

3.2 *Temperature control system*

The temperature controlling system consists of three Watlow cartridge heating elements with dimensions of 6.35 mm in diameter and 229 mm in length, which were fixed through the base of the cell. They heaters were arranged around the soil specimen to assure even and fast distribution of temperature. A 75420-00 water circulation pump from SHURFlo connected to the pressurized water inside the cell is used to ensure that the temperature of the water is uniform throughout the cell. A temperature controller was connected to the heating elements for controlling the temperature in the cell. A thermocouple was connected to the top of the cell to provide a feedback loop of the temperature applied to the triaxial cell in addition to using the relative humidity and temperature probe reading as a feedback to insure that the soil specimen having the same temperature as the water inside the cell.

3.3 *Mechanical loading system*

A Brainard-Kilman Model S-600 triaxial load frame was used to apply axial loads to the triaxial cell piston. This frame is appropriate for performing constant displacement rate test. Although a constant displacement rate was used, the axial displacement during shearing was also measured using a linearly variable deformation transformer (LVDT). A load cell was used to record axial loads applied to the specimen during shearing. In this test setup, soil specimen volume change due to heating inside the triaxial cell during both shearing and during application of high suction was measured using visual observation of the water level in graduated burettes connected to the water line of the cell pressure.

4 THERMAL CALIBRATION TESTS

The thermal expansion of the different parts of the triaxial cell, including porous stones, drainage lines, and the water filling them due to a temperature increase may affect the volume change measurements of the unsaturated soil specimen measured using the LVDT and cell water inflow or outflow. A calibration In order to calculate the actual volume change of the soil specimen during temperature changes, it is necessary to perform a thermal calibration tests. An aluminum cylinder with a diameter of 35.5 mm and a height of 71 mm was used to assess the thermal expansion of the system. The volumetric coefficient of thermal expansion of aluminum is 6.9×10^{-5} m/m°C. The volume calibration test began at room temperature (23 °C) by applying a confining pressure (50 kPa, 100 kPa and 200 kPa) followed by increasing the temperature in steps of 10 °C up to 70 °C over 6 hours intervals and monitoring the temperature at the bottom of the aluminum cylinder using the temperature probe until reaching steady state. After this, the temperature was decreased to 23 °C. During the heating-cooling cycle, the overall volume change was estimated using observation of water levels in a graduated burette.

The relative humidity controlled using the automated humidity system was calibrated by performing a test on a sand specimen used for the purpose of rapidly reaching steady state gas flow. The calibration test involved changing the wet and dry N_2 gas percentages to different values and monitoring the relative humidity recorded by the probe until reaching equilibrium. The test was repeated by maintaining a constant wet and dry N_2 gas percentage and

changing the temperature. The temperature was increased in increments up to 70 °C and changes in measured relative humidity were recorded.

5 CALIBRATION TESTING RESULTS

In order to insure that the cell temperature matches the soil specimen temperature, the controlled temperature applied to the water inside the triaxial cell using the temperature controller was compared to the equilibrium temperature recorded using the temperature probe, and a 1:1 relationship was obtained.

The observed volume change of the drainage system was corrected for the known value of volumetric thermal expansion and shrinkage of the aluminum during the heating-cooling cycles. The volume change of the aluminum specimen was subtracted from the measured volume change as follows:

$$\Delta V_{corr} = \Delta V_t - \frac{(d_o \Delta T \alpha_l)^2}{4} \pi L_o \qquad (2)$$

where ΔV_{corr} are the corrected volume change for the triaxial cell, α_1 is the volumetric coefficient of thermal expansion for aluminum, ΔV_t is the total volume change, and d_o and L_o are the original diameter and height of the aluminum specimen, respectively, at ambient temperature. The calibrated volume change with respect to testing temperature and confining pressure is shown in Figure 2.

The results indicate that the confining pressure has a slight effect on the volume change and this effect increases slightly at higher temperatures. For a heating-cooling cycle, about 75% of the induced thermal expansion was reversible. This information will be used later to correct the observed volume change for drained tests on soils at different temperatures. The data recorded from the relative humidity and temperature probes at ambient temperature and varies percentages of saturated and dry N_2 gas with respect to time is shown in Figure 3. This figure shows that a relative humidity of 26% corresponds to a mixture of 50% wet and 50% dry N_2 gases, and a relative humidity of 50% corresponds to 75% wet and 25% dry N_2 gases. The corresponding total suction for each relative humidity value is shown in Figure 4. These results show the wide range of total suction which can be applied using this method.

The relative humidity recorded from the relative humidity calibration test at elevated temperature and constant percentage of saturated and dry N_2 gas with respect to time is shown in Figure 5. The results show that increasing the temperature led to a clear drop in the relative humidity which affects the corresponding total suction applied.

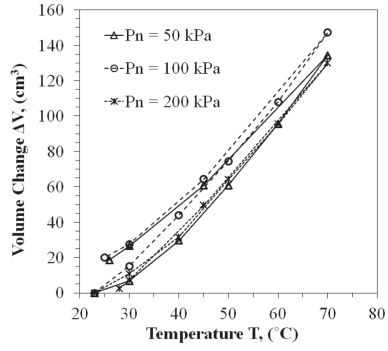

Figure 2. Volume change versus temperature at confining pressures of 50, 100 and 200 kPa.

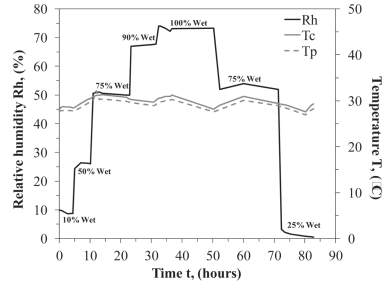

Figure 3. Relative humidity calibration with temperature.

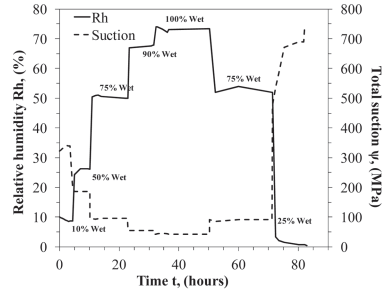

Figure 4. Relative humidity and total suction during testing.

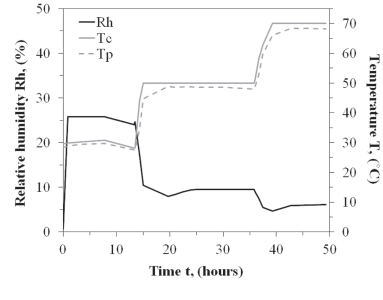

Figure 5. Relative humidity calibration at elevated temperature for 50% wet and 50% dry N_2 gas percentages.

6 CONCLUSION

A new triaxial cell is introduced to measure the shear strength of unsaturated soils under elevated temperatures and high suction magnitudes. In addition to details on the temperature and suction control systems, this paper presents the procedures used to calibrate the thermal deformation response of the cell and the suction control system using the vapor equilibrium technique under elevated temperature.

REFERENCES

Abdel-Hadi, O.N. & Mitchell, J.K. 1981. Coupled heat and water flows around buried cables. *J. of the Geot. Eng. Div*. ASCE. 107(11): 1461–1487.

Abuel-Naga, H.M., Bergado, D.T., Bouazza, A. & Pender, M. 2009. Thermomechanical model for saturated clays. *Géotechnique*. 59(3): 273–278.

Alsherif, N. & McCartney, J.S. 2012. Nonisothermal shear strength of unsaturated soils under high suction magnitudes. *2nd European Conf. on Unsat. Soils*, Italy. 8 pg.

Blatz, J.A. & Graham, J. 2000. A system for controlled suction in triaxial tests. *Géotechnique* 50(4): 465–478.

Blatz, J.A. & Graham, J. 2003. Elastic plastic modeling of unsaturated high-plastic clay using results from a new triaxial test with controlled suction. *Géotechnique* 53(1): 113–122.

Blatz, A.J., Cui, Y.J. & Oldecop, L.A. 2008. Vapour equilibrium and osmotic technique for suction control. *Geotech. Geol. Eng*. 26(6): 661–673.

Blight, G.E. 1967. Effective stress evaluation for unsaturated soils. *J. Soil Mech. and Found. Div.,* 93(SM2): 125–148.

Brandl, H. 2006. Energy foundations and other thermoactive ground structures. *Géotechnique.* 56(2): 81–122.

Chipera, S.J., Carey, J.W. & Bish, D.L. 1997. Controlled humidity XRD analyses: application to the study of Smectite expansion/contraction. *Adv. in X-ray Anal.* 39, 713 721.

Cui, Y.J., Sultan, N. & Delage, P. 2000. A thermomechanical model for clays. *Can. Geot. J.* 37(3): 607–620.

Cunningham, M.R., Ridley, A.M., Dineen, K. & Burland, J.B. 2003. The mechanical behaviour of a reconstituted unsaturated silty clay. *Geotechnique* 53(2): 183–194.

Delage, P., Cui, Y.J., Yahia-Aıssa, M. & De Laure, E. 1998. The unsaturated hydraulic conductivity of a dense compacted bentonite. *2nd Int. Conf. on Unsat. Soils*. Beijing, China, pp. 27–30.

Delage, P., Sultan, N. & Cui, Y.J. 2000. The thermal consolidation of Boom Clay. *Can. Geot. Journal*. 37: 343–354.

Escario, V. 1980. Suction controlled penetration and shear tests. *4th Int. Conf. on Expansive Soils.* Vol. II. Denver, American Society of Civil Engineers, pp. 781–797.

Fredlund, D. & Rahardjo, H. 1993. *Soil Mechanics for Unsaturated Soils*. John Wiley and Sons. New York.

Gens, A., Garcıa-Molina, A.J., Olivella, S., Alonso, E.E. & Huertas, F. 1998. Analysis of a full scale in situ test simulating repository conditions. *IJNAMG*. 22, 515–548.

Hueckel, T. & Baldi, M. 1990. Thermoplasticity of saturated clays: experimental constitutive study. *Journal of Geotechnical Engineering*, 116(12): 1778–1796.

Hueckel, T., François, B. & Laloui, L. 2009. Explaining thermal failure in saturated clays. *Géotechnique.* 59(3): 197–212.

Laloui, L. & Cekerevac, C. 2003. Thermo-plasticity of clays: an isotropic yield mechanism. *Computers and Geotechnics*. 30(8): 649–660.

Likos, W.J. & Lu, N. 2001. Automated measurement of total suction characteristics in the high suction range: application to the assessment of swelling potential. *Transp. Res. Record.* 17(55): 119–128.

Likos, W. & Lu, N. 2003. Automated humidity system for measuring total suction characteristics of clay. *Geotechnical Testing Journal.* 26(2).

Lloret, A., Villar, M.V., Sanchez, M., Gens, A., Pintado, X. & Alonso, E.E. 2003. Mechanical behaviour of heavily compacted bentonite under high suction changes. *Géotechnique.* 53(1): 27–40.

McCartney, J.S. 2012. Issues involved in using temperature to improve the mechanical behavior of unsaturated soils. *5th Asia-Pacific Unsat. Soils Conf*. Feb 29–March 2, 2012. Pattaya, Thailand.

Merchan, V., Vaunat, J., Romero, E. & Meca, T. 2008. Experimental study of the influence of drying on the residual friction angle of clays. *1st European Conf. on Unsat. Soils*, Durham, 423–428.

Nishimura, T. & Fredlund, D.G. 2000. Relationship between shear strength and matric suction in an unsaturated silty soil. *UNSAT ASIA 2000*, Singapore, May 18–19, 563–568.

Nishimura, T. & Fredlund, D.G. 2003. A new triaxial apparatus for high total suctions using relative humidity. *12th Asian Reg. Conf. on Soil Mech. and Geot. Eng.* Vol. 1. Singapore, pp. 65–68.

Pintado, X., Lloret, A. & Romero, E. 2009. Assessment of the use of the vapour equilibrium technique in controlled-suction tests. *Can. Geotech. J*. 46, 411–423.

Romero, E. 1999. Characterisation and thermo-hydromechanical behaviour of unsaturated boom clay: an experimental study. *These de l'Universite Polytechnique de Catalogne*, Barcelone, 405 pp.

Saix, C., Devillers, P. & El Youssoufi, M.S. 2000. Elément de couplage thermomécanique dans la consolidation de sols non saturés. *Can. Geotech. J.* 37, 308–317.

Tang, A.M. & Cui, Y.J. 2005. Controlling suction by the vapour equilibrium technique at different temperatures and its application in determining the water retention properties of MX80 clay. *Can. Geotech. J.* 42(1): 287–296.

Tessier, D. 1984. Etude experimentale de l'organisation desmateriaux argileux: hydratation, gonflement et structuration au cours de la dessiccation et de la rehumectation. *Ph.D. thesis, Universite de Paris VII*, Paris, France.

Uchaipichat, A. & Khalili, N. 2009. Experimental investigation of thermo-hydro-mechanical behaviour of unsaturated silt. *Géotechnique*. 59(4): 339–353.

Vaunat, J., Merchan, V., Romero, E. & Pineda, J. 2007. Residual strength of clays at high suctions. *2nd Int. Conf. on Mech. of Unsat. Soils*, Weimar, Germany, Vol. 2, 151–162.

Villar, M.V. 2000. Caracterizacion termo-hidro-mecanica deuna bentonita de Cabo de Gata. *Ph.D. thesis, Universidad Complutense de Madrid*, Madrid, Spain.

Advances in Unsaturated Soils – Caicedo et al. (eds)
© 2013 Taylor & Francis Group, London, ISBN 978-0-415-62095-6

Measurement of friction on piles over neutral plane in expansive soils

C. Mendoza
Department of Civil and Environmental Engineering, Los Andes University, Bogota, Colombia

ABSTRACT: Using pile foundations is a common solution to reduce the effect of expansive soils on foundations. Little experimental evidence exists concerning the behavior of piles installed in unsaturated expansive soils. The purpose of this research is to provide measurements of the skin friction and the lateral pressures on pile shaft and analyze their behavior during wetting. Reduce scale models in centrifuge are used for this purpose. Furthermore the effect of geofoam as an alternative to reduce friction is studied.

1 INTRODUCTION

Problems generated by expansive soils are more common and expensive than others like tide, earthquakes, landslides and hurricanes. Their effects are accentuated in regions with extreme climatic variations having high plasticity clays. Under these circumstances shallow foundations are affected by structural damages resulting for swelling and shrinkage. Deep foundations are good solutions to transmit the loads of deep layers of soil that are unaffected by expansion but foundations must be conceived to withstand negative skin friction or uplifting pile. The interaction between piles and expansive soils are not well known.

Davis & Poulos (1972) developed solutions for negative skin friction and swelling forces in piles. These models were based in elasticity and Mohr Coulomb criteria. Other traditional expressions are described by Das (2006) and others. Despite its numerical solutions are used for pile design in expansive soils, Alonso (1990) proof that expansive soils shows an unsaturated behavior, so the methods listed above don´t describe the real behavior of an expansive soil.

This paper looking for measuring friction forces in the active zone of piles using a centrifuge machine. Otherwise, expanded polystyrene EPS (geofoam) was used in centrifuge modeling to test their application as an alternative material to add to shaft pile to minimize the soil expansive effects.

1.1 *Review of measurement of friction forces in expansive soils*

Research about modeling of pile foundation in expansive soils, measurement of friction and neutral plane are not common. Fellenius (1988) showed that active zones finished in specific depths, depending on adjacent soil settlement and pile stiffness. Lee (1993) presented a load transference simplified approximation by mean of pile group in negative skin friction conditions. It depends of pile—soil interface stiffness, spaces between piles and piles number. Matyas & Santamarina (1994) estimated negative skin friction and neutral plane under an elastoplastic solution. Lee et al. (1993) presented tridimensional models to estimate negative skin friction on simple pile and groups. Hanna & Sharif (2006) create a numerical model to analyze piles in expansive soils, under a lineal model. Hanna & Azizul (2009) develop a coupled model to pile group settlement for consolidation in expansive soil, furthermore adding lime and fly ash to accelerate consolidation. Their contribution is an analysis of expansive—non expansive sequence, in contrast with other works that analyze one only expansive stratum.

1.2 *Review on geofoam as a material to swelling soil control*

To purposes of present research expect EPS geofoam to cover shaft pile over neutral plane. Geofoam material is made by blocks of polystyrene particles placed by mean of expansion and fusion process. Geofoam have been used in geotechnical engineering in slides, backfills and tunnels, this material proves their utility in reducing lateral pressures in walls using it in the backfill, also geofoam reduce filtrations and can seal cracks and can be used as vibration barriers (Minova Corp., 2010). However, this material hasn't been used in pile foundation construction. Fist numerical modeling to use geofoam in expansive soils is developed after Ayketin (1997), using how a compressible inclusion between foundation and soil. Laboratory study of geofoam in expansive soils is developed where is showed a comparative measure of pressures with and without geofoam.

2 CHARACTERIZATION OF EXPANSIVE SOIL USED IN PHYSICAL MODELING

2.1 *Soil used for modeling*

This research did not work a soil mixture created in laboratory, because it presents a low permeability stopping a quickly swelling during centrifuge modeling (Segura, 2010). In contrast, two natural expansive clays from Barranquilla and Tibu, Norte de Santander (Colombia—Venezuela border) were used. Both materials were tested in laboratory but only Tibu´s clay was used in the models since it present higher expansive characteristics.

2.2 *Geotechnical characterization of expansive soil*

The soil was tested in laboratory carrying out basic tests such as classification, compaction, free and controlled expansion and contraction limits as well as consolidation, direct shear and Triaxial CU tests, finding strength and deformability variables. Resume of test are given in Table 1.

The results are complemented with suction measure tests. Twelve suction tests were executed with using chilled mirror apparatus. Water retention characteristics representing suction in pF and water content are showed in Figure 1. High values of suction are observed for values of water content smaller than the natural moisture (15%), for these water contents the suction suction values are between 1 MPa to 27 MPa; while for water content values higher than 15% the suction values are less than 1 MPa.

Table 1. Characteristics of Tibu´s clay.

Variable	Value
Liquid limit (%)	60
Plastic limit (%)	21
Plasticity index (%)	40
Free expansion in a test tube (%)	110
Expansion pressure (kPa)	300
Contraction limit (%)	14
Dry density (kN/m^3)	16
Optimum moisture (%)	16.09
Friction angle CU triaxial test (°)	20
Es (kPa)	810
Cc	0.264
Cs	0.068
P'_0 (kPa)	21
OCR	0.5
Permeability K_y (m/s)	3E-9
Cohesion—direct shear (kPa)	25
Friction angle—direct shear (°)	17
Cohesion soil-EPS mixture (kPa)	31
Friction angle soil-EPS mixture (°)	32

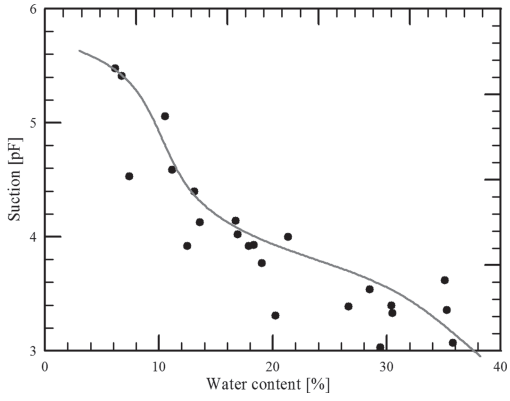

Figure 1. Graph suction vs. moisture for soil tested.

2.3 *Tests in oedometer apparatus with measure of suction and moisture*

Six tests were realized in an instrumented oedometer apparatus. This device allows measurement of water content during test, in which can be perform compaction and anisotropic consolidation, Figure 2. Test was made in charge-recharge five cycles, adding water to soil in last cycle to observe the effect of suction in tests; these results can be used for search parameters for constitutive modeling.

3 CENTRIFUGE MODELING

3.1 *Model features*

Models were conceived to be tested in a small centrifuge, which characteristics are given in table 2. Prototype—model scale was 1:30. It was only modeled the active zone, according to the characteristics given in ground for soil researched. Due to the difficult to measuring radial stresses in a scale model considering a circular section pile, a rectangular model (simulating a barrette) was selected. Pile model was created with aluminum blocks sliding on smooth fixing screws, set in acrylic base. On shaft pile model was attached a sandpaper to simulate the roughness of a pile concrete; also is added EPS geofoam as will be shown later.

Model has five load cells—range 500 N, to measure horizontal and vertical forces on pile model. Also, strain gages were calibrated to measure horizontal charges as a complementary measurement device, Figure 3. Displacement was measured with LVDT, and strains were assessed using a mesh

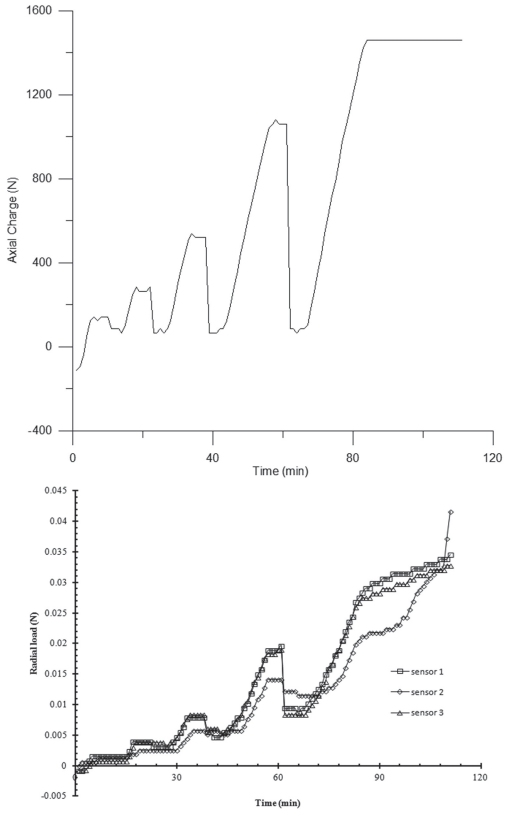

Figure 2. Graphs charge axial and radial vs. time.

Table 2. Centrifuge features.

Variable	Value
Type	Beam
Ratio (m)	0.56
Acceleration range (g)	10–300
Height model (mm)	120
Width model (mm)	70
Length model (mm)	140
Blocks dimensions (mm)	$25.4 \times 25.4 \times 69.0$

drawn in a face of model, which is obtained by means of photo sequence analysis. Dimensions of blocks and instruments are given in table 2. As explained in section 3.2, soil are compacted to achieve a maximum dry density compared with a proctor standard test. It requires optimum water content and taking into account the suction was lower, models were dried to reduce the moisture to values between 10% to 15%, where suction values were most high and therefore, expansive effects are most visible. Inundation was used as a system to increase water content in the model.

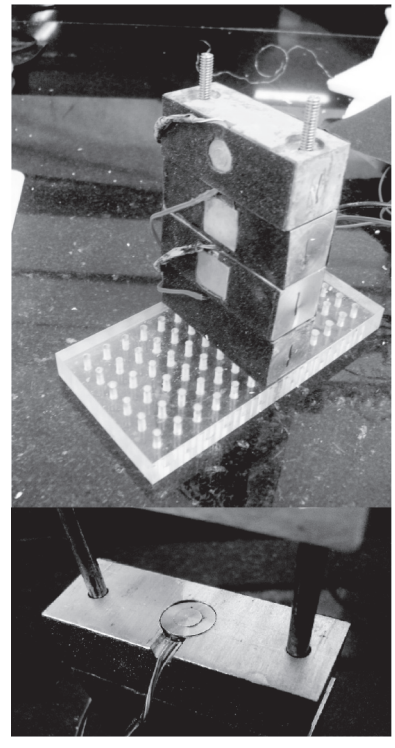

Figure 3. Pile model with horizontal and vertical load cells.

3.2 *Model verification*

Before carrying out models in centrifuge, the model behavior and the load cells capacity was verified at 1 g acceleration. For this purpose, six test models with different characteristics were proved (compacted or reconstituted and dried soils; soil placed in one or two faces of blocks; also one or many water content increases). Ideal results are given in a compacted and dried soil, where expansive effects are faster, since the cracks due to dry accelerates water infiltration. Figure 4 shows the evolution of lateral pressure during wetting during one of the verification tests.

3.3 *Expanded Polystyrene EPS—Geofoam*

Geofoam used is a commercial product for geotechnical works. In our case it is made by a mixture of two liquid chemical products: alcasylicate prepared with amines and diphenylmethane dusocianate, isomers. For research purposes was used a liquid commercial: its expansion factor is

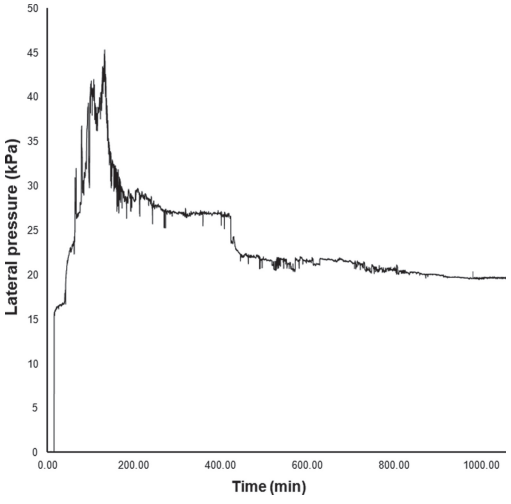

Figure 4. Skin friction forces on pile model under 1 g acceleration.

1:10 and it appears 30 s after the mixture of two components.

Laboratory test were made on EPS samples and with the couple of EPS-soil. The strength in a uniaxial compression test is 64 kPa and the elasticity modulus is 663 kPa. The unit weight is 1,3 kN/m^3. Direct shear tests for the couple of expansive soil with geofoam inclusions showed an increase of cohesion and friction angle values (31 kPa and 32° respectively).

3.4 *Centrifuge modeling*

Once model type has been selected, centrifuge models were flown. Table 3 shows the centrifuge protocol used. Centrifuge machine and model used are shown in Figure 5. Fifteen models are used to research the expansive soil behavior under different moisture content.

3.5 *Lateral pressures*

Figure 6 shows the typical behavior of the increase of lateral pressure during wetting. Force magnitude depends of degree of saturation, water content, suction and flow water direction. Major forces in models were developed with low water contents, ranging from 20 kPa to 200 kPa peak stress. In all cases, maximum stresses were reached in first 60 days (prototype time).

Figure 7 shows the lateral pressures for two models with both similar conditions of soils but with and without Geofoam. The results show a reduction of lateral pressures on the pile model having geofoam.

Table 3. Centrifuge protocol.

Variable	Description
Drying	In oven, 40 °C to reduce water content to the desired
Wetting	During fly by water inundation of camera, to simulate saturation in a winter season
Acceleration	Thirty (30) gravity
Time modeling	Four hours in model, equivalent in time scale to five months or 150 days in prototype
Type models	Eight (8) models with expansive soil only, five (5) models with sheets of geofoam and one (1) model with injection of liquid geofoam
Scale laws applied (model/ prototype ratio)	Time: n^2, force:$1/n^2$, stress: 1, length: 1/n

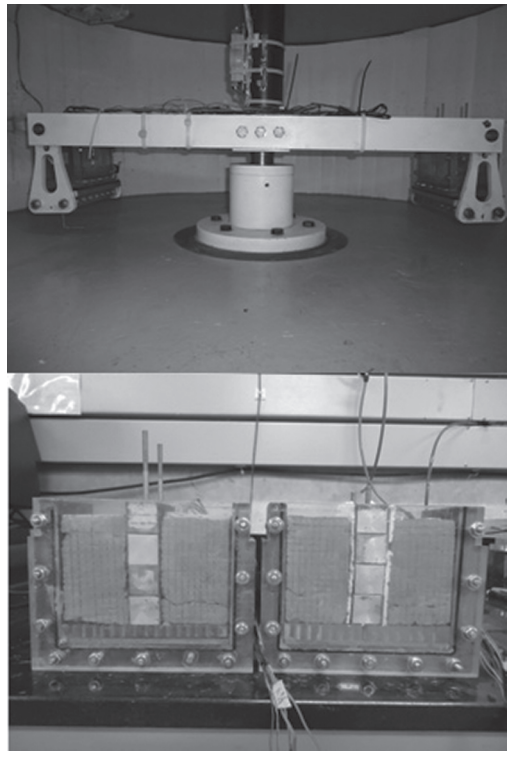

Figure 5. a) Centrifuge machine. b) Models with expansive soil and expansive soil-geofoam.

3.6 *Skin friction*

Behavior of pile model was clearly defined. On top pile, skin friction increased in positive magnitude, while at intermediate nodes, was decreased with time. In all tests internal nodes showed a decreasing

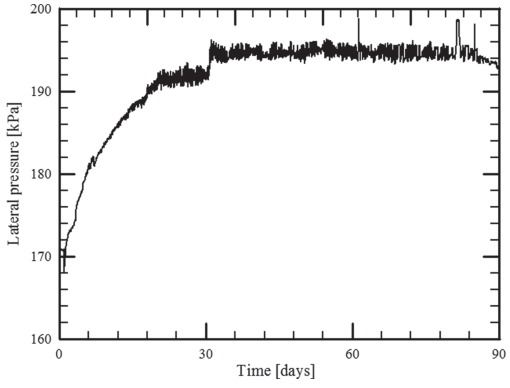

Figure 6. Lateral pressure stress vs. time on centrifuge testing.

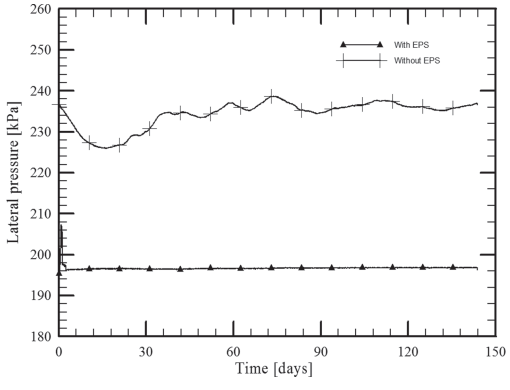

Figure 7. Comparison of lateral pressures with and without EPS geofoam for two models in similar conditions.

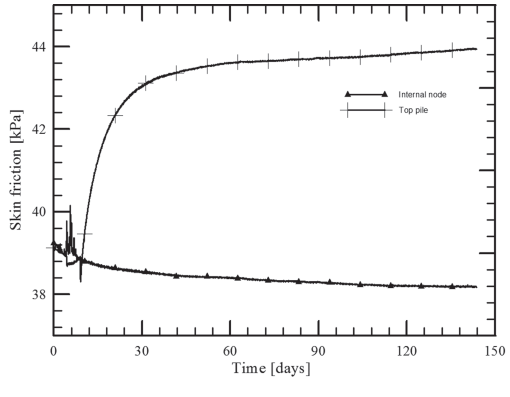

Figure 8. Comparison tests with and without EPS geofoam for two models in similar conditions.

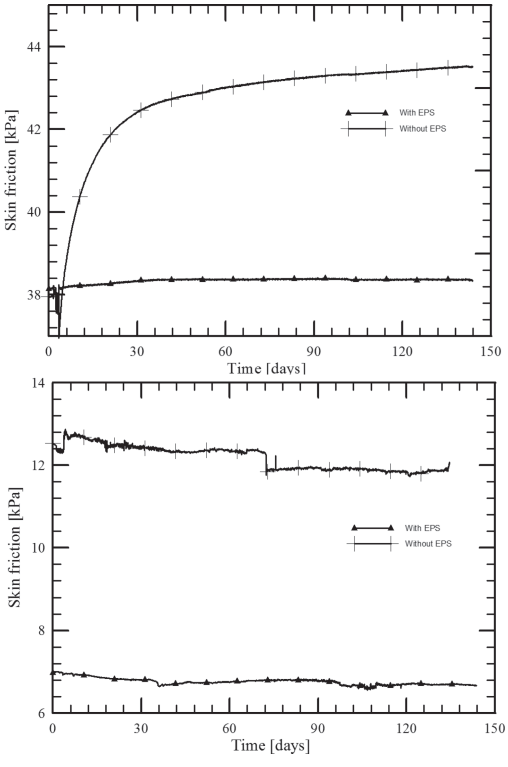

Figure 9. Comparison of skin friction with and without EPS geofoam for two models in similar conditions (a) top pile (b) internal nodes.

friction path, Figure 8 show these paths. EPS geofoam reduced the magnitude of skin friction in 12% approximately, as been seen in Figure 7.

4 CONCLUSIONS

Skin friction stresses depends on the degree of saturation and suction during the summer season, since the higher magnitudes were achieved in tests with lower suction and water content.

The expansive reaction appears in first 60 days of winter season or saturation period, after that remains constant or decreases.

Evolution of stress vs. time show a well defined tendency: an upward-sloping straight line, which reaches a peak stress; after, stresses are constant when soil is saturated or decreasing.

For practical purposes, can be considered the peak stress over neutral plane as a percentage between 12% to 15% comparing to controlled expansion pressure in oedometer test.

EPS geofoam restrict the lateral pressures in a percentage between 17% to 30%.

EPS Geofoam can reduce in 12% to 47% the magnitude of skin friction in piles during swelling.

Liquid injection of geofoam in construction of deep foundations can be considered as a new constructive alternative to reduce the swelling and shrinkage effects, both drilled and driven piles. Geofoam can react and move quickly on a given withering between soil and pile. Its quick reaction counteracts the gradual emergence of expansive effects of soil and fill all voids, as well as to increase the frictional strength in expansive clays. Nevertheless, high volumes and waste of geofoam used in research should be considered to generate an effective system of geofoam inclusion.

REFERENCES

Alonso, E. et al. 1990. Constitutive modeling for partially satured Soils. Géotechnique. 40: 405–430.

Aytekin, M. 1997. Numerical modeling of EPS Geofoam use with Swelling Soil. Geotextiles and Geomembranes. 15: 133–146.

Castro, J. 2008. Modeling of expansive and collapsible soils in centrifuge. Unpublished master´s thesis. University of the Andes, Bogota, Colombia.

Das, B. 2001. Principles of foundation engineering. México D.F: International Thomson Editors.

Fellenius, B. (1988). Unified design of piles and pile groups. Washington DC: Transportation Research Board.

Hanna, A. & Sharif, A. 2006. Drag force on a single pile in clay subjected to surcharge loading. International Journal of Geomechanics ASCE. 6(2): 89–96.

Hanna, A. & Azizul, M. 2009. Coupled consolidation model for negative skin friction on piles in clay layers. Geomechanics and Geoengineering. 4(2): 141–149.

Josa, A. 1988. An elastoplastic model for unsaturated soils. Unpublished doctoral dissertation. Polytechnic University of Catalonia. Barcelona. Spain.

Lee, C. et al. 1993. Pile groups under negative skin friction. Journal of Geotechnical Engineering ASCE. 119(10): 1585–1599.

Lee-Kuo Lin, Li-Hsien Chen, Chen & Roger H.L. 2010. Evaluation of geofoam as a geotechnical construction material. Journal of Materials in Civil Engineering. 22 (2): 160–170.

Lo, I., Zhang, J. & Ju, L. 2005. Soil & Sediment contamination. Centrifugue modeling of cadmium migration in satured and unsatured soils. New Jersey: Taylor and Francis Group, Inc.

Matyas, E. & Santamarina, J. 1994. Negative skin friction and neutral plane. Canadian Geotechnical Journal. 31: 591–597.

Minova International Limited. 2010. Geofoam construction system. Retrieved march 1 2011, the web site Minova InternationalLimited.www.minovausa.com/pdfs/products/geofoam.pdf.

Murillo, C., Thorel L. & Caicedo, B. 2009, July. Ground vibration isolation with geofoam barriers: Centrifugue modeling. Geotextiles and Geomembranes. 27: 423–434.

Nelson, J. & Miller, D. 1992. Expansive soils. New Jersey: John Wiley & Sons, Inc.

Poulos, H.G. & Davis E.H. 1980. Pile foundation Analysis and Design. Otawa: Rainbow—Bridge Book.

Segura, C. 2009. Shallow foundation in expansive soils. Unpublished master´s thesis. University of the Andes, Bogota, Colombia.

Advances in Unsaturated Soils – Caicedo et al. (eds)
© 2013 Taylor & Francis Group, London, ISBN 978-0-415-62095-6

On the use of unsaturated properties of a sandy material for centrifuge model preparation

W.F. Morales, J. Laue & S.M. Springman
Institute for Geotechnical Engineering, ETH Zurich, Switzerland

ABSTRACT: This contribution shows how the unsaturated properties of a uniform sandy material are used to create stable vertical surfaces when building dyke models for testing in a geotechnical drum centrifuge. The model is constructed inside a 1.0 m (length) × 0.54 m (depth) × 0.36 m (width) box with a semi-circular base, which must then be tilted through 90° to place the model into the channel of the centrifuge drum. A construction procedure has been developed to create unsaturated conditions in the sand so that the suctions are large enough to ensure that the 0.5 m high vertical walls remain stable for a short period of time until the centrifuge test can begin. This has been backed up by 3D numerical finite element calculations of the performance of the model in an unsaturated state.

1 INTRODUCTION

Centrifuge modeling is a technique in which small scale models are tested in an enhanced acceleration field. The increased acceleration subjects the model to the same stress level as at the prototype scale, providing key scaling laws are applied. Further information regarding this technique is presented, among others, by Schofield (1980) and modeling in a geotechnical drum centrifuge is described, for example, in Springman et al. (2001). Mayne et al. (2009) discuss ongoing challenges and solutions to modern centrifuge modeling.

In most centrifuge facilities, the increased gravity field is parallel to the horizon (neglecting the 1 g earth gravitational field). As this field has to be aligned with the depth direction of the prototype, the model surfaces simulating horizontal planes have to be vertical during the centrifuge test.

The small scale models are usually built in a laboratory and are then placed into the centrifuge facility before the test begins. This requires that some surfaces hold vertical and perpendicular to the planned test gravity for a period of time that will be long enough to prepare the test and start spinning the centrifuge. As shown by Fredlund & Rahardjo (1993), partially saturated, fine-grained reconstituted soils can hold significant suctions, which stabilize the ground. When these soils are fully saturated or, if sand is used, this task becomes more challenging.

In the following sections, it is shown how the unsaturated properties of a uniform sandy material are used to create stable vertical surfaces when building dyke models. The model is constructed inside a $1.0 \times 0.54 \times 0.36$ m box with a semi-circular base of constant curvature, which must be tilted through 90° to place and install the model in the drum centrifuge.

2 MODEL PREPARATION

2.1 *Material*

A uniform poorly graded sand from 15 km away from the coast nearby Perth, Australia, with a d_{50} of 0.23 mm, is used to model the dyke. The form of the grains is rounded as consequence of aeolian transportation (Buchheister, 2009).

Physical and mechanical parameters of the sand were determined in the laboratory and are presented in Table 1. γ_s is the dry unit weight. ν' is the Poisson's ratio, ϕ'_{max} *and* ϕ'_{crit} are the maximal and critical internal friction angles. d_{10}, d_{50}, d_{60} are particle sizes for which the 10, 50, 60% of the material has a smaller grain size. e_{min} and e_{max} are the minimal and maximal void ratios achieved.

In addition, knowledge on the hydraulic parameters under unsaturated conditions is needed to model the behavior of the soil properly. This includes the relationship between volumetric water content θ and the hydraulic conductivity, as a

Table 1. Physical and mechanical properties of Perth sand (some values from Nater, 2005; Buchheister, 2009).

γ_s [kN/m^3]	ν' [-]	ϕ'_{max} [°]	ϕ'_{crit} [°]	d_{10} [mm]	d_{50} [mm]	d_{60} [mm]	e_{max} [-]	e_{min} [-]
26.50	*0.3*	*37.5*	*30*	*0.17*	*0.23*	*0.25*	*0.85*	*0.53*

function of the water suction. The former is often referred to as the Water Retention Curve (WRC).

Figure 1 shows the curve obtained from a specimen of sand reconstituted to a predefined void ratio of 0.6 in a Fredlund apparatus, which uses the axis translation technique (Fredlund & Rahardjo, 1993), and is subjected to both drying and wetting paths. The void ratio of 0.6 is similar to that in the centrifuge models, after finishing sample preparation. It is a key point, as the WRC is non-unique and is highly dependent on density, as demonstrated e.g. by (Askarinejad et al., 2010) and (Morales et al., 2011).

The main parameters deduced from the WRC are the Air Entry Value *(AEV),* defined as the value of matric suction at which the air enters into the soil and begins to desaturate the soil matrix. The Water Entry Value (*WEV*), which is the value of matric suction at which the water starts to displace air in the porous medium soil during a wetting process (Wang et al., 2000). θ_{max} is defined as the volumetric water content when the material is saturated, whereas θ_{res} is the residual volumetric water content, i.e. the amount of water that remains trapped in the soil even at high matric suctions. A summary of the values obtained is given in Table 2.

The WRC presented in Figure 1 shows a hysteretic response when the specimen is subjected to a drying path followed by a wetting process. The drying path is horizontal until the Air Entry Value (AEV) of 2.4 kPa is reached. From that point on, it follows a relatively steep curve until it reaches the θ_{res}, whereupon the wetting process begins. Once the Water Entry Value (WEV) of 9.5 kPa is reached, the material begins to saturate. The curve does not overlap with that obtained for the drying path. Instead, it shows a flatter behavior.

The hydraulic conductivity function (Fig. 2) was deduced from the WRC as indicated by Fredlund & Xing (1994).

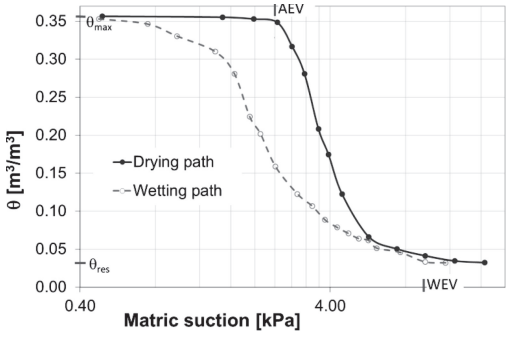

Figure 1. Water retention curve for perth sand, e = 0.60.

Table 2. Hydraulic properties of Perth sand under unsaturated conditions, e = 0.60.

AEV [kPa]	WEV [kPa]	θ_{max} [m^3/m^3]	θ_{res} [m^3/m^3]
2.40	*9.50*	*0.36*	*0.03*

2.2 *Strongbox*

The dyke model is built inside a new strongbox designed with the aim of modeling a dyke and its surroundings in realistic relative dimensions. This box (Fig. 3) is composed of two plates (bottom and top), two lateral walls, seven connecting struts and a curved modular base (Fig. 4), which is fixed to the channel of the drum centrifuge. The form of the box is an annular sector of dimensions $1.0 \times 0.54 \times 0.36$ m.

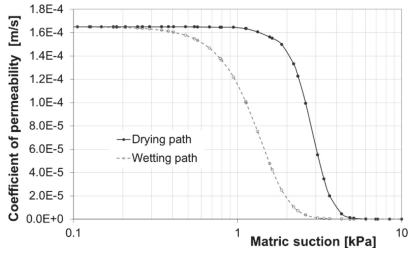

Figure 2. Hydraulic conductivity function for Perth Sand, e = 0.60.

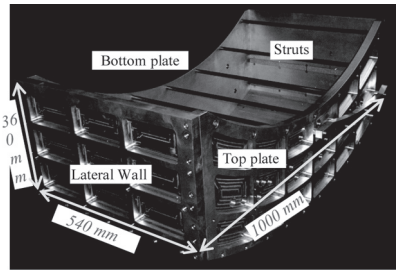

Figure 3. New semi-circular strongbox at ETH Zurich.

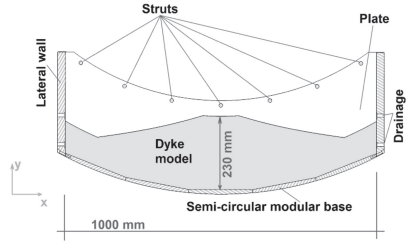

Figure 4. Cross section of the strongbox with dyke model.

Details about functionality and design aspects of the strongbox can be found in Morales et al. (2012a; 2012b).

2.3 *Construction procedure*

Morales et al. (2012a) present a detailed description of the construction procedure of the small scale model. A summary of the key points is given here.

The box is filled completely with sand by dry pluviation to start preparing the model dyke and its subsoil. This means that the material falls freely under gravity from a constant height of 0.60 m, and a dry unit weight of 17.4 kN/m^3 was achieved.

Then the sand is saturated by adding water from the bottom of the model through a drainage port in the lateral walls of the strongbox. Once the water table reaches the surface of the soil model, water is pumped out with a vacuum pressure of 3.5 kPa. Suction is applied until a gravimetric water content of 14% is reached.

The slopes are shaped next. Finally, the model is tilted through 90° to be placed in the drum channel (Fig. 5) using a crane, which can also cause unplanned vibrations and hence disturbance.

3 STABILITY CALCULATIONS

The stability of the model in the drum under 1 g was studied via 3D finite element analysis. This was carried out with TOCHNOG, an open source finite element method (FEM) software with emphasis on geotechnical calculations (Roddeman, 2003).

The boundary value problem was discretized with 29407 low order tetrahedra elements (TET4) (Fig. 6). The soil response was represented by an elastic-perfectly plastic material model following the Mohr-Coulomb failure criteria. The material model parameters are listed in Table 3, and explained in the next section.

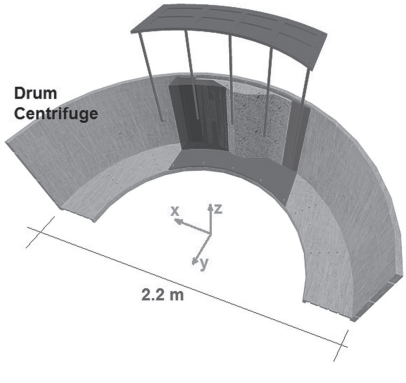

Figure 5. Model installed in the drum centrifuge with the box shown in 'exploded' mode.

3.1 *Parameters*

The bulk unit weight (γ) corresponds to the dry unit weight achieved (17.4 kN/m^3) multiplied by 1.14, to take water in the soil mass (w = 14%) into account.

The stiffness of the material in an unsaturated state has been determined from an oedometer loading test on a soil sample with a water content of 14%. As expected, maximum vertical total stress (z-direction) at the bottom of the rotated sample is 19.8 kN/m^3 × 0.5 m ≈ 10 kPa, with an expected suction of 3.65 kPa (see below), the drained Young's modulus (E') was calculated from Equation 1, in which E'_{oed} is the drained oedometric stiffness modulus for an effective normal stress of 13.65 kPa (E'_{oed} = 29.3 MPa) (cf. Table 4).

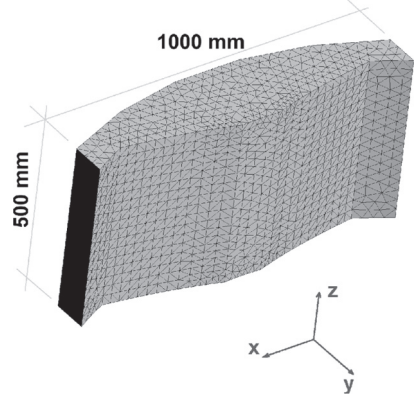

Figure 6. FEM mesh of the dyke boundary value problem.

Table 3. Material properties used in the FEM calculations.

γ [kN/m^3]	ν' [-]	ϕ' [°]	ψ [°]	E [MPa]	c' [kPa]	c'_{appa} [kPa]
19.8	*0.3*	*30*	*7.5*	*21.83*	*0*	*1.67*

Table 4. Results from the oedometer loading test.

σ' [kPa]	E'_{oed} [kPa]	E' [kPa]	e [-]
5.65	*18370*	*13646*	*0.648*
9.65	*73480*	*54585*	*0.648*
13.65	***29392***	***21834***	***0.648***
17.65	*5652*	*4199*	*0.646*
21.65	*2939*	*2183*	*0.644*
25.65	*993*	*738*	*0.638*
34.15	*1881*	*1398*	*0.630*
42.65	*1420*	*1055*	*0.620*

$$E' = \frac{(1+\nu')\cdot(1-2\nu')}{(1-\nu')}\cdot E'_{oed} \quad (1)$$

The apparent cohesion (c'_{appa}) was calculated as indicated by Sheng et al. (2011):

$$\begin{aligned}\tau &= c' + \overline{\sigma_n}\cdot\tan\phi' + \chi\cdot S\cdot\tan\phi' \\ &= c' + \overline{\sigma_n}\cdot\tan\phi' + c'_{appa}\end{aligned} \quad (2)$$

τ is the shear strength of the unsaturated soil, ϕ' is the effective angle of internal friction, c' is effective cohesion, $\overline{\sigma_n}$ is the net normal stress, S is matric suction. χ is a parameter originally assumed to be a function of the degree of saturation (S_r). However, Khalili & Khabbaz (1998) showed that it actually depends on suction and that χ is approximated as:

$$\chi = \begin{cases}\left(\dfrac{AEV}{S}\right)^{0.55} & \text{if } S \geq AEV \\ 1 & \text{if } S < AEV\end{cases} \quad (3)$$

The values for the AEV and S are taken from the drying path of the WRC. The gravimetric water content (w) of 14% corresponds to a volumetric water content (θ) of 0.2 m^3/m^3, then a suction of 3.65 kPa is determined as acting on the soil. Although the volume changed during the 1D loading test, which increases the volumetric water content by 1.7%, it was assumed negligible. From Equations 2 & 3:

$$\begin{aligned}c'_{appa} &= \chi\cdot S\cdot\tan\phi' \\ &= \left(\frac{AEV}{S}\right)^{0.55}\cdot S\cdot\tan\phi' \\ &= \left(\frac{2.40}{3.65}\right)^{0.55}\cdot 3.65\cdot\tan(30°) \\ &= \underline{1.67\ \text{kPa}}\end{aligned} \quad (4)$$

3.2 *Conditions for the analyses*

Displacements have been restrained in the normal direction of the nodes in contact with the strongbox.

The initial suction value of 3.65 kPa was defined for each element as an initial condition, and earth's gravity was applied in the z-direction.

Three analyses were carried out. A 3D static analysis to estimate the deformation after the system has been tilted, hence the surfaces are vertical. A stability analysis of the 3D models is done using the c′-phi reduction method (Brinkgreve & Bakker, 1991). It gives an indication of the global factor of safety of the model although this is a very rough method and is based on assumptions that any components of c′ or ϕ′ decay at the same rate. Finally, a two-dimensional limit equilibrium analysis, using the method from Morgenstern & Price (1965) of the central section was carried out.

3.3 *Results*

Figure 7a is a shaded plot of total displacements after the small scale model is tilted. A maximum displacement of 0.15 mm is expected in the top part of the model. The cross section in Figure 7b shows a deformed shape (scaled up 400 times) and the distribution of the displacement inside the soil. The surface does not remain perfectly vertical, as some lateral deformations are expected. However, they are assumed not to be large enough to affect the behavior of the model during the centrifuge testing.

The estimated factor of safety for stability of the model with the c-phi reduction procedure is 1.56 and the Morgenstern-Price method gives a value of 3.0. Both failure mechanisms are illustrated in Figure 8. A triangular wedge is obtained for the limit equilibrium analysis, which had been observed already in previous tests on very loose models (Laue et al., 2005). It contrasts with the displacements obtained with the c-phi reduction method (Fig. 8b). The difference in the failure mechanisms explains the variation in the estimated factors of safety.

Figure 9 presents a soil model after it had been built and tilted through 90°. No clear deformations

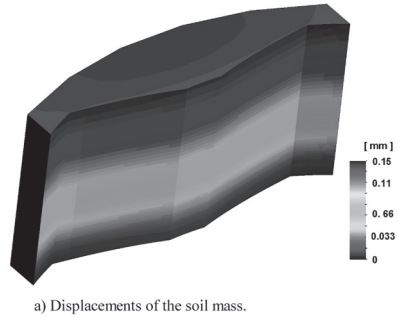

a) Displacements of the soil mass.

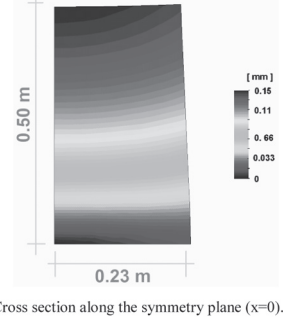

b) Cross section along the symmetry plane (x=0).

Figure 7. Total displacements after the model is tilted at 1 g (deformed shape scaled up 400 times).

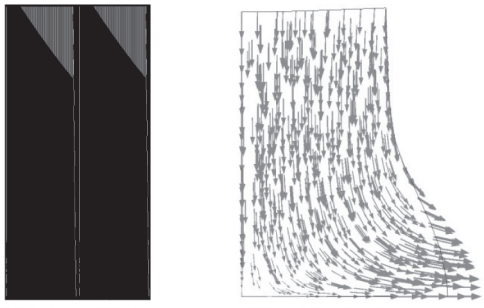

a) Limit equilibrium. b) c-phi reduction.

Figure 8. Failure mechanisms for both types of stability calculation.

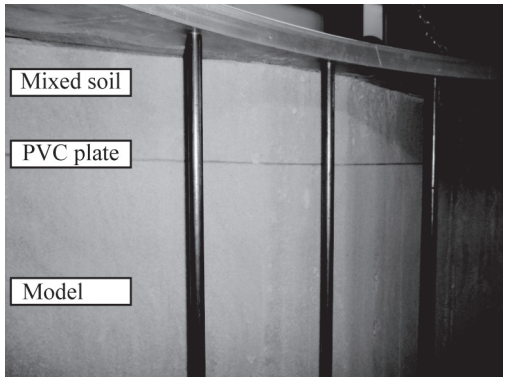

Figure 9. Dyke model after pluviation, partial saturation and tilting through 90°, all at 1 g.

are visible in the soil mass, indicating that the unsaturated material is appropriate in this state for building the small scale model.

4 INSTALLATION ISSUES

Notwithstanding the expected response of the model, a gap of approximately 0.5 mm typically develops while installing the model inside the drum centrifuge (Fig. Figure 10). This deformation is generally caused by vibrations when sliding the box containing the model into the drum channel.

When the test is running and the acceleration in the model is increased, the soil deforms and an active shear wedge is developed (cf. Fig. 10). This does not affect the stability of the model, but it leaves a loose zone behind it. Water then flows through that zone during the flooding phase, exceeding the supply and foiling the plans for overflow.

Two measures were adopted to prevent this. Firstly, a PTFE (generic term for Teflon®) film is stuck to the top face of the bottom annular ring

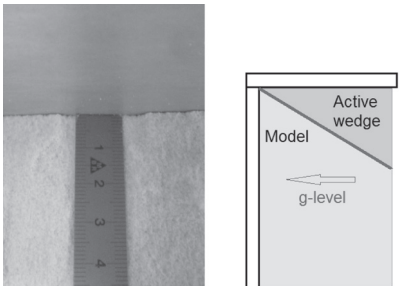

Figure 10. (left) Gap on top of the tilted sand model after installation inside the drum centrifuge; (right) active wedge that develops after increasing the g-level.

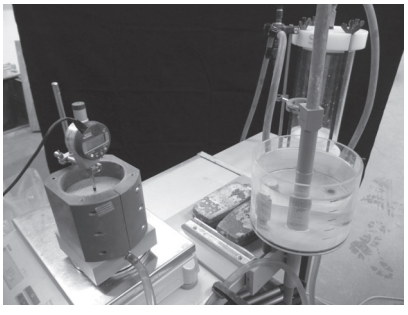

Figure 11. Setup for swelling test on a 100 mm diameter specimen of 85 mm height.

of the drum channel, as well as to the external lower face of the bottom of the strongbox. A Teflon-Teflon contact has an approximate coefficient of friction of 0.04, reducing the force required to push the strongbox into the drum.

A thin layer of a soil composed of a mix of the sand with an expansive material (bentonite MX-80) is placed at the upper part of the model separated from the model by a 1 mm thick PVC plate (cf. Fig. 9). This material does not prevent the gap from forming, but once it makes contact with water, the volumetric expansion of the material closes the gap. Further details about swelling potential of this bentonite can be found in Montes-H et al. (2003).

A swelling test was conducted to determine the expansion potential of different mixes of sand and bentonite. A cylindrical sample (100 mm diameter × 85 mm height) was connected to a water supply at the base in order to saturate the specimen from the bottom. A cap was placed on top of the specimen. The deformations of the sample were measured from the displacement of the cap (Figure 11).

Figure 12 shows the results from the swelling test. The content of bentonite changes the permeability of

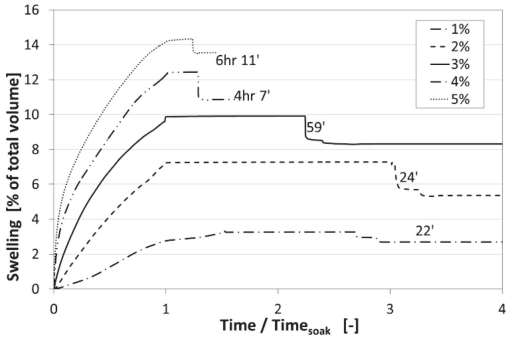

Figure 12. Swelling potential for different mixes of sand and bentonite.

the material, as well as the time required for saturation of the sample, which is given beside each curve.

The mix of 97% sand and 3% bentonite was chosen over the other mixes, as it gives a volumetric expansion potential of 10% within 1 hour after the mixture is in contact with water.

5 DISCUSSION

This contribution shows how the unsaturated properties of a uniform sand might be used successfully in the creation of a small scale model at 1 g, for subsequent testing in a centrifuge facility at ng. This requires some vertical surfaces, 0.5 m high, to remain stable during a period of time of 3 hours between the model preparation and the beginning of the test.

The numerical simulation estimates very small deformations in the upper part of the model, which can still affect the model behavior. However, vibrations occurring while placing the model inside the centrifuge lead to a small gap forming above the sand model at the interface with the upper drum annulus. This issue is faced by using a thin layer with a mix of the sand and bentonite. As water is absorbed, the bentonite expands, and the gap closes itself.

REFERENCES

Askarinejad, A., Francesca Casini, P. Kienzler, and S.M. Springman. 2010. Comparison between the in situ and laboratory water retention curves for a silty sand. in Unsaturated soils: Proceedings oh the 5th International Conference on Unsaturated Soils, Sep. 6–8, 2010, at Barcelona, ES.

Brinkgreve, R.B.J., and H.L. Bakker. 1991. Non-linear finite element analysis of safety factors. in 7th International Conference on Computer Methods and Advances in Geomechanics, at Cairs, USA.

Buchheister, J. 2009. Verflüssigungspotenzial von reinem und siltigem Sand unter multiaxialer Belastung. Ph.D. Dissertation, ETH Zurich, Zurich, CH.

Fredlund, D. G., and A. Q. Xing. 1994. Equations for the soil-water characteristic curve. Canadian Geotechnical Journal 31(4): 521–532.

Fredlund, D.G., and H. Rahardjo. 1993. Soil mechanics for unsaturated soils. Toronto, CA.: Wiley-Interscience.

Khalili, N., and M.H. Khabbaz. 1998. A unique relationship of chi for the determination of the shear strength of unsaturated soils. Géotechnique 48 (5).

Laue, J., S.M. Springman, P. Nater, E. Grämiger, and A. Ducksch. 2005. Creating seafloor conditions in geotechnical centrifuges. in 16th International Conference on Soil Mechanics and Geotechnical Engineering, at Osaka, JP.

Mayne, P.W., M.R. Coop, S.M. Springman, A.B. Huang, and J.G. Zornberg. 2009. Geomaterial behavior and testing. in 17th International Conference on Soil Mechanics and Geotechnical Engineering, Oct. 5–9, 2009, at Alexandria, EG.

Montes-H, G., J. Duplay, L. Martinez, and C. Mendoza. 2003. Swelling-shrinkage kinetics of MX80 bentonite. Applied Clay Science 22(6): 279–293.

Morales, W.F., J. Laue, and S.M. Springman. 2012a. Controlled water-level system for breach analysis of levees within an enhanced acceleration field in 2nd Eurofuge Conference, Apr. 23–24, 2012, at Delft, NL.

Morales, W.F., J. Laue, A. Zweidler, and S.M. Springman. 2012b. Design and analysis of centrifuge devices with a Product Lifecycle Management (PLM) system. in 2nd Eurofuge Conference, Apr. 23–24, 2012, at Delft, NL.

Morales, W.F., P.A. Mayor, and S.M. Springman. 2011. In-situ and laboratory water retention characteristics in a silty sand dyke. in 15th European Conference on Soil Mechanics and Geotechnical Engineering, Sep. 12–15, 2011, at Athens, GR.

Morgenstern, N.R., and V.E. Price. 1965. The analysis of the stability of general slip surfaces. Géotechnique 15(1): 79–93.

Nater, P. 2005. Belastungs- und Verformungsverhalten von geschichteten Bodensystemen unter starren Kreisfundationen. Ph.D. Dissertation, ETH Zurich, Zurich, CH.

Roddeman, D. 2003. Tochnog User's Manual—a free explicit/implicit FE program.

Schofield, A.N. 1980. Cambridge geotechnical centrifuge operations. Géotechnique 30(3): 227–268.

Sheng, D., A. Zhou, and D.G. Fredlund. 2011. Shear strength criteria for unsaturated soils. Geotechnical and Geological Engineering 29(2): 145–159.

Springman, S.M., J. Laue, R. Boyle, J. White, and A. Zweidler. 2001. The ETH Zurich Geotechnical Drum Centrifuge. International Journal of Physical Modelling in Geotechnics 1(1): 59–70.

Wang, Z., L. Wu, and Q.J. Wu. 2000. Water-entry value as an alternative indicator of soil water-repellency and wettability. Journal of Hydrology 231–232: 76–83.

Advances in Unsaturated Soils – Caicedo et al. (eds)
© 2013 Taylor & Francis Group, London, ISBN 978-0-415-62095-6

Application of electrical resistivity for the control of water content and density in loess

V. Rinaldi
National University of Córdoba, Argentina

ABSTRACT: Argentinean loess is a typical collapsible soil which strength and stiffness are mainly governed by water content and unit weight. Electrical resistivity of soils depends fundamentally from water content, porosity, and salt concentration in the pore fluid. The interest of this work is to discuss the applicability of electrical resistivity survey to predict variations in density and water content in loess. Samples of loess were prepared in laboratory at varied densities and water contents. The results show that loess resistivity depends mainly on water content and that soil density has little influence. Mapping water content distribution by means of resistivity measurements is possible if salt concentration in pore fluid is known in advance and assumed uniformly distributed in the whole soil mass. A real scale work is described here for which resistivity mapping was used successfully to evaluate distribution of water content in loess formation.

1 INTRODUCTION

The Argentinean loess is of eolian origin and can be classified in the unstable group of soils as collapsible (Aitchinson, 1973). The most relevant properties Argentinean deposit has been extensively described by Moll & Rocca (1991), and Rinaldi et al. (2007). Most loess deposits were naturally deposited by wind (primary loess) while others were removed and re-deposited by water (secondary loess). Additionally, is of common practice to improve the behavior of loess by means of static and dynamic compaction. In any case, natural water content and final density mainly governs shear strength, permeability and compressibility of the soil.

McCarter (1984), Kalinski & Kelly (1994), Knight, (1991), Abu-Hassanein et al. (1996) Zhou et al. (1997), and Rinaldi & Cuestas (2001) discussed the potential application of electrical conductivity (or its inverse value, the resistivity) to evaluate soil compaction. In general, electrical conduction in soils depends mainly on temperature and frequency of measurement, electrolyte type and concentration in the porous, water content and density. Minor influence can be attributed to soil structure and saturation history of the soil.

The possibility of monitoring soil density by means of an electrical methods is advantageous since the control in the field can be performed from the surface to any depth just working with different separation of electrodes when any of the four-electrode configuration is adopted (see for example ASTM G57). On the other hand, to the experience of the authors, measurement of conductivity is fast and little data processing is required in order to obtain accurate and repeatable results.

The purpose of this work is to present a fundamental study to discuss the applicability of electrical resistivity to predict water content and density of loess soil. Thus, various samples were prepared in the laboratory at different densities and water contents. Electrical conductivity was measured for each sample by using a two electrode device. The relationship between the electrical conductivity, soil density and water content is described in terms of the well known Archie´s law. An example of in-situ control by mean of conductivity measurement is presented.

2 BACKGROUND

The influence of the different parameters in the electrical conductivity of compacted specimens of loess was discussed elsewhere (Rinaldi & Cuestas, 2001). The most relevant are: frequency of measurement, electrolyte type and concentration (c), initial salt concentration in the soil, dry unit weight (γd), degree of saturation (S), and temperature (T). At a constant temperature and frequencies of measurement, these authors showed that the influence of the different variables in the electrical conductivity of the soil can be take in consideration by using the well known Archie´s expression

(Archie, 1942) which for saturated conditions can be expressed as:

$$F = a\, n^{-m} \tag{1}$$

where F is the formation factor defined from the slope of the σ_e vs. σ_s curves as:

$$F = \frac{\sigma_e}{\sigma_s} \tag{2}$$

Being σ_e and σ_s the electrical conductivity of the pore fluid and the saturated soil respectively, n is the porosity, a is the tortuosity factor, and m is the cementation factor. The value 1/F is also known as the resistivity index (RI).

For the unsaturated condition equation (1) can be extended as follows:

$$F_s = F\, S^{-p} \tag{3}$$

where S is the degree of saturation and p is the saturation exponent. Then, by replacing (1) in (3):

$$F_s = a\, n^{-m}\, S^{-p} \tag{4}$$

The values of a, m and n are normally determined from experiments for a given soil. Notice that for saturated samples $S = 1$, and $n = \theta_v$ and equations (4) reduce to equation (1), which was empirically obtained by Archie for some saturated rocks and then extensively validated in practice for a variety of porous formations. Equations (1) and (4) assume that in the porous media the particles and the air are non conductive phases and conduction takes place only through the fluid (Glover, 2010).

In terms of the volumetric water content (θ_v), equation (4) can be rewritten as:

$$F_s = a\, n^{(p-m)}\, \theta_v^{-p} \tag{5}$$

Thus, for soils in the saturated condition, the measured conductivity of the soil mass becomes:

$$\sigma_s = \frac{\sigma_e}{a} n^m \tag{6}$$

Equation (7) shows that electrical conductivity for saturated soils is mainly dependent on porosity or the volumetric water content (since $n = \theta_v$) and salt concentration of the pore fluid which governs the value of σ_e. The values of σ_e and a are difficult to be obtained in practice specially in fine grained soils.

Therefore, for a given soil in saturated conditions for which salt concentration in the pore fluid is approximately the same along the whole soil mass (σ_e = constant), there is always possible to find a correlation between the measured bulk conductivity and the porosity as follows:

$$\sigma_s = \alpha\, n^m \quad (saturated\ soil) \tag{7}$$

or alternatively,

$$\sigma_s = \alpha\, \theta_v^m \quad (saturated\ soil) \tag{8}$$

where α is a curve fitting parameter.

For unsaturated soils, the bulk electrical conductivity of the soil can be obtained from equation (5) as:

$$\sigma_s = \frac{\sigma_e}{a} n^{(m-p)}\, \theta_v^p \tag{9}$$

In a similar approach developed for the saturated conditions, it is always possible to find a more general expression for a given soils assuming that σ_e is constant everywhere in the soil mass of the type:

$$\sigma_s = \alpha\, n^{(m-p)}\, \theta_v^p \tag{10}$$

Equation (10) is a more general expression for soils at any compaction density and water content condition. It can be seen that for saturated soils ($n = \theta_v$) and equation (10) reduces to equation (8).

Notice that in equations (6) to (10) soil dry density is included in n and also in θ_v since:

$$\theta_v = \frac{\gamma_d}{\gamma_w} w \tag{11}$$

where (γ_d) is the dry unit weight of the soil, (γ_w) is the unit weight of water and (w) is the gravimetric moisture content.

Equations (10) and (11) are the basic relationship to determine water content and density from the measured soil resistivity of the soil. From these equations it becomes clear that soil conductivity depends on soil density and water content (w). In saturated soils, conductivity is directly related to volumetric water content. The parameters a and m depend mainly on mineral composition, grain size distribution and fabric. The exponent p for a given soil is slightly dependent on soil density.

3 TESTING PROGRAM

The soil tested here is the typical loess obtained from the campus of the Universidad Nacional de Córdoba which can be classified in USCS as ML. In natural state the dry density is $\gamma_d = 13.5$ kN/m^3, liquid limit LL = 31, and plasticity index PI = 26.

The electrical conductivity of the soil samples was measured in the two-electrode cell. Basically the cell consists on a cylindrical glass tube (33.4 mm internal diameter) and two circular electrodes of the same diameter located at both ends of the tube. Electrodes were made of cooper and coated with nickel. The measurements of conductivity were performed by means of a Stanford Research impedance analyzer SR715 at the frequency of 10 kHz. Specific details of the testing cell used here and its calibration procedure are described in Rinaldi & Cuestas (2001).

The natural samples of loess were air-dried, sieved through sieve No 40 and then oven dried at 105 ºC. The dried soil was then mixed with the different volumes of NaCl electrolyte prepared at concentrations between 0,5% and 2% by weight. The prepared soil specimens were then compacted to the desired density in the glass tube of the cell.

4 ARCHIE´S LAW FOR LOESS

Figure 1 display the variation of the formation factor obtained for a sample of loess saturated with NaCl solutions and compacted at various densities. The exponent of the correlation was $m = 2.6$ and the factor $a = 0.5$. The range of porosities included in Figure 1 range between 0.37 and 0.50 which are the maximum and minimum densities that may be observed in the field. The agreement of equation (1) is acceptable in the rage of densities tested. The values of the constants a and the exponent m may be different even for the same soil at other compaction densities.

Figure 2 shows the variation of the formation factor for samples prepared at various water content and concentrations of NaCl. Equation (5) was evaluated for porosities $n = 0.3$ and $n = 0.5$ and plotted in the same figure. The constant parameters were fixed as $a = 0.5$, $m = 2.6$ and $p = 2.4$. The variation of the exponent p is presented on Figure 3 for samples prepared at different densities and mixed with different concentrations of NaCl. Therefore, equation (5) can be written for the present results as:

$$\frac{\sigma_s}{\sigma_e} = \frac{1}{a} n^{(2.6-2.4)} \theta_v^{2.4} \tag{12}$$

From Figure 2 it can be observed that for the model porosity has negligible effect on the formation factor and that water content is the main parameter that governs conduction trough the soil.

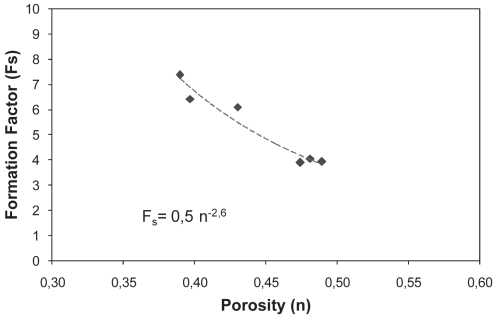

Figure 1. Formation factor of loess saturated with NaCl solutions at concentrations between 0.5% and 2% as a function of porosity (n).

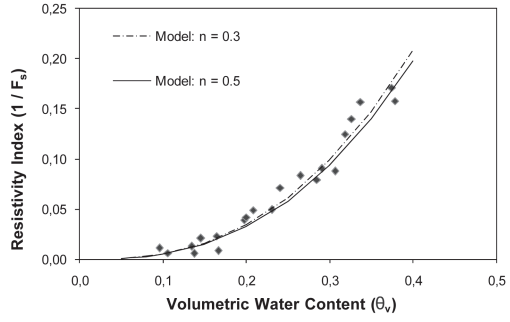

Figure 2. Formation factor of loess samples prepared with NaCl solutions at concentrations between 0.5% and 2% as a function of volumetric water content (θ_v).

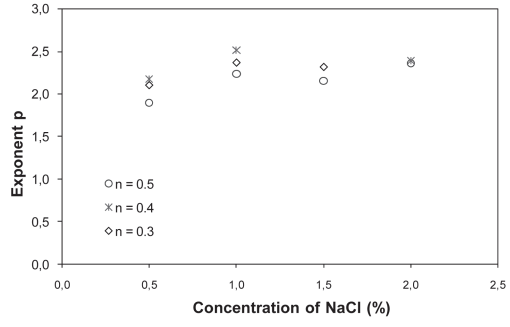

Figure 3. Variation of the exponent p for samples of loess of loess prepared at various porosities and mixed with NaCl solutions at concentrations between 0.5% and 2%.

This result can be explained from the close values obtained for the exponent p and m. The physical meaning of this result can be further clarified from the phase diagram for the soil displayed on Figure 4. Three conduction paths can be identified through the soil in the unsaturated condition: solid particles (σ_p), fluid (σ_e) and air (σ_a). Thus, the total conduction can be expressed in a simplified approach as:

$$\sigma_s = (1-n)\,\sigma_p + (n-\theta_v)\,\sigma_a + \theta_v \sigma_e \tag{13}$$

The second term of equation (12) vanishes since conductivity of the air is close to zero. Additionally, the first term also has a negligible influence for soils which particles can be considered as non-conductive. Then, the total conduction depends mainly from the volumetric water content of the soil. Notice from Figure 4 that for any variation in the fraction volume of solids and air (which changes soil density), conductivity through the fluid will remain practically unchanged.

The volumetric water content depends also from the soil unit weight (γ_d) according to equation (11) however, this parameter has not significant variation from the loosest to densest condition for most soils. For example in loess density usually ranges from 13,5 kN/m^3 to 16,5 kN/m^3 when heavily compacted which represent an increment of 20%. Conversely, water content (w) may vary from 2% in the air dry condition to almost 40% in the saturated condition which represent an increment of 2000%. Then for practical purposes and for loess, equation (12) can be simplified to: (5) as:

$$\frac{\sigma_s}{\sigma_e} = \chi\, \theta_v^p \tag{14}$$

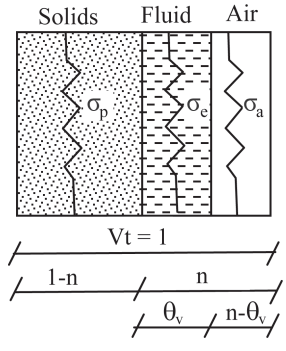

Figure 4. Phase diagram of soil and simplified conduction paths assumed.

That for the soil tested here yield:

$$\frac{\sigma_s}{\sigma_e} = 2.14\, \theta_v^{2.6} \tag{15}$$

In order to obtain the soil conductivity from equation (14) it is required to know in advance the conductivity of the pore fluid (σ_e). This parameter is normally unknown, however it is clear that for a given soil formation, the concentration of salt in the pore fluid can be assumed homogeneously distributed in the whole mass (due to ion diffusion) and thus the value of σ_e can be considered the same everywhere.

5 FIELD EVALUATION

Figure 5 displays the variation of electrical resistivity obtained in an area of 60 m × 150 m located at the south of the city of Córdoba. The thickness of loess formation at the site is larger than 60 m. Measurements were performed by using the four electrode configuration equally spaced 5 m apart. Separations of electrodes were kept constant and measurements of resistivity were performed at different points in the surface of the soil following a square grid of 20 m. The measured resistivity was estimated to correspond to an average thickness of 2.5 m.

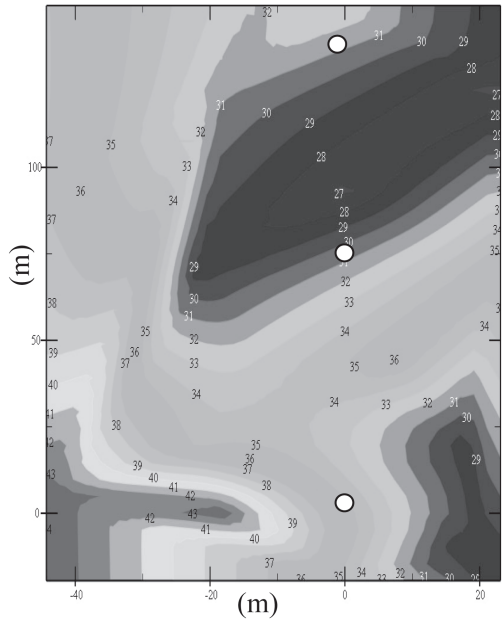

Figure 5. Resistivity variation obtained in an area of 60 m × 150 m of loess formation. Numbers on the figure display resistivity values in Ohm-m. White dots indicate the position of control points.

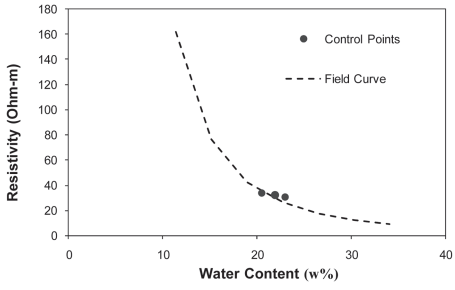

Figure 6. Variation of resistivity as a function of water content for the field test performed.

The range of resistivities values obtained in this test collapse in a narrow band between 22 Ohm-m and 43 Ohm-m, however, data are consistent. According to equation (14) the mapped resistivity is directly related to soil water content. In order to determine the relationship between the resistivity values and water content, the following procedure was used here:

a) Three field points of control were selected and from each point were determined moisture content ($w\%$) and soil density (γ_d). Figure 5 shows the location of each point.
b) Volumetric water content (θ_v) was determined for the three control points from equation (11).
c) For convenience, equation (14) was rewritten in terms of resistivity as:

$$\rho_s = \frac{\rho_e}{2.14}\,\theta_v^{-2.6} \tag{16}$$

d) From equation (15) the value of ρ_e was determined for the three control points since the values of θ_v and ρ_e are known.
e) Assuming constant density (γ_d) and fluid resistivity (ρ_e) everywhere, equation (15) is then the field curve that can be used to determine water content for any other point where resistivity is known.

Equation (15) is plotted on Figure 6 as a function of water content. The three control points are also shown on the same figure.

The study presented here assumes the validity of equation (14) obtained for loess formation. For any other formation, it is recommended to obtain in the laboratory a calibration of the model, or to increase the number of control points and to determine a field curve from these points.

6 CONCLUSIONS

The main conclusion of this work can be summarized as follows:

a) Resistivity or electrical conductivity of loess has a significant dependence on water content and is little influenced by density.
b) Archie´s equation can be used to model the dependence of electrical resistivty from water content for loess in saturated and unsaturated condition.
c) The main dependence of soil resistivity from water content was explained here by means of a simple physical model.
d) A field procedure was described here which allows mapping the distribution of water content from electrical resistivity measurements. The procedure assumes little variation in the conductivity of the soil mass under test.
e) Further studies are required to evaluate the influence of fine contents and to what extends can be applied Archie´s model.

REFERENCES

Abu-Hassanein Z., Benson C. and Blotz L., 1996, Electrical Resistivity of Compacted Clays, *Journal of Geotechnical and Geoenvironmental Engineering*, ASCE, No. 5, Vol. 122, pp. 397–406.

Aitchinson G.D. 1973, Structurally Unstable Soils; State of the Art. *Proc. VIII ICSMFE*, Moscu, pp.161–190.

Archie G.E., 1942, The Electrical Resistivity Log as an Aid in Determining Some Reservoir Characteristics, *Transactions of the American Institute of Mechanical Engineers*, 146, pp.54–67.

Glover P.W.J., 2010, A Generalized Archie's Law For N Phases, *Geophysics,* Vol. 75, No. 6, pp. 247–265.

Kalinski R.J. & Kelly W.E., 1994, Electrical-Resistivity Measurement for Evaluating Compacted-Soil Liners, *Journal of Geotechnical Engineering*, Vol. 120, No. 2, pp. 451–457.

Knight R., 1991, Hysteresis in the Electrical Resistivity of Partially Saturated Sandstones, *Geophysics*, Vol. 56, No. 12, pp. 2139–2147.

McCarter W.J., 1984, The Electrical Resistivity Characteristics of Compacted Clay, *Geotechnique*, No. 2, Vol. 34, pp. 263–267.

Moll L. & Rocca R. 1991, "Properties of Loess in the Center of Argentina". IX Panamerican Conference on Soil Mechanics and Foundations Engineering. Chile, Vol. 1.

Rinaldi V. & Cuestas G. 2001, The Ohmic Conductivity of a Compacted Silty Clay, *ASCE Journal of Geotechnical and Geoenvironmenta Engineering*. Vol 128, No. 10, pp. 824–835.

Rinaldi V.A., Rocca R.J. & Zeballos M.E. 2007, Geotechnical Characterization and Behaviour of Argentinean Collapsible Loess. *Characterisation and Engineering Properties of Natural Soils*. Tan, Phoon, Hight & Leroueil (eds). Balkema, London, Vol. 4, pp. 2259–2286.

Zhou D., Arbabi S. & Stenby E., 1997, A Percolation Study of Wettability Effect on the Electrical Properties of Reservoir Rocks, Transport in Porous Media, No. 29, pp. 85–98.

This page intentionally left blank

Advances in Unsaturated Soils – Caicedo et al. (eds)
© 2013 Taylor & Francis Group, London, ISBN 978-0-415-62095-6

A method for making a homogeneous specimen of unsaturated clay using micro-wave

H. Suzuki, Y. Okano, K. Ueno & R. Uzuoka
The University of Tokushima, Tokushima, Japan

ABSTRACT: Many laboratory tests related to unsaturated clay were usually made by compacted statically or dynamically. However, the methods for making were not explained in detail. We suggest distribution of water contents of a compacted clay sample is not uniform. A new method for making a specimen of unsaturated clay by using micro wave is proposed. The variations of water contents and dry densities within the specimens using micro wave method are compared quantitatively to those using dynamically compacted method. As a result, a distribution of water contents by micro wave was more homogeneous than that of compacted method. Finally, unconfined compression test is performed using the specimens made by the both methods. The strength of specimen made by micro wave was a little higher than that of compacted specimen, and amount of strain until failure of micro wave was larger than that of compacted method.

1 INTRODUCTION

Generally, it is very difficult to make a specimen with an initial degree of saturation exactly controlled by a method for making specimen of unsaturated clay. Most of the specimens in laboratory tests are made by compacted dynamically or statistically method, but concrete methods for making a specimen were not explained in detail on many past papers. Moreover, they are not always guaranteed that the water contents and the dry densities in the parts of specimen become uniformity. Although it is sometimes tried that the specimen is approached to the fixed suction state by suction-controlled apparatuses from the initial state, it is indispensable for the long time applying suction to a specimen to balance state. On the other hand, if homogeneity is secured, consider the method that apply the fixed suction to a saturated specimen formed from a clay sample which was pre-consolidated at a slurry state, however, it takes a long time to balance up the fixed suction in this case. For example, the researches of water retention curve, Romero & Vaunat (2000), Karube & Kawai (2001), Gallipoli (2003), Tarantino & Tombolate (2005). A. Tarantino (2010) etc., the developments of elasto-plastic behavior of unsaturated soils, V. Sivakumar et al. (2010a, b), and experimental studies of effective stress of unsaturated soils, Alonso et al. (2010), Alonso E. E. & Romero E. (2011) use compacted specimen. The axis translation technique, namely a method for controlling suction by applying air pressure to a specimen is commonly used in suction-controlled oedometer and triaxial compression tests. If a compacted specimen is used by the method, it takes a long time to balance to the fixed suction state within a specimen. Applying suction to a saturated specimen may keep homogeneous; it also takes a long time to balance to the fixed suction state within a specimen. They used Tensiometer method, vapor pressure method, psychrometer method and centrifugal method etc. except for pressure plate method to measure wide range matric suction in the many past investigations of water retention curve. Most of specimens are also compacted, therefore, cannot be homogeneity of specimen and rapidness of measurement which a specimen balances the fixed suction state. Suzuki & Okano (2011) investigated the simplified water retention curve which made by micro wave for unsaturated clay and then an amount of drying is in proportion to elapsed time. In this study, a method for making a specimen of unsaturated clay using micro wave is proposed and it will be able to prepare a rapidness and homogeneity to need to an initial state of specimen for water retention curve test, suction-controlled oedometer and unconfined compression tests. Firstly, a method for making a homogeneous and rapidness specimen of unsaturated clay using micro wave is proposed, and water contents and dry densities of the inner part of specimens compacted by a rammer to use unconfined compression and oedometer tests is compared with those of by micro wave. Next, unconfined compression test was performed.

2 PHYSICAL PROPERTIES OF SHIGARAKI CLAY

A sample used in this study is Shigaraki clay. Table 1 and Fig. 1 show physical properties and grain size accumulation respectively, therefore, it is classified as clay (CL) according to Japanese soil classification standard.

3 METHOD FOR MAKING SPECIMEN USING MICRO WAVE

A pre-consolidated saturated clay samples are made by loading 80 kPa considering to format easily specimens. A heating method by micro wave is the followings. Saturated specimens of oedometer and unconfined compression tests are formatted from the samples The specimens are entered into a microwave controlling the heated times (30 sec, 1 min, 2 min), and then are radiated by taking out it to measure a temperature and mass of drying specimen. Radiation times are double times of heating time namely, they are 1 min, 2 min, 4 min, respectively. These works for measuring temperature and mass must be done rapidly to become constant heated time. The microwave used in this experimental works is the frequency (2450 MHz) and the outputs (100–750 W). It is necessary to dry very slowly to make a homogeneous specimen avoiding a volumetric changes caused by rapid drying. Therefore, the output of this microwave is set up 100 W which is the lowest output and is adopted a usage avoiding volumetric change mentioned above. The optimum heated time is determined in the case of unconfined compression specimen (diameter 5 cm, height 10 cm). Fig. 2 (a), (b), (c) show temperatures after heating 30 sec, 1 min, 2 min, respectively, and the inner part of specimen is not so high temperature (30 ~ 50 °C), the temperatures are including after evaporation are shown in this figure. The temperatures are measured by taking out specimens from micro-wave after heating and evaporating and by inserting sensor in a part of specimens. These temperatures the inner parts of specimens are adequate to use tensiometer which can be used below 45 °C.

Fig. 3 shows elapsed time after heating and degree of saturation relations. The heated times are 30 sec, 1 min, 2 min and corresponding to radiated times are 1 min, 2 min, 4 min. As shown in this figure, the both curves of the heated times of 1 min and 2 min are almost same, but the curve of 30 sec heated time is very different from others caused by

Table 1. Physical property of Shigaraki clay.

Density of soil particle Gs(g/cm^3)	2.61
Liquid limit w_L (%)	43.9
Plastic limit w_P (%)	18.3
Plasticity index I_P(%)	25.6

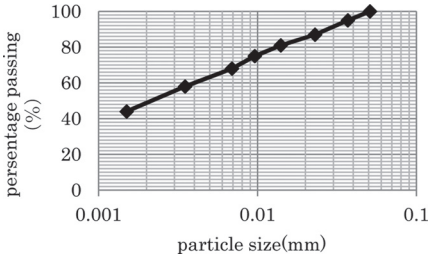

Figure 1. Grain size accumulation curve of Shigaraki clay.

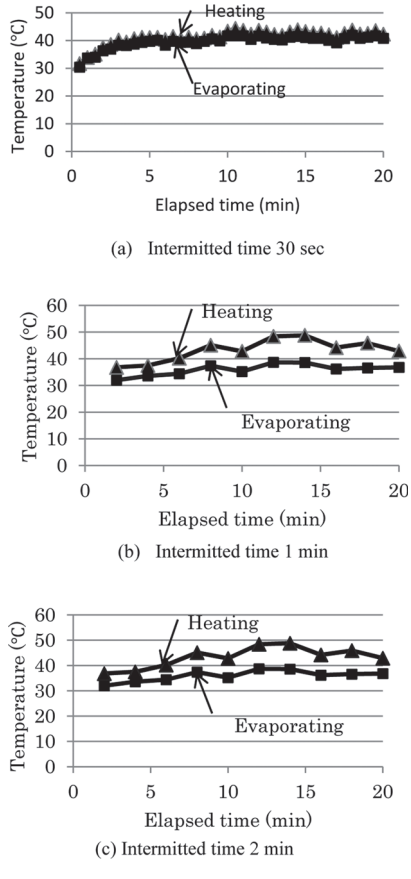

Figure 2. The temperatures of the specimens in heating and evaporating (Unconfined compression test specimen diameter 5.0 cm height 10.0 cm).

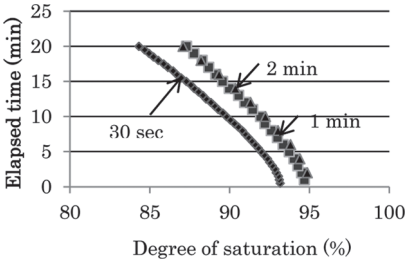

Figure 3. Determination of optimum a method for heating and evaporating (Specimens are same shape with Fig.2).

low initial degree of saturation. As a heating of micro wave can be uniformly evaporated moisture of a specimen, the heated times (1 min and 2 min) suit in order to reappear the curves. Moreover, the heated time is determined to 2 min considering not only reappear ability but also workability, The heated time is the summation of intermitted heated times but not successive heated times used in the below.

4 COMPARISON SIMPLIFIED AND MEASURED VALUES AT HEATED TIME AND DEGREE OF SATURATION RELATION

A simplified curve is defined by no volume change of a specimen after heated, namely it means a curve assuming that wet density is constant after heated. Therefore, the degree of saturation linearly decrees with increment of heated time of the simplified curve. On the other hand, a measured curve a volume of specimen after heated is measured by calipers method. In generally, to obtain a simplify curve is easy and high reappearance, however, an accuracy of these curves is not known. Therefore, the experimental works of the tow specimens of unconfined compression test (diameter 3.5 cm, height 7 cm and diameter 5.0 cm, height 10 cm) are performed in order to examine the accuracy.

Fig. 4 (a) shows the comparisons in the case of a specimen of diameter 3.5 cm. When a specimen is begun to heat, it has a high degree of saturation, therefore, the simplified values are rather different from the measured values, but they approach to them by repeating intermitted heating tests. Moreover, when degree of saturation is about 70%, the simplified values are exactly same with the measured values. The simplified curve can be used to make a specimen of low degree of saturation. Fig. 4 (b) shows the comparisons in the case of diameter 5.0 cm. From this figure, the simplified values and the measured values relation is almost

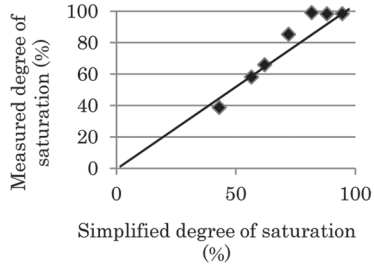

(a) Unconfined compression test specimen
Diameter 3.5 Height 7.0 cm

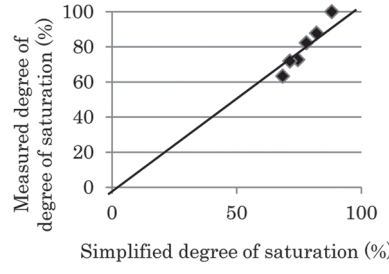

(b) Unconfined compression test specimen
Diameter 5.0 Height 10.0 cm

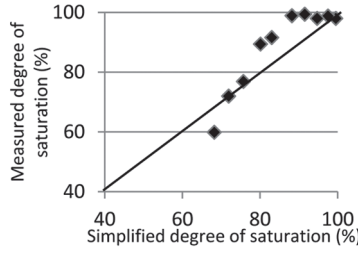

(c) Oedometer test specimen
Diameter 7.0 cm Height 3.0 cm

Figure 4. Comparison simplified degree of saturation with measured degree of saturation.

same as well as Fig. (a). Fig. 4 (c) shows the same results of oedometer specimen using the method mentioned above. As shown this figure, when a measured degree of saturation is approaching to 70% degree of saturation, a simplified degree of saturation is also almost same value, even if oedometer test specimen is. If oedometer test specimen with low degree of saturation is made, a specimen can be made by the simplified calculated curve. Therefore, degree of saturation using below this chapter is defined by the simplified curve method. Comparing simplified degree of saturation with that of measured, the more heating summation by micro wave, namely the lower degree of saturation,

the deference of them is smaller. It is recognized that a specimen by micro wave is evaporated uniformly with a little shrinkage of volume against the expectation at first.

5 HOMOGENEITY OF A SPECIMEN OF UNSATURATED CLAY

Fig. 5 shows the relation that the water content is 19% corresponding to degree of saturation 80%. This is that the compacted specimen 80% should be made by seven times compactions using 19% moisture powder clay at the compacted energy which is equal to 550 kJ/m^3. The variation of degree of saturation of each compacted specimen is examined on the condition that a specimen is made by same compacted method and same water content.

As shown Fig. 6, the measured values vary widely even if the same compacted method is used. Therefore, it is difficult to make a specimen with the controlled initial degree of saturation of compacted specimen. Owing to investigate homogeneity of oedometer specimen, Fig. 7 shows a method for dividing into three pieces in the horizontal direction and nine pieces in the vertical direction in order to make its squares. Therefore, specimen is divided totally into twenty seven pieces. It is important that a wet mass is measured rapidly not to dry. Fig. 8 shows the results of Distribution of water contents of compacted unconfined compression test specimen. On the other hand, Fig. 9 examines homogeneity of oedometer specimen made by micro wave. As shown these figures, the data of Fig. 8 is more various than that of Fig. 9. Since the deference of both figures cannot be clearly understood, coefficient of variation is used to evaluate quantitatively the variation of water contents. Comparing coefficient of variation of water contents of specimen made by micro wave with that of compacted specimen, the value (0.095) by micro wave becomes half of the value (0.175) by compacted method. It is clearly verified that specimen of micro wave is more homogeneous than that of compacted method at the inner part of specimen. The reason why water contents of compacted specimen are widely varied is to occur inhomogeneity of water contents for mixing imperfectly the powder clay and water and to be used different diameter of the rammer and the mould. Since the homogeneity of specimen in horizontal direction is verified mentioned above, next is examined in vertical direction using unconfined compression test specimen dividing into five pieces as shown Fig. 10.

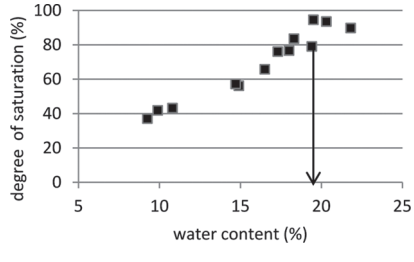

Figure 5. Change of degree of saturation for water content.

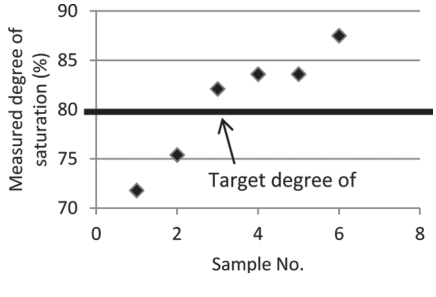

Figure 6. Accuracy of reproduction for degree of saturation obtained from compacted specimens.

Fig 7. A method for dividing oedometer test specimen to investigate the distribution of water contents.

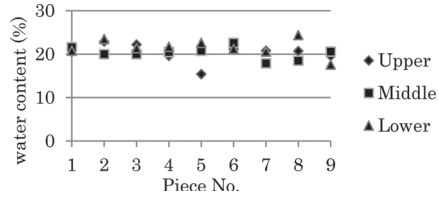

Figure 8. Distribution of water contents of compacted oedometer test specimen.

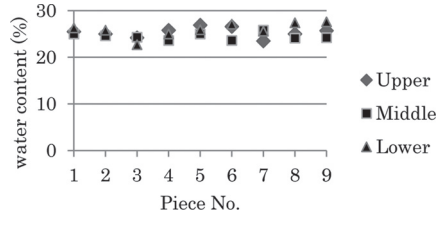

Figure 9. Distribution of water contents of oedometer test micro wave specimen.

The distribution of water contents by micro wave and compacted method are vertically almost same, as shown in Figs. 11 and 12, This is because each layer is given the same compaction energy to be same the diameters of rammer and mould used in the tests. Fig. 13 shows the variation of the densities of five pieces of compacted specimen to use unconfined compression test. Fig. 14 shows the distribution of dry densities of pieces by micro wave. As a result, micro wave specimen is more homogeneous dry densities than that of compact method. The dry density of compacted specimen becomes higher in order to many compacting times into the bottom direction.

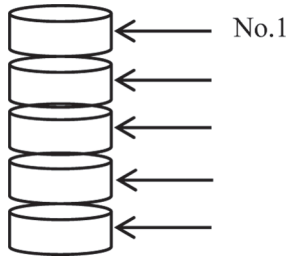

Figure 10. A method for dividing specimens of unconfined compression tests to investigate the distributions of water contents and dry densities.

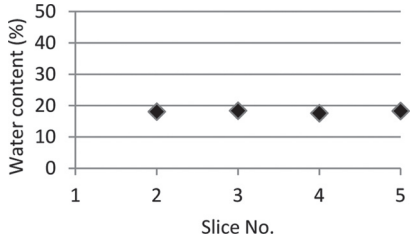

Figure 11. Distribution of water contents of compacted unconfined compression test specimen.

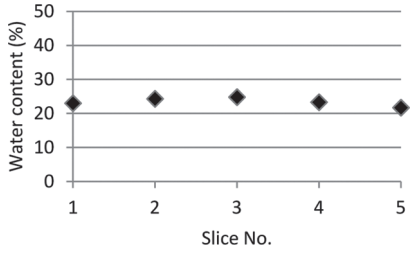

Figure 12. Distribution of water contents unconfined compression test specimen by micro wave.

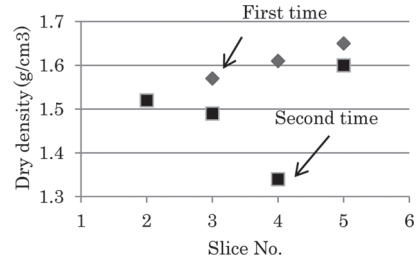

Figure 13. Distribution of dry densities compacted unconfined compression test specimen.

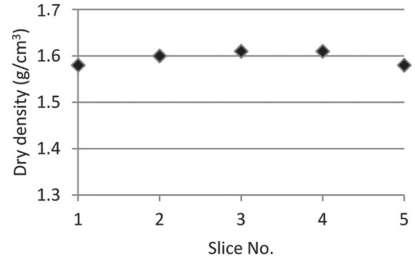

Figure 14. Distribution of dry densities of unconfined compression test specimen made by micro wave.

6 UNCONFINED COMPRESSION TEST USING MICRO WAVE AND COMPACTED SPECIMENS

The method for making a specimen using micro wave is better to make a homogeneous one comparing with compacted method. The stress-strain relation and strength of unconfined compression test of proposed micro wave method are compared to those of compacted method. The both specimens were made by mentioned above, and target degree of saturation is 80%. The sizes of them are diameter 5 cm height 10 cm. Fig. 15 shows the stress and strain relation. The strength by compacted method is a little larger than that of micro wave. As shown in Fig. 13, the reason is that the dry densities of compacted specimen are a little smaller and very various. The both stress-strain relations are very different, namely the peak strength of micro wave specimen appears at high strain level, on the other hand, that of compacted specimen appears at small strain level. It means micro wave specimen can be formed homogeneous suction among soil particles. From the observation of the shape of failure in Fig. 16, the specimen by micro wave appears a clear failure plane at final failure state, on the other hand, the compacted specimen is easily collapsed at the bottom. Therefore, micro wave method is better than compacted method.

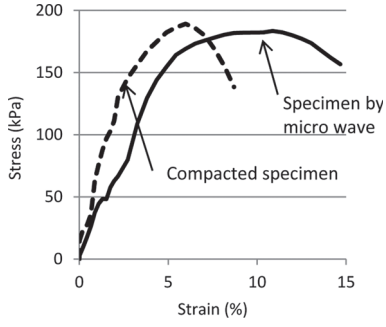

Figure 15. Comparison of stress-strain relations of compacted specimen with that of micro wave specimen on unconfined compression tests.

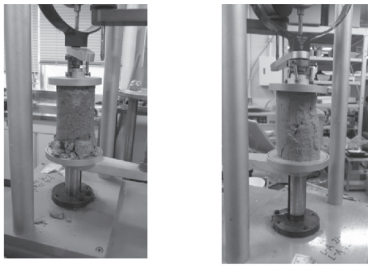

Compacted specimen Micro wave specimen

Figure 16. Failure shapes of compacted and micro wave specimens.

7 CONCLUSIONS

This study was to compare micro wave method with compacted method on a method for making a specimen of unsaturated clay. As a result, the following conclusions were obtained.

The method of optimum heated time which is heated time 2 min and radiated time 4 min was determined to obtain an optional target degree of saturation.

The usefulness of the method for making a specimen of unsaturated clay was examined by the homogeneity of distribution of water contents and dry densities of oedometer and unconfined compression tests specimens. The distribution of water contents of oedometer test specimen was 23%-27% and that of unconfined compression test specimen was 23%-24%, therefore, they were indicated the high homogeneity. A little deference of water content between micro wave and compacted specimens was dependent on pre-consolidated clay sample, if a specimen was made by micro wave, it made clear that both specimens became homogeneous. On the other hand, the distribution of water contents of compacted oedometer test specimen was 15%-24% to vary widely, however it of unconfined compression test specimen was uniformly 17%-18%. Therefore, it was difficult for the compacted method to make a specimen with a target degree of saturation. In micro wave specimen, if the rule of the method for heating time is obeyed, a specimen with target degree of saturation can be made easily, namely the method for making a specimen using micro wave is better than the compacted method.

Unconfined compression tests were performed using the both specimens. The strength of the micro wave specimen was a little high than that of compacted specimen. Observing the shapes of failure, the micro wave specimen were formed the failure plane at the specimen, on the other hand, the compacted specimen easily failed at the bottom. Therefore, it was made clear that a method for making a specimen of unsaturated clay gave the effects of mechanical properties.

REFERENCES

Alonso et al. 2010. A microstructurally based effective stress for unsaturated soils, *Geotechnique* 60(12), 913–925.

Alonso, E.E. & Romero, E. 2011. Experimental investigation on an effective stress law in compacted clayey/silty soil, *Proceedings of 5th Asia-Pacific Conference on Unsaturated Soils*, 331–336, 14–16, November, Thailand.

Gallipoli, D., Wheelwe, S.J. & Karstunen, M. 2003. Modeling the variation of degree of saturation in a deformable unsaturated soil, *Geotechnique* 53(1), 123–136.

Karube, D. & Kawai, K. 2001. The role of pore water in the mechanical behavior of unsaturated soils. *Geotech. Geolog. Engng* 19(Nos 3–4), 211–241.

Sivakumar, V., Sivakumar, E., J., Murray, P., Mackinnon & Boyd, J. 2010a. Mechanical behavior of unsaturated kaolin (with isotropic and anisotropic stress history), Part 1: wetting and compression behavior, *Geotechnique* 60(8), 581–594.

Sivakumar, V., Sivakumar, R., Boyd, J. & Mackinnon, P. 2010b. Mechanical behavior of unsaturated kaolin (with isotropic and anisotropic stress history), Part 2: performance under shear loading, *Geotechnique* 60(8), 595–609.

Suzuki, H. & Okano, Y. 2011. Characteristic stress-strain relationship of unsaturated soil by a method for making clay specimen using micro wave, *Proceedings of 5th Asia-Pacific Conference on Unsaturated Soils*, 437–442, 14–16, November, Thailand.

Tarantino, A. & Tombolato, S. 2005. Coupling of hydraulic and mechanical behavior in unsaturated compacted clay, *Geotechnique* 55(4), 307–317.

Tarantino, A. 2010. A water retention model for deformable soils, *Geotechnique*, 59(9), 751–762.

Advances in Unsaturated Soils – Caicedo et al. (eds)
© 2013 Taylor & Francis Group, London, ISBN 978-0-415-62095-6

Centrifuge modelling of wetting-induced collapse in embankment base

L. Thorel & I.M. Khokhar
LUNAM University, IFSTTAR, GER Department, Physical Modelling in Geotechnics Group, Bouguenais, France

V. Ferber
Entreprise Charier, France

B. Caicedo
Civil and Environmental Engineering Department, Universidad de los Andes, Colombia

ABSTRACT: The relevancy of the oedometer test used for the prediction of wetting-induced deformations in embankments is examined. Single-and double oedometer tests are carried out. A comparison between laboratory tests and geotechnical centrifuge modelling at 100 × g conducted to examine an inundated embankment made of a sand-clay mixture is made. A 20-cm high embankment model is built and instrumented. The material is compacted on the "dry side" of the optimum Proctor curve at a low compaction rate in order to emphasize settlement phenomena. The inundation simulation is conducted in two successive sequences during centrifuge flight up to a water table of five centimetres. The results prove that the prediction of the dry density after settlement due to inundation is good.

1 INTRODUCTION

The use of dry soil materials for the construction of roadway and railway embankments is limited to small heights, which, however, must plainly comply with compaction requirements (LCPC, 2003). The compaction of dry soils is energy consuming and does not prevent settlement from happening in case of soaking. The literature reveals that the compaction rate is one main parameter affecting long-term deformations of embankment bases (Lawton *et al.*, 1992; Auriol *et al.*, 2000). This problem is crucial for countries combining naturally dry soils and notable flood hazard, where highways programmes involving the construction of high embankments are developed. Therefore, we need to improve our understanding of dry compacted soil behaviour, in order to optimize embankment compaction for better stability regarding settlement risks.

Frequently, the wetting-induced behaviour of compacted soils results in "collapsing". Settlement mechanisms depend on (Lawton *et al.*, 1992):

- The compaction water content (or the suction) and the dry density after compaction. Collapse occurs mainly in dry and loose soils;
- The vertical stress applied during the inundation. Collapse settlement, indeed, increases with increasing vertical stress, i.e., collapse potential increases within the embankment deeper layers;
- The intrinsic properties of the soil, such as critical clay content (Rollins *et al.*, 1993) or plasticity index (Lim and Miller, 2004), which depends on the non clayey fraction of the soil. This critical clay content ranges between 10 to 40% (El Sohby & Rabbaa, 1984), depending on the vertical stress and probably on the grain size distribution of the non clayey fraction (Basma *et al.* 1992);
- The stress anisotropy during the inundation;
- The water content increase (or the suction decrease). The settlement increases non-linearly with the suction decrease (El-Ehwany & Houston, 1990; Pereira & Fredlund, 2000).

Regarding soil physical properties, the dry density after compaction is the main parameter affecting wetting-induced deformations under vertical stress (Lawton *et al.*, 1992; Rao *et al.*, 2000; Estabragh *et al.*, 2004; Ferber *et al.*, 2008). Moreover, the long-proposed experimental methods for the prediction of wetting-induced deformations, like the single or double oedometer tests (Jennings & Knights, 1957), though remaining pertinent (Basma *et al.*, 1992), need to be compared with observations like physical models. Physical modelling has been used to study the collapse of embankments (Miller *et al.*, 2001) without focusing on the relationships between initial dry density and settlements.

The study is conducted on a small scale embankment made of a dry and loosely compacted sand-clay mixture (SCM) using the IFSTTAR geo-centrifuge. The objective of the comparison with oedometer tests is to quantify the effect of a low compaction rate on settlement in case of inundation, and to assess the relevancy of laboratory test-based predictions. As the model is compacted in loose conditions, which do not represent actual field conditions, the results are presented at the model scale.

2 LABORATORY RESULTS

2.1 *Materials*

The SCM consists of a mixture of Speswhite kaolin and NE34 Fontainebleau sand (Table 1). The sand is characterized by a very narrow particle size range and a negligible fine content (Thorel *et al.* 2011). The clay is purified kaolin made of 77% clay particles and characterized by a plasticity index of almost 23. The optimum moisture content is 29% for MDD = 1.42 t/m^3. The clay fraction is mostly composed of kaolin minerals, among which some traces of illite have been detected. The SCM used for the tests is composed of 40% Speswhite kaolin and 60% Fontainebleau sand (Table 1). Therefore, the material characteristics are a combination of those of the clay and the sand. The clay content places it within the range of collapsible soils (El Sohby & Rabbaa, 1984). The compaction characteristics and the shape of the standard Proctor curve are similar to those of a clayey sand material and the plasticity index is low. The SCM water retention curve, obtained using the osmotic method, is presented as a function of suction and height of water above the water table (Fig.1).

Table 1. Geotechnical characteristics of the soil.

	Fontainebleau sand	Speswhite kaolin	40% kaolin 60% sand
C400 µm (%)	100	100	100
Fines content (%)	0.01	100	40
Clay content (% < 2 µm)	0	77	31
Liquid limit, wL (%)	-	55.1	25
Plastic limit, wP (%)	-	32.3	14
Plasticity Index, Ip (%)	-	22.8	11
Methylene blue abs. (g/100 g)	0.1	1.54	0.6
ρs (g/cm^3)	2.64	2.65	2.65
Std Proctor opt. w (%)	7	29	13.5
Std Proctor opt. MDD (g/cm^3)	1.51	1.42	1.87
Std Proctor opt. Sr (%)	24.7	88.7	85.8

2.2 *Single and double oedometer tests*

Collapse is a wetting induced phenomenon, which must be studied by describing accurately the effects of both inundation and vertical stress.

After sand and clay are mixed, tap water is added to reach the required water content. The material is kept in sealed bags during, at least, twenty-four hours. After curing time, the specimens are compacted directly in the oedometer cells (70-mm diameter and 19-mm thick) using a miniaturized dynamic hammer (Ferber *et al.*, 2008). Thus, the dry density is directly related to the number of blows of the hammer, i.e., to the compaction energy.

The tests consist in loading and/or soaking the specimens according to three different paths (Fig. 2):

– Loading unsaturated specimen at a constant water content (path 1), simulating the embankment construction;

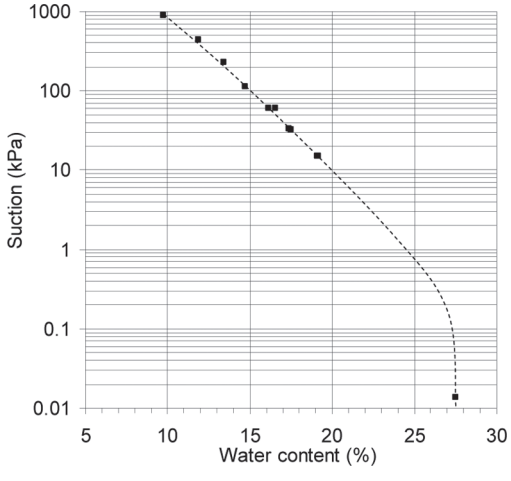

Figure 1. SCM water retention curve.

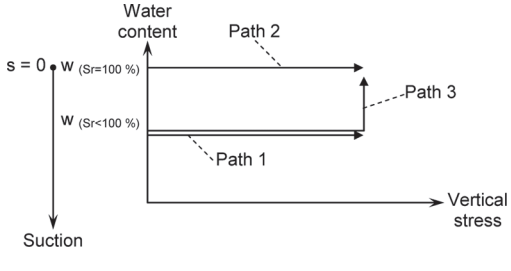

Figure 2 Hydro-mechanical paths.

– Loading saturated specimen (path 2) according to the conventional oedometer test;
– Soaking specimen after loading at a given vertical stress (path 3) to simulate the inundation of compacted fills occurring via, for instance, flooding.

Regarding path 1, the water content is kept constant during the test by protecting the cells from the ambient air using a plastic membrane (Delage & Fry, 2000). The increase in vertical stress is obtained by loading the frame with increasing masses. The specimen mass is measured before and after the test to determine water content variations, showing a decrease of 0.5 points at the highest water content (e.g., from 11 to 10.5%). The degree of saturation corresponding to a water content of 11% is 39% for an initial void ratio of 0.75 and 43% for e = 0.68.

Path 2 corresponds to a conventional oedometer test carried out on a soil compacted at a given water content and a given compaction energy, then loaded under a 3-kPa vertical stress, and finally soaked. Very small deformations result from this saturation since the soil is not expansive. The mechanical load is applied when all deformations are completed.

Paths 1 and 2 correspond to the elementary tests of the double-oedometer test procedure.

Path 3 is performed on specimens compacted at different dry densities but at the same water content. On the specimens are applied six different vertical loads between 3 and 800 kPa. These vertical stresses correspond to the stress undergone by a material found at the base of an approximately 40-m high embankment. The initial void ratio range between 0.39 and 0.74 corresponds to initial dry densities between 1907 kg/m^3 and 1526 kg/m^3.

The unsaturated and saturated oedometer tests results are plotted together in Fig. 3.

The unsaturated tests present a substantial pre-consolidation stress (400 to 800 kPa). It is the limit between the elastic (for low stresses) and plastic (for high stresses) zones, which is typical of the unsaturated behaviour of low plasticity compacted soils (Alonso *et al.*, 1990). The elastic compression index, which corresponds to the slope of the curve for a vertical stress lower than the pre-consolidation stress, is 0.01, whereas the plastic compression index determined from the data obtained at 800 and 1400 kPa, is 0.25. The unsaturated curves are located "above" the saturated curves for vertical stresses higher than 30–60 kPa. It shows that, above this threshold, the specimen is subject to settlements if water is added. On the contrary, below 30 kPa, swelling occurs with the addition of water.

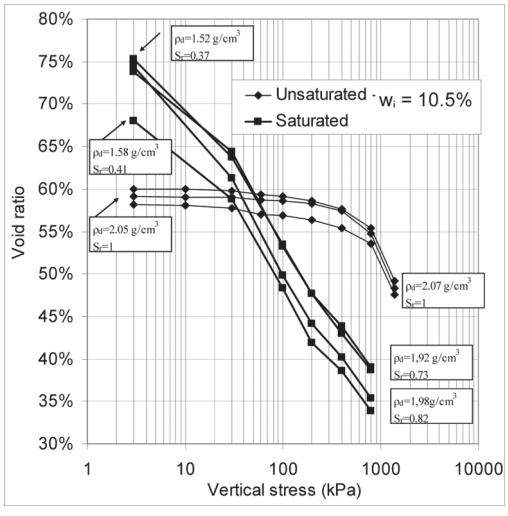

Figure 3. Double-œdometer tests on the compacted SCM.

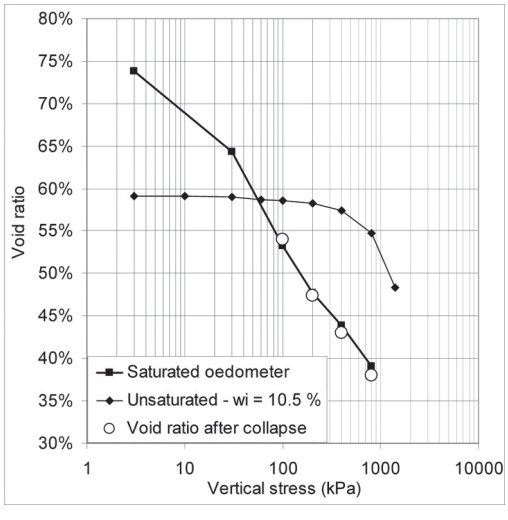

Figure 4. Comparison between the results of single and double oedometer tests.

When the final void ratio after collapse of loose specimens, obtained by single-oedometer tests according to path 3, is plotted versus vertical stress (Fig.4), the data are found on the compression curve of the saturated oedometer test.

This means that the conventional compression curve of the saturated oedometer test can be used to predict the void ratio after collapse and, consequently, the collapse deformations.

3 CENTRIFUGE TEST PREPARATION AND PROCEDURE

A two-dimensional SCM embankment scale model, represented on the 1/100 scale, is inundated during a centrifuge flight at 100 g.

3.1 *Experimental set up and preparation*

For the purposes of the experiment, a two-dimensional half cross-section of the embankment, which is assumed symmetrical, is built (Fig. 5) inside a strongbox consisting of:

- a main 20-cm wide and 60-cm long compartment, in which the material is compacted;
- some lateral compartments communicating with the main compartment, in which the height of water can be measured;
- a transparent wall in the main compartment, which is used to film the model during the test.

A 2-cm thick sand layer, surrounded by a geotextile, is laid on the strongbox bottom. This draining layer is used to simulate the water table rise below the embankment base before the inundation event. The SCM, with a water content of 10.5%, is compacted on the "dry side" of the Proctor curve in seven successive layers, each approximately 3 cm thick.

Each layer is compacted with 96 blows of a conventional standard Proctor hammer evenly distributed on the surface (Fig. 6). Loosely compacted material is needed here to emphasize the displacement phenomena caused by wetting.

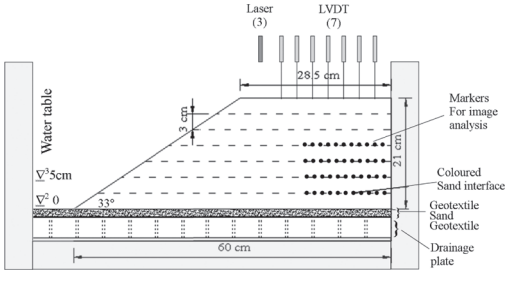

Figure 5. Cross-section of the embankment model in the strongbox.

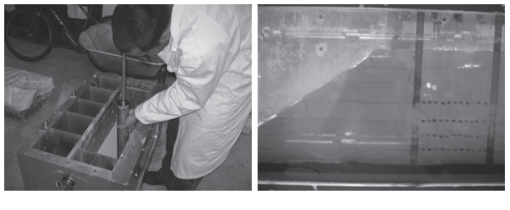

Figure 6. Compaction and final shape of the model cross-section (black points are the reference pins for local displacement measurements).

At the interface between each layer, circular pins are placed close to the transparent wall as geometrical reference points (Fig. 6). The image analysis makes it possible to follow the point displacements using a specially-dedicated LCPC piece of software (Thorel *et al.*, 2000). The results correspond to the mean value of the vertical displacement of the pins of each row.

After compaction, the structure is carved manually to form a slope of 33°, a classical inclination for actual road embankments filled with the same material (Fig. 6). The final lengths of both crest and base are 28.5 cm and 60 cm, respectively. The corresponding prototype embankment would be scaled by a factor 100 (Garnier *et al.*, 2007).

The water level (0 and 5 cm from the base of the embankment) is controlled using a Mariotte bottle (Thorel *et al.*, 2002) connected to the main compartment. The test is conducted according to three successive sequences: 1) no hydraulic connexion, 2) water table at the bottom of the embankment and 3) water table up to 50 mm above the base of the embankment.

The total displacement of the embankment crest is calculated using some laser transducers placed above the crest, at a few centimetres from the slope crest and an LVDT, regularly applied above the central part of the crest.

3.2 *Test sequences*

Three sequences simulating the stress states that embankment materials are susceptible to undergo, are described:

- Stress state 1—embankment construction with increasing vertical stress;
- Stress state 2—a possible water level rise beneath the embankment causing capillary rises;
- Stress state 3—a possible inundation event, leading to water infiltrations from both the slope and the base of the embankment.

These three stress states are simulated by three different sequences during the test:

- Phase 1—g-level application to the embankment model to increase the vertical stress in the soil;
- Phase 2—saturation of the sand layer under the embankment by maintaining the water table just above the sand-embankment interface level;
- Phase 3—inundation of the strongbox with a water table located 5 cm above the sand-embankment interface.

4 CENTRIFUGE TEST RESULTS

The objective of the centrifuge tests is to examine the wetting-induced settlements of the embankment model before comparison with laboratory results. The settlements are measured according to two different principles:

- for each layer, thanks to the reference points filmed by a camera placed in front of the transparent wall. Image analysis allows for the monitoring of the lowest four layers throughout a height of twelve centimetres;
- at the crest level.

The crest settlement due to inundation (for which the zero value corresponds to the beginning of the first inundation event, when the settlements have been stailized) are presented as measurements continuous with time (Fig. 7).

The first inundation event (phase 2) generates homogeneous settlements on the embankment crest. The second event (phase 3) generates more extensive settlements near the slope crest (laser sensors) because of a combination of lateral displacement. This lateral displacement combined to settlement has to be linked with the natural rotation of the stresses in the vicinity of the slope. Apparently, this phenomenon is not observed on the crest, far from the slope. This gives an indication that there is probably no rotation of the stresses in this zone, on which the study is focused on.

The average crest settlement shows that: 1) the saturation of the sand layer generates a 5-mm settlement; 2) the inundation with a water table of five centimetres generates an additional settlement of seven millimetres, re aching a total of 12-mm.

The image analysis gives more details on the settlement distribution within the layers (Fig. 8):

- the settlement of each layer increases with each inundation phase;
- the individual settlement of each layer increases with the depth of the layer. For instance, layer 1, located at the very base of the embankment presents a more extensive settlement than the three other layers. Conversely, the extent of the settlement of layer 4 is the less significant. Layer 3 appears as an exception, since its settlement is more extensive than the settlement of layer 2;
- the total settlement is 3.4 mm and 14.6 mm after the first and the second inundation sequences, respectively. These values are similar to the average values of 4.8 mm and 12 mm measured on the crest.

The inundation of the embankment generates extensive settlements due to the wetting-induced collapse behaviour of loosely compacted soils.

The maximum crest settlement after the last inundation sequence is higher than 12 mm (model scale), which corresponds to a 1.2-m settlement in a full-scale embankment. This value, probably due to the initial loose soil compaction rate (82% of the MDD), is not acceptable for a transportation embankment.

The settlement values (measured using transducers or image analysis) are consistent and increase with increasing depth and increasing water table height. This result is coherent considering that: 1)

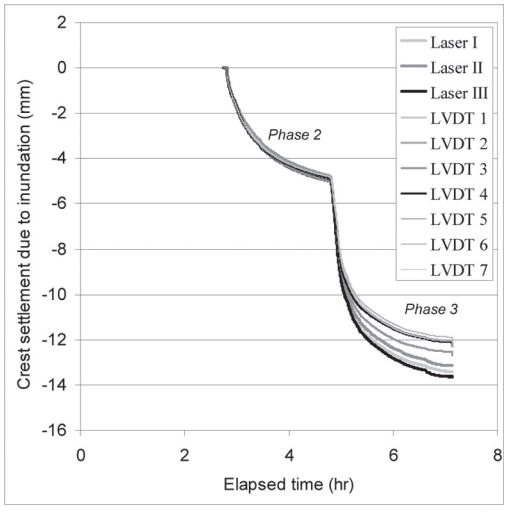

Figure 7. Cumulative crest settlement: focus on the inundation sequences (model time).

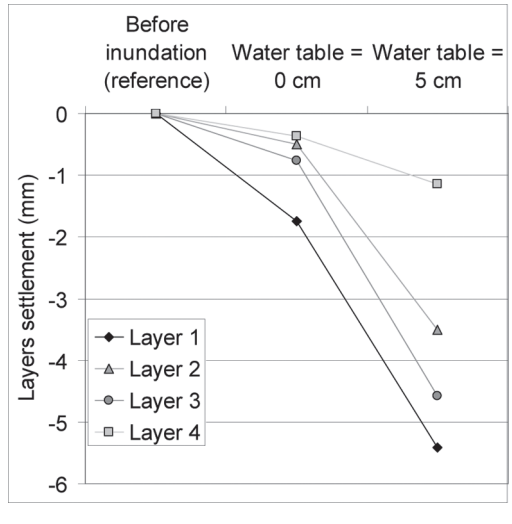

Figure 8. Layer settlement (variation in height) at the end of the two inundations measured by image analysis (model scale).

the vertical stress amplifies the deformation due to collapse; 2) the rise of the water table causes saturation, and consequently, the collapse of an increasing thickness of compacted material.

5 DISCUSSION

To compare void ratios obtained with the centrifuge test and with the oedometer tests, respectively, the following assumptions are made:

- In the embankment, only the zone far from the slope is taken into account;
- The dry density after compaction is equal to 1530 kg/m^3 in the embankment;
- The vertical stress, $\sigma(z)$, at a given depth, z, in the embankment, is related to the material height above this point by the initial density of the material. With a dry density after compaction of 1530 kg/m^3 and a water content of 10.4%, the wet bulk density, ρ, used for calculations is 1690 kg/m^3.

The variations of the void ratio observed during the different sequences (Fig.9) reveal that:

After the first inundation event (water table = 0 cm), the void ratio decrease is relatively small, and, except for the first layer, the value is very close to that of the void ratio predicted by the unsaturated oedometer test. Considering the high values obtained for crest settlement during this sequence (Fig. 7), layer 1 was probably already partly saturated because of capillary rises, which explains why the void ratio decrease is larger than the unsaturated oedometer test prediction (a difference of 0.2 mm is observed);

After the second inundation event (water table = 5 cm), the void ratio decreases in the three lowest layers because of the increasing water level. In the fourth layer, a limited decrease is observed, which can be explained by the fact that the capillary rise does not reach the full height of the fourth layer. The saturated oedometer test results give a good prediction of the final void ratio in layers 1 and 3 but a discrepancy occurs regarding the second layer.

A reasonable consistency is observed between oedometer and centrifuge tests. Assuming that the oedometer tests are representative of embankment settlements far from the slope (no horizontal displacements observed nor allowed), these tests are satisfactory for prediction. In the shallower zones and under the slopes, the stress ratio may notably modify performances (Lawton *et al.*, 1992), and this approach should not be used.

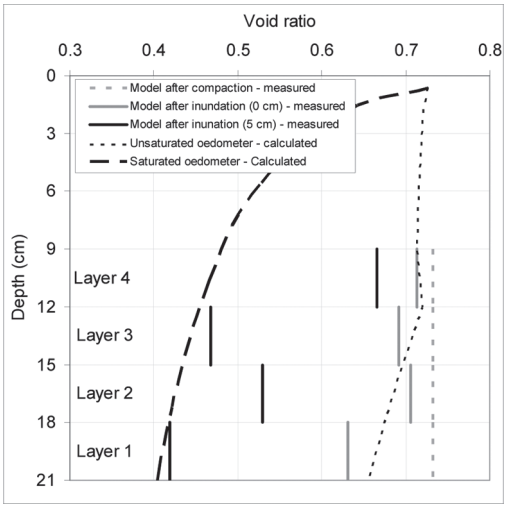

Figure 9. Comparison of void ratio measurements obtained with the centrifuge and œdometer tests (centrifuge model scale).

6 CONCLUSION

An inundation is simulated during a centrifuge test in two-dimensional geometry in order to examine the collapse behaviour of embankments. The test embankment model is built with a loosely compacted (82% MDD) clay-sand mixture to increase the collapse phenomenon. This material is studied by carrying out single and double oedometer tests.

The maximum water height reached during the inundation events is five centimetres, which causes 12-mm crest settlements at model scale (at full scale, a 20-m high field embankment subjected to a 5-m high inundation would settle by approximately 1 m).

It must be emphasized that the quality of the prediction depends mainly on the two following parameters: a) the height of the capillary rise; b) the dry density profile before inundation.

The settlements far from the slope (where there are no rotation of the stresses) can be roughly predicted on the basis of the double oedometer test. The method presented could also be used to define dry density objectives during the placement process depending on the embankment height. These objectives are given by the saturated oedometer test. The inundation simulation study conducted at the same time on a full scale embankment confirms the transposition potential of this approach (Vinceslas *et al.*, 2009). This method, however, would not be relevant for high plasticity clays (Ferber *et al.*, 2008) knowing that such soils are generally banned from common compacted fills.

REFERENCES

Auriol, J.C., Havard, H., Mieussens, C. & Queyroi, D. 2000. Résultats d'enquêtes sur la pathologie des remblais en service *Routes/Roads*, n°306, 57–74.

Alonso, E.E., Gens, A. & Josa, A. 1990. A constitutive model for partially saturated soils, *Géotechnique*, 40, 3, 405–430.

Basma, A.A. & Tuncer, E.R. 1992. Evaluation and control of collapsible soils. *J. of Geotech. Engng*, 118(10) 1491–1504.

Delage, P. & Fry, J.J. 2000. Comportement des sols compactés: apports de la mécanique des sols non saturés. *Revue française de Géotechnique*, N°92, 17–29.

El Sohby, M.A. & Rabbaa, S.A. 1984. Deformational behaviour of unsaturated soils upon wetting. P*roc. Eight Regional Conf. for Africa on Soil Mechanics and Foundation Engineering*, South African Inst. Civil Eng., Vol. 1, 129–137.

Estabragh, A.R., Javadi, A.A. & Boot, J.C. 2004. Effect of compaction pressure on consolidation behaviour of unsaturated silty soil. *Can Geotechnical Journal*, 41, 540–550.

El-Ehwany, M. & Houston, S.L. 1990. Settlement and moisture movement in collapsible soils. *J. Geotech. Engng*, 116(10).

Ferber, V., Auriol, J.C., Cui, Y.J. & Magnan, J.P. 2008. Wetting-induced volume changes in compacted silty clays and high-plasticity clays. *Can Geotechnical J.*, 45, 252–265.

Garnier, J., Gaudin, C., Springman, S.M., Culligan, P.J., Goodings, D., Konig, D., Kutter, B., Phillips, R., Randolph, M.F. & Thorel, L. 2007. Catalogue of scaling laws and similitude questions in geotechnical centrifuge modelling. *Int. J. Physical Modelling in Geotechnics*, 7, No. 3, 1–24.

Jennings, J.E. & Knight, K. 1957. The prediction of total heave from the double-oedometer test. *Transactions Symp. on Expansive Clays*, South African Inst. of Civ. Engng, 13–19.

LCPC. 2003. *Practical manual for the use of soils and rocky materials in embankment construction.* Techniques et méthodes des laboratoires des ponts et chaussées, LCPC Ed., ISSN 1151–1516, 60 p.

Lawton, E.C., Fragaszy, R.J. & Hetherington, M.D. 1992. Review of wetting-induced collapse in compacted soil. *Journal of Geotechnical Engineering*, 118, No. 9, 1376–1394.

Lim, Y.Y. & Miller, G.A. 2004. Wetting-induced compression of compacted Oklahoma soils. *Journal of Geotechnical and Geoenvironmental Engineering*, 130, No. 10, 1014–1023.

Miller, G.A., Muraleetharan, K.K. & Lim, Y.Y. 2001. Wetting-induced settlements of compacted-fill embankments. *Transportation Research Record,* 1755, 111–118.

Pereira, J.H.F. & Fredlund, D.G. 2000. Volume change behavior of collapsible compacted gneiss soil. *J. Geotech. & Geoenvironmental Engineering*, 126, No. 10, 907–916.

Rao, S.M. & Revanasiddappa, K. 2000. Role of matric suction in collapse of compacted clay soil. *Journal of Geotechnical and Geoenvironmental Engineering*, 126, No. 1, 85–90.

Rollins, K.M., Rollins, R.L., Smith, T.D. & Beckwith, G.H. 1993. Identification and characterization of collapsible gravels. *J. Geotechnical Engineering*, 120, No. 3, 528–542.

Thorel, L., Favraud, C. & Garnier, J. 2002. Mariotte Bottle in a Centrifuge: a device for constant water table level. Technical Note. *Int. J. Phys. Modelling Geotech,* 2, N°1, 23–26.

Thorel, L., Noblet, S., Garnier, J. & Bisson, A. 2000. Capillary rise and drainage flow through a centrifuged porous medium. *Int. Symp. Phys. Modelling & Testing in Env. Geotech, La Baule, 15–17 May 2000*. ISBN 2-7208-6050-6.

Thorel, L., Ferber, V., Caicedo, B., Khokhar, I.M. 2011. Physical modelling of the wetting-induced collapse of an embankment base. *Géotechnique* Vol. LXI, n°5, pp. 409–420.

Vinceslas, G., Khay, M., Sagnard, N. & Ferber, V. 2009. Moisture state variations on embankments located in flood zones: Instrumentation and behavioral monitoring of an experimental embankment. *Bulletin des Laboratoires des Ponts et Chaussées*, 274, 5–30.

This page intentionally left blank

Advances in Unsaturated Soils – Caicedo et al. (eds)
© 2013 Taylor & Francis Group, London, ISBN 978-0-415-62095-6

A practical method for suction estimation in unsaturated soil testing

M.F. Amaral & A. Viana da Fonseca
Department of Civil Engineering, University of Porto, Faculty of Engineering, Portugal

E. Romero & M. Arroyo
Department d'Enginyeria del Terreny, Universitat Politècnica de Catalunya, Barcelona Tech, Cartogràfica i Geofísica, Spain

ABSTRACT: This research presents an alternative methodology to estimate suction in triaxial tests carried out under constant water content. A preliminary determination of the retention curve is proposed using two complementary techniques, namely psychrometer measurements and mercury intrusion porosimetry results. Starting with the definition of a set of retention curves at different void ratios, an attempt is made for establishing a correspondence of the measured retention curves with the results of a high pressure isotropic compression test. From the stress-paths followed in a soil-cement specimen during isotropic compression, plotted in the void ratio—stress plane, the suction is interpolated by using the previously measured values and the evolution law describing suction as a function of the specimen's void ratio. For the aforementioned paths, the suction for all stress state points is estimated, including for the apparent yield pressure.

1 INTRODUCTION

It is recognized the difficulty of measuring and controlling suction in laboratory tests. Most standard techniques available in specialized laboratories, such as vapor transfer, axis translation and osmotic technique are time consuming and/or expensive (Ng et al., 2007). Indeed, they are not appropriate when the objective involves a considerable number of triaxial and/or oedometer tests in unsaturated conditions. For tests with suction control in hard soils—soft rocks or clayey soils it is not unusual to find triaxial tests taking between 1–6 months or more in the literature (Pineda, 2012). The present research is a small slice of a package with more than 30 isotropic compression tests under unsaturated conditions. Therefore, standard controlled suction tests would condition the experimental program accomplishment. Although it is not presented here, the objective of the research is to study the influence of water content (w), cement content (C) and void ratio (e) on the mechanical behavior of a specific soil. This fact promotes a large amount of isotropic and triaxial tests and originated the need for an efficient and quick suction monitoring.

Although temporally most economical, the suction measurement techniques are not always suitable for a wide suction range, for example, the suction evaluation with psychrometric measurements is only suitable for high suctions (higher than 1 or 2 MPa) [Romero et al. (1999), Romero & Simms (2008)]. Moreover, the axis translation technique is applied for low suction values (below 1 MPa) but these tests are known as time consuming and once again, they would delay the experimental program. As a result of this reduced overlapping range, it is indispensable to use alternative techniques to allow suction estimation for a larger bandwidth. Considering these factors the interest in more efficient suction measurements has grown among researchers.

This paper presents a triaxial test procedure based on the estimated suction, maintaining constant water content. It presents an empirical model that allows predicting suction as a function of cement content and void ratio for a silty soil remolded from granite residual soil of northern Portugal [Viana da Fonseca et al. (1997), Viana da Fonseca et al. (2009), Amaral et al. (2011a), Amaral et al. (2011b), Rios (2011)]. On one hand it is known that suction increases very steeply with interparticle cementation, while on the other hand, the retention curve is affected by the initial void ratio (e_0) of the samples, although for high suctions the effect of e_0 can be neglected.

For the fast and practical suction monitoring during isotropic compression tests, the retention curves were previously computed using two different methods. For low suction levels, the technique used was the mercury intrusion porosimeter (MIP) (Romero & Simms, 2008), while for high levels of suction (over 2 MPa), a chilled mirror dew point

psychrometer (WP4) was the selected method (Cardoso et al., 2007). This procedure allows covering all suctions in a range starting from 1 kPa up to 60 MPa. Retention curves are related to the pair of variables; cement content (C) and void ratio (e_0), allowing indirectly estimating suction for all stages of triaxial tests carried out in mixtures of soil-cement in unsaturated conditions.

2 EXPERIMENTAL PROGRAMME

2.1 *Soil characterization*

The soil used for this study is classified as a fine graded silty sand (SM), according to the unified classification with a specific gravity (G) of 2.72. Mineralogical analysis showed that the particles are predominantly kaolinite, with minor parts of mica and quartz. The grain size distribution (Amaral et al., 2012) shows an effective diameter (D_{50}) of 0.25 mm, and uniformity and curvature coefficients of 113 and 2.7, respectively. The Atterberg limits of the portion passing the #40 ASTM sieve reveals a liquid limit of 34% and a plastic limit of 31%, representing these values a practically non plastic soil. Maximum dry unit weight in Modified Proctor test is 18.9 kN/m^3 for a optimum water content (w_{opt}) of 13%. (Amaral et al., 2012).

A high strength Portland cement (CEM I 52.5 R), with G equal to 3.10, was used as cohesive agent to speed up the curing process and promote a fast stabilization of the soil-cement specimen's strength. Tap water was used for the specimen's compaction and cement hydration.

2.2 *Specimens preparation*

The tested specimens were molded to obtain cylinders with 50 mm diameter and 33 mm height, for MIP and WP4 tests and 50 mm diameter and 100 mm height, for the isotropic compression test. The hygroscopic water content was measured in the day before molding. Consequently, the amount of water to be added for the desired water content (w_{opt}) was defined. In the specimens preparation process the weight of fines was replaced with the quantity of cement to be added. Thus, the grain size distribution and Proctor compaction curve were maintained. The proportion of cement (C) and the water content (w) were calculated by dividing their weights with the dry soil weight.

The soil, cement and water were placed in a tray and mixed in order to get a fully homogeneous admixture. Then the mixture was placed in a cylindrical mold, which had an internal diameter of 50 mm, and was statically compressed until the required density. Samples for isotropic compression test (100 mm height) were compacted in three layers.

At the end of the described procedure, the assembled specimen was kept in a humid chamber. After 24 hours, the specimens were removed from the mold for weighing and measurement. Later, they were again placed in the humid chamber for another 27 days where they remained in curing. The tolerances for the specimen's acceptance were:

- Dry unit weight within ± 1% reference value;
- Water content within ± 0.5% reference value;
- Diameter within ± 0.5 mm;
- Height ± 1 mm.

After 28 days of curing, the specimens were removed from the humid chamber. Those samples that were prepared for isotropic compression tests were installed in the triaxial cell after a vapor equilibrium procedure (to dry/wet the specimens). The specimens aimed at the dew point psychrometer tests were trimmed to cylinders of approximately 30 mm diameter and 10 mm height. As for the MIP tests, a cube with 1 cm^3 was the final specimen's shape. Prior to pursue the MIP tests, the samples were dried using infrared light.

2.3 *Testing program*

The following tests were performed:

i An isotropic compression test in a triaxial cell (T) over a specimen of soil-cement (5%) with constant water content approximately equal to 16%.
ii 6 MIP tests (M) on two distinct percentages of cement content (0 and 5%) at different void ratios.
iii Two tests with the dew point psychrometer (W) which were necessary to interpolate at intermediate values of the retention curve [1, 2 MPa] and at both 0 and 5% cement contents.

The characteristics of the samples are presented in Table 1. γ_d is the dry unit weight, e_{micro} and e_{macro}, are the micro and macro void ratio, respectively, determined from MIP, and interpreted as shown in Figure 1.

In the MIP technique an absolute pressure (p) is applied to a non-wetting liquid (mercury) to enter the empty pores.

$$p = -\frac{4\sigma_{Hg}\cos(\theta_{nw})}{d} \quad (1)$$

where σ_{Hg} is the surface tension of mercury (0.484 N/m at 25ºC), θ_{nw} the contact angle between mercury and the pore wall and d the entrance pore diameter.

Table 1. Main characteristics of the tested specimens.

Specimen	Test type	c (%)	e	e_{micro}	e_{macro}	γ_d (kN/m^3)
M1	MIP	0	0.748	0.105	0.643	15.26
M2	MIP	0	0.581	0.108	0.473	16.88
M3	MIP	0	0.452	0.110	0.342	18.38
M4	MIP	5	0.544	0.251	0.293	17.38
M5	MIP	5	0.457	0.245	0.212	18.41
M6	MIP	5	0.511	0.249	0.262	17.76
W1	WP4	0	0.753	0.108	0.645	15.22
W2	WP4	5	0.585	0.248	0.337	16.93
T1	Triaxial	5	0.569	0.248	0.322	17.10

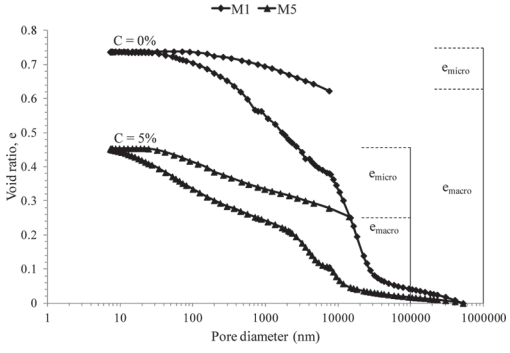

Figure 1. Determination of e_{micro} and e_{macro} values.

The injection of non-wetting mercury was assumed to be equivalent to the ejection of water by the non-wetting front advance of air (drying branch) for the same diameter of pores being intruded. Thus, p and matric suction (s) can be related by capillary equilibrium (Washburn's equation) as follows.

$$s = p\frac{\sigma_w \cos(\theta_w)}{\sigma_{Hg} \cos(\theta_{nw})} \quad (2)$$

where σ_w is the surface tension of water (0.072 N/m at 25ºC) and θ_w the contact angle between water and the pore wall.

From the analysis of the results in Table 1 it is possible to conclude that the value of e_{micro} does not depend on the initial void ratio, resulting from the compaction, i.e., during this process there is only a change in the macro voids (only e_{macro} varies). The changes in the values of e_{micro}, for specimens with distinct cement contents, are mostly due to the presence of more or less bonding agent. Samples with higher cement content present higher values of e_{micro}: (ex. W1 vs. W2, in Table 1).

2.4 *The inclusion of the suction factor*

The suction estimation in triaxial tests on non-saturated soils, from the assumption of the constancy of moisture content, is fairly reliable for low values of suction or for high degrees of saturation, corresponding to values below the air entry point. Figure 2 illustrates the retentions curves immediately calculated from MIP results for 5% cement content and shows a clear dependency on void ratio in the very low suction range. In the same figure, W2 test is also plotted.

Water saturation and the degree of mercury are related. Therefore, the specimens porosity (n), assumed as unaltered during mercury intrusion, the intruded porosity (n_v) and the specimen's water content can be related trough (Prapaharan et al., 1985).

$$w = \frac{1}{G}\frac{n - n_v}{1 - n} \quad (3)$$

According to the previous equation, the soil-water characteristic curve can be plotted. The interpolation area is defined according to Romero et al. (2011).

Figure 3 indicates that there are ranges of moisture/water content values that depend on the actual void ratio (e) value. Therefore, it is necessary to define a law that allows the verification of the variation of suction with the void ratio. This condition is determinant for low values of e, since its decrease tends to increase the air entry value. The shape of those laws is outlined in Figure 3.

Figure 3 can be constructed by determining s values which directly cross the vertical constant water content line represented in Figure 2. As observed in the figure, for void ratios larger than

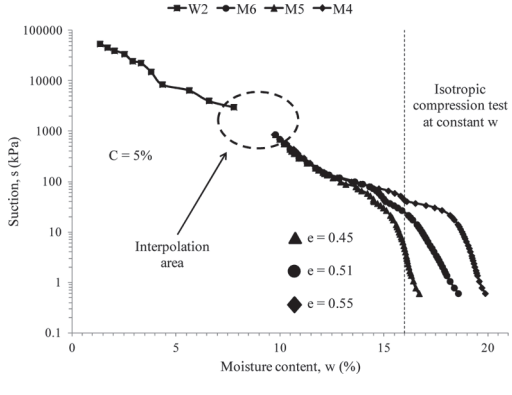

Figure 2. Retention curves for specimens with C = 5%, where a moisture content range is lacking for specific suction values.

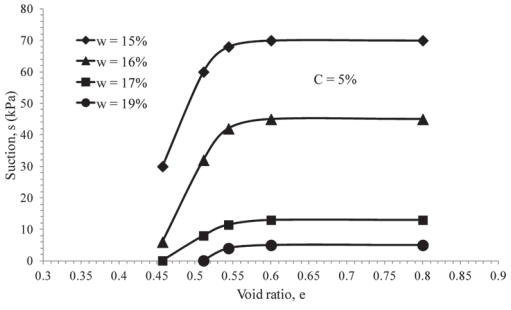

Figure 3. Suction variation with void ratio for distinct values of moisture content.

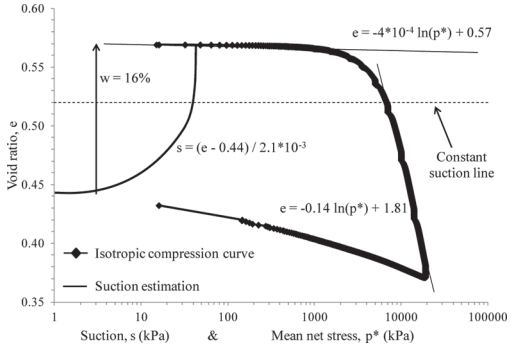

Figure 4. High pressure isotropic compression test under constant water content and derived suction curve.

0.54, the suction water content relationship can be considered not affected by void ratio.

From the analysis presented in Figure 3, it seems there is a void ratio value which establishes a suction increase stoppage. This limit, for the applied water content, is equivalent to the suction defined in the retention curve of the soil's maximum void ratio.

3 ISOTROPIC COMPRESSION TEST

The procedure described above has as main objective the suction determination not only for the apparent yielding pressure but also along all stress states of the isotropic compression curve.

After the specimen T1 removal, from the humid chamber, it was moistened (to improve w = 13% to w = 16%) and assembled to a Hoek type high pressure triaxial cell. The back pressure, in the specimen pores (BP), was kept at around 0 kPa. The sample remained for 24 hours under a mean net pressure (p^*) of 10 kPa, defined by:

$$p^* = \frac{(\sigma_1 - u_a) + 2(\sigma_3 - u_a)}{3} \quad (4)$$

where u_a is the air pressure.

The isotropic compression test ($\sigma_1 = \sigma_3$) was undertaken up to high pressures. The increase in confining pressure was performed by steps, with a constant stress rate between them (0.5 kPa/s), where u_a was kept almost constant at 0 kPa. The use of steps allowed a stabilized u_a and water pressure (u_w). The maximum confining pressure was of 19 MPa. Figure 4 shows the isotropic compression test results for the tested specimen with constant water content. Jointly, the suction estimation curve is presented.

From the analysis of the curves presented in Figure 4, it is concluded that for void ratios greater than approximately 0.52, the suction values are kept constant once it is not changed the moisture content. However, below this value, the suction is strongly conditioned by the specimen's updated void ratio. As a consequence, it is required to estimate this variation by using an equation similar to the linear one shown in Figure 4. It can also be inferred, from those results, for void ratios bellow 0.44, the specimen T1 remains saturated and water content is no longer constant under drained conditions. This situation could be visually checked while water was expelled from the specimen for confining pressures close to 15000 kPa. However, these stress levels are on the far away from the yielding net pressure.

Models such as those presented by Alonso & Gens (1993) and Alonso et al. (1994) formulate the yield surface of unsaturated cemented soils by fundamental variables such as yielding and suction. The methodology proposed here allows a very effective and accurate way of determining both variables, allowing a very practical methodology for such models application.

4 CONCLUSIONS

This research proposes an alternative methodology to evaluate fundamental variables for modeling unsaturated cemented soils. The method is based on performing isotropic compression tests on soil-cement specimens at constant water content, which allows reducing significantly testing time. The technique proved to be very competent and relatively easy to apply.

In parallel, the analysis of the retention curves patterns determined for specimens with and without cement, allowed to demonstrate that, first, the degree of compaction does not influence the micro voids, and, secondly, the amount of cement greatly influences the magnitude of the micro void ratio.

Concerning the high suction retention curves, measured with the dew-point psychrometer, they were calculated on a MIP result validation prospective. The interpolation area (in the ranges where both the suction devices are not appropriate) proved that the laws defined by dew-point psychrometer and MIP technique may be extended via a single logarithmic-linear segment.

ACKNOWLEDGEMENTS

This research was developed under the activities of FCT (Portuguese Foundation for Science and Technology) research unit CEC, in FEUP [PTDC/ECM/099475/2008], and financed by the European Community (QREN/UE/FEDER), Operational Program for Competitive Factors "COMPETE".

REFERENCES

Alonso, E.E., Gens, A. 1993. On the mechanical behavior of arid soils. *Proc. 1st Int. Symp. of Eng. Characterization. Arid soils*, London, UK. pp. 173–205.

Alonso, E.E., Gens, A., Gehling, W.Y.Y. 1994. Elastoplastic model for unsaturated expansive soils. *Proc. 3rd European conference of Numerical methods for geotechnical engineering*. Manchester. RU. pp. 11–18.

Amaral, M.F., Viana da Fonseca, A., Arroyo, M., Cascante, G., Carvalho, J. 2011a. Compression and shear wave propagation in cemented-sand specimens. *Géotechnique Letters*. Vol. 1, No. 3, pp. 79–84.

Amaral, M.F., Viana da Fonseca, A., Carvalho, J., Consoli, N.C. 2011b. Dynamic Poisson ratio analysis. *Proc. 15th European Conf. Soil Mech. Geotechnical Eng.* CD-Rom: pp. 115–120.

Amaral, M.F., Rios, S., Viana da Fonseca, A. 2012. Yielding in the isotropic compression of Porto silty sand. *Acta Geotechnica Slovenica*. Vol. 9, No. 1, pp. 31,45.

Cardoso, R., Romero, E., Lima, A., Ferrari, A. 2007. A comparative study of soil suction measurement using two different high-range psychrometers. Proc. 2nd Int. Conf. Mechanics of Unsaturated Soils, Weimar, Germany, March 7–9, 2007. Experimental Unsaturated Soil Mechanics. T. Schanz (ed.). Springer Proceedings in Physics, 112. Springer-Verlag, Berlin: 79–93.

Ng, C.W.W., Chiu, C.F., Chen, R., Delage, P. 2007. The axis-translation and osmotic techniques in shear testing of unsaturated soils: a comparison. *Soils and Foundations*. Vol. 47, No.4, pp. 678–684.

Pineda, J. 2012. Experimental and constitutive study in expansion and degradation of clayey soft rocks. PhD. Thesis. Polytechnic University of Catalunya, Spain.

Prapaharan, S., Altschaeffl, A.G., Dempsey, B.J., 1985. Moisture curve of a compacted clay: mercury intrusion method. *J. Geotech. Eng.* ASCE. Vol. 111, No. 9, pp. 1139–1143.

Rios, S. 2011. A general framework for the geotechnical characterisation of artificially cemented soil. DSc. Thesis. University of Porto, Portugal.

Romero, E. 1999. Characterization and thermo-hydro-mechanical behaviour of unsaturated Boom-clay: An experimental study. PhD. Thesis. Polytechnic University of Catalunya, Spain.

Romero, E., Della Vecchia, G., Jommi, C. 2011. An insight into the water retention properties of compacted clayey soils. *Géotechnique*. Vol. 61, No. 4, pp. 313–328.

Romero, E., Gens, A., Lloret, A. 1999. Water permeability, water retention and microstructure of unsaturated Boom clay. *Engineering and Geology*. Vol. 54, pp. 117–127.

Romero, E., Simms, P.H. 2008. Microstructure investigation in unsaturated soils: a review with special attention to contribution of mercury porosimetry and environmental scanning electron microscopy. *Geotechnical and Geological Engineering*. DOI: 10.1007/s10706-008-9204-5.

Viana da Fonseca, A., Caberlon Cruz, R., Consoli, N. 2009. Strength properties of sandy soil-cement admixtures. *Geotechnical and Geological Engineering*. Vol. 27, No. 6, pp. 681–686.

Viana da Fonseca, A., Matos Fernandes, M., Silva Cardoso, A. 1997. Interpretation of a footing load test n a saprolitic soil from granite. *Géotechnique*. Vol. 47, No. 3, pp. 633–651.

This page intentionally left blank

Advances in Unsaturated Soils – Caicedo et al. (eds)
© 2013 Taylor & Francis Group, London, ISBN 978-0-415-62095-6

Preparing unsaturated samples of decomposed granite for laboratory controlled CPTs

H. Yang & A.R. Russell
Centre for Infrastructure Engineering and Safety, School of Civil and Environmental Engineering, The University of New South Wales, Sydney, Australia

ABSTRACT: This paper focuses on the development of a procedure for the formation of large unsaturated samples made of decomposed granite in the UNSW calibration chamber for conducting laboratory controlled Cone Penetration Tests (CPTs). Static compaction was used, and the attainment of the target suction using axis translation was quickened following the development of a radial drainage system incorporating Geotextiles wrapped around the sample in the chamber. The CPT results shown, along with the moisture content profiles, indicate improved uniformity of samples and the success of the procedure.

1 INTRODUCTION

The CPT is often used by engineers to estimate the density, stiffness and shear strength parameters of soils (Lunne et al., 1997). The results of the CPT and their link to soil properties are usually analyzed through empirical or semi-theoretical solutions. As calibration chambers allow researchers to fully control the stress and strain history, boundary conditions, density and moisture content of the test beds, performing CPTs in chambers is often preferred over field conditions when developing the solutions.

Methods to prepare large samples for calibration chamber testing include slurry consolidation for clays (e.g. Sheeran & Krizek, 1971; Huang et al., 1988; Anderson et al., 1991; McManus & Kulhawy, 1991; Kurup et al., 1994) and pluviation for sands (e.g. Brandon et al., 1991). The compaction method has also been used, although is not well documented.

Each of the methods has been used to form saturated soil samples. For unsaturated soil samples, only two calibration chamber studies have been documented (Pournaghiazar et al., 2011; Tan, 2005). Pournaghiazar et al. (2011) used the pluviation method to place dry clean sand into a calibration chamber and then achieved the target suction by firstly saturating the sample by flushing with water and then using the axis translation technique (Hilf, 1956). Miller et al. (2002) and Tan (2005) used the static compaction method to place a silty sand in a chamber at a prescribed moisture content with reference to the pre-obtained soil-water characteristic curve to get the target suction, but post-test analysis showed that the density along the depth of the sample followed a sinusoidal curve.

The purpose of this study is to form large unsaturated samples of a decomposed granite (sand-silt-clay mixture) in a calibration chamber using static compaction, with a view to overcome some of the difficulties experienced by Tan (2005). Particular attention will be given to the uniformity of density and moisture content throughout the sample.

2 TEST SOIL

2.1 *Index properties*

The soil used in this study is decomposed granite from the catchment area of Lyell dam, NSW, Australia. It is classified as a silty sand (SM) according to the Unified Soil Classification System. Index properties are listed in the table 1, and a particle size distribution curve is shown in figure 1.

2.2 *Static compaction*

Static compaction tests were first conducted at bench scale to obtain compaction curves. Soils were firstly oven dried and then mixed with prescribed amounts of distilled water. Soil was then compacted into a 50 mm diameter mould in five layers, so the final compacted thickness of each layer was 20 mm. Specimens were weighed after compaction to calculate the dry density. Different compaction pressures were used to compact the soil and three compaction curves corresponding to static pressures of 60 kPa, 210 kPa and 600 kPa are shown in figure 2 to highlight the difference in the dry densities achieved.

Table 1. Index properties of Lyell dam soil.

Property	Value
Liquid Limit, %	15.2
Plastic Limit, %	N/A
Plasticity Index, %	N/A
Specific Gravity	2.55
Gravel, %	0
Sand, %	72.84
Fines, %	27.16
Clay Size Fraction, %	4.35
Unified Soil Classification System Classification	SM

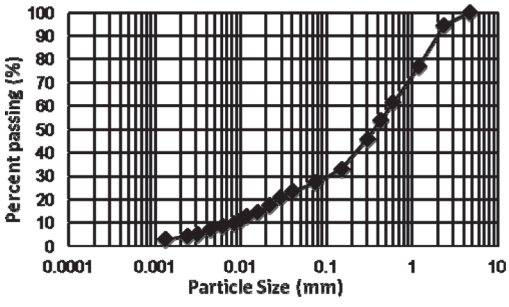

Figure 1. Particle size distribution curve.

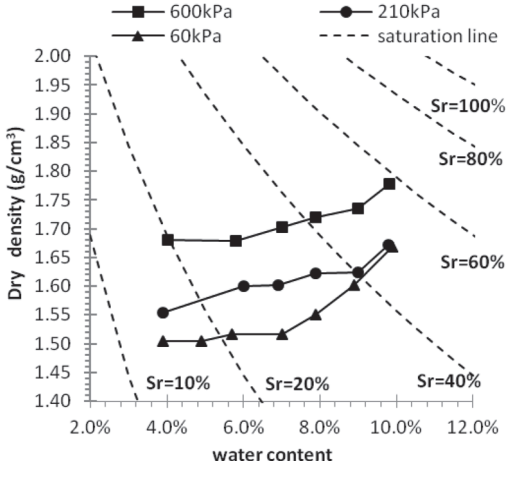

Figure 2. Static compaction curves.

2.3 *Soil water characteristics*

Soil-water characteristic curves were obtained using a pressure plate. Details of the equipment are given by Russell (2004). Nine specimens for use on the pressure plate were prepared (each being 50 mm dia. and 25 mm thickness) at three different void ratios by compacting them at the same moisture content but different static compaction pressures. Specimens were not saturated before pressure plate testing to avoid volumetric collapse. The testing involved increasing suction in increments until 450 kPa was reached (drying), then reducing suction in increments (wetting). Seven days were found to be sufficient for each increment to reach water equilibrium. The results are presented in figure 3 showing the moisture content vs. applied suction.

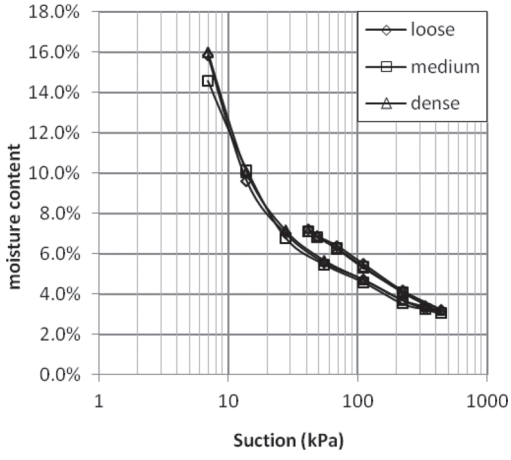

Figure 3. Soil-water characteristic curves, in the moisture content vs. log of suction plane. Loose indicates an initial void ratio of 0.68, medium an initial void ratio of 0.59 and dense an initial void ratio of 0.50.

3 TEST SETUP

3.1 *Calibration chamber system*

The UNSW calibration chamber used here was designed by Pournaghiazar et al. (2011). Key improvements over other designs include a novel sample formation system, a modified axial load application system and measurement and control of suction within the system. A cross section of the calibration chamber is shown in figure 4 and the control system is shown in figure 5.

In forming a sample soil was compacted directly into the chamber using a circular metal piston having a diameter of 450 mm, slightly less than the inner 460 mm diameter of the chamber.

The cone used in the testing was a miniature electrical cone, manufactured by A.P van den Berg (model ELC2), with diameter of 16 mm and cone tip area of 2 cm^2.

The machine used to push the cone was a HY-SON 100 kN single cylinder static cone

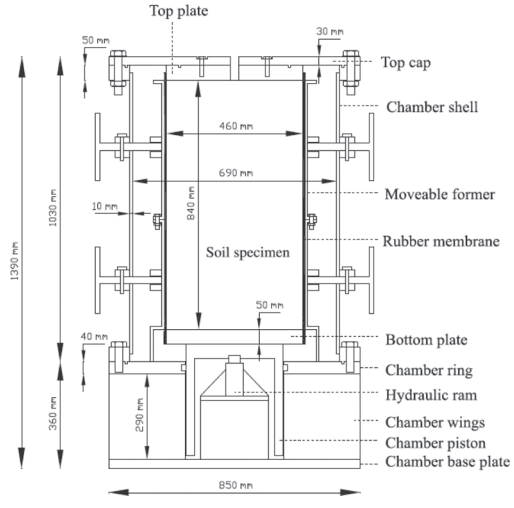

Figure 4. Cross-section of calibration chamber (after Pournaghiazar et al., 2011).

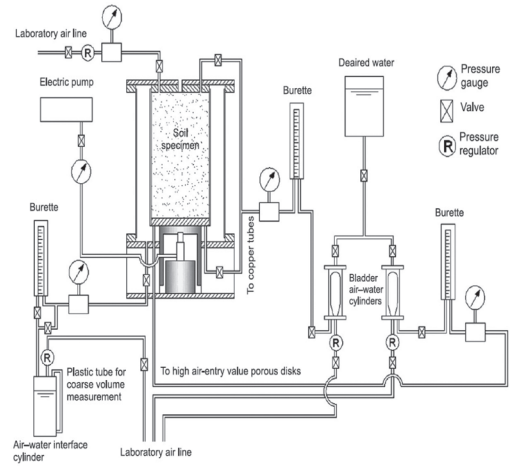

Figure 5. The calibration control system (after Pournaghiazar et al., 2011).

penetrometer powered by a petrol-driven power pack. A constant pushing rate of 0.2 to 2 cm/s was used. During the test the cone penetration resistance qc was recorded.

3.2 *General test procedure*

Before assembling the chamber, the High Air-Entry (HAE) ceramic discs embedded in the base plate were saturated under a pressure of 20 kPa for more than 24 hours. To ensure better contact between the soil and the HAE discs, a thin layer (about 3 mm) of kaolin was smeared across the top of the discs.

Then a rubber membrane of 8 mm thickness was fastened to the bottom plate using a 25 mm wide hose clamp. Once the membrane was in place, an o-ring coated with silica grease was carefully pushed into the groove at the base, and the chamber shell was bolted onto that.

A feature of the calibration chamber design is the four movable formers which can be fastened together to make a rigid cylindrical mould in which a sample can be compacted, preventing side bulging during compaction.

Soils were statically compacted to the target dry densities in thin layers. The surface of a compacted layer was scarified prior to compaction of the next layer. Seven layers in total were compacted. The first (bottom) layer had a thickness of 140 mm after compaction, while the six other layers had a post-compaction thickness of 110 mm. After compacting the seventh layer, 50 mm of gravel was put in place on top of the sample to ensure that the air pressure applied to the sample as part of the axis translation technique could evenly distribute across the top surface.

Another hose clamp was used to fasten the membrane to the top cap, after which the top cap was bolted to the shell with o-rings in between.

Vertical pressure and cell pressure were then applied, and to prevent localized drying near the top of the sample air was passed through a water bath cylinder as also done by Pournaghiazar et al. (2011). The vertical pressure, cell pressure and the air pressure were then increased in steps to target values and the axis translation technique was applied to achieve the target suction. The volume of water exiting through the base of the sample was recorded to indicate the rate of water expulsion.

3.3 *Assessing uniformity of soil samples*

The uniformity of a prepared soil sample was investigated by observing the uniformity of the cone penetration resistance profile and moisture content with depth. The moisture content was determined on sub samples obtained by coring post-test using a hand auger.

4 TEST RESULT

Two CPTs were conducted in two samples. After compaction each sample was subjected to a cell pressure of 200 kPa, vertical pressure at sample base of 160 kPa and pore air pressure (at the top) of 100 kPa and pore water pressure (at the ceramic discs) of 0 kPa, corresponding to a target base

vertical net stress of 60 kPa, target net cell pressure of 100 kPa and suction of 100 kPa.

After periods of allowing water to drain from the base of the samples, CPTs were performed in the centre of the sample at a rate of 1 cm/s. The boundary condition is illustrated in figure 6. And boundary influences are discussed in detail in Pournaghiazar et al. (2012a, 2012b).

During the application of suction and subsequent CPTs, a specially designed bush cylinder was positioned at the center hole of the chamber top cap to create a seal around the cone (Pournaghiazar et al., 2011).

4.1 *Test one*

For this test the sample was compacted at a static pressure of 60 kPa and moisture content of 6.15%. A dry density of 1.53 g/cm^3 (void ratio of 0.67) was targeted during compaction which is considered to correspond to a loose condition.

The cell, vertical and air pressures mentioned above were applied, and suction was induced. After 350 hours, the water exiting the sample had slowed considerably to a rate of 2.5 ml/hr. The sample volume change was recorded during this and the void ratio reduced to 0.64. The CPT was then performed and the result is shown in figure 7.

As shown, the cone penetration resistance is almost constant at depths ranging from 0.3 m to 0.5 m, where top and bottom chamber boundary influences are negligible (Pournaghiazar et al., 2011), although a slight increase in resistance with depth is observed in this depth range. The near uniform cone penetration resistance, in particular the absence of a sinusoidal pattern, indicates that the distribution of density is uniform and that

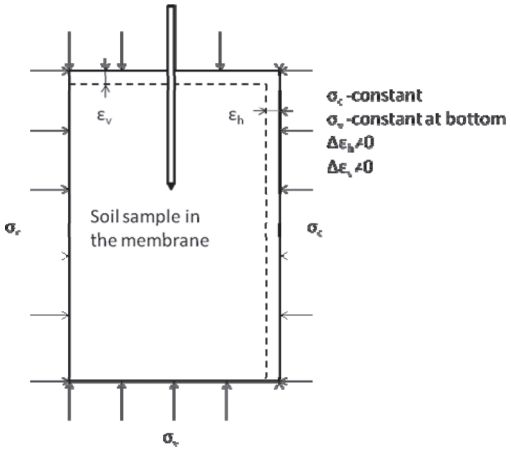

Figure 6. Boundary conditions.

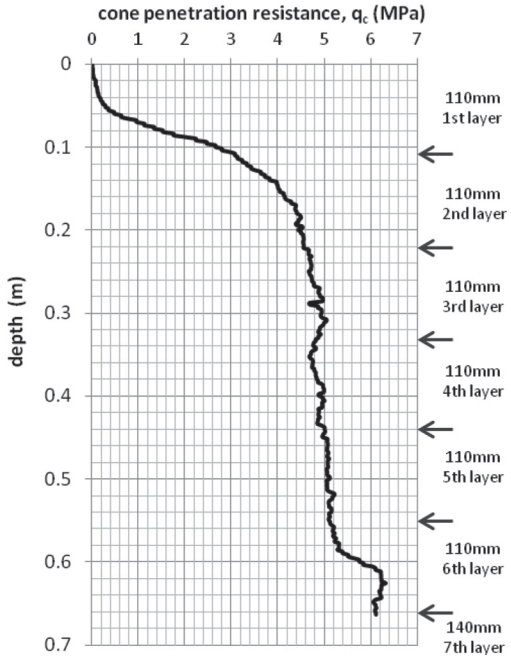

Figure 7. CPT result for test 1 with compaction layers indicated.

layering effects caused by static compaction are negligible or non-existent. However, as shown in figure 8, the distribution of moisture content has a slight gradient, being 5.8% at 0.3 m and 5.4% at 0.5 m, indicating moisture equilibrium had not been fully reached after 350 hours. The moisture gradient corresponds to a slight increase of suction with depth, and this may be the cause of the slight increase of cone penetration resistance with depth (4.9 MPa at 0.3 m to 5.1 MPa at 0.5 m).

4.2 *Test two*

In this test, to hasten moisture equilibrium being reached, strips of Geo-textiles were placed along the sides of the sample to permit radial drainage in addition to vertical drainage. Figure 9 shows the inside of the membrane with Geo-textile strips in position immediately prior to placement and compaction of soil.

The strips were submerged in distilled water and saturated prior to being taped onto the rubber membrane. The ends of the strips were laid horizontally across the top of the thin clay layer smeared across the ceramic discs.

Similar to test 1, the sample was compacted at a static pressure of 60 kPa and moisture content of 6.1%. A dry density of 1.53 g/cm^3 (void ratio of

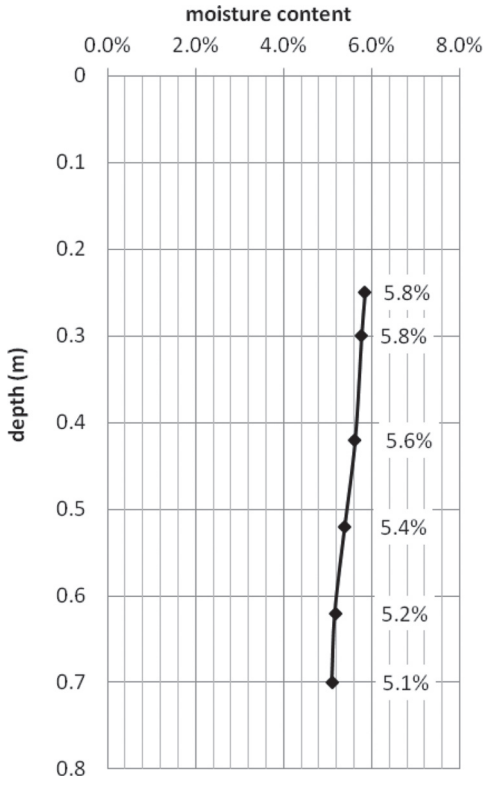

Figure 8. Moisture content distribution for test 1.

Figure 9. Cross section of the membrane with Geotextiles.

0.67) was targeted. After 592 hours, the water exiting the sample had slowed considerably to a rate of 1.7 ml/hr. The sample volume change was recorded during this and the void ratio reduced to 0.63. The CPT was then performed and the result is shown in figure 10 and the moisture content distribution in figure 11.

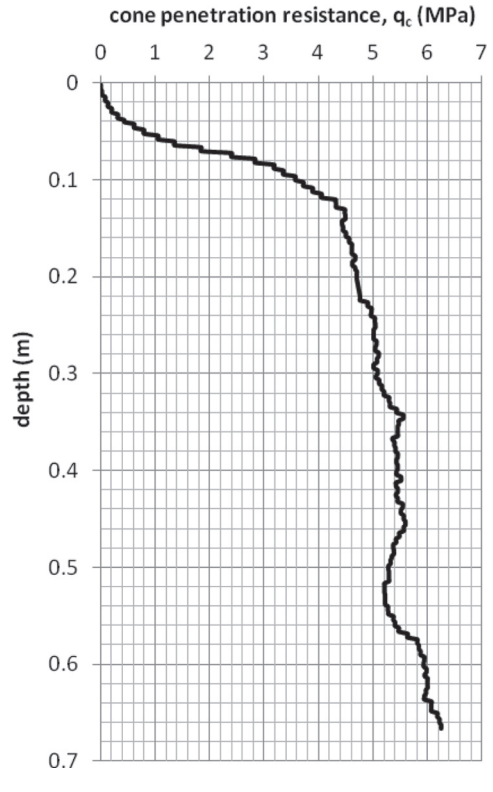

Figure 10. CPT result for test 2.

Again the cone penetration resistance is quite uniform between depths of 0.3 m and 0.5 m, increasing slightly from 5.2 MPa to 5.4 MPa. Again no sinusoidal pattern was observed.

The moisture contents at different depths achieved after 592 hours with the assistance of radial drainage are lower than those for 350 hours and vertical drainage, although a slight gradient still exists. However, near the base of the sample, that is from depths of about 0.5 m, the moisture content is constant and suction has reached the target value.

4.3 *Discussion*

The equilibrium stage was stopped only after observing the rate of water exiting the sample had slowed. A time of 592 hours was required for test 2 instead of 350 hours for test 1. The rate of water expulsion was quicker for test 2 than test 1, hastened by radial drainage.

Throughout the entire sample depth the moisture content distribution becomes more uniform with the assistance of radial drainage and a longer equilibrium time. The difference between

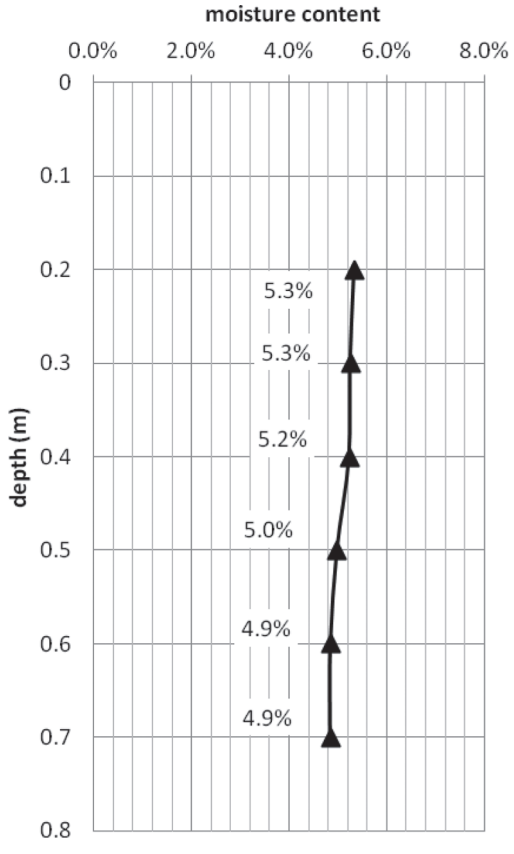

Figure 11. Moisture content distribution for test 2.

the largest and smallest values of moisture content with depth is 0.4% in test 2 compared to 0.7% in test 1. Also, the moisture contents are smaller in sample 2 than sample 1, implying higher suctions had been reached, although slight gradients were still present which is consistent with the slight increases of cone penetration resistances with depth being measured.

5 CONCLUSIONS

A static compaction method for preparing large unsaturated samples of decomposed granite in a calibration chamber has been investigated. Variations of cone penetration resistances and moisture contents with depth were measured to indicate sample uniformity. The absence of a sinusoidal pattern in the cone penetration resistances indicates that layering effects caused by static compaction are negligible or non-existent. However, slight gradients in the moisture contents with depth existed, although were less pronounced as the equilibrium times were increased and drainage was allowed to occur radially. The slight moisture content gradients correspond to a slight suction gradient, and is consistent with the slight increases of cone penetration resistances with depth. Even so, static compaction, and imposing suction using the axis translation technique, can enable large homogeneous unsaturated samples to be formed.

REFERENCES

Anderson, W.F., Pyrah, I.C. & Fryer, S.J. 1991. Clay calibration chamber for testing field devices. Geotechnical Testing Journal, 14: 440–450.

Brandon, T.K., Clough, G.W. & Rahardjo, P.P. 1991. Fabrication of silty sand specimens for large- and small-scale tests. Geotechnical Testing Journal, 14: 46–55.

Hilf, J.W. 1956. An investigation of pore pressure in compacted cohesive soils. US Bureau of Reclamation, U.S. Department of the Interior, Denver, Colo. Technical Memorandum 654.

Huang, A.B., Holtz, R.D. & Chameau, J.L. 1988. Calibration chamber for cohesive soils. Geotechnical Testing Journal, 11: 30–35.

Kurup, P.U., Voyiadjis, G.Z. & Tumay, M.T. 1994. Calibration Chamber Studies of Piezocone Test in Cohesive Soils. Journal of Geotechnical Engineering, 120: 81–107.

Lunne, N, Robertson, P.K., & Powell, J.J.M. 1997. Cone penetration testing in geotechnical practice. Blackie Academic & Professional,EF Spon/Routledge Publishers, New York.

McManus, K.J. & Kulhawy, F.H. 1991. Cohesive soil for large-size laboratory deposits. Geotechnical Testing Journal, 14: 26–34.

Miller, G.A., Muraleetharan, K.K., Tan, N.K., & Lauder, D.R. 2002. A calibration chamber for unsaturated soil testing. In Proceedings of the 3rd International Conference on Unsaturated Soils, UNSAT 2002, Vol. 2, Balkema, Lisse, pp. 453–457.

Pournaghiazar, M., Russell, A.R. & Khalili, N. 2011. Development of a new calibration chamber for conducting cone penetration tests in unsaturated soils. Canadian Geotechnical Journal, 2: 314–321.

Pournaghiazar, M., Russell, A.R. & Khalili, N. 2012a. Drained cavity expansions in soils of finite radial extent subjected to two boundary conditions. International Journal for Numerical and Analytical Methods in Geomechanics. (DOI: 10.1002/nag.1099).

Pournaghiazar, M., Russell, A.R. & Khalili, N. 2012b. Linking cone penetration resistance measured in calibration chambers and field. Geotechnique Letters, 2: 29–35.

Russell, A.R. 2004. Cavity expansion in unsaturated soils. Ph.D thesis. University of New South Wales.

Sheeran, D.E. & Krizek, R.J. 1971. Preparation of homogeneous soil samples by slurry consolidation. Journal of Materials, vol. 6, No. 2, 356–373.

Tan, N.K. 2005. Pressuremeter and Cone penetrometer testing in a calibration chamber with unsatrated Minco silt. Ph.D thesis. University of Oklahoma.

Advances in Unsaturated Soils – Caicedo et al. (eds)
© 2013 Taylor & Francis Group, London, ISBN 978-0-415-62095-6

Estimating soil hydraulic parameters from capillary rise tests

T.C. Zapata & O.M. Vilar
University of São Paulo, São Carlos, Brazil

ABSTRACT: The capillary rise is a simple and rapid test which measures the advancing wetting front, a typical phenomenon of unsaturated soils. This paper explores the potential of combining capillary rise tests and an optimization technique to estimate saturated hydraulic conductivity and hydraulic conductivity function. The optimization process uses the routine SOLVER and to describe the capillary rise the models of Terzaghi (1943) and Lu & Likos (2004b), which considers Gardner´s hydraulic function, were used. The proposed technique was tested against results available in the literature and tests with compacted soils. Capillary rise could be nicely fitted using Lu & Likos (2004b) and saturated hydraulic conductivities approached the measured ones for most of the soils analyzed. The Gardner parameters were of the same order of magnitude of reported values of similar soils. The technique seems promising and could be an interesting alternative for measuring hydraulic parameters of soils.

1 INTRODUCTION

The hydraulic conductivity is an essential property for solving various engineering problems. For an unsaturated soil, hydraulic conductivity depends on the hydraulic potential or on the soil suction, this dependence being expressed in the hydraulic conductivity function. This is function difficult to measure, both in lab and in the field: it demands expertise and some special instruments, such as tensiometers and moisture content transducers and is time consuming. To overcomed those difficulties, some alternative approaches have been developed to estimate such a function, many of them resting on the soil water retention curve (van Genutchen, 1980 among others). This is a logical option, since the tests to measure soil water retention can be seen as a kind of permeability test, performed under transient conditions.

The capillary rise is a well known physical phenomenon in which the suction height and the moisture content follow a relationship similar to the soil water retention curve. This similarity reflects a direct influence of hydraulic conductivity in the process of capillary rise that in turn becomes a possible alternative to evaluate the unsaturated hydraulic conductivity of soils. Besides, it is a simple laboratory test that demands a relatively short period of timeto be completed.

One of the first proposals to model the capillary rise in a soil was that of Terzaghi (1943). He developed an equation considering the hypothesis that during the process of capillary rise the soil was saturated and that the rate of capillary rise could be described by Darcy's law. The resulting solution of Terzaghi model is expressed in Equation 1.

$$t = \frac{n.h_c}{k_s}\left(\ln\frac{h_c}{h_c - z} - \frac{z}{h_c}\right) \quad (1)$$

where t—time; n—soil porosity; h_c—ultimate height of capillary rise; z—distance measured positive upward from the elevation of the water table and k_s—saturated hydraulic conductivity.

Lu & Likos (2004b), based on the original equation of Terzaghi (1943) and the observations of Lane & Washburn (1946) have presented a new alternative solution, using the hydraulic conductivity function of Gardner (1958), to represent the variation of the hydraulic conductivity in the process of capillary rise.

Gardner's equation is expressed as:

$$k(h) = k_s e^{(-\beta h)} \quad (2)$$

where k(h)—hydraulic conductivity at a given hydraulic potential, h, and β, a soil parameter representing the variation of hydraulic conductivity with hydraulic potential. The solution of Lu & Likos (2004b) is presented as a series function, as follows (Equation 3).

$$t = \frac{n}{k_s}\sum_{j=0}^{m=\infty}\frac{\beta^j}{j!}\left(h_c^{j+1}\ln\frac{h_c}{h_c - z} - \sum_{s=0}^{j}\frac{h_c^s.z^{j+1-s}}{j+1-s}\right) \quad (3)$$

On the other hand there is at present computational tools as the technique of the inverse problem,

which has proven effective for determining the hydraulic properties of soils. The inverse problem consists in obtaining the best estimator of the parameters of an equation that represents a physical phenomenon, based on prior information of these parameters through laboratory testing or documentation.This method was used, for instance, to estimate parameters affecting water flow and solute transport in unsaturated soils by Kool et al. (1987). It was also used by Eching & Hopmans (1993) to optimize thehydraulic conductivity function from transient flow tests and by Simunek et al. (1998) to determine the hydraulic conductivity from tests of evaporation of water from soil cores in the laboratory. All the cited authors obtained reliable optimized methods that fairly fitted experimental data.

Considering this background, the objective of this study was to verify the potential of parameter optimization method for estimating the hydraulic pro-perties based on capillary rise tests. The SOLVER parameters optimizer that is included in the EXCEL code was chosen for that purpose, together with the mathematical models of Terzaghi (1943) and Lu & Likos (2004b) to represent the process of capillary rise.

The first part of the study is devoted to check the potential of the optimization method by analyzing test data provided by Lane & Washburn (1946) and Zhang & Fredlund (2009) in order to determine the saturated hydraulic conductivity (k_s), maximum height of capillary rise (h_c) and Gardner parameter (β). The second part of the study is directed to obtain soil hydraulic parameters using the SOLVER routine considering test data from laboratory measurements of capillary rise in specimens of compacted soils, typical of the State of São Paulo, Brazil.

2 MATERIALS AND METHODS

2.1 *Samples*

The first part of this study was conducted using the data of tests carried out by Lane & Washburn (1946) for granular soils and Zhang & Fredlund (2009) for fine soils. Due to space limitations, the physical indices of those soils will not be presented. However the hydraulic parameters of interest will be shown in the section of test results.

For the second part of analysis, eight typical fine soils of the State of São Paulo, varying from clayey sand to silt, were tested to obtain the saturated hydraulic conductivity and the capillary rise with time. Table 1 presents the identification of the soils tested, together with some other characteristics, including the parameters from Standard Proctor test, w_{ot}, optimum moisture content and ρ_{dmax}, maximum dry density.

The permeability and capillary rise tests were performed with compacted specimens. All the soil samples were moistened to reach their optimum moisture content and dynamically compacted in five layers to obtain the correspondent maximum dry density. Final dimensions of specimens were 50 mm in diameter and 100 mm in height. The saturated hydraulic conductivities were measured using rigid wall permeameters, allowing for constant rate of flow to characterize saturation or near saturation of the specimen. Thus, the tests were performed without any additional phase to improve the saturation of the specimens, such as using backpressure.The results of variable head permeability tests are shown in Table 1.

2.2 *Capillary rise test*

To perform the capillary rise test ens were prepared similarly to the specimens used for permeability tests and then air dried. Thus, for this preliminary part of the research, the tests were intended to be performed on short length samples (50 mm diameter and 100 mm height) and in addition they were kept as simple as possible.

The capillary rise test was performed by placing the specimen of soil directly over a high permeability porous stone that was at the top of a cylindrical tank 5 cm in diameter. This tank was connected by a pipe to a water supplier tank, placed on the same level of the soil specimen. The water supplier tank was sitting on a scale with 0.01 g of resolution for the purpose of measuring the mass of water absorbed during the process of capillary rise. Relative humidity and temperatures were controlled and the water evaporation was measured during the tests. A millimetric ruler was placed on the side of the soil specimen for measuring the advancing front of wetting (z) with time (t). For each soil type at least two tests were performed to ensure repeatability of data.

2.3 *Method of the inverse problem*

The optimization method selected was the Solver optimization routine, which is part of the Excel program. It was chosen for its versatility and ease of use in solving various linear and nonlinear problems. The models selected to represent the process of capillary rise were those presented by Terzaghi (1943) (Equation 1) and Lu & Likos (2004b) (Equation 3). The objective to be minimized during the optimization process for the Terzaghi model is the time t, considered dependent on k_s and h_c parameters.

Regarding the model of Lu & Likos (2004b), the objective to be minimized is the time t, now considered dependent on k_s, h_c and β parameters.

Table 1. Soils tested in this research program.

Sample	SI	SC	TD	AV	DC	IG	MA	IP
% Sand	69	56	38	19	10	8	8	4
% Silt	8	10	21	33	50	10	48	18
% Clay	24	34	40	48	40	82	45	78
LL (%)	34	38	45	49	79	108	58	60
IP (%)	14	17	11	15	26	53	24	17
SUCS	SC	SC	ML	ML	MH	MH	MH	MH
ρ_s (g/cm^3)	2.566	2.690	2.587	2.894	2.98	2.657	2.749	2.666
ρ_{dmax} (g/cm^3)	1.890	1.800	1.46	1.520	1.46	1.272	1.563	1.430
w_{ot} (%)	12.1	14.5	26.7	24.8	31.5	37.7	22.9	29.8
k_s (cm/s)	4.2×10^{-7}	1.1×10^{-7}	1.2×10^{-6}	4.2×10^{-8}	1.3×10^{-6}	3.7×10^{-6}	7.8×10^{-6}	6.0×10^{-7}

The objective function of the optimization process was to minimize the sum of squared deviations between the estimated values of "t" and those observed in laboratory.

In the case of the model of Lu & Likos (2004b), besides considering t as a function of the three parameters (k_s, h_c and β), an additional analysis was performed considering $_s$ as a known parameter (the value measured in the lab tests) and varying h_c and β. In the graphs, the notation of the results obtained using this second option is: Lu & Likos (1).

As the solution of Lu & Likos (2004b) is in series, fits were made considering up to five terms of the series for each soil analyzed and choosing the results that better matched experimental results of capillary rise results.

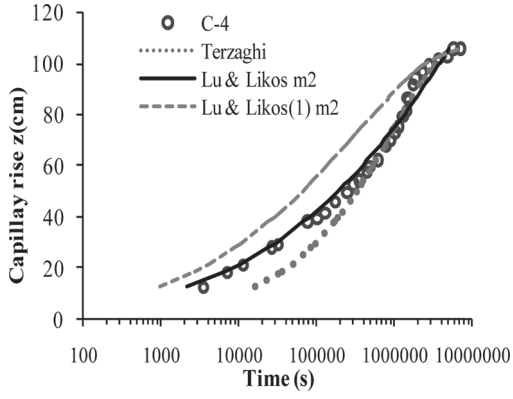

Figure 1. Experimental and modeled data of capillary rise. Soil C-4 of Lane & Washburn (1946).

3 RESULTS

3.1 *First part*

This part was intended to check the potential of the optimization technique in the determination of soil hydraulic parameters using available tests results. Figure 1 shows an example of the nice fitting between experimental and modeled capillary rise, using optimized parameters, for soil C4 of Lane & Washburn (1946).

As can be seen, Lu & Likos method using the second term of the series (m^2) tends to match the experimental data. The Terzaghi solution departs from experimental data for early rise times and the second option of Lu & Likos that considers known the saturated hydraulic conductivity, gives the poorer results.

Although not all the soils presented similar trends, specially the coarser ones, it was observed that the optimized parameters were capable of nicely reproduce experimental data, especially if the Lu & Likos (2004b) model is considered. The larger deviation was observed when using the Terzaghi model.

Table 2 shows a comparison between experimental and optimized saturated hydraulic conductivity. It can be seen that the Terzaghi model tends to yield values closer to the experimental ones or that deviates about an order of magnitude, exception made for the soils C5 and SM and SC. A similar behavior is noticed for the results of Lu & Likos model.

The exceptions in this case were the soils C1, C7 and SM.

As far as the values of the maximum height of capillary rise (h_c) are concerned, the obtained values were almost identical to the experimental ones as can be seen in Table 3. However, the second option of Lu & Likos that considers known k_s yields h_c that depart from experimental ones for some soils. In the case of the soils studied by Zhang & Fredlund (2009) the comparison was impaired by the fact that there is some doubt regarding the height of capillary rise reported since they could not be the maximum considering the length of the tube used as mold and the time spent in the tests.

A more difficult comparison is that of the parameter β of soil hydraulic function of Gardner (1958)

Table 2. Parameter (k_s) obtained by the methods of Terzaghi (1943) and Lu & Likos (2004b).

Soil	Experimental k_s cm/s	Terzaghi k_s cm/s	Lu & Likos k_s cm/s
Lane & Washburn (1946)			
C-1	1.1×10^{-1}	1.0×10^{-2}	1.0×10^{-3}
C-2	1.6×10^{-2}	1.0×10^{-3}	5.5×10^{-1}
C-3	7.1×10^{-3}	1.0×10^{-3}	1.6×10^{-2}
C-4	4.6×10^{-4}	1.6×10^{-5}	2.0×10^{-4}
C-5	1.1×10^{-4}	4.2×10^{-6}	7.2×10^{-4}
C-6	6.2×10^{-5}	1.6×10^{-5}	1.9×10^{-5}
C-7	9.6×10^{-6}	9.7×10^{-6}	1.8×10^{-4}
C-8	1.4×10^{-5}	1.9×10^{-5}	5.4×10^{-5}
Zhang & Fredlund (2009)			
CL	3×10^{-6}–3×10^{-5}	5.4×10^{-6}	5.6×10^{-6}
ML	1×10^{-5}–3×10^{-4}	1.2×10^{-5}	1.7×10^{-5}
SM	3×10^{-3}–5×10^{-2}	1.0×10^{-4}	3.8×10^{-5}
SC	2×10^{-5}–4×10^{-4}	5.6×10^{-6}	3.1×10^{-5}

Table 3. Parameter (h_c) obtained by the methods of Terzaghi (1943) and Lu & Likos (2004b).

Soil	Experimental h_c cm	Terzaghi h_c cm	Lu & Likos h_c cm	Lu & Likos (1) h_c cm
Lane & Washburn (1946)				
C-1	5.4	5.5	5.5	5.5
C-2	28.4	28.5	28.5	28.5
C-3	19.8	19.9	19.9	19.9
C-4	106	108	150	106
C-5	82	82	85	82.3
C-6	239.6	239.6	239.6	239.6
C-7	165.5	166	166	4000
C-8	360	361	360	467.6

since there are very few experimental data available. Zhang & Fredlund (2009) have used the instantaneous profile method to derive the hydraulic conductivity function. They have found that their experimental results could nicely be fitted using the two-parameter Gardner function (Gardner, 1958). Considering that, it was expect that the one parameter function should not fit the experimental data of those authors. However, an attempt was made to obtain optimized β and the results obtained are presented in Table 4.

Figure 2 shows an example of obtained function considering the two options of the Lu & Likos (2004b) model. As expected, the calculated curves departs from the experimental data, however they tended to follow it to some an extent, especially up to the air entry value of the soil.

Table 4. Parameter β of the soils tested by Zhang & Fredlund (2009) obtained by the optimization method.

Soil	Lu & Likos β cm^{-1}	Lu & Likos (1) β cm^{-1}
CL	0.01	0.027
ML	0.01	0.005
SM	0.50	1.000
SC	0.10	0.100

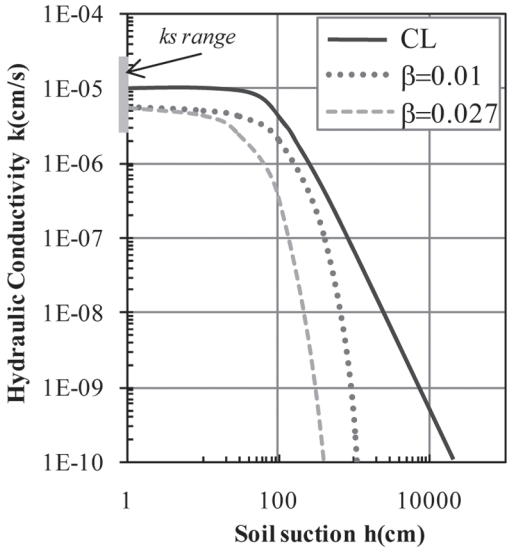

Figure 2. Experimental and calculated hydraulic conductivity function of soil CL tested by Zhang & Fredlund (2009).

3.2 *Second part*

Based on the promising results obtained so far for the k_s and h_c parameters, the optimization method of previewing the soil hydraulic properties was used to infer the properties of the eight different soils tested for capillary rise and saturated hydraulic conductivity.

3.2.1 *Capillary rise*

The results of the capillary rise test of the eight samples tested are presented in Figure 3. The maximum time to reach the top of the specimen (100 mm) occurred for soil AV and was of about 24 hours. At a first glance, this can be considered an advantage of this option of test to estimate soil hydraulic parameters, since other options of permeability tests demands much more time to be accomplished.

3.2.2 *Capillary rise prediction*

The same procedure used in the first part of this study was followed for the tested soils. All the test

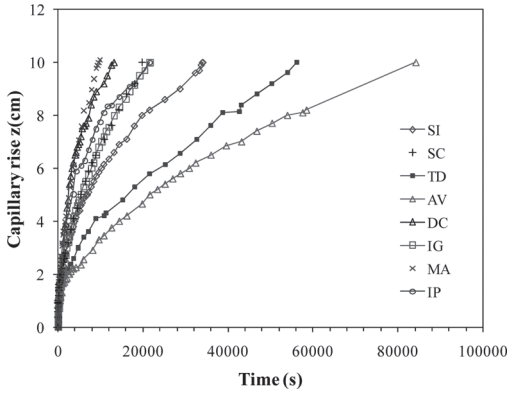

Figure 3. Capillary rise in the eight soils tested.

results of capillary rise were nicely fitted considering the optimized parameters and the models of Terzaghi (1943) and Lu & Likos (2004b). Figure 4 shows an example of such a fitting presenting the experimental data and fitted curves of soil SI. The fitting of experimental data considering the three options yields practically the same curves. This is not a coincidence but a result of the fact that both options of Lu & Likos (2004b) method gave the best optimized parameters using only the first term of the series. In this situation, the equations of Lu & Likos and of Terzaghi yield closer values.

3.2.3 *Saturated hydraulic conductivity (k_s)*

Table 5 shows a comparison between the experimental and the values obtained using the optimization technique and the models of Terzaghi (1943) and Lu & Likos (2004b).

In general values are closer or present variations of about one order of magnitude, with the optimized values larger than the experimental ones. A possible reason for this deviation rests in the fact that the tests were performed without any ancillary device to improve the saturation of the samples. Thus some air bubbles are retained in the air voids leading to hydraulic conductivities that are lower than the real ones.

3.2.4 *Maximum height of capillary rise (h_c)*

The values of the maximum height of capillary rise (h_c) obtained were comparable for many of the tested soils when the models of Terzaghi (1943) and Lu & Likos (2004b) are considered as shown in Table 6. However, for the method to accomplish the optimization process for the second option of the Lu & Likos method, some maximum height of capillary rise results unrealistic. The maximum height of capillary rise was not planned to be measured in the tests, since the specimens used were only 100 mm.

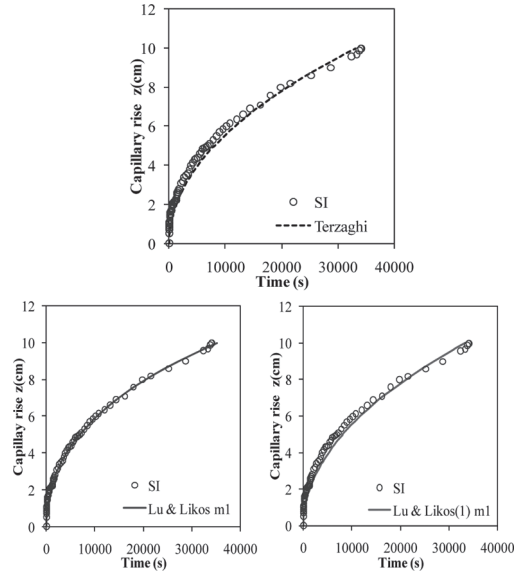

Figure 4. Experimental and previewed results using the models of Terzaghi (1943) and Lu & Likos (2004b) with parameters obtained from optimization analysis. Soil: SI.

Table 5. Values of experimental saturated hydraulic conductivity (k_s) and calculated using the optimization procedure.

Soil	Experimental k_s cm/s	Terzaghi k_s cm/s	Lu & Likos k_s cm/s
SI	4.3×10^{-7}	5.6×10^{-6}	8.7×10^{-6}
SC	1.1×10^{-7}	3.5×10^{-6}	3.6×10^{-6}
TD	1.3×10^{-6}	2.5×10^{-6}	1.8×10^{-6}
AV	4.2×10^{-8}	1.8×10^{-6}	4.9×10^{-7}
DC	1.8×10^{-6}	3.0×10^{-6}	3.0×10^{-6}
IG	3.7×10^{-6}	8.6×10^{-6}	4.5×10^{-6}
MA	7.8×10^{-6}	4.5×10^{-6}	3.5×10^{-6}
IP	6.0×10^{-7}	3.5×10^{-6}	3.6×10^{-6}

Table 6. Values of the maximum height of capillary rise (h_c).

Soil	Terzaghi h_c cm	Lu & Likos h_c cm	Lu & Likos (1) h_c cm
SI	80	80	1000
SC	300	300	9200
TD	150	210	293
AV	150	600	7830
DC	400	420	673
IG	150	300	351
MA	517	700	304
IP	350	600	3574

Table 7. Values of β (Gardner parameter).

Soil	SUCS	Lu & Likos β cm^{-1}	Lu & Likos (1) β cm^{-1}
SI	SC	0.100	0.007
SC	SC	0.008	0.001
TD	ML	0.010	0.001
AV	ML	0.010	0.037
DC	MH	0.010	0.001
IG	MH	0.013	0.005
MA	MH	0.010	0.001
IP	MH	0.100	0.107

Additional tests using longer soil specimens are planned and will help in checking the calculated values.

3.2.5 *Gardner parameter* β

Table 7 shows the values of parameter β, considering the model of Lu & Likos (2004b) in its two options. The option Lu & Likos(1) yielded, for most soils, values that are about one tenth of the values from Lu & Likos (2004). As in the case of h_c there are not measured values for comparison, however the obtained results from the first option of Lu & Likos (2004b) are comparable with some values suggested in the literature for similar soils (Lu & Likos, 2004a). Some permeability tests for unsaturated soil are also planned and it is expected that the technique could be improved by searching for solutions for capillary rise that considers also two parameter hydraulic function.

4 CONCLUSION

This paper focused primarily in exploring the potential of combining capillary rise tests in specimens of short height and a parameter optimization technique to estimate hydraulic parameters of soil. The option has showed promising, especially in reproducing the capillary ascension of water in a soil. The obtained saturated hydraulic conductivities were closer to the measured ones, or have shown deviations of about one order of magnitude for most of the soils tested. Regarding the unsaturated hydraulic conductivity, it was not possible to confirm the accuracy of prevision; however, for some of tested soils, the obtained results were close to the values reported in the literature. Additional tests and analysis are underway and it is expected that they could confirm the promising performance of capillary tests and optimization technique in obtaining hydraulic parameters of soils, especially those related to the hydraulic conductivity function.

REFERENCES

Eching, S.O. & Hopmans, J.W. 1993. Optimization of Hydraulic functions from transient outflow and soil water pressure data. *Soil science society of America*. 57(5): 1167–1175.

Gardner, W.R. 1958. Some steady state solutions of the unsaturated moisture flow equation with application to evaporation from a water table. *Soil Science.* 85(4): 228–232.

Kool, J.B., Parker, J.C. & Van Genuchten, M.Th. 1987. Parameter estimation for unsaturated flow and transport models. *A review, J. of Hydrol*. 91: 255–293.

Lane, K.S. & Washburn, D.E. 1946. Capillarity tests by capillarimeter and by soil filled tube. *Highway research board proceedings*. 26: 460–473.

Lu, N. & Likos, W.J. 2004a. *Unsaturated Soil Mechanics.* John Wiley & Sons, New Jersey, USA. p. 556.

Lu, N. & Likos, W.J. 2004b. Rate of Capillary rise in soil. *Journal of Geotechnical and Geoenvironmental engineering, ASCE*. 130(6): 646–650.

Simunek, J., Wendroth, O. &. Van Genuchten M.Th. 1998. A parameter estimation analysis of the evaporation method for determining soil hydraulic properties. *Soil Science Society of America Journal*. 12: 167–180.

Terzaghi, K. 1943. *Theoretical Soil Mechanic.* Wiley, New York.

Van Genutchen, M.Th. 1980. A closed-form equation for predicting the hydraulic conductivity of unsaturated soils. *Soil Science Society of America Journal*. 44: 892–898.

Zhang, X. Li. & Fredlund, D.G. 2009. Wetting front advancing column test for measuring unsaturated hydraulic conductivity. *Canadian Geotechnical Journal*. 46(12): 1431–1445.

Advances in Unsaturated Soils – Caicedo et al. (eds)
© 2013 Taylor & Francis Group, London, ISBN 978-0-415-62095-6

Geophysical investigation of cracking in unsaturated soils

G. Jones
University of Strathclyde, Department of Civil and Environmental Engineering, Glasgow, UK

M. Zielinski
University of Strathclyde, Department of Civil and Environmental Engineering, Glasgow, UK
Texas A&M University, Zachry Department of Civil Engineering, College Station, Texas, USA

P. Sentenac
University of Strathclyde, Department of Civil and Environmental Engineering, Glasgow, UK

ABSTRACT: Non-invasive investigations are fast growing methods that are currently being used for many engineering purposes. These, so-called geophysical techniques can provide very accurate information about the subsurface without causing any disturbance. This future is so important when dealing with the specific infrastructure that cannot be excavated (i.e., levees, road and railway embankments and earth dams). Most of these structures, which are located well below the ground water level, are considered unsatured. During their lifetime, they undergo series of complex hydro-physio-mechanical variations, which in many cases causes permanent changes in their structure (i.e., creation of cracks). In presented study, an Electrical Resistivity Tomography (ERT) is employed to track the formation of desiccation cracks in drying soil. A 3-D physical models containing two different types of soil were used in order to observe the changes in crack pattern during soil desiccation.

1 INTRODUCTION

Desiccation cracking in soils can result in considerable change in the hydraulic and mechanical properties of existing structures. The significant increase in the hydraulic conductivity of the soil caused by desiccation cracking (Dyer et al., 2009) can create preferential paths for contaminant transport in the substrata (Armstrong et al., 1994, Rounsevell et al., 1999). Desiccation cracking has also been recognised as one of the major causes of the reduced performance of landfill covers and clay liners (Melchior 1997, Albright et al., 2006) and may lead to enhanced seepage and progressive failures in flood embankments, as reported by Marsland (1957).

The formation of desiccation fissures in soils results from a rise in negative pore water pressure (suction) within the soil, due to an air-water interface entering into a saturated medium (Shin & Santamarina, 2011). The onset of fissuring corresponds to a change from the saturated solid-liquid state to the unsaturated solid-liquid-gas state (air-entry) where air begins to replace water in the soil pores (Peron et al., 2009), causing the volumetric moisture content of the soil to reduce.

Continuous desiccation results in the separation of the soil into polygonal blocks, divided by a network of fissures (Corte & Higashi 1964, Kodikara et al., 2000). Shrinkage acting on the blocks can lead to shear planes forming beneath the surface of the soil, resulting in horizontal subsurface fissuring, leading to the separation of the desiccated blocks from the rest of the soil structure (Konrad & Ayad 1997, Style et al., 2010). These fissuring networks may provide preferential flow paths when water levels are high, leading to embankment failures (Cooling & Marsland 1953, Marsland & Cooling 1958).

A typical condition survey of flood embankments consists of periodic, visual walk-along observations (Morris et al., 2007). Normally the surveys are carried out in the winter months, when vegetation is lower, allowing the soil surface to be observed (Perry et al., 2003, BS 7370-5:1998). However, vegetation can often remain sufficiently dense obscuring the soil surface and a general reduction in crack size during the wetter, winter months can make identification of fissures difficult, thus masking the severity of the problem.

To date, investigating the actual depth of fissuring has only been possible through the excavation of trenches (a destructive technique) as carried out by Cooling and Marsland (1954) and Dyer et al., (2009). A non-destructive technique which can be used to detect and characterise fissures in the subsurface and on the surface where direct visual identification is inadequate is required. In particular a

method which allows for the identification of fissure networks, through the characterisation of polygonal blocks at the soil surface and the detection of sub-surface fissuring would identify soil-barriers at risk of failure. Ideally such a method should also enable the monitoring of fissure development in earthwork structures, as well as tracking the seasonal changes in resistivity due to changes in soil moisture. Such monitoring would provide a better understanding of the soil mass behaviour when subjected to extreme weather patterns and could act as an early stage detection system for earthwork structures.

2 ELECTRICAL RESISTIVITY TOMOGRAPHY

2.1 *2-D and 3-D ERT in cracking detection*

Electrical Resistivity Tomography (ERT) is a commonly used geophysical method for the imaging of shallow sub-surface targets. Recent improvements in resistivity equipment have resulted in improved quality and efficiency of complex surveys and advances in inversion software and computer technology have allowed for better modelling of resistivity data. Common uses of ERT include water and contaminate flows (de Lima et al., 1995, Bensom 1997, Martínez-Pagán et al., 2010), in engineering site investigations (Rucker et al., 2009, Banham & Pringle 2011) locating buried artefacts or structures in Archaeological surveys (Tonkov & Loke 2006, Negri et al., 2008) as well as providing geological and hydrogeological site information (Ganerod et al., 2006).

Previous studies (Samouelian et al., 2003, Samouelian et al., 2004, Sentenac & Zielinski 2009) have identified Electrical Resistivity Tomography (ERT) as sensitive to fissures in the soil subsurface. Samouelian et al., (2003) first showed the sensitivity of ERT in mapping artificially created 2-D fissure in a silty loam. The study used a Wenner alpha Array and used the RES2DINV inversion software (Loke & Barker 1996, Loke 2010) to identify a contrasting area of high resistivity representing the fissure and lower resistivity representing intact soil. The authors concluded that in order to accurately resolve the desiccation fissures in a 2-D resistivity model, the creation of dedicated software was necessary. An inversion model for such software was discussed in a follow up paper by the same research team (Tabbagh et al., 2007).

In addition to their 2-D models, Samouelian et al., (2004) used 3-D resistivity monitoring to detect the onset of desiccation fissuring on a compacted block of compacted material. Square arrays were used in the study in order to identify the dip angle of the fissures as they formed. The study showed resistivity areas at the surface of the 3-D model with high resistivity, relating to the positions of the fissures in the soil, although no clear images of the fissuring network were obtained from the resistivity scan. In addition the study showed an increase in the measured resistivity values with drying time, indicating a relationship between the apparent resistivity and the soil moisture.

Sentenac & Zielinski (2009) employed the use of miniature electrodes in a clay model in order to monitor the onset of desiccation fissures in a 2-D plane. The material used in the study was compacted boulder clay reclaimed from a flood embankment located in East Yorkshire (England) near city Hull. In the study, the Wenner-Schlumberger array was used in order to ensure that the survey was sensitive to both vertical and horizontal fissures forming in the clay (Konrad & Ayad 1997). Importantly the study revealed improvements in the RES2DINV inversion software allowing the vertical fissures to be accurately resolved. The study accurately resolved the positions of the vertical fissures as they formed, and revealed possible horizontal discontinuity owing to fissuring beneath the shear plane. Additionally the use of a conductive gel tracer was investigated in order to better visualize the fissuring.

This study aims to build on the previous work and show that resistivity measurements taken in both 2-D and 3-D using conventional resistivity equipment can monitor and map the onset of fissuring using miniature electrodes in a laboratory, and compare the results with field measurements from a desiccated embankment.

3 LABORATORY STUDY

3.1 *3-D ERT model—material*

Two separate physical models were created using different types of soil sourced from existing embankments, with the aim of investigating the influence of soil type on resistivity measurements. The first material (silty clay) was reclaimed from a disused flood embankment located near Thorngumbald along the Humber estuary in England. A full description of the soil properties can be found in Ghataora et al., (2007). The second material (boulder clay) was obtained during the construction of a flood embankment near Galston in East Ayrshire, Scotland. The properties of the boulder clay are described in Zielinski et al., (2011).

3.2 *3-D ERT model—experimental setup*

The physical model used in this study was a square section of compacted embankment clay, designed to simulate a section of the embankment crest subjected to drying. The clay was contained within a wooden box of dimensions $0.6 \times 0.6 \times 0.2$ m,

which was lined with Perspex with an attached geo-membrane, which was used to minimise the shrinkage of the soil, thus simulating the restraining effect of a massive compacted structure.

Both soils were air dried, crushed and sieved in order to remove any stones and large organic matter that could influence the measurements. Once crushed, the soil was wetted by spraying water onto the dry soil and mixed manually. To achieve consistent moisture content, the soil was mixed in batches of 10 kg (dry mass) with the container placed on an electronic balance to monitor the water added. The target water content of the models was wet of optimum (i.e. at a water content greater than that required to achieve maximum density), at 22% for Thorngumbald and 20% for Galston, to ensure that a significant amount of shrinkage of the soil would occur. Once the soil was mixed it was stored in air tight containers for 48 hours to ensure further homogenisation of water content throughout the soil. The wet soil was then compacted using a wooden plate of 0.6 by 0.6 m onto which a 6 kg hammer was dropped from a height of approximately 0.5 m. This procedure ensured that a smooth surface was created during compaction enabling easy identification of early fissures. Once compacted the model was soaked by spraying water onto the exposed surface of the soil, which was then covered for three days to ensure homogenisation of the soil.

One hundred and forty four Electrodes were fabricated using 0.65 mm diameter stainless-steel pins (Fig. 1) and inserted into the soil to a depth of approximately 1 cm in the arrangement presented on Figure 2. The diameter was kept deliberately small to minimise the impact of the electrode on the surrounding soil so as not to influence the formation of the fissures and to minimise the deviation from an ideal point source due to the "electrode effect"; i.e. the effect of the physical size of an electrode on the apparent resistivity measurement.

The depth of electrode insertion was 1 cm which gave an electrode length to electrode spacing ratio of 0.22, just above the "critical" ratio of 0.2 defined by Rucker and Gunther (2011); a much deeper insertion would have increased the ratio resulting in greater uncertainty of measurement, whereas a shallower depth of insertion would have provided poorer contact between electrode and soil, increasing the contact resistance.

The contact resistance was observed to be high with values of close to 8000 ohms recorded for the model in the final stages of drying, compared to 600 ohms for the initial model. In order to achieve a good contact between the soil and electrodes, water was sprayed onto the base of the electrodes prior to each measurement which reduced the resistance to more acceptable value of around 1800 ohms.

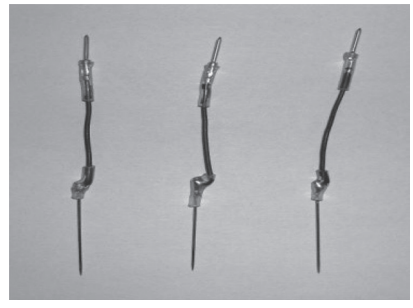

Figure 1. Miniature stainless-steel electrodes.

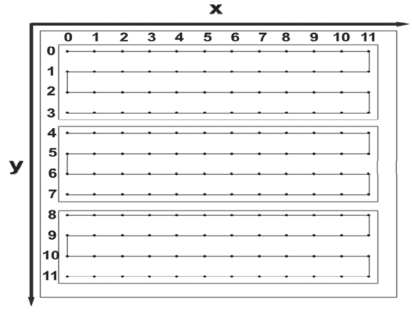

Figure 2. Electrodes and survey grids arrangement.

3.3 *3-D ERT model—experimental procedure*

The experiment using the Thorngumbald clay was allowed to desiccate naturally with the surface left exposed. Resistivity measurements were taken at regular intervals over the three sections with both the Schlumberger and Dipole-Dipole arrays. The period between scans was increased as observed model changes reduced. Measurements were discontinued after 65 days of drying, when no further evolution of fissuring was observed.

Slightly different procedure was applied to the second model containing Galston clay. Accelerated desiccation was induced in the Galston model by applying heat from a 1200 W infra-red (IR) lamp. Moreover, three separate drying and wetting periods were applied to the model in order to investigate the influence of changing hydraulic conditions on the crack formation and its detection using ERT. Measurements were taken regularly using the Schlumberger array and with the Dipole-Dipole array on the final model.

4 RESULTS AND DISCUSSION

4.1 *Surface fissuring*

The evolution of the surface fissuring pattern on the two soil models can be seen in Figure 3a and

4a, with the corresponding top layers of the 3-D resistivity models in Figures 3b and 4b. The Thorngumbald model showed a gradual growth of fissures evolving to a fully interconnected network at the surface after 9 days of drying time, with only a small increase in fissuring width, to a maximum of 1.5 cm observed. The Galston model as expected showed a more rapid evolution of the fissuring network, with initial fissures observed on the surface after 4 hours of IR drying. The fully developed fissuring pattern had evolved after a further 16 hours of IR drying and no increase in fissure width was observed after this point. In both cases the models displayed clear separations along the fissures into polygonal blocks demonstrating the surface interconnection as discussed by Corte and Higashi (1964), Kodikara et al., (2000) and Konrad and Ayad (1997).

Both Figures 4b and 5b show high resistivity anomalies corresponding with the positions of the fissures, contrasted with the lower resistivity of the intact soil. The results are consistent with the findings of previous works (Samouelian et al., 2003, Samouelian et al., 2004, Sentenac and Zielinski 2009).

Clear similarities can be seen between the shape and position of the high resistivity anomalies on the top surface of the resistivity models and the fissuring network observed on the physical soil model: the grids applied to the displayed models show that the position and lengths of the major fissures are consistent.

From these results it can be concluded that at this scale the surface fissuring network can be sufficiently mapped in terms of the psuedolocation of fissures and the characterization of the resultant polygonal blocks. The fissure width resolved using inversion software is larger than the fissure width observed on the physical model as can be seen in Figures 4 and 5. The fissures shown in the Voxler plot (Fig. 5) of the top layer of the Thorngumbald model show the width of the anomalies to be 4.5 cm, equal to the electrode spacing. From these results it can be concluded that at this scale the surface fissuring network can be sufficiently mapped in terms of the psuedolocation of fissures and the characterization of the resultant polygonal blocks.

The fissure width resolved using inversion software is larger than the fissure width observed on the physical model as can be seen in Figures 4 and 5. The fissures shown in the Voxler plot (Fig. 5) of the top layer of the Thorngumbald model show the width of the anomalies to be 4.5 cm, equal to the electrode spacing. This compares with the actual maximum fissure width of 2 cm measured on the physical model. This perhaps reveals a weakness of the method, in that two or more fissures falling between the same measured sections of an array would likely be resolved as a single anomaly.

This effect can be observed in the Galston model shown in Figure 6, where a large number of small

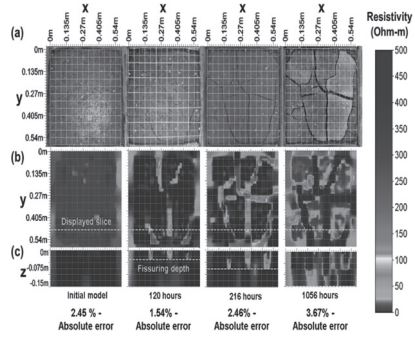

Figure 3. Development of fissuring for Thorngumbald model: (a) photographs showing surface fissures, (b) resistivity model from combined data sets; first model layer (z = 0.01 m), (c) vertical slice at x ≈ 38 cm.

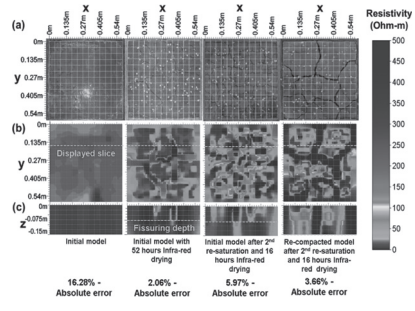

Figure 4. Development of fissuring for Galston model: (a) photographs showing surface fissures, (b) resistivity model from combined data sets; first model layer (z = 0.01 m), (c) vertical slice at x ≈ 38 cm.

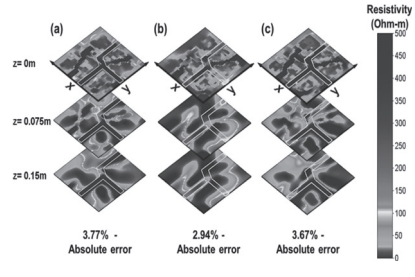

Figure 5. Depth slices for Thorngumbald 3-D lab model after 1056 hours showing relative position of bisecting fissures (a) Schlumberger (b) Dipole-Dipole (c) Combined model.

fissures fall between the electrodes at indicated points: these fissures can be seen as a single large anomaly, which in certain situations would act to mask the severity of the problem. This is of particular importance when considering field measurements, electrode spacings far larger than those used here will be required to make a field survey efficient.

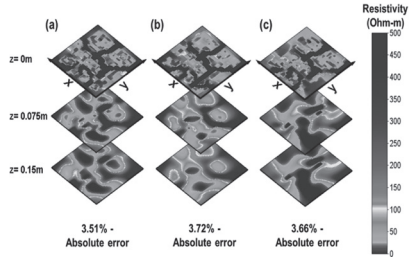

Figure 6. Depth slices for Galston re-compacted model (a) Schlumberger (b) Dipole-Dipole (c) Combined model.

4.2 *Subsurface fissuring*

The resistivity model shown in Figures 3c and 4c shows an apparent increase in fissure depth with drying time.

From the results of both models it can be observed that the combined array satisfactorily resolves the fissures forming in the subsurface in terms of their estimated depths and their surface positions. Figures 5 and 6 show orthogonal planes of the resistivity models for the Thorngumbald and Galston models displaying the resolution of fissures at the surface and in the subsurface.

In terms of the observed pattern of fissures and the polygonal blocks formed the Schlumberger and combined model provide accurate resolution of the surface fissuring in both the Thorngumbald (Figures 5a and c) and the Galston models (Figs. 6a and c).

The Dipole-Dipole model shows large inaccuracies in the mapped surface for both the Thorngumbald and Galston model (Figs 5b and 6b). The reason for the errors can perhaps be due to poor contact between the electrodes and the dry soil, which is known to affect Dipole-Dipole measurement.

From the models presented in Figure 5 and 6 it can be seen that both the Schlumberger and Dipole-Dipole arrays when combined can be used to map surface fissures in a clayey soil, although poor contact between the soil and electrodes may result in errors, particularly when using the Dipole-Dipole array.

This is particularly important when considering a long term ERT monitoring, where dry soil is likely to be encountered during the summer months. Additionally the use of Schlumberger, Dipole-Dipole and a combination of the two can be used to visualize fissuring in the subsurface, although as with all resistivity problems resolution is reduced with depth and inaccuracies can be observed particularly in regions with low data coverage. Additionally some overestimation of the fissuring depth was observed particularly from the Dipole-Dipole model. This again may be a result of inaccuracies due to high contact resistances or may also be due to the effect of the electrode length, which was slightly above the critical length required to result in increased uncertainties (Rucker & Gunther, 2011).

As expected a model created from a combined Dipole-Dipole and Schlumbeger data provided the most accurate model owing to the increased data coverage and the complementary nature of the two arrays. In particular the model shows improved accuracy when considering the resolution of fissures in the subsurface. The accuracy of the model is obviously dependent on the quality of the data obtained from both scans.

5 CONCLUSIONS

The study presented here has shown that under laboratory conditions desiccation fissuring in a soil mass can be monitored and mapped in 3-D using miniature ERT. The maps produced for the inverted resistivity data enabled the interconnection between fissures at the surface to be identified and the results presented indicate that fissuring in the subsurface was also detected. The polygonal blocks resulting from the fissured networks were successfully characterized and compare well with those observed on the physical model; their detection and monitoring in the laboratory suggests that where vegetation obscures the fissures 3-D ERT can be used as a diagnostic technique allowing the extent and severity of such defects to be analyzed.

Two array types were tested and it has been demonstrated that a combined survey using both Schlumberger and Dipole-Dipole array produced the most accurate resistivity maps, based on the surface fissures and on the observations made of exposed fissures after dissection. The Schlumberger method was found to be the better of the two and is recommended by the authors for future mapping of fissured networks where time constraints apply, due to its shorter survey time and sufficiently good resolution.

The method presented demonstrates an easily replicable technique which can be applied in the field; though further research is required into the effect of up-scaling the survey to a conventional size before the method can be used as a standard technique.

ACKNOWLEDGEMENTS

The authors would like to thank EPSRC for the support towards the funding for this research. The second author would like to acknowledge the financial support provided by the EU funded project RISMAC (*Grant agreement: PIOF-GA-2009-254794*) and the Royal Society.

REFERENCES

Albright, W.H., Benson, C.H., Gee, G.W., Abichou, T., McDonald, E.V., Tyler, S.W. & Rock, S.A., 2006. Field performance of a compacted clay landfill final cover at a humid site. *Journal of Geotechnical and Geoenvironmental Engineering.* (132)11: 1393–1403.

Armstrong, A.C., Matthews, A.M., Portwood, A.M., Addiscott, T.M. & Leeds-Harrison, P.B., 1994. Modelling the effects of climate change on the hydrology and water quality of structured soils. *In: Soil Responses to Climate Change. NATO ASI Series 23* [Rounsevell, M.D.A. & P.J. Loveland (eds.)]. Springer-Verlag, Heidelberg, Germany, 113–136.

Banham, S.G., & Pringle, J.K., 2011. Geophysical and intrusive site investigations to detect an abandoned coal-mine access shaft, Apedale, Staffordshire, UK. *Near Surface Geophysics* (9)5: 483–496.

Bensom, A.K., Payne, K.L., & Stubben, M.A., 1997. Mapping groundwater contamination using dc resistivity and VLF geophysical methods—a case study. *Geophysics* 62(1): 80–86.

BSI, 1998. Grounds maintenance. Part 5: Recommendations for the maintenance of water areas. *British Standards Institution*, Milton Keynes, BS 7370-5.

Cooling, L.F., & Marsland, A., 1954. Soil mechanics studies of failures in the sea defence banks of Essex and Kent. *Proceedings of the ICE* - North Sea Floods 31 January/1 February 1953: 58–73.

Corte, A., & Higashi, A., 1964. Experimental research on desiccation cracks in soils. *Research Report*, Materiel Command Cold Regions Research & Engineering Laboratory.

de Lima, O.A.L., Sato, H.K., & Porsani, M.J., 1995. Imaging industrial contaminant next term plumes with resistivity techniques. *Journal of Applied Geophysics* 34(2): 93–108.

Dyer, M., Utili, S., & Zielinski, M., 2009. Field survey of desiccation fissuring of flood embankments. *Proceedings of the ICE—Water Management* WM3: 221–232.

Ganerod, G.V., Ronning, J.S., Daslegg, E., Elvebakk, H., Holmoy, K., & Nilsen, B., 2006. Comparisson of geophysical methods for subsurface mapping of faults and fracture zones in a section of the Viggja road tunnel, Norway. *Bulletin Engineering Geology and Environment.*

Ghataora, G.S., Burns, B., Hassan, M., & Morris, M., 2007. Soil piping tests on Thorngumbald flood embankment. *Science Report FD2411/TR3*, Environment Agency.

Kodikara, J.K., Barbour, S.L., & Fredlund, D.G., 2000. Desiccation cracking of soil layers. *Proceedings of the Asian Conference in Unsaturated Soils*, UNSAT ASIA 2000, Singapore, May 18–19, 2000, Balkema: 693–698.

Konrad, R., & Ayad, J.M., 1997. Dessication of a sensitive clay: field experimental observations. *Canadian Geotechnical Journal* 34: 929–942.

Loke, H.M., 2010, Tutorial: 2-D and 3-D electrical imaging surveys. Geotomo: http://www.geoelectrical.com.

Loke, M.H., & Barker, R.D., 1996. Practical techniques for 3-D resistivity surveys and data inversion. *Geophysical Prospecting* 44, 499–523.

Marsland, A., 1957. The design and construction of earthen food banks. *Journal Institute of Water Engineers* 11(3): 236–258.

Marsland, A., & Cooling, L.F., 1958. Tests on full scale clay flood bank to study seepage and the effects of overtopping. Watford: *Internal Report No. C562*, Building Research Station.

Martínez-Pagán, P., Cano, Á.F., Da Silva, G.R., & Olivares, A.B., 2010. 2-D Electrical Resistivity Imaging to Assess Slurry Pond Subsoil Pollution in the Southeastern Region of Murcia, Spain. *Journal of Environmental and Engineering Geophysics* 14(1): 29–47.

Morris, M., Dyer, M., & Smith, P., 2007. Management of flood embankments: A good practice review. *R&D Technical Report*, FD2411/TR1, Joint Defra/EA Flood and Coastal Erosion Risk Management R&D Programme.

Negri, S., Leucci, G., & Mazzone, F., 2008. High resolution 3-D ERT to help GPR data interpretation for researching archaeological items in a geologically complex subsurface. *Journal of Applied Geophysics* 65(3–4): 111–120.

Peron, H., Hueckel, T., Laloui, L., & Hu, L.B., 2009. Fundamentals of desiccation cracking of fine-grained soils: experimental characterisation and mechanisms identification. *Canadian Geotechnical Journal* 46: 1177–1201.

Perry, J., Pedley, M., & Reid, M., 2003. Infrastructure embankments—condition appraisal and remedial treatment. CIRIA, London.

Reynolds, J.M., 1997. An introduction to applied and environmental geophysics, John Wiley and Sons, Chicester.

Rounsevell, M.D.A., Evans, S.P. & Bullock, P., 1990. Climate Change and Agricultural Soils: Impacts and Adaptation. *Climatic Change* 43(4): 683–709.

Rucker, D.F., Levitt, M.T., & Greenwood, W.J., 2009. Three-dimensional electrical resistivity model of a nuclear waste disposal site. *Journal of Applied Geophysics* 69(3–4): 150–164.

Samouelian, A., Cousin, I., Richard, G., Tabbagh, A., & Braund, A., 2003. Electrical resistivity imaging for detecting soil cracking at the centimetric scale. *Soil Science Society of America Journal* 67(5): 1319–1326.

Samouelian, A., Richard, G., Cousin, I., Guerin, R., Braund, A., & Tabbagh, A., 2004. Three-dimensional crack monitoring by electrical resistivity measurement. European *Journal of Soil Sciences* 55(4): 751–762.

Sentenac, P., & Zielinski, M., 2009. Clay fine Fissuring using miniature geoelectrical resistivity arrays. *Journal of Environmental Earth Sciences* 59(1): 205–214.

Shin, H., Santamarina, J., 2011. Desiccation Cracks in Saturated Fine-Grained Soils: Particle-Level Phenomena and Effective-Stress Analysis. *Géotechnique* 61(11): 961–972.

Style, R.W., Peppin, S.S.L., & Cocks, A.C.F., 2010. Mud peeling and horizontal crcak formation in drying clays. *Research Report* 10/44, Oxford Centre for Collaborative Applied Mathematics.

Tabbagh, J., Samouelian, A., Tabbagh, A., & Cousin, I., 2007. Numerical modelling of direct current electrical resistivity for the characterisation of cracks in soils. *Journal of Applied Geophysics* 62(4): 313–323.

Tonkov, N., & Loke, M.H., 2006. A Resistivity Survey of a Burial Mound in the 'Valley of the Thracian Kings'. *Archaeological Prospecting* 13: 129–136.

Zielinski, M., Sanchez, M., Romero, E., & Sentenac, P., 2011. Assessment of water retention behaviour in compacted fills. Compacted Fills: Assessment, Behaviour, Design and Construction. Proceedings of the Institution of Civil Engineers. Geotechnical Engineering. 64(GE2): 139–148.

Unsaturated soil behavior

Water retention behavior and hydraulic properties

This page intentionally left blank

Advances in Unsaturated Soils – Caicedo et al. (eds)
© 2013 Taylor & Francis Group, London, ISBN 978-0-415-62095-6

Preferential flow and mass transport modeling in a heterogeneous unsaturated soil

L.B. Bien, R. Angulo-Jaramillo, D. Predelus, L. Lassabatere & T. Winiarski
Université de Lyon, UMR5023 Ecologie des Hydrosystèmes Naturels et Anthropisés, Université Lyon 1, ENTPE, CNRS, Vaulx-en-Velin, France

ABSTRACT: This paper aims at studying the impact of soil heterogeneity on both flow and solute transport processes in a large physically based model, LUGH (Lysimeter for Urban Groundwater Hydrology) and 3D numerical modeling. Sand and a sand-gravel bimodal mixture soils were settled using a heterogeneous structure to represent the dip of layers of vadose zone heterogeneity observed under an infiltration basin of Lyon (France). Water and tracer were injected in a pulse mode using a rainfall simulator and 15 breakthrough curves were collected at the bottom. These data clearly pointed out the establishment of preferential flow resulting from both capillary barrier and soil layer dip effects. Numerical modeling helped to better identify the mechanisms responsible for heterogeneous transfers and to establish the link between soil structure heterogeneity and preferential flow and solute transfer.

1 INTRODUCTION

The structure of the vadose zone plays a major role in the transfer of water and solute. Its high heterogeneity is the cause of so-called preferential flow which is the source of a wide disparity in time of occurrence of pollutants in groundwater (Parker & Albrecht, 1987; Flury et al., 1994). It is therefore necessary to understand how the soil structural heterogeneity impacts both water and mass transfer in order to preserve the groundwater resource. From a hydrodynamic point of view, it is possible to consider that these preferential flows occur in areas involving significant variation of unsaturated hydraulic conductivity with respect to adjacent materials (Miyazaki, 1998; Kung, 1990; Steenhuis et al., 1990; Heilig et al., 2003).

For over 300 years, the lysimeters were developed for soil science (Grebet & Cuenca, 1991). Lysimeters, "a device which isolates, between the soil surface and a given depth, a volume of soil and comprises at its base a recovery system for percolating water" (Muller, 1996) are effective tools to study hydrological processes in the vadose zone and the transfers of pollutants applied from the soil surface (heavy metals, organic compounds, radionucleides…) (Lanthaler, 2004).

From data measured in lysimeter, numerical models for water and solutes transfer are verified and the results are then transferred to larger scales. A major challenge for research is the improvement of models with accurate measurement methods (Hansen et al., 2000). Today, the majority of lysimeters, especially in Europe, are implemented in the field (Lanthaler, 2004). The construction and monitoring of these large-scale experiments is accurate but time consuming and expensive. In addition, they have difficulties in interpretation associated with transient flow regimes coupled with the soil profile heterogeneity and the coupling between different physical, chemical and biological nonlinear processes (Kaskassian et al., 2009; 2012). Strong simplifying assumptions must then be applied. Therefore, laboratory lysimeters were developed to test and validate models that couple different processes (i.e., 3D process) and to be able to take into account the effect of heterogeneity. They constitute an intermediate approach between leaching behavior under field conditions and laboratory leaching tests like small laboratory columns (Hansen et al., 2000).

Lysimeters are generally classified according to their size, filling method and effluent collection method (Bergstrom, 1990). Those for which the soil profile is reconstructed are acceptable for gravelly or sandy soils and have a low-construction cost (Lanthaler, 2004). On the other hand, with a reconstructed soil, it is possible to control both the structural arrangement and texture of the materials. According to how the water is drained, there are two popular types of lysimeters: free drainage systems and suction-controlled (i.e., pressure-controlled) systems. For the first type, water flows freely outside the lysimeter by gravity. For the suction-lysimeter, percolated water is collected by applying suction pressure at the outlets

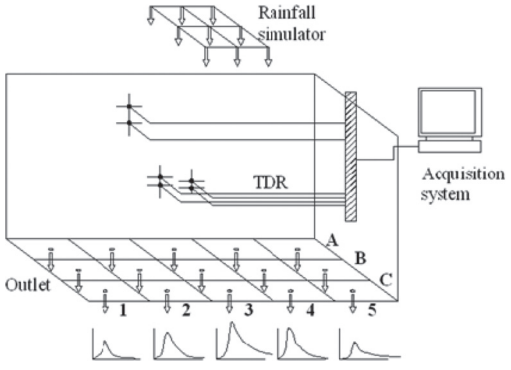

Figure 1. Schematic diagram of LUGH: simulated rainfall (water & tracer) on top, central computer for operation managing TDR multiplexing data acquisition, 15 breakthrough curves sampled for tracer analysis (row 1 till 5 and line A till C).

(suction plate or suction cups) (Lanthaler, 2004). The second type is generally more difficult to control (Bergstrom, 1990). In addition, the suction-application device can be altered by interactions with water and solutes and clogging mechanisms (Rimmer et al., 1995; Goyne et al., 2000).

Given the difficulty of studying the coupled processes between physical, geochemical and biological compartments, the device LUGH (Lysimeter for Urban Groundwater Hydrology) was developed to study the influence of unsaturated soils heterogeneity on mass transfer (Bien et al., 2011, Figure 1). The objective of this paper is to quantify the impact of soil heterogeneity on preferential flow of water and a conservative tracer under unsaturated conditions. We describe the results of our laboratory study on the effect of capillary barrier on preferential flow and non reactive solute transport. The conclusions are established on the basis of the comparison between experimental data and the numerical simulations.

2 FLOW AND TRANSPORT MODEL

The mass conservation of the fluid phase in a three-dimensional unsaturated condition can be represented by the Richards (1931) equation (Haverkamp et al., 2006):

$$C_a(h)\frac{\partial h}{\partial t} = \vec{\nabla}.\left[K(h)\vec{\nabla}H\right] \quad (1)$$

where, $C_a = \partial\theta/\partial h$ = capillary capacity [L^{-1}]; $K(h)$ = unsaturated hydraulic conductivity; h = capillary pressure head; $H = h + z$ = hydraulic head; z = vertical distance measured upward. Unsaturated hydraulic properties are represented by van Genuchten (1980) relationship and Mualem capillary model (1976):

$$\frac{\theta(h)-\theta_r}{\theta_s-\theta_r} = \left[1+(\alpha|h|)^n\right]^{-m} \quad (2)$$

$$K(h) = K_s\left(\frac{\theta(h)-\theta_r}{\theta_s-\theta_r}\right)^{0.8} \left[1-\left\{1-\left(\frac{\theta(h)-\theta_r}{\theta_s-\theta_r}\right)^{1/m}\right\}^m\right]^2; \quad (3)$$

where θ_r and θ_s = residual and saturated volumetric water content, respectively; α = scale parameter for capillary pressure head; n and m = shape parameters; K_s = saturated hydraulic conductivity.

The solute transport in porous media can be modeled by considering molecular diffusion, hydrodynamic dispersion, to obtain the following equation (Bear, 1972):

$$\frac{\partial \theta c}{\partial t} = \vec{\nabla}.(\theta D\vec{\nabla}C) - \vec{\nabla}.(\vec{q}C) \quad (4)$$

where C = solute concentration in the liquid; D = hydrodynamic dispersion coefficient; q = Darcy velocity for the liquid solution.

3 MATERIAL AND METHODS

LUGH consists of a monolith (1×1.6×1 m^3) of compacted soils. Two materials: sand (0–2 mm in diameter) and a bimodal mixture (50% sand-50% gravel 4–12 mm in diam.) were used to represent two layers of the same glaciofluvial deposit current in the region of Lyon (France) (Goutaland et al., 2008).

A rainfall-simulator is used to apply a constant flow at a fraction of surface (no flux for the rest) and create an unsaturated infiltration flow. It also allows to apply a conservative tracer (Br^-, C_0 = 0.01 M L^{-1}). The bottom of LUGH is composed by 15 blocks (0.32×0.32 m^2) that support the soil and allow both free drainage and separate collection of eluted water. The blocks are named in matrix form in 3 lines (A, B, C) and 5 rows (1 to 5, Figure 1). Soil volumetric water content is measured using 6 TDR sensors (Time Domain Reflectometry, model CS616, Campbell Scientific, Logan, UT) (Figure 2).

Two sets of experiments were performed: (1), test E1, LUGH filled only with the bimodal mixture sand-gravel and an infiltration flux q_1 of 3.28 m j^{-1} (40 L h^{-1}), and (2), test E2, LUGH filled with two layers of sand over bimodal mixture (Figure 2) and an infiltration flux q_2 of 0.328 m j^{-1} (4 L h^{-1}). Prior to

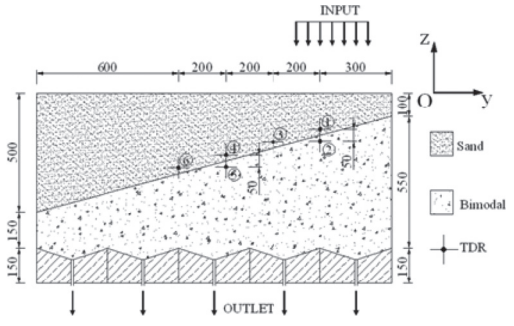

Figure 2. Heterogeneous soil profile mimicking a dip angle between two layers from a sedimentary deposit, location of 6 TDR probes along the interface.

Table 1. Dry bulk density (ρ_d) and hydraulic parameters (Eq. 2 and 3) for sand and bimodal mixture.

	ρ_d (kg m^{-3})	θr (m^3 m^{-3})	θs (m^3 m^{-3})	n (-)	α (m^{-1})	K_s (m s^{-1})
Sand	1634	0.023	0.377	3.28	4.40	8.9×10^{-5}
Mix	1794	0.019	0.329	3.30	10.15	8.3×10^{-5}

injection of the pulse of tracer, infiltration continues until the establishment of steady-state flow regime. The tracer is then applied for 45 minutes for test E1 in order to supply a volume of solute V_0, which is equivalent to ½ of the volume of water contained in the lysimeter (i.e., 30 L of solute), and during 8h for test E2 in order to supply the same quantity of solute as in E1 experiment (no tracer in the soil before the pulse injection). The 15 solute breakthrough curves of each experiment are analyzed using a system dynamics approach, i.e., moment method and resident time analysis (Gaudet & Vauclin, 2005). The hydrodynamic characteristics, $\theta(h)$ and $K(h)$, of sand and bimodal mixture are estimated using BEST (Lassabatere et al., 2006) and method of Mubarak et al. (2009) (Table 1). The hydrodynamic dispersion coefficient is obtained through numerically inverting the 15 experimental elution curves. COMSOL Multiphysics software package was used for both water and solute numerical calculations (COMSOL AB, 2008).

4 RESULTS AND DISCUSSION

Test E1, in a homogeneous medium, is used to validate both the model and the hydrodynamic parameters of the bimodal mixture. The results show a vertical-gravity-driven flow with a low lateral diffusion (Figure 3). The good agreement between measured and calculated elution curves allowed us to validate both the model and the estimated

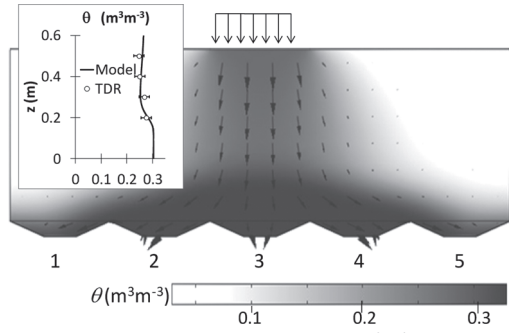

Figure 3. Volumetric water content field, θ(m^3 m^{-3}) and darcian flux vector field (arrows) for test E1; comparison of simulated (curve) and measured volumetric water content (dots + 0.03 m^3 m^{-3}) for the vertical hydric profile at the center of LUGH (output 3).

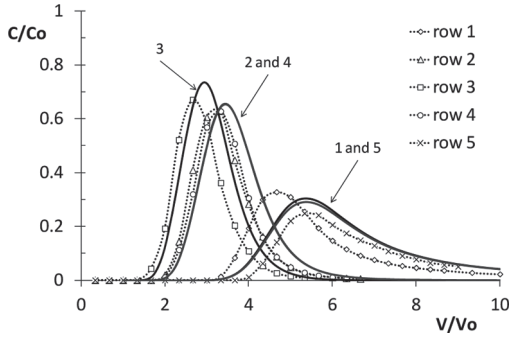

Figure 4. Bromide measured (dots) and calculated (lines) breakthrough curves for test E1 and in function to rows; each curve correspond to the line averaged elution curve.

hydrodynamic parameters at the LUGH scale (Figure 4). Breakthrough elution curves (BTC) are presented in dimensionless variables, C/C_0 as a function of V/V_0, where V = volume of water injected in the system since the beginning of solute pulse injection. These variables are used to compare the different experimental conditions. The BTC are analyzed by calculating the temporal moments of order 1 and 2. The first order moment allows for calculating both the solute mass balance and mean residence time. The variance of the breakthrough curve is obtained from the moments of order 1 and 2.

We found identical values for residence time from the experimental data or from modeling (Table 2). Bromide elution curves for test E1 can be divided into two groups with values of residence time of the same order of magnitude: a group with comparable peak concentrations (rows 2, 3 and 4) and a group with lower peaks on the sides (rows 1 and 5) (Figure 4). Modeling helps to understand these differences due

Table 2. Experimental values of solute residence time, *Ts* (h), for tests E1 and E2; each value is the average of rows A, B and C of the same output 1 to 5; values in parenthesis indicate the standard deviations.

Test	Tow 1	Row 2	Row 3	Row 4	Row 5
E1 exp	4.00 (±0.37)	2.23 (±0.14)	1.85 (±0.14)	2.31 (±0.20)	4.77 (±0.42)
E1 calc	4.70	2.42	1.97	2.42	4.72
E2 exp	120.2 (±0.1)	36.1 (±1.8)	24.3 (±5.4)	19.1 (±1.3)	26.0 (±3.6)
E2 clac	44.0	36.8	27.0	19.7	24.5

to the experimental setup. Indeed, the differences between the two groups are due to the effect of the experimental higher boundary condition (application of solutes and water) which produces a more humid area in the center thereby increasing pressure; the flow is then deflected laterally carrying the solute to outputs 1 and 5. This effect is due to the finite geometry of the lysimeter and would not have taken place in a semi-infinite soil profile.

The intersection of the curves $K(h)$ to the value of critical pressure head $h_c = -0.025$ m, shows the possibility of existence of a capillary barrier between the two materials depending on the hydric history (Figure 5). This is verified by modeling the test E2 where the values of water pressure heads calculated along the interface correspond to capillary pressure less than h_c. The capillary barrier deflects the flow within the sand layer and generates a preferential flow along the interface as shown by both the streamlines and velocity field (Figure 6). Below the interface, the flow returns to the vertical direction. The calculated and measured volumetric water content of the sand increases at the interface and even reaches saturation (data not shown) (Figure 7).

For outputs 4 and 5 located below the infiltration surface, the breakthrough curve of row 4 has a greater value of maximum concentration and with an earlier breakthrough as compared to row 5. Row 3 breakthrough curve shows both a greater maximum and smaller spreading than row 5 while it is furthest from the infiltration surface. However, their residence times are similar (Table 2). In the case of test E2, the maximum of the breakthrough curves row 4, 3, 2 and 1 progressively decreases as the distance to the infiltration area increases. This is the result of the combined effect of the capillary barrier, which depends on the history of water and the slope of which depends on the structure of LUGH. Moreover, it appears that the effect of preferential flow is slightly overestimated by the model because the calculated elution curve of row 1, test E2 (Figure 7) arrives later than the measured one due to a wall effect caused by the accumulation of water on the left side of LUGH (Figure 6).

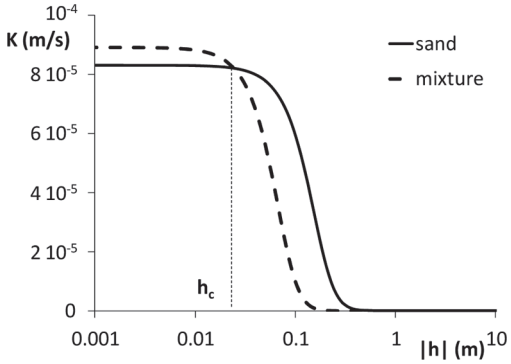

Figure 5. Hydraulic conductivity as a function of water pressure head, $K(h)$, using van Genuchten-Mualem relationship for sand and mixture sand-gravel; the critical pressure head is h_c = -0.025 m.

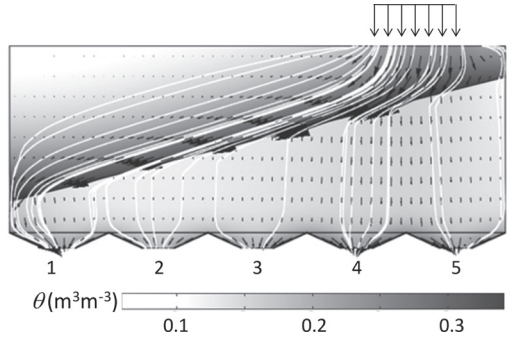

Figure 6. Volumetric water content field, θ (m^3 m^{-3}), darcian flux vector field (arrows) and stream-lines for test E2.

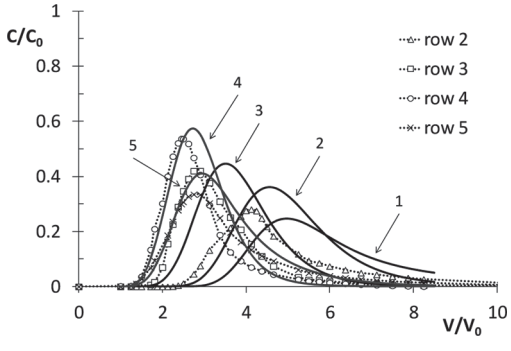

Figure 7. Bromide measured (dots) and calculated (lines) breakthrough curves for test E2; each curve is the average of rows A, B and C of the same output 1 to 5.

The standard error of the residence time calculated for rows A, B and C depend on the output row number. For E1, rows 1 and 5, the standard deviations are greater than for rows 2, 3 and 4 (Table 2). This is probably due to changes in the

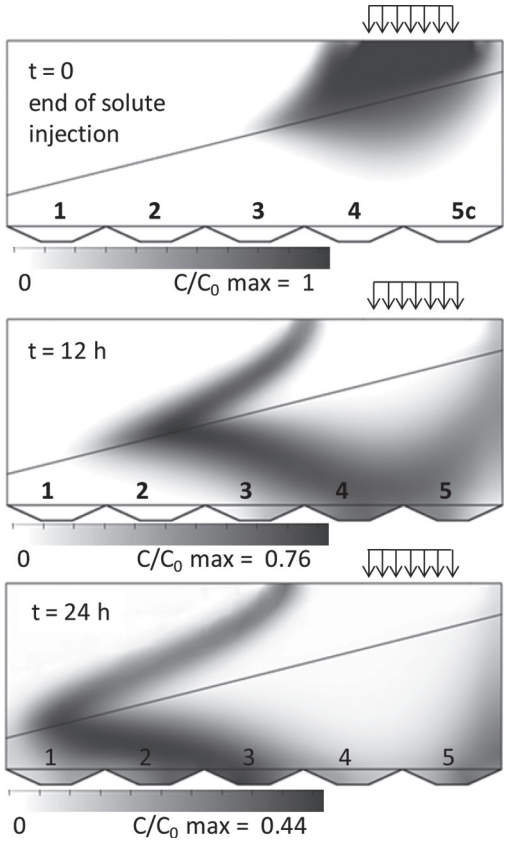

Figure 8. Relative concentration C/C_0-field at the end of the solute injection (t = 0, initial zero concentration) and after t = 12h and 24h of leaching; the plume of solute moves from the output 4 (below the input) to the outlet 2 due to the combined effect of capillary barrier and slope of the interface, for test E2.

infiltration rate; i.e., for an output that is away from the infiltration surface, the heterogeneity of the breakthrough curves will be more important.

For E2, under the combined effect of the capillary barrier, the slope of the interface and variations in the flow of infiltration, the standard deviations are large enough in rows 3 and 5 where the flow is mainly gravity driven, by comparison with row 2 where it has a higher capillary component (see the shape of the streamlines under the interface, Figure 6).

The solute is transferred homogeneously through the sand. The plume is then deformed by the presence of the capillary barrier and the slope of the interface (Figure 8). After stopping the supply of solute (t = 0), the amount of solute present in the soil is pushed by water along the preferential direction of flow (t = 12 and 24h). The maximum concentration moves along the interface showing the preferential transfer in the lysimeter.

5 CONCLUSIONS

LUGH results show the important and significant role played by the initial conditions and system boundaries on water flow and solute transport. Indeed, for the homogeneous case (test E1), we have seen that gravity flow process plays an important role in the flow pattern below the infiltration zone while capillary flow process determines both the spreading and velocity of the solute plume in areas on both sides of the lysimeter (rows 1 and 5). For the heterogeneous case (test E2), the results show a delay in transfer of solute due to the lateral extension of the plume at the interface between the materials. Water and solute are then deflected beyond the supply surface.

The comparison between experimental and modeled data is very satisfactory. Thus, the numerical simulations are of great interest in the explanation of the transfer process. It allows us to pre-design other tests by performing a flow-sensitivity analysis of all the hydrodynamic parameters and both the initial and boundary conditions. The first results of the pilot LUGH demonstrated the role of sedimentary type heterogeneity of the unsaturated zone on mass transfer processes.

The analysis of 15 elution curves and the calculation of residence time give comparable results, confirming the numerical modeling. Tests conducted at very low Darcy velocity will help us to better understand the relationship between the flow and mass transfer on one hand and behavior of the heterogeneous soil at low saturation on the other hand. In unsaturated soil condition, the effect of capillary barrier on the development of preferential flow is increased. This effect is highly dependent on soil water history.

This work shows the great interest to conduct a very precise 3D modeling to analyze laboratory experiments on a finite volume of soil, whatever its size. The variability of the velocity field, wall effects and the boundary conditions are parameters that must be taken into account when studying nonlinear solute transfer phenomena.

ACKNOWLEDGEMENTS

We thank the Rhone Basin Long Term Environmental Research Observatory (ZABR, Zone Atelier Bassin du Rhône) and the Field Observatory for Urban Water Management (OTHU, Observatoire de Terrain en Hydrologie Urbaine) for their financial support.

REFERENCES

Bear, J. 1972. Dynamics of fluids in porous media. *American Elsevier*, Mineola NY.

Bergstrom, L.F. 1990. Use of lysimeters to estimate leaching of pesticides in agricultural soils. *Env. Pollution* 67: 325–347.

Bien, L.B., Hehn, V., Lassabatère, L., Winiarski, T. & Angulo-Jaramillo, R. 2011. Transfert des solutés à travers un grand lysimètre de sol non saturé hétérogène, *36émes Journées Scientifiques du GFHN-8ème Colloque GEOFCAN réunis: milieux poreux et géophysique. Bulletin du Groupe Francophone d'humidimétrie et traNsferts en Milieux poreux (GFHN)*, 30 novembre-1 décembre, Orléans, France, pp. 82–86.

COMSOL, AB. 2008. COMSOL Multiphysics User's Guide, version 3.5a. *COMSOL AB ed:* Grenoble: 624p.

Flury, M., Flühler, H., Jury, W.A. & Leuenberger, J. 1994. Susceptibility of soils to preferential flow of water: a field study. *Water Resour. Res.* 30: 1945–1954.

Gaudet, J.P. & Vauclin, M. 2005. Rétention et transfert des pollutions des sols par les éléments traces - métaux lourds: mécanismes et modélisation numérique. In P. Delage (ed.), *Géomécanique environnementale*: 68–95. Lavoisier Pub.: Paris.

Goutaland, D., Winiarski, T., Dubé, J.S., Bièvre, G., Buoncristiani, J.F., Chouteau, M. & Giroux, B. 2008. Hydrostratigraphic characterization of glaciofluvial deposits underlying an infiltration basin using ground penetrating radar. *Vadose Zone J.* 7: 194–207.

Goyne, K.W., Day, R.L. & Chorover, J. 2000. Artifacts caused by collection of soil solution with passive capillary samplers. *Soil Sci. Soc. Am. J.* 64: 1330–1336.

Grebet, P. & Cuenca, R.H. 1991. History of lysimeter design and effects of environmental disturbances. Lysimeters for Evapotranspiration and Environmental Measurements, Am. Soc. Civil Eng. Irrigation and Drainage Division Symposium, Honolulu, Hawaii. pp. 10–18.

Hansen, J.B., Holm, P.E., Hansen, E.A. & Hjelmar, O. 2000. Use of lysimeters for characterisation of leaching from soil and mainly inorganic waste materials. Nordtest project 1494–00, Final Report, December 2000. *Technical report 473. Institute of Water Management,* Denmark.

Haverkamp, R., Debionne, S., Viallet, P., Angulo-Jaramillo, R. & de Condappa, D. 2006. Soil properties and moisture movement in the unsaturated zone: 6.1–6.59. In J.W. Delleur (ed.), *The handbook of Groundwater Engineering*. CRC: Boca Raton.

Heilig, A., Steenhuis, T.S., Walter, M.T. & Herbert, S.J. 2003. Funneled flow mechanisms in layered soil: field investigations. *J. Hydrol.* 279: 210–223.

Kaskassian, S., Chastagnet, J., Gleize, T., Côme, J.M., Getto, D., Barthes, V. & Angulo-Jaramillo, R. 2012. L'essai d'infiltration couplé à un traçage non réactif: un outil pour évaluer le transfert des polluants dans la zone non saturée des sols. *L'eau, l'industrie, les nuissances* 322: 38–45.

Kaskassian, S., Gaudet, J.P., Chastanet, J., Decung, F., Angulo-Jaramillo, R., Szenknect, S., Côme, J.M., Getto, D., Barthes, V. & Krimissa, M. 2009. Projet ANR-PRECODD/TRANSAT 2005–2009, Evaluation des temps de Transfert, dans la zone Non Saturée des sols, de contaminants dissous ou particulaires. *Guide technique:* 105 pages. http://www.burgeap.fr/page/fr/r-d.

Kung, K-J.S. 1990. Preferential flow in a vadose zone: 2. mechanism and implications. *Geoderma* 46: 59–71.

Lanthaler, C. 2004. Lysimeter Stations and Soil Hydrology Measuring Sites in Europe—Purpose, Equipment, Research Results, Future Developments. *Dipl. Thesis Mag. rer. nat., School of Natural Sciences,* Karl-Franzens-University, Graz.

Lassabatère, L., Angulo-Jaramillo, R., Soria Ugalde, J.M., Cuenca, R., Braud, I. & Haverkamp, R. 2006. Beerkan estimation of soil transfer parameters through infiltration experiments—BEST. *Soil Sci. Soc. Am. J.* 70: 521–532.

Miyazaki, T. 1988. Water flow in unsaturated soil layered slopes. *J. Hydrol*. 102: 201–214.

Mualem, Y. 1976. A new model for predicting the hydraulic conductivity of unsaturated porous media. *Water Resour. Res.* 12: 513–522.

Mubarak, I., Mailhol, J.C., Angulo-Jaramillo, R., Bouarfa, S. & Ruelle, P. 2009. Effect of temporal variability in soil hydraulic properties on simulated water transfer under high-frequency drip irrigation. *Agric. Water Management* 96: 1547–1559.

Muller, J.-C. 1996. Un point sur trente ans de lysimétrie en France (1960–1990). Une technique, un outil pour l'étude de l'environnement. *INRA, editions, Comifer, Paris*, 390p.

Parker, J. & Albrecht, K. 1987. Sample volume effects on solute transport predictions. *Water Resour. Res.* 23: 2293–2301.

Rimmer, A., Steenhuis, T.S., Selker, J.S. & Albrecht, G.J. 1995. Wick samplers: an evaluation of solute travel times. *Soil Science*, 159: 235–243.

Steenhuis, T.S. & Parlange, J.-Y. 1991. Preferential flow in structured and sandy soils. *Am. Soc. Agric. Eng.* 12–21.

van Genuchten, M.Th. 1980. A closed form equation for predicting the hydraulic conductivity of unsaturated soils. *Soil Sci. Soc. Am. J.* 44: 892–898.

Advances in Unsaturated Soils – Caicedo et al. (eds)
© 2013 Taylor & Francis Group, London, ISBN 978-0-415-62095-6

Influence of cracks on soil water characteristic curve

S. Azam, M. Ito & F. Khan
University of Regina, Regina, Saskatchewan, Canada

ABSTRACT: The soil water characteristic curve was determined for two cracked soils of Saskatchewan, Canada. Using high quality undisturbed field samples, both soils indicated bimodal curves comprising of two air entry values. The fissure AEV (associated with drainage through cracks) and the matrix AEV (related to seepage through soil matrix) were found to be 10 kPa and 300 kPa for the expansive clay in Regina and 5 kPa and 100 kPa for the cemented sandstone at Avonlea. The appropriate parameter on the ordinate for presenting the curve is water content for expansive soils and degree of saturation for erodible soils.

1 INTRODUCTION

The soil water characteristic curve (SWCC) is a continuous sigmoid function that correlates the presence of water with suction. This curve describes important features of soils when their saturation state is altered. Soils remain fully saturated with increasing suction up to the air entry value (AEV) when air starts to enter into pore spaces under capillarity. Thereafter, soils continuously lose water with increasing suction until the residual state. The remaining water is difficult to force out and complete soil desiccation requires a suction of 10^6 kPa. The curve comprises of three straight-line portions: a horizontal line from saturation to the AEV; a steep downward slope from the AEV to the residual state; and a flat downward slope from the residual state to the completely dry state. The curve shape is affected by the following soil properties: (i) grain sizes and soil microstructure that influences pore tortuousity; (ii) dry unit weight that is related to the total void space in a soil; and (iii) clay mineral types and amounts that dictate the amount of adsorbed water.

The above-mentioned SWCC works well for compacted clays and well-graded sandy soils. However, natural soils deviate from this conventional behavior owing to the presence of cracks that are primarily derived from over-consolidation and desiccation. This is particularly the case for surface soils where most construction activities take place. Theoretically, soil discontinuities affect the water flow pattern by encouraging the initial water migration through the cracks before the commencement of water movement through the pore system within the soil (Fredlund et al., 2010).

The surface sediments in southern Saskatchewan, Canada, are derived from extensive physical weathering (scraping, deposition, overburdening, and reworking of materials) by up to seven glacial advances and retreats (Christiansen & Sauer 2002). The last glaciation known as the Wisconsinan (23,000 years BP to 17,000 years BP) extended throughout the entire province. The up to 1000 m thick ice sheet started to retreat in the northeastwardly direction around 17,000 years BP. According to Mollard et al. (1998), this process was completed around 8000 years BP when the essential features of the present landform emerged including moraines and eskers. Two local soils are of particular concern because of their problematic engineering features. The expansive clay in Regina shows large swell-shrink deformations whereas the cemented sandstone at Avonlea exhibits extensive slope stability issues. Both of these soil responses are due to changes in water availability that, in turn, are derived from periodic weather variations in a predominantly semi-arid climate. Because of the glacial overburden removal, both of these soils show hair-line discontinuities within the surface layer. Clearly, a glacial geology and a semi-arid climate govern the behavior of natural soils in this part of the Canadian prairies.

The main objective of this paper was to understand the water retention behavior of two natural soils possessing cracks, namely; Regina clay and Avonlea sandstone. The geotechnical index properties of the materials were determined for preliminary soil assessment. Likewise, the soil water characteristic curves were determined using high quality undisturbed samples collected as part of separate site investigation programs.

2 GEOTECHNICAL INDEX PROPERTIES

The geotechnical index properties were determined according to the ASTM test methods as follows: (i) field water content (w) by the Standard Test Methods for Laboratory Determination of Water (Moisture) Content of Soil and Rock by Mass (D2216-05); (ii) field dry unit weight (γ_d) by the Standard Test Method for Density of Soil in Place by the Drive-Cylinder Method (D2937-10); (iii) specific gravity (G_s) by the Standard Test Methods for Specific Gravity of Soil Solids by Water Pycnometer (D854-10); (iv) liquid limit (w_l), plastic limit (w_p) and plasticity index (I_p) by the Standard Test Methods for Liquid Limit, Plastic Limit, and Plasticity Index of Soils (D4318-10); and (v) grain size distribution by the Standard Test Method for Particle-Size Analysis of Soils (D422-63(2007)). The entire grain size distribution data is not given in this paper.

Table 1 provides a summary of the geotechnical index properties of the investigated soils. Despite a closely matching specific gravity, the Regina clay had a dry unit of 1.34 g/cm^3 and a void ratio of 1.05 whereas the Avonlea sandstone had a dry unit of 1.61 g/cm^3 and a void ratio of 0.7. This indicates the finer and fissured nature of the former deposit and the coarser and dense nature of the latter sediment. Furthermore, the two materials were found to be quite different from one another in terms of their water adsorption capacity. The Regina clay was characterized by a high liquid limit (83%) and plasticity index (53%) that is attributed to the presence of expansive clay minerals in the soil (Ito & Azam 2009). In contrast, the Avonlea sandstone exhibited a lower liquid limit (39%) and plasticity index (8%) because of the predominance of non-clay minerals such as quartz, calcite, and feldspar (Imumorin & Azam 2011). These observations correlated well with the clay size fraction that measured 66% and 13% for the two sediments, respectively. Based on the Unified Soil Classification System (USCS), the Regina clay was classified as CH (clay with high plasticity) whereas the Avonlea sandstone was classified as SM (silty sand).

Table 1. Summary of geotechnical index properties.

Property	Regina clay	Avonlea sandstone
Field Water Content, w (%)	31	5
Field Dry Unit Weight, γ_d (g/cm^3)	1.34	1.61
Specific Gravity, G_s	2.75	2.73
Field Void Ratio, e*	1.05	0.7
Field Degree of Saturation, S (%)†	81	20
Liquid Limit, w_l (%)	83	39
Plastic Limit, w_p (%)	30	31
Plasticity Index, I_p (%)	53	8
Clay Size Fraction, C (%)	66	13
USCS Symbol	CH	SM

* $e = (G_s\, \gamma_w/\gamma_d) - 1$
† $S = w\, G_s/e$

3 WATER RETENTION BEHAVIOR

The SWCC was determined according to the ASTM Standard Test Methods for Determination of the Soil Water Characteristic Curve for Desorption Using a Hanging Column, Pressure Extractor, Chilled Mirror Hygrometer, and/or Centrifuge (D6836-02(2008)e2) on 10 mm thick samples obtained from undisturbed cores. Predetermined suction values were applied using pressure plate/membrane extractors manufactured by Soil Moisture Equipment Inc. The porous plates and the cellulose membranes were submerged in distilled and de-aired water for 24 hours to expel air bubbles. Thereafter, the specimens along with the retaining ring were placed on their respective porous plate or cellulose membrane and allowed to saturate. Next, the excess water was removed and each plate or membrane was placed in the designated extractor. For each suction value, the expelled water from the samples was monitored in a graduated burette. When two consecutive readings nearly matched over a 24 hour period, the test was terminated and the sample water content was determined.

For Regina clay, test data were compared with estimations using a unimodal equation (Fredlund et al., 2000) that utilized the geotechnical index properties (w, G_s, and γ_d) and the best fit of the measured GSD data (Fredlund et al., 2002). Based on a physico-empirical approach, the computer software of SoilVision Systems Ltd. divided the GSD into uniform particle sizes, each size assigned an individual SWCC calculated from the database of measured SWCC, and all summed to develop the entire curve.

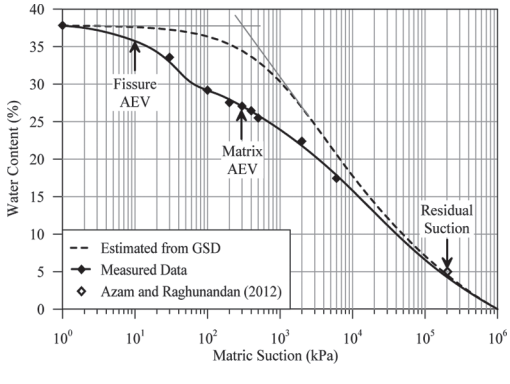

Figure 1. SWCC of Regina clay.

Figure 1 gives the SWCC of Regina clay. The estimated SWCC followed the typical theoretical trend. The full saturation water content equaling 38% remained constant up to the AEV of 300 kPa. Desaturation occurred at an increased rate between the AEV and the residual suction of 2000,000 kPa (at $w = 5\%$) and the curve finally joined the abscissa at 10^6 kPa under completely dry soil conditions.

The measured data fitted well to a bimodal distribution with two air entry values: a lower value (10 kPa) corresponding to drainage through fissures followed by a higher value (300 kPa) associated with seepage through the soil matrix. When the undisturbed samples were gradually desatuarted, air first entered into the fissures at low suction. Although these fissures are sealed due to hydration of expansive soils (Azam & Wilson 2006), numerous swell-shrink cycles over geologic time render these discontinuities to have much lower tensile strengths than the soil aggregates. This led to a quick drainage through these paths of least resistance. Subsequent application of suction affected the soil aggregates and eventually forced air to enter into the pore system of the aggregate. The matrix AEV matched the one obtained from GSD estimation because water movement through an aggregate is governed by the arrangement of individual particles. Furthermore, the downward SWCC shift of the undisturbed soil is attributed to its flocculated morphology in contrast to a dispersed fabric for the GSD sample (dispersion was ensured using sodium hexametaphosphate). The corresponding larger pores in the geologic samples were easy to dewater because of a reduced capillarity. This resulted in a greater water content reduction at the same matric suction. Beyond the residual state, the two curves converged as the water present in both of the samples was electrochemically attached to the clay surfaces. The 5% residual water corresponded to the adsorbed water, as confirmed through thermogravimetric analysis (data not given in this paper).

The SWCC given in the form of water content versus matric suction is the best representation for expansive soils. The measured value of gravimetric water content is independent of volume increase due to sample saturation. The use of the degree of saturation on the ordinate is not appropriate because it depends on void ratio. Furthermore, the definition of the degree of saturation for fissured expansive soils is not straight forward. Since such soils consist of discontinuities and soil aggregates, the calculated degree of saturation pertains to an average value for the entire soil mass. A more accurate approach for this calculation is to consider only the soil aggregates as saturated (up to the matrix AEV) and the fissures as air filled cracks. This is close to an equilibrium field microstructure that allows alternate swelling and shrinkage (Ito & Azam 2010). In this approach, the change of water volume in the soil mass equates to the volume change of the soil aggregates and that of the cracks. Gens & Alonso (1992) explained the two levels of soil structure in their framework as follows: the microstructure is governed by physicochemical interactions between the expansive clay minerals thereby forming aggregates whereas the macrostructure includes both the aggregates and the fissures.

Figure 2 presents the SWCC of Avonlea sandstone. Once again, the measured data fitted well to a bimodal distribution with two air entry values: a lower value (5 kPa) corresponding to drainage through cracks followed by a higher value (100 kPa) associated with flow through the soil matrix. When the field samples were progressively desaturated, air first entered into the discontinuities at low suction. Material erosion and dissolution during water flow enlarged these features thereby resulting in a lower fissure AEV compared to that of Regina clay. The fissures originate from geologic overburden removal and grow over time under the harsh climate prevalent in the area. Seasonal variations in water availability (snow melt in spring and rainfall in summer) and water deficiency (low rainfall and freezing in fall and winter) result in physical and chemical weathering of the deposit at Avonlea (Imumorin & Azam 2011). The associated reduction in grain sizes precludes the use of GSD for SWCC estimation. Furthermore, the finer particles get trapped in the relatively bigger soil pores left behind by the coarser particles and impart dual porosity to sandstone. Water flow through the newly formed smaller pores result in a high matrix AEV, albeit three times lower than that of Regina clay. Finally, the residual suction was found to be only 1200 kPa at $S = 15\%$. The low matrix AEV and residual suction are attributed to the low clay content of the sandstone.

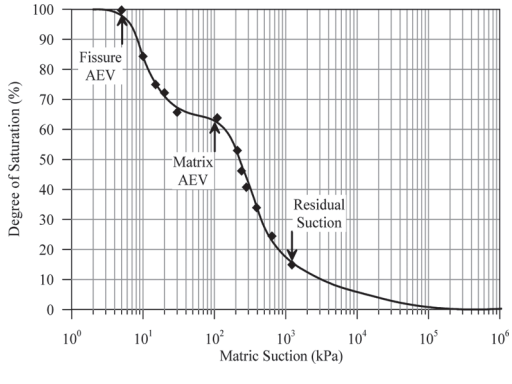

Figure 2. SWCC of Avonlea sandstone.

The SWCC in Figure 2 is given in the form of degree of saturation versus matric suction. This is the most suitable parameter for erodible soils exhibiting dual porosity because of its direct applicability to field conditions. In this representation, the SWCC pertains to the intact soil for which the degree of saturation can be calculated with reasonable accuracy because soil volume change is negligible. The commonly observed mass wasting due to erosion and dissolution in the field is different from changes in void ratio that are calculated using the three phase soil-water-air system.

4 SUMMARY AND CONCLUSIONS

The water retention behavior of natural soils possessing cracks is different from that of compacted soils or well-graded sandy soils. This is particularly true for swelling soils and erodible soils of southern Saskatchewan, Canada. Glacial geology and harsh climate govern the SWCC of the expansive clay in Regina and the cemented sandstone at Avonlea. The removal of glacial overburden has resulted in the development of hair-line discontinuities within the surface layer of these sediments. Seasonal weather variations lead to swelling and shrinkage in the clay and erosion and dissolution in the sandstone. The overall influence of geology and climate on the behavior of these two natural soils was investigated. The main conclusions of this research are summarized as follows:

- The SWCC for cracked soils is characterized by a bimodal distribution with two air entry values: a lower value corresponding to drainage through fissures followed by a higher value associated with seepage through the soil matrix.
- The fissure AEV and the matrix AEV, obtained by using high quality undisturbed field samples, were found to be 10 kPa and 300 kPa for Regina expansive clay and 5 kPa and 100 kPa for Avonlea cemented sandstone.
- The most appropriate way of presenting the SWCC of expansive soils is to use water content versus matric suction because the measured gravimetric water content is independent of volume increase due to sample saturation.
- The best way to understand field behavior of erodible soils with dual porosity is to plot the SWCC in the form of degree of saturation versus matric suction because of negligible volume changes in such soils.

ACKNOWLEDGEMENTS

The authors would like to acknowledge the financial support provided by the Natural Science and Engineering Research Council of Canada. Thanks to the Saskatchewan Ministry of Highways and Infrastructure for providing material support, the University of Regina for providing laboratory space, and SoilVision Systems Ltd. for providing the computer software.

REFERENCES

Azam, S. & Raghunandan, M.E. 2012. Rheological and desaturation characteristics of a clay slurry. *Proceedings, 65th Canadian Geotechnical Conference*, Winnipeg, Canada. Accepted.

Azam, S. & Wilson, G.W. 2006. Volume change behavior of a fissured expansive clay containing anhydrous calcium sulfate. *Proceedings, 4th International Conference on Unsaturated Soils*, Carefree, Arizona, USA. 1: 906–915.

Christiansen, E.A. & Saure, E.K. 2002. Stratigraphy and structure of Pleistocene collapse in the Regina low, Saskatchewan, Canada. *Canadian Journal of Earth Science,* 39:1411–1423.

Fredlund, M.D., Fredlund, D.G. & Wilson, G.W. 2000. An equation to represent grain-size distribution. *Canadian Geotechnical Journal,* 37: 817–827.

Fredlund, D.G., Houston, S.L., Nguyen, Q. & Fredlund, M.D. 2010. Moisture movement through cracked clay soil profiles. *Geotechnical and Geological Engineering,* 28: 865–888.

Fredlund, M.D., Wilson, G.W. & Fredlund, D.G. 2002. Use of the grain-size distribution for estimation of the soil-water characteristic curve. *Canadian Geotechnical Journal,* 39:1103–1117.

Gens, A. & Alonso, E.E.1992. A framework for the behaviour of unsaturated expansive clays. *Canadian Geotechnical Journal,* 29: 1013–1032.

Imumorin, P. & Azam, S. 2011. Effect of precipitation on geologic development of badlands in arid regions. *Bulletin of Engineering Geology & the Environment,* 70(2):223–229.

Ito, M. & Azam, S. 2009. Engineering characteristics of a glacio-lacustrine clay deposit in a semi-arid climate. *Bulletin of Engineering Geology & the Environment,* 68: 551–557.

Ito, M. & Azam, S. 2010. Determination of swelling and shrinkage properties of undisturbed expansive soils. *Geotechnical and Geological Engineering*, 28: 413–422.

Mollard, J.D., Kozicki, P. & Adelman, T. 1998. Some geological, groundwater, geotechnical and geoenvironmental characteristics of the Regina area, Saskatchewan, Canada. *Urban Geology of Canadian Cities*. In P.F. Karrow and O.L. White (eds), Department of Earth Science and Quaternary Sciences Institute, University of Waterloo, Canada.

Advances in Unsaturated Soils – Caicedo et al. (eds)
© 2013 Taylor & Francis Group, London, ISBN 978-0-415-62095-6

Influence of suction on the permeability of unsaturated soils

B. Melbouci & F. Ghanem
Laboratoire Géo Matériaux Environnement et Aménagement,
Université Mouloud Mammeri de Tizi-Ouzou, Algérie

ABSTRACT: In this research, we explore the possibility to relate permeability to the phenomenon of suction. The permeability coefficient of unsaturated soil is strongly related to particle size and pore's size distribution and it can be predicted from the curve of suction. By looking at the statistical model "of Fredlund," the suction has a significant influence on the permeability of unsaturated soils and is more pronounced when the dimensions of the pores are very small. The suggested formula of permeability is based on the use of suction curves. It is used to different types of soil suction curves which are obtained from models Pedo-Transfer Function (PTF) and Pore Size Distribution (PSD).

1 INTRODUCTION

Saturated soil is a biphasic medium (solid and liquid), whereas an unsaturated soil is a triphasic medium containing the solid skeleton, water and air. The interaction of gas-water-solid makes the mechanical behavior of unsaturated soil more complex than that of a saturated soil [Li XL., 1999], according to Fredlund and D. G. (2005), it is a soil containing water and air in the voids separated by a skin called meniscus and pore water pressure is less than that of air. An unsaturated soil is found in arid, semi arid in compacted soils. The influence of air on the soil behavior depends largely on the degree of saturation. When the gas phase is continuous, its effect on the hydro mechanical behavior results in the suction effect. Whereas, when the gas phase is discontinuous and is in the form of air bubbles trapped in the water for example, the fluid phase (mixture of water and air bubbles) from the ground behaves like a very compressible liquid.

2 THE TYPES OF SUCTION

The suction pressure is lower than that of air. It acts on the water inside the grains and leads to water movement so it's a negative pressure of the pore water. According to Bakkari A. (2007), the suction is a measure of the attraction between the soil and water. This allows water to rise to a height greater than that of the natural state. Suction is the most important parameter of hydraulic and mechanical behavior of un-saturated soils. (Blatz JA et al., 2008) listed three components of suction in unsaturated soils: matric suction, adsorption in the case of clay minerals, and osmotic suction.

2.1 *Matrix suction*

The matrix suction expresses the ability of water retention of soil components. There are two types:

*Capillary suction: is due to the difference between the pressures of air and water (pore pressure) and this pressure difference results in the existence of a meniscus between the air and water.

*Adsorption Suction: is due to the actions of physic-chemical adsorption of clays and they are as negatively charged particles.

2.2 *Osmotic suction*

Osmotic suction is the ability to retain water by the salts present in dissolved form in the pore water.

2.3 *Total suction*

The total soil suction can be seen as the sum of two components:

*Matrix suction; ψ_m
*Osmotic suction π;

$$\text{So: } \psi = \pi + \psi_m \quad (1)$$

3 FACTORS AFFECTING SOIL PERMEABILITY

Soil characteristics that influence the hydraulic conductivity (k) are: the total porosity and distribution of pore size and tortuosity (geometry porous). The characteristics of the fluid that affect conductivity are the density and viscosity of the fluid.

Flows in porous media are through complex and tortuous paths through a series of interconnected pores and different sizes and shapes.

Parameters that affect the permeability can be classified into three categories:

- Mineralogy composition, size distribution of pores, etc.
- Environmental: compaction conditions, structure, saturation, etc.
- Associated factors for measuring permeability: test method, test condition, etc.

4 PERMEABILITY OF UNSATURATED SOIL

In an unsaturated soil, the permeability coefficient is not constant, it varies depending on the combination of the void ratio and degrees of saturation and, it is strongly influenced by the variation of the suction. Several analytical expressions have been developed to predict the permeability of unsaturated soils. The fundamental principle of the application of these models is the availability of hydraulic properties of unsaturated soil, the water retention and soil hydraulic conductivity functions. The models most widely used are those of Corey-Books (1964) and Van Genuchten (1980) and recently the formula of Fredlund et al. (1994).

The hydraulic properties of unsaturated soils are needed to address problems of flow and mass transfer through the soil. One of hydraulic properties is essential retention curve of soil water. Direct measurements of this property are costly and time, and consequently models are developed to predict on the basis of soil textural indices. These models are known as "pedotransfer functions" PTFs (Pedo-Transfer functions). Given the simplicity and economy that characterizes the procedure; it is interesting to estimate indirectly the characteristic curve.

4.1 *Fredlund and Xing equation (1994)*

$$\theta(\psi) = C(\psi)\left[\frac{\theta_s}{\left[\ln\left[e+\left(\frac{\psi}{a}\right)^n\right]\right]^m}\right] \tag{2}$$

where:

- e: is the base of natural logarithms, which equals 2.71828,
- a: is approximately the value of the point corresponding to the suction air inlet of the soil,
- n: is a soil parameter connected to the slope of the curve of water retention, at the inflection point,
- m: is a parameter related to the residual water content,
- θs: is the saturated volumetric water content,
- C (ψ): is a correction function defined as:

$$C(\psi) = 1 - \frac{\ln\left(1+\frac{\psi}{\psi_r}\right)}{\ln\left(1+\frac{10^6}{\psi_r}\right)} \tag{3}$$

With:

- ψ_r: is suction corresponding to residual water content θ_r,

4.2 *Functions of pedi-transfer*

The Pedi-transfer functions can be classified into two groups [M. Huang et al., 2008].

The first group of PTFs using statistical estimates of soil properties to describe the curve of suction or water retention. Soil properties are: particle size and volume properties—mass.

The second group of TFPs uses a physic-empirical that converts the particle size distribution by the distribution of pore size.

4.3 *Application of the method of Fredlund*

To study this permeability parameter, we were inspired by the method of Fredlund et al. (1994) which is a statistical method which exploits the suction curve and deduce the function of hydraulic conductivity k(ψ). The principle consists in subdividing the curve of suction (Figure V-1), represented in the plane Θ(s) along the axis into n segments equal Θ, Θ is defined by the following relationship:

$$\theta = \frac{\theta - \theta_r}{\theta_s - \theta_r} \tag{4}$$

The permeability function k(Θ) is given by the expressions below:

$$K(\Theta_i) = \frac{k_s}{k_{sc}} \frac{T_s^2 \rho_w g}{2\mu_w} \frac{\theta_s^p}{n^2} \Sigma_{j=i}^m \left[(2j+1-2i)\,\psi_j^{-2}\right] \tag{5}$$

$$k_{sc} = \frac{T_s^2 \rho_w g}{2\mu_w} \frac{\theta_s^p}{n^2} \Sigma_{i=1}^m \Sigma_{j=i}^m \left[(2j+1-2i)\psi_j^{-2}\right] \tag{6}$$

i = 1,2, ..., m

j: i varies from to m

With:

- $k(\theta_i)$: permeability function of the effective volumetric water content (θ_i) corresponding to the i_{th} interval.

k_s: coefficient of saturated permeability, measured in the laboratory.
k_{sc}: Permeability calculated at saturation.
T_s: surface tension;
m: Total number of intervals between the volumetric water content at saturation θ_s and the minimum volumetric water content θ_r on soil-water characteristic curve.
ψ_j: suction corresponding to point to the center of the j_{th} interval.
i: interval number which increases with the decrease in water content by volume.
m: is the number of intervals between the saturated water content (θ_s) and the minimum moisture con-tent (θ_l) in the curve of suction;
n: number of intervals between the saturated water content (θ_s) and the water content of zero ($\theta = 0$) ($n = m\ [\theta s / ((\theta s\text{-}\theta l))]$);
g: acceleration of gravity;
ρ_w: water density;
u_w: absolute viscosity of water;

The above formula can also be expressed as relative permeability kr (θi), as follows:

$$k_r(\Theta_i) = \sum_{j=i}^{m} \frac{2(j-i)+1}{\psi_j^2} \Big/ \sum_{j=i}^{m} \frac{2(2j-i)}{\psi_j^2} \qquad (7)$$

5 INFLUENCE OF SUCTION ON THE PERMEABILITY OF UNSATURATED SOIL

The presentation and interpretation of results obtained by applying the method of Fredlund et al. (1994) was used in our case on several soil types in order to study the influence of suction on the permeability. The influence of residual water is then processed. Using this method, whose principle is to use suction curves, helped plot the curves of relative permeability of the soil. In this study, we considered two cases in order to know the influence of the residual water content on the permeability. First Case: In this case, we used suction curves (volumetric water content in terms of suction), neglecting the residual water content ($\Theta = 0$). Second case: First we plotted the curves of suction pressure versus normalized water content (Θ), in order to know the influence of the latter on the permeability of unsaturated soils.

In the graphs below (Fig. 1), the curves $Kr = f(\psi)$ show the influence of suction on the unsaturated permeability of different soils existing through the gravelly sand, medium, fine, silt sand, the loam, sandy loam soil, the clay and bentonite.

Based on the above curves (fig. 1), we find that the permeability coefficient does not vary linearly. For sandy soils, the unsaturated permeability is instantaneous in a small range of suction that does not exceed 10 kPa, because the pores are emptied suddenly, while, soil permeability purpose is not instantaneous and can reach a range of very high suction exceeding 100,000 kPa as fine soils have a high capacity to retain water. This is due to the plasticity of soil, particle size, and soil texture and the tortuosity and connectivity of pores.

The prediction of the permeability coefficient for clay soils is generally less accurate than sandy soils. Therefore, the prediction of relative permeability soil becomes less accurate when the suction increases.

We also note that the permeability of the capillary is constant with increasing suction. The soil is plastic over the capillary is very important.

5.1 *Comparison of the relative permeability between the two cases*

In the first, the suction curves as a function of normalized water content (Θ) have been established (taking into account the residual water content) in order to know the influence of the latter on not saturated soil permeability. We, then, plotted the relative permeability curves using the same procedure. A comparison was made between the permeability curves of the first case and that of the second case for each soil type, to show the influence of the residual water content of the unsaturated permeability. The results are shown in Figures 2.

According to the different figures obtained on different materials, we observe that the residual content does not affect the permeability of unsaturated soils. The permeability curves obtained are similar to those provided by the literature for similar materials. The small offset between the curves may be due to calculation errors.

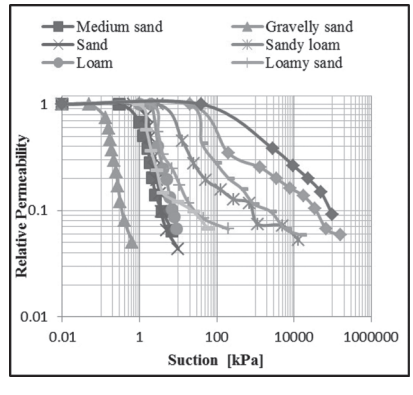

Figure 1. Synthesis of the permeability curves of un-saturated soils.

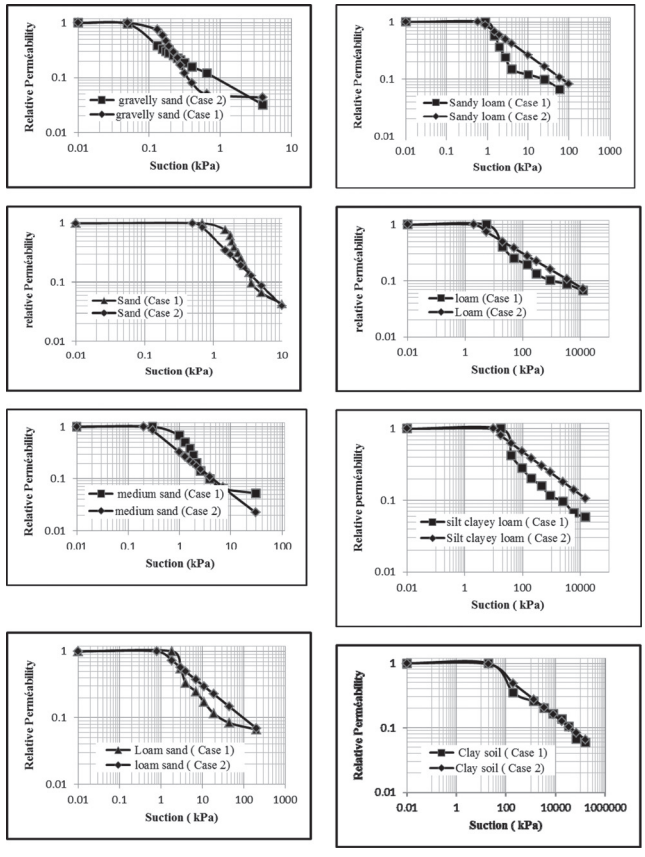

Figure 2. Comparison of unsaturated permeability curves between the first and second case.

6 CONCLUSIONS

The permeability of unsaturated soils is an important parameter for understanding soil behavior. It is mainly determined by the distribution of pore size. The coefficient of permeability of an unsaturated soil is also strongly related to particle size and it can be predicted from the curve of suction. The suction has a significant influence on the permeability of un-saturated soils. This influence is naturally more marked when the pore dimensions are very small. The method thus established in this work is applicable to different soil types in a range of suction from 0 to 106 kPa. It is very helpful in cases where experimental data are not available.

REFERENCES

Bakkari, A. (2007). Observation et modélisation d'ouvrages en terre soumis à des processus de séchage et d'humidification; thèse doctorat l'école nationale des ponts et chaussées.

Blatz, J.A., Cui, Y.J. & Oldecop, L. (2008). Vapour Equilibrium and Osmotic Technique for Suction Control; Geotech. Geol Eng 26: 661–673.

Brooks, R.H. & Corey, A.T. (1964). Hydraulic properties of porous media, Hydrology Paper N° 3, Colorado State University, Fort Collins, CO.

Fredlund, D.G. (2005). Teaching Unsaturated Soil Mechanics as Part of the Undergraduate Civil Engineering Curriculum; Visiting Professor Kobe University, Kobe, Japan.

Fredlund, D.G, Xing, A. & Huang, S. (1994). Predicting the permeability function for unsaturated soils using the soil-water characteristic curve; Journal géotechnique canadien, 31(3): 521–532.

Huang, S., Barbour, S.L. & Fredlund, D.G. (1998). Development and verification of a coefficient of permeability function for a deformable unsaturated soil; Department of Civil Engineering, 57 Campus Drive, University of Saskatchewan, Saskatoon, SK S7 N 5 A9, Canada.

Li, X.L. (1999). Comportement Hydromécanique des Sols Fins: de l'état saturé à l'état non saturé; Thèse de doctorat Université de Liège, Faculté des Sciences Appliquées (Belgique).

Van Genuchten, M.Th. (1980). A closed-form equation for predicting the hydraulic conductivity of unsaturated soils. Soil Sci. Am. J., 44, 892–898.

Advances in Unsaturated Soils – Caicedo et al. (eds)
© 2013 Taylor & Francis Group, London, ISBN 978-0-415-62095-6

Evaluation of the suction calibration curves for Whatman 42 filter paper

K.V. Bicalho, K.F. Cupertino & A.I. Bertolde
Federal University of Espirito Santo, Vitoria, ES, Brazil

ABSTRACT: The filter paper method is probably the simplest of the methods available for estimating a wide range of soil suction. The method is highly dependent on the suction calibration curve employed (i.e., the water retention or characteristic curve of the filter paper). Several calibration functions for ash-less filter paper have been published in the literature, and significant discrepancy exists among them. Most of the functions are called "bilinear" (i.e., two different equations). The possibility of using a smooth function representing the best-fit curve for fictional points obtained from seven published calibration curves is evaluated. The suggested function incorporates a power law and a logarithmic dependence of water content on suction as observed in most published soil water retention functions. The variability of the suggested function compared to the seven published calibration curves for Whatman 42 filter paper for different levels of suction is quantified.

1 INTRODUCTION

The filter paper method (FPM) is probably the simplest of the methods available for estimating suction of soils for essentially the full range of interest for fluid and vapor transport and other geotechnical applications (Houston et al.,1994).The method calculates soil suction indirectly by measuring the filter paper water content at equilibrium that is related to soil suction through a predetermined suction calibration curve. The calibration function defines the water retention curve (or characteristic curve) of the filter paper.

A number of calibration functions for ash-less filter papers have been published in the literature. Bicalho et al. (2009) show that significant discrepancy exists among the several published calibration functions for the filter paper Whatman 42. Most of the functions are called "bilinear" (i.e., two different equations) with an inflection point occurring at a filter paper gravimetric water content value somewhere between 30 and 50% (120 kPa > corresponding suction > 60 kPa).

The possibility of using a smooth function representing the best-fit curve for fictional points obtained from seven published calibration curves is evaluated in this paper. The function assumes the non-linearity between pairs of filter paper gravimetric water content and suction (logarithmic scale) as observed in most mathematical formulations of the published soil water retention functions. The variability of the suggested function compared to seven published calibration curves for Whatman 42 filter paper for different levels of suction is quantified. This paper is a continuation of the earlier papers (Bicalho et al., 2009, 2011), and for providing continuity, the previous papers are briefly summarized here.

2 FILTER PAPER TECHNIQUE

The FPM calculates the soil suction indirectly from previous calibration. Basically, the filter paper comes to equilibrium with the soil either through vapor (total suction measurement) or liquid (matric suction measurement) flow. At equilibrium, the filter paper and the soil will have the same suction value. After equilibrium is established between the filter paper and the soil in a relatively constant temperature environment, the gravimetric water content of the filter paper disc is measured, and converted to suction using a calibration curve for the type of paper used. This is the basic approach suggested by the American Society for Testing and Materials (ASTM) standard D5298 for the measurement of either matric suction using the contact filter paper technique or total suction using the non-contact filter paper technique. The ASTM D5298 employs a single calibration curve that has been used to infer both total and matric suction measurements and recommends the filter papers to be initially oven-dried (16 h or overnight) and then allowed to cool to room temperature in a desiccator. The ASTM D5298 calibration curve is a combination of both wetting and drying curves. However, because of the marked hysteresis on wetting and drying of the filter paper, the calibration curve for initially dry

filter paper is different from that of the initially wet filter paper. Muñoz-Castelblanco et al. (2010) show that the gap between the drying and wetting filter paper calibration is more remarkable at higher levels of suction (> 100 kPa). Some publications presents calibration for the wetting path, with the paper initially air dry (Chandler & Gutierez 1986; Chandler et al., 1992; Ridley 1993; and Marinho 1994).

The contact FPM is used for measuring matric suction of soils. In the method, water content of an initially dry filter paper increases due to a flow of water in liquid form from the soil to the filter paper until both come into equilibrium. Therefore, a good contact between the filter paper and the soil has to be established. The contact FPM becomes inaccurate in high matric suction range since water transport is dominated by vapor transport (Fredlund & Rahardjo 1993).

2.1 *FPM calibration curves*

The calibration curve for the filter paper matric suction measurement is commonly established using a pressure plate apparatus (e.g., Al-Khafaf & Hanks 1974; Hamblin 1981; Greacen et al., 1989). It is important to note that only ash-less filter papers should be used in the filter paper technique. Although there are several ash-less filter papers available, only Whatman 42 and Sleicher and Schuell 59 (or SS 59) are commonly used.

A number of calibration functions for Whatman No. 42 filter papers have been published in the literature. The functions share a number of similarities, allowing them to be written in a general form as (Bicalho et al., 2011):

$$Log_{10}(s) = A - Bw \quad (1)$$

where s = suction (kPa), w = gravimetric water content (%) of the filter paper at equilibrium, and A, B = the fitting parameters. Chandler & Gutierrez (1986) presented a calibration curve for suctions in the range of 80 kPa and 6000 kPa that included their own results and also those from Fawcett & Collis-George (1967) (i.e., A = 5.777 and B = 0.06) and Hamblin (1981) (i.e., A = 6.281 and B = 0.0822), therefore, the obtained calibration curves are similar with obtained A = 5.85 and B = 0.0622.

Figure 1 shows some calibrations (wetting paths) presented in the literature for the filter paper Whatman 42 with an inflection point occurring at a filter paper gravimetric water content value around 47% (suction 60 kPa). Marinho & Oliveira (2006) suggest a calibration function for the filter paper Whatman 42 with an inflection point occurring at a filter paper gravimetric water content equal to 33% (suction 115 kPa). The calibration curves proposed by Chandler et al. (1992), ASTM Standard D5298

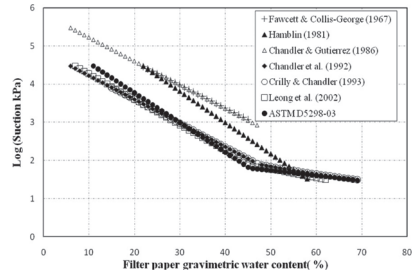

Figure 1. Evaluated calibration curves (wetting paths) for Whatman 42 filter paper.

and Leong et al. (2002)-Matric suctions are similar with A in Equation 1) ranging from 4.842 (Chandler et al., 2002) to 5.327 (ASTM D5298) and B ranging from 0.0622 (Chandler et al., 1992) to 0.0779 (ASTM D5298). A similar agreement can be seen in the suctions derived using the curves proposed by Chandler et al. (1992), ASTM D5298 and Leong et al. (2002)-Matric suctions. Considerable variability is observed between their results and those of Fawcett & Collis-George (1967), Hamblin (1981) and Chandler & Gutierrez (1986) (which seem to overestimate the values of suction).

Although Leong et al. (2002) suggested the use of different calibration curves for matric and total suctions, caution is recommended when using published total suction calibration curves since such curves are expected to be valid only for the equalization time used during the corresponding calibration. If the equilibrium between the filter paper and the soil has not yet been achieved, the total suction calibration curve might give total suction estimations smaller than corresponding matric suction estimations, yielding an unrealistic negative value of osmotic suctions. Marinho & Oliveira (2006) suggest a unique calibration for matric and total suctions.

3 EXPERIMENTAL RESULTS

Tests were performed on a residual silty sand, hereafter called Perafita sand, resulting from weathered granite, which has been used as a building material for a road in the north of Portugal. It contains about 20% of grains smaller than 80 μm, with a layered structure similar to that of clay particles. The liquid limit of the Perafita sand is 32.6%, the plastic limit is 25%, clay fraction is 2.5%, specific gravity is 2.66, standard Proctor optimum water content is 17.6% and the corresponding dry density is 16.8 kN/m^3, modified Proctor optimum water content is 13.2% and the corresponding dry density is 18.6 kN/m^3. The preparation procedure of samples is the same for all the tests: the soil is sieved to avoid the presence of coarse grains (maximum size 4.75 mm), then

it is mixed up with the right quantity of water; after that, it is placed in a sealed plastic bag for 24 hours to allow the hydric equilibrium to establish. The contact filter paper tests were carried out on soil specimens compacted to the modified Proctor optimum water content (13.2%) and nearly maximum density (18.6 kN/m^3). The compacted soil specimen sizes were 102 mm in diameter and 23.35 mm high.

The test procedure involves placing a piece of initially air dry filter paper against the compacted soil specimen whose matric suction is required and sealing the whole to prevent evaporation. The filter paper then wets up to water content in equilibrium with the magnitude of the soil matric suction, and careful measurement of the water content of the filter-paper enables the soil matric suction to be obtained from a previously established correlation. This provides a measure of the matric suction, which is assumed to be the same numerically as the capillary pressure (the reference being the atmospheric pressure). The Whatman 42 filter paper was used in all tests.

The other techniques (i.e., tensiometers, and the osmotic technique) used to measure or control the negative pore water pressure in the compacted soil specimens are not discussed in this paper since the purpose herein is to discuss the filter paper technique only. Details of the experimental techniques are given in Fleureau et al. (2002).

4 STATISTICAL ANALYSIS

The suctions inferred from filter paper measurements depend on the used calibration function, and there is a variability and uncertainty associated with the used calibration. In practice, an engineer is unlikely to evaluate the several calibrations functions proposed in the literature. Therefore, it may be convenient to know what variability can be expected from choosing one of the many cited calibration functions for Whatman No. 42 filter papers.

In this paper, a regression line (known as the *least squares line*) is used to examine the linear w-Log$_{10}$ (suction) relationship (Eq. 1) and to quantify the variability around the best estimate function. A best fitted calibration function that "minimizes the squared residuals" is defined for all data (fictional points) obtained from the seven calibration functions previouly discussed for suction values between 30 and 30000 kPa. Since the regression model is usually not a perfect predictor, there is also an error term in the Equation 1. The coefficient of determination (r-squared, R^2) is the square of the correlation coefficient. Its value may vary from zero to one.

Initially, two best fitted calibration functions that "minimizes the squared residuals" is defined for all fictional data points obtained from the evaluated seven calibration functions. It is assumed an inflection point occurring at a filter paper gravimetric water content value of 47% (see Fig. 2). The resulted functions based on the correlation coefficient criterion are:

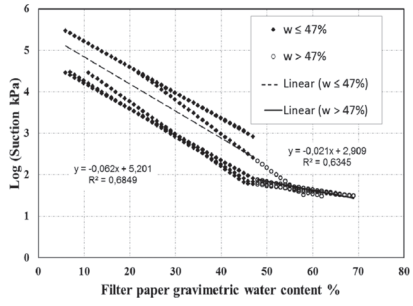

Figure 2. Two linear calibration functions resulted from the seven evaluated calibration curves for Whatman 42 filter paper.

for w ≤ 47%

$$Log_{10}(s) = 5.201 - 0.062w \quad (2a)$$

for w > 47%

$$Log_{10}(s) = 2.909 - 0.021w \quad (2b)$$

Figure 2 shows a large discontinued data in the ordinates (y) represented by suction values in logarithmic scale such as: if the filter paper gravimetric water content (w) is near 47%, the corresponding suction lies between 84 kPa (Eq. 2b) and 194 kPa (Eq. 2a). Therefore, it was calculated an alternative model to the linear models adopted by the evaluated calibration functions to verify the possibility of non-linearity between pairs of filter paper gravimetric water content and Log (suction) as observed in most mathematical formulations of the published soil water retention curves (Brooks & Corey, 1966; van Genuchten, 1980; Fredlund & Xing 1994).

In the Equation 2 the data were treated using linear statistical models, where pairs of data are converted into a straight line. When a nonlinear statistical model (where exponential functions, potential or reciprocal are applied) can be expressed by a straight line it is called intrinsically linear.

Thus, the exponential function shown in Equation 3 can be considered intrinsically linear because it can be transformed into a straight line through the logarithmic transformation.

$$Log_{10}(s) = Ae^{-Bw} \quad (3)$$

The resulted function obtained from the seven calibrations presented in Figure 1 is given by:

$$Log_{10}(s) = 6.0635e^{-0.022w} \quad (4)$$

Figure 3 shows the resulted function based on the correlation coefficient criterion ($R^2 = 0.8654$). To quantify the variability around the best estimate calibration function define by Equation 4, the predicted suctions obtained by each evaluated calibration function were compared with the suction values from the best fitted defined by Equation 4 for each level of w. The variability is evaluated by using the mean error (ME) and the root mean squared error (RMSE) defined by:

$$ME = \frac{1}{N}\sum_{i=1}^{N}(\hat{Y} - \hat{Y}_M) \quad (5)$$

$$RMSE = \sqrt{\frac{1}{N}\sum_{i=1}^{N}(\hat{Y} - Y_M)^2} \quad (6)$$

where $\hat{Y}$ = Log (s) obtained by Equation 4, Y_M = Log (s) of each evaluated calibration function for the corresponding w, and N is the number of data points. The results are presented in Table 1 for nonlinear analysis.

When comparing regression models that use the same dependent variable and the same estimation period, the RMSE goes down as adjusted R^2 goes up. In the regression nonlinear analysis, the calibration function proposed by Crilly & Chandler (1993) has the lowest RMSE and ME values thus it is the one that best adjust the resulted calibration function defined by Equation 4 (see Table 1). The same was not observed in the RSME and ME values of Fawcett & Collis-George (1967), Chandler & Gutierrez (1986) and Hamblin (1981) that presented the highest when compared with the best fitted calibration function's results defined by Equation 4.

When comparing regression models that use the same dependent variable and the same estimation period, the RMSE goes down as adjusted R^2 goes up. In the regression nonlinear analysis, the calibration function proposed by Crilly & Chandler (1993) has the lowest RMSE and ME values thus it is the one that best adjust the resulted calibration function defined by Equation 4 (see Table 1). Fawcett & Collis-George (1967) presented the highest RMSE and ME values.

It is also determined a best fitted calibration function that "minimizes the squared residuals" defined for all data points (i.e., suction values between 30 and 30000 kPa) obtained from the calibration functions proposed by Chandler et al. (1992), ASTM Standard D5298 and Leong et al. (2002) called here local calibration function. The local calibration function based on the correlation coefficient criterion was calculated in nonlinear analysis ($R^2 = 0.976$). The best fitted calibrations in non linear analysis are given by (see Fig. 4):

$$Log_{10}(suction)(kPa) = 5.328e^{-0,022w} \quad (7)$$

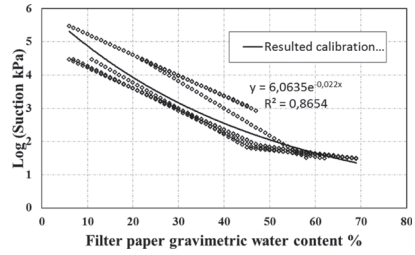

Figure 3. Resulted nonlinear calibration function from the seven evaluated calibration curves for Whatman 42 filter paper.

Table 1. Values of RSME and ME for the evaluated calibration functions compared to Equation 4.

References	RSME	ME
Fawcett & Collis-George (1967)	0.833	–0.832
Hamblin (1981)	0.497	–0.408
Chandler & Gutierrez (1986)	0.724	–0.695
Chandler et al. (1992)	0.310	0.211
Crilly & Chandler (1993)	0.198	0.140
Leong et al. (2002)	0.323	0.289
ASTM D5298-03	0.215	0.164

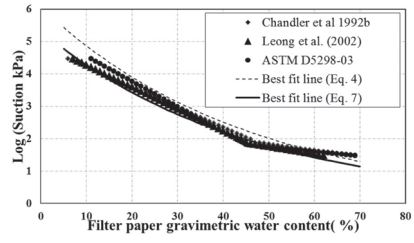

Figure 4. Best fit line resulted from the three evaluated calibration curves for Whatman 42 filter paper.

Table 2 presents the obtained RMSE and ME values for the three evaluated calibration functions compared to Equation 7. The RMSE and ME values goes down indicating small variability among the calibration functions proposed by Chandler et al. (1992), ASTM Standard D5298 and Leong et al. (2002) and the resulted best line. In Figure 4 the solid line represent Equation 7 (the best adjusted function to the three evaluated calibration functions for Whatman 42 filter paper in the nonlinear analysis).

A confidence interval gives an estimated range of values which is likely to include an unknown population parameter, the estimated range being calculated from a given set of sample data. The level C of a confidence interval gives the probability that the interval produced by the method employed includes the true values of the parameter. Figure 5 shows a pair of 80% confidence intervals (upper and lower

Table 2. Values of RSME and ME for the evaluated calibration functions compared to Equation 7.

References	RSME	ME
Chandler et al. (1992)	0.092	0.019
Leong et al. (2002)	0.119	0.081
ASTM D5298–03	0.170	0.004

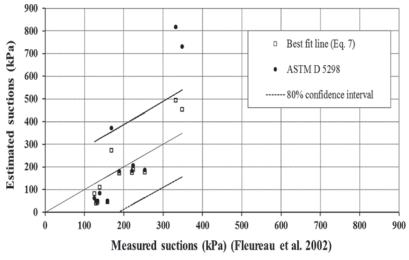

Figure 5. A pair of 80% confidence intervals (upper and lower limits) calculated from Eq. (7) and ASTM calibration function.

limits) calculated from each calibration line, but varies from calibration line to calibration line, although obtained under the same experimental conditions. The results, presented in Figure 5, are the estimated suctions determined by the contact filter paper tests using the calibration functions proposed by Equation 7 and ASTM D5298 and the measured suctions of compacted Perafita sand specimens resulting from several methods used by Fleureau et al. (2002). It is observed a general agreement between the FPM test results using the calibration curves ASTM D5298 and a non linear function proposed by this paper (Eq. 7) and other techniques used to measure or control suctions in the compacted soil specimens for 100 kPa < suction < 300 kPa. The values given by Equation 8 are inserted within the confidence interval and therefore it is the one that best adjust the investigated data.

Various functions are published at literature to describe the water retention curve (Brooks & Corey, 1966; van Genuchten, 1980). Usually they are successful at high and medium water contents but often give poor results at low water contents (Nimmo, 1991; Ross et al., 1991). Another issue related to these functions is that they either do not allow water content to be zero, an assumption that is physically unrealistic (Nimmo, 1991), or they allow it to be zero only at infinite suction. Additionally, these functions are largely empirical and disconnected from basic soil properties, such as pore geometry and adsorption (Hillel 1980). Besides the mentioned limitations these functions are often cited. Therefore, the fitting of the Brooks & Corey (1966) equation to the three chosen data sets is also discussed here.

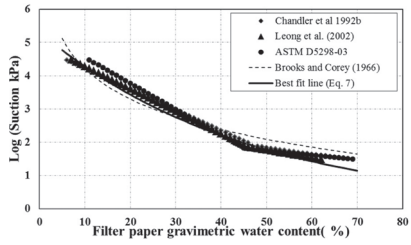

Figure 6. Best fit line resulted of nonlinear analysis from the three evaluated calibration curves for Whatman 42 filter paper.

Brooks & Corey (1966) represent the normalized dimensionless effective saturation, S_e, as a power function of suction, s:

for $s \le s_c$

$$S_e = \left(\frac{s}{s_c}\right)^{-\lambda} \tag{8a}$$

for $s > s_c$

$$S_e = 1 \tag{8b}$$

where $S_e = (S - S_r)/(1 - S_r)$, S = the degree of saturation corresponding to suction s, S_r = the residual saturation, and s_c, λ = the fitting parameters. The parameter s_c is commonly termed the air entry value, and λ is a positive value. Equation (8a) can be rewritten as:

$$s = s_c \left(\frac{G_s w}{e} - S_r\right) \Big/ (1 - S_r) \tag{9}$$

where G_s = the specific gravity, and e = void ratio for the used Whatman No. 42 filter papers. Marinho (2012) suggests the value of s_c around to 4.95 kPa, G_s = 1.8 and e = 2,6 for the used paper (Whatman No. 42).

Figure 6 shows results of fitting the Brooks & Corey (1966) to the three chosen data sets. The values of the Brooks & Corey (1966) parameters used in the analysis are: $\lambda = 0.33$ and $S_r = 0$. The fitting is generallv very good for both equations. Although Brooks & Corey (1966) provide fits inferior to those of the Equation 7, more measured data are required to support the validity of the proposed equation. Moreover, the use of the functions should be limited to the range of the original data on which they are based.

5 CONCLUSIONS

An evaluation of using different filter paper calibrations in the contact filter paper test for measurement of soil suction was conducted in this

paper. The method offers a simple technique for the determination of soil suction, provided that an adequate calibration curve is used. It is always recommended to verify if the calibration can be used without causing significant errors in the suction values to be determined. A similar agreement can be seen in the suctions derived using the calibration functions for Whatman No. 42 filter papers (wetting path) proposed by Chandler et al. (1992), ASTM D5298 and Leong et al. (2002)-Matric suctions. Considerable variability is observed between their results (Chandler et al. (1992), ASTM D5298 and Leong et al. (2002)-Matric suctions) and those of Fawcett & Collis-George (1967), Hamblin (1981) and Chandler & Gutierrez (1986) which seem to overestimate the values of suction.

It is defined a smooth function representing the best-fit curve for fictional points obtained from the often cited calibration curves: Chandler et al. 1992, ASTM D5298 and Leong et al. 2002. The suggested function assumes the non-linearity between pairs of filter paper gravimetric water content and Log (suction) as observed in most mathematical formulations of the published soil water retention curves.

It is observed a general agreement between the FPM test results using the suggested suction calibration function and other techniques used to measure or control suctions in the compacted silty sand specimens for 100 kPa < suction < 300 kPa.

ACKNOWLEDGEMENTS

The authors are grateful for sponsorship by the Brazilian government agency CNPq and FAPES FACITEC. The discussions with Professor Fernando Marinho about the filter paper method are very much appreciated.

REFERENCES

Al-Khafaf, S. and Hanks, R.J. 1974. Evaluation of the filter paper method for estimating soil water potential. *Soil Sci.* 117, 194–199.

ASTM Standard D5298-03. 2007. Standard Test Method for Measurement of Soil Potential (Suction) Using Filter Paper, Annual Book of ASTM Standards, *Soil and Rock* (I), 4(8), ASTM International,West Conshohocken, PA.

Bicalho, K.V., Marinho, F.A.M., Fleureau, J.M. and Correia, A.G. 2011. Evaluation of filter paper calibrations for indirect determination of soil suctions of unsaturated soils, *Proc. of 5th Int. Conf. on Unsaturated Soils*, Barcelona, 609–613.

Bicalho, K.V., Marinho, F.A.M., Fleureau, J.M., Correia, A.G. and Ferreira, S. 2009. Evaluation of filter paper calibrations for indirect determination of soil suctions of an unsaturated compacted silty sand. *17th International Conference on Soil Mechanics and Geotechnical Engineering*, 1, 777–780.

Brooks, R.H. and Corey, A.T. 1966. Properties of Porous Media affecting fluid flow. *J. Irrig. and Drain. Div.* ASCE, 92(2), 61–88.

Chandler, R.J., Crilly, M.S. and Montgomery-Smith, G. 1992. A low-cost method of assessing clay desiccation for low-rise buildings. *Proc. Instn. Civ. Engrs Civ. Engng.* 92, May, 82–89.

Chandler, R.J. and Gutierrez, C.I. 1986. The filter paper method of suction measurement. *Geotechnique* 36(2): 265–268.

Crilly, M.S. and Chandler, R.J. 1993. A method of determining the state of desiccation in clay soils. *BRE Information Paper IP 4/93 Garston*, Construction Research Communications Ltd.

Fawcett, R.G. and Collis-George, N. 1967. A filter paper method for determining the moisture characteristics of soil. *Amt. J. Exp. Agric. Anim. Husb.* 7, 162–167.

Fleureau, J.-M., Hadiwardoyo, S., Dufour-Laridan, E. Langlois, V. and Gomes Correia, A. 2002, Influence of suction on the dynamic properties of a silty sand. *Unsaturated Soils*, Jucá, de Campos and Marinho (eds), Sweets and Zeitlinger, Lisse, 2, 463–471.

Fredlund, D.G. and Rahardjo, H. 1993. *Soil mechanics for unsaturated soils.* Wiley & Sons, New York.

Fredlund, D.G. and Xing, A. 1994. Equations for the soil-water characteristic curve. *Can. Geotech. J*. 31: 521–532.

Greacen, E.L., Walker, G.R. and Cook, P.G. 1989. Procedure for the Filter paper method of measuring soil water suction, Division of soils, Report 108, CSIRO *Division of Water Resources*, Glen Osmond, Australia.

Hamblin, A.P. 1981. Filter paper method for routine measurement of field water potential. *J. Hydrol.* 53, 355–360.

Hillel, D. 1980. *Fundamentals of Soil Physics,* Academic Press, Inc, San Diego, California.

Houston, S.L., Houston, W.N. and Wagner, A. 1994. Laboratory filter paper suction measurements, *Geotechnical Testing Journal*, 17(2): 185–194.

Leong, E.C., He, L. and Rahardjo, H. 2002. Factors Affecting the Filter Paper Method for Total and Matric Suction Measurements, *Geotech. Test. J.*, 25(3): 322–332.

Marinho, F.A.M. 1994. Shrinkage behavior of some plastic clays. PhD Thesis, Imperial College, University of London.

Marinho, F.A.M. and Oliveira, O.M. 2006. The filter paper method revised. *ASTM geotechnical testing journal,* USA, 29(3): 250–258.

Marinho, F.A.M. 2012. Personal communication.

Muñoz-Castelblanco, J.A., Pereira, J.M., Delage, P. and Cui, Y.J. 2010. Suction measurements on a natural unsaturated soil: a reappraisal of the filter paper method, *UNSAT 2010*, Barcelona, Spain.

Nimmo, J.R. 1991. Comment on the treatment of residual water content in "A consistent set of parametric models for the two-phase flow of immiscible fluids in the Subsurface" by Luckner et al., *Water Resour. Res.*, 27, 661–662.

Ridley, A.M. 1993. The measurement of soil moisture suction. PhD thesis, University of London.

Ross, P., Williams, J.J. and Bristow, K.L. 1991. Equation for extending water-retention curves to dryness, *Soil Sci. Soc. Am. J.*, 55, 923–927.

van Genuchten, M. 1980. A closed form equation for predicting the hydraulic conductivity of unsaturated soils. *Soil Sci.* 44, 5, 892–898.

Advances in Unsaturated Soils – Caicedo et al. (eds)
© 2013 Taylor & Francis Group, London, ISBN 978-0-415-62095-6

Soil water characteristic curves of lime-treated highly expansive soils

T.Y. Elkady
King Saud University, Riyadh, Saudi Arabia
Cairo University, Giza, Egypt

A.M. Al-Mahbashi
King Saud University, Riyadh, Saudi Arabia

ABSTRACT: Estimation of the long-term performance of lime-treated expansive subgrade requires information on its unsaturated behavior. This paper aims at investigating the effect of the lime treatment on the soil-water characteristic curves of expansive soils. Tests were performed on compacted samples of lime-treated expansive clay from Saudi Arabia considering lime contents of 0%, 2%, and 4% and curing periods of 7 and 28 days. Soil water characteristic curves were determined by axis translation technique and filter paper method to cover a wide suction range. Test results revealed that lime content had a significant effect on the shape of the soil water characteristic curves; while, curing period had a less markable effect on the SWCC of lime-treated soil.

1 INTRODUCTION

Civil engineers are always challenged with the design and construction of safe and durable pavements. One problem that engineers face is the design and construction of pavements on expansive soils. Expansive soils are soils that undergo significant swelling or shrinkage due to changes in water content. These changes cause extensive damage to pavements that are manifested in the form of irregular deformations (bumps), cracking, and rutting of the pavement surface.

Expansive soils are found in many locations in Saudi Arabia. Information regarding expansive soil sites, their geological origin, and swelling characteristics has been well documented in the technical literature (Erol & Dhowian 1990, Abduljauwad & Al-Sulaimani 1993, Azam et al., 1998, Azam et al., 2003, Sabtan 2005, Aiban 2006). Expansive clays located in eastern region of Saudi Arabia are characterized to be moderately to highly expansive (Abduljawad, 1994).

One common mitigation method for the improvement of expansive subgrade involve the addition of lime for the purpose of arresting the swell potential and provide support for the pavement structural system. Many studies (Basma & Tuncer 1991, Afès & Didier 2000, Nalbantoglu & Tuncer 2001, Al-Rawas 2005, Alper et al., 2006) showed that the addition of lime content beneficially reduces swelling potential, swelling pressure, plasticity index, and compressibility, and increases shear strength and stiffness.

Lime-treated expansive soils are typically in a state of unsaturated condition in the field due to in-situ compaction. Therefore, its engineering behavior can be further understood by considering the influence of matric suction on its behavior. The soil water characteristic curve (SWCC) is considered a tool used for predicting and interpreting the engineering behavior of unsaturated soils. SWCC describes the relationship between water content (whether gravimetric or volumetric) and soil suction.

The technical literature comprise few researches on the SWCC curves of lime-treated soils with even more limited research directed towards the SWCC of lime-treated expansive soils (Bilsel & Oncu 2005, Kattab & Al-Taie 2006, Puppala et al., 2006, Yang et al., 2011). Recently, Stoltz et al. (2012) has studied the effect of the wetting and drying during SWCC determination on the micro—and macro-scale distribution of lime treated expansive soils.

The main objective of this research is to investigate the effect of lime content and curing period on the soil water characteristic curves of lime-treated expansive soils. Tests were performed considering 2% and 4% lime content and curing periods of 7 and 28 days.

2 MATERIAL AND METHODS

This section provides a description of materials and experimental techniques used in this study.

2.1 *Material used*

In this study, expansive clay obtained from the city of Al-Qatif was used. Al-Qatif is a historic, coastal oasis region located on the western shore of the Arabian Gulf in the eastern province of Saudi Arabia (26° 56′0″ N, 50° 1′0″ E). Several researches conducted to investigate the swelling characteristics of Al-Qatif expansive clay revealed that the soil is highly expansive in nature due to the presence of high smectite mineral content (Abduljauwad & Al-Sulaimani 1993, Azam et al., 1998, Azam et al., 2003). Soil samples were obtained from open pits excavated to a depth of 1.5–3.0 m below ground surface. Samples were transferred to laboratory for full characterization as summarized in Table 1.

Mineralogical characterization of Al-Qatif soil was performed using Bruker D8 Advance system. Samples were scanned from 2° to 60° (2θ) using 2.2 kW Cu anode long fine focus ceramic X-ray tube at a scanning rate of 1 degree per minute. The X-Ray diffraction analysis concluded that Al-Qatif clay consist of montmorillonite and palygorsite which are typical swelling minerals.

Compaction characteristics of lime-treated expansive clay as a function of lime content are presented in Figure 1. From Figure 1, as the lime content increased the optimum water content increased and the maximum dry density decreased.

Lime used in this study was analytical grade calcium hydroxide (assay 90%), supplied by Winlab Chemicals, UK. Lime contents considered included 2% and 4% (by dry weight of clay) because they are typically specified in expansive soil improvement projects.

Table 1. Soil characterization data for Al-Qatif soil.

Test	Value
Specific Gravity, Gs	2.71
Liquid Limit, w_L (%)	137
Plastic Limit, w_P (%)	60
Shrinkage Limit, w_{sh} (%)	12
% passing Sieve No. 200	99
Unified soil classification	CH

2.2 *Sample preparation*

Compacted samples of lime-treated expansive clay were prepared for the determination of the soil water characteristic curves. All samples are prepared at optimum water content and maximum dry density. Soil samples obtained from the field were air dried, pulverized and sieved using sieve No. 40. Expansive clay and lime were mixed thoroughly at target water content and stored in plastic bags for 24 hours to allow for the mix to homogenize. Samples were statically compacted to desired maximum dry density and stored in humid environment (95% relative humidity) for a curing period of 7 and 28 days.

3 EXPERIMENTAL PROGRAM

3.1 *Swell potential*

The swell potential for untreated and lime-treated expansive clay under different lime content and curing periods was evaluate using one-dimensional swell test as per ASTM D4546. Results of the tests shown in Figure 2 revealed that the addition of lime resulted in significant reduction in swelling potential of tested samples. On the other hand, the curing period had a less markable effect on the reduction of swelling potential of lime treated expansive clays.

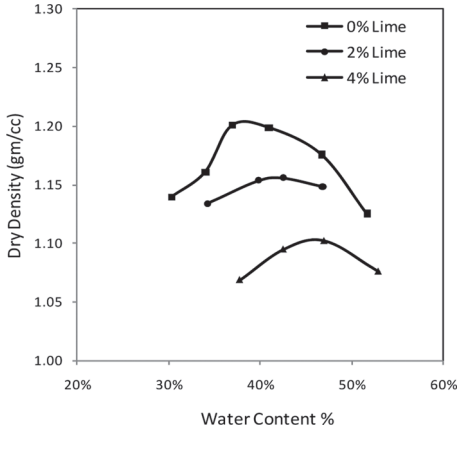

Figure 1. Standard compaction curves of lime-treated expansive clay for different lime contents.

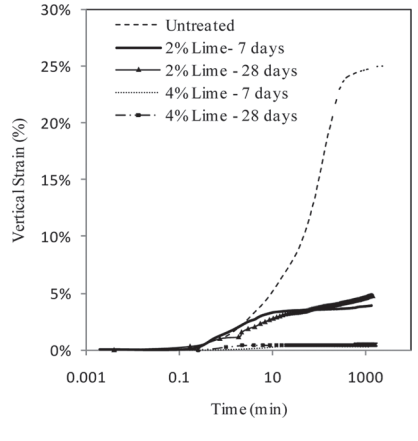

Figure 2. Swell versus time curve for treated and untreated expansive clay.

3.2 *Soil water characteristic curves*

SWCC of lime-treated expansive soils was evaluated using axis translation technique and filter paper method to cover a wide suction range. Axis translation technique using Fredlund SWCC device was used to evaluate the SWCC for suction levels up to 1500 kPa (using a ceramic disc with air entry value of 15 bar). The water in the compartment below the ceramic disc was connected to a graduated burette to monitor the amount of water egress from samples during suction application.

For Fredlund SWCC device, samples' dimensions were 50 mm in diameter and 20 mm thick. After curing period, samples were transferred to consolidometer and saturated for 24 hours or until full swell was attained. Samples were then transferred to the Fredlund SWCC device and suction was applied incrementally up to 1500 kPa and allowed to equilibrate under each suction level. Equilibrium was attained when water level in burettes did not change within 24 hours. After equilibrium, soil samples were weighed to determine reduction in water content due to suction application. At the end of the test, final water content of samples were determined using gravimetric methods and water content at each suction was back-calculated based on the cumulative water content loss measured at each stage.

The filter paper method was used to evaluate the soil water characteristic curves of the lime-treated expansive clays for suction values greater than 1500 kPa. Matric suction was measured using contact techniques in accordance with ASTM D5298-94. In this method, Whatman No. 42 filter paper discs (50 mm in diameter) was placed between two identical compacted samples of 70 mm in diameter and 20 mm high. To avoid contamination due to potential bacterial growth and organic matter, the testing filter paper was encased between protective filter papers. To determine the boundary drying curves, samples were allowed to evaporate under laboratory environment to reach desired water contents. The desired water contents were beyond the range of water content obtained using the axis translation technique. Attainment of desired water content was confirmed by continuous weighing of samples. After reaching desired water content, initial sample weight and volume were recorded. Samples with filter paper were sealed in glass jars and stored in temperature controlled environment (22 ± 1°C) for a period of 14 days. After equilibration, water content of filter paper was determined using gravimetric techniques and using balance with resolution of 0.0001 g. Suction values corresponding to filter paper water content was evaluated based on filter paper calibration curve developed by Oliveira and Marinho (2006). Verification of calibration curve for filter paper batch used in this study was performed as shown in Figure 3.

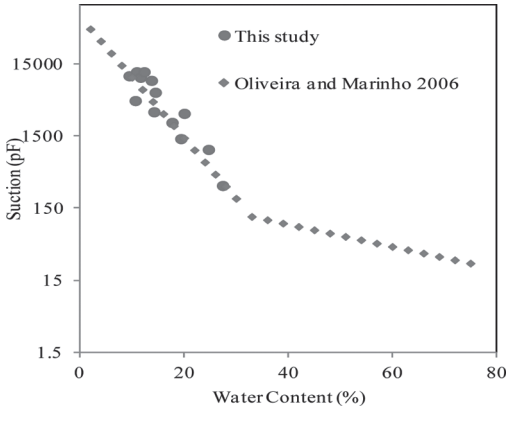

Figure 3. Verification of ASTM filter paper calibration curve.

4 RESULTS AND DISCUSSION

The SWCC of lime treated expansive clay as a function of lime content and for curing period of 7 days were shown in Figures 4 to 6. In these figures, the soil water characteristic curves were expressed in terms of gravimetric water content. The effect of lime content on soil water characteristic curves was illustrated in Figure 4. From Figure 4, it was apparent that the rate of desaturation in low suction range (less than 1500 kPa) decreases with addition of lime. An in depth examination of soil water characteristic curves, illustrated in Figure 5, revealed that the rate

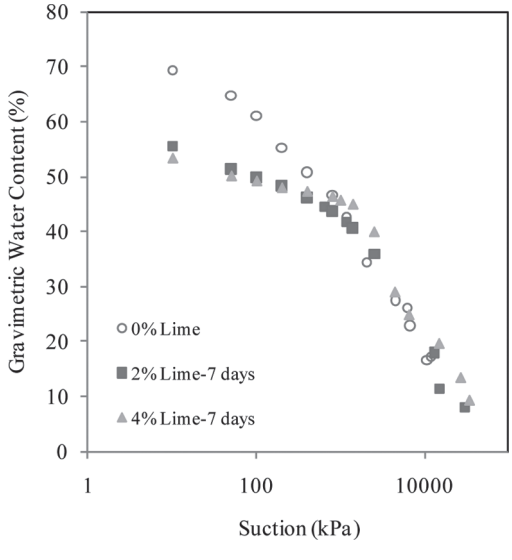

Figure 4. SWCC of untreated and lime-treated expansive clay.

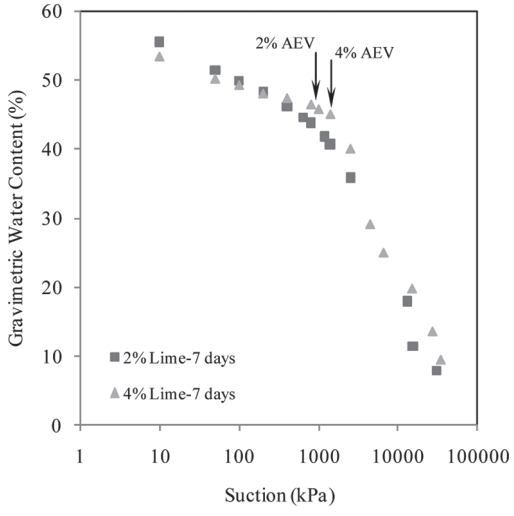

Figure 5. Effect of lime content on the SWCC of lime-treated expansive clay.

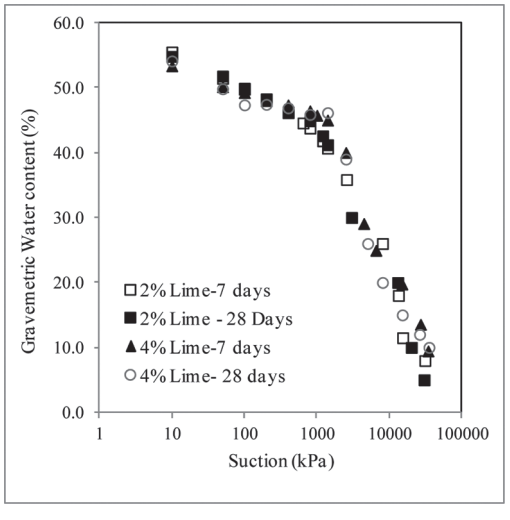

Figure 6. Effect of curing period on the SWCC of expansive clay.

of de-saturation continues to decreases with increase in lime content; however, on a less pronounced scale. In the high suction range, no difference between soil water characteristic curves was observed.

Figure 5 depicts changes in the shape of the SWCC with lime content. Specifically, it was observed that the SWCC for 2% lime content shows a smooth transition from the low suction range (less than 1500 kPa) to the high suction range (greater than 1500 kPa) similar to that for untreated soil. On the other hand, the SWCC for 4% lime shows a bi-linear relationship with a breaking point identifying the air entry value.

Based on the aforementioned observations, a bi-linear relationship was fitted to express the SWCC of lime treated expansive soils using the following equations:

$$w = -0.693 \log(\psi) + 56.723 \quad \psi \leq 1500 \text{ kPa} \qquad (1)$$

$$w = -4.690 \log(\psi) + 122.37 \quad \psi > 1500 \text{ kPa} \qquad (2)$$

where w = gravimetric water content (%) and ψ = matric suction (kPa).

The air entry value (AEV) defines the matric suction at which air begins to enter the pores and it marks the transformation from saturated to unsaturated conditions. By visually inspecting Figure 5, it was observed that the air entry value increased with the increase in lime content. This can be attributed to the reduction in pore size as a result of more lime filling the voids and inducing a more stabilized clay matrix.

The effect of curing period on the soil water characteristic curves of lime-treated soil is illustrated in Figure 6. This figure reveals that for the study soil the curing period has a negligible effect on the characteristics of lime-treated SWCCs. Because the SWCC are mainly dependent on the pore size distribution of soil, it can be inferred that the long-term pozzolanic reactions due to lime has a slight effect on pore size distribution of lime treatment.

5 CONCLUSIONS

This research examined the effect of the lime content and curing period on the soil water characteristic curves. These curves can be incorporated in advanced pavement design procedures (e.g., mechanistic enhanced integrated climate model) to predict moisture distributions in pavements with lime-treated subgrade as functions of depth and time. Main conclusions drawn from this research can be summarized as follows:

- Lime content had a paramount effect on the SWCC curves of lime-treated expansive clay.
- The water retention capacity of lime-treated soils represented by the air entry value deduced from SWCC has shown to increase with increase in lime content.
- The appearance of the SWCC of lime treated expansive soils depends on lime content. For this study, SWCC transition from the low suction to the high suction transforms from a smooth curve to a bilinear relationship as lime content increases.
- The curing period has a negligible effect on the soil water characteristic of lime treated soils.

ACKNOWLEDGEMENTS

This paper is a part of a research project supported through NPST program by King Saud University, Project No. 11-BUI1901-02. The authors also thank the technicians of Bugshan Research Chair in Expansive Soils for their help and support.

REFERENCES

Abduljauwad, S.N. 1994. Swelling behavior of calcareous clay from the eastern province of Saudi Arabia. *Quarterly Journal of Engineering Geology* 27: 333–351.

Abduljauwad, S.N. & Al-Sulaimani, G.J. 1993. Determination of swell potential of Al-Qatif clay. *Geotechnical Testing Journal* 16(4): 469–484.

Afès, M. & Didier, G. 2000. Stabilization of expansive soils: the case of clay in the area of Mila (Algeria). *Bulletin of Engineering Geological Environment* 59(1): 75–83.

Aiban, S.A. 2006. Compressibility and swelling characteristics of Al-Khobar Palygorskite, eastern Saudi Arabia. *Engineering Geology* 87: 205–219.

Alper, S., Gozde, I., Recep, Y.H. & Kambiz, R. 2006. Utilisation of a very high lime fly ash for improvement of Izmir clay. *Building and Environment* 42(2): 150–155.

Al-Rawas, A.A., Hago, A.W. & Al-Sarmi, H. 2005. Effect of lime, cement and Sarooj (artificial pozzolan) on the swelling potential of an expansive soil from Oman. *Building and Environment* 40(5): 681–687.

ASTM D4546. 2000. Standard Test Method for One-Dimensional Swell or Settlement Potential of Cohesive Soils, West Conshohocken, PA.

ASTM D5298. 1994. Standard Test Method for Measurement of Soil Potential (Suction) Using Filter Paper, West Conshohocken, PA.

Azam, S., Abduljauwad, S.N. & Al-Amoudi, O. 2003. Volume change of arid calcareous soils. *Natural Hazards Review*, *ASCE* 4(2): 90–94.

Azam, S., Abduljauwad, S.N., Al-Shayea, N. & Al-Amoudi, O. 1998. Expansive characteristics of gypsiferous/anhydritic soil formations. *Engineering Geology* 51: 89–107.

Basma, A.A. & Tuncer, E.R. 1991. Effect of lime on volume change and compressibility of expansive clays. *Transportation Research Record* 1295: 52–61.

Bilsel, H. & Oncu, S. 2005. Soil Water Characteristic and volume change behavior of an artificially cemented expansive clay. In Romero and Cui (eds.) *Advanced Experimental Unsaturated Soil Mechanics, Tarantino:* 331–335.

Erol, A.O. & Dhowian, A.W. 1990. Swell behavior of arid climate shales from Saudi Arabia. *Quarterly Journal of Engineering Geology* 33: 243–254.

Kattab, S.A. & Al-Taie, L.I. 2006. Soil Water Characteristic curves (SWCC) for lime treated expansive soils from Mosul City. In Miller G., Zapata, C., Houston, S.L. and Fredlund, D.G. (eds) *Fourth International Conference on Unsaturated Soils, Carefree, Arizona on April 2–5:* 1671–1682.

Nalbantoglu, Z. & Tuncer, E. 2001. Compressibility and hydraulic conductivity of chemically treated expansive clay *Canadian Geotechnical Journal* 38: 154–160.

Oliveira, O.M. and Marinho, F.A.M. 2006. Evaluation of filter paper calibration. UNSAT 2006: 1845–1851.

Puppala, A.J., Punthutaecha, K. & Vanapalli, S.K. 2006. Soil-Water Characteristic Curves of Stabilized Expansive Soils. *Journal of Geotechnical and Geoenvironmental Engineering* 132(6): 736–751.

Sabtan, A.A. 2005. Geotechnical properties of expansive clay shale in Tabuk, Saudi Arabia. *Journal of Asian Earth Sciences*, 25: 747–757.

Stoltz, G. Cuisiner, O. & Masrouri, F. 2012. Multi-scale analysis of the swelling behavior of the swelling and shrinkage of a lime-treated expansive clayey soils. *Applied Clay Science* 61: 44–51.

Yang, H., He, C. & Zhan, W. 2011. Analysis of the improvement effect of expansive soil water characteristic curve In GeoHunan International Conference II: Emerging Technologies for Design, Construction, Rehabilitation, and Inspections of Transportation Infrastructures, (GSP 222), June 9–11, 2011, Hunan, China: 272–278.

This page intentionally left blank

Advances in Unsaturated Soils – Caicedo et al. (eds)
© 2013 Taylor & Francis Group, London, ISBN 978-0-415-62095-6

Water retention properties of a demolition waste

A.M.J. Gómez, M.M. Farias, M.P. Cordão-Neto & M.V.R. Souza
Universidade de Brasilia, Brasilia, Brazil

I.F. Otálvaro
Pontificia Universidad Javeriana Seccional Cali, Cali, Colombia

ABSTRACT: Construction and Demolition Wastes (CDW) present a high amount of aggregate chips covered with mortar. This results in high absorption of water with a direct impact in particle breakage or disaggregation. It is supposed that intra particle suction plays an important role is the phenomenon. However, Water Retention Curves (WRCs) of CDW are not well understood. In this work, the WRCs of dynamically compacted specimens of the CDW from the demolition of the National Stadium in Brasilia are studied. The objective of this study is to obtain WRCs of the recycled materials by using a pressure-plate and filter paper method. The breaking effect during compaction is quantified from the grain size distribution curves. The particle breakage during compaction increases when the energy augmented. The results from the WRCs were incorporated into a pore size capillary model to predict pore size distribution.

1 INTRODUCTION

The amount of construction and demolition waste (CDW) generated in global and local levels are significant. The volume of these materials is increasing with the construction of new buildings and the demolition of old structures that have reached the end of its useful life, or due to natural hazards like earthquakes, storms and floods and anthropic disasters like wars.

Around 300 million tons/year of CDW is generated in Europe, about 170 million tons/year in the United States and 68 million tons per year are produced in Brazil. The Federal District (Brasilia) has a daily production of 6000 tons, equivalent to an annual production of 2.2 million tons/year (Gómez 2011).

Innovation and development of wastes recycling technology try to make these materials suitable for reuse. Applications of CDW, recycled concrete aggregates (RCA), and reclaimed asphalt pavement (RAP) in civil engineering works and infrastructure are now common practice in many countries (Rahardjo et al., 2010). Several researches show that CDW is an attractive alternative material for bases and sub-bases due to its high resistance and its non-expansive behavior (Leite et al., 2011, Gómez 2011, Hendriks et al., 2001, Park 2003).

Engineering properties like volume change, hydraulic conductivity and shear strength is significantly controlled by suction. However, the unsaturated characteristics of CDW materials have not been fully investigated. The purpose of this paper is to obtain the water retention curves of the recycled materials and evaluate its influence on the breaking of particles during compaction. Some conclusions and recommendations are presented.

2 WATER RETENTION CURVE

The water retention curve (WRC) can be defined as the relationship between the amount of water in a porous material and its matrix suction. It is related to properties such as, pore size distribution, unsaturated volume change, unsaturated shear strength, and unsaturated permeability (Nimmo 2004, Thu et al., 2007, Vanapalli et al., 1996, Romero et al., 1999).

The shape of the WRC depends on the pore size distribution and compressibility of the porous material with respect to suction (Marinho 2005). Figure 1 shows the relationship between the pore-size distribution and the WRC. Each pore-size is associated with a suction value due to the capillarity. In a material with multiple pore sizes, the WRC has an "S" shape and presents a more gradual reduction in water content with as suction increases.

Several laboratory techniques are available for determining water retention curves of natural and compacted materials. The pressure-plate and the filter paper methods are two low cost alternatives. In the pressure-plate method the Axis Translation

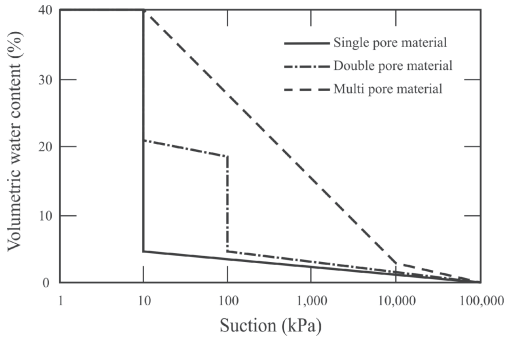

Figure 1. General shape of water retention curve according to pore size distribution (Marinho 2005).

Technique (ATT) is used. The ATT consists in increasing artificially the atmospheric pressure in a porous material sample. The matric suction can be controlled, regulating the air pressure in a test cell, as well as the pressure in water using a saturated porous filter in contact with the sample. Because the base element allows drainage, the amount water that flows through the sample can be quantified, and under constant pressures the flow of water ceases when equilibrium is reached. The WRC is constructed by relating suction and the volume of stored water when the drainage ceases.

The filter paper method (FPM) has been used since 1937, when it was presented by Gardner. Since then, many researchers have used filter papers for suction measurements (Marinho & Oliveira 2006). This method is based on the principle that, when a wet soil is placed in contact with a drier filter paper inside a sealed container, the paper absorbs water from the soil until both materials reach equilibrium of suction. When the filter paper is in intimate contact with the soil water, the water absorbed by the filter paper has the same concentration as the soil. In this way, the matric suction is measured (Marinho & Oliveira 2006). The equilibrium suction is estimated from the measured water content of the filter paper using its calibration equation.

2.1 *Materials*

A typical construction and demolition waste is a mixture of reinforced concrete blocks, mortar, steel, plastic and wood.

The recycled material investigated in this research was collected from demolition waste of National Stadium of Brasilia. For this study a representative sample of about 1.6 tons of CDW aggregate was used for the laboratory evaluation. Two grinding process were necessary for obtain the CDW aggregate required for this investigation.

3 PHYSICAL CHARACTERISTICS OF THE CDW

3.1 *Composition*

In order to determine the composition of the CDW used in this study, the coarse aggregate fraction retained in the 4.75 mm sieve was examined by visual analysis. The CDW aggregate was separated into four main groups: (i) cementitious materials (the major component of the CDW aggregate, comprised mainly of concrete and mortar, 41%); (ii) crushed rocks (about 15%); (iii) red ceramics (bricks and roof tiles, 1%); and (iv) white ceramics (floor and wall tiles, 1%). The fine aggregate fraction represented 42% of the total sample. Undesirable materials such as metals wood and plastic represented only a very small proportion of 0.6%, far below the limit value of 3% required by Brazilian standards.

3.2 *Properties of CDW*

The physical properties of CDW used in this research were determined using Brazilian (NBR) and American standards (ASTM).

Tests like water absorption, grain shape, grain-size distribution, sand equivalent, soundness, Atterberg limits were used to determine the physical properties of recycled aggregate and define whether it was suitable as base material for highways. The results are summarized in Table 1.

4 MECHANICAL AND HYDRAULIC PROPERTIES

4.1 *Compaction of CDW*

Proctor process was used for the compaction of CDW specimens. Modified and Intermediate Proctor energy (1263 kN-m/m^3) were used. The laboratory compaction test was carried out based on the American Standard procedure (ASTM D1557-07). The values of optimum moisture content and maximum dry density identified were 13.0% and 17.5 kN/m^3, respectively, for intermediate energy.

The grain size distribution used for investigation was the lower limit of gradation C prescribed in Brazilian standard DNIT 141/10-ES. This gradation is commonly used for base and sub-base materials in highways with medium to heavy traffic volume. The original and after compaction grain size distribution curves for different initial values of moisture content (8%, 10%, 14% and 19%) are shown in Figure 2.

The CDW aggregate specimens for determination of the WRC were compacted with this gradation C using intermediate Proctor energy and

Table 1. Summary of physical characteristics of CDW aggregate.

Properties	CDW investigated
Uniformity coefficient (*Cu*)	61
% Passing sieve N°40	15
% Passing sieve N°200	3% coarse aggregate 12% fine aggregate
Swelling	0.0%
Liquid limit	32%
Plasticity index	NP
Sand equivalent	70%
Absorption	7%
Soundness in Magnesium sulfate	6% coarse aggregate 11% fine aggregate
Los Angeles abrasion	35%

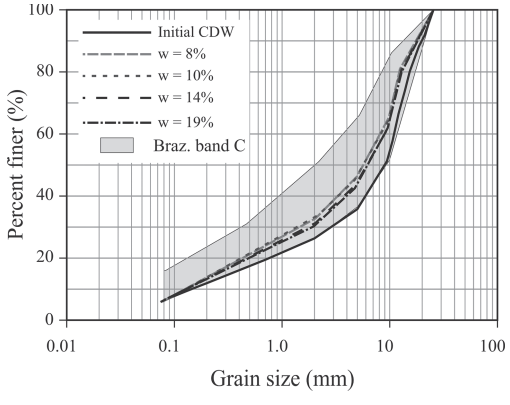

Figure 2. Grain-size distribution of the recycled material and moisture compaction effect.

different moisture content (9%, 13% and 17%). The samples obtained were 100 mm in diameter and 35 mm in height.

4.2 *CDW particles breakage*

The most important engineering properties of granular materials such as stress-strain and strength behavior, volume change and pore-pressure developments, and variation in permeability depend on the integrity of the particles or the amount of particle crushing that occurs due to changes in stress. Therefore, it is important to be able to identify and quantify the effects of particle crushing on these engineering properties (Lade et al., 1996).

In order to evaluate the breaking process due compaction in CDW aggregates, the grain-size distribution before and after the compaction process were compared and Marsal (1975) breakage factor (B_g) was calculated to quantify this breakage. Figure 2 presents the variation of grain-size distribution for CDW at different moisture contents after compaction.

Marsal (1975) developed his measure of particle breakage in connection with the design and construction of earth and rockfill dams. While performing large-scale triaxial compression tests, he noticed significant amount of particle breakage. His method involves the changes in individual particle sizes between the initial and final grain size distributions. The difference in the percentage retained is computed for each sieve size. This difference will be positive or negative. Marsal's breakage factor is the sum of the differences having positive sign.

4.3 *Testing details for the WRC*

The water retention tests were performed using a pressure-plate apparatus (Fig. 3) and the filter paper method. The pressure-plate consists of four main parts: i) an aluminum cell where a relatively permeable porous disk with an air-entry value of 300 kPa is sealed to the base; ii) a 50-mL glass burette for measuring the volume of water extracted from the soil sample by the applied suction; iii) air pressure regulation system with Fairchild precision regulator model 10 N for applying middle suctions between 3 to 200 kPa and a pressure gauge; and iv) a GCTS hanging column for applying low suctions (i.e., 1 to 5 kPa).

The testing method was carried out based on the American standard procedure ASTM D6836-02. The porous ceramic stone was previously immersed in deaired water during a period of 16 hours. Afterwards the saturation of ceramic stone was checked by a simple permeability test under constant water head.

After compaction, the samples were saturated by capillarity. The specimens were placed on a porous stone, covered with a filter paper, and place in a container filled with deaired water up to the base of the compaction mold. Then, the samples were weighed and mounted on the pressure plate.

The lower suctions (i.e., 1 to 5 kPa) were applied maintaining the connection valve between the pressure regulator and the GCTS hanging column open. Initially the water outlet was closed and the desired air pressure set up. After air pressure stabilization, the water outlet was opened and the equilibrium was reached (i.e., the water volume of the burette stayed constant). Matric suction was applied until equilibrium was observed what could be verified by plotting the water volume of the burette with respect to time in logarithmic scale. The same procedures were applied to the next higher values of matric suction until the maximum pressure allowed by the air capacity of regulator (equal or less than 200 kPa).

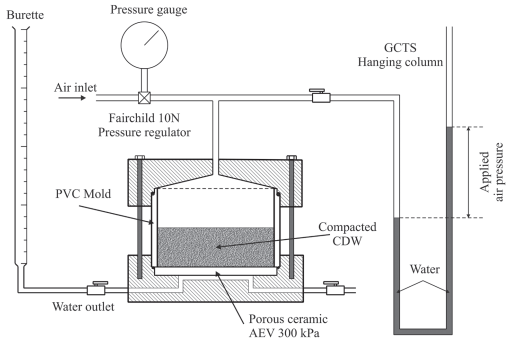

Figure 3. Schematic of a pressure-plate with ceramic porous stone coupled with GCTS hanging column.

Suction values higher than 100 kPa were determined using filter paper technique. This required the compaction of a sample for each point. After compaction the specimens were saturated and then air-dried in the lab to attain the chosen moisture value.

A sandwich composed by three pieces of filter paper was placed at the base of each sample after reaching the required humidity. Both papers were used straight after removal from the box air-dry condition. Each filter paper was carefully handled with a stainless steel tweezers to avoid changing its original characteristics. The sample with both filter papers was wrapped with two layers of PVC film, and then placed within a plastic bag, and stored in the EPS box in a temperature-controlled room for 14 days. The equilibrium suction was obtained from the Chandler et al. (1992) calibration equation.

5 RESULTS AND DISCUSSION

5.1 *Breaking effect on CDW*

The change of grain sizes was evident from the leftwards shift in the curves in Figure 2. These curves represent samples with different initial water content. The most significant changes occurs for the samples with lower initial water content (8%).

Marsal's degradation indices (B_g) were computed for all samples with different compaction energies. Figure 4 shows lines of equal degradation.

Note that by increasing the energy of compaction, there is an increased factor of breakage of the grains and the same parameter decreases with increasing moisture content.

5.2 *Water retention properties*

The water retention curves were obtained primarily by following a drying or desorption process. Figure 5 shows the WRCs of the CDW that

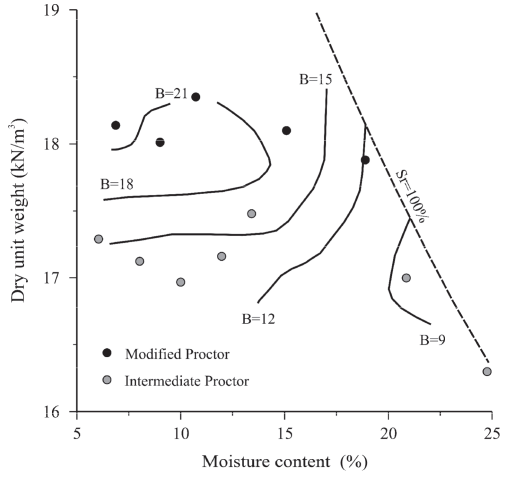

Figure 4. Lines of equal degradation indices according to sample water content and compaction energy.

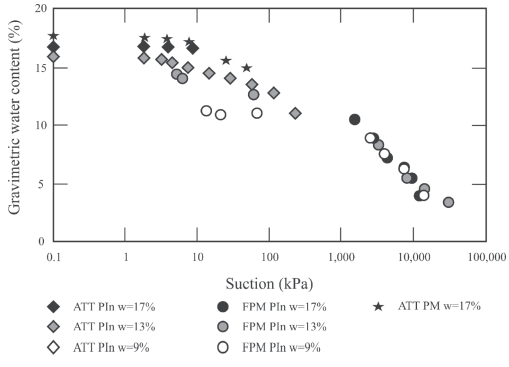

Figure 5. Water retention curve of CDW.

describes the change in gravimetric water content with respect to the change in matric suction. It is noted that for suction values below 100 kPa, where the desaturation process of CDW begins, the results of with the filter paper are lower than those obtained by the axis translation technique.

This situation may result from: i) at high moisture values the filter paper loses repeatability because it stores more water than its own weight and is therefore hard to calibrate; or ii) in the ATT the curvature of the air–water interface will increase because of the compression of the entrapped air cavity as a result, the pressure differential between air and water, which is controlled by the meniscus curvature, will increase (Marinho et al., 2008).

The shape of each curve suggests a multi-modal distribution of pores. By applying a capillarity model for the WRC at 13% moisture, it is possible to distinguish three dominant pore sizes (see Figure 6).

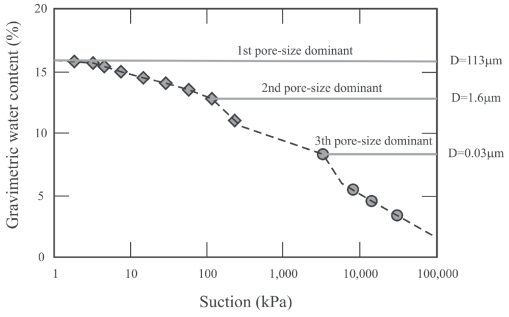

Figure 6. Multi pore shape in the water retention curve for the compaction moisture of 13%.

The shapes of the WRCs for low suctions (i.e., <100 kPa) were affected by compaction moisture.

As compaction moisture content grows, the magnitude of the first air entry value increases; this value is related to the largest pore size. The final part of the curves converges. This occurs for moisture values lower than 9%, which is equivalent to the amount of water absorpted by the recycled aggregates studied.

6 CONCLUSIONS

The water retention curves for three specimens of construction and demolition wastes were obtained. The axis translation technique combined with filter paper method allowed characterizing the water retention properties in samples compacted in the intermediate Proctor energy with different moisture contents.

The equipment's and techniques used to obtain the WRCs constitute an effective and low cost tool for determining the water retention properties of the construction and demolition waste materials.

The shape of each curve suggests a multi-modal distribution of pores. For the sample compacted with 13% moisture content, it was possible identify three dominant pore sizes using a model that relates the suction capillarity with the pore diameters.

Under the studied laboratory test conditions it was shown that compaction humidity affects the initial part of the WRC, while the end portion remains unchanged. Thus, changes in the initial form of the WRC have a connection with the breakage of the particles during the compaction process.

ACKNOWLEDGEMENTS

The authors would like to thank of the "Conselho Nacional de Desenvolvimento Científico e Tecnológico" CNPq and "Coordenação de Aperfeiçoamento de Pessoal de Nível Superior" CAPES of Brazil for providing the financial support for this research.

REFERENCES

Chandler, R.J., Crilly, M.S. & Montgomery-Smith, G. 1992. "A Low-cost Method of Assessing Clay Desiccation for Lowrise Buildings," Proceedings, Institute of Civil Engineering, 92(2): 82–89.

Gómez, A.M.J. 2011. Estudo Experimental de um Resíduo de Construção e Demolição (RCD) para Utilização em Pavimentação. Dissertação de Mestrado, Publicação G.DM-196/11, Faculdade de Tecnologia, Departamento de Engenharia Civil e Ambiental, Universidade de Brasília, Brasília, DF, 123 p.

Hendriks, Ch.F. & Janssen, G.M.T. 2001. Reuse of construction and demolition waste in the Netherlands for road constructions. *Heron*, 46(2): 109–117.

Lade, P.V., Yamamuro, J.A. & Bopp, P.A. 1996. Significance of Particle Crushing in Granular Materials. *Journal of Geotechnical Engineering*, 122(4): 309–316.

Leite, F.D.C, Motta, R.S., Vasconcelos, H.L. & Bernucci, L.L.B. 2011. Laboratory Evaluation of Recycled Construction and Demolition Waste for Pavements. Construction and Building Materials, 25: 2972–2979.

Marinho, F.A.M. 2005. Nature of soil–water characteristic curve for plastic soils. *Journal of Geotechnical and Geoenvironmental Engineering* 131(5): 654–661.

Marinho, F.A.M. & Oliveira, O.M. 2006. The Filter Paper Method Revisited. *Geotechnical Testing Journal* 29(3): 1–9.

Marinho, F.A.M., Take, A. & Tarantino, A. 2008. Tensiometeric and axis translation techniques for suction measurement. *Geotechnical and Geological Engineering* 26(6): 615–631.

Marsal, R.J. & Resendiz, D. 1975. *Earth and Earth-Rock Dams* (in Spanish). Limusa, Ciudad de Mexico, Mexico, 546 p.

Nimmo, J.R. 2004. Porosity and Pore Size Distribution. In Hillel D. editor. *Encyclopedia of Soils in the Environment*. London. Elsevier.

Park, T. 2003. Application of Construction and Building Debris as Base and Sub-base Materials in Rigid Pavement. *Transportation Engineering, ASCE*, 129(5): 249–264.

Rahardjo, H., Vilayvong, K. & Leong, E.C. 2010. Water Characteristics Curves of Recycled Materials. *Geotechnical Testing Journal*, 34(1): 1–7.

Romero, E., Gens, A. & Lloret, A. 1999. Water permeability, water retention and microstructure of unsaturated compacted Boom clay. *Engineering Geology* 54: 117–127.

Thu, T.M., Rahardjo, H. & Leong, E.C. 2007. Elastoplastic model for unsaturated soil with incorporation of the soil-water. *Canadian Geotechnical Journal* 44(1): 67–77.

Vanapalli, S.K., Fredlund, D.G. & Pufahl, D.E. 1996. Model for the prediction of shear strength with respect to soil suction. *Canadian Geotechnical Journal* 33: 379–392.

This page intentionally left blank

Advances in Unsaturated Soils – Caicedo et al. (eds)
© 2013 Taylor & Francis Group, London, ISBN 978-0-415-62095-6

Water infiltration in final cover layer of landfills in northeast region of Brazil

R.L. Lopes
Federal Institute for Education, Science and Technology of Rio Grande do Norte (IFRN), Natal/RN, Brazil

J.F.T. Jucá
Federal University of Pernambuco (UFPE), Recife-PE, Brazil

M.O.H. Mariano
Federal University of Pernambuco (CAA-UFPE), Caruaru-PE, Brazil

ABSTRACT: Final cover layers in landfills often suffer changes in their characteristics due to climatological cycles. This paper presents the behavior in two different configurations, performed on an experimental landfill, located in northeastern Brazil. The layers were instrumented with water content and temperature sensors, and a lysimeter to measure infiltration. The soil was characterized in laboratory and water retention curve allowed the suction evaluation and correlation with climatological variations. The total annual infiltration for the two layers was close to that recommended by USEPA for humid climate. Both layers presented infiltration rates in months of rainfall above 280 mm and saturation above 80%. When daily precipitation events were below 50 mm and the degree of saturation was below 60%, no infiltration was recorded. The two layers showed a very similar behavior with respect to infiltration, although the methanotrophic layer has always displayed saturation slightly above the capillary barrier.

1 INTRODUCTION

Cover layers' design should aim at a system that minimizes percolation to environmentally safe values. Landfill cover layer have been conventionally designed using "resistive barriers," in which leachate generation is reduced using materials with low saturated hydraulic conductivity (typically 10^{-9} m/s or less), where the percolation control is achieved by maximizing overland flow (Zornberg et al., 2003).

Final cover layers are necessary for environmental protection and different types of materials and designs can be used to improve performance, especially preventing water infiltration and biogas emissions as shown by Benson & Khire (1995), McCartney & Zornberg (2002), Albright et al. (2004), Cabral et al. (2010) and Melchior et al. (2010). The cover layers are submitted to climate changes all over the year and it is necessary to establish adequate relations between climate and material characteristics for a better evaluation of the long-term performance.

Two different cover layers were put on an experimental cell constructed in Muribeca Landfill, in the Metropolitan Region of Recife, Pernambuco, Brazil, in alternative to conventional cover layer with only compacted soil. The alternative cover layer called methanotrophic (MET01) was made by mixing soil and compost (50% v/v) above of the compacted soil layer. Another alternative layer, called capillary barrier layer (BAC), was made with compacted soil above gravel of big dimensions with geotextile on the interface.

The layers are performed aiming at infiltrations and biogas emissions studies with different materials and design. This article presents the results of the investigation of water infiltration along eighteen months in these two top covers, as well as moisture variations in depth and *in situ* permeability in both coverages.

2 THE EXPERIMENTAL COVERS

The total experimental cell dimensions are 65 m × 85 m (area), with 9 m height. It was filled up with 36,659 t of urban waste from June/2007 to February/2008. The investigation was conducted in two types of cover layer of the cell as shown in Figure 1, according to the following characteristics:

Methanotrophic layer (MET): layer composed of 0.30 m of compacted soil under a mix of soil and compost layer. The proportion of the compost

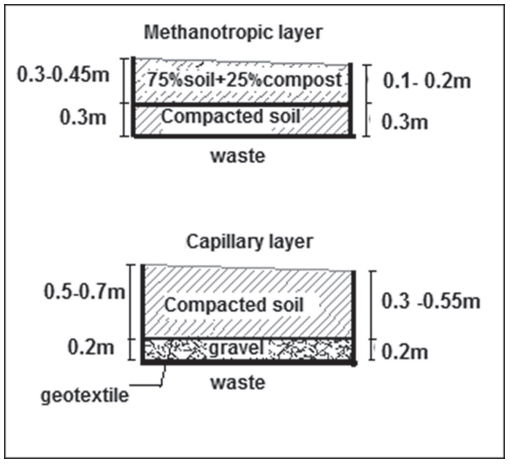

Figure 1. Cover types of the experimental cell.

is 50% volume in mix with soil, which corresponds to 75% soil and 25% organic compost (w/w). The depth of the MET layer varies from 0.40 to 0.75 m and covers an area of 590.2 m².

Capillary barrier (BAC): layer composed of 0.20 m of gravel under a compacted soil layer with total thickness varying from 0.50 to 0.90 m. The superficial area is 500.3 m². Geotextile was used in the soil-gravel interface.

3 METHODOLOGY

3.1 *Soil characterization*

Several samples were taken in field during the cover layers execution to determine granulometry, compaction curve, Atterberg limits and water permeability according to Brazilian Association of Technical Standards procedures to soil classification.

The Soil-Water Retention Curve (SWRC) was made from field samples collected from the surface of each layer of coverage, in 0 to 0.15 m depth. The samples were collected in metal rings with a diameter of 0.07 m and height of 0.03 m, covered with PVC and aluminum foil, stored in a thermal box to preserve moisture and immediately sent to the laboratory. The method used was that of paper filter described by Marinho (1994).

The saturated permeability was determined in samples taken from PVC rings with 0.10 m diameter and 0.15 m height, in order to preserve field conditions. The test was done according to ASTM D5084-10 (ASTM, 2010) in a flexible wall permeameter following the procedures adopted by Maciel (2003) and Mariano (2008). The moisture field capacity was estimated from the water

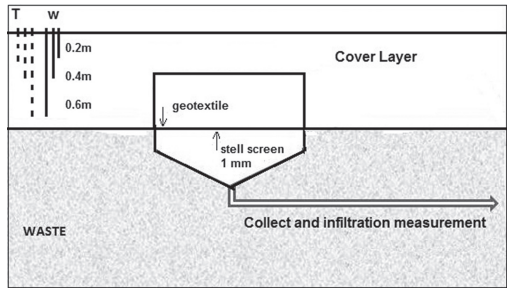

Figure 2. Lysimeter to infiltration measure.

retention curve according to Maia et al. (2005) considering tension of 10 kPa.

3.2 *Water infiltration and in situ permeability*

The infiltration assessment was done within June 2009 to December 2010. The infiltrated water was daily measured in a lysimeter with dimensions 0.60 m × 0.60 × 0.45 m, made of 3 mm carbon steel plates carried with anticorrosion treatment located below the top cover as illustrated in Figure 2.

Next to the lysimeter, water content and temperature sensors were installed within 3 depths and the water infiltrated was collected daily through a tap installed on the lateral slope. The field permeability was determined from *in situ* daily infiltration measurements at specific times in both cover layers. The effective permeability field was determined from the ratio between the height of water infiltrated in a given period and the period of time during which the drainage was measured and related to the saturation of the cover layer in the period. It was made as proposed in the simplification by Albright et al. (2006) assuming a balance of flow and vertical hydraulic gradient unit.

3.3 *Climatological data*

Rainfall data were obtained from INMET (Curado Station—Recife/PE), the nearest climatological station to the experimental cell's and evapotranspiration was determined by Thornthwaite's method modified by Camargo et al. (1999).

4 RESULTS AND DISCUSSIONS

4.1 *Material characterization*

The soil used as cover for the experimental landfill has grain size distribution as shown in Table 1 and Figure 3. The SWRC data for the two materials as shown in Figure 4 and it had been fitted with Van Genuchten's model (Van Genuchten, 1980).

Table 1. Soil characterization.

Geotechnical characterization		Soil (BAC)	Soil/compost (50/50) v/v (MET01)
Size (mm)	0.002	25	23
	0.002–0.06	24	29
	0.06–0.2	15	20
	0.2–0.6	19	15
	0.6–2.0	15	16
	>2.0	2	7
% fines (<0.075 mm)		55	54
LL		43	52
LP		31	39
IP		12	13
Gs (kN/m^3)		2.62	2.45
γdmáx (kN/m^3)		16.6	13.0
W_{opt} (%)		19.0	22.3
K_{sat} (m/s)		4.4×10^{-8}	2.8×10^{-6}
Wcc*		20.4	28.7
porosity		0.43	0.52
Organic content (%)		0.5	11.6

*Wcc = water content in field capacity

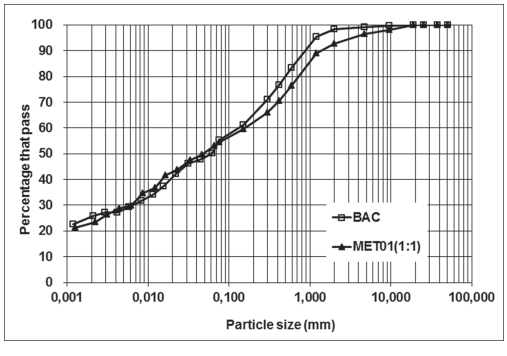

Figure 3. Grain size distribution.

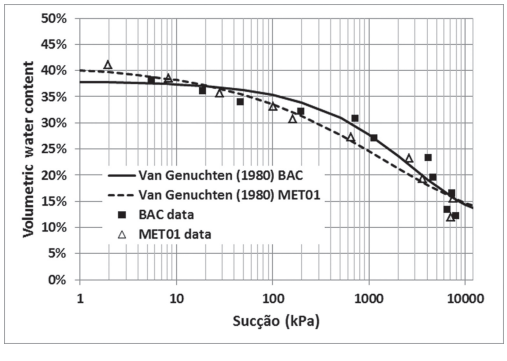

Figure 4. Soil Water Retention Curve (SWRC).

The addition of organic compost led to substantially increase the organic content in the mixture soil/compost, modifying some characteristics, such as increased porosity, permeability and saturated field capacity, although the granulometric curve is similar to that observed by Cabral et al. (2011). These characteristics are important to evaluate the infiltration behavior through the cover layer.

Experimental data indicates that for the same range of suction (0 to1.000 kPa) MET01 loses or gains moisture faster than the BAC. Studies about unsaturated condition soil in landfill cover layers are important to understand the behavior of the material and establish water content intervals to minimize water infiltrations.

4.2 *Water infiltration*

The climatological regime during the period analyzed ranged from dry to intense rainfall periods. Some failures were observed in the first and second month running in BAC lysimeter, in a period of heavy rains, when leaks were found. Thus the total values of infiltration in this period to BAC lysimeter are unreliable. After fixing and reinstalling, the measurements were taken during the 16 months.

According to climate measurements, the initial period was marked by high infiltration rate in the initial months due to high intensity rainfall in a short period of time (109 mm/day), occurred in June 2009 in the region, so that the moisture quickly topped the field capacity. Infiltrations measured and precipitation are shown in Figure 5.

The infiltration was measured in periods when the precipitation was above 50 mm and when both the moisture of the surface layer and compacted soil exceeded moisture field capacity in MET01. Similar in BAC, infiltrations were measured when the interface of the soil/geotextile/stones reaching moisture field capacity, leading to capillary break effect.

In October 2009, rains were of short duration and magnitude, discontinuous, with higher daily rainfalls of 9 mm and a cumulative 16.3 mm. From October 2009 to March 2010, the infiltration dropped considerably, with insignificant measures due to increasing temperature and decreasing rainfall. Measurements above 1 mm/month were only recorded in the next rainy season, starting in April 2010 to MET 01, and May 2010 to BAC.

In June 2010 rains were heavy, of large duration and magnitude, with daily maximum of 149.7 mm and accumulated 543.9 mm. Between 16 and 18 July there was a huge rainfall of 348.5 mm and both cover layers were saturated. Maximum monthly drainage was 34,3% of total precipitation in MET, and it was measured at the beginning of lysimeter installation.

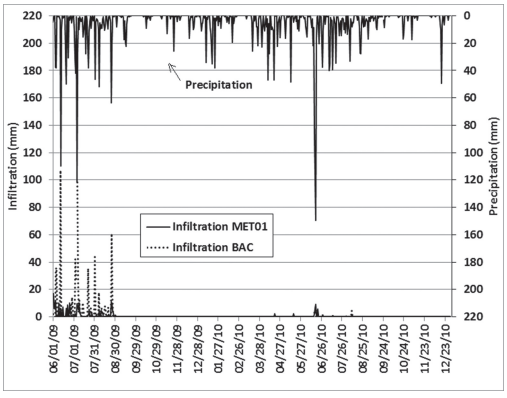

Figure 5. Precipitation and infiltration measured.

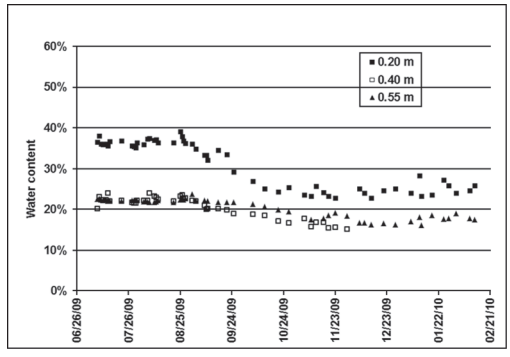

Figure 6. Water content variation in depth on dry season (MET01).

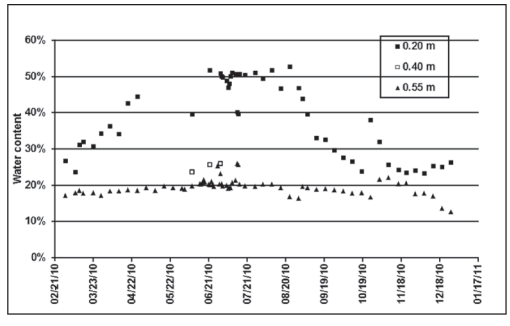

Figure 7. Water content variation in depth on wet season (MET01).

The leakage rate measured at the BAC in the beginning of operation is greater than those measured by Albright et al. (2004). In the second year, infiltration of 30.5 mm approached the leakage measured by Suzuki et al. (2005) in a capillary barrier in a humid climate.

Both cover layers in 2010 had already established a continuous regimen, between dry and wet seasons. The total infiltration measured was 29.4 mm in MET01 and 30.6 mm in BAC, representing 1,5% and 1,6% of total precipitation, closer to that recommended by the Environmental Protection Agency (USEPA) as 30 mm/year for humid climates (ratio Precipitation/evapotranspiration greater than 0.50).

4.3 *Water content*

Figure 6 and 7 show water content variation in depth on MET01 layer in dry and wet seasons respectively.

During the low precipitation it was observed reduced water content in MET01 because the amount of precipitated water was not sufficient to increase the moisture due to local evaporation. There was tendency to uniform profile due to low water availability for the phenomenon evapotranspiration during the dry season.

It was observed similar pattern of increased water content in profile as a function of rainfall over time. However, the compacted soil layer underneath mix soil/compost showed slower changes in water content. This is due to lower permeability (1.5×10^{-9} m/s) than the layer above (2.8×10^{-6} m/s). Thus, even with the high rainfall, occurred until 22 June 2010, the moisture at 0.55 m depth remained constant and only after that there was a change of soil moisture, increasing their permeability and consequently causing the water flow.

The largest variations in water content was held at the surface layer in MET01 (mixture of soil with compost), decreasing from 40.5% to 18.0% by evapotranspiration potential in drier periods (September to February). Unlike, water content increased again during the rainy season (March to August). The surface layer is greatly influenced by climatological conditions with wide range of water content, due to characteristics shown in SWRC to the MET01, gaining or losing moisture faster in the surface layer than in the compacted layer underneath.

Due to higher proportion of organic compost in MET01, this cover layer settled vegetation characterized by grasses soon after the start of implementation. The vegetation covering 100% of the upper surface and adjacent slopes, from January 2009, increased the moisture extract from soil through plant transpiration during dry periods, and promote the retention of moisture in rainy periods. However, this cover layer presented large cracks in the beginning.

To BAC layer the water content ranged from 15.5% to 25.1% in the surface layer and 13.2% to 25.4% at a depth of 0.40 m. These variations are somewhat smaller than those observed in MET01.

The sensor at a depth of 0.40 m depth failed in June 2010 and the moisture distribution over different periods of dry and rainy in capillary barrier could not be clearly determined in BAC.

It appears that in dry periods surface moisture is greater than the depth of 0.40 m, suggesting formation of a layer of water on the storage surface of the BAC, and for high rainfall intensity, moisture tends to be constant in the profile. This storage layer may have been provided by the presence of the geotextile at the interface soil /rock, which has a similar permeability to a sand medium/coarse (10^{-2} m/s to 10^{-3} m/s, according to the manufacturer's catalog), taking into account the stone large particle size act as drain, since it does not retain water. Figure 8 shows moisture variations on BAC layer.

The water content profile shows a tendency almost constant in dry periods, below field capacity, with lower water content next to interface soil/geotextile/rocks. It was observed that when the interface reached the field capacity (w = 20.4%), the cover layer started to drain. Below this valor, the cover layer was able to store water due to capillary effects for existing differences between the fine soil permeability, the geotextile and capillary block.

The profile reached water content field capacity in rainy season, presenting direct relation with increasing precipitation, and over time, decreasing in rainfall, the most superficial layer loses moisture more rapidly due to water availability for evaporation.

A vegetation layer with the same characteristics (grass) was developed in 85% of the area of capillary barrier in the beginning of 2009, as in MET01. The vegetation was less intense near the interface with a conventional layer (not shown in this study) and side slope, which remain during the study period, even in months with low precipitation.

Similar studies in capillary barrier concluded that it was overloaded during periods of heavy rainfall, causing suction break (discontinuity) (Hupe et al., 2003, Berger & Melchior 2009).

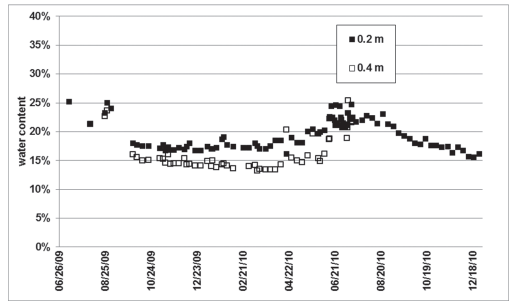

Figure 8. Water content variation in depth on BAC.

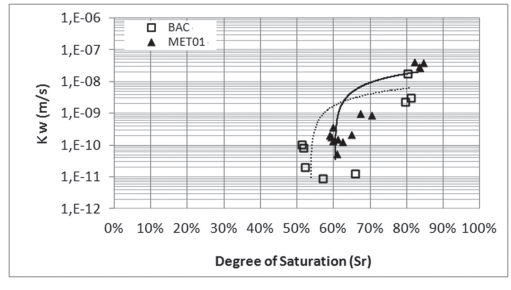

Figure 9. In situ permeability and degree of saturation.

4.4 *In siu permeability*

The in situ permeability measured over infiltration in the time and correlated with saturation degree is shown in Figure 9.

There was a tendency to a drastic reduction of water permeability to saturation degree below than 60% in the MET01 and 55% in the BAC. Maximum permeability is reached in MET01 for saturation degree above 95% and to BAC for saturation degree above 80%, coinciding precisely with the periods of infiltration.

In the period monitored MET01 showed degree of saturation ranging from 45% to 100% in 0.2 m depth and from 45% to 91% in the layer of compacted soil (0.3 to 0.6 m), with 75% measurements below 76.% in the interface soil/waste. BAC layer showed degree of saturation ranging from 49% to 94% in 0.2 m depth and from 38% to 98% in 0.4 depth with 75% measurements below 61% next to interface soil/waste. These cover layers were in the unsaturated condition, during almost any time, thus representing conditions of low permeability, and consequently without infiltration.

5 CONCLUSIONS

This study indicates that for regions with similar rainfall occurrences those of the northeastern coast of Brazil, with incidences of rainfall concentrated in just over four months a year and the remaining time with low rainfall, alternative cover layers can be used in final cover of landfill, presenting infiltration in safe values as recommended by the Environmental Protection Agency (USEPA) for humid climates.

Methanotrophic layers have been studied as an alternative to reduce fugitive emissions. This study has shown that a change in physical characteristics by the addition of organic compost in the soil did not lead to significant increases in infiltration through the layer. Also the large amount of organic content promoted establishment of a vegetation

that protect against erosion and helped the control of water content in depth.

The capillary barrier presented similar behavior to methanotrophic layers. Unstable flows were observed when saturated, resulting in high rates of flow into the landfill, but in short time. It is recommended to include a surface layer of protection above the compacted soil barrier, with mix soil/compost, to prevent high infiltration rates. Also, it is necessary to evaluate other materials to be used as capillary block, in order to minimize the unstable flows and increase the water retention in the layer above, because of the large permeability differences in the interface material.

ACKNOWLEDGEMENTS

The authors gratefully acknowledge CAPES and CNPq for sponsoring exchange among three Brazilian universities for this research field and research funding.

REFERENCES

Albright et al. 2004. Field Water Balance of Landfill Final Covers. *Journal of Envinonmental Quality*. 33: 2317–2332.

ASTM. 2010. D5084-10. Standard Test Methods for Measurement of Hydraulic Conductivity of Saturated Porous Materials Using a Flexible Wall Permeameter. American Society for Testing and Materials. Volume 04.08. Soil and Rock (I): D420–D5876.

Benson, C.H & Khire, M.V. 1995. Earthen Covers for Semiarid and Arids Climates. In: Landfill Closures—Environmental Protection and Land Recovery. ASCE, *Geotechnical Special Publication*. n°. 53, R. Jeffrey Dunn and Udai P. Singh (Eds.) New York, N.Y. 201–217.

Berger, K. & Melchior, S. 2009. Landfill capping and water Balance of cover systems. In: Proceedings Sardinia 2009, Twelfth International Waste Management and Landfill Symposium, S. Margherita di Pula, Cagliari, Italy.

Cabral et al. 2010. Biocover Performance of Landfill Methane Oxidation: Experimental Results. *Journal of Environmental Engineering. ASCE*. 136: 785–793.

Cabral et al. 2011. Geotechnical issues in the design and construction of PMOBs. In Alonso & Gens (eds). *Unsaturated Soils*. 1361–1367.

Camargo et al. 1999. Ajuste do método de Thornthwaite para estimar a evapotranspiração potencial em climas árido e super úmidos, baseados na amplitude de temperatura diária. *Revista Brasileira de Agrometeorologia*. 7(2): 251–257.

Hupe et al. 2003. Investigations of alternative landfill surface sealing systems in test fields. In: Proceedings Sardinia 2003, Ninth International Waste Management and Landfill Symposium. S. Margherita di Pula, Cagliari, Italy.

Maciel, F.J. 2003. Estudo da geração, percolação e emissão de gases no aterro de resíduos sólidos da Muribeca/PE. *Dissertação de Mestrado*. Universidade Federal de Pernambuco. 173p.

Maia et al. 2005. Capacidade de campo, ponto de murcha permanente e água disponível para as plantas em função de doses de vermicomposto. *CAATINGA*, Mossoró, v. 18, n. 3, p. 195–199.

Mariano, M.O.H. 2008. Avaliação da retenção de gases em camadas de cobertura de aterro de resíduos sólido. *Tese de Doutorado*. Universidade Federal de Pernambuco. CTG. Engenharia Civil. Recife-PE. 243p.

Marinho, F.A.M. 1994. Shrinkage behaviour of some plastic soils, *PhD Thesis*, Imperial College, London, UK. 216p.

McCartney, J.S. & Zornberg, J.G. 2002. Design and Performance Criteria for Evapotranspirative Cover Systems. In: *Proceedings of the Fifth International Conference on Environmental Geotechnics*, A.A. Balkema, 1: 195–200.

Melchior et al. 2010. Results from 18 years of In situ performance Testing of Landfill cover systems in Germany. *Journal of Environmental Engeneering*. 136(8): 815–823.

Suzuki et al. 2005. Substantiations and analysis for the capping with the capillary barriers. In: *Proceedings Sardinia 2005. The Tenth International Landfill Symposium*, Sardinia, Itália.

Van Genuchten, M. Th. 1980. A closed form equation for predicting the hydraulic conductivity of unsaturated soils. *Proc. Soil Sci. Soc. Am*. 44(5): 892–898.

Zornenberg et al. 2003. Analysis and design of evapotranspirative cover for hazardous waste landfill. *Journal of Geotechnical and Geoenvironmental Engineering*, 129(6): 427–438.

Advances in Unsaturated Soils – Caicedo et al. (eds)
© 2013 Taylor & Francis Group, London, ISBN 978-0-415-62095-6

Water retention properties of a residual soil from Caracas

A. Luis & D. Marcial
Universidad Central de Venezuela, Caracas, Distrito Capital, Venezuela

ABSTRACT: The hills of the South Eastern side of Caracas are actually in an intense urbanism process of certain rural zones where deep residual soil profiles develop. Elsewhere, necessary topography modifications generate slopes that require appropriate stability analysis. A research program is currently starting up at the soil mechanics laboratory of Universidad Central de Venezuela to determine the influence of suction in the hydro mechanical properties of these residual soils in unsaturated conditions. Within the framework of this research, the water retention curves of two residual soils from the referred site were determined using the pressure plate method. Soil specimens are tested after compacted to optimal water content and maximal Modified Proctor dry density. Results, obtained in a range of suction from 10 to 600 kPa, allow obtaining the air entry value, residual volumetric water content and, in general terms the sensitivity of these soils to suction changes.

1 INTRODUCTION

During the last two decades, several important geotechnical events, related to intense and long rains, have occurred in Venezuela. After Gonzalez et al. (2002), when rain events persists during hours or days, they might cause shallow mass movements, like mud flows but the climatic changes and their effects on the soil infiltration can induce also deeper movements in the soil mass, with more harmful consequences.

A history case to highlight this aspect is the rain event that occurred during late 1999 in Vargas estate, Venezuela. Then, important debris flow occurred in many locations along the north slopes of Avila formation that killed thousands of peoples. More recently, from late 2008, mass movements of shallow soil layers occur very often in several of the residential areas in South Eastern side of Caracas. These subsurface soils are most likely residual soils in natural o compacted state. In this investigation, the selected soil samples correspond to residual soils of slopes close to El Volcán hill, where the outcropping geological formation is named Las Brisas.

This geological formation is mainly composed of metamorphic mica schist rocks that allow deep residual soil profiles to develop. The locations of sampling sites are indicated in Figure 1. One of the samples corresponds to a cut slope at the north side of Los Guayabitos road in Baruta municipality. A second sample corresponds to a nearby rural sector called El Gavilán in El Hatillo municipality. Both places are within the limits of the Protected Zone of Caracas, named this way because of a restricted urban development to protect natural environments near Caracas city. However, because of social pressure due the growth of population, there have been a lot of new habitation buildings lately.

Alfaro (2008) indicates that soils mechanics studies often consider that the soil porosity is saturated because this state represents a critical one for several work conditions. However, most of human population is established in places where soils are in a non saturated state.

To initiate case studies on unsaturated soils behaviour, it is first necessary to determine the water retention curve WRC of each considered soil layer. This curve establishes the relationship between soil suction and its water content. Figure 2 shows a typical water retention curve, presented by Fredlund et al. (1994) obtained both, from a saturated state (desorption curve) or from an air dried state (adsorption curve) in silty soils. Note the difference of position between curves obtained with different initial conditions. This behaviour of great hysteresis is typical in granular soils, in which a big amount of air gets trapped in the soil pores during a wetting path from a low degree of saturation as initial condition.

In high plasticity clayey soils, water retained by adsorption forces predominate over water retained by capillarity, so the hysteresis is often much lower in this type of soils.

The WRC is the base element to determine other geotechnical parameters of unsaturated soils, such as permeability, which experimental method has been adequately solved by Daniel (1982). Daniel's method is based on the WRC and the monitoring of suction variations at different positions within an infiltration column. Once it is known the hydraulic conductivity in unsaturated conditions, there can

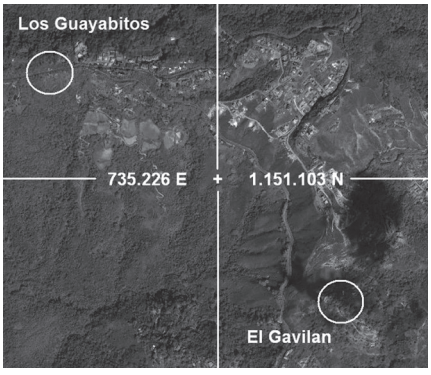

Figure 1. Location of sampling sites.

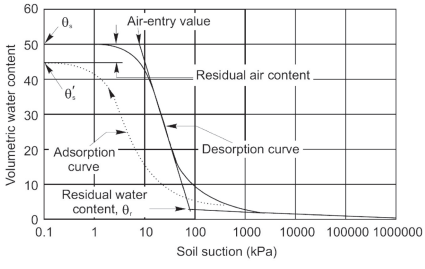

Figure 2. Typical desorption and adsorption curves for a silty soil Fredlund et al. (1994).

be done more precise estimations of water infiltration in unsaturated profiles, during rain events.

Also, the WRC gives a good idea of the range of suctions that must be investigated to obtain sensibility of resistance parameters (cohesion and internal friction angle) to suction changes.

Thus, valuable information is obtained and used to adequately approach slope stability problems in unsaturated soils.

2 MATERIALS AND METHODS

There are several methods to determine the WRC in a wide range of suctions. Their major applications are related to agronomy studies, but they have been also adapted to geotechnical engineering, see Fredlund (2005). The most common methods used to obtain WRCs cover specific suction ranges, but none method apply for the whole range. Therefore when the soil need to be investigated in a large range of suctions, it is necessary to combine different methods. Most common methods are: electric conductivity method, the tensiometer, the porous plate apparatus, the filter paper method, the vapour phase method and the osmotic method. For sandy and silty soils the sensibility range to suction changes is relatively low. Thus, they can be boarded with techniques like the porous plate apparatus or the osmotic method. These methods cover suction ranges up to 1500 kPa. However, for clayey soils, water retention properties might vary in a large range of suctions, frequently beyond 100 MPa. Therefore it is necessary the combination of two or more methods, including the vapour phase method that permit to apply very high suction values.

The residual soil samples studied are sandy low plasticity silts. The grain size distribution curves of both samples are plotted in Figure 3. Note that the contents of fine particles are 68 and 78% for Los Guayabitos and El Gavilan sites respectively. Also, colloidal size particles contents are 17 and 19% for Los Guayabitos and El Gavilan samples respectively. The main particle sizes d_{50} of both soils are 0,042 and 0,05 mm respectively for Los Guayabitos and El Gavilan samples. Concerning soil plasticity, the soil from Los Guayabitos is not plastic and the soil from El Gavilan has very low plasticity.

For this type of soils, the pressure plate method should be well adapted to obtain the WRCs in the range of suction changes sensitivity of both soils. This method was developed by Richards (1941) and in the last 60 years it has been one o the most common methods to investigate water retention properties of soils in the suction range of 10 to 1500 kPa.

The method basis is to apply an air pressure to a wet soil sample, placed on water saturated ceramic porous stone of known air entry value. Since air pressure is lower than air entry value of the porous plate, the applied air pressure is considered to be equal to soil matrix suction. At a certain suction level, water exchanges between with the soil sample occurs trough the porous plate until equilibrium is reached. When equilibrium is reached, water flow through the porous plate ceases and then applied air pressure corresponds to the soil suction. The sample is withdrawn from the apparatus and the water content is measured. This way, applying different air pressures, the WRC is obtained in the range of the air entry value of the pressure plate. The upper side of Figure 4 shows the schematic set up of pressure plate method. The lower side of Figure 4 shows the process of placing soil specimens in the pressure plate used in this work.

The initial conditions of tested soil samples correspond to static compaction with optimum water content to the modified Proctor maximal dry density. This is 13.4% and 1.79 Mg/m^3 for Los Guayabitos site and 12.65% and 1.90 Mg/m^3 for El Gavilán site.

The air dried soil was sieved by ASTM #10 and mixed with distilled water to the corresponding water content and stoked in a hermetic recipient during at least 24 hours to homogenize. Then soil is statically compacted in 50 mm in diameter and

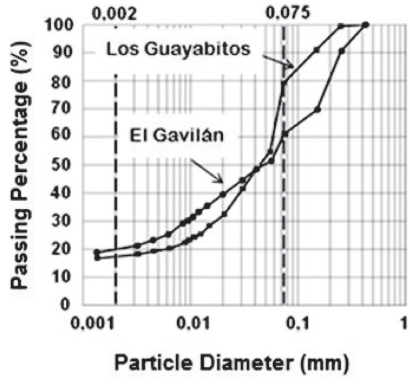

Figure 3. Particle size distribution of studied samples.

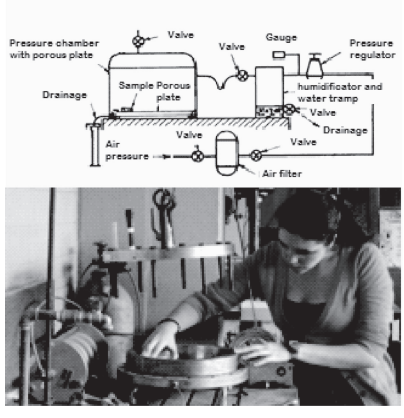

Figure 4. The pressure plate method.

Figure 5. Views of compaction device and prepared samples.

20 mm height rings. Compaction rate was about 1 mm per minute. Compacted samples were then air dried to obtain the wetting path of WRC. For drying path samples were saturated by capilarity. To do so, samples were placed over water saturated layers of absorbent paper until constant weight is reached. The compaction device (left side), air dried samples and saturated samples are shown in Figure 5. Note that some swelling occurs during saturation of samples. However, no volume changes are observed when air drying the samples.

Each sample was placed in the porous plate within a compaction ring to avoid the collapse of the sample.

3 RESULTS AND DISCUSSIONS

The first aspect to be established was the equilibrium time between the applied suction and water content of both saturated and air dried samples. To do so, 8 samples with different initial state were placed in the pressure plate under a corresponding suction of 200 kPa. Each sample permits to determine the water content a different time, from a few hours to about 4 days. After each period of time is reached, samples are withdrawn from de pressure plate, weighed and oven dried to measure the corresponding water content. Changes of water content with time are presented in Figure 6 for El Gavilan site. Note that samples in drying path reach equilibrium first than samples in wetting path. The equilibrium time for drying path is about 24 hours but for wetting path is about 40 hours. After verifying equilibrium times with 10 and 1500 kPa, equilibrium time was fixed to 48 hours for the whole suction range. Note also important hysteresis between drying and wetting paths, typical of non plastic soils.

After equilibrium time was established, WRCs were obtained with at least two samples per each suction value. This was considered in order to account for possible heterogeneity due to soil composition or sample preparation. These results are presented in Figure 7. Note that studied suction range was limited to 600 kPa. This was because of limitations of the working pressure of the compression unit available to run the tests.

Concerning Los Guayabitos soil, both wetting and drying paths cross at a suction value of 600 kPa. The observed residual water content for this soil is of about 4.8 percent and the wetting path is quite stable from 250 to 600 kPa. However, no stabilisation is observed at the lower suction rage. Note also that at the lower value of 1 kPa, one obtain a very high dispersion of water content. This may be due to the fact that air pressure regulators do not show a fine control at this range of pressures. Thus, to adequately define de WRC of these residual soils, one may have to use a finer method like the porous plate method.

Concerning the WRC of El Gavilan soil, the range of water content changes are quite similar that los Guayabitos one. However, slight differences

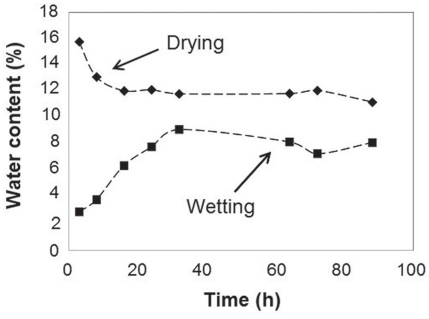

Figure 6. Water content changes with time for 200 kPa suction.

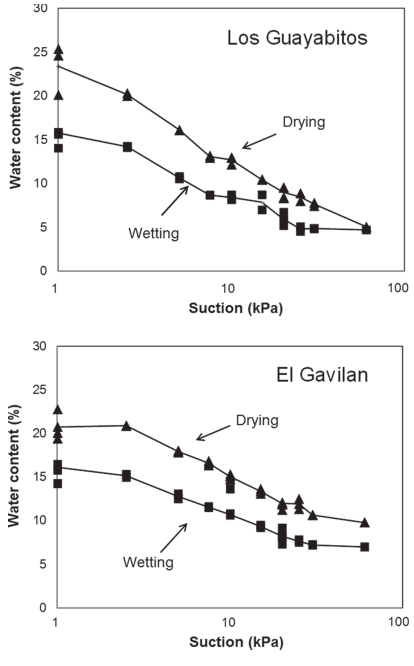

Figure 7. WRCs of Los Guayabitos and El Gavilan sites.

can be observed. In this case, wetting and drying path do not cross at the suction value of 600 kPa. Also, the residual water content observed with the wetting path is 7.0 percent, higher than 4.8 percent obtained with Los Guayabitos soil. In this case, also dispersion of results at a suction value of 1 kPa is quite important, but the initial part of the drying path indicates that the air entry value appears to be very low (a few kPa).

In general terms, obtained WRCs show that the different stages of desaturation, as indicated by Vanapalli et al. (1999), were covered: the boundary effect stage, the transition stage and the residual stage of unsaturation.

Although both residual soils are located very close and they are in the same geological formation, they have slight differences in terms of soil composition that are reflected in the WRCs.

4 CONCLUSIONS

Drying and wetting water retention properties of two residual soils from Caracas hills were investigated using the Richards or so called pressure plate method. The obtained results show that the different stages of desaturation were covered and indicate that this method is well adapted to obtain the WRCs of investigated soils. Thus, mechanical properties should be also studied by adapting Richards method to triaxial test. However, some improvements must be incorporated. A higher working pressure compressor unit must be used to obtain the water retention properties in the full range of the method (up to 1500 kPa). For very low suction values of about 1 kPa the pressure control must be finer to avoid dispersion of results that is very important. If it is not possible others methods, like the suction plate, must be used to obtain precise information in the lower suction range, like the air entry value.

ACKNOWLEDGEMENTS

The ceramic porous stones and other laboratory accessories to control suction were acquired with resources from the Scientific and Humanistic Development Council of the Universidad Central de Venezuela.

REFERENCES

Alfaro, M.A. 2008. Geotecnia en suelos no saturados. *Revista de la Academia Colombiana de Ciencias* 32(125): 471–481.

Bolt, G.H. 1956. Physico-chemical analysis of the compressibility of pure clays. *Geotechnique* 6: 86–93.

Daniel, D.E. 1983. Permeability test for unsaturated soil. *Geotechnical Testing Journal* 6(2): 81–86.

Fredlund, D.G., Xing, A. & Huang, S. 1994. Predicting the permeability function for unsaturated soils using the soil—water characteristic curve. *Canadian Geotechnical Journal* 31(3): 521–532.

Fredlund, D.G. 2005. A new soil—water characteristic curve device. Proceedings of advanced experimental unsaturated soil mechanics-an international symposium. Italy: Eperus.

Gonzalez, L., Ferrer, M., Ortuño, L. & Oteo, C. 2002. Ingeniería Geológica. Madrid: Pearson Education.

Richards, L.A. 1941. A pressure membrane extraction apparatus for soil suction. *Soil Science* 51(5): 377–386.

Vanapalli, S.K., Fredlund, D.G. & Pufahl, D.E. 1999. The influence of soil structure and stress history on the soil—water characteristics of a compacted till. *Géotechnique* 49(2): 143–159.

Advances in Unsaturated Soils – Caicedo et al. (eds)
© 2013 Taylor & Francis Group, London, ISBN 978-0-415-62095-6

Air permeability of cover soil from the Bandeirantes landfill in São Paulo, Brazil

F.A.M. Marinho
University of São Paulo, Brazil

P.F. Teixeira
Nove de Julho University, Brazil

ABSTRACT: The cover system of any landfill is responsible for controlling the water movement in and out of the landfill. For municipal solid waste landfills in particular, the generation of gases create another important design aspect for the cover system. If the cover system is not adequately designed, the gas will escape to the atmosphere without control. One important parameter for cover design is the gas or air permeability. Usually, the soils used for the cover system come from different locations, and this may create heterogeneities within the cover system. This paper presents the results of an experimental study to obtain the coefficient of air permeability of unsaturated soil specimens from the cover system of a Brazilian landfill located in São Paulo state.

1 INTRODUCTION

The placement of municipal solid waste (MSW) in landfills started many years ago, and it is still used today. The biochemical processes within the landfill generate what is called biogas. The average compositions of the main components of biogas are 54% methane (CH_4), 42% carbon dioxide (CO_2), and 3% nitrogen (N_2). With the implementation of the Kyoto protocol, the emission of greenhouse gases should be restricted. The enhancement (anthropogenic) of the greenhouse effect has to be avoided by reducing the emission of gases such CO_2 and CH_4. Considering that CH_4 is 25 times more potent in increasing the greenhouse effect, the emission of CH_4 should be avoided when possible. Reductions in the emission of greenhouse gases can be used to obtain carbon credits, which can be an important source of resources (e.g., La Rovere et al., 2006).

In places where there is some control, the municipal solid waste (MSW) is placed in sanitary landfills. According to IBGE (2008) in Brazil, 64.6% of the MSW is placed in sanitary landfills, 15.6% is placed in controlled landfills and 17.6% is simply dumped in an unspecific area. The remainder goes to other destinations, such as recycling or incineration. Apart from sanitary landfills, all other forms of MSW disposition do not satisfy the requirements of existing legislation and the technical specifications that should be met. Beyond that fact, all the procedure used for MSW disposition could minimise their environmental effects if an appropriated cover system is used. The cover or better saying the cover system, of MSW is one of the key elements for environmental protection.

A cover system should serve the following functions:

- Work as a barrier for infiltration (which generates leachate).
- Help prevent the outflow of gases and odour.
- Avoid the presence of animals that could transmit diseases.
- Work as a support for vegetation.

The biogas that is generated within a landfill can be used for energy generation, as has been done at Bandeirantes landfill in São Paulo, Brazil (e.g., Kaimoto et al., 2006). The cover system is also extremely important for controlling the emission of biogas to the atmosphere. Apart from the application mentioned above, the studies related to air permeability have direct application in remediation techniques. A comprehensive understanding of soil characteristics in terms of gas flow is important for any problem that involves gas or air flow in porous media.

This paper presents the results of an experimental study to obtain the coefficient of air permeability of samples at different degrees of saturation. The tests were performed with specimens obtained from an undisturbed block taken from the cover system of the Bandeirantes landfill in Brazil.

2 LANDFILL FUGITIVE GAS

The traditional way to design a cover suggests that it has to have a very low permeability. Although in many situations, this is not the best way to design a cover for MSW, most landfills have a low hydraulic conductivity cover system. The use of soil with a low hydraulic conductivity may induce cracks due to accommodation of the waste and also due to desiccation. Cracks, bad compaction zones and a low water content in the cover create an easy path for the gas to escape and avoid the drainage system when one exists. Although there are indications that forced extraction of the biogas can capture up to 80% of the gas generated (e.g., Park and Shin, 2001), the amount of fugitive gas in landfills can be significant. Many solutions can be applied to cases in which the fugitive emission is high. The identification of hot spots is the first step in obtaining the solution in many cases. It is not the objective of this paper to discuss solutions for fugitive emissions of biogas. However, some alternatives to reduce fugitive emissions are compaction, increasing the water content and the use of biofilters with methanotrophic bacteria (e.g., Barlaz et al., 2004).

In any case, the material to be used as a cover should be evaluated in relation to its permeability to air (or gas).

3 AIR PERMEABILITY

The Darcy law was formulated for the flow of a viscous and incompressible fluid within a porous media under laminar conditions. The volumetric flow (Q) of a gas in porous media can be described by the following expression:

$$Q = \frac{k}{\mu} A \frac{dP}{dx} \tag{1}$$

Q = volumetric flow rate (L^3/T)
k = permeability (L^2)
μ = dynamic viscosity (PT)
dP/dx = pressure gradient (P/L)

For compressible fluids, assuming that the gas behaves like an ideal gas, the volumetric flow is given by the following equation:

$$Q = \frac{k}{\mu} A \frac{P_{in}^{\,2} - P_{atm}^{\,2}}{2 P_{atm} L} \tag{2}$$

The permeability is:

$$k = \frac{2 \mu L P_{atm} Q}{A(P_{in}^{\,2} - P_{atm}^{\,2})} \tag{3}$$

P_{in} = pressure in (absolute pressure)
P_{out} = pressure out (here, it is the atmospheric pressure, P_{atm}).

When the applied pressure is relatively small in relation to the atmospheric pressure, the air compressibility can be ignored without significant errors, although is very simple to take it into account.

The coefficient of permeability (L/T) is given by:

$$K = \frac{k \rho g}{\mu} \tag{4}$$

ρ = density of the air (1.205 kg/m^3 at 20°C)
μ = dynamic viscosity (1.85 * 10S^{-5} Pa s)
g = acceleration due to gravity (9.81 m/s^2)

The gas permeability differs from the permeability to liquids, and it is dependent on the applied mean pressure, temperature and nature of the gas. *Ceteris paribus*, the lower the pressure, the higher the permeability. The Klinkenberg effect is responsible for this behaviour.

According to Klinkenberg (1941), the gas permeability at a finite pressure is given by

$$k = k_{\text{int}} \left[1 + \frac{b}{P_{av}} \right] \tag{5}$$

where k_{int} is the intrinsic permeability (or the Klinkenberg permeability), b is the Klinkenberg factor, which is dependent on the pore structure of the medium and the temperature for a given gas. P_{av} is the average pressure.

Figure 1 presents a schematic representation of the determination of the parameters for the Klinkenberg empirical equation. Note that the intrinsic permeability represents the value obtained under very large gas-phase pressure, and it depends

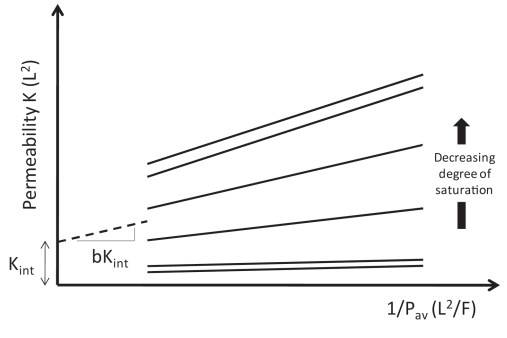

Figure 1. Schematic representation of the relationship between the mean pressure and the apparent coefficient of permeability (modified from Abbas et al., 1999).

only on the porous media. It is independent of the nature of the fluid. The figure shows the effect of the degree of saturation, which acts as part of the soil structure.

Many authors have shown that the Klinkenberg permeability and Klinkenberg factor (b) depend on the degree of saturation (e.g., Estes et al., 1956, using oil and Abbas et al., 1999 using water). Qingjie et al. (2002) presented a model that reproduces the variation of the Klinkenberg factor (b) with the degree of saturation. Estes and Fulton (1956) showed that the variation of b with the degree of saturation is clearer for degrees of saturation below 50%. In the model presented by Qingjie et al. (2002), that value is approximately 20%.

The Klinkenberg effects are significant in any situation in which the mean free path of gas molecules in porous media approaches the pore dimension. The concept of free-molecule flow is useful to understand the mean free path because it describe a situation in which gas molecules collide more frequently with flow boundaries (soil particles) than with other gas molecules. A large free path means that significant molecular collisions occur with the soil particles rather than with other gas molecules. The gas permeability is then enhanced by 'slip flow'. Therefore, it is expected that the Klinkenberg effect is significant for clay and silts and small for sands. Abbas (1999) suggested that when the pressure tends towards infinity, the flow become a viscous flow. Depending on the type of soil used for the cover system, the Klinkenberg effect may be significant. When it is necessary to determine the air permeability of the cover system, it is recommended that one determine how the Klinkenberg effect is affecting the flow for the soil investigated.

In this paper, the tests were performed using an atmospheric flow mode under constant differential pressure. In this case, the air leaving the specimen is allowed to flow directly to atmosphere. McPhee and Arthur (1991) suggested that the test be performed under back pressure. However, the use of back pressure for compressible materials requires the use of a high confining pressure. A high confining pressure may induce significant changes in the void ratio and therefore change the air permeability. It should be noted that the soil compressibility creates difficulties for interpreting the Klinkenberg effect.

4 MATERIALS AND METHODS

4.1 *Soil from the cover of the Bandeirantes landfill*

The soil tested is sandy silt (39% silt, 46% sand, 11% clay and 4% gravel) with a low plasticity. The Atterberg limits are w_l = 39% and w_p = 31%, and the specific density of the solids is 2.77. The soil-water retention curve was obtained from undisturbed samples using a suction plate (from 0 to 30 kPa), a pressure plate (from 30 kPa to 500 kPa) and filter paper (above 500 kPa). Figure 3a presents the retention curves for two samples and the results from suction measurements made with the samples used for the permeability test.

4.2 *Specimen preparation*

The specimens were obtained from undisturbed blocks obtained from the cover system of the Bandeirantes landfill. The specimens were trimmed to a diameter of 38 mm and a height of approximately 80 mm. The initial conditions of the specimens tested are presented in Table 1. The specimens are named according to the two series of tests performed. Specimens from serie A were tested under the same air pressure an specimens from series B were tested under different air pressures to evaluate the Klinkenberg effect.

4.3 *Air permeability cell*

All tests were performed using air for operational safety reasons. The tests were carried out at the soil mechanics laboratory of the Politechnique School of São Paulo University.

The air permeability cell consists of a triaxial cell adapted to perform air permeability tests. Figure 2 presents the details of the equipment used.

At the base and at the top of the specimen, a dry, coarse porous material was used. After the specimen was placed on the pedestal of the cell, a membrane was placed, and the soil was isolated using "orings". A cell pressure was applied to avoid flow between the samples and the membrane. The air pressure is adjusted at the base

Table 1. Characteristics of the specimens tested.

Specimen	Suction (kPa)	w_{nat} (%)	γ_d (kN/m³)	e	S (%)
A1-48	48	20.8	14.4	0.885	65.0
A1-61	61	18.9	14.8	0.831	63.1
A1-165	166	13.4	14.6	0.853	43.6
A1-230	231	13.4	14.5	0.875	42.5
A1-433	434	13.4	14.2	0.904	41.1
A1-530	531	13.44	13.9	0.953	38.9
A2-67	67	17.89	13.6	0.991	49.9
A2-100	100	14.7	14.1	0.861	45.6
A2-200	200	11.9	14.2	0.909	36.2
B1	61	23.2	14.2	0.910	70.2
B2	162	14.5	14.3	0.900	44.4

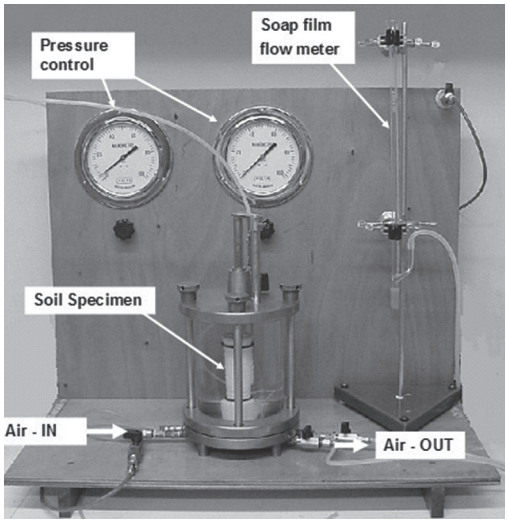

Figure 2. Setup of the permeability cell.

of the specimen, and atmospheric pressure was maintained at the top.

The flow of air was measured using a soap film flow meter (Barr, 1934). Two flow meters were used with a total volume of 25 ml and 50 ml. The soap used was an ordinary detergent diluted with water. The wall of the flow meter was cleaned and wetted before use. After a series of repeatable measurements (a minimum of 15 were performed) the time and volume of the flow was recorded and associated with the specimen condition.

4.4 *Air permeability tests results*

The coefficient of air permeability (K) is given by the following equation:

$$K = \frac{2\rho g L P_{atm} Q}{A(P_{in}^{\ 2} - P_{atm}^{\ 2})} \tag{6}$$

From the above equation, it can be observed that the air flow is not proportional to ΔP but to the pressure squared ($P_{in}^{\ 2} - P_{atm}^{\ 2}$). In our case, P_2 is atmospheric pressure (e.g., Vangpaisal and Bonazza, 2004).

The intrinsic permeability and the air permeability obtained are presented in Table 1. The results from series B are shown in Figure 4.

Figure 3a presents data from soil water retention tests performed in two representative specimens and individual data obtained from the specimens used for permeability tests, according to Table 1. The results indicate that the air entry value of the soil is low; it is less than 10 kPa.

Table 2. Intrinsic permeability and air permeability of the specimen tested.

Specimen	k (m^2)	K_a (m/s)
A1-48	3.00×10^{-13}	1.87×10^{-7}
A1-61	2.70×10^{-13}	1.69×10^{-7}
A1-165	3.11×10^{-13}	1.98×10^{-7}
A1-230	2.6×10^{-13}	1.60×10^{-7}
A1-433	2.86×10^{-13}	1.76×10^{-7}
A1-530		2.51×10^{-7}
A2-67	9.00×10^{-13}	5.60×10^{-8}
A2-100	1.1×10^{-12}	6.96×10^{-7}
A2-200	8.00×10^{-13}	5.60×10^{-7}
A3-500	1.17×10^{-12}	7.21×10^{-7}

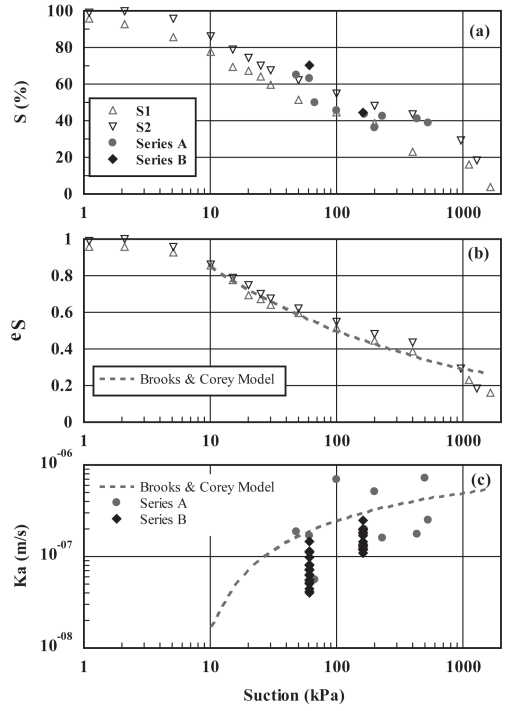

Figure 3. Coefficient of permeability, effective degree of saturation and degree of saturation versus suction.

In Figure 3b, the results are shown in terms of the effective degree of saturation along with the fitting obtained using the Brooks and Corey model (Brooks and Corey, 1966). The suction measurements were obtained using a suction plate (1 to 30 kPa), a pressure plate (30 to 500 kPa) and filter paper (> 500 kPa). Figure 3c presents the relation between the coefficient of permeability and the suction and the Brooks and Corey model. The parameters of the model are $(u_a - u_w)_b$ = 7 kPa

(which is the air entry value) and $\lambda = 0.25$ (which is the pore size distribution index).

Figure 4 presents the relation between the intrinsic permeability and the inverse of the mean applied pressure for series B. The results obtained within series A showed a significant variability. Although data from series A were obtained using different specimens from the same undisturbed sample, no measured parameter could be identified that could explain the variability. The specimens that presented a higher permeability had a degree of saturation of approximately 40%. However, from the five specimens that presented a lower permeability, three also had a degree of saturation of approximately 40%.

McPhee and Arthur (1991) mentioned that the determination of Klinkenberg parameters is extremely sensitive to the test methods and procedures used. To obtain the Klinkenberg parameters, all points from both series were considered. The intrinsic permeability (K_{int}) (or Klinkenberg permeability) obtained was 1.59 * 10–13 m^2, and the b parameter was 9.45 kPa (Eq. 5). It should be noted that when testing soil, the compressibility of the specimen may create different pore sizes during the increase of the confining pressure that is required to be able to increase the air pressure. The increase in suction also induces changes in pore size.

The Klinkenberg coefficient may be estimated using the empirical equation proposed by Jones (1972), where the intrinsic permeability k is given in m^2 and b is given in kPa.

$$b = 1.89 * 10^{-4} * k^{-0.36}$$

Applying the above equation, b = 6.8 kPa, which, although different from the result presented above, yields a reasonable trend (see Figure 4) considering that the porosity of the specimen tested changes with increasing pressure. The use of the equation proposed by Heid et al. (1950) gives also a reasonable trend. It should be noted that the use of other equations, such as the one suggested by Jones and Owens (1980), can give very different results. It can be concluded that the use of empirical equations is difficult for many reasons, including differences in the pore size distribution and the compressibility of the specimen.

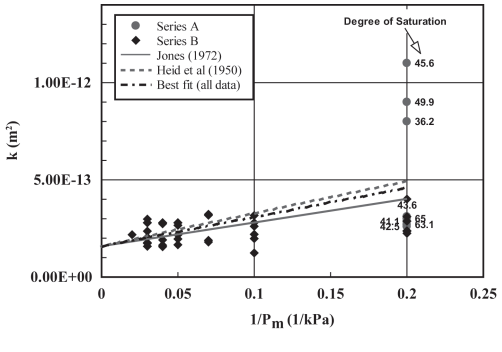

Figure 4. Determination of the intrinsic permeability.

Considering the permeability (k) for a low pressure (5 kPa), the coefficient of permeability (K) can vary from 3.3 * 10^{-7} m/s to 1.8 * 10^{-7} m/s using the values obtained experimentally and the one based on Jones (1972). If the Klinkenberg effect is not taken into account, the coefficient of permeability for low pressures would be 1.4 * 10^{-7} m/s. It can be conclude that the Klinkenberg effect is negligible for this case because the variability of the coefficient of permeability for the soil is much higher than this value. Apart from the actual variability, the determination of the Klinkenberg permeability is strongly affected by the accuracy of the pressure measurement and also by the setup used to apply the pressure. According to McPhee and Arthur (1991), the use of atmospheric mode induces significant variability in the results due to instabilities of the pressure system.

5 CONCLUSIONS

The soil obtained from the cover of the landfill represents a specific point of the cover system. The results obtained suggested that the material has an air entry suction value of approximately 7 kPa, which may facilitate fugitive emissions of biogas during the dry season. The air entry value of the soil tested is too close to the pressure values that can be found below landfill covers. Landfill covers should be designed and constructed by considering, among others parameters, the air entry value of the compacted soil used. The Klinkenberg effect was negligible for the material and level of pressure tested. Considering that the pressure of the biogas at the cover system interface is usually low (< 5 kPa) the Klinkenberg effect can be ignored. The air permeability decreases rapidly for degrees of saturation above 60%. Based on field measurements performed in São Paulo City, the suction at approximately 30 cm deep may reach a value of approximately 100 kPa close to the surface. Based on this, the air permeability of the cover may increase up to 2 * 10^{-7} m/s.

ACKNOWLEDGEMENTS

We thank Dr. Rosana Vazoller, the company Biogás energy ambiental s/a and the city of São Paulo administration for making it possible to

obtain the undisturbed sample. The authors also thank the following Brazilian Agencies: CAPES and CNPq.

REFERENCES

Abbas, A. Carcasses, M. & Ollivier, J.P. (1999). Gas permeability of concrete in relation to its degree of saturation. Materials and Structures, Vol. 32, Jan.–Feb., pp. 3–8.

Barlaz, M.A., Green, R.B., Chanton, J.P., GoldSmith, C.D. & Hater, G.R. (2001). Evaluation of a Biologically Active Cover for Mitigation of Landfill Gas Emissions. Environ. Sci. Technol. 38: 4891–4899.

Barr, G. (1934). Two designs of flow meter, and a method of calibration. The Journal Scientific Instruments, 11. pp. 321–324.

Brooks, R.H. & Corey, A.T. (1966). Properties of Porous Media Affecting Fluid Flow. Journal of Irrigation and Drainage Division., IR 2, 61–68.

Estes, R.K. & Fulton, P.F. (1956). Gas Slippage and Permeability Measurements. Petroleum Transactions, AIME. Technical Note 370. pp. 338–342.

Heid, J.G., McMahon, J.J., Nielsen, R.F. & Yuster, S.T. 1950. Study of the permeability of rocks to homogeneous fluids, Am Petroleum Institute Drilling Production Practices, p. 230–246.

IBGE. (2008). Instituto Brasileiro de Geografia e Estatística, Pesquisa Nacional de Saneamento Básico. Available at http://www.ibge.gov.br. Acesso em maio de 2012.

Jannot, Y., Lasseux, D., Vizé, G. & Hamon, G. (2007). A detailed analysis of permeability and Klinkenberg coefficient estimation from unsteady-state pulse-decay or draw-down experiments. International Symposium of the Society of Core Analysts held in Calgary, Canada, 10–12 September.

Jones, F.O. & Owens, W.W. (1980). A laboratory study of low-permeability gas sands: paper SPE 7551-PA, Journal of Petroleum Technology, Vol. 32, No. 9, pp. 1631–1640. DOI: 10.2118/7551-PA.

Kaimoto, L.S.A., Leite, E.F. & Coelho, M.G. (2006). Considerações sobre aproveitamento do Biogás em Aterro Sanitário. Simpósio Internacional de Tecnologias e Tratamento de Resíduos Sólidos—Rio de Janeiro—abril. (in Portuguese).

La Rovere, E.L. Costa, C.V. & Dubeux, C.B.S. (2006). Aterros Sanitários no Brasil e o Mecanismo de Desenvolvimento Limpo (MDL): Oportunidades de promoção de desenvolvimento sócio-ambiental. Simpósio Internacional de Tecnologias e Tratamento de Resíduos Sólidos—Rio de Janeiro—abril. (in Portuguese).

McPhee, C.A. & Arthur, K.G. (1991). Klinkenberg Permeability Measurements: Problems and Practical Solutions, in Advances in Core Evaluation: Accuracy and Precision in Reserves Estimation, ed. P.F. Worthington, pp. 447–462.

Park, J.W. & Shin, H.C. (2001). Surface emission of landfill gas from solid waste landfill. Atmospheric Environment 35: 3445–3451.

Qingjie, L., Baohua, L., Xianbing, L. & Shouguo, Y. (2002). The Effect of Water Saturation on Gas Slip Factor by Pore Scale Network Modeling. International Symposium of the Society of Core Analysts.

Vangpaisal, T. & Bouazza, A. (2004). Gas Permeability of Partially Hydrated Geosynthetic Clay Liners. Journal of Geotechnical and Environmental Engineering, ASCE. Vol. 130, No. 1, pp. 93–102.

Advances in Unsaturated Soils – Caicedo et al. (eds)
© 2013 Taylor & Francis Group, London, ISBN 978-0-415-62095-6

Water retention curves for a tropical soil contaminated by vinasse

M.G. Miguel & S.Y. Pereira
State University of Campinas, Campinas, São Paulo State, Brazil

ABSTRACT: The ethanol production has increased considerably and also the generation of one of its main effluents, called vinasse, in Brazil. The area studied presents an unsaturated tropical soil profile where sugar cane was grown. This research aims to evaluate the influence of the vinasse in the physical, chemical and water retention characteristics of this soil profile. Pitcher sampling with Denisson tube was used to collect disturbed and undisturbed soil samples in areas with and without vinasse until 24 meters deep. These soil samples were submitted to geotechnical, mercury intrusion porosity, X-ray fluorescence and filter paper tests. All the soil samples were classified as clayey-silt sands and fine particle aggregations were observed for soil samples with vinasse. The water retention curves were influenced by the macro and microposity. The pore distribution and the symmetry of the curves in both pathways can be affected by the presence of vinasse.

1 INTRODUCTION

In Brazil, the program to motivate alcohol and biodiesel production has favored extending sugarcane agriculture and created more factories in the country because of the demand for clean fuels. Extending alcohol production has substantially increased one of the main effluent generations, called vinasse.

Silva & Orlando Filho (1981) report some chemical elements present in the composition of vinasse as C, N, P, K, Ca, Mg, S, Fe, Cu, Zn and Mn, in addition to pH obtained in chemical analyzes of several samples of vinasse from Brazilian sugar and alcohol mills. High concentrations in terms of macro and micronutrients and in pH values were found in these samples.

Physical and soil water retention characteristics suffer changes with vinasse presence (Cunha *et al.*, 1987, Aguiar 1992, Cruz *et al.*, 1991, Luz *et al.*, 2010), from them the organic matter concentration increase, pH increase, expanding salinity and compression resistance.

The research studies the influence in water retention capacity of the soil profile contaminated by vinasse and located in productive Aquifer System from São Paulo State, in Brazil.

This research study area is located at Assentamento Sepé Tiaraju, in the Municipalities of Serra Azul and Serrana, in Ribeirão Preto region, State of São Paulo, Brazil, with UTM projections: 234000 and 7647200. In this area, there were sugar cane crops irrigated with raw vinasse as natural fertilizer by means of aspersion and effluent channels.

The region relief is depicted as slightly wavy, with altitudes varying from 450 to 650 m and declivities from 0 to 30%. In hydrogeological terms, there are two main aquifer systems: Sistema Aqüífero Guarani (Guarani Aquifer system) and Sistema Aqüífero Serra Geral (Serra Geral Aquifer system). Sistema Aqüífero Guarani consists of two geological formations called Pirambóia and Botucatu. Serra Geral Formation composes the Serra Geral Aquifer System.

Particularly, it is proposed to assess characteristic changes, being physical, chemical and water retention of unsaturated soil layer in a certain place from such region, used as natural tank (opencast digging without waterproofing) to arrange vinasse during 20 years.

Geophysical electro-resistivity test was performed outside and inside the area of the tank by using electric conductivity method until 20 m depth. Conductive anomalies in electric conductivity lines are pointed out inside the tank (Da Cruz, 2008, Da Cruz *et al.*, 2008).

From such anomalies, direction and flow direction of greater intensity were defined, as Figure 1 indicates, where the two collect points of disturbed and undisturbed soil samples were presented, inside and outside tank area, chosen to perform standardized experiments of geotechnical and chemical characterizations and determine soil water retention curves, using paper filter method in laboratory.

Chemical characterizations are not present in this research; however, they can be seen in Arcaro *et al.* (2010).

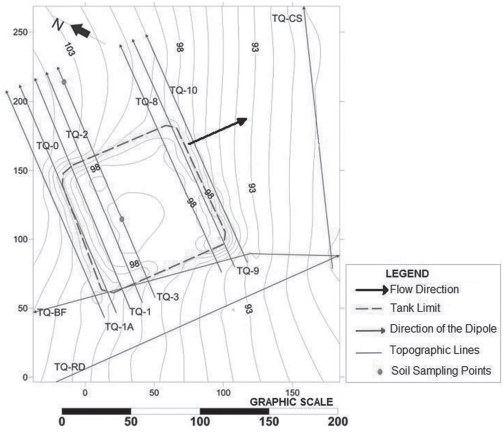

Figure 1. Area studied (Modified from Da Cruz, 2008).

2 MATERIAL AND METHODS

Disturbed soil samples were collected into the deactivated tank pit by the auger drilling probe every meter of depth, from the ground level. The maximum depth reached was 24 m, in which the table water was found.

Undisturbed soil samples were collected by Pitcher sampling, with Denisson casing, until maximum depth of 24 m. These soil samples were collected every 1.5 m of depth, from the ground level.

Some disturbed soil samples were submitted to geotechnical characterization tests, as following: grain-size distribution (ASTM, 1998a) and Liquid and Plastic Limits (ASTM, 1998b).

The soil samples used to determine the soil-water retention curves were a) undisturbed soil samples with vinasse collected at depth ranges: 0 m to 0.3 m; 1.5 m to 2.2 m; 10.5 to 11.2 m; and 15.0 to 15.6 m; and b) undisturbed soil samples without vinasse collected at depth ranges: 0 m to 0.3 m; 1.5 m to 2.0 m, and 10.5 to 11.0 m. The first soil samples were symbolized for S1-WV; S2-WV, S3-WV and S4-WV, respectively. The last soil samples were symbolized for S1-NV; S2-NV and S3-NV.

Theses soil samples were submitted to porosimetry tests with mercury intrusion, except the samples collected at 0 m to 0.3 m depth and at 10.5 m to 11.0 m without vinasse.

Soil-water retention curves (SWRC) were obtained by filter paper technique (ASTM, 2004), with drying and wetting pathways. Two to three specimens were prepared from each soil samples, using stainless steel rings of 0.05 m diameter and 0.02 m height.

Paper filter Whatman No. 42 was used and Chandler *et al.* (1992) calibration equations proposed. Experimental points of water retention curves were fitted with van Genutchen (1980) equation, expressed as Equation 1:

$$w = w_r + \frac{(w_{sat} - w_r)}{[1 + (\alpha_v \psi)^n]^m} \quad (1)$$

where: ψ is the matric suction (kPa); w, gravimetric moisture content (%); w_{sat}, gravimetric moisture content at saturation (%); w_r, residual gravimetric moisture content (%); α_v, fitting parameter (kPa^{-1}); n and m, fitting parameters related to the pore distribution and curve symmetry, respectively.

3 RESULTS AND DISCUSSION

Average values of solid unit weight (γs), liquid limit (LL) and plasticity index (PI) obtained for soil samples with and without vinasse are presented in Table 1. Discreet decreasing of the plasticity along the depth and low variation of solid unit weight were observed.

Grain-size distribution curves with and without deflocculant (WD and ND, respectively), during the sedimentation phase of the tests are presented in Figure 2. The percents of each fraction regarding the depth range of collection (z) are shown in Table 2.

Although there were differences in the grain-size distribution curves obtained using or not the deflocculant, all soil samples were classified as clayey-silty sands. The sand fraction increased and the clay fraction decreased along the depth, according to PI (Table 1).

All the experimental SWRC presented bimodal pore-size distribution, with macro and micropores, except experimental SWRC at 0 m to 0.3 m depth. Macro and micro structures of the soil samples can also be seen in Figure 5. The micropore frequencies (about between 0.01 to 0.1 μm) were high for all soil samples, but they were slightly lower for deeper samples (S5). Macropore frequencies (about between 1 to 100 μm) were different: S2-WV sample presented the highest macropore frequencies, followed by S2-NV, S3-WV, S5-WV and S5-NV samples. However, the macropores frequencies between about 40 to 100 μm were higher for S2-WV.

Experimental SWRC obtained over drying and wetting pathways are presented in Figures 3 and 4, respectively. SWRC representative of each depth were considered. Bulk density (ρ_d) and void ratio (e) values of specimens are showed in Table 3. Logarithm curves of the differential volume *versus* pore diameter obtained by porosimetry tests are presented in Figure 5.

Table 1. Average value of physical indexes.

Depth range of collection (m)	LL %	PI	γ_s kN/m³
2–3	30.3	10.1	28.17
6–7	28.3	9.0	28.06
9.5–10	31.3	11.7	28.13
12–13	27.7	7.9	28.07
15–16	24.7	6.8	27.53
18–19	29.5	11.0	27.71
20–21	23.9	6.1	28.09
23–24	21.3	3.1	27.66

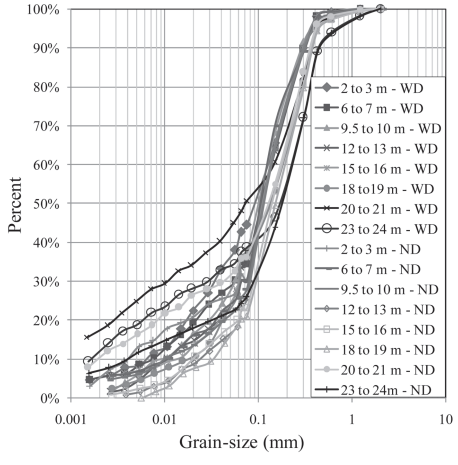

Figure 2. Grain-size distribution curves with and without deflocculant.

Table 2. Fraction percent.

	With deflocculant			Without deflocculant		
z (m)	Clay %	Silt %	Sand %	Clay %	Silt %	Sand %
2–3	22.0	21.1	57.0	18.7	25.7	55.7
6–7	20.6	24.0	55.3	14.3	27.3	58.4
9.5–10	25.1	24.6	50.3	20.5	21.0	58.5
12–13	18.9	25.6	55.5	16.4	21.2	62.5
15–16	19.0	24.4	56.5	15.9	23.9	60.2
18–19	15.0	25.6	59.4	10.7	28.3	61.0
20–21	17.4	28.9	53.6	10.9	22.5	66.6
23–24	12.3	23.5	64.2	7.2	15.8	77.0

Void ratio values decrease along the depth (Table 3) except the soil samples at 0 m to 0.3 m depth, because of the densification process by agricultural machinery. This fact suggests that the shallower soil samples have been suffering leaching process presenting microaggregation (Table 2) and

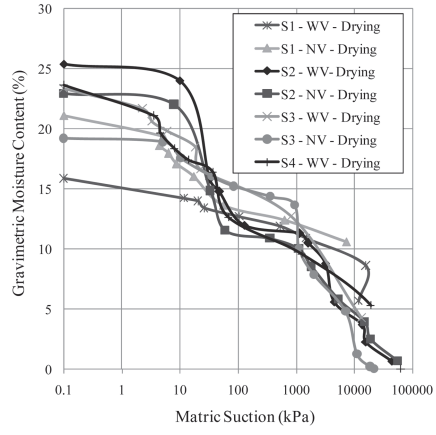

Figure 3. Experimental SWRC for drying pathway.

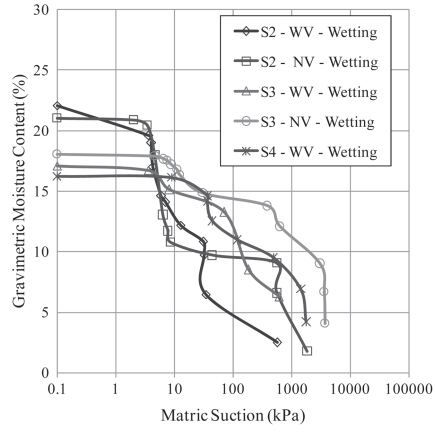

Figure 4. Experimental SWRC for wetting pathway.

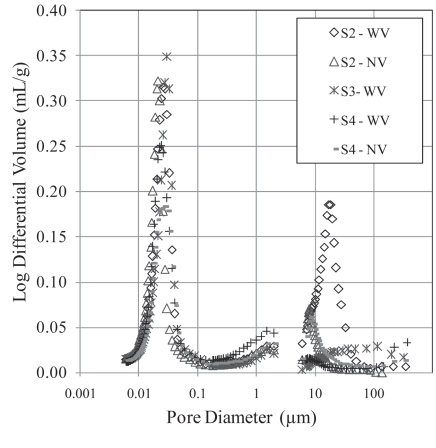

Figure 5. Curves of logarithm of the differential volume *versus* pore diameter.

Table 3. Physical indexes of the specimens.

Soil sample	z m	ρ_d g/cm^3	e	Pathway
S1-WV	0–0.3	1.91	0.47	Drying
S1-NV	0–0.3	1.85	0.50	Drying
S2-WV	1.5–2.2	1.63	0.63	Drying
S2-NV	1.5–2.0	1.83	0.50	Drying
S3-WV	10.5–11.2	1.95	0.35	Drying
S3-NV	10.5–11	1.95	0.36	Drying
S4-WV	15–15.6	1.94	0.45	Drying
S2-WV	1.5–2.2	1.65	0.65	Wetting
S2-NV	1.5–2.0	1.81	0.51	Wetting
S3-WV	10.5–11.2	1.82	0.53	Wetting
S3-NV	10.5–11	1.81	0.54	Wetting
S4-WV	15–15.6	1.79	0.58	Wetting

Table 4. Stretches considered in the fitting.

Soil sample	Pathway	1st Stretch kPa	2nd Stretch kPa
S1-WV	Drying	0.1–1,500	–
S1-NV	Drying	0.1–7,500	–
S2-WV	Drying	0.1–1,000	2,000–90,000
S2-NV	Drying	0.1–1,000	2,000–90,000
S3-WV	Drying	0.1–800	1,000–90,000
S3-NV	Drying	0.1–15	20–90,000
S4-WV	Drying	0.1–40	50–20,000
S2-WV	Wetting	0.1–30	40–90,000
S2-NV	Wetting	0.1–10	15–90,000
S3-WV	Wetting	0.1–10	15–90,000
S3-NV	Wetting	0.1–300	400–90,000
S4-WV	Wetting	0.1–200	300–2,000

macro and micro porosity (Fig. 5). The deeper soil samples, although present microporosity, showed less expressive macroporosity, which can be associated with geostatic stress action.

SWRC obtained for drying pathway (Fig. 3) at different depths presented differences between them mainly for matric suction values between 0.1 to 35 kPa. SWRC also presented differences for the matric suction values between 35 kPa e 1000 kPa, except the S1 samples. SWRC obtained for wetting pathway (Fig. 3) at different depths were distinct for any matric suction values. The values of gravimetric moisture content at saturation for the SWRC obtained were very distinct. The values of gravimetric moisture content at saturation were very distinct for all the SWRC (Figs. 3 and 4).

These differences among curves are related to pore distribution of the samples, mainly of the macropores, according to Figure 5 and to decreases of the clay fraction amount and the void ratio along the depth (Tables 2 and 3).

The van Genuchten (1980) equation was used to fit the experimental SWRC. For the bimodal SWRC, the curves were divided in two stretches: 1st stretch related to macroporosity and 2nd stretch related to microporosity. Each curve presented different values for these stretches, according to Table 4.

The fitting parameter values from van Genuchten (1980) are presented in Tables 5 and 6, respectively for drying and wetting pathways. Experimental and fitted SWRC, for the drying and wetting pathways are presented in Figures 6 and 7, respectively.

The "n" and "m" fitting parameter values showed divergent for the S1 samples with and without vinasse (Table 5). For the S2 samples, few differences were found. Nonetheless, for the S3 samples, different "α_v" values for the two stretches and different "m" values in the stretch related to microporosity were found. The fitting parameter values in the stretch related to macroporosity for the S4-WV sample were closer to S3—for WV sample, however, the fitting parameter values in the stretch related to microporosity were very distinct of other samples.

Table 5. Fitting parameter values from van Genuchten (1980) for drying pathway.

Soil samples	1st Stretch-macro			2nd Stretch-micro		
	α_v kPa^{-1}	n	m	α_v kPa^{-1}	n	m
S1-WV	0.35	1.4	0.12	–	–	–
S1-NV	0.30	7.4	0.06	–	–	–
S2-WV	0.05	3.8	0.65	0.0004	1.85	0.46
S2-NV	0.05	3.3	0.70	0.0005	1.78	0.44
S3-WV	0.50	2.0	0.50	0.0005	0.75	0.80
S3-NV	0.09	2.0	0.50	0.00008	1.00	4.20
S4-WV	0.40	1.8	0.40	0.00012	0.05	2.50

Table 6. Fitting parameter values from van Genuchten (1980) for wetting pathway.

Soil samples	1st Stretch-macro			2nd Stretch-micro		
	α_v kPa^{-1}	n	m	α_v kPa^{-1}	n	m
S2-WV	0.26	2.8	0.64	0.06	1.70	0.41
S2-NV	0.22	6.0	0.86	0.06	1.50	0.33
S3-WV	0.20	4.8	0.79	0.0004	1.15	12.0
S3-NV	0.08	5.0	0.80	0.00009	1.90	9.0
S4-WV	0.03	5.5	0.50	0.001	1.90	1.7

These observations indicate that the presence of vinasse in the soil samples may have decreased the air-entry values of the macro and micropores and the symmetry of the SWRC in the microporosity stretch.

The fitting parameter values presented in Table 6 for the S2 samples indicated more expressive differences for the "n" and "m" parameters refering to macro and microporosity. This fact suggests that the pore distribution and the symmetry of the

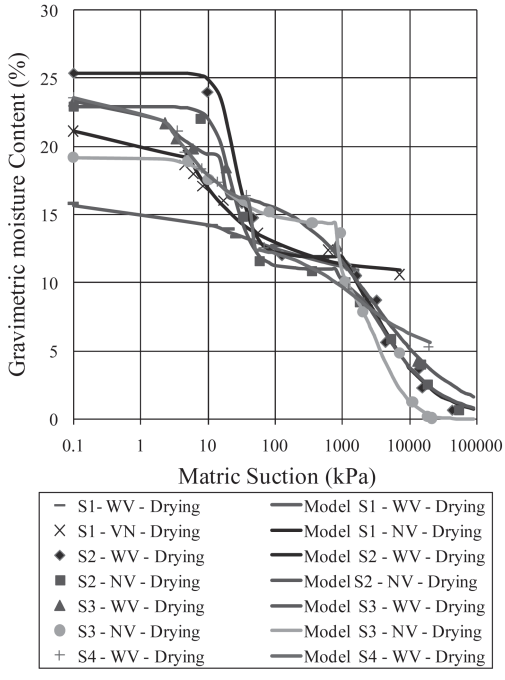

Figure 6. Experimental and fitted SWRC for drying pathways.

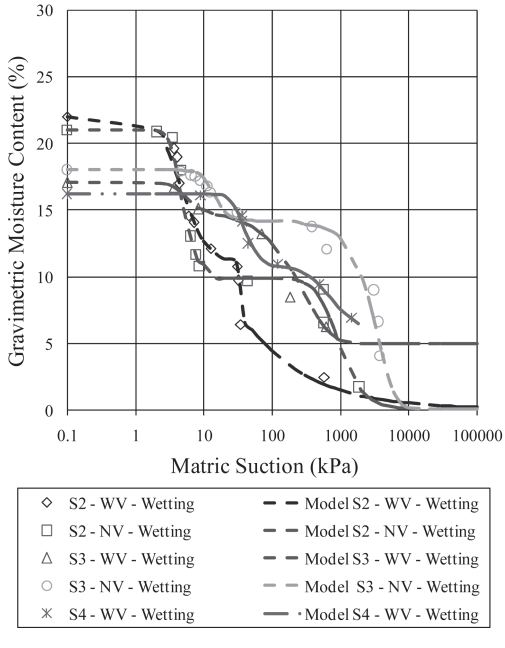

Figure 7. Experimental and fitted SWRC for wetting pathways.

curves during the wetting process can be affected by presence of vinasse. The "α_v" parameter values in the stretch relates to macro and microporosity and the "n" and "m" parameter values in the microporosity stretch were significantly changed with the presence of vinasse for the deeper samples.

4 CONCLUSIONS

The research studied the influence in water retention capacity of the soil profile contaminated by vinasse and some considerations could be highlighted.

The soil samples collected along soil profile were classified as clayey-silt sand, regardless whether or not the deflocculant is used in the sedimentation tests. The amount of sand fraction increased along the depth with consequent reduction of the plasticity.

The soil water retention curves (SWRC) obtained in the drying and the wetting pathways presented bimodal pore distribution, except the shallower samples due to densification processes by use of the agricultural machinery. The porosimetry tests confirmed the presence of macro and micro pores in the soil samples, with high frequency of macropores for the shallower samples.

SWRC obtained in distinct depth presented differences that can have relation with pore distribution, mainly the macropores, of the soil samples, and with the decreases of the clay fraction amount and the void ratios along the depth.

In general, the pore distribution and the symmetry of the SWRC in both pathways can be affected by the presence of vinasse.

ACKNOWLEDGEMENTS

The authors wish to thank FAPESP (Research Support Foundation of São Paulo) for their assistance in the research under process 2007/05323-1, INCRA (National Institute for Colonization and Agrarian Reform) for logistical support, and ENGESOLOS Engineering and Foundations Ltd., for supporting the implementation of field tests.

REFERENCES

Aguiar, M.A. 1992. Vinasse incorporation in the soil: effects on the strength characteristics of the obtained material. material Thesis. Agricultural Engineering Faculty. State University of Campinas—São Paulo State-Brazil. 74 p. (In Portuguese).

Arcaro, N.P., Pereira, S.Y., Miguel, M.G. & Aguiar, D.P.O. 2010. Study of soil contaminated by vinasse applying leach test In: XXXVIII International Association of Hydrologists, Cracóvia/Polonia. IAH 2010, 2: 2151–2158.

ASTM Standard D4318-98. 1998a. Test method for liquid limit, plastic limit and plasticity index of soils. American Society for Testing and Materials, West Conshohocken, Pa.

ASTM Standard D422-98. 1998b. Test method for particle-size analysis of soils. American Society for Testing and Materials, West Conshohocken, Pa.

ASTM Standard D5298-03. 2007. Standard test method for measurement of soil potential (suction) using filter paper. Vol. 04.08. American Society for Testing and Materials, West Conshohocken, Pa.

Chandler, R.J., Crilly, M.S. & Montgomery-Smith, G. 1992. A low-cost method of assessing clay desiccation for low-rise buildings. Proc. of The Institution of Civil Engineering. 92(2): 89–89.

Cunha, R.C.A., Costa, A.C.S., Maset Filho, B. & Casarini, D.C.P. 1987. Effects of irrigation with vinasse and the dynamics of its constituents in the soil: I—physical and chemical aspects. *Water Science and Technology*. 10(8): 155–165.

Cruz, R.L., Righetto, A.M. & Nogueira, M.A. 1991. Experimental investigation of soil and groundwater impacts caused by vinasse disposal. *Water Science and Technology*, 24(11): 77–85.

Da Cruz, J.I. (2008). Detection of the vinasse influence in the soil resistivity by geophysics data analysis: a case study in the settlement Sepé-Tiarajú-SP. Thesis. Geosciences Institute. State University of Campinas. Campinas—São Paulo State-Brazil. 165 p. (In Portuguese).

Da Cruz, J.I., Portugal, R.S., Ustra, A.T., Elis, V.R., Fachin, S.J.S. & Borges, W.R. 2008. Evaluation of the influence of vinasse diposal on soil by dc-resistivity data analysis. Source: Society of Petroleum Engineers. In 70th European Association of Geoscientists and Engineers Conference and Exhibition—Incorporating SPE EUROPEC, 5: 2903–2907.

Luz, B.S., Miguel, M.G. & Pereira, S.Y. 2010. Physical, chemical and water retention characteristics of a tropical soil with vinasse in Brazil In: 6 International Congress on Environmental Geotechnics, 6ICEG. New Delhi/India: Tata Mc Graw Hill Education Private Limited, 2: 1349–1352.

Silva, G.M. de A. & Orlando Filho, J. 1981. Characterization of chemical composition from several types of Brazilian vinasse. *Bol. Tec. PLANALSUCAR*, 3: 5–22. (In Portuguese).

Van Genuchten, M.T. 1980. A Closed-form equation for prediciting the hydraulic conductivity of unsaturated soils. *Soil Science Society of America Journal*. 44(5): 892–898.

Advances in Unsaturated Soils – Caicedo et al. (eds)
© 2013 Taylor & Francis Group, London, ISBN 978-0-415-62095-6

Permeability studies with blend of fly Ash and Rice Husk Ash stabilized soil subgrade

N.L. Patil, Sanjay Sharma & Hemant Sood
Department of Civil Engineering, National Institute of Technical Teachers Training and Research, Chandigarh, India

ABSTRACT: Permeability of soil subgrade plays a vital role in sustainable subgrade strength. Fly Ash and Rice Husk Ash (RHA) are the waste products which can be utilized as a potential stabilization material. Present study addresses effects of fly ash and RHA on permeability characteristics of CL and CL-ML (USCS classification) soil subgrade. Experimental investigations for class-F fly ash and uncontrolled burnt RHA have been performed in varying proportions independently and in blended combinations with the subgrade soils. The laboratory investigations for permeability modification reported significant increase in permeability (10^{-9} to 10^{-5} cm/sec) with fly ash and RHA stabilization for CL and CL-ML soil with good regression. The effects of fly ash and RHA stabilization on change in voids ratio and degree of saturation during the permeability measurement have also been reported. The improvements in permeability are beneficial for improving the drainage properties of the subgrade soil.

1 INTRODUCTION

Various types of stabilizers are used for improving the subgrade soil properties. Present study mainly focuses on modification of permeability characteristics of soil subgrade. Effect of class-F fly ash and uncontrolled burnt Rice Husk Ash (RHA) on permeability of CL and CL-ML (USCS) soil stabilizers is discussed in the ensuing paragraphs.

Selvig & Gibson (1956) carried out experimentations with more than 600 fly ash samples in United States. They found that coal ash was composed of Silica (SiO_2), ferric oxides (Fe_2O_3), alumina (Al_2O_3) and small quantities of calcium oxide (CaO), potassium oxide (K_2O) and sodium oxide (Na_2O). Diamond (1985) examined the chemical and mineralogical compositions of class-F fly ash obtained from bituminous coal and concluded that this type of fly ash has very consistent contents of ($SiO_2 + Fe_2O_3 + Al_2O_3$) (typically more than 90%).

Pandian (2004) and Santos Fabio et al. (2011) studied permeability and various other geotechnical properties of fly ash. The study reported that fly ash has good potential for use in subbase and embankment works. Muhardi et al. (2010) carried out permeability studies with class-F fly ash and reported that permeability of soil stabilized with fly ash depends on grain size and pozolonic activity of fly ash.

Experimental studies carried out by Roy, T.K. & Chattopadhyay, B.C. (2008) with pond ash and fly ash indicated significant improvements in index properties and CBR of alluvial soils. Musa Alhassan & Alhaji Mohamad Mustafa (2007) studied effect of soil stabilization performance with Laterite soils (A-7-decrease 6). The study reported decrease in MDD and increase in optimum moisture content of lateritic soil. Investigations on CBR and UCS of these soils have shown considerable increase in CBR and UCS property of soil. Gidde & Jivani (2007) have shown the potential of utilization of RHA for various geotechnical purposes. Yulianto & Mochtar (2010) have used RHA and lime for peat soil stabilization. The stabilization with RHA and lime has good improvement in physical and engineering behaviour of peat soil.

Present study mainly aims at modifying the permeability of CL and CL-ML soil subgrade (USCS) using class-F fly ash and uncontrolled burnt RHA. Experimental investigations have been performed to assess the permeability behaviour of stabilized soil. Correlations with respect to voids ratio and degree of saturation during the permeability measurement have also been reported. Permeability of stabilized soil has been determined by variable head method in the laboratory with standard compaction. The study was carried out in the Highway Research laboratory at National Institute of Technical Teachers Training and Research, Chandigarh, India.

2 MATERIAL PROPERTIES

Subgrade soils samples collected from road construction sites near Chandigarh, India were categorized for the geotechnical properties. Fly ash (class-F) was collected from the Guru Gobind Singh Thermal Power Plant (GGSTPP) Ropar, Punjab. Uncontrolled burnt RHA was brought from Punjab Chemicals and Crop Protection Limited (PCCPL) Industries, Derabassi, near Chandigarh. Geotechnical properties of subgrade soils, fly ash and RHA have been listed in Table 1. Chemical composition of GGS Thermal Power Plant fly ash from Ropar, Punjab and uncontrolled burnt RHA from Derabassi near Chandigarh India are highlighted in Table 2.

Table 1. Geotechnical properties of soils, fly ash and RHA.

Property	CL soil	CL-ML soil	Fly ash	RHA
Liquid Limit %	26.38	23.17	42.18	163.31
Plastic Limit %	15.61	17.51	NP	NP
Plasticity Index	10.77	5.66	NP	NP
OMC (Standard Proctor)	13.1	11.02	17	67.45
MDD (Standard Proctor)	1.91	1.98	1.31	0.69
Permeability (cm/sec)	4.34×10^{-8}	9.90×10^{-8}	2.9×10^{-5}	3.69×10^{-4}
Unsoaked CBR %	11.28	11.44	26.28	7.29
Soaked CBR %	2.17	7.65	1.53	4.1

Table 2. Chemical composition of GGSTPP fly ash and uncontrolled burnt RHA.

Constituents	GGSTPP fly ash (Percent content)	RHA (Percent content)
SiO_2	60.53	86.01
Fe_2O_3	4.18	0.01
Al_2O_3	27.27	1.40
CaO	1.04	1.90
MgO	0.40	–
Loss on ignition	2.11	5.66

3 EXPERIMENTAL PROGRAMME

All experimental investigations have been carried out as per the relevant Indian standards. Compaction characteristics are obtained for standard proctor compaction. Variable head method was adopted for determination of permeability of stabilized soil. Fly ash was used in 10%, 20%, 30% and 40% proportions by dry weight of soil. RHA was mixed in proportions of 8%, 12%, 16% and 20% by dry weight of soil. Investigations are performed for fly ash and RHA independently and in combinations to determine the effect of blend on stabilization of subgrade soil. Permeability measurements were noted for average temperature during the measurement. Voids ratio and degree of saturation are noted for fully saturated soil sample during the permeability measurement.

4 RESULTS AND DISCUSSION

4.1 *Compaction characteristics of fly ash RHA stabilized soils*

Compaction characteristics of the soils under investigations have been established for performing the permeability tests using fly ash and RHA blends. It was observed that OMC of the soil increases with increase in fly ash and RHA content. Higher OMC of such stabilized soils was due to higher water retention of fly ash and RHA. The maximum dry density was reported to decrease with increase in percentages of both fly ash and RHA. The obvious reason for reduction in dry density could be the stabilization with light weight fly ash and RHA. Figure 1 and 2 shows respectively the effect of fly ash and RHA on optimum moisture content of CL and CL-ML soils. Figure 3 and 4 shows the variation in maximum dry density respectively for fly ash and RHA stabilization with CL and CL-ML soils.

4.2 *Voids ratio and degree of saturation*

Voids ratio and Degree of saturation of the soil has a direct effect on permeability of soil. Permeability of soil increases with increase in voids ratio and degree of saturation. Void ratio of CL and CL-ML soil increased with increase in percentage of fly ash and RHA. Figure 5 and 6 shows the variation in voids ratio of CL and CL-ML soil respectively with fly ash and RHA stabilization. Voids ratio and degree of saturation of the soil have been worked out when the soil is completely saturated during the permeability measurement. As both fly ash (CaO = 1.04) and RHA (CaO = 1.90) used for stabilization are non-cementitious, voids ratio of the stabilized soil shows perceptible increase.

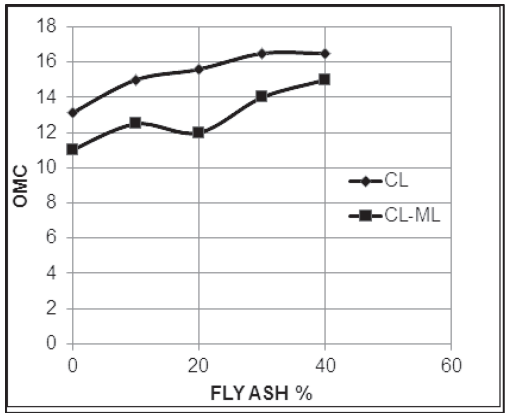

Figure 1. Effect of fly ash on OMC of CL and CL-ML soils.

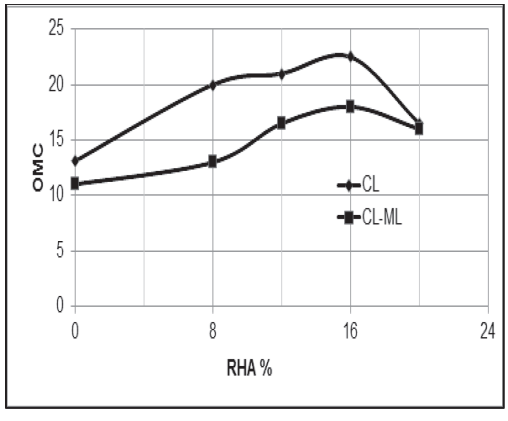

Figure 2. Effect of RHA on OMC of CL and CL-ML soils.

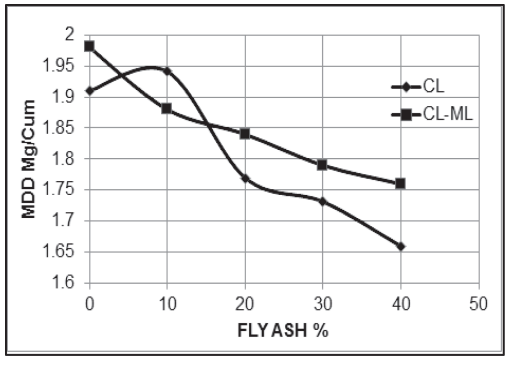

Figure 3. Effect of fly ash on MDD of CL and CL-ML soils.

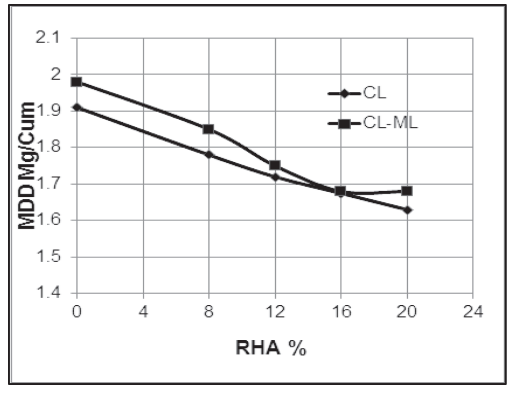

Figure 4. Effect of RHA on MDD of CL and CL-ML soils.

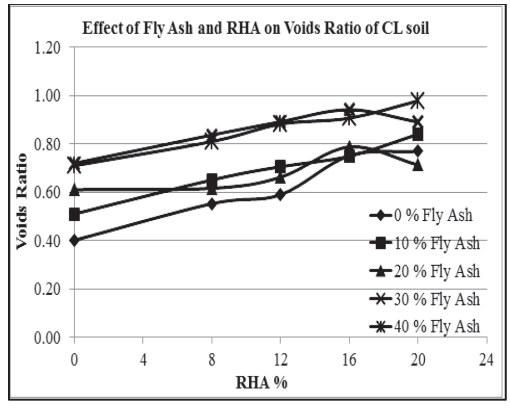

Figure 5. Effect of fly ash and RHA on voids ratio of CL soils.

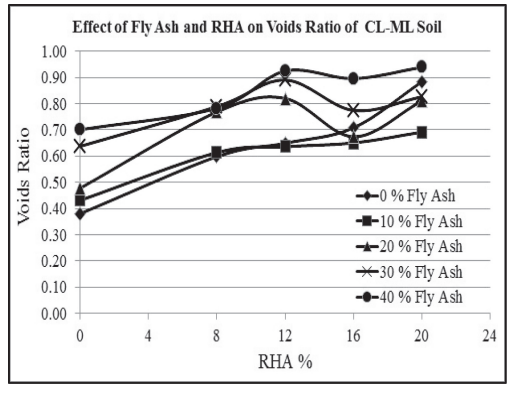

Figure 6. Effect of fly ash and RHA on voids ratio of CL-ML.

Degree of saturation of the soil has been observed to be increased for higher content of fly ash and RHA. The effect of fly ash and RHA blending on CL and CL-ML soil is shown in Figure 7 and 8 respectively.

4.3 *Permeability behaviour of fly ash, RHA stabilized soil*

Permeability modification of soil subgrade is important for easy drainage of roadway. Permeability of CL and CL-ML soil has shown marked improvement with stabilization using class-F fly ash and uncontrolled burnt RHA. Permeability of stabilised soil was measured after complete saturation of the soil sample. Samples were prepared at OMC and MDD values established for this study. Permeability measurements were carried out with varying head method. Permeability values were corrected for temperature correction. It was observed that permeability of CL and CL-ML soil increased with increase in fly ash and RHA content. Due to increased voids ratio and increased degree of saturation the permeability of the soil increased with fly ash and RHA stabilization. Permeability variation with respect to RHA for different fly ash contents is shown in Figure 9 and 10 for CL and CL-ML soil respectively. For both the soils under investigations permeability variation reported a good correlation for different RHA as well as fly ash contents.

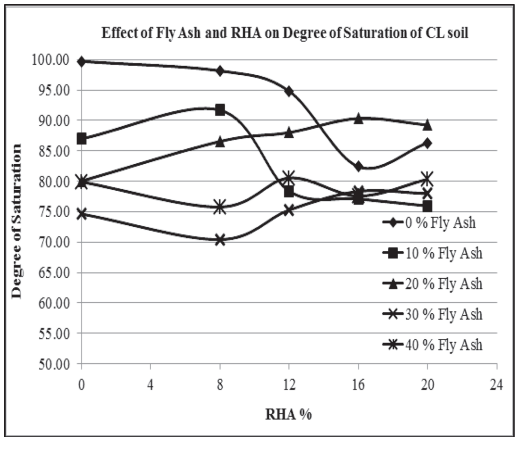

Figure 7. Effect of fly ash and RHA on degree of saturation of CL soil.

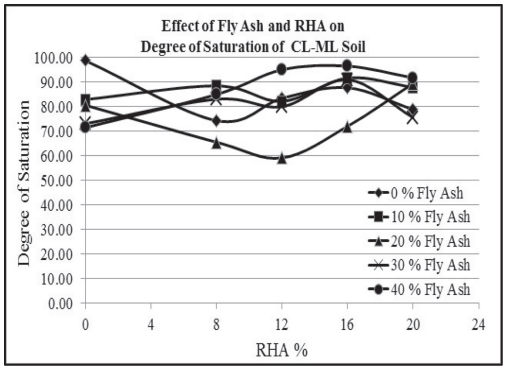

Figure 8. Effect of fly ash and RHA on degree of saturation of CL-ML soil.

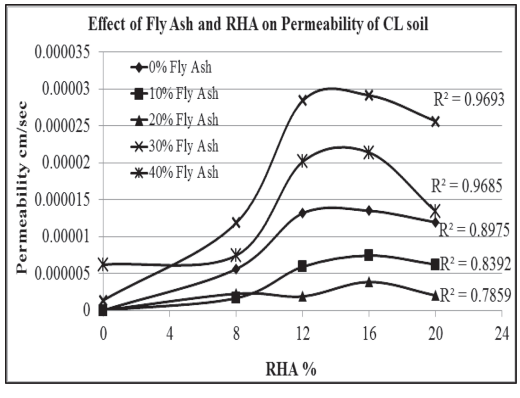

Figure 9. Effect of fly ash and RHA on permeability of CL soil.

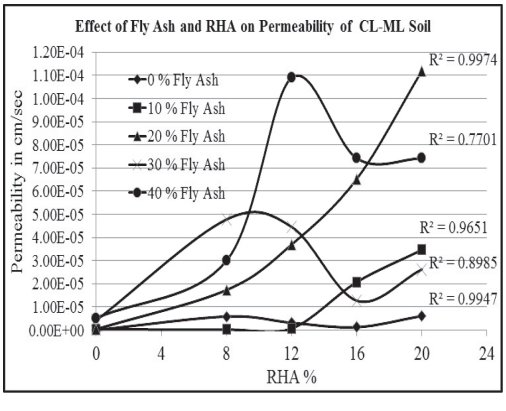

Figure 10. Effect of fly ash and RHA on permeability of CL-ML soil.

5 CONCLUSIONS

Following are the inferences drawn from the study.

- Class-F Fly ash and uncontrolled burnt Rice Husk Ash (RHA) can be used for improving the various index and geotechnical properties of subgrade soils.
- Optimum moisture content of the soil increases with increase in class-F fly ash and uncontrolled burnt RHA content for CL and CL-ML soils.
- Maximum Dry density of CL and CL-ML soil reduces with increased amount of class-F fly ash and uncontrolled burnt RHA.
- Voids ratio of the CL and CL-ML soil increases with increased content of class-F fly ash.
- Voids ratio of CL and CL-ML soil increases with increased percentage of uncontrolled burnt RHA.
- Degree of saturation of both CL and CL-ML soil increases at higher percentage of fly ash as well as RHA.
- Permeability of CL and CL-ML soil increased considerably with fly ash and RHA stabilization.
- Permeability of CL soil increased from 4.34×10^{-8} to 1.20×10^{-5} cm/sec at 30% fly ash and 12% RHA content.
- Permeability of CL-ML soil increased from 9.9×10^{-8} to 1.18×10^{-4} cm/sec with 40% fly ash and 12% RHA content.

REFERENCES

Alhassan, Musa & Mustafa, A.M. 2007. Effect of Rice Husk Ash on Cement Stabilized Laterite. *Leonardo Electronic Journal of Practices and Technology*, 6(11): 47–58.

Diamond, S. 1985. Selection and use of fly ash for highway concrete. *Report No. FHWA/IN/JHRP-85/8. Final Report. Purdue Univ.*, W Lafayette, Ind.

Gidde, M.R. & Jivani, A.P. 2007. Waste to wealth-Potential of Rice Husk Ash in India a Literature Review. *Proceedings of International Conference on Cleaner Technologies and Env. Management, Pondicherry, India*. 586–590.

Muhardi, Marto, A., Kassim, K.A., Makhtar, A.M., Lee Foo Wei & Yap Shih Lim. 2010. Engineering characteristic of Tanjung Bin Coal ash, *Electronic Journal of Geotechnical Engineering,* 15(K): 1117–1129.

Pandian, J. 2004. Fly ash characterization with reference to geotechnical applications, *Journal. of Indian Institute of Science, Banglore, India*. 84: 189–216.

Roy, T.K. & Chattopadhyay, B.C. 2008. A Study on the Effect of Cement on Alluvial Soil Strengthened With Pond and Rice Husk Ash for Construction of Road Subgrade, *The 12th International Conference of International Association for Computer Methods and Advances in Geomechanics (IACMAG), Goa, India*. 3508–3513.

Santos, Fabio. Lin, Li. Yadong, li & Farshad, Amini 2011. Geotechnical properties of Fly ash and soil mixture for use in highway embankment, *World of coal ash (WOCA) Conference, Denvar.* CO, USA.

Selvig, W.A. & Gibson, F.H. 1956. Analysis of ash from United States coals; Bulletin 567, Bureau of Mines.

Yulianto, Faisal, E. & Mochtar, Noor, E. 2010. Mixing of Rice Husk Ash (RHA) and Lime for Peat Stabilization, *Proceedings of the First Makassar International Conference on Civil and Engineering (MICCE2010)*.

This page intentionally left blank

Advances in Unsaturated Soils – Caicedo et al. (eds)
© 2013 Taylor & Francis Group, London, ISBN 978-0-415-62095-6

Capillary rise in pores with rough walls

L.E. Vallejo
Department of Civil and Environmental Engineering, University of Pittsburgh, Pittsburgh, USA

ABSTRACT: When a smooth circular tube of small diameter, d, is immersed in water, the water rises in the tube to a height of capillary rise, h, which can be calculated from: $h = (4T_s \cos \theta)/(\gamma_w d)$. In this equation, T_s is the surface tension of the water, θ is the contact angle, and γ_w is the unit weight of the water. However, pores in soils and rocks are not circular nor smooth but rough. This study presents a method to calculate the height of capillary rise in tubes with rough walls. To obtain this height, capillary rise experiments using a wedge were employed. The wedge was formed by two flat surfaces meeting at a corner. The capillary rise depended upon the angle of the wedge and the distance from the corner of the wedge. These findings were used to interpret the way water flows in the pores of shales.

1 INRODUCTION

When a smooth circular tube of small diameter, d, is immersed in a container with water, the water rises in the tube to a height called the height of capillary rise, h (Fig. 1). The height of capillary rise, h, is easily calculated and is equal to: $h = 4T_s \cos \theta/\gamma_w d$. In this equation, T_s is the surface tension of the water, θ is the contact angle, and γ_w is the unit weight of the water. However, pores in soils and rocks are not circular nor smooth but rough. The present study presents a method to calculate the height of capillary rise in tubes with rough walls. The implications of the results of this study are extended to analyze the slaking of shales.

2 CAPILLARY RISE IN ROUGH TUBES

The pore system in soils and rocks have boundaries that are rough and do not resemble the smooth circular profile of the tube shown in Fig. 1. An example of how the boundaries of the pores in a sample of shale from Tennessee looks like is shown in Fig. 2. This figure shows that the profiles of the pores in the shale are made of jagged irregularities of different dimensions and aperture angles. Little is known about how these irregularities of the pore profiles influence the movement of water as a result of capillarity forces and how these forces influence the slaking of shales.

2.1 *The influence of pore roughness on capillary rise*

According to Ransohoff and Radke (1988) when a capillary tube with either square or triangular cross section as shown in Fig. 3 is immersed in water, the water advance in the capillary tube up to a distance h, after which the water advances to very

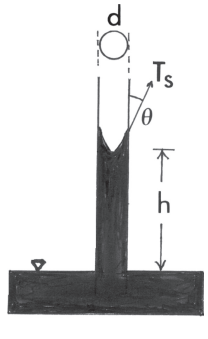

Figure 1. Capillary rise in a smooth circular tube of diameter d.

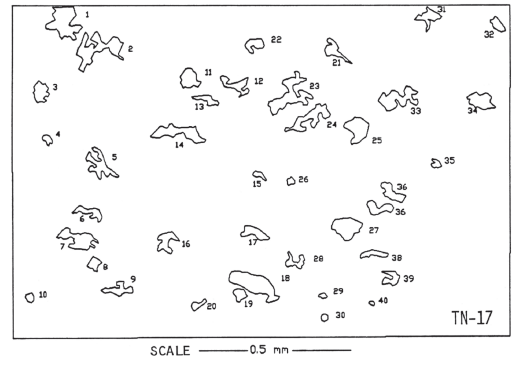

Figure 2. Pore profiles in a shale sample from Tennessee (TN-17, average pore diameter = 0.056 mm).

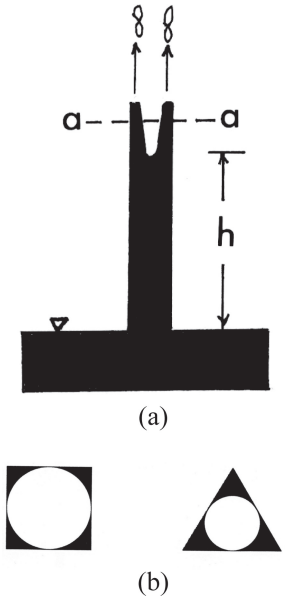

Figure 3. (a) Capillary rise in a tube with either a square or triangular cross sectional area, (b) Water location in the square or triangular tube on a section a-a in Fig. 3(a).

large distances following the corners of the tube. The distance h can be obtained from: $h = 4Ts/\gamma_w d$, where d is the radius of the inscribed circle in the square or triangular areas (Fig. 3).

In order to explain why the water reaches very large distances in the corners of the tube, a laboratory investigation developed by Greenslade (1992) is presented next. Greenslade (1992) conducted a laboratory experiment that consisted in immersing in water a wedge made of two glass plates as shown in Fig. 4. The angle of the wedge formed by the two glass plates was varied in the experiments. According to Greensdale, the water meniscus in the wedge formed a curve (Fig. 4). The height of the curve reached a maximum value at the corner of the wedge and decreased in height as the meniscus moved away from the corner of the wedge. The height of the capillary rise between the glass plates depended of the angle between the plates.

In order to explain the shape of the capillary rise in the wedge shown in Fig. 5 the following analysis is presented. Fig. 5 shows a wedge with an opening angle equal to α. Let's assume the area ABO is filled with capillary water. The height of the capillary water in the wedge in each of the inscribed circular tubes of varying diameter d in Fig. 5 can be obtained from the following relationship,

$$h = (4T_s \cos \theta)/\gamma_w d \quad (1)$$

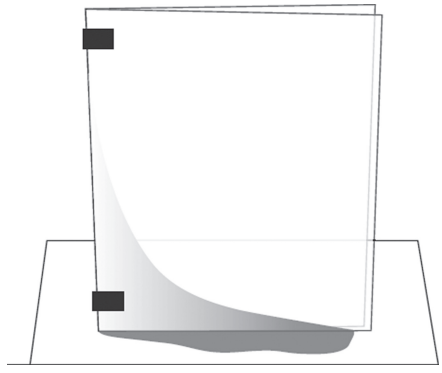

Figure 4. Capillary rise in a wedge formed by two glass plates (after Greenslade, 1992).

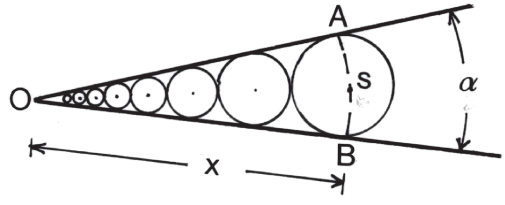

Figure 5. A wedge with inscribed circles of decreasing diameters and filled with capillary water.

The arch s in Fig. 5 is approximately equal to the diameter of the circles tangent to the sides of the wedge, and can be obtained from,

$$s \approx d = \alpha x \quad (2)$$

After replacing the value of the variable d (diameter of circles) given by Eq. (2) into Eq. (1), we obtain,

$$h = (4T_s \cos \theta)/(\gamma_w \alpha x) \quad (3)$$

If one analyzes Eq. 3, it is determined that the value of h in the cylindrical tubes between the two glass plates shown in Fig. 4 depends of α and x (Fig. 5). The value of h in the cylinder located in the corner of the wedge reaches extremely high values because either α or x have very small values. In fact, as the value of α or x tends to a zero value, the value of h tends to an infinite value as shown in Fig. 3(a).

3 IMPLICATIONS OF THE PREVIOUS RESULTS ON THE SLAKING OF SHALES

3.1 *Slaking of shales by pore air compression*

There are different mechanisms discussed in the geotechnical literature which explain the slaking

of shales when immersed in water (Surendra et al., 1991; Vallejo, 2011). One slaking phenomenon is attributed to the compression of entrapped air in the pores of the shales when water enters them as a result of capillary suction (Terzaghi and Peck, 1968). This entrapped air in the pores exerts tension on the solid skeleton, causing the material to fail in tension. According to Moriwakii (1974), pore-air compression is the predominant slaking mechanism in shales composed primarily made of kaolinite.

The mechanism for pore-air compression that breaks the shales was first presented by Vallejo (2011) and is shown in Fig. 6. Fig. 6 shows a shale sample with a system of cylindrical macro-pores that run continuously through it [Fig 6(A)]. These macro-pores which are assumed to be not connected, resemble small cylindrical tubes inside the shale.

When the sample is immersed in water, water will be pulled into the individual macro-pores as a result of capillary forces, and the air that originally filled the macro-pores will be subjected to compression [Fig 6(B)]. The system of forces acting at the interface between the air and the water in a macro-pore are presented in Fig. 6(C). At equilibrium conditions the following relationship applies:

$$\pi d T_s - p(\pi d^2)/4 + u(\pi d^2)/4 = 0 \quad (4)$$

where d is the diameter of the cylindrical macropore, T_s is the surface tension of water acting on the meniscus, p is the air pressure, and u is the pore water pressure at the level of the macropore.

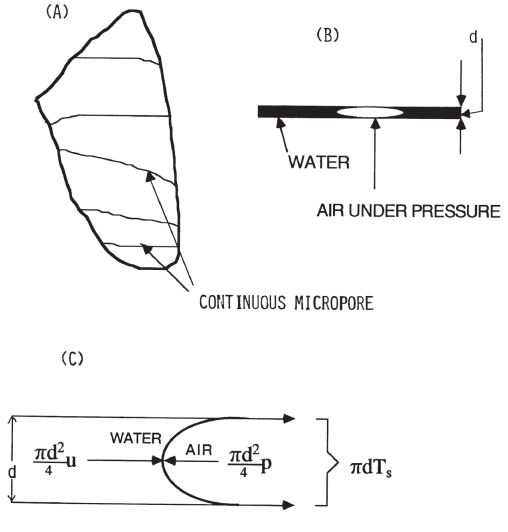

Figure 6. Forces acting in a macro-pore in a shale sample.

From, Eq. (4), the following relationship can be obtained:

$$p = u + (4T_s)/d \quad (5)$$

An analysis of Eq. (5) indicates that the pore air pressure, p, in the portion of the macro-pore filled with air [Fig. 6(B)] increases as the diameter, d, of the cylindrical macro-pore decreases. Thus, the smaller the diameter of the macro-pore, the larger is the pore air pressure, p. Since pore-air compression is favored by small pore radii, slaking of the shales by air compression will be more pronounced in those shales containing macro-pores with small diameters. In addition, small diameter macro-pores more readily confine the air pressure developed during the suction process. That is, the diffusion of the air pressure will decrease with a decrease in surface area (which is a function of the diameter of the macro-pore) of the pore that is in contact with the air. Thus, the diameter of the macro-pores in shales has a marked influence on their slaking with water.

3.2 *Diameter of pores and the slaking of shales*

To check the validity of Eq. (2), sixty eight shale samples (containing large portions of kaolinite) from Appalachia were tested for their durability when immersed in water. Dry pieces of the shales were immersed for 24 hours in a cylindrical container with water (soak test). At the end of the 24 hour period, the shales were examined with respect to their durability. Fourteen samples had degraded into soil, and fifty four of the samples remained unchanged (Figs. 7 and 8). In order to determine the size of the pores of the samples that degraded into soils and the size of the pores in the samples that experienced no change, thin section analysis of the shale samples was carried out.

Photographs of the thin sections were made using a polarizing microscope. From the photographs, the cross sectional areas and shapes of the perimeters of the pores in the shales were obtained. Using standard digitizing procedures, the profiles of the pores were obtained from the photographs of the thin sections. Fig. 9 shows the typical results of the process for the case of shales TN-5 and TN-9 (Figures 7 and 8).

The average diameter of the pores of the TN-5 sample was equal to 0.053 mm. The average diameter of the pores of TN-9 sample was equal to 0.107 mm. Thus, according to Eq. (2), the size of the pores has an influence on the slaking of shales. Shales with smaller pores slake as a result of the pore air compression mechanism (Figs. 7 and 9).

Of the sixty eight shale samples tested, fourteen samples slaked into soils and had average diameters

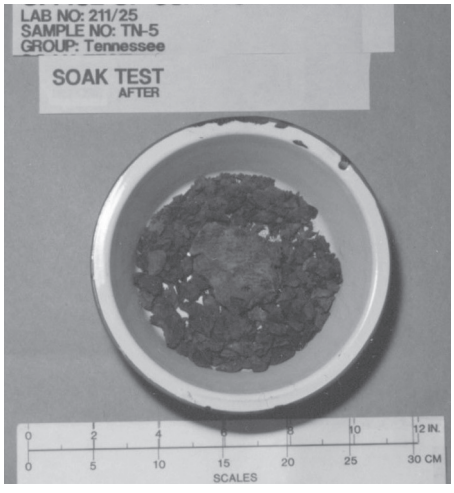

Figure 7. Shale sample TN-5 after the soak test. The sample degraded into soil.

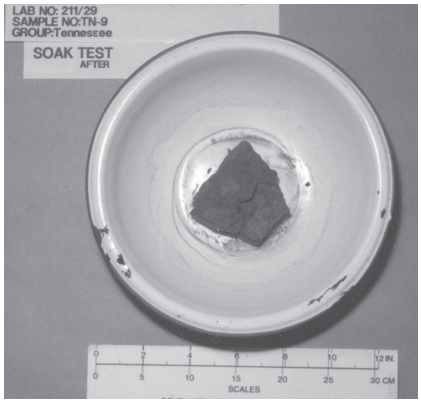

Figure 8. Shale sample TN-9 after the soak test. The sample remained unchanged.

that were equal or smaller that 0.06 mm. Fifty four samples did not slake. Of these fifty four samples, forty six samples had pores with diameters greater than 0.06 mm, however, eight shale samples had pores with diameters that were smaller than 0.06 mm and did not slake. An example of this type of shale samples is TN-17 given in Fig. 2 that had an average diameter equal to 0.056 mm. What cause the eight shale samples with an average diameter smaller than 0.06 mm not to slake? The answer seems to be related to the degree of roughness of their pore profiles. The degree of roughness of the eight profiles that did not slake was measured using the fractal dimension concept from fractal theory.

3.3 *Measurement of pore roughness in the shales*

The roughness of the pore boundaries was evaluated using fractal theory. Fractal theory makes use of a number called the fractal dimension, D, to evaluate the degree of irregularity of objects in nature (Mandelbrot, 1977). In this study the fractal dimension was used to measure to measure the degree of roughness of the pore boundaries of the eight shale samples with pore diameters less than 0.06 mm that did not slake as well as the pore boundaries of samples TN-5 and TN-9 (Fig. 9). The fractal dimension of the pore boundaries were calculated using the area-perimeter method (Korvin, 1992; Hyslip and Vallejo, 1997). The fractal dimension, D, is obtained from the slope, m, of the best fit line that connects the values of the area and perimeter for each of the pores in a shale sample (Fig. 9). Fig. 10 shows this plot for the samples TN-5 and TN-9.

Once the slope, m, is obtained, the dimension is calculated from the ratio between 2 and m (that is D = 2/m). The fractal dimension, D, measures the average roughness of the pore boundaries in the shale samples. The higher the value of D, the rougher are the pore boundaries in the shales.

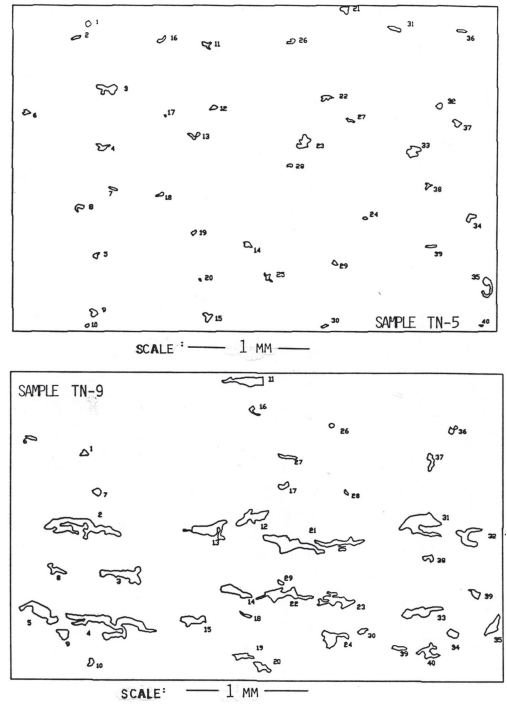

Figure 9. Pore geometry of samples TN-5 (average diameter = 0.053 mm) and TN-9 (average diameter = 0.107 mm).

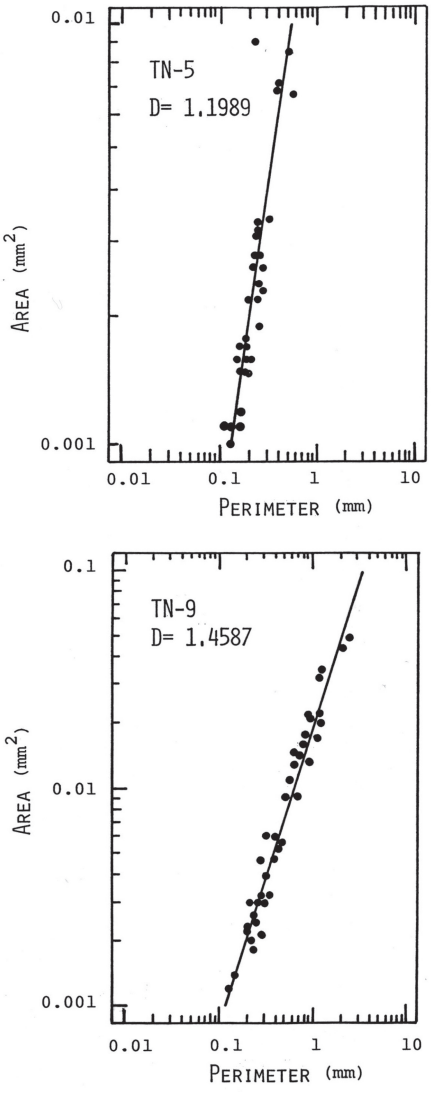

Figure 10. Area-perimeter method to obtain fractal dimension values for samples TN-5 and TN-9.

The fractal dimension, D, for the pore boundaries of sample TN-5 was equal to 1.1989. D for sample TN-9 was equal to 1.4587 (Figures 9 and 10).

Even though the size of the pores in shales is a good indicator for the slaking susceptibility, it was not a parameter that indicated without a doubt the slaking behavior of shales. Table 1 shows the results of the jar slake tests and the fractal analysis on the 8 samples that did not slake even though the average size of their pores was less than 0.06 mm. The fractal analysis for these shales indicated that their pore walls were very rough (Fig. 2). These high degree of roughness of the pore walls is reflected on the high values of the fractal dimension for the pore perimeters. An explanation for the lack of slaking of the shales of Table 1 that have small (pore diameters < 0.06 mm) but rough pores (D > 1.4) seems to rest on the degree of roughness of the pore boundaries (Fig. 2).

Table 1. Properties of the eight shale samples that did not slake.

Sample	Pore diameter, mm	Fractal dimension, D
TN-7	0.056	1.7767
TN-16	0.045	1.4246
TN-17	0.056	1.4762
KY-19	0.052	1.4907
KY-22	0.051	1.4900
KY-32	0.055	1.6020
WV-8	0.052	1.5473
WV-14	0.051	1.4406

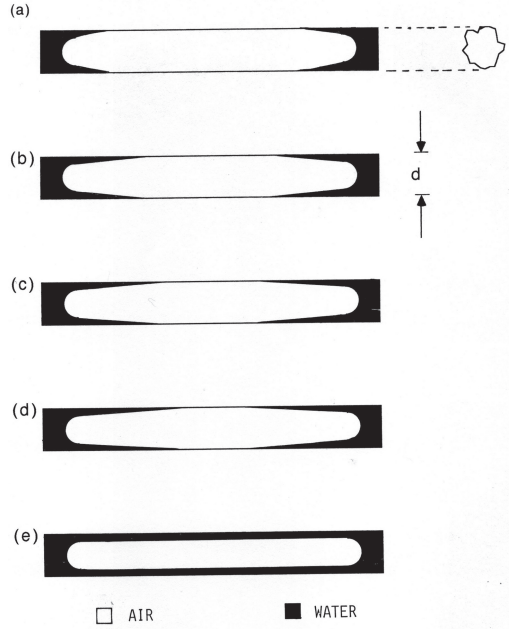

Figure 11. Advancement of water in a rough macropore. No pore air compression develops.

3.4 *Influence of the degree of roughness of the pore profiles on the slaking of shales*

According to Ransohoff and Radke (1988) when a capillary tube with either square or triangular cross section as shown in Fig. 3 is immersed in

water, the water does not completely advance in the capillary tube following the whole cross sectional area, but advances to large distances in the tube following the corners and crannies of the tube. This partial filling of the tube cross sectional area will prevent the development of air pressure that is necessary to cause the slaking of the shales [Fig. 6(B)]. Fig. 11 shows how water will advance in a rough pore such as that shown in Fig. 2. The water at the extreme portions of the macro-pore will cover its whole cross sectional area, however, after a short distance from the ends of the macro-pore, the water will follow the corners and crannies of the pore walls (Figs. 2 and 11). This movement of the water through the corners and crannies of the pore walls will prevent the development of the air pressure that is required to cause the breakage of the shale [Fig. 6(B), Eq. (2)]. Thus, the roughness of the boundaries of the pores (measured by the fractal dimension) has a significant influence on the slaking of the shales and needs to be considered in any evaluation of the durability of shales in water.

4 CONCLUSIONS

The capillary rise of water in tubes with small diameter but having rough profiles have been analyzed. The implication of the way water rises in rough tubes on the slaking of shales has also been investigated. From this study the following conclusions can be made:

1. The degree of roughness of the boundaries in capillary tubes influences the way capillary water advance in the tubes. The standard capillary rise uses the diameter of the inscribed circle in the rough cross sectional area. After which, the water moves large distances through the irregular sections of the tube.
2. The slaking of the shales studied was the result of pore air compression.
3. The slaking by pore air compression was directly related to the average pore diameter and the roughness of the pore boundaries. The smaller the diameter and the smoother the boundaries of the pores, the more pronounced was the slaking of the shales by air compression.
4. The roughness of the pore boundaries in the shales was determined using the fractal dimension concept from fractal theory. The larger the fractal dimension, the rougher were the boundaries of the pores.
5. Regardless of the diameter of the pores, shales with very rough pores did not slaked as a result of pore air compression. These rough pores moved the capillary water through their corners and crannies. Thus, the water did not move through the whole cross sectional area of the rough pores. This type of water movement prevented the development of pore air compression that is needed for the breaking of the shales.

REFERENCES

Greenslade, T.B. 1992. Capillary phenomenon. The Physics Teacher, 30: 300–301.

Hyslip, J.P. & Vallejo, L.E. 1997. Fractal analysis of the roughness and size distribution of granular materials. Engineering Geology, 48(3,4): 231–244.

Korvin, G. 1992. Fractal Models in the Earth Sciences. Elsevier, Amsterdam.

Mandelbrot, B.B. 1977. Fractals: Form, Chance and Dimension. W.H. Freeman, San Francisco.

Moriwaki, Y. 1974. Causes of Slaking of Argillaceous Materials. Ph.D. Dissertation, Dept. of Civil Engineering, University of California at Berkeley.

Ransoff, T.C. & Radke, C.J. 1988. Laminar flow of a wetting liquid along corners of predominantly gas occupied non- cicular pores. Journal of Colloidal and Interface Sciences, 121(2): 391–401.

Surendra, M., Lovell, C.W. & Wood, L.E. 1981. Laboratory studies of the stabilization of non-durable shales. Transportation Research Record, 79: 33–40.

Terzaghi, K. & Peck, R.B. 1968. Soil Mechanics in Engineering Practice. John Wiley & Sons, New York.

Vallejo, L.E. 2011. Mechanics of the slaking of shales. Geomechanics and Engineeing, 3(3): 219–231.

Volumetric and elastic behavior

This page intentionally left blank

Advances in Unsaturated Soils – Caicedo et al. (eds)
© 2013 Taylor & Francis Group, London, ISBN 978-0-415-62095-6

Multi-dimensional swelling behavior of Al-Qatif expansive soils

M.F. Abbas, T.Y. Elkady & M.A. Al-Shamrani
King Saud University, Saudi Arabia

ABSTRACT: Volume change behavior of expansive soil is typically studied in the laboratory environment under one-dimensional conditions. In the field, expansive soils may undergo different swelling behavior due to different stress conditions. Attention, therefore, should be focused on the real behavior of expansive soil in a multi-dimensional stress conditions. The objective of this study is to investigate the swelling behavior of expansive soils under triaxial loading conditions. The testing program investigated the effect of stress ratio (K) on expansive soil behavior. Monitored parameters included axial swell strain and total volume changes. The ratio of axial swell strain to volumetric swell strain (Swell Ratio, SR) was assessed and the influence of test conditions on this ratio was highlighted. Finally, test results were compared with that obtained from one-dimensional swelling tests. This information is useful in the estimation of more realistic volume changes in expansive soils given that stress conditions are known.

1 INTRODUCTION

Extensive areas throughout the world, mainly in arid and semi-arid regions, experience foundation problems caused by expansive clays. Geotechnical investigation has shown that the causes of the problem are attributed to significant volume changes. The swelling characteristics of such soils are considered important design parameters for designing several structures such as pavements, shallow foundations, shallow tunnels, retaining walls, canal linings and underground conduits. Discrepancies were observed between swelling characteristics obtained from laboratory tests and that observed in the field. This was attributed to differences in stress conditions and degree of wetting between field and laboratory (El Sayed & Rabbaa 1986, Dhowian 1990, Al-Shamrani & Al-Mhaidib 1995).

This motivated researchers to evaluate heave and swelling pressure of expansive soils under stress states conditions identical to that existing in the field. This will minimize the negative effects of unrealistic estimation for these parameters, either from the safety or economical point of views. Several researchers studied the multi-dimensional volume change using triaxial testing under isotropic conditions (Dakshanamurty 1979, Tisot & Aboushook 1983, Al Shamrani & Al Mhaidib 1995, 1999, and Al Shamrani & Dhowian 2003). Few researchers examined the volume change of expansive soils under anisotropic conditions (Dakshanamurty 1979, Tisot & Aboushook 1983, Jotisankasa 2005, Jotisankasa et al., 2007 and Chen & Ng 2005) in attempt to replicate field conditions. Dakshanamurty (1979) showed that the volumetric strain depends on the mean stress. Tisot & Aboushook (1983) mentioned that the prediction of heave may be improved by applying anisotropic stress during triaxial testing. However, the test duration makes the triaxial testing useless.

Some researchers proposed corrections to oedometer heave to account for different stress conditions. Dhowian et al. (1990), Erol (1987) and Al-Shamrani & Dhowian (2003) reported that this correction, based on field tests, was in the order of one-third.

Al-Shamrani (2004) reported that the ratio of triaxial ultimate vertical swell—under isotropic conditions—to that obtained from oedometer varied between one-third and two-third. This ratio increased with applied load and decreased with increase in initial moisture content and dry unit weight. Furthermore, Al-Shamrani (2004) noted that the swell ratio, SR, defined as the ratio of vertical swell to the volumetric swell, increased with the application of confining pressure with an average value of 0.57.

This research aims at examining the volume change behavior of expansive soil under different stress states using triaxial testing. A comparative study between the volume change behavior predicted from triaxial and one-dimensional loading conditions was performed. The swell ratio, SR, was assessed and the influence of test conditions on this ratio was demonstrated. Moreover, the heave reduction factor, R_f, was obtained and related to the applied stress conditions.

Table 1. Physical properties of Al–Qatif soil.

Physical property	Value
Specific gravity	2.71
Liquid limit (%)	140
Plastic limit (%)	60
Shrinkage limit (%)	20
Plasticity index (%)	80
% Finer than 200 μm	99
USCS classification	CH

2 TESTED MATERIAL

Soil used for this study were obtained from the city of Al-Qatif located in the eastern province of Saudi Arabia (latitude 26° 56' N and longitude 50° 01' E). Al-Qatif expansive clay is considered highly expansive in nature. Soil samples were obtained from a test pit at a depth of about three meters below ground surface. Laboratory testing including routine classification and physical property tests were conducted. The physical properties of Al-Qatif clay used in the present study are provided in Table 1.

3 SAMPLE PREPARATION

In order to minimize variations in test results, remolded samples were used in the testing program. Disturbed samples obtained from the field were air dried, pulverized and screened through sieve No. 40. Individual samples were thoroughly mixed with distilled water at optimum moisture content (32%) and stored in air-tight plastic bags for not less than 24 hours to allow for uniform distribution of moisture content. Finally, samples were statically compacted to maximum dry density (12.0 kN/m^3) and the corresponding moisture content. It should be mentioned that the sample dimensions for both oedometer and triaxial testing were 20.0 mm height and 50.0 mm diameter.

4 EXPERIMENTAL PROGRAM

The volume change behavior of expansive soil was investigated for samples under various stress ratios and boundary conditions. Stress ratio applied on test samples were 0.5, 1.0, and 1.5. Boundary conditions considered include complete lateral restrained condition (oedometer test) and controlled lateral restrained condition (triaxial test). A description of testing performed is as follows.

4.1 *Oedometer testing (at rest conditions)*

Testing was performed to evaluate the swelling characteristics (axial swell strain and swelling pressure) of expansive clay under complete lateral restraint (at rest conditions). Testing was performed in accordance with ASTM D4546 test methods. Tests performed included the following:

- *Method A* (*O_A*): the swell potential was evaluated under vertical stress of 1.0 kPa. After full swell was attained, vertical stress was incrementally increased. The pressure that returns the sample back to its original state (i.e., void ratio or height) is defined as swell pressure.
- *Method B* (*O_B*): the swell potential under target vertical stresses (40 kPa) was estimated. In addition, the swelling pressure corresponding to the pressure that returns the sample back to its initial volume was obtained.
- *Method C* (*O_C*): this method was used to evaluate the swelling pressure corresponding to the pressure that prevents sample from swelling.

4.2 *Triaxial testing (isotropic and anisotropic conditions)*

A series of triaxial tests were performed to characterize the swelling behavior of expansive soil under different boundary (partial lateral restraint) and stress conditions (isotropic and anisotropic). Testing was performed using GDS stress path triaxial device. Cell and back-pressures were applied using computer controlled pressure volume controllers (PVC). Volume change measurements were performed using the double cell technique and PVC while axial deformation was measured using LVDT connected to the loading ram. Two variations of bottom pedestal were considered to investigate their effect on the swell duration as described in Section 5.

In these tests, as-compacted samples were initially subjected to a total axial stress (σ_1) of 50 kPa with a confining pressure corresponding to stress ratios ($K = \sigma_3/\sigma_1$) of 0.5, 1.0 and 1.5. Samples were allowed to equilibrate under target stress conditions until no volume change was recorded. Secondly, samples were inundated from the drainage port in the top cap and by applying a backpressure of 10 kPa. During sample inundation, two types of tests were performed as described below:

- *Constant confining pressures tests* (*TR_CP*): samples were permitted to swell in both axial and lateral directions under target stress ratio. Axial and volumetric swell were recorded until full swell was attained.
- *Constant volume tests* (*TR_CV*): For this test, both the axial loading ram and PVC ram were

restrained from movement. Axial and lateral swell pressures were evaluated as increase in deviator and radial stresses. A summary of conditions for each test are presented in Table 2.

5 RESULTS AND ANALYSIS

The results of the experimental program were analyzed with respect to the swell behavior after inundation and the swelling pressure. The difference in swell behavior of expansive clay under both one-dimensional and multi-dimensional conditions was illustrated. Summary of the test results are presented in Table 2.

5.1 *Swell potential*

The axial swell strain estimated using oedometer test for different procedures (method A, B, and C) are shown in Figure 1. It should be noted that the axial swell strain from method C was estimated from the rebound slope, c_r (ASTM D 4546). It is observed from Figure 1 that, for the same axial stress of 40 kPa, free swell test (*O_A*) provides the highest axial swell strain. This indicates that axial swell strain is stress path dependent. This behavior has been reported by several researchers (e.g., Erol et al., 1987, Dhowian et al., 1990).

The axial swell strain obtained under *TR_CP* test conditions are illustrated in Figure 2 and summarized in Table 2. From these tests, it is apparent

Table 2. Summary of the experimental program.

Sample ID	Water content (%)		K	σ_1 (kPa)	Swell strain (%)		Swelling pressure (kPa)
	Initial	Final			Axial	Vol.	
O_A	30.5	55.9	K_o	1	30.0	30.0	460
O_B	30.5	56.9	K_o	40	16.8	16.8	470
O_C	31.8	41.8	K_o	40	N.A.	N.A.	300
TR_CP_1	32.0	54.6	1.0	50	9.7	14.6	335
TR_CP_2	32.1	66.0	1.0	50	9.1	13.6	–
TR_CP_3	31.3	68.7	1.0	50	8.8	14.8	–
TR_CP_4	31.9	55.5	0.5	50	6.5	12.0	–
TR_CP_5	31.4	67.2	1.5	50	13.7	19.5	–
TR_CP_6	31.6	69.5	1.5	50	14.9	18.7	–
TR_CP_7	31.8	51.4	1.5	50	14.2	18.5	–
TR_CP_8	32.4	70.8	1.0	50	8.3	13.3	–
TR_CP_9	31.7	60.9	0.7	72	7.5	13.1	–
TR_CV	31.2	–	1.0	50	N.A.	N.A.	240

Note: *O* refers to the oedometer testing and *TR* refers to the triaxial testing. The numbers in the abbreviation refer to the number of the test.

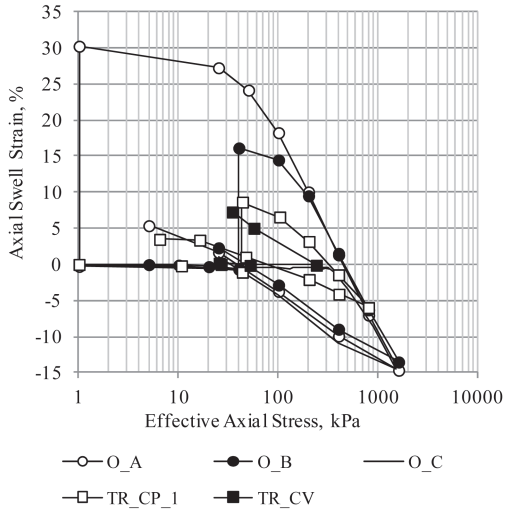

Figure 1. Different procedures to obtain the swelling potential and swelling pressure.

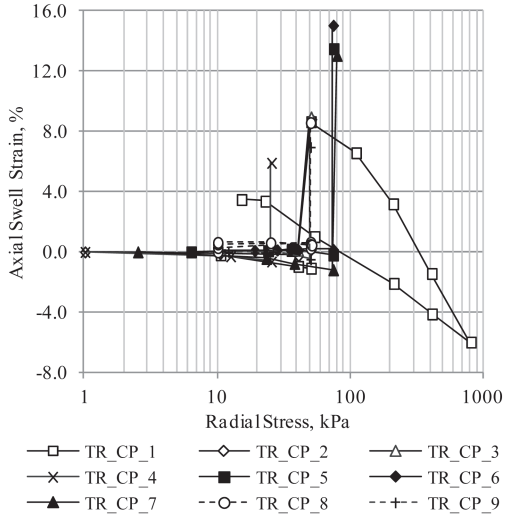

Figure 2. Effect of stress ratio on the axial swell strain obtained by triaxial testing.

that as the stress ratio increased (i.e., radial stress increased) the axial swell strain increased. This is attributed to increase in the level of lateral restraint as a result of radial stress increase.

A comparison between axial swell stain obtained using oedometer and triaxial isotropic test conditions (*TR_CP_1*) are provided in Figure 1. As shown in Figure 1, the axial swell strain predicted by triaxial testing is less than that obtained by oedometer (*O_A* and *O_B*) for the same vertical

stress. Similar observations were reported by (Al-Shamrani & Al-Mhaidib 1999). The same conclusion was arrived for triaxial test under other stress ratios considered in this study (see Table 2).

Moreover, the slopes of loading and unloading curves deduced from oedometer tests shown in Figure 1 were the same. On the other hand, the loading and unloading characteristics for triaxial testing showed a more stiff behavior.

A plot for the variation of axial swell strain and the stress ratio is illustrated in Figure 3. Based on test data, an exponential relationship was fitted between stress ratio, *K*, and axial swell strain as presented in Figure 3. This relationship can be used to estimate field axial swell potential provided that in-situ stress ratio can be assessed. It can be seen also that a stress ratio value of 1.73 should be applied in triaxial testing in order to obtain an axial swell strain equal to that obtained in oedometer. In other word, the estimated stress ratio in oedometer testing under a vertical stress of 40 kPa, similar to the vertical stress applied in triaxial is about 1.73.

A similar relationship between applied stress ratio and measured volumetric swell strain exists as shown Figure 4. From this figure, it could be inferred that the equivalent triaxial stress ratio yielding volumetric strain equal to that obtained from the oedometer test is about 1.3.

Curves for axial swell strain versus time for oedometer and *TR_CP* tests are depicted in Figure 5. For the sake of clarity, only one curve representative of each stress ratio was considered. As previously deduced, Figure 5 indicates that the axial swell strain increased with increase in stress ratio. Furthermore, it is apparent that the time to reach

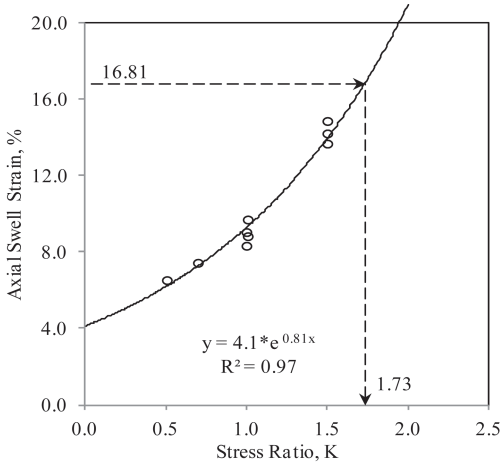

Figure 3. Relationship between the axial swell strain and stress ratio applied in triaxial testing.

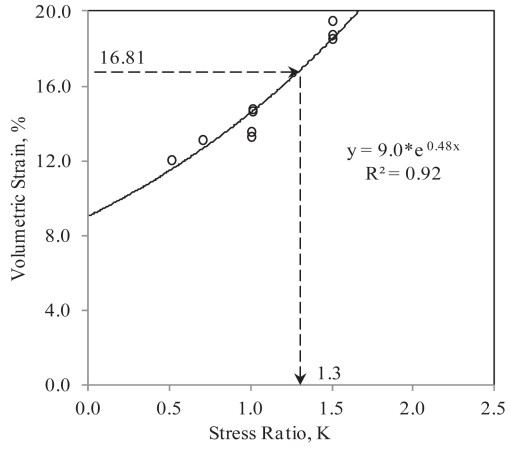

Figure 4. Relationship between the volumetric swell strain and stress ratio applied in triaxial testing.

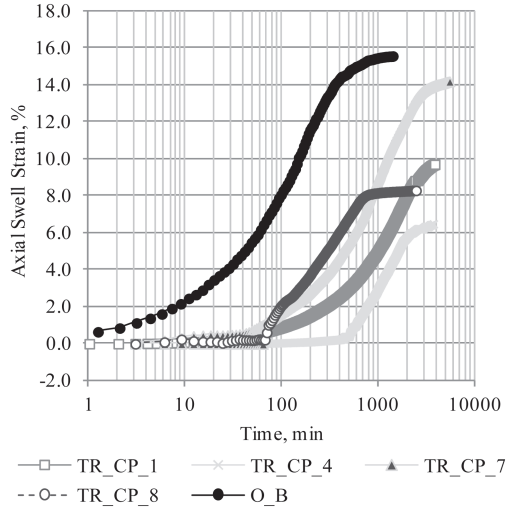

Figure 5. Time-swell strain for selected oedometer and triaxial test results.

full swell deduced from oedometer test is faster than that for triaxial test. This is attributed to differences in inundation procedures followed during oedometer and triaxial testing.

In oedometer tests, samples were soaked using free access of water while air in voids exited freely from the sample. The soaking conditions for triaxial tests were different. For *TR_CP_1* through *TR_CP_4*, tests, a ceramic disc with air entry value of 500 kPa was mounted on the bottom pedestal. For *TR_CP_5* through *TR_CP_9*, the bottom pedestal had a porous stone. For both cases, samples

were inundated by admitting water through the top drainage port and by applying backpressure from top drainage port. For both soaking cases, there is limited opportunity for air encountered in voids to drain out.

From Figure 5, it is apparent obvious that samples *TR_CP_1* and *TR_CP_4* have a slow response time compared to other triaxial tests. This can be explained by the presence of the ceramic disc. It is also shown from Figure 5 that the swell strain rate is independent of the stress ratio applied but depends on the permeability of the bottom pedestal drainage discs. Furthermore, the secondary swell in case of using ceramic disc is higher than that in case of using conventional porous stones (oedometer and triaxial).

5.2 *Swelling pressure*

Table 2 summarizes the swelling pressures deduced from different oedometer and triaxial tests. For oedometer testing, the swelling pressure deduced from *O_A* and *O_B* test procedures were approximately the same (460 and 470; respectively). However, swelling pressure deduced using *O_C* test showed a much lower value of 300 kPa. This trend was observed by many researchers and attributed to the difference of definition of swelling pressure.

Comparison of constant volume tests performed using oedometer (*O_C*) and triaxial (*TR_CV*) revealed that the swelling pressure deduced from the *TR_CV* was less than that deduced from *O_C*. This is attributed to the difference in boundary conditions acting on test samples. This highlights the importance of considering boundary conditions for the proper estimation of swell pressure.

Tests were performed to evaluate the effect of triaxial stress path on the magnitude of swelling pressure. Swelling pressure obtained from plots of volumetric strain versus mean stress ($(\sigma_1 + 2\sigma_3)/3$) for *TR_CP_1* and *TR_CV* are illustrated in Figure 6. Swelling pressure from *TR_CP_1* test is defined as the mean stress that returned the sample back to its initial volume. From Figure 6, it is observed that swell pressure deduced from *TR_CP_1* is nearly equal to that deduced from triaxial constant volume test (*TR_CV*) with values of 208 and 215 kPa; respectively.

5.3 *Heave reduction factor and swell ratio*

From triaxial test results, the heave reduction factor, R_f, was plotted versus stress ratio as shown in Figure 7. R_f is defined as ratio of the axial swell strain obtained from triaxial to that obtained from oedometer. Similar trend for the relationship between heave reduction factor and stress ratio

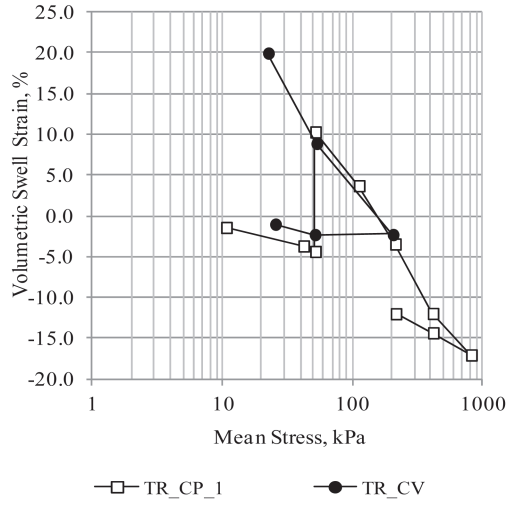

Figure 6. Obtaining the volumetric swelling mean stress.

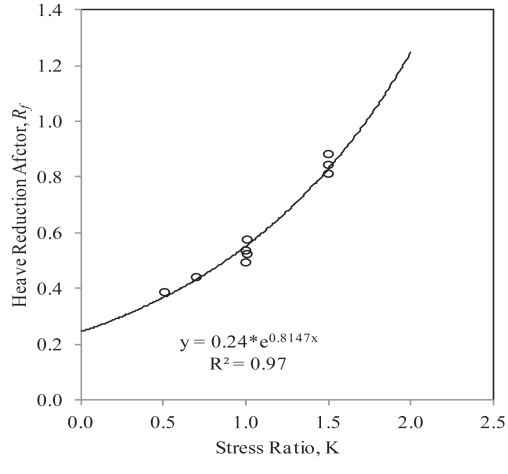

Figure 7. Heave reduction factor, R_f versus stress ratio, *K*.

was observed by McKeen (1992); however, with a linear relationship.

The swell ratio (*SR*) as defined by Al-Shamrani (2004) was calculated and plotted with respect to the stress ratio as shown in Figure 8. From Figure 8, the swell ratio exponentially increased with increase in stress ratio. Knowing the field stress ratio, axial swell strain and by performing a conventional oedometer test we can estimate the actual axial swell strain besides the volumetric swell strain by the aid of Figures 7–8.

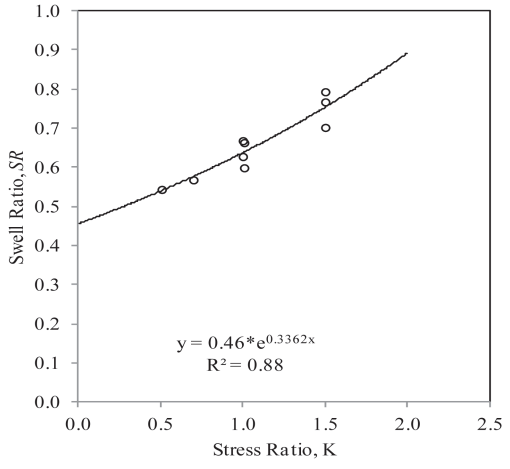

Figure 8. Relationship between swell ratio, *SR*, and stress ratio, *K*.

6 CONCLUSIONS

In order to explain the field swell behavior which differs from that predicted by using one-dimensional oedometer testing, an experimental study was performed and investigated the swell behavior under multi-dimensional loading conditions and different stress and boundary conditions. By comparing the oedometer methods for predicting the swell potential, it is noted that there is a discrepancy between the results which gives the importance of reviewing the field conditions before selecting the appropriated method for prediction the swell volume change.

The study has emphasized the effect of the stress ratio on the swelling behavior in seek of interpret the inconsistency between the field and laboratory results obtained by several researchers. Based on tests results compiled from this study, it is observed that each of the axial and volumetric swell strain, heave reduction factor and the swell ratio exponentially related to the stress ratio, *K*. Moreover, the study suggested a procedure for obtaining the swell potential in the field by conducting an oedometer test and knowing the field stress ratio, *K*.

ACKNOWLEDGEMENT

This research was supported by Eng. Abdullah Bugshan Research Chair in Expansive Soils, Civil Engineering Department, King Saud University.

REFERENCES

Abdullah, W.S. 2002. Bidimensional swell effect on accuracy of footing heave prediction. *Geotechnical Testing Journal*, 25(2): 177–186.

Al-Shamrani, M.A. & Al-Mhaidib, A.I. 1995. Multi-Dimensional Swell Behaviour of Expansive Shales. *Proc., 11th African Regional Conference on Soil Mechanics and Foundation Engineering, XI ARCS-MFE*, Cairo, Egypt, 1995: 161–174.

Al-Shamrani, M.A. & Al-Mhaidib, A.I. 1999. Prediction of Potential Vertical Swell of Expansive Soils Using a Triaxial Stress Path Cell. *The Quarterly Journal of Engineering Geology*, 32: 45–54.

Al-Shamrani, M.A. & Dhowian, A.W. 2003. Experimental Study of Lateral Restraint Effects on the Potential Heave of Expansive Soils. *Engineering Geology*, 69 (1–2): 63–81.

Al-Shamrani, M.A. 2004. Influence of Lateral Restraint on the Swelling Behavior of Expansive Soils. *Journal for Southeast Asian Geotechnical Society*, 35 (3): 101–111.

ASTM. D 4546-03. Standard Test Methods for One-Dimensional swell or settlement potential of cohesive soils. West Conshohocken, PA.

Chen, F.H. & Huang, D. 1987. Lateral expansion pressure on basement walls. *Proceedings of the 6th International Conference Expansive Soils*, New Delhi, 1: 55–59.

Dakshanamurthy, V. 1979. A stress-controlled study of swelling characteristics of compacted expansive clays. *Geotechnical Testing Journal*, 2 (1): 57–60.

Dhowian, A.W. 1990. Heave prediction techniques and design consideration on expansive soils, *Journal of King Saud University, Engineering Science*, 2: 355–377.

El-Sayed, S.T. & Rabbaa, S.A. 1986. Factors affecting behaviour of expansive soils in the laboratory and field—a review. *Geotechnical Engineering*, 17(1): 89–107.

Erol, A.O., Dhowian, & Youssef, A. 1987. Assesemnt of oedometer methods for heave prediction. *Proceedings 6th International Conference on Expansive Soils*, New Delhi, India, 1: 99–103.

Jotisankasa, A., Croop, M. & Ridley, A. 2007. The development of a suction control system for a triaxial apparatus. *Geotechnical Testing Journal*, 30 (1): 1–7.

Tisot, J.P. & Aboushook, M. 1983. Triaxial study of swelling characteristics. *Proceedings, 7th Asian Regional Conference on. Soil Mechanics and Foundation Engineering*, Haifa, 1: 94–97.

Advances in Unsaturated Soils – Caicedo et al. (eds)
© 2013 Taylor & Francis Group, London, ISBN 978-0-415-62095-6

Soil characterization and compressibility parameters of Bogotá clay due to suction changes

G.E. Ávila
Universidad Nacional de Colombia, Bogotá, Colombia

A. Ledesma & A. Lloret
Universitat Politècnica de Catalunya, UPC, Barcelona, Spain

ABSTRACT: Parameters such as soil fabric, mineral composition, plasticity and grain size distribution together with soil-volume behavior are essential for the evaluation of shrinkage and cracking processes in soils. This paper presents the results of a laboratory testing program conducted on surface Bogotá clay to evaluate basic geotechnical properties and compressibility soil parameters due to suction changes. Water retention curves and suction controlled oedometer tests, were used to evaluate the effects of suction changes. Calibration of suction imposed with Polyethylene Glycol of 35000 g/mol (PEG 35000) is presented here because it was only available for PEG 20000 and of lower molecular mass. Results show that the air entry value of the Bogotá clay is high, that there is an important hysteretic behavior of the clay during drying and wetting cycles and that suction cycles produce a significant increase in the preconsolidation stress and in the stiffness parameters of the soil.

1 INTRODUCTION

This paper presents the procedures and results of a laboratory program conducted for the evaluation of the compressibility parameters of Bogotá clay. The tests were performed on undisturbed samples of medium plasticity clay taken from the Soft Soil Zone of Bogotá city, according to the city Microzoninig (Ingeominas and Universidad de Los Andes, 1997). Water retention curves and two techniques of suction controlled oedometer tests were applied for the soil characterization. A particular calibration of the osmotic pressure imposed by PEG 35000 was also developed which is useful for testing high plasticity soils because it generates higher suction values than the traditionally used PEG 20000.

The study of soil volumetric changes due to suction variations is of interest for evaluation of shrinkage and cracking of surface soils that in many cases are the main cause of structural damages in roads, houses or small building. Also the soil volumetric changes may be related to the periodical surface level variations in vast areas of the city, caused by weather oscillations (Blanco et al., 2010, Ávila and Castro, 2011).

2 GEOLOGICAL AND GEOTECHNICAL CONTEXT OF BOGOTÁ CLAY

Bogota city is located at 2600 m over sea level and has two main geomorphologic zones. One corresponds to a plain area where most of the city is placed, locally named Bogotá Sabana and the other is the mountain zone that borders the city in the Eastern and Southwestern sectors.

According to Van Der Hammen et al., 1973, Van der Hammen and Hooghimstra, 1995 and Caro et al., 1996, the plain zone soil has been formed by a sedimentary process from an ancient lake of tectonic-sedimentary origin that received lacustrine, fluvial and fluviar-glacier materials from Pliocene period until its desiccation about 30,000 years ago.

The upper stratum of the plain zone is called Sabana Formation, composed by dark-gray and green colored clays of medium to high plasticity, with Liquid limits that may vary between 30 and more than 200% in the upper 60 m (Ingeominas and Univeridad de Los Andes, 1997) with inter stratifications of sand and organic soils. Sabana Formation is very thick because it has 780 m depth in the Western part of the deposit and this

depth gradually reduces as it approaches to the mountain area. The depth of the deposit in the site of sampling is 180 m (located in INGEOMINAS offices).

2.1 *Basic geotechnical properties*

Undisturbed samples recovered at depths between 2 and 4 m. were used for this investigation. This soil corresponds to a brown to grey clay with some red shades, of medium consistency and plasticity. According to USCS is a CH material very close to Casagrande A line. Table 1 shows the basic geotechnical parameters of the clay.

Gaviria et al. (2004) present five thematic profiles of the Sabana Formation up to 160 m depth from a borehole drilled very near the site of sampling of the present study. These profiles were originally made to investigate stratigraphy and paleo-climate history but they also permit to complement the geological and mineralogical description of the soils. It was found in that study the prevalence of clayey materials in the upper 50 m, with some interlayer of organic matter. From 50 m to 160 m, clay soils continue but there appear many layers of silts, sands and organic matter. The clayey minerals are more abundant than other minerals as feldspars, quartz and carbonates and the feldspar/quartz relation indicates the predominance of quartz which is more resistant to degradation than feldspar. Relative proportions of the clay materials (<2 microns) indicate that near 50% correspond to Kaolinite and in less proportion there appear smectite, illite and chlorite respectively.

Relative proportion of clayey minerals between 2 and 4 m depth, deduced from Gaviria et al. (2004) are summarized in Table 2.

Table 1. Basic geotechnical parameters of Bogotá clay in INGEOMINAS sector between 2 and 4 m depth.

Parameter	Symbol	Unit	Interval
Natural water content	wn	%	42–46
Liquid limit	LL	%	62–65
Plastic limit	LP	%	28–32
Plasticity index	IP	%	30–35
Specific gravity	Gs	–	2.6–2.7
Unit weight	γt	kN/m^3	16.5–18.0
Void ratio	e	–	1.25–1.27
Degree of saturation	Sr	%	96–100
Clay fraction (<0.002 mm)	C	%	61–63
Activity	A	–	0.52–0.57
Undrainded shear strength	Su	kPa	55–65

Table 2. Mineral composition of Bogotá clay at INGEOMINAS site between 2 and 4 m depth (deduced from Gaviria et al., 2004).

	Clay	Feldspars	Quartz	Total
Global composition	75%	3%	22%	100%
	Kaolinite	Smectite	Illite	Clorite
Clay fraction composition	55%	17%	15%	13%

The predominance of Kaolinite (of low activity) and the relatively low presence of smectite (of high activity) produce a moderate activity of the Bogotá clay (A = 0.55) compared with other soils reported in literature (Skemptom (1953) in: Lambe and William, 1979) as London clay (A = 0.95) and Shellhaven (A = 1.33).

3 SUCTION CONTROLLED LABORATORY TESTING

3.1 *Retention curves*

Different techniques were used to determine the water retention curves of the studied clay, as transistor psycrhrometer, vapor equilibrium technique, pressure plate and filter paper, as shown in Figure 1 from Ávila (2001).

Here it is important to note the high air entry value of Bogotá clay. Such a characteristic means that the clay may be in saturated condition under suction values up to 1 MPa.

3.2 *Suction calibration of PEG 35000*

A particular calibration of the suction imposed by PEG 35000 was conducted because calibrations of this kind were only available for PEG 20000 or of lower molecular mass. For the calibration an Imperial College Suction Probe (Rydley and Burland, 1993) was used in conjunction of a semi permeable membrane type Spectra/Por 5 MWC0 12-14000 normally employed for medical dialysis. This membrane has two sheets (it comes in tubular shape) but for the experiment it was cut and open to live only one sheet.

The membrane was placed in distilled water for a period of 2 hours until a soft consistency was reached. After that it was cut to fit the oedometer diameter and then placed in the upper and lower sides of the soil sample. A thin clay layer was placed between the membrane and the suction probe in order to avoid early cavitation of the water in the system.

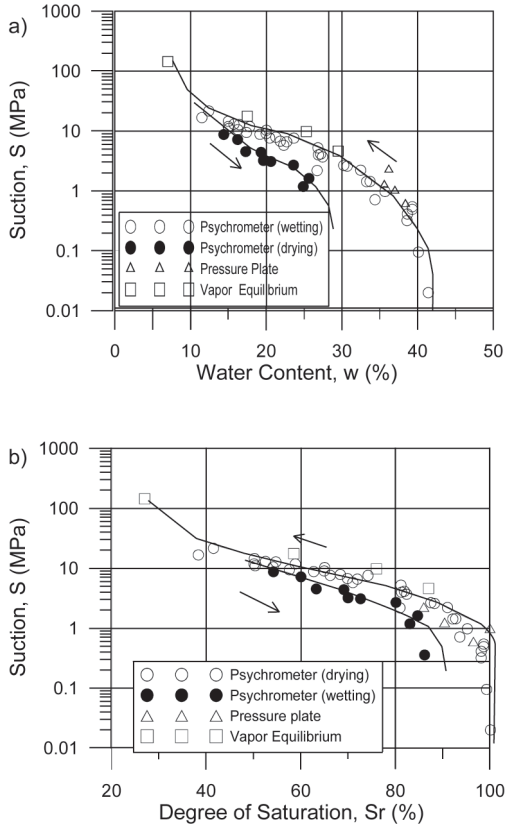

Figure 1. Water Retention Curves of a Bogotá Clay obtained with four different techniques: a) water content—suction, b) degree of saturation—suction. From Ávila (2001).

Solution was prepared mixing PEG 35000 (commercially available if form of dry grains) with distilled water, using PEG concentrations from 5% to 40% with increments of 5% (weight of PEG respect to weight of water).

For PEG concentrations lower than 15% suction stabilization was reached in less than 40 min. For concentrations between 15% and 35% suction stabilization lasted between 100 and 120 min and for the PEG concentration of 40% it was not possible to determine the imposed suction because the system presented cavitation at a suction of 1350 kPa, before equilibrium was reached.

Calibration curve of the suction imposed by different PEG 35000 concentrations is presented in Figure 2, together with calibrations reported for different author, using PEG with lower molecular masses (Gens and Romero, 2000).

All these calibrations are in a narrow zone indicating that for the same concentrations, the

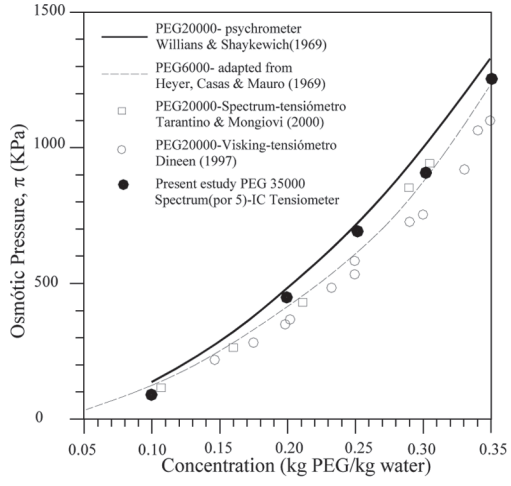

Figure 2. PEG 35000 calibration in conjunction with other calibrations presented by Gens and Romero (2000).

molecular mass of the PEG salt does not generate significant changes in the imposed suctions.

3.3 *Oedometer tests*

Conventional and suction controlled One-dimensional compression test permitted to evaluate the volume changes generated for load and suction variations. The conventional oedometer test was used as a reference behavior under saturated conditions whereas two types of procedures were used to impose suction: vapor transfer technique and osmotic technique by means of Polietylene Glyclol 35000 (PEG 35000).

A sketch of the vapor transfer technique set up is presented in Figure 3.

In the osmotic technique oedometer test, a PEG 35000solution at different concentrations was used to impose suction at the sample base with the aid of a peristaltic pump. The set up is similar to that developed by Dineen (1997) based in previous works of Kasiff and Ben Shalom (1971) and Delage et al. (1992) and it is sketched in Figure 4.

3.4 *Results*

In the tests with vapor control, for the compression test an initial small vertical stress of 48 kPa was applied to adjust the sample and the equipment, after what two suction increments were applied in a drying path: the first one of 40 MPa by means of a NaCl vapor solution and the second one of 144.3 MPa using sulfuric acid vapor solution. Volumetric deformation caused

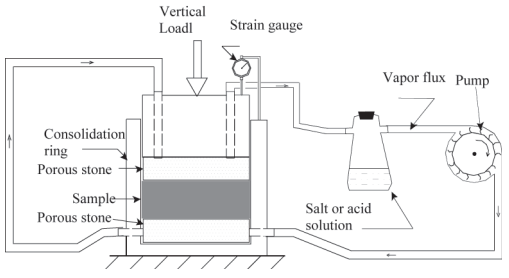

Figure 3. General set up of the consolidation test with vapor transfer technique.

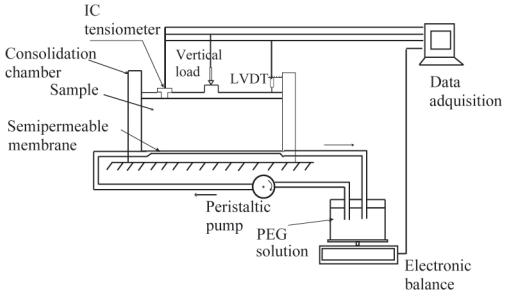

Figure 4. General set up of the consolidation test with osmotic suction.

by the suction were about 9% and maximum volume change was caused by the initial suction of 49 MPa whereas the second suction increase only produced a small sample contraction. In the wetting path suction was decreased again to 40 MPa and finally distilled water was used in the circuit to reduce suction to zero and a small volumetric increase was registered. The volumetric deformations produced by suction changes are presented in Figure 5.

In the tests using osmotic control, the suction increase produced vertical strains in the sample in a way similar to that caused by direct loading and it was observed that the greatest volume change was caused during the application of a 20% PEG concentration in the drying path.

The maximum PEG concentration used was 30% after what a total volume change of about 20% was experienced by the sample, indicating that possibly this method of application of suction is more efficient that the vapor transfer technique. Wetting path was imposed reducing PEG concentrations and this suction reduction produced a volume increase near to 5%, indicating a hysteretic behavior. The volumetric deformations as function of osmotic suction are shown in Figure 6.

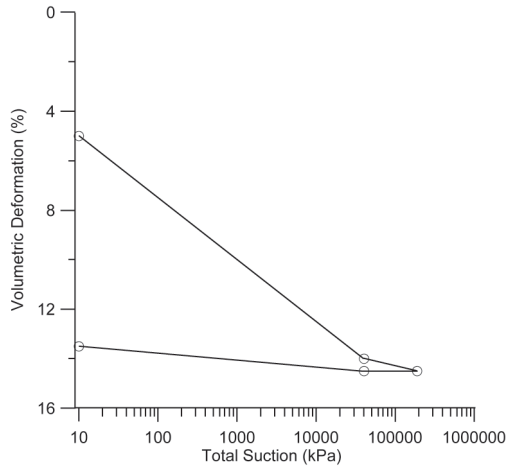

Figure 5. Volumetric deformation produced by suction application in oedometer test using vapor transfer technique.

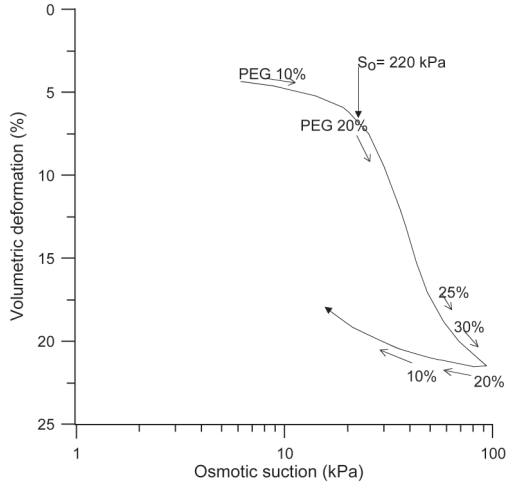

Figure 6. Volumetric deformation produced by suction application in oedometric test using osmotic technique.

In that figure is also indicated the PEG concentration used to impose suction and the fluency suction (So) defined in the Barcelona Model (Alonso et al., 1990) characterized by the slope change in the drying path, which represents the maximum past suction experienced by the soil.

Suction cycles were followed by conventional loading and unloading using dead weights to see their effect in the rigidity of the clay. The conventional consolidation test showed an effective

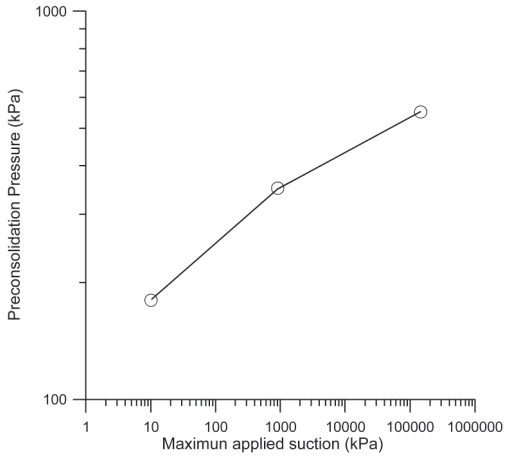

Figure 7. Effect of maximum applied suction on apparent preconsolidation stress.

preconsolidation stress of 180 kPa, indicating that the soil is over-consolidated (OCR = 3) and of moderated compressibility characteristics (Cc = 0.35 and Cr = 0.11). As predicted by Alonso et al. (1990), applied suction cycles to the samples, previous to direct loading caused a significant increase in preconsolidation stress as shown in Figure 7.

The important volume changes caused by suction variations have influence in the active zone of Bogotá soils, which extends to about 5 m depth. This may explain seasonal variations of the land surface level measured in Bogotá City and probably it is contributing to the soil subsidence registered in some areas of the soft soils of Bogotá city (Ávila, 1998, Blanco et al. (2010), Ávila and Castro, 2011), and in the countryside where significant surface soil deformations and big cracks are evident especially during very dry weather periods.

4 CONCLUSIONS

A systematic study of composition and compressibility parameters of a surface Bogotá clay shows that it corresponds to a medium to high plasticity soil (CH), with liquid limit between 62% and 65%, plasticity index between 61% and 63% and moderate activity between 0.52 and 0.57. Clay fraction is composed predominantly by Kaolin followed by smectite and in lower proportions ille and chlorite.

Retention curves performed by different methods showed consistent results and they revealed an air entry value of the clay of about 1 MPa, which is high, meaning that the soil stays in saturated conditions for relatively high suction values.

Compressibility parameters of the Bogotá clay were evaluated using conventional and suction controlled consolidation tests. Suction was imposed by two techniques vapor transfer technique and osmotic technique, using a Polietylen Glyclol 35000 solution. For this solute a particular calibrations of the imposed suction was conducted and it was found that for similar PEG concentrations, suctions imposed by PEG 35000 is of the same order that the suction imposed with PEG of lower molecular masses. Also, it was observed that the method is efficient for inducing significant moisture changes in the soil sample placed the consolidation chamber.

Suction cycles previous to loading produced important increments in the preconsolidation stress of the clay, changing the OCR for the imposed suctions from 3 to 9.

Volumetric deformations showed a non-linear relation to suction, that is, the clay suffers significant shrinkages for certain suction values and this contractions produce and increase in stiffness in the soil. For that reason, further suction increments only generate residual contractions. Suction reductions generate hysteretic rebounds in the drying path that are of lower than in the wetting path. This may explain periodical surface level variations recently measured in Bogotá soils for subsidence evaluations.

REFERENCES

Alonso, E.E., Gens, A. & Josa, A. (1990). A constitutive model for partially saturated soils. *Géotechnique* 40 (3): 405–430.

Ávila, G. (2001). Curvas de retención de agua de una arcilla de Bogotá. XI Jornadas Geotécnicas de la Ingeniería Colombiana y IV Foro sobre Geotecnia de la Sabana de Bogotá. Bogotá, octubre 2001.

Ávila, G. & Castro, N. (2011). Avances en el estudio de subsidencia de la ciudad de Bogotá. VIII Seminario Colombiano de Geotecnia—Seminario Internacional de Geotecnia Urbana. Bogotá.

Blanco, P., Barreto, A. & Ortiz, A. (2010). La interferometría diferencial DInSar—Una técnica para el monitoreo de la subsidencia en Bogotá D.C. Boletín Colombiano de Geotecnia ed. 13–2012: 1–16.

Caro, P., Padilla, J. & Vergara, H. (1996). Mapa geológico de Santafé de Bogotá. VI Congreso Colombiano de Geología. Soc.Col. Geología—Ingeominas. Santafé de Bogotá.

Delage, P., Vicol, T. & Suraj de Silva, G.P.R. (1992). Suction controlled testing of non-saturated soils with osmotic controlled consolidometer. 7a ICES, Dallas, pp. 206–211.

Dineen, K. (1997). The influence of soil suction on compressibility and swelling. Tesis de PhD, London University.

Gaviria, S., Duarte, R., Romero, F., Thorez, J. & Berrio, J.C. (2004). Procesos de erosión, transporte y depósito durante el Cuaternario. En: Aspectos Geoambietales de la Sabana de Bogotá. Publicaciones Geológicas Especiales de Ingeominas. 27: 169–217.

Gens, A. & Romero, A. (2000). Ensayos de laboratorio. Simposio sobre geotecnia de las infraestructuras del transporte: Barcelona: 17–43.

Ingeominas and Universidad de Los Andes. (1997). Microzonificación sísmica de Santa Fe de Bogotá. Convenio interadministrativo 01–93.

Lambe, T.W. & Withman, R.V. (1979). Soil Mechanics. John Wiley and Sons, Inc. New York.

Ridley, A.M. & Burland, J.B. (1993). A new instrument for measuring soil moisture suction. Technical Note, *Gèotechnique* 4 (2).

Van Der Hammen, T., Werner, J.H. & Van Dommelen, H. (1973). Palynological record of the upheaval of the Northern Andes: a study of the Pliocene and the lower Quaternary of the Colombian Eastern Cordillera and the early evolution of its high Andean biota. Review Paleobotany and Palynilogy, 16: 1–122.

Advances in Unsaturated Soils – Caicedo et al. (eds)
© 2013 Taylor & Francis Group, London, ISBN 978-0-415-62095-6

Cyclic behavior of unsaturated unbound aggregates for pavements

B. Caicedo
Universidad de los Andes, Bogotá, Colombia

O. Coronado
Universidad Nacional de Colombia, Bogotá

J.M. Fleureau
Ecole Centrale Paris & CNRS, Châtenay Malabry, France

A. Gomes-Correia
Universidade do Minho, Guimarães, Portugal

ABSTRACT: The results of an experimental work on three road granular materials from La Sabana de Bogotá are presented. These works include small strains precision triaxial tests under cyclic loading with measurement of the negative pore water pressure (suction). The influence of different initial conditions of density, water content and fines content was studied. The interpretation of the results, in the quasi-elastic domain, is based on total stress and effective stress analyses, the latter allowing to take into account the effects of both total stresses and negative pressure, in the perspective of a more rational design of pavement structures.

1 INTRODUCTION

The empirical nature of traditional pavement design methods has been discussed in road engineering for many years. These methods rely on empirical rules based on experience under particular conditions. The main limitation of empirical methods is that they cannot be extrapolated with confidence beyond those conditions on which they are based (Lekarp et al., 2000).

On the other hand, mechanistic pavement design is based on rational methods using Young' modulus (E) and Poisson's ratio (ν). A conditional prerequisite for the success of the mechanistic approach is that the behavior of the constituent materials is properly understood. Numerous research has been conducted on the behavior of unbound granular materials (U.G.M.) used in flexible pavements. Most of these works has been carried out on good quality granular materials whose index properties are based on the recommendations of empirical methods.

Non standard granular materials could have characteristics like higher fines content, higher plasticity index, higher blue methylene value and more crushable grains than good quality U.G.M. Most of these characteristics increase the role of the water on the mechanical behaviour of U.G.M. For this reason, to analyze the role of index parameters on the performance of flexible pavements it is essential to take in to account the influence of negative pore pressure on the Young' modulus (E) and Poisson's ratio (ν).

In the laboratory, the negative pore water pressure, or suction ($u_c = u_a - u_w$), is not easy to measure in coarse materials and their derivation requires the use of elaborate tests.

Several authors have studied the effect of the negative pore water pressure on the small strains behavior of partially saturated soils (Brull 1980, Wu et al., 1989, Kheirbek-Saoud 1994, Picornell and Nazarian 1998, Balay et al., 1998). In most cases, the analysis of the results is made in total stresses, and the role of the stress tensor is considered separately from that of the negative pore water pressure. Other authors (Wu et al., 1989, Biarez et al., 1991, Coussy & Dangla 2002, Fleureau et al., 2003) showed that an effective stress approach could be used to take in account the effect of the capillary pressure in the interpretation of the data in the very small strains domain.

In this study, small strains triaxial tests with measurement of negative pore water pressure have been performed on three "non standard"

unbound granular materials (U.G.M.) used in Bogotá Colombia. The Colombian materials have recomposed in order to attain different plasticity index, methylene blue value, crushability and fines content. Wetting tests have been carried out to determine suction and water content changes in the material during wetting. One of the goals of this paper is to show how to take moisture changes into account in the pavement design analysis using an effective stress approach.

2 MATERIALS AND METHODS

2.1 *Materials*

The materials used in this study are gravels made of sandstones coming from three different locations near Bogotá—Colombia. The grain particles of the three gravels (Servitá, Vista Hermosa and Soacha) have different degrees of cementation that affects their state properties. Also two alluvial sands were used in order to prepare mixtures with controlled characteristics. The state properties of the five materials are summarized in Table 1.

Using these five basic materials, a total of 25 different mixtures were prepared. These mixtures have different fine contents, plasticity indexes, blue methylene, fragmentability and water content values as shows in Table 2.

2.2 *Cyclic triaxial tests*

The cyclic tests were carried out in a classic triaxial cell, allowing a direct measurement of the stiffness modulus and Poisson's ratio for homogeneous strains ranging between 10^{-6} and 10^{-2}. To be able to explore the domain of the very small strains with sufficient accuracy, the force and strain measurements are done on the specimen itself. The force transducer is placed inside the cell directly on the head of the specimen, which permits a precise measurement of the force applied to the specimen and eliminates the bearing-piston friction problems. The measure of the axial strains is achieved by means of three LDT strain sensors placed in the central zone of the specimen, in order to avoid the influence of the constrictions of the bases on the measures. Radial strains are derived from the variations of the perimeter of the specimen measured by a deformable belt placed to mid-height and equipped with a LDT sensor. The LDT sensors are constituted of 4 strain gauges forming a complete Wheatstone bridge fixed on a deformable blade made of beryllium bronze; they were manufactured at the Ecole Centrale Paris on the model of the sensors developed at the university of Tokyo in the team of Professor Tatsuoka (Goto et al., 1991). Supports for the sensors are put in place in the specimen during the compaction. The accuracy of the strain measurements is approximately10^{-5} with a 21 bits Agilent A/D converter. To prepare the specimens, water is added to the dry mixture in a homogenous way. Dynamic compaction of the specimen, 150 mm in diameter and 300 mm in height, is achieved by hand by means of a Modified Proctor hammer, in 12 layers with 56 strokes of rammer per layer. During the manufacture of the specimens, special attention is paid to the setting up of the six supports of the vertical sensors. Then, the axial and radial strain sensors are put in place, as well as the force transducer.

Table 1. Main state properties of the materials.

	Plasticity index %	Blue methylene (g/100 g)	Abrassion coeff. Los Angeles %
Vista Hermosa	9	1.40	20
Servitá	10	1.46	34
Soacha	16	1.90	56
Guamo sand	–	0.90	–
Suarez sand	–	0.50	–

To determine the reversible behavior of the materials, preliminary conditioning of the specimens is carried out in order to simulate the real conditions of laying down of the soil: it consists in 20000 loading-unloading cycles under an isotropic stress of 40 kPa and a deviatoric stress of 280 kPa. After the pre-conditioning, the specimen is submitted to 20 successive paths with increasing levels of stress (Figure 2a). All the tests are made under constant confining stress σ_3.

Each loading is applied during 100 cycles. The reversible strains of the specimen are measured during the 100th cycle. An example of the measurements is shown on Figure 2b, where the deviatoric stress q is represented versus the axial, radial and volumetric strains (ε_1, ε_3 and ε_v, respectively).

These cycles illustrate the non linearity of the behavior, i.e. the increase in the modulus with q, when the axial strain exceeds the elastic limit of the material (about10^{-5}).

The secant module is defined in the following way:

$$E_{\text{sec}} = q / \varepsilon_1^r \tag{1}$$

The measurements are made for axial strain ε_1^r approximately equal to 10^{-4}.

Table 2. Characteristics of the mixtures.

Sample N°	Fractions: Coarse 20/0.5	Fine 0.315/0	w_L %	PI %	VB g/100 g	LA %	Grain size distribution: 12.5 mm %	2 mm %	80 µm %	2 µm %	w %	ρ_d kg/m^3	e	S_R %	w_{comp}
V3	VH	GS	17	3	0.9	20	84.0	44.0	11	0.2	4.1	1980	0.33	33	W_{OPM}-2.7%
V7	VH	GS	16	3.6	0.7	20	77.5	37.4	9.8	0.2	5.2	1980	0.33	42	W_{OPM}-1.6
V8	VH	GS	15	3	0.8	20	81.0	41.0	9.67	0.2	4.0	1980	0.35	31	W_{OPM}-2.8
V14	VH	SS	–	–	0.25	20	87.0	38.0	8.92	0.1	3.1	1980	0.36	23	W_{OPM}-3.7
V15	VH	SS	–	–	0.5	20	84.0	37.0	9.38	0.1	4.7	1960	0.37	34	W_{OPM}-2.1
V16	VH	SS	–	–	0.25	20	84.0	39.0	9.08	0.1	5.8	1970	0.37	43	W_{OPM}-1.0
V6	VH	SO	27	15.7	1.9	20	80.0	36.0	12	0.2	4.4	1980	0.33	36	W_{OPM}-2.6
V11	VH	SO	27	16.4	1.9	20	88.0	54.0	32	1.6	5.0	1970	0.33	39	W_{OPM}-2.0
V13	VH	SO	26	16	1.9	20	75.0	30.5	5.1	0.1	4.5	1960	0.35	34	W_{OPM}-2.5
V17	VH	SO	26	14.5	1.25	20	82.0	37.0	11.3	1.4	3.2	1980	0.34	25	W_{OPM}-3.8
V18	VH	SO	26	14	1.25	20	82.0	37.0	12.7	1.5	4.6	1970	0.34	35	W_{OPM}-2.4
V19	VH	SO	26	14.2	1.5	20	82.0	37.0	13	1.5	6.0	1980	0.34	46	W_{OPM}-1.0
S2	SE	GS	15	5.1	0.9	34	84.0	47.0	19	0.6	3.5	2010	0.31	30	W_{OPM}-3.0
S4	SE	SO	24	12	1.6	34	84.0	46.0	19.9	0.6	4.9	2040	0.28	46	W_{OPM}-2.6
S5	SE	VH	22	22	1.3	34	82.4	46.7	21	0.6	4.8	2030	0.29	43	W_{OPM}-2.0
S21	SE	GS	–	–	1.0	34	–	–	10	–	0	1930	0.36	0	W_{OPM}-6.5
SO1	SO	GS	23	12	1.5	56	74.5	45.9	29	1.5	6.3	1960	0.33	48	W_{OPM}-2.0
SO9	SO	GS	23	12	1.4	56	94.0	59.4	29.9	1.5	4.0	1980	0.33	30	W_{OPM}-4.0
SO10	SO	SO	27	16.1	1.9	56	89.0	59.0	30	1.6	6.5	1940	0.35	40	W_{OPM}-1.5
SO22	SO	GS	–	–	1.0	56	–	–	10	–	0	1940	0.37	0	W_{OPM}-8.0

W_L liquid limit; PI plasticity index; VB methylene blue value; LA Los Angeles abrasion coefficient; w water content, ρ_d dry unit weight; e void ratio; S_r saturation degree; w_{comp} compaction water content.

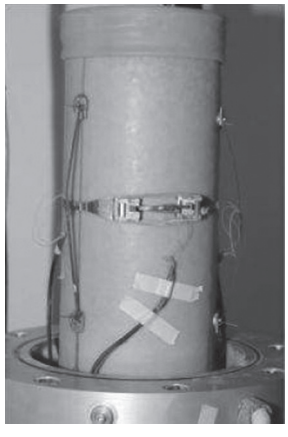

Figure 1. Triaxial sample with vertical and radial LDT transducers.

2.3 *Triaxial tests with measurement of the negative pore water pressure*

The device consists of a triaxial cell with a semi-permeable ceramics placed in the base; the porous stone with high air entry pressure (1,5 MPa, from Soil Moisture) does not permit the passage of air in the water circuit. The device can be used either as a tensiometer (with $u_a = 0$ and $u_w < 0$) to measure negative pore water pressures between 0 and 50 kPa, or with an air overpressure at the head of the specimen for higher negative pressures. Pore water pressure measurements are done by means of an absolute pressure sensor with a range of 1000 kPa and a sensitivity of 0,1 kPa/mV. Data logging is achieved by means of a 16 bits data acquisition system from GDS.

The size of the specimens is 100 mm in diameter and 200 mm in height.

Specimens were dynamically compacted by means of a Modified Proctor hammer in 4 layers, with 56 strokes per layer. A thin layer of kaolinite is placed on the ceramics to ensure a good contact with the specimen and the continuity of the water phase.

2.4 *Wetting tests on tensiometric plates*

To impose negative pore water pressures ranging between 0 and 30 kPa, tensiometric plates were

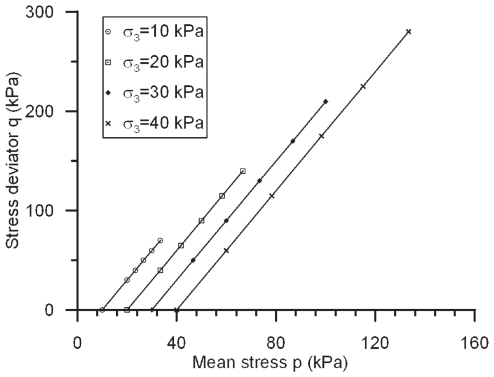

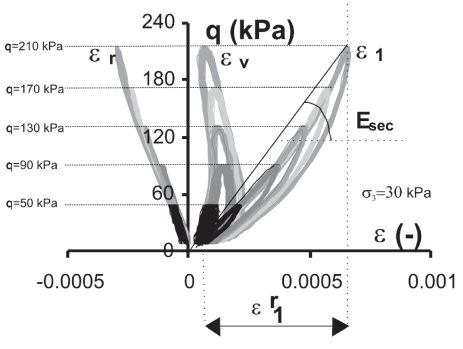

Figure 2a. Stress paths for the determination of the elastic properties of the materials.
Figure 2b. Example of measurement of the stress deviator vs. axial, radial and volumetric strains.

used. They are made of a low porosity sintered glass filter that plays the role of the semipermeable separation, set in a glass funnel. The specimen is placed on the filter to the atmospheric pressure, in contact with a reservoir filled with de-aired water. Imposing a difference of level between the filter and the measurement tube results in controlling the depression of the water placed in the reservoir, and therefore the negative pore water pressure in the specimen.

At the end the cyclic triaxial tests, the specimen is cut into several pieces that are placed on the tensiometric plate. The exchanges of water between the specimen and the reservoir are derived from the displacement of the water meniscus in a horizontal measurement tube connected to the reservoir. When the negative pore water pressure in the specimen reaches the imposed value, generally at the end of 5 days, the total volume of the specimen and its water content are derived from immersion in kerdane followed by drying in an oven; the water content, void ratio and degree of saturation of the material are derived from these data.

3 INTERPRETATION OF THE RESULTS IN TOTAL STRESS, ROLE OF THE PLASTICITY INDEX AND FINES CONTENT

Two sets of tests were performed on materials having 10% of fines: one set corresponds to a plasticity index of 16% (IP = 16%) and the other to an IP = 0. Figures 3 and 4 illustrate the variation of the secant modulus with the isotropic stress p in two planes (logp – log E_{sec}) and (p – E_{sec}) for different water contents ranging from 3.0% to 5.8%. One notes the sensitivity of the material to this parameter: under the same isotropic stress, the modulus is higher when the water content is smaller because of the increase in the capillary forces in the menisci that form themselves between the grains.

As previously noted (Fleureau et al., 2003), the lines are more or less parallel for the different wet soils; this is particularly clear on the logarithmic plan.

The logarithmic plan allows the use of exponential models like the K-θ model. On the other hand, the results on the linear plan adjust to straight lines having different slope depending on the plasticity index. This kind of plan allows the normalization of the results using the modulus E_{0p} corresponding to zero total mean stress (p = 0).

The linear interpretation allows the normalization of the results dividing by the modulus E_{0p} (figure 5). This figure shows that all the points for the same plasticity index are grouped along the same line. We remark that the higher the plasticity index, the smaller the slope of the line. Equations 2 and 3 describe the variation of the secant modulus for 0% and 16% plasticity index and for 10% of fine content.

It's well known that the modulus increases as the water content reduces (Balay et al., 1998;

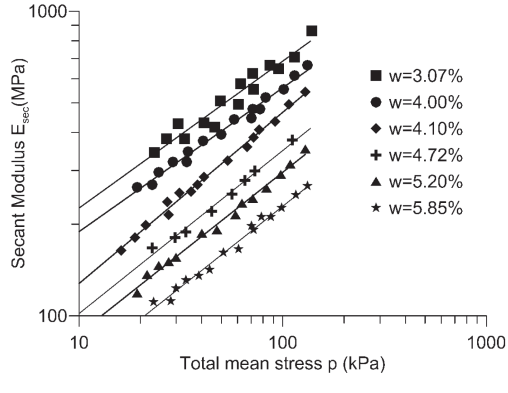

Figure 3. Results for zero plasticity index (bleu value = 0.5 g/100 g), logarithmic scale.

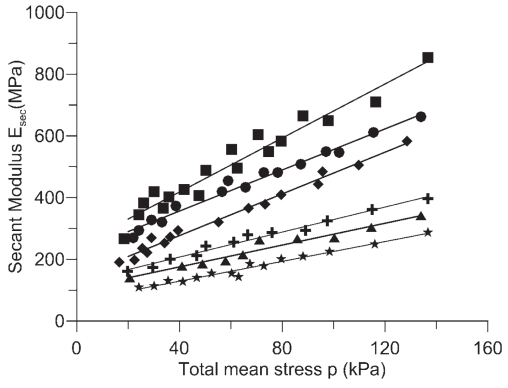

Figure 4. Results for zero plasticity index (bleu value = 0.5 g/100 g), linear scale.

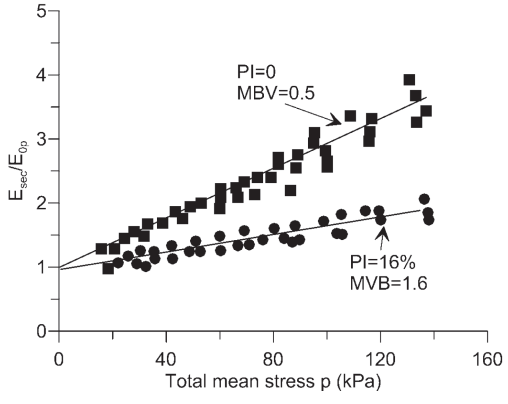

Figure 5. Normalization of the secant modulus as a function of the total mean stress p for plasticity indexes 0% and 16% and 10% of fines.

Fleureau, et al., 2002). This is particularly clear for the modulus at zero total mean stress (E_{op}). Furthermore, since water content and suction are directly related, the modulus E_{op} depends on suction. Figure 8 shows the increase of E_{0p} with suction and therefore with the effective stress.

$$\frac{E_{\sec}}{E_{0p}} = 1 + 0.02 p_a \left(\frac{p}{p_a} \right) \quad \text{IP} = 0 \tag{2}$$

$$\frac{E_{\sec}}{E_{0p}} = 1 + 0.008 p_a \left(\frac{p}{p_a} \right) \quad \text{IP} = 16\% \tag{3}$$

where p_a is the atmospheric pressure.

Figure 6 shows the normalized modulus E_{sec}/E_{op} in the plane (E_{sec}/E_{op}–p) for materials having 20% of fines and different plasticity indexes (5% and 12%). Also in this case, the slope of the lines increases as the plasticity index decreases but the variation is less significant than for the case of 10% of fines and plasticity indexes of 0% and 16%. Equations 4 and 5 describe the variation of modulus for the different plasticity indexes. Figure 8 shows the modulus E_{0p} related to suction for the material having 0 plasticity index and 10% of fines.

$$\frac{E_{\sec}}{E_{0p}} = 1 + 0.012 p_a \left(\frac{p}{p_a} \right) \quad \text{IP} = 5\% \tag{4}$$

$$\frac{E_{\sec}}{E_{0p}} = 1 + 0.006 p_a \left(\frac{p}{p_a} \right) \quad \text{IP} = 12\% \tag{5}$$

In the case of 30% of fines, we found that the plasticity index has a less significant role in the normalized plane that in the cases with smaller fine

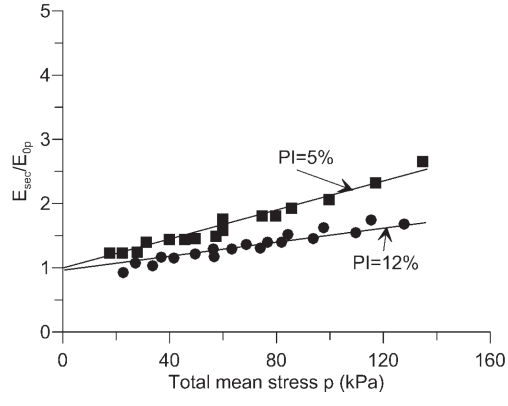

Figure 6. Normalization of the secant modulus as a function of the total mean stress p for a plasticity index of 5% and 12% and 20% of fines.

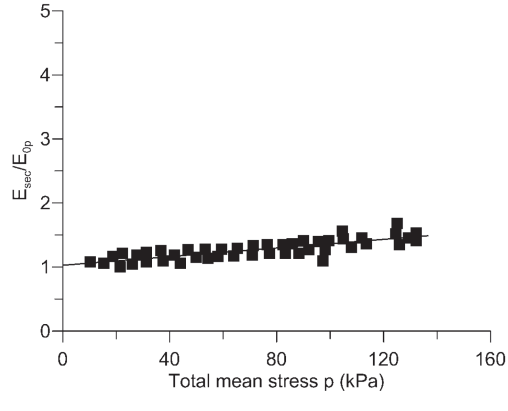

Figure 7. Normalization of the secant modulus as a function of the total mean stress p for 30% of fines and different plasticity indexes.

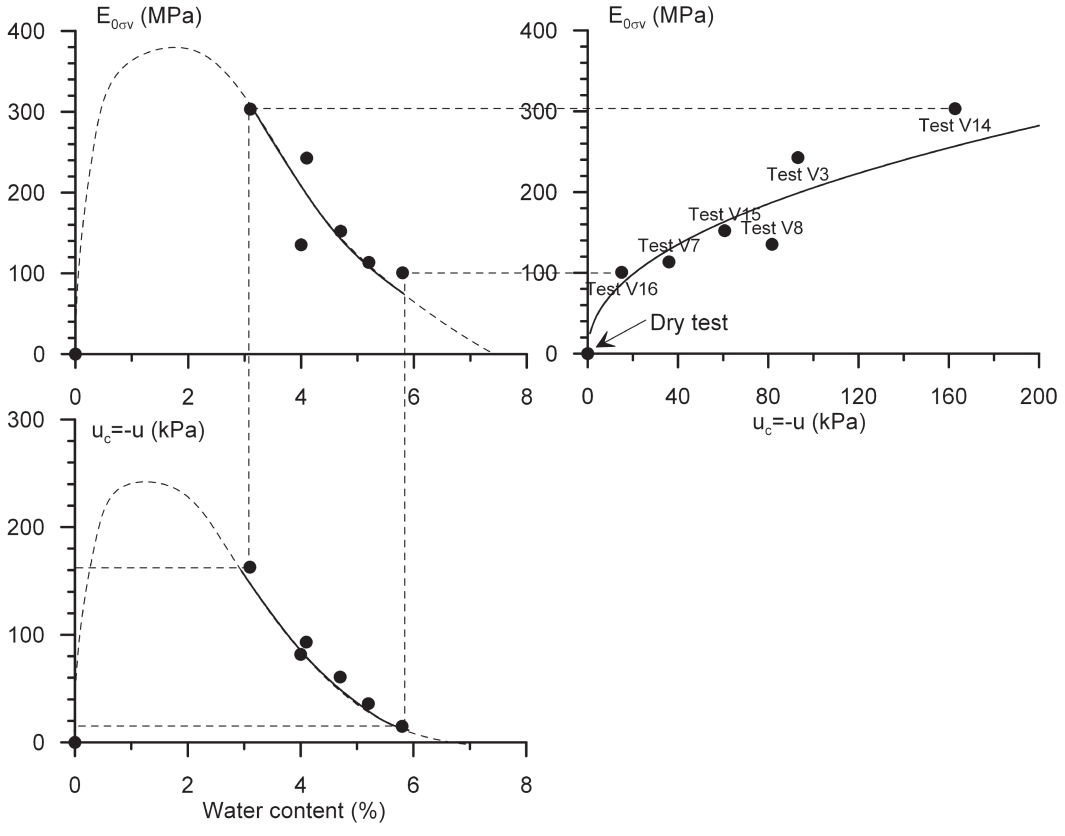

Figure 8. Relationship between the modulus $E_{0\sigma v}$, the water content and the suction for 10% of fines and PI = 0%.

contents. In fact, Figure 7 shows that the slope of the lines in the plane (E_{sec}/E_{op}–p) is the same for the different plasticity indexes.

$$E_{0p}(e = 0.33) = bP_a \left(\frac{u_a - u_w}{P_a} \right)^n \quad (6)$$

The effect of suction on E_{0p} can be obtained using equation 6 (see Figure 8), with this equation the role of the negative pore water pressure on the modulus at zero total stress depends on the parameters *b* and *n*. These parameters for different materials are presented in Caicedo *et al.,* 2008.

4 INTERPRETATION OF THE RESULTS USING EFFECTIVE STRESSES

Different expressions have been proposed to calculate the effective stress in an unsaturated medium. In the case of high negative pore water pressures and low degrees of saturation, the approach developed at the Ecole Centrale Paris is based on a micromechanical model composed of regular arrangements of non-deformable balls of the same diameter d (Fleureau et al., 2003).

The increase in negative pore water pressure due to the reduction of the degree of saturation leads to an increase in the intergranular forces, which increases the moduli and the shear strength of the soil. For a regular arrangement of spheres, an elementary calculation based on Laplace's law results in the following expression of the capillary stress p'_u that represents the contribution of the negative pore water pressure to the cohesion of the material. The capillary stress is a function of suction and of the diameter d. In the case of a real grain size distribution, the parameter d must be determined. The expression to pass from total stresses to effective stresses is therefore:

$$\sigma'_V = \sigma_V + p'_u \quad (7)$$

To compare the results of the tests carried out at different void ratios, it is necessary to normalize

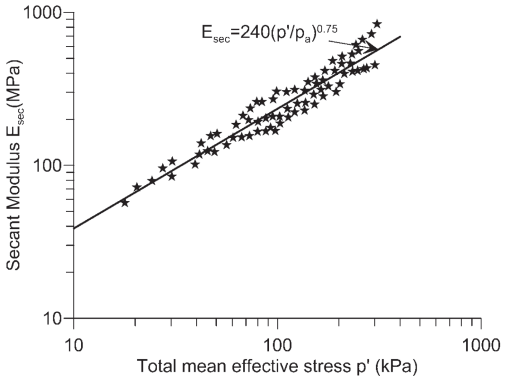

Figure 9. E_{sec} as a function of the isotropic effective stress for all the mixtures with Vista Hermosa Material.

the moduli to the same value of void ratio. The relation of Iwasaki et al. (1978) was used to bring the moduli back to a void ratio of 0.33:

$$E_{(e=0.33)} = E_e \frac{f(e=0.33)}{f(e)} \quad f(e) = \frac{(1.93-e)^2}{1+e} \quad (8)$$

For the Colombian materials, a simplified effective stress law has been used. This relationship was the Terzaghi law using the measured negative pore pressure. Figure 9 shows all the results of moduli obtained for the Vista Hermosa material in function of the effective isotropic stress. All the results can be described by a power equation.

5 CONCLUSIONS

The precision triaxial tests performed on three road unbound granular materials highlight the non linear behavior of these materials. The effect of the water content, plasticity index and fines content on the secant modulus is important. The interpretation of the results in terms of effective stresses based on suction measurements shows that it is possible to take into account the effect of water content on the reversible parameters. The role of the grain size distribution and crushability are directly related to the changes in suction.

These results allow generalizing the constitutive laws developed for dry untreated unbound granular materials to larger conditions of water content, representative of the real conditions in pavements.

REFERENCES

Balay, J., Gomes Correia, A., Jouve, P., Hornych, P. & Paute, J. 1998. Etude expérimentale et modélisation du comportement mécanique des graves nos traitées et des sols support de chaussées, Bull. Ponts & Ch., 216: 3–18.

Biarez, J., Fleureau, J.M. & Kheirbek-Saoud, S., 1991. Validité de s' = s—uw dans un sol compacté, 10th E.C.S.M.F.E., Firenze, 1: 15–18.

Brull, A. 1980. Caractéristiques mécaniques des sols de fondation de chaussées en fonction de leur état d'humidité et de compacité, Coll. Int. Compactage, Presses Ponts & Chaussées, Paris, 1: 113–118.

Coussy, O. & Dangla, P. 2002. Approche énergétique du comportement des sols non saturés, in Mécanique des sols non saturés, Hermès, Paris: 137–174.

Goto, S., Tatsuoka, F., Shibuya, S., Kim Y.-S. & Sato, T. 1991. A simple gauge for local small strain measurements in the laboratory, Soils and Foundations, 31(1): 169–180.

Fleureau, J.-M., Hadiwardoyo, S. & Gomes Correia, A. 2003. Generalised effective stress analysis of strength and small strains behaviour of a silty sand, from dry to saturated state, Soils and Foundations, 43(4): 21–33.

Iwasaki, T., Tatsuoka, F. & Takagi, Y. 1978. Shear Moduli of Sands under Cyclic Torsional Shear Loading, Soils and Foundations, 18(1): 39–50.

Kheirbek-Saoud, S. 1994. PhD Thesis, Ecole Centrale Paris.

Lekarp, F., Isacson, U. & Dawson, A. 2000. State of the art I: Resilient response of unbound aggregates. Journal of transportation engineering, February 2000.

Picornell, M. & Nazarian, S. 1998. Effects of soil suction on the low-strain shear modulus of soils, 2nd Int. Conf. on Unsat. Soils, Beijing, 2: 102–107.

Wu, S., Gray, D.H. & Richart, F.E. 1989. Capillary effects on dynamic modulus of sands and silts, Geot. Eng. Div. J., ASCE, 110(9): 1188–1203.

This page intentionally left blank

Advances in Unsaturated Soils – Caicedo et al. (eds)
© 2013 Taylor & Francis Group, London, ISBN 978-0-415-62095-6

Small strain shear modulus of an unsaturated sandy soil

G.B. Georgetti & O.M. Vilar
University of Sao Paulo, Sao Carlos, Sao Paulo, Brazil

ABSTRACT: This paper aims to present and discuss the preliminary results of a set of tests performed to determine the maximum shear modulus of a compacted sandy soil tested both on saturated and on unsaturated conditions. The methodology consisted on installing certain matric suction on soil specimens using the axis translation technique, and testing them in triaxial cells coupled with bender elements. In the cells, isotropic consolidation was allowed, keeping suction at constant values. After that, shear waves were transmitted through the soil and their travelling times were obtained in the time domain. Results corresponding to wave path length to wavelength ratio greater than 3.0 were considered in the analysis. The comparison of test results with different soil conditions showed that small strain shear modulus increased with both suction and confining pressure.

1 INTRODUCTION

The shear modulus is recognized as an important design parameter of the soil and has been obtained through laboratory and field tests. Bender element technique is a relatively new alternative on laboratory tests, which has been increasingly used in Soil Mechanics due to the simplicity of obtaining the maximum shear modulus of the soil (Dyvik & Madshus 1985, Jovičić et al., 1996, Brignoli et al., 1996).

The maximum shear modulus is associated with small strains and is useful to evaluate the initial condition of geotechnical constructions, in general, and also the surroundings of loaded areas in the ground, where small strains occur (Burland 1989). When unsaturated soils are concerned, the induced strains are even smaller due to the higher stiffness provided by soil suction.

Investigations of small strain shear modulus of unsaturated soils using bender elements are still incipient, and few authors have been reported its relation with suction, as for example Marinho et al. (1995), Hoyos et al. (2008) and Nyunt et al. (2011). Marinho et al. (1995), testing a highly plasticity statically compacted clay, reports that the small strain stiffness increases up to a critical value of suction and that the peak value of stiffness is associated with the general air entry point of the specimen. Hoyos et al. (2008) investigated the influence of compaction-induced suction of clayey and sandy soils on small strain shear modulus (G_o) via bender elements and resonant column, noting considerable increase of G_o at the highest values of suction. Nyunt et al. (2011) show that the relationship between the small strain stiffness and matric suction of a compacted unsaturated sand is non linear. The range of soil suctions used in the tests was 0 to 20 kPa, while the net confining stresses varied between 50 and 100 kPa. In general, G_o increased at a faster rate with suction, up to the air entry value of the sand. The authors also report that for constant suction, G_o tends to increase almost linearly with net confining stress.

This paper deals with small strain stiffness measured using the bender element technique. Some preliminary test results of a compacted lateritic soil tested at saturated and unsaturated conditions are presented and discussed.

2 SOIL PROPERTIES

This study used a soil of colluvial origin which was subjected to a typical pedogenetic process of tropical areas termed laterization. The soil is clayey medium to fine sand, classified as SC, according to the Unified Soil Classification System. Other physical indices and properties are specific gravity of 2.64, liquid limit of 32%, plastic limit of 16%, maximum dry density and optimum moisture content from standard Proctor compaction of 1.80 g/cm^3 and 13.8%, respectively.

The preliminary tests were carried out on specimens compacted at 95% of the maximum dry density and at optimum moisture content. The soil-water retention curve defined on drainage path for this compaction condition is shown in Figure 1. The experimental data were obtained via porous plate funnel method (ASTM 2002) and filter paper technique (ASTM 2003). The experimental data

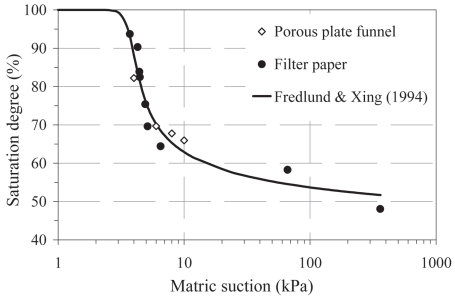

Figure 1. Soil-water retention curve.

were fitted using Fredlund & Xing (1994) model and the resulting fitting equation was

$$Sr = 33.6 + \frac{100 - 33.6}{\left\{\ln\left[e + (\psi / 3.617)^{12.718}\right]\right\}^{0.320}} \quad (1)$$

where *Sr* is the saturation degree in percentage and ψ is the matric suction in kPa.

As can be seen, this is a typical curve of sandy soil. Large part of desaturation takes place at relatively low suction variation, between 4 and 10 kPa. In accordance with the soil sandy nature and voids arising from the relatively low dry density, the air entry value of the soil is of the order of 4 kPa.

3 BENDER ELEMENT TESTS

Bender element technique is a non-destructive dynamic method of obtaining the small strain shear modulus of the soil. Basically, the bender elements work in pairs and each element consists of two thin piezoceramic plates rigidly bonded to a central metal plate with an epoxy resin coating. When subjected to a voltage signal, the opposite polarization of the piezoceramic plates produces bending in a direction normal to the plane of the element, which is a reversible function.

The bending movement of a bender element is capable of transmitting shear wave through soils. Then, placing a pair of bender elements at opposite sides of a soil sample, one transmits the shear wave that travels through the soil and is received by the other element. Both the input and output electrical signals associated to the shear wave are captured by oscilloscope, allowing the travel time to be obtained. The measurement of wave travel time leads to the shear modulus of the soil by simple calculation. As the maximum shear strain induced by this method is less than 10^{-5} (Dyvik & Madshus 1985), the shear modulus determined via bender element technique is the small strain or maximum shear modulus of the soil.

In this experimental program, tests on saturated and non-saturated specimens were performed with bender elements coupled to top caps and base pedestals of triaxial cells, where soil was allowed to consolidate under different isotropic stress levels.

3.1 *Specimens*

The soil specimens were dynamically compacted to reach 95% of the maximum dry density and optimum moisture content. Due to the availability of testing equipment, saturated specimens were 70 mm diameter and 140 mm height, while non-saturated specimens were 50 mm diameter and 100 mm height. Table 1 presents physical indices of specimens.

3.2 *Saturated test procedure*

On the saturated bender element test, backpressure was used to saturate the specimen and backpressure was continued until a B value larger than 95% was reached. After that, the sample was isotropically consolidated to the desired target consolidation stresses. In doing that, different loading conditions were applied to the specimen. The first loading path started at an effective isotropic stress of 10 kPa. In sequence the effective confining stress was raised in steps until 500 kPa. After that, the specimen was gradually unloaded in steps until 25 kPa, and then the specimen was reloaded and effective pressure reached 250 kPa.

At the end of each stage of consolidation, bender elements transmitted shear waves through the soil for later evaluation of soil stiffness at that specific stress state.

3.3 *Unsaturated test procedure*

Specimens tested under non-saturated condition followed a pre-test procedure to reach the target suction prior to testing. First, the specimens had suction reduced to zero by capillarity rising and then, target suctions of 50 and 100 kPa were

Table 1. Physical indices of the compacted specimens.

Soil condition at the test	ρ_d g/cm³	*w* %	*Sr* %	*e*
Saturated	1.700	13.9	66.4	0.553
Suction of 50 kPa	1.708	13.9	67.2	0.546
Suction of 100 kPa	1.711	13.9	67.6	0.543

ρ_d is the dry density, *w* is the moisture content, *Sr* is the saturation degree and *e* is the void ratio.

imposed in auxiliary chambers using the axis translation technique (Hilf 1956). Suction equilibrium was considered to be reached when the mass of the specimens leveled off.

The bender element tests comprised a suction equilibrium stage before consolidation, which intended to reestablish pressures that were disturbed during test assembly. The consolidation stages and propagation of shear waves followed the same procedure as described for the saturated test. Pore air and water pressures were kept constant throughout the unsaturated tests. A porous plate of 500 kPa air entry at base pedestal of the triaxial cell enabled suction to be controlled using axis translation.

3.4 *Shear wave and small strain shear modulus*

Several frequencies of shear waves were propagated through the soil at the end of each stage of consolidation. The input signal was chosen as sinusoidal pulses, in accordance with the suggestion of Viggiani & Atkinson (1995). The amplitude of the pulses was 14 V and the frequencies ranged between 1 and 16.7 kHz for the saturated soil and between 1 and 50 kHz for the unsaturated soil. The calculation of the small strain shear modulus (G_o) considered that soil behaves as an isotropic homogeneous elastic medium at small strains. For each confining pressure and frequency, G_o was determined using Equation 2:

$$G_o = \rho . V_s^2 \quad \text{with} \quad V_s = \frac{L}{t} \tag{2}$$

where ρ is the density of the soil; V_s is the shear wave velocity; L is the wave path length, taken as the distance between the tips of source and receiver bender elements (Dyvik & Madshus 1985, Viggiani & Atkinson 1995); and t is the shear wave travel time.

The main source of error on bender element tests is the subjectivity of the determination of the travel time used to calculate V_s (Jovičić et al., 1996). Several methods on time or on frequency domain have been used to infer t, as the first major deflection of the received signal, the peak of the transmitted signal and the first major peak of the received signal, the cross-correlation of both signals and the cross-power spectrum method. Nevertheless, there is no agreement among researchers about which is the most reliable method yet (Viggiani & Atkinson 1995, Leong et al., 2005, Arroyo et al., 2010, Chan 2010). Considering the preliminary nature of tests, in this paper, the wave travel time was taken as the first major deflection of the received signal, which is a straightforward method and contributes to the simplicity of the interpretation of bender element tests.

Other important aspect regarding the determination of the shear wave travel time is the quality of the received signals. These signals are affected by near-field effects, which can be minimized by choosing high excitation frequencies for the input pulses. The wave path length to wavelength ratio (L/λ) can be used as a guide to select the signal input frequency, where the wavelength may be estimated from the relation between V_s and the input frequency. Sanchez-Salinero et al. (1986) showed through numerical analysis that the near-field effects are not significant when the wave path length to wavelength ratio (L/λ) is greater than 2. Considering experimental investigations, Jovičić et al. (1996) confirmed this tendency, and Leong et al. (2005) concluded that L/λ of at least 3.33 is reasonable to improve the quality of the received signal.

4 RESULTS AND ANALYSIS

On the tests performed, the saturated specimen and the specimen under 100 kPa of suction followed the path of first loading, unloading and reloading, while the specimen under 50 kPa of suction experienced only the first loading path due to contretemps during the test.

From the results, the travel time was obtained by taking the first major deflection of the received signal, and the wave velocity was calculated. Figures 2 to 4 show the shear wave velocities plotted against the wave path length to wavelength ratio. In these figures a dashed line represents the lower limit of L/λ, chosen through analysis of the behavior of the curves. It can be noticed that beyond the value of 3.0 the curves show a tendency of increasing velocities, and forward, this property tends to stabilization. Therefore, the near-field effect is

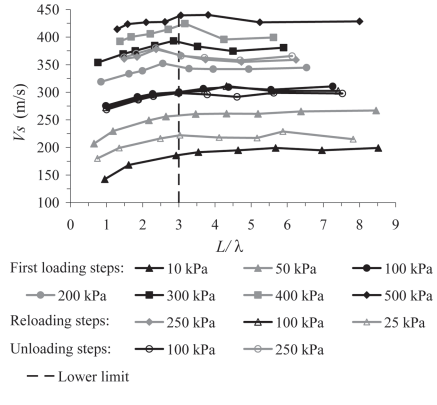

Figure 2. Shear wave velocity as a function of wave path length to wavelength ratio for the soil tested on saturated condition.

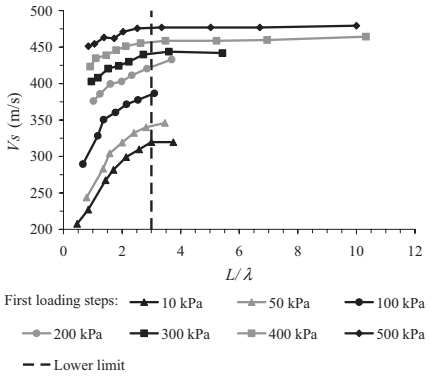

Figure 3. Shear wave velocity as a function of wave path length to wavelength ratio for the soil tested under suction of 50 kPa.

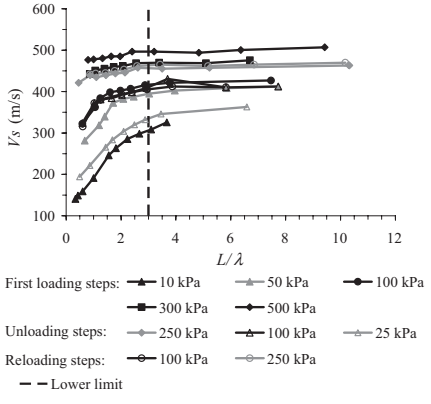

Figure 4. Shear wave velocity as a function of wave path length to wavelength ratio for the soil tested under suction of 100 kPa.

probably affecting the analysis of signals with corresponding L/λ minor than 3.0. Such behavior is more pronounced on unsaturated soils under small loadings, i.e. on relatively stiff soils. Based on these evidences, the maximum shear modulus of the soil in each stress state was computed as the average of V_s with the associated L/λ greater than 3.0.

Figure 5 presents the variation of V_s with confining stress on the first loading path. For all the soil conditions, shear wave velocities exhibit the same trend of increasing until 100 kPa of confining pressure and follow towards constant values after that. Additionally, the influence of suction on increasing V_s can be observed. In general, it has been reported that shear wave velocity tends to increase with net confining pressure and with soil suction. In this sense, the test results of saturated specimens shown in Figure 5 are in accordance

Table 2. Small strain shear moduli from bender element tests.

Isotropic stress at the loading path (kPa)	G_o (MPa) on soil condition		
	Saturated	Suction of 50 kPa	Suction of 100 kPa
First loading			
10	79	196	203
50	144	230	317
100	195	286	342
200	245	359	–
300	301	376	427
400	347	406	–
500	399	437	481
Unloading			
250	272	–	406
100	194	–	334
25	102	–	240
Reloading			
100	185	–	324
250	276	–	416

with the results of Brignoli et al. (1996) who tested saturated sand and clays. The non-saturated specimens, compared with the test results of sand (Nyunt et al., 2011) show larger shear wave velocities what seems logical, considering the suctions used in the present tests.

Table 2 summarizes the maximum shear moduli obtained from the tests, which varied from 79 to 481 MPa. Examining the data, it can be readily noticed that G_o increases with loading and suction, as expected. Besides, on each soil condition, the moduli show quite close values for the same loading pressures, independently of the loading path concerned. This suggests that G_o was barely affected by the stress path. However, this must be confirmed by additional tests.

In order to better analyze the influence of confining stress on soil stiffness, data of small strain shear modulus at first loading stages were plotted against effective or net confining stresses.

The curves obtained when linear scale was used are similar in shape to the curves presented in Figure 5. However, the experimental points show alignment using logarithmic scale, as can be seen in Figure 6, and a potential fit may be made for each soil condition. Equation 3 shows the fitted equation and Table 3 reports the constants resulting from the fits.

$$G_o = a.\left(\sigma_3 - u_a\right)^b \tag{3}$$

where G_o is in MPa, $(\sigma_3 - u_a)$ represents both effective or net confining stress in kPa, and a and b are the constants of the potential fit.

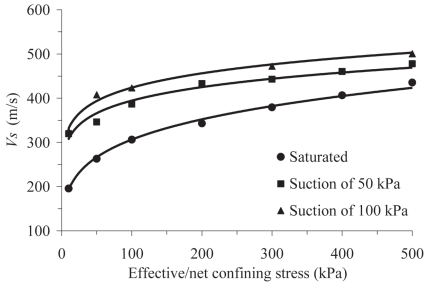

Figure 5. Variation of the shear wave velocity with confining stress on the first loading path.

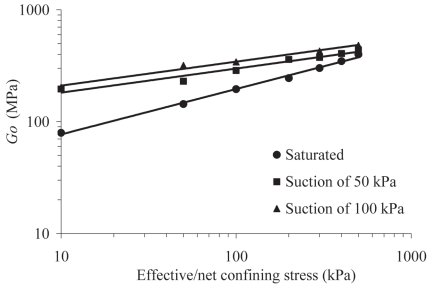

Figure 6. Variation of the small strain shear modulus with confining stress on the first loading path.

Table 3. Constants of the potential fits.

Soil condition	a	b	r^2
Saturated	30.2	0.406	0.99
Suction of 50 kPa	100.7	0.215	0.96
Suction of 100 kPa	128.3	0.214	0.98

The constant b indicates the inclination of the curves and according to Table 3, it is greater for the saturated condition than for the non-saturated condition. This suggests that the non-saturated soil is less suitable to changes in G_o due to changing in the net confining stress when compared to the saturated soil. Such behavior can be attributed to the rigidity of soil skeleton that has arisen from suction.

The influence of suction on the increment of soil stiffness can also be observed in Figure 7. Data show that G_o continuously increase with suction within the suction range tested, which is in accordance with the results of Hoyos et al. (2006).

Nyunt et al. (2011) found non-linear relationship between maximum shear modulus and matric suction while testing sand. The changing point was near the air-entry value of the soil. In the test results here reported, this possible behavior of the soil could not be confirmed. Probably, the reason for that is the suction range used in these preliminary tests, since the lower soil suction used was 50 kPa, which is larger than the soil air entry value. Additional tests are underway and will help to elucidate this point.

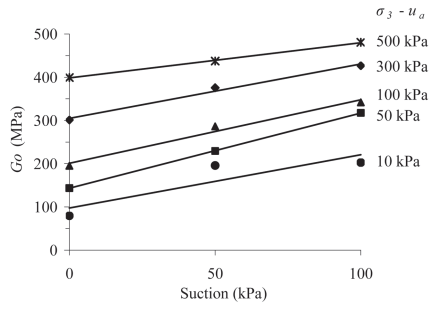

Figure 7. Variation of the small strain shear modulus with suction on the first loading path.

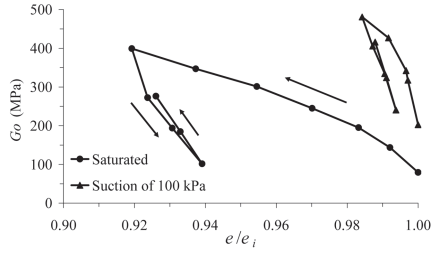

Figure 8. Variation of the small strain shear modulus with the relation between void ratio and initial void ratio.

In analyzing the data of Table 2 and Figure 7 it is possible to verify that the soil suction is more effective in increasing the small strain stiffness when compared to the net confining stress. For instance, considering the tests with net confining stress of 100 and 300 kPa, this increase of confining stress results in an increase of about 50% in the shear moduli, while an increase of 100 kPa in the suction results in almost the same increase in the shear moduli. That is, to obtain shear modulus of the same order of magnitude it is necessary to apply an increment of net confining stress that must roughly be twice the increment of soil suction.

Figure 8 shows how G_o varied with void ratio on the tests with saturated soil and soil with 100 kPa of suction. The change in void ratio can be observed through the relation between void ratio and initial void ratio of the specimens. Arrows were used to indicate the followed path.

Maximum void ratio changes were registered on the first loading path, and were of 8.1% for saturated soil, while for soil under suction this value corresponded to 1.6%. These results indicate that volume change on the unsaturated soil was small and more difficult to measure in comparison to the saturated soil. During unloading and reloading, less void ratio variation happened. However, the shear modulus continued to vary and suffered little influence of reloading after unloading.

5 CONCLUSION

This paper presented results of tests performed on saturated and unsaturated compacted sandy soil using the bender element technique. These are preliminary data from a research that has been carried out at the University of Sao Paulo.

Bender elements were associated to triaxial cells and proved to be a simple method to obtain the small strain shear modulus of the soil.

Experimental results showed that a wave path length to wavelength ratio greater than 3.0 provided almost constant values for shear wave velocities and matched values suggested by other authors. Thus, it was considered appropriated to determine the shear wave velocity for saturated and non-saturated soil specimens.

Small strain shear modulus showed tendency to increase with confining pressure and also suction. While shear modulus *versus* confining pressure were plotted in logarithm scale and fitted to potential curves, shear modulus *versus* suction showed linearity in linear scale. Analysis of data indicated that the small strain shear modulus suffers negligible interference of the stress path. Furthermore, soil stiffness has shown to be more influenced by an increment of suction than by the same increment of confining pressure.

ACKNOWLEDGEMENTS

The authors acknowledge CAPES (Coordenação de Aperfeiçoamento de Pessoal de Nível Superior) and FAPESP (Fundação de Amparo à Pesquisa do Estado de São Paulo) for the financial support given to this research.

REFERENCES

Arroyo, M., Pineda, J.A. & Romero, E. 2010. Shear wave measurements using bender elements in argillaceous rocks. *Geotechnical Testing Journal* 33(6).

ASTM. 2002. Standard test methods for determination of the soil water characteristic curve for desorption using a hanging column, pressure extractor, chilled mirror hygrometer, and/or centrifuge—D6836. In *Annual Book of ASTM Standards, Vol. 04.09*. West Conshohocken: American Society for Testing Materials.

ASTM. 2003. Standard test method for measurement of soil potential (suction) using filter paper—D5298. In *Annual Book of ASTM Standards, Vol. 04.09*. West Conshohocken: American Society for Testing Materials.

Brignoli, E.G.M., Gotti, M. & Stokoe, K.H.II. 1996. Measurement of shear waves in laboratory specimens by means of piezoelectric transducers. *Geotechnical Testing Journal* 19(4): 384–397.

Burland, J.B. 1989. Ninth Laurits Bjerrum Memorial Lecture: Small is beautiful—the stiffness of soils at small strains. *Canadian Geotechnical Journal* 26(4): 499–516.

Chan, C.-M. 2010. Bender element test in soil specimens: identifying the shear wave arrival time. *Electronic Journal of Geotechnical Engineering* 15(M): 1263–1275.

Dyvik, R. & Madshus, C. 1985. Laboratory measurements of G_{max} using bender elements. In V. Khosla (ed.), *Advances in the art of testing soil under cyclic loading; Proc. Annual Conv. ASCE, Detroit*. New York: American Society of Civil Engineers.

Fredlund, D.G. & Xing, A. 1994. Equations for the soil-water characteristic curve. *Canadian Geotechnical Journal* 31(3): 521–532.

Hilf, J.W. 1956. *An investigation of pore-water pressure in compacted cohesive soils.* PhD Thesis, Faculty of Graduate School of the University of Colorado, Denver.

Hoyos, L.R., Takkabutr, P., Puppala, A.J. & Hossain, M.D.S. 2008. Dynamic response of unsaturated soils using resonant column and bender element testing techniques. In D. Zeng, M.T. Manzari & D.R. Hiltunen (eds), *Geotechnical Earthquake Engineering and Soil Dynamics IV; Proc. conf., Sacramento, 18–22 May 2008*. Reston: American Society of Civil Engineers.

Jovičić, V., Coop, M.R. & Simić, M. 1996. Objective criteria for determining G_{max} form bender element tests. *Géotechnique* 46(2): 357–362.

Leong, E.C., Yeo, S.H. & Rahardjo, H. 2005. Measuring shear wave velocity using bender elements. *Geotechnical Testing Journal* 28(5).

Marinho, F., Chandler, R. & Crilly, M. 1995. Stiffness measurements on an unsaturated high plasticity clay using bender elements. In E.E. Alonso & P. Delage (eds) *1st International conference on unsaturated soils; Proc. int. conf., Paris, 6–8 September 1995.* Rotterdam: Balkema.

Nyunt, T.T., Leong, E.C. & Rahardjo, H. 2011. Strength and smaal-strain stiffness characteristics of unsaturated sand. *Geotechnical Testing Journal* 34(5).

Sanchez-Salinero, I., Roesset, J.M. & Stokoe, K.H.II. 1986. *Analytical Studies of body wave propagation and attenuation.* Report No. GR 86-15. Austin: Civil Engineering Department, University of Texas at Austin.

Viggiani, G. & Atkinson, J.H. 1995. Interpretation of bender element tests. *Géotechnique* 45(1): 149–154.

Advances in Unsaturated Soils – Caicedo et al. (eds)
© 2013 Taylor & Francis Group, London, ISBN 978-0-415-62095-6

Swelling behavior of expansive clays incorporating mineralogy and pore size distribution via SWCC

A. Pedarla, A.J. Puppala & L.R. Hoyos
Civil Engineering Department, University of Texas at Arlington, Texas, USA

ABSTRACT: Understanding the behavior of expansive soils with moisture content provides useful information. However, swell properties of these clays are dependent on both pore size distribution and clay mineralogy, which was the major focus of this research. Information regarding micro fabric structure of compacted soils was obtained with Mercury Intrusion Porosimetry (MIP). Two expansive clayey soils having different mineralogy and basic soil parameters were selected as test soils. Soil-water characteristic curves were obtained using pressure cell and filter paper test methods. On companion specimens, MIP studies were also conducted to determine the variations of fine and coarse pores in the tested soil specimens. Test results showed that the swelling behavior of soils was equally influenced from percent expansive clay mineral and pore size distribution. This signifies the importance of including fabric details in better swell characterization.

1 INTRODUCTION

Expansive soils are quite unstable and cause damage to the structures overlying them due to their volume changes. The swell shrink behavior of expansive soils causes damages to structures that are much higher than the damages caused by other natural disasters like earthquakes and floods (Jones & Holtz 1973). The behavior of these fine grained soils is better understood with their type of constituent mineral and the pore size distribution. The seasonal moisture variation of the field governs the expansive soil behavior (Nelson & Miller 1992).

This unsaturated behavior of expansive soil makes it very problematic to measure the actual pore space. The moisture absorption characteristic of a soil is mainly dependent on the pore size distribution, suction and mineralogy of a soil (Mitchell 1993). Hence it is important to study both pore size distribution and clay mineralogy in better understanding the soil behavior.

1.1 *Background*

Aung et al. (2001) conducted research on Singapore residual soils and compared soil-water characteristic curve (SWCC) with soil-air characteristic curve (SACC) obtained from the pore size distribution studies. Results showed a close resemblance between these two curves. In a study conducted by Simms & Yanful (2002), predictions of the SWCCs using pore size distributions (PSD) measured both before and after the SWCC tests significantly under-predicted the values when compared to measured values from mercury intrusion porosimetry test.

Rao & Revanasiddappa (2005) studied undisturbed and remolded soils and conducted suction and MIP tests. They concluded that the matrix suctions of the undisturbed and remolded residual soil specimens are greatly influenced by the relative abundance of the inter-aggregate porosity and intra-aggregate porosity.

Zhang & Li (2010) conducted MIP tests on coarse grained soils and found that soils having coarse contents larger than 70% are considered to have coarse controlled structures. Also, it was found out that the predicted SWCC from MIP tests was in good accordance with the measured SWCC for fine grained soils. Cui & Tang (2011) studied pore structures of different soils using MIP and Scanning Electron Microscope (SEM) devices and studied the micro and macro mechanisms of land subsidence caused by a high-rise building group.

Chittoori & Puppala (2011) used basic soil properties like total potassium (TP), specific surface area (SSA) and cation exchange capacity (CEC) to predict the expansive clay mineral contents in a soil. Predictions of test results are in good agreement with the known standard values.

The present research targets the effects of clay mineralogy, moisture content and pore size distribution on expansive clays behavior. These three parameters are in turn dependent on each other. SWCC

frame work is used to explain all these parameters and their influence on overall swell behavior.

2 EXPERIMENTAL STUDY

Two expansive clays were selected for the present research study. These soils were selected from two different regions having different geological formations and distinct behavior.

2.1 *Basic soil tests*

Standard laboratory tests were conducted on both the soil specimens in order to identify their behavior. The optimum moisture content and dry density properties were determined using Standard Proctor Test and these results are summarized in Table 1.

The mineralogy of the soil was identified with the help of standard procedure based on CEC, SSA and TP contents (Chittoori & Puppala 2011, Pedarla et al. 2012). The soil from Texas was classified as fat clay which comprises of 60% of Montmorillonite and Illite (expansive clay minerals) in its clay fraction. The soil from Oklahoma was low compressible lean clay but exhibited a higher content of both Montmorillonite and Illite (90%).

2.2 *Macro swell behavior*

Soils used in the present research were pulverized after oven drying and allowed to pass through U.S. No. 40 sieve. Soil specimens were compacted to 25 mm height and 62.5 mm in diameter at their OMC—MDD condition. The specimens were compacted statically at a strain rate of 2.27 mm/min. Prepared samples were then transferred to the consolidation setup. The samples were then tested for swell strains at an overburden load of 7 kPa (ASTM D4546–08). Figure 1 shows the variation of maximum 1D vertical swell with elapsed time.

The maximum vertical swell strain exhibited by the Texas soil was 9.3%, whereas Oklahoma soil exhibited a vertical swell strain of 4.4%. It was observed that though Oklahoma soil exhibited higher amounts of expansive minerals, the swell strains are less when compared to the same of Texas soil. Reason for this behavior is explained in the later sections.

Table 1. Basic soil characterization.

Property	Texas soil	Oklahoma soil
Liquid limit, w_L (%)	55	41
Plasticity index, w_P (%)	37	21
USCS classification	*CH*	*CL*
% passing U.S. Sieve No. 200	92	90
Specific gravity, G_s	2.72	2.83
% Montmorillonite & Illite	60	90
Maximum dry density, MDD (Mg/m^3)	1.64	1.59
Optimum moisture content, OMC (%)	17	24

2.3 *SWCC measurements*

Replicate samples compacted as specified before were used in suction studies. Soil-water characteristic curve (SWCC) was measured using a pressure cell apparatus at low matric suction range and filter paper technique at high matric suction range. The pressure cell apparatus with a 500 kPa ceramic plate was used for measuring the SWCC following the drying path in the suction range of 0 to 500 kPa (ASTM D6836-02). The filter paper technique (ASTM D5298-10) was then used for measuring the matric suction for a range of 500 to 10,000 kPa. For this technique, Whatman No. 42 filter paper was used in the present experimental program.

Figure 2 shows the SWCCs measured for the suction range of 0 to 10,000 kPa. At select suction cycles, the specimen dimensions were measured. The volumetric changes measured were then determined and applied to the calculations of volumetric water contents corresponding to the respective values of suction pressures.

The change in volume is predominant in expansive clays during application of suction conditions which alters the volumetric water content in the compacted soil specimens. Hence forth, care is taken to measure the volumetric changes during SWCC studies.

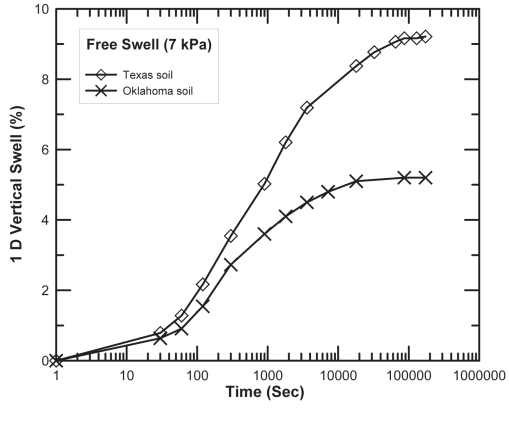

Figure 1. 1-D vertical swell response from both test soils.

2.4 *Mercury intrusion porosimetry studies*

Mercury Intrusion Porosimetry (MIP) is based on the premise that a non-wetting liquid will only intrude capillaries under particular pressure. MIP method for measuring pore size distribution of porous solids was first proposed by Washburn (1921). In order to interpret pressure values, the pressure is usually converted into equivalent pore radii by applying the following Washburn (1921) equation (1):

$$r = -2r\cos\theta/\mathrm{p} \quad (1)$$

where θ is the contact angle between the mercury and a surface of the solid material tested and r is the surface tension of mercury. The mercury was intruded into the sample tube under the vacuum condition. The low pressure analysis was conducted which is preceded by the high pressure analysis $\psi_a = 150$ kPa.

The test samples were prepared at their maximum dry densities. A sample of 5 mm size was carefully cut from the soil specimen and was tested for MIP. Replicate specimens from matric suction measurement are freeze dried. The soil specimens are dried completely in order to study the pore distribution at that state. The pore distribution of the soil specimen varies with moisture content which is in turn influenced by the mineralogy of the soil. Hence, the present research studies the pore distribution of the soil specimen at its initial dry state.

The volume of mercury forced in to the specimen after each increment was automatically recorded. Each pressure increment pushes mercury into the accessible soil pores of a diameter larger than or equal to that calculated by the Washburn (1921) equation for the given pressure. The extrusion curve does not coincide with the intrusion curve because there is some mercury retained in the pores of soils.

3 LINKING SWELL POTENTIAL WITH PORE STUDIES

The variation of total pore volume for a given pore radius is presented in Figure 4. The pores corresponding from 6 to 60 μm are classified as coarse pores. Pores from 0.01 to 6 μm are classified as medium pores and the pores from 0.01 μm to 0.002 μm are regarded as fine pores. The total volume corresponding to the pores at that pore size is calculated and presented in Table 2. Figure 3 shows the variation of pore size for both the soil specimens.

Texas soil exhibits a lower total pore volume of 14.8 cm^3/g when compared to Oklahoma soil which is 18.4 cm^3/g.

The distribution of pore size is a governing parameter for the hydraulic conductivity of the

Table 2. Summary of test results.

Property	Texas soil	Oklahoma soil
1-D swell (%)	9.3	4.4
Air-entry value ψ_a (kPa)	150	80
Saturated water Content (%)	36	27
Average pore diameter (μm)	0.0306	0.022
Micro Pore vol. (%)	18	26
Medium Pore vol. (%)	60	64
Total pore volume (cm^3/g)	14.8	18.4
Pore gradation	Uniform/well	Gap

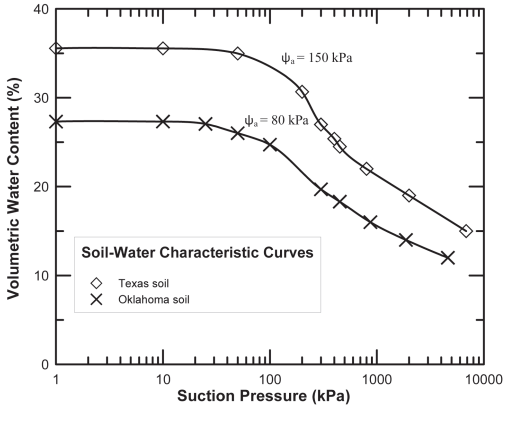

Figure 2. Soil-water characteristic curves for Texas and Oklahoma soils. (ψ_a – Air entry pressure).

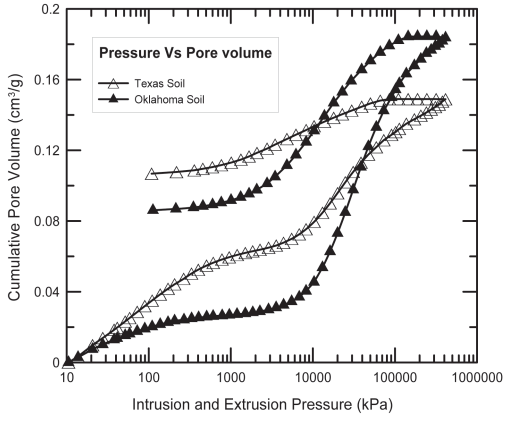

Figure 3. Patterns of intrusion and extrusion of mercury from both soil specimens.

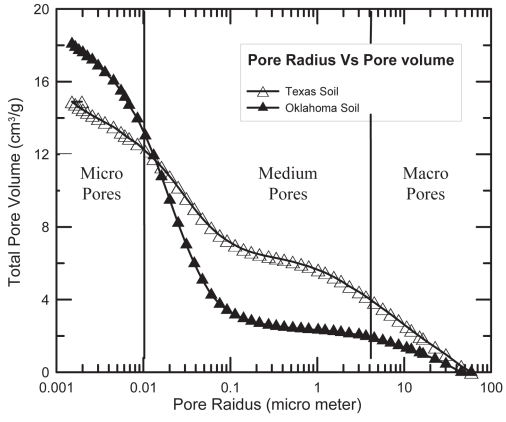

Figure 4. Variation of total pore volume with pore radius.

soil medium. Figure 4 shows that the pore sizes for Texas soil are more uniform and well distributed when compared to the Oklahoma soil. The majority of pore volume for Oklahoma soil is concentrated between 0.01 to 0.1 µm. This uneven distribution of pore radius curve leads to lack of interconnectivity between pore radii in Oklahoma soil and influenced moisture distribution across the soil specimen. Hence it can be stated that due to uniform pore gradation and lesser micro pore sizes, Texas soil will have more open fabric and hence has higher moisture movement within the soils. This explains the reasons for Texas soil to exhibit high swelling potential than the Oklahoma soil which contains gap graded type of pore distribution and higher micro pore volume. Consequently this resulted in less heaving in the Oklahoma soil.

4 SUMMARY AND CONCLUSION

Two expansive clays were selected for the present study. After the basic soil testing it was concluded that Texas soil was fat clay having more swell strain than Oklahoma soil. Oklahoma soil exhibited more expansive mineral content than Texas soil. However, macro swell tests showed that Texas soil samples experienced larger swelling.

SWCC measured along the drying path of the specimens revealed the variation of air entry value and saturated moisture contents between these soils. The higher moisture capacity for Texas soil is attributed due to the uniformly graded pores and lesser micro pores which have allowed for more moisture access to clay minerals in the compacted specimens. This results in larger swelling in Texas soils.

Overall, the results here indicate that the clay mineralogy and pore distribution are needed to understand the swelling capacities of sub-soils. The present research is limited to two expansive soils. Hence, research on more soils is required to determine the effects of pore space distribution on swelling behavior of expansive clays.

ACKNOWLEDGEMENTS

The authors would like to acknowledge National Science Foundation (Program Director: Dr. Richard J. Fragaszy) for supporting this research under NSF Grant No.1031214. Authors would also acknowledge the support of Dr. Qinhong Hu from Department of Earth and Environmental Sciences for allowing the use of MIP device for the present studies. Any findings, conclusions, or recommendations expressed in the present material are those of the authors and do not necessarily reflect the views of NSF.

REFERENCES

Aung KK, Rahardjo H, Leong EC & Toll DG (2001). Relationship between porosimetry measurement and soil water characteristic curve for an unsaturated residual soil, Geotechnical and Geological Engineering, 19:401–416.

Chittoori BCS & Puppala AJ (2011). Quantitative estimation of clay mineralogy in fine grained soils, *Journal of Geotechnical and Geoenvironmental engineering*, 137(11):997–1008.

Cui Z & Tang Y (2010). Microstructures of different soil layers caused by the high-rise building group in Shanghai, *Environmental Earth Sciences*, 63:109–119.

Jones DE & Holtz WG (1973). Expansive soils-the hidden disaster, *Civil Engineering*, ASCE, 43, pp. 49–51.

Mitchell JK (1993). Fundamentals of soil behavior. John Wiley & Sons, New York.

Nelson DJ & Miller DJ (1992). Expansive Soils, Problems and Practice in Foundation and Pavement Engineering. New York: John Wiley and Sons Inc.

Pedarla A, Puppala AJ, Chittoori BS, Hoyos LR, Zapata C & Houton SL (2012). Influence of Mineral Montmorillonite on soil suction modeling parameters, GeoCongress 2012, 1126–1135.

Pedarla A, Puppala AJ, Hoyos LR, Vanapalli SK & Zapata C (2012). SWRC Modeling Framework for evaluating volume change behavior of expansive soils, Unsaturated soils: Research and Applications, 3:221–228.

Rao SM & Revanasiddappa K (2005). Role of micro fabric in matricsuction of residual soils, *Engineering Geology*, 80: 60–70.

Simms PH & Yanful EK (2002). Predicting Soil water characteristic curves of compacted plastic soils from measured pore size distributions, *Geotechnique*, 52(4):269–278.

Washburn EW (1921). Note on a method of determining the distribution of pore sizes in a porous material. Proceedings of the *National Academy of Sciences* 4:115–116.

Zhang LM & Li X (2010). Microporosity structure of coarse granular soils, *Journal of Geotechnical and Geoenvironmental Engineering*, 135(10):1425–1436.

Advances in Unsaturated Soils – Caicedo et al. (eds)
© 2013 Taylor & Francis Group, London, ISBN 978-0-415-62095-6

Drying-wetting tests on sand—silt mixtures: Impact of volumetric changes on the retention curves

M. Morvan
Institut Pascal UMR 6602, Polytech Clermont-Ferrand, Université Blaise Pascal, Clermont-Ferrand, France

D. Branque, H. Wong & B. Colin
Département Génie Civil et Bâtiment, Ecole Nationale des Travaux Publics de l'Etat, Université Lyon I, France

ABSTRACT: This paper presents the first results of a comprehensive experimental program with the objective to characterize the retention properties of sand–silt mixtures, and particularly to investigate the impact of volumetric changes on the retention curves of these materials. During our tests carried out with a suction-controlled oedometer cell, the samples are subjected to drying and wetting paths under null total stress. To control suction, the axis translation technique, is used. Volumetric variations of the samples are measured continuously during drying-wetting cycles. Samples with different proportions of sand and silt and different initial void ratios are tested. Influence of the proportion of silt on the volumetric changes and on the retention curve is studied, followed by the influence of the initial void ratio on the retention curves. Moreover, effects of volume change during loading are also analyzed.

1 INTRODUCTION

The Department of Civil Engineering of ENTPE has been performing theoretical and experimental research on partially saturated soils since several years. The objective is to develop a data base and computational tools capable of simulating the hydromechanical behavior of unsaturated geomaterials (soils or soft rocks) taking into account complex hydro-mechanical loading paths that can be encountered in practice.

Within the framework of this research, Pereira et al. (2005) first proposed a general methodology to take into account suction effects in constitutive models originally developed for dry or saturated soils. Based on this work, Morvan et al. (2009) subsequently developed a constitutive model of unsaturated soils based on the concept of "Bounding Surface Plasticity" (Dafalias et al., 1986). This model, with thirteen parameters, well-adapted to the case of sandy and silty soils, has shown its ability to reproduce a number of interesting features not treated so far by other existing models (post-peak softening, evolution from contractant to dilatant behavior during undrained shearing, gradual transition from purely elastic to elastic-plastic behaviour). In a third stage, Morvan et al. (2011) have introduced additional mechanisms in this model in order to account for hysteretic effects which appeared during or drying-wetting cycles.

While the validation of these models requires necessarily the confrontation with reliable and complete experimental data (in regard to the range of loading paths tested), we were quickly confronted with the lack of data in this domain of our theoretical work. This deficiency arises from the fact that laboratory characterization of partially saturated soils requires unconventional experimental equipment and exceptionally long durations of time to perform.

This lack of experimental data concerns in particular the phenomena of hydric irreversibility usually associated with hysteresis effects occurring during drying-wetting cycles, and their coupling to mechanical irreversibility, especially related to volumetric variations. This high degree of hydro-mechanical coupling in unsaturated soils has in particular been demonstrated experimentally by Sun et al. (2007). Indeed, in addition to exerting an influence on the mechanical behavior, the retention curve itself is conversely influenced by variations in porosity. From the point of view of modeling, some authors (Sun et al., 2007a, Sun et al., 2008, Khalili et al., 2008, Nuth et al., 2008a) assume that the retention curve is translated by an amount depending on the change of void ratio.

This lack of experimental data motivated the development of a set of laboratory equipment in ENTPE to study the hydromechanical coupling in partially saturated soils. In particular, a set of oedometric cells and a trixial cell, both with

suction control using axis translation technique, were developed. This paper presents the results and analyses of the first tests performed with the oedometric cell, by applying drying-wetting cycles on sand–clay mixtures with different clay contents and different void ratio.

2 EXPERIMENTAL DEVICE AND PROCESS

2.1 *Experimental device*

The oedometer used in our tests is based on Fredlund SWCC device (Padilla et al., 2005, Perez-Garcia et al., 2008). This apparatus is schematically presented in Figure 1, where suction is imposed by axis-translation technique. To achieve this, the base of the oedometer is equipped with a removable porous stone with high air-entry suction (100 kPa or 500 kPa according to the material studied). Being voluntarily kept at full saturation, the porous stone guarantees the continuity between water contained in the soil sample and water inside the pressure-volume controller. The latter device which allows to impose water pressure on the porous stone has the following characteristics: maximum pressure (1500 kPa), precision of pressure (± 0.5 kPa), maximum volume (180 cm^3), accuracy of volume measurements (1 mm^3). In parallel, air pressure is imposed on the entire volume inside the cell using a circuit of pressurized air regulated using a pressure regulator with a precision of 0.1 kPa.

The soil sample to be tested is mounted in a rigid cylinder with a height of 20 mm and a diameter of 70 mm, and placed on the porous stone. Only the axial strain parallel to the axis of the cylinder is allowed, the radial strain being inhibited by the rigid cylinder. Its upper face is in contact with the piston of the cell by which a uniformly distributed vertical load is applied on the soil sample. The guiding rod of the piston passes through the cover of the cell while ensuring water-tightness, and has a system for compensating air pressure in order to prevent any uplift of the loading device due to increasing air pressure in the cell.

The vertical displacement of the piston is measured using a LVDT sensor with a maximum stroke of 5 mm. The command of the pressure—volume controller for water and data acquisition (air and water pressures imposed, water volume exchanged, vertical displacement of the piston) are ensured by an automatic computerized system.

2.2 *Materials tested*

To this date, two experimental campaigns to study the hydromechanical couplings in partially saturated soils during drying-wetting cycles have been performed with this device. The first was conducted on a reference sand (Hostun S28 sand) and the second on a mixture of sand (Hostun S28 sand) and clay (kaolin powder) with a clay mass content of 10%. The grain size distribution of these two materials is presented in Figure 2.

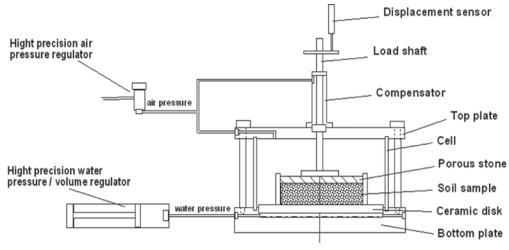

Figure 1. Schematic representation of the suction-controlled oedometer cell developed in ENTPE.

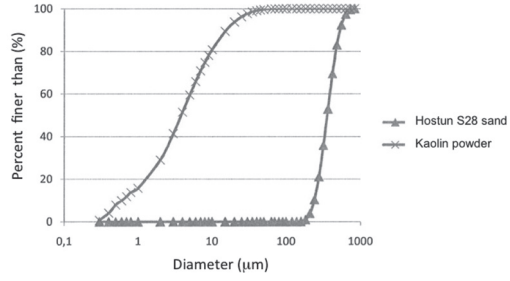

Figure 2. Grain size distribution of Hostun S28 sand and kaolin powder.

Two tests were conducted on pure sand, each with a different density: one loose (Dr = 39% corresponding to a void ratio e = 0.85) and one dense (Dr = 70%, e = 0.74), to study the translation of retention curve due to change of initial density. For both tests, the samples were prepared by pluviation of dry sand. Two different drop heights were used to obtain the targeted densities.

In the case of sand–clay mixture, two drying-wetting tests were performed on specimens with comparable void ratios: 0.71 and 0.72. Beforehand, a protocol for sample preparation in order to ensure their homogeneity and reproducibility was developed. In this protocol, the sand and kaolin powder (10% of the dry mass of the mixture) are initially mixed and then moistened to a water content of 6.5% (the optimum Proctor of the mixture being obtained at a water content of 11%). The wet mixture is then compacted by layer inside a Proctor mold. The soil sample to be tested is then extracted

using the ring oedometer and is then placed in the oedometer cell.

2.3 *Preliminary modeling*

For each of these tests, a preliminary simulation was performed to determine the shape of the retention curve and the order of magnitude of the air-entry suction in order to optimize the increments of suction to be imposed hence the test duration. The analytical model used in this preliminary simulation is the modified model of Kovacs (MK Model, Aubertin et al., 2003). This model was chosen because it is suitable for granular materials and it takes into account the influence of physical parameters (liquid limit, void ratio) on the retention curve. Using this model, we obtain for the Hostun S28 sand an estimated value of the air-entry suction about 1 kPa thus at the limit of the precision of measurement of our equipment. For the sand-clay mixture studied, air-entry suction is estimated to be about 30 kPa (Fig. 3), which is fully consistent with the characteristics of the experimental setup used.

2.4 *Testing procedure*

Firstly, the porous stone is saturated with water. To achieve this, it is placed on the oedometer cell and then subjected to a circulation of deaerated water using the pressure-volume controller of water at a pressure of about 10 kPa. The porous stone is turned over several times during this procedure. The soil sample is then put into contact with the porous stone and is then saturated with a slow and ascending circulation of water in the oedometer cell. After full saturation, the drying-wetting test can begin. Different levels of suction are imposed by steps by increasing the air pressure while keeping a constant water pressure (usually set at 10 kPa). The test duration for each level of suction depends on the time required to reach equilibrium for the water exchange between the controller and the sample. In our tests, equilibrium is considered to be attained when no change in the volume of water contained in the sample is observed for three straight hours.

Once the drying phase is completed, a wetting phase is imposed by step-wisely decreasing the air pressure. At the end of the test, the cell is demounted and the entire sample is recovered to measure its water content and void ratio. Note that the full test, comprising a drying and wetting cycle, lasts about two months. Figure 4 presents the raw measurements of air pressure and volume of water exchanged at one of the drying-wetting tests on sand. We can thus visualize the different steps of suction increments

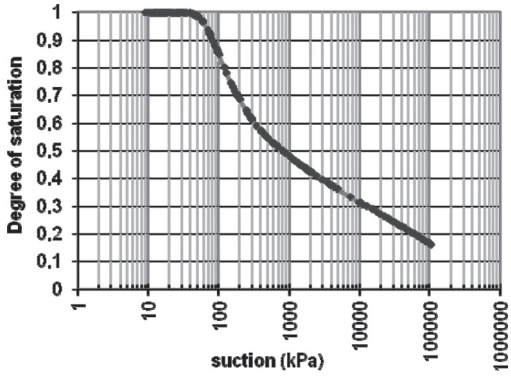

Figure 3. Retention curve of the sand–silt mixture computed with the modified Kovacs model.

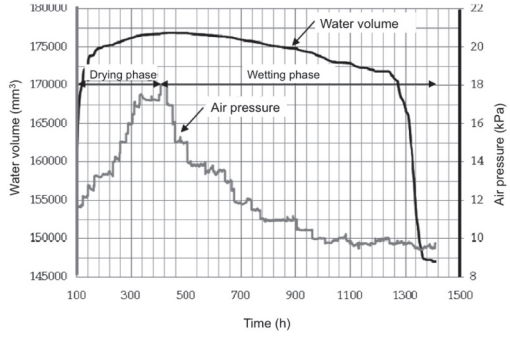

Figure 4. Examples of steps of imposed air pressure and volume of water exchanged during a drying-wetting test on sand.

imposed (water pressure is kept constant and equal to 9.5 kPa).

3 TESTS ON SAND

3.1 *Tests on loose sand*

Figure 5 shows the drying-wetting curve obtained for loose sand (Dr = 39%). This presents a classic form where the branch corresponding to the drying phase is above that obtained during wetting. To obtain the same degree of saturation, one needs a higher suction during drying than during wetting. The material studied presents only a small hysteresis between the wetting and the drying curves. This may result from the loose state of the sand studied and its narrow grain size distribution which favors a uniform pore size.

Figure 5 also shows the very good capacity of the experimental device to accurately measure a very low air-entry suction (in the order of 1 kPa for loose sands) as well as a very low residual suction

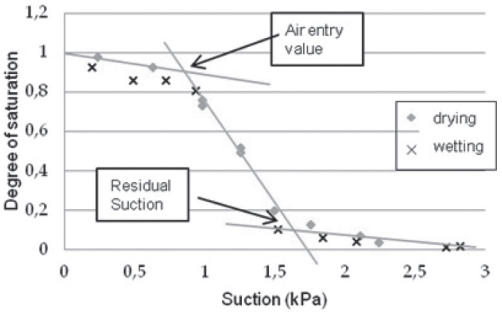

Figure 5. Retention curve of loose Hostun S28 sand obtained during our tests.

(in the order of 1.5 kPa for the material studied). Note that these measurements are possible thanks to the use of a high-precision (less than 100 Pa) air pressure regulator.

3.2 *Tests on dense sand*

Figure 6 shows the retention curve obtained in the case of Hostun sand in the dense state (Dr = 70%) during a drying-wetting cycle. Contrary to the case of loose sand, this figure shows a strong hysteresis between wetting and drying phases, which seems to reflect a higher dispersion of pore size. Note however that the air-entry suction measured on dense sand (of the order of 1.5 kPa) is close to that measured on loose sand. The air-entry suction therefore appears little influenced by the density of the granular material studied in this paper.

3.3 *Comparison of two densities*

Figure 7 compares the retention curves of Hostun S28 sand obtained for a drying path for both densities studied. It shows that the retention curve of the granular material is significantly influenced by the initial density of the sample. In our case, this difference is especially important for suctions above the air-entry value. Indeed, if the measurements obtained tend to confirm the logarithmic dependence of the degree of saturation on suction during drying, they also show that this dependence (slope of the drying curve) is also influenced by the state of initial density of the material. Hence, due to the presence of smaller pores in a dense material, it seems logical that a higher suction is necessary to drain this sample than in the case of loose material.

3.4 *Comparison of saturation degree*

For classic experimental design, either water volume or water mass exchanges are measured which would then allow to deduce changes in water

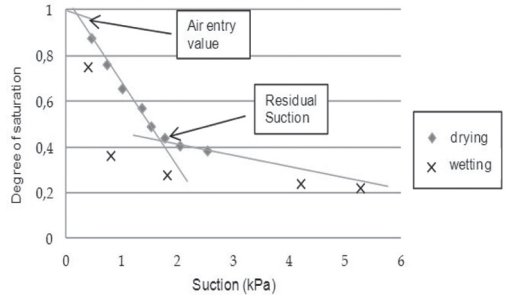

Figure 6. Retention curve of dense Hostun S28 sand obtained during our tests.

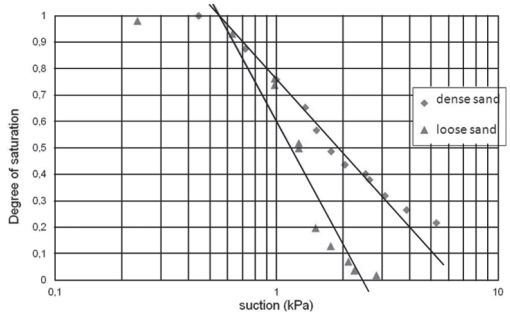

Figure 7. Comparison between retention curves (upon drying) of Hostun sand at loose and dense states.

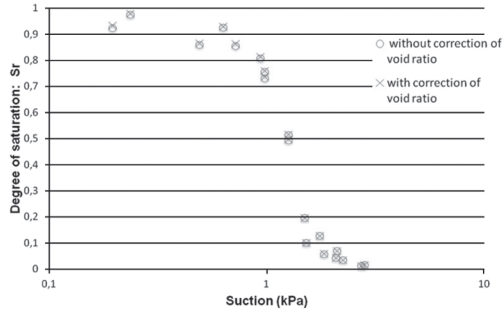

Figure 8. Influence of the variations of void ratio on the deter-mination of the degree of saturation in the case of loose Hostun S28 sand.

content (w) of the sample. To determine the degree of saturation (Sr) from measurements of water content, it is necessary also to monitor changes of void ratio (e) of the sample during the test since:

$$S_r = \frac{\rho_s}{\rho_w}\frac{w}{e}$$

where ρ_s and ρ_w represent the densities of solid grains and water.

Thanks to an accurate and continuous measurement of the variations of the height of the sample during the test, our experimental device allows this correction. Figure 8 illustrates the effects of this correction in the case of loose Hostun S28 sand. Note that despite its low initial density, this granular material shows no significant volume change during the drying-wetting cycle which justifies the first order correction on the degree of saturation.

4 TESTS ON A SAND-SILT MIXTURE

During the retention tests on the sand-clay mixture presented in Section 2.2, it appeared that the time required to reach equilibrium for water exchange between the controller and the sample at each suction increment was much longer than in the case of pure sand (approximately ten times longer). Only the initial part of the drying curve was then studied. This work allows us in particular to verify the capacity of our experimental device to characterize the behavior of sand-clay mixtures close to saturation.

Figure 9 shows the drying curves of the sand—clay mixture obtained for two initial void ratios (0.71 and 0.72) close to each other, where only a very small difference can be observed. This demonstrates the good reproducibility of the soil samples studied. The one corresponding to the denser material is slightly translated towards higher suctions. Both curves have similar slopes, with an air-entry suction of the order of 10 kPa, logically greater than those observed on pure sand.

Figure 10 shows the corresponding variations of void ratio. Both samples show a similar decrease of their void ratio, indicating shrinkage of the material during drying. Due to the presence of a granular matrix, this shrinkage is low (3% variation of the void ratio at 50 kPa suction).

Figure 11 compares the corrected and uncorrected values of the degree of saturation of the sand-clay mixture according to the consideration or not of its volume changes during drainage. This comparison is made for the mixture of initial void ratio 0.72. Note that the effect of this correction on sand-clay mixture is more pronounced than for pure sand but remains relatively unimportant (around 3%). This figure shows fewer differences than those due to the imperfect reproducibility of the samples in the case of sand-clay mixtures studied (Figure 9). On the other hand, this result shows the capacity of our experimental device to take into account the volume changes of the material, even small, during the drying-wetting cycle. It confirms its interest compared to more conventional devices, such as the Richards' apparatus for example.

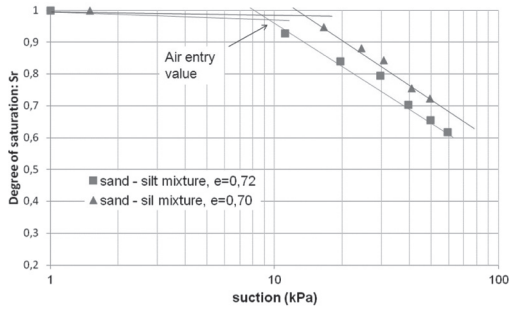

Figure 9. Retention curves (drying path) obtained on sand-clay mixture.

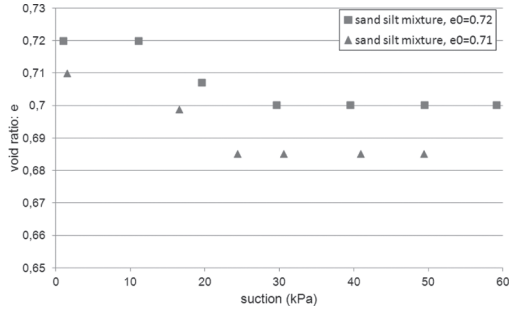

Figure 10. Variations of void ratio of sand-clay mixture during drying tests.

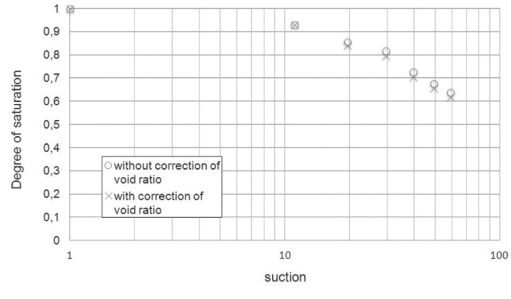

Figure 11. Influence of variations of void ratio on the determination of degree of saturation in the case of loose Hostun S28 sand.

5 COMPARISONS BETWEEN THE TWO MATERIALS

Figure 12 compares the drying curves obtained for the two materials studied: dense sand and sand-clay mixture with a void ratio of 0.72. Due to pores of smaller sizes, it seems logical that the drying curve of the sand-clay mixture (air-entry suction around 10 kPa) is shifted towards higher suctions compared to that of sand (air-entry suction around 0.5 kPa).

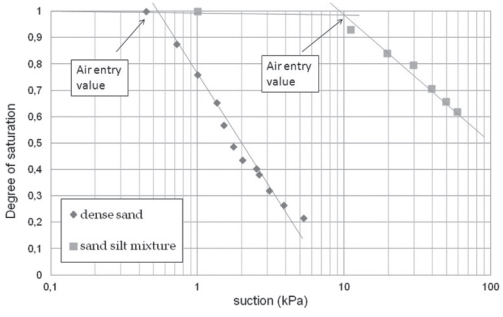

Figure 12. Comparison of retention curves (drying path) of dense sand and of sand-clay mixture.

Moreover, the measurements effectuated on pure sand as well as on sand-clay mixture confirm the logarithmic dependence of the degree of saturation on suction during drying (coefficient of correlation above 0.97). This observation confirms the relevance of using this kind of relationship in the model of Morvan et al. (2009, 2011). More importantly, our tests also provide evidence on the influence of the grain size distribution and density on the constant of proportionality of this logarithmic dependence.

6 CONCLUSION

The paper presents the first results of a comprehensive experimental program set out to characterize the retention properties of pure sand and sand–silt mixtures, and more particularly to investigate the impact of volumetric changes on the retention curves of these materials. During our tests carried out using an oedometer cell with controlled suction, the samples are subjected to drying and wetting paths under null total stress. The axis-translation technique (with excess air pressure) is employed for suction control. Volumetric variations of the samples are also measured continuously during the drying-wetting cycles. Mixture samples with different proportions of sand and silt and different initial void ratios are tested.

These first tests showed the ability of our experimental device to study the hydromechanical behaviour of sand-clay mixtures with good precision and reproducibility, particularly in the domain of low suctions. Different physical phenomena, such as hysteresis between drying and wetting and offset of the retention curve towards higher suction with decreasing pore size, have been studied and quantified in the case of sand and sand-clay mixtures. Similarly, the logarithmic dependence of the degree of saturation on suction during drying was analyzed for the materials tested. The relevance of a correction in the determination of the degree of saturation taking into account the volume change of the material has also been discussed.

REFERENCES

Aubertin, M., Mbonimpa, M., Bussiere, B. and Chapuis, R.P. (2003). A model to predict the water retension curve from basic geotechnical properties. Canadian Geotechnical Journal 40: 1104–1122.

Dafalias, Y.F. (1986). Bounding Surface Plasticity I: Mathematical Fondation Hypoplasticity. Journal of engineering mechanics 112: 966–987.

Khalili, N., Habte, M.A. and Zargarbashi, S. (2008). A fully coupled flow deformation model for cyclic analysis of unsaturated soils including hydraulic and mechanical hystereses. Computers and Geotechnics 35: 872–889.

Morvan, Wong, H. and Branque, D. (2009). An unsaturated soil model with minimal number of parameters based on bounding surface plasticity Int. J. for Numerical and Analytical Methods in Geomechanics, 34:1512–1537.

Morvan, M., Wong, H. and Branque, D. (2011). Incorporating porosity-dependent hysteretic water retention behavior into a new constitutive model of unsaturated soils Canadian Geotechnical Journal, 48:(12) 1855–1869.

Nuth, M. and Laloui, L. (2008a). Advances in modelling hysteretic water retention curve in deformable soils. Computers and Geotechnics 35: 835–844.

Padilla, J.M., Perera, Y.Y., Houston, W.N. and Fredlund, D.G. (2005). A new soil-water characteristic curve device. Advanced experimental unsaturated soil mechanics, Trento, Italy, Balkema.

Pereira, J.M., Wong, H., Dubujet, P. and Dangla, P. (2005). "Adaptation of existing models to unsaturated states: application to CJS model." International Journal for Numerical and Analytical Methods in Geomechanics 29(11): 1127–1155.

Perez-Garcia, N., Houston, S.L., Houston, W.N. and Padilla, J.M. (2008). An oedometer-type pressure plate SWCC apparatus. Geotechnical Testing Journal 31(2): 115–123.

Sun, D., Sheng, D., Cui, H.B. and Sloan, S.W. (2007a). A density-dependent elastoplastic hydro-mechanical model for unsaturated compacted soils. International Journal for Numerical and Analytical Methods in Geomechanics 31: 1257–1279.

Sun, D., Sheng, D., Xiang, L. and Sloan, S.W. (2008). elastoplastic prediction of hydro-mechanical behaviour of unsaturated soils under undrained conditions. Computers and Geotechnics 35: 845–852.

Sun, D., Sheng, D. and Xu, Y.F. (2007b). Collapse behaviour of unsaturated compacted soil with different initial densities. Canadian Geotechnical Journal 44: 673–686.

Advances in Unsaturated Soils – Caicedo et al. (eds)
© 2013 Taylor & Francis Group, London, ISBN 978-0-415-62095-6

Collapse behaviour of a natural loess from Northern France

J.A. Muñoz-Castelblanco
Ecole des ponts ParisTech, now in Cathie Associates, Nanterre, France

P. Delage, J.M. Pereira & Y.J. Cui
Ecole des Ponts ParisTech, Navier/CERMES, Champs-sur-Marne, France

ABSTRACT: An investigation of the collapse behaviour of an intact loess samples extracted close to the high speed train line (TGV Nord linking Paris to Brussels and London) has been conducted in relation with some stability problems observed during heavy rain episodes. The effect of initial water content on the collapse obtained when soaking samples under the standard 200 kPa stress has been investigated, with significantly higher collapse potential in drier states. The effect of the applied stress has also been considered by running tests under 200 kPa (standard value) and the considerably smaller value 19 kPa (close to in-situ vertical stress of 16 kPa). Tests were performed by using two techniques: Constant Strain Rate (CSR) tests and Step Loading (SL) tests. The changes in suction upon loading were measured by means of an in-house constructed high capacity tensiometer. The results showed a higher collapse strain under the small in-situ vertical stress. Microstructure observation (SEM) suggested that the resistance of the microstructure should not be homogeneous given the irregular position of silt grains-clay aggregations between a metastable arrangement of clean silt grains. Clearly, collapse under wetting should occur by the densification of the areas where grains are clean with large pores around them. The zones in which the porosity is filled by clay aggregation should be more resistant and locally less sensitive to collapse.

1 INTRODUCTION

Extensive areas in northern regions of France are covered by aeolian loess layers that have been deposited during the last glaciation by a constant North-West wind blowing from the Channel, close to the limit of the ice sheet at the time of the last glaciation (Figure 1).

As seen in the Figure, the North high speed train railways (TGV Nord between Paris and Brussels/London) crosses the loess deposits, particularly in an area in which significant instabilities have been observed, close to the city of Amiens in Picardie.

A typical illustration of the surface instabilities is illustrated in the photo of Figure 2. Impressive sinkholes were observed during the TGV construction period when shallow loess layers that were previously protected from rain by an upper superficial illuviated clayey layer (Antoine *et al.,* 2003) were exposed to climatic effects (drying and raining) during the railways construction.

This kind of instability with respect to water inundation led to further investigate the collapse susceptibility of these loess deposits (e.g., Cui *et al.,* 1995, 2004, Delage *et al.,* (2005).

In this work, the change in collapse susceptibility of the loess with respect to water content is first examined. Then, the collapse susceptibility is further investigated by carrying out various oedometer compression tests including standard step loading tests and constant rate of strain (CRS) tests. One of the performed CRS tests comprised collapse upon wetting under vertical load of 19 kPa (closer to the in-situ vertical total stress of 16 kPa) smaller than the standard 200 kPa value. The results obtained are analysed with respect to microstructure considerations.

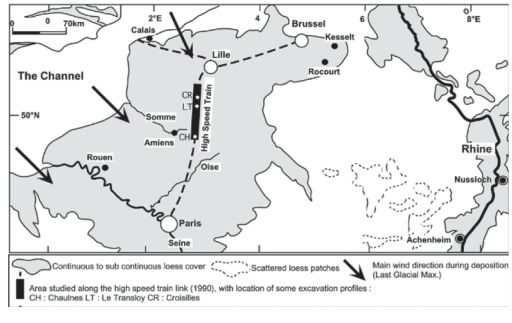

Figure 1. Extension of loess deposits in Northern France (Antoine 2002).

Figure 2. Collapse behaviour in shallow layers of loess directly exposed to climatic variations.

2 CHANGES IN COLLAPSE WITH WATER CONTENT

The effect of initial water content on collapse was investigated on good quality specimen trimmed from blocks extracted close to the village of Croisilles (CR in Figure 1) at a depth of 2.2 m. The geotechnical parameters of the loess of Croisilles are given in Table 1.

The loess has a 6 plasticity index and contains 12% carbonate, a component known to provide some bonding between particles due to the alteration of primary carbonates ($MgCO_3$ or $CaCO_3$) followed by re-precipitation ("Loess is not just the accumulation of dust", Pécsi 1990).

Standard collapse tests were run by soaking specimens that have been previously compressed up to 200 kPa at constant values of water content (23, 14 and 4% respectively).

Figure 3 (Cui & Marcial 2003) presents the effect of the initial water content on the collapse behaviour of loess samples from the village of Croisilles along the TGV line. This investigation was conducted to better understand the response of loess surfaces exposed to the atmosphere like that of Figure 2, given that it appeared that drier loess layers presented more dramatic instabilities.

Clearly, the collapse settlement (2, 4.4 and 7.5% respectively) is larger in drier samples. The data show that all compression curves after soaking follow the compression curve of an initially soaked sample (under 3 kPa), confirming the validity of Jennings & Knight's double oedometer technique. Indeed, the drier the sample, the larger the collapse strain. Since all collapse sequences end up along the same saturated compression curve, the increase in collapse in drier specimens is due to their larger rigidity that allows less deformation during the constant water content compression phase prior to soaking.

Table 1. Geotechnical characteristics of the Croisilles loess.

Sample depth	2.2 m
Natural water content w (%)	18.1
Dry unit mass ρ_d (Mg/m^3)	1.39
Natural degree of saturation S_r	0.53
Natural suction (HTC) (kPa)	34
Clay fraction (% < 2 μm)	16
Plastic limit w_p	22
Liquid limit w_l	28
Plasticity index I_p	6
Carbonate content (%)	12

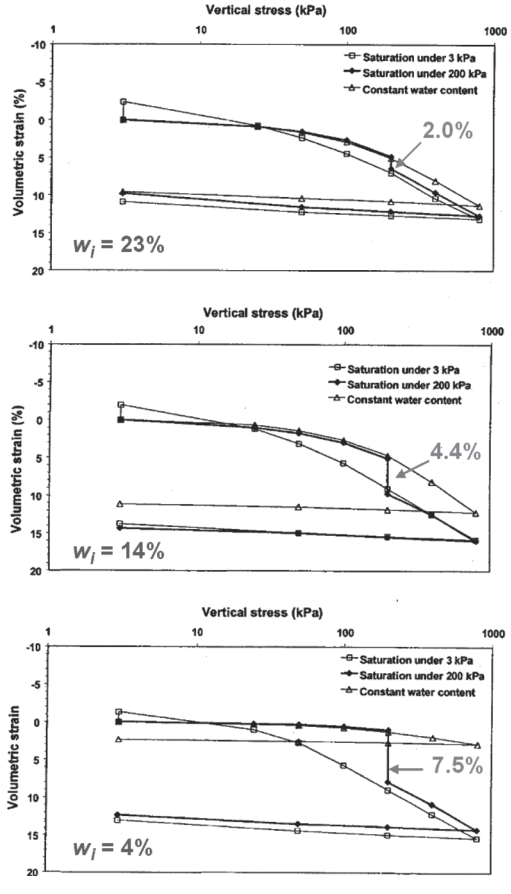

Figure 3. Effects of initial water content on collapse.

This recalls that the collapse strain upon wetting observed under a given stress depends of the unsaturated compression strain obtained during the compression phase conducted prior to the soaking sequence, giving particular importance to the choice of the stress value under which soaking

is performed. This is now further explored by conducting soaking tests under both low and large stresses.

3 EFFECT OF APPLIED STRESS ON COLLAPSE UPON WETTING

Tests were performed on good quality samples trimmed from a block that was manually extracted at a depth of 1 m close to the village of Bapaume. The geotechnical characteristics of the samples are presented in Table 2. Their water retention properties have been investigated in details in Muñoz-Castelblanco *et al.* (2012) in relation to microstructure features. The loess has a higher plasticity index (9) compared to the Croisilles loess and contains less carbonate (6%), it is also slightly denser (ρ_d = 1.45 Mg/m^3 compared to 1.39 Mg/m^3).

A series of oedometric compression tests (Table 2) in which suction changes were monitored by using an in-house constructed high capacity tensiometer (HCT, Cui et al. 2008) at the base of the sample as described in Delage et al. (2007) was carried out.

Tests were performed at constant water content starting from the natural unsaturated state (w_i between 14.3% and 14.9%) with initial suctions s_i between 38 and 47 kPa. Most tests were standard step loading tests (SL001 to 004), but two constant rate of strain (CRS03 and 05) were also conducted. As noted by Tarantino & De Col (2008), it is preferable to run constant rate of strain tests when monitoring suction changes during oedometer compression.

In test SL004, the sample was soaked at very low stress (1.5 kPa) prior to compression, providing the "saturated" reference compression curve. Constant water content tests were made to compare the unsaturated compression behaviour (with preserved initial structure) with the saturated one, like in the double oedometer test (Jennings & Knight 1957).

Table 2. Geotechnical characteristics of the Bapaume loess.

Sample depth	1 m
Natural water content w (%)	14.4
Natural void ratio e	0.84
Dry unit mass ρ_d (Mg/m^3)	1.45
Natural degree of saturation S_r	0.46
Natural suction (HTC) (kPa)	40
Clay fraction (% 2 µm)	16
Plastic limit w_p	19
Liquid limit w_l	28
Plasticity index I_p	9
Carbonate content (%)	6

The data presented in Figure 4 come from test SL001 (step loading test at constant initial water content of 14.6%), test CRS03 at constant rate of strain of 0.059%/mn and at constant water content (w = 14.4%) that presents excellent correspondence with test SL001, test SL002 (step loading test of a sample previously soaked under 1.5 kPa with no collapse observed), test CRS05 carried out after soaking under 3 kPa (with no collapse observed) that presents excellent correspondence with test SL002, test SL003 (step loading collapse test with soaking at 205 kPa). Excellent correspondence is observed between tests SL001 and CRS03 before collapse, and between tests SL002 and CRS05 after collapse.

The Figure also shows the data of the SL004 step loading test with collapse at 19 kPa (a stress slightly larger than the in-situ stress of 16 kPa).

Note that all the initial states have the same initial void ratio (0.85), showing fairly good homogeneity within the block. The responses in suction are reasonably constant in all tests, showing that the same suction decrement occurs during both collapses at 205 and 19 kPa.

There is excellent correspondence between all tests, showing the good quality and homogeneity of the samples tested and the good quality of the experimental procedures. The unloading response of the unsaturated test SL001 at w = 14.4% (S_{rf} = 65%) is comparable to that of the tests where unloading has been made after soaking (SL005, SL004, SL003, SL002), showing little influence of

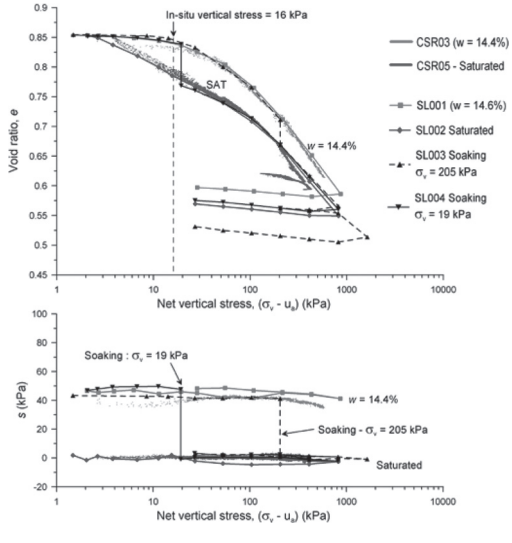

Figure 4. Collapse and compression tests performed.

suction on the rebound elastic response. A gross yield stress of 55 kPa can be derived from step loading test SL001, a value close to that obtained from test CRS003 (67 kPa, 0.059%/mn). Irreversible strain appears to start from the beginning in tests on samples at zero suction (CRS05, SL002), with little evidence of pre-yield pseudo-elastic behaviour. Both tests exhibit same unloading curves.

Tests SL003 and SL004 confirm the validity of Jennings & Knight's double oedometer method and of the state surface concept of Matyas & Radhakrishna (1968), initially developed from data of compacted soils. The maximum collapse is observed under 30 kPa. Below, the unsaturated sample is less compressible than the saturated one (in agreement with one of the main assumptions of the BBM model, Alonso *et al.* 1990). This is no longer true above 30 kPa where the unsaturated sample is more compressible than the saturated one. This feature, described in Alonso et al. (1987) and observed by Sivakumar & Wheeler (2000), has been integrated in some constitutive models that account for the maximum of collapse (e.g. Josa *et al.* 1992, Georgiadis *et al.* 2008).

Suction changes during compression are small, like in compacted soils dry of optimum (Li 1995, Gens *et al.* 1995, Tarantino & De Col 2008). The collapse strain at 19 kPa (3.8%) is larger than at 205 kPa (2.3%). Indeed, 19 kPa appears to be located just below the start of irreversible strains in the compression curve of tests SL004, SL001 and CRS03 whereas compression up to 205 kPa produces a plastic strain of about 10%.

The constant water content curves progressively converge towards the "saturated" compression curve, as also shown in Figure 4 that compares both compression curves. The changes in collapse with vertical stress indicate a maximum collapse at 30 kPa.

During compression at constant water content, the degrees of saturation increase from approximately 47% to 62% (Table 2) with no water expulsion. The small suction changes observed can be related to the low initial saturation of the samples. As observed in the scanning electron microscope observations performed on the same loess by Muñoz-Castelblanco *et al.* (2012) and presented in Figure 5, the largest pores of the loess are dry inter-grains pores (with an average entrance diameter of 8 μm) located between clean silt grains of 30 μm average diameter.

The clay fraction appears to be irregularly scattered in the grains assembly, forming local aggregates in which loess grains are embedded. Due to the low degrees of saturation, compression should only affect, like in soils compacted dry of optimum (Delage 2009), the largest dry pores while remaining intact the clay/grain aggregates (that are very likely saturated at these low suction levels and that govern suction changes). So there is little impact of compression on suction, like in soils compacted dry of optimum (Li et al. 1995, Gens et al. 1995, Tarantino & De Col 2009).

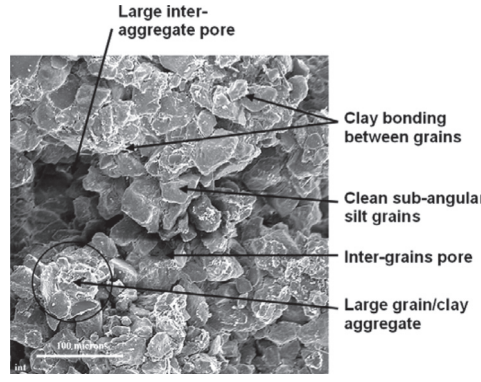

Figure 5. SEM microstructure observation on intact Bapaume loess samples at initial intact state (Muñoz-Castelblanco et al. 2012).

Observation of the SEM photography suggests that the resistance of the microstructure should not be homogeneous based on the irregular position of existing clay aggregations between a metastable arrangement of silt grains. Clearly, collapse under wetting should occur by the densification of the areas where grains are clean with large pores around them. The zones in which the porosity is filled by clay aggregation should be more resistant and locally less sensitive to collapse.

Compression at constant water content affects a loose assembly of dry grains bonded together by hydrated carbonate links that are apparently sensitive to changes in water content. In loess samples from the same deposit, preliminary mercury intrusion tests carried out before and after collapse (Cui *et al.*, 2004, Delage *et al.*, 2005) and more recent investigation of the loess microstructure (Muñoz-Castelblanco *et al.*, 2012) showed that collapse occurred in some large dry pores between clean grains. At any stress, collapse brings the representative point from the constant water compression curve down to the "saturated" compression curve.

4 CONCLUSIONS

Two aspects of the collapse behaviour of loess deposits from northern France were investigated. The effects of initial water content has been explored by running collapse upon wetting tests under a standard stress value 200 kPa on loess samples from Croisilles that have been put at various initial water contents prior to compression.

The magnitude of the collapse settlement appeared to depend on the initial water content. Since all final points after soaking reached the "saturated" compression curve as expected, the larger collapse observed in drier is due to the higher stiffness of the drier samples that allows for a larger void ratio under any stress, resulting in a final larger collapse settlement under 200 kPa.

Since significant collapse can also occur under low stress as observed in the instabilities of shallow layers exposed to the atmosphere in Figure 2, the effect of applied stress on collapse has been examined on samples from the city of Bapaume. This effect is well illustrated by comparing the compression curves at constant natural water content and after saturation under low stress that evidence the existence of a maximum collapse. Indeed, significant collapse can be observed under stress as low as 19 kPa, a value slightly larger than the in-situ vertical stress at 1 m depth (16 kPa).

This shows that the standard 200 kPa stress value under which collapse tests are carried out might not be relevant in some cases, since most collapse susceptibility could be erased by previous compression.

The microstructure of the loess appears to be heterogeneous with on the one hand some zones constituted of clean silt grains and large pores and on the other hand zones formed of silt grains aggregated by clay particles. Collapse occurs in the weakest zones and hence corresponds to some rearrangements in the looser zones made up of clean grains. The usual interpretation based on the weakening of clayey bridges by wetting is then not verified for the loess studied here.

Finally, the photos of Figure 2 can be further commented by adding that such impressive sinkholes are likely due to the combined effects of drying and wetting, since it has been showed that significantly higher collapse occurred in drier conditions, with values as high as 7.5% in the dry state.

REFERENCES

Alonso E., Gens A. & Hight A. (1987). Special problems soils. Gen. Report, *Proceedings 9th European Conference on Soil Mechanics and Foundation Engineering*., Dublin 3, Balkema. 1087–1146.

Alonso E., Gens A. & Josa, A. (1990). A constitutive model for partially saturated soils. *Géotechnique* 40 (3). 405–430.

Antoine P. (2002). Les loess en France et dans le Nord-Ouest européen. *Revue Française de Géotechnique* 99. 3–21.

Antoine P., Catt J. & Sommé J. (2003). The Loess and Coversands of Northern France and Southern England. *Journal of Quaternary Sci.* 18. 309–318.

Cui Y.J., Schlosser F., Delage P., Wojnarowicz M. & Durand F. (1995). Comportement mécanique des loess sur le tracé du TGV Nord. *CR XIème Congrès Européen de Mécanique des Sols et des Travaux de Fondation*, Copenhague, vol. 7, Balkema. 45–50.

Cui Y.J. & Marcial D. (2003). Etude de comportement des limons non saturés soumis aux vibrations ferroviaires (Lot1). *Rapport SNCF*. 47 pages.

Cui Y.J., Marcial M., Terpereau J.M., Delage P., Antoine P., Marchadier G. & Ye W.M. (2004). A geological and geotechnical characterisation of the loess of Northern France. *A.W. Skempton Memorial Conference*, vol. 1. 417–428.

Cui Y.J., Tang A., Mantho A. & De Laure E. (2008). Monitoring Field Soil Suction Using a Miniature Tensiometer. *Geotechnical Testing Journal 31* (1). 95–100.

Delage P. (2009). Compaction behaviour of clay: discussion. *Géotechnique* 59 (1), 75–76.

Delage P., Cui Y.J. & Antoine P. (2005). Geotechnical Problems related with Loess deposits in Northern France. *Proceedings of International Conference on Problematic Soils.* 517–540.

Delage P., Le T.T., Tang A.M., Cui Y.J. & Li X.L. (2007). Suction effects in deep Boom clay block samples. *Géotechnique* 57 (1). 239–244.

Gens A., Alonso E.E., Suriol J., & Lloret A. (1995). Effect of structure on the volumetric behavior of a compacted soil. In Unsaturated Soils: *Proceedings 1st International Conference on Unsaturated Soils / UNSAT 95*, Paris. 83–88.

Georgiadis K., Potts D.M. & Zdravkovic L. (2008). An improved constitutive model for unsaturated and saturated soils. *In Unsaturated Soils: Advances in Geo-Engineering, Proceedings of the 1st European Conference on Unsaturated Soils*, Durham, UK, CRC Press. 581–588.

Jennings J.E. & Knight K. (1957). The additional settlement of foundation due to collapse of sandy soils on wetting. *Proceedings of the 4th International Conference on Soil Mechanics and Foundation Engineering* 1. 316–319.

Josa A., Balmaceda A., Gens A. & Alonso E.E. (1992). An elasto-plastic model for partially saturated soils exhibiting a maximum of collapse. *Proceedings of 3rd International Conference on Computational Plasticity*, Barcelona, vol. 1. 815–826.

Li Z.M. (1995). Compressibility and collapsibility of compacted unsaturated loessial soils. *Proceedings 1st International Conference on Unsaturated Soils UNSAT'95 1*. Balkema. 139–144.

Matyas E.L. & Radhakrisna H.S. (1968). Volume change characteristics of partially saturated soils. *Géotechnique* 18 (4). 432–448.

Muñoz-Castelblanco J., Pereira J.M., Delage P. & Cui Y.J. (2012). The water retention properties of a natural unsaturated loess from Northern France. *Géotechnique* 62 (2), 95–106.

Pécsi M. (1990). Loess is not just the accumulation of dust. *Quaternary International* 7/8. 1–21.

Sivakumar V. & Wheeler S.J. (2000). Influence of compaction procedure on the mechanical behaviour of an unsaturated compacted clay. Part 1: Wetting and isotropic compression. *Géotechnique* 50 (4), 359–368.

Tarantino A. & De Col E. (2008). Compaction behaviour of clay. *Géotechnique* 58 (3). 199–213.

This page intentionally left blank

Advances in Unsaturated Soils – Caicedo et al. (eds)
© 2013 Taylor & Francis Group, London, ISBN 978-0-415-62095-6

Elastic response of unsaturated soils

C. Murillo
Department of Civil and Agricultural Engineering National University of Colombia, Bogotá, Colombia

B. Caicedo
Department of Civil and Environmental Engineering University of Los Andes, Bogota, Colombia

L. Thorel
Université Nantes Angers Le Mans, IFSTTAR, Département Géotechnique Eau et Risque, Bouguenais, France

C. Dano
Research Institute in Civil and Mechanical Engineering, Ecole Centrale Nantes, Nantes, France

ABSTRACT: The elastic behavior of unsaturated soils subjected to very small strains (smaller than 10^{-5}) was studied in the past years using different experimental devices (mainly resonant columns). The bender elements technique, now extensively used in soil mechanics, offers an efficient alternative to measure elastic properties of soils. Furthermore to enrich the common bender elements testing results providing only shear modulus values, an evolution of the bender elements technique, named bender-extender elements is presented here. The present study provides new results about the elastic properties of intermediate unsaturated soils made of mixtures of sand and clay. The results in terms of elastic properties are presented as a function of the suction level.

1 INTRODUCTION

The identification of elastic parameters is an essential topic in geotechnical engineering. In particular in this paper, the elastic behavior of compacted soils subjected to very small strains (smaller than 10^{-5}), currently involved in many geotechnical structures such as roads or railways, embankments, earth structures is investigated. Their serviceability is clearly determined by soil elastic properties which depend on the water content and suction level.

Small-strain stiffness of soils was studied in the past years using different experimental devices (mainly resonant columns but also local small strain devices). The bender elements technique nowadays extensively used in soil mechanics offers an efficient alternative even if some shortcomings relative to interpretation methods remain questionable. The most common bender element device was developed by Shirley and Hampton (1977): it allows the propagation of shear waves, and then only the shear modulus G is directly measurable. An evolution of the bender elements technique, named bender-extender elements, was developed by Lings and Greening (2001). This device allows the simultaneous measurement of the shear and compression wave velocities. Consequently two independent elastic constants are determined on the same sample avoiding indirect estimations.

Most of the studies involving bender elements have been performed on purely frictional sands or soft cohesive soils (clays). The present study provides new results about the elastic properties of intermediate unsaturated soils made of mixtures of sand and clay, identified using the bender—extender elements testing device.

The resulting values of elastic properties of intermediate compacted soils are presented taking into consideration the suction level into soil specimens. Finally a model describing the elastic behavior of these unsaturated soils is proposed.

2 TESTED SOILS

The tested compacted soils are reconstituted in the laboratory from different mixtures, defined by their weight percentage of Speswhite kaolin (SPW), and Missillac sand (MS). The index properties of the SPW clay are a liquid limit of 55.1%, a plastic limit of 32.3%, and a specific gravity G_s of 2.62, the specific gravity G_s of the sand fraction MS is 2.65. Figure 1 shows the grain size distributions of these soils.

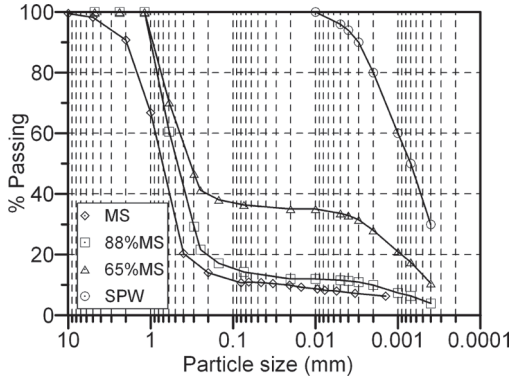

Figure 1. Particle size distribution for Speswhite Kaolin (SPW or S1), Missilac Sand (MS) and mixtures S2 and S3.

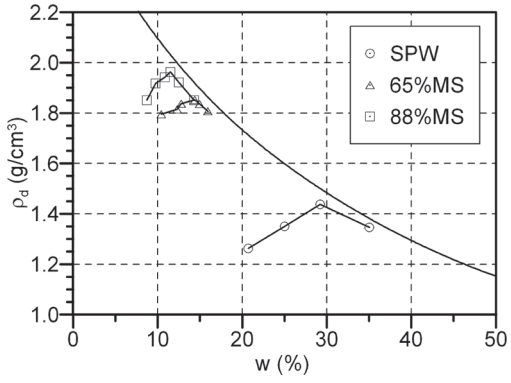

Figure 2. Proctor test results.

Three different mixtures of soils were studied. These mixtures fall in three different categories of soils according to the French Road Soil Classification System (LCPC 1992) that is based mainly on the grain size distribution and on the Methylene blue absorption. In this system the soils are respectively classified as A3, B6 and B31, according to AASHTO soils classification system these soils are ranked as A-7-5, A-1-a, and A-2-7 respectively. In the following paragraphs the soils used in this study are designed as S1 for A3 or AASHTO A-7-5; S2 for B6 or AASHTO A-1; and S3 for B31 or AASHTO A-2-7. The mass percentage of MS for each of these soils is 0% (S1), 65% (S2) and 88% (S3); and the Methylene blue absorption values are 1.54, 1.21, and 1.11 g/100 g for the S1, S2, and S3, respectively.

Soil S3, which includes the smallest percentage of kaolin, has the highest dry maximum unit weight measured following the standard Proctor test (Figure 2) by comparison with S2 and S1.

2.1 *Soil samples preparation and characteristics*

Sand is sifted in different fractions whose maximum grain size is respectively 1 mm, 0.5 mm, 0.2 mm and 80 µm. Fractions lower than 1 mm is then mixed in a 0.14 m^3 concrete mixer to reconstitute the material, avoiding segregation. Kaolin is then added and mixed for three minutes to obtain a dry and homogeneous mixture. 28%, 11% and 13% of water is added to obtain S1, S3 and S2 soils, respectively. The optimum Proctor water contents are 29.2%, 11.5%, and 14.4% respectively.

The mixture is introduced into a 30 cm large and 40 cm high cylindrical container in three successive layers of about 10 cm each. The soil mass is then subjected to a compressive vertical stress (σ_v) using a pressure-controlled hydraulic actuator. The final vertical stress is equal to 2 MPa for S1 and 2.5 MPa for S2 and S3. The static compaction on specimens is applied for 10 minutes on each soil layer. After 10 minutes of compaction no additional settlement is measured. The obtained density is calculated classically as the ratio of the mass and the volume of the sample. These values allow obtaining a homogeneous material having a dry density close to the maximum Proctor density (Murillo et al. 2009a, 2009b). Four steel cores (10 cm in diameter, 20 cm long) are finally placed on the top surface of the compacted soil. Using a hydraulic actuator, the steel cores are fully driven in the soil mass. Finally, each core sample is taken out from the mould.

Table 1 summarizes the main characteristics of the samples: the water content, the dry density ρ_d and the initial void ratio e_i are similar for each sample of the same compacted soil showing good homogeneity from the compaction procedure. Furthermore initial water content (or initial degree of saturation S_{ri}) is approximately the same for the samples of each soil, except for S2, in order to examine the effect of the saturation degree. Samples of compacted soils are taken to measure their suction value using a pressure plate cell apparatus for soil S3 and a WP4-T chilled mirror apparatus for soils S1 and S2. The mean suction values of the three different soils are presented in Table 1, the matric suction of the samples cover a broad range from 60 kPa for soil S3 having 88% sand to 8000 kPa for soil S1 having 100% of kaolin; soil S2 having 65% of sand was tested at two water contents: 11% and 15% corresponding to 1500 kPa and 300 kPa matric suction respectively.

Table 1. Soil sample properties.

Soil	w (%)	ρ_d (gr/cm^3)	e_i	Sr_i (%)	$u_a - u_w$ kPa
S1	28.28	1.44	0.837	90	8000
	28.32	1.46	0.815	92	
S2	11.74	1.84	0.484	63	1500
	15.5	1.81	0.487	85	300
S3	11.13	1.94	0.374	80	60
	11.29	1.93	0.384	78	

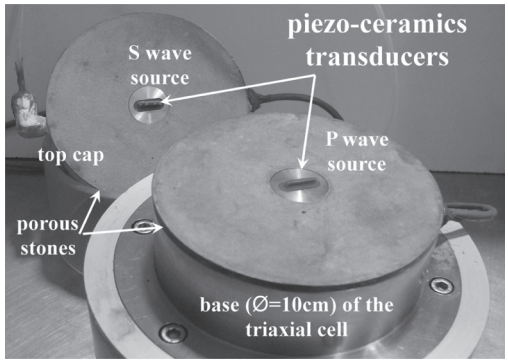

Figure 3. Bender extender elements.

3 EXPERIMENTAL DEVICES

3.1 *Bender-extender elements*

A couple of piezo-ceramics transducers, called bender-extender elements (Figure 3), is used to measure both compression (P-waves) and shear (S-waves) waves. This device is extensively described in Lings and Greening (2001). The bender-extender elements withstand a relatively large range of confining pressures, and they can be excited with different input signal frequencies and shapes.

The piezo-ceramics transducers are embedded into the top cap and the base of a triaxial compression test apparatus. The upper element is excited by an electrical pulse which initiates a shear wave through the specimen. On the other hand, compression wave is generated upwards by the lower element. When each wave reaches the opposite element, the mechanical movement is then converted into an electric signal. Both input and output signals are recorded.

Each sample is pressed on the lower element to maintain a perfect contact between the tested material and the transducer. The upper element is also pressed onto the sample. As a result, both elements penetrate into the sample over a depth of 2.5 mm. Special attention is also given to the alignment and the position of the two elements for polarization and signals quality reasons. The cell pressure is controlled with a 2 MPa hydraulic actuator which has a total volume of 200 cm^3.

During tests, the shape (sine, square) and the frequency (5, 6.7, 8.3, and 10 kHz) of the excitation signal are imposed by the user through the software interface. The sampling rate is 10^5 samples per second (100 kHz), and the amplitude of the signal is ± 5 volts. Tests were carried out on samples having 10 cm diameter and 7 or 10 cm high. Records of wave propagation were performed for different confining pressures varying from 0 (before filling the cell with water) to 500 kPa, along isotropic loading stress paths. The samples are protected from the confining fluid by a thin 0.5 mm thick latex membrane, adding a confining stress of 0.3 kPa.

Variations of the sample height under pressure are assessed by an external gauge. Measurement errors are unavoidable because of the bedding effect and the compliance of the system (Scholey et al., 1995). The errors, however, remain small because of the specimen stiffness (approximately 200 MN/m^2 for the mean value of the shear modulus). The size (diameter and height) and the mass of the specimens are initially carefully measured.

Assuming isotropy and homogeneity, the elastic parameters characterizing the linear elastic behavior (E, G) are related to the wave velocities in the framework of the mechanics of continuous media:

$$G = \rho \cdot V_s^2 \tag{1}$$

$$E = \frac{\rho V_s^2 (3V_p^2 - 4V_s^2)}{V_p^2 - V_s^2} \tag{2}$$

where V_s is the shear wave velocity, V_P is the compression wave velocity, and ρ is the density of the soil. The velocity of the waves is given by:

$$V = \frac{L}{T} \tag{3}$$

where L is the effective tip-to-tip distance between the two bender-extender elements, corrected to take into account the shortening of the sample during the test, in compliance with the recommendations by Viggiani & Atkinson (1995), Jovičić et al. (1996), and Brignoli et al. (1996) and T is the wave travel time relative to the compression wave, T_p, or the shear wave, T_s.

The identification of T_P is relatively easy since it corresponds to the time interval between the

input signal initial point and the output signal first deviation, usually clear enough, even if the amplitude of the P-wave is ten times lower than the amplitude of the shear wave.

Different methods can be used to identify the travel time of the shear wave T_s: (e.g., peak-to-peak time method, cross-correlation method).

According to Viggiani and Atkinson (1995), Lohani et al. (1999) and Kawaguchi et al. (2001), the travel time that corresponds to the peak-to peak distance between input and output signals might globally be wrong except for high frequency input signals. The difficulty to establish the peak in the output signal may generate errors mainly for square waves where no clear peak appears, particularly at low frequencies, for which the wave period is large.

The cross-correlation method (Mancuso et al., 1989, Viggiani and Atkinson 1995, Mohsin and Airey 2003) is a mathematical tool that provides a reliable indication on the similarity between the signals and on the degree of distortion. This method allows assessing the travel time of both shear and compression waves.

4 SHEAR AND YOUNG MODULI FOR UNSATURATED INTERMEDIATE SOILS

A critical review of the literature shows that the shear and Young moduli of unbound granular materials mainly depends on the void ratio e and on the effective principal stresses σ'_1 and σ'_3. For isotropic loading stress paths, the shear and Young moduli are expressed as a function of the void ratio and of the mean effective stress p' or the confining effective stress σ'_3 such as (Hardin & Richart, 1963; Iwasaki & Tatsuoka, 1977; Biarez & Hicher, 1994; Lo Presti et al., 1997):

$$\frac{G}{G_{ref}} = \frac{K_G}{f_G(e)}\left(\frac{\sigma'_3}{\sigma'_{3,ref}}\right)^n \quad (4)$$

$$\frac{E}{E_{ref}} = \frac{K_E}{f_E(e)}\left(\frac{\sigma'_3}{\sigma'_{3,ref}}\right)^n \quad (5)$$

where K_E, K_G and n are material constants, $f_{G,E}(e)$ a function of the void ratio (Table 2) and G_{ref}, E_{ref}, $\sigma'_{3,ref}$ are parameters that normalizes the equations. As observed, the power n reported in literature, which characterizes the nature of grain-to-grain contacts, is close to 0.5. The deviation from the predictions of the Hertz's theory (n = 1/3) can be explained by the nature of the contacts, not necessarily punctual (Dano and Hicher 2002). For cohesive and frictional soils, the cementation of particles also makes the power n to decrease, up to 0 if the cementation is strong.

Table 2. Relations between G, E, e and σ'_3.

Reference	Modulus	n	Ff(e)	Comments
Hardin & Richart (1963)	G	0.5	$(2.17 - e)^2/(1 + e)$	Rounded grains
Iwasaki & Tatsuoka (1977)	G	0.4		Cu < 1.8
Biarez & Hicher (1994)	G, E	0.5	$1/e$	All soils
Lo Presti et al. (1997)	G	0.45	$1/e^{1.3}$	Sands

For the intermediate unsaturated materials used in this study, the variation of Young and shear moduli as a function of the confining stress depends on the sand fraction (or clay content) and on the suction as follows: (i) the higher the percentage of sand is, the higher shear and compression wave velocities are. Furthermore, sandy soils are more pressure sensitive than pure clay: indeed, when a binder like clay or cement-type materials is added to the granular skeleton, the contact area between the grains increases and the effect of the pressure is softened (Chang and Woods 1987); (ii) On the other hand it is well-known that matrix suction has an effect on the shear wave velocity (Wu et al., 1984), even in the drying-wetting process (Xu et al., 2008).

The shear and Young moduli measured reveal that for unsaturated intermediate materials, there is non-null moduli for zero confining stress. This effect is related to capillary forces present in these materials. However this result is in disagreement with equations 4 and 5 for which zero moduli are expected for zero confining stress. To reproduce the effect of suction, equations 4 and 5 could be modified in two ways: (i) using a generalized effective stress analysis (Fleureau et al., 2003), or (ii) consider the suction effect on the modulus at zero stress, and the effect of confining net stress separately (Caicedo et al., 2009). The second approach is used in this paper due to the difficulties in the definition of effective stresses in unsaturated soils. Then to describe the variation of Young and shear moduli of intermediate unsaturated soils the following two power laws can be used:

$$\frac{G}{G_{ref}} f_G(e) = \frac{G_{0\sigma_3}}{G_{0\sigma_{3,ref}}} + K_G\left(\frac{\sigma_3}{\sigma_{3,ref}}\right)^n \quad (6)$$

$$\frac{E}{E_{ref}} f_E(e) = \frac{E_{0\sigma_3}}{E_{0\sigma_{3,ref}}} + K_E \left(\frac{\sigma_3}{\sigma_{3,ref}} \right)^n \quad (7)$$

where $E_0\sigma_3$, $G_0\sigma_3$ are the moduli for zero confining stress.

Equation 6 leads present good agreement with experimental values as shows in Figure 4. This fitting permits obtaining the moduli for zero confining stress for all tests, these moduli are presented in Figure 5 that represents the Young and shear moduli for zero confining vertical stress, $E_0\sigma_3$, $G_0\sigma_3$ (normalized to $e = 0.45$ using the equations suggested by Iwasaki & Tatsuoka (1977) for shear modulus and Biarez & Hicher (1994) for Young modulus) as a function of suction, $(u_a - u_w)$. As described, the moduli for zero total stress grows up as the suction increases. In fact, for zero total stress the stiffness of the material appears as a result of the capillary forces acting on the contacts between granular particles. These results agree with the results presented by Fleureau et al. (2003), and Caicedo et al. (2009). Figure 5 also shows that for zero suction, Young and shear moduli for zero confining stress goes to zero; this value agree with equations 4 and 5. On the other hand, when suction increases, the modulus at zero confining stress trends to a maximum asymptotic value. This behavior can be described using the following hyperbolic equations:

$$G_{0\sigma_3} = \frac{u_a - u_w}{a_G + b_G(u_a - u_w)} \quad (8)$$

$$E_{0\sigma_3} = \frac{u_a - u_w}{a_E + b_E(u_a - u_w)} \quad (9)$$

Figures 6 and 7 show the evolution of the component of shear and Young modulus that vary with the confining net stress, ($E_{e=0.45} - E_0\sigma_3$, and $G_{e=0.45} - G_0\sigma_3$ vs. $\sigma_3 - u_a$). Table 3 shows the values

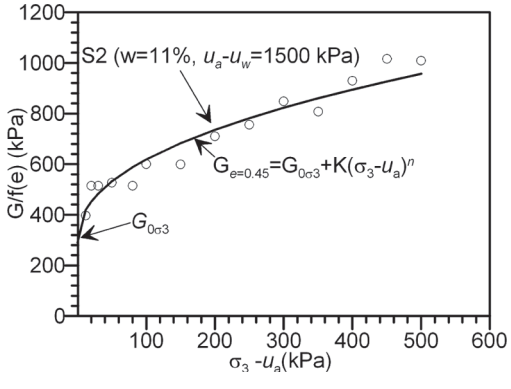

Figure 4. Shear modulus vs net confining stress fitted using equation 8.

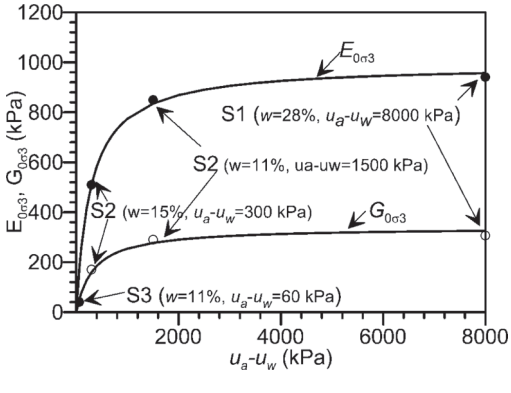

Figure 5. Relationship between the modulus $E_{0\sigma3}$, $G_{0\sigma3}$, and suction.

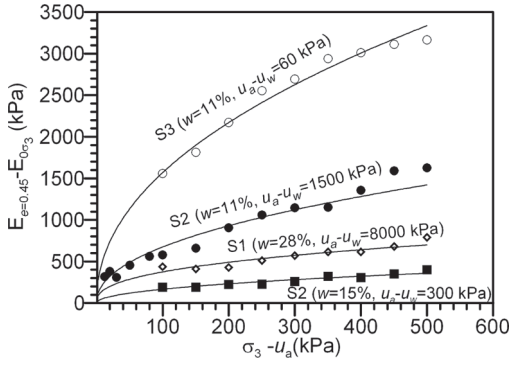

Figure 6. Relationship between the component $E_{e=0.45} - E_{0\sigma_3}$ of Young modulus vs confining net stress $\sigma_3 - u_a$.

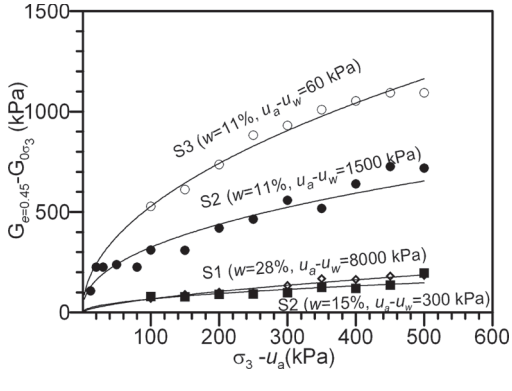

Figure 7. Relationship between the component $G_{e=0.45} - G_{0\sigma_3}$ of shear modulus vs confining net stress $\sigma_3 - u_a$.

Table 3. Constants used in equations 10 and 11.

	Shear modulus kPa					Young Modulus kPa				
Soil	a_G	b_G	f(e)	K_G	n	a_E	b_E	f(e)	K_E	n
S1	0.99	$3\ 10^{-3}$	$(2.17 - e)^2/(1 + e)$	8.3	0.48	0.28	$1\ 10^{-3}$	1/e	38.3	0.48
S2 (w = 11%)				43.3	0.43				79.9	0.46
S2 (w = 15%)				7.0	0.49				18.5	0.48
S3				55.07	0.49				180.8	0.48

of the constants used to fit the experimental results in to equations 10, and 11. The results of the exponent *n* vary between 0.43 and 0.49 for all the soils of this study, and for either Young or shear moduli; these values are similar than those presented in Table 4 corresponding to saturated unbound soils. This last result confirms that equations 4 and 5 can be used for intermediate unsaturated soils but only to describe the effect of the net confining stress separately of the modulus for zero confining stress.

$$Gf_G(e) = \frac{u_a - u_w}{a_G + b_G(u_a - u_w)} + K_G(\sigma_3 - u_a)^n \qquad (10)$$

$$Ef_E(e) = \frac{u_a - u_w}{a_E + b_E(u_a - u_w)} + K_E(\sigma_3 - u_a)^n \qquad (11)$$

As observed in Table 3, exponent *n* is similar for all the soils studied, however the constant *K* in equations 10 and 11 depends on the type of soil and suction value.

Figures 8 and 9 show the evolution of Young and Shear modulus vs suction and confining net stress, these figures show how equations 10 and 11 describe the different growing rate of modulus when either the suction or the net confining stress remain constant.

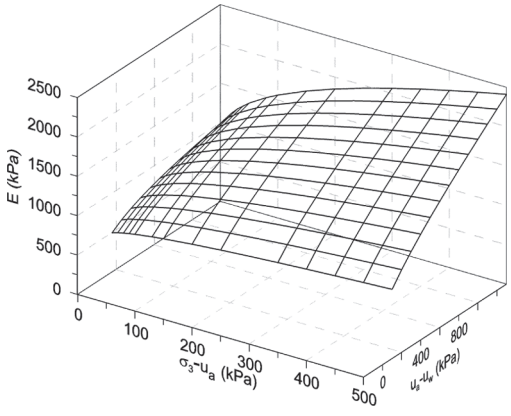

Figure 8. Young modulus vs confining net stress $\sigma_3 - u_a$ and suction $u_a - u_w$ for soil S2.

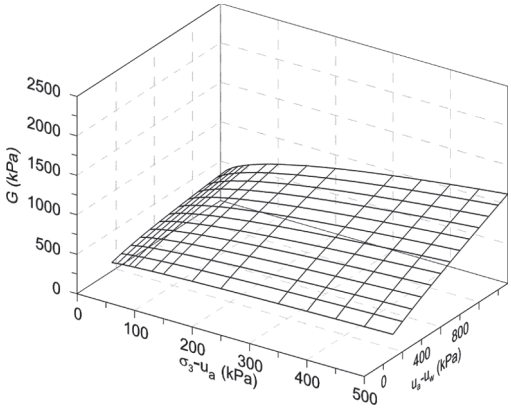

Figure 9. Shear modulus vs confining net stress $\sigma_3 - u_a$ and suction $u_a - u_w$ for soil S2.

5 SUMMARY AND CONCLUSIONS

Wave propagation velocities are experimentally determined for S1, S2 and S3 soils subjected to isotropic stresses. The statically reconstituted samples tested, which are both cohesive and frictional, are mixtures of kaolin SPW and Missillac sand, which represent a subgrade material.

The results of the Young and shear moduli have been interpreted in the framework of unsaturated soils, for zero net confining stress, non null Young and shear moduli appears as a result of the suction pressure for all the soils that is in contradiction with the power law used to describe the evolution of these modulus as a function of the confining stress. Due to the difficulties in the definition of generalized effective stress law for unsaturated soils two relations are proposed to describe the evolution of Young and shear modulus in compacted

intermediate soils. With these laws the Young and shear modulus grow depending on the increase in suction and the increase in the confining net stress separately. Using this description the exponent of the power law for unsaturated soils fall in similar values than the exponent characteristic of the power law used for saturated soils in effective stress, however more tests are required to elucidate the variation of parameters K_G and K_E for different soils and conditions.

REFERENCES

Biarez, J. and Hicher, P.-Y. (1994): Elementary mechanics of soil behaviour–saturated and remoulded soils, Balkema.

Brignoli, E., Gotti, M. and Stokoe, K.H. (1996): Measurement of shear waves in laboratory specimens by means of piezoelectric transducers, Geotechnical Testing Journal, 19, (4), 384 –397.

Caicedo, B., Coronado, O., Fleureau, J.M. and Gomes Correia, A. (2009): Resilient behaviour of non-standard unbound granular materials, Int. J. Road Materials and Pavement Design, X(2) 287–312.

Chang, T.S. and Woods, R.D. (1987): Effect of confining pressure on shear modulus of cemented sand. Developments in geotechnical engineering, *Soil structure Interaction*. Elsevier,New York, ch. 43, 193–208.

Dano, C. and Hicher, P.Y. (2002): Evolution of elastic shear modulus in granular materials along isotropic and deviatoric stress paths, *Proc*. 15th *ASCE Engineering Mechanics Conference, Columbia University.* 6 p.

Fleureau, J.-M., Hadiwardoyo, S. and Gomes Correia, A. (2003). Generalised effective stress analysis of strength and small strains behaviour of a silty sand, from dry to saturated state, *Soils and Foundations,* 43(4), 21–33.

Hardin, B.O. and Richart, F.E. (1963): Elastic wave velocities in granular soils, *Journal of the Geotechnical Engineering Division, ASCE,* 89(1), 33–65.

Iwasaki, T. and Tatsuoka, F. (1977): Effects of grain size and grading on dynamic shear moduli of sands, *Soils and Foundations,* 17(3), 19–35.

Jovičić, V., Coop, M. and. Simic. M. (1996): Objective criteria for determining Gmax from bender element tests, Géotechnique, 46(2), 357–362.

Kawaguchi, T., Mitachi, T. and Shibuya, S. (2001): Evaluation of shear wave travel time in laboratory by bender element test, *Proc 15th Int Conf. Soil Mechanics Foundations*, Istanbul, 1, 155–158.

LCPC—Laboratoire Central des Ponts et Chaussées (1992): *Réalisation des remblais et des couches de forme*, " France, Fascicules I 98p et II 102p.

Lings, M.L. and Greening, P.D. (2001): A novel bender/extender element for soil testing, *Géotechnique*, 51(8), 713–717.

Lo Presti, D.C.F., Jamiolkowski, M., Pallara, O., Cavallararo, A. and Pedroni, S. (1997): Shear modulus and damping of soils, *Géotechnique*, 47(3), 603–617.

Lohani, T.N., Imai, G. and Shibuya, S.T. (1999): Determination of shear wave velocity in bender element test, Proceedings of the second International Conference on Earthquake Geotechnical Engineering, Lisbon, 1, 101–106.

Mancuso, C., Simonelli, A.L. and Vinale, F. (1989): "Numerical analysis of in situ S-wave measurements", Proc. of the 12th International Conference on Soil Mechanics and Foundation Engineering, Rio de Janeiro, 1, 277–280.

Mohsin, A.K.M. and Airey, D.W. (2003): Automating Gmax measurement in triaxial test. Deformation characteristics of Geomaterials, Proceedings of the 3rd International Symposium ISLyon. Balkema, Lyon, 73–80.

Murillo, C., Thorel, L. and Caicedo, B. (2009a): Spectral Analysis of Surface waves technique to evaluate the shear wave velocity in centrifuge models. *J. Applied Geophysics.* June, 68, 135–145. doi: 10.1016/j.jappgeo.2008.10.007.

Murillo, C., Caicedo, B. and Thorel, L. (2009b). A miniature falling weight for non destructive characterization of soils. Technical Note. *Geot. Testing J.ASTM,* 32(5), 465–474.

Scholey, G.K., Frost, J.D. and Jamiolkowski, M. (1995): A review of instrumentation for measuring small strains during triaxial testing of soils specimen, *Geotechnical Testing Journal*, 18(2), 137–156.

Shirley, D.J. and Hampton, L.D. (1977): Shear wave measurements in laboratory sediments". *J. Acoust. Soc. Am.,* 63(2), 607–613.

Viggiani, C. and Atkinson, J.H. (1995): Interpretation of bender element tests". Géotechnique, 45(1), 149–154.

Wu, S., Gray, D.H. and Richart, Jr. (1984): Capillary effects on dynamic modulus of sands and silts". *J. Geotechnical Engineering"., ASCE*, 110(9), 1188–1203.

Xu, J., Ng, C.W.W. and Yung, S.Y. (2008): Drying and wetting effects on shear wave velocity of an unsaturated soil, *Unsaturated soils; advances in Geo-engineering*. Toll et al. (eds), Taylor & Francis, 525–530.

This page intentionally left blank

Advances in Unsaturated Soils – Caicedo et al. (eds)
© 2013 Taylor & Francis Group, London, ISBN 978-0-415-62095-6

Evaluation of soil matric suction, microstructure and its influence on collapsible behavior

J. Ramos & Y. Valencia
National University of Colombia, Medellín

ABSTRACT: This paper examines the role of microstructure and matric suction in the collapse behavior of residual soils, were carried out a series of physical classification tests,the microstructure of the specimens was examined by Scanning Electron Microscope (SEM), and the ASTM Filter Paper Method was used to determine their matric suction; Results evidenced that the collapse phenomenon is linked to breaking open the soil microstructure showing grains of quartz bound together by clays (kaolinite) or oxides and hydroxides of iron or aluminum (hematite, gibbsite) and the sharp reduction on matric suction during wetting of the sample which affects the stability of the slopes, furthermore some trend was observed for collapsible and non-collapsible soils in water retention curve.

1 INTRODUCTION

Residual soils occur in most countries of the world but the greater areas and depths are normally found in tropical humid areas. In these places, the residual soil (also known as tropical residual soils) forming processes are still very active and the weathering development is much faster than the erosive factor. The origin, formation and occurrence of tropical residual soils have been described in detail by [Singh and Huat, 2004].

Deep groundwater condition is not unusual in tropical residual soils especially within steep slopes. Soils above the groundwater are certainly unsaturated, hence negative pore water pressure also known as matric suction plays an important role in controlling the shear strength and consequently the stability of many steep slopes.

Ignorance or lack of understanding of the geotechnical behavior of soil in the partially or unsaturated state has caused a lot of damages to infrastructures, buildings and other structures. For instances, the collapsibility and volume change of partially saturated soils in connection with the drying or wetting causes a lot of damage in foundation, roads and other structures. It is also observed that many shallow slope failures involve a slumping (collapse) type of failure. As such, the development of extended soil mechanics, which embraces the soil in the unsaturated state or subjected to soil suction, is essential as detailed by Azlan et al.

Most residual soil exhibit high suctions for most of the year. The absence of positive pore water pressure except immediately after rain makes conventional soil mechanics for saturated soil not so relevant. In particular, the effective stress theories of saturated soil are not applicable at the practical level.

1.1 *Theorical framework*

A general partial differential equation to describe the one-dimensional consolidation of an unsaturated soil [Fredlund and Hasan, 1978] can be rewritten for a collapsible soil [Tadepalli and Fredlund, 1991] as follows,

$$\frac{\partial u_w}{\partial t} = \frac{1}{C_v^w}\frac{\partial^2 u_w}{\partial^2 y} + \frac{\partial C_v^w}{\partial y}\frac{\partial u_w}{\partial y} \tag{1}$$

where:

u_w = pore-water pressure.
C_v^w = coefficient of consolidation with respect to the water phase.
y = vertical Cartesian coordinate.
t = time.

The constitutive relations for unsaturated soils can be used to predict the volume change of a collapsible soil during inundation. The equation

can be written as follows [Tadelli and Fredlund, 1991].

$$\frac{dV_w}{V_0} = m_2^s \, d(-u_w) \tag{2}$$

where:

dV_v = change in total volume.
V_o = initial volume of the soil.
$d(-u_w)$ = change in pore water pressure.
M_2^s = coefficient of total volume change with respect to a change in matric suction at a constant net normal stress.

As we can appreciate the equation, the collapse phenomenon is primarily related to the reduction of the matric suction during inundation, matric suction is one of the two stress-state variables that control the behavior of an unsaturated soil; there is a one-to-one relationship between matric suction and total volume change for a soil exhibiting collapse behavior during inundation.

Factors influencing collapse behavior of unsaturated soils include water content, degree of saturation, relative compaction and particle size [Olsen and Langfelder, 1965; Krahn and Fredlund, 1972; Houston et al., 1994; Rao and Revanasiddappa, 2000]. Besides the above mentioned factors, the microstructure is expected to influence soil collapse and also matric suction of unsaturated soils as it determines the relative abundance of different types of pores (large, small, etc.), soil collapse is referred to high porous media, and presence of clay minerals and iron oxide.

The arrangement and bonding that occur between micro-structure units determines the relative abundance of macropores and micropores in an undisturbed soil. Visual illustration of microstructure features of an undisturbed is presented by the scanning electron microscope (SEM) in Fig. 1.

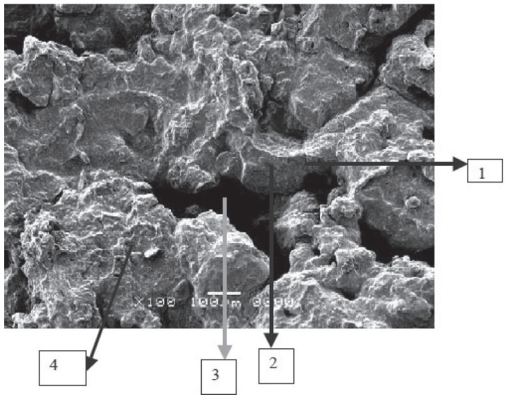

Figure 1. SEM showing micro-structure of undisturbed red soil sample: (1) inter-granular contact, (2) sand particle, (3) macropore, (4) clay aggregate. (Sudhakar).

2 MATERIAL AND TEST METHODS

2.1 *Collection and data properties of specimens*

Undisturbed soil specimens were collected from different locations for collapsible and non-collapsible behavior to determine the influence that soil structure and soil suction on collapsible phenomenon, the laboratory data obtained was processed, details the in-situ properties of the undisturbed soil specimens from the locations are displayed later.

2.2 *Soil suction measurement*

The ASTM Filter Paper Method (ASTM D5928-94 Standard Test Method for Measurement of Soil Suction) determined the matric suction of the undisturbed and remolded specimens in the unsaturated state.

The in-contact filter paper technique is used for measuring matric suction of soils. Direct contact between the filter paper and the soil allows water in the liquid phase and solutes to exchange freely. [Fredlund et al., 1995], In the in-contact filter paper technique, water content of an initially dry filter paper increases due to a flow of water in liquid form from the soil to the filter paper until both come into equilibrium. Therefore, a good contact between the filter paper and the soil has to be established. After equilibrium is established between the filter paper and soil, the water content of the filter paper is measured. Then, by using the appropriate filter paper calibration curve, the suction of the soil is estimated.

2.3 *Index properties*

Index property tests such as grain size distribution and Atterberg limit tests were performed on

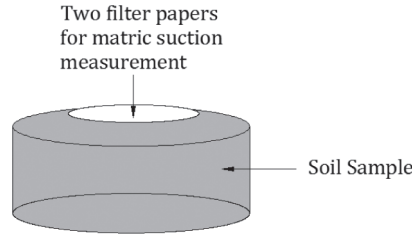

Figure 2. Suction Test Scheme.

Table 1. Index properties of soil samples.

Location	Index Properties		In-Situ Moisture (%)
	LL	IP	
Barbosa1	38	2	19
Barbosa2	28	6	22
Barbosa3	34	5	25
Marinilla	46	12	18
Caldas	77	22	48
Santa Elena	64	12	44
Santuario	39	2	18
Medellín	55	NP	19
Brasil*	–	–	–

representative soils collected from the test pits. Two laboratory tests are commonly used to determine the grain size distribution of soils, namely the sieve analysis and hydrometer test. The sieve analysis determines the grain size distribution of particles larger than 75 Am (gravel and sand termed as coarse-grained soils). Hydrometer analysis gives insight in the distribution of finer particles (silts and clays termed as finegrained soils). Natural soils almost always contain a variety of particle sizes mixed together. The Atterberg limits assess the plasticity of a soil and its consistency at various moisture contents. The commonly performed Atterberg limits tests are the liquid limit test and the plastic limit test. The liquid limit (LL) of a soil represents the water content at which a soil transits from liquid to plastic state. The plastic limit (PL) of a soil represents the water content at which a soil transits from plastic to semi-solid state. Plasticity index (PI) defined as the difference between liquid limit and plastic limit represents the range of water content in which the soil is plastic, i.e., can be easily molded without cracking or breaking. Soils with large clay content remain plastic over a wide range of water content and thus have large plasticity index. The plasticity index is important in classifying finegrained soils based on Casagrande's plasticity chart.

2.4 *Soil structure analysis*

A scanning electron microscope (SEM) is a type of electron microscope that images a sample by scanning it with a beam of electrons in a raster scan pattern. The electrons interact with the atoms that make up the sample producing signals that contain information about the sample's surface structure, composition, and other properties such as electrical conductivity.

One of the newer and most promising qualitative methods for studying and, where possible quantifying, the arrangements of aggregations/particles and voids in unsaturated soils is the environmental scanning electron microscopy (SEM). SEM is a special type of scanning electron microscope that works under controlled environmental conditions and requires no conductive coating on the specimen. This makes it possible to examine wet samples and to preserve their natural characteristics for further testing, A schematic cross section of the equipment is shown in Fig. 3. As observed in the figure, the sample chamber is at a higher pressure (absolute pressure up to 3 kPa) and separated from the increasing vacuum regions by the pressure-limiting apertures.

It is expected that vacuum will not diffuse from one level to another through the small holes bored in the aperture discs, allowing maintaining a very good vacuum in the electron gun (10–5 Pa) as shown in the figure and a poor vacuum in the specimen chamber.

2.5 *Double oedometer collapse test*

The quantification of volume change occurs when soil undergoes collapse is obtained from oedometer test. Once the geotechnical engineer recognizes the possibility of collapsible soils is present, this mainly done depending on the density and consistency limits measurements [Lutenegger & Saber 1988].

Two identical samples are placed in oedometers; one tested at in-situ natural moisture content, and the other is fully saturated before the test begins, and then subjected to identical load-

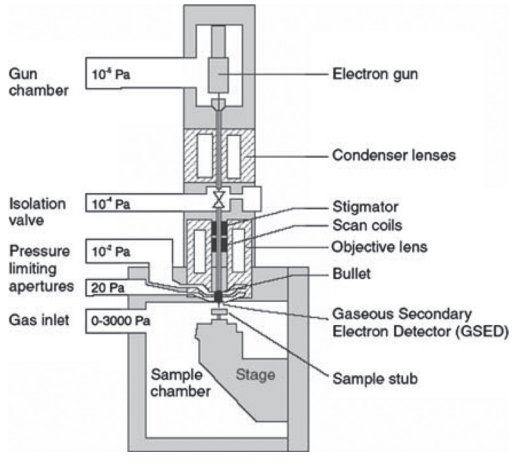

Figure 3. Schematic cross section of an SEM (Danilatos 1993).

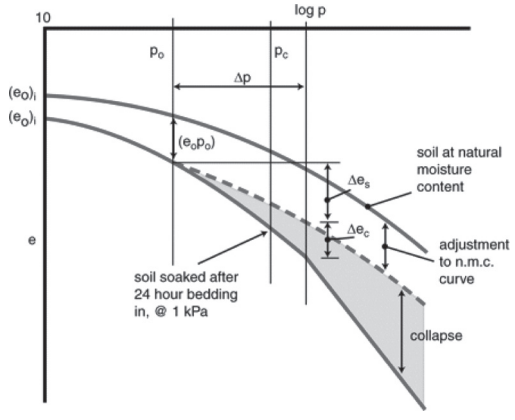

Figure 4. Typical collapse potential test result.

ing. Two stress versus strain curves are generated. The difference between the compression curves is the amount of deformation that would occur at any stress level at which the soil get saturated. An idealized view of double oedometer test is shown in figure 4. Critical stress (σcr) represents the stress level at which the dry sample loose structure breaks down and beyond it the two curves converge. This behavior could be explained also by that at high stress level, the limiting void ratio for the saturated sample is approached for particles packing. It is common for natural soil that the initial void ratio of the two samples are not initiating from the same point; in this case adjustment of the two curves according to the procedure proposed by [Jennings, J. E. and Knight, 1975] shall be adopted.

3 RESULTS AND DISCUSSIONS

3.1 *Soil structure analysis*

As [Bishop and Blight 1963] postulate we can appreciate that collapse is due to wetting induced reduction in strength of clay bridges existing between unweathered grains in an open structure below existing applied stress.

Soil structure and X-Ray diffraction showing grains of quartz bound together by clays (kaolinite) or oxides and hydroxides of iron or aluminum (hematite, gibbsite) and the sharp reduction on matric suction during wetting of the sample which affects the stability of the slopes, furthermore some trend was observed for collapsible and non-collapsible soils in water retention curve, it is now understood that collapse produced by a system of macropeds deforming to displace

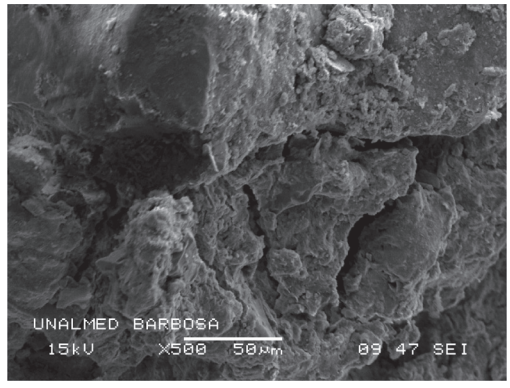

Figure 5. Results from SEM (Barbosa).

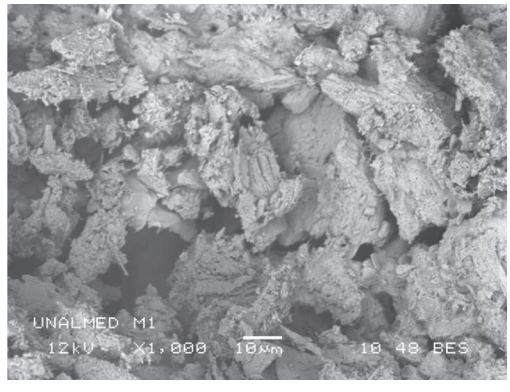

Figure 6. Results from SEM (Santa Elena).

Figure 7. Results from SEM (Marinilla).

air from a network of inter aggregate pores, and is strongly related to the relative abundance of the different pore sizes within a soil matrix [Rao & Revanasiddappa, 2006].

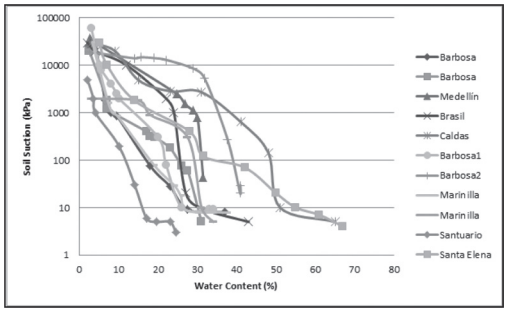

Figure 8. Results from soil suction test and data.

3.2 *Soil collapse analysis*

The deflection under each load was appreciated along with the matric suction values. An important change in matric suction was commonly observed during the loadings during inundation. The soil specimens was left in the inundated condition for 24 hours for each change of load. Most of collapse occurred in the first few minutes after inundation, that would explain the general objective of this paper that relate the first deflection of the soil retention curve on with the collapse behavior, soil specimens that do not have double oedometer test was classified by [Lutenegger and Saber 1988] methodology that relate the liquid limit and natural dry density with collapse potential.

3.3 *Soil suction analysis*

Collapsible and Non-collapsible soil curves were plotted,the suction curves of collapsible soils tend to have more deflection than non-collapsible early, plus these have a residual behavior, while non-collapsible note is achieved without a marked as asymptotic trend.

4 CONCLUSIONS

- Differences in matric suctions and pore-size distributions of (a) undisturbed residual soil specimens from the same location, (b) undisturbed residual soil specimens from different locations and imply that the micro-structure has a major influence on the matric suction of the residual soil specimens in the undisturbed and remolded conditions.
- In traditional soil mechanics theory an increase in effective stress results in a volume decrease. Conversely, an effective stress decrease results in a volume increase. For a soil with a collapsible structure this does not necessarily hold true.
- Micro-structure determines the relative abundance of different types of pores in a soil. SEM results indicated that the pore-size distribution of the undisturbed and residual soil specimens has bi-modal character. Based on the findings of the earlier researchers as Sudhakar, it is inferred that the large pore mode contributes to the inter-aggregate porosity constituted by the macropores. The small pore mode contributes to the intra-aggregate porosity constituted by the micropores. The matrix suction of the undisturbed residual soil specimens is greatly influenced by the relative abundance of the interaggregate porosity and intra-aggregate porosity suggested by the matrix suction results of the residual soil specimens in the undisturbed conditions.
- Collapsible and Non-collapsible soils show a trend in characteristic curve, this indicate that exist some relationship between soil suction curve shape and collapse behavior. The microstructure has an important role because the types and sizes of pore determine the interaggregate soil.

REFERENCES

Alonso, E.E. & Gens, A. 1994. On the mechanical behaviour of arid soils. Proceedings First International Symposium on Engineering, Characteristics of Arid Soils, London, pp. 173–205.

ASTM D5298-03. Standard Test Method for Measurement of Soil Potential (Suction) Using Filter Paper.

Barden, L., Mcgown, A. & Collins, K. 1973. The collapse mechanism in partly saturated soils. Engineering Geology 7: 49–60.

Burland, J.B. 1961. Discussion on collapsible soils. Proceedings 5th International Conference on Soil Mechanics and Foundation Engineering, Paris, vol. 3, pp. 219–220.

Carvalho, D. & Albuquerque, P.J.R. 2007. Analisé do Comportamento colapsíble de uma argila laterítica, de origen coluvionar da regiao de campinas. 6° Simpósio sobre Solos Não Saturados.

Carvalho, J.B.Q. & Simmons, J.V. 1997. Mineralogy and microstructure. In: Blight, G.E. (Ed.), Mechanics of Residual Soils. Balkema, Rotterdam, pp. 95–152.

Jennings, J. E. & Knight, K. 1975. A guide to construction on or with materials exhibiting additional settlement due to collapse of grain structure. 6 th regional conference for Africa on soil mechanics and foundation engineering Durban, South Africa, 99–105.

Lutenegger, A.J. & Saber, R.T. 1988. Determination of collapse potential of soils. Geotechnical Testing Journal 11(3): 173–178.

Ortiz, J. & Valencia, Y. 2010. Caracterización físico—química, mineralógica y mecánica de un suelo tropical

de la margen izquierda del río Medellín a la altura de Barbosa. XIII Congreso Colombiano de Geotecnia—VII Seminario Colombiano de Geotecnia, Manizales.

Ramos, J. & Valencia, Y. 2010. Evaluación de la colapsabilidad de los suelos en la doble calzada Hatillo-Barbosa. XIII Congreso Colombiano de Geotecnia—VII Seminario Colombiano de Geotecnia, Manizales.

Rao, S.M. & Revanasiddappa, K. 2000. Role of matric suction in collapse of compacted clay soil. ASCE Journal of Geotechnical and Geoenvironmental Engineering 126: 85–90.

Rao, V. & Revanasiddappa, D. 2006. Influence of cyclic wetting and drying on collapse behaviour of compacted residual soils. Geotech. Geol. Eng. 24: 725–734.

Revanasiddappa, K. 2000. Collapse behaviour of red soils of Bangalore District, Indian Institute of Science, Doctoral thesis.

Singh, H. & Huat, B.B.K. 2004. Origin, formation and occurrence of tropical residual soils. Tropical Residual Soils Engineering. Huat et al. (Ed). Leiden. Balkema, pp. 1–20.

Sudhakar, M. & Raoa, K. Revanasiddappa, Role of micro-structure in matrix suction of residual soils, Indian Institute of Science.

Velez, M., Valencia, Y. & Echeverri, O. 2010. Comparativo entre la succión medida en laboratorio y la succión medida en campo de la capa superficial de una ladera del corregimiento de Santa Elena, Antioquia. XIII Congreso Colombiano de Geotecnia—VII Seminario Colombiano de Geotecnia, Manizales.

Advances in Unsaturated Soils – Caicedo et al. (eds)
© 2013 Taylor & Francis Group, London, ISBN 978-0-415-62095-6

An experimental study on the stiffness of a lime-treated clayey soil

A.M. Tang, M.N. Vu & Y.J. Cui
Ecole des Ponts ParisTech, Marne-la-Vallée, France

ABSTRACT: The present work investigates the stiffness of a compacted lime-treated clayey soil using bender elements. The studied soil was sieved through various target maximum grain size (D_{max}), humidified to reach the target water contents w_i, then mixed with 3% of quick lime powder prior to static compaction at a dry density of 1.60 Mg/m^3. Two initial water contents and four maximal grain sizes were accounted for. The soil stiffness was then monitored in variable time intervals until reaching stabilization. Afterwards, the soil specimen was subjected to full saturation followed by air-drying to come back to its initial water content. The results show that the soil stiffness after lime-treatment is significantly dependent on the aggregates size. The wetting-drying cycles seem to slightly increase the soil stiffness in the case of lime-treated specimens and decrease the soil stiffness in the case of untreated specimens.

1 INTRODUCTION

Lime treatment is a well-known technique in civil engineering applications such as road construction, embankments, slab foundations and piles. Adding lime to clayey soils leads to various reactions such as cation exchange, flocculation, carbonation and pozzolanic reaction (Boardman et al., 2001). These reactions give rise to improvement of their hydro-mechanical properties. Indeed, the treatment reduces the swelling potential (Tonoz et al., 2003, Al-Rawas et al., 2005), increases the shear strength (Bell 1996, Osinubi & Nwaiwu 2006, Sivapullaiah et al., 2006, Consoli et al., 2009), increases the elastic modulus (Bell 1996, Rogers et al., 2006, Sakr et al., 2009), modifies the compaction properties (Bell 1996, Osinubi & Nwaiwu 2006, Consoli et al., 2009). The water retention properties of clays can be also modified by the lime treatment (Clare & Cruchley 1957). Microstructural investigations on lime-treated clays show that the treatment changes the soil fabric significantly (Cai et al., 2006, Russo et al., 2007, Shi et al., 2007, Le Runigo et al., 2009, Sakr et al., 2009). Moreover, the above studies have shown equally that the effects of lime treatment depend on lime content, soil water content, soil type, curing time, temperature, stress state, etc.

Even though numerous studies have been performed to analyze the effect of lime treatment, almost all works have involved soil specimens prepared in laboratory conditions. Investigations of the lime-treated soil specimens taken from the field still remain rare. Bozbey & Guler (2006) investigated the feasibility of using a lime-treated silty soil as landfill liner material by conducting tests on both laboratory and field scales. They found that the hydraulic conductivity measured on the specimens prepared in laboratory was one order of magnitude lower than that of undisturbed samples taken from the field. Cuisinier & Deneele (2008) performed suction-controlled oedometer tests on soil samples taken from an embankment 3 years after the construction. They also performed the same tests on untreated soil and treated specimens prepared in the laboratory. The results show that the swelling potential of the lime-treated samples taken from the field is significantly larger than that prepared in the laboratory but still remains lower than that of the untreated samples. They attributed this loss of stabilization efficiency in field conditions to the effects of drying-wetting cycles related to climatic changes. The impact of cyclic wetting/drying on swelling properties of lime-stabilized clays was also investigated by Rao et al. (2001), Guney et al. (2007) and Khattab et al. (2007) showing the reduction of the efficiency of lime treatment with wetting-drying cycles.

One of the main reasons for the difference between lime-treated soil samples prepared in the laboratory and the treated soil samples taken from the field could be the difference in aggregates size. Indeed, prior to compaction in the laboratory, the soil is usually sieved at a few millimeters and then mixed with lime. On the contrary, in the field, the dimension of clay clods may reach several centimeters before the treatment.

The present work aims at investigating the effects of grains size on the efficiency of lime treatment. For this purpose, air-dried soils were grounded and sieved at 4 values of passing dimension (0.4, 1, 2, and 5 mm) prior to lime-treatment and compaction. The shear moduli of soil specimens were

monitored using the bender element method. When reaching the stabilization of the shear moduli, wetting-drying cycles were applied in order to investigate the weathering effects.

2 SOIL STUDIED AND EXPERIMENTAL TECHNIQUES

The soil used in this study is a soil taken at a site near Tours, a city in central France. Its main geotechnical properties are shown in Table 1. The clay fraction (<2 μm) is about 26%. After sampling, the soil was air-dried, ground and finally passed through one of the four target sieve sizes (0.5, 1.0, 2.0, and 5.0 mm). The remained soil was ground again and passed though the sieve until the entire soil mass passed though the target sieve. The soil was then humidified by spraying distilled water to reach the target moisture content and sealed in plastic box for at least 48 h for moisture content homogenization. For each sieve size, two water contents were considered: 14% and 18%. Prior to compaction, the moist soil and lime were thoroughly mixed and then poured in a cylinder mould of 50 mm in diameter. Static compaction was then carried out to a dry density of 1.6 Mg/m^3 with a final height of the soil specimen of 50 mm. After the compaction, the soil specimen was taken out of the mould and then wrapped by plastic film in order to prevent from any moisture exchange between soil and atmosphere.

The bender elements technique was used to monitor the shear modulus. The experimental set-up is shown in Figure 1. The soil specimen was put in contact with two bender elements: the transmitter one embedded on the top base and the receiver one embedded on the bottom base. Both bender elements were connected to a control and data logging system. When performing a measurement, a triggered sinusoidal signal was sent to the transmitter; the response of the receiver was recorded. The travel time (Δt) of the shear wave can be then determined. Considering the travel length, l, which is equal to the specimen height (50 mm) minus the protrusions of the bender transmitter and receiver into the soil specimen (2 mm), the shear wave velocity can be then calculated as follows: $V_s = l/\Delta t$. The soil density (ρ) was verified after each measurement by weighing the soil specimen, and it was used for the determination of the small strain shear modulus, G_{max}, as follows: $G_{max} = \rho V_s^2$. This experimental technique is similar to that recently used by Puppala et al. (2006) when monitoring the shear modulus of chemically treated sulfate-bearing expansive soils.

Table 1. Geotechnical properties of soil studied.

Properties	*Value*
Liquid limit, w_L (%)	45
Plastic limit, w_P (%)	21
Plasticity index, I_p (%)	24
Value of blue of methylene, *VBS*	4.86
Carbonates content (%)	0.35
Specific gravity, G_S	2.70

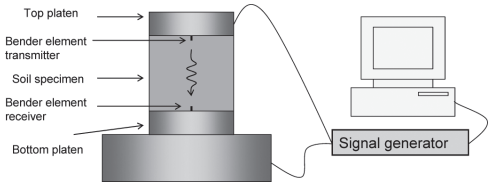

Figure 1. Experimental set-up.

The cyclic wetting/drying was applied according to the following procedure. When the stabilization of G_{max} after treatment was reached, the soil specimen was first wetted. Water was added to the soil specimen carefully using a sprayer and the weight of the specimen was monitored. A water content of 21% (corresponding to a degree of saturation S_r = 82%) was chosen. Actually, at this water content, adding more water on the upper surface of the soil specimen would lead to water drainage from its lower surface; this value of water content correspond therefore to the maximum value that the soil specimen can retain. After reaching the target water content, the soil specimen was wrapped again by plastic film and let for at least 24 h for moisture homogenization prior to the G_{max} measurements. For the drying, the plastic film was removed and the soil was air-dried until the target water content was reached. Afterwards, the soil specimen was wrapped again by plastic film and let for at least 24 h.

To sum up, the following parameters were considered in this study: 2 molding water contents (14 and 18%); 4 maximum grain diameters (0.5, 1, 2, and 5 mm). In each case, both treated and untreated specimens were tested. Moreover for each test, 3 identical specimens were investigated for replicate. That corresponds to 48 soil specimens in total.

3 EXPERIMENTAL RESULTS

After compaction, the small strain modulus G_{max} was monitored in order to follow its changes versus time. In Figure 2, the mean value of G_{max} (measured on 3 identical specimens) is plotted versus time for the soil passed through 0.4 mm sieve. Just after the compaction, G_{max} of untreated specimens

was equal 65 MPa for an initial water content w_i = 14% and 44 MPa for an initial water content w_i = 18%. The values increased slightly with time and stabilized after 100 h at 73 MPa and 50 MPa, respectively. In the case of treated specimens, G_{max} was equal 108 MPa for w_i = 14% and 80 MPa for w_i = 18%. Comparison with the values of untreated specimens shows that the lime-treatment has a significant effect on G_{max} just after the compaction. With time G_{max} increased also and stabilized after 200 h at 121 MPa for w_i = 14% and 122 MPa for w_i = 18%. The increase was more significant in the case of higher water content (w_i = 18%). Interestingly, the stabilized G_{max} value has been found to be similar for both water contents.

Similar observation can be made from the results of soil passed through other sieves: i) an immediate effect of lime-treatment after compaction, characterized by a significant increase of G_{max}; ii) a slight increase of G_{max} with time for untreated specimens; iii) an increase of G_{max} with time for treated specimens especially in the case of higher water content (w_i = 18%); iv) stabilization of G_{max} about 200 h after the treatment, with similar final values for both water contents.

In order to analyze the effect of maximum grain size D_{max} on G_{max}, the mean final values of G_{max} and the error bars (measured on 3 identical specimens) are shown in Figure 3 versus D_{max}. For the treated soil compacted at w_i = 14% (Fig. 3*a*), G_{max} was found to be decreasing with D_{max}, the highest value is 120 MPa for D_{max} = 0.4 mm and the lowest value is 103 MPa for D_{max} = 5.0 mm. Similar observation can be made for the treated soil compacted at w_i = 18% (Fig. 3*b*): the higher the maximum grain size the lower the value of G_{max}. For the untreated specimens, the effects of D_{max} on G_{max} were not significant for the wetter specimen (w_i = 18%). For the drier specimen (w_i = 14%), the curve shows a decrease of G_{max} followed by an increase with the lowest value at D_{max} = 2 mm.

Cyclic wetting/drying was carried out by controlling the water content of the soil specimen. In Figure 4, G_{max} is presented versus elapsed time for the soil passed through 0.4-mm sieve. The corresponding water content at each measurement is also added. The starting points (t = 0) correspond to the last points shown in Figure 2. At the initial water content w_i = 14% (the corresponding degree of saturation is S_r = 55%), the initial value of G_{max} was equal to 73 MPa (Fig. 4*a*) for the untreated specimen. Wetting to a water content of 21% (S_r = 82%) decreased G_{max} to 28 MPa. The subsequent drying to the water content of 14% (at t = 100 h) increased G_{max} to 50 MPa. Cracks were observed after the subsequent wetting/drying path that explains the decreases of G_{max}.

For the specimen treated at the initial water content of 14% (Fig. 4*a*), wetting to a water content of 21% decreased slightly G_{max} from 121 to 114 MPa.

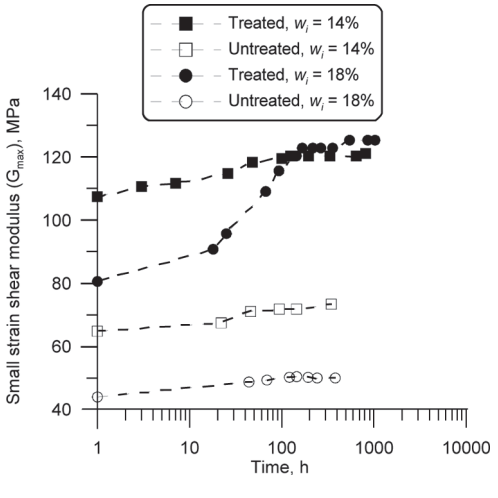

Figure 2. Small-strain shear modulus versus time after compaction. (for G_{max} = 0.4 mm).

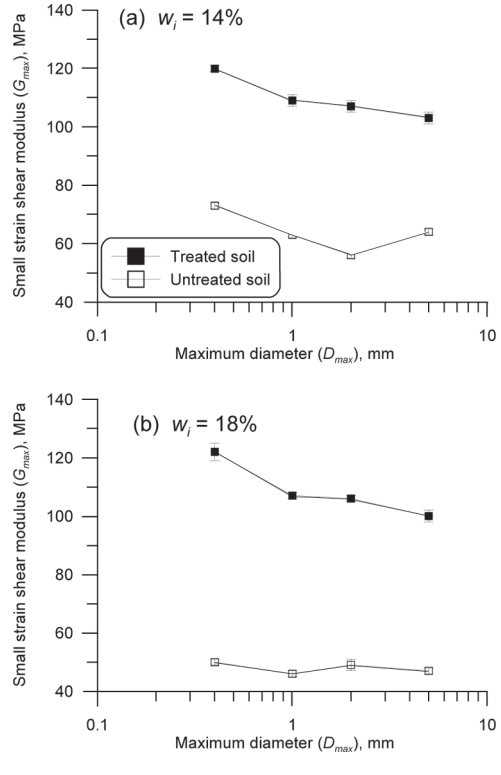

Figure 3. Small-strain shear modulus after stabilization versus maximum diameter.

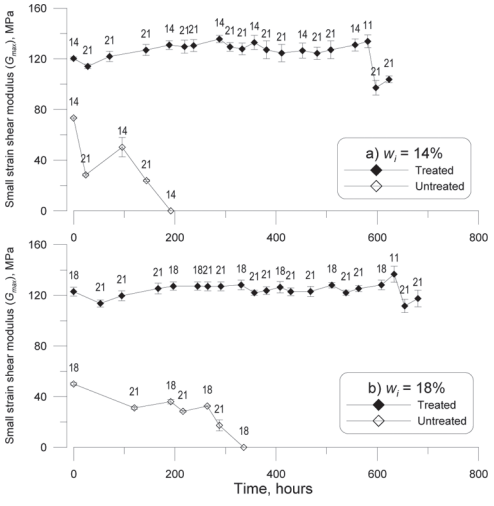

Figure 4. Changes in small-strain shear modulus upon cyclic wetting/drying for D_{max} = 0.4 mm (the corresponding water content is given above each point).

Nevertheless, when this high value of water content was maintained, G_{max} was increasing and reached 127 MPa after 100 h. The subsequent wetting and drying only induced slight decrease and increase of G_{max}. For the last drying stage (at t = 580 h), the water content was reduced to 11%, lower than the initial value. This more intensive drying resulted in a significant decrease of G_{max} when the soil was wetted again to a water content of 21%: G_{max} decreased from 134 to 97 MPa. This can be explained by the apparition of micro-cracks observed on the soil specimens.

For the soil specimen compacted at the initial water content of 18%, micro-cracks appeared on the untreated specimens after 3 wetting/drying cycles, leading to a decrease of G_{max} to zero (Fig. 4*b*). For the treated specimens, the phenomena observed were similar to that of 14% water content: i) a slight increase after the first wetting; ii) small changes upon cyclic wetting/drying; iii) after an intensive drying with the water content decreased to 11%, the subsequent wetting resulted in a drastic decrease due to appearance of micro-cracks.

For the others values of D_{max}, it was equally observed that the untreated specimens compacted at a drier state (initial water content of 14%) showed a decrease of G_{max} to 0 after 3 wetting/drying cycles. It is however not the case for the untreated specimens compacted at a wetter state (initial water content of 18%) except the specimens having D_{max} = 0.4 mm. Indeed, for these specimens, cyclic variations were observed with wetting-drying cycles. For the lime-treated specimens, wetting-drying cycles only induced a small decrease and increase of G_{max}. These changes become significant only when wetting the soil after an intensive drying, up to a water content of 11%. In addition, the effect of this intensive drying seems to be more significant for the drier specimen (initial water content of 14%). The effect of D_{max} upon cyclic wetting/drying has been found to be not significant since the behavior of the soil specimens having different values of D_{max} was quite similar. More details on these results can be found in Tang et al. (2011).

4 DISCUSSION

The bender elements method is usually used to monitor changes in shear wave velocity in triaxial cell under confining conditions. In this case, good contact between the bender elements and the soil specimen can be ensured (Leong et al., 2009, Ng et al., 2009). Application of this method is much more difficult in the case of the present study where the evolution of G_{max} needs to be monitored during several days and on a large number of soil specimens; it was not realistic to use one triaxial cell for each specimen. For this reason, in the present work, the bender elements were put in contact with the soil specimen only during the measurement. In addition, no confining pressure was applied. In order to minimize the test errors, three specimens were tested for each parameter studied. The results showed the good repeatability of the procedure used (see error bars in Fig. 3). Note that Puppala et al. (2006) used equally this technique to study the changes of G_{max} with time for chemically stabilized sulfate-bearing cohesive soils.

The changes of G_{max} of compacted soil specimens were monitored until reaching the stabilization. A slight increase of G_{max} with time was observed for the untreated specimens. This can be explained by the aging effects of compacted clay soils. Indeed, Delage et al. (2006) observed significant changes in microstructure of a compacted expansive soil after compaction. They explained these changes as follows: after the compaction, water situated in the inter-aggregate porosity is absorbed to the intra-aggregate porosity, giving rise to increase of the intra-aggregate porosity. Tang et al. (2008) also observed this phenomenon characterized by a slight increase of soil suction after compaction. The effect of suction on G_{max} was also evidenced in the present study: untreated soil compacted at lower water content (higher suction) has a higher G_{max}. This is in agreement with the observation by Sawangsuriya et al. (2008).

For the treated soil specimens, G_{max} obtained just after the compaction has been found to be

significantly higher than that of untreated soil specimens having the same molding water content. The values of G_{max} of treated specimens are comprised between 80 and 130 MPa. Rogers et al. (2006) performed cyclic triaxial tests and obtained equally a resilient modulus of 80–140 MPa for a compacted clay treated with 2.5% of lime. The increase of G_{max} with lime-treatment can be explained partly by the decrease of water content after treatment. That increases the soil suction and as a consequence increases the value of G_{max}. A second explanation is related to the various reactions within the treated soil such as cation exchange, flocculation, carbonation and pozzolanic reactions. These reactions are probably more significant at a wetter state with more water supply For this reason, the results showed more significant increase of G_{max} with time for the wetter specimens (w_i = 18%, see Fig. 2).

As far as the effect of the maximum grain size (D_{max}) is concerned, the results of the treated specimens showed a lower value of G_{max} for a larger value of D_{max}. This effect was not observed for the untreated specimens. Actually, for a smaller D_{max}, the total surface of aggregates was larger; and therefore more soil-lime reaction can be expected. Note that this observation on the effect of maximum grain size is of importance from a practical point of view. Indeed, laboratory tests are usually performed on small grain size (less than few millimeters) while the grain size of clay aggregates in the field may reach several centimeters. As a consequence, particular attention should be paid when using the parameters determined in laboratory for field application design.

The effects of cyclic wetting/drying on G_{max} were investigated in this study. It has been observed that wetting induced a decrease and drying induced an increase of G_{max}. This phenomenon can be explained by the effect of suction: wetting decreased the soil suction thus the soil stiffness while drying increase the soil suction thus the soil stiffness. The same phenomenon was observed by Ng et al. (2009) when performing measurements of G_{max} in a suction-controlled triaxial cell. Comparison between the treated specimens and untreated specimens shows that the effect of suction change on G_{max} of treated specimen is less significant than that of untreated specimen. This shows that lime-treatment reinforces the soil and makes it less sensitive to suction changes.

For the untreated specimens, it has been observed that wetting/drying cycles resulted in a decrease of G_{max}, especially for drier specimens. That can be explained by the creation of micro-cracks by cyclic wetting/drying under unconfined conditions (Yesiller et al., 2000). In the work of Ng et al. (2009), as the tests were performed under confined conditions the creation of micro-cracks was avoided. For the treated specimens, the first wetting path equally induced a decrease of G_{max}. Nevertheless, after this decrease, the value of G_{max} increased slightly. The immediate decrease of G_{max} can be explained by the effect of suction, while the subsequent increase of G_{max} after wetting can be attributed to the onset of various reactions by water addition. This explains why Kavak & Akyarh (2006) recommended watering the lime-treated soil 1 week after the treatment.

5 CONCLUSION

The small strain shear modulus G_{max} of a compacted lime-treated clayey soil was investigated using bender elements. The following conclusions can be drawn:

1) The lime treatment increases significantly G_{max}. For the two molding water contents considered, G_{max} obtained after the stabilization (about 200 h after the treatment) has been found to be independent of the molding water content.
2) For the four maximal grain sizes D_{max} considered, it has been observed that the larger the value of D_{max} the lower the value of G_{max}. This conclusion is of importance from a practical point of view for earthworks involving lime-treated soil. Indeed, the results obtained show that designing earthworks based on the parameters determined from laboratory tests can be misleading, because D_{max} of the soil tested in laboratory is usually less than few millimeters while D_{max} of clay aggregates in the field may reach several centimeters.
3) Cyclic wetting/drying induced significant decrease of G_{max} of untreated specimens, due to the appearance of micro-cracks. Only an intensive drying to water content much lower than the initial one can induce micro-cracks and thus decrease of G_{max}.
4) For the treated specimens, only the first wetting induced a decrease of G_{max}. And on the contrary the subsequent cycles induced a slight increase of G_{max}. If the decrease due to wetting can be explained by the suction effect, the slight increase by further wetting-drying cycle should be attributed to the onset of various physico-chemical reactions within the soil by water addition.

ACKNOWLEDGEMENT

The authors address their deep thanks to the French National Research Agency for funding the present study which part of the project Terdouest "Sustainable earthworks involving treated soils".

REFERENCES

Al-Rawas, A.A., Hago, A.W. & Al-Sarmi, H. 2005. Effect of lime, cement and Sarooj (artificial pozzolan) on the swelling potential of an expansive soil from Oman. *Building and Environment* 40(5): 681–687.

Bell, F.G. 1996. Lime stabilization of clay minerals and soils. *Engineering Geology* 42(4): 223–237.

Boardman, D.I., Glendinning, S. & Rogers, C.D.F. 2001. Development of stabilisation and solidification in lime-clay mixes. *Géotechnique* 50(6): 533–543.

Bozbey, I. & Guler, E. 2006. Laboratory and field testing for utilization of an excavated soil as landfill liner material. *Waste Management* 26(11): 1277–1286.

Cai, Y., Shi, B., Ng, C.W.W. & Tang, C.S. 2006. Effect of polypropylene fibre and lime admixture on engineering properties of clayey soil. *Engineering Geology* 87(3–4): 230–240.

Clare, K.E. & Cruchley, A.E. 1957. Laboratory experiments in the stabilization of clays with hydrated lime. *Géotechnique* 7(2): 97–111.

Consoli, N.C., Lopes, L.S. & Heineck, K.S. 2009. Key parameters for the Strength Control of Lime Stabilized Soils. *Journal of Materials in Civil Engineering* 21(5): 210–216.

Cusinier, O. & Deneele, D. 2008. Impact of cyclic wetting and drying on the swelling properties of a lime-treated expansive clay. *Journées Nationales de Géotechnique et de Géologie de l'Ingénieur* JNGG'08—Nantes: 18–20.

Delage, P., Marcial, D., Cui, Y.J. & Ruiz, X. 2006. Ageing effects in a compacted bentonite: a microstructure approach. *Géotechnique* 56(5): 291–304.

Guney, Y., Sarib, D., Cetinc, M. & Tuncan, M. 2007. Impact of cyclic wetting–drying on swelling behavior of lime-stabilized soil. *Building and Environment* 42(2): 681–688.

Kavak, A. & Akyarlı, A. 2007. A field application for lime stabilization. *Environ Geol*. 51(6): 987–997.

Khattab, S.A.A., Al-Mukhtar, M. & Fleureau, J.M. 2007. Long-Term Stability Characteristics of a Lime-Treated Plastic Soil. *Journal of Materials in Civil Engineering* 19(4): 358–366.

Le Runigo, B., Cuisinier, O., Cui, J.Y., Ferber, V. & Deneele, D. 2009. Impact of initial state on the fabric and permeability of a lime-treated silt under long-term leaching. *Can. Geotech. J.* 46(11): 1243–1257.

Leong, E.C., Cahyadi, J. & Rahardjo, H. 2009. Measuring shear and compression wave velocities of soil using bender-extender element. *Can. Geotech. J.* 46(7): 792–819.

Ng, C.W.W., Xu, J. & Yung, S.Y. 2009. Effect of wetting-drying and stress ratio on anisotropic stiffness of an unsaturated soil at very small strain. *Can. Geotech. J.* 46(9): 1062–1076.

Osinubi, K.J. & Nwaiwu, G.M. O. 2006. Compaction Delay Effects on Properties of Lime-Treated Soil. *Journal of Materials in Civil Engineering* 18(2): 250–258.

Puppala, A.J., Kadam, R., Madhyannapu, R.S. & Hoyos, L.R. 2006. Small-Strain Shear Moduli of Chemically Stabilized Sulfate-Bearing Cohesive Soils. *Journal of Materials in Civil Engineering* 132(3): 322–336.

Rao, S.M., Reddy, B.V.V. & Muttharam, M. 2001. The impact of cyclic wetting-drying on the swelling behaviour of stabilized expansive soils. *Engineering Geology* 60(1–4): 223–233.

Rogers, C.D.F., Boardman, D.I. & Papadimitriou, G. 2006. Stress Path Testing of Realistically Cured Lime and Lime/Cement Stabilized Clay. *Journal of Materials in Civil Engineering* 18(2): 259–266.

Russo, G., Vecchio, S.D. & Mascolo, G. 2007. Microstructure of a Lime Stabilised Compacted Silt. *Experimental Unsaturated Soil Mechanics—Springer Proceedings in Physics* 112: 49–56.

Sakr, M.A., Shahin, M.A. & Metwally, Y.M. 2009. Utilization of Lime for Stabilizing Soft Clay Soil of High Organic Content. *Geotech Geol Eng.* 27(1): 105–113.

Sawangsuriya, A., Edil, B.T. & Bosscher, P.J. 2008. Modulus-suction-moisture relationship for compacted soil. *Can. Geotech. J.* 45(7): 973–983.

Shi, B., Liu, Z., Cai, Y. & Zhang, X. (2007). Micropore Structure of Aggregates in Treated Soils. *Journal of Materials in Civil Engineering* 19(1): 99–104.

Sivapullaiah, P.V., Sridharan, A. & Ramesh, H.N. 2006. Effect of sulphate on the shear strength of limetreated kaolinitic soil. *Ground Improvement* 10(1): 23–30.

Tang, A.M., Cui, Y.J. & Barnel, N. 2008. Compression-induced suction change in a compacted expansive clay. *Unsaturated Soils: Advances in Geo-Engineering, Proc. 1st European Conf. on Unsaturated Soils,* Durham, UK (ed. Toll, D.G., Augarde, C.E., Gallipoli, D. & Wheeler, S.J.), Leiden: CRC Press/Balkema: 369–374.

Tang, A.M., Vu, M.N. & Cui, Y.J. 2011. Effects of the maximum grain size and cyclic wetting/drying on the stiffness of a lime-treated clayey soil. *Géotechnique* 61(5): 421–429.

Tonoz, M.C., Gokceoglu, C. & Ulusay, R. 2003. A laboratory-scale experimental investigation on the performance of lime columns in expansive Ankara (Turkey) Clay. *Bull Eng Geol Env*. 62: 91–106.

Yesiller, N., Miller, C.J., Inci, G. & Yaldo, K. 2000. Dessication and cracking behavior of three compacted landfill liner soils. *Engineering Geology* 57(1–2): 105–121.

Advances in Unsaturated Soils – Caicedo et al. (eds)
© 2013 Taylor & Francis Group, London, ISBN 978-0-415-62095-6

Effects of relative humidity cycling on the hydro-mechanical behaviour of two clayey rocks from North-East Spain

J.A. Pineda
ARC Centre of Excellence for Geotechnical Sciences and Engineering, The University of Newcastle, Australia (formerly at Universitat Politécnica de Catalunya, Barcelona)

E. Romero
Department of Geotechnical Engineering and Geosciences, Universitat Politécnica de Catalunya, Barcelona, Spain

ABSTRACT: The paper describes the results of an experimental research aimed at studying the effects of relative humidity cycling on the degradation phenomena of two clayey rocks from North-East Spain, with particular emphasis on peak shear strength, low-strain stiffness and water permeability. Undisturbed samples were subjected to an extreme relative humidity cycle (between 15% and 99%) using the vapour transfer technique, before performing triaxial compression and water permeability tests. Rock stiffness was evaluated by ultrasonic pulse tests. Test results showed clear differences in stiffness and shear strength response between undisturbed and degraded samples, highlighting the relevance of hydraulically induced degradation phenomena on this type of materials.

1 RELATIVE HUMIDITY SENSITIVITY OF CLAYEY ROCKS

One of the key features of clayey rocks is the enhancement of their water sensitivity when excavated and exposed to the environment such as in slopes, tunnels and excavations. The irreversible consequences of their exposure to relative humidity changes have been recognized and studied by several authors (see e.g., Vales et al., 2004, Alonso & Pineda 2006, Cardoso 2009, Picarelli & DiMaio 2010, Martinez-Bofill et al., 2011, Pineda 2012, to name a few). If chemical processes are not involved, the mineralogical composition, anisotropy, the current stress level as well as the specific hydraulic path applied has been recognized to control the degradation process of clayey rocks (Pineda 2012). In the case of slopes, for instance, the face of the slope is continuously exposed to environmental seasons (including raining periods). It may leads to fast degradation at the surface when extreme suction changes take place. However, the maximum depth of the weathering front will depend on factors described above because they control the evolution of the hydro-mechanical properties of the rock during relative humidity cycling.

In this paper, the dependency of the hydromechanical properties of two clayey rocks (strength, stiffness and permeability) to relative humidity cycling is evaluated. The increase of rock degradation when using liquid water is also analyzed.

2 TESTED MATERIALS AND EXPERIMENTAL PROGRAM

Rocks tested in this work were obtained from two slopes located in two national roads at Idiazabal (IM-18) and Ormaiztegui (OM-9) sites in the North-East Spain (Guipuzkoa). It is interesting to note that similar stability problems have been reported during last decades despite both slopes are so far each other. Representative undisturbed samples where used to carried out a preliminary study aimed to evaluate the degradation potential of both materials. Rocks tested corresponds to argillites from the Upper Cretaceous period mainly composed by (Martinez-Bofill et al., 2011): quartz (OM-9:27%; IM-18:29%), clayey fraction (50%; 60%) being the illite-moscovite the predominant clayey mineral. The percentage of carbonates was around 20% (OM-9) and 9% (IM-18). From characterization tests (clayey fraction) liquid limit and plasticity index showed similar values in both cases (27% and 13%, respectively) whereas density of solids was around 2.78 Mg/m^3.

Triaxial samples (38 × 76 mm) were obtained by dry-coring to minimize alteration induced by liquid water. Even so, only ten undisturbed samples (five from each slope) could be obtained for triaxial testing. Table 1 shows the main properties of tested samples. It can be seen the lower natural gravimetric water content and initial void ratio as well as the higher initial degree of saturation of the specimens.

Table 1. Initial properties of tested samples.

Samples	w_o (%)	ρ_d (Mg/m^3)	e_o (–)	Sr (–)
IM-18_S1	2.11	2.62	0.062	0.95
IM-18_S2	2.12	2.61	0.063	0.94
IM-18_S3	2.12	2.61	0.063	0.94
IM-18_S4	2.12	2.62	0.063	0.94
IM-18_S5	2.11	2.62	0.061	0.96
OM-9_S1	1.78	2.64	0.052	0.95
OM-9_S2	1.78	2.65	0.051	0.97
OM-9_S3	1.50	2.67	0.042	0.99
OM-9_S4	1.79	2.64	0.052	0.96
OM-9_S5	1.79	2.65	0.051	0.97

2.1 *Relative humidity cycling test*

Rock degradation was induced by applying a relative humidity cycle (wetting-drying) on undisturbed specimens via vapour transfer technique. Distilled water inside a desiccator was used to apply the wetting path (RH ≈ 99%) whereas drying was applied using saturated lithium chloride solution (LiCl, RH ≈ 15%). Relative humidity and temperature measurements were continuously monitored using a digital hygrometer placed inside the desiccator. During both wetting and drying paths, a continuous record of sample total density evolution was made using volume and mass measurements.

The evolution of the rock stiffness during relative humidity cycling was tracked by means of small-strain Young modulus measurements. E_0, under unstressed conditions, was determined by measuring longitudinal wave velocities, V_L, using an ultrasonic pulse device (V-Meter®). This device is used to determine the travel time (t_p) of a high frequency (54 kHz) and high voltage compression wave travelling alongside the sample axis. Longitudinal wave velocity and Young modulus were determined as:

$$V_L = \frac{l}{t_p}; \quad E = \rho V_L^2 \tag{1}$$

being l and ρ the sample height and total density, respectively.

2.2 *Triaxial compression tests*

Saturated triaxial compression tests were carried out on both undisturbed and degraded (after hydraulic cycling) specimens. Three stages were applied in each test: (i) saturation, (ii) consolidation, and (iii) shearing. Samples were saturated under total net stresses, p, between 100–500 kPa whereas back pressure, u_w, varied between 50–150 kPa. During this process, the top drainage line was maintained open to the atmosphere. Both p and u_w were maintained at least for three days. Water permeability, k_w, was determined during the last 24 hours of saturation, by assuming steady state conditions, through the Darcy's law as: $k_w = q/(i.A)$, with q being the outflow of water, A the cross section of the sample and i the hydraulic gradient applied. Afterwards, the top drainage line was closed to the atmosphere and the same water back-pressure was applied on both top and bottom during consolidation process. Consolidation stage was maintained during three additional days. Finally, each sample was subjected to shearing at drained conditions until reach the failure of the samples. Back-pressure was maintained at both top and bottom of the samples during shearing. A strain rate equal to 1×10^{-5}%/min was used in all tests.

3 HYDRO-MECHANICAL PROPERTIES OF UNDISTURBED MATERIALS

Five samples were used to determine the hydro-mechanical properties of undisturbed materials (three from IM-18 and two from OM-9). Two different responses were obtained for the outflow water volume registered during the last 24h of saturation process. For samples from IM-18 the water flux (between 0.088 and 0.096 mm^3/min) was around 2 orders of magnitude lower compared with samples from OM-9 (between 0.202 and 4.98 mm^3/min). Water permeability ranged around 10^{-11} m/s (IM-18) whereas k_w ranged between $10^{-11}/10^{-10}$ m/s for samples from OM-9. Table 2 includes the final states of the specimens at the end of saturation.

Figure 1 shows the stress-strain curves obtained during shearing stage. Higher stiffness as well as peak deviatoric stress was observed for samples from OM-9. Tangent modulus, E_{TAN}, obtained for the linear part of the stress-strain curve (typically between 0.2–0.6% of axial strain) ranged between 2350–2600 MPa and between 1400–1560 MPa for specimens from OM-9 and IM-18, respectively. This behavior may be attributed to the high carbonate content (mainly CaCO3) of samples from OM-9 (around 20%).

A linear failure criterion was assumed to determine the peak envelops as observed in Figure 2. The peak stress ratio q/p' was equal to 2.42 and

Table 2. Permeability measurements and consolidation.

Samples	p' (kPa)	w_o (%)	ρ_d (Mg/m^3)	e_o (–)	k_w (m/s)
IM-18_S1	50	2.90	2.57	0.080	–
IM-18_S2	250	3.00	2.57	0.083	2.2×10^{-10}
IM-18_S3	400	2.90	2.57	0.081	1.0×10^{-11}
OM-9_S1	50	2.39	2.61	0.067	4.6×10^{-11}
OM-9_S2	150	2.38	2.61	0.066	3.7×10^{-10}

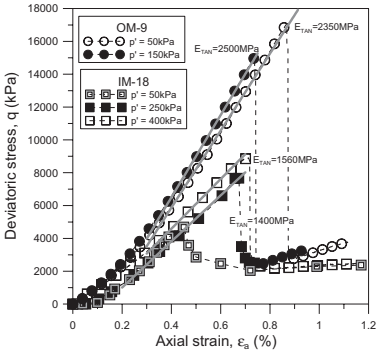

Figure 1. Stress-strain curves for undisturbed materials.

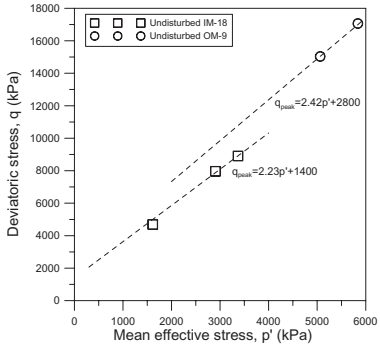

Figure 2. Peak strength envelops for undisturbed materials.

2.23 whereas cohesion intercepts were 2800 and 1400 kPa for OM-9 and IM-18, respectively. Thus, effective friction angles, ϕ', ranged from 59 and 54° whereas effective cohesion, c', varied between 1970 and 870 kPa.

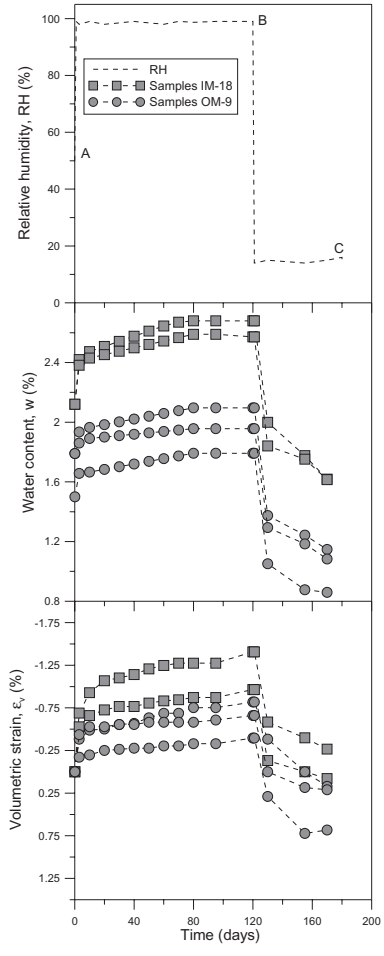

Figure 3. Temporal evolution of w and ε_v during RH cycling.

4 RELATIVE HUMIDITY CYCLING AND HYDROMECHANICAL PROPERTIES OF DEGRADED MATERIALS

Five samples were subjected to relative humidity cycling under unstressed conditions (two from IM-18 and three from OM-9). The vapour transfer technique was used to induce extreme changes in relative humidity from around 99% (using distilled water, $\psi \approx 1.5$ MPa) to 15% (Lithium chloride, LiCl, $\psi \approx 256$ Mpa). Figure 3 shows the temporal evolution of gravimetric water content and volumetric strain during the application of the relative humidity cycle (path A-B). Relative humidity measurements obtained using a digital hygrometer has been also included in this figure. Gravimetric water content increased from around 2.17 to 2.65% for samples from IM-18 whereas a smaller increase was obtained for samples from OM-9 (from 1.79 to around 2.05%). The small variation in gravimetric water content was in agreement with the high initial degree of saturation of the samples. Despite of that, wetting was maintained during 120 days until obtain the equilibrium in both water content and volumetric strains. Hydraulic equilibrium was observed after around 100 days of wetting. Drying reduced the gravimetric water content towards 1.75% and 1.15% for samples from IM-18 and OM-9, respectively. Drying was more efficient (in time) to reach the hydraulic equilibrium so it was maintained only during 60 days.

The average volumetric strain obtained at the end of wetting varied between –1% and –0.70% for samples from IM-18 and OM-9, respectively. Drying induced volumetric shrinkage in all samples. It leads to final average volumetric strains (compression) around 0.10% and 0.25%, espectively. Thus, a small net volumetric shrinkage took place after

RH cycling. As observed in Figure 4, two different fissuring patterns (i.e., rock degradation) came into view during drying which indicates different anisotropic responses. For OM-9, a set of parallel fissures were observed following a dip of around 45°. In the case of samples from IM-18 both horizontal and vertical fissures formed a "quadrilateral" net of fissures. Higher fissuring degree was observed in samples from IM-18 which is consistent with the lower CaCO3 content (around 9%). Table 3 shows values of w, e and S_r obtained at the end of drying.

The evolution of Young modulus during hydraulic cycling is showed in wwwwwwwure 5 as a function of the relative humidity applied. Degradation of Young modulus, E/E_0, was higher for samples from IM-18. It is worth noting the important decreasing in E_0 modulus observed during wetting (between 30–55%) despite the high initial degree of saturation of tested.

Table 3. Final conditions at the end of drying.

Samples	w_f (%)	ρ_{df} (Mg/m^3)	e_f (–)	Sr (–)	E/E_0
IM-18_S4	1.62	2.61	0.065	0.69	0.65
IM-18_S5	1.61	2.62	0.060	0.74	0.57
OM-9_S3	0.85	2.67	0.040	0.59	0.72
OM-9_S4	1.15	2.65	0.050	0.64	0.74
OM-9_S5	1.08	2.66	0.044	0.68	0.73

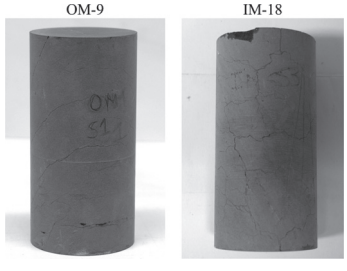

Figure 4. Fissuring patterns developed during RH cycling.

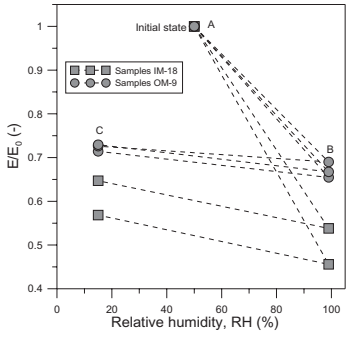

Figure 5. Evolution of young modulus during RC cycling.

Drying increased rock stiffness though the undisturbed value was not recovered in any case. For samples from IM-18, E/E_0 reduced to 0.55 at the end of wetting. Young modulus increased around 0.65 during drying due to the influence of total suction. For OM-9, E/E_0 reduced to 0.70 during wetting and then a smaller increase (up to 0.75) was observed at the end of drying.

The irreversible stiffness reduction observed for both materials but in particular for samples from IM-18 was in agreement with the important loss of mass continuity (fissuring) and the lower CaCO3 content described above. Values of E/E_0 obtained at the end of drying have been also included in Table 3.

After hydraulic cycling, each sample was resaturated via vapour transfer (RH = 99%) before to place inside the triaxial apparatus. This stage was carried out to avoid high suction gradients inside the specimens leading to additional fissuring (if liquid water is used). Samples were left to wet until reach a water content similar to the initial value (Sr > 0.89). It took typically 30 days. During this process volume changes were not measured to avoid sample damage and only the final states could be registered (see Table 4). Then, each sample was saturated and consolidated inside the triaxial apparatus under mean effective stresses between 50 and 350 kPa. Water permeability for degraded specimens was evaluated only in two samples (one for each type of rock) under p' = 50 kPa (p = 100 kPa and u_w = 50 kPa). The registered water flux increased around one order of magnitude for samples from OM-9 (36.7 mm^3/min). On the other hand, such increase was around two orders of magnitude for samples from IM-18 (442 mm^3/min). Thus, water permeability for degraded samples was equal to 8.2×10^{-9} m/s (OM-9) and 1×10^{-7} m/s (IM-18), respectively. The comparison with permeability values obtained for undisturbed specimens showed an irreversible increase in rock permeability which is attributed to the application of the previous relative humidity cycle. Such increase was around one order of magnitude for samples from OM-9 whereas for samples from IM-18 k_w increased up to three orders of magnitude. Water content and void ratio obtained at the end of saturation stage

Table 4. Volumetric properties of degraded samples before triaxial tests.

Samples	w (%)	ρ_d (Mg/m^3)	e (–)	Sr (–)
IM-18_S4	2.25	2.59	0.068	0.92
IM-18_S5	2.27	2.58	0.071	0.89
OM-9_S3	1.60	2.64	0.050	0.89
OM-9_S4	1.90	2.62	0.058	0.91
OM-9_S5	1.80	2.63	0.055	0.91

were around $w_f \approx 3.08\%$, $e_f \approx 0.085$ (OM-9) and $w_f \approx 3.51\%$, $e_f \approx 0.1$ (IM-18), respectively.

Figure 6 shows the stress-strain curves obtained during shearing stage for degraded specimens. Again, samples from OM-9 showed a higher stiffness and peak deviatoric stress compared with IM-18 specimens. However, such differences smaller if compared with undisturbed materials. The comparison showed the strong reduction of peak deviatoric stress after the application of the hydraulic cycling. It was accompanied by an increase in the axial strain at peak. The maximum q_{peak} for degraded materials was around 4000 kPa compared with 17000 kPa obtained for undisturbed specimens. Tangent modulus, E_{TAN}, obtained for the linear part of the stress-strain curve, ranged between 460–565 MPa (OM-9) and between 380–415 MPa (IM-18), respectively. It means a reduction between 3–4 times in rock stiffness induced by the previous hydraulic cycling.

Figure 7 shows the peak strength envelops for both undisturbed and degraded materials (assuming a linear failure criterion in all cases). Residual envelope, obtained from ring shear tests on remoulded material has been also included for comparison. The same residual conditions were obtained for both materials which suggest similar intrinsic properties (at fully degraded state). It is worth noting that peak conditions for degraded materials (both OM-9 and IM-18) were defined by the same linear failure envelope. For degraded specimens the stress ratio q/p' was equal to 1.64 whereas cohesion intercept was around 1100 kPa. It corresponds to an effective friction angle, ϕ', equal to 40° and effective cohesion, c', of 564 kPa. A drop in friction angle around 14° took place as a consequence of the previous relative humidity cycling. It suggests that a similar degradation path could be followed by both rocks irrespective differences observed at undisturbed state.

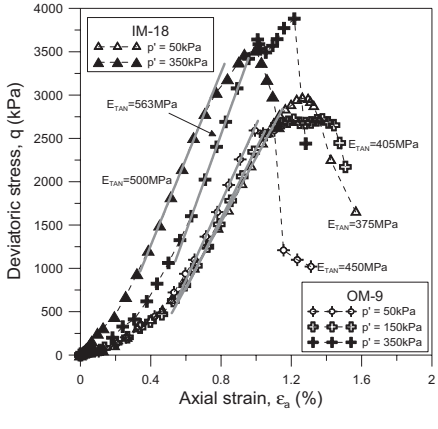

Figure 6. Stress-strain curves for degraded materials.

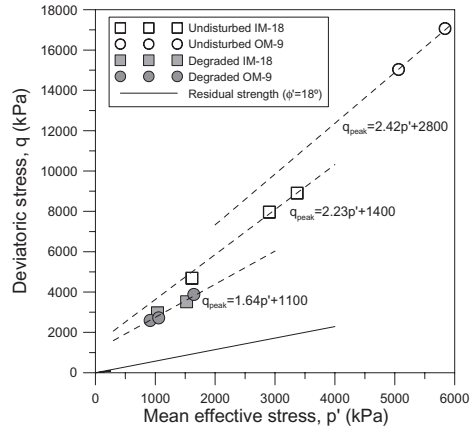

Figure 7. Peak strength envelopes for degraded and undisturbed specimens.

5 DISCUSSION

Despite the few experimental data, previous results suggest that the application of relative humidity cycles tend to similar degradation states in both materials, or at least to follow a similar degradation path irrespective of their different initial states. The most relevant aspects observed from the experimental study presented in this paper can be summarized as follows:

- under undisturbed (saturated) state, specimens from OM-9 showed higher peak stress, and rock stiffness (E_{TAN}). Effective cohesion was also higher for OM-9 specimens whereas similar friction angles were observed for both rocks;
- k_w (undisturbed varied between 10^{-10} and 10^{-11} m/s) in both materials;
- RH cycling induced smaller volumetric changes for samples from OM-9 (at the end of drying). Rock stiffness showed an irreversible reduction in both materials although it was more evident for samples from IM-18;
- k_w (degraded) increased up to four orders of magnitude for samples from IM-18 (suggesting large degradation)
- at degraded (saturated) state, both materials showed an important reduction in q_{peak} and rock stiffness (E_{TAN}). This behavior was more important for specimens from OM-9 (suggesting large degradation during shearing may be induced by debonding). This way, both materials tended towards a "unique" strength envelope.

From the above there is not completely clear why specimens from OM-9 experienced higher degradation during shearing, in terms of q_{peak} and $E_{TAN,}$ taking into account they showed lesser volumetric changes and lower stiffness degradation during RH cycling. This behavior is attributed to the increase of

the rock sensitivity to liquid water after RH cycling which was fully displayed during shearing for samples from OM-9. New opened fissures, induced during RH cycling, are an easy way for liquid water flow that leads to the softening of the rock and increases their maximum water retention capacity (w_{sat}). Thus, high permeability would be expected for high fissures samples (as observed for specimens from IM-18).

Figure 8 shows the volumetric paths followed by two specimens (undisturbed and degraded) from OM-9 and IM-18. For undisturbed specimens, saturation was performed directly in the triaxial apparatus, i.e., only liquid water was used during path A-1. In this case, peak envelopes were determined for samples located at point 1. The stress state for samples from OM-9 showed lower values for both w and e. Therefore, higher peak stress and rock stiffness registered could be expected for those specimens.

Samples subjected to wetting via vapour transfer (path A-B) reached their maximum water retention capacity at lower values (vertical dotted lines) compared with saturated samples using liquid water. Irreversible volume changes and stiffness reduction took place during RH cycling, path B-C, where higher degradation was registered for samples from IM-18. Then, samples were re-saturated using vapour transfer (path C-D). At that point (unsaturated), samples were fully saturated inside the triaxial apparatus using liquid water (path D-E). Re-saturation using liquid water induced additional volumetric swelling but also an increase in the maximum water retention capacity in both materials. A higher increase in water permeability was observed for IM18 due to the large fissuring developed during RH cycling. Peak strength envelopes were determined at point E which was located so far from point 1. The distance 1-E, specifically the increment in void ratio Δe, could give a measured of the induced degradation in each material. Nevertheless, there is not included the additional degradation induced during shearing which seems to be related with a debonding process (as observed for OM-9) activated by the previous hydraulic process.

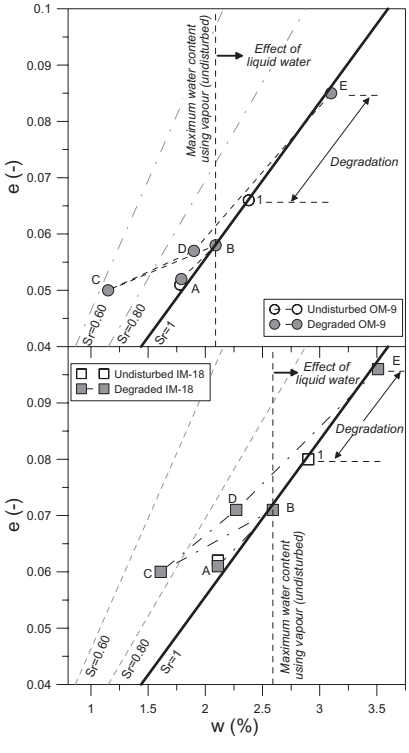

Figure 8. Volumetric paths followed by tested samples.

6 CONCLUSIONS

The behavior of two clayey rocks from the North-East Spain has been studied in this paper. Preliminary results obtained from triaxial tests showed a strong dependency of hydro-mechanical properties (permeability, stiffness and strength) to the application of RH cycles. The influence of using liquid water on the induced degradation was enhanced when previously RH cycling were applied. It seemed to leads to follow similar degradation paths.

REFERENCES

Alonso, E.E. & Pineda, J.A. (2006). Weathering and degradation of shales: experimental observations and models of degradation. VI South American Conference in Rock Mechanics, Cartagena de Indias, National University Press, 249–296.

Cardoso, R. (2009). Hydro-mechanical behaviour of compacted marls. PhD Thesis, Instituto Superior Técnico, Lisbon.

Martinez-Bofill, J., Soler, A., Tauler, E, Corominas, J, Otero, N. & Agelet, J. (2011). Influencia de la mineralogía en la durabilidad de rocas blandas: aplicación a taludes en Gipuzcoa. Revista Sociedad Española de Mineralogía, No. 15, 125–126.

Picarelli, L. & DiMaio, C. (2010). Deterioration processes of hard clays and clay shales. G.S.L. Special publication 23, 15–32.

Pineda, J.A. (2012). Swelling and degradation of argillaceous rocks induced by relative humidity effects: an experimental study. PhD Thesis, Universitat Politécnica de Catalunya.

Vàles, F., Nguyen Minh, D., Gharbi, H. & Rejeb, A. (2004). Experimental study in the influence of the degree of saturation on physical and mechanical properties in Tournemire shale (France). Applied Clay Science, vol. 26, pp. 197–207.

Advances in Unsaturated Soils – Caicedo et al. (eds)
© 2013 Taylor & Francis Group, London, ISBN 978-0-415-62095-6

Laboratory experiments on swelling due to crystal growth in sulphate argillaceous rocks

A. Deu & E.E. Romero
Department of Geotechnical Engineering and Geosciences, Universitat Politècnica de Catalunya, Barcelona, Spain

I.R. Berdugo
Department of Civil and Environmental Engineering, Universidad del Norte, Barranquilla, Colombia

ABSTRACT: Crystal growth is a frequent cause of expansive deformations in natural soils, compacted soils, rocks and concrete. The sulphate crystallization in discontinuities and cracks due to evaporation of highly mineralized solutions can contribute in an important way to displacements and swelling pressures that usually appear in tunnels and deep foundations in argillaceous rocks. The present work is aimed to study the basic mechanisms that control the hydrated sulphate mineral growth in anhydritic-gypsiferous argillaceous rocks due to the evaporation of groundwater. The paper presents some laboratory works including mineralogical and micro-structural analysis, as well as the design and development of new free swelling tests which were developed focusing on the capacity to discern the role carried out by the geochemical properties of the water, the main environmental variables and the degree of cracking on undisturbed sulphate argillaceous samples from different zones of the Lower Ebro Basin (Catalonia, Spain).

1 INTRODUCTION

Sulphate argillaceous rocks manifest high mechanical competences in undisturbed state, but when subjected to unload processes or when exposed to atmospheric agents often exhibit important degradation and large swelling pressures that occur during a large period of time without signs of attenuation. Some examples of this behavior can be found in several tunnels and deep foundations excavated in anhydritic-gypsiferous rocks in Central Europe. These cases have been studied by Kovári & Descoeudres (2001), Amstad & Kovári (2001) and Wittke (2006), among others.

Some severe swelling problems have been studied recently in tunnels excavated in sulphate argillaceous rocks from the Tertiary Lower Ebro Basin, in the northeastern Spain. These cases have been deeply studied by Alonso et al. (2004), Berdugo (2007), Deu (2008), among others.

Swelling in sulphate argillaceous rocks is a complex phenomenon in which key factors are not deeply defined. Sulphate mineral crystal growth in open discontinuities due to evaporation of groundwater can contribute to explain large displacements and high swelling pressures recorded in both field observations and laboratory tests. The supersaturation in sulphates of groundwater could be consequence of both environmental conditions and dissolution of anhydrite.

The paper describes a new swelling test designed to take into account conditions related to environmental conditions and chemical composition of groundwater, which were no represented in swelling tests developed before. Some samples from the east margin of the Tertiary Lower Ebro Basin were tested in varying conditions and detailed geological characterizations of samples before and after tests were also carried out.

2 SWELLING IN SULPHATE ARGILLACEOUS ROCKS

Since the early experimental studies of swelling in sulphate argillaceous rocks, a theory was assumed to explain both swelling pressures and swelling strains. It is based on two uncoupled mechanisms that occur when the rocks are soaked. The first is a short term physical swelling due to the clay matrix expansion. The second is a long term chemical swelling due to the transformation of anhydrite into gypsum in a reversible reaction conditioned by temperature, salt concentration in water and the open character of the system. In an open system, the theoretical volumetric increase is about 63%.

A swelling pressure is generated if the volumetric increase is totally o partially inhibited. This classic interpretation is shown in Figure 1.

A detailed discussion regarding swelling tests on anhydritic-gypsiferous clayey materials from the Lower Ebro Basin and Germanic Basin—as well as on test results on expansive hard soils-soft rocks and inert materials-, is presented in Berdugo (2007). The dependence of anhydrite gypsification is also discussed. According to this author, gypsification of anhydrite is not a reasonable explanation for swelling these materials. A new interpretation of swelling in sulphate argillaceous rocks is proposed by Berdugo (2007). It is suggested that precipitation of hydrated sulphate crystals in open discontinuities due to supersaturation of groundwater could be a more realistic cause.

Supersaturation of groundwater can be induced by both evaporation of sulphate solutions and dissolution of anhydrite in the presence of gypsum. The precipitation of sulphate crystals in open discontinuities allows the generation of new fissures where neo-formations of crystals are able to precipitate, causing swelling. Following this interpretation some factors must be taken into account in order to study the swelling phenomenon: saturation conditions of groundwater regarding gypsum, environmental conditions that may induce vapor and water flow, mineralogical properties of argillaceous rocks and the presence of open discontinuities in the rock, usually related to fissures and slickenside surfaces.

Nevertheless, this interpretation only explains part of the problem. According to Ramon & Alonso (2012), factors that lead to swelling phenomena are not well known. Actually, the presence of sulphate formations does not always imply the development of swelling.

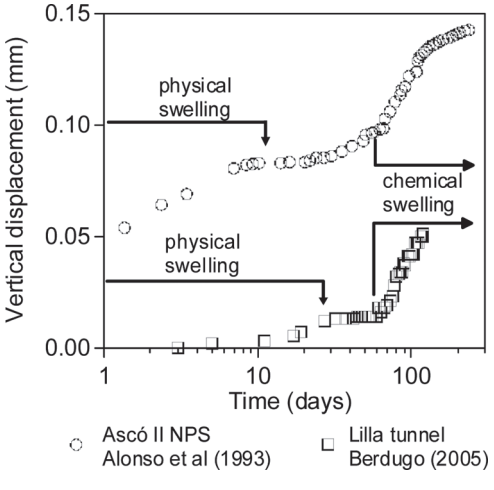

Figure 1. Classic interpretation of swelling in sulphate argillaceous rocks (Alonso et al., 2007).

3 GEOLOGICAL SETTING

Triassic and Tertiary sulphate argillaceous rocks occur in extensive zones of the Iberian Peninsula. It is well known that anhydritic-gypsiferous rocks out-crop in 7.2% of the Spanish territory. Samples for this study were recovered from boreholes in two sites of the eastern margin of the Lower Ebro Basin: (1) Rajadell and (2) Lilla (see Figure 2). Both rocks are claystones containing anhydrite, gypsum and carbonates, interbedded with limestones and sand-stones.

A geological characterization of samples before and after free swelling tests was carried out. It was implemented in order to study mineralogy and micro-structure variations in samples as a result of test protocols. Studies included mineralogical quantitative analysis by means of X-ray diffraction analysis on both randomly and oriented aggregates. In addition, mineral phases and their relationships were studied in detail using petrographic protocols and electronic microscopy.

3.1 *Rajadell claystone*

Rajadell claystone contain a red clayey matrix with sulphate nodules and veins interbedded in variable proportions. The mineralogical composition of the rock is summarized in Table 1. Slickenside surfaces were no detected in the rock massif. The occurrence of an anhydrite vein in the clayey host matrix is shown in Figure 3.

3.2 *Lilla claystone*

Lilla claystone has a sulphate crystalline fraction constituted basically by anhydrite and gypsum, in a porous host matrix constituted by not active

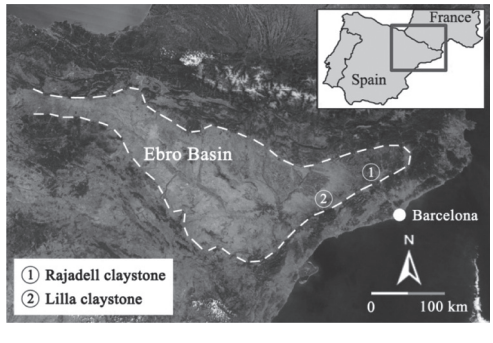

Figure 2. Location of Rajadell and Lilla claystones in the eastern margin of the Lower Ebro Basin.

Table 1. Mineralogical composition of Rajadell claystone.

Mineral	Relative content (%)
Dolomite	29
Quartz	5
Orthoclase	4
Anhydrite	18
Gypsum	1
Mica + Illite	37
Chlorite + Kaolinite	6

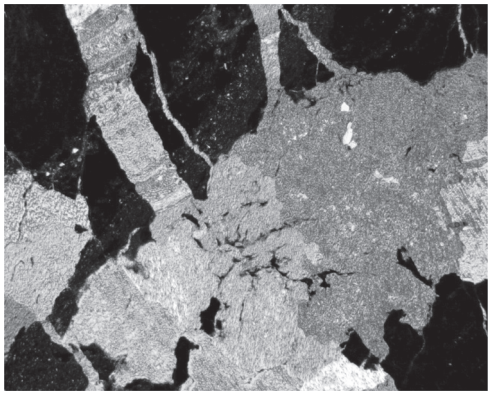

Figure 3. Anhydrite vein in the clayey host matrix of Rajadell claystone (x5 increases).

Table 2. Mineralogical composition of Lilla claystone.

Mineral	Relative content (%)
Dolomite	11–13
Quartz	2–7
Anhydrite	13–28
Gypsum	1–7
Illite + Paligorskite	51–67

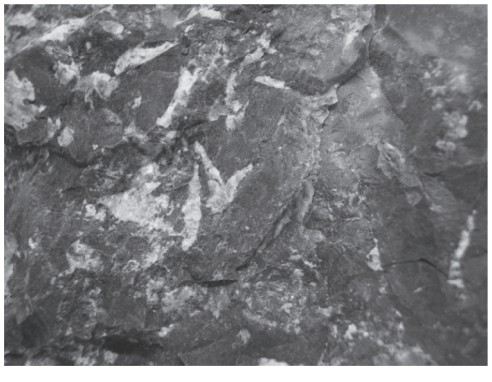

Figure 4. A detail of Lilla claystone illustrating the clayey host matrix and the sulphate fraction.

phyllosilicates (paligorskite and illite), by minerals rich in magnesium and calcium (dolomite) and, to a lesser extent, by quartz. Expansive clayey minerals, particularly smectite, were only detected in isolated samples of the host matrix. A persistent system of low-angle slickenside surfaces was observed and associated with the regional tectonic events during Upper Eocene. The mineralogical composition of Lilla claystone is summarized in Table 2, and a detail of Lilla claystone is shown in Figure 4.

It is important to remark that while only some slight differences in the mineralogical composition of sulphate fraction and clayey matrix have been described, the presence of the deep system of slicken-side surfaces in Lilla claystone is the main geomechanical difference between both materials.

4 SWELLING TESTS

The expansive behavior of sulphate argillaceous rocks at laboratory scale has been studied in detail during decades. The Huder-Amberg oedometer test (1970), which initiates with a stage of loading-unloading followed by swelling after soaking and swelling under load, is the referent in the Swiss and German practice.

However, Pimentel (2007) suggests that the main shortcoming of Huder-Amberg test is that the initial loading causes damage in the microstructure of samples, generating high swelling values as a result of imposed initial destructuration.

The interpretation of swelling phenomena in sulphate argillaceous rocks implies a great complexity, involving variables related to mineralogy and tectonic history of samples, as well as chemical composition of groundwater and environmental conditions. Following this idea, a new protocol is proposed for free swelling tests (unconfined state) in which hydraulic/environmental boundary conditions can be controlled. The protocol was developed focusing on the possibility to discern the rule carried out by main variables in the swelling phenomena. In this sense, an extensive mineralogical and micro-structural analysis is highly recommended before test. A simplified sketch of the new swelling test chamber is shown in Figure 5.

The chamber is divided by an impermeable membrane in order to establish two different environments. A cylindrical sample is used in contact with both environments of the chamber and covered by a latex skin. In the bottom part the sample is soaked with a constant water level with a previously determined chemical composition. In addition, environmental conditions (relative humidity and temperature) in the upper part of the chamber are controlled by a constant vapor flow associated with a saturated hygroscopic solution. The sample is only confined by a low vertical load.

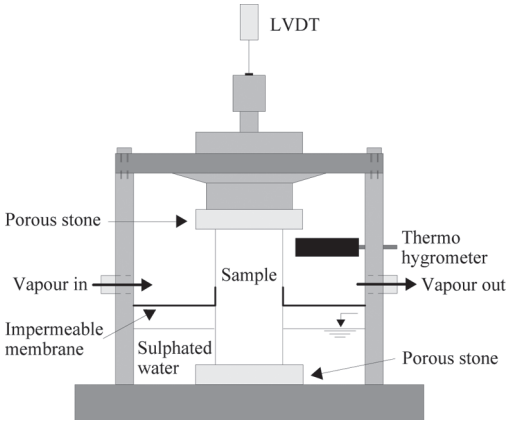

Figure 5. Sketch of the swelling test chamber including hydraulic/environmental boundary conditions.

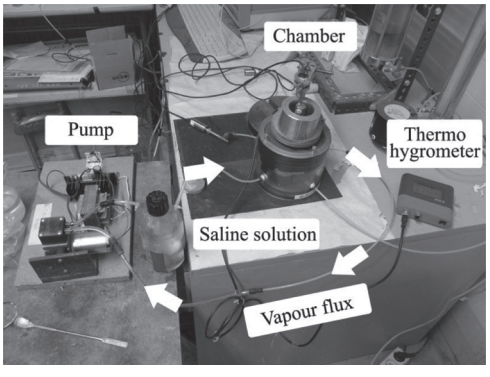

Figure 6. Experimental setup of the swelling test. The vapor flux in the upper part of the chamber induces a vapor flow through the sample.

In order to avoid relative humidity equilibrium in the chamber, and to induce vapor and water fluxes through the sample, the membrane must be impermeable. Suction values in the sample are modified by imposing variations in the relative humidity in the upper part of the chamber. In order to ensure that the vapor and water fluxes through the sample are upwards, the relative humidity imposed in the upper part should be lower that the relative humidity imposed by the soaking water. Thermohygrometers and LVDT sensors are used in order to monitoring environmental conditions and swelling strain during the test. The evaporation of the sulphate soaking water through the sample leads to supersaturation in hydrated sulphate minerals, which growth in open discontinuities. Therefore, new discontinuities are generated. The experimental setup of swelling tests is presented in Figure 6.

5 SWELLING TEST RESULTS

Free swelling tests under unconfined conditions were carried out on natural samples of Rajadell and Lilla claystones during more than 160 days. In the first case, a constant relative humidity of about 75% was imposed during the entire test in the upper part of the chamber; so the suction in the sample remained almost constant. On the other hand, in the case of Lilla claystone variations in the relative humidity were imposed in order to evaluate the effect of this variable on the axial swelling rate. The summary of both protocols is presented in Table 3.

Rajadell sample was not affected by either axial or radial deformations after 170 days of test. The relative humidity in the upper part of the chamber was kept between 70% and 75% during the test, and the relative humidity imposed by the soaking water was around 88%. The evolution of swelling strain and relative humidity in both environments of the chamber are shown in Figure 7.

Test in Lilla calystone was carried out imposing three different values of relative humidity in the upper part of the chamber. In the first part of the test a relative humidity between 40% and 60% was imposed by the vapor transferred by a $K_2CO_3 \cdot 2H_2O$ saturated solution. In the second part a high suction in the sample was induced by imposing a relative humidity of about 21%. A saturated solutions of $CaCl_2 \cdot 6H_2O$ was used in this case.

Finally, environmental conditions in the upper part were similar to the imposed in the soaking zone by the vapor transferred by a KCl saturated solution. Therefore, the suction value in the sample was reduced significantly. The soaking water imposed an almost constant relative humidity of about 94%. Although a swelling behavior throughout the test was observed, some variations in axial swelling rate related to the difference in the relative humidity imposed by both soaking water and vapor transfer were observed. The evolution of swelling strain and relative humidity in both environments of the chamber are shown in Figure 8.

Although mineralogical properties in both samples were similar, clear differences in swelling behaviour were observed during the tests. As shown in Figure 8, swelling strain rate increases when suction in the sample is high (0,078 mm/day); and it reduces if the imposed environmental conditions approach to the conditions in the soaking zone (0,027 mm/day).

At the beginning large axial deformations were observed until a second phase, in which minor but constant deformations without any signs of decreasing in time were recorded up to changes in environmental conditions. The short term swelling may be considered as a result of the expansion of clays in the matrix, which has been observed in isolated samples

Table 3. Summary of protocols for free swelling tests on Rajadell and Lilla claystones.

Sample	Time (days)	Soaking water (bottom chamber)	Hygroscopic solution (upper chamber)
Rajadell	170	$MgSO_4 \cdot 7H_2O$	NaCl
Lilla	160	$CaSO_4 \cdot 2H_2O$	$K_2CO_3 \cdot 2H_2O$ $CaCl \cdot 6H_2O$ KCl

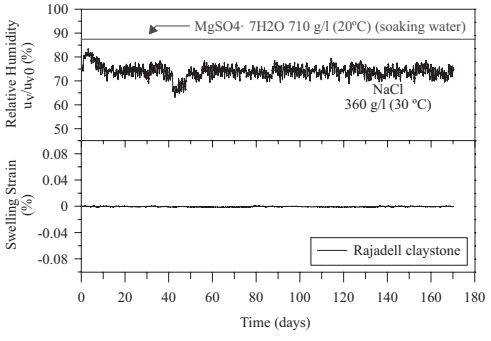

Figure 7. Swelling strain and relative humidity in both environments of the chamber in the test on Rajadell claystone.

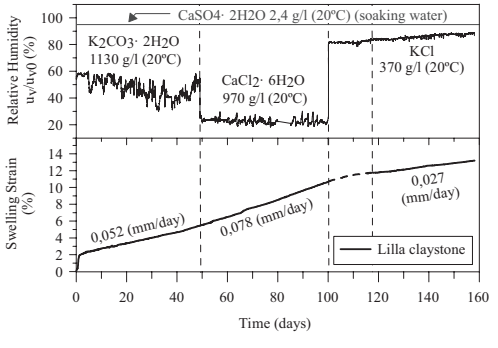

Figure 8. Swelling strain and relative humidity in both environments of the chamber in the test on Lilla claystone.

of the host matrix. During the second phase, which is controlled the by the vapor transfer, dry conditions in the upper part of the sample activate the swelling mechanisms. After 160 days of test, an axial swelling strain of about 13% was measured.

6 ANALYSIS AFTER SWELLING TEST

A study of samples after tests was carried out in order to evaluate variations in mineralogical composition and micro-structure due to soaking and swelling. The study included X-ray diffraction on both randomly and oriented aggregates, as well as petro-graphic and electronic microscopy in different parts of tested samples.

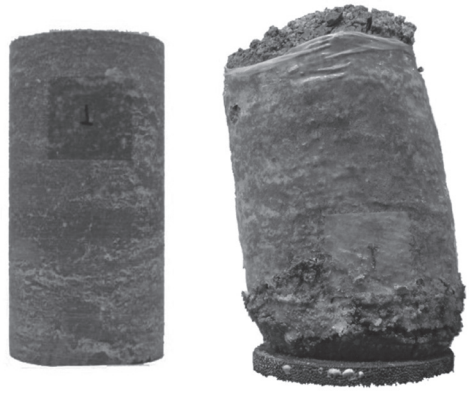

Figure 9. Appearance of Lilla claystone before and after swelling test.

6.1 *Rajadell claystone*

Rajadell sample was not affected after 170 days of test. No volumetric deformations or variations in mineralogical properties were observed.

$MgSO_4 \cdot 7H_2O$ crystallizations in the surface of the soaked zone were detected, but epsomite crystal growth was not observed at interstitial level of the sample. In addition, neither precipitations of hydrated sulphate mineral in open discontinuities nor generation of new fissures were observed.

6.2 *Lilla claystone*

Since the beginning of the test, swelling of Lilla claystone was clearly detected and chemo-mechanical degradation of the sample was observed throughout the test. A vertical swelling strain of about 13% was registered by the LVDT, and large lateral deformations were measured.

The precipitation of hydrated sulphate minerals in open discontinuities, both in the soaked and the dried part of the sample was clearly observed. The appearance of the sample before and after the test is shown in Figure 9.

As shown in Figure 9, the sample was extensively degraded during the test, ion particular where the clayey matrix was the principal component. Growth of gypsum crystals due to the evaporation of soaked water and supersaturation in hydrated calcium sulphate were clearly observed in discontinuities. The precipitation of gypsum crystals caused the opening of new fissures, filled

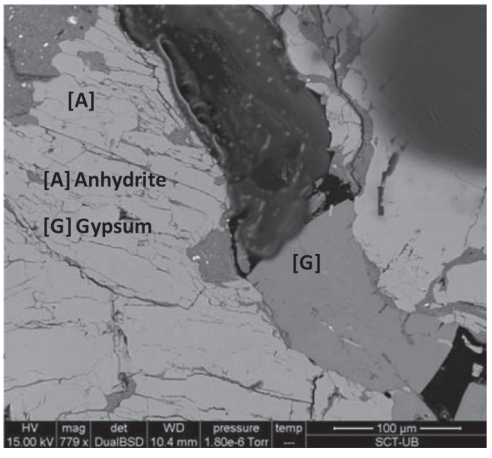

Figure 10. Neo-formation of gypsum crystals in an open discontinuitie Lilla claystone as a result of swelling under drying.

by new gypsum crystals and generating new ones. Electronic microscopy images make it possible to visualize the degradation of the sample and neo-formation of gypsum crystals in open discontinuities. A gypsum crystal filling a neo-formed fissure is shown in Figure 10.

7 CONCLUSIONS

Evidences presented in the paper reveal that swelling induced by crystal growth in sulphate argillaceous rocks is a consequence of drying, an opposite effect of drying in argillaceous materials; namely, the development of shrinkage strains. This understanding seems to be consistent with a large number of observations in tunnels and deep foundations in evaporite formations.

It is concluded that the most important mechanism in the observed long term expansive phenomena in sulphate argillaceous rocks is precipitation of sulphated minerals, although co-precipitation of sulphate-carbonated species is also possible. It has been shown that under appropriate relative humidity conditions the precipitation of gypsum and other types of hydrated sulphates from mineralized water is thermodynamically possible. Therefore, swelling phenomena could be related partially with crystal growth in discontinuities and evolve systematically in time if an effective vapour transfer from the water to the atmosphere is permitted.

ACKNOWLEDGEMENTS

The Ministry of Public Works of Spain was the financial supporter for this study. The authors wish to thank the support provided by their colleagues Prof. Eduardo Alonso, Prof. Antonio Gens, Prof. Marcos Arroyo, Dr. Eng. Juliana Knobeldorff and Eng. Dani Tarragó.

REFERENCES

Alonso, E.E., Berdugo, I.R., Gens, A. & Romero, E.E. 2004. Expansive phenomena in an instrumented tunnel excavated in anhydritic-gypsiferous argillaceus rocks. In W. Schubert (ed.), *Proc. EUROCK 2004 & 53rd Geomechanics Colloquium., Salzburg, October 6–8 2004*: 241–244. Essen: VGE.

Alonso, E.E., Berdugo, I.R., Tarragó, D. & Ramon, A. 2007. Tunnelling in sulphate claystones. Keynote Paper. In Cuéllar et al. (eds), *Proc. 14th European Conference on Soil Mechanics and Geotechnical Engineering, Madrid, September 24–27, 2007*: 103–122. Rottherdam: Millpress,

Amstad, C. & Kovári, K. 2001. Untertagbau in quellfähigem fels. Eidgenössisches Departement für Umwelt, Verkehr, Energie und Kommunikation (UVEK) & Bundesamt für Strassen. Zürich: ASTRA.

Berdugo, I.R. 2007. Tunnelling in sulphate-bearing rocks—expansive phenomena. Dr. Thesis, Universitat Politècnica de Catalunya.

Deu, A. 2008. Estudio experimental del crecimiento de minerales sulfatados en argilitas anhidrítico-yesíferas. Tesina d'Especialitat, Universitat Politècnica de Catalunya.

Huder, J. & Amberg, G. 1970. Quellung in Mergel, Opalinuston und Anhydrit. Schweizerische Bauzeitung, Jhrg: 88–43.

Kovári, K. & Descoeudres, F. 2001. Tunnelling Switzerland. *Swiss Tunnelling Society*. Zürich.

Pimentel, E. 2007. A laboratory testing technique and a model for the swelling behaviour of anhydritic rocks. In Ribeiro e Sousa et al. (eds), *Proc. 11th ISRM Congress, Lisbon, 9–13 July 2007*: 143–146. London: Taylor & Francis Group.

Ramon, A. & Alonso, E. 2012. Gypsum growth in tunnels. In Qian & Zhou (ed.), *Harmonisin Rock Engineering and the Environment*, *Beijing, 18–21 October 2011*: 1797–1802. London: Taylor & Francis Group.

Wittke, M. 2006. Design, construction, supervision and long-term behaviour of tunnels in swelling rocks. In Van Cotthen et al. (eds), *Proc. Eurock 2006, Liège, 9–12 May 2006*: 211–216. London: Taylor & Francis Group.

Shear and tension behavior

This page intentionally left blank

Advances in Unsaturated Soils – Caicedo et al. (eds)
© 2013 Taylor & Francis Group, London, ISBN 978-0-415-62095-6

Solute suction and shear strength in saturated soils

V.Y. Katte & G.E. Blight
University of the Witwatersrand, Johannesburg, Gauteng Province, South Africa

ABSTRACT: So far limited experimental data are available that demonstrate the contributions of the independent suction components (matrix and solute suctions) to the shear strength of unsaturated soils. Previous experimentation on the capillary model (Katte & Blight, 2012) concluded that relatively small changes in surface tension occur upon addition of solutes to the pore water. These have little or no effect on the shear strength at constant matrix suction even though the solute suction may be large. The objective of this paper is to validate the former by carrying out consolidated drained tests on saturated cohesionless soils with varying solute concentration hence solute suction while assessing the shear strength.

1 INTRODUCTION

In a recent paper (Katte & Blight, 2012) it was shown that the surface tension of water is relatively unaffected by dissolving sodium chloride in the water to the extent of 2 mol/L. It was concluded that the capillarity is purely a physical effect and does not depend on the internal stresses in a solution that gives rise to solute (i.e., osmotic) suction.

This is a worrying conclusion because, according to Raoults' laws, the relative humidity H in equilibrium with an aqueous solution is given by

$$H = \frac{n_w}{n_w + n_s} \tag{1}$$

where

n_w = number of moles of solvent and
n_s = number of moles of solute.

Also according to Kelvin's equation (see, Aitchison, 1965), the total suction is given by the equation

$$h\gamma_w = \frac{R\theta}{m_w} \log_e \left[\frac{n_w}{n_w + n_s} \right] \tag{2}$$

where h is the height to which a solution in equilibrium with a relative humidity H would rise in a capillary of given radius; R is the universal gas constant; θ is the absolute temperature and m_w is the molecular mass of water.

Substituting for H in (2)

$$(u_a - u_w)\, total = \frac{R\theta}{m_w} \log_e \left[\frac{n_w}{n_w + n_s} \right] \tag{3}$$

It appears that the more concentrated the solution in the capillary tube, the higher the capillary rise h should be, but the experimental results and simple static equilibrium deny this.

Katte & Blight (2012) went on to show that the shear strength of unsaturated soils is little affected by the presence of solutes in the pore water. It can be said, on the available evidence, that the shear strength of unsaturated soils is controlled entirely by the effective stress written as

$$\sigma' = (\sigma - u_a) + [\chi(u_a - u_w)]\, matrix \tag{4}$$

A survey of unsaturated soil mechanics literature found no similar work on the effect, if any, on the shear strength of soil. The nearest are the experiments by Tang & Graham (2002). However they worked on a mixture of applied total stress and measured total suction and assumed a constant value for osmotic suction.

Since writing the Katte & Blight 2012 paper, the following additional experiments have been carried out:

- Near-identical capillary tubes have been set up, side by side, but each within its own sealed air space, with one tube dipping into pure water and the other into 1.0 molar NaCl solution. These were left for several weeks to see if, with time, the capillary rises would change as the humidity of the air above the menisci equilibrated with the liquid forming each meniscus. The capillary rises did not change in either case.
- The capillary tubes were left untouched and the two containers of liquid swapped, ie a tube filled with pure water now dipped into a container of salt solution, and vice-versa. Again the capillary rises were unchanged.

In another recent paper (Blight, 2011), it was shown that if a fine pored porous material (concrete in this case) is dried to a constant mass at a temperature of 50°C and then allowed to equilibrate in atmospheres of 86% to 96% relative humidity, the material immediately increases in water content, but initially shrinks by 400–500 linear microstrain, before beginning to swell. This is put down to compressive stresses generated by water menisci reforming at the solids contacts as water from the humid air condenses in the void spaces of the porous material. As the menisci grow and increase in radius, the capillary compression reduces, allowing the material to start swelling.

In this case, solute suction trays of saturated salt solution controlled the relative humidity of the pore air but the condensation consisted of pure water. Therefore the compression must have resulted from the generation of matrix suction, followed by its reduction as wetting proceeded and the menisci grew in size. Here also the entire contractions were produced by changes in matrix suction.

For the present paper, it was decided to check if solute suction plays any role in the shear strength of saturated soils. Field observations by (Casagrande, 1965) have earlier indicated that osmotic suction plays little part in the strength of saturated soil. The soils used for this paper were granular materials. These were chosen so as to eliminate the physico-chemical interactions which are more pronounced in soils having some form of clay due to the double layer. For example, Olson & Mesri (1970) found that the void ratio at an effective consolidation pressure of 100 psf were lower for kaolinite and illite than for smectite when the pore fluid was either sodium or calcium aqueous solutions. Similar results were obtained when carbon tetrachloride was replaced as the pore fluid. Also, smectite gave a much higher swell index than illite and kaolinite respectively, when the pore fluid was either aqueous sodium or calcium solutions. Therefore the soil materials used for this paper can be considered inert.

2 SAMPLE PREPARATION AND PORE SUCTION CONTENT RELATIONSHIPS

Limestone powder (finer than 0.6 μm), quartz powder (finer than 1.18 μm) and glass beads (finer than 1.18 μm) were separately mixed in batches with distilled water, 1 M NaCl solution and detergent solutions at contents of between 2 and 10% by mass. The samples were stored in sealed plastic bags and left for at least 48 hours to allow the water and solution contents to equilibrate with the solids before subsequent testings.

The results of thermocouple psychrometer measurements carried out on limestone powder, quartz powder and glass beads at a range of solution contents using distilled water, 1 M NaCl solution and 2 g/l detergent are given in Figures 1–3.

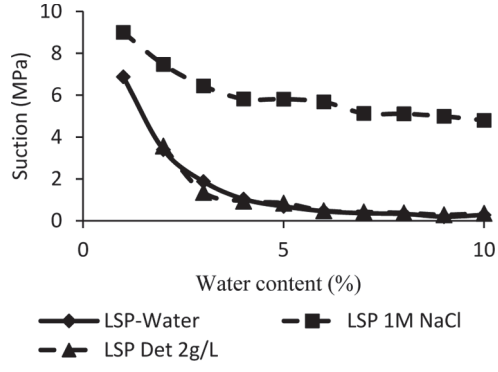

Figure 1. Water content—total suction curve for limestone powder.

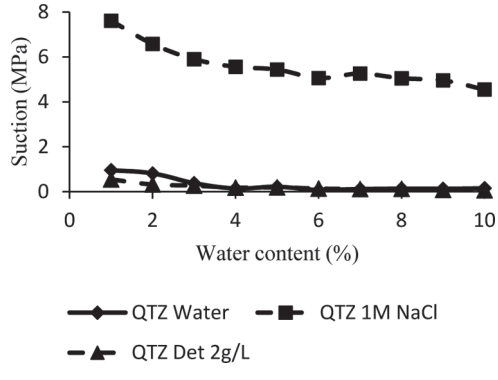

Figure 2. Water content—total suction curve for quartz powder.

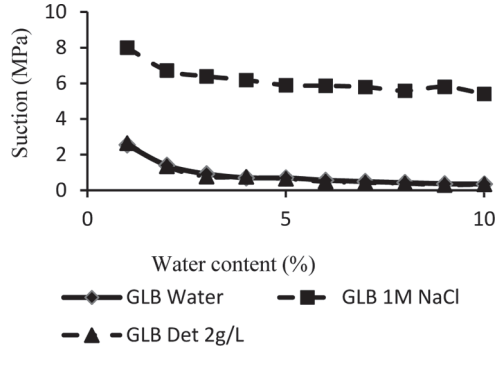

Figure 3. Water content—total suction curve for glass beads.

For the distilled water, the suction must be entirely matrix suction and the addition of detergent makes very little difference. For 1 M NaCl, the suction must be almost entirely solute suction at higher water contents, with an appreciable matrix suction component at low water contents. At high water contents where matrix suction is low, the measured solute suction is very close to that calculated from Equation (3).

3 TRIAXIAL SHEAR TESTS

Specimens of 38 mm diameter and 76 mm height were made by compacting 50.0 g soil materials (limestone powder and quartz powder) in a cylindrical mould in three layers. These were sealed to the pedestal of a triaxial cell using a rubber membrane. The glass beads were sealed in a similar manner with measured weights of the glass beads compacted in a split mould mounted on the pedestal. A positive back pressure using the appropriate distilled water, 1 M NaCl solution or 2 g/l detergent solution was applied through the triaxial base. The following notations are used to differentiate the specimens: water-water denotes the specimen mixed with distilled water with a back pressure applied by distilled water. Subsequently the first word denotes the solution mixed with the soil and the second denotes the back pressure solution.

Once a B-value of about 0.9 was achieved in the back pressured specimen, it was sheared drained with the back pressure maintained constant, at a rate of 2% per hour. The constant back pressures and maximum deviator stresses obtained are incorporated into Figures 4–6. In all five cases the results obtained indicate that the presence of solutes has no bearing on the shear strength of the specimens, in order words the strengths were independent of solute suction. It also made no difference if the solute suction of the solution mixed with the soil differed from that of the back pressure solution.

The ϕ' values of the soils are given in Table 1. For each of the respective soil mixes, the difference in the ϕ' values from those of water-water specimens

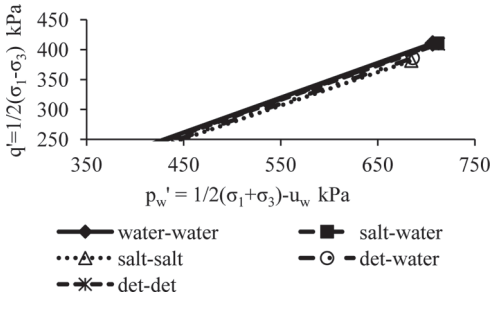

Figure 4. p′– q′ diagram for limestone powder.

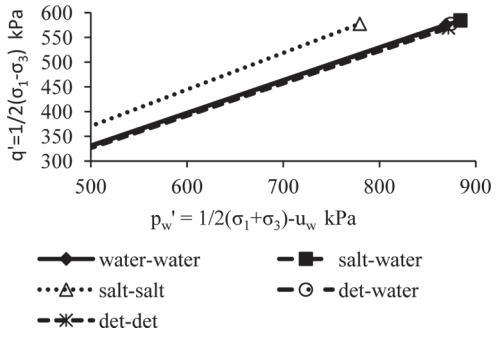

Figure 5. p′– q′ diagram for quartz powder.

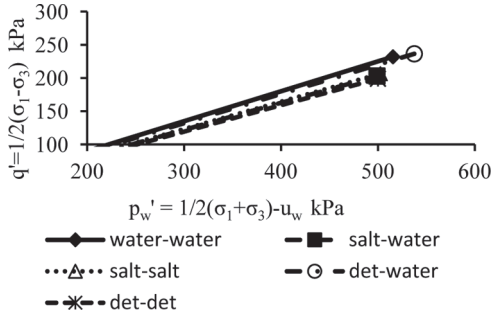

Figure 6. p′– q′diagram for glass beads.

Table 1. The ϕ' values of the soil.

Soil	Mix	ϕ'
Limestone powder	water-water	35.6°
	salt-salt	33.8°
	salt-water	35.3°
	det-det	35.3°
	det-water	34.3°
Quartz powder	water-water	42.4°
	salt-salt	48.4°
	salt-water	42.4°
	det-det	40.5°
	det-water	42.4°
Glass beads	water-water	26.4°
	salt-salt	23.8°
	salt-water	23.8°
	det-det	23.4°
	det-water	26.0°

is minute. If these results were plotted in terms of the total suction the respective ϕ' angles obtained would have been about 4°.

4 CONCLUSIONS

From these experiments it can be concluded that, as was the case with unsaturated specimens, solutes have little or no direct effect on the shear strength of a saturated soil in which the soil particles are inert. This is so despite the high solute suctions that were obtained with all the samples upon mixing with 1M NaCl solution. Solute suction may play an indirect role in the volume change of soils (see Katte & Blight, 2012) but has no effect on the shear strength of saturated chemically inert soils.

REFERENCES

Aitchison, G.D. (ed). 1965. Moisture equilibria and moisture changes in soils beneath covered areas. Sydney: Butterworths.

Casagrande, A. 1965. Role of calculated risk in earthwork and foundation engineering. Journal of Soil Mechanics and Foundation Engineering, ASCE, 91(SM4): 1–40.

Blight, G.E. 2011. Shrinkage during wetting of fine pored materials: Does this accord with the principle of effective stress? In Unsaturated soils (ed.), Alonso, E. & Gens, A.: 205–209. Leiden: CRC Press.

Katte, V. & Blight, G. 2011. The roles of solute suction and surface tension in the strength of unsaturated soil. Unsaturated soils (ed.), Mancuso, C., Jommi, C. & D'Onza, F., Heidelberg: Springer.

Olson, R. & Mesri, G. 1970. Mechanisms for controlling the compressibility of clay. Journal of the Soil mechanics and foundation division, ASCE, 96: 1863–1878.

Advances in Unsaturated Soils – Caicedo et al. (eds)
© 2013 Taylor & Francis Group, London, ISBN 978-0-415-62095-6

Effect of pre-shearing/suction histories on residual shear strength of unsaturated soils

L.R. Hoyos, C.L. Velosa & A.J. Puppala
University of Texas at Arlington, Arlington, Texas, USA

ABSTRACT: Results from a series of multi-stage, suction-controlled ring shear tests conducted on statically compacted samples of silty sand are presented. The experiments were accomplished in a fully servo/suction-controlled ring shear apparatus suitable for unsaturated soil testing via axis-translation technique. The present work focuses primarily on one crucial aspect of compacted soil behavior, namely, the effects of pre-shearing and/or suction histories on residual shear strength response of compacted silty sand. Results from multi-stage ring shear tests corroborate the critical role played by matric suction on residual shear strength properties of unsaturated soils. Test results also show that the residual shear strength of compacted silty sand is virtually independent of both the original soil structure and its pre-shearing/suction histories.

1 INTRODUCTION

A vast majority of geotechnical infrastructure, made of compacted soil or resting on unsaturated ground, undergoes a wide range of deformations. Calculation of foundation settlement, for instance, requires good estimation of soil stiffness at relatively small strains. Analysis of engineered earth slopes, embankments, and soil bearing capacity, on the other hand, requires good estimation of shear strength from peak to residual. To date, however, there is very limited experimental evidence of unsaturated soil behavior under large deformations, and their corresponding residual shear strength properties, while the soil is being subjected to controlled-suction states. This type of research has been deterred in the past by the lack of suitable testing tools and techniques. It is, hence, in this context that a suction-controlled ring shear (RS) apparatus plays a key role in the thorough characterization of this type of materials.

Only a short handful of researchers have recently begun experimental trials with new test methodologies, including Vaunat et al. (2007), Infante Sedano et al. (2007), and Merchán et al. (2011). Despite the crucial findings of these dedicated few, highlighting the key role played by matric suction, a comprehensive experimental effort has yet to be undertaken to investigate one crucial aspect of compacted soil behavior, namely, the effects that both the original soil structure and the pre-shearing/suction histories may have on the residual shear strength response of the test soil. The present work is motivated by these research needs.

In this work, results from a series of multi-stage, suction-controlled ring shear tests conducted on statically compacted samples of silty sand are presented. The tests were accomplished in a fully servo/suction-controlled RS apparatus suitable for unsaturated soil testing via the axis-translation technique. A detailed description of its development, including main components, calibration, and its performance verification against a standard Bromhead device, is presented by Hoyos et al. (2011).

Silty sand was selected in this work because of its poor gradation and low plasticity, hence minimizing the time suitable for pore-fluids equalization during suction-controlled RS testing. The relatively significant content of fine-grained material is also expected to minimize potential wall-friction effects between the soil specimen and the concentric rings of the RS apparatus.

2 RING SHEAR DEVICE: BASIC FEATURES

The RS apparatus allows for application of vertical loads up to 8 kN, monotonic torque up to 113 N-m, and unlimited angular rotation. It features three main modules: (1) Main cell with pneumatic actuator for normal loads, and electromechanical rotary actuator for torque loads; (2) DA/PC system with data reduction software for calculation of normal/shear stresses, and average linear/angular displacements; and (3) PCP-15U suction control panel for implementation of the axis-translation technique.

An orderly step-by-step setting-up procedure was established as follows:

1. A small piece of wet filter paper is placed over the top of each HAEV disk, prior to soil compaction, in order to ensure phase continuity between the pore-water in the soil and the water in the saturated disk: Figure 1(a).
2. The 15-mm (0.59-in) thick sample is statically compacted into the bottom annular platen: Figure 1(b). The sample is transferred to the RS frame and the platen tightly fixed onto the bottom base plate: Figure 1(c).
3. The vertical load shaft is brought up via a servo controller and the upper annular platen affixed to the top of the piston shaft: Figure 1(c). A vertical sitting load of 25 N is applied to bring the upper platen in full contact with the soil.
4. All drainage and flushing lines are filled with de-aired water and flushed several times to avoid any trapped air in the whole system.
5. The main cell is set into place and the top cover plate affixed to the main cell: Figure 1(d). A pore-air pressure line, originated from the PCP-15U panel, is connected to the cover plate of the main cell via a quick connector.
6. Readings of the load-torque transducers are reset, and both the LVDT and the angular deformation sensors are re-zeroed, prior to RS testing.
7. The sample is then subject to a suction-controlled multi-stage RS test using the $s = u_a$ ($u_w = 0$) test approach.

In order to ensure phase continuity between the water compartment beneath the HAEV ceramics and the pore-water in the soil, the 5-bar ceramics are to be saturated prior to RS testing. An in-place saturation procedure was adopted, which can be summarized as follows. The ceramics are first immersed in de-aired distilled water in a beaker for at least 24 hrs. A vacuum of 30 in Hg is then applied for 48 hrs to remove occluded air bubbles in the ceramics: Figure 2(a). The ceramics are then mounted and sealed into a stainless steel ring as part of the bottom annular platen assembly: Figure 1(a). The annular cavity, reserved for the soil specimen, is filled with de-aired distilled water to a height of about 25 mm (1 in): Figure 2(b). Once the main cell and top cover plate are set into place, the water film is subjected to an air pressure of 200 kPa for at least 48 hrs. During this period, any remaining air in the ceramics is expected to dissolve in water. After saturation of the ceramics, the main cell is removed and the remaining water film eliminated via a suction pipette. (The ceramics, however, remain covered with water until the soil is ready to be compacted.)

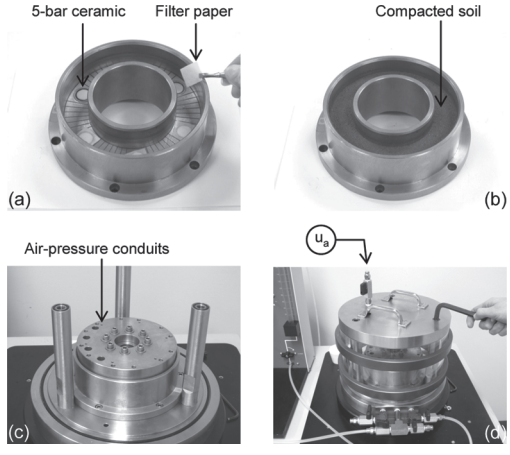

Figure 1. Suction-controlled RS assembling process: (a) lower platen, (b) test sample, (c) top platen, (d) main cell.

Figure 2. Saturation of HAEV ceramics: (a) vacuum beaker, (b) in-place water bath.

3 BASIC PROPERTIES OF TEST SOIL

The test soil classifies as silty sand (SM) according to the USCS. The soil has 83.6% sand, 9.8% silt, and 6.6% clay; with optimum moisture content, OMC = 10.5%; maximum Proctor dry density, $\gamma_{d\text{-}max} = 1.84$ g/cm^3; and specific gravity, $G_s = 2.68$. The soil does not exhibit plastic characteristics. The corresponding soil-water characteristic curve (SWCC), assessed via pressure plate testing, is shown in Figure 3.

All RS test samples were prepared directly into the lower annular platen via in-place static compaction: Figure 1(b). The upper annular platen is used to compress one single lift of a loose soil-water mix to a target dry unit weight of 95% of the corresponding $\gamma_{d\text{-}max}$. A monotonic force is applied by means of a triaxial loading frame at a constant compaction displacement rate of 1.25 mm/min (Hoyos et al., 2011). Samples of SM soil were prepared at water contents corresponding to suction values slightly less than 25, 50, or 100 kPa, according to the SWCC in Figure 3.

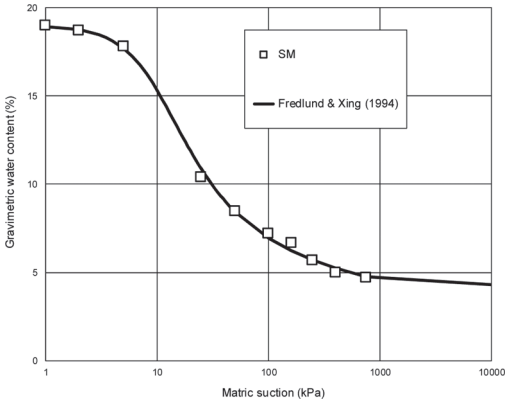

Figure 3. Soil-water characteristic curve from SM soil.

4 GENERAL RESPONSE OF SM SOIL

The first stage of a multi-stage suction-controlled RS test requires bringing the soil to an initial net normal stress, $(\sigma_n - u_a) = 25$ kPa, and matric suction, s = 25, 50, 75, or 100 kPa. A vertical load is first monotonically applied via the upper annular platen to induce a normal stress 25 kPa greater than the target value of suction; the soil is then allowed to consolidate.

The pore-air pressure u_a is then raised in the main cell, as shown in Figure 1(d), to target suction value, $s = u_a$. The vertical load is adjusted accordingly to keep the net normal stress constant at 25 kPa. The time required for consolidation-equalization ranged from 50 to 90 hrs. Suction-controlled RS tests were then performed on compacted samples of SM soil, under constant-suction states, s = 25, 50, 75, or 100 kPa, by following a multi-stage scheme in which residual strength assessments were made at three net normal stress values, $(\sigma_n - u_a) = 25$, 50, and 75 kPa. All tests were conducted at an equivalent horizontal displacement rate of 0.025 mm/min, which corresponds to a rotational speed of 0.023°/min.

Figure 4 shows the shear stress vs. horizontal displacement responses of compacted SM soil, during first shearing stage, under suctions, s = 50 kPa and 100 kPa; including the corresponding change in vertical soil displacement. The curve for saturated condition (s = 0) is reproduced from Hoyos et al. (2011). Matric suction is observed to have a significant influence on residual shear strength, with a considerable increase for s = 100 kPa. Because of the predominantly coarse-grained nature of SM soil, all samples exhibit a certain degree of dilatancy toward a critical state. These results evidence the enhancement of soil brittleness and soil dilatancy with increasing suction. Furthermore,

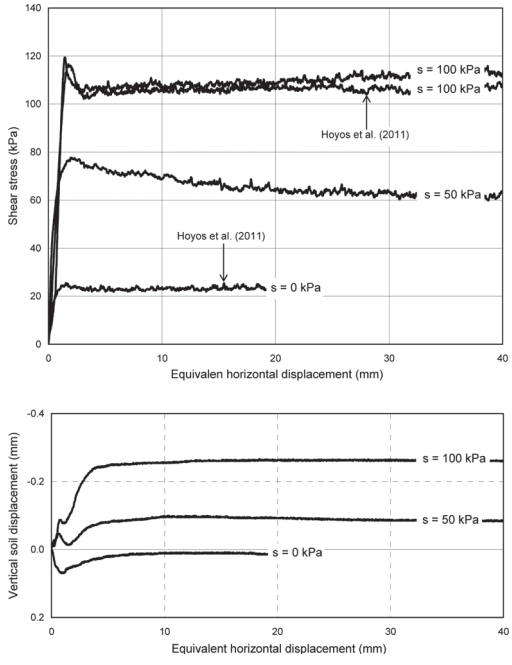

Figure 4. Results from s-controlled RS tests on compacted SM soil under net normal stress, $(\sigma_n - u_a) = 25$ kPa.

results from first shearing stage of the RS test performed under s = 100 kPa, are remarkably similar to those reported by Hoyos et al. (2011) under identical conditions, which further demonstrates the reliability of the newly developed RS apparatus.

5 EFFECT OF PRE-SHEARING HISTORY

In order to evaluate the dependency of residual shear strength of SM soil over its past pre-shearing history, a new statically compacted sample was subjected to a multi-stage RS test under net normal stress values, $(\sigma_n - u_a) = 25$, 50, and 75 kPa, and constant suction, s = 25 kPa, as depicted by path AF in Figure 5. Results are compared with those reported by Hoyos et al. (2011) from a single-stage test under net normal stress, $(\sigma_n - u_a) = 75$ kPa, and same suction. Results from both tests are shown in Figure 6, including the corresponding changes in vertical soil displacement. It is observed that when the last-stage shearing (path EF) is induced on the pre-sheared soil (paths AB and CD), both the peak and dilatant behaviors are virtually suppressed. However, the residual stress is reasonably close to that induced by a single-stage shearing under same stress state.

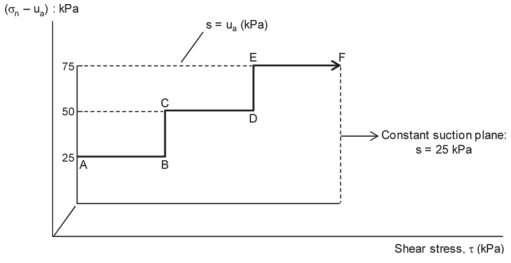

Figure 5. Multi-stage RS test path (AF) at constant suction, s = 25 kPa.

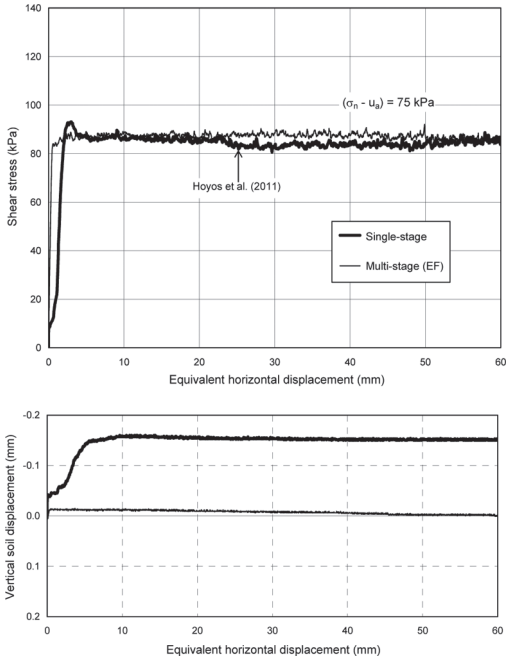

Figure 6. Results from single—and multi-stage RS tests on compacted SM soil at constant suction, s = 25 kPa.

These results seem to confirm previously reported observations that the residual shear strength of compacted soils only depends upon the applied level of net normal stress, and not the initial soil structure or the induced pre-shearing history (Bishop et al., 1971, Bromhead & Curtis 1983, Vaunat et al., 2006).

6 EFFECT OF SUCTION HISTORY

In order to evaluate the dependency of residual shear strength of SM soil over its past suction history, a new statically compacted sample was subjected to a multi-stage RS test under constant

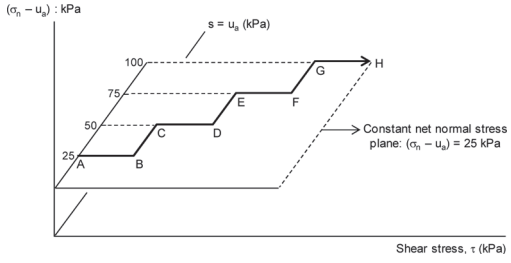

Figure 7. Multi-stage RS test path (AH) at constant net normal stress, $(\sigma_n - u_a) = 25$ kPa.

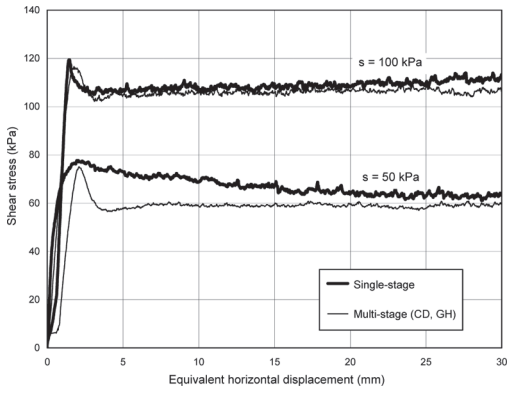

Figure 8. Results from single—and multi-stage RS tests on compacted SM soil at constant suction, s = 25 kPa.

net normal stress, $(\sigma_n - u_a) = 25$ kPa, and suctions, s = 25, 50, 75, and 100 kPa, as depicted by path AH in Figure 7.

Results are compared with those generated during first shearing stage of the two tests conducted under same net normal stress and suctions, s = 50 kPa and 100 kPa (Fig. 4). Results from these three tests are shown in Figure 8. It can be noticed that when shearing is applied on a pre-sheared soil, i.e., path CD for s = 50 kPa, or path GH for s = 100 kPa, the residual stress response is virtually same as that from a single-stage shearing under same stress state. These results also seem to corroborate that the residual shear strength of a compacted soil is virtually independent of its original structure and/or its past suction history (Vaunat et al., 2006, 2007).

7 COMBINED EFFECTS OF PRE-SHEARING AND SUCTION HISTORIES

Finally, with the aim of evaluating the simultaneous effects of pre-shearing and suction histories over the residual shear strength of compacted

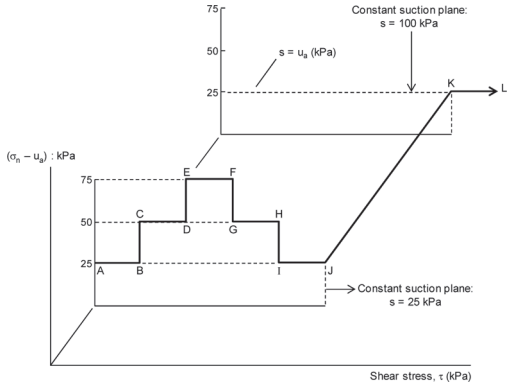

Figure 9. Multi-stage RS test path (AL) to assess the combined effects of pre-shearing/suction histories on compacted SM soil.

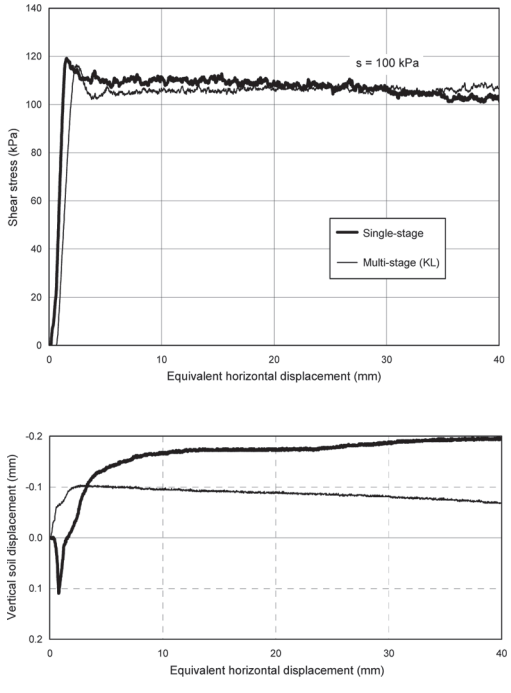

Figure 10. Combined effects of pre-shearing/suction histories on compacted SM soil under multi-stage RS testing.

SM soil, a new statically compacted sample was subject to a multi-stage RS test that involved a constant-suction load-unload net normal stress path, followed by a suction-increase path, as depicted by path AL in Figure 9. The soil was initially sheared (path AJ) under constant suction, s = 25 kPa, following a load-unload sequence of net normal stresses, $(\sigma_n - u_a)$ = 25, 50, 75, 50, and 25 kPa. The soil was then dried via axis-translation (path JK) to a suction state, s = 100 kPa, and re-sheared (path KL) under constant net normal stress, $(\sigma_n - u_a)$ = 25 kPa. Results from this multi-stage RS test are compared with those from a single-stage test conducted on a separate sample under net normal stress, $(\sigma_n - u_a)$ = 25 kPa, and matric suction, s = 100 kPa. The results from both tests are shown in Figure 10. In both cases, the residual stress response of compacted SM soil is observed to be, once again, virtually the same.

It can also be noted that the drying process (path JK) stiffens the pre-sheared soil, which is manifested by both the peak and dilatant behaviors during last-stage shearing (path KL). This dilatancy, however, is still less pronounced than that induced during single-stage shearing. It can thereby be concluded that the effect of matric suction on residual strength of compacted soils is more significant than that of net normal stress, since the peak and dilatant behaviors apparently are not fully suppressed if the soil is subject to a drying process after pre-shearing. An increase in dilatancy with suction was also reported by Vaunat et al. (2006).

8 CONCLUDING REMARKS

Results from a series of suction-controlled ring shear tests, conducted on statically compacted samples of silty sand (SM) soil, were presented. The tests were conducted in a newly developed, fully servo/suction-controlled ring shear (RS) apparatus. The results reflect the critical role played by matric suction on residual shear strength of compacted soil. Results from multi-stage RS tests seem to confirm that the residual shear strength of compacted silty soil is not affected by the original structure or its past pre-shearing or suction histories.

ACKNOWLEDGEMENTS

The core system of the RS apparatus was developed under U.S. National Science Foundation Award # CMS-0626090. This support is gratefully acknowledged. Any findings, conclusions, or recommendations expressed in this material are those of the authors and do not necessarily reflect the views of the National Science Foundation.

REFERENCES

Bishop, A.W., Green, G.E., Garga, V.K., Andresen, A., and Brown, J.D. (1971). "A new ring shear apparatus and its application to the measurement of residual strength." Géotechnique, 21(2), 273–328.

Bromhead, E.N., and Curtis, R.D. (1983). "A comparison of alternative methods of measuring the residual strength of London clay." Ground Engineering, 16(4), 39–41.

Fredlund, D.G., and Xing, A. (1994). "Equations for the soil-water characteristic curve." Canadian Geotechnical Journal, 31, 521–532.

Hoyos, L.R., Velosa, C.L., and Puppala, A.J. (2011). "A servo/suction-controlled ring shear apparatus for unsaturated soils: development, performance, and preliminary results." Geotechnical Testing Journal, ASTM, 34(5), 413–423.

Infante Sedano, J.A., Vanapalli, S.K., and Garga, V.K. (2007). "Modified ring shear apparatus for unsaturated soil testing." Geotechnical Testing Journal, ASTM, 30(1), 1–9.

Merchán, V., Romero, E., and Vaunat, J. (2011). "An adapted ring shear apparatus for testing partly saturated soils in the high suction range." Geotechnical Testing Journal, ASTM, 34(5), 433–444.

Vaunat, J., Amador, C., Romero, E., and Djeren-Maigre, I. (2006). "Residual strength of a low plasticity clay at high suctions." Proceedings of Fourth International Conference on Unsaturated Soils, Carefree, Arizona, vol. 1, 1279–1289.

Vaunat, J., Merchán, V., Romero, E., and Pineda, J. (2007). "Residual strength of clays at high suctions." Proceedings of the Second International Conference on Mechanics of Unsaturated Soils, Weimar, Germany, vol. 2, 151–162.

Advances in Unsaturated Soils – Caicedo et al. (eds)
© 2013 Taylor & Francis Group, London, ISBN 978-0-415-62095-6

Review of factors affecting formation of cracks in clay layers

C. Lozada
Department of Civil and Environmental Engineering, Universidad de los Andes, Bogotá, Colombia

ABSTRACT: Clays exhibit volumetric changes when exposed to different environmental conditions. Particularly desiccation process in clays produces vertical settlements and cracks can appear as a consequence of shrinkage. The mechanisms in which the environment, the soil properties, and the geometric configuration as a whole affect cracking characteristics are not yet understood; even if numerous experimental tests have been realized in thin layers of clay to evaluate the influence of different variables. Variables studied in abundant research include the effect of: air temperature, thickness of soil layer, bottom surface material, and tensile strength. The aim of this paper is to present a review of the experimental results made by different researchers, highlighting their main contributions, and relevant aspects for future works.

1 INTRODUCTION

Desiccation is the process in which the soil loss water and becomes unsaturated, this process can be produced by different conditions such as: decrease in water table due to groundwater production, temperature increase by extreme drought periods, loss of vegetation as a protective layer of soil. When clayey soil in saturated state is exposed to desiccation, a zone appears above water table in which the pore water pressure is negative. Under these circumstances shrinkage occurs and tension stresses appears within the soil mass. In this zone, once tension forces exceed the tensile strength of the soil cracking initiates (Nahlawi & Kodikara 2006; Thusyanthan et al., 2007; Morris, et al., 1992).

Despite the huge advance of knowledge achieve in unsaturated soils mechanics in the last decades, the whole effects affecting shrinkage cracking due to shrinkage of fine-grained soil is not yet understood. The state of knowledge in this area consists in laboratory test made by many authors that have studied shrinkage cracking in thin clay samples and few numerical studies that describes this process. This paper presents a review of the main contributions of different authors, and present relevant aspects for future works.

2 CRACK CHARACTERIZATION

Crack formation depends on the intrinsic and state properties of soil and the boundary conditions of the desiccating layer. Intrinsic and state properties of soil includes: fines content, Atterberg limits, mineralogy, moisture content, tensile strength, and dry density. On the other hand, boundary conditions include the external variables that affect cracking: roughness of the soil base, temperature gradient, humidity, thickness of the soil layer, wind velocity, size of the sample of soil, radiation, and the number of hydraulic cycles of wetting and drying. Trabelsi et al. 2011; Corte & Higashi 1960; Miller et al. 1998 carried out laboratory tests including different intrinsic soil properties and controlling different boundary conditions.

The cracked soil can be characterized in terms of the resulting geometry as: Number of cracks, cells per unit area (the amount of soil separated by cracks), crack spacing, depth of cracks, length of cracks, and cracked area. Also, it is common to specify the value of the humidity at which cracks open.

Image analysis is the principal way to measure characteristics of cracked soil. Recent technological advances permit trough the quantification of pixels in binary image determine the quantity of pixels that corresponds to cracking and non-cracking zones (Trabelsi et al., 2011; Tang et al., 2008; Vogel et al., 2005; Yesiller et al., 2000; Serra 1982). Furthermore, fractal dimension allow to characterize the degree of cracking and the interconnectivity of cracks (Vallejo 2009).

To describe the evolution of cracks during a desiccation test or in the field, two definitions have been implemented: CIF (Crack Intensity Factor) and LF (Density of Length of Fissure). CIF is the area of cracks with respect to the total area, and LF is the length of cracks with respect to the total length. The evolution of CIF and LF with time are described by Trabelsi et al. (2011) and Miller et al. (1998). The curves plotted against time present a linear region at the beginning of the

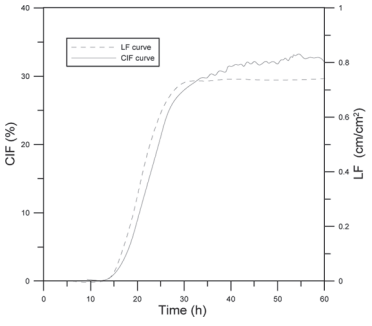

Figure 1. Evolution of CIF and LF versus time. Experimental results (Adapted from Trabelsi et al. (2011)).

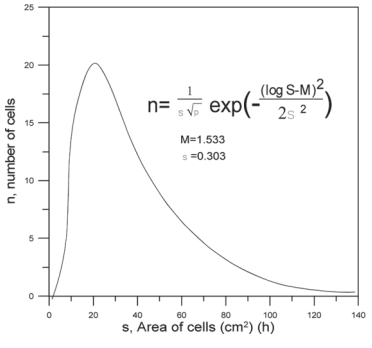

Figure 2. Log-normal distribution of size of cells. Experiment 29, thickness 8 mm, wood bottom, and dry density 1.8 (Adapted from Corte & Higashi (1960)).

desiccation process and then reached a steady state (see figure 1).

Corte & Higashi (1960) and Nahlawi & Kodikara (2006) measured the size of cells at the end of the desiccation process and found that size of cells coincide with a log-normal distribution. The distribution of size of cells obtained in the test of Corte & Higashi (1960) is show in figure 2. In these tests the soil sample is drying in a room which temperature was kept about 22°C and humidity was about 30–40%.

3 VARIABLES THAT AFFECT CRACKING PATTERN

To explain the formation of cracks in soil it is accepted that cracking is initiated when tension forces exceed the tensile strength during drying process (Nahlawi & Kodikara 2006; Thusyanthan et al., 2007; Abu-Hejleh & Znidarčić 1995). Different apparatus have been developed to measure tensile strength. Some tests to measured tensile strength and the main relationships between two or more characteristics are presented below.

3.1 *Tensile strength*

The most common tests to measured tensile strength in soils are: bending test, indirect tension test, direct tension test, and triaxial tension test. The main disadvantages in tensile strength measurements using bending tests are the nonlinear behavior of the soil and the non-homogeneous stress field. On the other hand, in direct tension tests the stress path is controlled, but shear stresses appear because the differential of lateral strain. Another disadvantage with these two methods is the difficulty to control the pore water pressure. To solve these problems Bishop & Garga (1969) developed a modification of triaxial cell in order to create a tension test. This test consists in a sample with a reduced middle section involved in a membrane, (see figure 3). The sample is fixed on one side and tension load is induced by the confining pressure.

Tensile strength test in unsaturated soils also has been measured by Rodriguez 2002; Nahlawi et al. 2004; Lu et al. 2009; and Kim et al. 2012. The authors developed different test that varies in dimensions, shape of the device, and formulation to calculate the tension strength. The device developed by Rodriguez et al. (2002), consists in 3 main parts: two pieces of trapezoidal shape and a central part that is allowed to remove at the beginning of the test (see figure 4).

The purpose of this device is to measure the tensile strength in the middle of the device by the application in one half of the mold a tension load and fixing the other side.

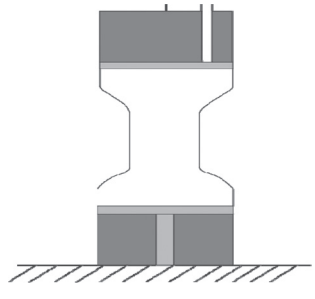

Figure 3. Triaxial tension test (Adapted from Bishop & Garga, 1969).

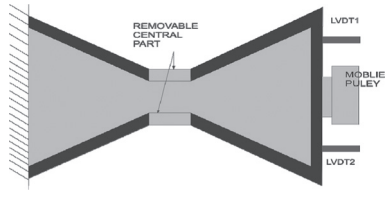

Figure 4. Direct tension test device (Adapted from Rodriguez (2002)).

Prat et al. (2008) made some tests to measure the tensile strength using this dispositive varying the moisture content. Figure 5 shows the resultant curves for two densities, the difference in the shape of the curve in the wet-side is smaller than in the dry-side of the curve. This result is consistent with the results obtained by Favaretti 1996; Tamrakar et al. 2005; and Rodríguez 2006. For these tests, the authors do not mentioned the control of environmental conditions.

Also, Trabelsi et al. (2011) made some tests in the same device, but they fixed the environmental conditions (temperature 20°C ±2°C and constant relative humidity 50% ± 5%). Each test was realized with water content in the range of 65% to 120%. Because the soil initially is in slurry state, two pieces in the central part are fixed to maintain the correct shape of the clay during drying. When the soil acquires consistency by drying the load is applied. Figure 6 shows an exponential curve that represent the results of the experiments in which tensile stress increases as water content decreases. Indeed, these curves are different in comparison to figure 5 because the drying process.

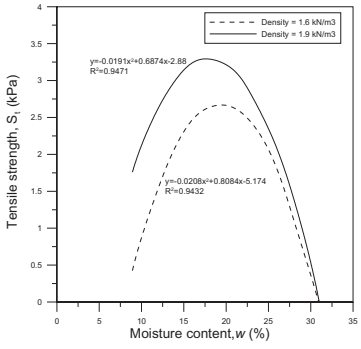

Figure 5. Tensile strength curve for different moisture content (Adapted from Prat et al. (2008)).

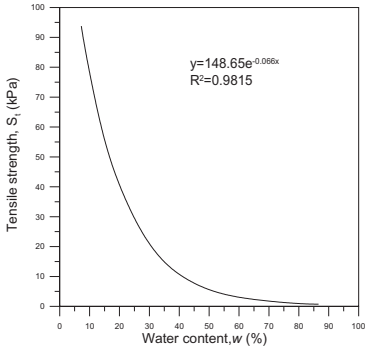

Figure 6. Tensile strength curve (Adapted from Trabelsi et al. (2011)).

Nahlawi et al. (2004) carried out a testing equipment based in the same principle developed by Rodriguez (2002). This device is made with two rectangular blocks in which the first are fixed and displacement is allowed on the second block (see figure 7). Authors made tests in clayey soil prepared with initial water content between 122% and 21.5%. Figure 8 shows the decrease in the tensile strength with increase the water content in contrast to the increase of tensile strain at failure with the increase of water content.

Additionally, recent researches such as Thusyanthan et al. (2007), argued that combination between shear and tensile strength stresses are developed at the beginning of cracking in soils. First test for determines this stress combination was made by Vesga (2009). The author developed an apparatus that measure the tensile shear strength of unsaturated clays called direct tensile shear test (DTS) (see Figure 9). The principle of this test is the application of a tensile force and subsequently a shear strength that produce failure by tension.

In most tensile strength tests it is questionable the uniformity in the stress distribution and the possible stress concentration and friction between the mold. Some solutions to these problems are based on the removal of corners in the mold and in eliminating the corners and lubricating the mold to avoid friction effects. Other important effects are the temperature and humidity regulation, for that reason, the use of

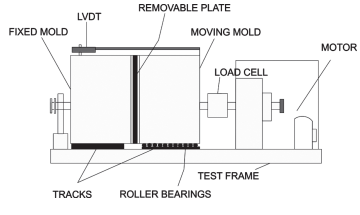

Figure 7. Shear strength device (Adapted from Nahlawi et al. (2004)).

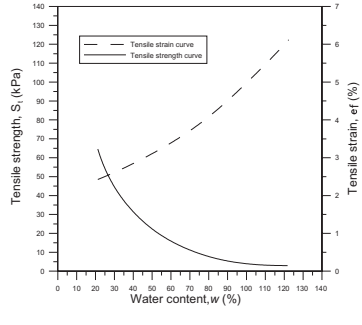

Figure 8. Tensile strength and tensile strain versus water content (Adapted from Nahlawi et al. (2004)).

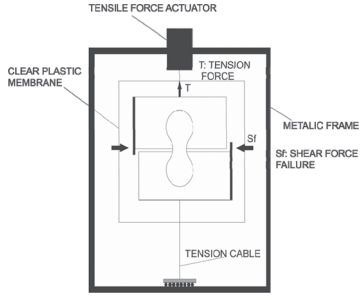

Figure 9. Direct tensile frame for DTS service (Adapted from Vesga (2009)).

membranes and isolating chambers to control and measure some conditions are the best solution.

3.2 *Effect of the plasticity index*

Tang et al. (2008) made tests in order to determine the influence of different factors in shrinkage cracks formation. The test procedure consists in three main steps: (1) the slurry clay is prepared with 90% water content (2) the slurry is put into square glass plates of 16 cm, and (3) the plates are located in a drying oven. Four factors were varied: Temperature, thickness, wetting and drying cycles, and soil types. The test results demonstrated that width opening and CIF (Crack Intensity Factor) are greater in soils with higher amount of fines content and plasticity index. Also, similar trends are found by Rayhani et al. (2008). Nevertheless, experiments made by Miller et al. (1998), show larger values of width and depth, using a soil with a low plastic index and optimum compacted dry density. The difference of the results showed that cracking not only depends to fines contents and plasticity index, but also of the soil density.

3.3 *Temperature*

Tang et al. (2008) selected three temperatures (30°C, 40°C and 50°C) to make desiccation experiments, and concluded that the average length, width of cracks, and average area of aggregates increased with increasing temperature. Also, Tang et al. (2010) determine that CIF values increases with increasing temperature (see figure 10). During tests the temperature and relative humidity was imposed at: 22°C and 55 ± 5% RH, 60°C and 5 ± 2RH, and 105°C and 0% RH.

As is stated above, cracks initiated when tensile stress exceeds tensile strength. Unfortunately, the behavior of tensile strength with temperature is not understood yet. However, some authors as Cui et al. (2005) and Mitchell (1964) found that in general shear strength decreases with temperature. For that reason, the increase of cracking with increase of temperature can be attributed to the suction increase rate and lower tensile strength.

3.4 *Thickness*

Tang et al. (2008) selected three thicknesses (5 mm, 8 mm, and 11 mm) to make some desiccation experiments, the authors showed that the number of intersections and crack segments decreases with an increase in thickness of soil layer (see figure 11). Soil layer thickness increase is accompanied by an increase on average length, width of cracks, average area of aggregates, and CIF. Same trend was found by Corte & Higashi (1960) and Nahlawi & Kodikara (2006), they observed that area of cells increase as increase the soil thickness and consequently the total length of cracks decreases with an increase of thickness (see figure 12).

Also, Corte A and Higashi A (1960) conclude that soil water content presents an exponential trend in function to depth. This behavior is due to the desiccation velocity of the soil surface.

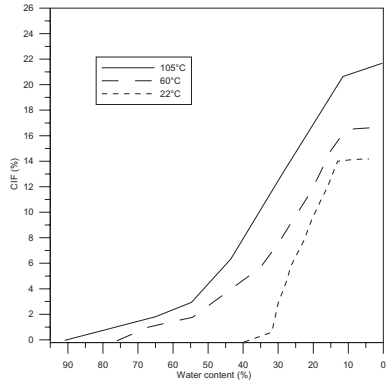

Figure 10. Relations between CIF and water content for three temperatures (Adapted from Tang et al. (2010)).

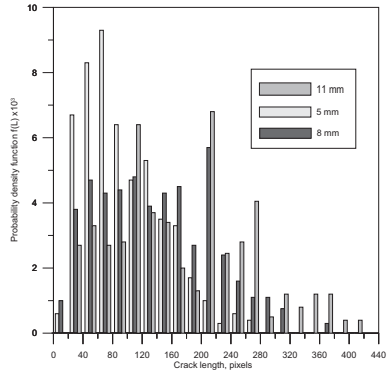

Figure 11. Relations between total length of cracks and thickness (Adapted from Tang et al. (2008)).

3.5 *Bottom surface material*

Corte and Higashi (1960) determine that if the thickness of soil is the same in two samples with different base materials, wood and glass, the soil with wood base presents larger cells than the soil with glass base. Also, the authors determine that the size of cracking cells are more dependent of the base material than of the difference in soil density, this is due to the property of adhesion of soil. Figure 13 presents the relation obtained by the authors for wood and glass with the Equation 1.

$$S = ad^{b} \quad (1)$$

where, a and b are constants, S is the mean area of cells; and d is the thickness.

3.6 *Wetting and drying cycles*

To understand environmental cycles Tang et al. (2008), realized in multiple wetting-drying cycles probability density functions of: cracked area, width of cracks, and length of cracks. The authors found that with increasing of wetting-drying cycles, the soil surface becomes more cracked, cracking cells are smaller, more cracks are close together, and

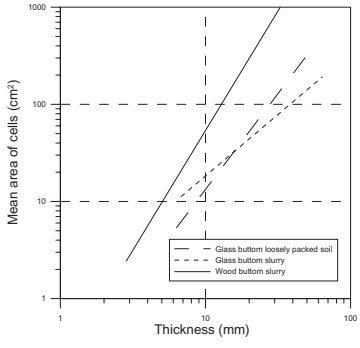

Figure 12. Relations between mean area of cells and thickness (Adapted from Corte & Higashi (1960)).

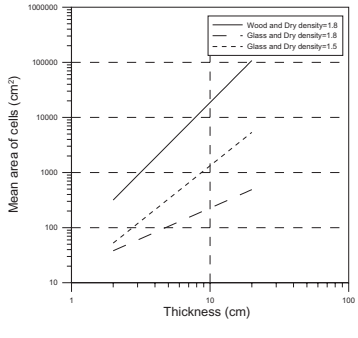

Figure 13. Relations between mean area of cells and thickness for wood and glass (Adapted from Corte & Higashi (1960)).

CIF decreases. On the contrary, Yesiller et al. (2000) observed that the CIF increased after the first wet-dry cycle. The difference in both results could be due to the effects of compaction conditions.

However, size effects in samples and all environmental conditions are not well controlled. Hence, to reproduce environmental conditions as a rainfall, heat flux, and evaporation, authors as Take & Bolton (2002) and Tristancho and Caicedo (2008), developed a climatic chamber to implement in a centrifuge machine.

However, despite the existence of climatic chambers, there are not studies about cracking desiccation in soil using this device. A deduction of scaling laws of environmental characteristics was made by Tristancho et al. (2012).

4 CONCLUSIONS

During desiccation process, clayey soil cracks when the tensile stress is greater than the tensile strength. For this reason, different devices have been developed to measure tensile strength in soil. Principal devices are: indirect tension test, direct tension test, and triaxial tension test. However, some disadvantages are presented as the assumption of linear behavior of soil, homogeneous stress field, and the impossibility to measure pore pressure. The best solution to these problems could be a triaxial test adaptation in order to measure soil extension.

Some tests on soil with different water content show that tensile strength of soil increases to a maximum value, and then decreases with an increase of water content. However, this behavior depend of the compaction of the soil.

On the other hand, the main cracks characteristics and factors that influenced desiccation cracking on soils are:

- Cracking Intensity Factor (CIF) and Density of Length of Fissure (LF) increases with time linearly at the beginning and then reached a steady state.
- The size of cells presents a log-normal distribution with time.
- Width opening and CIF are greater with higher amount of fines content and plasticity index. However these results can be influenced by compaction of the soil.
- CIF, average length, width of cracks and average cell area increases with increasing of temperature.
- With an increase of thickness, the average of length decrease, width of cracks increase, and area of cells increase.
- With respect to bottom surface material, mean area of cells depending of the adhesion property of bottom material.

Although cracked soil behavior largely depends on the tensile strength, the relation with the variables listed above have not been studied. Also, it is important to realize tests with greater depth and size in order to eliminate border and scale effects. An alternative to solve these problems and control soil climatic conditions is the use of reduced scale models in the centrifuge machine. With the correct use of the laws that governs the problems in centrifuge test, cracking desiccation test could be more accuracy and appropriated.

REFERENCES

Abu-Hejleh, A.N. & Znidarčić, D. 1995. Desiccation Theory for Soft Cohesive Soils. *Geotechnical Engineering*. 121(6): 493–502.

Bishop, A.W. & Garga, V.K. 1969. Drained Tension Tests on London Clay. *Géotechnique* (19): 309–313.

Corte, A. & Higashi, A. 1960. Experimental research on desiccation cracks in soils. *U.S. Army Snow ice and permafrost research establishment*. Research report No. 66. Corps of engineering, Wilmette, Illinois, USA.

Cui, Y.J., Lu, Y.F., Delage, P. & Riffard, M. 2005. Field simulation of in-situ water content and temperature changes due to ground-atmospheric conditions. *Géotechnique* 55(7): 557–567.

Favaretti, M. 1996. Tensile strength of compacted clays. *State of the art in unsaturated* soils. First international conference on unsaturated soils-UNSAT'95 Edited *by E.E. Alonso and P. Delage.* eds, Balkema, Rotterdam: 51–56.

Kim, T-H., Kim, T-H., Kang, G-C. & Ge, L. 2012. Factors influencing crack-induced tensile strength of compacted soil*, Journal of Materials in Civil Engineering*. 24: 315–320.

Lu, N., Kim, T.H., Sture, S. & Likos, W.J. 2009. Tensile strength of unsaturated sand. *Journal of Engineering Mechanics*. 135(12): 144–154.

Miller, C.J., Mi, H. & Yesiller, N. 1998. Experimental analysis of desiccation crack propagation clay liners. *Journal of the American Water Resources Association*. 34(4): 677–686.

Mitchell, J.K. 1964. Shearing resistance of soils as a rate process. *ASCE Journal of Soil Mechanics and Foundation*, Engineering Division 90(1): 29–61.

Morris, P.H., Graham, J. & Williams. 1992. Cracking in drying soils. *Canadian geotechnical journal.* 29: 263–277.

Nahlawi, H., Chakrabarti. S. & Kodikara, J.K. 2004. A direct tensile testing method for unsaturated materials. *Geotechnical testing journal ASTM*. 27(4): 1–6.

Nahlawi, H. & Kodikara, J.K. 2006. Laboratory experiments on desiccation cracking of thin soil layers. *Geotechnical and Geological Engineering*. 24(6): 1641–1664.

Prat, P.C., Ledesma, A., Lakshmikantha, M.R., Levatti, H. & Tapia, J. 2008. Fracture mechanics for crack propagation in drying soils. *Proc., 12th Int. Conf. Int. Assoc. for Computer Methods and Advances in Geomechanics,* Indian Institute of Technology, Mumbai, India: 1060–1067.

Rayhani, M.H.T., Yanful, E.K. & Fakher, A. 2008. Physical modeling of desiccation cracking in plastic soils. *Engineering Geology*. 97: 25–31.

Rodríguez, R. 2002. Estudio experimental de flujo y transporte de cromo, níquel y manganeso en residuos de la zona minera de Moa (Cuba): influencia del comportamiento hidromecánico. *Ph.D. thesis, Universitat Politècnica de Catalunya—BarcelonaTech*, Barcelona, Spain.

Rodríguez, R. 2006. Hydrogeotechnical characterization of a metallurgical waste. *Canadian Geotechnical Journal.* 43: 1042–1060.

Serra, J. 1982. *Image analysis and mathematical morphology*. Academic Press. London.

Take, W.A. & Bolton, M.D. 2002. An atmospheric chamber for the investigation of the effect of seasonal moisture changes on clay slope, *In: International Conference on Physical Modelling in Geotechnics, ICPGM '02, 10-7-2002 to 12-7-2002, St. John's,* Newfoundland, Canada: 765–770.

Tamrakar, S.B., Toyosawa, Y., Mitachi, T. & Itoh, K. 2005. Tensile strength of compacted and natural soils using newly developed tensile strength measuring apparatus. *Soils and Foundations.* 45(6): 103–110.

Tang, C., Shi, B., Liu, C., Zhao, L. & Wang, B. 2008. Influencing factors of geometrical structure of surface shrinkage cracks in clayey soils. *Engineering geology*. 101(3–4): 204–217.

Tang, C.S., Cui, Y.J., Tang, A.M. & Shi, B. 2010. Experimental evidence on the temperature of desiccation cracking behavior of clayey soils. *Engineering geology.* 114: 261–266.

Thusyanthan, N.I., Take, W.A., Madabhushi, S.P.G. & Bolton, M.D. 2007. Crack initiation in clay observed in beam bending. *Géotechnique* 57(7): 581–594.

Trabelsi, H., Jamei, M., Zenzri, H. & Olivella, S. 2011. Crack patterns in clayey soils: Experiments and modeling. *International Journal for Numerical and Analytical Methods in Geomechanics.* Published online in Wiley Online Library.

Tristancho, J. & Caicedo, B. 2008. Climatic Chamber to model soil-atmosphere interaction in the centrifuge. *Unsaturated Soils: Advances in Geo-Engineering—Toll et al. (eds) Taylor & Francis Group*. London: 117–121.

Tristancho, J., Caicedo, B., Thorel, L. & Obregón, N. 2012. Climatic chamber with centrifuge to simulate different weather conditions. *Geotechnical Testing Journal.* 35(1): 1–13.

Vallejo, L.E. 2009. Fractal analysis of temperature induced cracking in clays and rocks. *Géotechnique*. 59(3): 283–286.

Vesga & Luis, F. 2009. Direct tensile-shear test (DST) on unsaturated kaolinite clay. *Geotechnical testing journal.* 32(5): 1–13.

Vogel, H.J., Hoffmann, K. & Roth, K. 2005. Studies of crack dynamics in clay soil: I. Experimental methods, results, and morphological quantification. *Geoderma.* 125(3–4): 203–211.

Yesiller, N., Miller, C.J., Inci, G. & Yaldo, K. 2000. Desiccation and cracking behavior of three compacted landfill liner soil. *Engineering geology.* 57: 105–121.

Advances in Unsaturated Soils – Caicedo et al. (eds)
© 2013 Taylor & Francis Group, London, ISBN 978-0-415-62095-6

Evaluating the impact of thermal variations on the penetration test parameters

G. Franchomme, S. Rosin-Paumier & F. Masrouri
LEMTA (CNRS, UMR 7563), Université de Lorraine, Vandoeuvre-lès-Nancy Cedex, France

ABSTRACT: Geostructures with thermo-active function establish direct thermal exchange between the ground and the building. The cost of geostructures is lower than the usual geothermal solutions. However, adapting foundation piles to produce energy piles raises questions regarding the impact of temperature variations on the geotechnical parameters of the soil. In this study, a high resolution mini-penetration test, adapted from the current static penetration test, was developed to characterize laboratory samples. Samples of a kaolinite/sand mixture were prepared with various water contents and dry densities and submitted to thermal variations. The cone tip resistance and the sleeve friction are measured. These parameters depended strongly on the water content of the material. We demonstrated that temperature variations with a constant water content do not affect the measured shear stress parameters. The proposed penetration test can be carried out to compare the impact of thermal curing on soil parameters.

1 INTRODUCTION

Thermo-active geostructures are sustainable structures that enable thermal exchange with the ground through a liquid that flows through a closed-loop circulation system integrated into the geostructure. These systems use the subsurface as a heating or cooling source. Geostructures may be piles, diaphragm walls, tunnel linings, basement slabs or walls (Fromentin et al., 1999, Laloui et al., 2003, Brandl 2006). The standard use of thermo-active foundations modifies the current ground temperature (12°C) over a scale of 1 to 30°C (Peron & Laloui 2011). To study geo-exchange systems in ground structures, the complex interactions between temperature variations and induced stresses or deformations, which may affect building performance, must be considered (McCartney et al., 2010).

Foundation piles function through a combination of two effects: the cone tip resistance and the sleeve friction along the pile. The sleeve friction can be associated with the shear resistance, which is the relative resistance of the ground against the sliding caused by a load. The impact of temperature on the shear resistance is complex. Some authors such as Mitchell (1964), Sherif & Burrous (1969), de Bruyn & Thimus (1996), Lingnau et al. (1996) and Wiebe et al. (1998) reported that ground heating decreases the shear resistance, whereas Noble & Demirel (1969), Houston et al. (1985), Tanaka et al. (1996) and Cekerevac & Laloui (2004) obtained the opposite results. In fact, heating and loading cause opposite effects. On the one hand, heating decreases the viscosity of the interstitial water, which reduces the resistance between aggregates as well as the shear resistance. On the other hand, heating a material under mechanical stress densifies the ground, which results in increased contact between aggregates. In consequence, the resistance between aggregates and the shear resistance increase. The two different conclusions found in the literature result from the combination of these two effects in different soils.

Considering that thermo-active foundations may be built in a large variety of soils and the difficulty of predicting how temperature variations can affect the shear resistance of a material, it seems necessary to develop a quick and easy-to-use test to compare the impacts of thermal stresses on the soil parameters. In this study, a high-resolution mini-penetration test was developed. The method supplies parameters like those of the penetrometer test currently used to calculate the bearing capacities of piles. The aim of the test is to rapidly determine the impact of thermal variation on the shear resistance of different soils.

In this paper, the proposed mini-penetration test is first introduced. Then, test results on a mixture of kaolinite and fine sand are presented and discussed. Several samples were prepared at the Proctor optimum point and submitted to temperature variations from 1 to 50°C, which is equal to the maximal variations of the soil temperature induced by current implementations of thermal piles.

2 MATERIAL AND METHODS

2.1 *Preparation and characterization of the samples*

The tested material was a mixture of 50% kaolinite from the Charente basin and 50% Hostun sand (France). The materials were dried separately for at least 24 hours in an oven (60°C) and then mechanically mixed in the desired proportion. Water was added to obtain different initial water contents between 9 and 19%. The mixture was then packed in hermetic bags and left to homogenize for at least 24 hours (Table 1).

The liquid limit (LL), the plastic limit (PL) and the plasticity index (PI) of the soil were 26.9, 15.4 and 11.5%, respectively.

The particle size distribution of the mixture was determined using a Laser Fritsch analysette 2© (Figure 1).

Table 1. Initial water contents (w_i), dry densities (ρ_d), temperatures (T) and final water contents of the samples after the penetration test (w_f).

Test	w_i %	ρ_d Mg/m³	T °C	w_f %
E1	9.3	1.60	20	9.3
E2	11.3	1.74	20	11.3
E3	11.9	1.82	20	11.9
E4, E*4	12.3	1.87	20	12.3
E5, E*5	13.0	1.88	20	13.0
E6	13.2	1.89	20	13.2
E7, E*7	14.2	1.85	20	14.2
E8, E*8	15.1	1.82	20	15.1
E9, E*9	16.9	1.73	20	16.9
E10, E*10	18.5	1.66	20	18.5
E11, E*11	13.5	1.90	1	13.4
E12, E*12	13.5	1.90	30	13.2
E13	13.4	1.87	50	12.5

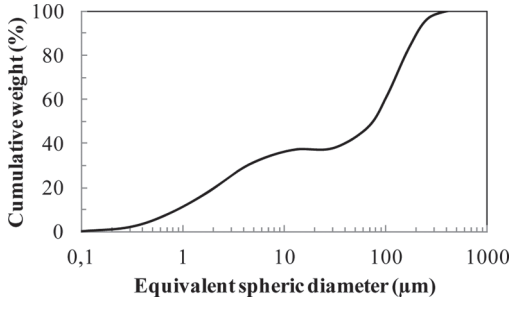

Figure 1. Particle size distribution of the kaolinite—sand mixture.

The material was compacted in 6 layers using a mold 152 mm in diameter and 152 mm in height. The applied energy was the same as that used in the Proctor method. Compaction in 6 layers was used to ensure the homogeneity of the material in the mold (Table 1). The obtained compaction curve was superimposed onto the standard Proctor curve (Figure 2). The optimum water content and the maximum dry density were 13% and 1.88 Mg/m³, respectively (Figure 2).

2.2 *Thermal cure*

The initial temperature of all samples was 20°C.

Samples were thermally cured at 1, 30 or 50°C and were equipped with thermal sensors to determine the minimal duration of thermal curing (Table 2).

2.3 *Mini penetration test*

The mini-penetration test is a laboratory test adapted from the normalized static penetration test (NF P94-113, AFNOR 1996). In our test, a probe consisting of a cone with a 60° apex penetrates the sample continuously at 30 mm/s (Figure 3). Two stainless steel probes named P1 and P2 were used

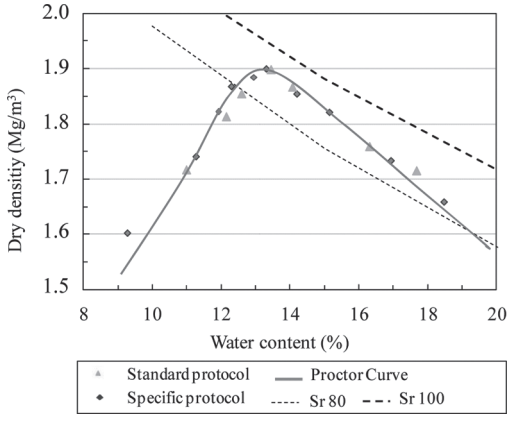

Figure 2. Comparison between the Proctor curve and the specific compaction curve of the material. Sr: Saturation rate.

Table 2. Parameters of the thermal curing protocol.

Climatic chamber temperature (°C)	1	30	50
Duration of the thermal cure (h)	9h20	4h20	12h50
Sample temperature (°C)	1.5	29.3	48.8

(Figure 3). The lengths (250 mm), angles (60°) and maximal external diameters (12 mm) of the two cones were similar. The diameter of P1 was 10 mm, the diameter of P2 was 12 mm, and the maximum penetration length of both probes was 100 mm. The cone tip resistance was measured with P1, whereas P2 measured a combination of the cone tip resistance and the sleeve friction.

Three mini-penetration tests were carried out in each mold at the equilibrium temperature. The position of each penetration test was fixed to prevent edge effects (Figure 4).

Three penetration velocities were tested: 1 mm/min, 30 mm/min and 90 mm/min. The velocity of the probe determines the duration of the test, which should be minimized to avoid changes in the water contents of the samples. Preliminary tests found that the probe penetration velocity had no impact on the measured parameters, and so the intermediate speed of 30 mm/min was used in all further tests.

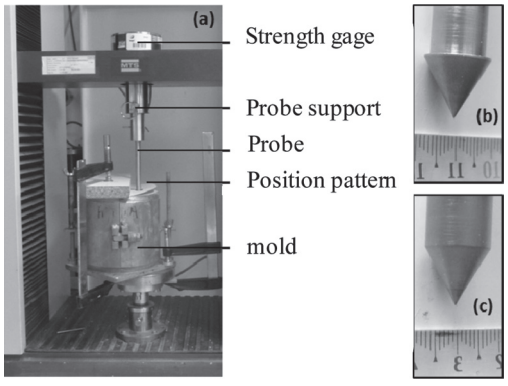

Figure 3. a. Mini-penetration test with traction-compression machine and probes for mini-penetration test (b. P1; c. P2).

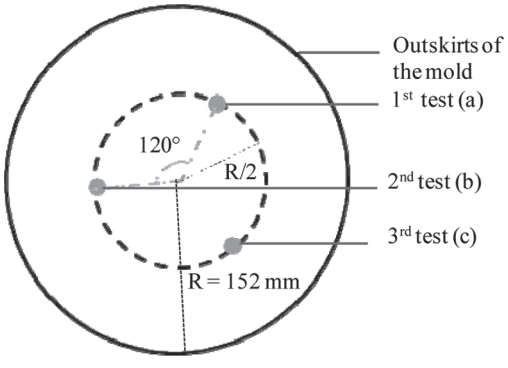

Figure 4. Positions of penetration tests in the mold.

3 RESULTS

3.1 *Mini-penetration curves typology*

The penetration curves obtained by probes P1 and P2 were named E and E* tests, respectively (Table 1). The behavior of the total strength versus depth is presented in Figure 5. In the first part of the curves (a), the apex of the probe penetrated into the soil. This part of the test is similar for both probes, as their angles and the diameters of their conical apexes are identical. Part b of the curves is specific to P1. As the sleeve friction was unmeasured, the strength variation in Part b was constant for a homogeneous soil. Part c of the curves is specific to P2. The strength increased as the probe came into contact with the soil.

The cone tip resistance (q_c) was calculated by averaging the strengths obtained in the linear part (b) of the P1 test. Equations 1 and 2 transform the measured stresses into resistance values.

$$q_c = F_c/(\pi R_1^2) \quad (1)$$

$$fs = (Ft - Fc)/(2\pi R_2(L - Lp)) \quad (2)$$

where F_c = the cone tip strength; R_1 = the radius of the conical apex, R_2 = the probe radius; fs = the sleeve friction; L = the penetration length and Lp = the height of the cone apex.

3.2 *Coupled influence of water content and dry density at 20°C*

This section presents the results of tests on the samples described in Table 1 carried out at 20°C.

3.2.1 *Cone tip resistance*

Figure 6 presents the P1 penetration strengths measured from samples with different water

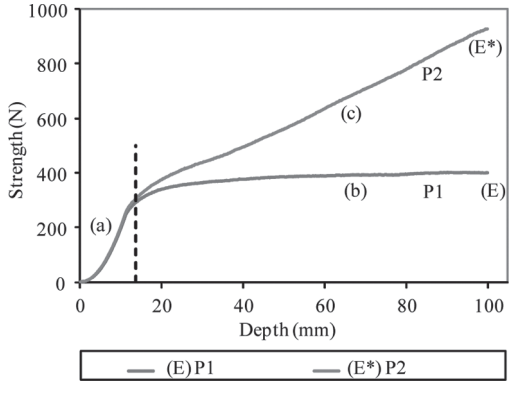

Figure 5. Total strength versus depth measured using probes P1 (E) and P2 (E*).

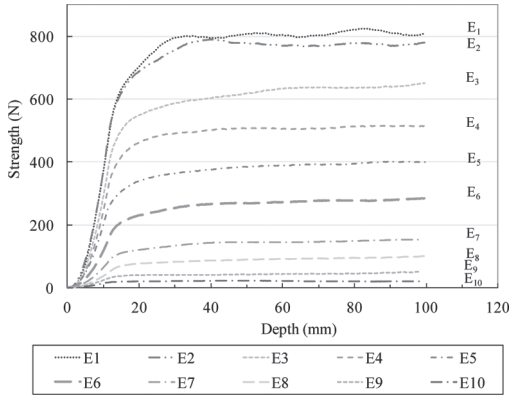

Figure 6. Strength measured along the penetration of P1 in samples with different water contents and dry densities.

contents and dry densities. The b parts of the curves are constant, which indicates that the prepared samples are homogeneous. The maximal strength measured during the tests increased as the water contents of the samples decreased.

The samples E3 and E8 were prepared at the same initial dry density (1.82 Mg/m^3), so the 750 N difference between the measured strengths could be only due to the difference in water contents: w = 11.9% for E3, and w = 15.1% for E8. Variations in the dry density were generally observed to less strongly affect these results.

Figure 7 superimposes the cone tip resistance at a penetration depth of 90 mm onto the compaction curve. As the water content decreases, the tip resistance increases. The cone tip resistance varies more rapidly on the dry side (w < 14.5%, Equation 3) than on the wet side (w > 14.5%, Equation 4) of the compaction curve. The equations of these two curves were determined and used as references in further tests.

$$q_c = -2028.2w + 29770 \quad (3)$$

$$q_c = 49.589w^2 - 1875.2w + 17919 \quad (4)$$

3.2.2 *Sleeve friction*

Tests with both P1 and P2 were performed on each sample. The difference between the two curves provides the sleeve friction (Figure 8), and comparing the sleeve friction at different water contents and dry densities provides the same conclusion as the cone tip resistance: As the water content of the samples decreases, the sleeve friction increases (Figure 9). Equations 5 and 6 describe the sleeve friction curves for water contents from 12% to 14.5% and from 14.5% to 19%, respectively.

$$fs = -74.353w + 1113.9 \quad (5)$$

$$fs = 1.5969w^2 - 59.743w + 571.35 \quad (6)$$

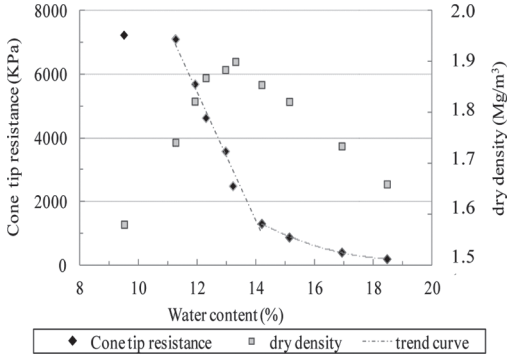

Figure 7. Comparison between the compaction curve and the cone tip resistance at a penetration depth of 90 mm.

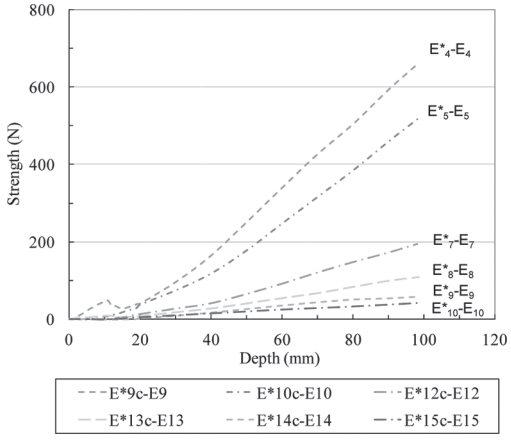

Figure 8. Sleeve frictions at different water contents and dry densities calculated from penetration tests using P1 and P2.

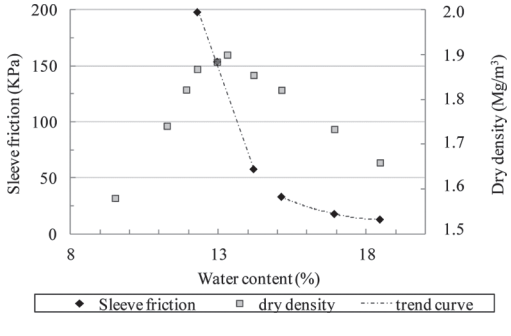

Figure 9. Comparison between the sleeve friction at 90 mm penetration depth and the compaction curve.

3.3 *Impact of a thermal cure on the cone tip resistance and sleeve friction*

The results of penetration tests carried out on different samples (E11 to E13) after thermal curing at 1, 30, and 50°C were compared to the results of the E6 test at 20°C (See Table 1 and Table 3).

The cone tip resistance and the sleeve friction were not strongly affected by temperature variations between 1 and 30°C. However, increasing the temperature to 50°C dramatically increased both of these parameters (Figure 10). The variation could be due to variations in the water content (from 13.2% to 12.5%) caused by heating the sample, though the mold was completely covered during the thermal curing process. As already demonstrated in Figures 7 and 9 (Equations 3 and 5), this decrease in water content could dramatically increase both the cone tip resistance and the sleeve friction (dry side).

Test E4 was performed at 20°C on a sample with a similar water content and dry density as E13. The measured cone tip resistance was similar to that of E13 (Table 3), but the measured sleeve friction was lower. This observed difference may be due to the effects of temperature changes, but further experiments are necessary to confirm this result.

Table 3. Measured and theoretical cone tip resistance (q_c) and sleeve friction (f_s) at a penetration depth of 90 mm.

Sample number	Temperature °C	q_c KPa	f_s KPa
E11	1	2323	105
E6	20	2504	131*
E12	30	2336	106
E13	50	4075	317
E4	20	4633	154

*Calculated with equation 5.

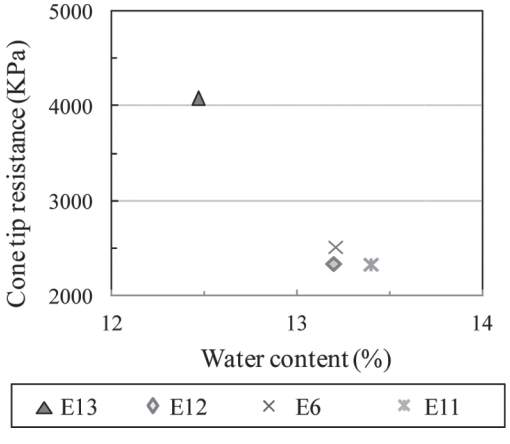

Figure 10. Comparison of the cone tip resistances at 90 mm penetration depth of sample E11, E6, E12 and E13, which were cured at 1, 20, 30 and 50°C, respectively.

4 CONCLUSION

The purpose of this study was to develop a high-resolution mini-penetration test and propose a simple method to quickly define the effects of temperature variations on the cone tip resistance (q_c) and sleeve friction (f_s) of a soil. The results demonstrated that the test is repeatable and reliable.

The study was divided into several phases: (1) definition of the adapted compaction protocol, (2) definition of the thermal curing protocol, (3) and definition of the penetration test conditions (depth, velocity, …). The effects of the water content, the dry density and the thermal curing temperature on the penetration test parameters were studied.

We demonstrated that decreasing the water content of the samples increased both the cone tip resistance and the sleeve friction. The dry density of the sample has less impact on the penetration parameters than the water content. The cone tip resistance and the sleeve friction both vary more sharply on the dry side of the compaction curve (w < 14.5%, Equation 3) than on the wet side (w > 14.5%, Equation 4). The results demonstrate that thermal curing between 1 and 30°C has little effect on the penetration parameters of the studied kaolinite/Hostun sand mixture. Thermal curing at a higher temperature (50°C) led to a decrease of the sample water content, and resulting increases in the cone tip resistance and the sleeve friction were observed.

REFERENCES

Afnor, 1996. NF P94-113. Sols: reconnaissance et essais; Essai de pénétration statique. *Association Française de Normalisation*, Paris, France, 16 p.

Brandl, H. 2006. Energy foundations and other thermo-active ground structures. *Geotechnique* 56(2): 81–122.

Cekerevac, C. & Laloui, L. 2004. Experimental study of thermal effects on the mechanical behaviour of a clay. *International journal for numerical and analytical methods in geomechanics* 28: 209–228.

De Bruyn, D. & Thimus, J.F. 1996. The influence of temperature on mechanical characteristics of Boom clay: The results of an initial laboratory program. *Engineering Geology* 41: 117–226.

Fromentin, A., Pahud, D., Laloui, L. & Moreni, M. 1999. Pieux échangeurs: Conception et règles de prédimensionnement, *Revue française de génie civil* 3(6): 387–421.

Houston, S.L., Houston, W.N. & Williams, N.D. 1985. Thermo-mechanical behavior of seafloor sediments. *Journal of Geotechnical Engineering* 111(11): 1049–1263.

Laloui, L., Moreni, M. & Vulliet, L. 2003. Comportement d'un pieu bi-fonction, fondation et échangeur de chaleur. *Canadian Geotechnical Journal* 40(2): 388–402.

Lingnau, B.E., Graham, J., Yarechewski, D., Tanaka, N. & Gray, M.N. 1996. Effects of temperature on strength and compressibility of sand-bentonite buffer. *Engineering Geology* 41: 103–115.

McCartney, J.S., LaHaise, D., LaHaise, T. & Rosenberg, J. 2010. Application of Geoexchange Experience to Geothermal Foundations. In Hussein, M.H., Anderson, J.B. & Camp, W.M. (eds) *Proceeding of The Art of Foundation Engineering practice, Geotechnical special publication 198*, 411–423.

Mitchell, J.K. 1964. Shearing resistance of soils as a rate process. *Journal of the Soil Mechanics and Foundations Division, ASCE* 90: 29–61.

Noble, C.A. & Demirel, T. 1969. Effect of temperature on strength behavior of cohesive soil. In Effects of Temperature and Heat on Engineering Behavior of Soils, Special report 103, Highway Research Board.

Peron, H. & Laloui, L. 2011. A method for the geotechnical design of heat exchanger piles, *Proceedings of the Geo-Frontiers Conference, ASCE Conf. Proc. doi:10.1061/41165(397)* 49.

Sherif, M.A. & Burrous, C.M. 1969. Temperature effects on the unconfined shear strength of saturated, cohesive soil. Effects of Temperature and Heat on Engineering Behavior of Soils, *Special report 103, Highway Research Board*: 267–272.

Tanaka, N., Graham, J. & Crilly, T. 1996. Stress-strain behaviour of reconstituted illitic clay at different temperatures. *Engineering Geology* 47: 339–350.

Wieibe, B., Graham, J., Tang, G.X. & Dixon, D. 1998. Influence of pressure, saturation and temperature on the behaviour unsaturated sand-bentonite. *Canadian Geotechnical Journal* 35: 194–205.

Advances in Unsaturated Soils – Caicedo et al. (eds)
© 2013 Taylor & Francis Group, London, ISBN 978-0-415-62095-6

Using fracture mechanics theory to evaluate the unconfined compressive strength of unsaturated fissured clays

L.E. Vallejo
Department of Civil and Environmental Engineering, University of Pittsburgh, Pittsburgh, USA

ABSTRACT: This study reports laboratory and theoretical investigations on the mechanics of fissure propagation and failure of unsaturated clay samples subjected to unconfined compressive loads. The theoretical investigation used Linear Elastic Fracture Mechanics (LEFM) theory. The samples tested had fissures inclined at 15, 30, 45, 60 and 75 degrees with the vertical. They had water contents of 3, 9, and 15%. The samples were found to behave like brittle materials and their failure was the result of a fissure-induced tension. At failure, the samples developed secondary tensile cracks that propagated form the original cracks in a direction parallel to the uniaxial compressive load direction. The strength of the samples that failed in tension was found to increase with an increase in water content. This behavior was explained using the pendular, funicular, and saturated water distribution in the samples. LEFM theory predicted very well the failure mode of the fissured clay samples.

1 INTRODUCTION

Some clays forming part of slopes and earth dams exist in the fissured state (Duncan and Dunlop, 1969, Sherard, 1973). For the assessment of the short-term stability of these earth structures, the unconfined compressive, σ_c, of the clays is needed. Very little is known about the role fissures play in the failure process of unsaturated clays when subjected to compressive loads. The purpose of this study is to report laboratory and theoretical investigations designed to understand the role of water content and its distribution on the unconfined compressive strength of fissured clays.

2 LABORATORY ANALYSIS

2.1 *Laboratory preparation of samples*

For the experimental investigation, laboratory prepared samples of kaolinite clay with pre-existing cracks were used. The kaolinite used in the experiments had a LL = 58% and PL = 28%. The dry kaolinite was mixed with distilled water to form a soft soil mass with water content of about 40%. After the mixing was done, the clay-water mixture was placed in plexiglass containers that measured 7.62 cm in length, 7.62 cm in width and 4 cm in thickness. The samples were consolidated in these containers using a weight that applied a normal pressure of 25.7 kPa for a period of 5 days. After removal of the weight, the samples had consolidated and measured 7.62 in length and width and about 2.54 cm in thickness. Immediately after removal of the samples, when their water content (w) was about 30%, cracks were artificially made in the samples by a process of inserting and removing thin glass sheets 1 mm in thickness and 2,5 cm in width in a direction normal to the sample's face. The cracks were made at 15, 30, 45, 60 and 75 degrees with the direction of uniaxial compressive load (vertical direction).

In order to investigate the effect of water content (w) on the uniaxial compressive strength of the fissured clay samples, groups of clay samples with 3 different water contents were tested in the laboratory. These three different water contents were developed in the samples by allowing them to air dry after the cracks were made in the samples (w = 30%). By allowing the samples to air dry (air temperature = 20°C) for about 2 hours, 4 hours, and 2 days, the final water contents in the samples were measured to be 15, 9, and 3%. After these final water contents were reached in the samples, they were tested under a uniaxial compressive stress conditions. The rate of deformation used in the testing was 0.5 mm/min.

2.2 *Mode of failure of the samples*

Figures 1 to 4 shows the mode of failure under uni-axial compression of the prismatic clay samples containing pre-existing (primary) cracks at 15, 30, 45, 60 and 75 degrees with respect to the vertical. The text should fit exactly into the type area of 187 × 272 mm (7.36" × 10.71"). For correct settings of margins in the Page Setup dialog box (File menu) see Table 1.

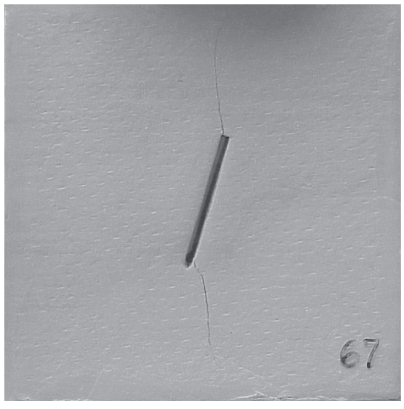

Figure 1. Secondary cracks developed at failure of a clay sample containing a primary crack inclined at 15 degrees with respect to the vertical.

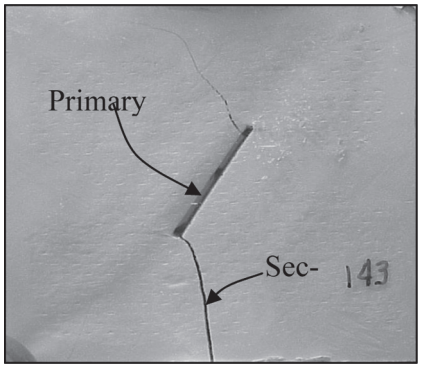

Figure 2. Secondary cracks developed at failure of a clay sample containing a primary crack inclined at 30 degrees with respect to the vertical.

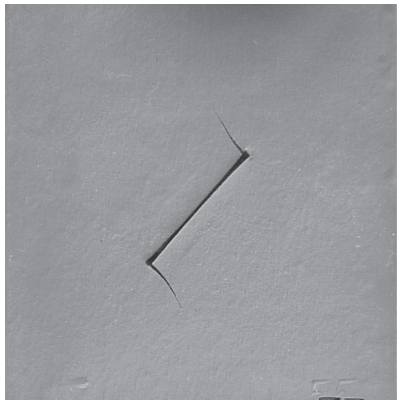

Figure 3. Secondary cracks developed at failure of clay sample containing a primary crack inclined at 45 degrees with respect to the vertical.

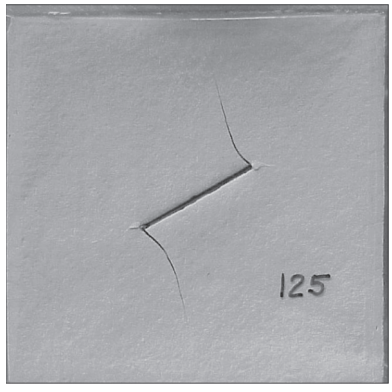

Figure 4. Secondary cracks developed at failure of a clay sample containing a primary crack inclined at 60 degrees with respect to the vertical.

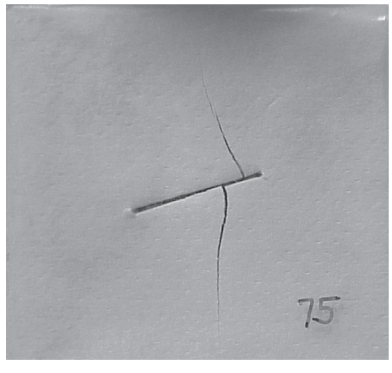

Figure 5. Secondary cracks developed at failure of a clay sample containing a primary crack inclined at 75 degrees with respect to the vertical.

An analysis of Figures 1 to 5 indicates that under uniaxial compression, the samples experienced failure by developing secondary cracks that started from the face or the tips of the original cracks and propagated in a direction that was parallel to the uniaxial compressive stress direction. The samples shown in Figures 1 to 5 had a w = 3%. The samples with water contents of 9 and 15% failed in a similar manner as the samples with w equal to 3%.

2.3 *Influence of the crack inclination and water content on the failure of the samples*

Figure 6 shows a plot of the uniaxial compressive strength (given by the maximum uniaxial compressive stress, σc, versus the inclination of the pre-existing fissures in the samples, β. The uniaxial compressive strength reported in Figure 6 is the one at which the samples failed in tension by the developing of secondary cracks (Figures 1

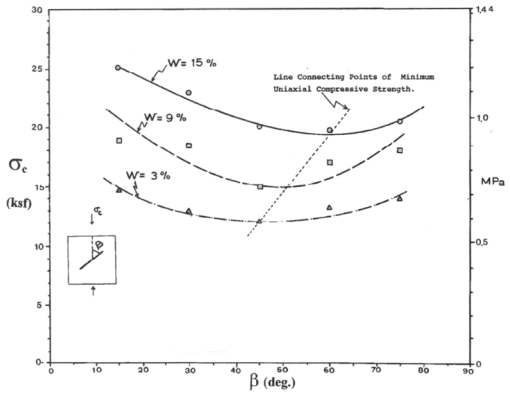

Figure 6.

through 5). The plot in Figure 6 has also been done for samples having three different water contents.

Figure 6 shows that the inclination of the pre-existing cracks have a marked influence on the compressive strength of the fissured clay samples. For the case of the samples with water contents (w) between 3 and 15%, Figure 6 shows that the compressive strengths reached minimum values when the pre-existing cracks in the samples reached a critical angle, β, that varied between 45° and 60°. Figure 6 also indicates that for the brittle samples (w = 3 to 15%), their uniaxial compressive strength increased in value with an increase in water content in the clay. This behavior is explained next using the type of stresses that caused the failure of the samples and the influence of the water content and its distribution in the unsaturated clay samples.

3 THEORETICAL ANALYSIS

In order to evaluate the type of stresses that caused the failure of the prismatic samples of brittle clay containing primary cracks inclined at 15 to 75 degrees with the vertical, Linear Elastic Fracture Mechanics (LEFM) theory will be used.

3.1 *Stresses around pre-existing crack*

For an evaluation of the type of stresses that caused the secondary cracks in the clay samples (Figures 1 to 5), the principles of LEFM theory will be used. According to Jayatilaka (1979), the tangential stress σ_θ the radial stress σ_r, and the shear stress $\tau_{r\theta}$, in the vicinity of a pre-existing crack in a sample of clay under uniaxial compression, σ_c (Figure 7), can be obtained from the following relationships,

$$\sigma_r = [1/(2\pi r)^{1/2}] \cos(\theta/2)\{K_I [1 + \sin^2(\theta/2)] + (3/2)\, K_{II} \sin\theta - 2K_{II} \tan(\theta/2)\} \quad (1)$$

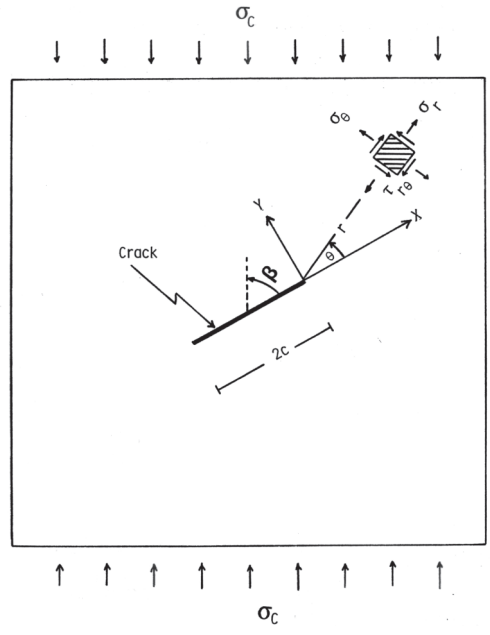

Figure 7. System of stresses in the intact clay regions near the pre-existing crack.

$$\sigma_\theta = [1/(2\pi r)^{1/2}] \cos(\theta/2)\{K_I \cos^2(\theta/2) - (3/2)\, K_{II} \sin\theta\} \quad (2)$$

$$\tau_{r\theta} = [1/2(2\pi r)^{1/2}] \cos(\theta/2)\{K_I \sin\theta + K_{II}(3\cos\theta - 1)\} \quad (3)$$

where:

$$K_I = \sigma_c (\pi c)^{1/2} \sin^2\beta \quad (4)$$

and

$$K_{II} = \sigma_c (\pi c)^{1/2} \sin\beta \cos\beta \quad (5)$$

The terms in Equations (1) through (5) are shown and defined in Figure 6. K_I and K_{II} are the stress intensity factors.

The principal stresses σ_1 and σ_3 and their directions can be obtained from the following relationships,

$$\sigma_{1,3} = (\sigma_r + \sigma_\theta)/2 \pm \{[(\sigma_r - \sigma_\theta)/2]^2 + [\tau_{r\theta}]^2\}^{1/2} \quad (6)$$

$$\psi = (1/2) \tan^{-1}[2\, \tau_{r\theta}/(\sigma_r - \sigma_\theta)] \quad (7)$$

$$\lambda = \psi + \pi/2 \quad (8)$$

where ψ is the angle of inclination with respect to the X axis (Figure 7) of the principal plane on which σ_1 acts. λ represents the inclination with respect to the X axis (Figure 7) of the principal plane on which σ_3 acts. A computer program that uses Eqs. (1) through (8) was written in order to

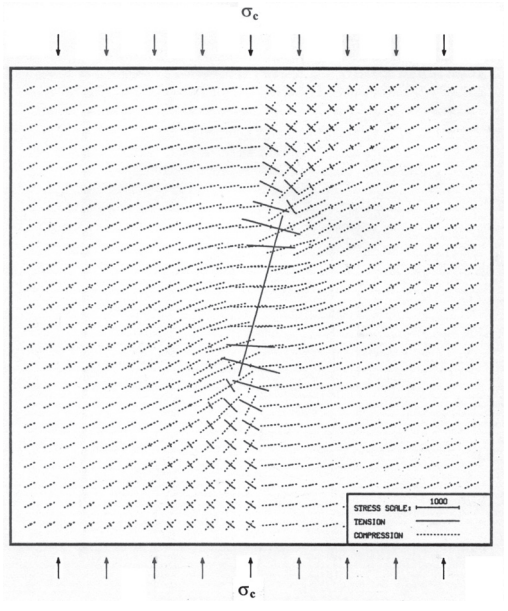

Figure 8. Magnitude and direction of the principal stresses in regions near and around a pre-existing crack inclined at 15 degrees with the vertical. The uniaxial stress used was equal to 2000 units of stress (full lines are tension, dotted lines are compression).

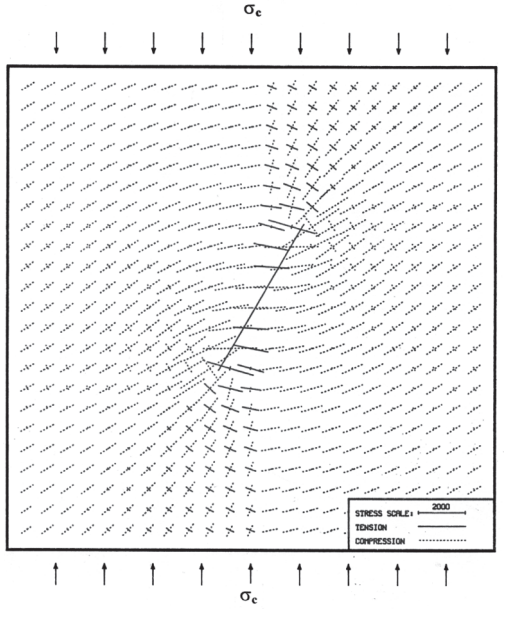

Figure 9. Magnitude and direction of the principal stresses in regions near and around a pre-existing crack inclined at 30 degrees with the vertical. The uniaxial stress was equal to 2000 units of stress (full lines are tension, dotted lines are compression).

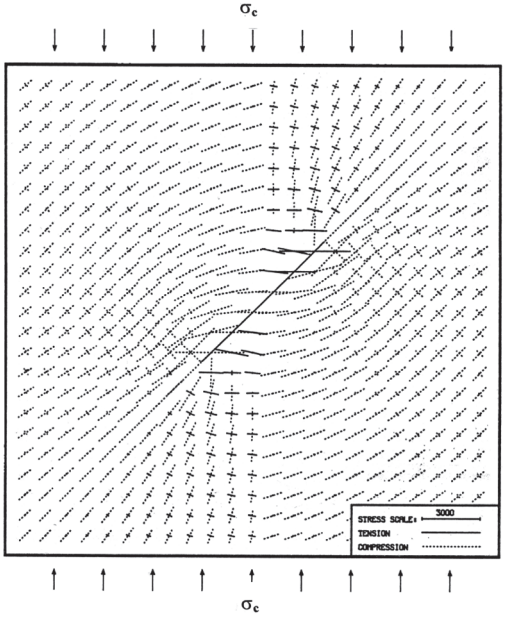

Figure 10. Magnitude and direction of the principal stresses in regions near and around a pre-existing crack inclined at 45 degrees with the vertical. The uniaxial stress used was equal to 2000 units of stress (full lines are tension, dotted lines are compression).

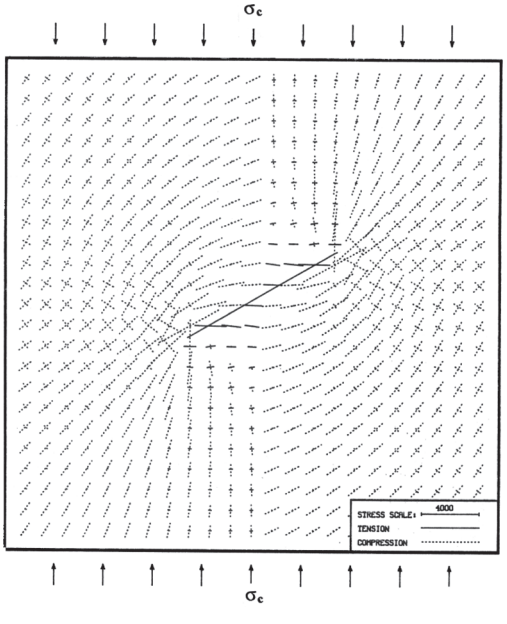

Figure 11. Magnitude and direction of the principal stresses in regions near and around a pre-existing crack inclined at 60 degrees with the vertical. The uniaxial stress used was equal to 2000 units of stress (full lines are tension, dotted lines are compression).

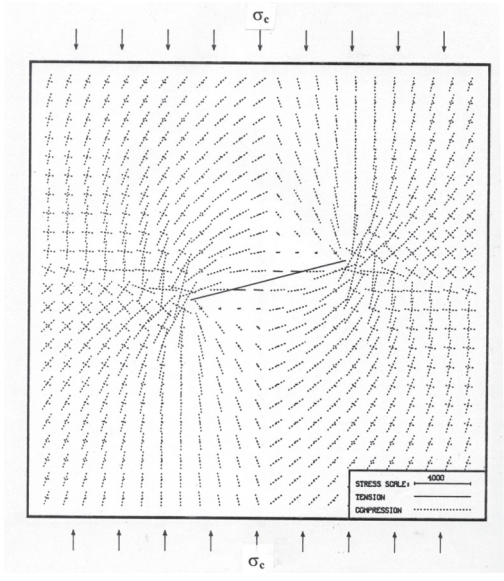

Figure 12. Magnitude and direction of the principal stresses in regions near and around a pre-existing crack inclined at 75 degrees with the vertical. The uniaxial stress used was equal to 2000 units of stress (full lines are tension, dotted lines are compression).

plot the magnitude and direction of the principal stresses σ_1 and σ_3 in regions near and around the cracks of Figures 1 through 5. The plot of the principal stresses and their directions are shown in Figures 8 through 12.

3.2 *Type of stresses*

An analysis of Figures 8 through 12 indicates distinctive zones of high tensile stresses develop on the left section of the upper tip and on the right section of the lower tip of the pre-existing crack. These areas of tensile stresses coincide with the location of secondary cracks that the samples developed and shown in Figures 1 through 5. Thus, the failure of the samples started in the zones of tension and not in the zones of compression since is known that clays are weaker in tension and stronger in compression. Recent research conducted by Vesga et al. (2008) that used DEM to study crack propagation in clays have found similar results as the findings outlined in the present study.

4 BEHAVIOR OF THE UNSATURATED FISSURED CLAYS

In order to explain why the brittle fissured clay samples experience an increase in uniaxial compressive strength with an increase in water content,

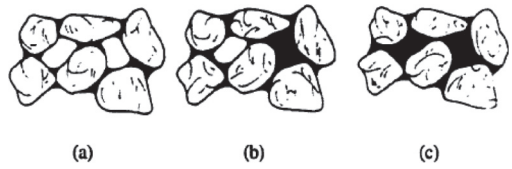

Figure 13. Degree of saturation in unsaturated soils: (a) pendular, (b) funicular, and (c) saturated (after Schubert et al., 1975).

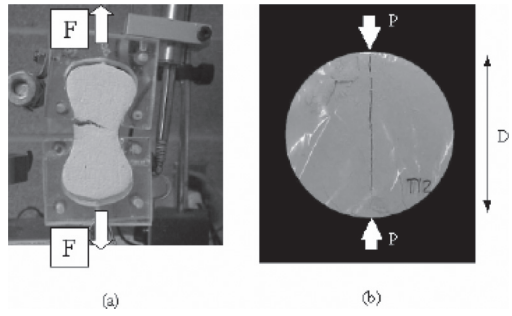

Figure 14. Direct and indirect tensile strength tests on kaolinite clay samples (Vesga & Vallejo, 2005, 2006).

the amount of water and its distribution in the samples will be used.

According to Schubert et al. (1965) and Kim and Hwang (2000) the state of water saturation in soils can be either pendular, funicular or saturated (Figure 13). The amount of water in the unsaturated samples increased in value as well as in its distribution in the samples from the pendular, funicular and finally in the saturated state. These states create negative pore water pressures in the samples. The effect of the negative pore water pressures is to pull together the clay particles in the samples. This pulling together of the clay particles by the negative pore water pressures will make the samples more resistant against failure in tension (Figures 8 to 12 show tension zones in the samples). Also the higher the water con-tent in an unsaturated sample, the larger the number of clay particles affected by the negative pore water pressures and thus the larger the tensile strength of the tensile strength of the samples. As the sample become close to saturation ($w \approx 25\%$), the samples tend to develop positive pore water pressures when subjected to compression. These positive pore water pressures will cause a decrease in compressive strength in the samples.

Recent reports by Vesga and Vallejo (2005, 2006) on the tensile strength of unsaturated kaolinite samples with varying degrees of water content seem to substantiate the previous contention. Vesga and Vallejo (2005, 2006) conducted direct and indirect tensile strength tests on samples of kaolinite with different water contents. The indirect tensile tests were of the Brazilian type. Figure 14 shows

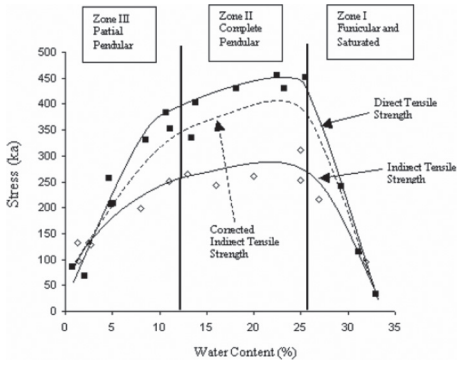

Figure 15. Tensile strength of unsaturated kaolinite clay samples with different states of unsaturation (Vesga & Vallejo, 2006).

the type of tensile strength tests conducted by Vesga and Vallejo (2005, 2006), Figure 15 shows the results of the strength tests in function of the water content in the samples.

An analysis of Figure 15 shows that as the degree of saturation increases in the unsaturated samples (from pendular to funicular), the tensile strength of the samples increases. An increase in tensile strength in the samples will also represent an increase in uniaxial compressive strength (Figure 6). Figure 15 also shows that as the water content in the samples reaches the saturation value ($w \approx 25\%$), the tensile strength of the samples decreased in value with an increase in water content.

5 CONCLUSIONS

Laboratory and theoretical investigations designed to understand the effect of fissures in unsaturated samples of clay subjected to unconfined compression strength tests indicated the following:

1 The inclination of cracks in unsaturated fissured clays had a marked influence on their unconfined compressive strength. There is a critical crack inclination in a sample that corresponds with its minimum unconfined compressive strength. If the crack inclination increases or decreases from this critical one, the unconfined compressive strength always increases. The critical crack inclination is a function of the water content in the clay sample.
2 Cracks in unsaturated clays under uniaxial compression induce tensile stresses in the intact material surrounding the cracks. These tensile stresses cause the clay to fail in tension, with secondary cracks being the end result. Linear Elastic Fracture Mechanics (LEFM) theory predicted very well the formation and propagation of these secondary tensile cracks.
3 The secondary tensile cracks originated at the tip or edges of the pre-existing cracks and extended in a direction parallel to the direction of the uniaxial compressive stress.
4 It was determined that the uniaxial compressive strength of the unsaturated fissured clay samples increased in value with an increase in their un-saturated water content. This result can be explained by the negative pore water pressures induced in the samples when their water content increased from a pendular to a funicular state. Indirect and direct tensile strength tests in clay samples indicated that their tensile strength increased in value as their unsaturated water content increased in value from a pendular to a funicular state. An increase in tensile strength with water content will represent an increase in un-confined compressive strength in the fissured clay samples.

ACKNOWLEDGEMENTS

The works described herein was supported by NSF Grant No. ECE-8414931. This support is gratefully acknowledged.

REFERENCES

Duncan, J.M. & Dunlop, P. 1969. Slopes in stiff fissured clays and shales. Journal of the Soil Mechanics and Foundation Division, ASCE, 95(2), 467–491.

Jayatilaka, A. 1979. Fracture of Engineering Brittle Materials. Applied Science Publishers, London.

Kim, T.H. & Hwang, C. 2003. Modeling of tensile strength on moist granular earth material at low water content. Engineering Geology, 69, 233–244.

Schubert, H., Herrmann, W. & Rumpf, H. 1975. Deformation behavior of agglomerates under tensile stresses. Powder Technology, 11, 121–131.

Sherard, J.L. 1973. Embankment dam cracking. In: Embankment Dam Engineering, Casagrande Volume. Hirschfield R.C. & Poulos, S.J. (Eds). Wiley Intersciences, New York, 271–353.

Vesga, L. & Vallejo, L.E. 2005. Strength of an unsaturated kaolinite clay under suction pressures. Proceedings of the 16th International Conference on Soil Mechanics and Geotechnical Engineering, Osaka, Japan, 2, 611–614.

Vesga, L.F. & Vallejo, L.E. 2006. Direct and indirect tensile tests for measuring the equivalent effective stress in a kaolinite clay. In: Unsaturated Soils, ASCE's Geotechnical Special Publication No. 147, Miller, G.A., Zapata, C.E., Houston, S. & Fredlund, D.G. (Eds), 1290–1301.

Vesga, L.F., Vallejo, L.E. & Lobo-Guerrero, S. 2008. DEM analysis of the crack propagation in brittle clays under uniaxial compression tests. International J. for Numerical and Analytical Methods in Geomechanics, 32(11), 1405–1415.

Advances in Unsaturated Soils – Caicedo et al. (eds)
© 2013 Taylor & Francis Group, London, ISBN 978-0-415-62095-6

Fractal evaluation of the fragmentation of clays due to desiccation

L.E. Vallejo
Department of Civil and Environmental Engineering, University of Pittsburgh, Pittsburgh, USA

ABSTRACT: The evolution of cracks in clays as result of desiccation is studied. When desiccation starts, few cracks form. With time, these original cracks interconnect producing the fragmentation of the clay. At the end of the fragmentation process, the clay is formed of fragments of different sizes. The fragmentation fractal dimension (D_d) concept from fractal theory is used to measure the size distribution of the fragments. The fractal analysis was conducted on bentonite clay samples desiccated in the laboratory and on the giant desiccation clay polygons located in the southwestern part of the United States. These polygons have three very distinctive shapes: regular random, irregular random and orthogonal polygon. The D_d was equal to 2.21 for the regular random polygons, 1.96 for the irregular random polygons, and 3.894 for the orthogonal desiccation polygons. The effect of fragmentation on the type of landslides that the desiccated clays could develop is also discussed.

1 INTRODUCTION

High temperatures resulting from climatic fluctuations can cause cracking in clays. The cracking in the clays is the result of evaporation and shrinkage. The present study deals with the formation and the evolution of the cracks in clays in the laboratory as well as in the field. The level of fragmentation of the desiccated clays is measured using the fractal dimension concept from fractal theory (Turcotte, 1986). Also, the effect of the level of fragmentation on the type of landslides that the desiccated clay areas could develop is also discussed in this study.

2 LABORATORY INVESTIGATION OF CRACKING

2.1 *Laboratory preparation of samples*

To investigate how temperature induced desiccation cracks form, evolve, and interconnect in clays, a prismatic sample of bentonite clay was prepared in the laboratory. The clay used in the experiments had a liquid limit equal to 418%, a plastic limit equal to 120%, a shrinkage limit equal to 10%, and a specific gravity equal to 2.82. For the experimental investigation, a mixture made of 0.73 kg of bentonite clay, 2.73 kg of water, and 0.24 kg of calgon (hexametaphosphate used as a clay dispersant) was placed in a container where it was mixed thoroughly until a uniform slurry was obtained. A portion of this slurry was then placed in an open faced plexiglass container. The container with an open face measured 37 cm in length, 29.5 cm in width, and 2.5 cm in depth. The clay slurry in the container measured 36 cm in length, 28.5 cm in width, and 1 cm in depth. The open face of the container allowed photographic recording of the evolution of cracking in the clay during the desiccation process.

2.2 *Evolution of temperature induced desiccation cracking in clay samples*

Figure 1 shows the progression of cracking on the free surface of the bentonite clay sample. The cracking was the result of water being removed by evaporation from the clay sample. This water removal caused the desiccation cracking of the clay. The water evaporation from the sample took place under a constant air temperature that was equal to 25°C. The first crack developed after 110 hours of desiccation and penetrated 0.5 cm into the depth of the clay layer [Figure. 1(A)]). The degree of cracking shown in Figures 1(B), 1(C), and 1(D) was recorded at 114, 123, and 155 hours of desiccation respectively. Fig. 2 shows a photograph of the clay sample at the end of the desiccation process [Figure 1(D)].

The fracture networks in the desiccated clay are quite complex. As a result of the temperature induced desiccation process, the clay sample first developed a series of long isolated cracks that affected only a small area [Figs. 1(A) and 1(B)]. These cracks are the first generation cracks. As desiccation time progressed, second generation cracks formed.

These cracks are shorter, and connect the first generation cracks. The second generation

cracks are orthogonal to the first generation cracks. Network connectivity was complete after 123 hours of desiccation [Fig. 1(C)]. As the desiccation time increased, new cracks formed that in general were shorter, more diversely oriented, and increased network connectivity greatly. These new cracks generally defined small, irregular polygonal blocks bounded by first and second generation cracks [Fig. 1(D)]. Also, at the end of the desiccation process, when most of the water had evaporated from the clay sample, it experienced extensive fragmentation [Fig. 1(D)].

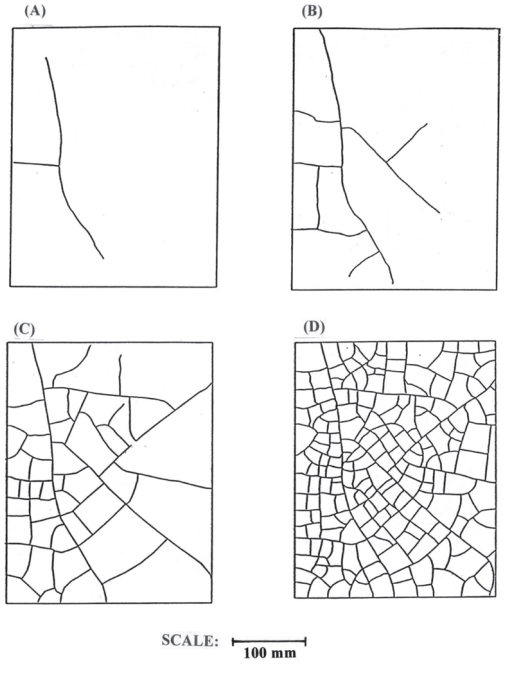

Figure 1. Evolution of cracks in the laboratory clay sample.

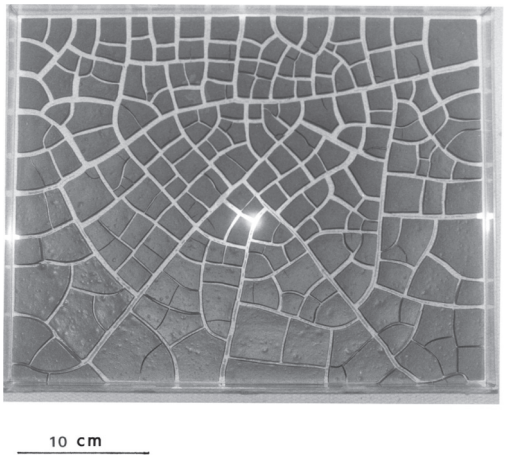

Figure 2. Complete fragmentation in the laboratory clay sample corresponding to Fig. 1(D) in Figure 1.

3 FIELD INVESTIGATION OF CRACKING

The complex crack pattern depicted in Fig. 1(D) has also been reported by Neal et al. (1968) to occur in large basin clay playas located in the western part of the United States (in the states of Nevada, California Arizona and New Mexico) under air temperatures in excess of 57° C. These temperature induced desiccation cracks not only covered the surface of the playas (with areas in excess of 15000 m^2), but penetrated the playas to depths equal to 5 meters. At the end of the desiccation cracking, the clay developed polygons that were regular random [Fig. 3(A)], irregular random [Fig. 3(B)], and orthogonally oriented [Fig. 3(C)].

4 FRACTAL EVALUATION OF THE CLAY FRAGMENTATION

Fractal geometry is a relatively new mathematical concept developed by Mandelbrot (1977, 1982) to quantitatively describe complex patterns in nature

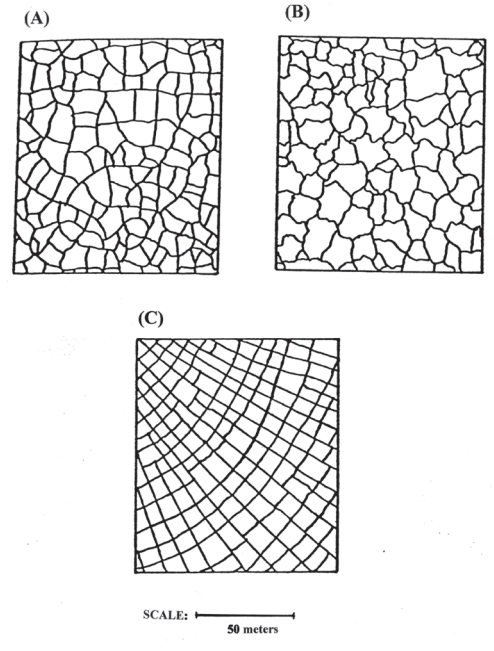

Figure 3. Type of cracks in large basin clay playas: (A) regular random, (B) irregular random, and (C) orthogonal (after Neal et al., 1968).

such as those formed by the cracks in the bentonite clay or the clays in the field (Figs. 1 and 3). Recently, engineers and earth scientists have successfully used concepts of fractal theory to analyze phenomenon such as the roughness of rock and soil particles and rock joints (Vallejo, 1995; Carr and Warriner, 1989); the distribution of rock fragments resulting from blasting (Perfect, 1997); the persistence of fault segments in the earth crust (Hirata, 1989); and the structure and distribution of pores in clays and sedimentary rocks (Vallejo, 1996; Schlueter et al., 1997). In this study, fractal theory is used to quantify the degree of fragmentation of the clays when the desiccation process is complete [Figs. 1(D), 2, and 3]. The degree of fragmentation is obtained using the fragmentation fractal dimension.

4.1 *Degree of fragmentation in the clay samples*

Grain size distribution of naturally occurring soils have been found by Tyler and Wheatcraft (1992) and Hyslip and Vallejo (1997) to be fractal. According to Mandelbrot (1977, 1982) and Turcotte (1986) the distribution of grains by size in a natural soil can be obtained using the following equation:

$$N(D > d) = kd^{-Dd} \quad (1)$$

where $N(D > d)$ is the total number of particles (N) with linear dimension D (diameter of the particle) greater than a given size d; k is a proportionality constant; and D_d is the fragmentation fractal dimension of the size distribution of the grains. The distribution of sizes in the soil will be reflected in the values of D_d. In the present study, the soil grains are represented by the clay fragments after complete fragmentation of the clay as shown in Figures 1(D), 2, and 3.

In order to obtain the fragmentation fractal dimension Dd for Figs. 1(D) and 3, one plots in a log-log paper the number of fragments (N) in the sample with diameter larger than certain value d, versus the diameter of the fragment d [Eq. (1)]. One then draws the best fitting line through the plotted points. The absolute value of the slope of the line represents the fragmentation fractal dimension value, D_d (Turcotte, 1986). Following this procedure, the fragmentation fractal dimension has been obtained for Figure 1(D) and is shown in Figure 4. The fragmentation fractal dimension for the cases shown Figure 3 was also obtained following the same procedure and are shown in Figures 5, 6, and 7.

An analysis of Figures 4, 5, 6, and 7 indicates that the best fitting lines that are used to obtain D_d have reasonable correlation coefficients (R^2). These correlation coefficients vary between 0.711 and 0.987.

Figures 5, 6 and 7 show that most of the data plotted in the middle portion of the graphs within

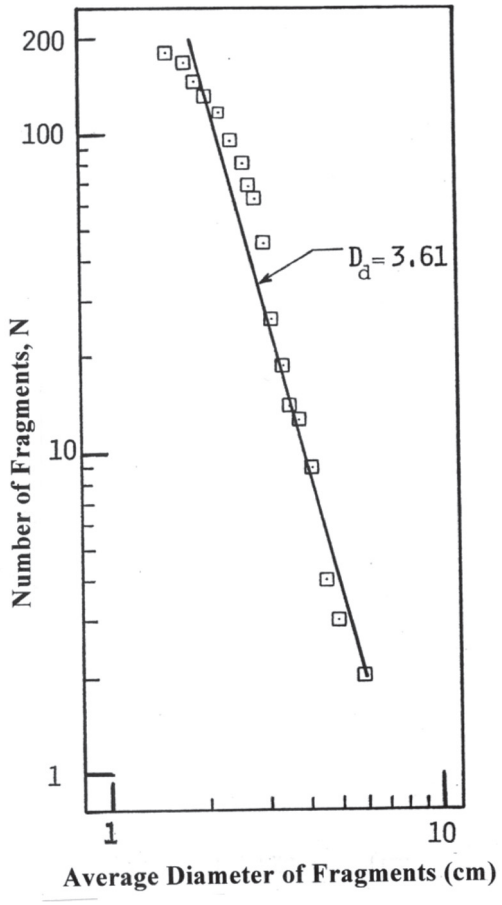

Figure 4. Fragmentation fractal dimension Dd = 3.61 (correlation coefficient R2 = 0.987) for clay desiccation shown in Figures. 1(D) and 2.

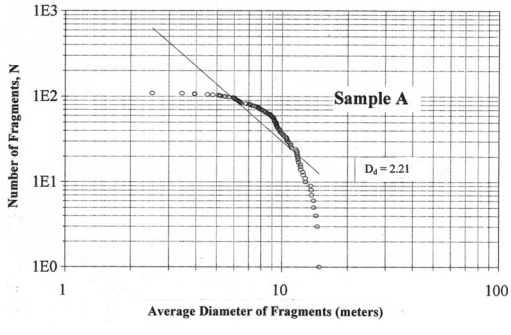

Figure 5. Fragmentation fractal dimension Dd = 2.21 (correlation coefficient R2 = 0.723) for clay desiccation shown in Figure. 3(A).

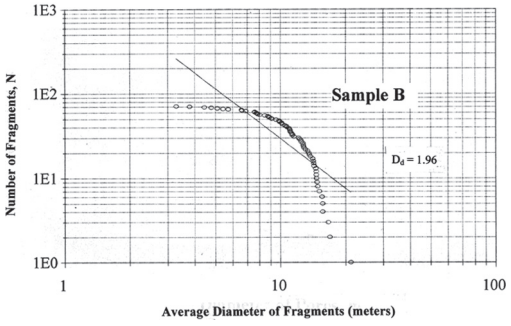

Figure 6. Fragmentation fractal dimension Dd = 1.96 (correlation coefficient R2 = 0.711) for clay desiccation shown in Figure 3(B).

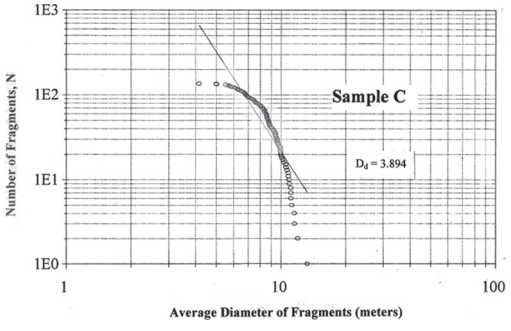

Figure 7. Fragmentation fractal dimension Dd = 3.894 (correlation coefficient R2 = 0.811) for clay desiccation shown in Figure 3(C).

a range of fragments that varied between 5 and 15 meters in diameter. This indicates that the majority of the fragments had average diameters that vary between 5 and 15 meters, with a few fragments outside this range. Thus, the best fitted lines represent the fragmentation fractal dimension for the mentioned range of clay fragments.

5 INFLUENCE OF THE FRAGMENTATION OF THE CLAYS ON THE TYPE OF POTENTIAL LANDSLIDES

According to Tyler and Wheatcraft (1992), when the fragmentation fractal dimension D_d is between 0 and 3, it indicates a greater number of larger fragments in the size distribution of fragmented clay. The cracked samples shown in Figs. 3(A) and 3(B) have this type of size distribution. When the fragmentation fractal dimension D_d is greater than 3, it indicates a greater number of the smaller fragments in the size distribution of fragmented

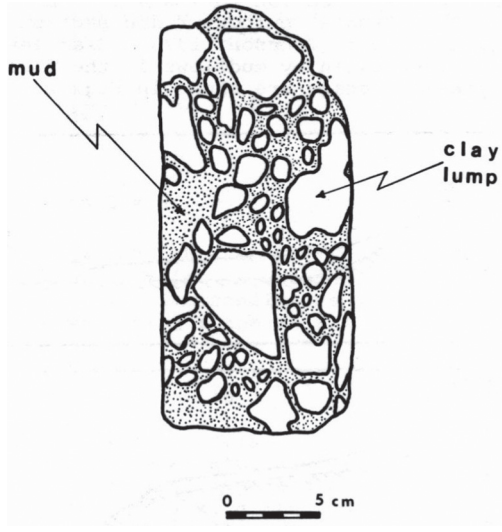

Figure 8. Fabric of a mudflow in the London Clay at Beltinge, North Kent (after Skempton and Hutchinson, 1969).

clay. The cracked samples shown in Fig. 2 and 3(C) have this type of size distribution.

If rain takes place, water will mix with the smaller clay fragments producing mud. The larger fragments will remain relatively intact. If the mixture of mud (or water) and large clay fragments are located on a slope, the mixture will move as either a mudflow or a debris flow. The mixture that originally had a fragmentation fractal dimension greater than 3 will become a mudflow because the sample was originally controlled by the smaller clay fragments that will readily mix with the rain water producing a liquid mud that will contain some large clay fragments. The large clay fragments will be dispersed in the muddy matrix. An example of this type of mudflow structure was found on a slope in the London Clay at Beltinge, North Kent and was recorded by Skempton and Hutchinson (1969) and is shown in Figure 8. Figure 8 shows the fabric of the mudflow composed of a muddy matrix in which large clay fragments are in dispersion.

When the cracked clay has a fragmentation fractal dimension between 0 and 3, the larger clay fragments will control the size distribution of the fragmented clay. After rain takes place, a mixture of water and clay fragments will result. If this mixture

is located on a slope, a potential failure will be made of a mixture of large clay fragments and water resembling that of debris flow. With time, however, due to the slaking in water of the large clay fragments, part of these fragments will mix with the water producing as a result a mudflow structure,

that is, a muddy matrix in which the survivor large clay fragments are dispersed (Figure 8).

6 CONCLUSIONS

The present study deals with the formation and the evolution of the cracks in clays in the laboratory as well as in the field. The level of fragmentation of the desiccated clays is measured using the fractal dimension concept from fractal theory. Also, the effect of the level of fragmentation on the type of land-slides that the desiccated clay areas could develop is also discussed in this study. From this study, the following was determined:

1. Clay samples in the laboratory and in the field as a result of evaporation induced by high temperatures develop cracks in their structure. These cracks produced the complete fragmentation of the clays.
2. After complete fragmentation, the clay samples studied developed a size distribution of fragments that is fractal in nature.
3. The fragmentation fractal dimension of the cracked clays varied in value between 1.96 and 3.894. Fragmentation fractal dimension values between 0 and 3 represents samples that are controlled by larger clay fragments. Fragmentation fractal dimension values greater than 3 represents samples that are controlled by smaller clay fragments.
4. Fragmented clays with fragmentation fractal dimension values between 0 and 3 have the potential to develop into debris flows. Fragmented clays with fragmentation fractal dimension values greater than 3 have the potential to develop into mudflows.

ACKNOWLEDGEMENTS

The works described herein was partially supported by NSF Grants No. ECE-8414931 and CMS-0301815. This support is gratefully acknowledged.

REFERENCES

Carr, J.R. and Warriner, J.B. (1989). Relationship between the fractal dimension and joint roughness coefficient. Bulletin Association of Engineering Geologists, 26, 253–263.

Hirata, T. (1989). Fractal dimension of fault systems in Japan. Pure and Applied Geophysics, 131, 157–170.

Hyslip, J.P. and Vallejo, L.E. (1997). Fractal analysis of the roughness and size distribution of granular materials. Engineering Geology, 48 (3–4), 231–244.

Mandelbrot, B.B. (1977). Fractals: forms, chance and dimension. Freeman, San Francisco.

Mandelbrot, B.B. (1982). The Fractal Geometry of Nature. Freeman, San Francisco

Neal, T.J., Langer, A.M. and Kerr, P.F. (1968). Giant desiccation polygons of great basin playas. Geological Society of America Bulletin, 79, 69–90.

Perfect, E. (1997). Fractal models for the fragmentation of rocks and soils: a review. Engineering Geology, 48, 185–198.

Skempton, A.W. and Hutchinson, J.N. (1969). Stability of natural slopes and embankment foundations. Proceedings of the 7th Int. Conf. on Soils Mechanics and Foundations Eng.,State of the Art Volume, Mexico, 291–340.

Schlueter, E.M., Zimmerman, R.W., Witherspoon, P.A. and Cook, N.G.W. (1997). The fractal dimension of pores in sedimentary rocks and its influence on permeability. Engineering Geology, 48, 281–290.

Tyler, S.W. and Wheatcraft, S.W. (1992). Fractal scaling of soil particle-size distribution analysis and limitations. Soil Science Society of America Journal, 56(2), 47–67.

Turcotte, D.L. (1986). Fractals and fragmentation. J. of Geophysical Research, 91(B2), 1921–1926.

Vallejo, L.E. (1995). Fractal analysis of granular materials. Geotechnique, 45 (1), 159–164.

Vallejo, L.E. (1996). Fractal analysis of the fabric changes in a consolidating clay. Engineering Geology, 43, 281–290.

This page intentionally left blank

Advances in Unsaturated Soils – Caicedo et al. (eds)
© 2013 Taylor & Francis Group, London, ISBN 978-0-415-62095-6

Critical combination of tensile and shear stresses causing the crack propagation path in brittle clays subjected to uniaxial compression

L.F. Vesga
Domeight Research Institute, Bogotá, Colombia

L.E. Vallejo
Department of Civil Engineering, University of Pittsburgh, PA, USA

ABSTRACT: In this study, the evolution of crack propagation in specimens that are subjected in the laboratory to a uniaxial compressive stress and that have a pre-existing crack inclined at 60° with respect to the uniaxial compressive stress direction was modeled using theoretical and numerical analyses. The theoretical path analyses used the direct tensile-shear strength of the soil, the LEFM, the proximity to failure concept and the incremental crack propagation analysis. The numerical analyses used the DEM method implemented in the PFC2D V3.0 computer program. The theoretical and numerical analyses predict very well the crack propagation path of the pre-existing crack.

1 INTRODUCTION

Cracks can be formed or exist in clays during desiccation, swelling and shearing processes. Cracks decrease the resistance of soils because they produce stress concentrations at the crack tips. Open cracks also increase the hydraulic conductivity affecting projects that require water barriers such as dams, reservoirs and landfills.

The propagation of cracks in stiff clayey soils has been previously studied in the laboratory and analyzed theoretically and numerically. Linear Elastic Fracture Mechanics (LEFM) theory and laboratory tests on brittle kaolinite clay specimens having a pre-existing primary crack have been used by Vallejo (1993) and Bobet et al. (1998) to study crack propagation in soils.

Bobet et al. (1998) mentions that the theoretical models are, in general, based on three fundamental theories: the maximum tangential stress (Erdogan and Sih, 1963), the maximum energy release rate theory (Hussain et al., 1974), and the minimum energy density theory (Sih, 1974). These methods reasonably predict tensile crack initiation in tension and in compression, but they have been unsuccessful for shear crack initiation (Bobet et al., 1998) and do not properly predict the crack propagation path in compression (Vesga, 2005).

Crack numerical models have been recently developed by Vásárhelyi and Bobet (2000), Vogel et al. (2004), Svahn et al. (2006), Cervera and Chiumenti (2006) for incorporating tensional and shear strength components in the crack propagation analyses. Thusyanthan et al. (2007) proved in the laboratory that crack initiation on kaolinite beams subjected to flexion occurs by at points subjected to tension and shear.

In this study, laboratory tests as well as theoretical and numerical analyses were used to analyze the evolution of crack propagation in specimens that are subjected to a uniaxial compressive stress. The crack propagation path follows a line of points subjected to combination of tensile and shear stresses which produce the contact bonds between particles to break and the crack to propagate.

The theoretical analyses used the Direct Shear and Tensile (DTS) strength of the clay, the Linear Elastic Fracture Mechanics (LEFM), the proximity to failure concept (Bourne and Willemse (2001), and the crack incremental analyses (Sih and de Oliveira, 1984). The numerical analyses used the Discrete Element Method (DEM). Very good agreement was found between the predicted numerical and theoretical crack propagation path and the laboratory results.

2 SWCC AND EES

The soil water characteristic curve (SWCC) of the soil used in this research is presented in Figure 1. The EES in an unsaturated soil as defined by Cho and Santamarina (2001) is the capillary force acting between two particles (F) divided by the effective area that corresponds to that contact (A_{eff}).

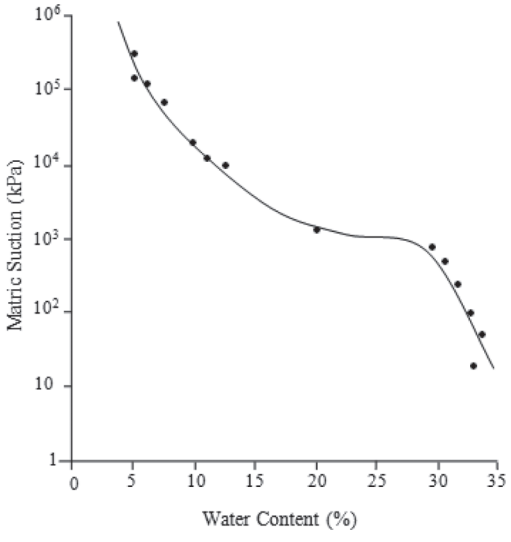

Figure 1. SWCC of the clay utilized in the research.

Inter-particle forces acting in unsaturated soils are divided in three different groups by Lu and Likos (2006). Active skeletal forces, local forces, and passive particle-particle contact forces form these groups. The local forces include physico-chemical forces as van der Waals forces (VDW), electrical double-layer forces, cementation forces, and capillary forces. Scott (1963), Lambe & Whitman (1969), Kézdi (1974), and more recently Santamarina et al. (2001) present detailed description of origin of inter-particle forces in soils.

The capillary attraction force is the most important force type acting in usaturated soils and is produced from two components (Cho and Santamarina, 2001; Lu and Likos, 2006). As determining the individual resultant force in each one of all the different contacts in a soil is almost impossible, direct tensile tests can be used to measure the sum of forces from all contacts acting together in a cross-sectional area of the soil, and extend these results to determine the EES.

As there is no confinement in the tension tests, the total stress is zero and the only stress acting in the soil is the equivalent effective stress EES, which represents the combination of forces acting between particles in a cross section of a soil. The EES in a soil is defined as

$$EES = \frac{\sum F_p}{A} \tag{1}$$

where F_p is the force component of the sum of inter-particle forces acting in a cross section of a soil that is parallel to the considered direction of EES and A is the normal total area of the cross—section considered. This concept is very helpful in understanding the strength of soils subjected to suction.

3 DTS STRENGTH

The Direct Tensile and Shear (DTS) strength is the soil strength when it is subjected to simultaneous tensile and shear stresses. The procedure for determining the DTS strength in soils is presented by Vesga (2009) however a general description of the test method is presented below.

3.1 *Equipment description*

The DTS apparatus measures the tensile-shear strength of unsaturated clays. The apparatus is composed of two clamps through which a transverse force to a pre-tensioned bowtie-shaped specimen is applied (see Figure 2). The tensile force is applied using a MTS hydraulic testing machine and the shear force is applied using two calibrated, instrumented and parallel springs located at the front and back of the specimen and applying a centralized load that prevents torsion in the specimen. The DTS device including the specimen is maintained inside a plastic membrane in order to maintain constant water content during the test (see Figure 2). A selected tensile force is applied to the specimen and maintained at a constant level while a shear force is applied and increased until the sample fails.

3.2 *Specimen neck stresses in the DTS test*

The average tensile and shear stresses in the horizontal plane of the neck are given by

$$\sigma_y = T/A_s \tag{2}$$

$$\tau_{xy} = S_f/A_s \tag{3}$$

where T is the tension force, S_f is the failure shear force, and A_s is the cross sectional area of the neck. Analyses of Mohr diagrams show that the failure occur by tension even if the failure is induced applying a shear stress in the pre-tensioned specimen. Figure 3 shows the relationship between the applied vertical and shear stresses in the specimen's neck of specimens at an average water content of 15% (water distribution in the complete-pendular state). A good linear relationship can be observed and also that as higher the tensile stress applied the lower the shear stress to produce failure.

Five triaxial tests were performed over prismatic kaolinite samples prepared with the same procedure used for the DTS tests. The air phase in the triaxial tests was maintained at atmospheric pressure

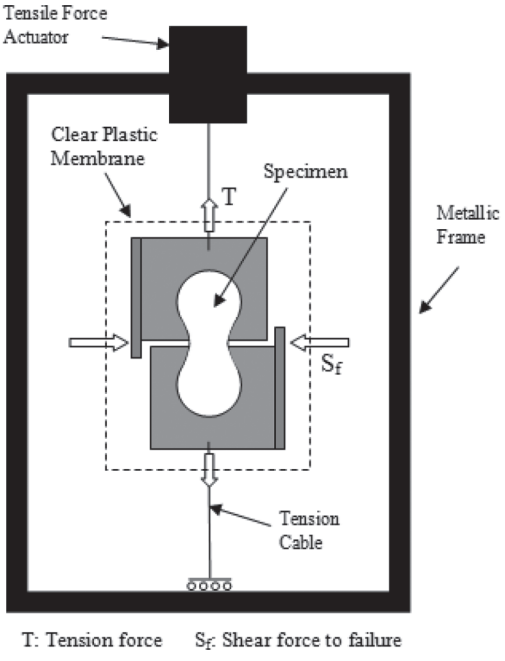

Figure 2. Direct tensile and shear (DTS) test device (Adapted from Vesga, 2009).

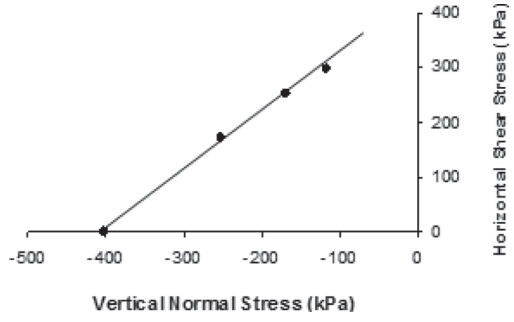

Figure 3. Vertical normal stress (σ_y) and horizontal shear stress τ_{xy} at failure in the specimen's neck.

during the tests (drained) and the water content remained constant. No special technique was used to provide an air drained phase different to the configuration of a traditional triaxial drained test; the only difference is that the soil is unsaturated. triaxial tests results show a failure envelope inclined 25° with respect to the horizontal which represents the total stress friction angle. However, this is the same effective friction angle of this clay.

If the total stress friction angle in the unsaturated triaxial test is the same value of the effective stress friction angle of the material, consequently no excess pore water pressure was developed during the

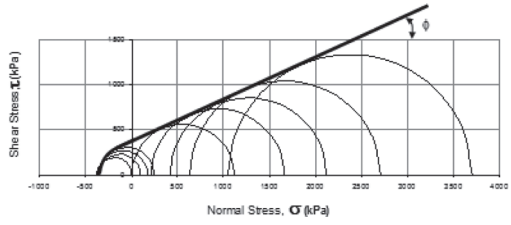

Figure 4. Failure envelope from DTS tests and unsaturated triaxial tests (total stresses). The unsat tests are for constant water content at w = 15% and air drained. The Mohr's circles for DTS are those for which the minor principal stress is negative. (Adapted from Vesga, 2009).

loading process in the unsaturated triaxial tests. This occurs because the clay has a pore water distribution in the complete-pendular state and variations of suction in this state produce no influence in the EES (Vesga, 2008 and 2009). If this hypothesis is true then by analogy it is possible to say that no excess pore water pressures developed in the DTS tests since the soil is in such complete-pendular state. In consequence, Mohr diagrams using results from triaxial unsaturated air-drained and constant-moisture tests can be plotted together with the DTS tests results (Figure 4). In total, there are results from nine tests that closely match a failure envelope that is a combination of a straight (frictional) portion with an inclination angle equal to the friction angle of the kaolinite and a circular sector in the tension zone.

Figure 5 shows the detail of this Mohr-Coulomb-Tensile failure envelope near the origin of stresses. There is a unique Mohr circle of total stresses that represents the state of failure by shear and by tension at the same time and has a center at p_t and a radius q_t given by the following expressions (Vesga, 2009).

$$p_t = \frac{\sigma_t - c \cdot \cos\varphi}{1 - \sin\varphi} \tag{4}$$

$$q_t = \frac{c \cdot \cos\varphi - \sigma_t \sin\varphi}{1 - \sin\varphi} \tag{5}$$

By using the above expressions, it is now possible to define the Mohr-Coulomb-Tensile failure envelope of a soil when the angle of internal friction, the apparent cohesion intercept, and the tensile strength are known. These expressions are valid for tests on samples which do not develop excess pore pressures during the tests (Vesga, 2009).

Figure 5 presents also the Mohr-Coulomb-Tensile failure envelope in terms of effective stresses which results from displacing horizontally the total stress failure envelope a distance equivalent to the EES due to the soil unsaturation.

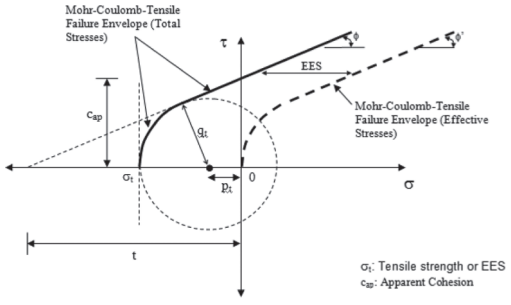

Figure 5. Mohr-Coulomb-Tensile failure envelope in terms of total and effective stresses that is a combined straight line and a sector of a circle. The circle represents the state of stresses at failure that occurs simultaneously by shear and by shear and by tension (Adapted from Vesga, 2009).

4 LABORATORY TESTS

The laboratory tests of crack propagation used prismatic pre-fissured specimens of brittle kaolinite clay subjected to uniaxial compression following the procedure presented by Vallejo (1986). The primary crack had an inclination angle (β) of 60º with respect to the vertical. The specimens had a moisture content of 15% and a degree of saturation of 51%. The moisture content corresponds to a pore water distribution in the complete-pendular state. Figure 11a presents the results from the laboratory tests. The secondary crack propagates from the pre-existing crack tips following a curved path until the cracks reach the direction of the applied maximum stress. Similar results can were observed by Vallejo (1986).

5 LEFM

According to Linear Elastic Fracture Mechanics (LEFM) theory, a crack or fissure in clay can be stressed in three different modes as is shown in Figure 6 (Vallejo, 1994). The stress normal to the crack walls produce a Mode I type of cracking for which the disarrangements of the crack surfaces are perpendicular to the plane of the crack. The Mode II type of cracking is produced by shear stresses along the crack plane and causes the walls of the crack to slide in the crack plane. The Mode III is the tearing mode and crack dislodging is caused by out of-plane shear stresses. Cracks can propagate in materials as a result of one or a combination of two or three type modes (Vallejo, 1994).

According to LEFM, the tangential stress (σ_θ), the radial stress (σ_r) and the shear stress ($\tau_{r\theta}$) in the material located in the vicinity of a crack subjected

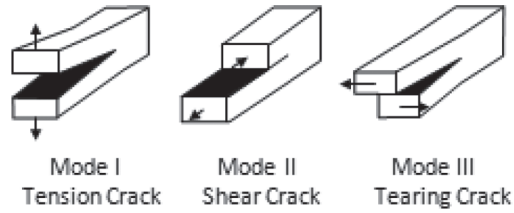

Figure 6. The three modes of cracking (Vallejo, 1994).

to a mixed mode type of loading (Mode I plus Mode II) can be obtained from the following relationships (Vallejo, 1994).

$$\sigma_\theta = \frac{1}{\sqrt{2\pi r}}\cos\frac{\theta}{2}\left[K_I\cos^2\frac{\theta}{2} - \frac{3}{2}K_{II}\sin\theta\right] \quad (6)$$

$$\sigma_r = \frac{1}{\sqrt{2\pi r}}\cos\frac{\theta}{2}\left[K_I\left(1+\sin^2\frac{\theta}{2}\right) - \frac{3}{2}K_{II}\sin\theta - 2K_{II}\tan\frac{\theta}{2}\right] \quad (7)$$

$$\tau_{r\theta} = \frac{1}{\sqrt{2\pi r}}\cos\frac{\theta}{2}\left[K_I\sin\theta + K_{II}(3\cos\theta - 1)\right] \quad (8)$$

Parameters in the equations above are explained in Figure 7 and K_I and K_{II} are the stress intensity factors for an open crack under Mode I and Mode II type of loading and are given by (Vallejo, 1994):

$$K_I = 1.1215\sigma_n(\pi\cdot c)^{1/2} \quad (9)$$

$$K_{II} = 1.1215\tau_n(\pi\cdot c)^{1/2} \quad (10)$$

where σ_n is the normal stress that acts perpendicular to the plane of the open crack and τ_n is the shear stress that acts parallel to the crack, and c is the semi-length of the crack.

The principal stresses can be deducted from the tangential, radial and shear stresses presented above. The maximum and minimum principal stresses and the center (p) and the radius (q) of the Mohr's circle that represents the stresses at a point are given by

$$\sigma_1 = \frac{(\sigma_\theta+\sigma_r)}{2} + \sqrt{\left(\frac{\sigma_\theta+\sigma_r}{2}\right)^2 + (\tau_{r\theta})^2} \quad (11)$$

$$\sigma_3 = \frac{(\sigma_\theta+\sigma_r)}{2} - \sqrt{\left(\frac{\sigma_\theta+\sigma_r}{2}\right)^2 + (\tau_{r\theta})^2} \quad (12)$$

$$p = \frac{(\sigma_1+\sigma_3)}{2} \quad q = \frac{(\sigma_1+\sigma_3)}{2} \quad (13 \text{ and } 14)$$

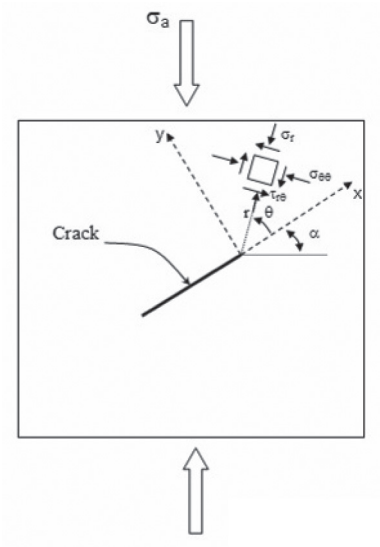

Figure 7. Tangential, radial, shear stresses around a crack tip.

6 PROXIMITY TO FAILURE CONCEPT

The proximity to failure concept proposed by Bourne and Willemse (2001) consists basically in that the failure of the material would occur by the failure mode for which its failure envelope is closer to the Mohr's circle of stresses. In Figure 8, the proximity to failure by shear and tension are represented by *v* and *w* as per Eq. 15 and 16

$$v = tp \times \sin\varphi - q \tag{15}$$

$$w = \sigma_t - \sigma_3 \tag{16}$$

After the failure envelope is determined, the proximity to failure concept is applied. The material is analyzed before it fails. Figure 8 shows the Mohr-Coulomb-Tensile curved envelope and three Mohr's circles that represents different state of stresses around and close to a crack tip. The proximity to failure (*w*) of the circle 1 is by tension. The proximity to failure (*v*) of circle 2 is by shear.

There is another state of stresses represented by the circle 3 that is very critical because has proximity by tension and by shear at the same time. This hypothesis is proposed by Vesga (2005) for establishing the direction of the primary pre-existing crack propagation. The point close to the crack tip at which the propagation of the primary crack starts is the one that has a state of stresses for which the material fails by tension and by shear at the same time ($w = v$). The hypothesis is called

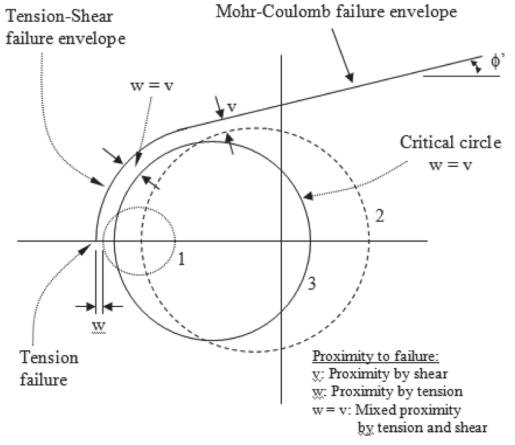

Figure 8. Tangential radial and shear stresses around a crack tip.

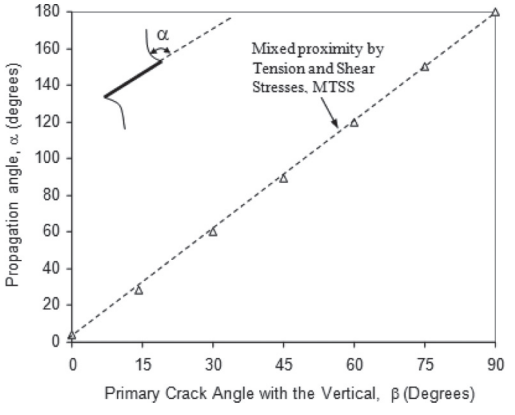

Figure 9. Crack propagation angle derived using the MTSS criterion.

Mixed Tension and Shear Stress (MTSS) criterion. Figure 9 shows the angle of crack propagation α as a function of the primary crack inclination angle β derived from the MTSS criterion for specimens that are subjected to uniaxial stress.

7 THEORETICAL CRACK PROPAGATION

Sih and de Oliveira (1984) proposed a methodology for analyzing the secondary crack propagation path of pre-cracked specimens. At the moment at which the crack propagation occurs, new crack tips are developed that are separated a distance from the former crack tips. A new equivalent straight crack is considered as formed between the new tips (Fig. 10). The incremental analysis consists in considering a new crack with a small arbitrary crack

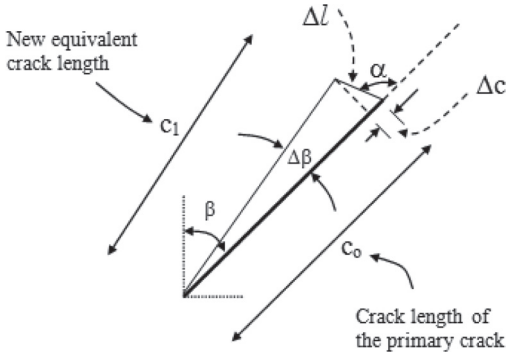

Figure 10. Incremental crack growth initiated from an inclined primary crack.

length (Δl) that propagates in the direction of the theoretical crack propagation angle (α) presented in Figure 9.

The new tips are separated a given distance from the former crack tips and a new, equivalent, straight crack is formed. With incremental analysis, a new crack with a new length (c_1) and orientation (β_1) that depends on the length (c_0) and orientation (β) of the previous equivalent crack is presumed. The process is repeated again and again with successive small length increments (Δl) of the secondary propagated crack. The equations resulting from Figure 10 are

$$c_1 = \sqrt{(c_0 + \Delta l \cos\alpha)^2 + (\Delta l \sin\alpha)^2} \quad (17)$$

$$\Delta\beta = \sin^{-1}\left[\frac{\Delta l \times \sin\alpha}{c_1}\right] \quad (18)$$

The theoretical analyses of crack propagation use EES, DTS, LEFM, proximity to failure concept, and crack incremental analysis. The MTSS criterion of crack propagation angle presented in Figure 9 was developed using the first four concepts. Applying the MTSS criterion and the crack incremental analyses (Eq. 17 & 18) the theoretical crack propagation path presented in Figure 11b was derived. Crack length increments equivalent to 10 percent of the primary crack length were utilized in the analyses. The theoretical analyses represent very well the crack propagation path observed in the specimens tested in the laboratory (Fig. 11a).

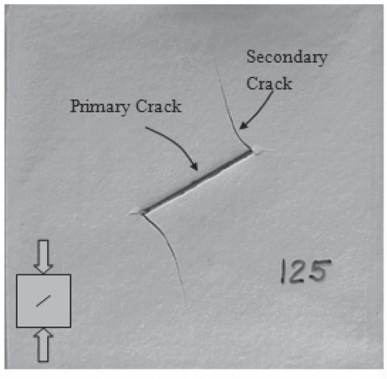

(a) Laboratory test result of uniaxial compression.

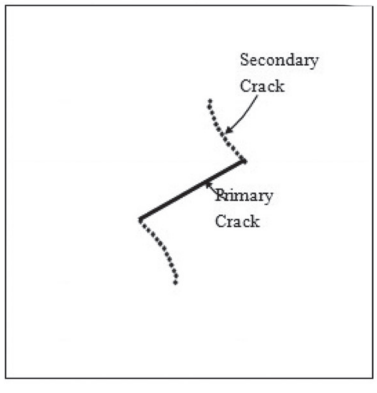

(b) Theoretical analysis.

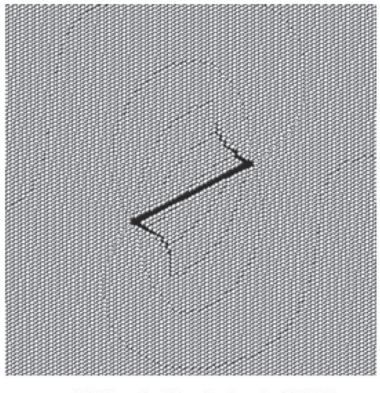

(c) Numerical analysis using DEM.

Figure 11. Comparison of laboratory tests results and theoretical and numerical analyses of crack propagation.

8 DEM ANALYSES

The DEM analyses of the pre-fissured specimens used PFC2D V3.0 program (Itasca, 2002). The simulated specimens were generated by more than 9000 equal sized disk particles (Vesga, 2007). DEM can be used in the simulation of continuum materials such as rocks and clays (Itasca, 2002) if contact bonds between the DEM particles are implemented. For each bond, PFC2D uses a normal tensile and a shear maximum load as well as normal and shear stiffness (Itasca, 2002). When a contact bond

breaks, a separation between particles occurs. The modeling used a uniaxial compression stress level (σ_c) high enough to produce a crack propagation path clearly visible. Figure 11c presents the results obtained. The DEM analyses predicted very well the crack propagation path observed in the laboratory and the path predicted with the theoretical analyses

9 CONCLUSIONS

Theoretical and numerical analyses were performed to study how cracks propagate in brittle clay. The theoretical analyses used the Linear Elastic Fracture Mechanics, the direct tensile-shear (DTS) resistance of the clay, the proximity to failure concept and incremental crack propagation analyses. The numerical analyses used the Discrete Element Method (DEM). The theoretical and DEM results were compared with those obtained in laboratory samples. The laboratory tests used stiff clay samples with one crack inclined 60° with respect to the uniaxial stress direction. The crack propagation path resulting from the theory, the DEM, and the laboratory results compared very well. The crack propagation path is formed by points subjected to critical combinations of tensile and shear stresses.

REFERENCES

Bourne, S.J. and Willemse, E.J.M. (2001). Elastic stress control on the pattern of tensile fracturing around a small fault network at Nash Point, UK. Journal of Structural Geology 23, 1753–1770.

Cho, G.C. and Santamarina, J.C. (2001). "Unsaturated particulate materials—Particulate-level studies". Journal of Geotechnical and Geoenvironmental Engineering. ASCE. Vol. 127, No. 1, pp. 84–96.

Thusyanthan, N.I., Take, W.A., Madabhushi, S.P.G. and Bolton, M.D. (2007). "Crack initiation in clay observed in beam bending." Geotechnique, Vol. 57, No. 7, pp. 581–594.

Vallejo, L.E. (1986). "Mechanics of crack propagation in stiff clays". Geotechnical Aspects of Stiff and Hard Clays. ASCE's Geotechnical Special Publication No. 2. Khera, R.P., and Lovell, W., eds., pp. 14–27.

Vallejo, L.E. (1993). "Shear stresses and the hydraulic fracturing of earth dams soils". Soils and Foundations, Vol. 33, No. 3, pp. 14–27.

Vallejo, L.E. (1994). "Application of fracture mechanics to soils: an overview". Fracture Mechanics Applied to Geotechnical Engineering. ASCE's Geotechnical Special Publication No. 43. Vallejo, L.E. and Liang, R.Y., Editors, pp. 1–20.

Vásárhelyi, B. and Bobet, A. (2000). "Modeling of Crack Initiation, Propagation and Coalescence in Uniaxial Compression". Rock Mech. and Rock Eng. Vol. 33(2).

Vesga, L.E. (2005). Mechanics of crack propagation in clays under dynamic loading. Ph.D. Thesis. University of Pittsburgh.

Vesga, L.F. (2008). "Equivalent Effective Stress and Compressibility of Unsaturated Kaolinite Clay Subjected to drying", JGGE, ASCE, Vol. 134, No. 3.

Vesga, L.F. (2009). "Direct Tensile and Shear (DTS) Test in Unsaturated Kaolinite Clay". Geot. Testing J., under review.

Vesga, L.F., Vallejo, L.E. and Loboguerrero, S. (2007). "DEM Analysis of the Crack Propagation in Brittle Clays under Uniaxial Compression", Int. J. Num. An. Methods in Geomechanics. DOI: 10.1002/nag.665.

This page intentionally left blank

Advances in Unsaturated Soils – Caicedo et al. (eds)
© 2013 Taylor & Francis Group, London, ISBN 978-0-415-62095-6

Crack propagation and threshold strength of fissured clays subjected to cyclic loading

L.F. Vesga
Domeight Research Institute, Bogotá, Colombia

L.E. Vallejo
Department of Civil Engineering, University of Pittsburgh, PA, USA

ABSTRACT: The mechanics of crack propagation in clay under uniaxial cyclic stresses is presented. Prismatic samples of kaolinite clay with induced cracks at different inclination angles were tested. The level of uniaxial stress at which the cracks do not propagate (the threshold strength) is investigated. The samples with the induced cracks were unsaturated with water contents variable between 3% and 25%. The strength of the samples to cyclic loading was found to vary with water contents because the capillary effects in the samples. The tests also indicated that the pre-existing cracks in the clay samples propagated from their tips in a direction parallel to the applied uniaxial compressive stress. In addition, the threshold strength at which the cracks did not propagate in the samples varied between 30% and 70% of the static stress that caused the sample failure.

1 INTRODUCTION

Over-consolidated clays and shales forming part of the core section of zoned earth dams and natural slopes have been found to exist in the fissured state (Bishop, 1967; Covarrubias, 1969; Duncan and Dunlop, 1969; Marsland, 1972; Morgenstern, 1977; Peterson et al., 1966; Rizkallah, 1977; Sherard, 1973; Skempton, 1964; Skempton and La Rochelle, 1965; Terzaghi, 1936; Vallejo, 1986; Williams and Jennings, 1977). According to Covarrubias (1969), fissures or cracks exist in the core section of earth dams as a result of deformation of the materials in the dam or in the foundation due to their weight; abrupt changes in the cross section of a valley; large deformations caused by saturation of the materials in the dam; excessively rapid filling of the reservoir that causes high rates of strain, especially of the materials undergoing substantial movement upon saturation; large transient stresses caused by earthquakes; large differences in stress-strain properties of materials in adjacent zones or layers. In the case of stiff clays forming natural slopes, Williams and Jennings (1977) found that fissures develop as a result of a variety of processes, the most important of which are: consolidation, swelling of the clay as a result of a decrease in overburden pressure, chemical reactions in the clay that induce volume distortions, tectonic stresses, desiccation of the clay, weathering process inherited from bedrock and large lateral stresses.

Sherard (1973) reports 15 cases of embankment dam cracking that have occurred around the world. He notes that 150 to 300 small dams (20–75 ft. high) are constructed in the United States each year and that most of the cracking in the dams in the U.S. results from embankment soils that are especially brittle and so susceptible to cracking.

Clay deposits subjected to desiccation often develop in-tense cracking that extends deep below the surface. Arizona, Mexico City and Bogota are examples of areas particularly affected by such deep cracking. Vesga et al. (2003) found intensive deep cracking in the high plastic Bogota (Colombia) clay deposit that affects a flat area of 90000 ha located in a zone characterized by high seismic hazard: hundreds of kilometers of roadways and hundreds of small buildings in this area have been severely damaged or collapsed as a result of deep cracking caused by desiccation.

The present research addresses the question of what happens to fissured soil deposits when they are subjected to dynamic loading such as that generated by earthquakes, wave action, traffic load, or machinery vibration.

2 PREVIOUS RESEARCH

Vallejo (1986, 1988, 1989, 1994) and Vallejo and Shettima (1995) report several important findings related to the behavior of clays with pre-existing

cracks. Vallejo and co-workers did several tests using rectangular kaolinite specimens with single or multiple cracks prepared in accordance with a special process that he developed; cracks of different orientations and specimens with different water contents were used. The specimens were subjected to monotonic uniaxial, biaxial, triaxial and shear stress fields. The research used Linear Elastic Fracture Mechanics (LEFM) to theoretically study the tension and compression stress concentrations around the cracks.

Four important conclusions can be derived from their findings as follows. (1) The critical pre-existing crack inclination, which corresponds to the condition of the lowest compression strength for crack propagation, varies between 45º and 60º with respect to the direction of the applied principal stress. (2) The maximum tangential stress criterion for a sharp crack of the type earlier proposed by Erdogan and Sih (1963) was used to predict the angle between the pre-existing crack plane and the crack propagation direction; this criterion was selected by Vallejo et al. (1995) as the closest to their findings between of all the criteria that were applied; (3) Fissures propagate as a result of constant compressive stresses (creep), which are much less than the crack-propagation compression strength of monotonically loaded clays (Vallejo and Shettima, 1997). (4) Multiple cracks will make the clay weaker, especially if superposition of tensile-stress concentration zones develops (Vallejo, 1994).

Lefebvre et al. (1988) studied the cyclic undrained resistance of non-fissured, intact saturated Hudson Bay clay and described the threshold as the stress level below which the soil suffers no failure regardless of the number of applied cycles. The researchers used the term cyclic stress ratio to describe this stress level which relates to both the applied triaxial cyclic stress and the triaxial compression strength of the intact clay. They found that for the saturated Hudson Bay clay, the stability threshold is defined by a cyclic stress ratio of between 0.60 and 0.65. In a similar way, the stability threshold concept is applied in this research to the study of crack propagation in clays under dynamic loads.

3 STABILITY THRESHOLD APPLIED TO FISSURED CLAYS

The stability threshold research will now be extended to fissured clays. The laboratory tests for this research focused on specimens of fissured clays that were subjected to cyclic loads; the loads applied were just a fraction of the static loads that caused the failure of the clay (Vesga, 2005). The research investigated the influence of the resulting fatigue on the propagation of cracks in unsaturated kaolinite clay and on the threshold stress with respect to cyclic loads levels below which the cracks do not propagate. Samples of fissured clays were subjected to uniaxial cyclic stress conditions. The cyclic stress ratio was defined as the ratio between the applied deviator dynamic vertical stress (σ_d) on a fissured specimen and the monotonic compression strength (σ_u) of a similar specimen having the same water content and crack geometry. The cyclic stress ratio is given as:

$$r_d = \frac{\sigma_d}{\sigma_u} \tag{1}$$

The purpose of the dynamic-load testing was to find the threshold load (fraction of the static load), expressed as the cyclic stress ratio r_d, at which, regardless of the number of cycles applied, there is no crack propagation in an unsaturated kaolinite clay subjected to dynamic loading conditions.

4 DESCRIPTION OF LABORATORY TESTS

Prismatic kaolinite specimens were prepared for the tests. The liquid, plastic and shrinkage limits of the kaolinite are 44, 26 and 24 respectively and the specific gravity is 2.59. The SWCC curve of the clay used in this research is described by Vesga (2008). The sample preparation was done with the following process:

1. Mixing the dry powdered kaolinite with distilled water to moisture content of 40% and until a smooth and uniform paste was obtained.
2. Casting the paste into molds (prismatic of 7.5 cm × 7.5 cm × 2.5 cm or cylindrical 6.35 cm in diameter and 2 cm thick).
3. Applying a vertical pressure of 30 kPa for consolidation during 24 hours in a closed environment with 75% of relative humidity (RH).
4. Extracting the specimens from the molds and inducing the primary crack with inclination angles of 15º, 30º, 45º, 60º and 75º with respect to the horizontal; samples were still saturated during this stage. Each crack was made using a blade which produced a crack having a length of 25 mm and a thickness of 1 mm.
5. Subjecting the specimens to a drying process into an environment with a RH ~30%.
6. After each specimen reached the desired moisture content (between 2% and 34% with intervals of around 3%) it was stored into a plastic membrane during a minimum 24 hour period in order to obtain equilibrium of the moisture through the sample.

Uniaxial constant water content tests were done using both intact and pre-cracked specimens (Fig. 1). Each sample tested was maintained inside

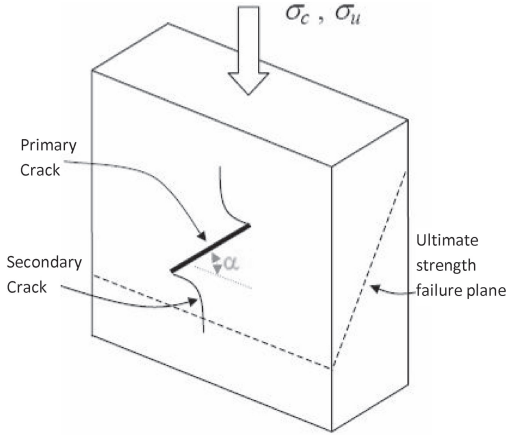

Figure 1. Specimen and failure modes.

a plastic membrane in order to prevent water content changes during the tests.

A MTS hydraulic compression machine was used for the dynamic loading tests. The purpose of these tests was to find the threshold cyclic stress ratio (fraction of the ultimate static strength) at which there is no crack propagation under dynamic loading conditions regardless of the number of applied cycles. The cyclic stress ratio r_d was defined as the ratio between the applied dynamic vertical stress and the ultimate monotonic compression strength of a similar specimen having the same water content and the same crack inclination. Thus, the cyclic axial load was a fraction of the static load at which the specimen failed.

Dynamic uniaxial compression tests were performed on pre-fissured specimens. A sine wave loading type with a frequency of 1 Hz was applied to the specimens. The data acquisition system DATAQ ID-194 (Dataq Instruments, 2003) recorded the load and deformation of the samples occurred during the tests. The level of the cyclic stress ratio r_d was changed in order to determine the crack propagation threshold.

5 RESULTS FROM LABORATORY TESTS

Two stress levels were registered for each uniaxial compression loading test performed on fissured specimens. With the stress level of σ_c, crack propagation occurred in the front and rear faces of the specimen. Secondary crack initiation was established visually with continuous inspection of the specimen faces. With the stress level of σ_u—which is the maximum stress specimens' were able to withstand—a shear failure plane appeared in the lateral faces of the specimen (Fig. 1).

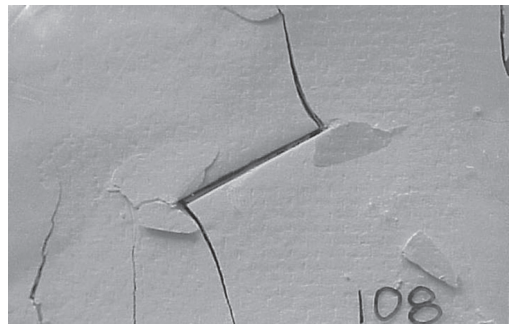

Figure 2. Failed specimen. Secondary crack curved to follow the direction of the principal stress.

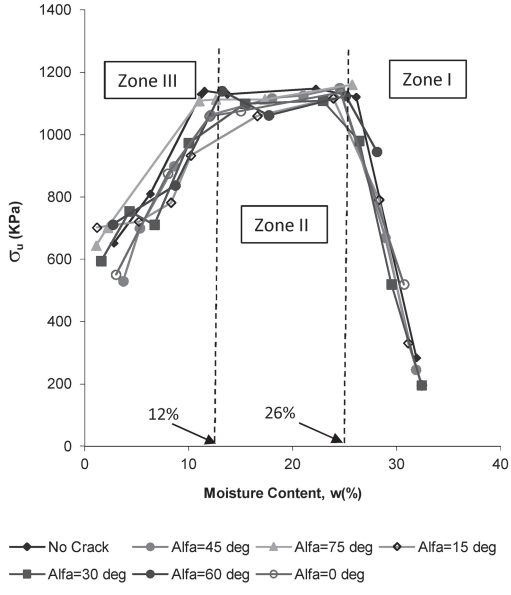

Figure 3. Uniaxial ultimate compression strength in intact and cracked specimens σ_u.

The ultimate monotonic uniaxial compressive strength σ_u of the intact and pre-fissured specimen is presented as a function of the water content in Fig. 3. σ_u for intact specimens and for specimens with a crack is very close and this indicates that the presence of the primary crack has no effect on the ultimate uniaxial compressive strength of the tested specimens. A shear failure plane was observed in the lateral face of all of the specimens (Fig. 1). This indicates that the two types of failure occur independently one of each other.

The uniaxial stress that produces the crack to propagate (σ_c) is presented in Fig. 4. Both, σ_u and σ_c indicate similar curve shapes. The strength increases as the soil is dried for moisture contents

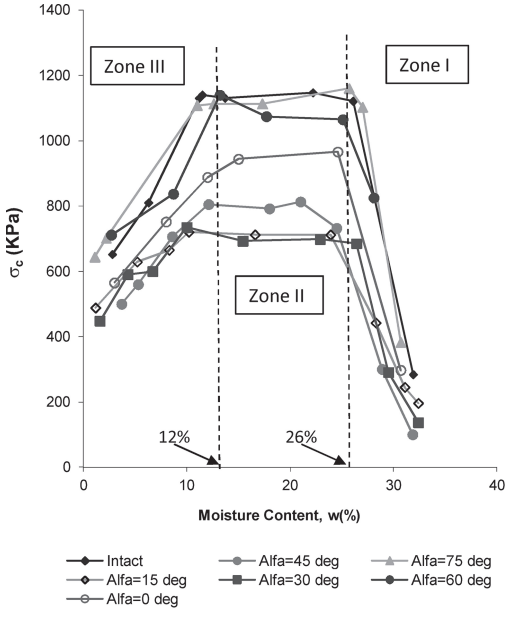

Figure 4. Vertical stress producing crack propagation σ_c.

above 26% (Zone I), the strength is almost constant for the intermediate interval between 12% and 26% (Zone II) and reduces as the soil is dried below 12% (Zone III).

Vesga and Vallejo (2006) explain the observed variation of the soil strength with the moisture content using the concept of equivalent effective stress (EES) proposed by Cho and Santamarina (2001). Vesga and Vallejo (2006) propose that the EES is dependent on the water distribution in the pores of the clay: saturated, funicular and pendular states as defined by German (1989). All the pores within the soil are full of water in the saturated state, air penetrates in the soil but water phase is still continuous in the funicular state and capillary meniscus between particles (discontinuous water phase) exist in the pendular state (German, 1989). Zone I corresponds to saturated-funicular state, in which since the water phase is continuous then the strength increases as the suction stress in the soil is increased (Vesga, 2008). Zone II corresponds to complete-pendular state in which the soil strength remains almost constant. Zone III corresponds to partial-pendular state in which strength diminishes as the water content is reduced below 12%.

Vesga (2005) subdivides the pendular state in complete pendular and partial-pendular states. All the contacts between particles in the soil have capillary meniscus in the complete-pendular state (Zone II) and some capillary contacts break in the partial-pendular state (Zone III) as the soil is dried. When suction is increased in the partial-pendular state the soil strength does not change; this statement can be supported not only experimentally as shown here, but also theoretically (Vesga, 2008). On the other hand, a capillary contact can break for two principal reasons: cavitation pressure in the water is reached as the soil is dried, or the particles forming the contact are separated a distance and the capillary neck cannot survive if the water volume is reduced and some distance between particle remains. Capillary neck breakings produce the soil to be weaker as the soils is dried (suction stress is increased) in the Zone III. The soil has a minimum resistance after it is completely dried; its resistance depends on the van der Waals inter-particle attractions (Vesga, 2005).

Soil behavior in the complete-pendular and partial-pendular states as explained here in invalidate the empirical soil strength equations based on the suction stress as proposed by several authors. In other words, measuring the suction stress in soils for evaluating strength or compressibility is waste of time if the soil is in such pendular states. Other efforts of expressing the strength in terms of tensile strength or the equivalent effective stress seem to be more reasonable and scientifically sound (Lu, 2008, Lu et al., 2009; Vesga 2008).

Comparison of results from different tests does not show important variation of the crack propagation angle with water content. After the secondary crack started the propagation, the crack curved towards the vertical direction which is the orientation of the principal stress applied on the specimens (Fig. 1 and 2).

The cyclic stress ratio was earlier defined as the ratio between the applied dynamic vertical stress and the ultimate monotonic compression strength of a similar specimen (with the same water content and the same primary crack inclination). The purpose of the dynamic loading test was to find the threshold load (fraction of the static load) at which no crack propagation occurred under dynamic loading conditions regardless of the number of applied cycles.

Figures 5 and 6 show the obtained results; the cyclic stress ratio is expressed as a function of the water content in the specimens. The dark points in this figure represent the cyclic stress ratios (r_d) for which crack propagation occurred; the clear points represent the cases for which no crack propagation was observed after 7200 cycles of load applications.

The general trend observed in these tests was that the crack stability threshold is almost constant regardless of the moisture content for water contents of less than 26% (complete-pendular and partial-pendular states). For water content above 26% in funicular-saturated state, the crack stability threshold diminishes noticeably; at a moisture content of 30%, the threshold was found to be as

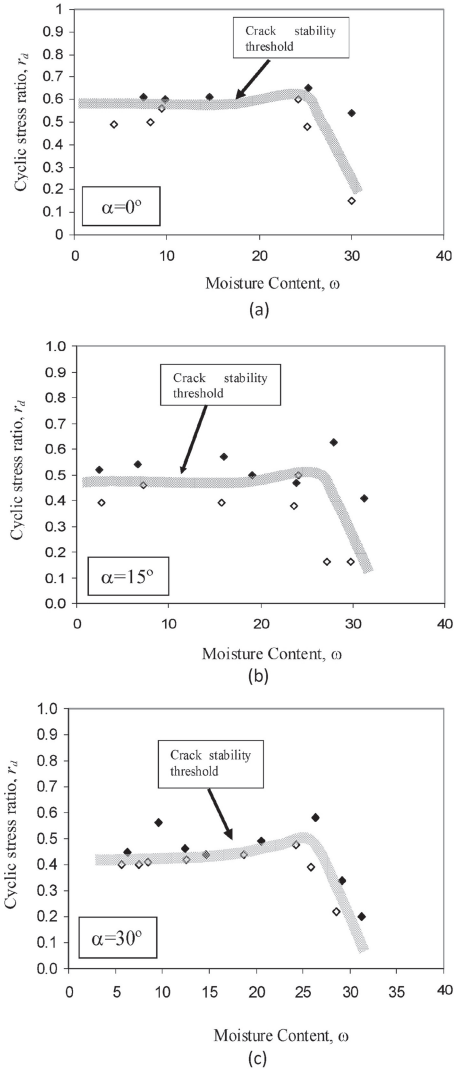

Figure 5. Crack propagation threshold α = 0, 15, and 30 deg.

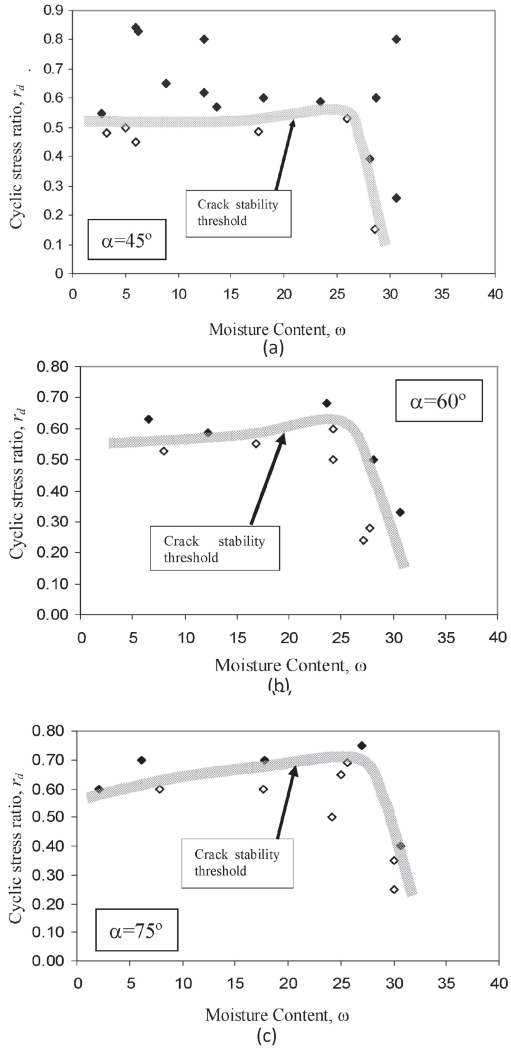

Figure 6. Crack propagation threshold α = 45, 60, and 75 deg.

low as 0.15. As noted, the reduction in the crack stability threshold for high moisture contents is very significant and is very possible to be related to locally developed pore pressures in the compression zones (local liquefaction) around the crack (stress concentrations around crack tips are evaluated by Vallejo, 1995). These pore pressures can be developed when the material is close to saturation because the water phase is continuous through the clay in the saturated-funicular state.

Pore pressures in unsaturated clays subjected to dynamic loading are not easy to be measured and even more difficult would be measuring local pore pressures around the crack tips in the clay.

6 CONCLUSIONS

The crack stability threshold is defined as the cyclic stress ratio r_d, at which, regardless of the number of cycles applied, there is no crack propagation in a clay specimen subjected to uniaxial dynamic loading conditions. Uniaxial static and dynamic laboratory tests were performed in order to measure the crack stability threshold on kaolinite clay specimens having a crack at different inclination angles and different moisture contents. The threshold is almost constant under moisture contents of 26% in the complete-pendular and partial-pendular states of water distributions in the pores

of the clay and diminishes remarkably for higher moisture contents when the water distribution is in the saturated-funicular state.

More research is necessary in order to confirm that the low threshold values observed for high moisture contents close to saturation (saturated-funicular state) are due to the pore pressures developed in the clay during dynamic loading and if there occurs local liquefaction around the crack tips due to the high compressive stress concentrations which produce the pore pressure to rise and the crack to propagate.

REFERENCES

Bishop, A.W. "Progressive failure with special reference to the mechanism causing it". Proc. Geotech. Conf., Oslo, Vol. 2, pp. 142–150. 1967.

Broek, D. " Elementary engineering Fracture Mechanics". Martinus Nijhoff Publishers, Boston. p. 469. 1984.

Cho, G.C and Santamarina, J.C. "Unsaturated particulate materials—Particulate-level studies". Journal of Geotechnical and Geoenvironmental Engineering. ASCE. Vol. 127, No. 1, pp. 84–96. 2001.

Covarrubias, S.W. "Cracking of earth and rockfill dams". Harvard Soil Mechanics Series, 82. 1969.

Dataq Instruments. "Waveform recording systems". 2003 Catalog. Akron, OH. 2003.

Duncan, J.M. and Dunlop, P. (1969). "Slopes in stiff fissured clays and shales". Journal of the Soil Mechanics and Found. Div. ASCE, Vol. 95, No. 2, pp. 467–491. 2003.

Erdogan, R. and Sih, G.C. "On the crack extension in plates under plain loading and transverse shear". Journal of Basic Eng. ASME, Vol. 85, pp. 519–527. 1963.

German, R.M. Particle packing characteristics. Metal Powder Industries Federation. Princeton, New Jersey. 1989.

Lefebvre, G., LeBoeuf, D. and Demers, B. "Stability threshold for cyclic loading of saturated clay" Canadian Geotechnical Journal. Vol. 26, pp. 122–131. 1988.

Lu, N. "Is s matric suction an independent stress variable?".J. of Geot. And Geoenv. Eng. ASCE, Vol. 134, No. 7, 2008.

Lu, N., Kim, T.-H., Sture, S. and Likos, W. "Tensile Strength of Unsaturated Sand".J. of Eng. Mech. Vol. 135, No. 12, 2009.

Marsland, A. "The shear strength of stiff fissured clays". Stress strain behavior of soils, R.H. Parry, ed., G.T. Foulis and C., London England, pp. 59–68. 1972.

Morgenstern, N. "Slopes and excavations in heavily overconsolidated clays". Proceedings of the Ninth Int. Conf. on Soil Mech. and Found. Eng., State of the Art Report, Tokio, Japan. Vol. 2, pp. 567–581. 1977.

Morris, P.H., Graham, J. and Williams, D.J. "Cracking in drying soils". Canadian Geotechnical Journal. Vol. 29, pp. 263–277. 1992.

Peterson, R., et al. "Limitations of laboratory shear strength in evaluating the stability of high plastic clays", Proc. ASCE Res. Conference on the Shear Strength of Cohesive Soils, Boulder, Colorado, pp. 701–765. 1996.

Rizkallah, V. "Stress strain behavior of fissured stiff clays". Proceedings of the Ninth Int. Conf. on Soil Mech. and Found. Eng., Tokio, Japan. Vol. 1, pp. 217–220. 1977.

Saada, A.S., Bianchi, G.F. and Liang, L. "Cracks, bi-furcation and shear bands propagation in saturated clay". Geotechnique, Vol. 44, No. 1, pp. 35–64. 1994.

Saada, A.S., Chudnovsky, A. and Kennedy, M.R. "A fracture mechanics study of stiff clays". Proceedings of the Eleventh Int. Conf. on Soil Mech. and Found. Eng., San Francisco, Calif., Vol. 2, pp. 637–640. 1985.

Sherard, J.L. "Embankment dam cracking". Embankment Dam Engineering, Hirchfeld, R.C. and Poulos, S.J., eds., John Wiley and Sons, New York, pp. 271–353. 1973.

Skempton, A.W. "Long term stability of clay slopes". Geotechnique, Vol. 14, No. 2, pp. 77–102. 1964.

Skempton, A.W. and LaRochelle, P. "The Bradwell slip: a short term failure in London Clay". Geotechnique, Vol. 15, No. 3, pp. 221–242. 1965.

Terzaghi, K. "Stability of slopes in natural clays". Proceedings of the First Int. Conf. on Soil Mech. and Found. Eng., Cambridge, Mass., Vol. 4, pp. 2353–2356. 1936.

Vallejo, L.E. "Mechanics of crack propagation in stiff clays". Geotechnical Aspects of Stiff and Hard Clays. ASCE's Geotechnical Special Publication No. 2. Khera, R.P. and Lovell, W., es., pp. 14–27. 1986.

Vallejo, L.E. "The brittle and ductile behavior of clay samples containing a crack under mixed-mode loading". Theoretical and Applied Fracture Mechanics, Vol. 10, pp. 73–78. 1988.

Vallejo, L.E. "Fissure parameters in stiff clays under compression". Journal of Geotech. Eng., ASCE, Vol. 115, No. 9, pp. 1303–1317. 1989.

Vallejo, L.E. "Application of fracture mechanics to soils: an overview". Fracture Mechanics Applied to Geotechnical Engineering. ASCE's Geotechnical Special Publication No. 43. Vallejo, L.E. and Liang, R.Y., Editors, pp. 1–20. 1994.

Vallejo, L.E., Al-Saleh, S. and Shettima, M. "Evaluation of fracture criteria for fissured clays". Proc. Tenth Pan. Conf. on Soil Mech. and Found. Engineering, Mexico. 1995.

Vesga, L.F. "Crack Propagation Threshold in Fissured Clays". 4th Int. Conf. Geotechnical Earthquake Engineering, Thesaloniki, Greece, 2007.

Vesga, L.F. "Equivalent Effective Stress and Compressibility of Unsaturated Kaolinite Clay Subjected to Drying". J. Geot. Geoenv. Eng. ASCE. Vol. 134, No. 3, 2008.

Vesga, L.F. Mechanics of Crack Propagation in Clays under Dynamic Loading. Ph.D. Dissertation. Department of Civil and Environmental Eng. University of Pittsburgh. 2005.

Vesga, L.F., Caicedo, B. and Mesa, L.E. "Deep cracking in the 'Sabana de Bogota' clay". Proceedings of the Twelfth Panamerican Conf. on Soil Mech. and Geotech. Engineering. Cambridge, Mass. pp. 737–742. 2003.

Vesga, L.F. and Vallejo, L.E. "Direct and Indirect Tensile Tests for Measuring the Equivalent Effective Stress in a Kaolinite Clay". 4th International Conference on Unsaturated Soils. ASCE. Arizona, USA. 2006.

Williams, A.A.B. and Jennings, J.E. "The in-situ shear behavior of fissured soils". Proceedings of the Ninth Int. Conf. on Soil Mech. and Found. Eng., Tokio, Japan. Vol. 2, pp. 169–176. 1977.

Constitutive modelling and microstructure

This page intentionally left blank

Advances in Unsaturated Soils – Caicedo et al. (eds)
© 2013 Taylor & Francis Group, London, ISBN 978-0-415-62095-6

Hydro-mechanical formulation considering fluid compressibility

Sylvia Regina C. Brant-P-de-Jesus & Manoel Porfírio Cordão-Neto
Universidade de Brasília, Brasilia, Brazil

Igor Fernandes-Gomes
Universidade Federal de Pernambuco, Recife, Brazil

ABSTRACT: Traditional numerical modeling for geotechnics and reservoir geomechanics use formulations which take into consideration many simplifying hypotheses for the representation of complex phenomena of porous media physical behavior. However, these simplifications may neglect effects which could contribute in model's accuracy. In this paper, a fully coupled hydro-mechanical formulation considering fluid and solids compressibility is presented. The hydraulic behavior during consolidation in a soil column is simulated with this model and results of fluid pressure are evaluated. The permeability of the medium is determined by a permeability function and the effect of permeability changes is verified. Therewith, it is possible to define porosity changes influence in porous media physical behavior. Also, variations in fluid compressibility are considered. The fluid compressibility does not interfere in flow tendency through the medium; it causes delay in fluid pressure dissipation during consolidation. The effect of permeability variation is not related to fluid compressibility.

1 INTRODUCTION

1.1 *Theme contextualization*

There are two principles which may be referred to as essentials to describing soils and rocks behavior. The mechanical behavior is associated to the law of conservation of linear momentum, allowing forces balance analysis and the hydraulic behavior is characterized by mass conservation law.

These phenomena are related: stress-strain state is affected by fluid pressures and vice-versa. Therewith, it is intuitive the importance of coupled analyses, which describe more precisely how mechanical and hydraulic behavior are related.

There are cases in which specific features of the porous medium can influence the analysis. Changes in stress-strain state induce porosity variation in the solid matrix and considering this in modeling may enhance simulation.

In most formulations for porous media behavior representation, many hypotheses are considered in order to simplify complex phenomena which take place. However, some of those simplifications may interfere in model responses, with simulation results not correspondent to the observed behavior of the studied case.

The compressibility of the solids which form the solid matrix of a porous medium and the compressibility of the fluids within this medium are not taken into account in traditional models in geotechnics or related areas, such as reservoir geomechanics, in petroleum engineering. This kind of consideration could enhance modeling, contributing to more accurate results in behavior prediction.

1.2 *Objectives*

When solids and fluid compressibility influence in porous media behavior is considered possible, a new type of approach for mechanical and hydraulic behavior may be presented.

A fully coupled hydro-mechanical formulation with this consideration was presented by Jesus (2012). This formulation was fully described by the author, followed by its implementation, validation and calibration in ALLFINE (Farias, 1993; Cordão Neto, 2005; Jesus, 2012).

In this paper, results for hydraulic behavior simulation of this numerical model are presented. The effect of permeability variation during incompressible and compressible fluid flow is studied. Therewith, it is possible to study the combined effect of compressibility changes in the fluid and permeability of the medium for each type of fluid.

With this model assumption, a theoretical case of consolidation is analyzed, with verification of fluid pressure results.

2 FORMULATION

The presented formulation was organized and fully described by Jesus (2012). Here, a brief summary

of the equilibrium and the mass conservation equations of the model is shown.

2.1 *Equilibrium equation*

The equilibrium equation for a porous medium can be described as:

$$\frac{\partial \sigma_{ij}}{\partial x_j} + b_i = 0 \tag{1}$$

where: σ_{ij} is the stress tensor, b_i is the body forces vector and x_j corresponds to the coordinate system.

The stress-strain relation here presented is based on the definition of the generalized effective stress. Also, the influence of solids compressibility on solid matrix stress state is considered. Thus, the effective stress principle is defined as (Li et al., 1999):

$$\{\sigma'\} = \{\sigma\} - \alpha_b \{m\} p \tag{2}$$

where: $\{\sigma'\}$ is the effective stress vector, $\{\sigma\}$ is the total stress vector, α_b is the Biot parameter, $\{m\}^T = \{1\ 1\ 1\ 0\ 0\ 0\}$ for a 3D analysis and p is the fluid pressure (for a saturated analysis).

The Biot parameter (α_b) is defined by the following expression:

$$\alpha_b = 1 - \frac{\{m\}^T \left[D^{ep}\right] \{m\}}{9k_s} \tag{3}$$

where: $[D^{ep}]$ is the constitutive matrix and k_s is the bulk modulus of solids.

The Principle of Virtual Work is employed to solve the equilibrium equation in space using FEM (Zienkiewicz, 1977).

The matrixes that represent the solved equilibrium equation are assembled and may be written as:

$$[K]\{\dot{u}\} + [C]\{\dot{p}\} = \{\dot{F}\} \tag{4}$$

where:

$$[K] = \int_{\Omega} [B]^T [D][B] d\Omega$$

$$[C] = \int_{\Omega} [B]^T \alpha_b \{m\} \left[N^p\right] d\Omega$$

$$\{\dot{F}\} = \int_{\Omega} [N]^T \{\dot{b}\} d\Omega + \int_{\Gamma} [N]^T \{\dot{\tau}\} d\Gamma$$

$[K]$ is the stiffness matrix, $\{\dot{u}\}$ is the nodal displacements rate vector, $[C]$ is the solids-fluid coupling, $\{\dot{p}\}$ is the nodal fluid pressure rate vector and $\{\dot{F}\}$ is the external forces rate vector.

2.2 *Mass conservation equation*

The mass conservation equation used in this paper involves both liquid and solid phases. The mass conservation equation for the liquid phase is defined by the following expression:

$$\frac{\partial}{\partial t}\left(\theta \rho^f\right) + \frac{\partial}{\partial x_i}\left(\theta \rho^f \dot{U}_i\right) = 0 \tag{5}$$

where: θ is the volumetric water content, ρ^f is the fluid density and $\dot{U}_i$ is the real fluid velocity.

The real fluid velocity can be expressed as:

$$\dot{U}_i = \dot{u}_i + \frac{w_i^f}{\theta} \tag{6}$$

where: $\dot{U}_i$ is the real fluid velocity vector, $\dot{u}_i$ is the velocity of the solids vector, w_i^f is the fluid velocity due to percolation vector and θ is the volumetric fluid content of the medium.

The real fluid velocity assumption implies on taking into account the effects of porosity changes in the porous medium. The velocity of the solids $\dot{u}_i$ is related to the displacements of the medium.

The mass conservation equation for the solid phase may be presented as:

$$\frac{\partial}{\partial t}\left[(1-\phi)\rho^s\right] + \frac{\partial}{\partial x_i}\left[(1-\phi)\rho^s \dot{u}_i\right] = 0 \tag{7}$$

where: ϕ is the material porosity, ρ^s is the solids density and $\dot{u}_i$ is the solids velocity vector.

In order to represent the mass conservation of porous media, the volume of solids and the volume of fluid within a finite element should be balanced in a total element volume approach (Li et al., 1999).

The variation of the density of liquid fluids (Peaceman, 1977; Rosa et al., 2006) and solids (Li et al., 1999) is expressed as:

$$\frac{d\rho^f}{\rho^f} = \frac{1}{k_f} dp \tag{8}$$

where: ρ^f is the fluid density, k_s is the bulk modulus of the fluid and p is the fluid pressure.

$$\frac{(1-\phi)}{\rho^s}\frac{D\rho^s}{Dt} = \left[\frac{(\alpha_b - \phi)}{k_s}\frac{Dp^R}{Dt} - (1-\alpha_b)\dot{u}_{i,i}\right] \tag{9}$$

where: ρ^s is the solids density, k_s is the bulk modulus of rock crystals, α_b is the Biot parameter, ϕ is

the porosity of the rock and p^R is the pressure of the fluids (for saturated medium $p^R = p$).

The spatial solution for the mass conservation equation via FEM can be made with Galerkin method, a weighted residual method (Zienkiewicz, 1977).

The matrixes that represent the solved mass conservation equation are assembled and written as:

$$[M]\{\dot{p}\} + [L]\{\dot{u}\} + [R]\{p\} = \{Q\} \tag{10}$$

where:

$$[M] = \int_{\Omega} \left[N^P\right]^T \left[\frac{(\alpha_b - \phi)}{k_s} + \frac{\phi}{k_f}\right] \left[N^P\right] d\Omega$$

$$[L] = \int_{\Omega} \left[N^P\right]^T \alpha_b \{m\}^T [B] d\Omega$$

$$[R] = \int_{\Omega} \left[N^P\right]^T \left[\frac{(\alpha_b - \phi)}{k_s}\{\dot{u}\} + \frac{\phi}{k_f}\left(\{\dot{u}\} + \frac{\{w^f\}}{\phi}\right)\right] \left[B^P\right] d\Omega + \int_{\Omega} \left[B^P\right]^T \frac{[K]}{\mu} \left[B^P\right] d\Omega$$

$$\{Q\} = \left[\int_{\Omega} \left[B^r\right]^T \frac{[K]}{\mu} \rho_f \{g\} (\nabla . y) d\Omega\right] - \int_{\Gamma_2} \left[N^r\right]^T \overline{q} d\Gamma$$

$[M]$ is the mass matrix, $\{\dot{p}\}$ is the nodal fluid pressure rate vector, $[L]$ is the fluid-solids coupling matrix, $\{\dot{u}\}$ is the nodal displacements rate vector, $[R]$ is the flow matrix, $\{p\}$ is the nodal fluid pressure vector and $\{Q\}$ is the external discharges vector.

2.3 *Coupling of equations and time solution*

The spatial solution of equilibrium and mass conservation equations may be put together in order to assemble a system of equations. This system permits the time solution of the problem at a later stage. Considering both Equations 4 and 10, we have:

$$\begin{bmatrix} 0 & 0 \\ 0 & [R] \end{bmatrix} \begin{Bmatrix} \{u\} \\ \{p\} \end{Bmatrix} + \begin{bmatrix} [K] & [C] \\ [L] & [M] \end{bmatrix} \begin{Bmatrix} \{\dot{u}\} \\ \{\dot{p}\} \end{Bmatrix} = \begin{Bmatrix} \{\dot{F}\} \\ \{Q\} \end{Bmatrix} \tag{11}$$

Then, with this, the system of equations may be expressed by:

$$[W]\{x\} + [Y]\{\dot{x}\} = \{Z\} \tag{12}$$

Considering the studied phenomenon is transient, this system of equations should be solved in time. Finite Difference (FDM) was the chosen method for the time discretization of the system of equations, already solved in space. This choice was based on the ease of application of FDM for that matter. Evaluating Equation 12 in time stage $t+\alpha\Delta\tau$, the solution of the equation system is:

$$\left[\Delta t \alpha [W]_{t+\alpha\Delta t} + [Y]_{t+\alpha\Delta t}\right]\{\Delta x\} = \Delta t \{Z\}_{t+\alpha\Delta t} - \Delta t [W]_{t+\alpha\Delta t} \{x\}_t \tag{13}$$

3 METHODOLOGY

3.1 *Description of the problem*

The studied case consists of a laterally confined column of soil, one meter high and supporting an uniform load of a 10000 kPa, as illustrated in Figure 1.

This soil sample is assumed to be totally saturated with fluid flow restricted in the laterals of the column and free at the top surface. The dominium is discretized in a non-uniform mesh of 10 elements (3-D 8-noded elements, as shown in Figure 2) and 44 nodes. The loading induces a consolidation process in the sample. The constitutive model employed for these simulations was the linear elastic.

The permeability is defined as function of porous medium void ratio and the simulations are performed for three different configurations of this function. Also, the fluid compressibility is varied for the simulations, with a fluid bulk modulus value of $k_f = 1 \times 10^{12}$ kPa for incompressible fluid

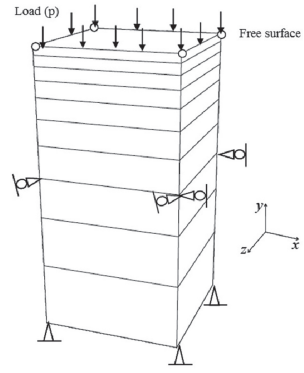

Figure 1. One-dimensional consolidation problem (modified Cordão Neto, 2005).

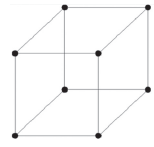

Figure 2. 8-noded 3D element.

and $k_f = 1 \times 10^5$ kPa for compressible fluids. This allows the verification of the combined effect of compressibility and permeability changes. The values of fluid bulk modulus and solids bulk modulus used in these simulations do not necessarily correspondent to real values of these parameters. They have been established to facilitate the visualization of the effects of compressibility in the model results. However, depending on the stress state the porous media is subjected to, it is possible to visualize the same effects here presented with real values of this parameter.

The evaluation of the simulation results is made with the values of fluid pressure, which are monitored over time during the consolidation process.

3.2 *Permeability functions*

In general, permeability is assumed constant during consolidation. This hypothesis may not be accurate considering mechanical and hydraulic phenomena which take place during this process. The solid matrix suffers stress changes and straining, implying on void closing.

The pore volume reduction influences permeability. So, these two features are related and can be expressed as permeability functions. In this study, a permeability function is suggested:

$$k = A\frac{\exp(Be)}{\exp(BC)} \tag{14}$$

where: k is the permeability and e is the void ratio.

Parameter A corresponds to the initial permeability (k_0) and parameter C is equivalent to a reference void ratio value, the initial void ratio (e_0) for the simulations presented in this paper.

Parameter B was used to calibrate the void ratio variation range of the function. With its variation, it was possible to define three different formats for the permeability function. The function reaches constant values of permeability (function k_1), values 10 times lower than the initial (function k_2) or values 100 times lower than the initial (function k_3) for the final void ratio of 0,87. The values for each parameter are presented in Table 1 and its corresponding permeability functions are shown in Figure 3.

Table 1. Calibration parameters for the permeability function.

A		$1{,}0 \times 10^{-6}$
B	For function k_1	0,0
	For function k_2	95,8
	For function k_3	191,9
C		0,90

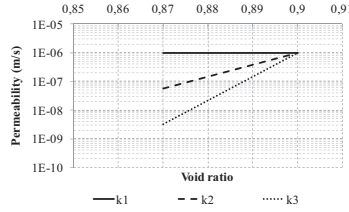

Figure 3. Permeability functions.

4 RESULTS AND DISCUSSION

The analyses performed use the parameters shown in Table 2. The values of permeability vary according to the permeability functions defined in section 3.2.

For the performed simulations, the final void ratio is 0,895, regardless the permeability function used. The volume change is small, but the effects of permeability variation can be noticed in fluid pressure results. The evolution of the fluid pressure during the simulation of the consolidation process is monitored for specific time factors (T = 0; 0,2; 0,5 e 0,8). The results for incompressible fluid analysis are presented in Figures 4 to 7.

For the first time stage (T = 0), the fluid pressure is the same for all permeability functions. In this stage, there is no fluid flow. The fluid pressure corresponds only to the load applied on the soil. The numerical model used in this simulation does not provide results with discontinuity. This justifies the smoothed format of the curve.

For the following time stages, the effect of varying permeability due to void ratio changes can be noticed in fluid pressure results, because it dissipates faster over time when the medium is more permeable. Thus, the values of fluid pressure decrease more rapidly for the constant permeability function (k_1 function) and slower for the function which reaches a permeability value 100 times lower than the initial value (k_3 function), as expected. It can be noticed that the results of fluid pressure are influenced by permeability even for low void ratio variation.

The following simulation was performed for a compressible fluid. The analysis results are presented in Figures 8 to 11.

The results for simulations with the compressible fluid follow the same behavior tendency of the incompressible fluid. For the first time stage, fluid pressure is equal for all permeability functions. Then, for the following time stages, fluid pressure dissipates faster for the constant permeability function (k_1 function) and slower for the function which reaches a permeability value 100 times lower than the initial value (k_3 function).

The difference observed between fluid pressure results is related to the fluid compressibility, with no influence of the permeability functions.

Table 2. Parameters for the consolidation simulation.

Young modulus (E)	2500000 kPa
Poisson coefficient (ν)	0,31
Initial void ratio (e_0)	0,90
Density of the solids (ρ^s)	2,65 kg/m³
Solids bulk modulus (k_s)	$1,0 \times 10^{15}$ kPa
Density of the fluid (ρ^f)	1,00 kg/m³

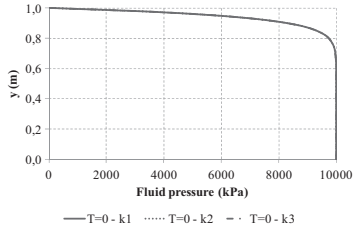

Figure 4. Results of fluid pressure for incompressible fluid simulation (T = 0).

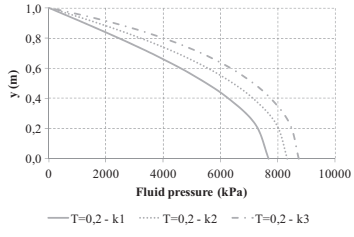

Figure 5. Results of fluid pressure for incompressible fluid simulation (T = 0,2).

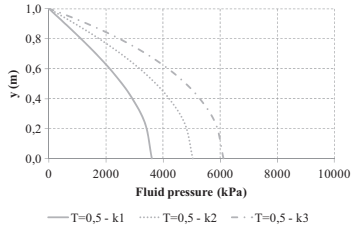

Figure 6. Results of fluid pressure for incompressible fluid simulation (T = 0,5).

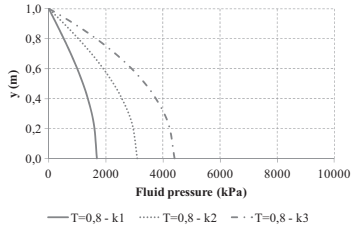

Figure 7. Results of fluid pressure for incompressible fluid simulation (T = 0,8).

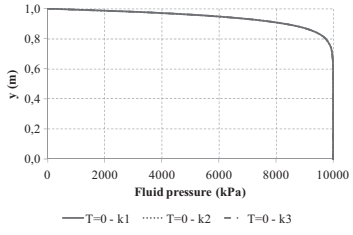

Figure 8. Results of fluid pressure for compressible fluid simulation (T = 0).

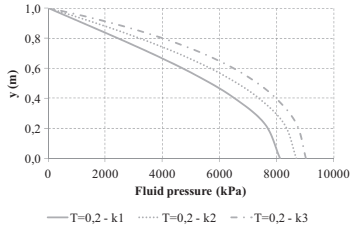

Figure 9. Results of fluid pressure for compressible fluid simulation (T = 0,2).

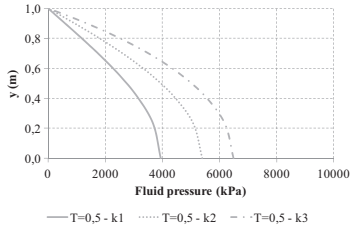

Figure 10. Results of fluid pressure for compressible fluid simulation (T = 0,5).

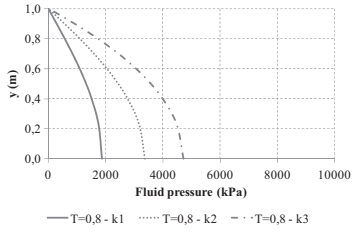

Figure 11. Results of fluid pressure for compressible fluid simulation (T = 0,8).

By analyzing the format of the fluid pressure curves over time, it can be noticed that fluid flow tendency is the same (the shape of the curves is maintained), regardless the fluid compressibility.

The compressibility of the fluid causes an effect of delay in fluid pressure dissipation, given by volume changes the fluid suffers. The effect of fluid compressibility in a consolidation process in a porous medium is detailed in Jesus (2012).

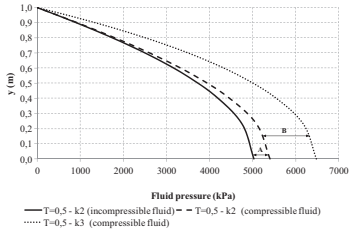

Figure 12. Comparison between results of incompressible and compressible fluid simulation for different permeability functions (T = 0,5).

Finally, the results for incompressible and compressible fluid simulations were compared, as shown in Figure 12.

Analyzing the results, two zones are distinguished. Zone A corresponds to the difference in fluid pressure values associated to fluid compressibility. The results of the curves that delimitate zone A are governed by the same permeability function (k_2), making zone A correspondent only to the fluid compressibility effect.

Zone B is referred to the difference of fluid pressure values due to permeability changes. The curves delimitating zone B correspond to results of simulations made with the same fluid bulk modulus value. However, they are governed by different permeability functions, k_2 and k_3. Thus, zone B corresponds only to the permeability effect.

With this approach, one can observe the limit of effect for each parameter, allowing more accurate analyses of causes for fluid pressure increase in porous media during consolidation.

5 CONCLUSIONS

In this paper, the effects of permeability variation in fluid pressure dissipation during a consolidation process were investigated. Furthermore, the combined effect of permeability changes and fluid compressibility is analyzed.

The analyses performed for permeability influence evaluation prove that the effect of permeability functions affects significantly soil responses. So, there is need of developing appropriate constitutive models for porous media hydraulic behavior.

Verifying fluid compressibility effect, it can be stated that it does not alter percolation through the porous medium. Fluid flow takes place with the same tendency observed in incompressible fluid simulations. However, an effect of fluid pressure dissipation delay is still registered, only related to fluid compressibility.

Finally, the results of incompressible and compressible fluid simulations are compared for two different permeability functions. Considering that fluid compressibility does not influence fluid flow tendency, it can be made a division of zones of causes for fluid pressure delay in dissipation, one correspondent only to fluid compressibility influence, other to permeability decrease influence.

With the achieved results, it can be noticed that the presented formulation is appropriate to studies of petroleum engineering, more specifically, reservoir geomechanics. Behavior predictions can be made using the presented model, with results that should represent reservoir behavior more accurately, given the consideration of factors which are usually disregarded in reservoir simulations. The mechanical and the hydraulic behavior of reservoirs can be affected by the compressibility of the oil within the reservoir-rock and the reservoir-rock itself. Considering this, this formulation is appropriate for reservoir behavior prediction.

Ultimately, the presented results are interesting for further research of models for multiphase fluids in porous media, with fluid and solids compressibility taken into consideration. The simulation of traditional geotechnics problems can be performed with this model and more precise results can be achieved on account of considering fluid and solids compressibility.

ACKNOWLEDGEMENTS

The authors would like to acknowledge the support given by Brazilian research organizations CAPES and CNPq and University of Brasília.

REFERENCES

Cordão Neto, M.P. (2005). *Análise hidro-mecânica de barragens de terra construídas com materiais colapsíveis.* Doctorate thesis, G.TD—028/05, Civil and Environmental Engineering Department, University of Brasília, Brasília, DF, 152 p.

Farias, M.M. (1993). *Numerical analysis of clay core dams*. Ph.D. Thesis, University of Wales—University College of Swansea. 161 p.

Jesus, S.R. C.B. P. de (2012). *Coupled Hydro-mechanical Analysis Considering Fluid and Solids Compressibility*. Master dissertation, G.DM-207/12, Civil and Environmental Engineering Department, University of Brasília, Brasília, DF, 124 p.

Li, X., Thomas, H.R. & Fan, Y. (1999). Finite element method and constitutive modeling and computation for unsaturated soils. *Computer methods in applied mechanics and engineering*. 169, 135–159.

Peaceman, D.W. (1977). *Fundamentals of numerical reservoir simulation*. Elsevier, Amsterdan, Netherlands. 192p.

Rosa, A.J., Carvalho, R. de S. & Xavier, J.A.D. (2006). *Engenharia de reservatórios de petróleo*. Interciência, 1 ed. 808 p.

Zienkiewicz, O.C. (1977). *The Finite Element Method*. McGraw-Hill, London, United Kingdom, 3 ed., 787 p.

Advances in Unsaturated Soils – Caicedo et al. (eds)
© 2013 Taylor & Francis Group, London, ISBN 978-0-415-62095-6

Volumetric behavior of unsaturated-reconstituted soils

G.J. Burton & D. Sheng
School of Engineering, The University of Newcastle, Callaghan, New South Wales, Australia

E. Romero
Department of Geotechnical Engineering and Geosciences, Universitat Politècnica de Catalunya, Barcelona, Spain

ABSTRACT: The vast majority of unsaturated soil research is completed on compacted soils. Due to ease of laboratory testing, specimens are typically prepared dry of optimum and often with high void ratios (low dry density) to capture the phenomena of collapse. Compacted soils have significant impacts on infrastructure, but the inherent effects of structure within each sample are difficult to differentiate from the effects of suction (and degree of saturation) in the laboratory. Although significant advances have been made with techniques such as MIP and ESEM. The difficulties of producing and unsaturated sample from slurry have largely limited the amount of published literature on samples reconstituted from slurry. In this paper, the available published data sets of Jennings and Burland (1962), Vicol (1990) and Cunningham (2000) are reviewed. Predictions of the volume change behavior are then made.

1 INTRODUCTION

Unsaturated soil mechanics has and still is receiving a lot of interest in the research community. A large number of constitutive models have been proposed to simulate the behavior of unsaturated soils. Most of these have been developed based on the observed behavior of compacted soils while reconstituted soils have received comparatively less attention. Laboratory testing of compacted soils has the benefit of starting from an initially unsaturated state and allows the use of the axis-translation technique.

A fundamental ingredient of all constitutive models is the volume change equation which defines the volume change of the soil under stress and suction changes. Volume change of soils subject to cycles of wetting and drying can cause significant damage to lightly loaded foundations and structures. The volume change behavior also affects the shear strength, yield stress and hydraulic behavior of the soil.

In this paper we briefly note some points in relation to compacted and reconstituted soils followed by some predictions made using a modified form of the Sheng-Fredlund-Gens (SFG) volume change equation proposed by Sheng et al. (2008).

2 COMPACTED VERSUS RECONSTITUTED

The development of unsaturated soil mechanics is by and large based on the results of laboratory testing of samples prepared in the laboratory by compaction. Compaction may be kneading, dynamic (e.g., Standard Proctor or Modified Proctor) or static. The choice of which is up to the specific researcher. Static compaction is commonly adopted to provide controllable final density and knowledge of the past maximum vertical stress.

The division between compacted and reconstituted soils has however recently been suggested by Tarantino (2011) as being vague. This suggests that study of the behavior of reconstituted soils should enhance the understanding of both compacted soils and unsaturated soils in general. The complexities arising from compacted soils may partly obscure the effects of suction or degree of saturation on the behavior.

The process of compaction, not matter what type, inherently introduces some form of structure to the sample. Structure is taken here include both fabric and stability of the inter-particle contacts (Mitchell and Soga, 2005). In unsaturated soil research the discussion on structure has typically focused around the role of double-structure or double porosity (micro and macro pores) developed as a result of compaction.

Similarly in preparing reconstituted samples for testing the water content at which the slurry is prepared affects the initial portion of compression (Cerato and Lutenegger, 2004, Hong et al., 2010). Due to the logarithmic relationship between void ratio and effective stress the differences at higher stress become less pronounced.

Naturally occurring saturated structured soils have been found to be poorly described using the

Modified Cam Clay (MCC) model. The "structure permitted" space for the compression of a saturated structured soil was coined by Leroueil and Vaughan (1990). Structured saturated soils are able to maintain a higher void ratio at certain effective stresses in comparison to an unstructured soil that may be reconstituted in the laboratory. The plastic volumetric strain caused by compression or shearing is effective in destroying the structure developed in saturated structured soils. This behavior may be seen as analogous to that for a compacted unsaturated soil which is particularly well demonstrated with the one dimensional compression results of Jotisankasa (2005). Discerning the effects of structure (fabric) from the effects of suction becomes difficult.

3 VOLUME CHANGE MODELS

Perhaps the most striking features of unsaturated soil behavior are the swelling and collapse phenomenon which occur under constant total stress. The genesis of these mechanisms may take years to form under natural circumstances and can lead to significant financial costs (Holtz, 1983).

Constitutive models abound in the literature for unsaturated soils. A complete review cannot be completed here but a comparison of selected volume change equations is presented. Here it is also noted that we hold no preference over a net stress and suction approach or an effective stress approach.

Firstly the development of a constitutive model should ideally extend from accepted saturated soil models. The most common of which are the Cam Clay model proposed by Roscoe and Schofield (1963) and the Modified Cam Clay (MCC) model proposed by Roscoe and Burland (1968). The isotropic volume change adopted by MCC takes a linear relationship between specific volume and the logarithm of effective stress:

$$v = N - \lambda \ln p' \tag{1}$$

where v is the specific volume, N is the specific volume when $p' = 1$ kPa typically, λ is the slope of the normal compression line (NCL) and p' is the effective mean stress. Modifications of this model have been proposed to capture the distinct behaviors of structured soils (e.g., Rouainia and Wood, 2000, Liu and Carter, 2002).

In terms of models for unsaturated soils, by far the most widely cited model is the Barcelona Basic Model (BBM) proposed by Alonso et al. (1990). This model does suffer from the limitations that it does not incorporate the hydraulic behavior and an ever increasing collapse volume predicted. The latter of which can be overcome through the selection of parameters (Wheeler et al., 2002). Coupling the BBM with a hydraulic model is however difficult (Vaunat et al., 2000, Gens, 2010). The BBM separates the effects of net stress and suction on the volume change behavior through the equation:

$$v = N(s) - \lambda(s) \ln \frac{\overline{p}}{\overline{p}_c} \tag{2}$$

where $\overline{p}$ is the mean net stress, $N(s)$ is the specific volume at suction s and net stress $\overline{p}_c$, and $\lambda(s)$ is the compression index as a function of suction. In the original model $\lambda(s)$ was assumed to reduce with increasing suction. Such a function ignores the key role played by the non-zero air-entry suction where for suctions less than the air-entry value the compressibility is equal to the saturated compressibility.

To capture the coupling between hydraulic and mechanical behaviors, neglected by the BBM, Wheeler et al. (2003) adopted a form of Bishop's effective stress (Bishop, 1959) and a modified suction.

$$p^* = \overline{p} + S_r s \tag{3}$$

and modified suction:

$$s^* = ns \tag{4}$$

where S_r is the degree of saturation, n is the porosity. The volume change equation adopted by Wheeler et al. is similar in form to the volume change equation of MCC (Equation 1) but is complicated through the coupled movement of the loading collapse (LC), suction-increase (SI) and suction-decrease (SD) yield surfaces and through the incorporation of both suction and degree of saturation into the effective stress.

To overcome some of the limitations of the both net stress and effective stress approaches Sheng et al. (2008) proposed an incremental form of the volume change equation for normally consolidated soils:

$$d\varepsilon_v = -\frac{dv}{v_0} = \lambda_{vp} \frac{d\overline{p}}{\overline{p} + f(s)} + \lambda_{vs} \frac{ds}{\overline{p} + f(s)} \tag{5}$$

where λ_{vp} is the virgin compression index due to stress increase and λ_{vs} is the virgin compression index due to suction increase interpreted from a $d\varepsilon_v$: $\ln \overline{p}$ plot. The variation of λ_{vs} with suction is given by:

$$\lambda_{vs} = \begin{cases} \lambda_{vp} & s < s_{sa} \\ \lambda_{vp} \dfrac{s_{sa}}{s} & s \geq s_{sa} \end{cases} \tag{6}$$

where s_{sa} is defined by the saturation suction. The saturation suction (and air-entry value) are not intrinsic parameters which may depend on previous stress history of the soil (e.g., Ng and Pang, 2000), as shown with the results for Jossigny silt discussed below. In a hydro-mechanical coupled model, the water retention behavior is coupled with the stress-strain relationship and hence the saturation suction (or air-entry value) will change with stress or volume (Wheeler et al., 2003, Sheng and Zhou, 2011).

In Equation 5 originally Sheng et al. adopted $f(s) = s$ for the term in the denominator. This function was shown by Zhou and Sheng (2009) to provide a reasonable prediction of a number of sets of data. There is one specific limitation with the adoption of this function and that is that there is a discontinuity between saturated and unsaturated states. To overcome this Sheng (2011) suggested an alternative form of $f(s) = sS_r$ be adopted. In addition the loading-collapse (LC) and zero shear strength functions may be derived from the SFG model:

$$\bar{p}_y = \begin{cases} \bar{p}_{y0} - s & s < s_{sa} \\ \bar{p}_{y0} - s_{sa} - s_{sa} \ln \dfrac{s}{s_{sa}} & s \geq s_{sa} \end{cases} \quad (7)$$

$$\bar{p}_0 = \begin{cases} -s & s < s_{sa} \\ -s_{sa} - s_{sa} \ln \dfrac{s}{s_{sa}} & s \geq s_{sa} \end{cases} \quad (8)$$

where $\bar{p}_y$ is taken at the LC yield surface and $\bar{p}_0$ the zero shear strength surface.

4 PREDICTIONS

To make predictions of the volume change of unsaturated soils a number of questions need to be answered. The separation of behavior into elastic (pre-yield) and plastic (post-yield) is of fundamental importance. The difficulty arises for compacted soils in providing an adequate definition of the yield stress based on the compaction history. This is particularly true for dynamic compaction when an effective stress approach is adopted. The suction experienced by the soil compacted on the wet side of optimum (high degree of saturation) is observed to decrease with increasing stress (Tarantino and De Col, 2008). However the suction on the dry side remains relatively constant (e.g., Romero et al., 1999) but is rarely measured throughout compaction. More commonly the suction is measured after compaction and unloading process at which point the suction has increased.

The data sets adopted for this comparison of the modified SFG volume change equations include Jennings and Burland (1962), Vicol (1990) and Cunningham (2000). In these data sets the interpretation of a yield stress is simplified as for Jennings and Burland the soils are compressed at the maximum suction experienced, Vicol the sample is dried during loading and for Cunningham the yield stress is below the air-entry value.

Jennings and Burland (1962) tested a silt and silty sand clay and a silty clay in one dimensional and isotropic compression. The samples were initially brought to the desired suction using a pressure membrane apparatus. The measured and predicted soil-water characteristic curve (SWCC) for the silty clay is shown in Figure 1(a). The SWCC was fitted using the Fredlund and Xing (1994) equation and with only three points reported should be considered a coarse estimate. The saturation suction is adopted for the SFG model; here however it is taken as equal to the air-entry value of 300 kPa.

The samples were trimmed and placed in a high pressure isotropic cell. No suction control was attempted through the test. Although suction was not controlled thorough the test of Jennings and Burland, from the test results of Sivakumar (1993) and Sharma (1998), albeit on compacted samples, the water content during compression at constant suction remained essentially constant. It may be assumed, with limited accuracy, that the suction remained constant through the compression phase. Interestingly Romero et al. (2011) identified that there appears to be a critical magnitude of suction, above which the water content-suction relationship is practically identical regardless of void ratio. The predictions are made based on the assumption that suction remains constant through compression.

The drying curve was also measured for one sample with the results shown in Figure 1(b). The predicted response according to Equation 8 is shown. The initial point for the drying curve was based on the void ratio at the liquid limit ($e_0 = w_L G_s$). The slope of the normal compression line (NCL) was estimated from the reconstituted sample ($C_c = 0.262$).

The results of the compression testing are shown in Figure 1(c) for the sample dried to an initial degree of saturation of 0.504 ($S_{r,i} = 0.504$). The predicted behavior provides as good approximation to the observed results. The predicted and observed results show the potential for collapse with the compression curve for the unsaturated soil crossing the NCL of the saturated sample. This so-called 'collapse' may not be due to the development of soil structure, rather the change of the soil compressibility with suction. In Equation 5, even if the compression index is assumed to be

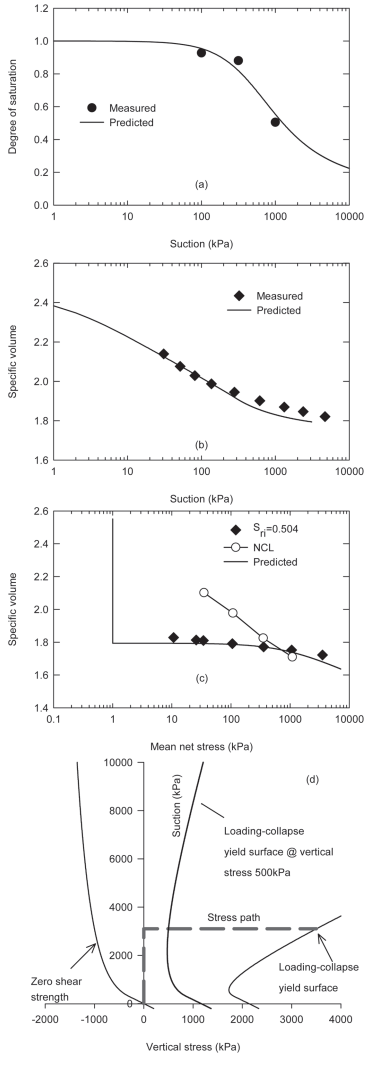

Figure 1. Data of Jennings and Burland (1962) $S_{ri} = 0.504$, a) Measured and predicted SWCC, b) Measured and predicted drying, c) Measured and predicted isotropic compression, d) Predicted evolution of modified SFG zero shear strength and loading-collapse yield surface.

constant, increasing suction will lead to a stiffer soil and hence a flatter NCL, due to the term $\bar{p} + f(s)$ in the denominator. Examining this in relation to the LC yield surface obtained from Equation 8 in Figure 1(d), we can see that drying and loading was sufficient to flatten the LC yield surface. From Figure 1(c) we can see that the NCL and $S_{r,i} = 0.504$ curves crossed at a vertical stress of approximately 500 kPa. Plotting the yield surface at this point we see that it is essentially vertical in Figure 1(d) which indicates that on wetting the sample is likely to swell.

Jossigny silt from 25 km west of Paris was tested by Vicol (1990). Osmotic suction control was employed. The samples were prepared from slurry at roughly 1.5 times the liquid limit. Vicol completed drying at vertical stress of 50 kPa, 100 kPa and 200 kPa on normally consolidated and over consolidated samples.

The wetting branch of the SWCC for Jossigny silt was obtained by Vicol (1990) and also by Fleureau et al. (1993, 2002) with an interpreted saturation suction of around between 10 kPa (Vicol, 1990, Fleureau et al., 2002) and 100 kPa (Fleureau et al., 1993).

The predicted compression and drying of Jossigny silty is shown in Figure 2(a) and 2(b). The drying prediction has been completed for both saturation suctions due to the difficulty clarifying

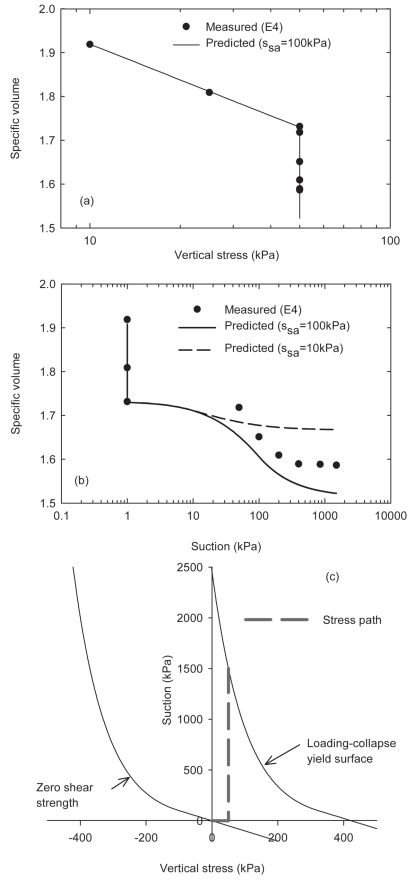

Figure 2. Jossigny silt sample E4 of Vicol (1990), a) Measured and predicted compression, b) Measured and predicted drying, c) Predicted Modified SFG zero shear strength and loading-collapse yield surface evolution.

which is more representative. The predictions provide an upper lower bound of the observed drying behavior. The characteristics of the behavior are however well predicted. The evolution of the LC yield surface is shown in Figure 2(c). It is interesting to note that the first drying process up to 100 kPa suction produces virtually no volume change. The volume change from drying to 50 kPa suction should be equal to the volume change caused by a stress change of the same magnitude, if the air entry value is larger than 50 kPa. However, the experimental results show much less volume change, which is inconsistent with the effective stress principle for saturated soils. Fleureau et al. (2002) tested the same soil, but observed much larger volume change during the first drying phase. The LC yield surface indicates no potential for collapse on wetting.

Cunningham (2000) completed a suite of laboratory tests on a blend of 70% silt, 20% Speswhite kaolin and 10% London clay reconstituted in the laboratory. The samples were prepared by first consolidating the reconstituted material mixed at a water content 1.5 times the liquid limit to a vertical stress of 200 kPa (mean stress of 130 kPa, $K_0 = 0.475$).

The SWCC is shown in Figure 3(a), with the SWCC fitted using the Fredlund and Xing (1994) equation. The air-entry value was interpreted as 400 kPa. The predicted and measured volume change for the sample tested at a suction of 650 kPa is shown in Figure 3(b). The evolution of the LC yield surface is shown in Figure 3(c). The yield point used for the predictions was a mean effective stress of 130 kPa. For this sample we see that there is a small potential for collapse developed through the flattening of the yield surface. The more pronounced behavior in a laboratory test during wetting may be swelling however.

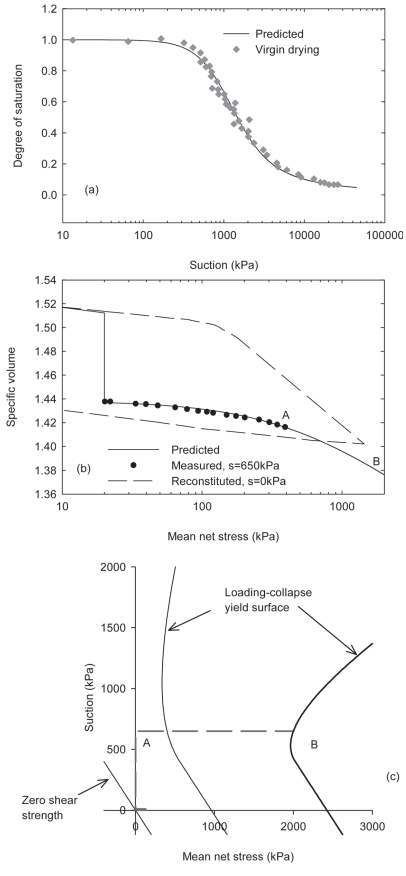

Figure 3. Data of Cunningham (2000), a) Measured and predicted SWCC, b) Measured and predicted isotropic compression, c) Predicted evolution of modified SFG zero shear strength and loading-collapse yield surfaces.

5 DISCUSSION

From a review of the literature on reconstituted unsaturated soils, and the predictions made, the following points are noted:

- Drying a reconstituted soil to sufficiently high suction and then compressing it to sufficiently high stress can make the soil 'collapsible'. This collapsibility is due to the change of the soil stiffness with suction, rather than the soil structure.
- For collapse to occur relatively low saturation suction is required—this point defines the inflexion point on the LC yield surface. Or a relatively high vertical stress is required—but not so high that compression of the macro-pores has already been completed.
- In the case of Cunningham's the evolution of the LC yield surface using the SFG model predicts that for these materials the dominant behavior likely to be observed in the laboratory tests, had wetting been completed, would have been swelling.

6 CONCLUSIONS

The volume change behavior of a number of reconstituted soils has been collated and discussed. Predications of the behavior have been made using a modified form of the volume change equations originally presented in the SFG model.

While the results of testing on reconstituted may not exhibit the potential for collapse at the stress ranges commonly tested in the laboratory,

the testing of reconstituted soils avoids some of the problems associated with the definition of structure in compacted soils.

A simple modification to the proposed SFG model has been found to equally well predict the observed volume change behavior of unsaturated reconstituted soils.

REFERENCES

Alonso, E.E., Gens, A. & Josa, A. 1990. A constitutive model for partially saturatred soils. *Géotechnique*, 40, 405–430.

Bishop, A.W. 1959. The principle of effective stress. *Tecknish Ukeblad*, 106, 859–863.

Cerato, A.B. & Lutenegger, A.J. 2004. Determining intrinsic compressibility of fine-grained soils. *Journal of Geotechnical and Geoenvironmental Engineering*, 130, 872–877.

Cunningham, M.R. 2000. *The mechanical behaviour of a reconstituted, unsaturated soil*. PhD Thesis, Imperial College of Science, Technology and Medicine, London.

Fleureau, J.M., Kheirbeksaoud, S., Soemitro, R. & Taibi, S. 1993. Behavior of clayey soils on drying–wetting paths. *Canadian Geotechnical Journal*, 30, 287–296.

Fleureau, J.M., Verbrugge, J.C., Huergo, P.J., Correia, A.G. & Kheirbek-Saoud, S. 2002. Aspects of the behaviour of compacted clayey soils on drying and wetting paths. *Canadian Geotechnical Journal*, 39, 1341–1357.

Fredlund, D. & Xing, A.Q. 1994. Equations for the soil-water characteristic curve. *Canadian Geotechnical Journal*, 31, 521–532.

Gens, A. Some issues in constitutive modelling of unsaturated soils. *In*: Buzzi, O., Fityus, S. & Sheng, D., eds. Unsaturated Soils: Theoretical and Numerical Advances in Unsaturated Soil Mechanics, 2010. 613–626.

Holtz, W.G. 1983. The influence of vegetation on the swelling and shrinking of clays in the United States of America. *Geotechnique*, 33, 159–163.

Hong, Z.S., Yin, J. & Cui, Y.J. 2010. Compression behaviour of reconstituted soils at high initial water contents. *Geotechnique*, 60, 691–700.

Jennings, J.E.B. & Burland, J.B. 1962. Limitations to the use of effective stresses in partly saturated soils. *Géotechnique*, 12, 125–144.

Jotisankasa, A. 2005. *Collapse behaviour of a compacted silty clay*. PhD Thesis, Imperial College London.

Leroueil, S. & Vaughan, P.R. 1990. The general and congruent effects of structure in natural soils and weak rocks. *Geotechnique*, 40, 467–488.

Liu, M.D. & Carter, J.P. 2002. A structured Cam Clay model. *Canadian Geotechnical Journal*, 39, 1313–1332.

Mitchell, J.K. & Soga, K. 2005. Fundamentals of Soil Behavior (3rd Edition). John Wiley & Sons.

Ng, C.W.W. & Pang, Y.W. 2000. Influence of stress state on soil-water characteristics and slope stability. *Journal of Geotechnical and Geoenvironmental Engineering*, 126, 157–166.

Romero, E., Gens, A. & Lloret, A. 1999. Water permeability, water retention and microstructure of unsaturated compacted Boom clay. *Engineering Geology*, 54, 117–127.

Romero, E., Della Vecchia, G. & Jommi, C. 2011. An insight into the water retention properties of compacted clayey soils. *Geotechnique*, 61, 313–328.

Roscoe, K.H. & Schofield, A.N. Mechanical behaviour of an idealised 'wet clay'. Proc. 2nd European Conf. on Soil Mechanics and Foundation Engineering, Wiesbaden, 1963. 47–54.

Roscoe, K.H. & Burland, J.B. On the generalised stress-strain behaviour of wet clay. *In*: Heyman, J. & Leckie, F.A., eds. Engineering Plasticity, 1968 Cambridge. Cambridge University Press, 535–609.

Rouainia, M. & Wood, D.M. 2000. A kinematic hardening constitutive model for natural clays with loss of structure. *Geotechnique*, 50, 153–164.

Sharma, R.S. 1998. *Mechanical Behaviour of Unsaturated Highly Expansive Clays* Doctor of Philosophy PhD Thesis, University of Oxford.

Sheng, D., Fredlund, D.G. & Gens, A. 2008. A new modelling approach for unsaturated soils using independent stress variables. *Canadian Geotechnical Journal*, 45, 511–534.

Sheng, D. 2011. Review of fundamental principles in modelling unsaturated soil behaviour. *Computers and Geotechnics*, 38, 757–776.

Sheng, D. & Zhou, A.-N. 2011. Coupling hydraulic with mechanical models for unsaturated soils. *Canadian Geotechnical Journal*, 48, 826–840.

Sivakumar, V. 1993. *A critical state framework for unsaturated soils*. PhD Thesis, University of Sheffield.

Tarantino, A. & De Col, E. 2008. Compaction behaviour of clay. *Geotechnique*, 58, 199–213.

Tarantino, A. Compacted versus reconstituted states. *In*: Alonso, E.E. & Gens, A., eds. Unsaturated Soils, 2011. CRC Press, 113–136.

Vaunat, J., Romero, E.E. & Jommi, C. An elastoplastic hydromechanical model for unsaturated soils. *In*: Tarantino, A. & Mancuso, C., eds. Experimental evidence and theoretical approaches in unsaturated soils., 2000. Rotterdam: Balkema, 121–138.

Vicol, P.T. 1990. Comportement Hydraulique et Mechanique D'un Sol Fin Non Sature: Application a la Modelisation. Thèse de doctorat, École Nationale des Ponts et Chaussée, Paris, France.

Wheeler, S.J., Gallipoli, D. & Karstunen, M. 2002. Comments on use of the Barcelona Basic Model for unsaturated soils. *International Journal for Numerical and Analytical Methods in Geomechanics*, 26, 1561–1571.

Wheeler, S.J., Sharma, R.S. & Buisson, M.S.R. 2003. Coupling of hydraulic hysteresis and stress-strain behaviour in unsaturated soils. *Geotechnique*, 53, 41–54.

Zhou, A.N. & Sheng, D.C. 2009. Yield stress, volume change, and shear strength behaviour of unsaturated soils: validation of the SFG model. *Canadian Geotechnical Journal*, 46, 1034–1045.

Advances in Unsaturated Soils – Caicedo et al. (eds)
© 2013 Taylor & Francis Group, London, ISBN 978-0-415-62095-6

Micromechanical study of the compressibility of unsaturated granular materials

R. Barata & R. Cardoso
Instituto Superior Técnico, Technical University of Lisbon, Lisbon, Portugal

ABSTRACT: The compressibility of granular soils is studied by adopting a micromechanical approach in which soil is considered as a set of particles and volume changes result from their interaction. Oedometric tests were performed in four different granular materials which grains have different stiffness and water sensitivity. The tests were performed in dry (relative humidity of the laboratory) and in saturated conditions in order to analyze how full saturation and stress changes affect the compressibility of individual grains and thus explain global compressibility. Other complementary tests were performed where the changes in grains stiffness and geometry due to the different loading paths were investigated to explain the volumetric changes measured in the oedometer tests.

1 INTRODUCTION

The mechanics of continuum media provides the framework to solve the large majority of equations used to solve soil mechanics problems. This is a macromechanical approach because soil is a particulate media and the contribution of single particles to global behaviour is not taken into account in a direct manner. With computational advances, the use of discrete elements methods to solve problems related to soils is becoming more feasible and can provide alternative methods to solve engineering problems in granular materials. This happens because some particularities of behaviour can be better reproduced when the presence of grains is considered explictly.

The most important engineering properties of granular materials, such as stress-strain and strength behaviour, volumetric changes and permeability variations, depend on the integrity of the particles or the amount of particle crushing due to stress changes (Lade et al., 1996). For soils, the intergranular stress provides shear and compressive strength, and any change in linear and volumetric strains is controlled by these stresses (Lade & de Boer 1997).

Fragments of four different granular materials are investigated (Fig. 1): Abadia marls, dry kaolin, limestone (gravel) and LECA (Lightweight Expanded Clay Aggregate). Marls and kaolin were chosen because their grains suffer physical degradation in contact with water and therefore the granular material becomes a clayey material after full saturation. The two other materials were chosen because their fragments do not degrade in the presence of water and therefore the granular structure of the aggregate when wetted is not lost.

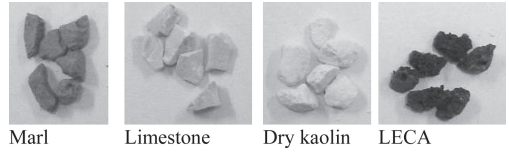

Figure 1. Fragments of the materials tested (2 mm < D < 4,5 mm).

Oedometric tests were performed, in dry and saturated conditions. They were complemented with saturated permeability tests, the measurement of grading size distribution after the different stress paths applied and with crushing tests of the grains with the two suctions. The interpretation of the results allows identifying how grains are affected by stress and wetting and how their behaviour affects the volumetric behaviour of the granular medium.

2 GRAINS AND GRANULAR STRUCTURE

Compressibility of soils is usually represented by plotting specific volume or void ratio against the logarithm of mean stress or vertical effective stress, as shown in Figure 2. In this figure, region 1 indicates small deformations mainly due to particle rearrangement. Stress increases until yielding stress, which is identified by a change in the slope of the curves and is when region 2 is attained. In this

region void ratio decreases with stress increment at a higher rate. Also, irrecoverable deformations occur when stress increments are in region 2. The curve in region 2 corresponds to the normal compression line and its slope is the compressibility index, C_c. When stress continues to increase, the curve shows another slope change because the void ratio starts to decrease at a lower rate. This is evident for the dense carbonate sand which differs from silica sand since the crushing resistance of carbonate sand grains is smaller than that of silica grains. Grain crushing due to loading corresponds to clastic yielding, where most irrecoverable deformations occur.

The interpretation of plots showed in Figure 2 explains soil behaviour from a micromechanical point of view, which is the approach followed in this study. However the use in practice of the curves consists in a macromechanical approach because there is no need to consider the existence of the grains or fragments of the material, neither their breakage nor interaction.

Lade et al. (1996) showed that the amount of particle crushing is affected by stress level (proximity to failure), stress magnitude and stress path. These authors indicated that larger grains have higher probability of having imperfections and therefore higher probabilities of breaking than smaller grains. Adding to this, well-graded soils do not break down as easily as uniformly graded soils and, as the relative density increases, the amount of particle breakage decreases. Both these factors are based on the fact that with more particles surrounding each particle (large coordination number or large number of neighbours), the average stress tends to decrease. This was also established by McDowell et al. (1996).

Rocks physical weathering results in their breakage and disaggregation. The resulting fragments or grains have more or less strength depending on the rock type. For example, grains coming from hard rocks have more strength and therefore are less compressible than those that came from soft rocks. Therefore, stress affects differently the grains according to their nature. Water presence also affects the grain mechanical properties. Grains coming from rocks with clayey minerals are more alike to be softened when wetted. On the other hand, for materials without clay minerals, such as those usually used as rockfills, water accelerates crack propagation and thus accelerates particle breakage. This phenomenon is known as "water corrosion" (Oldecop & Alonso 2001). It can be concluded that in materials with no clay minerals (such as hard rocks), water enhances crack opening. However many other granular materials, including very dry clayey materials, can show this type of behaviour.

To conclude, soils are made of grains. Their global volumetric behaviour can be explained by changes in granular rearrangement mainly caused by stress changes and wetting. Grains rearrangement (their shape do not change), breakage (division into smaller grains), erosion (detachment of small pieces of a grain) or be softening (loss of internal bonds), depend on their nature. Some of those behaviours can coexist. With the tests performed in this study, the mechanisms mentioned will be seen and further explained in results analysis.

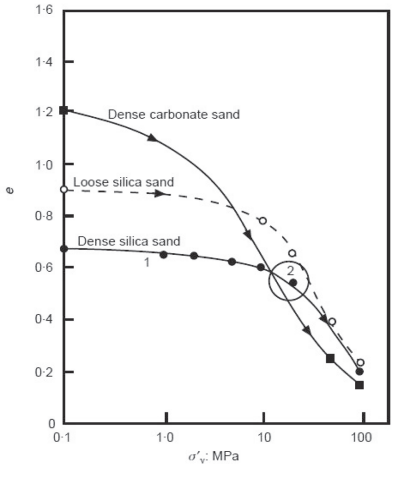

Figure 2. One-dimensional compression plots for different granular materials (McDowell & Bolton 1998)

3 CHARACTERIZATION OF THE MATERIALS

Fragments of Abadia marls, limestone gravel, dry kaolin aggregates and LECA were studied.

Abadia marls from Arruda dos Vinhos (Portugal) are classified as hard-soils/soft-rocks. The mechanical and hydraulic proprieties of marls change due to wetting-drying cycles, among others weathering processes. This evolutive behaviour is characterized by crack opening and/or loss of bonding, having in general negative impact on the strength and compressibility of the material. The mineral composition of Abadia marls is quartz, calcite, rutile, gypsum and clay minerals. The existing expansive minerals are montmorillonite and gypsum. The marls specific density is 2.74 (Cardoso 2009). When sets of fragments of Abadia marls are dried and intact they behave as rockfill materials. However, when suction cycles or stress changes are applied they become soft and

the degraded material behaves such as compacted clays (Cardoso 2009). Important deformations will occur due to softening therefore it is expected to see important volume changes due to breakage and particles rearrangement.

The gravel studied in this paper is a crushed limestone used for concrete production. The specific density of this gravel limestone is estimated to be 2.75 and its porosity is very low.

Kaolin is a white clay mineral often used in the ceramic industry, as well as in rubber industry. Kaolin specific density is 2.63. Mercury Intrusion Porosimetry (MIP) tests were performed in dry aggregates. They are in accordance with its clayey nature.

LECA is an aggregate of natural clay expanded by thermal treatment. The specific density of this material is 1.70. LECA is generally presented as a set of round shaped elements. Every one of these elements is composed by a vitreous cover surrounding a porous core, as seen on Figure 3. The pore geometry, induced by the fabric process, makes the full saturation of this material very difficult. As the material loses water, capillary forces retain the water in the pores (Caldeira et al., 2010). The main minerals existing in LECA elements are silicate in vitreous phase, heronite, iron oxide, quartz and feldspars. Clayey minerals are almost absent and LECA matrix is non-plastic. More detailed information about these materials can be found in Barata (2011).

4 SAMPLES PREPARATION

Mainly oedometric tests were performed in this study, which information provided was complemented with crushing and permeability tests. Four samples of each material were prepared by adopting a uniform grading size distribution (between 2 mm and 4.75 mm).

The specimens of the four materials were prepared with similar void ratios in order to compare their compressibility, considering only the influence of the grains nature. Nevertheless, even if each material has similar grain size, their grain shapes are not similar and therefore the initial rearrangement can be different. Void ratio e provides an indirect measurement of this rearrangement, however it accounts with the voids between the fragments (macrostructural void ratio e^M) and the voids of the fragments (microstructural void ratio e^m). For this reason, void ratio is the sum of the last two ($e = e^M+e^m$) and specimens preparation must take into account the macroscopical void ratio instead of e because of the different nature of grains used. Similar e^M indicates similar number of neighbours for each grain independently from the material.

Void ratio, e, can be estimated using Equation 1,

$$e = \frac{G_s \times \gamma_w}{\gamma_d} - 1 \quad (1)$$

where G_s is the specific density, γ_w the water unit weight and γ_d the dry unit weight of the material. Therefore it is controlled through the soil mass to be set within the oedometer ring (73.12 cm^3 volume). Abadia marls were the first material tested and are adopted as reference. The mass of fragments of Abadia marls set within the oedometer was 92.7 g, which corresponds to a void ratio of 1.16.

The number of particles contained in the oedometer ring can be estimated dividing the total mass by the mass of a single particle (average values in Table 1, measured in a set of 50 and 100 fragments (Barata 2011). During samples preparation the mass proportions could not be attained (total mass in relation to Abadia marls in Table 1) since the grains of each different material have different shape, stiffness and strength and thus break or adjust differently during sample preparation process. The real mass in the oedometers for each material is the one indicated in the first row of Table 1 and the number of particles indicated in that table was estimated using that real total mass and the mass of individual particles. Finally, it is possible to determine the microstructural void ratio (Table 1) (Barata 2011). As seen in this table, the materials

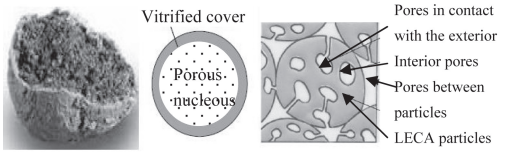

Figure 3. LECA detail (Caldeira *et al.,* 2010).

Table 1. Computation of the number of particles in the rings.

	Marls	Gravel	Kaolin	LECA
Mass inside the ring (g)	92.7	122.7	79.8	29.0
Mass of a single particle (g)	0.064	0.101	0.072	0.019
Particles per unit volume (nr/cm^3)	19.6	16.6	15.2	20.9
Total void ratio e	1.16	0.64	1.41	3.28
Microvoid ratio e^m	0.596	0.003	0.671	2.517
Macrovoid ratio e^M	0.564	0.637	0.739	0.762

with high total void ratios have also high microvoid ratios (which mean they are porous). Comparing the macrovoid ratios they are considered to be similar enough so that results of tests performed on the different samples can be compared.

Since the microstructural value is very different for each material type, another way to achieve similar granular structures for the materials is to prepare specimens with the same number of grains. This corresponds, for the same value, to similar number of contacts between particles. The number of particles was not counted because they were more than 1000 for each sample and for this reason it was estimated indirectly through the mass placed in the oedometer ring. The estimated mass of one single particle of each material can be seen in Table 1. The proportional mass in relation to Abadia marls is 1.58 for gravel, 1.13 for kaolin and 0.29 for LECA. As observed in Table 1, the number of grains is slightly different for each granular material studied. It can be admitted that differences will not significantly affect the results, at least in qualitative manner.

5 EXPERIMENTAL RESULTS

5.1 *Compressibility*

Oedometric tests were performed in dry and saturated environment for each material. Samples were prepared as indicated previously in Table 1. The increment of vertical stress was applied with 48 h interval. Maximum vertical stress reached was 1.18 MPa. The samples to be tested under saturated conditions were fully saturated by imbibition with distilled water for 48 h under the vertical stress of 12.5 kPa. Initial suction was 85 MPa corresponding to the relative humidity of the laboratory (HR = 56%, T = 20ºC).

Compressibility index, C_c, swelling index, C_s, and time-dependent compressibility index, λ^t were measured. The results of all the oedometric tests performed are plotted in Figure 4. The compressibility and swelling indexes C_c and C_s are shown in Table 2 as well as the effective yielding stress, σ'_y. For the dry material it is assumed that effective stress is equal to total stress as there is no water in the voids between the fragments ($u = 0$).

From the analysis of Table 2 and Figure 4, the four materials can be divided into two groups. One containing Abadia marls and kaolin, because they are water sensitive, and another containing gravel and LECA, since they do not seem to be water sensitive. The compression indexes obtained from saturated tests of the water sensitive materials marls and kaolin are very similar to the compression indexes obtained in tests performed with reconstituted materials for marls (Cardoso 2009) and kaolin, also presented in Table 2. This confirms structure loss.

The materials from the first group show similar compression indexes when dry and saturated tests are compared separately and they both suffered collapse when wetted under the vertical stress of 12.5 kPa. This means that water disrupts fragments physically. The grains lose internal boundaries, therefore become softer and thus the set of fragments become similar to clayey materials. Figure 5 shows the different granular structures observed for marl fragments. Initial structure is shown in Figure 5a. The increment of vertical stress in dry conditions leads to significant crushing but fragments can still be distinguished (Fig. 5b). The individual fragments are no longer visible if vertical stress is applied in full saturated conditions (Fig. 5c). Similar behaviour was observed for kaolin.

For kaolin, the disruption of its structure does not only occur if water is present. In fact, at the

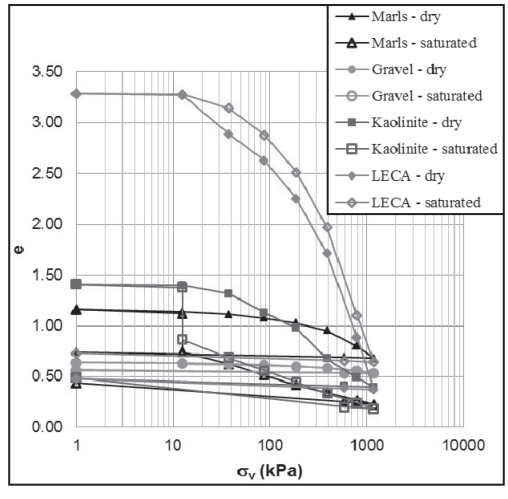

Figure 4. Results of the oedometric tests performed for all the materials.

Table 2. Data from the oedometer tests.

		Marls	Gravel	Kaolin	LECA
Dry test	C_c	0.670	0.140	0.526	2.870
	C_s	0.030	0.017	0.042	0.037
	σ'_y (kPa)	230	300	55	120
Saturated test	C_c	0.223	0.135	0.320	2.554
	C_s	0.082	0.017	0.062	0.044
	σ'_y (kPa)	–	260	–	120
Reconstituted	C_c	0.325	–	0.323	–

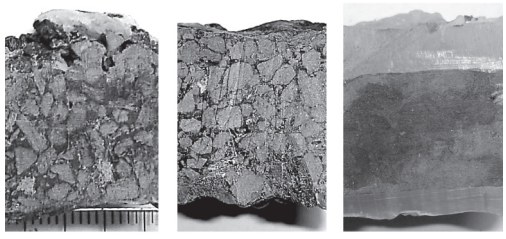

a) Dry - no load b) Dry with loading c) Wet with loading

Figure 5. Structural changes suffered by marl aggregates subjected to different loading conditions.

vertical stress of 387.5 kPa an inflexion can be observed, which means the void ratio starts to decrease with further stress increment. This can be explained by severe particles crushing and higher strain energy is necessary for further crushing. This will also be observed in the next sections.

The second group, containing gravel and LECA, does not seem to be water sensitive because the results of each material have no significant differences between their dry and wet tests. The higher compressibility of LECA is explained by particle breakage, erosion and rearrangement. Since the maximum tension attained in oedometric tests did not reach the maximum strength of gravel, the volume changes observed during the compression of this granular material is only due to rearrangement.

Another distinction can be made for the four materials when dry tests are analysed. Marls and gravel are much more resistant than kaolin and LECA. The mineral composition and the compacted structure of each grain explain the strength of the first two materials and this strength explains the lower decrease in void ratios for marls and gravel, unlike the observed for kaolin and LECA ($\Delta e_{marls} = 0.481$; $\Delta e_{gravel} = 0.104$; $\Delta e_{kaolin} = 1.013$; $\Delta e_{LECA} = 2.914$).

5.2 *Grading size distribution and crushing tests*

For granular materials such as those studied in this work, applied stress is equilibrated by intergranular forces. These forces can increase with applied stress and can be very large, explaining therefore particle breakage or even crushing. For this reason, changes in grading size distribution caused by loading and/or wetting depend on the strength of the fragments of the granular material. Those changes can be described by the Hardin index, B_r, which measures particles relative breakage having initial grading size distribution curve as reference (McDowell et al., 1996). That index varies between 0 (no breakage) and 1 (theoretical limit of full breakage).

The Hardin indexes presented in Table 3 were computed considering the results of the tests previously presented in Figure 4, as well as for the case of the full saturated material where vertical stress was not applied. They show that gravel is the material which fragments break less, marls are the material which fragments break more but only when fully wetted, high breakage is found for kaolin for both dry and saturated tests, as well as for LECA. For this last material, however, breakage occurs only when vertical stress is applied. Also, erosion occurs besides breakage due to its porous matrix and is independent from water presence. Detached grains rearrange and thus explain the large reduction in void ratio observed in the oedometer tests.

The differences observed can be explained by the individual strength of particles. Crushing tests were performed on single particles of the different materials (Barata 2011). These tests were performed on dry and saturated conditions and the results are presented in Table 4. The measured strength follows the sequence gravel, marls, LECA, kaolin, from the strongest to the weakest dry material, and follows the sequence gravel, LECA, marls, kaolin, from the strongest to the weakest wet material. LECA and gravel have approximately the same strength either dry or wet, but marls and kaolin have both three times more strength dried then when wetted. This data is in accordance with the compressibility values obtained for the different materials (see Table 2) and confirms the micromechanical origin of the volumetric behaviour of the granular materials studied.

The results of the crushing tests confirm the changes in grading sizes distribution curves. Gravel is the strongest material, dry or wet, thus it was expected to be the material with the lowest relative breakage. On the other hand, kaolin is the material with lowest strength; however this material

Table 3. Hardin indexes, B_r.

Test	Marls	Gravel	Kaolin	LECA
Dry*	0.191	0.007	0.398	0.351
Saturated**	0.460	0.000	0.329	0.019
Saturated*	0.495	0.009	0.278	0.347

* after the oedometer test; ** without any stress increment.

Table 4. Compressive strength measured in the crushing tests.

	Marls	Gravel	Kaolin	LECA
Dry (kN)	0.093	0.490	0.008	0.070
Saturated (kN)	0.030	0.490	0.003	0.052

presents the highest B_r only for the dry test, which can be explained by experimental error during sieving process. The differences observed by comparing the water sensitive materials, kaolin and marls, were not expected because B_r should increase for the full saturated case. In fact, after wetting marls, individual grains are still visible, whereas for kaolin this is not possible. This result is expected because kaolin grains become softer than marls grains because this soft rock preserves some bonds after wetting.

Gravel shows practically no breakage increase and LECA almost none when wetted without any load. This corroborates the fact that they are not water-sensitive. Since gravel is stronger than LECA it has lowers B_r but greater than 0. These are explained by abrasion that occurs due to particle rearrangement forced by the loading. For LECA, the high B_r is explained by particle breakage and erosion.

5.3 *Permeability*

Void ratio and its evolution with loading affect the circulation of water between the large pores of the granular materials studied. Therefore, the comparison of the values of saturated permeability is another way of comparing structural changes associated to grain breakage and softening.

Taylor's method was used to derive saturated permeability of the marls and kaolin from the saturated oedometer tests, for which the values for the initial and final loading in fully saturated conditions are presented in Table 5. Permeability of Abadia marls and kaolin decreases about 10,000 times with stress increment. Water and stress applied destroy their granular structure. The aggregate material becomes a clayey soil, which is in accordance with the permeability value measured (about 10^{-12}) usual for clayey materials.

Saturated permeability was measured in a permeameter cell for the gravel and LECA, without loading, because the fragments do not convert into clay and therefore Taylor's method is not valid. These two materials show a permeability expected for coarse sands, as expected accordingly with their grading size distribution curves.

The reduction in void ratio during the test experienced by the marls and kaolin explains the strong permeability reduction during the increment of vertical stress. The higher the void ratio reduction, the higher is the permeability reduction. Therefore it can be expected that permeability of gravel does not change meaningfully during the experiment, but the permeability of LECA probably reduces significantly. Nevertheless LECA has no clay minerals in its constitution, thus have no high water absorption capacity and therefore its final permeability is probably higher than those of the marls and kaolin.

Table 5. Permeability according to test instant (m/s).

	Marls	Gravel	Kaolin	LECA
initial	8.2×10^{-8}	4.87×10^{-7}	1.3×10^{-8}	4.53×10^{-7}
final	2.4×10^{-12}	–	5.7×10^{-12}	–
Δe	0.515	0.099	0.682	2.632

5.4 *Time-dependent compressibility*

Time-dependent compressibility index, λ^t (Eq. 2), against vertical stress is plotted in Figure 6. It indicates how these materials behave under constant stress during a certain time. The increment of this index with increasing vertical stress (slope of the linear relationship of the figure) indicates particles breakage (Oldecop & Alonso 2001).

$$\lambda^t = \frac{d\varepsilon}{d(\ln t)} \tag{2}$$

It can be observed that the compressibility evolution in time of all the materials, when dried, is function of applied stress. This is a rockfill-type behaviour, expected because the grains of the granular materials break and rearrange under constant stress.

Increasing slopes of the linear relationships in Figure 6 are in accordance with fragments strengths. In fact, gravel is the strongest material and water insensitive, and therefore the linear relationship is almost horizontal. After gravel come the marls, then LECA and kaolin, at the end, with the highest slope.

Gravel and LECA show similar behaviour whether they are dry or wet, i.e. their time-strain

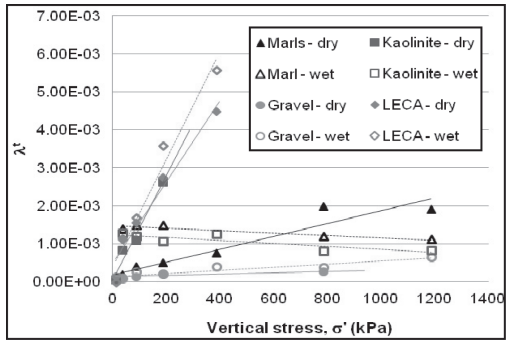

Figure 6. Time-dependent compressibility versus vertical stress: dry (—) and wet (- - -).

relationship is stress dependent. Nevertheless, the slopes of the linear relationships are higher when water is present, which means their grains break and rearrange more easily with water. This is the rockfill-type behaviour mentioned, and water is acting as a corrosive agent. When fully saturated, marls and kaolin develop strains regardless of stress level. This can be explained by the fact that these two materials when wetted behave as clayey materials in which viscous effects rule the volumetric behaviour instead of fragments breakage.

6 CONCLUSIONS

The compressibility of the granular materials studied can be explained from a micromechanical point of view. Deformations due to particle breakage and some erosion occur for materials that have some stiffness but have low strength in comparison with the stresses applied. This is the main mechanism for all the materials when dried. The deformations increase in full saturated conditions when crushing strength of the materials decrease due to their water sensitivity. For the marls and kaolin, water acts breaking internal bonds and the particles shape of these two materials change and the grains become softer. As consequence, these materials behaviour becomes similar to that of clayey materials, strong collapse deformations are observed with large reduction in the void ratio and compressibility becomes close to the value found for reconstituted materials.

REFERENCES

ASTM (1998). Standard Test Method for Particle-Size Analysis of Soils. Designation: D422–63.

Barata, R. (2011). Micromechanical explanation for the compressibility of granular materials. MSc Thesis, Instituto Superior Técnico, Lisbon.(in Portuguese).

Caldeira, L., Cardoso, R. & Maranha das Neves, E. (2010). Comportamento estrutural de aterros de argila expandida (LECA). 12th Nac. Cong of Geotechnics (in Portuguese).

Cardoso, R. (2009). Hydro-mechanical behaviour of compacted marls. PhD Thesis. Instituto Superior Técnico, Lisbon.

Lade, P.V. & de Boer,R. (1997). The concept of effective stress for soil, concrete and rock. Géotechnique 47(1), 61–78.

Lade, P., Yamamuro, J. & Bopp, P. (1996). Significance of Particle Crushing in Granular Materials. Journal of Geotechnical Engineering.

McDowell, G.R. & Bolton, M.D. (1998). On the micromechanics of crushable aggregates. Géotechnique 48(5), 667–679.

McDowell, G.R., Bolton, M.D. & Robertson D. (1996). The Fractal Crushing of Granular Materials. J. Mech. Phys. Solids, Vol. 44, No. 12, pp. 2079–2106.

Oldecop, L.A. & Alonso, E.E. (2001). A model to Rockfill Compressibility. Géotechnique 51(2), 127–139.

This page intentionally left blank

Advances in Unsaturated Soils – Caicedo et al. (eds)
© 2013 Taylor & Francis Group, London, ISBN 978-0-415-62095-6

Progressive emergence of double porosity in a silt during compaction

F. Casini, J. Vaunat & E. Romero
Departamento de Ingeniería del Terreno, Cartográfica y Geofisica, Universitat Politècnica de Catalunya, Barcelona, Spain

A. Desideri
Dipartimento di Ingegneria Strutturale e Geotecnica, Sapienza Università di Roma, Roma, Italy

ABSTRACT: The paper deals with an experimental investigation of water retention properties of a statically compacted unsaturated low plasticity silt. The objective is a deeper understanding of the evolution of an aggregate type fabric at different initial conditions in terms of void ratio and water content. A series of Mercury Intrusion Porosimetry tests (MIP) were performed to provide information about factors influencing fabric changes (effect of mechanical stress due to sample compaction) and fabric-properties relationships (water re-tention curve related to porosimetry). The arrangements of aggregation/particles are also investigated with Environmental Scanning Electron Microscopy (ESEM). The experimental data has been used to calibrate a multimodal water retention model for aggregate which is obtained by linear superposition of sub-curves of the van Genuchten type modified. By comparing the WRC obtained by MIP and under suction controlled conditions it has been found a good agreement between the two method for the drying path.

1 INTRODUCTION

The soil structure of compacted soils depends on void ratio and water content at compaction. The ad-vent of techniques such as mercury intrusion porosimetry (MIP), useful to study the pore size distribution, and environmental scanning electron microscopy (ESEM), able to visualize microstructural features at different hydraulic state led to important understanding of the soil structure evolution during hydro-mechanical paths (e.g., Monray et al., 2010; Casini et al., 2012).

The structure of most coarse-grained, or granular, soils display a mono-modal pore size distribution, as there is little tendency of the grains to adhere to each other and to form aggregates. The actual arrangement and internal mode of packing of the grains de-pends upon the distribution of grain sizes and shapes, as well as upon the manner in which the material has been deposited or formed in place. In soils with an appreciable content of clay, the primary particles tend, under favorable circumstances, to group themselves into structural units known as secondary particles, or aggregates. Such aggregates are not characterized by any universally fixed size, nor are they necessarily stable. The visible aggregates, which are generally of the order of several millimeters to several centimeters in diameter, are often called peds, or macro-aggregates.

As pointed out by various author (e.g., Romero et al., 2000) two main mechanisms generally govern the storage of water inside a soil: the first mechanism is mainly related to free water flow inside the macropores between aggregates/grain; the second one is related to water adsorption at the intra-aggregate level. While the second mechanism is virtually independent of the void ratio, the first one is coupled with the mechanical response of the soil (e.g., Vaunat et al., 2000; Casini 2012; Casini et al., 2012b).

In the literature few works on the microstructural behaviour on compaction are devoted to low activity soils with clay content less than 25%. These silty soils have a low tendency to form aggregates and are characterized by a mono-modal pore size distribution, which makes them no so attractive for the study of microstructural features. Nevertheless, under certain circumstances these low activity soils develop an aggregated structure (double porosity), which enhances their microstructural sensitivity to loading and water content changes. The current paper specifically focuses on the development and changes undergone on an aggregated structure induced by different initial conditions applied on a silty material. This kind of aggregated microstructure has important consequences on the water retention properties. To properly describe its evolving water retention character, a multimodal retention model is proposed by considering a

linear superposition of two sub-curves of the van Genuchten (1980) type, which allow having a better insight into the micro-structural features and their consequences at macro-structural level.

1.1 *Material*

The material used in the tests is an aeolian silt extracted from a layer of alluvial soil located at Jossigny, East of Paris, France. The behaviour of the saturated and unsaturated state of this material was studied by various authors (Cui (1993), Casini (2008), D'Onza et al., 2011).

The soil is classified as low plasticity silt (CL) (Figure 1) with presence of a significant fraction of clay (25%). Clay minerals determined by X-ray difractometry are illite, kaolinite and inter-stratified illitesmectite. No significant swelling properties have been observed on wetting (Cui and Delage, 1996). In situ water content is around 22%.

The grain size distribution of the soil and the grain size distribution function are reported in figure 1. The soil is classified as silty clay of low plasticity according to the USCS.

Several samples of Jossigny silt compacted at different void ratio and water contents were saturated for a vertical stress σ_v = 200 kPa by Casini (2008). The results of the saturation phase are reported in Figure 2 in the plane axial strain induced by saturation $\Delta\varepsilon_{asat}$ versus initial void ratio e_0. The samples exhibit collapse (compression) behaviour upon wetting that decreases with the initial void ratio.

1.2 *Experimental program*

Twenty MIP tests were performed at five different void ratios e (0.5–0.9) and four gravimetric water content w (%) (13–21) (Figure 3a). Some MIP tests have been also repeated adding dissolved salt (NaCl) 0.5–3 molar (circles in Figure 3). The tested sample, the saturation line and the Proctor curve are reported in Figure 3 in the plane void ratio e gravimetric water content w (%). The samples were prepared by one-dimensional static compression. The appropriate mass of loose soil was initially mixed to the target water content and then compacted statically with a press with the readings of the compaction forces. In figure 3b are reported the vertical stress needed to reach the target void ratio for each MIP sample. The compaction vertical stress increases as the void ratio decreases, changing the water content the trend is similar. The curves are shifted to the right as the wa-ter content decreases. The value range between 50 kPa (w = 21% e = 0.9) and 2800 kPa (w = 13 e = 0.5) (Casini et al., 2012).

Some MIP tests have been also repeated adding salt (NaCl) 0.5–3 molar (circles in Figure 3).

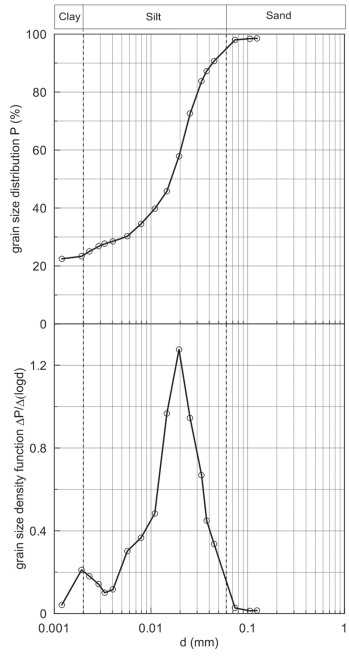

Figure 1. Jossigny silt: (a) Grain Size Distribution; Grain Size Density Function.

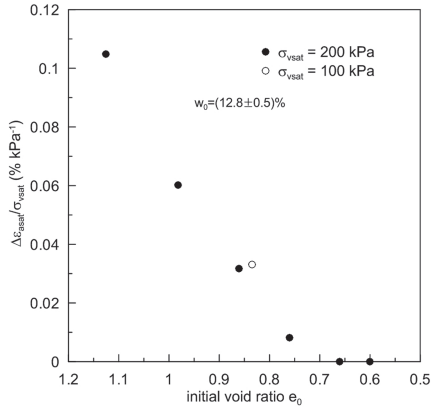

Figure 2. Deformation at saturation stage for different initial void ratios (after Casini et al., 2012).

The salt was added in order to modify the activity of the finer particle and to check if the structure is essentially related to the activity of the clay fraction. The salt has been used as an artificial way to deeper understand the phenomena of the double porosity emergency and its evolution. The salt was dissolved in the water and the mixture was added to the ovendried soil powder as for the others samples.

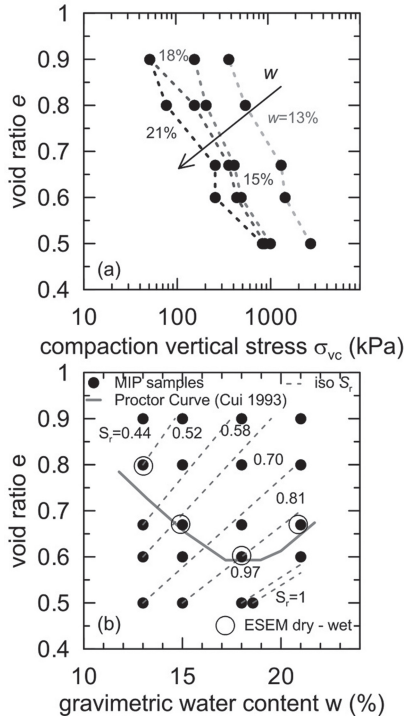

Figure 3. Tests: (a) MIP samples (with salt circle), ESEM (circle) with and without salt, Proctor Curve and iso Degree of Saturation Sr in the plane w–e; (b) compaction vertical stress measured versus void ratio measured for compacted the samples at target void ratio e and w.

2 EXPERIMENTAL RESULTS

In Figure 4 are reported the results of the MIP tests for the same gravimetric water content and different void ratio e in terms of $PSD^* = PSDenw/e$ where PSD = $-\Delta e_{nw}/\Delta(\log d)$ is the Pore Size Distribution, $e_{nw} = V_{nw}/V_s$ the void ratio of non wetting fluid, d the pore diameter, V_{nw} the volume of non wetting fluid and V_s the volume of solid particles. The shape of the PSD^* is given by w. It is interesting to note for the lower $w = 13\%$ the PSD^* is quasi mono-modal, the peak value is centered around a diameter $D = 5$ mm (about 25% of the bigger peak diameter of the grain size density function Fig. 4a) while as the w increase a new "pore family" appears ($w = 15\%$ Fig. 4b). This emergence of the double porosity move progressively as the water content increases ($w = 18\%$ Fig. 4c) and tend to disappear for $w = 21\%$.

The results are also reported in Figure 5 for the same void ratio and different water content. The curves trend are similar for the different void ratio. It is evident the quasi mono-modal structure of the lower water content which progressively

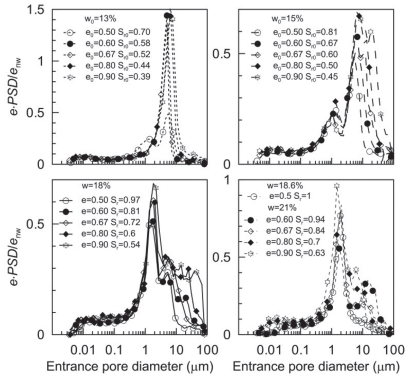

Figure 4. Normalised $PSD/enw \bullet e$ versus pore diameter for the same gravimetric water content w: (a) $w = 13\%$; (b) $w = 15\%$; (c) $w = 18\%$; (d) $w = 21\%$.

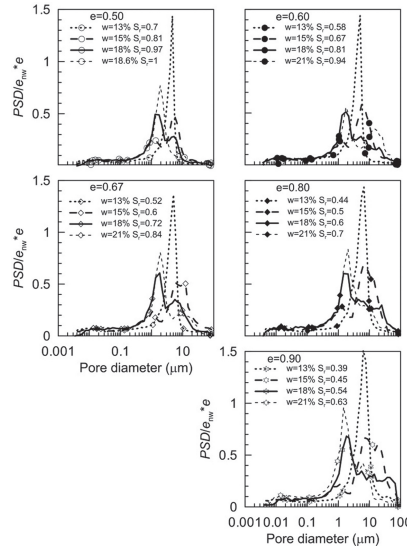

Figure 5. Normalised PSD/enw^*e versus pore diameter for the same void ratio e: (a) e = 0.50; (b) e = 0.60; (c) e = 0.67; (d) e = 0.80; (e) e = 0.90.

change to a double porosity structure where the macro (M) peak value move to D_M = 8–10 mm and a macro-micro (M_m) porosity emerge for a D_{Mm} = 1 mm. While for the higher water content the double porosity became narrow with a D_{Mm} = 1.5–2 mm and D_M = 7–9 mm (exception $e = 0.6$ $w = 21\%$).

The results are compared with the no-salty samples in figure 6 in order to investigate the stability of smaller pores with an elettrolitical solution. The structure related to the increasing water content and to the subsequent swell of the aggregates is inhibit by the presence of salt. The micro

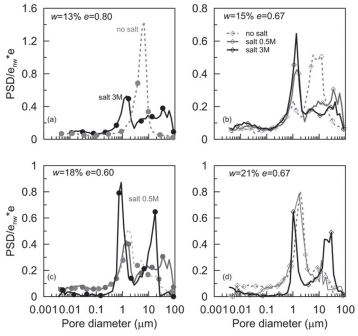

Figure 6. Comparison samples with-without dissolved salt *PSD** versus pore diameter: (a) w = 13%; e = 0.80; (b) w = 15%; e = 0.67; (c) w = 18%; e = 0.6; (d) w = 21%; e = 0.6.

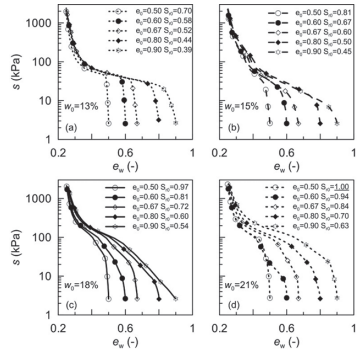

Figure 7. Drying path of Water Retention Curve deduced from MIP: (a) same water content.

aggregation is blocked. The pores size diameters are smaller with salt. During a drying process in salty soils the salt is deposited.

3 CONSEQUENCES ON WATER RETENTION PROPERTIES

The MIP results can be used to obtain the relationship between the suction and the degree of saturation or water content at constant void ratio. The mercury intrusion is assimilated to the air-intrusion (non-wetting fluid) during the drying path of the water retention curve. Thus the injection of mercury with a contact angle is equivalent to the drain-age of the water induced by air front advancing for the same diameter of pores intruded. Under the hypothesis of non-deformable soil skeleton, the volume of pores non intruded by the mercury should be used to evaluate the degree of saturation or the water content corresponding to the equivalent applied air overpressure. Anyway, the non-intruded porosity by the mercury should be taken into account for estimating the residual water content in the evaluation of the water content. The WRC obtained is valid in the range where the capillarity is the predominant physics mechanisms, usually for suction $s < 2$ MPa.

The water ratio $e_w = V_w / V_s = S_r \cdot e$ is estimated by the following equations:

$$\begin{aligned} e_{nw} + e_w &= e \\ e_w &= e - e_{nw} = (1 - S_{rnw})e \end{aligned} \tag{1}$$

Where e_{nw} is the non wetting ratio (mercury), S_r and S_{rnw} the degree of saturation of water and non—wetting fluid respectively ($S_r + S_{rnw} = 1$) for a two fluid mixture).

In Figure 7 are reported the WRC obtained after the correction for taking into account the non-intruded porosity and the adsorbed water. The residual water ratio as been taken e_{wres} in agreement with the measures performed with a WP4 at different void ratios.

The water ratio $e_w = V_w / V_s$ where V_w is the volume of water and e_{wres} is the residual water ratio. The results are reported in the plane water ratio e_w-suction s for the same water content (Figure 7a) and the same void ratio (Figure 7b). As the void ratio decreases, the air entry value increases and the curves are steeper. This trend is consistent for the four gravimetric water content investigated (Figure 7a). The increase of the compaction water content let the curves more dispersed in the higher range of suctions ($s \geq 100\ kPa$).

The driest samples (w = 13%) shows a more rigid behaviour before the air entry value, after that curves are flatter than the more wetted samples (Figure 7b). This behaviour persisting for the five void ratios explored. For the same compaction water content the form of the curves are similar while the void ratio affect the air entry values of the curves.

Here the heterogeneity of the pore system induced by the compaction process is taking into account using a multimodal retention model, defined by Durner (1994) as a linear superposition of sub-curves of the Van Genuchten (1980) type with the following equation:

$$E_w = \frac{e_w - e_{wres}}{e - e_{wres}} = \sum_{i=1}^{k} w_i \left[\frac{1}{1 + (\alpha \cdot s)^{n_i}} \right]^{m_i} \tag{2}$$

where E_w is the effective water ratio equal to the effective degree of saturation, k is the number of sub-system that assembled together give the global pore size distribution, w_i are weighting factors for each sub-curves subjects to $0 < w_i < 1$ and $\sum w_i = 1$. For the parameters of the sub-curves (α_i, n_i, m_i)

must be imposed the condition $\alpha_i > 0$, $m_i > 0$, $n_i > 1$. Here is imposed the additional constraint $n_i = 1/(1-m_i)$.

Each sub-curve in Equation 2 differentiated two times with respect to the suction s give the relation between the suction pressure at the inflection point and the parameters given by the following expression: where $s_{p_i} = m_i^{1-m_i} / \alpha_i$ is the suction at the in-flection point in the E_{w-s} plane. Obtained α_i from Equation (3) and substituting in equation (2) the water storage mechanisms in an heterogeneous porous medium became:

$$E_w = \frac{e_w - e_{wres}}{e - e_{wres}} = \Sigma_{i=1}^{k} w_i \left[1 + m_i \left(\frac{s}{s_{p_i}} \right)^{1/1-m_i} \right]^{m_i} \quad (3)$$

The equation 2 is used for model the WRC data obtained by MIP. The experimental data are modelled with a bi-modal water retention model, obtained setting k = 2 in the above equation.

The pore capillary density function (PCF) is defined as: $PCF = \Delta E_w / \Delta \log(s)$ where E_w is the effective degree of saturation as defined above.

The model is calibrated best fitting the PCF obtained by experimental results as reported in Figure 8a. The area below the peak of lower suction is de-fined as w_1 (macro area below the PCF) while w_2 (micro area) is given by $w_2 = 1 - w_1$ because the area below the curve corresponds to the unity. The suction at inflection points are named respectively s_{pM} and s_{pm} as reported in Figure 8a (Casini et al., 2012).

The parameters obtained by the multimodal model have been calibrated as a function of void ratio and gravimetric water content.

A comparison between the model prediction and the experimental data is reported in Figure 8b, the model well fit the experimental results in the entire range of suction. Furthermore the model is able to well capture the change in shape of the retention curve at the inflection points for all the water content investigated (Fig. 9).

The data of drying path obtained under suction con-trolled conditions under oedometer conditions has been compared with the model prediction in Figure 10. Two drying curves have been

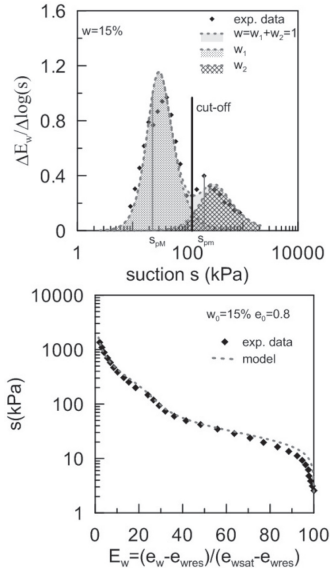

Figure 8. Laboratory versus model prediction: (a) Pore capillary function (PCF) macro micro; (b) WRC derived from PCF (Casini et al., 2012).

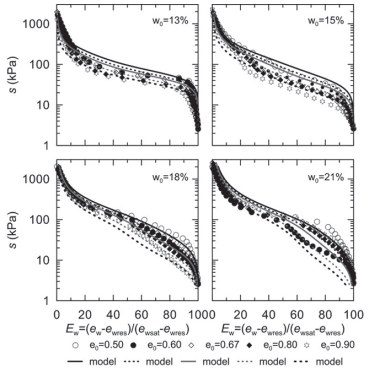

Figure 9. Comparison model—data for different gravimetric water content.

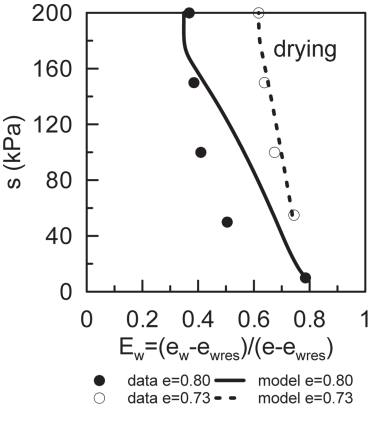

Figure 10. Comparison along drying paths between experimental data under suction controlled conditions and model predictions (Casini et al., 2012).

simulated, one for the path at lower density (void ratio at the beginning of the drying path e0 = 0.80) and the second for the path at higher density (void ratio e0 = 0.73). Curves have been normalised in order to fit the initial and final water contents of each path. The evolution is reasonable reproduced by the model for both changes in suction and vertical load.

4 CONCLUSION

An extended microstructural investigation (MIP and ESEM) have been performed on Jossigny silt statically compacted at different initial void ratio and water content. The objective was a deeper under-standing of the evolution of microstructures changing on a silty soil and its consequences on the water retention properties. As highlighted by the experimental results the shape of the pore size distribution is induced by the compaction water content. The PSD is monomodal for the driest tested conditions, because the water is not in half to form aggregates for this kind of soil. The aggregates increasing in size and uniformity with the water content until to cover the silt/sand particles for the wettest tested conditions moving back to a quasi monomodal distribution.

Some tests were also repeated adding dissolved salt (NaCl) in the water. The salt has been used as an artificial manner to understand the evolution of double porosity. The swelling of aggregates has been inhibited by the salt, the microstructure has been blocked by the interaction between salt and clay fraction. During the drying the salt is deposited, it is a way to investigate the stability of smaller pores with an electrolitical solution.

The drying path of the water retention curve obtained by MIP has been modelled with a multimodal retention model, where the weighted parameters are related to the area below the pore capillary distribution and the suctions at inflection points to the peak value of the distribution. The agreement be-tween the measured and the estimated WRC indicates that the multimodal prediction method lead to more realistic estimation of the retention properties of soils. The model parameters are related to the pore capillary distribution and have a clear physical meaning.

The comparison between the WRCs obtained with MIP and oedometer under suction controlled condition were satisfactory. The two approach gives results in agreement under the same initial conditions, while some difference are highlight due to the change of microstructures induced by different stress path followed between oedometer and MIP tests.

The model is quite simple and must be validated for such engineering application involved compacted soils where a commonly applied unimodal retention function is inadequate for conductivity estimation because they lack the necessary flexibility in the range of characteristic pores.

REFERENCES

Casini, F. (2008). Effetti del grado di saturazione sul comporta-mento meccanico di un limo, PhD Thesis, Universitá degli Studi di Roma “La Sapienza”, Italy.

Casini, F. (2012). Deformation induced by wetting: a simple model. Canadian Geotechnical Journal 49, 954–960.

Casini, F. (2012). Hydromechanical behaviour of a silty sand from a steep slope triggered by artificial rainfall: from un-saturated to saturated conditions. Canadian Geotechnical Journal, in print ISSN 0008-3674.

Casini, F., Vaunat J., Romero E. and Desideri, A. (2012). Conse-quences on water retention properties o fdouble-porosity features in a compacted silt. Acta Geotechnica 7: 139–150 DOI10.1007/s11440-012-0159-6.

Cui Y.J. (1993). “Etude du comportement d’un limon non saturé et de sa modélisation dans un cadre élasto-plastique” PhD Thesis, ENPC, Paris, France.

Cui, Y.J. and Delage, P. (1996). Yielding and plastic behavior of an unsaturated compacted silt. Géotechnique 46, No. 2, 291–311.

D’Onza, F., Gallipoli, D., Wheeler, S., Casini, F., Vaunat, J., Khalili, N., Laloui, L., Mancuso, C., Masin, D., Nuth, M., Pereira, J.M. and Vassallo, R. 2011. Benchmark of consti-tutive models for unsaturated soils. Géotechnique 61(4): 283–302.

Durner, W. (1994). Hydraulic conductivity estimation for soils with heterogeneous pore structure. Water Resources Research 30(2): 211–223.

Monroy, R., Zdravkovic, L. and Ridley, A. (2010). Evolution of micro-structure in compacted London Clay during wetting and loading. Géotechnique 60(2): 105–119.

Romero, E. and Vaunat, J. (2000). Retention curves of deformable clays. Proc Int Workshop on Unsat Soils: Exp evid and Theor Approaches, Trento (Italy), Balkema: 91–106.

van Genuchten, M.T. (1980). A closed-form equation for predicting the hydraulic conductivity of unsaturated soil. Soil Science Society American Journal, 44: 892–898.

Vaunat, J., Romero, E. and Jommi, C. (2000). An elastoplastic hydro-mechanical model for unsaturated soils Proc Int Workshop on Unsat Soils: Exp evid and Theor Approaches, Trento (Italy), Balkema: 121–138.

Advances in Unsaturated Soils – Caicedo et al. (eds)
© 2013 Taylor & Francis Group, London, ISBN 978-0-415-62095-6

State surface of wetting-drying cycles at the equilibrium stage

E. Jahangir & F. Masrouri
Laboratoire Environnement Géomécanique & Ouvrages (LAEGO), Université de Lorraine, Vandoeuvre-lès-Nancy, France

H. Nowamooz
LGECO, INSA de Strasbourg, Strasbourg Cedex, France

ABSTRACT: It is generally accepted that swelling soils, after undergoing several suction cycles, present cu-mulative (swelling or shrinking) strains and can reach an elastic range called the equilibrium stage. It is im-portant to predict the final state of soil after it has undergone a sufficient number of cycles in order to investi-gate the long-term behavior of soil submitted to several wetting and drying cycles. In this paper, the equilibrium state for a mixture of bentonite/silt was investigated. Using the state surface approach, the cyclic cumulative strains of loosely and densely compacted samples were studied. A unique state surface was pro-posed at the end of several drying and wetting cycles for the final equilibrium state. Using the proposed mod-el, the cumulative behavior of an intermediately compacted sample during several suction cycles was appro-priately predicted.

1 INTRODUCTION

Expansive soils are subjected to natural hydration cycles, which lead to the shrink-swell characteristics of soils that depend on the drying-wetting paths. The occurrence of shrink-swell hazards in clayey soils could affect the performance of surrounding lightly loaded structures. The shrink-swell phenomenon is also recognized as a costly natural hazard throughout the world because the cycles cause differential settlement beneath shallow foundations. This settlement causes cracks in facades and structural elements, especially in unreinforced masonry elements (Chen, 1965; Nelson and Miller, 1992; Fityus et al., 2004). Hence, understanding the behavior of unsaturated expansive clays is essential in the design and construction of individual structures, embankments and roads.

After swelling soils experience several suction cycles, it is accepted that the strain reaches an elastic range called the equilibrium stage. Tests on expansive soils reported by Dif and Bluemel (1991), Al-Homoud et al. (1995), Alonso et al. (2005) and Airo Farulla et al. (2010) showed the cumulative shrinkage of expansive soils exposed to cyclic wetting and drying, which increases at higher vertical stresses. This behavior was explained by the continuous rearrangement of the soil particles leading to a less active microstructure. However, Chu and Mou (1973) and Pousada (1984) observed the opposite effect, where the swelling strains increase with the number of successive cycles. All of these prior tests showed that the equilibrium elastic state can be reached at the end of several cycles.

In this context, it is important to predict the long-term behavior of the soil after it has undergone a sufficient number of hydraulic cycles. This paper proposes a model for the cumulative strain of loosely, intermediately and densely compacted swelling samples during hydration cycles by using the state surface approach.

2 STATE SURFACE

The hydro-mechanical behavior of unsaturated expansive soils has been studied by several authors (e.g. Alonso et al., 1990, Fredlund and Rahardjo 1993, Gens et al., 2006, Sheng et al., 2008, Zemenu et al., 2009). These authors concluded that the swelling behavior of unsaturated expansive clays can be described as a coupled response of soil to suction changes and applied stresses. There are relatively few models that integrate this coupled hydro-mechanical response in a unified framework. The most frequently used model is the Barcelona Expansive Model (BExM) proposed by Alonso et al. (1999). The BExM can be considered a theoretical reference framework (22 parameters) for studying the unsaturated expansive clay's behavior. A simpler method, the state surface approach, correlates the volume change to two independent stress state variables. The concept of state surface was first proposed by Matyas

and Radhakrishna (1968) and was later used by Fredlund and Morgenstern (1977), Lloret and Alonso (1985), Fredlund and Rahardjio (1993), Gatmiri and Delage (1995) and Sheng *et al*. (2008) Jahangir *et al*. (2012). They showed that the stress state variables, net stress and suction, are necessary to describe the hydro-mechanical behavior of an unsaturated soil. The state surface was used as a simplified method in some practical problems with a simple stress path (Zhang and Lytton, 2009). Alonso et al. (1990) determined that the state surface approach, with its unique constitutive surface used to describe unsaturated soil behavior, cannot explain the stress-path dependency and hysteresis behavior. Fredlund and Morganstern (1976) conducted a series of monotonic loading stress paths on unsaturated swelling Regina clay and concluded that, under monotonic loading conditions, a unique state surface can be considered. However, in the case of hydration cycles, each cycle requires a separate state surface. Moreover, Zhang and Lytton (2009) presented a modified state surface approach that is able to consider the suction hardening behavior. This approach produced results similar to the BExM (Alonso et al., 1999). Vu and Fredlund (2006) reported that estimated volume change using the state surface approach should be adequate for most engineering analysis.

Lloret and Alonso (1985) proposed several analytical functions of state surfaces for different types of plastic soil. Vu (2003) proposed six functions to fit the void ratio constitutive surfaces of an unsaturated expansive soil and tested these functions on swelling clay from Regina (Saskatchewan—Canada). Herein, his first function (*Unsat-1*) was considered because of the small number of parameters (three) and its ability to model the experimental results (equation 1).

$$e = a - b\log[1 + (\sigma - u_a) + c(u_a - u_w)] \quad (1)$$

In equation 1, a is the void ratio at zero net stress and suction. Parameter b represents the total volume change due to suction and stress changes. Parameter c represents the rate of volume change during a variation of suction and may be related to the swelling characteristic of the soil, such as plasticity index (Vu and Fredlund, 2006). The fitting parameters *a, b and c* can be obtained by oedometric or triaxial suction controlled tests. Figure 1 shows the state surface for a swelling soil (Regina clay).

The concept of state surface, as defined by Vu (2003), is used in this study to quantify the volume change during a drying or wetting phase with a simple stress path, taking into account the coupled hydro-mechanical behavior.

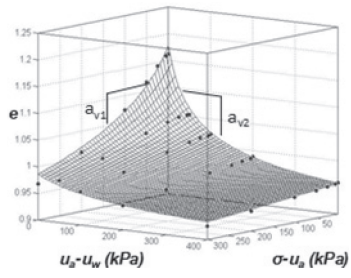

Figure 1. The state surface for expansive clay, proposed by Vu (2003) and fitted for Regina clay.

3 EXPERIMENTAL RESULTS

Nowamooz and Masrouri (2008, 2009a, 2010) studied the hydromechanical behavior of an artificial compacted mixture of 40% silt and 60% bentonite after several wetting and drying cycles at the equilibrium stage. The samples, with an initial water content of 15%, were compacted at three different initial states: loose, intermediate and dense. The initial dry densities of the compacted soils are 1.27 ± 0.01, 1.48 ± 0.01 and 1.55 ± 0.01 Mg/m^3, under a vertical pressure of 1,000, 2000 and 3,000 kPa. The initial matric suction, measured by the contact filter paper method (ASTM 1995a), was between 20 and 25 MPa for all compacted samples.

Nowamooz and Masrouri, (2010) previously demonstrated that the strain accumulation of the swelling soils can be related to their initial state. Figure 2 shows the variation of the void ratio during successive wetting and drying cycles between 0 and 20 MPa without applying any vertical stress. The loose samples demonstrated shrinkage whereas the dense samples demonstrated swelling. The experiment shows that the samples exhibit reversible behavior, where different initial densities have a trend to reach the same state of void ratio after undergoing weting-drying cycles.

Figure 3 presents the variation of the void ratio for loosely, intermediately and densely compacted soils during wetting and drying cycles between 0 and 8 MPa with applied vertical stresses of 15, 30 and 60 kPa, respectively. The first wetting path from 20 to 8 MPa produced an expansion for all samples. During the following successive cycles of 0 and 8 MPa, the loose samples had a shrinkage accumulation whereas the intermediate and dense samples had a swelling accumulation. At the end of the suction cycles, the volumetric strains converged once more towards a unique equilibrium stage.

The applied stress intensity influenced the amount of shrinkage or swelling accumulation, particularly at the end of the first wetting and drying cycle. It can be concluded that, as the applied stress

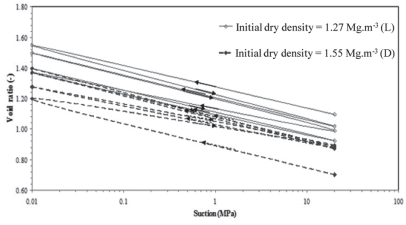

Figure 2. Variation of the void ratio, in cyclic controlled-suction paths at a null vertical stress, for densely and loosely compacted bentonite and silt mixtures (Nowamooz and Masrouri, 2010).

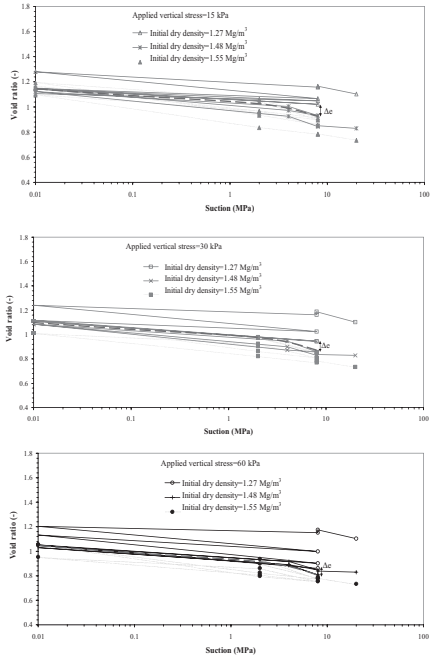

Figure 3. Variation of the void ratio in cyclical controlled suction paths for loose, intermediate and dense compacted bentonite and silt mixtures a) at a vertical stress of 15 kPa, b) at a vertical stress of 30 kPa and c) at a vertical stress of 60 kPa.

is increased, the shrinkage accumulation increases and the swelling accumulation decreases.

4 MODELING RESULTS

The experimental results from loosely and densely compacted samples (1.27 and 1.55 Mg/m^3) were interpreted using the state surface proposed by Vu (2003). Using the fitted parameters of this model at two different initial states, the cumulative behavior of the intermediate sample (1.48 Mg/m^3) during several suction cycles was predicted.

After three suction cycles between 0 and 8 MPa for loose and dense samples, it was thought that the equilibrium stage was reached. The fitted state surface for each wetting and drying path is presented in Figure 4, and the parameters of these surfaces (equation 1) are summarized in Table 1.

Table 1 shows that parameter a, which represents the void ratio value under zero suction and stress, decreases gradually with increasing cycles for the loose sample (cumulative shrinkage), whereas it increases regularly for the dense sample (cumulative swelling). There is a similar tendency for parameter b.

Subsequently, the evolution of the state surface parameters *a* and *b* can be related to the cycle number with the following equations:

$$a = \alpha n^{\beta} \tag{2}$$

$$b = \gamma n^{\lambda} \tag{3}$$

Variable n is the cycle number and α, β, γ and λ are the soil parameters depending on initial state

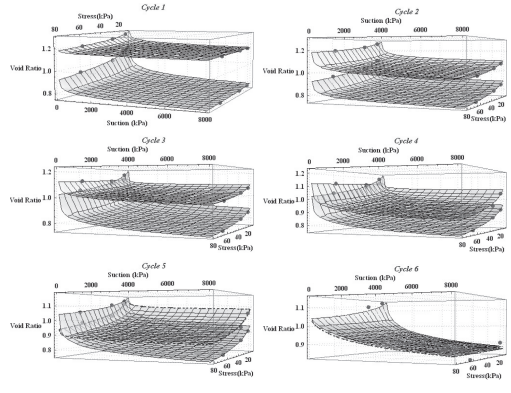

Figure 4. State surface fitted using equation 1 for each cycle of compacted samples (1.27 and 1.55 Mg/m^3).

Table 1. Fitted Parameters of surface for each wetting and drying path.

Soil type parameters	Loose (γ_d = 1.27 Mg/m^3)			Dense (γ_d = 1.55 Mg/m^3)		
	a	b	c	a	b	c
1-Wetting	1.554	0.2	0.01	1.1	0.085	0.5
1-Drying	1.539	0.176	0.15	1.15	0.106	0.15
2-Wetting	1.4	0.17	0.011	1.23	0.11	0.5
2-Drying	1.392	0.148	0.15	1.27	0.13	0.15
3-Wetting	1.33	0.146	0.015	1.29	0.135	0.4
3-Drying	1.31	0.141	0.15	1.3	0.142	0.15

of soil. Table 2 presents these parameters for the two studied samples.

The parameters α and γ correspond to values *a* and *b* for the first wetting path in Table 2. The parameters β and λ correspond to cumulative behavior of the sample during the suction cycles in relation to its initial loose and dense state. For the loose samples, these parameters are negative, causing a decrease in the parameters a and b with increasing cycle number. This produces a cumulative shrinkage during the wetting and drying cycles. The opposite variation of β and λ parameters can be observed for the dense samples.

Parameter c remains constant during the drying paths and varies slightly during the wetting paths (Table 1). To estimate the variation of this parameter with the cycle number, the average values for the wetting path (0.43 for the dense sample and 0.015 for the loose sample) and the value for the drying path (0.15 for both dense and loose samples) were used. This difference may be related to the hysteresis phenomenon. For the loose sample where a cumulative shrinkage was observed during the cycles, the drying cycle products higher volume variation. In this case, parameter c is higher for the drying cycle than for the wetting cycle. For the dense sample, the trend is opposite, and the parameter c is higher for the wetting phases.

Figures 5-a, -b, and—c show the evolution of parameters a, b and c during wetting-drying paths as well as their estimated values. The figure illustrates that parameters a and b of the loose and dense samples reach the same value after undergoing 7 wetting and drying paths. The last drying path (cycle 6 in Figure 4) presents the critical state surface of the equilibrium stage for both loose and dense samples, with the estimated parameters coming very close to each other. The critical state at the equilibrium stage will present a unique shape during the following drying paths expressed by:

$$e = 1.30 - 0.41 \times Log_{10}(1 + \sigma + 0.15s) \qquad (4)$$

The proposed model was used to predict the cyclical behavior of the intermediate samples (initial dry densities of 1.48 Mg/m^3). To estimate the parameters for the intermediate samples, a linear regression was performed between the loose and dense soils parameters presented in Table 3.

Table 2. Parameters of equations 2 and 3 for the loose and dense samples.

		α, γ	β, λ
Loose γ_d = 1.27 Mg/m^3	a	1.569	–0.088
	b	0.197	–0.148
Dense γ_d = 1.55 Mg/m^3	a	1.104	0.087
	b	0.091	0.209

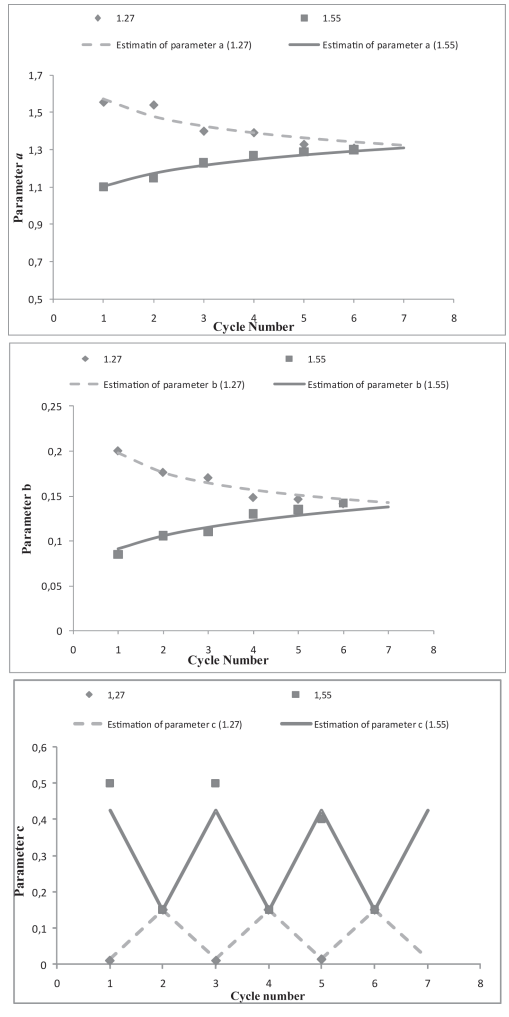

Figure 5. Evolution of the surface parameters for loose and dense samples as a function of cycle number.

Because the values of parameter β are positive, cumulative swelling strains are expected during wetting and drying cycles. Figures 6-a, -b and—c show the evolution of the estimated parameters a, b and c during wetting-drying paths with cycle number.

The estimated parameters of the model make it possible to predict the cyclic behavior of the intermediate sample. Figures 7-a, b and c show the model predictions for the applied stresses of 15, 30 and 60 kPa compared to the experimental results.

Table 3. Parameters of equations 3 and 4 for the intermediate sample.

Parameter	a	b	c
Intermediate $\gamma_d = 1.48$ Mg/m^3	$\alpha = 1.220$	$\gamma = 0.0436$	Wetting = 0.15
	$\beta = 0.0915$	$\lambda = 0.114$	Drying = 0.32

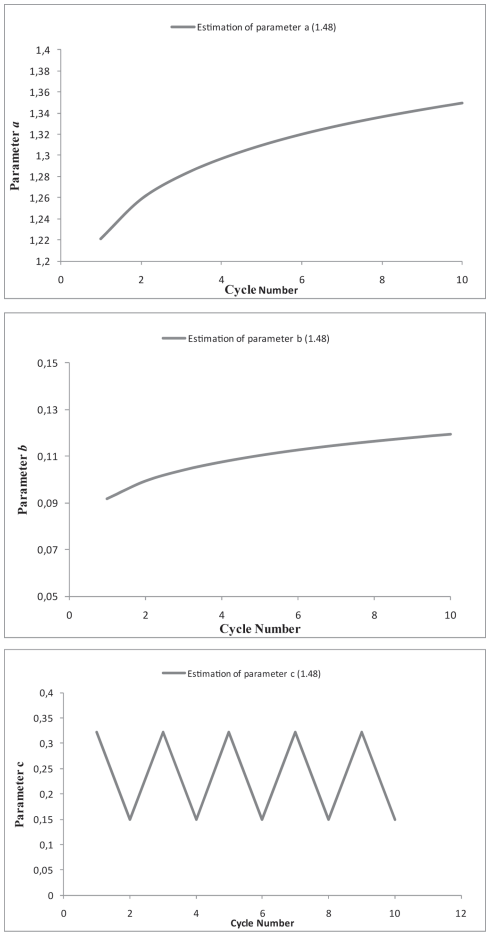

Figure 6. Evolution of the surface parameters for the intermediate sample as a function of cycle number.

A high correlation can be observed between the modeling and experimental results.

5 CONCLUSION

In this paper, the influence of consecutive wetting and drying cycles on expansive compacted loose and dense soil samples was studied. The

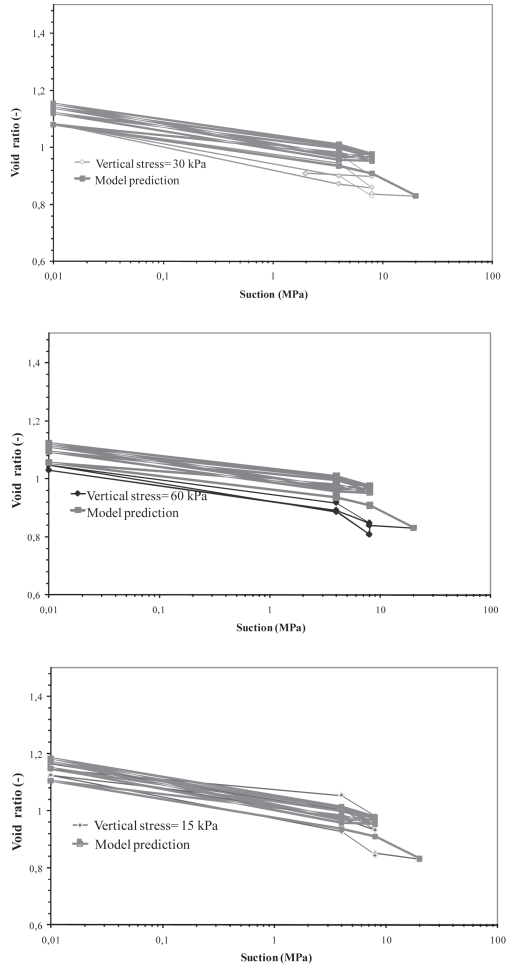

Figure 7. Model prediction for the intermediate samples with vertical stresses of: 15 kPa, 30 kPa and 60 kPa.

wetting and drying cycles were applied under different values of constant vertical net stress. The dense samples showed cumulative swelling strains, whereas the loose samples showed an accumulation of volumetric shrinkage. At the end of several wetting and drying cycles, the volumetric strains converged to an equilibrium stage.

The equilibrium state for a mixture of bentonite/silt was primary investigated. Using the state surface approach, the cyclic cumulative strains of loosely and densely compacted samples were studied. This datum allowed for a unique state surface to be proposed at the end of several drying and wetting cycles. Using this approach, the cumulative behavior of an intermediately compacted sample during several suction cycles was appropriately predicted.

REFERENCES

Al-Homoud, A.S., Basma, A.A., Husein Malkawi, A.I. & Al-bashabsheh, M.A. (1995). Cyclic swelling behavior of clays. Journal of Geotechnical Engineering, vol. 121, pp. 562–565.

Airo Farulla, C., Ferrari, A. & Romero, E. (2010). Volume change behaviour of a compacted scaly clay during cyclic suction changes. Can. Geotech. J. n°47, 668–703.

Alonso E.E., Gens A. & Josa A. (1990). A constitutive model for partially saturated soils, Géotechnique, 40, n°3, 405–430.

Alonso E.E., Vaunat J., Gens A. (1999). Modeling the mechanical behaviour of expansive clays. Engineering Geology 54, 173–183.

Alonso, E.E., Romero, E., Hoffemann, C. & García-Escudero, E. (2005). Expansive bentonite/sand mixtures in cyclic controlled suction drying and wetting. Engineering Geology, vol. 81, pp. 213–226.

Chen, F.H. (1965). The use of piers to preventing the uplifting of lightly structured founded on expansive soils. Proceedings, Engineering effects of moisture changes in soils, International research and engineering conference on expansive clay soils, Texas A & M press, college station, TX.

Chu, T.Y. & Mou, C.H. (1973). Volume change characteristics of expansive soils determined by controlled suction tests. Proc. 3rd Int. Conf. Expansive Soils, Haïfa, vol. 2, pp. 177–185.

Dif, A.E. & Bluemel, W.F. (1991). Expansive soils under cyclic drying and wetting. Geotechnical Testing Journal, vol. 14, pp. 96–102.

Fredlund, D.G. & Morgenstern, N.R. (1977). Stress state variables for unsaturated soils. Journal of Geotechnical Engineering, vol. 103, pp. 447–466.

Fredlund, D.G. & Rahardjo, H. (1993). Soil Mechanics for unsaturated soils, A Wiley- Interscience Publication.

Fityus, G., Smith, D.W. & Allman, M. (2004). Expansive Soil Test Site Near NewCastle. Journal of Geotechnical and Geoenvironmental engineering 130(7): 686–695.

Gatmiri, B. & Delage, P. (1995). A new void ratio state surface formulation for the nonlinear elastic constitutive modeling of unsaturated soil-Code UDAM. 1st Int. Conf. on unsaturated soils, Paris, 1049–1056.

Gens, A., Sanchez, M. & Sheng, D. (2006). On constitutive modelling of unsaturated soils. Acta Geotechnica, 1,137–147.

Jahangir, E., Deck, O. & Masrouri, F. (2012) Estimation of the ground settlement beneath foundations due to the shrinkage of clayey soils. Can. Geo. J. In Press.

Lloret, A. & Alonso, E.E. (1985). State surfaces for partially saturated soils, In: Proceedings 11th International Conference on Soil Mechanics and Foundation Engineering, vol. 2, San Francisco, 557–562.

Matyas, E.L. & Radhakrishna, H.S. (1968). Volume change characteristics of partially saturated soils. Géotechnique 18 (4), 432–448.

Nelson, J. & Miller, D. (1992). Expansive soils: Problems and practice in foundation and pavement engineering, John Wiley & sons Ltd, New York.

Nowamooz, H. & Masrouri, F. (2008). Hydromechanical behaviour of an expansive bentonite/silt mixture in cyclic suction-controlled drying and wetting tests, International Journal of Engineering Geology, n°101 (3–4), 154–164.

Nowamooz, H. & Masrouri, F. (2009a). Density-dependent hydromechanical behaviour of a compacted expansive soil: experimental and analytical aspects, Engineering Geology, n°106 (3–4), 105–115.

Nowamooz, H. & Masrouri F. (2009b). Shrinkage-swelling of compacted clayey dense and loose soils, Comptes Rendus Mécanique, n°337 (11–12), 781–790.

Nowamooz, H. & Masrouri, F. (2010). Influence of suction cycles on the soil fabric of compacted swelling soil, Comptes rendus Géoscience, n°342 (12), 901–910.

Pousada, E. Deformabilidad de arcillas expansivas bajo succión controlada, Doctoral Thesis, Universidad Politecnica de Madrid, Spain (1984).

Sheng, D., Fredlund, D.G. & Gens, A. (2008). A new modeling approach for unsaturated soils using independent stress variables, Can. Geotech. J., n°45, 511–534.

Vu, H.Q (2003). Uncoupled and coupled solutions of volume change problems in expansive soils. Thesis University of Saskatchewan.

Vu, H.Q. & Fredlund, D.G. (2006) Challenges to modeling heave in expansive soils, Canadian Journal of Geotechnics, n° 43, 1249–1272.

Zhang, X. & Lytton, R.L. (2009). Modified state-surface approach to the study of unsaturated soil behaviour. Part I and II. Canadian geotechnical journal, n°46, 553–570.

Zemenu, G., Audiguier, M. & Cojean, R. (2009). Analyse du comportement d'un sol argileux sous sollicitations hydriques cycliques. Engineering Geology and the Environment, n° 68: 421–436.

Advances in Unsaturated Soils – Caicedo et al. (eds)
© 2013 Taylor & Francis Group, London, ISBN 978-0-415-62095-6

Assessment of the critical state strength of unsaturated aggregated soils

E.J. Murray & R.M. Jones
Murray Rix Geotechnical, Earl Shilton, Leicestershire, UK

V. Sivakumar
Queens University Belfast, Northern Ireland, UK

ABSTRACT: Engineers frequently have to assess the strength of the ground from limited observational and laboratory test data. The problem becomes particularly difficult when dealing with unsaturated soils. The paper examines the strength of unsaturated fine-grained soils and the possibility of assessing appropriate critical state strength parameters for analyses from limited information. The derivation of parameters and applicability in stability analysis are discussed.

1 INTRODUCTION

Determination of the strength of unsaturated soils requires complex laboratory testing which is time consuming and may in practice be deemed prohibitively expensive. Such testing is at present limited mainly to research facilities. Commercial laboratories have been slow to expand their testing capabilities into unsaturated soil testing and practicing engineers are not in a position to utilise unsaturated soil mechanics principles on a routine basis.

Testing under unsaturated conditions may be deemed essential for large prestigious projects, such as underground nuclear waste depositories, large earth dams, major slope stability projects and the like. But practicing engineers are frequently called on to assess stability of small, though perhaps important projects, where because of monetary, time or client restraints detailed testing is not undertaken. This might include excavation stability as in quarries where the faces are to stand open for a limited time period, design of embankment or cutting slopes for transport systems where variable ground conditions and significant changes in environmental factors during their lifetime require engineering judgment, and foundation stability situations where the perception of ground movement is a major consideration to occupants of buildings. Particular problems are encountered with fine-grained soils. In such circumstances the engineer frequently reverts to assumptions of saturated conditions (or in the case of granular soils possibly to perfectly dry soil mechanics principles) and thankfully usually provides a reliable though probably conservative answer.

How might a practicing engineer get a handle on the strength of a soil in an unsaturated state and use the information to assess stability? This is the question posed and an attempt is made to provide some guidance and to raise discussion.

2 CRITICAL STATE STRENGTH

Murray and Sivakumar (2010a and b) developed an analysis for the critical state strength of unsaturated fine-grained soils. Such soils are shown to form aggregates comprising the soil particles and water which influence soil strength. The analysis is based on the following controlling stress equation determined from thermodynamic equilibrium considerations:

$$p_c' = \overline{p} + s\frac{v_w}{v} \tag{1}$$

where, p_c' is defined as the coupling stress; $\overline{p}$ is the mean net stress ($p - u_a$); s is the matric soil suction ($u_a - u_w$); u_a is the pore air pressure (generally the datum of atmospheric pressure in practice and equated to zero); u_w is the pore water pressure (negative in unsaturated soils); v_w is the specific water volume ($v_w = 1 + S_r e$); v is the specific volume ($v = 1 + e$); e is void ratio; S_r is degree of saturation; p is the mean stress (under triaxial conditions $p = (\sigma_1 + 2\sigma_3)/3)$); σ_1 is the axial stress under triaxial conditions; σ_3 is the cell pressure or lateral stress under triaxial conditions

Figure 1 shows a plot of q/s (where the deviator stress q is given by $(\sigma_1 - \sigma_3)$) against p_c'/s for kaolin from the results of Sivakumar (2005) and Sivakumar *et al.* (2009). The results show a consistent trend with a slope of M_a and an intercept $\Omega = 0.6$ on the q/s axis at $p_c'/s = 1$. Similar relations have been show for a range of soil types and test protocols where aggregation of particles

is known to occur (Sivakumar, 1993 and Wheeler and Sivakumar 1995 and 2000 for kaolin; Toll 1990 for Kiunyu gravel; Toll and Ong 2003 for Jurong soil; Maâtouk *et al.* 1995 for Trois-Rivières silt). The results are summarised in Table 1. Though M_a varies with soil type and in some cases with test protocol, $\Omega = 0.6$ appears constant provided aggregation occurs.

The following relationship may be derived from Figure 1.

$$\frac{q}{s} = M_a \left[\frac{p_c'}{s} - 1 \right] + \Omega \tag{2}$$

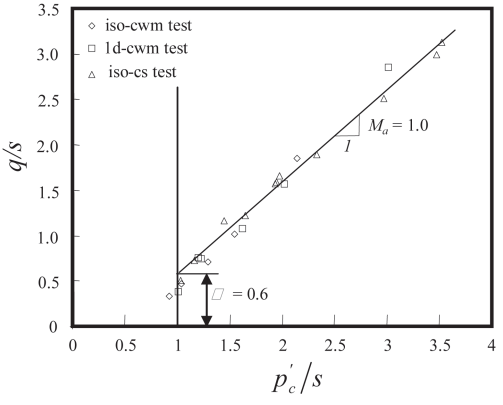

Figure 1. q/s against p_c'/s at critical state from iso-cs, iso-cwm and 1d-cwm test results of Sivakumar (2005) and Sivakumar *et al*. (2009) for unsaturated kaolin. 1d and iso stand for specimens initially one dimensionally and isotropically compressed respectively; cs and cwm stand for shearing under constant suction and constant water mass respectively.

Table 1. Summary of soil properties and analyses.

Material	kaolin	kaolin	Kiunyu gravel	Jurong soil	Trois-rivieres silt
Test designation	1d-cs	iso-cwm, 1d-cwm, iso-cs	1d-cwm	1d-cwm	1d-cs
LL* (%)	70	70	–	36	–
PL** (%)	34	34	–	22	–
PI*** (%)	36	36	–	14	7
Clay (%)	80	80	8 to 9	–	18
Silt (%)	20	20	6	–	66
Sand (%)	0	0	–	–	16
M	0.82	0.82	1.62	1.23	1.63
M_a	0.86	1	1.77	1.27	1.63

*Liquid Limit; **Plastic Limit; ***Plasticity Index

Substituting for p_c' from Equation 1, this may be written as,

$$q = M_a \overline{p} + M_b s \tag{3}$$

where,

$$M_b = M_a \left[\frac{v_w}{v} - 1 \right] + \Omega \tag{4}$$

M_a and M_b are the total and suction stress ratio parameters but should not be confused with those of Toll 1990, which were determined in a different manner. In the above analysis the only unknown strength parameter that needs to be determined from experimentation is M_a, the other variables including M_b are reliant on only the readily measurable or assessed soil properties of s, v_w/v and $\overline{p}$. The term $M_a \overline{p}$ in Equation 3 represents the deviator stress component influenced by the net stress $\overline{p}$ and $M_b s$ the additional component due to the suction s within the aggregates which contain the water phase.

Murray and Sivakumar (2010b) report the following theoretical equation for Ω, which is presented for completeness. This has been shown to give a value of $\Omega = 0.6$ for kaolin (as well as the other soil types of Table 1) consistent with the determination of Figure 1.

$$\Omega = M_a n^* \tag{5}$$

where, n^* is the porosity for a loose dry aggregated soil.

3 DETERMINATION OF CRITICAL STATE STRENGTH FROM TRIAXIAL TESTS

Test data analysed by Murray and Sivakumar (2010a and b) indicate that testing in the triaxial cell can give rise to variations in M_a not just between material types but between tests on the same material if different test procedures are employed. For example, tests on kaolin on specimens initially one dimensionally compressed and then tested under constant suction conditions (1d-cs) (Sivakumar, 1993 and Wheeler and Sivakumar 1995 and 2000) gave a value of $M_a = 0.86$ while specimens initially isotropically prepared and tested under constant suction (iso-cs) and specimens initially isotropically or one-dimensionally prepared but tested under constant water mass (iso-cwm and 1d-cwm respectively) gave a value of $M_a = 1.00$ as in Figure 1 (Sivakumar, 2005 and Sivakumar *et al*., 2009). This highlights the importance of any testing undertaken being representative of the conditions

likely to be experienced in practice. It is apparent from analysis that not only the test method but the method of specimen preparation influenced the form of the aggregates and soil structure and thus the strengths determined.

It is also important to note that while tests in the laboratory may be carefully controlled with specimens prepared to uniform quality, these may not represent site conditions. In the field, strata variations both laterally and vertically, ground stress history and environmental factors such as the weather play their part and the engineer has to make judgments based on experience when assessing ground properties and stability. This may necessitate looking at a likely range of soil strength parameters and other properties and carrying out sensitivity analysis to identify the risks and key variables and uncertainties. This includes assessment of values of M_a.

If laboratory testing is carried out to determine M_a, it is likely that the amount of testing will be limited on most projects. While the analysis indicates that only one good quality, representative strength test would be necessary to determine M_a and thus the strength under a wide range of suction and saturation conditions, it would be necessary to establish a relationship between s and v_w/v for the material being examined in order to determine M_b. This could be established by field and/or laboratory determinations. Figure 2 shows a plot of M_b against v_w/v for the tests on kaolin of Figure 1. Suction in-situ may be determined by various means either by recovering samples and testing in the laboratory (in this instance removal of confining stress needs to be taken into account) or by measurements in-situ which can present their own practical difficulties. Suction measurements in the field frequently differ from those that might be expected from theoretical considerations. Further reading on suction measurements is given by Fredlund and Rahardjo (1993), Lu and Likos (2004), Rahardjo and Leong (2006), Ng and Menzies (2007), Delage *et al*. (2008) and Murray and Sivakumar (2010b).

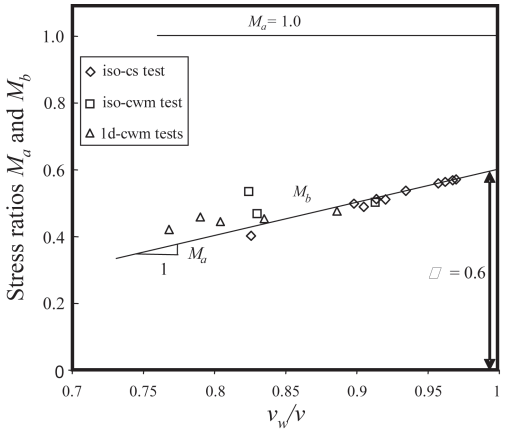

Figure 2. Suction stress ratios M_a and M_b plotted against v_w/v from iso-cs, iso-cwm and 1d-cwm test results of Sivakumar (2005) and Sivakumar *et al*. (2009) for unsaturated kaolin.

Though not determined on a statistical basis, examination of available experimental data suggests that if only one triaxial strength test is carried out that the value of M_a determined is likely to be within ±30% of the mean of a series of tests. The greater the value of p_c'/s and the greater the number of tests undertaken, the error in determining the inclination M_a will be reduced considerably.

4 STABILITY ANALYSES

A review of commercially available stability programs has not been undertaken, but those with which the authors are familiar are not written in terms of M_a and M_b and it is necessary to convert these parameters into the more conventional angle of shearing resistance ϕ' and cohesion c'. The following equations can be used:

$$\phi' = \sin^{-1}\left[\frac{3M_a}{6+M_a}\right] \text{ and } c' = M_b\left[\frac{3-\sin\phi'}{6\cos\phi'}\right]s \quad (6)$$

The equation for ϕ' is the same as that for a saturated soil at the critical state but with M_a replacing M. Essentially ϕ' in Equation (6) is the friction angle for an aggregated soil and can be expected to be greater than ϕ' for a non-aggregated, saturated soil. At what suction the aggregates break down during shearing is uncertain but the results for kaolin suggest that this is below s = 100 kPa. Monroy *et al.* (2010) noted that the transition from an aggregated to a matrix structure in unsaturated London clay took place as the suction in wetting tests was reduced from 40 kPa to 0. Aggregates in unsaturated soils effectively represent larger, though somewhat deformable, soil 'particles'. Accordingly, M_a can be expected to be greater or equal to M, as shown by the experimental evidence.

Commercial stability analysis programs allow for negative pore water pressures to be taken into account. Analysis is usually performed using effective stress parameters based on saturated soil testing. A positive water pressure below the water table reduces the effective stress and thus the ground strength. A negative pore water pressure above the water table increases the effective

stress and the soil strength. Such analysis ignores the aggregation effect in unsaturated fine-grained soils and its influence on soil strength. Equations 3 and 4 demonstrate that the component of deviator stress $M_a \overline{p}$ is controlled by changes in the net stress (normally the total mean stress if the air pressure is taken as atmospheric) while the component $M_b s$ is controlled by the suction and degree of saturation. Converting M_a to ϕ' and $M_b s$ to c' using Equation 6 automatically accounts for the negative pore water pressures above the water table, which should not be included as a further component in the analysis.

Use of the critical state strength in stability analysis rather than peak strength means that there is surety that the soil strength adopted can be relied on in first-time slip situations. This assumes that the critical state strength can be reasonably determined but may justify a reduced factor of safety in analysis from that employed if the peak strength parameters are used.

5 ASSESSMENT OF CRITICAL STATE STRENGTH

In saturated soil mechanics, there are innumerable relationships between index properties, such as the plasticity index, and soil parameters, such as angle of shearing resistance, compressibility, swelling and shrinkage potential. What are the possibilities of developing a relationship between M_a for unsaturated soil and the plasticity of cohesive deposits? Any such relationship is likely to have a margin of error as suggested by the test data analysed in Table 1 though there are clear indications of increasing clay content and plasticity leading to reduced values of M and M_a. The overall soil grading is also important and too few fines may mean aggregation does not occur or has little or no influence on soil strength.

The important conclusion that $M_a \geq M$, as illustrated in Figure 1 and Table 1, where M is the stress ratio for a saturated soil, effectively places a lower limit on the value of M_a and may be used as at least a first approximation in analyses.

There is a further possible means of assessing M_a without carrying out detailed laboratory strength tests. Loose granular materials when stockpiled stand at their angle of repose. This is close to the angle of shearing resistance of the material ϕ' at critical state though some argue that there is a fundamental difference. Nevertheless, determination of the angle of repose gives a measure of the friction angle at the critical state. Atkinson (1993) describes two tests that can be used to assess ϕ' for a dry granular material that may prove of use in determining the critical state ϕ' for a dry aggregated soil, as these behave in many respects as a granular soil. The tests which determine the maximum slope angle at which loose materials stand are: (i) rotating a soil sample in a drum, and (ii) creating a mound as in Figure 3. The figure shows a small mound of loose dry aggregated kaolin. This stands at an inclination close to the angle of friction and it may be possible to assess M_a based on Equation 6. However, there is limited test information to justify this approach though it is considered to warrant further research. A major difficulty would be to obtain a representative loose aggregate material, particularly from in-situ samples, noting earlier comments that the aggregate formation has an influence on the strength of unsaturated fine-grained soils.

Figure 3. Sieved dry aggregated kaolin.

6 CONCLUSIONS

The paper has outlined some of the considerations that practicing geotechnical engineers face in attempting to determine unsaturated soil strength for stability problems. An analytical interpretation of critical state strength is explained and it is shown that it only requires a limited amount of experimental data to obtain the strength of an unsaturated aggregated fine-grained soil over a wide range of suctions (and degrees of saturation). However, strata variability in-situ and changing environmental factors mean the engineer has to make judgments based on experience as well as the available information. Some tentative guidance is given on the likely variability in the interpreted critical state strength from triaxial test data and alternative methods of assessing it that might prove useful.

REFERENCES

Atkinson, J. (1993). An Introduction to the Mechanics of Soils and Foundations. McGraw-Hill, London.

Delage, P., Romero, E. and Tarantino, A. (2008). Recent developments in the techniques of controlling and measuring suction in unsaturated soils. Unsaturated Soils: Advances in Geo-Engineering, Proc. 1st European Conference on Unsaturated Soils, E-UNSAT, Durham, UK, Ed. Toll, D.G. *et al*., 33–52.

Fredlund, D.G. and Rahardjo, H. (1993). Soil mechanics for unsaturated soils. New York: John Wiley and Sons, Inc.

Lu, N. and Likos, W.J. (2004). Unsaturated soil mechanics. J. Wiley and Sons Inc, Hoboken, New Jersey, USA.

Maâtouk, A., Leroueil, S. and La Rochelle, P. (1995). Yielding and critical state of a collapsible unsaturated silty soil. Geotechnique, 45(3), 465–477.

Monroy, R. Zdravkovic, L. and Ridley, A. (2010). Evolution of microstructure in compacted London Clay during wetting and loading. Geotechnique, 60(2), 105–199.

Murray, E.J. and Sivakumar, V. (2010a). A fundamental interpretation of the critical state of unsaturated soils. Unsaturated Soils, Proceedings of the Fifth International Conference on Unsaturated Soils, Barcelona, Spain, Ed., Alonso, E. and Gens, A., Taylor and Francis Group, London.

Murray, E.J. and Sivakumar, V. (2010b). Unsaturated Soils (A Fundamental Approach to the Interpretation of Soil Behaviour). Wiley-Blackwell, UK.

Ng, C.W.W. and Menzies, B. (2007). Advanced Unsaturated Soil Mechanics and Engineering. Taylor Francis, London and New York.

Rahardjo, H. and Leong, E.C. (2006). Suction measurements. Unsaturated Soils: Proc. 4th Int. Conf. on Unsaturated Soils, UNSAT 2006, Carefree, Arizona, ASCE Special Publication No. 147, 1, 81–104.

Sivakumar, R. (2005). Effects of anisotropy on the behaviour of unsaturated compacted clay. Thesis submitted to the Queen's University of Belfast for the degree of Doctor of Philosophy.

Sivakumar, V. (1993). A critical state framework for unsaturated soils. Thesis submitted to the University of Sheffield, UK for the degree of Doctor of Philosophy.

Toll, D.G. (1990). A framework for unsaturated soil behaviour. Geotechnique, 40(1), 31–44.

Sivakumar, V., Sivakumar, R., Boyd, J. and MacKinnon, P. (2010). Mechanical behaviour of unsaturated kaolin (with isotropic and anisotropic stress history). Part 2: performance under shear loading. Geotechnique, 60(8), 581–594.

Toll, D.G. and Ong, B.H. (2003). Critical state parameters for an unsaturated residual sandy soil. Geotechnique, 53(1), 93–103.

Wheeler, S.J. and Sivakumar, V. (1995). An elasto-plastic critical state framework for unsaturated soils. Geotechnique, 45(1), 35–53.

Wheeler, S.J. and Sivakumar, V. (2000). Influence of compaction procedure on the mechanical behaviour of an unsaturated compacted clay. Part 2: Shearing and constitutive.

This page intentionally left blank

Advances in Unsaturated Soils – Caicedo et al. (eds)
© 2013 Taylor & Francis Group, London, ISBN 978-0-415-62095-6

Incorporating a microstructural state variable in constitutive modeling

N.M. Pinyol
Centre de Mètodes Numèrics en Enginyeria (CIMNE), Barcelona, Spain
Department of Geotechnical Engineering and Geo-Sciences. Universitat Politècnica de Catalunya, Barcelona, Spain

E.E. Alonso & A. Gens
Department of Geotechnical Engineering and Geo-Sciences. Universitat Politècnica de Catalunya, Barcelona, Spain

ABSTRACT: The selection of constitutive variables has been extensively discussed when modeling unsaturated soils. In general, suction and degree of saturation have been involved in the definition of constitutive variables. Recently, microstructural features have also been included due to their relevant effects on the mechanical and hydraulic soil response. This is the case of a model recently published by the same authors which includes a state variable in the definition of the constitutive variables to take into account microstructural effects. Details of the performance of this model, which has a relatively simple elastoplastic formulation, are presented. The simulation of isotropic stress paths illustrates the capabilities of the model and the effect of the microstructural state variable.

1 INTRODUCTION

The pore size distribution provides a measure of the microstructure of soils. The presence of two pore size domains is explained by the aggregation of clay particles into larger units which reach dimensions comparable to silt and fine sand particles. Such a structure has been reported for colluvial and tropical soils (Mascarenha et al., 2011), and more commonly for compacted soils on the dry side (Simms and Yanful, 2001; Thom et al., 2007; Merchán, 2010). However alluvial soils and soils compacted on the wet side often exhibit a monomodal pore size distribution. In the first case a micro-macro double structure seems to be well justified. In the second case it is more difficult to distinguish a micropore (or macropore) domain. Despite this difficulty, which is discussed further below, Mercury Intrusion Porosimetry (MIP) data and its interpretation in terms of a macrostructure (associated with capillary effects) and a microstructure in which physicochemical attraction of clay platelets governs water action, seems to be a simplified but useful way of interpreting unsaturated soil behavior.

Selecting appropriate state variables is a starting point to constitutive modeling. Void ratio and water content are an obvious choice. The alternate selection of isotropic saturated preconsolidation stress and suction provides advantages discussed in Alonso and Pinyol (2008) in the context of soil compaction. However, the additional effect of soil microstructure on observed experimental behaviour, reported by several authors (Lambe, 1958; Lawton et al., 1989, 1991; Fredlund and Rahardjo, 1993; Wheeler and Sivakumar, 2000; Jotisankasa et al., 2007, 2009, Alonso et al., 2010, 2012) suggests that an additional state variable is required to improve model capabilities.

A relevant question is how to include the microstructural information in constitutive modeling. One option is to adopt a commonly accepted set of "constitutive" stresses (net stress and suction; Bishop—or intergranular-stress and suction) and to transfer to the constitutive model formulation the task of including microstructural effects. A second alternative is to explore first if microstructure may be included in the definition of constitutive stresses and to develop a constitutive model afterwards. The second alternative has some promise of leading to a simpler class of models. This alternative was proposed in Alonso et al. (2012) and it is further discussed in this paper.

2 EFFECTIVE STRESS IN A STRUCTURED SOIL

Gens and Alonso (1992) and Alonso et al. (1999) proposed a model which explicitly introduced a double structure through the consideration of a microstructural void ratio. Constitutive models

were defined for each of the structural levels defined, as well as an interaction between them. The elastoplastic model was defined in terms of net stress and suction (either "macro" or "micro"). This model uses the first alternative as defined above. The model is well adapted to describe the volumetric behavior of expansive clays. This is shown for instance in Lloret et al. (2003). Figure 1, taken from this paper, shows the calculated evolution of the micro and macro void ratios of a compacted bentonite during a path involving wetting at low stress and compression under saturated conditions.

This is an interesting capability, but the model is relatively complex and parameter calibration is not a simple task.

A simpler way of including microstructure was advanced by a number of researchers who examined particular aspects of unsaturated soil behaviour, essentially strength and elastic stiffness (Vanapalli et al., 1996; Khalili and Khabbaz, 1998; Vaunat et al., 2000; Toll and Ong, 2003; Tarantino and Tombolato, 2005; Jotisankasa et al., 2009). The idea was to propose that the mechanical effect of suction is only explained by the capillary action on the macrostructure.

Alonso et al. (2010) formalized this concept for the entire range of degrees of saturation and defined a microstructural void ratio, $\xi_m = e_m/e$, which marks the transition of a water volume filling microvoids to free or capillary water occupying the macrovoids. It was shown that indirect determinations of ξ_m through backanalysis of strength and stiffness data were similar to direct determinations of ξ_m by means of MIP.

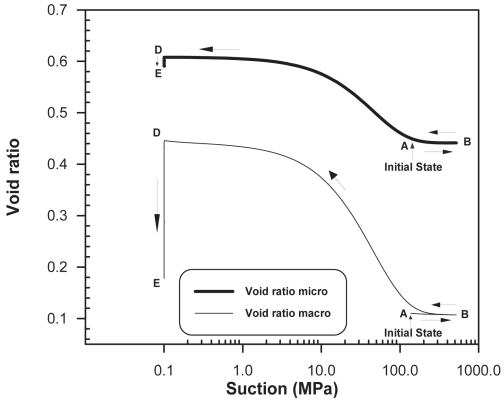

Figure 1. Calculated evolution during wetting at low stress and compression under saturated conditions of the micro and macro void ratio of a compacted bentonite (Lloret et al., 2003).

An effective degree of saturation was defined as follows:

$$\overline{S}_r = \frac{S_r - \xi_m}{1 - \xi_m} \quad \text{for} \quad S_r > \xi_m \tag{1a}$$

$$\overline{S}_r = 0 \quad \text{for} \quad S_r \le \xi_m \tag{1b}$$

Alternative smooth approximations for Equation (1) are

$$\overline{S}_r = \left(S_r\right)^{\alpha} \tag{2a}$$

$$\overline{S}_r = \frac{S_r - \xi_m}{1 - \xi_m} + \frac{1}{n}\ln\left[1 + \exp\left(-n\frac{S_r - \xi_m}{1 - \xi_m}\right)\right] \tag{2b}$$

where n is a smoothing parameter.

The third expression has been used in the formulation of the model outlined below.

3 MODEL HYPOTHESIS AND MODEL FORMULATION

The model is formulated in terms of a Bishop (1959) based stress (Eq. (3)) and the "effective suction" (Eq. (4)):

$$\overline{\sigma} = \sigma - p_g + \overline{s} \tag{3}$$

$$\overline{s} = \overline{S}_r s \tag{4}$$

where σ is the total stress, p_g is the air pressure, s, the matric suction ($s = p_g - p_w$, p_w: pore water pressure) and $\overline{S}_r$ the effective degree of saturation.

Elastic volumetric changes in void ratio (e) are calculated as follows:

$$de = \overline{\kappa}\frac{d\overline{p}}{\overline{p}} \tag{5}$$

where $\overline{p}$ is the mean effective stress (calculated through Eq. (3)) and $\overline{\kappa}$ the elastic volumetric compressibility assumed constant in this paper.

Expression (5) implies that a change in net stress leads to the same elastic mechanical effect as a change in effective suction of the same magnitude. This assumption was investigated by Alonso and Romero (2012). They subjected samples of compacted low plasticity Barcelona silty clay of alternative proving tests, by applying increments of isotropic net stress and suction from a common initial state. Probing tests remained in the elastic region. Measured volumetric strains were interpreted with the help of Equation (5).

Volumetric plastic changes are defined at post yield stress level as follows:

$$de = \bar{\lambda}\frac{d\bar{p}_0}{\bar{p}_0} \tag{6}$$

where $\bar{p}_0$ is the mean yield stress at the current effective suction and $\bar{\lambda}$ the plastic volumetric compressibility in the void ratio—logarithmic effective stress (Eq. (3)) plane. The structure of $\bar{\lambda}$ will be discussed below.

The effect of non-saturation in the plastic compressibility has been reported by many authors. In particular, the effect of suction in the slope of normal compressibility lines in the void ratio—logarithm of net stress has been extensively corroborated by experimental data (Alonso et al., 1987; Barrera, 2002; Benatti et al., 2010). Toll (1990), Wheeler et al. (2003) and Jotisankasa et al. (2007) discuss not only the suction effect but also the effect of the degree of saturation on the compressibility. The proposal of Alonso et al. (2012) is that the unsaturated plastic compressibility, $\bar{\lambda}$, depends on the virgin compressibility index for saturated conditions (effective suction equal to zero), $\bar{\lambda}(0)$, and of the current effective suction ($\bar{s}$, Eq. (4)). Loading stress paths in terms of effective stress (Eq. (3)) at constant effective suction (Eq. (4)) are characterized by linear compression lines.

Notice that these stress paths cannot be directly reproduced in the laboratory. However, this fact should not be an important drawback in the simulation of laboratory tests or typical loading situations in which net stress, suction or degree of saturation are controlled or measured. Once the model is formulated, conventional stress paths can be simulated and the results can be given in any stress space since net stress, suction, degree of saturation and macro and micro void ratios are known or are computed at each calculation step. The main disadvantage of formulating the model in a set of stress variables different from the variables used in laboratory tests lies in the difficulty of parameter calibration.

Collapse is also dependent on microstructure. This effect was shown in Suriol et al. (1998) and it is further discussed in Alonso et al. (2012). Since collapse is directly related to yield behavior, the isotropic yield locus should be made dependent on a microstructural state variable. Therefore a loading collapse (LC) yield function will be defined in the space $\bar{p} - \bar{s}$. The LC yield function may be selected on the basis of phenomenological observations. In Alonso et al. (2012), the LC is linked with the volumetric compression index, $\bar{\lambda}$, by the expression:

$$\frac{\bar{p}_0}{\bar{p}_c} = \left(\frac{p_0^*}{\bar{p}_c}\right)^{\frac{\bar{\lambda}(0)-\bar{\kappa}}{\bar{\lambda}(\bar{s})-\bar{\kappa}}} \tag{7}$$

In Equation (7), p_0^* is the preconsolidation isotropic stress for saturated states (zero effective suction) and $\bar{p}_c$ is a reference mean effective stress corresponding to the point where virgin compression lines cross for different effective suctions.

Note that the microstructure does not affect p_0^* The model assumes that a unique normal saturated consolidation line exists. Therefore, the preconsolidation stress for saturated conditions only depends on the void ratio and not on the compaction conditions (results of Honda et al. (2003) and Jotisankasa (2007) confirm this hypothesis). The hardening law was made dependent on plastic volumetric strain.

An advantage of using a Bishop-based stress as an effective stress for unsaturated soils (instead of a net stress) is that Terzaghi effective stress is immediately recovered when saturation is reached ($S_r = 1$). Therefore no additional procedures have to be added in order to ensure the continuity of the stress variable at the saturated/unsaturated transition.

However, experimental evidence for the behavior of soils subjected to a suction lower than the air entry value (s_e) should also be considered. In these cases $S_r = 1$ and Terzaghi effective stress controls soil behavior. This necessary consistency is not automatically ensured by defining a Bishop-based stress variable as "effective" stress in a constitutive model for unsaturated soils. The effect of the second constitutive variable should also vanish when saturation is reached (and not just when suction is zero).

The saturated behavior is automatically recovered in those constitutive models in which the second stress variable is a function of the degree of saturation (Wheeler et al., 2003; Tamagnini, 2004; Buscarnera and Nova, 2009; Zhou et al., 2012a, b). This is not the case of models in which the compressibility index and the yield function are expressed in terms of suction (e.g., Alonso et al., 1990 (BBM), Sun et al., 2007). This drawback can be easily solved by prescribing that the variables depending on suction recover their corresponding saturated values for suctions lower than s_e. This idea is proposed in Loret and Khalili (2002), Pereira et al. (2005) and Sheng et al. (2008).

The same problem is observed in models in which the second constitutive variable is a function of the product $S_r{\cdot}s$. At saturation, this product can be different from 1 if suction is higher than zero but lower than s_e. Then, some parameters of the model which depend on $S_r{\cdot}s$ may not recover saturated values. In order to recover saturated behavior, Alonso et al. (2012) propose that the plastic stiffness increase due to non-saturation is linked with the air entry value (s_e). This is done by defining the reduction of $\bar{\lambda}$ by including information taken

from the WRC. This may be achieved if parameter $\bar{\lambda}$ is computed with the following expression:

$$\bar{\lambda}(\bar{s}) = \lambda(0)\left[\bar{r} + (1-\bar{r})\left[1 - \left(\frac{\bar{s}}{\bar{s}_\lambda}\right)^{1/(1-\bar{\beta})}\right]^{-\bar{\beta}}\right] \quad (8)$$

which adopts a form taken from the equation proposed by Van Genuchten (1980) for the WRC.

Equation (8) is plotted in Figure 2 for different values of the parameters $\bar{s}_\lambda$, $\bar{r}$ and $\bar{\beta}$. The first parameter, $\bar{s}_\lambda$, depends on the air entry value and it takes the same value adopted for the water retention curve. When suction reaches a value lower than s_e and the degree of saturation is equal to one, suction and effective suction take the same values and the compression index becomes equal to $\lambda(0)$. Parameter $\bar{r}$ controls the minimum value of $\bar{\lambda}$. The shape of the curve, and the suction at which a minimum value of $\bar{\lambda}$ is reached, is determined by parameter $\bar{\beta}$.

4 MODEL PERFORMANCE

The performance of the model is illustrated for a soil characterized by the model parameters and initial state variables summarized in Table 1. Isotropic loadings tests at constant suction (1 MPa) and a subsequent saturation at constant mean net stress are simulated on samples with different values of e_m (0.1, 0.15, 0.2, 0.25). The parameter e_m quantifies the initial microstructure. It was assumed to remain constant afterwards. Evidence of this behavior was given in Alonso et al. (2012) for some reported tests on compacted soils. The initial void ratio is equal to 0.6 for all samples. It leads to different initial values of ξ_{m0}.

A unique set of constitutive parameters describe the "intrinsic" properties of the compacted soils. As—compacted conditions are defined by two initial stress states: suction and (saturated) yield stress. Based on experimental data collected by Romero et al. (2011) on Boom clay, bentonite and Barcelona silty clay, the selected values of e_m could be appropriate for a low or medium plasticity clay compacted at both dry conditions (low values of e_m) and wet conditions (high values of e_m). A Van Genuchten curve has been selected to represent the water retention features (Table 1).

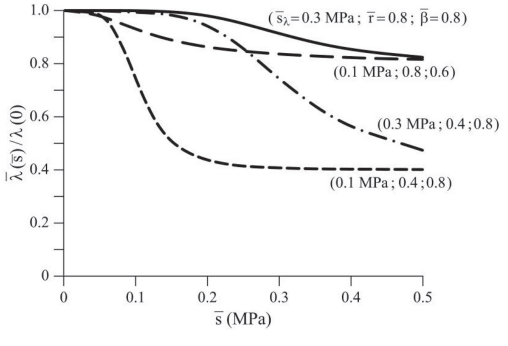

Figure 2. Variation of isotropic compressibility, $\bar{\lambda}$, with effective suction, $\bar{s}$, for different parameter values.

Table 1. Model parameters used in model performance.

Parameter	Definition	Units	Values
Mechanical parameters			
$\bar{\kappa}$	Elastic compressibility	–	0.01
$\bar{\lambda}(0)$	Plastic compressibility at zero effective suction	–	0.1
$\bar{p}_c$	Reference stress	MPa	0.02
$\bar{s}_\lambda$	Minimum value of effective suction affecting plastic volumetric compressibility. It is equivalent to an air entry value (P_0)	MPa	0.05
$\bar{r}$	Parameter that establishes the minimum value of the compressibility coefficient for high values of effective suction	–	0.5
$\bar{\beta}$	Parameter that controls the rate of increase in stiffness with effective suction	MPa^{-1}	0.32
n	Parameter that defines the degree of smoothing in Eq. (2b)	–	10
Water retention curve. Van Genuchten model			
$S_{r\min}$	$\frac{S_r - S_{r\min}}{S_{r\max} - S_{r\min}} = \left(1 + \left(\frac{s}{P_0}\right)^{\frac{1}{1-\lambda}}\right)^{-\lambda}$	–	0
$S_{r\max}$		–	1
P_0		MPa	0.05
λ		–	0.27
Initial conditions			
e_0	Initial void ratio	–	0.6
p_0^*	Yield stress at zero effective suction	MPa	0.2
s_0	Initial suction	MPa	1
ξ_{m0}	Initial microstructural state variable	–	Sensitivity analysis

Figure 3 shows the computed compression curves. The normal compression line for saturated

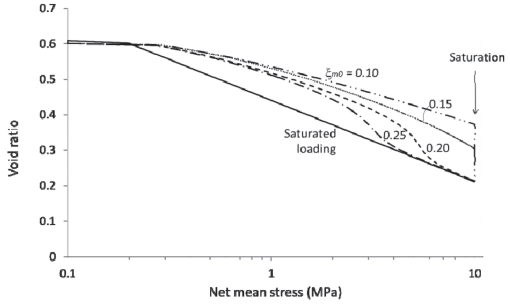

Figure 3. Isotropic loading curves at constant suction (1 MPa) and saturation at 10 MPa of net stress for different values of ξ_{m0}.

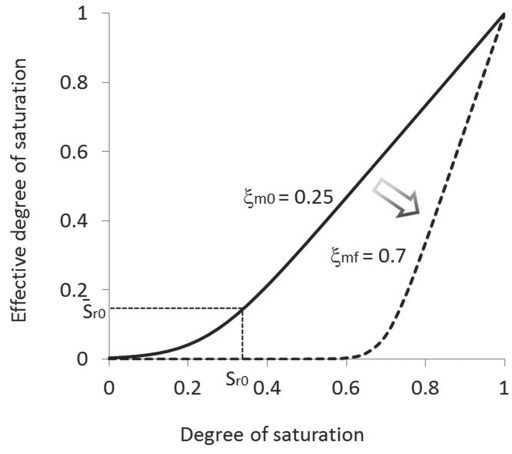

Figure 4. Change of effective degree of saturation during loading at constant suction for $\xi_{m0} = 0.25$.

conditions is also plotted. Compression lines are not linear in the $p - s$ space. At relatively low stress levels, all unsaturated compression curves exhibit a higher stiffness than the saturated compression curve. This is an effect of the current effective suction. As applied stress increases, the curvatures are more pronounced and they converge toward the fully saturated normal consolidation line. This is consequence of the progressive reduction of void ratio during compaction. Since e_m is assumed to remain constant the state variable $\xi_m = e_m/e$ increases continuously and the effective suction, which controls compressibility, decreases.

In the calculated example the WRC is unique and the degree of saturation is maintained during loading. Therefore, the amount of water existing in the sample reduces progressively during loading. Capillary water will eventually disappear (water will remain inside aggregates), the effective suction will reduce to zero and the compressibility will approach the saturated value. Since all samples are subjected to the same suction, samples with higher values of ξ_{m0} reach the saturated compression lines faster since they have a lower proportion of macropores. Given a microstructure, an initial suction and a WRC, the shape of the compression curves is determined by the shape of the function selected for $\overline{\lambda}(\overline{s})$.

The evolution of effective degree of saturation during loading for $\xi_m = 0.25$ is represented in Figure 4. Initially, the effective degree of saturation ($\overline{S}_{r0} = 0.17$) is defined by $S_{r0} = 0.36$ and $\xi_{m0} = 0.25$. During loading, void ratio reduces (from $e = 0.6$ to 0.21) and ξ_m increases (up to 0.7) reducing the effective degree of saturation. Eventually, ξ_m may become higher than the degree of saturation (which remains constant) and then the effective degree of saturation becomes essentially zero and the loading curve reaches the saturated normal consolidation line.

In the simulated cases, samples were saturated when the isotropic net stress reached 10 MPa. The smaller collapse of samples compacted at a higher water content (higher ξ_{m0}) can be observed in Figure 3 (distance between unsaturated and saturated loading curves). Note also that the model is able to reproduce the collapse variation with the applied net stress as observed experimentally (Suriol and Lloret, 2007; Rodriguez and Vilar, 2011). The collapse initially increases with the vertical stress, it reaches a maximum value and finally decreases at higher values of net stress.

5 CONCLUSIONS

The constitutive model for compacted soils presented in Alonso et al. (2012) has been discussed and its capabilities have been illustrated by simulating isotropic loadings.

The model is defined in terms of the constitutive stress proposed in Alonso et al. (2010) and an effective suction. Both constitutive variables include microstructural information.

Based on this, the proposed model formulation is relatively simple. It can be defined as a modification of the Barcelona Basic Model (Alonso et al., 1992) using different constitutive variables. Despite the simplicity in the formulation, the model is able to reproduce some particular features of compacted soils.

The performance of the model was illustrated in the calculated response against isotropic loading paths. A unique set of parameters was selected and the initial value of the microstructural state variable, which is a measured of the compacted conditions, was varied to perform a sensitivity analysis.

The model is able to reproduce the following features:

- In the elastic region, changes in net stress have the same effect on the soil deformation as changes in effective suction of the same magnitude.
- In compacted soils, dry compaction results in a higher apparent preconsolidation stress. Compressibility indices increase when compaction water content increases.
- Wetting induced collapse depends on the applied net stress. It increases first at relatively low values of net stress, reaches a maximum and decreases at higher compression values.

REFERENCES

Alonso, E.E., Gens, A. & Josa, A. 1990. A constitutive model for partially saturated soils. *Géotechnique* 40 (3): 405–430.

Alonso, E.E., Gens, A. & Hight, D. 1987. Special problem soils. General Report. *Proc. 9th Eur. Conf. on Soil Mech. and Found. Engng,* (Dublin, Ireland) 3: 1087–1146.

Alonso, E.E., Pereira, J.M. Vaunat, J. & Olivella, S. 2010. A microstructurally based effective stress for unsaturated soils. *Géotechnique* 60(12): 913–925.

Alonso, E.E. & Pinyol, N.M. 2008. Unsaturated soil mechanics in earth and rockfill dam engineering. *Proc. 1st Eur. Conf. on Unsaturated Soils* (Durham, UK) 1: 3–32.

Alonso, E.E., Pinyol, N.M. & Gens, A. 2012. Compacted soil behaviour: initial state, structure and constitutive modeling. *Géotechnique*, to be published.

Alonso, E.E. & Romero, E. 2012. Experimental investigation of an effective stress law in compacted clayey/silty soil. *Proc. 5th Asian Conference on Unsaturated Soils*. Pattaya, Thailand: 331–336.

Alonso, E.E., Vaunat, J. & Gens, A. 1999. Modelling the mechanical behaviour of expansive clays. *Engineering Geology* 54: 173–183.

Barrera, M. 2002. Estudio experimental del comportamiento hidromecánico de suelos colapsados. *PhD Thesis*. Universitat Politècnica de Catalunya, Barcelona, Spain.

Benatti, J.C.V., Miguel, M.G., Rodrigues, R.A. & Vilar, O.M. 2010. Collapsibility study for tropical soil profile using oedometric tests with controlled suction. *Unsaturated Soils*. Alonso & Gens (eds). Vol. 1: 197–198.

Bishop, A.W. 1959. The principle of effective stress. *Tecknisk Ukeblad*, 106(39): 859–863.

Buscarnera, G. & Nova, R. 2009. An elastoplasti strainhardenint model for soil allowing for hydraulic bonding-debonding effects. *Int. J. Numer. Anal. Meth. Geomech. 3*: 1055–1086.

Fredlund, D. & Rahardjo, H. 1993 *Soil mechanics for unsaturated soils.* Wiley (London): 517 p.

Gens, A. & Alonso, E.E. 1992. A framework for the behaviour of unsaturated expansive soils. *Canadian Geotechnical Journal* 29(6): 761–773.

Honda, M., Seguchi, H., Kim, E., Hawai, K., Iizuka, A. & Karube, D. 2003. A study of the relation between volume change characteristics of compacted soil and the condition of compaction. *Proceedings of the 2nd Asian Conference on Unsaturated Soils.* April, Osaka, Japan: 177–180.

Jotisankasa, A., Coop, M. & Ridley, A. 2009. The mechanical behaviour of an unsaturated compacted silty clay. Géotechnique 59(5), 415–428.

Jotisankasa, A., Ridley, A. & Coop, M. 2007. Collapse behavior of compacted silty clay in suction-monitored oedometer apparatus. *Journal of Geotechnical and Geoenvironmental Engineering* 133(7): 867–877.

Khalili, N. & Khabbaz, M.H. (1998). A unique relationship for the determination of the shear strength of unsaturated soils. *Géotechnique* 48(5): 681–687.

Lambe, T.W. 1958. The engineering behaviour of compacted clay. *J. Soil Mech. Found. Div.* 84(SM2) Asce: 1–35.

Lawton, E.C., Fragaszy, R.J. & Hardcastle, J.H. 1989. Collapse of compacted clayey sand. *J. Geotech. Engng.* 115(9) ASCE: 1252–1267.

Lawton, E.C., Fragaszy, R.J. & Hardcastle, J.H. 1991. Stress ratio effects on collapse of compacted clayey sand. *J. Geotech. Engng*. 117(5) ASCE: 714–730.

Lloret, A.,Villar, M.V., Sánchez, M., Gens, A., Pintado, X. & Alonso, E.E. 2003. Mechanical behaviour of heavily compacted bentonite under high suction changes. *Géotechnique* 53(1): 27–40.

Loret, B. & Khalili, N. 2002. An effective stress elastic-plastic model for unsaturated porous media. *Mechanics of Materials* 34: 97–116.

Merchán, V. 2011. Small strain stiffness and residual strength of unsaturated Boom clay: A micro-structural insight. *PhD Thesis*. Universitat Politècnica de Catalunya. Barcelona, Spain.

Pereira, J.M., Wong, H., Dubujet & Dangla, P. 2005. Adaptation of existing behaviour models to unsaturated states: Application to CJS model. *Int. J. Numer. Anal. Meth. Geomech. 29*: 1127–1155.

Rodriguez, R.A. & Vilar, O.M. 2011. Experimental study of collapsible beaviour of tropical unsaturated soil. *Unsaturated Soil.* Alonso & Gens (eds.). Vol. 1: 353–357.

Romero, E., Della Vecchia, G. & Jommi, C. 2011. An insight into the water retention properties of compacted clayey soils. *Géotechnique* 61(4): 313–328.

Sheng, D., Fredlund, D.G. & Gens, A. 2008. A new modeling approach for unsaturated soils using independent stress variables. *Can. Geotech. J.* 45(4): 511–534.

Simms, P.H. & Yanful, E.K. 2002. Predicting soil-water characteristic curves of compacted plastic soils from measured pore-size distributions. *Géotechnique* 52(4): 269–278.

Sun, D., Sheng, D. & Sloan, S.W. 2007. Elastoplastic modelling of hydraulic and stress-strain behavoiur of unsaturated soils. *Mechanics of Materials* 39: 212–221.

Suriol, J., Gens, A. & Alonso, E.E. 1998. Behaviour of compacted soils in suction-controlled oedometer. *Proceedings of the 2nd International Conference on Unsaturated Soils*. Beijing (China). International Academic Publishers (eds): 438–443.

Suriol, J. & Lloret, A. 2007. Cambios en la estructura de suelos compactados frente a humedecimiento y secado. *Ingeniería Civil* 147: 67–76.

Tamagnini, R. 2004. An extended Cam-clay model for unsaturated soils with hydraulic hysteresis. *Géotechnique* 54(3): 223–228.

Tarantino, A. & Tombolato, S. 2005. Coupling of hydraulic and mechanical behaviour in unsaturated compacted clay. *Géotechnique* 55(4): 307–317.

Thom, R., Sivakumar, R. Sivakumar, V. Murray, E.J. & Mackinnon, P. 2007. Pore size distribution of unsaturated compacted kaolin: the initial states and final states following saturation. *Géotechnique* 57(5): 469–474.

Toll, D.G. 1990. A framework for unsaturated soil behaviour. *Géotechnique* 40(1): 31–44.

Toll, D.G. & Ong, B.H. 2003. Critical-state parameters for an unsaturated residual sandy clay. *Géotechnique* 53(1): 93–103.

Vanapalli S.K., Fredlund, D.E., Pufahl, D.E. & Clifton A.W. 1996. Model for the prediction of shear strength with respect to soil suction. *Can Geotech. J.* 33(3): 379–392.

van Genuchten, M.T. 1980. Closed-form equation for predicting the hydraulic conductivity of unsaturated soils. *Soil Sci. Soc. Am. J.* 44(5): 892–898.

Vaunat, J., Romero, E. & Jommi, C. 2000. An elastoplastic hydromechanical model for unsaturated soils. *Experimental evidence and theoretical approaches in unsaturated soils* (eds A. Tarantino and C. Mancuso): 121–138. Rotterdam. A.A. Balkema.

Wheeler, S.J., Sharma, R.S. & Buisson, M.S.R. 2003. Coupling hydraulic hysteresis and stress-strain behaviour in unsaturated soils, *Géotechnique* 53(1): 41–54.

Wheeler, S.J. & Sivakumar, V. 2000 Influence of compaction procedure on the mechanical behaviour of an unsaturated compacted clay. Part 2: Shearing and constitutive modelling. *Géotechnique* 50(4): 369–376.

Zhou, A-N, Sheng, D., Sloan, S. & Gens, A. 2012a. Interpretation of unsaturated soil behaviour in the stress. Saturation space I: Volume change and water retention behaviour. *Computers and Geotechnics* 43: 178–187.

Zhou, A-N, Sheng, D., Sloan, S. & Gens, A. 2012b. Interpretation of unsaturated soil behaviour in the stress. Saturation space II: Constitutive relationships and validation. *Computers and Geotechnics* 43: 111–123.

This page intentionally left blank

Advances in Unsaturated Soils – Caicedo et al. (eds)
© 2013 Taylor & Francis Group, London, ISBN 978-0-415-62095-6

Effect of loading and suction history on time dependent deformation of coarse crushed slate

E. Romero, C. Alvarado & E.E. Alonso
Universitat Politècnica de Catalunya BarcelonaTech, Barcelona, Spain

ABSTRACT: The paper presents the results of an experimental investigation aimed at evaluating the time-dependent compressibility of coarse crushed quartzitic slate, focusing on the effects of the previous loading and hydraulic history. Long-term and large diameter compression tests under oedometer conditions were performed at different total suctions (relative humidity values) and vertical stresses but following different loading and hydraulic paths. A finding, which has practical implications in earthwork constructions, is that pre-compressing at increasing overconsolidation ratios or pre-soaking the crushed material at constant and elevated stresses leads to the progressive vanishing of long-term deformations.

1 INTRODUCTION

Rockfill mechanical behavior is sensitive to the action of water, which is of particular concern during the design and performance stage of rockfill and zoned dams. These structures exhibit long term deformations, which tend to depend linearly on the logarithm of time as indicated by field records (Oldecop & Alonso 2007). Breakage of rock particles and subcritical crack propagation in corrosive environment are the main underlying physical mechanisms that explain these phenomena, which depend on the strength of individual particles (toughness), the size and shape of particles, the stress level and the relative humidity prevailing at the rockfill voids—or alternatively the activity of the liquid filling these voids—(Oldecop & Alonso 2001, Romero *et al.*, 2005).

This paper particularly explores the time-dependent compressibility, focusing on the effects of the previous hydraulic and loading history—as considered, for instance, by the overconsolidation ratio *OCR*—on rockfill delayed deformations. A crushed quartzitic slate was tested at constant relative humidity—or total suction—and at different *OCR* values in large diameter oedometer cells. The dependence of creep deformation on *OCR* is by no means an academic issue. In fact, it has important practical implications, since the long term settlements could be controlled by pre-conditioning techniques (pre-compression at high stresses or pre-soaking at constant and elevated stresses).

2 MATERIAL USED IN THE RESEARCH

A crushed quartzitic Cambric slate from the Pancrudo River outcrop (Aragón, Spain), which was used in the zoned earth and rockfill Lechago Dam, was tested. The behavior of this material has been studied by several authors (Oldecop & Alonso 2001, Chávez & Alonso 2003, Chávez *et al.*, 2009). Some properties of the rock material are summarized in Table 1.

The material obtained in the quarry was further crushed and sieved. Figure 1 shows the grain

Table 1. Properties of the quartzitic slate.

Property	Value
Uniaxial compression strength*	14.2–31.9 MPa
Density of solids*	2.75 Mg/m^3
Water absorption (saturation)	2.9%
Void ratio (mercury intrusion porosimetry)	0.081
Slake durability (5th cycle) (ASTM D4644)	96.5%
Flakiness index	19%

* Oldecop & Alonso 2001, Chávez & Alonso 2003.

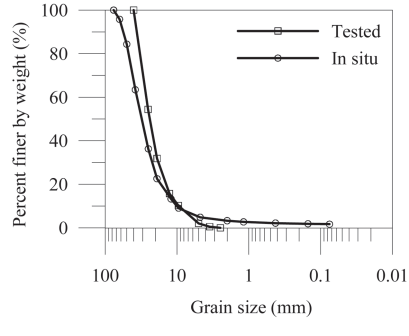

Figure 1. Grain size distribution curve of the crushed quartzitic slate.

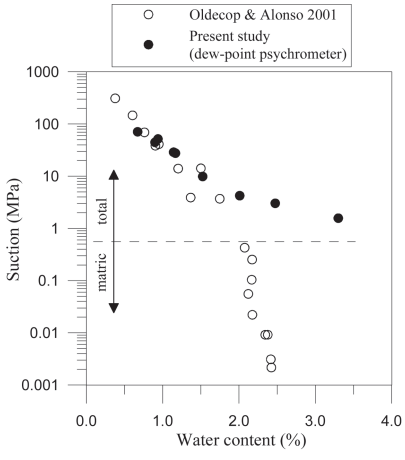

Figure 2. Retention curve along a drying path for crushed quartzitic slate.

size distributions of the *in situ* and tested rockfill material. Before static compaction, the maximum particle size was fixed at 40 mm with 10% passing 10-mm sieve and coefficient of uniformity of 2.9. The water retention curve of the material along a drying path obtained by axis translation (matric suction), vapor equilibrium technique and dew-point psychrometer measurements (total suction) is shown in Figure 2.

3 EXPERIMENTAL PROGRAM

An oedometer test program was carried out in a large diameter cell (300 mm in diameter and approx. 200 mm high) with a relative humidity control system using vapor transfer technique driven by an air pump. Figure 3 shows the rockfill oedometer test setup. The crushed slate was statically compacted in four layers inside the oedometer ring at a void ratio $e_0 = 0.55 \pm 0.03$ and water content around $w = 0.6\%$ in equilibrium with the relative humidity prevailing at laboratory conditions (approx. 50%). Pre-compression tests involved loading-unloading paths at saturated state and at constant relative humidity of the air (75% and 30%, corresponding to total suctions 39 MPa and 160 MPa, respectively). Different overconsolidation ratios ('NC' normally consolidated and 'OC' overconsolidated states) were analyzed as described in Table 2 and as shown in Figure 4 for the different stress paths followed. Pre-soaking tests were associated with soaking and drying paths at a constant vertical stress of 1 MPa. During soaking, compression (collapse) strains developed due to important particle breakage at the stress level tested. On subsequent drying by vapor transfer technique to different total

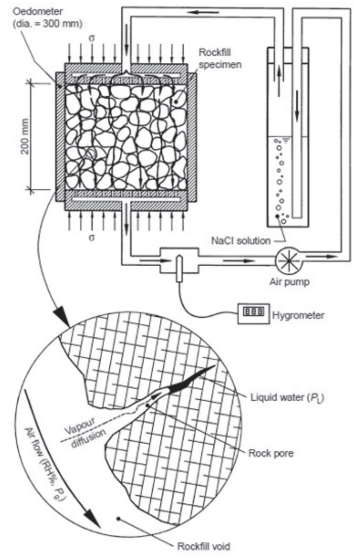

Figure 3. Rockfill oedometer test setup with relative humidity control (Oldecop & Alonso 2001).

Table 2. Description of the pre-compression test program performed.

Ref.	Wetting stage	Total suction	Stress applied in long term tests
1	Water at 0.05 MPa	0	NC*: 0.1; 0.5 and 1 MPa OC**: 0.87; 0.67 and 0.25 MPa
2	Vapor	39 MPa	NC*: 0.1; 0.5 and 1 MPa OC**: 0.87; 0.67 and 0.25 MPa
3	Vapor	160 MPa	NC*: 0.1; 0.5 and 1 MPa OC**: 1.0; 0.87; 0.67 and 0.25 MPa

* Normally consolidates state. **Overconsolidated states.

suctions—varying between 39 MPa and 160 MPa–, the material was at an overconsolidated state that was hydraulically induced.

4 EXPERIMENTAL RESULTS

The evolution of the vertical strain along a loading-unloading path under saturated conditions (ref. 1 in Table 2 and Fig. 4) is shown in Figure 5. A step loading approach was followed with maximum load duration of 72 hours for overconsolidated states (unloading stages after pre-compression) and 24 hours for normally consolidated conditions (loading stages).

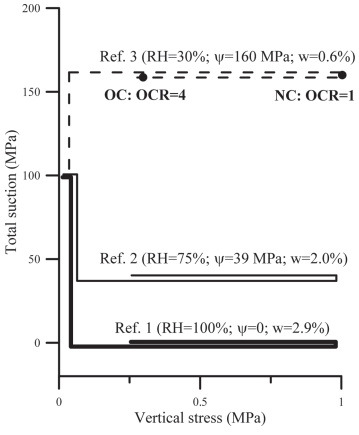

Figure 4. Stress paths followed at different and constant relative humidity for the pre-compression tests at normally and overconsolidated states.

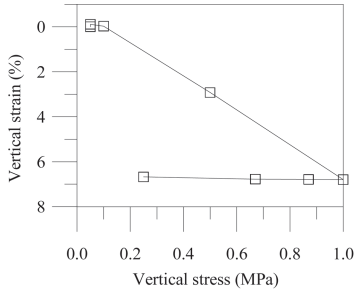

Figure 5. Volume change results under saturated conditions along a loading-unloading path.

The time evolution of the volume change response under saturated and normally consolidated conditions is presented in Figure 6, in which a larger time-dependent compressibility is observed at higher vertical stresses (the different loading steps are indicated in the figure).

The slope of the vertical strain (ε_v)—log time curves previously presented provides information for the determination of the secondary (time-dependent) compressibility index according to the following equation, which was calculated for elapsed times since load application larger than 100 min

$$C_\alpha = \frac{\Delta\varepsilon_v(1+e_o)}{\Delta\log t} = -\frac{\Delta e}{\Delta\log t} \quad (1)$$

The time dependent compressibility index under normally consolidated conditions $C_{\alpha NC}$ and at different total suctions (refer to Table 2 and Fig. 4) are plotted in Figure 7 as a function of the vertical

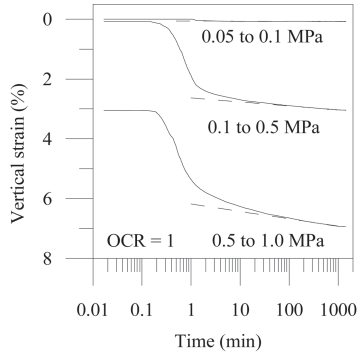

Figure 6. Time evolution of vertical strain in normally consolidated and saturated samples.

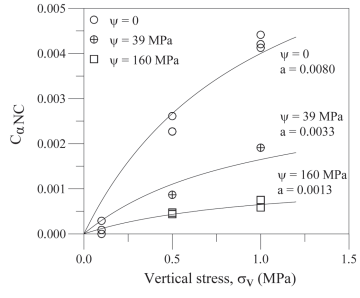

Figure 7. Time-dependent compressibility index of normally consolidated samples against vertical stress for different constant total suctions.

stress σ_v applied, in which the dependence on total suction is readily observed. An equivalent behavioral response was presented by Oldecop & Alonso (2007), in which samples in dry environments displayed nearly null index, consistent with the low crack propagation velocity obtained from the stress corrosion curves at low relative humidity values and with the conceptual model proposed by Oldecop & Alonso (2001). In addition, the compressibility indexes tend to level off at high vertical stresses (usually between 1 and 2 MPa, as shown by Oldecop & Alonso 2007). To limit maximum levelling off, the following empirical expression was used to fit experimental data (Fig. 7) with parameter *a*, which as a first approximation can depend on total suction

$$C_{\alpha NC} = a\,\sigma_v \Big/ \left(1\text{MPa} + \sigma_v\right) \quad (2)$$

On regarding the time dependent compressibility index under overconsolidated states obtained during the unloading stages and after pre-compression, Figure 8 presents its evolution

with *OCR*. An important reduction in the secondary compressibility was detected at $OCR > 1$, which follows a behavioral response similar to soils (see for instance, Alonso *et al.*, 2000).

The variation of $C_\alpha/C_{\alpha NC}$ for different *OCR* values was described by the following empirical equation, where α and β are constant parameters that allow reproducing the measured data ($\alpha = 0$ and $\beta = 15$ are used to plot the curves in Fig. 8).

$$C_\alpha/C_{\alpha NC} = (1-\alpha)e^{-\beta(OCR-1)} + \alpha \quad (3)$$

The time dependent compressibility index at constant vertical stress 1 MPa and at different total suctions under normally consolidated states and after undergoing the soaking and drying paths—that induced overconsolidated states–, is plotted in Figure 9. Again, some reduction in the time dependent compressibility index is detected in the overconsolidated samples (samples previously subjected to soaking-drying), which presents a consistent and equivalent behavioral response to the pre-compression tests.

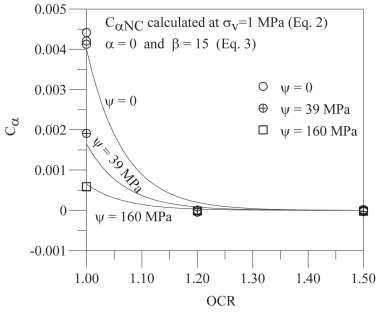

Figure 8. Time-dependent compressibility index against *OCR* for different constant total suctions.

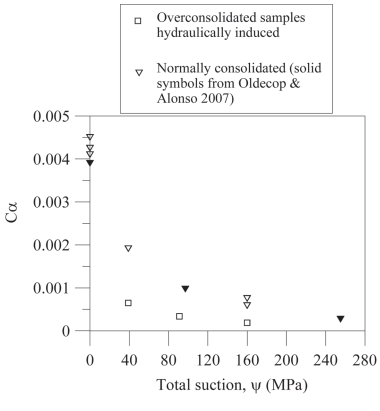

Figure 9. Time-dependent compressibility index against total suction at a constant vertical stress of 1 MPa. Normally consolidated samples and overconsolidated samples after undergoing the soaking-drying paths at 1 MPa.

5 CONCLUSIONS

A crushed quartzitic slate, used in previous investigations on rockfill behavior, was tested to study the effects of the previous loading and the hydraulic history on material delayed deformations. Typical tests involved loading-unloading samples at constant relative humidity—or total suction—and at different *OCRs*, as well as soaking-drying paths at constant and elevated stress, which were performed in special large diameter oedometer cells (300 mm in diameter). A finding is that preloading the crushed slate at increasing *OCRs* leads to the progressive vanishing of creep deformations, following a behavioral response similar to soils. An equivalent response was observed at overconsolidated states after the soaking-drying paths. The reduction has practical applications, since the long term settlements of rockfill materials could be controlled by pre-compression and pre-soaking technique at elevated stress. If at each point of the rockfill embankment an $OCR = 1.1$ is ensured by pre-loading, a reduction to 22% of the normally consolidated long-term settlement would be expected.

ACKNOWLEDGEMENTS

The financial support given by the Universidad de Carabobo (Venezuela) to the second author is greatly acknowledged.

REFERENCES

Alonso, E.E., Gens, A. & Lloret, A. (2000). Precompression design for secondary settlement reduction. *Géotechnique* 50(6): 645–656.

Chávez, C. & Alonso, E.E. (2003). A constitutive model for crushed granular aggregates which includes suction effects. *Soils and Foundations* 43(4): 215–227.

Chávez, C., Romero, E. & Alonso, E.E. (2009). A rockfill triaxial cell with suction control. *Geotech. Testing J.* 32(3): 219–231.

Oldecop, L.A. & Alonso, E.E. (2001). A model for rockfill compressibility. *Géotechnique* 51(2): 127–139.

Oldecop, L.A. & Alonso, E.E. (2007). Theoretical investigation of the time-dependent behaviour of rockfill. *Géotechnique* 57(3): 289–301.

Romero, E., Alonso, E.E. & Hueso, O. (2005). Effect of water composition on rockfill compressibility. Proc. 16th Int. Conf. on Soil Mechanics and Geotechnical Engineering, Osaka, 12–16, September 2005. Vol. 3. Millpress, Rotterdam: 1913–1916.

Advances in Unsaturated Soils – Caicedo et al. (eds)
© 2013 Taylor & Francis Group, London, ISBN 978-0-415-62095-6

DEM modeling of unsaturated rockfill. Scale effects

M. Tapias, E.E. Alonso & J.A. Gili
Department of Geotechnical Engineering and Geosciences, UPC, Barcelona, Spain

ABSTRACT: The large size of the particles in rockfill structures prevents the appropriate laboratory testing. Moreover, the humidity is a key point to explain changes in the long term deformability of rockfill. Therefore, prediction of field behavior requires the development of models that integrate size effects and humidity changes. The Distinct Element Method has been used to develop a numerical model that includes assemblies of several spherical particles in a pyramidal shape. These "macroparticles" break when a rupture criterion involving the subcritical propagation of cracks within grain is achieved. This propagation is a function of stress state, defect size and relative humidity. Size effects for particles ranging from 0.28 to 56 cm of average diameter have been investigated. The results were validated against some real oedometer tests. The present work demonstrates the capabilities of the method as an useful tool to extend the laboratory tests on gravels to the actual rockfill dimensions.

1 INTRODUCTION

Rockfill is often used in large civil engineering structures such as embankments and dams. Particle sizes range from a few millimetres to more than one meter.

The Relative Humidity (RH) prevailing in pores affects the short and long term mechanical behavior of coarse aggregates (gravels, rockfill). Changes in RH explains the observed response of tested samples as well as large retaining structures (Alonso et al., 2005, Oldecop & Alonso 2007).

Testing the rockfill used in dams and embankments under oedometric, direct shear or triaxial conditions is unreasonable because of the size of particles. Published experimental information on the mechanical behaviour of rockfill is based on tests on scaled grain size distributions.

Scale effects are present in particle breakage, a key phenomenon controlling all aspects of the stress-strain-time behaviour of rockfill. Therefore, a procedure to extrapolate laboratory results to the scale of prototypes should be devised. On the other hand, parameters used in constitutive models are expected to change with the size of particles.

The Distinct Element Method (Cundall et al., 1979) offers an interesting possibility of simulating size effects provided it is capable of integrating properly grain failure mechanisms (Alonso et al., 2012). In this paper the capability of the DEM to handle particle breakage is reviewed. The effect of RH on particle breakage will also be introduced. The model developed will be applied to the simulation of oedometer tests.

2 PARTICLE BREAKAGE CRITERIA

A classical explanation of size effects, observed in brittle materials, is associated with concepts of fracture mechanics. Failure is explained by the full propagation of an existing defect or crack. Under a simple tensile stress state (Mode I of failure) of intensity σ, crack propagation occurs when the stress intensity factor:

$$K = \beta\sigma\sqrt{(\pi a)} \tag{1}$$

becomes equal to the material toughness, Kc. In Equation (1) a is the initial length of the propagating crack and β is a dimensionless factor which embodies the geometry of the particle, the position of the crack, the direction and point of application of loads and the relative size of the crack in relation to the particle size. It is a function of the ratio a/D where D is taken as the average diameter of the particle. In the simulations performed, parameter $\beta(a/\mathrm{D})$ was approximated by the expression given in Tada et al. (1985) and Oldecop & Alonso (2007) for a disk of a perfectly elastic-brittle material containing a central crack.

If a given rock mass is assumed to host a distribution of cracks of different lengths, the larger the particle under consideration the higher the probability of having large-size cracks within the particle. In other words, the size of the particle and the size of maximum crack are equivalent. The particle fracture, in view of Equation (1), will be dependent on particle size.

The next step would be to relate the macroscopic behaviour to the scale dependent particle breakage. This is an 'automatic' outcome of a DEM simulation. Therefore, size effects will be obtained if scale dependent laws are used to simulate particle breakage.

3 NUMERICAL MODEL FOR UNSATURATED ROCKFILL

The numerical model presented here follows previous experimental and theoretical research on the behaviour of rockfill (Oldecop & Alonso 2001, 2007, Alonso et al., 2012). The possibilities offered by the Distinct Element Method (Cundall & Strack 1979, Potyondy & Cundall 2004, Itasca 2008) to investigate scale effects are analyzed here. The basic numerical tool used in simulations is the computer program PFC3Dv4 (Itasca 2008) which has been programmed to simulate a number of necessary features mainly associated with the mechanisms of particle breakage.

Model particles approximate the real shape by aggregating several spheres as a rigid body. Initial macroparticles (or "clumps") integrate 14 spheres in the work developed.

Figure 1 shows the picture of a limestone gravel taken from a experimental program referred to later, the pyramidal shape of the selected macroparticles and the initial arrangement of 471 macroparticles which define the oedometer sample analyzed. The selection of the number of spheres simulating a particle was a trade-off between the capability of the assemblage to reproduce a realistic initial shape of particles and the computational cost of the model. A clump of 14 spheres allows a basic three dimensional pyramidal shape which was judged adequate. Macroparticles interact through contact friction and normal and shear stiffness coefficients (Table 1).

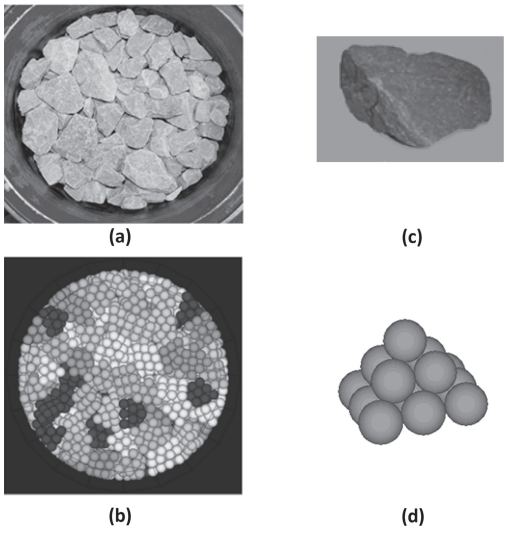

Figure 1. (a) Crushed gravel in oedometer cell (Alonso et al., 2009) (b) DEM model of Oedometer test; (c) Limestone gravel (approximate size: 2.5 cm) tested by Ortega (2010); (d) 14 spheres macroparticle (DEM model).

The determination of the tensile stress σ necessary to calculate K, follows the analysis given by Russell & Muir Wood (2009) and Alonso et al. (2012).

Defects are attributed randomly to all particles, keeping their maximum length limited by the initial size of particles. Maximum defect length was limited to half the size of the particle. A uniform probability density function was simply selected for the distribution of crack sizes among particles.

Particles will fail if, at some instant during sample loading, $K = Kc$. However, particles may also fail even if $K < Kc$. This is known as a "subcritical" failure condition, analyzed in Atkinson (1984), Wiederhorn et al. (1980) and Oldecop & Alonso (2001, 2007) in the context of rockfill behaviour. Fractures propagate in time at a velocity controlled by K and the prevailing relative humidity (RH). Crack growth rates reported in several experiments are collected in terms of (K/Kc) in Figure 2.

Crack propagation velocity, V, is described by a modified Charles law (Oldecop & Alonso 2007):

$$V = \frac{da}{dt} = V_0 \left(\frac{K}{K_c} \right)^n \tag{2}$$

where V_0 is a reference velocity taken as $V_0 = 0.1$ m/s in view of the data given in Charles (1958) and exponent n depends on current suction (relative humidity), see Figure 3.

For a given time increment dt, the crack length increment da is calculated following equations (2) and (1). In this work, the time increment has a value of 1000s and this is the real time. Crack lengths are updated at each step in calculations, $a = a_0 + da$, where a_0 is the previous crack length. The particle is assumed to be broken when the updated crack length reaches the mean dimension of the particle.

Table 1. Properties of the discrete particles in DEM model.

Contact stiffness, *kn*:	4 E 6 *N/m*
Shear stiffness, *ks*:	4 E 6 *N/m*
Friction Coefficient, μ:	0.3
Toughness, *K*:	5 E 6 *Pa*√*m*

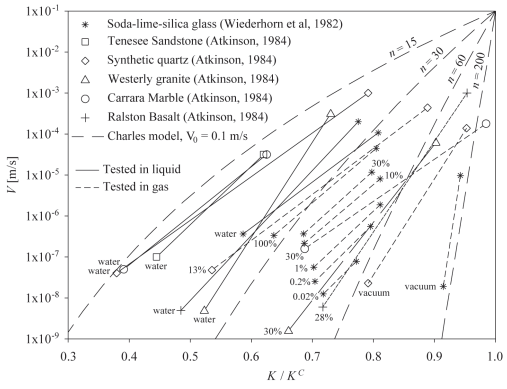

Figure 2. Crack propagation rates for different rocks, quartz and glass. The testing condition (immersed in water, imposed RH or vacuum) is shown next to each curve. Also indicated are curves of Charles model. (Oldecop & Alonso 2007).

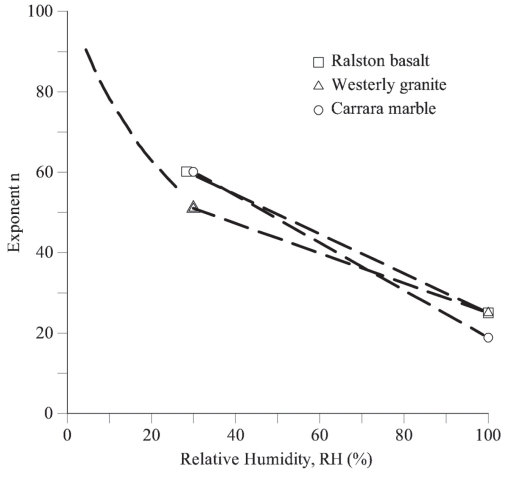

Figure 3. Relationship between exponent n of Charles law and Relative Humidity (Alonso et al., 2009).

Figure 4 shows the breakage time in terms of defect size a and RH, for the following set of parameters.

Particle diameter: $D = 500$ mm; reference velocity in Charles law: V_o = 0,1 m/s, tensile stress: $\sigma = 7$ MPa and toughness: $K_c = 1$ MPa•m$^{0.5}$. Note that small changes in the size of the initial defect leads to a very large change of the rupture time. This is a characteristic of fracture phenomena which is explained by Charles law.

In the simulation the macroparticle divides following an arbitrary criterion which takes into account the number of particles integrated in a "clump" and its pyramidal shape. The following

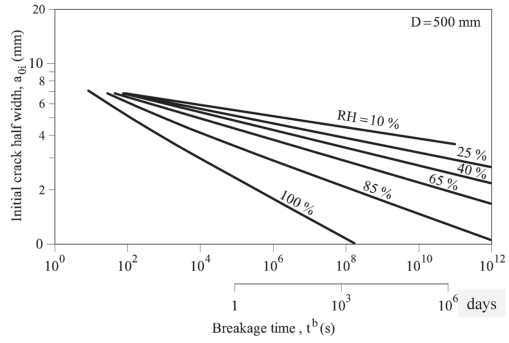

Figure 4. Breakage times for varying initial crack lengths and prevailing suction (modified from Alonso et al., 2009).

division rule is applied: 14 → 8 + 6; 8 → 4 + 4; 6 → 3 + 3; 4 → 2 + 2; 2 → 1 + 1. It tends to divide particles into two new particles of approximately equal shape and size.

Calculation of stresses, the determination of failure criteria for particles as well as the conditions and performance protocol of oedometer tests were introduced in a program developed in FISH language, which is included in the program PFC3D v4. Any clump which reaches the established failure criterion (length of crack reaching the clump size) divides in the manner described above. The two new particles (clumps) are integrated into the model. Therefore, the number of clumps increases continuously during the "test" and the grain size distribution is modified accordingly.

4 SOME RESULTS OF DEM SIMULATION OF UNSATURATED ROCKFILL

Some results obtained during the simulation of oedometer tests are presented in this section. Sample dimensions, initial porosity and initial equivalent diameter of particles are given in Table 2.

Maximum particle size covers the range 2.8 mm –560 mm. This wide range helps to identify scale effects. It is also a range of particles that may be easily found in practice. Initial porosity is essentially the same in all cases (0.53) to avoid density effects.

4.1 *Compressibility*

Model parameters (Table 1) were adjusted to simulate results of real oedometer tests performed on uniform limestone gravel (Ortega 2010). Ortega tested 40–30 mm, 30–25 mm, 25–20 mm and 20–25 mm hard limestone gravels having an initial porosity of 0.49 in a 300 mm diameter by 200 mm

Table 2. Dimensions of sample and macroparticles in the numerical simulation of oedometer tests (Alonso et al., 2012).

Sample	Scale	Sample size		Equivalent macroparticle diameter (mm)	Initial porosity
		Height (mm)	Diameter (mm)		
S25	0.1	25	25	2.8	0.5314
S250	1	250	250	28	0.5314
S1250	5	1250	1250	140	0.5337
S5000	20	5000	5000	560	0.5314

height cell. Figure 5a shows the experimental results for the 30–25 mm range of particles. The figure provides plots of deformations measured along time for a series of increasing stress increments. In all cases the RH was maintained constant and equal to RH = 10%. Once a final target stress was reached the sample was fully flooded. The sample reacted by reducing volume (collapsing) at a relatively high deformation rate.

Experimental results may be compared with the numerical simulations of oedometer tests performed on a sample of uniform initial size of 28 mm (Fig. 5b).

The agreement of the experimental and DEM simulated deformation-time records demonstrate the capability of the model to reproduce rockfill deformation phenomena. All time records follow a similar pattern: An immediate deformation is followed by a delayed accumulation of strains. Calculated deformations are very similar to experimental results.

If deformations for a particular instant (5×10^8 s was selected) are plotted in terms of vertical stress, conventional deformation-stress plots are calculated (Fig. 6). They show the type of compression behaviour reported by Oldecop & Alonso (2003) for samples of uniform compacted gravel of slate. Scale effects are clearly shown. Larger size particles result in an increase in compressibility, defined as:

$$\lambda = \frac{d\varepsilon_v}{d(\ln \sigma_v)} \tag{3}$$

Size effects on λ for $\sigma_v = 2.8$ MPa and RH = 10% are plotted in Figure 7 when the grain size changes from 0.28 cm to 56 cm (200 times). Also plotted are λ values measured by Ortega (2010) for three test series. They show the expected scale effect but points are concentrated in a narrow range of sizes. A regression curve may be approximated by:

$$\lambda = 0.004(D)^{0.7} \tag{4}$$

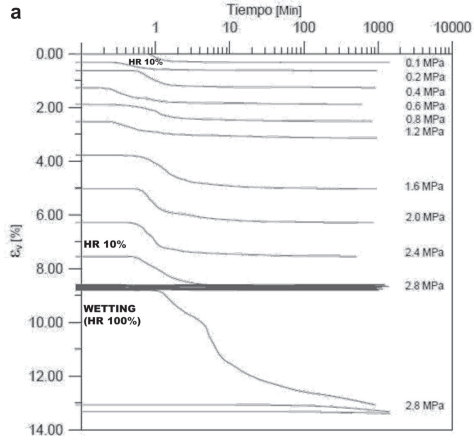

Figure 5a. Experimental results: Measured deformation—time records in an oedometer test on compacted limestone gravel having equivalent diameter sizes in the range 25–30 mm (Ortega 2010).

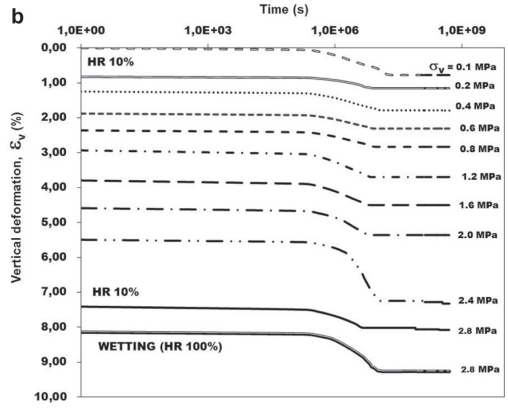

Figure 5b. DEM simulation: Calculated deformation—time records, under the vertical stresses indicated. Equivalent particle size: 28 mm.

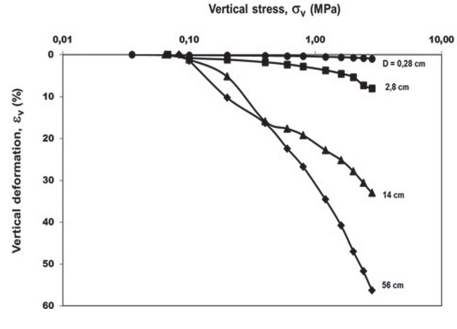

Figure 6. Calculated compressibility of samples of increasing initial equivalent particle size, D. RH = 10% (Alonso et al., 2012).

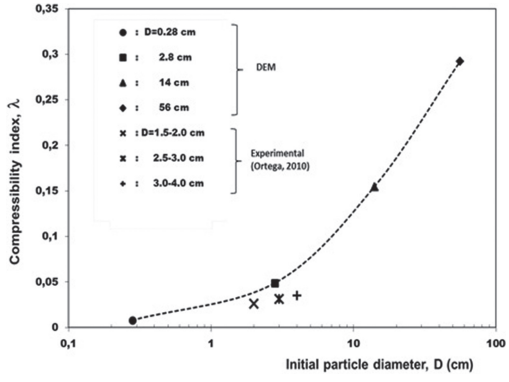

Figure 7. Variation of compressibility indices with initial particle diameter at σ_v = 2.8 MPa. RH = 10% (Alonso et al., 2012).

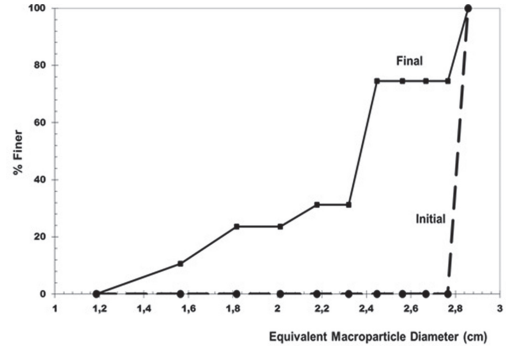

Figure 8. Calculated grain size distribution of test D = 2.8 cm at the end of the test (σ_v = 2.8 MPa, RH = 10%), (Alonso et al., 2012).

4.2 *Particle breakage*

Figure 8 shows an example of the evolution of the grain size distribution of the 2.8 cm particle size sample when the vertical stress reached 2.8 MPa. The final grain size distribution is not a continuous function which is probably a result of the limited number of particles defining a macroparticle but, also, of the relatively low number of "clumps" used in the simulation.

5 CONCLUSIONS

In this work, a model of unsaturated rockfill assemblies has been implemented using the DEM. A particle breakage criterion incorporating the mechanics of crack propagation in brittle materials is a key point of the model. This opens the possibility of quantifying scale effects in rockfill, a subject of practical interest.

The shape for the initial clumps of particles is roughly pyramidal; each one is composed by several spheres. The clump incorporates an inner defect that will grow with time following a modified Charles law under a mode I type of loading. The crack propagation velocity and the size of the defect increase progressively with time until the clump breaks.

Crack propagation is controlled by the initial distribution (in the entire sample) of defects and its initial length as well as on stress intensity, current suction (or relative humidity) and time.

For the calibration of the parameters of the model, data from real oedometer tests performed on samples having an average particle diameter of 2.8 cm were used.

Numerical simulations were then carried out, testing particle sizes in the range 0.28–56 cm (initial particle average size) in order to evaluate the compressibility of the rockfill at different scales. The model is capable of a precise reproduction of long-term (oedometer) tests. Short-term compressibility increases with particle size.

The model provides also information of the evolution of grain size distribution during loading of specimens and an example for an initial set of uniform particles having a size of 2.8 cm is given in the paper.

Thus, the model presented here can be used as a virtual laboratory to explore size effects and the behavior of rockfill in real situations.

REFERENCES

Alonso, E.E., Tapias, M. & Gili, J. 2012. Scale effects in rockfill behaviour. *Géotechnique Letters*. In press.

Alonso, E.E., Oldecop, L. & Pinyol, N.P. 2009. Long term behavior and size effects of coarse granular media. In D. Kolymbas & G. Viggiani (eds): *Mechanics of Natural Solids*: 255–281. Berlin: Springer-Verlag.

Alonso, E.E., Olivella, S. & Pinyol, N.P. 2005. A review of Beliche Dam. *Géotechnique* 55(4): 267–285.

Atkinson, B.K. 1984. Subcritical crack growth in geological materials. *J. Geophysical Research* 89(B6): 4077–4114.

Charles, R.J. 1958. Static fatigue of glass. *Journal of Applied Physics* 29(11): 1549–1560.

Cundall, P.A. & Strack, O.D.L. 1979. A discrete numerical model for granular assemblies. *Géotechnique* 29(1): 47–65.

Itasca, 2008. Manuals of PFC3D v.4.0: *Theory and Background*, 4th edn. Minneapolis, USA: Itasca Consulting Group Inc.

Oldecop, L. & Alonso, E.E. 2001. A model for rockfill compressibility. *Géotechnique* 51(2): 127–139.

Oldecop, L.A. & Alonso, E.E. 2003. Suction effects on rockfill compressibility. *Géotechnique* 53(2): 289–292.

Oldecop, L. & Alonso, E.E. 2007. Theoretical investigation of the time-dependent behaviour of rockfill. *Géotechnique* 57(3): 289–301.

Ortega, E. 2010. *Comportamiento de materiales granulares gruesos—Efecto de la succión*, PhD Thesis, Department of Geotechnical Engineering and Geosciences, Technical University of Catalonia. UPC. Barcelona, Spain.

Potyondy, D.O. & Cundall, P.A. 2004. A bonded-particle model for rock. *International Journal of Rock Mechanics and Mining Sciences* 41: 1329–1364.

Russell, A. & Muir Wood, D. 2009. Point load tests and strength measurements for brittle spheres. *Int. J. Rock Mechanics & Mining Sciences* 46: 272–280.

Tada, H., Paris, P.C. & Irwin, G.R. 1985. *The stress analysis of cracks handbook*. 2nd Edition. St. Louis, MO: Paris Productions.

Wiederhorn, S.M., Fuller, E.R. & Thomson, R. 1980. Micromechanisms of crack growth in ceramics and glasses in corrosive environments. *Met. Sci.* 14(Aug.–Sept.): 450–458.

Advances in Unsaturated Soils – Caicedo et al. (eds)
© 2013 Taylor & Francis Group, London, ISBN 978-0-415-62095-6

Incorporation of the soil-water characteristic curve hysteresis in pavement design

D.C. Rosenbalm & C.E. Zapata
Arizona State University, Tempe, Arizona, USA

ABSTRACT: The Mechanistic Empirical Pavement Design Guide (MEPDG) incorporates unsaturated soil mechanics into the analysis and pavement design. This task is accomplished by using climatic and soil properties to estimate the suction, which along with the Soil-Water Characteristic Curve (SWCC) are used to determine the degree of saturation. Although large strives have been made to incorporate unsaturated soil mechanics in pavement design, the MEPDG does not incorporate the hysteretic behavior of the SWCC but rather, the analysis is performed using only the drying branch. This paper presents a stochastic evaluation of the models used in the MEPDG to estimate the water content of the unbound/granular materials considering the hysteretic behavior of the SWCC. It was found that the prediction of the resilient modulus is overly conservative for any climatic condition when hysteresis is not considered and therefore, consideration of the SWCC hysteresis in pavement design and analysis is necessary and recommended.

1 INTRODUCTION

The MEPDG is one of the first analysis tools for pavement engineers that incorporates unsaturated soil mechanics into the pavement design via the Enhanced Integrated Climatic Model (EICM). The EICM uses climatic conditions and soil properties of the design location to estimate equilibrium soil suction values by using the TMI-Matric Suction model (Witczak et al., 2006). The soil matric suction is then used to estimate the water content at equilibrium condition by making use of the soil water characteristic curve (SWCC) models. This procedure yields an environmental factor, which is, in simple terms, the normalized moisture content to the as-constructed moisture content, usually at optimum conditions. The environmental factor is then applied to the resilient modulus at optimum condition, which yields the modulus used in the prediction of important pavement distresses such as permanent deformations or rutting.

The EICM makes used of the Fredlund and Xing (F&X) SWCC model into the design for mathematical modeling purposes. However, the Fredlund and Xing SWCC model only incorporates the drying branch of the SWCC. It has been proven that the SWCC exhibits hysteresis during the pore wetting and drying processes (Fredlund & Rahardjo 1993). Therefore, there is a need to incorporate the wetting SWCC curve into the EICM to improve the prediction of the moisture content of the soil at equilibrium conditions. This paper presents a procedure envisioned to incorporate the wetting SWCC into the ECIM using the Feng and Fredlund (F&F) hysteresis model (Feng & Fredlund 1999). The resilient modulus estimated is compared to the results from the current MEPDG model for the Levels 1 and 3 analyses. A stochastic evaluation is incorporated into the analysis to accurately consider pavement design reliability.

2 OBJECTIVES

The objectives of this paper were:

1. Present a procedure that allows for the incorporation of the wetting SWCC branch into the EICM model for the prediction of the moisture content of unbound materials.
2. Determine the effects of considering the SWCC hysteretic behavior in the prediction of the degree of saturation.
3. Determine the effects of considering the SWCC hysteretic behavior in the prediction of resilient modulus at equilibrium.

The analysis was performed under a stochastic framework and the results included pavement reliability considerations.

3 SWCC HYSTERESIS

The SWCC hysteresis curves are shown in Figure 1. The two main hysteresis curves, the primary drying (2) and primary wetting (3) curves, are called the

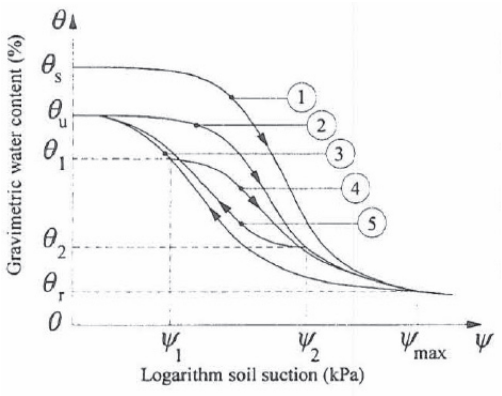

Figure 1. Schematic illustration of different hysteresis curves (modified from Hogarth et al., 1988).

main hysteresis loop. The initial drying curve (1) is a unique theoretical curve that is mainly used for engineering applications. This curve starts at the saturated water content, θ_s, or porosity of the soil. The existence of intermediate wetting and drying curves such as the drying scanning curve (4) and the wetting scanning curve (5), makes the problem even more difficult to solve.

The difference between the wetting and drying processes is significant; therefore, taking into account the effects of hysteresis is necessary.

4 INCORPORATING THE SWCC HYSTERESIS INTO A STOCHASTIC EICM EVALUATION

4.1 *Feng and Fredlund model*

In 1999, Feng and Fredlund presented a simple model that was able to fit both the wetting and dry curve with a good-fit (Feng & Fredlund 1999). The Feng and Fredlund model is presented in Equation 1.

$$S(\psi) = \left[1 - \frac{\ln\left(1+\frac{\psi}{\psi_r}\right)}{\ln\left(1+\frac{10^6}{(2.7b)^{1/d}}\right)}\right]\frac{S_u b + c\psi^d}{b + c\psi^d} \quad (1)$$

where S_u = degree of saturation (%S) at 0 suction; and b,c,d = regression coefficients.

As shown in Equation 1, the Feng and Fredlund model is presented with the 1994 Fredlund and Xing correction factor that forces the function to zero degree of saturation when the suction reaches 1,000,000 kPa.

4.2 *Predicting the wetting SWCC using the Feng & Fredlund hysteresis model*

Using the Pham et al. (2005) equations the Feng and Fredlund drying curve can be modified by the following equations:

$$c_w = c_d \quad (2)$$

$$b_w = \left[\frac{b_d}{\left(10^{D_{SL}}\right)^{d_d}}\right]^{\frac{1}{R_{SL}}} \quad (3)$$

$$d_w = \frac{d_d}{R_{SL}} \quad (4)$$

$$S_{uw} = 0.9 S_{ud} \quad (5)$$

where c_w, b_w, *and* d_w = wetting curve regression coefficients; c_d, b_d, *and* d_d = drying curve regression coefficients; R_{SL} and D_{SL} = slope and distance ratios between the boundary curves (values shown in Table 1), respectively; S_{uw} = degree of saturation at 0 suction for the wetting branch; and S_{ud} = degree of saturation at 0 suction for the drying branch.

S_{uw} adjustment was based on Pham et al. (2005) recommendation that 90% of the boundary drying curve will suffice due to the entrapped air that is encountered when the soil begins to dry and then wet again or water leaving or entering a pore within the soil skeleton (Fredlund & Rahardjo 1993).

4.3 *Fitting the Fredlund & Xing model*

With the wetting and dry boundary curves developed, the 1994 Fredlund and Xing equation can be fit to both, the wetting and drying SWCC curves, using Equation 6:

$$S(\psi) = \left[1 - \frac{\ln\left(1+\frac{\psi}{\psi_r}\right)}{\ln\left(1+\frac{10^6}{(2.7b)^{1/d}}\right)}\right]\left[\frac{1}{\left[\ln\left[\exp(1)+\left(\frac{\psi}{a_f}\right)^{b_f}\right]\right]^{c_f}}\right] \quad (6)$$

where ψ = suction in kPa; ψ_r = residual suction; and a_f, b_f and c_f = fitting parameters.

Table 1. R_{SL} and D_{SL} values (modified from Pham et al., 2005).

Soil type	RSL	DSL
Sand	2.0	0.20
Sandy loam	2.5	0.25
Silt loam and clay loam	1.5	0.50
Compacted silt and sand	1.0	0.35

4.4 *Appling coefficients of variation*

After obtaining the wetting and drying coefficients for the Fredlund and Xing model, the coefficients of variation from Rosenbalm (2011) can be applied to create an upper and lower confidence bound curves to the wetting and drying curves. Table 2 shows the coefficient of variations for the drying curve obtained by Rosenbalm (2011) studies. The CV's for the regression constants shown in Table 2 where based only on drying SWCC curves; however, for this study it was assumed that the CV's for the wetting curve will be similar to those found for the drying SWCC curves.

Using Equation 7, the standard deviation of the regression coefficients can be determined:

$$\sigma = CV * \mu_f \tag{7}$$

where σ = standard deviation; CV = coefficient of variation; and μ_f = mean regression coefficient which applies to a_f, b_f, or c_f coefficients.

4.5 *Creating descriptive statistics for SWCC hysteresis*

The standard deviation determined from Equation 7 can be applied to the mean value by adding or subtracting 1.96σ, which creates the upper and lower confidence bounds to the SWCC curves. The value of 1.96 corresponds to a 95% confidence interval for a normal distribution. It was assumed that measured properties (Level 1 analysis) will follow normality since the soils within a given project are tested and determined to be statistically the same or statistically different. With the upper and lower bound determined, Table 3 can be use as a reference to determine the descriptive statistics for the SWCC parameters. The alpha and beta shape factors, shown in Table 3, are associated with the beta distribution, which is coupled with the Monte Carlo Simulation presented below to obtained error bars, as shown below. More details can be found in *Reliability Associated with the Estimation of Soil Resilient Modulus at Different Hierarchical Levels of Pavement Design* (Rosenbalm 2011).

Figure 2 shows an example of the upper and lower confidence bounds associated with the wetting and drying curve for a clayey soil. The drying curve in this example was obtained from measured suction values, while the wetting curve was predicted using the steps outlined above.

Table 2. Coefficients of variation for Fredlund & Xing regression coefficients (modified from Rosenbalm 2011).

Soil type	F&X Regression constants		
	a_f	b_f	c_f
Sand	42.98%	1.03%	5.73%
Silt	13.79%	0.46%	9.29%
Clay	7.82%	37.96%	41.28%

Table 3. SWCC descriptive statistics.

Descriptive Statistic	F&X Regression constants a_f, b_f, or c_f
Mean, μ	Obtained from testing and fitting F&X
Variance, σ^2	σ^2
Standard deviation	$\sigma = CV*\mu$
Minimum, a	$a = \mu - 1.96\sigma$ (from wetting SWCC)
Maximum, b	$b = \mu - 1.96\sigma$ (from drying SWCC)
Alpha shape factor (Johnson et al., 1994)	$\alpha = \left(\frac{\mu-a}{b-a}\right)\left\{\frac{\left(\frac{\mu-a}{b-a}\right)\left(1-\left(\frac{\mu-a}{b-a}\right)\right)}{\frac{\sigma^2}{(b-a)^2}}-1\right\}$
Beta shape factor (Johnson et al., 1994)	$\beta = \left(1-\left(\frac{\mu-a}{b-a}\right)\right)\left\{\frac{\left(\frac{\mu-a}{b-a}\right)\left(1-\left(\frac{\mu-a}{b-a}\right)\right)}{\frac{\sigma^2}{(b-a)^2}}-1\right\}$

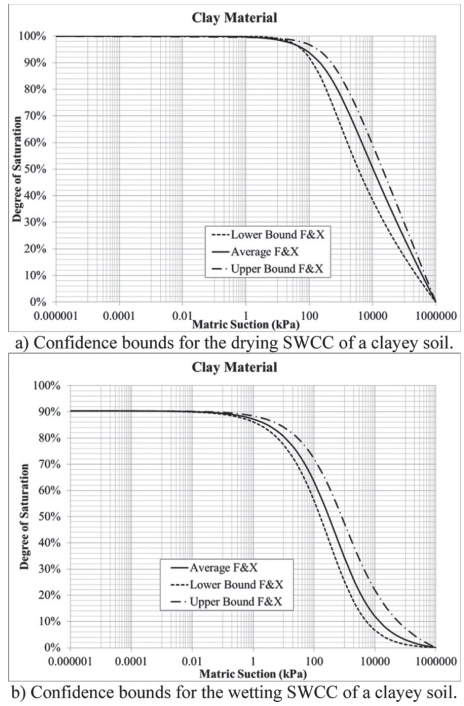

a) Confidence bounds for the drying SWCC of a clayey soil.

b) Confidence bounds for the wetting SWCC of a clayey soil.

Figure 2. Upper and lower boundaries for the wetting and drying curves.

Based on the information provided above, the following steps can be followed to generate a wetting curve for use in a stochastic evaluation of the EICM:

Fit the drying SWCC points to the Feng and Fredlund (F&F) drying Model.

1. Predict the wetting SWCC using the Feng and Fredlund Model.
2. Fit the Fredlund and Xing (F&X) model to the Feng and Fredlund model to obtain the EICM fitting parameters.
3. Fit the drying SWCC points to the Fredlund and Xing Model.
4. Apply coefficients of variations (CV's) (Rosenbalm 2011) to the wetting and drying curve fitting parameters to create an upper and lower bound for the SWCC.
5. Using the upper and lower confidence bound for the Fredlund and Xing fitting parameters, create descriptive statistics for the SWCC input.

5 DEGREE OF SATURATION COMPARISON

Once the SWCC hysteresis was incorporated into the analysis procedure, the degree of saturation as well as the resilient modulus at equilibrium were estimated and compared to those values obtained without considering the SWCC hysteric behavior. The analysis was performed with Level 1 data (measured properties) and Level 3 data (estimated properties).

The comparison was performed on a clayey material for four different climatic locations: Phoenix (AZ), Amarillo (TX), Salem (OR) and Eureka(CA). The climatic information used is presented in Table 4, which includes the mean annual air temperature (MAAT), annual precipitation, and the Thornthwaite moisture index (TMI). Positive TMI values represent regions where precipitation exceeds evaporation, whereas negative TMI values represent regions where evaporation exceeds precipitation.

Table 4. Climatic information for comparison (Rosenbalm & Zapata 2012).

	MAAT (^{0}C)		Precipitation (cm)		TMI (unitless)	
City	μ	σ^2	μ	σ^2	μ	σ^2
Eureka, CA	10.86	0.07	125	455.6	85.9	296.7
Salem, OR	11.73	0.08	108	360.6	57.8	476
Amarillo, TX	13.98	0.23	58.0	150.3	–15.4	172.8
Phoenix, AZ	23.90	0.16	17.9	31.2	–58.2	5.7

The soil properties used for Level 1 and Level 3 analyses are not presented in this document due to space limitations but they can be found in Rosenbalm (2011). The soil used is classified as A-6 by AASHTO classification; it has a percent passing #200 of 74%, a liquid limit of 43% and a plasticity index of 21%. The SWCC regression parameters for Level 1 analysis when hysteresis is considered are presented in Table 5. It should be noted that for this example, it was assumed that the mean values of all soil properties considered at Level 1 and Level 3 analyses were the same. Obviously, the CV's associated with Level 1 soil properties are different than those associated with Level 3 soil properties.

The degree of saturation results for all locations for the Level 1 analysis, with and without hysteresis; and Level 3 results are shown in Figure 3 and Table 6. The error bars shown in Figure 3, correspond to two standard deviations, and were obtained by running a Monte Carlo Simulation coupled with the beta distribution. As shown in Figure 3, the mean value for the degree of saturation for Level 3 and Level 1 without including the hysteresis is similar while the values for

Table 5. SWCC regression constants considering hysteresis.

	F&X regression constants		
Descriptive statistic	a_f	b_f	c_f
Mean	206.32	0.5768	1.0339
Variance	9602.6	0.0901	1.1727
Standard deviation	97.99	0.3002	1.0829
Minimum	100.32	0.1605	0.0304
Maximum	317.15	1.0938	2.6962
Alpha shape factor	1.4210	1.4210	1.4210
Beta shape factor	1.4210	1.4210	1.4210

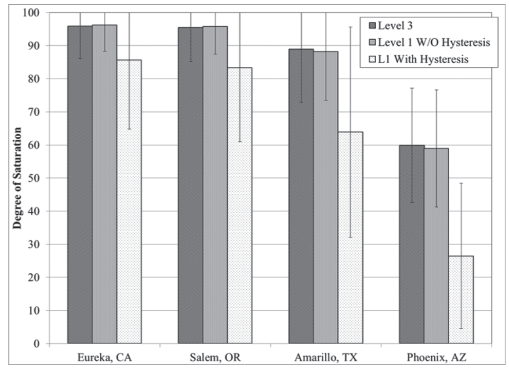

Figure 3. Degree of saturation for different climatic locations.

Table 6. Degree of saturation results for the comparison.

Eureka, CA			
Property	L3	L1 w/o Hysteresis	L1 Hysteresis
μ	95.9	96.1	85.6
σ^2	23.7	15.5	108.6
σ	4.9	3.9	10.4
a	73.6	80.9	51.6
b	100.0	100.0	100.0
Salem, OR			
Property	L3	L1 w/o Hysteresis	L1 Hysteresis
μ	95.4	95.7	83.3
σ^2	26.5	17.3	124.2
σ	5.1	4.2	11.1
a	74.0	78.9	47.4
b	100.0	100.0	100.0
Phoenix, AZ			
Property	L3	L1 w/o Hysteresis	L1 Hysteresis
μ	59.9	58.9	26.5
σ^2	74.6	78.2	120.9
σ	8.6	8.8	11.0
a	34.2	36.0	8.6
b	94.4	93.6	80.1
Amarillo, TX			
Property	L3	L1 w/o Hysteresis	L1 Hysteresis
μ	88.9	88.1	63.9
σ^2	64.9	54.2	252.1
σ	8.1	7.4	15.9
a	59.3	62.3	26.6
b	100.0	100.0	100.0
Phoenix, AZ			
Property	L3	L1 w/o Hysteresis	L1 Hysteresis
μ	59.9	58.9	26.5
σ^2	74.6	78.2	120.9
σ	8.6	8.8	11.0
a	34.2	36.0	8.6
b	94.4	93.6	80.1

Level 1 with hysteresis are lower and present larger error bars. In addition, the effects of the SWCC hysteresis are more pronounced for the arid and semi-arid climate of Phoenix (AZ) and Amarillo (TX); whereas, the effects of the SWCC hysteresis in the estimation of the degree of saturation is less pronounced in the wet climate of Eureka (CA) and Salem (OR).

6 COMPARISON OF RESILIENT MODULUS PREDICTION

It was shown that the degree of saturation prediction is different when the hysteric behavior of the SWCC is incorporated into the stochastic analysis, when compared to the predicted values obtained by using the drying SWCC. Therefore, it is expected that the predicted values of the resilient modulus at equilibrium conditions of unbound and granular materials change as well. As outlined above, the resilient modulus at equilibrium is a function of the resilient modulus at optimum condition and the environmental factor representing climatic conditions and soil properties (Witczak et al., 2006). The environmental factor on the other hand, is a function of the degree of saturation, the initial (as-constructed) moisture content, and the soil index properties such as plasticity index and grain-size distribution. Thus, changes in the limits of the degree of saturation will either increase or decrease the environmental factor.

Using the same climatic locations and soil properties for the A-6 soil previously presented, the log transformation of the resilient modulus at equilibrium values were estimated. The results are presented in Table 7. Figure 4 shows the results of

Table 7. Log of resilient modulus at equilibrium conditions.

Eureka, CA			
Property	L3	L1 w/o Hysteresis	L1 Hysteresis
μ	3.94	3.97	4.206
σ^2	0.026	0.013	0.066
σ	0.161	0.116	0.257
a	3.555	3.735	3.736
b	4.46	4.347	4.878
Salem, OR			
Property	L3	L1 w/o Hysteresis	L1 Hysteresis
μ	3.949	3.981	4.258
σ^2	0.028	0.015	0.073
σ	0.166	0.123	0.27
a	3.545	3.729	3.75
b	4.55	4.385	4.956
Amarillo, TX			
Property	L3	L1 w/o Hysteresis	L1 Hysteresis
μ	4.097	4.156	4.631
σ^2	0.051	0.036	0.087
σ	0.225	0.19	0.296
a	3.566	3.744	3.765
b	4.77	4.691	5.172
Phoenix, AZ			
Property	L3	L1 w/o Hysteresis	L1 Hysteresis
μ	4.689	4.743	5.106
σ^2	0.026	0.023	0.009
σ	0.16	0.15	0.097
a	4.012	4.128	4.568
b	5.162	5.077	5.303

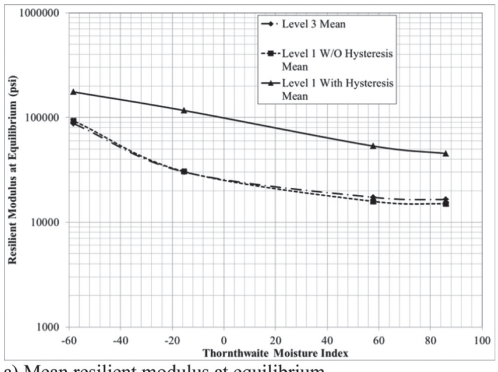

a) Mean resilient modulus at equilibrium.

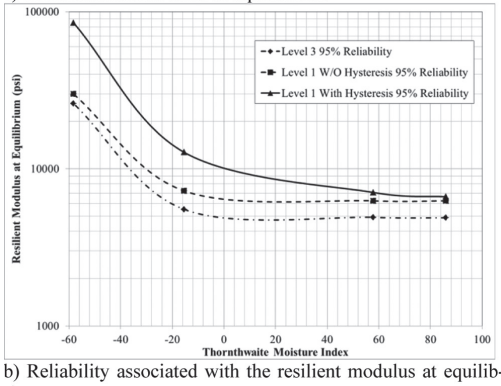

b) Reliability associated with the resilient modulus at equilibrium.

Figure 4. Differences in resilient modulus at equilibrium.

the resilient modulus at equilibrium in terms of reliability.

When looking at the results of the resilient modulus at equilibrium in terms of the mean values, both Level 3 and Level 1 without the hysteresis produce similar results, while Level 1 considering the hysteretic behavior is considerably and statistically different. On the other hand, when looking at a 95% reliability level, all three comparisons yield different results. As the TMI increases (the climate changes from arid to wet climate), the results obtained for Level 1 analysis with and without hysteresis begin to merge. This is due to the proximity of the moisture content to saturated conditions. In addition, all three results are statistically different. The results of the statistical analysis obtained for the comparison can be seen in Table 8. The "accept" or "reject" corresponds to accepting or rejecting the null hypothesis.

Table 8. Statistical analysis of the resilient modulus at equilibrium mean values.

Eureka, CA			
	Level 3	Level 1 w/o	Level 1 With
Level 3	**Accept**	Reject	Reject
Level 1 w/o	Reject	**Accept**	Reject
Level 1 With	Reject	Reject	**Accept**
Salem, OR			
	Level 3	Level 1 w/o	Level 1 With
Level 3	**Accept**	Reject	Reject
Level 1 w/o	Reject	**Accept**	Reject
Level 1 With	Reject	Reject	**Accept**
Amarillo, TX			
	Level 3	Level 1 w/o	Level 1 With
Level 3	**Accept**	Reject	Reject
Level 1 w/o	Reject	**Accept**	Reject
Level 1 With	Reject	Reject	**Accept**
Phoenix, AZ			
	Level 3	Level 1 w/o	Level 1 With
Level 3	**Accept**	Reject	Reject
Level 1 w/o	Reject	**Accept**	Reject
Level 1 With	Reject	Reject	**Accept**

* Null hypothesis: $Mean_i = Mean_j$

7 SUMMARY AND CONCLUSIONS

As shown above, the incorporation of the main wetting curve into the prediction of the degree of saturation of unbound materials in the EICM model used in pavement design reduces the degree of saturation predicted in all climatic regions analyzed and hence, it increases the predicted resilient modulus values. Due to the uncertainty associated with the model used to estimate the wetting branch of the SWCC, the variance associated with the prediction of the degree of saturation increases. However, the variance will decrease if a measured wetting SWCC curve is used in the design process.

The results obtained are dramatically important for the pavement design in arid regions. It was observed that as the TMI decreases (the climate becomes more arid), the resilient modulus predicted increases exponentially. It implies that the addition of the SWCC hysteresis into the most current pavement design guide (MEPDG) available, increases the resilient modulus design value in arid regions, which in turn reduces the pavement cross-section when compared with the pavement cross-sections estimated with the resilient modulus at equilibrium for Level 3 and Level 1 without the incorporation of the SWCC hysteresis.

Finally, the results showed that regardless of the method used to obtain the main wetting SWCC curve, the incorporation of hysteresis in the models used to predict the resilient modulus will yield

results that are less conservative and therefore, represents a more accurate and sustainable solution for an important material property needed in pavement infrastructure design.

REFERENCES

Feng, M. & Fredlund, D.G. 1999. Hysteretic influence associated with thermal conductivity sensor measurements. *In* Proceedings *From Theory to the Practice of Unsaturated Soil Mechanics,* 52nd Canadian Geotechnical Conference and the Unsaturated Soil Group, Regina, Sask., 23–24 October 1999: 14:2:14–14:2:20.

Fredlund, D.G. & Xing, A. 1994. Equations for the Soil-Water Characteristic Curve. *Canadian Geotechnical Journal* 31(4): 521–532.

Fredlund, D.G. & Rahardjo, H. 1993. *Soil Mechanics for Unsaturated Soils*. John Wiley & Sons.

Hogarth, W.L., Hopmans, J., Parlange, J.-Y. & Haverkamp, R. 1988. Application of a simple soil-water hysteresis model. *Journal of Hydrology*, 98: 21–29.

Johnson, N.L., Kotz, S. & Balakrishnan, N. 1994. *Continuous Univariate Distributions:* Volume 2. New York: Wiley—Interscience.

Pham H.Q., Fredlund, D.G. & Barbour, S.L. 2005. A study of hysteresis models for soil-water characteristic curves. *Canadian Geotechnical Journal* 42: 1548–1568.

Rosenbalm, D.C. 2011. *Reliability Associated with the Estimation of Soil Resilient Modulus at Different Hierarchical Levels of Pavement Design*. Master Thesis, Arizona State University.

Rosenbalm, D.C. & Zapata, C.E. 2012. Incorporating Stochastic Evaluation in the Estimation of Soil Resilient Modulus. In *Proceedings for the 2012 GeoCongresss,* ASCE. Oakland, CA. March 2012. CD ROM.

Witczak, M.W., Zapata, C.E. & Houston, W.N. 2006. *Models Incorporated into the Current Enhanced Integrated Climatic Model. NCHRP 9–23 Project Findings and Additional Changes after Version 0.7*. Tempe, Arizona: Arizona State University, NCHRP 1–40D Final Report, Inter Team Technical Report.

This page intentionally left blank

Advances in Unsaturated Soils – Caicedo et al. (eds)
© 2013 Taylor & Francis Group, London, ISBN 978-0-415-62095-6

Results of unsaturated tests on metastable soils

J.C. Ruge & R.P. da Cunha
University of Brasilia, Brasilia D.F., Brazil

D. Mašín
Charles University, Prague, Czech Republic

ABSTRACT: The main objective of the current research is to analyze through the use of elemental simulations, unsaturated tests executed on soils with metaestable characteristics (Brasilia porous clay), which due to high porosity and kind of cementation, presents a structure temporally unstable when undergoing an increasing of wetting and/or variation of the stress state, resulting in the most of cases in a significant change of volume denominated collapse. The tests were done in the Geotechnical Lab from the University of Brasilia and Geological Institute from Charles University in Prague, considering characterization tests for the identification of the basic properties, tests for determination of the characteristic curve, consolidation, direct shear and triaxial, in both conditions saturated and unsaturated, as well as the porosimetry test, for the study of the mechanical behavior. The tests were reproduced using numerical modeling to elemental level, involving a hypo-plastic model for the unsaturated soils behavior.

1 INTRODUCTION

The numerical simulations based on element tests, currently are useful when the researcher wants to have an initial approaching of the behavior of a sample, especially if it is reproduced through of the constitutive model selected for the stage of numerical modeling of a geotechnical structure in particular. Depending on the constitutive theory this kind of simulation is an additional tool when calibrating the parameters necessary for a subsequent phase of modeling (Moya, 2011).

The constitutive model used as a reference in this work is based on hypoplasticity with an extension for unsaturated response of the soil (Mašín & Khalili, 2008). The constitutive equations were developed taking into account the critic state concept of the soils and the effective stress principle, giving a special importance to stiffening effect of the suction on the mechanical behavior and the collapse phenomenon upon wetting. The peculiar characteristics of the porous clays from Brasilia are perfectly suitable to the reference model, due to the fact that the mechanical response presented is governed by the partial saturation and the collapse.

2 GEOLOGICAL AND GEOTECHNICAL CHARACTERISTICS

The typical soil form the region is a lateritic red clayey soil, denominated as porous clay, presents low strength to the penetration (SPT between 1 to 6 blows), low strength of tip (CPT between 0.6 to 2.3 MPa), low bearing capacity, low saturation level and high permeability (10^{-3}–10^{-4} m/s). Due to high porosity and kind of cementation, the soil presents a structure highly unstable when it is subjected to sub-stantial increases of humidity and/or alteration of stress state (Cunha et al., 1999) (Figure 1).

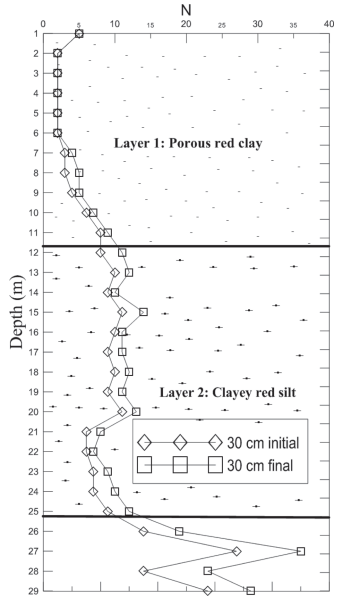

Figure 1. Results from SPT in the site.

The typical soil profile can be divided in the next layers (Mota, 2003 and Guimaraes, 2002):

- 0 to 3.5 m—clayey-silty porous sand, with predominance of gibbsite, macrospores and aggregates, high void ratio (1.27–1.60), solid specific weight around of 26.5 kN/m3 and PI about 10. It is important to emphasize that the properties between 3 to 4 meters correspond to the transition zone;
- 3.5 to 8.5 m—Sandy-silty clay, zone of physical, mineralogical, and microstructural properties that goes gradually varying until to find the residual soil to 8.5 m. In this layer the gibbsite, porosity, macroporosity decreases, the void ratio begins to reduce (1.27 to 0.89), solid specific weight and PI are similar to the previous layer.
- 8.5 to 26.0 m—In this depth the soil has a silty texture, characterized for the increasing of the void ratio (0.96 to 1.08), solid specific weight (around of 27.4 kN/m3) and PI (average value of 17) with a more homogenous pore distribution. The solid specific weight (around of 26.5 kN/m3), consisting of clayey mineral as kaolinite (γ_s = 25.5 kN/m3), quartz (γ_s = 26.0 kN/m3) and ferric hydroxide (hematite; (γ_s = 51.0 kN/m3) and alumina (gibbsite; γ_s = 24.0 kN/m3). The increasing of γ_s from 8 m must be due to the disappearing of the gibbsite, while the hematite contain is maintained.

3 CHARACTERIZATION OF THE MATERIAL

3.1 *Basic characterization*

By means of physical and chemical tests executed, a complete characterization of the material, in the Table 1 it is possible to analyze some basic properties and geotechnical parameters from the soil in study.

Table 1. Basic characterization of the material under analysis.

Sample	1B	2 A
Depth (m)	6.0	9.0
w (%)	26.8	19.6
γ_s [kN/m^3]	28.01	28.02
γ_d [kN/m^3]	11.39	12.88
γ [kN/m^3]	14.70	15.51
Gs	2.81	2.82
LL (%)	48	50
PL (%)	29	30
IP (%)	19	20
IC	1.13	1.55

In the Figure 2, in terms of the granulometry, is shown that the samples present large differences when the tests are done with or without deflocculant, this difference is due to presence of bonding in the form of lump in the soil, since the existing particles of the clay and silt form packages in the soil similar to the sand grains. i.e. it exists clearly a distribution of macrospores and microspores (bimodal) in the sample tested.

Although the granulometric curve is unimodal in both cases, this behavior can be evidenced in the analysis of the porosimetry test and the water retention curve.

It was also carried out a porosimetry test with mercury intrusion, which permits to determine the pore size and distribution, as well as, the apparent density and packaging of a porous medium nucleus (soil).

This process is based on the injection of mercury in the pores of the sample, in order to estimate the capillary pressures, being the pore size inversely proportional to the applied pressure. The test determines the pore volume and size distribution (Fig. 3).

It's important in the Figure 3 (derivative of the cumulative pore volume vs. pore radius); to observe that the variations of inflection in the graph in the form of peaks show that there is presence of micropores and macropores in the sample.

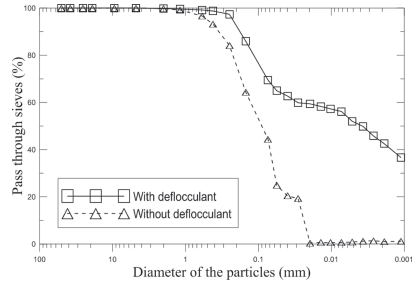

Figure 2. Granulometry of the porous clay from Brasilia.

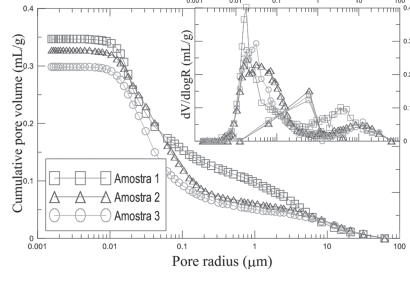

Figure 3. Results of the porosimetry test.

3.2 *Mineralogical and chemical characterization*

X-ray diffractometry (XRD), which is a valuable tool to mineralogical characterization of clayey minerals and other components, was used. Also were executed analysis for samples of 6 and 9 m, in a diffractometer Xt'Pert Pro, in the Geochemical, Mineralogy and Minerals Resources Laboratory of the Charles University in Prague. Table 2 shows the list of patterns of the mineral found in the sample located to 6 m of depth.

Using these technics was possible to identify minerals as quartz, kaolinite, gibbsite and hematite coinciding with the work reported by Cardoso (1995), being important to review that a factor that affects the results of the (G_s) for values higher than the typical (2.60–2.68), generally is influenced by the presence of ferric and aluminum minerals that increases the value of G_s.

In addition it is significant to highlight that although the quantity of these minerals is relatively low, they can have an influence on the cementation of the clay, generating it a metastable behavior according to Sultan (1969), who mentioned that the collapsible soils are part of a metastable soil group, where the initial structure is broken due to environmental variations, in agreement with Vargas (1973) who defined collapsible soils as all the lateritic porous surface, characterized for the partial saturation and ferric oxide bonding. In accordance the fine fraction of lateritic soils is predominately kaolinite with aluminum and ferric oxide, which are interconnected of stable way in a porous fabric.

3.3 *Geomechanical characterization*

3.3.1 *Strength and consolidation tests*

For the tests that supplied the mechanical behavior of the material, out two phases of lab tests were carried, being the first in the Geotechnical Laboratory from the UnB, where were tested undeformated samples in saturated state.

The second phase was executed in the Geological Institute from Charles University in Prague. Figure 4 shows the results of oedometric tests located at 9 m of depth in saturated, unsaturated conditions and reconstituted sample.

Table 2. Result of XRD phase analysis—List of patterns.

Compound	Score	Total lines	Scale Factor	Semi-quant (%)
Quartz	69	12	1.010	63
Gibbsite	45	69	0.117	11
Kaolinite	42	116	0.121	21
Hematite	57	10	0.063	5

In the saturated curve it is possible to confirm the response from a partially structured soil, where the bonding has few influence in the strain of the sample (natural and fabric only), in the ln p vs. e space that is characteristic of a normally or lightly overconsolidated clay (Brasilia Clay) that presents a metastable structure where the stress sensitivity decreases with the loading.

$$S_\sigma = \frac{p_{nat}}{p_{rec}} \tag{1}$$

In relation with the drained triaxial tests in saturated conditions in the Figure 5 it is possible to analyze the results for different confining stress (left), as well as the triaxial tests in unsaturated conditions (right).

The reference model, which will be studied in the next chapter needs, for an adequate calibration of the parameters, the results of a compression isotropic test presented in the Figure 6, where was

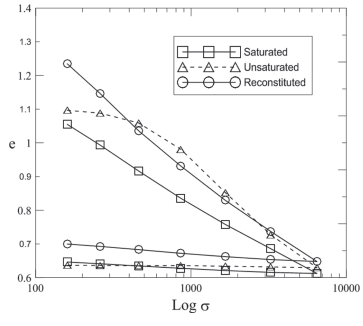

Figure 4. Oedometric test of Brasilia Clay.

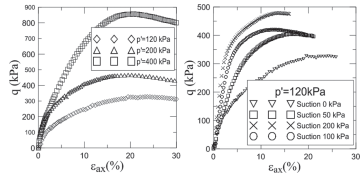

Figure 5. Triaxial tests of Brasilia Clay.

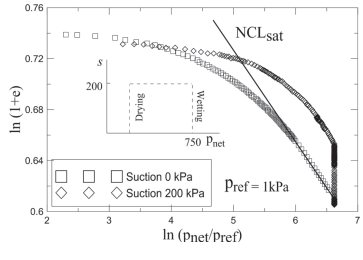

Figure 6. Compression isotropic test.

subjected the sample to suction of 200 kPa and induced the collapse by wetting when the net pressure was 750 kPa.

3.4 *Hydraulic characterization*

The relation between suction and humidity represents an important function in the characterization of an unsaturated soil, this relation can be evidenced by means of the comparison between the stored water and the soil suction, called suction water characteristic curve (SWCC) that reveals the relation between the pore distribution and soil structure. Figure 7 shows the SWCC of the studied soil obtained trough of the axis translation technic reaching a maximum suction of 1500 kPa that corresponds a value of 35% of residual volumetric wet content according to the distribution pore in the water retention of the macro-spores.

The characteristic curve of the soil (SWCC) is used to estimate the hydraulic parameters of the water flux in the subsoil in the unsaturated zones, generally above of the phreatic level. The mathematic model selected to simulate the behavior of the water retention in the Brasília clay was proposed by van Genuchten (1980) by means of the equation 2 that relates the saturation with the pressure head.

$$S_{(\phi_p)} = S_{res} + (S_{sat} + S_{res})\left[1 + \left(g_a \mid \phi_p \mid^{g_n}\right)\right]^{g_c} \qquad (2)$$

Where S_{res} is the residual saturation, which denotes the liquid portion that remains in the pores, even to high head pressures, g_a is a fit parameter related to the air entry value of the soil, S_{sat} is a value always lower than 1, since the pores generally in saturated conditions are not completely filled with water because the air can avoid the saturation. g_n and g_c are another fit parameters which is function of the water extraction rate of the soil when the entry air value was exceeded.

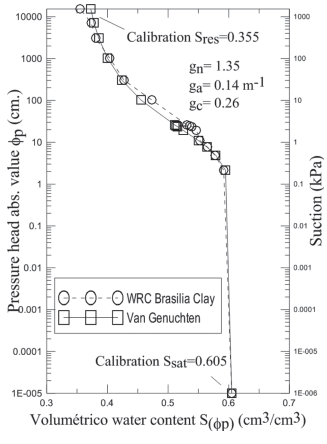

Figure 7. Compression isotropic test.

4 REFERENCE MODEL

This research is based as reference model the hypoplasticity theory for unsaturated soils, the constitutive equations were developed based in critical state concept and the effective stress principle, taking in account the effect of stiffness increasing, governed by the variation of the suction on the mechanical response and the collapse phenomenon by wetting (Mašín & Khalili, 2008).

4.1 *Constant suction model*

As was mentioned in the previous paragraph the reference model is supported in the concept proposed by Mašín & Khalili (2008) where the suction influences the effective tension and the normal forces on the interparticles contacts improving the skeleton stiffness of the soil, since the particles are close and therefore interacting stronger. In other words, this behavior increases the state boundary stress (SBS) analogously like are bonded the soil particles in ce-mented saturated geomaterials (Masin & Herle 2005).

In these conditions, the SBS size for unsaturated soils is defined by the NCL based on the compression law of Butterfield (1979) for the critical state line as is showed in the next equation.

$$\ln(1+e) = N(s) - \lambda^*(s)\ln\frac{p}{p_r} \qquad (3)$$

From where e is the void ratio, considered like state variable in the constitutive model. The expressions $N(s)$ and $\lambda^*(s)$ predicts the position of the inclination of the compression virgin line in the space $ln(p/p_r)$ *vs* $ln(1+e)$ for determined suction s, and the model parameters N and λ^* define the values for unsaturated conditions. The equation 4 shows the expression for equivalent tension of Hvorslev on the NCL for a given suction (Hvorslev, 1960).

$$p_e = p_r \exp\left[\frac{N(s) - \ln(1+e)}{\lambda^*(s)}\right] \qquad (4)$$

Mašín (2007) modified the values of the barotropy f_s and picnotropy f_d, since demonstrated that the incorporation of the virgin compressibility in the intercept $N(s)$ affects the origin values

proposed by Gudehus (1996), above the picnotropy factor:

$$f_d = \left(\frac{2p}{p_e}\right)^{\alpha} \tag{5}$$

P_e is found according with the equation 5, and the barotropy factor is:

$$f_s = -\frac{trT}{p_e}(3 + a^2 - 2^{\alpha}\sqrt{3})^{-1} \tag{6}$$

The scalar factor α is in function of the parameters λ^* and κ^* this can be consulted in Mašín & Khalili (2008), as well as the factor a.

4.2 *Model for any state of overconsolidation*

The next assumptions are used to complement the constitutive equation for any state and load condition:

- The suction controls the stability of contacts be-tween particles, increasing the suction under constant effective tension.
- The more open is the soil structure, the lower is the number of interparticle contacts; hence, each contact must transmit larger shear forces (Mašín & Khalili, 2008).

$$\overset{\circ}{\mathrm{T}} = f_s(L : D + f_d \mathrm{N}\|\mathrm{D}\|) + f_u H \tag{7}$$

With

$$H = \frac{T}{p_e}\frac{\partial p_e}{\partial s}\left\langle \overset{\square}{s} \right\rangle \tag{8}$$

Where s is introduced to consider the first assumption, and f_u, the new picnotropy factor that controls the tendency of soil structure to collapse, reproduce the second. The factor must be equal to 1 to states in the SBS (in this case the structure is as open as possible and collapse being controlled by **H** only), instead f_u tends to zero for $OCR = p_e/p$ tends to infinite (no wetting induced interparticle slippage occurs in highly overconsolidated soil). The following expression for the factor f_u satisfying these requirements is proposed:

$$f_u = \left(\frac{p}{p^{SBS}}\right)^{m} \tag{9}$$

Where p^{SBS} is the effective mean stress at the SBS corresponding to the current normalized stress **T**/*tr***T** and the current void ratio e and m is a model parameter controlling the influence of overconsolidation on the wetting-induced collapse.

4.3 *Parameters of the model*

Besides of the parameters of the hypoplastic model for saturated soils (ϕ, N, λ^*, κ^*, r) according to (Mašín, 2006), the extension of the proposed model needs consider the influence of the suction on N and λ, respectively denote as $N(s)$ and $\lambda(s)$, being that m controls the collapse of the structure along the wetting paths and s_e is the value of suction at the air entry and/or air expulsion. n and l are scalar quantities included inside of the formulation of $N(s)$ and $\lambda(s)$ controlling the unsaturated NCL.

$$N(s) = N + n\ln\left(\frac{s}{s_e}\right) \tag{10}$$

$$\lambda^*(s) = \lambda^* + l\ln\left(\frac{s}{s_e}\right) \tag{11}$$

5 SIMULATION WITH ELEMENT TESTS

Figure 8 shows the results of an oedometric test and the calibration process for the parameters N, λ^* and κ^*, using a element test program that has involved the constitutive theory selected inside of the program structure, the Figure 9 reveals the behavior of the SBS where the shape depends of the soil parameters specially of λ^*, κ^* and ϕ_c.

Using the equations 10 and 11, it is possible to find the parameter n, also it is important to note that the parameter l is zero, due to that the inclination of the saturated NCL is equal as the unsaturated. Figure 10 reveals the parameter m that controls the collapse by wetting for a suction of 200 kPa. In the Table 3 it is possible to observe the

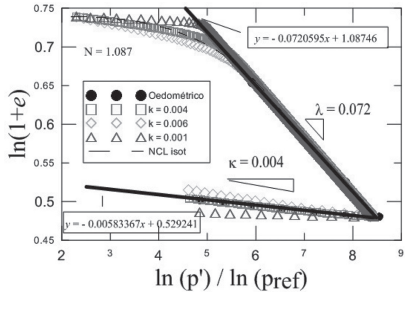

Figure 8. Process of model calibration in an oedometric test.

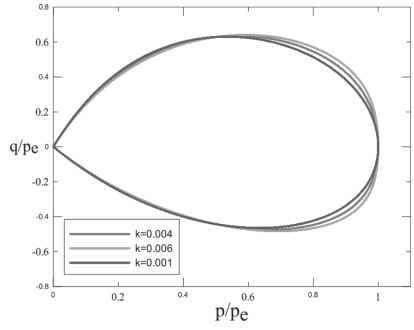

Figure 9. Behavior of the SBS model according with κ^*.

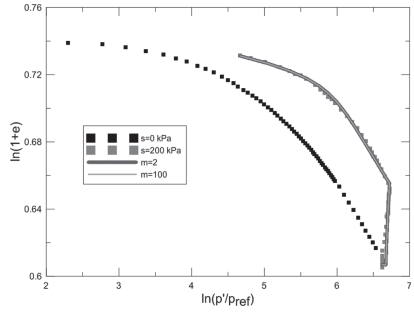

Figure 10. Calibration of the parameter *m.*

Table 3. Hypoplastic parameters of the Brasilia Clay.

ϕ_c	λ^*	κ^*	N	r	n	l	m	S_e
31.3	0.072	0.004	1.087	0.1	0.032	0	2	39

final parameters for the Brasilia Clay according with the hypoplastic constitutive model for unsaturated response of the soil.

6 CONCLUSIONS

– The program element test are very useful when the research requires to calibrate parameters of a constitutive model, in this case of an unsaturated model.
– In particular this element test program developed in Charles University is fitted only for unsaturated test, therefore when is necessary calibrate saturated parameters, it must use another kind of element test program.
– This procedure of calibration by means of element test, is still in process of improvement, so the cur-rent results are considered preliminaries.

REFERENCES

Butterfield, R. 1979. A natural compression law for soils. Geotechnique, 29 (4), 469–480.
Cardoso, F. 1995. Anàlise Quimica, Mineralogica e Micromor-fologica de Solos Tropicais. Colapsiveis e o Estudo da Dinamica do Colapso. Publicacao G.DM-026 A/95. Master's thesis, Dep. de Eng. Civil e Ambiental, Univ. de Brasília.
Cunha, R., Jardim, N. & Pereira, J. 1999. In situ characterization of a tropical clay via dilatometer tests. Geo-Congress 99 on Behavorial Characteristics of Residual Soils, ASCE Geotechnical Special Publication 92, Charlotte, (pp. 113–122).
Gudehus, G. 1996. A comprehensive constitutive equation for granular materials. Soils and Foundations, 36 (1), 1–12.
Guimaraes, R. 2002. Anàlise das Propriedades e Comportamento de um Perfil de Solo Lateritico Aplicada ao estudo do Desempenho de Estacas Escavadas, Publicacao G.DMU 091 A/02. Master's thesis, Departamento de Engenharia Civil e Ambiental, Universidade de Brasilia, Brasilia, DF.
Hvorslev, M. 1960. Physical components of the shear strength of saturated clays. In Shear Strength of Cohesive Soils, proc. ASCE Research Conf. Boulder.
Masin, D. 2006. Hypoplastic models for fine-grained soils. Ph.D. thesis, Institute of Hydrogeology, Engineering Geology and Applied Geophysics, Charles University, Prague.
Masin, D. 2007. A hypoplastic constitutive model for clays with metastable structure. Canadian Geotechnical Journal, 44 (3), 363–375.
Masin, D. & Herle, I. 2005. State boundary surface of a hypo-plastic model for clays. Comp.& Geotechnics, 6(32), 400–410.
Masin, D. & Khalili, N. 2008. A hypoplastic model for me-chanical response of unsaturated soils. Int. Journal for Num. & Analytical Methods in Geomechanics, 1(32), 1903–1926.
Mota, N. 2003. Ensaios avancados de campo na argila porosa nao saturada de Brasilia: interpretecao a aplicacao em proje-tos de fundacao. Ph.D. Thesis, Departamento de Engenharia Civil e Ambiental, Universidade de Brasilia, Brasilia, DF.
Moya, J. 2011. Propagación de ondas en medios no lineales. Master's thesis, Facultad de Ingeniería, Departamento de In-genieria Civil y Ambiental, Univ.de los Andes, Bogota, Col.
Niemunis, A. 2008. INCREMENTAL DRIVER user manual.
Sultan, H. 1969. Collapsing soils: State-of-the-art. VII Interna-tional Conference on Soil Mechanics and Foundation Engi-neering, Mexico, (pp. 1–17).
van Genuchten, M. 1980. A closed-form equation for predict-ing the hydraulic conductivity of unsaturated soils. Soils Sci-ence Society of America Journal, 44 (5).
Vargas, M. 1973. Structurally unstable soils of southern Brazil. VIII Int. Conf. on Soil Mechanics and Foundation Engineer-ing, Moscou, 2 (2), 232–249.

Advances in Unsaturated Soils – Caicedo et al. (eds)
© 2013 Taylor & Francis Group, London, ISBN 978-0-415-62095-6

Numerical analysis of unsaturated soil behaviour under large deformations

B.C.F.L. Lopes & M.P. Cordão-Neto
University of Brasília, Brasília, Brazil

ABSTRACT: Along the years Finite Element Method (FEM) has become an essential tool in engineering, specifically when dealing with complex situations. However, in order to simplify the simulations some hypotheses had to be assumed. Although nowadays many of those hypotheses have been abandoned, some still remained in use. Among the conditions that are rarely reproduced numerically are the large deformations that play an important role in some geotechnical problems, such as installation process of piles, slope stability analysis, settlement problems in embankments within others, and the condition of partially saturated soils that are the condition in which the majority of soils are found in nature. Therefore, this paper will introduce the general formulation of large deformations through the continuum mechanic method of Updated Lagrangian (UL) and propose a literature review of the constitutive modelling of unsaturated soils, emphasizing BBM-Subloading constitutive model (Cordão Neto et al., 2009).

1 INTRODUCTION

The complexity of geotechnical problems has been encouraging the use of numerical modelling to simulate soil behaviour. Among the most popular numerical modelling used is the finite element method. In order to make its use practical, several simplifications had to be imposed to real problems. However, along the years and with the advances in the numerical techniques, those simplifications have been gradually abandoned. Therefore, it is possible to have simulations closer enough to real situations.

Nevertheless, some simplifications are still remaining, such as the two highlighted in this paper: the hypothesis in which the deformations will be infinitesimals when compared to the problem's dimensions and the hypothesis of fully saturated soils or dry soils. Both hypotheses are rough simplifications since in some cases the deformations imposed to the soil can be relatively large and the conditions of fully saturated are exceptions, not rule.

This paper aims to introduce the general formulation of large deformations and it proposes a bibliography review of the constitutive modelling of unsaturated soils along with a detailed section of the model BBM-Subloading (Cordão Neto et al., 2009).

2 LARGE DEFORMATIONS

In the classical Finite element analysis it is assumed implicitly that deformations are small. In other words, it means that the geometry of the elements change very slightly during loading, therefore a consideration in which the deformations are of first order, infinitesimal and linear can be assumed (Zienkiewicz, 1977).

Indeed, those hypotheses turned out to be truth in most of the geotechnical problems analysed, since, in such cases, relatively small deformation are enough to cause collapse or lost in functionality of those structures. However, there are some situations where these hypotheses are not suitable. In such cases, it is necessary to consider the geometric non-linearity of the problem. In order to illustrate the difference in results, Hanssen (2010) performed slope stability analyses of an embankment considering the classical solution for small deformations and the Updated Lagrangian Method (UL) for large deformations. The results are shown in Figure 1.

It could be easily seen that the failure surface are very different in both cases. Furthermore, UL

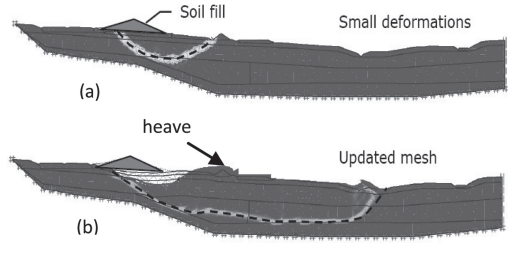

Figure 1. Slope stability analyses (a) small deformations (b) Large deformations (Hanssen, 2010).

method can reproduce heave, while conventional small deformation analysis cannot. Moreover, it can be observed that in the UL method the volume of material mobilised is greater than in the case simulated by small deformations theory.

2.1 *Geometric non-linearity*

According to Carter et al. (1977) there are, basically, two possible ways to describe deformations in a continuum medium, which are: Lagrangian Description, proposed by Lagrange, where the motion of the continuum medium is described by a function of the material coordinates and time. In this description, the mesh moves along with the material, as shown in Figure 2a. The other way is the Eulerian Description, proposed by Euler, where the motion of the continuum medium is described by a function of the spatial coordinates and time. There should be a distinction between spatial and material systems. In this case, the mesh is undistorted and the material is free to move along the mesh, as illustrated in Figure 2b.

The Lagrangian description of deformations is the description used in classic finite element methods (Qiu et al., 2010), while the Eulerian is the description used, for example, in the Material Point Method (MPM).

There are proposals in the literature of intermediate methods, between Lagrangian and Eulerian, and improvements of the original descriptions, as Total Lagrangian (TL) and Updated Lagrangian (UL), both modifications of the original Lagrangian Method, as alternatives to describe deformations.

TL and UL methods were developed to fill the gap left by the Lagrangian description itself, since it is not able to reproduce large deformations. The focus of this paper is the UL Method.

In the UL method the deformations occur in an incremental way. For each loading increment there is a change in the geometric position of the mesh nodes, together with changes in the stress state of its elements. These changes generate a new updated mesh. This process is repeated until the end of the loading increments.

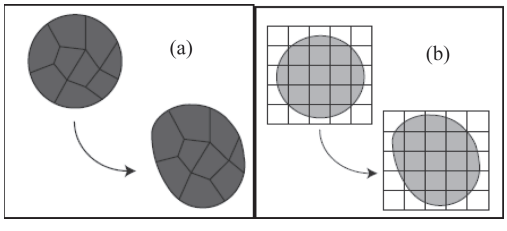

Figure 2. (a) Lagrangian description (b) Eulerian description (Qiu et al., 2010).

UL Method is easily implemented in conventional Finite Element codes and it is also able to produce generally good results. However, if the deformations are exceedingly large UL method generate large mesh distortions, which produce negative Jacobian. As a result the simulation stops abruptly and no results are obtained.

In the literature, the number of published papers related to large deformations applied to geotechnics is not expressive. Nevertheless, there is an increase in the topic's interest.

3 UPDATED LAGRANGIAN (UL)

Zienkiewicz (1977) presents in a simplified approach a Total Lagrangian formulation for large deformations. In the following it is shown the Updated Lagrangian formulation in the places where it differs from the Conventional Lagrangian Formulation adopted in traditional Finite Element Methods, namely Deformation-Displacement Total Matrix and Total Tangential Stiffness Matrix, based on Zienkiewicz (1977) and Khoei et al. (2011).

3.1 *Deformation-displacement total matrix* ($\overline{B}$)

$$\overline{B} = B_{\mathrm{o}} + B_{NL} \tag{1}$$

where B_o is the Deformation-Displacement Linear Matrix for small deformations and B_{NL} is the Deformation-Displacement Non-linear Matrix for Large Deformations.

If k represents the degree of freedom of the system and n the nodes number, and if the problem is 3D (as in the following example) $\overline{B}$ is a matrix of 6 lines, thereby:

$$B_{NL[6xkn]} = B_o \times B' \tag{2}$$

$$B_i^0 = \begin{bmatrix} \frac{\partial N_i}{\partial x} & 0 & 0 \\ 0 & \frac{\partial N_i}{\partial y} & 0 \\ 0 & 0 & \frac{\partial N_i}{\partial z} \\ \frac{\partial N_i}{\partial y} & \frac{\partial N_i}{\partial x} & 0 \\ 0 & \frac{\partial N_i}{\partial z} & \frac{\partial N_i}{\partial y} \\ \frac{\partial N_i}{\partial z} & 0 & \frac{\partial N_i}{\partial x} \end{bmatrix}_{[6xkn]} \tag{3}$$

$$B_i^{NL} = \begin{bmatrix} \frac{\partial N_i}{\partial x} & 0 & 0 \\ 0 & \frac{\partial N_i}{\partial y} & 0 \\ 0 & 0 & \frac{\partial N_i}{\partial z} \\ \frac{\partial N_i}{\partial y} & \frac{\partial N_i}{\partial x} & 0 \\ 0 & \frac{\partial N_i}{\partial z} & \frac{\partial N_i}{\partial y} \\ \frac{\partial N_i}{\partial z} & 0 & \frac{\partial N_i}{\partial x} \end{bmatrix}_{[6\,x\,kn]} \times \begin{bmatrix} \frac{\partial N_i}{\partial x} u_i & 0 & 0 \\ 0 & \frac{\partial N_i}{\partial y} v_i & 0 \\ 0 & 0 & \frac{\partial N_i}{\partial z} w_i \end{bmatrix}_{[knxkn]} \quad (4)$$

where $\partial N_i / \partial x$ represents the derivative of the function forms of i node in relation to x axis (the same is valid for y and z) and u_i, v_i and w_i represent the displacements in x, y and z directions, respectively, of i node.

3.2 *Total tangential stiffness matrix (K_T)*

$$K_{T[kn\ x\ kn]} = K_{o[kn\ x\ kn]} + K_{NL[kn\ x\ kn]} + K_{\sigma[knxkn]} \quad (5)$$

where K_o is the tangential stiffness matrix for small deformations, K_{NL} is the tangential stiffness matrix for large deformations and K_σ is the matrix of stress state. In this way:

$$K_o = \int_V B_o^T D B_o dV \quad (6)$$

$$K_{NL} = \int_V (B_o^T D B_o + B_{NL}^T D B_{NL} + B_{NL}^T D B_o) dV) \quad (7)$$

Or

$$\overline{K} = K_o + K_{NL} = \int_V \overline{B}^T D \overline{B} dV \quad (8)$$

$$K_\sigma = \int_V G^T M G dV \quad (9)$$

$$G = \begin{bmatrix} \frac{\partial N_1}{\partial x} & 0 & 0 & & \frac{\partial N_n}{\partial x} & 0 & 0 \\ 0 & \frac{\partial N_1}{\partial x} & 0 & & 0 & \frac{\partial N_n}{\partial x} & 0 \\ 0 & 0 & \frac{\partial N_1}{\partial x} & & 0 & 0 & \frac{\partial N_n}{\partial x} \\ \frac{\partial N_1}{\partial y} & 0 & 0 & & \frac{\partial N_n}{\partial y} & 0 & 0 \\ 0 & \frac{\partial N_1}{\partial y} & 0 & \cdots & 0 & \frac{\partial N_n}{\partial y} & 0 \\ 0 & 0 & \frac{\partial N_1}{\partial y} & & 0 & 0 & \frac{\partial N_n}{\partial y} \\ \frac{\partial N_1}{\partial z} & 0 & 0 & & \frac{\partial N_n}{\partial z} & 0 & 0 \\ 0 & \frac{\partial N_1}{\partial z} & 0 & & 0 & \frac{\partial N_n}{\partial z} & 0 \\ 0 & 0 & \frac{\partial N_1}{\partial z} & & 0 & 0 & \frac{\partial N_n}{\partial z} \end{bmatrix}_{[knxkk]} \quad (10)$$

$$M = \begin{bmatrix} \sigma_x I_{kxk} & \tau_{xy} I_{kxk} & \tau_{xz} I_{kxk} \\ & \sigma_y I_{kxk} & \tau_{yz} I_{kxk} \\ sim. & & \sigma_z I_{kxk} \end{bmatrix}_{[kkxkk]} \quad (11)$$

where D is the constitutive matrix of the material, σ_x, σ_y, σ_z, τ_{xy}, τ_{yz}, τ_{xz} compose the material stress state vector.

Due to the dependency of the B_{NL} matrix and consequently K_{NL} matrix, in relation to the displacements and M matrix and consequently K_σ matrix in relation to the stress state of the element, $\overline{B}$ and K_T matrices have to be updated at each increment of loading as well.

4 CONSTITUTIVE MODELLING FOR UNSATURATED SOILS

Constitutive models are mathematical tools used to analyse materials behaviour. Until 1999, the majority of proposals of representation of unsaturated soil behaviour were restrained to the reproduction of its mechanical behaviour. Barcelona Basic Model (BBM) proposed by Alonso et al. (1990) represents an important mark in this sense. BBM is an elasto-plastic model, derived from the established Modified Cam-Clay Model for saturated soils.

Lately, there are developments of models that couple hydraulic and mechanical soil behaviours. However, what it is seen in the literature, nowadays, are proposals of new models that only improve previous models results, adding to it more parameters. These new constitutive models, if it could be called this, do not offer any change in the paradigm. The concept of Subloading incorporated

to elasto-plastic models is an example of change in paradigm, since it modifies the concept of elastic and elasto-plastic. Another example of such a change is the introduction of Pore Size distribution (PSD) information into constitutive models.

Nakai et al. (2008) propose a model in which two parameters are added to represent the effects of fabric of the soil. As a result, the model is then able to reproduce either natural and remoulded clay soils.

Figure 3 briefly presents the evolution along the years of constitutive models for unsaturated soils.

One of the current trends is the development of constitutive models that incorporate the microstructure characteristics of the soil. Within this context, Hashiguchi (1980) highlighted yet that for an accurate description of the unsaturated soil behaviour its necessary succeed in the identification of the internal variables that control the relationship between stress-deformation-resistance.

5 BBM-SUBLOADING (CORDÃO NETO ET AL., 2009)

Subloading theory was originally proposed by Hashiguchi (1980), followed by Pedroso et al. (2005); Nakai et al. (2008); Farias et al. (2008) among others. The model is an enhanced extension of elastoplastic models. The inclusion of Subloading concept in a model allows it to describe the following features (Cordão Neto et al., 2009): 1. inelastic strains during re-loading; 2. smooth transition between normally consolidated states; 3. cyclic loads and 4. strain hardening behaviour with positive dilatancy (very typical behaviour of unsaturated soils). Adding to it only one state variable.

5.1 *Subloading concept*

Two components need to be added in order to improve models (Cordão Neto et al., 2009). These are: an addition yield surface, called Subloading yield surface (SL) (Figure 4); and the plastic void ratio for over-consolidated states, which is the new variable (Figure 5).

As a result the new model has two yield surfaces (Figure 4) both having the same shape with SL being always smaller than NS, or at least coincident with NS, which implies that in this point the soil becomes normally consolidated.

In subloading models the stress-strain constitutive matrix is always evaluated on the SL yield surface, which for BBM is expressed as follows:

$$f^{SL} = q^2 - M^2(p_m^{SL} - p)(p + p_s) \tag{12}$$

where p_m^{SL} is the stress variable adopted to define the size of the subloading yield surface; M is the

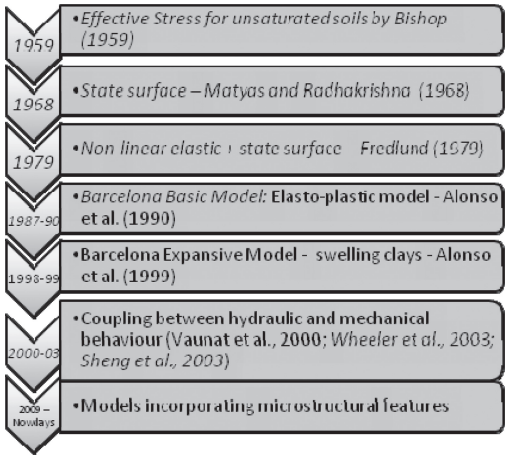

Figure 3. Highlights into constitutive modelling for unsaturated soils (Cordão Neto, 2011).

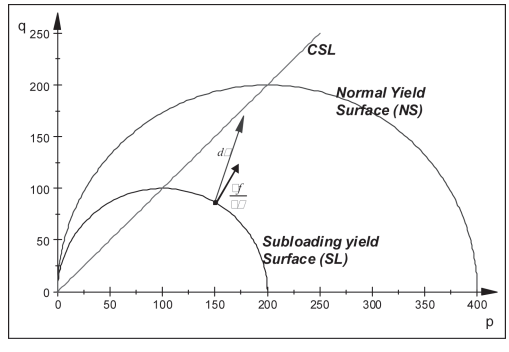

Figure 4. Normal and subloading yield surfaces (Cordão Net et al., 2009).

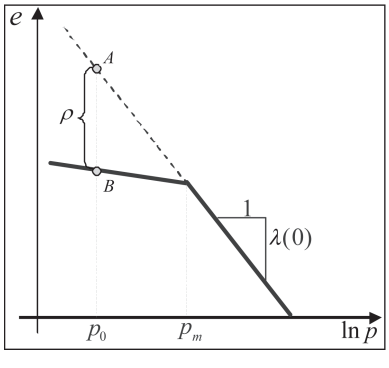

Figure 5. Representation of the plastic void ratio (Cordão Net et al., 2009).

slope of the critical state line, p is the net mean stress; q is the deviatoric stress (i.e., $q = \sigma_1 - \sigma_3$); and p_s considers the dependence of shear stress on suction (Alonso et al., 1990).

The new variable, called plastic void ratio (ρ) (Figure 5), is the distance between the current state and a hypothetical state over the normal compression line at the same stress level. Then, the plastic void ratio variable is a measure of the degree of over-consolidation of the soil (Cordão Neto et al., 2009).

A Subloading model needs the definition of an additional hardening law, which considers both: the plastic volumetric strains associated with the normal yield surface (i.e. $d\varepsilon_v^{p}$); and the plastic volumetric strains associated with the SL yield surface. This new law can be expressed as (Cordão Neto et al., 2009):

$$dp_m^{SL} = \frac{p_m^{SL}(1+e)}{\lambda(0)-\kappa}\left(d\varepsilon_v^{p(SL)} + d\varepsilon_v^{p(NS)}\right) \tag{13}$$

5.2 *Extension of subloading concepts to the unsaturated condition*

Cordão Neto et al. (2009) considered ρ as a function of suction (s), differently from Pedroso (2006) which assumed it independent of suction.

BBM was the model chosen as the reference framework. BBM assumes that the slope of the normally consolidated line 'λ(s)' depends on suction (Figure 6). This implies that the plastic void ratio is no longer the distance between points F-G, but the distance between E-H (Figure 6).

Therefore, the plastic void ratio should be expressed as:

$$\rho(s) = \rho(0) + \left[\lambda(0) - \lambda(s)\right]\ln\frac{p^o}{p^r} \tag{14}$$

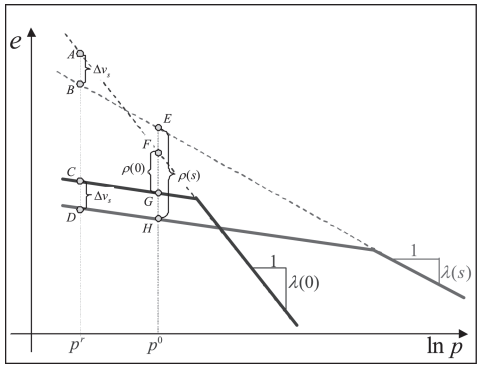

Figure 6. Effect of suction on plastic void ratio. (Cordão Net et al., 2009).

where p^o corresponds to the current stress state and p^r is the mean net stress such that: $e_A - e_B = e_C - e_D$. This variable has been defined in a similar way as p_c in Alonso et al. (1990). Note that the definition of $\lambda(s)$ does not require the addition of a new model parameter; as the dependence of ρ on suction is accounted by $\lambda(s)$ (which is in turn defined according to Alonso et al., 1990). The mechanical constitutive relation for stress-strain-suction in unsaturated soils is expressed as:

$$d\sigma_{ij} = D_{ij}^{e}\left(d\varepsilon_j - \Lambda\frac{\partial g}{\partial \sigma_j} - H_j ds\right) \tag{15}$$

where D_{ij}^{e} is the elastic stress-strain matrix; $d\varepsilon_j$ is the increment of the total strain; and H_j is the vector that relates elastic strains with suction changes.

It is assumed that once yield occurs (i.e. $f^{SL} = 0$), the stresses must remain on the yield surface during plastic deformation. This constraint is enforced by the consistency condition as follows:

$$df^{SL} = \frac{\partial f^{SL}}{\partial \sigma_i}d\sigma_i + \frac{\partial f^{SL}}{\partial \varepsilon^{p}}d\varepsilon^{p} + \frac{\partial f^{SL}}{\partial s}ds = 0 \tag{16}$$

From equations above the plastic multiplier can be expressed as:

$$\Lambda = \frac{\frac{\partial f^{SL}}{\partial \sigma_i}D_{kl}d\varepsilon_k}{A-B} + \frac{\left(\frac{\partial f^{SL}}{\partial s} - \frac{\partial f^{SL}}{\partial \sigma_i}D_{kl}H\right)_k ds}{A-B} \tag{17}$$

where

$$A = \frac{\partial f^{SL}}{\partial \sigma_i}D_{ij}^{e}\frac{\partial g}{\partial \sigma_j} \tag{18}$$

and,

$$B = \frac{\partial f^{SL}}{\partial \varepsilon_v^{p}}\left(\frac{\partial g}{\partial \sigma_i}m_i + \frac{G(\rho)}{p}\right) \tag{19}$$

where m $m_i = [1,1,1,0,0,0]$

6 CONCLUSIONS

This paper presented the Updated Lagrangian Method to describe Large Deformations and a literature review of constitutive modelling for unsaturated soil, emphasising BBM-Subloading model proposed by (Cordão Neto et al., 2009).

Updated Lagrangian Method is a good first attempt to describe large deformations, by the fact that it is easily implemented in Conventional Finite

Element Methods and it produces good results. However, care should be made when dealing with very large deformations, as the mentioned method can generate negative Jacobian as a result, making the solution of the problem unpractical.

Cordão Neto et al. (2009) highlighted that the incorporation of subloading concepts in the formulation of the BBM allows a smooth transition between over-consolidated and normally consolidated states, which is close to the actual behaviour observed in over-consolidated unsaturated samples. Moreover, models formulated in the context of subloading theory have additional advantages, such as: they are able of reproducing irreversible strains during re-loading and they are able of describing the strain hardening behaviour with positive dilatancy (very typical behaviour of unsaturated soils) and cyclic loads. The proposed new subloading model therefore has significant additional capability, requiring only one extra parameter with respect to a conventional unsaturated elasto-plastic model, such as BBM.

Although it is relevant in some cases, very few authors attempt to analyse problems considering the unsaturated condition of the soil and large deformations. Slope stability analyses are great examples of problems that need to be examined using the theory described in this paper.

REFERENCES

Alonso, E.E, Gens, A. & Josa, A. 1990. A constitutive model for partly saturated soil. *Géotechnique*, 40 (3): 405–430.

Alonso, E.E., Vaunat, J. & Gens, A. 1999. Modelling the mechanical behaviour of expansive clays. *Engineering Geology* 54 (1999): 173–183.

Bishop, A.W. 1959. The principle of effective stress. *Lecture delivered in Oslo*, Norway 106 (39): 859–863.

Carter, J.P., Booker, J.R. & Davis, E.H. 1977. Finite deformation of an elasto-plastic soil. *Int. J. Numer. Anal. Meth. Geomech. 1*: 25–43.

Cordão Neto 2011. Notas de aulas de mecânica dos solos não saturados. *Universidade de Brasília*: Brasília.

Cordão-Neto M.P., Sanchez, M., Karstunen, M. & Farias, M. 2009. Extension of the Barcelona Basic Model Considering Sub-loading Concepts. *4th Asia-Pacific Conference on Unsaturated Soils.* 23–25 November 2009. Newcastle, Australia.

Farias, M.M., Pedroso, D. & Nakai, T. 2008. Automatic substepping integration of the subloading tij model with stress path dependent hardening. *Comput Geotech.*

Fredlund, D.G. 1979. Appropriate concepts and technology for unsaturated soils. *Canadian Goetechnical Journal*, 16(1): 121–139.

Hanssen, S.B. 2010. Numerical Simulations of Progressive Failure and Localized Deformation. MSc. Dissertation. Norwegian *University of Science and Technology, Faculty of Engineering Science and Technology, Department of Civil and Transport Engineering*: 120.

Hashiguchi, K. 1980. Constitutive equation of elastic-plastic materials with elastoplastic transition. *J. Appl Mech, ASME* 1980. 102(2): 266–272.

Khoei, A.R., Anahid, M., Zarinfar, M., Ashouri, M. & Pak, A. 2011. A large plasticity deformation of unsaturated soil for 3D dynamic analysis of lower san-fernando dam. *Asian J. of Civil Eng. (Building and Housing)*. 12 (1): 1–25.

Matyas, E.L. & Radhakrishna, H.S. 1968. Volume change characteristics of partially saturated soils. *Géotechnique*, 18(4): 432–448.

Nakai, T., Zhang, F., Kyokawa, H., Kikumoto, M. & Shahin, H.M. 2008. Modelling the influence of density on geomaterials. *Geotechnics of soft soils—Proceedings of the second international workshop on geotechnics of soft soil, Glasgow*, UK. 65–76.

Pedroso, D. 2006. Mathematical representation of the cyclic mechanical behavior of saturated and unsaturated soils (In Portuguese). PhD Thesis—*University of Brasilia*. 224.

Pedroso, D, Farias, M.M. & Nakai, T. 2005. An interpretation of subloading tij model the contect of conventional elastoplasticity theory. *Soils Found*. 45(4): 61–77.

Qiu, G., Henke, S. & Grabe, J. 2010. Application of a Coupled Eulerian–Lagrangian approach on geomechanical problems involving large deformations. *Computers and Geotechnics* 38 pp. 30–39.

Sheng, D., Sloan, D.S.W., Gens, A. & Smith, D.W. 2003. Finite element formulation and algorithms for unsaturated soils. Part I: Theory. *Int. J. Numer. Anal. Meth. Geomech.* 27: 745–765.

Vaunat, J., Cante, J.C., Ledesma, A. & Gens, A. 2000. A stress point algorithm for an elastoplastic model in unsaturated soils. *International Journal of Plasticity.* (16): 121–141.

Wheeler, S.J., Sharma, R.S. & Buisson, M.S.R. 2003. Coupling of hydraulic hysteresis and stress-strain behaviour in unsaturated soils. *Géotechnique* 53: 41–54.

Zienkiewicz, O.C. 1977. The Finite Element Method. London: *McGraw-Hill*: 787.

Numerical modelling

This page intentionally left blank

Advances in Unsaturated Soils – Caicedo et al. (eds)
© 2013 Taylor & Francis Group, London, ISBN 978-0-415-62095-6

Study of the influence of climatic effects on the soil temperature and suction changes

K.V. Bicalho & G.P.W. Vivacqua
Federal University of Espirito Santo, Vitoria, ES, Brazil

Y.J. Cui
Université Paris-Est, CERMES-ENPC, Marne-la-Vallée, France

ABSTRACT: This paper focus on predicting of temperature and suction response to climatic changes in a soil profile during a long term period by considering the soil atmosphere interface interactions, with emphasis on evaporation. A one-dimensional model is used to calculate the evaporation rate and heat flux on the soil surface; water (liquid and vapor) transport equations coupled to heat flow equation are solved to determine the soil profiles. The investigated site, in France, has been instrumented with a meteorological station in order to monitor solar radiation, precipitation, wind speed, air temperature, and air relative humidity. A water deficit is observed in most of time throughout the instrumented years. The results show that the active zone is about 1.5 m deep in the investigated region and the actual monitored meteorological data, and would fluctuate 3 m by using the average data. Calculated and direct measurements were compared and satisfactory results were obtained.

1 INTRODUCTION

Adequate measurements of soil variables and atmospheric fluxes are often not available to study the various stages of the soil atmosphere interface interactions. This paper focus on predicting of in situ soil suction and temperature response to climatic changes during a long term period by using a soil-atmosphere interface model based on the meteorological data obtained in the field.

A one dimensional explicit finite difference program developed by Gao (2006) is used to identify the importance of various interactions related to surface evaporation.The program models the coupled water flow and heat flow in unsaturated soil and uses an energy estimation method for determining the evaporation rate of water from a wet soil (Xu & Qiu 1997). The model was validated with several data sets and able to satisfactorily predict soil profiles for non-cohesive and cohesive soils by Cui et al. (2005, 2010).

In this paper, the effects of the thermal conductivity of solid on the predict data is discussed. The influence of climatic effects on the soil temperature and suction (or water content) changes by using the actual monitored meteorological and the average meteorological data is also evaluated. The investigated site, in Mormoiron, located between the Mont Ventoux and the Vaucluse plateau, France, has been instrumented with a meteorological station in order to monitor solar radiation, precipitation, wind speed, air temperature, and air relative humidity for 42 years from 1964 to 2005. A water deficit is observed in most of time throughout the instrumented years. It seems that there was a seasonal trend in meteorological changes. Therefore, in this study, it is investigated the years of 2004 and 2005 that correspond to drier conditions where the recharge of the water table did not take place.

To overcome the limitations of some unknown input data (model parameters and initial conditions), earlier papers (Bicalho & Cui 2009; Bicalho et al. 2011) have already evaluated the sensitivity of predicted temperature changes in the region due to ground-atmospheric interactions to the variations of some not measured parameters, such us soil albedo and saturated hydraulic conductivity, and the initial soil temperature profile which may change during the day. This paper is a continuation of the earlier papers, and for providing continuity, the previous papers are briefly summarized here.

2 SOIL-ATMOSPHERE INTERFACE MODEL

The model computes the evaporation rate from soil by solving a coupled water (liquid and vapor) transport equations (Darcy's law and Fick's law), heat flow equation (de Vries 1963) analysis, and the surface energy balance used for defining a reliable

boundary setting method for extended periods of evaporation simultaneously.

2.1 *Soil heat and mass flow models*

Similar one-dimensional model was also used by Wilson et al. (1994); Cui et al. (2005, 2010), and Bicalho et al. (2011) to describe the heat and groundwater flow in unsaturated porous media. In this model, the transient equation of liquid water and water vapor is:

$$\frac{\partial(h_w)}{\partial t} = C_w \frac{\partial}{\partial z}(k_w \frac{\partial(h_w)}{\partial z}) + C_v \frac{\partial}{\partial z}(D_v \frac{\partial P_v}{\partial z}) \quad (1)$$

where t (s) is the time, z (m) the elevation, h_w(m) the total hydraulic head (the sum of capillary head and elevation head z), P_v (kPa) the vapor pressure, C_w (m) and C_v (m^4 kg^{-1}) the modulus of volume change with respect to liquid phase and vapor phase respectively, D_v (kg m kN^{-1} s^{-1}) the diffusion coefficient of water vapor through soil, P_v may be related to the h_w by Kelvin's equation, k_w is the water hydraulic conductivity depending on capillary head.

The calculation of the vapor pressure P_v in Equation 1 depends on the saturated vapor pressure P_{vs} and the soil temperature T (°C). Hence, the temperature profile of the soil must be determined simultaneously. The heat flow due to both conductivity and latent heat diffusion is (Wilson et al. 1994):

$$c_h \frac{\partial T}{\partial t} = \frac{\partial}{\partial z}(\lambda \frac{\partial T}{\partial z}) + L_v + \frac{P + P_v}{\partial z} \frac{\partial}{\partial z}(D_v \frac{\partial P_v}{\partial z}) \quad (2)$$

where C_h(J m^{-3} $°C^{-1}$) is the volumetric specific heat capacity, representing the thermal storage capacity of the volume element considered, λ (J s^{-1} m^{-1} $°C^{-1}$) is the thermal conductivity of soil, L_v (J kg^{-1}) is the latent heat coefficient of vaporization of water (4.186×10^3(607–0.7T)).

2.2 *Soil-atmosphere interface boundary condition*

The energy balance equation expressing the net radiation flux, R_n *(* Wm^{-2}*),* for the surface is (Blight 1997):

$$R_n = LE + H + G \quad (3)$$

where LE *(* Wm^{-2}) is the latent energy transfer (positive for evaporation and negative for condensation), H *(* Wm^{-2}) is the sensitive heat flux for the air (positive when energy is used to warm the air and negative when the air loses energy due to cooling), and *G (* Wm^{-2}) is the ground heat transfer (positive when energy is transferred to the subsurface and negative when energy is transferred to the atmosphere).

The energy estimation method proposed by Xu & Qiu (1997) is used for determining the evaporation rate of water from a wet soil. In this approach, *H* and *LE* are calculated from the turbulent exchange equations by:

$$H = \frac{\rho_a C_{pa}(T_s - T_a)}{r_a} \quad (4)$$

$$LE = \frac{L_V M_w (p_{vz0} - p_{vza})}{RTr_a} \quad (5)$$

where ρ_a is the air density, C_{pa} is the specific heat of air equal to 1.013×10^3 J/(kg.K), T_s is the soil surface temperature, T_a is the air temperature at reference height Z_a, T is the average temperature and $T \approx (T_a + T_s)/2$, p_{vz0} is the vapor pressure at the soil surface, p_{vza} is vapor pressures of in the air at reference height Z_a, r_a is the aerodynamic resistances for the sensible and latent heat fluxes, L_v is the latent heat of vaporization, M_w is the molecular mass of water equal to 0.018 kg/mol, *R* is the gas constant equal to 8.314 J/(mol.K). These equations take into account both the soil-atmosphere resistance (r_a), depending on the wind velocity (u_a), the soil-atmosphere temperature (T_s-T_a) or vapor pressure (p_{vz0}-p_{vza}) gradients. *G* is calculated from the energy balance. Aerodynamic resistances r_a is calculate as:

$$r_a = r_{a0} \frac{1}{\left(1 + Ri\left(T_s - T_a\right)\right)^{\eta}} \quad (6)$$

where $\eta = 0.75$ in unstable condition ($T_s > T_a$), and $\eta = 2$ in stable condition ($T_s < T_a$), R_i is the Richardson Number and r_{a0} is the aerodynamic resistances derived from a logarithmic wind profile:

$$Ri = \frac{5g(z_a - d)}{u_a^2 T_a}, r_{a0} = \frac{\left[\ln\left(\frac{z_a - d}{z_0}\right)\right]^2}{k^2 u_a} \quad (7)$$

where z_0 is the roughness length parameters for momentum (wind) and sensible heat transport, Z_a is the measurement height for wind speed u_a and relative humidity *d* is the displacement height, and $d = 0$ for bare soil, *k* is a constant equal to 0.41. Details of the used method are discussed in Cui et al. (2005, 2010).

2.3 *Soil constitutive functions*

To solve the governing equations the suction-volumetric water content and suction-unsaturated hydraulic conductivity relationships must be

known. The relationships are (Juarez-Badillo 1992):

$$\theta_w = \frac{\theta_{ws} - \theta_r}{1 + \left(\frac{\theta_{ws} - \theta_r}{\theta_{w1} - \theta_r} - 1\right)\left(\frac{s}{s_1}\right)^{\varsigma}} + \theta_r \tag{8a}$$

$$k_w = \frac{k_s}{1 + \left(\frac{k_s}{k_{w1}} - 1\right)\left(\frac{s}{s_1}\right)^{\xi}} \tag{8b}$$

where θ_{ws} is the saturated volumetric water content, θ_r is the residual volumetric water content, θ_{w1} is the value of water content corresponding to suction s_1, and ς is the parameter that controls the shape of the s-θ_w curve, k_s is the water permeability at $s = 0$, and k_{w1} is the hydraulic conductivity corresponding to suction s_1.

The thermal conductivity of soil, λ, is (de Vries 1963):

$$\lambda = \frac{f_s\theta_s\lambda_s + f_w\theta_w\lambda_w + f_a\theta_a\lambda_a}{f_s\theta_s + f_w\theta_w + f_a\theta_a} \tag{9a}$$
$$\lambda_a = \lambda_{dry-air} + \lambda_{water-vapor}$$

The thermal conductivity of solid, λ_s, is (Johansen 1975):

$$\lambda_s = \lambda_q^{(q)}\lambda_0^{(1-q)} \tag{9b}$$

where q is the quartz volume fraction, for q = 0, λ_s = 2.0 W/mK and q = 100%, λ_s = 7.7 W/mK, the thermal conductivity of water λ_w (0.57 W/m °C), $\lambda_{dry-air}$ (0.025 W/m °C), $\lambda_{water-vapor}$ (0.608 θ_w), f_s, f_w and f_a are the weight coefficient for solid, water and air respectively and f_w = 1.0,

$$f_s = \left[1 + \left(\frac{\lambda_s}{\lambda_w} - 1\right)\right]^{-1} \tag{10}$$

$$f_a = \frac{1}{3}\sum_{i=1}^{3}\left[1 + \left(\frac{\lambda_a}{\lambda_w} - 1\right)g_i\right]^{-1} \tag{11}$$

where g_i are called shape factors ($g_1 + g_2 + g_3 = 1$) (Gao 2006):

For $\theta_w > 0.121$,

$$g_1 = g_2 = \frac{0.333 - 0.105}{0.236 - 0.121}(\theta_w - 0.121) + 0.105$$

For $\theta_w < 0.121$,

$$g_1 = g_2 = \frac{0.105 - 0.015}{0.121}\theta_w + 0.015)$$

3 NUMERICAL SIMULATIONS

The soil heat and mass flow equations were solved using the explicit finite difference method (Gao 2006). It is assumed that the soil skeleton is rigid. For the investigated clay soil, the specific gravity is 2.72, the liquid limit ranges from 52% to 60%, the plastic limit ranges from 23 to 28%; and activity from 0.4 to 1.16. The input data are θ_{ws} = 0.49–0.4, θ_r = 0.08, θ_{w1} = 0.24, s_1 = 700–200 kPa, and ς = 1.1, $k_{sat} = 1.2 \times 10^{-11}$–$2.4 \times 10^{-10}$ m/s) and $k_{w1} = 1.2 \times 10^{-14}$ m/s, s_1 = 40 kPa, ς" = 1.25. The thermal coefficients C_w (4.15×10^6 J/m^3 °C), C_s (2.24×10^6 J/m^3 °C), and q = 50% and λ_s = 3.92 W/mK. Since the actual value of the thermal conductivity of solid, λ_s is not known, it is investigated in this paper the sensitivity of predicted volumetric water content (or pore-water pressure) and temperature profiles to the λ_s changes.

The investigated site in Mormoiron, France, has been instrumented with a meteorological station in order to monitor solar radiation, energy, precipitation, runoff, wind speed, air temperature, and air humidity for 42 years from 1964 to 2005. Examination of the atmospheric water balance at the site has shown that evapotranspiration often exceeds precipitation during the instrumented years. The annual average daily continuous precipitation measurements range from about 1 mm/day to 2.75 mm/day. The highest annual average precipitation rate (2.75 mm/day) was recorded in 2002. The annual average values do not change much from 1964 to 1999.

Even though, a detailed atmospheric water balance for each year shows a variable water deficit throughout the year. It seems that there was a seasonal trend in meteorological changes during this time period. Therefore, in this study, it is investigated the years of 2004 and 2005 that correspond to drier conditions where the recharge of the water table did not take place. A water deficit is observed in most of time throughout the studied years except for a brief period in December 2003, October 2004, April and October 2005.

The climatic data recorded at the Mormoiron site from December 2003 to December 2005 (i.e., solar radiation (0.05 to 0.35 $kW.m^{-2}$), energy, precipitation, runoff, wind speed (2 to 14 m/s), air temperature (0 to 25 °C), and air humidity) were used to set the soil-atmosphere interface boundary condition. It is observed that the air temperature changes correlate well with solar radiation. The air relative humidity varies between 30 and 100%, but it does not necessary follow the precipitation pattern. The air relative humidity depends not only on precipitation, but also on air temperature and wind speed (Cui & Zornberg 2008).

The analyses performed employed the same values of the depth of the analysis (ZMAX = 5.25 m), the constant spacing (Δz = 0.005–0.05 m), the time step (Δt = 0.5 s), the runtime, TMAX (s), bottom volumetric water content boundary (θ_b = 0.30), bottom temperature boundary (T_b = 14°C), and initial volumetric water content profile. Numerical analyses were made in one dimensional idealized case where the actual land soil cover is replaced by two layers homogeneous soil column.

To overcome the limitations of some unknown input data (model parameters and initial conditions), Bicalho et al. (2011) have already evaluated the sensitivity of predicted temperature changes in the region due to ground-atmospheric interactions to the variations of the not measured parameters, such us soil albedo and saturated hydraulic conductivity, and the initial soil temperature profile (ITP) which may change during the day.

Bicalho et al. (2011) investigated the sensitivity of predicted volumetric water content (or pore-water pressure) and temperature profiles to the variation of 5°C in the ITP. The dependence of the soil temperature on the soil water retention curve was not considered in the numerical simulations. It was observed that the value of the ITP can affect the temperature profiles and the influence of the considered changes (i.e., 5°C) on the suction (or volumetric water content) profiles is very small. The volumetric water content and pore water pressures at depth > 1.5 m are almost constant. The influence is more accentuated for the near surface layers, where more extreme variations in temperature occur. The results show that the temperatures increase with the depth during the cold season (January to March 2004) and decrease with the depth during the warm season (April to July 2004). Bicalho et al. (2011) observed the insensitivity of the simulations using different saturated hydraulic conductivities (case B—$k_{sat} = 1.2 \times 10^{-11}$–$2.4 \times 10^{-10}$ m/s; case B4 - $k_{sat} = 1.2 \times 10^{-9}$–$2.4 \times 10^{-8}$ m/s). The years of 2004 and 2005 correspond to drier conditions (high suction values) and changes of k_{sat} of this magnitude have not significant effect on the considered suction-unsaturated hydraulic conductivity relationship.

In order to investigate the effects of the thermal conductivity of solid, λ_s, two different values are used in the numerical simulations, i.e., λ_s = 3.92 W/mK (case B) and λ_s = 2.00 W/mK (case B9). The numerical simulations of volumetric water content profiles using different values of λ_s suggest that the differences between Cases B and B9 are very small for the investigated region and meteorological data. The sensitivity of predicted temperature changes to the variations of λ_s is presented in Figure 1.

The effects of the thickness of the upper layer (Z) in the two layers homogeneous soil column were investigated by Bicalho et al. (2011). The numerical simulations of volumetric water content profiles using different thicknesses of the upper layer, i.e., Z_1 = 3.45 m and Z_2 = 0.5 m, suggest that the differences between the two cases are very small.

The changes in soil profiles during a given period depend on the ratio of reflected to incident solar radiation (i.e., the soil albedo value). It is a function of several surface parameters including soil color, water content, roughness and vegetation cover, usually being lower for wet and rough conditions. The albedo value ranges from 0 to 1. The value of 0 refers to a blackbody, a theoretical media that absorbs 100% of the incident radiation. Albedo ranging from 0.1–0.2 refers to dark-colored, rough soil surfaces, while the values around 0.4–0.5 represent smooth, light-colored soil surfaces. The value of 1 refers to an ideal reflector surface (an absolute white surface) in which all the energy falling on the surface is reflected. The sensitivity of predicted temperature changes to the variations of the soil albedo is investigated in Figure 2, where case B (soil

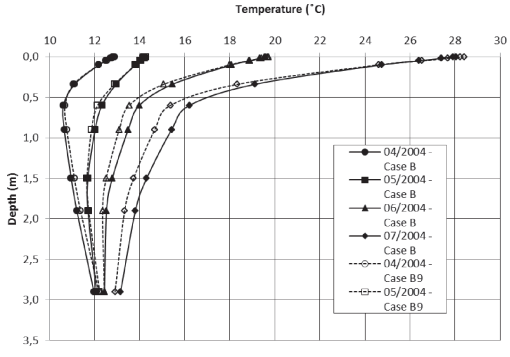

Figure 1. Influence of λ_s on the soil temperature profiles.

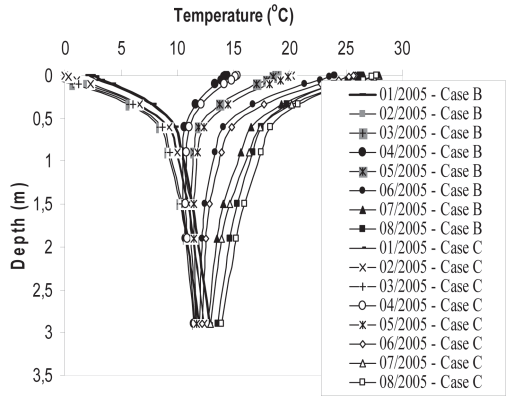

Figure 2. Influence of the soil albedo values on the temperature profiles (2005).

albedo = 0.15) and case C (soil albedo = 0.05). The insensitivity of the results (Cases B and C) during the cold season (January to March 2005) is shown in Figure 2. Small changes in the soil temperature values (increase) due to the variation (decrease) of the soil albedo (case C) are observed during the warm season (April to August).

The results of the simulations indicate that the active zone is generally about 1.5 m deep in the investigated region. For investigating it, the results of the simulations using the actual (measured) climatic input data (case B) and the mean month input data (case G) are present in Figures 3, 4, 5 and 6. The results show that the use of mean climatic data (dashed lines, case G) increases the soil temperature and the soil suction values, and the active zone about 3.0 m. However, more data should be investigated before anything very definite can be said about it.

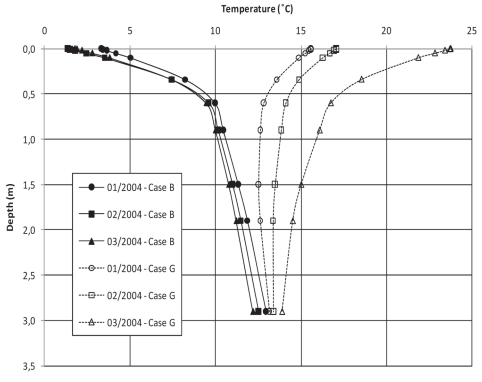

Figure 3. Influence of climatic data on the soil temperature profiles during cold season (months 01, 02 and 03, 2004).

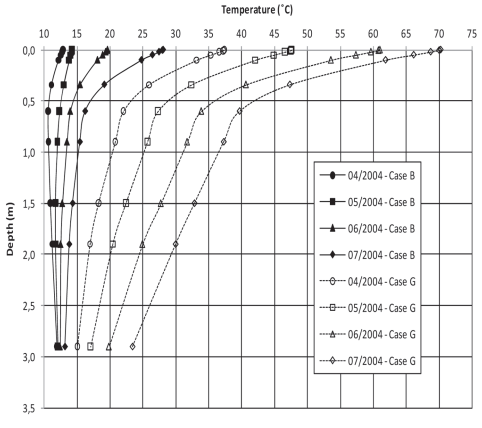

Figure 4. Influence of climatic data on the soil temperature profiles during warm (months 04, 05, 06, 07, 2004).

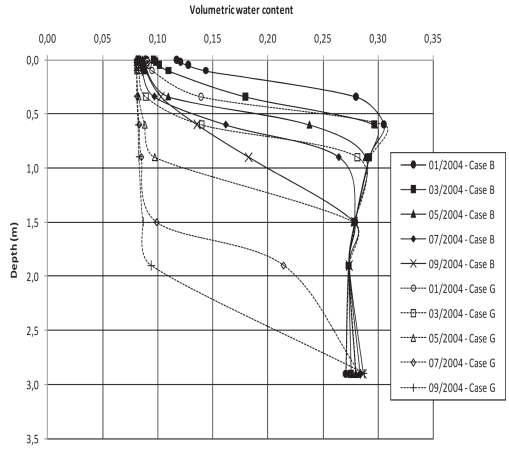

Figure 5. Influence of climatic input data on the volumetric soil water content profiles (2004).

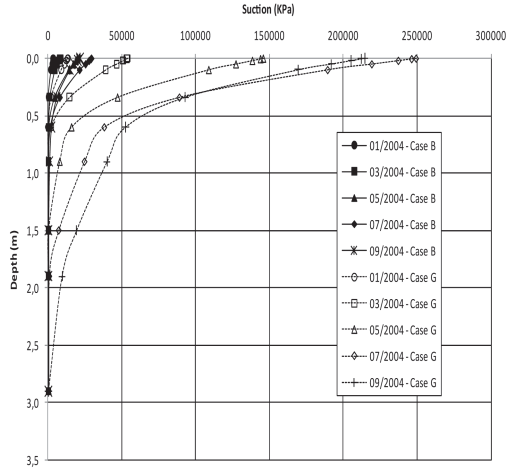

Figure 6. Influence of climatic input data on the soil suction profiles (2004).

Figure 7 presents the comparison of predicted and measured changes in soil temperature at three different depths (0.5 m, 1.5 m, and 2.5 m) during 2005 in Mormoiron, France. The results suggest that in the near the surface layers the simulations were less satisfactory due to probably vegetation effects or other mechanical phenomena (i.e., soil cracking). A sensitivity analysis of temperature and water content profiles to the changes to the variations of other unknown parameters (i.e., soil water content that depend on the soil temperature) should also be investigated. Cui et al. (2005) proposed to consider the superficial zone independently, using different values of the soil parameters.

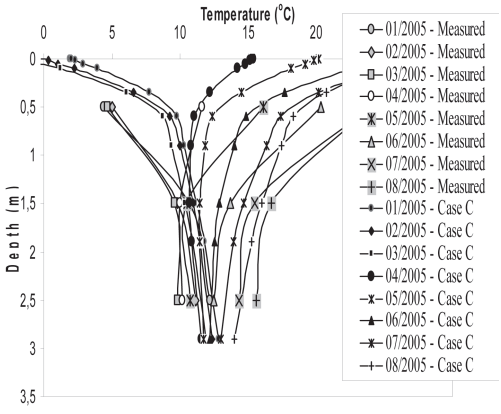

Figure 7. Comparison of predicted and measured changes in temperature profiles during 2005.

4 CONCLUSIONS

A preliminary sensitivity analysis was performed first by the authors to investigate and identify important factors in the model with many parameters. It was observed that the value of the ITP can affect the temperature profiles and the influence of the considered changes (i.e., 5°C) on the suction (or volumetric water content) profiles is very small. In contrast to soil moisture heat enters and leaves the soil surface easier and faster. The numerical analyses also reveal the insensitivity of water content (or suction) and temperature changes to the variations of the saturated hydraulic conductivity k_{sat}. The investigated years correspond to drier conditions (high suction values) and changes of k_{sat} of this magnitude (i.e., 100 times) have not significant effect on the considered suction-unsaturated hydraulic conductivity relationship. For the investigated soils, the changes in the thickness of the upper layer in the two layers homogeneous soil column may only slight affect the soil temperature and water content profiles. During the cold season, precise albedo values are not very important nor very sensitive in influencing the water balance.

This paper shows that the active zone is generally about 1.5 m deep for the investigated region and measured meteorological data. The results also suggest that the active zone may change about 3 m by using the average meteorological data. The comparison of predicted and measured changes in temperature profiles suggest that in near the surface layers the simulations are less satisfactory due to probably vegetation effects or other mechanical phenomena (i.e., soil cracking).

ACKNOWLEDGEMENTS

The first author is grateful for sponsorship by the Brazilian government agency CNPq and FAPES/ FACITEC. This work has been performed within the French ANR-RGCU project: ARGIC. The meteorological data was provided by Météo France and the soil data by BRGM.

REFERENCES

Bicalho, K.V. and Cui, Y-J. 2009. Simulations of in situ water content and temperature changes due to ground-atmospheric interactions. *Proceedings of the 17th International Conference on Soil Mechanics and Geotechnical Engineering: The academia and practice of geotechnical engineering*, Alexandria, Egypt, Publisher IOS Press, 534–537.

Bicalho, K.V., Vivacqua, G.P.D. and Cui, Y-J. 2011, Influences of the soil-atmosfere interface interactions on the soil water contente and temperature profiles. *Unsaturated soils,* Alonso & Gens (eds), 2, 1103–1108.

Blight, G.E. 1997. Interactions between the atmosphere and the earth. *Geotechnique*, 47 (4): 715–767.

Choudhury, B.J., Reginato, R.J. and Idso, S.B. 1986. An analysis of infrared temperature observations over wheat and calculation of latent heat flux. *Agric. For. Meteorol.*, 37:75–88.

Cui, Y.J., Lu, Y.F., Delage, P. and Riffard, M. 2005. Field simulation of in site water content and temperature changes due to ground-atmospheric interactions. *Geotechnique,* 55 (7): 557–567.

Cui, Y.J. and Zornberg, J. 2008. Water Balance and Evapotranspiration Monitoring in Geotechnical and Geoenvironmental Engineering. *Journal of Geotechnical and Geological Engineering,* 26 (6), 783–798.

Cui, Y.J., Gao, Y.B. and Ferber, V. 2010. Simulating the water content and temperature changes in an experimental embankment using meteorological data. *Engineering Geology* 114, 456–471.

De Vries, D.A. 1963. Thermal properties of soils. In physics of plant environment (ed. W.R. Van Wijk), pp. 210–235. Amsterdam: north-Holland.

Gao, Y.B. 2006. From Meterological data to the predication of embankment stability. *Technical report,* CERMES-ENPC, Paris, France.

Johansen, O. 1975. Thermal conductivity of soils. *Ph.D. thesis,* Trondheim, Norway. (CRREL Draft Translation 637, 1977). ADA 044002.

Juarez-Badillo, E. (1992). Leyes naturals en geomecanica. Volumen Raul J. *Marsal 31*. Mexico: SMMS.

Wilson, G.W., Fredlund, D.G. and Barbour, S.L. 1994. Coupled soil-atmosphere modeling for soil evaporation. *Can. Geotech. J.* 31: 151–161.

Xu Qin and Qiu Chong-Jian 1997. A variational method for computing surface heat fluxes from ARM surface energy and radiation balance system. *J. of App. Meteorology*, 36 (1):3–11.

Advances in Unsaturated Soils – Caicedo et al. (eds)
© 2013 Taylor & Francis Group, London, ISBN 978-0-415-62095-6

Numerical analysis of effect of rainfall infiltration on unsaturated soil

E.F. Garcia, C.A. Riveros & J.C. Saldarriaga
University of Antioquia, Medellin, Colombia

ABSTRACT: This paper presents an application for analysis of unsaturated layered soil-structures (embankment or levee) subjected to rainfall infiltration and seepage flow. A three-phase coupled infiltration-deformation method for unsaturated soil, which is based on the fundamental concept of the theory of porous media, is used for the numerical analyses. The effects of the water permeability on the distribution of seepage flow velocities and generation of deformations were investigated for an unsaturated layered embankment. The results illustrated that the generation of deformation on the embankment surface highly depends on the water permeability of the soil. This seepage-deformation coupled method can be useful and advantageous to analyze the behavior and response of many complex engineering problems for soil-structures, which involves different geometries, boundary conditions, and non-linear variables.

1 INTRODUCTION

1.1 *Brief review*

One of the main reasons why landslides are induced is due to the seepage flow caused by the increase of water levels inside the soil structures after a rainfall event. They often occur on initially stable slopes that consist of different types of soil.

Some researchers have studied the seepage-induce slope failure problem during and after rainfall from the experimental point of view (Orense et al., 2004, Tofani et al., 2006). Although, experimental studies allow the direct measurement of the variables involved in the infiltration process, which can be related to the decrease of the shear strength of the soil and slope failure; experimental tests have the disadvantage of being costly and time consuming.

Recently, to overcome these problems, numerical solutions have been used to analyze both, saturated and unsaturated soil (Alonso et al., 2003, Ehlers et al., 2004). Numerical analyses for soil structures are inexpensive and they permit to include complicated initial and boundary conditions, multilayered soils, non-uniform rainfall intensities, complex geometries of many engineering problems, and parametric studies, whereas experimental studies are difficult to implement.

In this paper, a numerical study to show the effect of the rainfall infiltration and the seepage flow on the deformation of unsaturated slopes is carried out. To do that, two-dimensional numerical analyses are performed for a layered embankment. The case corresponds to a three layered embankment which is subjected to both, the effect of rainfall infiltration and seepage flow from the mountain side. In the simulation, a rainfall record composed of a non-uniform intensity which induces the variation of the water level inside of a river embankment is used for the analyses.

The numerical analyses are carried out using a seepage-deformation coupled method for unsaturated soil (Oka et al., 2009). The analyses presented here are based on Biot's theory (Biot 1962) extended by the theory of porous media (Bowen 1976). Common constitutive and hydraulic parameters that represent the soils are employed in the simulations. The mechanism of the seepage flow direction and strain localization on the slope surface are discussed mainly with respect to the water permeability of the soil. From the numerical results, it was observed that the deformation of the embankment significantly depends on the water permeability of the soil and it is localized on the slope surface at the river side; the larger the water permeability of the soil, the larger the velocity of the seepage flow, and the larger the deformation on the surface of the river embankment.

2 MULTIPHASE ANALYSIS METHOD

2.1 *Governing equations*

Terzaghi (1943) defined the concept of a stress tensor for water-saturated materials. In the case of unsaturated soils, however, the concept needs to be redefined in order to consider compressible materials. In the present formulation, skeleton stress σ'_{ij} is defined and then used for the stress variable in the constitutive relation for the soil skeleton.

Total stress tensor σ_{ij} is obtained as the sum of the partial stresses, namely,

$$\sum \sigma_{ij}^{\alpha} = \sigma_{ij} \tag{1}$$

$$\sigma_{ij}^{S} = \sigma'_{ij} - n^{S} u_F \delta_{ij} \tag{2}$$

$$\sigma_{ij}^{W} = -n^{w} u_W \delta_{ij} \tag{3}$$

$$\sigma_{ij}^{G} = -n^{G} u_G \delta_{ij} \tag{4}$$

where u_W and u_G are the pore water pressure and the pore air pressure, respectively, n is the porosity, n^{α} is the volume fraction of phase α ($\alpha = S$: Solid, W: Water, G: Air), and u_F is the average pore pressure calculated according to saturation s as follows:

$$u_F = s u_W + (1-s) u_G \tag{5}$$

From Equations (1) to (5) we have,

$$\sigma'_{ij} = \sigma_{ij} + u_F \delta_{ij} \tag{6}$$

The skeleton stress is used as the basic stress variable in the model for unsaturated soils.

The conservation of mass is given by the following equation:

$$\frac{D}{Dt}\left(n^{\alpha}\rho_{\alpha}\right) + n^{\alpha}\rho_{\alpha} v_{i,i}^{\alpha} = 0 \tag{7}$$

in which D/Dt denotes the material time derivative, ρ_{α} is the material density and v_i^{α} is the velocity of each phase, the conservation laws for water and air phases are expressed as functions of s and n, that is

$$s D_{ii} + \dot{s} n = -V_{i,i}^{W} \tag{8}$$

$$(1-s) D_{ii} - \dot{s} n + (1-s) n \frac{\dot{\rho}_G}{\rho_G} = -V_{i,i}^{G} \tag{9}$$

where D_{ii} is the volumetric stretching and V_i^{α} is the apparent velocity of phase α. The rate type of equilibrium equation is expressed as follows:

$$\int_V \dot{S}_{ji,j} dV = 0 \tag{10}$$

in which S_{ij} is the deviatoric stress tensor. The above incremental equilibrium equation is used for the Updated Lagrangian formulation of the boundary value problem.

The relation between saturation and suction is given by the equation proposed by van Genuchten (1980).

$$s = s_{\min} + (s_{\max} - s_{\min})\left[1 + \left(\alpha P^{C}\right)^{n'}\right]^{-m} \tag{11}$$

in which α, n' and m are fitting parameters that describe the shape of the soil water characteristic curve, and the relation $m = 1 - 1/n'$ is assumed, s_{max} and s_{min} are the maximum and the minimum limiting values of saturation, respectively.

The effects of the degree of saturation on permeability for water and air are assumed as:

$$k^{W} = k_s^{W} s^{a}\left[1 - \left(1 - s^{1/m}\right)^{n'}\right] \tag{12}$$

$$k^{G} = k_s^{G} (1-s)^{b}\left[1 - \left(1 - s^{1/m}\right)^{n'}\right] \tag{13}$$

where a and b are material parameters, k_s^{W} is the coefficient of permeability for water under saturated conditions and k_s^{G} is the coefficient of permeability for air under fully dry conditions.

An elasto-viscoplastic model based on the over-stress-type of viscoplastic theory with soil structure degradation for saturated soil has been extended to unsaturated soil using the skeleton stress and the suction effect in the constitutive model (Oka et al., 2006). In this model it is assumed that there is an overconsolidation boundary that delineates the normally consolidated (NC) region, $fb \geq 0$, and the overconsolidated region (OC), $fb < 0$, it is described as follows:

$$f_b = \overline{\eta}_{(0)}^{*} M_m^{*} \ln\left(\sigma'_m / \sigma'_{mb}\right) = 0 \tag{14}$$

$$\overline{\eta}_{(0)}^{*} = \sqrt{\left(\eta_{ij}^{*} + \eta_{ij(0)}^{*}\right)\left(\eta_{ij}^{*} + \eta_{ij(0)}^{*}\right)} \tag{15}$$

where, σ'_m is the mean skeleton stress, M_m^{*} is the value of η^{*} when the volumetric strain increment changes from contraction to dilation. σ'_{mb} is the strain-hardening–softening parameter that controls the size of the boundary surface. The suction effect on the unsaturated soil is incorporated as:

$$\sigma'_{mb} = \sigma'_{ma} \exp\left(\frac{1+e_0}{\lambda - \kappa} \varepsilon_{kk}^{vp}\right)\left[1 + S_I \exp\left(-S_d\left(\frac{P_i^{C}}{P^{C}} - 1\right)\right)\right] \tag{16}$$

where ε_{kk}^{vp} is the viscoplastic volumetric strain, λ and κ are the compression and the swelling indexes, respectively, and e_0 is the initial void ratio. P_i^{C} is the initial suction value, P^{C} is the present suction value, S_I is the material parameter that denotes the strength increment when suction is P_i^{C}. S_d is the parameter which controls the rate of increasing or decreasing strength. σ'_{ma} is a strain-softening

parameter used to describe the degradation of the material caused by structural changes.

The static yield function is given by:

$$f_y = \overline{\eta}^*_{(0)} + M^*_m \ln\left(\sigma'_m / \sigma'^{(S)}_{my}\right) = 0 \quad (17)$$

More details about the seepage-deformation coupled FE formulation can be found in Garcia et al. (2010).

3 NUMERICAL ANALYSES

3.1 *Methodology*

The numerical analyses have been carried out using the seepage-deformation coupled formulation presented in the previous section. Visual FORTRAN was used a compiler to run the simulations. Geometry, boundary conditions that represent the soil structure; and constitutive and hydraulic parameters that represent the main soil of a layered embankment are described in the following section and used in the simulations. Finally, the mechanisms of the soil deformation and strain localization at the river side of the embankment are discussed mainly with respect to the saturated water permeability of the soil.

3.2 *Layered embankment*

The cross section and the boundary conditions for the numerical analysis of rainfall infiltration and seepage flow through an unsaturated river embankment are shown in Figure 1. The top surface of the river embankment has and inclination of 1°. The slopes of the embankment have gradients of 1V:1H at the upper part and 1V:3H at the middle of the embankment, respectively. For displacement, the embankment is fixed at the bottom in both horizontal and vertical directions; the lateral boundaries are fixed only in horizontal direction. The initial negative pore water pressure distribution (suction) in the top sandy-soil is considered to be linear. The initial water level in the soil is assumed to be located at 21.2 m at the river side and at 24.3 m at the mountain side and its

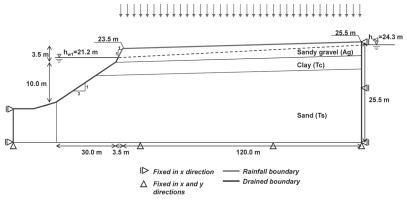

Figure 1. Cross section of the embankment used for the analysis.

inclination is about 1.5°. The flux of air is allowed for the entire boundaries and the initial air pressure, is assumed to be zero.

The embankment is composed of three materials, but only the upper layer (sandy gravel) is unsaturated and subjected to the changes in suction due to the rainfall infiltration. The sandy gravel layer is about 3.0 m in height and it overlies on a clay layer; the bottom of the embankment corresponds to a thick sandy layer. The material parameters that compose the upper layer of the embankment are listed in Table 1. The soil parameters for the clay and sand layers are irrelevant because these layers are below the water table, i.e. saturated soil.

In order to study the effect of the rainfall infiltration and seepage flow into the unsaturated layered embankment, a rainfall record of 170 hours is used for the numerical analysis. Figure 2 shows the intensity distribution of the rainfall. The maximum hourly rainfall corresponds to 14 mm and total precipitation is 106 mm. This rainfall pattern is applied through the numerical analysis on top and slope of the layered embankment, which reduces the suction levels inside the soil-structure. The initial degree of saturation for the sandy gravel is set to be 60%.

3.3 *Analyzed cases*

To investigate the effect of the water permeability on the development of deformation in an unsaturated layered embankment, when it is subjected to

Table 1. Material parameters for the soil.

Material parameter		Sandy gravel
Viscoplastic parameter	m'	40.0
Viscoplastic parameter (1/s)	C_1	1.0×10^{-15}
Viscoplastic parameter (1/s)	C_2	2.0×10^{-15}
State ratio at critical state	Mm	1.27
Compression index	λ	0.0804
Swelling index	κ	0.0090
Elastic shear modulus (kPa)	G_0	3000
Initial void ratio	e_0	0.344
Structural parameter	β	5.0
Structural parameter	$\sigma'_{maf}/\sigma'_{mai}$	0.60
Vertical water permeability (m/s)	k^W_{sv}	****
Gas permeability (m/s)	k^G_s	1.0×10^{-13}
Van Genuchten parameter (1/kPa)	α	0.10
Van Genuchten parameter	n'	4.0
Suction parameter	S_I	0.20
Suction parameter	S_d	0.20
Maximum saturation	s_{max}	0.97

**** The permeability depends on the case.

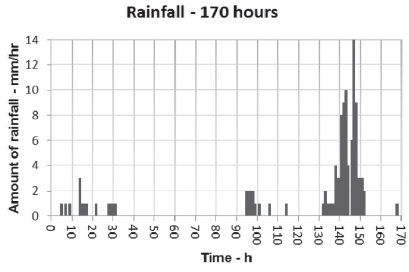

Figure 2. Rainfall record used for the numerical analysis.

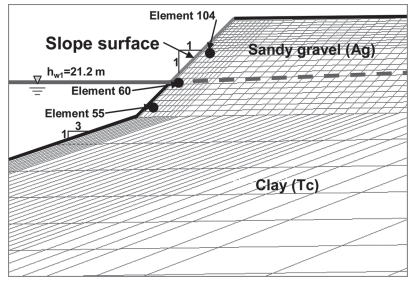

Figure 3. Finite element mesh at the slope of the embankment.

rainfall infiltration, different cases are analyzed. The analysis cases consist of different combinations of water permeabilities for the upper sandy-gravel layer and the slope surface. The cases are divided as: Cases 1–4; the saturated permeability for the sandy-gravel layer is increased, i.e. $k^W_{sv} = 1.0 \times 10^{-6}$, 3.0×10^{-6}, 6.0×10^{-6}, and 1.0×10^{-5} m/s, respectively, while the permeability of the slope surface is considered the same, i.e. $k^W_{sv} = 1.0 \times 10^{-7}$ m/s.

3.4 *Numerical results*

Cases 1–4 have been analyzed assuming that the slope surface of the layered embankment has smaller permeability than the layered soils. This difference among the permeabilities may be attributed either to a better compaction during the construction process of the slope or to a covering of the slope surface (e.g., concrete, vegetation, improved material, etc.). A detail of the mesh close to the slope of the embankment at the river side is shown in Figure 3. The mesh is finer close to the surface where larger gradients and deformations due to the rainfall infiltration are expected.

The magnitudes of water velocity vectors for cases 1–4, after 151 hours rainfall, are shown in Figures 4–7. These figures show that the velocity of the water flow increases when the permeability increases and it is more intense at the bottom of the slope surface. It is observed that the water flow tends to be more horizontal when water permeabilities become larger.

Similarly, Figures 8–11 present the distribution of the accumulated viscoplastic shear strain for the same cases at the time $t = 151$ h. These figures show that the accumulation of viscoplastic shear strain is localized along the slope surface and it grows when the water permeability increases. In Case 4 a large amount of accumulated viscoplastic strain (up to 49%) is generated.

Figure 12 shows the comparison of the accumulated shear strain-time histories for elements 55, 60 and 104 between times $t = 140$ and $t = 168$ hours. The location of the elements in the finite element

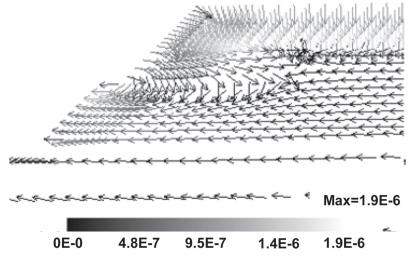

Figure 4. Water flow vectors for Case 1: $k^W_{sv} = 1.0 \times 10^{-6}$ m/s.

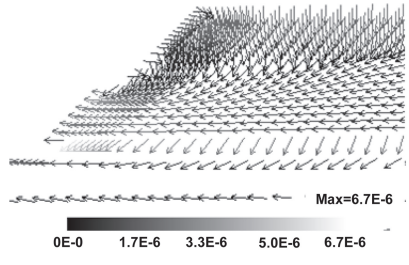

Figure 5. Water flow vectors for Case 2: $k^W_{sv} = 3.0 \times 10^{-6}$ m/s.

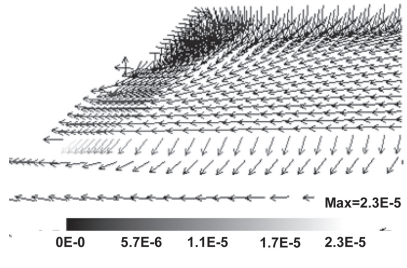

Figure 6. Water flow vectors for Case 3: $k^W_{sv} = 6.0 \times 10^{-6}$ m/s.

mesh is shown in Figure 3, which corresponds to the bottom, middle, and middle-top of the slope at the back of the concrete face, respectively. It can be seen from this figure that the viscoplastic shear strain starts to accumulate in the elements 60 and

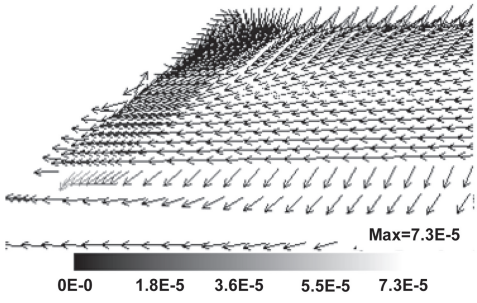

Figure 7. Water flow vectors for Case 4: $k^{W}_{sv} = 1.0 \times 10^{-5}$ m/s.

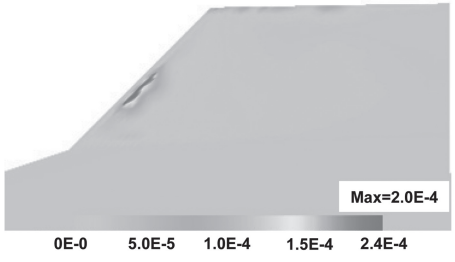

Figure 8. Accumulation of viscoplastic shear strain for Case 1: $k^{W}_{sv} = 1.0 \times 10^{-6}$ m/s.

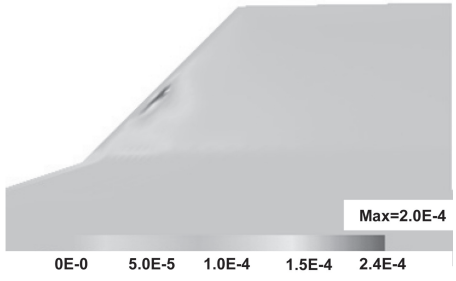

Figure 9. Accumulation of viscoplastic shear strain for Case 2: $k^{W}_{sv} = 3.0 \times 10^{-6}$ m/s.

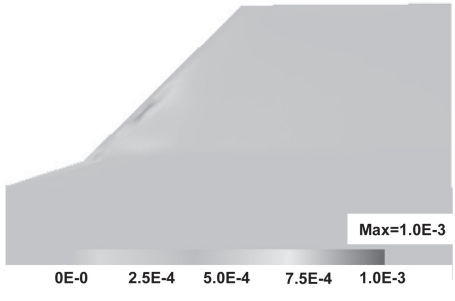

Figure 10. Accumulation of viscoplastic shear strain for Case 3: $k^{W}_{sv} = 6.0 \times 10^{-6}$ m/s.

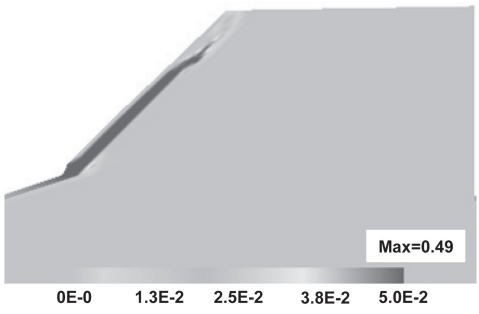

Figure 11. Accumulation of viscoplastic shear strain for Case 4: $k^{W}_{sv} = 1.0 \times 10^{-5}$ m/s.

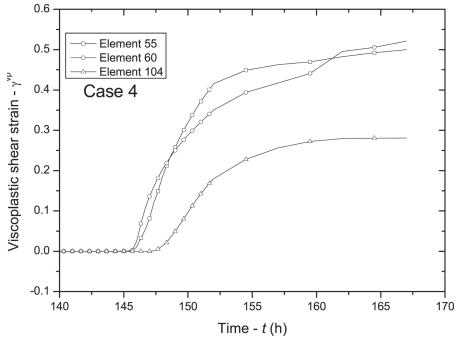

Figure 12. Time history of viscoplastic shear strain for elements 55, 69 and 104 (Case 4).

55 at time t = 145 h. Later at time t = 147 h, it is possible to see that the viscoplastic shear strain appears at the middle-top of the embankment (Element 104). This sequence in the development of the viscoplastic strain shows that the localization of deformation stared at the middle-high of the slope and rapidly propagates toward the crest of the slope.

3.5 *Discussion of the results*

Comparison of the previous figures shows that the larger the water permeability of the sandy-gravel layer, the larger the velocity of the seepage flow, and the larger the accumulation of deformation localized on the middle of the layered embankment. Orense et al. (2004) performed an experimental study on rainfall infiltration and seepage flow on small-scale unsaturated model slopes and reported a similar result that when the water table approaches to the slope surface, a highly unstable zone developed in that area and slope failure may be induced.

In the case of the simulations, the water accumulated inside the embankment resulted in the

increase of deformation of the soil on the slope surface (erosion). This accumulation of deformation is induced not only by the rainfall infiltration but also by the generation of pore water pressure and seepage flow when the water table increases near the slope surface. It could be explained by the accumulation of the water inside the embankment owing to the impediment of the water to flow out because of the lower permeability of the slope surface; as a result, larger pore water pressures and flow velocities emerge at the back of the slope that may induce erosion at the surface. It suggests that some geotechnical solutions to avoid the rainfall infiltration into the slopes, such as concrete faces, cement-soil mixtures, surface compaction, etc., can be harmful for the local stability of the embankments if they are not accompanied by additional measures to reduce the water levels generated by the seepage flow from the mountain sides during the rainfall infiltration. It supports the importance of the subsurface drainage of the soil structures in the improvement of their local and general stability.

4 CONCLUSIONS

Seepage-deformation coupled methods can be useful and advantageous to analyze the behavior and response of many complex engineering problems for soil-structures, which involve complex geometries, different boundary conditions, and non-lineal variables. This method is useful to analyze the hydraulic and deformation behavior, simultaneously.

In this paper, two-dimensional numerical simulations of a layered embankment subjected to rainfall infiltration and seepage flow were carried out. The distribution of the water velocity vectors and the pattern of deformations were investigated. In the analyses, the mechanism of the surface deformation and the strain localization on the layered embankment surface were discussed mainly with respect to the saturated water permeability of the soil. From the numerical results, it was found that the deformation of the embankment significantly depends on the water permeability of the soil and it was localized on the slope surface at the river side; the larger the water permeability of the soil, the larger the velocity of the seepage flow, and the larger the deformation on the surface of the layered embankment.

The localized deformation of the slope surface was induced by the accumulation of the water behind the slope surface owing to the impediment of the water to flow toward the river.

ACKNOWLEDGEMENTS

The work presented in this paper is part of the research project "Análisis Numérico del Proceso de Infiltración de Agua en Suelos Parcialmente Saturados" sponsored by University of Antioquia—CODI. The first author of this paper would like to thank Prof. Fusao Oka of Kyoto University for his constant support and advice during the development of this research.

REFERENCES

Alonso, E.E., Gens, A. & Delahaye, C.H. 2003. Influence of rainfall on the deformation and stability of a slope in overconsolidated clays: a case study. *Hydrogeology Journal* 11: 174–192.

Biot, M.A. 1962. Mechanics of deformation and acoustic propagation in porous media. *Journal of Applied Physics* 33(4): 1482–1498.

Bowen, R.M. 1976. "Theory of Mixtures". In A.C. Eringen (ed), C*ontinuum Physics*: 1–127. New York: Academic Press.

Ehlers, W., Graf, T. & Amman, M. 2004. Deformation and localization analysis of partially saturated soil. *Computer Methods in Applied Mechanics and Engineering* 193: 2885–2910.

Garcia, E.F., Oka, F. & Kimoto, S. 2010. Instability analysis and simulation of water infiltration into an unsaturated elasto-viscoplastic material. *International Journal of Solids and Structures* 47(25–26): 3519–3536.

Oka, F., Kimoto, S., Takada, N. & Higo, Y. 2009. A multiphase elasto-viscoplastic analysis of an unsaturated river embankment associated with seepage flow. In Oka, F., Murakami, A. & Kimoto, S. (eds.), *Prediction and Simulation Methods for Geohazard Mitigation*; *Proc. intern. symp., Kyoto, Japan, 127–132*.

Oka, F., Kodaka, T., Kimoto, S., Kim, Y.S. & Yamasaki, N. 2006. An elasto-viscoplastic model and multiphase coupled FE analysis for unsaturated soil. In Miller, G.A., Zapata, C.E., Houston, S.L. & Fredlund, D.G. (eds.), *Fourth international conference on unsaturated soil*; *Proc. intern. symp., Carefree, Arizona, 2–6 April 2006*. Geotechnical Special Publication: ASCE.

Orense, R.P., Shimona, S., Maeda, K. & Towhata, I. 2004. Instrumented model slope failure due to water seepage. *Journal of Natural Disaster Science* 26(1): 15–26.

Terzaghi, K. 1943. *Theoretical Soil Mechanics*. New Jersey: John Wiley & Sons.

Tofani, V., Dapporto, S., Vannocci, P. & Casagli, N. 2006. Infiltration, seepage and slope stability mechanisms during 20–21 november 2000 rainstorm in Tuscany, Central Italy. *Natural Hazards and Earth System Sciences* 6: 1025–1033.

Van Genuchten, M. 1980. A closed-form equation for predicting the hydraulic conductivity of unsaturated soil. *Soil Science Society of America Journal* 44: 892–899.

Advances in Unsaturated Soils – Caicedo et al. (eds)
© 2013 Taylor & Francis Group, London, ISBN 978-0-415-62095-6

The impact of moisture diffusion on the structural degradation of asphalt mixtures

S. Caro
Universidad de Los Andes, Bogotá, Colombia

ABSTRACT: Moisture damage in asphalt mixtures is defined as the progressive loss of structural integrity caused by the presence of moisture in the microstructure of the material. This degradation process includes the simultaneous development of adhesive damage at the interfaces between aggregates and asphalt binder, and cohesive damage within the asphalt binder. This paper presents a summary of the mechanisms explaining the phenomenon of moisture damage, as well as a numerical model that was developed to study the impact of the internal void structure of the mixtures on the structural degradation caused by moisture diffusion processes. The results of this study showed that the numerical model is able to account for adhesive and cohesive degradation caused by the presence of moisture and that the void structure of the mixtures plays a main role in determining the extent of moisture degradation.

1 INTRODUCTION

Hot mix asphalt (HMA) constitutes the most commonly used material in the construction of road infrastructure. This composite results from the combination of asphalt binder—an organic residue product of the distillation of crude oil—and mineral aggregates, at temperatures typically ranging from 140 to 160ºC (Roberts et al., 1996). The proportion of the asphalt binder in the mixture is determined during the mix design process (e.g., by using Marshall, Superpave, Hveem or other design methodologies), and it usually varies among 4.5 to 6.5% by total weight. Once the mixture is fabricated, it is transported to the area of the project, extended and compacted. Generally, asphalt courses are compacted to reach an overall 4 to 7% of air void content by the total volume of the mixture.

Field compacted mixtures are subjected to the passing traffic on the surface of the pavement and to the existing climate conditions in the area of the project. Fatigue cracking, permanent deformations and low temperature cracking or thermal cracking are the three main phenomena used as control during the mechanistic design of flexible pavements (Huang 2003). Field observations, however, have shown that there exist other mechanisms that could strongly contribute to the premature deterioration of asphalt pavements. Among these, moisture damage in asphalt mixtures has been recognized as one of the most important phenomena in promoting premature degradation of pavement structures (Hicks 1991).

Moisture damage can be defined as the progressive loss of the structural integrity of the material due the presence of water, in liquid or vapor state. There are two different processes responsible for this structural degradation: 1) adhesive deterioration at the interfaces between aggregates and asphalt binder, and 2) cohesive deterioration of the fine aggregate matrix, FAM (i.e., combination of asphalt binder with the finest portion of the aggregates). The difficulty in understanding and characterizing moisture damage is that it is a complex phenomenon that includes mechanical, physical, and chemical mechanisms that act simultaneously but at different rates and intensities.

As a main degradation factor, most transportation agencies have shown interest in controlling and/or mitigating moisture damage for the last 20 years. However, it has been only in the last decade that the fundamentals of this phenomenon have been explored through several research efforts. Many of these efforts include the application of concepts and experimental and modeling techniques that had been already used for several decades to study the properties and response of unsaturated soils. Caro et al. (2008a, b) present a detailed explanation of the advancements provided in the literature on this topic.

This paper focuses on the impact of moisture diffusion on the mechanical degradation of asphalt mixtures. The first part of the paper explains the mechanisms of moisture damage and the factors affecting the moisture sensitivity of asphalt mixtures. This is followed by an overview of the role of the internal void structure of the mixtures in

the development of moisture damage. Then, a micromechanical model of moisture damage due to moisture diffusion is described and, finally, the main conclusions of the study are presented.

2 TRANSPORT MODES AND FACTORS AFFECTING MOISTURE DAMAGE

The initiation of moisture damage in an asphalt mixture requires the presence of moisture in its internal structure. There exist three different modes by which moisture can reach this internal structure: 1) infiltration of water, 2) moisture diffusion, and 3) capillary rise.

Infiltration of water through the void structure is considered the main transport mode used by moisture to penetrate the microstructure of the mixture. It is speculated that the flow of water within the microstructure can generate erosion of the fine portion or matrix of the mixture. Besides, under saturated conditions, it is also speculated that pore pressure caused by the mechanical loading induced by traffic can generate micro-cracks and other mechanical degradation processes in the mixture (Kringos et al., 2008).

Moisture diffusion also plays an important role in promoting moisture damage. Its is believed that the main responsible for adhesive deterioration is the water vapor that is able to pass trough the FAM and reach the interface between the aggregates and the matrix of the mixture. Once vapor water reaches these interfaces, a separation or detachment of the existing asphalt film will occur due to preference of aggregates to be covered by water instead of asphalt binder (i.e., adhesive failure).

Finally, the existence of capillary rise in asphalt mixtures was recently demonstrated (Masad et al., 2007), but this transport mode is considered less critical as compared to the other two.

On the other hand, there are several factors determining the extent of moisture damage in a compacted asphalt mixture. Some of those factors are exclusively related to the characteristics and properties of the material itself or internal factors, while others are related to the environmental and mechanical loading characteristics of the area where the pavement is located or external factors (Arambula 2007).

Internal factors include specific properties of the aggregates (e.g., mineralogy composition, porosity, morphological properties, cleanliness, etc.), properties of the asphalt binder (chemical composition, aging susceptibility, viscosity, etc.), and some properties of the mixture (e.g., percent of asphalt binder, percent of air voids, air voids size and distribution, typical film thickness of the asphalt binder coating the aggregates, etc.). External factors depend exclusively on the climate conditions of the zone where the mixture is located (e.g., rainfall, relative humidity, etc.), as well as on other characteristics of the project (e.g., drainage quality).

Naturally, the combination of both internal and external factors will ultimately determine the actual propensity of a mixture to develop moisture damage.

3 INTERNAL VOID STRUCTURE

Voids have been recognized as the main path of air and moisture access to the microstructure of the mixtures (Brown et al., 2004). Although the relationship between the total amount of air voids and the different modes of moisture transport is well recognized, the relationship between the internal air void structure of a mixture and its moisture sensitivity is neither simple nor evident.

X-ray Computed Tomography techniques have been used in combination with image analysis procedures to provide a better understanding of the internal air void structure of asphalt mixtures (Masad et al., 2006, Masad et al., 2007). In general, these studies have shown that the internal void structure of asphalt mixtures is highly complex and that the classical use of the total air void content might be insufficient to fully characterize it since other information like the location of the voids, size distribution, and connectivity are also critical in determining the susceptibility of asphalt mixtures to moisture damage. Figure 1 illustrates the significant variability of the internal void structures in mixtures. This Figure shows the vertical distribution of air void content in a compacted asphalt course, obtained after conducting X-Ray CT analysis on field cores (Tashman et al., 2001).

There exist two common ways of including the air void phase in the numerical modeling of asphalt mixtures at the microscale level: 1) as part of the viscoelastic bulk matrix, FAM, or, 2) as an independent entity (i.e., a separate phase). In the first case, the FAM is modeled as a continuum

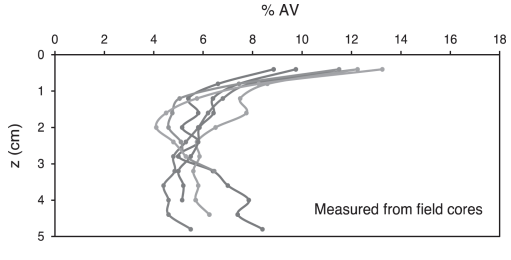

Figure 1. Air void content distribution with depth in field cores (modified after Tashman et al., 2011).

with effective material properties (Caro et al., 2010, Kringos et al., 2008). However, the main shortcoming of this approach is that the characteristics of the internal air void structure and its variability within the FAM phase are neglected. The second possibility is more desirable, since it is a better representation of an actual mixture, but its main difficulty is that it usually implies important computational costs.

4 DEGRADATION BY MOISTURE DIFFUSION

The amount of water vapor and the rate at which it accumulates in an asphalt mixture depend on three primary factors: 1) relative humidity gradient, 2) diffusion coefficients, and 3) storage rate and storage capacity. Relative humidity depends on the environmental conditions, whereas diffusion coefficients and storage capacity are material properties.

The strong impact of moisture diffusion on the structural degradation of asphalt mixtures has been verified in a recent experimental work conducted by the Geomaterials and Infrastructure Systems group at Universidad de Los Andes (Echeverria 2011). In this work, the impact of relative humidity on the fatigue resistance of regular dense mixtures was quantified. In these experiments, different specimens were subjected to a controlled relative humidity environment, and standardized strain-controlled fatigue tests were conducted after a steady state was reached within the mixture. Figure 2 presents the corresponding fatigue laws (i.e., the number of cycles to failure, N_f, caused by the application of constant strain levels, ε_t). These experimental observations corroborate that moisture diffusion plays a main role on the generation of moisture damage.

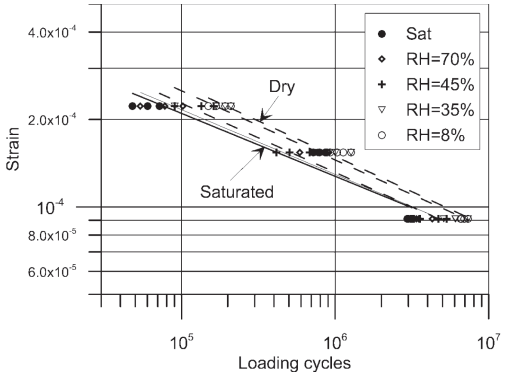

Figure 2. Impact of relative humidity on the fatigue resistance of asphalt mixtures (modified after Echeverría 2011).

5 MICROMECHANICAL MODEL OF MOISTURE DAMAGE

A proposed two-dimensional micromechanical model of moisture damage has been developed to study the impact of moisture diffusion in the structural degradation of asphalt mixtures. The mixture was modeled in the commercial finite element package Abaqus® after assuming that the material is composed by three different phases: 1) coarse aggregates, 2) voids, and 3) a FAM or fine aggregate matrix. It is interesting to note that this model considers air voids as an independent phase, a characteristic that—as mentioned in the previous section—is usually overlooked when modeling asphalt mixtures.

5.1 *Adhesive degradation*

The model simulates the impact of the presence of diffused moisture within the microstructure by affecting the mechanical cohesive properties of the FAM, and the adhesive properties of the FAM-aggregate interfaces. However, the model gives especial attention to the adhesive deterioration by including interfaces between the aggregates and the FAM using the Cohesive Zone Modeling (CZM) approach.

This modeling technique permits to simulate the initiation and propagation of cracks through the adhesive areas of the mixture. Details of the characteristics of the CZM technique herein used can be found elsewhere (Ortiz & Pandolfi 1999). As a summary, this approach uses rectangular elements that are able to carry on traction up to the point where certain distance or separation between its faces is reached. At this point, a softening process occurs leading to a progressive degradation of the traction capability of the material. When the element completely losses its structural capacity, it physically disappears from the model in what is interpreted as the initiation of a crack. Then, there are three parameters determining the mechanical response of these elements: 1) the initial stiffness of the element, 2) the distance or separation between the faces of the element where damage initiates, and 3) the total energy required to fully degrade the traction capacity of the material or critical energy release rate.

Both adhesive and cohesive degradation are simulated by making the viscoelastic material properties of the FAM and the mechanical properties of the adhesive bonds (i.e., adhesive bond strength and fracture energy) dependent on the amount of moisture that is diffused within the mixture.

5.2 *Modeling approach*

The micromechanical model was developed using a sequentially coupled moisture diffusion-mechanical response scheme.

Moisture diffusion within the microstructure of the asphalt mixture was assumed to follow Fick's second law and it was modeled using an implicit scheme, where the aggregates and the FAM are modeled using 3-nodes first order mass diffusion elements (type DC2D4 in Abaqus®), and the interfaces are modeled using 4-nodes linear mass diffusion elements (type DC2D3).

The mechanical simulation was solved using an implicit scheme in which the asphalt matrix is modeled as a linear viscoelastic material and the aggregates are modeled as linear elastic materials. Aggregates and FAM were discretized using first order triangular elements (elements type CPE3 in Abaqus®) while the interfaces were modeled using adhesive zones using "zero-thickness" adhesive elements (elements type COH2D4 in Abaqus®).

5.3 *Geometry*

Figure 3 presents the geometry of the 50 mm by 50 mm representative volume element of an asphalt mixture used for the simulations. This figure also presents a detail of the finite element implementation of the microstructure.

Although not visible in this figure, the model also includes the above-mentioned interfaces between every aggregate and the FAM. In this general model, however, the air void phase is missed. Unfortunately, the actual internal void structure within a mixture is difficult to determine since it strongly depends on the compaction process used during the construction of the pavement. Thus, it was decided to produce several probable sets of air voids distributions within the mixture. In order to do so, an air void size distribution obtained by Masad et al. (2006) after analyzing the images captured from a 10 cm diameter cylindrical specimen by means of X-ray CT was used to generate sets of circular air voids within the asphalt mixture.

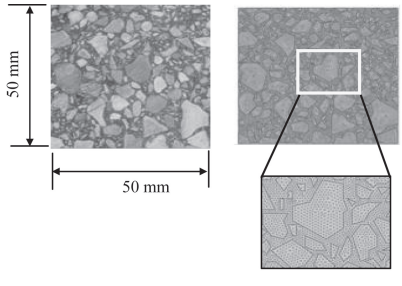

Figure 3. Geometry of the two-dimensional asphalt mixture.

In order to study the impact of the total amount of air voids in a mixture on the moisture degradation of the microstructure, three different values of total air void content were considered: 4%, 7% and 10%. For each case, ten different sets of circular air voids following the above-mentioned air void size distribution were produced. Once a set of voids was produced, it was randomly located within the mixture, as shown in Figure 4. This figure shows two cases of randomly produced air voids structures at 4 and 10%, and the final geometry of one of the modeled mixtures. In summary, thirty different geometries were considered at the three main levels of air void contents.

5.4 *Material properties*

In terms of moisture diffusion coefficients, the values for each phase were as follows (Arambula et al., 2010): aggregates: $1.28*10^{-3}$ mm^2/s, FAM (with no voids): $1.27*10^{-5}$ mm^2/s, air voids: 26 mm^2/s.

In terms of the mechanical properties, the linear viscoelastic material properties of the FAM correspond to the Prony Series reported by Kim et al. (2005), while the aggregates were assumed to be linear elastic with an elastic modulus of $5.0*10^{10}$ Pa, and Poisson's ratio of 0.3. The air voids were assumed to have zero structural resistance. Finally, the adhesive elements at each interface were characterized by the following parameters: 1) before the initiation of damage, the response of the elements is linear elastic with a modulus equivalent to that of the FAM phase, 2) the damage initiation criterion was assumed to be the same in the normal and shear modes and equal to 0.1 mm, and 3) the critical energy release rates of the material in normal and shear mode were estimated as 15% of the area within the elastic part of the traction-separation law.

The influence of moisture on the mechanical response of the FAM was accounted for by linearly reducing the relaxation modulus of this material as the moisture content increased. Thus, the relaxation modulus of the FAM at any time, t, was set to decrease linearly from its original value, in dry conditions, to 90% of that value, when fully saturated

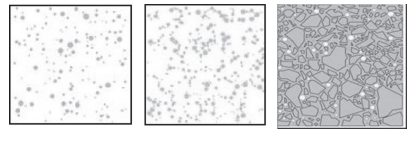

Figure 4. Randomly generated air void structures and a complete mixture model with the corresponding air void phase.

conditions. The Poisson's ratio of the FAM was assumed to be time and moisture independent. In terms of the impact of moisture on the mechanical properties of the adhesive zones it was modeled by reducing both the adhesive strength and the fracture toughness of the element as a function of the moisture content (0% reduction if there is no moisture to 80% reduction if the element is saturated).

5.5 *Modeling methodology*

The asphalt mixtures were initially subjected to a controlled loading simulation in the dry condition. The simulation consisted of loading and unloading the microstructure for a total of 30 s at a monotonic rate of 0.16 N/s. Simultaneously, identical undamaged specimens or microstructures were subjected to a ten-day moisture diffusion period after applying a saturated moisture boundary condition to the external edge of the model. Finally, the moisture-conditioned samples were subjected to the same mechanical scheme described in the initial step. This simulation can be understood as an experimental setup in which different replicates of asphalt mixtures with different air void content levels were subjected to mechanical loading under two different conditions: 1) in a *dry* state, and 2) after a ten-day moisture-conditioning process or *wet* state.

In all cases, the total dissipated energy (DE) by the mixture during the mechanical experiment (i.e., area under the overall force-displacement curve) was selected as the mechanical performance indicator of the material.

5.6 *Results and analysis*

Figure 5 presents the moisture profile of one mixture after the diffusion conditioning process, and Figure 6 presents the force-displacement curves obtained for this model in the case were moisture was not present (dry case) and in the case were the mixture was subjected to moisture diffusion (wet case).

Figure 7 presents a compilation of the results obtained for the 30 simulations conducted in dry conditions and the 30 simulations conducted after moisture conditioning, for the three total air void contents.

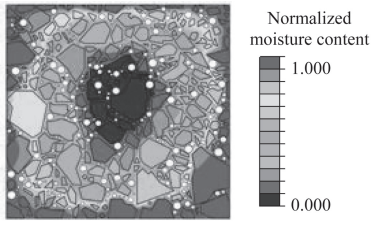

Figure 5. Moisture diffusion profile for a mixture after ten days of moisture diffusion.

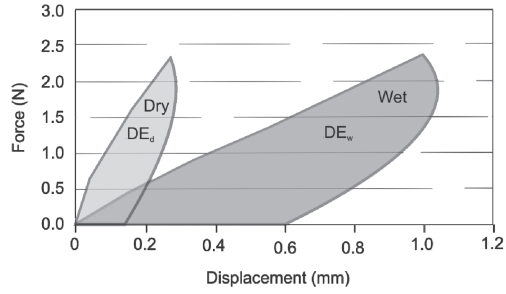

Figure 6. Force-displacement curves obtained when the load was applied in dry and wet conditions.

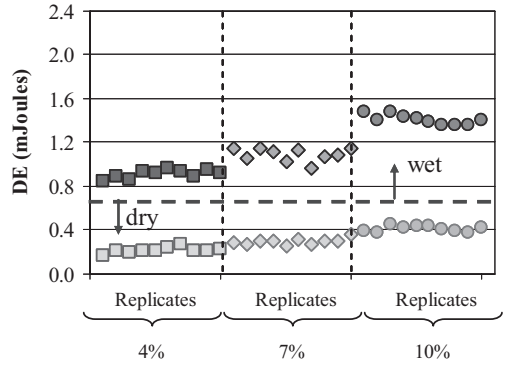

Figure 7. Summary of dissipated energy (DE) results for different percent of air voids.

Two main observations can be extracted from this figure:

- An increase in the percent of air voids in the mixture produces a reduction in the structural integrity of the mixtures (i.e., a reduction in the bulk specific gravity of the mixture), and an increase in the amount of moisture that reaches the interior of the microstructure after the moisture-conditioning period. These two effects increase the total energy dissipated by the moisture-conditioned mixtures (i.e., the dissipated energy is always larger in the wet cases).
- A reduction in the structural resistance of the mixtures caused by an increase of air voids (in the absence of moisture) was a major contributor to the overall loss of structural capacity of the microstructures. However, the data show that the marginal increase of the mechanical degradation per unit of air void content that is exclusively due to the presence of moisture grows faster than in the dry microstructures.

These observations can be explained if considered that an increase in the total air voids of a mixture naturally weakens the mechanical resistance of the composite (i.e., there is less mass to resist force), and that the presence of more voids facilitates the diffusion of more moisture to the inner part of the microstructure. This, in combination with the coupling capacity of the model, produces an increase in the overall cohesive and adhesive damage.

6 SUMMARY AND CONCLUSIONS

Moisture damage in asphalt mixtures is a phenomenon that strongly affects the durability of flexible pavements. The study of this degradation process requires the identification of the internal characteristics of the mixture and the external conditions of the environment that can make a mixture more prone to develop moisture damage.

This paper explains the main mechanisms associated with the development of moisture damage, including moisture transport modes and the role of the internal void structure in the development of moisture degradation.

The paper also presents a micromechanical model that was developed to study the impact of moisture diffusion on the mechanical response of asphalt mixtures that are characterized by different internal air void structures. The model has two main characteristics that make it different from other efforts conducted on this direction: 1) it randomly includes the internal void structure of the mixture as an independent phase of the mixture, and 2) it is able to simulate cohesive degradation (i.e., degradation of the viscoelastic properties of the fine matrix of the mixture) and adhesive failure (i.e., propagation of cracks at the interface of the aggregates and the fine matrix of the mixture) that are caused by the presence of moisture. The results show that an increase in the amount of voids in an asphalt mixture promotes faster moisture diffusion processes, and, as a consequence, induces more internal damage that is mainly caused by the degradation of the adhesive strength between the aggregates and the fine aggregate matrix of the mixture.

REFERENCES

Arambula, E. 2007. Influence of fundamental material properties and air void structure on moisture damage of asphalt mixes. Ph.D. dissertation, Texas A&M University, College Station, Texas.

Arambula, E., Caro, S. & Masad, E. 2010. Experimental Method and Numerical Simulation of Water Vapor Diffusion trough Asphalt Pavement Materials. Journal of Materials in Civil Engineering (ASCE) 43(7): 897–911.

Brown, E.R., Haini, M.R., Cooley, A. & Hurley, G. 2004. Relationship of air voids, lift thickness, and permeability in hot mix asphalt pavements. Rep. No. NCHRP 531, Transportation Research Board of the National Academies, Washington, D.C.

Caro, S., Masad, E., Bhasin, A. & Little, D. 2008a. Moisture Susceptibility of Asphalt Mixtures, Part I: Mechanisms. International Journal of Pavement Engineering 9(2): 81–98.

Caro, S., Masad, E., Bhasin, A. & Little, D. 2008b. Moisture Susceptibility of Asphalt Mixtures, Part II: Characterization and Modeling. International Journal of Pavement Engineering 9(2): 99–114.

Caro, S., Masad, E., Bhasin, A. & Little, D. 2010. A Coupled Micromechanical Model of Moisture-Induced Damage in Asphalt Mixtures. Journal of Materials in Civil Engineering (ASCE) 22(4): 380–388.

Echeverria, E. 2011. Influencia del contenido de humedad sobre la resistencia a la fatiga de una mezcla asfáltica tipo MDC-2. Master Thesis, Universidad de Los Andes, Bogotá, Colombia.

Hicks, R.G. 1991. Moisture damage in asphalt concrete: Synthesis of highway practice. Rep. No. NCHRP 175, National Cooperative Highway Research Program, Washington, D.C.

Huang, Y.H. 2003. Pavements analysis and design. Second Edition. Prentice Hall, NY.

Kim, Y.R., Allen, D.H. & Little, D.N. 2005. Damage-induced modeling of asphalt mixtures through computational micromechanics and cohesive zone fracture. Journal of Materials in Civil Engineering (ASCE) 17(5): 477–484.

Kringos, N., Scarpas, A., Kasbergen, C. & Selvadurai, P. 2008. Modelling of combined physical-mechanical moisture-induced damage in asphaltic mixes, part 1: Governing processes and formulations. International Journal of Pavement Engineering 9(2): 115–118.

Masad, E., Arambula, E., Ketcham, R.A., Abbas, A.R. & Martin, A.E. 2007. Nondestructive measurements of moisture transport in asphalt mixtures. Journal of the Association of Asphalt Paving Technologists (AAPT) 76: 919–952.

Masad, E., Castelblanco, A. & Birgisson, B. 2006. Effects of air void size distribution, pore pressure, and bond energy on moisture damage. Journal of Testing and Evaluation 34(1): 1–9.

Ortiz, M. & Pandolfi, A. 1999. A class of cohesive elements for the simulation of three-dimensional crack propagation. International Journal for Numerical Methods in Engineering 44: 1267–1282.

Roberts, K., Brown, P.S., Lee D-Y., & Kennedy T.W. 1996. Hot asphalt materials, mixtures and construction. National Center for Asphalt Technology, NAPA (Research and Education Foundation). Second Edition.

Tashman, L., Masad, E., Peterson, B. & Saleh, H. 2001. Internal structure analysis of asphalt mixes to improve the simulation of Superpave gyratory compaction to field conditions. Journal of the Association of Asphalt Pavement Technologists (AAPT) 70: 605–645.

Advances in Unsaturated Soils – Caicedo et al. (eds)
© 2013 Taylor & Francis Group, London, ISBN 978-0-415-62095-6

Shafts by the Sequential Excavation Method: Mechanical vs Hydro-mechanical calculations

C.C. Dias & A.T. Gomes
Faculdade de Engenharia da Universidade do Porto, Porto, Portugal

J. Vaunat
Universitat Politècnica de Catalunya, Barcelona, Spain

ABSTRACT: This paper presents the comparison study between a coupled Hydro-Mechanical (HM) and a mechanical (M) calculation of a sequential excavation for circular shafts. The sequential excavations are normally carried out with the water table lowering which leads to an unsaturated condition in the surrounding ground, affecting its geomechanical behavior. This work introduces the numerical analysis for shafts using sequential excavations in unsaturated conditions. Initially, general guide lines of the Sequential Excavation Method (SEM) are described and the modeling for both calculations is presented. The final part of the paper analyzes the main results, from global behavior of excavation to forces in the support.

1 INTRODUCTION

The Sequential Excavation Method (SEM) has been, in the past, typically used for the excavation of tunnels. Recently it has been adapted to the excavation of shafts with remarkably success as was the case of Porto Light Rail Metro (Topa Gomes 2009). At this city the common geotechnical scenario corresponds to granite but with superficial horizons corresponding to residual soils with depths that may reach more than 20 m (Viana da Fonseca 1996).

The excavation of shafts with this technique in residual soils implies usually that the water table is lowered, creating a non-saturated condition with important consequences, both in the mechanical and hydraulic behavior of the excavation. This paper intends to discuss the most important differences resulting from a simple mechanical calculation of the excavation or, alternatively, a coupled calculation, incorporating in the numerical model the mechanical and hydraulic behavior and solving them simultaneously.

2 SEQUENTIAL EXCAVATION METHOD

2.1 *Brief description of the method*

The SEM takes full advantage of the arch effect in the ground, redistributing the initial stress state in the three spatial directions, minimizing the loads over the support as the ground contributes decisively to the final equilibrium. The shape of the excavation is the most important aspect of the method. It should be, optimally, circular or alternatively elliptical. This contributes for the mobilization of the arch effect of the ground, reducing to a minimum the thickness of the lining.

The application of the SEM in the vertical direction allows shaft excavations, using the phases shown in Figure 1 and explained below:

i. The 1st phase can involve water table (WT) variations or not and the WT lowering can happen before (as shown in Fig. 1) or while the excavation takes place. At the same time takes place the construction of the capping beam;
ii. Excavation of the 1st ring;
iii. Construction of the support of the 1st ring;
iv. to vi. Repeat phase ii and iii to the remaining rings ending with the excavation of the last ring (v) and construction of the respective support (vi).

Each ring can be excavated in phases or integrally. The shotcrete lining ensures the stability of the excavated ground. The capping beam guarantees the adequate stiffness in case of non-symmetric load, especially if they occur at surface, as is the case of equipment transporting heavy materials.

After the excavation the works proceed with the construction of the internal structures, however that works are not the aim to the present study.

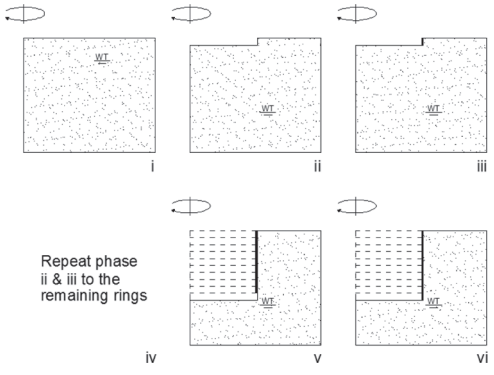

Figure 1. Main phases for the excavation sequence of a circular shaft.

Figure 2. Final excavation phase for Salgueiros Station (Topa Gomes et al., 2008).

2.2 *SEM used in metro stations excavations*

This method can be used to build large diameter shafts such as metro stations. The construction of Porto Light Rail Metro constitutes an excellent example of the application of this methodology. Several shafts were constructed, with diameters ranging from about a ten of meters to the case of Salgueiros Station, with a total length of around 80 m and a width of roughly 40 m. The excavation resulted from the intersection of two ellipses (Fig. 2) and details can be found in (Topa Gomes et al., 2008).

3 MODELING

In the present section, mechanical (M) and hydro-mechanical (HM) calculations are presented. Considering the water table lowering, the M calculation assumes it is lowered previously to the excavation and the HM calculation assumes the water table is lowered while the excavation is performed as will be shown.

3.1 *Code_Bright*

For the analysis presented in this paper, Code_Bright (vr. 4), a finite element program developed at the Department of Geotechnical Engineering and Geosciences of the Technical University of Catalonia (UPC), Spain, was adopted. It allows solving coupled thermo-hydro-mechanical problems in geological media (Vaunat & Olivella 2002). For the present paper Code_Bright has been used as a solver while GiD (vr. 10.0.3), also developed at UPC, as pre and postprocessor.

Table 1 presents the constitutive equations of the code. As the thermo condition was not part of this study, not all the equations were applied.

Considering the mechanical behavior, an elastoplastic model (Pinyol et al., 2007) was adopted to model Salgueiros soil matrix, with Mohr—Coulomb failure criterion. Regarding hydraulic model, retention curve and generalized power equations were used.

Besides the Finite Element Method, Code_Bright uses the Finite Differences Method for time analysis.

3.2 *The analyzed excavation*

Figure 3 shows the studied excavation consisting of a circular shaft, 30 m diameter and with a total depth of 20 m. To reach this depth 10 rings, each with a height of 2 m, were adopted. The only support element is a shotcrete membrane with 0.3 m thickness.

The geometry to mode the HM calculation is presented in Figure 3. In the M problem the width is 100 m and all residual soil is dry.

3.3 *Assumed geotechnical parameters*

The granite residual soil of Salgueiros is a saprolitic material, preserving the natural fabric of the original rock, with less than 10% clay, around

Table 1. Constitutive equations presents at Code_Bright, (Olivella & Vaunat 2006).

Equation	Variable name
Darcy´s law**	Liquid and gas advective flux
Fick´s law	Vapor and air non advective fluxes
Fourier´s law	Conductive heat flux
Retention curve**	Liquid phase degree of saturation
Mechanical model* **	Stress tensor
Phase density* **	Solid and liquid density
Gases law	Gas density

* Used in M calculation ** Used in HM calculation

20% silt and almost 70% sand (Topa Gomes et al., 2008).

The solid density of the particles was considered 2.65, with an average porosity of 0.35. These values represent a dry unit weight of 16.9 kN/m^3 and a saturated unit weight of 20.3 kN/m^3. Table 2 presents the remaining assumed parameters to model the residual soil.

Concerning the soil water characteristic curve, Equation 1 proposed by (Van Genuchten 1980), with the parameters presented in Table 2 was adopted:

$$S_e = S_{rl} + (S_{ls} - S_{rl}) \times \left| 1 + \left(\frac{\psi}{l} \right)^{1-\lambda} \right| \quad (1)$$

where S_e is the saturation degree; S_{rl} the residual saturation; S_{ls} the maximum saturation; λ the shape function; P_0 the pressure measured at 20ºC and ψ the suction.

To consider the influence of the unsaturated condition in the permeability, a generalized power law (Eq. 2), was used:

$$k_0 = A S_s^{\lambda_0} \quad (2)$$

where k_0 is the relative permeability; A and λ_0 the adjusting parameters.

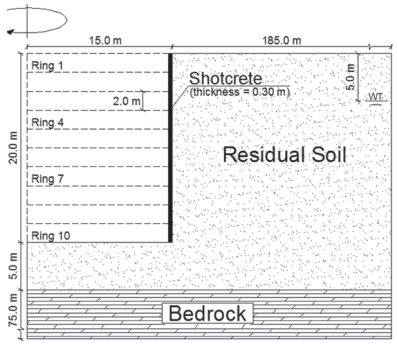

Figure 3. Geometry of the hydro-mechanical calculation.

Table 2. Residual soil of Salgueiros—hydraulic and mechanical parameters.

Mechanical parameters	Hydraulic parameters
c' = 20.0 kPa	k = 6.5 × 10^{-6} m/s
ϕ' = 35.0º	P_0 = 6.0 MPa
E = 100.0 MPa	λ = 0.25
ν = 0.375	S_{rl} = 0
Associated flow law	S_{ls} = 1
	A = 1
	λ_0 = 3

The bedrock was assumed linear elastic with a Young modulus of 1.0 GPa and a permeability coefficient of 6.5 × 10^{-10} m/s.

The shotcrete was also assumed linear elastic with Young modulus 30.0 GPa, Poisson's coefficient of 0.2, solid density of the particles 2.6 and permeability coefficient 10 × $^{-10}$ m/s.

3.4 *Finite element meshes and excavation time*

Quadrangular elements with one Gauss point were adopted for residual soil and bedrock elements, while similar elements with four Gauss points were used for shotcrete lining. The dimension of the used meshes is significantly different between a pure mechanical calculation and the hydro-mechanical calculation. In fact, while in the first the influence of the excavation reaches around two times the excavation depth, in the second this influence is much bigger due to the hydraulic conditions. Thus, in the pure M calculation a width of 100 m was considered while in the HM calculation 200 m were adopted.

Therefore the mechanical calculation presents 3368 quadrangular elements and 3454 nodal points (Fig. 4) while the mesh used to model the hydro-mechanical calculation has 3750 quadrangular elements and 3852 nodal points (in this calculation the bedrock does not exist).

Full excavation takes place in 80 days, 7 days to excavate each ring and 1 day to complete the shotcrete lining. The time for generating the initial state stress was placed as negative, 50 days for the Mechanical and 400 days for the Hydro-Mechanical calculation.

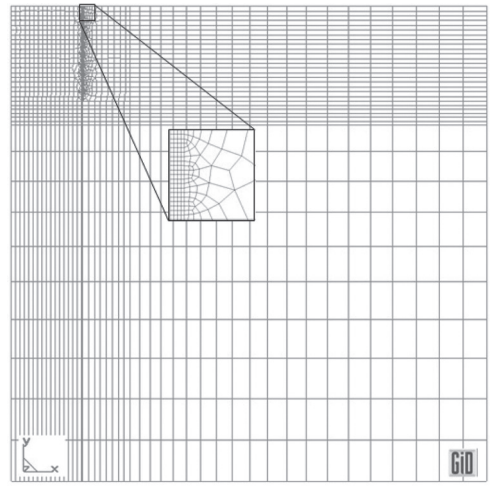

Figure 4. Mesh used to model the mechanical calculation.

4 RESULTS

In this section the results will be presented focusing in the main differences between the M and HM calculations. For this situation two distinct moments will be considered, one corresponds to the end of the excavation and another corresponding to the moment where a steady state flow is reached.

4.1 *Global behavior of the excavation*

To initiate the analysis in Figure 5 only M calculation results are shown. This figure presents the evolution of the horizontal ground displacements with increase of excavation height h.

The horizontal displacement of the shaft increases with depth, reaching a maximum horizontal displacement of 1.6 cm in the last but one ring. Beyond this continuous growth with depth, the displacement reaches relative maximums in each ring roughly at its mid-height. This phenomena result from the fact that each panel is partially supported by the shotcrete lining, above, and the ground below the excavation, this last acting like a brace.

It must also be referred that the continuous growth of the displacements with depth results from the growth of the ground stress with depth allied with the fact that the Young modulus was considered constant for all the residual soil. In conditions as the used in this calculation it is expected that the last but one ring presents always the maximum horizontal displacement.

Figure 6 presents the ground displacements for both calculations.

Considering the ground movements, these are bigger in the M calculation. This fact is mainly due to the bigger stress release in the first case as it corresponds to the total stress. In any case this result does not traduce exactly the ground behavior as the soil is partially saturated. Furthermore, for engineering purposes this procedure is conservative.

Considering the support (Fig 7), the HM calculation produces higher deformations as it has to carry the additional load corresponding to the "weight" of the water. The horizontal displacement of the support reaches a relative maximum in the bottom of each ring due to construction sequence. Considering the high stiffness of the shotcrete, it can be said that the main contribution to the support displacement is the ground movements that happen immediately before.

Another relevant aspect to mention is associated with the importance of the arch effect corresponding to the mobilization of shear stress when each ring is excavated. This phenomenon is well visible in Figure 8 and represents the vital importance of the ground strength in the overall equilibrium of this type of shafts.

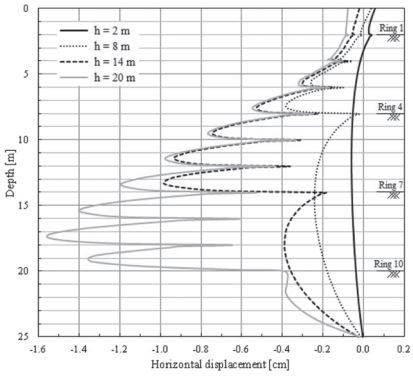

Figure 5. Horizontal displacement of the ground at the limit of excavation during certain phases. M calculation.

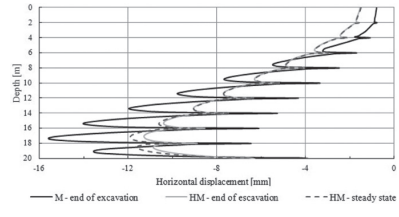

Figure 6. Horizontal displacement of ground face of excavation.

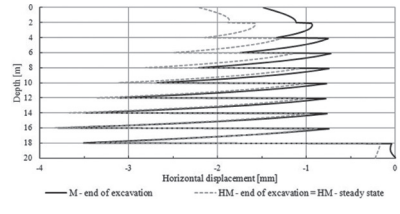

Figure 7. Horizontal displacement of support.

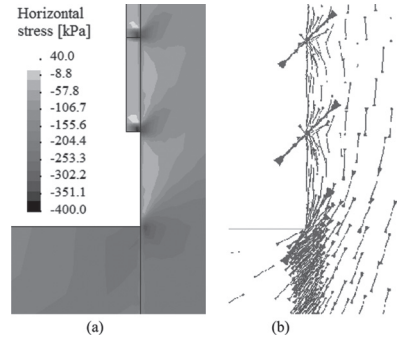

Figure 8. Arch transference in the vertical direction—excavation of the 8th ring. (a) Horizontal stress [kPa]; (b) main stress vectors. M calculation.

4.2 *Settlement at the surface*

Figure 9 shows that the values of the settlement are four times bigger for the HM calculation due to increase on the effective stress associated with the excavation and in particular the lowering of water table. For the distance corresponding to four times the height of the shaft, the settlement value of 3.5 mm is higher than the settlement at the excavation limit in the M calculation. At the face excavation the settlement is approximately four times the settlement of the M calculation.

Naturally these important differences results from the fact that the water table lowering was not simulated by any process in the M calculation. As residual soil is stiff enough to guarantee that lowering the water table produces satisfactory results, a common strategy assumes that it is possible to consider only the M calculation without the influence of water.

4.3 *Water table variation*

The water table was initially 5.0 m below the surface. With the excavation, the flow of water into the excavation lowers the water table to 13.2 m below the surface, at the end of the excavation, corresponding approximately to a suction of –130 kPa (Fig 10). An excavation in this condition is not capable to fix the water table at the bottom of the excavation unless a forced draw down is pursuit. This is a very important aspect and can represent a vital aspect to be improved in this type of works.

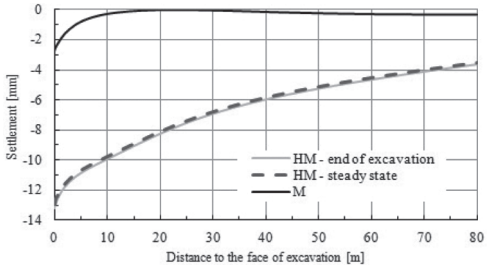

Figure 9. Settlement at the surface.

Figure 10. Pore-water pressure [kPa].

Figure 11 presents the position of the water table with the distance to the excavation face for various phases considered in the numerical calculations. The steady state is achieved in a very short period of time due to a high permeability of the ground.

Figure 12 shows that there are three areas to describe the seepage: downward behind the support, upward at the bottom of excavation and in the vicinity of the ring being excavated. The maximum seepage velocity is achieved in the steady state and is around 6.0×10^{-3} mm/s.

4.4 *Flow into the excavation*

Figure 13 shows, for the HM calculation, the flow per phase of excavation and the total volume during the construction period. As the transient state is very short, the figure represents the steady state after the 80th day. The figure shows that the maximum flow rate is reached while excavating the last

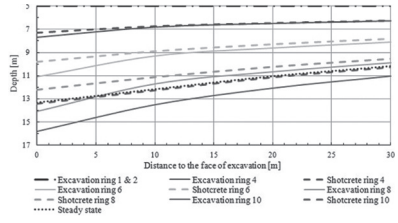

Figure 11. Depth of the water table during certain phases of the excavation.

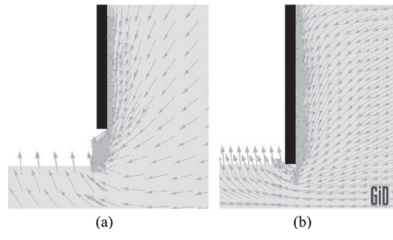

Figure 12. Velocity field of the water particles. (a) After excavate the last ring; (b) last shotcrete lining.

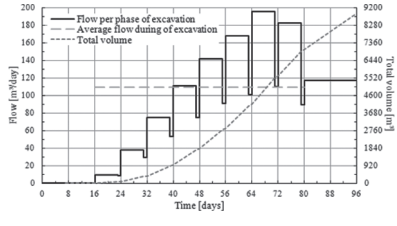

Figure 13. Flow and total volume during the excavation procedures.

but one ring, corresponding approximately to 195 m^3/day. This information should be considered as estimation but is a reference when it comes to the choice of the pumps to withdraw the water from the excavation.

Considering environmental aspects, the 7100 m^3, reached at the end of excavation, represents a huge volume of water that might affect the local aquifers, so it is from paramount importance to build the bottom slab immediately.

4.5 *Forces in the support*

Figure 14 shows the forces in the support for the 2 calculations under analysis. For the HM model two distinct moments were selected.

For the majority of the situations, regarding both the type of load and position it seems there are no important differences between the 3 different calculations. The only exceptions are the axial forces that seem to be bigger in the HM calculation. This is a direct consequence of the observed differences in the support displacements, bigger in the HM calculation as a direct consequence of the consideration of the additional load resulting from the water content corresponding to the unsaturated condition.

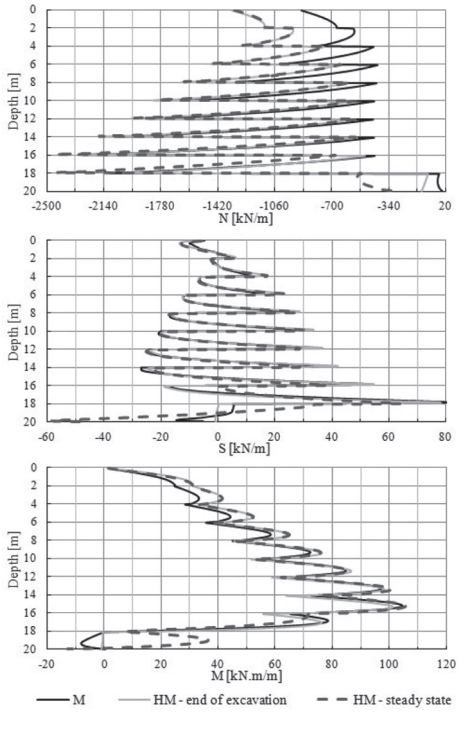

Figure 14. Forces in the support. From the top to bottom: axial force, shear force and bending moment.

5 CONCLUSIONS

The comparison between a simple mechanical calculation and a coupled hydro-mechanical calculation, taking into account the unsaturated condition of the ground above the water table, shows some important differences. First of all a pure M calculation is not able to model the settlements associated with the water table lowering which may be, in certain circumstances, of the same order of magnitude of the movements produced by the excavation of a shaft.

Also important is the fact that the coupled analysis produces differences in all the variables analyzed: soils displacement, support forces and displacements and, naturally, in the hydraulic condition obtained. These discrepancies were obtained even if the differences in stiffness resulting from the unsaturated condition were not considered.

Therefore it must be said that with the software capabilities available nowadays the study of coupled hydro-mechanical problems should be object of further and detailed studies as the results seem to enhance the importance of this type of analysis.

REFERENCES

Olivella, S. & Vaunat, J. 2006. *Application of Code_Bright—GiD to geotechnical problems.* Proc. 3rd GiD Conference, Barcelona, Spain, Vol. p. 10.

Pinyol, N., Vaunat, J. & Alonso, E.E. 2007. *A constitutive model for soft clayed rocks that includes weathering effects.* Géotechnique, Vol. 57, N. 2, pp. 137–151.

Topa Gomes, A. 2009. *Elliptical shafts by the Sequential Excavation Method. The case of Porto Metro.* PhD thesis, Civil Engineering Department, Faculty of Engineering of University of Porto.

Topa Gomes, A., Silva Cardoso, A., Almeida e Sousa, J., Andrade, J.C. & Campanhã, C.A. 2008. *Design and behavior of Salgueiros station for Porto Metro.* Proc. 6th International Conference on Case Histories in Geotechnical Engineering, Arlington, VA, 11–16 August, 2008.

Van Genuchten, M.T. 1980. A closed-form equation for predicting the hydraulic conductivity of unsaturated soils. Soil Science Soc. American Journal. Vol.44, pp. 892–898.

Vaunat, J. & Olivella, S. 2002. *Code_Bright/GiD: A 3-D program for thermo-hydro-mechanical analysis in geological media*. International Center for Numerical Methods in Engineering.

Viana da Fonseca, A. 1996. *Geomechanical of Porto granite residual soils. Foundations design criteria.* PhD thesis, Civil Engineering Department, Faculty of Engineering of University of Porto.

Advances in Unsaturated Soils – Caicedo et al. (eds)
© 2013 Taylor & Francis Group, London, ISBN 978-0-415-62095-6

A lattice model for liquid transport in unsaturated porous materials

C. Fahy & P. Grassl
University of Glasgow, Glasgow, UK

D. Gallipoli
Université de Pau et des Pays de l'Adour, France

ABSTRACT: A pressure driven mass transport model is proposed for describing the movement of liquid moisture through porous materials. The model employs a lattice, created from a random dual Delaunay and Voronoi tessellation, to discretise the material domain. Constitutive laws developed for describing the liquid retention and permeability behaviour of partially saturated soils are implemented in the above lattice model and applied to the analysis of two distinct capillary rise problems in different types of unsaturated porous materials. Analyses were carried out by using both 1D and 2D lattices, with results being compared to those reported in the literature to assess the accuracy of the proposed formulation.

1 INTRODUCTION

Compacted clay, concrete and masonry are some of the most common building materials to suffer from water ingress. They are found in structures such as dams, embankments, tunnels, piers and bridges, which are all subject to degradation due to water penetration. Given that porous materials are widely used in all aspects of construction, transport models are often needed for predicting the extent of moisture movement and, hence, to gauge the condition of structures.

In this context, a mass transport model is proposed to describe the movement of liquid through partly saturated porous materials. The proposed model is implemented in the numerical code OOFEM (Patzák & Bittnar, 2001) based on a lattice approach that uses a randomly generated dual Delaunay and Voronoi tessellation of the material domain (Grassl, 2009). The constitutive retention and permeability laws of the porous material are based on the hydraulic functions originally proposed by van Genuchten-Mualem (Mualem, 1976, van Genuchten, 1980) for unsaturated soils and subsequently modified by Vogel et al. (2000). The lattice model incorporating the above constitutive laws is applied to two benchmark problems (in 1D and 2D, respectively) to demonstrate its numerical robustness and ability to describe liquid movement through porous media.

2 LATTICE TRANSPORT MODEL

A two-dimensional lattice model is used to describe the movement of liquid under gradients of hydraulic potential in a partly saturated porous material. The lattice is obtained by overlying the material domain with a random Delaunay triangulation (shown by solid lines in Figure 1a) which is taken as the basis for the construction of a dual Voronoi polygonization (showed by dotted lines in

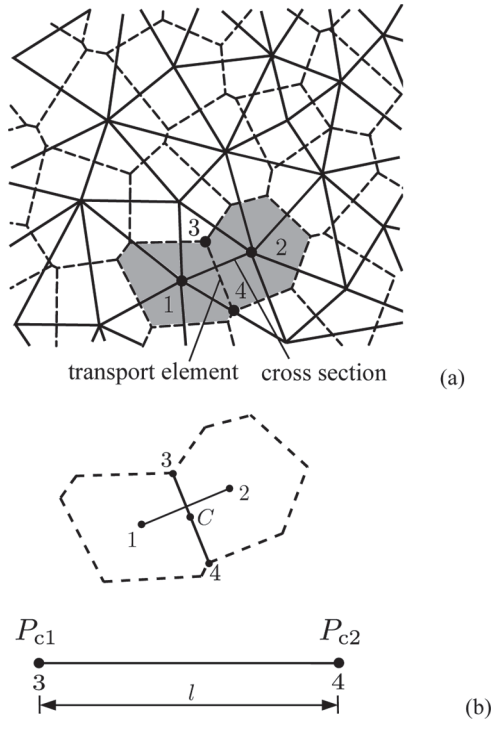

Figure 1. (a) Transport model, (b) Transport element.

Figure 1a). Transport elements are placed along the facets of the Voronoi polygons and their cross-sectional areas are calculated from the length of the corresponding edges of the dual Delaunay triangles.

Transport elements are idealized as one-dimensional conductive "pipes", according to the proposal by Bolander & Berton (2004). The gradient of hydraulic head, which governs flow rate along each transport element, is calculated from the liquid pressures P_c at the two extremities. Figure 1b shows one transport element, together with the capillary pressures acting at the nodes and the associated cross-sectional area as obtained from the dual Delaunay triangle.

In this work we restrict our attention to the case where pore water is in tension and, in the following, liquid pressure is therefore referred to as capillary pressure.

3 CONSTITUTIVE LAWS

The mass balance equation describes the change in moisture inside a porous element as a consequence of liquid flow and solid-liquid retention. A positive sign is assumed for liquid tension, unlike the convention of soil mechanics which assumes compression positive. This is made to facilitate future coupling of the transport formulation with fracture models currently implemented in OOFEM where tensile stresses are assumed positive.

In the balance equation, the flux (i.e. the liquid flow across a unit area of porous material) is related to the pressure gradient through Darcy's law as follows:

$$\mathbf{q} = k\nabla\left(\frac{P_c}{\rho g} - z\right) \tag{1}$$

where $\mathbf{q}$ is the flow vector, k is the hydraulic conductivity, P_c is the capillary pressure, ρ is the density of water, g is the acceleration of gravity and z is the capillary height. By introducing Darcy's law in the moisture balance equation, the following differential expression is obtained:

$$c\frac{\partial P_c}{\partial t} - \frac{k}{g}\mathrm{div}\left(\nabla\left(P_c - \rho g z\right)\right) = 0 \tag{2}$$

where c is the mass capacity and P_c is the time-dependent pressure field to be determined.

Boundary conditions are imposed either as prescribed values of capillary pressure (on boundary Γ_1) or as prescribed values of flux (on boundary Γ_2). The latter boundary condition can then be related to the gradient of capillary pressure through Darcy's law. This results in the following two mathematical constraints on P_c:

$$P_c = g(\mathbf{x}) \text{ on } \Gamma_1 \quad \text{and} \quad \frac{\partial P_c}{\partial \mathbf{n}} = f(\mathbf{x}) \text{ on } \Gamma_2 \tag{3}$$

where $\mathbf{n}$ denotes the direction normal to the boundary while $g(\mathbf{x})$ and $f(\mathbf{x})$ are functions of the spatial coordinate vector $\mathbf{x}$.

In Equation 4, the capacity c is defined as:

$$c = -\rho\frac{\partial \theta}{\partial P_c} \tag{4}$$

where θ is the water content which is calculated by a modified version of van Genuchten's retention model as proposed by Vogel et al. (2000):

$$\theta = \begin{cases} S_e(\theta_s - \theta_r) + \theta_r & \text{if } P_c > P_{c(aev)} \\ \theta_s & \text{if } P_c < P_{c(aev)} \end{cases} \tag{5}$$

where $P_{c(aev)}$ is the air-entry value of capillary pressure which separates saturated states ($P_c < P_{c(aev)}$) from unsaturated states ($P_c > P_{c(aev)}$), S_e is the effective degree of saturation (varying between zero and one when P_c tends to infinity and $P_{c(aev)}$ respectively), θ_r is the residual water content corresponding to $S_e = 0$ and θ_s is the saturated water content corresponding to $S_e = 1$.

From the physical point of view, air breaks into an initially saturated material when capillary tension exceeds $P_{c(aev)}$ (hence inducing a drop of degree of saturation). Conversely, water floods all pores of an initially unsaturated material when capillary tension falls below $P_{c(aev)}$ (hence attaining a degree of saturation of one). It is intuitive that the smaller the pore size of the material, the larger the value will be of $P_{c(aev)}$.

The effective degree of saturation S_e is related to capillary pressure P_c by the following modified version of van Genuchten's model (Vogel et al., 2000):

$$S_e = \frac{\theta_m - \theta_r}{\theta_s - \theta_r}\left(1 + \left(\frac{P_c}{a}\right)^{\frac{1}{1-m}}\right)^{-m} \tag{6}$$

in which θ_m, a and m are all model parameters. The role of parameter θ_m is illustrated in Figure 2 which provides a graphical representation of Equation 6. In particular, parameter θ_m is equal to or greater than the saturated water content θ_s.

If $\theta_m = \theta_s$, the original van Genuchten model is recovered from Equation 6 (Fig. 2). If $\theta_m > \theta_s$, a horizontal cut-off line at $S_e = 1$ is introduced (Fig. 2) to avoid values of effective degree of saturation

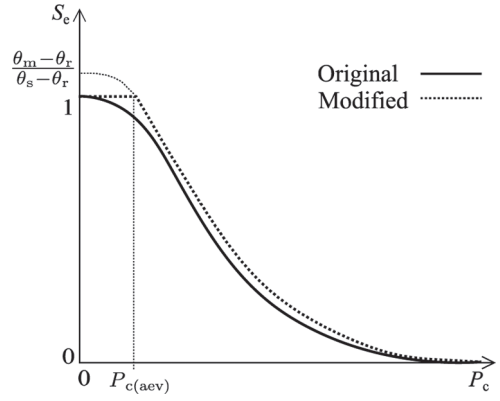

Figure 2. Effective degree of saturation versus capillary pressure.

greater than one. This line intersects the modified van Genuchten graph (Equation 6) at $P_c = P_{c(aev)}$.

Hence, the air-entry value of capillary pressure $P_{c(aev)}$ is calculated by imposing $S_e = 1$ in Equation 6 as:

$$P_{c(aev)} = a\left(\left(\frac{\theta_m - \theta_r}{\theta_s - \theta_r}\right)^{1/m} - 1\right)^{1-m} \tag{7}$$

The hydraulic conductivity k in Darcy's law (Equation 1) is next expressed in terms of intrinsic conductivity κ, relative conductivity κ_R, density of water ρ and absolute (dynamic) viscosity of water μ as:

$$k = \begin{cases} \dfrac{\rho g \kappa}{\mu}\kappa_R & \text{if } P_c > P_{c(aev)} \\ \dfrac{\rho g \kappa}{\mu} & \text{if } P_c < P_{c(aev)} \end{cases} \tag{8}$$

where κ_R is a function of the effective degree of saturation S_e according to the following modified version of van Genuchten's model (Vogel et al., 2000):

$$\kappa_R = \sqrt{S_e}\left(\frac{1-\left[1-\left(\dfrac{\theta_s-\theta_r}{\theta_m-\theta_r}S_e\right)^{1/m}\right]^m}{1-\left[1-\left(\dfrac{\theta_s-\theta_r}{\theta_m-\theta_r}\right)^{1/m}\right]^m}\right)^2 \tag{9}$$

As before, if $\theta_m = \theta_s$, Equation 9 reduces to the expression of the relative conductivity for the original van Genuchten model.

4 ANALYSES

4.1 *1D analysis*

To verify that the constitutive equations of Section 3 are correctly implemented in OOFEM, the 1D capillary infiltration problem modelled by Vogel et al. (2000) was modelled again in this work by using OOFEM. Table 1 gives the parameter values of the original and modified van Genuchten models (Vogel et al., 2000) as used in the simulations while Figure 3 shows the corresponding variations of volumetric water content θ, water capacity c and relative conductivity κ_R with capillary pressure P_c.

Note that the modified van Genuchten model assumes a value of θ_m that is very close to the value of θ_s, which results in a very small air-entry capillary pressure $P_{c(aev)} = 1.962 \times 10^{-4}$ MPa. Due to this, it is very difficult to notice any difference between the variations of volumetric water content with capillary pressure predicted by the original and modified models, respectively (Fig. 3a).

Prior to the start of the analysis, the 1000 mm soil column is assumed to be in hydraulic equilibrium with an imposed capillary pressure of 0.0981 MPa at the bottom (see Fig. 4). This value of capillary pressure corresponds to an imposed pressure head of –1000 cm as specified in Vogel et al. (2000). At time zero, atmospheric pressure was imposed at the bottom of the column combined with a zero flux at the top (Fig. 4), leading to an upward infiltration (i.e., an infiltration against gravity).

Figure 5 compares the pressure distribution along the soil profile as predicted by OOFEM and by Vogel et al. (2000), respectively, at different times during the infiltration process. As can be seen, the wetting fronts predicted by OOFEM lag slightly behind those predicted by the alternative numerical formulation of Vogel et al. (2000). However, when the modified version of the van Genuchten model is employed in Figure 6, the results obtained by OOFEM are in much better agreement with those presented by Vogel et al. (2000).

The predicted infiltration rate over time (calculated at the bottom of the soil column) is plotted

Table 1. Parameters for 1D soil column analysis.

θ_s	0.380
θ_r	0.068
θ_m	0.3803
$P_{c(aev)}$ [MPa]	1.962×10^{-4}
μ [t /(mm*s)]	1×10^{-9}
κ [mm^2]	5.6634×10^{-8}
m	0.0826
a [MPa]	0.0123

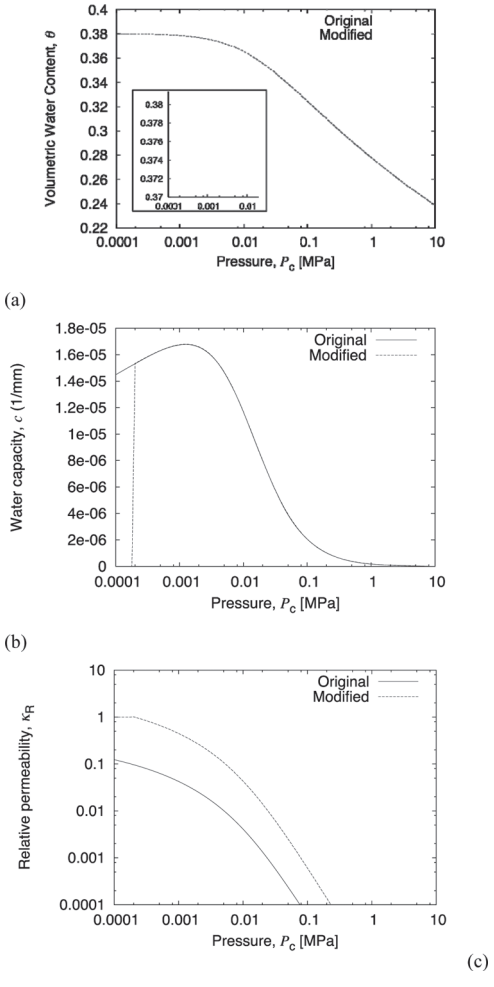

Figure 3. Predicted variation of (a) Volumetric water content, (b) Water capacity and (c) Relative conductivity with capillary pressure.

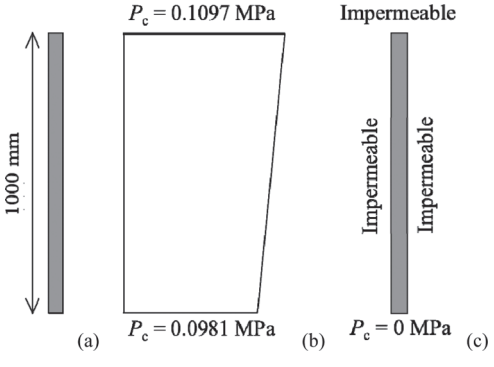

Figure 4. (a) Geometry, (b) Initial pressure distribution, i.e. prior to start (t < 0) and (c) Boundary conditions at start of the analysis (t = 0).

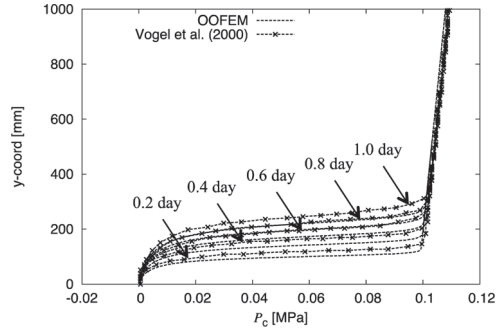

Figure 5. Comparison of capillary pressure distribution at different times predicted by OOFEM model and by Vogel et al. (2000) using the original van Genuchten model.

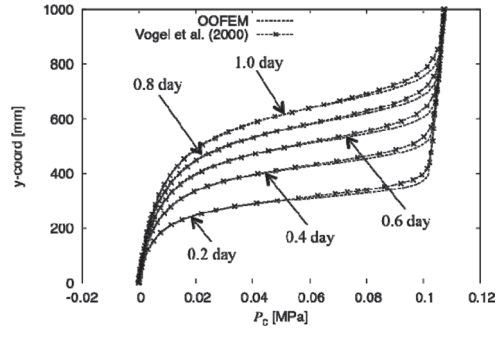

Figure 6. Comparison of capillary pressure distribution at different times predicted byOOFEM and by Vogel et al. (2000) using the modified van Genuchten model.

in Figures 7 and 8 for different degrees of lattice refinement.

When the original van Genuchten model is used, large oscillations of the infiltration rate occur at the start of the analysis, which persist longer in the case of a coarser mesh. As time increases, these oscillations smooth out and results no longer depend on mesh size (Fig. 7).

However, when the modified van Genuchten model is used, oscillations are greatly reduced and only occur at the very initial times for the coarser mesh (Fig. 8). Figure 8 shows clearly that after about 500 seconds no oscillations occur and results become independent of mesh size.

4.2 *2D analysis*

In order to further verify the accuracy and robustness of the flow model presented in Section 4.1 with reference to a 2D lattice, the laboratory test by Wittmann et al. (2008) was simulated using OOFEM. This test involved measurement of

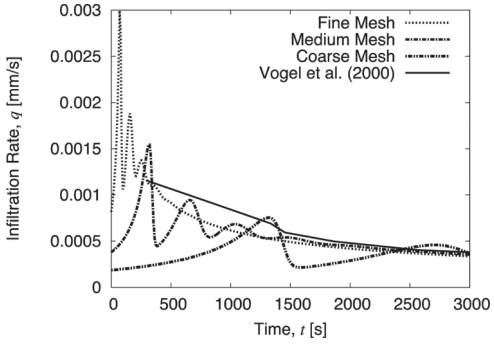

Figure 7. Infiltration rate calculated by OOFEM using original van Genuchten model.

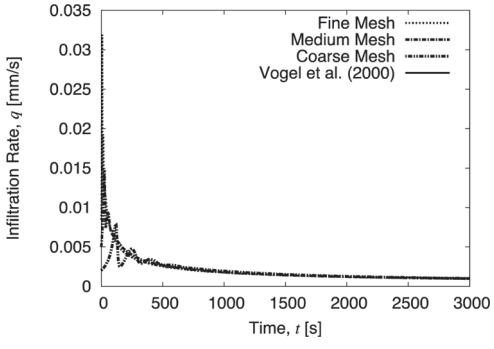

Figure 8. Infiltration rate calculated by OOFEM using modified van Genuchten model.

capillary infiltration through a concrete beam whose bottom surface was put in contact with free water. The concrete beam was modelled by means of a 2D lattice whose hydraulic properties were described by the modified van Genuchten model (because the modified van Genuchten model has been shown to be more accurate than the original model).

Prior to the start of the infiltration process, a uniform capillary pressure of 39.585 MPa (corresponding to an assumed effective degree of saturation of 0.5) is assumed throughout the beam. Subsequently, at time zero, the water pressure along the bottom of the beam is changed to zero (i.e., atmospheric) while the top and side boundaries are assumed to be impermeable to water (see Fig. 9). This leads to an upward capillary infiltration similarly to the previous case of a 1D soil column. The parameters used for the analysis were taken from the literature and are listed in Table 2 (Wittmann et al., 2008, Baroghel-Bouny et al., 1999).

As no value of the intrinsic permeability κ was available from the literature, this was chosen so to give optimum predictions of changes in water content at an early time. A comparison of the changes in water content predicted by the model over the depth of the beam (along the centre line) at different times against the experimental results presented by Wittmann et al. (2008) is shown in Figure 10. Inspection of Figure 10 indicates that, at the beginning of the infiltration process, the model agrees relatively well with the measured increase of water content (which is unsurprising given that the intrinsic permeability κ was chosen to fit experimental results at an early time). However, at later stages, the increase of water content is over predicted. It is still unclear as to why this over-prediction occurs. However, this might be due to the fact that concrete is incorrectly treated as a homogeneous material and the presence of aggregates, which slow down moisture movement, is ignored (Wang & Ueda, 2011).

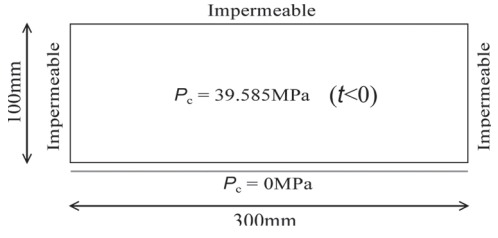

Figure 9. Geometry and boundary conditions.

Table 2. Parameters for 2D beam analysis.

θ_s	0.092
θ_r	0.000
$P_{c(aev)}$ [MPa]	1.962×10^{-4}
μ [t/(mm*s)]	1×10^{-9}
κ [mm^2]	1.0×10^{-13}
M	0.4396
a [MPa]	18.6237

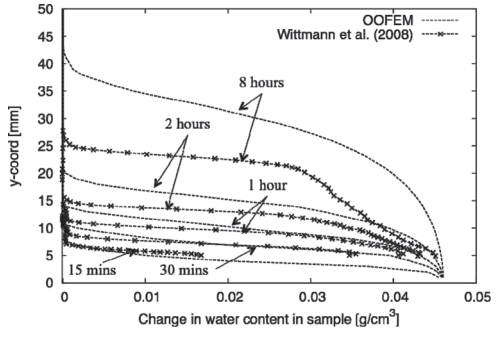

Figure 10. Change in water content versus depth of beam.

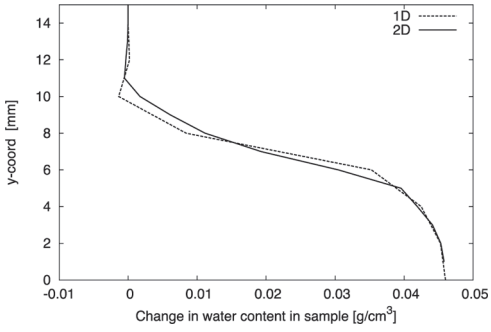

Figure 11. Comparison of 1D and 2D results for time equal to 30 minutes.

A simplified 1D model of the same infiltration problem (i.e., using the same parameter values given in Table 2) was also created to verify the results obtained from the 2D analysis. Figure 11 shows the change in water content calculated at time 30 minutes by the 2D and 1D models, respectively. Inspection of Figure 11 indicates that the two profiles are very similar which corroborates the precision of the predictions by OOFEM.

5 CONCLUSIONS

This paper presents a pressure driven mass transport lattice model that can accurately describe the movement of moisture through porous materials. The lattice model was constructed by placing 1D transport elements along the edges of Voronoi polygons with their cross-sectional properties determined from the length of the edges of the corresponding Delaunay triangles.

The robustness and accuracy of the implementation of a modified van Genuchten model by Vogel et al. (2000) in the numerical code OOFEM was demonstrated by simulating water movement through a soil column and a concrete beam (modelled by 1D and 2D lattices, respectively). The accuracy of both predictions was verified by comparison with published results.

This study confirms the work of Vogel et al. (2000) which states that the modified van Genuchten model is superior to the original van Genuchten model in terms of numerical robustness. This work has also shown that the modified van Genuchten model is superior in terms of accuracy and mesh dependency to the original model.

REFERENCES

Baroghel-Bouny, V., Mainguy, M., Lassabatere, T. & Coussy, O. 1999. Characterization and identification of equilibrium and transfer moisture properties for ordinary and high-performance cementitious materials. *Cement and Concrete Research*, 29: 1225–1238.

Bolander, J.E. & Berton, S. 2004. Simulation of shrinkage induced cracking in cement composite overlays. *Cement and Concrete Composites*, 26: 861–871.

Grassl, P. 2009. A lattice approach to model flow in cracked concrete. *Cement and Concrete Composites*, 31: 454–460.

Mualem, Y. 1976. A new model for predicting the hydraulic conductivity of unsaturated porous media. *Water Resources Research*, 12: 513–522.

Patzák, B. & Bittnar, Z. 2001 Design of object oriented finite element code. *Advances in Engineering Software*, 32: 759–767.

Van Genuchten, M.Th. 1980. A closed-form equation for predicting the hydraulic conductivity of unsaturated soils. *Soil Science Society of America*, 44: 892–898.

Vogel, T., van Genuchten, M.T. & Cislerova, M. 2000. Effect of the shape of the soil hydraulic functions near saturation on variably-saturated flow predictions. *Advances in Water Resources*, 24(2): 133–144.

Wang, L. & Ueda, T. 2011. Mesoscale modeling of water penetration into concrete by capillary absorption. *Ocean Engineering*, 38: 519–528.

Wittmann, F.H., Zhang, P., Zhao, T., Lehmann, E. & Vontobel, P. 2008. Neutron radiography, a powerful method for investigating water penetration into concrete. *In Advances in Civil Engineering Materials. Proceedings of The 50-year Teaching and Research Anniversary of Prof. Sun Wei*, Nanjing, China.

Advances in Unsaturated Soils – Caicedo et al. (eds)
© 2013 Taylor & Francis Group, London, ISBN 978-0-415-62095-6

Numerical simulation of a shallow foundation on an unsaturated silt

N.A. González & A. Gens
Technical University of Catalonia, Barcelona, Spain

ABSTRACT: This paper presents a coupled flow-deformation finite element analysis of a shallow foundation on an unsaturated loosely compacted silt subjected to variations in the water level. The behaviour of the silt foundation was simulated using the Barcelona Basic Model (BBM) which was implemented into the PLAXIS finite element code. Material parameters were calibrated from laboratory tests reported in the literature. The influence of partial soil saturation and of fluctuations of the groundwater level on the behaviour of footing is investigated. Constitutive equations were solved using two stress integration procedures, an explicit stress integration scheme with automatic substepping and error control techniques and a fully implicit stress integration scheme based on the Backward-Euler algorithm with substepping. Their performances during the numerical simulation are evaluated.

1 INTRODUCTION

A common engineering problem which often involves unsaturated soils is that of shallow foundation that rests above the ground water table. In many cases a capillary zone exists above the groundwater level (G.W.L), where the soil unsaturated. Typical footing analyses ignore this zone and assume that the soil above the ground water table is dry. This type of analyses underestimates the soil strength but, more importantly, ignores well known features of unsaturated soils such as collapse upon wetting.

This paper presents a series of unsaturated finite element analysis of a strip footing on an unsaturated loosely compacted silt performed with PLAXIS program using a fully coupled flow-deformation analysis (Galavi, 2010). Soil behaviour is described using the well-known BBM (Alonso et al., 1990), it has been implemented into PLAXIS as a user defined soil model. The influence of partial soil saturation and of fluctuations of the G.W.L. on the behaviour of footing is investigated.

Local constitutive equations are solved using two stress integration procedures, an explicit stress integration scheme with automatic substepping and error control techniques (Sloan et al., 2001; Sheng et al., 2003; González & Gens, 2010) and a fully implicit stress integration scheme based on the Backward-Euler algorithm with substepping (Pérez et al., 2001; González & Gens, 2010). The numerical performance of the algorithms was evaluated for an element test in González & Gens (2010) and González (2011). This paper, however, goes a step further as the algorithms are evaluated in a practical geotechnical boundary value problem. According to Sheng et al. (2003), because of the singularity at the footing edge and the strong rotation of the principal stresses during loading, this problem is a challenging test for the evaluation of the numerical algorithms.

2 NUMERICAL FORMULATION

2.1 *Constitutive relations*

The main features of the model used herein are:

i) to use the BBM formulation to account for the behaviour of unsaturated soils.

ii) to adopt Bishop stress and suction as the constitutive stress variables,

$$\sigma'_{ij} = \sigma_{ij} - P_a \delta_{ij} + S_e \left(P_a - P_w\right) \delta_{ij} \tag{1}$$

$$s = P_a - P_w \tag{2}$$

where, σ_{ij} is the total stress vector, P_a the air pressure, P_w the water pressure, S_e the effective degree of saturation and δ_{ij} the Kroneckers's delta. PLAXIS assumes that P_a is constant and equal to atmospheric; therefore, suction is negative of pore pressure (Galavi, 2010).

iii) Hydraulic hysteresis effects are not considered in the formulation. van Genuchten (1980) equation is adapted for the description of the relationship between degree of saturation and suction,

$$S_e = \frac{S_r - S_{res}}{S_{sat} - S_{res}} = \left[1 + \left(g_a \frac{P_w}{\gamma_w}\right)^{g_n}\right]^{g_c} \tag{3}$$

where, S_e is the effective degree of saturation, S_r the degree of saturation, S_{res} the residual saturation at

very high value of suction, S_{sat} the saturation of saturated soil and g_a [m^{-1}], g_n and g_c are fitting parameters, g_c is often used as ($1/g_n$-1).

The permeability for unsaturated states in PLAXIS is computed as,

$$k_i = k_{rel} k_i^{sat} \quad i = x, y, z \tag{4}$$

where k_i^{sat} is the permeability for saturated soils and k_{rel} is the relative permeability defined by,

$$k_{rel} = \left(S_e\right)^{g_l} \left[1 - \left(1 - S_e^{\left(-\frac{1}{g_c} \right)} \right)^{(-g_c)} \right]^2 \tag{5}$$

where, g_l is a fitting parameter.

Full details of the constitutive model are given in González (2011) and González & Gens (2010) and details of the fully coupled flow deformation analysis are given in Galavi (2010).

2.2 *Numerical integration algorithms*

Incremental stress-strain-suction equations are solved using both explicit and implicit integration algorithms adapted to unsaturated conditions.

Explicit algorithm is based on the Modified Euler procedure, uses the gradients of the yield surface and plastic potential at the start of the strain increment, and their accuracy is controlled by breaking up the strain increment into sub-increments (or substeps), special automatic local substepping and error control techniques were implemented following the proposals of Sloan et al. (2001) and Sheng et al. (2003).

The fully implicit stress integration algorithm is based on the Backward-Euler procedure with substepping techniques (Pérez et al., 2001). In the implicit algorithm, all gradients are estimated at an advanced stress state (which is unknown) and then the resulting non-linear constitutive equations are solved by iteration. As in the explicit algorithm, the strain increment can be subdivided in smaller size (substeps), in case that no convergence is reached in the iterative process of residual minimization.

In both algorithms, the suction variable is treated as an additional strain component and it is assumed that it may be sub-incremented at the same rate as the other strain components.

In the case the prescribed maximum number of time substeps (or sub-increments) is reached, the finite element program is asked to reject the current step and to decrease the size of the global step. Full details of the numerical algorithms employed in this work are given in González (2011) and González & Gens (2010).

3 MODEL CALIBRATION

A set of oedometer and triaxial laboratory tests on an unsaturated compacted silty soil (Jossigny silt) reported by Casini (2008) has been selected for the calibration of the constitutive model and the shallow foundation analysis performed in this work. Jossigny silt is a low plasticity silt (w_P = 19, w_L = 37, I_P = 18), the normal Proctor optimum characteristics are γ_{opt} = 16 kN/m^3 and w_{opt} = 18%. It was compacted at low values of dry density and water content (γ_{dry} = 14.5 kN/m^3 and w = 13%) to ensure significantly susceptibility to wetting. Mechanical and hydraulic calibrated model parameters are presented in Table 1 and Table 2, respectively.

Table 1. Mechanical properties for the Jossigny silt.

Parameter	Value	Description
ν	0.3	Poisson's ratio
κ	0.005	Slope of the unloading-reloading line
λ_0	0.12	Slope of the saturated consolidation line
k_s	0.14	Parameter to control the increase in apparent cohesion with suction
M	1.45	Slope of the critical state line
e_0	0.81	Initial void ratio
P_o* [kPa]	55	Saturated preconsolidation pressure
p_r [kPa]	1.0	Reference pressure
r	0.5	Parameter to control the maximum soil stiffness with suction
β [kPa^{-1}]	0.005	Parameter to control the rate of increase of stiffness with suction
α	1.0	Non-associated parameter

Table 2. Hydraulic properties for the Jossigny silt.

Parameter	Value	Description
S_{res}	0.39	Residual degree of saturation
S_{sat}	1.0	Maximum degree of saturation
g_a [m^{-1}]	0.7	Fitting parameter for van—Genuchten
g_n	2.083	Fitting parameter for van—Genuchten
g_c	–0.52	Fitting parameter for van—Genuchten
k_x, k_y [m/day]	0.0864	Intrinsic permeability
g_1	0	Fitting parameter for relative permeability

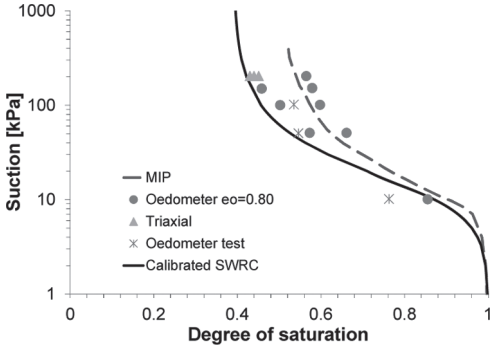

Figure 1. Soil Water Retention Curve of Jossigny silt (Experimental data from Casini, 2008).

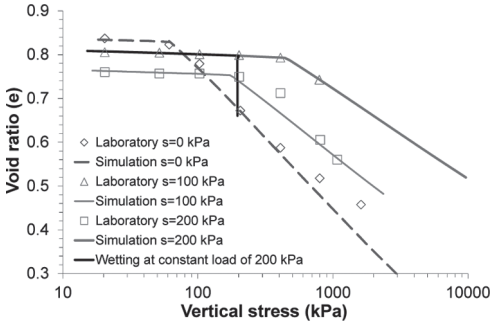

Figure 2. Predicted and experimental behavior of oedometer tests on Jossigny silt (Experimental data from Casini, 2008).

The soil water retention curve (SWRC) obtained experimentally by different techniques (Casini, 2008) and the calibrated curve are plotted in Figure 1. The experimental results showed the existence of hysteresis in the SWRC, however, the calibrated curve employed in this work is representative of the wetting branch.

Predicted and experimental results of oedometer tests performed under saturated conditions (s = 0 kPa) and at constant suctions of 100 and 200 kPa are plotted in Figure 2, a good agreement between predicted and experimental behavior is observed. Figure 2 also shows the results of a wetting test (starting from s = 200 kPa) under a vertical stress of 200 kPa for which it is evident the reduction in volume induced by saturation (collapse behavior).

Predicted and experimental results of a triaxial test involving anisotropic loading prior to shearing at constant suction of 200 kPa are plotted in Figure 3. Predicted behaviour also shows a reasonably good agreement with experiments.

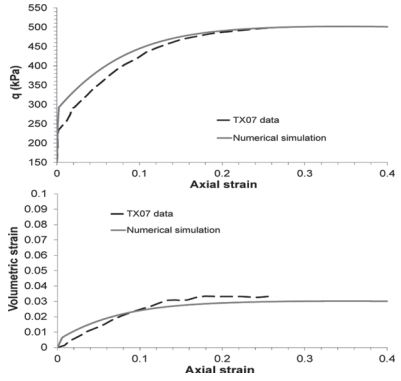

Figure 3. Predicted and experimental behavior of a triaxial test on Jossigny silt (Experimental data from Casini, 2008). (a) Deviatoric stress (q) against axial strain; (b) Volumetric strain against axial strain.

4 SHALLOW FOUNDATION ANALYSIS

In this section numerical simulation of a smooth strip footing, resting on the compacted Jossigny silt is presented. Figure 4 shows the FE mesh and the boundary conditions used for the analysis. The mesh consists of 415 15-noded triangular elements with a fourth order interpolation for displacements and for pore pressure and 12 gauss points for each element. The width and height of the model are 10 m and the width of the footing is 1 m. The initial position of the G.W.L. is on the surface. This level is changed during drying and wetting processes. The top, left and right boundaries are closed for flow, and drying and wetting are only applied through the bottom boundary by linearly changing the water head with time.

The soil parameters used in the analysis are those given in Table 1 and Table 2. The initial stresses are generated using the loads corresponding to the total soil unit weight (γ= 16.5 kN/m^3) and the K_0-value (K_0 = 0.416). The yield surface locations for the fully saturated conditions were set considering a preoverburden pressure (POP) of 55 kPa at the ground surface, where POP is defined as the difference between the vertical effective stress and the vertical preconsolidation pressure.

Two set of analysis were considered. In the first analysis, the footing was loaded considering three different depths of the G.W.L.: *a)* a deep water level (10 m depth), *b)* a water level at 5 m depth and *c)* a water level at the ground surface (saturated condition). In the second analysis the footing was loaded to a certain load with the G.W.L. at 5 m depth and subsequently the G.W.L. was raised to the ground surface at constant applied load. Three

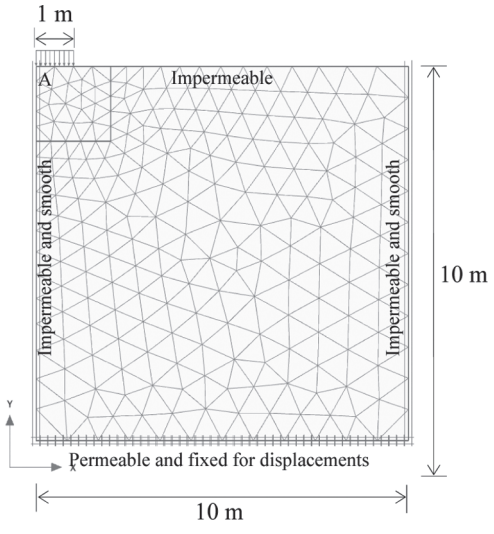

Figure 4. Geometry and FE mesh used for the footing problem.

different loads were considered: 75 kPa, 100 kPa and 125 kPa.

4.1 *Rigid footing at different groundwater levels*

To simulate the behavior of a rigid foundation, the analysis is performed under displacement control with vertical displacements applied to the soil surface below the position of the footing and an equivalent pressure is computed by summing the appropriate vertical nodal reactions. Before applying these displacements, the initial position of the G.W.L. was varied in order to set different initial suction profiles. Three initial positions were analyzed: 0 m, 5 m and 10 m, corresponding to suction values of 0 kPa, 50 kPa and 100 kPa on the top boundary, with the first value corresponding to a fully saturated condition. After the drying phase, the footing was loaded to a total displacement of 0.2 m. This displacement was applied over a time period of 1000 days, so that the rate of loading was slow enough to ensure fully drained conditions.

The predicted load-displacement curves for the three different initial positions of the G.W.L. are shown in Figure 5. The figure shows an increase of the predicted footing load with the G.W.L. depth. The footing load has not reached its limiting value at the maximum displacement achieved in the analysis. The load-displacement behavior is largely controlled by the increase of the elastic domain as illustrated in Figure 6, which plots the stress path followed for a stress point located directly underneath the footing (point A in Figure 4).

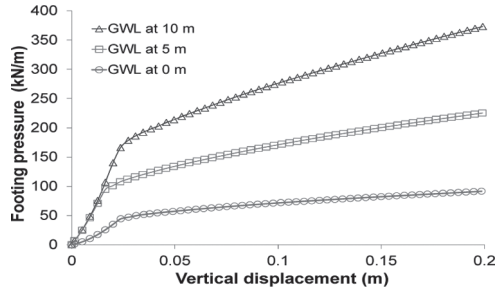

Figure 5. Load-settlement curves of rigid footing with different groundwater levels.

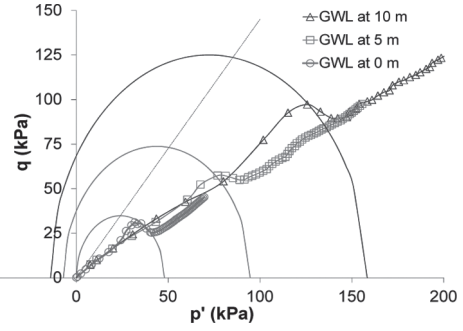

Figure 6. Stress-paths followed by footing for a point located directly underneath the foundation.

4.2 *Flexible footing with rise of groundwater level*

This analysis considers that the strip footing is vertically loaded to three different loads: 75, 100 and 125 kPa with the initial water level at 5.0 m. Then, the surface soil adjacent to the footing is wetted to zero suction (G.W.L. at the ground surface). These boundary conditions were imposed over a time of 1000 days in order to maintain fully drained conditions. As the footing is loaded by a uniform vertical pressure, and not by uniform imposed vertical displacements, it is taken to be perfectly flexible.

Figure 7 shows the relationships between vertical displacements against vertical effective stresses predicted by the three different loads. In the same figure the stress-displacement curves for G.W.L. at 5.0 m and G.W.L. at 0 m (presented in the previous section) are also plotted for comparison. It can be seen in this figure that the higher the load at which wetting took place the larger the induced settlement. In fact, there is an important reduction in displacement (or swelling behavior) rather than significant settlements when the wetting path is carried out at a load of 75 kPa, while, the wetting paths at loads of 100 kPa and 125 kPa initially exhibited only a small decrease in displacement

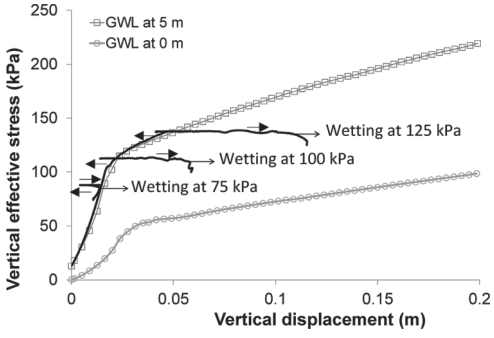

Figure 7. Vertical stress-displacement curves for unsaturated wetting analysis.

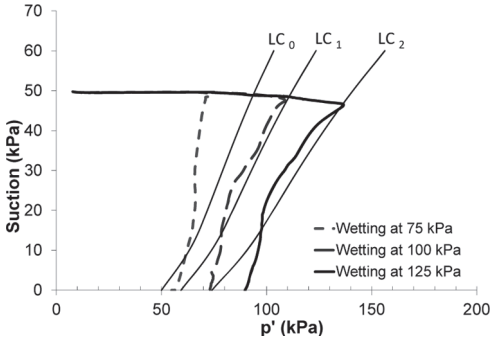

Figure 8. Stress paths for the wetting analysis in a point located directly underneath the foundation. LC_0: initial position of LC curve; LC_1: LC position after load to 100 kPa; LC_2: LC position after load to 125 kPa.

(swelling), followed by larger settlements (or collapse behavior).

This behavior is controlled depending on the location of the stress state with respect to the yield surface, as is illustrated in Figure 8, which plots the stress paths in the mean Bishop's stress against suction plane. Initial position of the Loading-Collapse (LC) curves just before wetting is also plotted in the figure. It is observed that in the three cases, the wetting paths first occur in the elastic domain until the LC curves are crossed, where, larger irreversible displacements are predicted. However, it is observed that most of the wetting path at a constant load of 75 kPa lies in the elastic domain and therefore a significant elastic swelling is predicted.

The vectors of total displacements after load to 125 kPa and after wetting at constant load of 125 kPa are presented in Figure 9. The orientation of these vectors indicates the direction of movement and their length the relative magnitude of movement (scaled by 40). Wetting of the soil leads to significantly increase of displacements of the

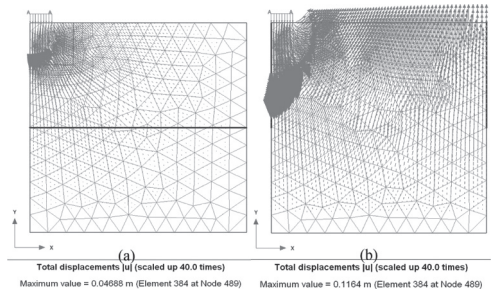

Figure 9. Vectors of total displacements. (a) After load to 125 kPa; (b) after wetting to the ground surface.

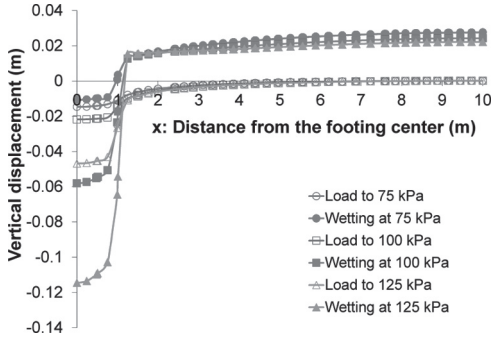

Figure 10. Vertical displacements at the ground surface induced by loading and wetting at three different loads.

nodes below the footing while the nodes away the footing heave.

The displacement pattern for the three analyses is better represented in Figure 10, where the computed vertical displacements after load and after wetting along a cross section at the ground surface are plotted. Negative displacements indicate settlements whereas positive displacements indicate heave of the ground surface. Since the footing is flexible, loading at constant GWL of 5.0 m it causes differential movements with the maximum settlements at its center (x = 0), a reduced settlements at the footing edge (x = 1 m) and an almost zero settlements at the distance of 10 m from its center.

During wetting phase, the ground surface heaves or continues to settle, depending on the distance from the footing center and on the applied load before wetting. At the centre of the footing a further settlement is predicted when the applied loads before wetting are of 100 kPa and 125 kPa, it is not the case when the applied load is of 75 kPa, which causes a settlement reduction. Just underneath the edge of the footing (at x = 1 m), the vertical displacements after wetting begin to change rapidly

from settlement to heave. At distances higher than about 1.25 m away from the footing center, the ground surface rises. Due to the fact that the Jossigny silt has a low swelling index (κ) of only 0.005 (see Table 1) heave is relatively small.

5 PERFORMANCE OF THE NUMERICAL ALGORITHMS

In this section, the performance of the integrations algorithms (explicit and implicit) used to solve the unsaturated constitutive equations is evaluated. Standard settings of PLAXIS regarding global convergence were maintained. For the local integration (at a gauss point level), the yield surface tolerance was fixed at YTOL = 10^{-8}; this parameter was also used to control the convergence of the residual in the implicit algorithm. Control error tolerance of the explicit algorithm was set to STOL = 10^{-4}, these set of values is considered as typical for practical applications as was suggested by Sheng et al. (2003).

Comparisons of the algorithms are presented in terms of the number of global steps (*Steps*), maximum number of global iterations (*Max.iter*), maximum number of local substeps (strain or suction subincrements) (*Max.substep*) and CPU time. It is important to note that *Steps* are controlled internally by PLAXIS and the user cannot modify this value. For a critical element and gauss point located underneath the edge of the footing, the total number of global iterations (*Iter.elm*) and local substeps (*Substep.elm*) are also compared. All CPU times presented are for an Intel Core i7 (2.8 GHz).

Table 3 shows a comparison of the algorithms for the rigid footing at different G.W.L. (see section 4.1). It is observed that, as the suction of the ground surface increases, the maximum number of global iterations and local substeps decreases. This observation is also consistent with the total number of iterations and substeps spent for the critical analysed element. Regarding efficiency of the numerical algorithms, for load footing at constant suction, explicit algorithm requires greater amount of work to integrate the constitutive equations and the global equations than implicit algorithm. CPU time does not vary significantly with the integration algorithm and the consideration of unsaturated soil.

Table 3. Numerical performance for the rigid footing.

	Load at GWL = 0 m		Load at GWL = 5 m		Load at GWL = 10 m	
	Expl.	Impl.	Expl.	Impl.	Expl.	Impl.
Steps	542	540	539	539	539	539
Max.iter	33	18	12	10	10	12
Max.substep	7	3	5	1	4	1
CPU time (s)	325.1	351.7	327.6	337.8	314.0	340.7
Iter.elm	6999	6464	6190	6103	5926	5915
Substep.elm	973	971	933	929	877	863

The efficiency of the numerical algorithms for the flexible footing subjected to a rise of the G.W.L. (see section 4.2) is summarized in Table 4. As expected, an increase of the footing load before wetting demands larger values of global iterations and local substeps. Footing load to 75 kPa is elastic (see Figure 8) and therefore it does not require local substeps. A rise of G.W.L. to the ground surface demands significantly greater amount of numerical work (at local and global levels) than loading at constant G.W.L. During wetting, the limit set of global maximum iterations (100) is reached in all cases. The higher the applied load before wetting the more local substeps are required. In general, the implicit algorithm demands more substeps and iterations than the explicit one during wetting, with the exception of the case with the lowest applied load (75 kPa), as illustrated in Figure 11, this leads to an increase of the computational cost.

Table 4. Numerical performance for the flexible footing.

	Load to 75 kPa		Wetting at 75 kPa	
	Expl.	Impl.	Expl.	Impl.
Steps	539	539	653	630
Max.iter	4	4	100	100
Max.substep	0	0	13	3
CPU time (s)	304.6	314.5	565.4	506.4
Iter.elm	4470	4470	69416	34853
Substep.elm	0	0	1727	581
	Load to 100 kPa		Wetting at 100 kPa	
	Expl.	Impl.	Expl.	Impl.
Steps	539	539	768	771
Max.iter	10	9	100	100
Max.substep	3	1	11	28
CPU time (s)	317.4	312.3	765.0	985.1
Iter.elm	5013	4890	129758	130952
Substep.elm	188	166	2397	2292
	Load to 125 kPa		Wetting at 125 kPa	
	Expl.	Impl.	Expl.	Impl.
Steps	539	539	766	768
Max.iter	15	9	100	100
Max.substep	5	1	41	100
CPU time (s)	339.1	343.6	742.8	1080
Iter.elm	6990	6377	88724	90691
Substep.elm	605	529	2576	2612

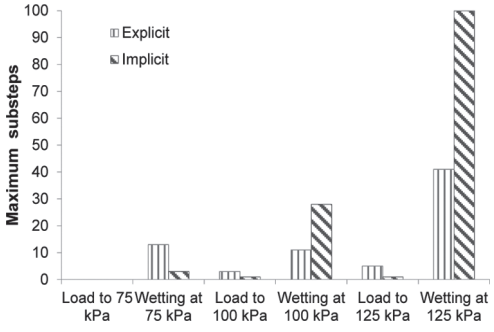

Figure 11. Maximum local substeps required for a flexible footing subjected to a rise of the G.W.L.

These results seem consistent with those presented for an element test in González & Gens, (2010), where the wetting path of a triaxial test demanded both a higher computational cost and more substeps when Bishop's stress and the implicit scheme were used.

6 CONCLUSIONS

The influence of partial soil saturation on the behaviour of a strip shallow foundation lying on a compacted silty soil was investigated through a series of FE analysis. Predicted ultimate footing load increases for larger depths of the G.W.L. Collapse of the foundation was computed when the G.W.L. rises to the ground surface, the higher the applied load before wetting the higher the settlements.

Regarding efficiency of the numerical algorithms employed to solve the constitutive equations, implicit algorithm seems to be more efficient than explicit one for load footing at a given G.W.L., however, when the G.W.L is raised, the implicit algorithm requires greater amount of work to integrate the constitutive equations and the global equations than the explicit algorithm, particularly when higher loads are applied to the foundation before wetting.

REFERENCES

Alonso, E., Gens, A. & Josa, A. (1990). A constitutive model for partially saturated soils. Géotechnique 40: 405–430.

Casini, F. (2008). Effetti del grado di saturazione sul comportamento meccanico di un limo. PhD Thesis, Sapienza Università di Roma, Italy.

Galavi, V. (2010). Groundwater flow, fully coupled flow deformation and undrained analysis in PLAXIS 2D and 3D. Technical internal report, Plaxis BV 2010.

González, N.A. & Gens, A. (2010). Evaluation of a constitutive model for unsaturated soils: stress variables and numerical implementation. A: Fifth International Conference on Unsaturated Soils. E. Alonso, A. Gens (Eds.) Unsaturated Soils, Vol 2. pp. 829–835.

González, N.A. (2011). Development of a family of constitutive models for geotechnical applications. PhD Thesis, Technical University of Catalunya, UPC-BarcelonaTech.

Pérez, A., Rodríguez, A. & Huerta, A. (2001). Consistent tangent matrices for substepping schemes. Comput. Methods Appl. Mech. Engrg. 190: 4627–4647.

Sheng, D., Sloan, S.W., Gens, A. & Smith, D.W. (2003). Finite element formulation and algorithms for unsaturated soils. Part I: Theory. Part II: Verification and application. Int. J. Numer. Anal. Methods Geomech. 27: 745–790.

Sloan, S.W., Abbo, A.J., Sheng, D. (2001). Refined explicit integration of elasto-plastic models with automatic error control. Engineering Computations; 18:121–154.

This page intentionally left blank

Advances in Unsaturated Soils – Caicedo et al. (eds)
© 2013 Taylor & Francis Group, London, ISBN 978-0-415-62095-6

Cyclic macroelement for shallow footing over unsaturated soil

B. Kafle & F. Wuttke
Geomechanical Modeling, Faculty of Civil Engineering, Bauhaus-Universität Weimar, Weimar, Germany

ABSTRACT: Settlement behaviour of foundation over unsaturated soil under the action of cyclic loading can be described by the inclusion of soil structure interaction considering nonlinear soil behaviour by the use of Macroelement formulation. The aim of this paper is to develop a framework of macroelement consisting of coupled system of forces, foundation and the nonlinear behaviour of multiphase granular soil. The model simulates the ratchetting behaviour during cyclic loading of multiphase soil. This is achieved by modifying the bounding surface to account for the change in hardening behaviour of the soil during cyclic loading. The mathematical control over the ratchetting behaviour is established by obtaining the distance of the current stress state from the established image point. The modification of bounding surface as a mathematical control is done to simulate the cyclic accumulation of displacement for the soil under multiphase condition.

1 INTRODUCTION

1.1 *Macroelement for shallow foundation*

Macroelement is a space constituting coupled system of forces from super structure, soil half space and the boundary between them. The complex behaviour of soil structure interaction can be conceived by the use of elastoplastic strain hardening macroelement constituting the interaction between different structural forces acting on foundation. The use of granular model like macroelement constituting of few constitutive parameter and capable of delivering high ended results of Soil structure interaction reduces the ambiguity of model response and the complexity in the analysis of the system under consideration. Figure 1. shows the pictorial representation of macroelement consisting of forces from structure and the arbitrary elasto-plastic region of soil under consideration of macroelement.

Macroelement for the dry sand has been proposed by several authors including (Gottardis & Butterfield 1988, Nova & Montrasio 1991, Butterfield and Gottardi 1994, Houlsby & Cassidy 2002, Grange 2008, Chatzigogos et al., 2009 etc.).

Macroelement for unsaturated soil has been proposed by (Wuttke et al., 2012) in which the model from (Nova and Montrasio 1991) has been extended to acount for multiphase behaviour.

1.2 *Macroelement for cyclic loading*

The repeating behaviour of cyclic loading leads to the several unique behavioral changes in the properties of soil. The small and repeated cycles with very low frequency gives rise to the behaviour

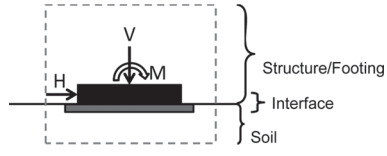

Figure 1. Pictorial representation of macroelement of shallow footing (after di Prisco & Pisano 2011).

of cyclic loading under drained condition. Whereas the rapid and transient cyclic loading leads to the similar behaviour as that of cyclic loading under undrained condition. Accumulation of strain during the cyclic loading is taken as the fundamental soil properties for the prognosis of structural resilience. A macroelement capable to simulate cyclic loading will take into account of several important features of soil structure interaction including interaction of forces from structures, nonlinear soil behaviour, interaction of the soil structure interface. (di prisco et al., 2002), proposed the cyclic macroelement model as an extension of static macroelement model from(Nova & Montrasio 1991) by combining two constitutive model, bubble model proposed by (Al-Tabbaa & Wood 1989) and the bounding surface model proposed by (Dafalias & Herrmann 1982). The proposed model is able to simulate the behaviour of foundation under cyclic loading and is also able to provide the prognosis of accumulation of cyclic strain.

This paper proposes a cyclic macroelement for multiphase granular soil by the modification of constitutive parameters of (Nova & Montrasio 1991) as proposed by (Wuttke et al., 2012) and introducing it in the cyclic macroelement as

proposed by (di prisco et al., 2002) to account for the prognosis of accumulation of cyclic displacement with the change in soil suction.

2 EXPERIMENTAL STUDIES FOR MULTIPHASE GRANULAR MATERIAL

2.1 *Properties of material used*

The material used for the present investigation is Hostun sand (Flavigny et al., 1990). According to the USCS classification Hostun sand is poorly graded sand (SP). Main parameters of Hostun sand are provided in Table 1 and the grain size distribution is shown in Figure 2.

The SWCC of the Hostun sand was determined in the laboratory using modified pressure plate apparatus (Schanz et al., 2011) Figure 3. The modified pressure plate is able to measure soil suction in small steps by using hanging water column connected to the base of the pressure plate. The low suction values were determined by the hanging water column technique. For the higher suction values from 3 to 100 kPa the air pressure is applied from the top and the water drained from the bottom of the sample is measured for the balanced atmospheric pressure.

The volumetric water content, θ corresponding to the applied suction values was computed from back calculations. Air-entry value ψ_{aev} and residual suction ψ_r is approximated to 1.9 kPa and 3.3 kPa respectively from SWCC of hostun sand presented in Figure 3.

Table 1. Properties of hostun sand.

Properties	Hostun sand
Specific gravity	2.65
C_u	1.50
C_c	1.11
Classification (USCS)	SP
D_{50}	0.35 mm

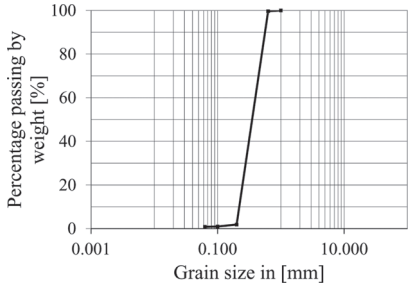

Figure 2. Grain size distribution of hostun sand used in the experimental investigation.

2.2 *Bearing capacity test*

Being capacity of a rough surface model square footing with the size 100 mm x 100 mm was determined in a box, shown in Figure 4.

The box is capable of draining water from four of its opening located at the bottom so as to obtain desired suction in the specimen. The box has the dimension of 980 mm in length, 480 mm in height and 480 mm in width. Tentative value of suction was obtained by measuring the location of water table on the specimen from the surface. Precise measurement of suction is done by the use of tensiometer located at the different depth of the specimen from the surface.

(Bolton & Lau 1988, Cerato & Lutenegger 2006) performed study of scale effect on the bearing capacity of granular soil. A notable effect on the bearing capacity of model footing was observed from numerical and experimental results. (Kusakabe 1995, Herle & Tejchamn 1997) proposed the threshold value of $B/D_{50} \geq 100$ to avoid particle size effect on model test. With the dimension of footing 100 mm x 100 mm and $D_{50} = 0.35$ mm; B/D_{50} of used hostun sand is greater than the threshold value for the effect of particle size on the bearing capacity test. The height of the specimen is obtained by considering the general shear failure mechanism under the static vertically loaded footing such that the failure mechanism due to the footing will occur within the box and the boundary effect in the vertical direction can be ignored.

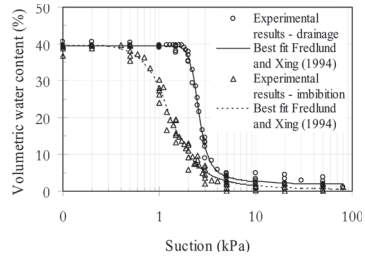

Figure 3. Soil-water characteristic curve of hostun sand (Wuttke et al., 2012).

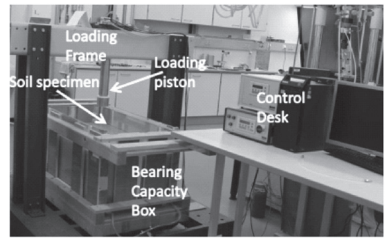

Figure 4. Experimental setup for bearing capacity test.

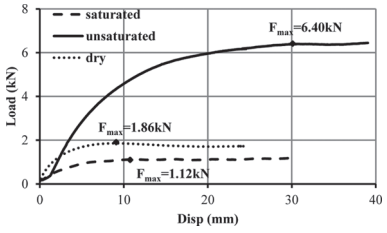

Figure 5. Experimental results of load versus settlement tests.

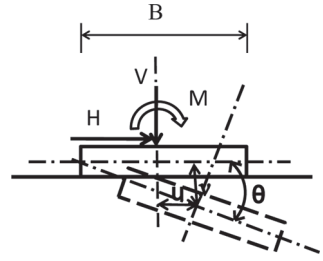

Figure 6. Forces acting over macroelement and the associated displacement (Wuttke et al., 2012).

The sample was prepared by filling the sand in layers and compacted to obtain same void ratio of 0.7 ± 0.02 in each test. After the preparation of the sample de-aired water was slowly filled from bottom of the specimen to obtain saturated specimen. Form the saturated specimen, water was drained to set the water table to a desired level from the surface. The suction of the specimen was measured by the use of tensiometer embedded in the specimen at different depth. The average value of measured suction up to the depth of 1.5B is calculated to homogenize the soil suction over the depth of specimen and designated as the suction of specimen. During the test the suction is precisely controlled and kept constant in the soil sample by connecting the box with the water reservoir. The friction angle of the specimen (Hostun Sand) is obtained from (Schanz & Vermeer 1996) for non-lubricated foundation with the friction angle $\phi = 41.8^{\circ}$. Automated data logging system was used to collect all the experimental data. Figure 5 summarizes the test result for load versus settlement curve.

The bearing capacity box was placed in a loading frame as shown in Figure 4. Three different specimen; dry, saturated and unsaturated with an average suction of 2.1 kPa (approximately. equal to ψ_{aev})was prepared. Displacement controlled loading with the constant rate of 0.0025 mm/s was applied on the footing until a failure load was reached.

3 CONSTITUTIVE MODEL

Assessment of cyclic displacement on the foundation can be done by the use of constitutive models which uses general coupling behaviour of soil and structure during cyclic loading in the form of spring and dash-pods and can be simplified by the use of strain hardening elasto-plastic theory. The system of springs can be substituted by elastoplastic macroelement from (Wuttke et al., 2012) which takes into account of multiphase soil behavour. The different forces acting over the foundation and their corresponding displacement are shown in Figure 6.

The different forces and displacement associate with macroelement can be expressed mathematically as generalized force vector $\boldsymbol{Q}$ and the associated displacement vector $\boldsymbol{q}$. The forces in generalized force vector are normalized with uniaxial limiting vertical force and moment is normalized additionally by width to obtain dimensional homogeneity Eq. (1). For the fulfillment of criteria of work conjugate, associated displacement vector is scaled with uniaxial limiting vertical force Eq. (2). The generalized force and displacement vectors and the extended formulation of macroelement for unsaturated soil from (Wuttke et al., 2012) is expressed as,

$$\mathbf{Q}(\psi) = \begin{Bmatrix} \xi(\psi) \\ h(\psi) \\ m(\psi) \end{Bmatrix} = \frac{1}{[V_m(\psi)]} \begin{Bmatrix} V \\ H/\mu \\ M/\left(\psi_M(\psi).B\right) \end{Bmatrix} \quad (1)$$

$$\mathbf{q}(\psi) = \begin{Bmatrix} \eta(\psi) \\ \varepsilon(\psi) \\ \zeta(\psi) \end{Bmatrix} = [V_m(\psi)] \begin{Bmatrix} v \\ \mu u \\ \psi_M(\psi).\theta.B \end{Bmatrix}, \quad (2)$$

where, (ψ) represents suction dependency of parameters, H denotes horizontal load, M, generated moment, V, vertical load and $V_m(\psi)$ maximum centric uniaxial vertical load capacity of macroelement for particular soil suction. μ, slope of failure envelope at the origin in H—V plane, $\psi_M(\psi)$, slope of failure envelope at the origin in M-V plane, B, width of foundation, v and u are displacement in vertical and horizontal direction and θ angle of rotation.

3-D failure surface of macroelement for multiphase soil from (Wuttke et al., 2012) is expressed as

$$[h(\psi)]^2 + [m(\psi)]^2 - [\xi(\psi)]^2 \left[1 - \xi(\psi)\right]^{2\beta(\psi)} = 0 \quad (3)$$

where, $\beta(\psi)$ is a constitutive parameter which controls the shape of the failure envelope.

The loading function of macroelement for multiphase soil is postulated as the function of load

vector $\boldsymbol{Q}$, the history of macroelement ρ_c and the soil suction as;

$$f(\mathbf{Q},\rho_c,\psi)=\left[h(\psi)\right]^2+\left[m(\psi)\right]^2 -\left[\xi(\psi)\right]^2\left[1-\frac{\xi(\psi)}{\rho_c}\right]^{2\beta(\psi)}=0. \tag{4}$$

The ρ_c lies in the interval $(0,1)=\{\rho_c\in R|0<\rho_c\le 1\}$. When $\rho_c=1$ loading function coincides with failure surface.

The plastic potential which defines the direction of plastic strain is defined as function of load vector varying with soil suction as,

$$g(\mathbf{Q},\psi)=\left[\lambda\cdot h(\psi)\right]^2+\left[\chi(\psi)\cdot m(\psi)\right]^2 -\left[\xi(\psi)\right]^2\left[1-\frac{\xi(\psi)}{\rho_g}\right]^{2\beta(\psi)}=0. \tag{5}$$

where, $\lambda=\mu/\mu_g$, $\chi(\psi)=\psi_M/\psi_g$ and ρ_g is a dummy variable and its numerical value has no significance in flow rule. μ_g and ψ_g are constitutive parameters. Hardening function ρ_c is introduced containing nondimensional constitutive parameters α and γ, and the initial slope of the tangent of force displacement curve for centric vertically loaded foundation, $R_0(\psi)$ *as*, Eq. (6),

$$\rho_c(\psi)=1-\exp\left(-\frac{R_0(\psi)\sqrt{\upsilon^2+(\alpha\iota)^2+\left(\gamma(\psi)B\theta\right)^2}}{[V_m(\psi)]}\right). \tag{6}$$

The incremental plastic strain $d_q^p(\psi)$for a given state of stress is obtained as, Eq. (7),

$$d\mathbf{q}^p(\psi)=\Lambda(\psi)\frac{\partial g(\psi)}{\partial\mathbf{Q}(\psi)}, \tag{7}$$

In formulating cyclic behaviour we need to have parameters which can define several behaviours observed during cyclic loading. For this achievement we need to modify the constitutive relation which is capable of generating realistic cyclic behaviour. The model from (di Prisco et al., 2002) is followed with amendment on it to describe the cyclic phenomenon of multiphase soil. A bounding surface with the same shape that of yield surface is assumed to be located in between failure envelope and origin Figure 7. The co-ordinates of Current stress point *p* lies well within the region of bounding surface. The cap of the cone is assumed to be spherical. The cone evolves during the monotonic loading and remains in elastic state and can change in shape and size while maintaining the elastic state. The cap of the cone maintains the boundary between the elastic and plastic state of stress. By locating the image point on the bounding surface which is obtained by connecting the current state of stress with the path of the cyclic stress and introducing a parameter which locates the distance of current state of stress from image point, plastic accumulated strain during the cyclic loading when the current state of stress is well within the bounding surface can be obtained.

The modified plastic generalized strain proposed by (di Prisco et al., 2002) is further extended with the proposed formulation from (Wuttke et al., 2012) to account for the cyclic loading under multiphase soil as,

$$dq(\psi)^p=\Lambda_I(\psi)\phi_c\left(\delta,\rho_k,\psi\right)\left(\frac{\partial g(\psi)}{\partial\mathbf{Q}(\psi)}\right)_I \tag{8}$$

where subscript *I* represent the value at the image point. The term $\phi_c(\psi)$ considers the cyclic behaviour of soil during cyclic loading and can be expressed in matrix form as,

$$\phi_{cii}(\psi)=e^{-\left[\varsigma_i(\psi)\sqrt{\frac{\delta(\psi)}{\frac{\xi(\psi)}{\rho_c(\psi)}}}+\kappa_i(\psi)\rho_k(\psi)\right]} \tag{9}$$

The term $\phi_{cii}(\psi)$ consists of the constitutive parameters $\varsigma(\psi)$, $\kappa(\psi)$ and the memory parameter $\rho_k(\psi)$ expressed in Eq.(10) which is updated when a new memory surface is reached during cyclic loading. The extended ρ_k from (di Prisco et al., 2002) to account for the memory retaining properties during cyclic loading for multiphase soil is expressed as;

$$d\rho_k(\psi)=\left(1-\rho_k(\psi)\right)\frac{R_0(\psi)}{\left[V_m^2(\psi)\right]} \left[d\eta+\alpha\frac{d|\varepsilon|}{\mu}+\gamma(\psi)\frac{d|\zeta|}{\psi_M(\psi)}\right] \tag{10}$$

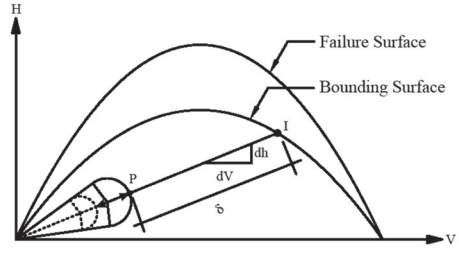

Figure 7. Extended bounding surface with current state of stress and location of image point for cyclic loading, (di Prisco et al., 2002).

4 NUMERICAL RESPONSE

Numerical response of unsaturated soil is obtained by extracting the model dependency parameters from the experimental results. As outlined by (Wuttke et al., 2012) few of the model parameters are influenced by the multiphase behaviour of the soil and other parameters can be taken as a constant as forwarded by (Montrasio & Nova 1997). The parameters influnced by multiphase condition of soil are $V_m(\psi)$ and $R_0(\psi)$. $V_m(\psi)$ and $R_0(\psi)$ are obtained from the experimental result as outlined in Figure 5 and Figure 8. respectively. The different values of $R_0(\psi)$ and $V_m(\psi)$from experimental results obtained from Figure 5 are presented in Table 2.

For the numerical simulation of cyclic loading amplitude of 0.1 kN with the static load of 0.8 kN was used. The initial displacement corresponding to the static load of 0.8 kN obtained from experimental results from Figure 5. was used as the starting point of the cyclic load. The model is simulated to obtain the response for the small frequency and for the drained condition. The ratchetting behaviour and the accumulation of plastic displacement for saturated, dry and unsaturated sand are shown in Figure 9–14. The values of cyclic parameters associated with the model are presented in Table 3.

5 CONCLUSION

The Numerical model formulated herein was able to simulate the ratchetting behaviour of sand under the saturation of different fluid and unsaturated condition for small amplitude under

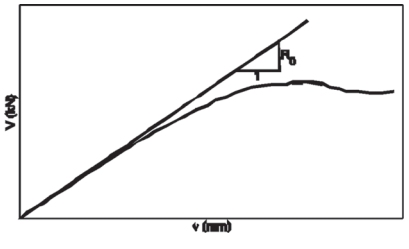

Figure 8. Slope of initial tangent R_0 for the centric vertical loading for the a particular value of suction (Wuttke et al., 2012).

Table 2. Variation of ultimate load and slope of initial tangent with soil suction (from Figure 5).

Suction (kPa)	V_m (kN)	R_0 (kN/mm)
0	1.12	0.252
2.1	6.4	0.822
Dry	1.86	0.533

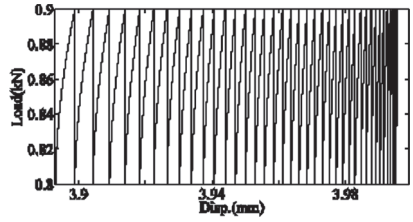

Figure 9. Numerical response of ratchetting behaviour of saturated sand.

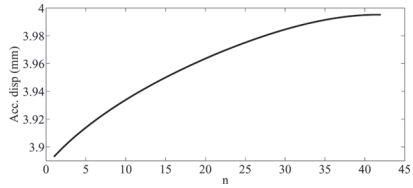

Figure 10. Numerical response of accumulation of plastic displacement of saturated sand with number of cycles (n).

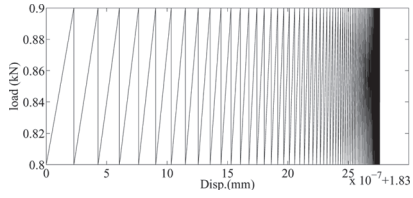

Figure 11. Numerical response of ratchetting behaviour of unsaturated sand with suction 2.1 kPa.

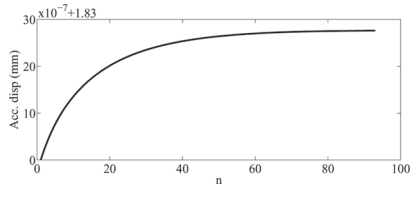

Figure 12. Numerical response of accumulation of plastic displacement of unsaturated sand (2.1 kPa) with number of cycles (n).

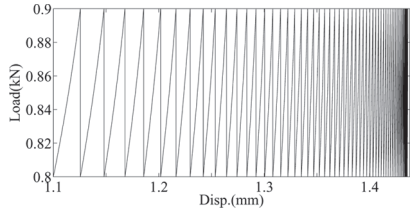

Figure 13. Numerical response of ratchetting behaviour of dry sand.

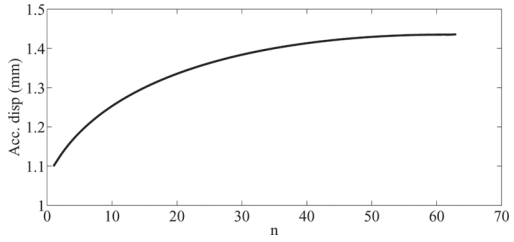

Figure 14. Numerical response of accumulation of plastic displacement of dry sand with number of cycles (n).

Table 3. Parameters associated with the model.

			$\zeta(\psi)$			$\kappa(\psi)$		
λ	α	β	Sat.	Dry	Unsat.	Sat.	Dry	Unsat.
1/3	3	0.95	50	50	8	8	8	50

drained condition. The influence of the suction dependent soil parameters $R_0(\psi)$ and $V_m(\psi)$ over the ratchetting behaviour was observed from the accumulation curve. The unsaturated sand has quantitatively lower accumulation of plastic displacement compared to water saturated and air saturated sand. The higher value of ultimate load $V_m(\psi)$ and the slope of initial tangent $R_0(\psi)$ for the unsaturated sand have shown the significant influence on the accumulation behaviour of the plastic strain during cyclic loading. The influence of soil suction on the cyclic constitutive parameters of the model, $\zeta(\psi)$ and $\kappa(\psi)$ is also observed. The model has shown its competence for simulating the cyclic accumulation of plastic displacement for the change in soil suction. However due to the small number of experimental result the values of constitutive parameters is not obtained for the wide range of suction and for the variety of existing soil type.

ACKNOWLEDGEMENTS

The authors would like to thank the support of the German Research Foundation DFG for funding the Research Training Group GRK 1462.

REFERENCES

Al-Tabbaa, A. & Wood, D.M. 1989. An experimentally based bubble model for clay, Pietruszczak, S. and Pande, G.N. (eds.), *NUMOG III*: 91–99. Niagara Falls: Elsevier applied science.

Bolton, M.D. & Lau, C.K. 1988. Scale effects arising from particle size. Corte´ J.F. (ed.), *Centrifuge 88*: 127–131. Rotterdam: Balkema.

Butterfield, R. & Gottardi, G. 1994. A complete three dimensional failure envelope for shallow footings on sand. *Geotechnique* 44: 181–184.

Cerato, A.B. & Lutenegger, A.J. 2006. Bearing capacity of square and circular footings on a finite layer of granular soil underlain by a rigid base. *J. Geotech. Geoenviron. Eng., ASCE* 132(11): 1496–1501.

Chatzigogos, C.T., Pecker, A. & Salencon, J. 2009. Macroelement modeling of shallow foundations. *Soil Dynamics and Earthquake Engineering* 29: 765–781.

Dafalias, Y.F. & Herrmann, L.R. 1982. Bounding surface formulation. Pande G.N. and Zeinkiewicz, O. C. (eds.), *Soil Mechanics-Transient and cyclic loading*: John Wiley and Sons Ltd.

di Prisco, C., Nova, R. & Sibilia, A. 2002. Analysis of soil-structure interaction of towers under cyclic loading. Pande, G.N. and Pietruszczak, S. (eds.), *NUMOG VIII*: 637–642. Rome: Rotterdam: Balkema.

di Prisco, C. & Pisano, F. 2011. Seismic response of rigid shallow footings. di Prisco, M., La Borderie, C. & Nicot, F. (eds.), *European Journal of Environmental and Civil Engineering*: 185–221. Paris: Lavoisier.

Flavigny, E., Desrues, J. & Player, B. 1990. note technique, le sable d'hostun RF. *Revue Française de Geotechnique* 53: 67–70.

Gottardis, M. & Butterfield, R. 1988. Displacements of footing on sand under eccentric and inclined loads, *Can. Geotech. J.* 25(2), 199–212.

Grange, S. 2008. Modélisation simplifiée3Dde l'interaction sol-structure: application au génie parasismique. Ph. D. Thesis.

Herle, I. & Tejchman, J. 1997. Effects of grain size and pressure level on bearing capacity of footings on sand. Asaoka, A., Adachi, T. & Oka, F. (eds.), *IS-Nagoya'97: Deformation and progressive failure in geomechanics*: 781–786 Pergamon.

Houlsby, G.T. & Cassidy, M.J. 2002. A plasticity model for the behaviour of footings on sand under combined loading, *Geotechnique* 52(2): 117–129.

Kusakabe, O. 1995. Foundations. *Geotechnical centrifuge technology*, R.N. Taylor, (eds.), Blackie Academic and professional, London.

Montrasio, L. & Nova, R. 1997. Settlement of shallow foundations on sand: geometrical effects, *Geotechnique* 47(1): 49–60.

Nova, R. & Montrasio, L. 1991. Settlement of shallow foundations on sand. *Geotechnique*, 41(2): 243–256.

Schanz, T., Lins, Y. & Vanapalli, S.K. 2011. Bearing capacity of a strip footing on unsaturated sand. *Proc., 5th Int. Conf. on Unsaturated soils*: 1195–1200. Barcelona, Spain: Taylor and Francis Group.

Schanz, T. & Vermeer, P.A. 1996. Angles of friction and dilatancy of sand, *Geotechnique* 46(1): 145–151.

Wuttke, F., Kafle, B., Lins, Y. & Schanz, T. 2012. A macroelement for statically loaded shallow strip foundation resting on unsaturated soil. *Int. J. Geomech.* (in Press).

Advances in Unsaturated Soils – Caicedo et al. (eds)
© 2013 Taylor & Francis Group, London, ISBN 978-0-415-62095-6

BEST method: Characterization of soil unsaturated hydraulic properties

L. Lassabatere, R. Angulo-Jaramillo & T. Winiarski
UMR5023 Ecologie des Hydrosystèmes Naturels et Anthropisés, Université Lyon 1, ENTPE, CNRS, Vaulx-en-Velin, France

D. Yilmaz
Centre Scientifique et Technique du Bâtiment, Nantes, France

ABSTRACT: BEST—Beerkan Estimation of Soil Transfer parameters—is an algorithm for estimating the entire set of unsaturated soil hydraulic properties using the inverse analysis of particle size distribution and the water cumulative infiltration curve obtained by the Beerkan method (single ring infiltration test at zero water pressure head). The required both experimental setup and data are presented. BEST physical principles are discussed with regards to both field experimental and analytically generated data. Examples of specific cases are detailed to point at method applicability (i.e., soil-dry initial condition, soils with no hydrophocity). BEST is discussed regarding its ease of use, efficiency and robustness. Perspectives are proposed for its ongoing development and improvement.

1 INTRODUCTION

Modeling water fluxes in the vadose zone linking surface water with groundwater is important for understanding the hydrological cycle and the transfer of water-transported contaminants. Unless preferential flow is involved (Feddes et al., 1988), variably-saturated water flow is usually modeled using the Richards' equation, written as following with cylindrical coordinates:

$$C(h)\frac{\partial h}{\partial t}=\frac{\partial}{\partial r}\left(\frac{K(h)}{r}\frac{\partial h}{\partial r}\right)+\frac{\partial}{\partial z}\left(K(h)\left(1+\frac{\partial h}{\partial z}\right)\right) \quad (1)$$

where h stands for water pressure head, $C(h)$ is the hydraulic capacity corresponding to the derivative of volumetric water content, θ with respect to capillary pressure head, h. In any case, modeling requires knowledge of soil hydraulic properties, such as the water retention curve, $\theta(h)$ and the hydraulic conductivity function, $K(\theta)$.

Analysis of water infiltration experiments has become a widely used practice for obtaining soil hydraulic properties (Perroux & White, 1988). Several experimental devices, often based on the tension disc infiltrometer or in situ lysimeters, have been developed for this purpose. Water infiltration data are then inversely analyzed using either analytical or numerical models (Simunek & van Genuchten, 1996; Mallants et al., 1997; Angulo-Jaramillo et al., 2000).

Among many water infiltration experiments, the Beerkan method, consisting of infiltrating water from a single ring at a zero pressure head (Braud et al., 2005), proved to be a low cost and robust method for characterizing soil hydraulic properties, even at the watershed scale. Lassabatere et al. (2006) proposed the BEST (Beerkan Estimation of Soil Transfer parameters) algorithm for estimating the complete set of unsaturated soil hydraulic properties using the inverse analysis of particle size distribution and the water cumulative infiltration curve obtained by the Beerkan method.

This article aims at presenting BEST method and reviewing its recent improvement. Two main versions were proposed, the original version (Lassabatere et al., 2006) and a new version modified for coarse material (Yilmaz et al., 2010). The main difference between the two methods lies in the inversion algorithm of infiltration, but the physical principles remain the same. Recently, works focused on the improvement and the validation of the inversion procedure using analytical generated data. In addition, a new Graphical User Interface (GUI) has been developed in order to ease the use of BEST algorithm. All these aspects are presented successively with prospects for future development.

2 BEERKAN INFILTRATION EXPERIMENT

2.1 *Beerkan field data*

Beerkan infiltration experiment consists of three types of measurements and sampling: an undisturbed soil core to measure both the initial

volumetric water content, θ_0 ($L^3\ L^{-3}$) and dry bulk density, ρ_b (ML^{-3}); the particle size distribution (PSD) and an axisymmetric water infiltration test. The experimental cumulative infiltration is measured using a ring of a radius r_d, with a constant zero pressure head at the soil surface. A series of known volumes of water ($k = 1$ to n_{tot}, n_{tot} = number of volumes of water) is poured into the cylinder and time is recorded when water has infiltrated into the soil (Figure 1). Experimental data are represented as the cumulative infiltration depth, I_k as a function of time, t_k. It is recommended to perform the experiments at uniform initial volumetric water content less than $0.25\theta_s$.

2.2 *Soil hydrophobicity restriction*

The use of BEST algorithm to estimate unsaturated hydraulic parameters proved to be efficient to characterize several soil-types either at local, plot or catchment scales (Mubarak et al., 2008; 2009a,b; Souza et al., 2008; Lassabatere et al., 2010; Gonzalez-Sosa et al., 2010; Cannavo et al., 2010 and many others). Otherwise, when the soils are extremely dry and/or with high organic matter content, soil hydrophobicity impacts the soil hydraulic behavior. Such effect is depicted in Figure 2. Hydrophobicity reduces flow at the very beginning of infiltration. Once the soil becomes wetter, the hydrophobicity decreases inducing lower resistance to flow, resulting in an increase in infiltration rate. This leads to the specific convex shape (Figure 2, hydrophobic soil) whereas cumulative infiltration should exhibit a concave shape (Figure 2, non-hydrophobic soil). In some cases, hydrophobicity can be strong enough to completely prevent water infiltration. In the case of hydrophobic soils, BEST should not be used even if the restriction $\theta_0 < 0.25\theta_s$ is satisfied.

Figure 1. Beerkan infiltration test at null pressure head.

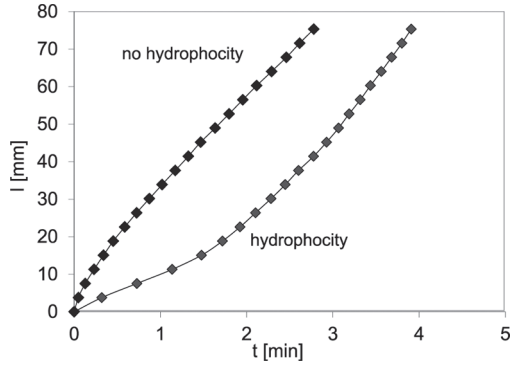

Figure 2. Effect of hydrophobicity on cumulative infiltration on a sandy soil: under dry initial condition (θ_0 = 0.02 $m^3\ m^{-3}$) and for wetter initial condition (θ_0 = 0.10 $m^3\ m^{-3}$); in both cases the condition $\theta_0 < 0.25\theta_s$ is satisfied; BEST can be used only when the soil exhibits no hydrophobicity effect.

3 BEST METHOD

3.1 *BEST-SLOPE algorithm*

The BEST (Beerkan Estimation of Soil Transfer parameters) algorithm (described below) assumes that the soil water retention function, θ (h) referred to as VG-WRF is described using the van Genuchten's equation (van Genuchten, 1980) and hydraulic conductivity function is described by a Brooks and Corey along with Burdine's capillary model:

$$\theta(h) = \theta_r + \frac{(\theta_s - \theta_r)}{\left[1 + (\alpha|h|)^n\right]^m} \tag{2a}$$

$$\frac{K(\theta)}{K_s} = \left(\frac{\theta - \theta_r}{\theta_s - \theta_r}\right)^{\eta} \tag{2b}$$

$$m = 1 - \frac{2}{n} \tag{2c}$$

$$\eta = \frac{2}{n-2} + 3 \tag{2d}$$

where, α ($= h_g^{-1}$) = inverse of scale parameter for the pressure head, θ_r and θ_s = residual and saturated volumetric water contents, respectively, n and m = water retention curve shape parameters, K_s represents the saturated hydraulic conductivity, and η is the shape parameter of hydraulic conductivity relationship.

BEST algorithm assumes that $\theta_r = 0$ (Haverkamp et al., 2006; Leij et al., 2005) and θ_s is known, whether measured in-situ, or estimated from the soil porosity. Then, BEST estimates firstly the

Table 1. Equations for particle size distribution (PSD) and analytical cumulative infiltration model (CI) used in BEST.

$$\text{PSD}\,F(D) = \left[1 + \left(\frac{D_g}{D}\right)^N\right]^{\left(1-\frac{2}{N}\right)} \quad (3)$$

CI—quasi exact implicit model (Haverkamp et al., 1994)

$$\frac{2\Delta K^2}{S^2}t = \frac{1}{1-\beta}\left[\frac{2\Delta K}{S^2}\left(I_{1D} - K_0 t\right)... \right.$$
$$\left. ... - \ln\left(\left(\exp\left(2\beta\frac{\Delta K}{S^2}\left(I_{1D} - K_0 t\right)\right) + \beta - 1\right)\Big/\beta\right)\right] \quad (4a)$$

$$I_{3D} = I_{1D} + AS^2 t \quad (4b)$$

CI—transient model (short time, $t \to 0$)

$$I_{trans}(t) = S\sqrt{t} + \left[BK_s + AS^2\right]t \quad (5)$$

CI—steady state model (asymptotic model, $t \to +\infty$)

$$I_{sst}(t) = \left[K_s + AS^2\right]t + C\frac{S^2}{K_s} \quad (6)$$

CI—maximum time for validity of transient model

$$t_{\max} = \frac{1}{4(1-B)^2}t_{grav} \quad (7a)$$

$$t_{grav} = \frac{S^2}{K_s^2} \quad (7b)$$

CI—model constants

$$A = \frac{\gamma}{r_d \Delta\theta} \quad (8a)$$

$$B = \left(\frac{2-\beta}{3}\right)\left(1 - \left(\frac{\theta_0}{\theta_s}\right)^\eta\right) + \left(\frac{\theta_0}{\theta_s}\right)^\eta \quad (8b)$$

$$C = \frac{1}{2(1-\beta)\left(1 - \left(\frac{\theta_0}{\theta_s}\right)^\eta\right)}\ln\left(\frac{1}{\beta}\right) \quad (8c)$$

hydraulic shape parameters (i.e. *n, m* and η) from the analysis of both soil porosity and particle size distribution and secondly the scale parameters (i.e., α or h_g and K_s) from the analysis of cumulative infiltration. The experimental PSD is fitted to Eq. (3) to derive the textural shape parameter *N* and the related texture shape index (Haverkamp et al., 2006) (Figure 3). Hydraulic parameter *n* is deduced from the value of texture shape parameter through pedotransfer functions detailed in Lassabatere et al. (2006).

Steady state infiltration rate, $q_{+\infty}$, is estimated through fitting the steady state model (Eq. 6) on the *i* last points of the experimental infiltration curve; by default $i = 3$. Then, the transient model (Eq. 5) is fitted to the experimental cumulative infiltration in order to estimate the sorptivity *S* (Figure 4). The model inversion is performed assuming the following relation between sorptivity, *S* and saturated hydraulic conductivity, K_s:

$$K_s = q_{+\infty} - AS^2 \quad (9)$$

The best-fit is performed incrementally for truncated datasets with *k* data points ((t_1, I_1) … (t_k, I_k)) with $k \le n_{tot}$ (Lassabatere et al., 2006). For each subset, optimum values of S_k, $K_{s,k}$ and $t_{max,k}$ are calculated and by a iterative selection process, the final value *S* and K_s are chosen for the largest t_k that fulfills the condition $t_k \le t_{max,k}$; t_{max} denotes the limit validity time of the transient flux equation (Table 1, Eq. 7).

Finally, the retention curve scale parameter, h_g, is calculated using the following equation:

$$h_g = -\frac{S^2}{c_p K_s\left(\theta_s - \theta_0\right)\left[1 - \left(\frac{\theta_0}{\theta_s}\right)^\eta\right]} \quad (10)$$

Where c_p = a proportionality constant calculated from shape parameters of the soil hydraulic functions (Lassabatere et al., 2006). Then, the set of hydrodynamic parameters (i.e., *n, m,* η, α, K_s, θ_r and θ_s) and the related hydraulic characteristic

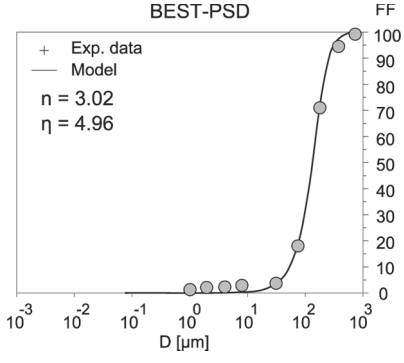

Figure 3. Particle size distribution PSD measured and fitted model and hydraulic shape parameters using BEST for a sandy soil.

curves are completely determined. This method is referred to as BEST-SLOPE since it uses the slope of the steady state model to define a constraint between sorptivity S and saturated hydraulic conductivity K_s during the inversion procedure.

3.2 *BEST-INTERCEPT algorithm*

The use of BEST-SLOPE algorithm has proven adequate in many cases. Yet, in certain cases, this algorithm led to erroneous negative values for saturated hydraulic conductivity. This results from the subtraction of too large value for AS^2 to steady state infiltration rate $q_{+\infty}$ in Eq. (9). This may occur when $AS^2 >> K_s$ and when $q_{+\infty}$ is underestimated, in particular for coarse soils (Yilmaz et al., 2010). Under such conditions, Eq. (9) is inappropriate.

Instead of considering the slope of the cumulative infiltration, the BEST-INTERCEPT method considers the intercept, $b_{+\infty}$ of the steady state model Eq. (6) to fix the relationship between sorptivity, S and saturated hydraulic conductivity, K_s (Figure 4):

$$K_s = \frac{C S^2}{b_{+\infty}} \tag{11}$$

Eq. (11) constraint between S and K_s avoids negative values for the estimation of K_s. This version of BEST is found to be less sensitive to experimental errors, in addition to being more robust and able of performing an efficient inverse analysis of cumulative infiltration for coarse soils.

3.3 *Analytical validation of BEST algorithms*

Infiltration data were generated using the quasi-exact implicit analytical model (Table 1, Eqs. 4) for a unit reference sorptivity, S_{ref} and saturated hydraulic conductivity, $K_{s,ref}$ to be used as reference data. We suppose dry initial conditions and K_0 as negligible. Then, the whole reference infiltration was truncated to provide different data subsets. The calculations were also performed for several r_d values. For the largest, quasi infinite radius, cumulative infiltration corresponds to 1D water infiltration. The smallest radius was taken as one fifth of the scale parameter for water pressure head, h_g, which is quite usual for most field studies.

Figure 6 depicts the evolution of the ratio between estimated and target values in function to the maximum time of the infiltration subset. Time is scaled using the gravity time t_{grav} defined by Philip (1969). If steady state is not reached ($t^* < 5$, Figure 6), estimations of steady state slope and intercept are erroneous (data not shown) and K_s and S are misestimated. In particular, K_s can be overestimated by several orders of magnitude. Overestimation of K_s, and underestimation of S, lead to significant underestimations of water pressure head scale-parameter, h_g (see Eq. 10). In opposite, when steady state is reached and $t^* > 5$, R_S and R_K tend towards unity for both BEST-SLOPE and BEST-INTERCEPT proving that the estimations of S, K_s and then h_g are accurate.

Moreover, it can be shown that the disc radius plays an important role (data not shown) regarding the choice of the method. Better estimations are obtained with BEST-INTERCEPT for very small disc radii and with BEST-SLOPE for larger radii. Indeed, in all cases, both BEST algorithms can be considered as trustful with errors less than

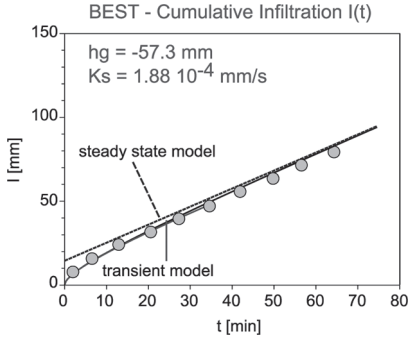

Figure 4. Fitting transient model Eq. (5) and steady state model Eq. (6) to cumulative infiltration data and estimation of hydraulic scale parameters of a sandy soil.

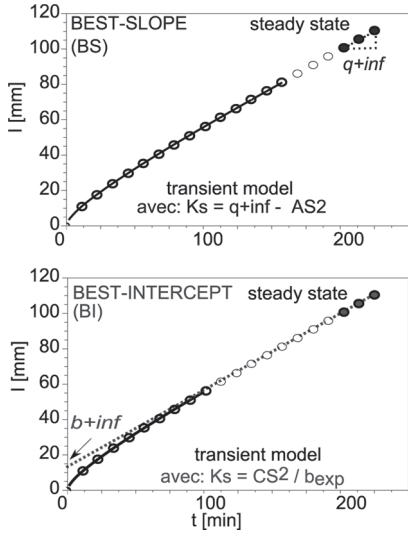

Figure 5. BEST-SLOPE and BEST-INTERCEPT for the analysis of cumulative infiltration coarse material.

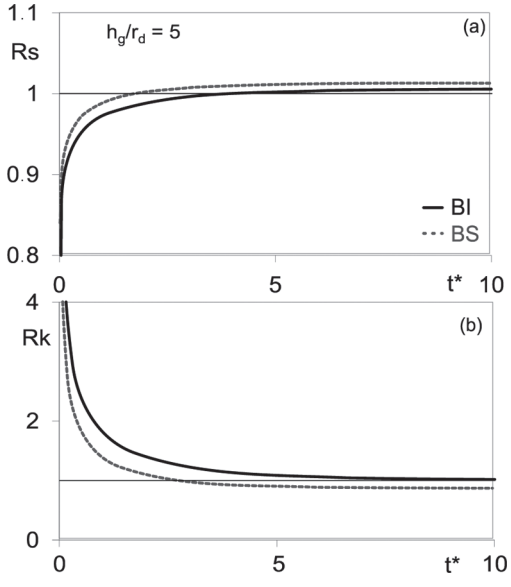

Figure 6. Analytical validation: ratios estimations / target values for sorptivity (R_S) and saturated hydraulic conductivity (R_K) in function to the truncation non-dimensional time of cumulative infiltration data $t = t_{max}/t_{grav}$ (Eq. (7b)).

5% on both sorptivity and hydraulic conductivity, provided that steady state is reached.

4 GRAPHIC USER INTERFACE, GUI

A GUI (Graphical User Interface) was developed to ease the use of BEST. BEST was encoded in the Windows® environment using Scilab free software (Campbell et al., 2006). BEST is available from the authors of this paper upon request, for the two versions BEST-SLOPE and BEST-INTERCEPT (Figure 7; Lassabatere & Angulo-Jaramillo, 2012). The inputs (i.e. dry bulk and mineral densities, initial volumetric water contents, disc radius, PSD and cumulative infiltration) are introduced as a "input.txt" file. The user opens and launches BEST file through the Scilab editor interface. Then the user follows step by step the instructions printed on dialog boxes. BEST ask first for the location of the input file. Then, the user selects the data to be fitted to PSD model. Aftermath, the user selects also the water infiltration data to be fitted to the transient and steady states models. Eventually, the cumulative infiltration can be truncated and reinitialized at the beginning in case of unusual strong infiltration for the one or two first volumes of water. After the process, the results are printed out

Figure 7. Example of BEST-GUI windows for visualization of data, simulated infiltration and results of estimated unsaturated hydraulic parameters (Lassabatere & Angulo-Jaramillo, 2012).

as graphs dialog boxes. All calculated parameters and user's choices are saved into a "result.txt" file.

5 CONCLUSIONS

BEST algorithms aim at the analysis of single-ring water infiltration experiments under null water pressure head (the so-called Beerkan method) for the complete estimation of soil hydraulic parameters. It proposes a robust, easy and inexpensive method. This article reviews the versions from Lassabatere et al. (2006) and Yilmaz et al. (2011). Then, the algorithms are validated against experimental and analytically generated data, which helps in pointing out at some limitations. At last, the article presents the recent developments and the ongoing works. BEST seems to be a promising, low cost and efficient method to get the complete set of soil hydraulic parameters. This is the first step required for the modeling of water infiltration in the vadose zone and for the understanding of water cycle at the catchment scale.

ACKNOWLEDGEMENTS

This work was partially supported by the French Ministry of Ecology as part of the research project "Formation and evolution of an anthropogenic soil and evaluation of its filtration function" of the research program GESSOL 3.

REFERENCES

Angulo-Jaramillo, R., Vandervaere, J.-P., Roulier, S., Thony, J.-L., Gaudet, J.-P. & Vauclin, M. 2000. Field measurement of soil surface hydraulic properties by disc and ring infiltrometers: A review and recent developments. *Soil Till. Res.* 55: 1–29.

Braud, I., de Condappa, D., Soria, J.M., Haverkamp, R., Angulo-Jaramillo, R., Galle, S. & Vauclin, M. 2005. Use of scaled forms of the infiltration equation for the estimation of unsaturated soil hydraulic properties (the Beerkan method). *European J. Soil Sci.* 56: 361–374.

Campbell, S.L., Chancelier, J.-P. & Nikoukhah, R. 2006. *Modeling and Simulation in Scilab, Scicos*. Springer: Paris.

Cannavo, P., Vidal-Beaudet, L., Bechet, B., Lassabatere, L. & Charpentier, S. 2010. Spatial distribution of sediments and transfer properties in soils in a stormwater infiltration basin. *J. Soil Sed.* 10: 1499–1509.

Feddes, R.A., Kabat, P., van Bakel, P.J.T., Bronswijk, J.J.B. & Halbertsma, J. 1988. Modelling soil water dynamics in the unsaturated zone—state of the art. *J. Hydrol.* 100: 69–111.

Gonzalez-Sosa, E., Braud, I., Dehotin, J., Lassabatere, L., Angulo-Jaramillo, R., Lagouy, M., Branger, R., Jacqueminet, C., Kermadi, S. & Michel, K. 2010. Impact of land use on the hydraulic properties of the top soil in a french catchment. *Hydrol. Proc.* 24: 2382–2399.

Haverkamp, R., Debionne, S., Viallet, P., Angulo-Jaramillo, R. & de Condappa, D. 2006. Soil properties and moisture movement in the unsaturated zone: 6.1–6.59. In J.W. Delleur (ed.), *The handbook of Groundwater Engineering*. CRC: Boca Raton.

Lassabatere, L. & Angulo-Jaramillo, R. 2012. BEST-Beerkan Estimation of Soil Transfer parameters software, *University of Lyon, Laboratoire d'Ecologie des Hydrosystèmes Naturels et Anthropisés, LEHNA UMR 5023 CNRS, ENTPE, UCB-Lyon 1*, January, Vaulx-en-Velin; software available for free: laurent.lassabatere@entpe.fr or angulo@entpe.fr.

Lassabatere, L., Angulo-Jaramillo, R., Goutaland, D., Letellier, L., Gaudet, J.P., Winiarski, T. & Delolme, C. 2010. Effect of the settlement of sediments on water infiltration in two urban infiltration basins. *Geoderma* 156: 316–325.

Lassabatere, L., Angulo-Jaramillo, R., Soria Ugalde, J.M., Cuenca, R., Braud, I. & Haverkamp, R. 2006. Beerkan estimation of soil transfer parameters through infiltration experiments—BEST. *Soil Sci. Soc. Am. J.* 70: 521–532.

Lassabatere, L., Angulo-Jaramillo, R., Soria-Ugalde, J. M., Simunek, J. & Haverkamp, R. 2009. Numerical evaluation of a set of analytical infiltration equations. *Water Resour. Res.* 45; W12415.

Leij, F. J., Haverkamp, R., Fuentes, Zatarain, F. & Ross, P.J., 2005. Soil Water Retention. *Soil Sci. Soc. Am. J.* 69: 1891–1901.

Mallants, D., Jacques, D., Tseng, P.-H., van Genuchten, M.T. & Feyen, J. 1997. Comparison of three hydraulic property measurement methods. *J. Hydrol.* 199: 295–318.

Mubarak, I. Mailhol, J.C., Angulo-Jaramillo, R., Ruelle, P., Boivin, P. & Khaledian, M. 2009a. Temporal variability in soil hydraulic properties under drip irrigation. *Geoderma* 150: 158–165.

Mubarak, I. Mailhol, J.C., Angulo-Jaramillo, Bouarfa, S. & Ruelle, R. 2009b. Effect of temporal variability in soil hy-draulic properties on simulated water transfer under high-frequency drip irrigation. Agricultural Water Management 96: 1547–1559.

Philip, J.R. 1969. Theory of infiltration. *Adv. Hydroscience* 5: 215–296.

Perroux, K.M. & White, I. 1988. Designs for Disc Permeameters. *Soil Sci. Soc. Am. J.* 52: 1205–1215.

Simunek, J. & van Genuchten, M.Th., 1996. Estimating Unsaturated Soil Hydraulic Properties from Tension Disc Infiltrometer Data by Numerical Inversion. *Water Resour. Res.* 32: 2683–2696.

Souza, E.S., Antonino, A.C.D., Angulo-Jaramillo, R.A. & Maciel Netto, A. 2008. Caracterização hidrodinâmica de solos: Aplicação do método Beerkan. *Revista Brasileira de Engenharia Agrícola e Ambiental* 12(2): 128–135. (in Portuguese)

van Genuchten, M.Th. 1980. A closed form equation for predicting the hydraulic conductivity of unsaturated soils. *Soil Sci. Soc. Am. J.* 44: 892–898.

Yilmaz, D., Lassabatere, L., Angulo-Jaramillo, R., Deneele, D. & Legret, M. 2010. Hydrodynamic Characterization of Basic Oxygen Furnace Slag through an Adapted BEST Method. *Vadose Zone J.* 9: 107–116.

Advances in Unsaturated Soils – Caicedo et al. (eds)
© 2013 Taylor & Francis Group, London, ISBN 978-0-415-62095-6

Unsaturated flow of unfrozen water in frozen soils

A. Shastri & M. Sanchez
Texas A&M University, College Station, USA

A. Lizcano
Geotechnical Engineering, SRK Consulting, Canada

ABSTRACT: The permanently frozen ground in the northern latitudes is known as permafrost. The behavior of frozen soils has some particular features that go beyond the classical soil mechanics theory. Some typical problems associated with them are (amongst others): frost heaving and thaw settlement. Civil infrastructure and buildings in frozen areas are strongly affected by such kind of phenomena. A good understanding of the water transfer process in frozen soils and its interaction with the mechanical problem are crucial for describing correctly the permafrost behavior. In frozen soils the void space is partially filled by ice and partially filled by unfrozen water. The amount of unfrozen water in a frozen soil depends on a number of factors, such as: freezing temperature, type of soil and void size. The ability of a frozen soil to retain unfrozen water can be related to the cryogenic suction (i.e. difference between the ice and liquid pressures). The flow of unfrozen water in frozen soils can be explained using concept of unsaturated water flow in soils. This paper focuses mainly on the transfer of unsaturated water in frozen soils and its modeling. The approach is based on a formulation for unsaturated soils, which has been adapted to the particular conditions of frozen soils. Laboratory tests related to the flow of unfrozen water in permafrost are analyzed and discussed.

1 INTRODUCTION

Geotechnical investigations on the behavior frozen soils have received particular attention for the last six decades. Permafrost underlies about 24% of the Northern hemisphere landmass and the resource and transport development in these areas requires the performance of major engineering works. Engineering problems include, freezing of foundations, thawing settlement/distress, glacial and periglacial slope movements, construction of roads, railways, bridges and pipelines to transport essential commodities including oil. These effects are also important in lieu of effects of global warming which could potentially alter regions that were once permanently frozen.

Originally it was understood that the behavior of frozen soil is only a consequence of the expansion caused due to phase transformation of water to ice. It was then theorized (Taber, 1929), water may be present well below freezing temperature. This was later quantified by Beskow (1935) and Everett (1961) and experimentally proved by Tice et al. (1988), using the pulse nuclear magnetic resonance technique. The movement of this "unfrozen water" is attributed to be one of the causes of frost heave and the formation of ice lens in the soil. It is also seen to a have major influence on the thermal and hydraulic behavior of the frozen soil. Therefore studying this migration of the unfrozen water forms an essential component in understanding frozen soil behavior.

There have been several streams of work which have been conducted to replicate the behavior of frozen soils based on the equilibrium between the frozen and unfrozen components. These include the hydrodynamic model (Harlan, 1973), the rigid ice model (Miller, 1978), the segregation potential model (Konrad & Morgenstern, 1981) based on this relation.

The interaction between the frozen and unfrozen components in frozen soils was observed to be similar to the interaction between the phases of (unfrozen) unsaturated soils. The representation of the three phases for the unfrozen unsaturated soils and frozen soil is seen in Figure 1. The cryogenic suction can be defined as the excess of the ice pressure over liquid pressure. Clausius–Clapeyron equation can be used to relate temperature, liquid and pressures.

A coupled thermo-hydro mechanical (THM) framework for frozen soils based on the behavior of unsaturated soils was proposed by Nishimura et al., (2008). Previous studies (Thomas et al., 2009, Selvadurai et al., 1999, Nishimura et al., 2008) were mainly focused on systems which have (unlimited)

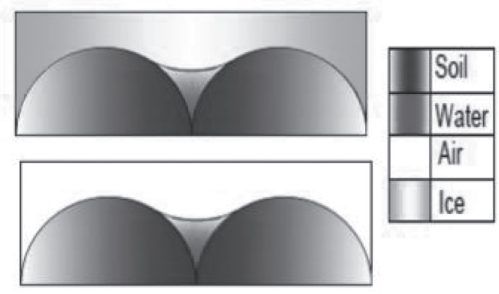

Figure 1. The three phases in frozen soils (top) and unfrozen unsaturated soils (bottom).

access to free water (open system). There is limited information about systems which do not have the access to free water (closed system).The current work focuses on the movement of unfrozen water in frozen soils in closed system. For hat end the numerical program CODE_BRIGHT (Olivella et al., 1996) has been adapted to deal with the presence of ice and unfrozen water in porous media.

2 FLOW MODELING IN UNFROZEN SOILS

The similarity found between the behavior of frozen soils and the behavior of unsaturated unfrozen soils is well observed and documented (e.g. Thomas et al., 2009, Liu and Yu 2011). Noting this similarities Nishimura et al. (2009), proposed a coupled THM formulation to model the behavior of frozen soils.

The equilibrium of the chemical potentials between liquid water and ice phases is described by the Clausius–Clapeyron equation, which can be expressed as

$$-(s_1 - s_2)dT + v_1 dP_1 - v_2 dP_2 = 0 \tag{1}$$

where s and v are the specific entropy and the specific volume respectively, T is the temperature on the thermodynamic scale, P is the pressure, subscripts 1 and 2 represent the two phases. The differential form can be integrated using atmospheric pressure and the temperature 273.15 K as references, to give

$$P_i/\rho_i - P_l/\rho_l = l \ln\left(T/273.15\right) \tag{2}$$

where P_i and P_l are the ice and liquid water pressures respectively, T is in °K, ρl is the liquid density, ρ_i is the ice density, and l is the latent heat of fusion.

The freezing characteristic curve relates the degree of saturation of the unfrozen water to the difference in the pressure of the ice and liquid water, which is designated as cryogenic suction 's' (i.e. $s = P_i - P_l$). The van Genuchten (1980) model has been employed here to represent the freezing characteristic function given by,

$$S_l = \left[1 + \left(\left(P_i - P_l\right)/P\right)^{1/1-\lambda}\right]^{\lambda} \tag{3}$$

where, S_l is the degree of saturation of unfrozen water, P and λ are model parameters.

Mass conservation of pore water is expressed as,

$$\partial/\partial t\left(\rho_l S_l \phi + \rho_i S_i \phi\right) + \nabla\left(\rho_l \mathbf{q}_l\right) = f^w \tag{4}$$

where, ϕ is the porosity, q_l is the liquid flux and f^w is the water sink/source term. The flux is calculated from Darcy's law as,

$$\mathbf{q}_l = k_{rl}/\mu_l \,\mathbf{k}\left(\nabla P_l - \rho_l \mathbf{g}\right) \tag{5}$$

where, k_{rl} is the relative permeability, μ_l is the viscosity, and k is the intrinsic permeability. The liquid relative permeability depends on the degree of saturation through, for example, the cubic law given as follows,

$$k_{rl} = S_l^{\lambda} \tag{6}$$

where, λ is a model. The viscosity of liquid (μ_l in [Pa s]) is calculated using the following expression.

$$\mu_l = 2.1\text{x}10^{-6} \exp\left(\frac{1808.5}{273.15 + T}\right) \tag{7}$$

The mathematical formulation is completed with the balance of internal energy as detailed in Olivella et al. (1994). A main assumption behind the mass balance of energy is that thermal equilibrium between the three phases (i.e. solid, ice and liquid).

A schematic representation of a frozen ground with a possible variation of temperature in depth is presented in Figure 2. The minimum temperature is acting at the ground surface, a temperature equal to zero °C is assumed at the top of the unfrozen zone (i.e. at the contact between partially frozen zone and the unfrozen one), and a linear variation of temperature (joining these two points) is also assumed. Obviously, actual (changing) conditions may vary from this hypothetical case.

The probable distribution of liquid pressure, ice pressures, liquid and ice saturations resulting from

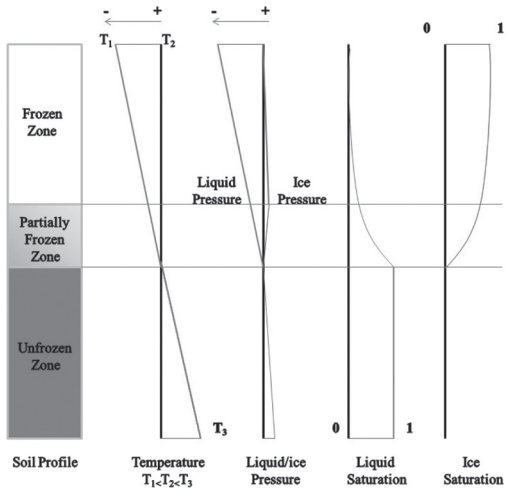

Figure 2. Schematic representation of a frozen soil profile; showing a tentative variation of temperature in depth, alongside with the variation of liquid and ice pressure, and liquid and ice saturations

the assumptions presented above are also presented in Figure 2 (e.g. obtained after working with equations 2 and 3).

Three zones can be distinguished: i) the frozen zone, where the soil is completely frozen (and ice saturation is nearly equal to one); ii) the unfrozen zone, where the soil is partially saturated with ice and liquid; and iii) the unfrozen zone where the unfrozen water takes place in the unfrozen zone.

The significant gradients of liquid pressure generally develop in natural freezing conditions drive the movement of unfrozen water in frozen soils. The following section presents an already published experimental campaign looking at the flow of water in frozen soils.

3 LABORATORY TESTS ON FROZEN SAMPLES

Xu et al. (1998) investigated the mechanism of frost heave and salt expansion in soils primarily found in regions in and around China. The experimental setup analyzed here is based on the water migration in freezing soils for a closed system (Xu et al., 1998).

The properties of the soil specimen used for this test are given in Table 1. Details of the experimental preparation are provided in Xu et al. (1998). Remolded Lanzhou Sand was first air dried and mixed with distilled water to reach the desired water content.

Water seepage was prevented by wrapping the soil in a plastic film. The soil was then consolidated for three days. Soil columns were then cut down to 12 cm to be used for testing. The samples were then placed in a constant temperature chamber.

Thermocouples were fixed at every 2 cm along the wall of the soil box. The perimeter of the box was insulated using a 10 cm thick insulation material. The temperature of the soil sample was controlled using plates at the top and the bottom of the sample. A linear temperature gradient was applied. The linear profile of temperature was established across the soil specimens as shown in Figure 3.

Similar experiments were performed for Mongolian sand, silt and clayey soil samples, but the samples were cut to 15 cm. The properties of the silt and the Lanzhou samples are listed in Table1.

The final water content of the sample was determined for the samples at different depths. Figure below show some typical results from Xu et al. (1998) study. The observation for the samples for the silt sample is shown in Figure 4. It can observe that, the flow rate is greater at high temperature end of the samples and the flow rate recedes with

Table 1. Properties of soil samples used on the experiment.

Property	Silt	Lanzhou sand
Salinity (%)	0.3	0.3
Dry density ρ_d (g/cm^3)	1.56	1.52
Initial water content (%)	23.23	15.99
Temperature gradient grad θ (°C/cm)	0.26	0.13
Specific gravity	2.71	2.71

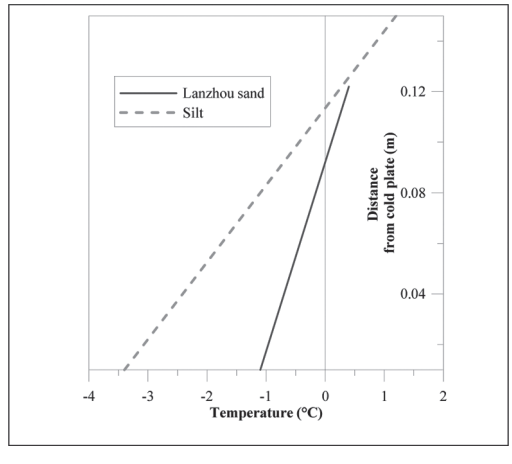

Figure 3. Linear profile of temperature for silt and Lanzhou sand.

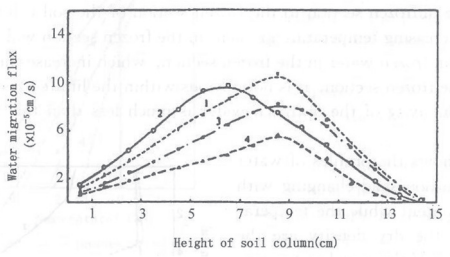

Figure 4. Variation of water migration for different silt samples.

a decrease in temperature. The following section focuses on the modeling of some of these experiments.

4 CASE STUDY MODELING

The finite element analyses were conducted to replicate the conditions in the silt and Lanzhou sand samples (Xu et al., 1998). As mentioned, the program CODE_BRIGHT was used for the numerical simulations. Figure 5 presents a schematic representation of the solved problem together with the mesh adopted for the numerical simulations (366 elements for the case of the Lanzhou sand).

Table 2 presents the parameters adopted for the retention curve (3), intrinsic permeability (5) and relative permeability (6). The parameters have been back calculated from the experiments.

Figure 6 presents the variation of the relative permeabilities (both liquid and ice) with the degree of saturation based on the cubic law (6).

The variation of degree of saturation with cryogenic suction represented through the retention curve for Lanzhou sand and silt are shown in Figure 7.

The comparison of the flux across the samples for the model and test data is shown in Figures 8 and 9 for the silt and Lanzhou sand respectively. The modeling results of the flow rate are seen to be in concurrence with the experimental results

The decrease is attributed to the formation of a greater fraction of ice, thereby reducing the degree of water saturation in the soil. The drop in the degree of saturation reduces the relative permeability and lowers the flow rate

The comparison of the behavior of the silt and Lanzhou samples it can be seen that the water migration is higher in the Lanzhou sand. The Lanzhou sand is seen to have a more open structure and produces a higher flow rate. However despite an increase in the intrinsic permeability, the higher suction produced as a result of higher temperature gradient in the silt produces a large flow rate.

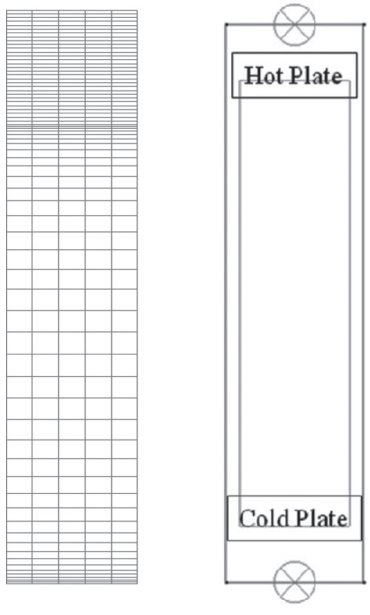

Figure 5. Finite element mesh and the schematic representation of the numerical model.

Table 2. Model Parameters.

Equation	Parameters designation	Silt	Lanzhou sand
Retention Curve	P (MPa)	4.2	1.3
	λ	0.63	0.84
Intrinsic permeability	k (m^2)	4.0E-18	9.8E-18
Relative permeability	λ	3	3

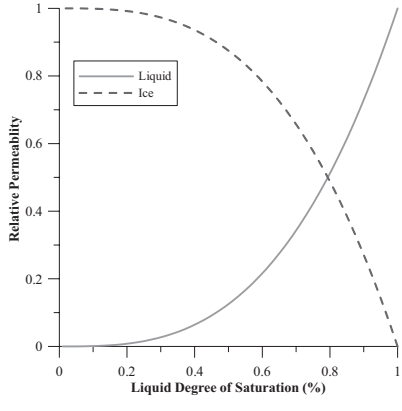

Figure 6. Variation of relative permeability with the degree of saturation.

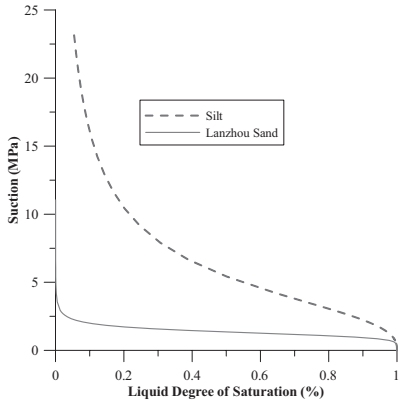

Figure 7. Retention curve for silt and Lanzhou sand.

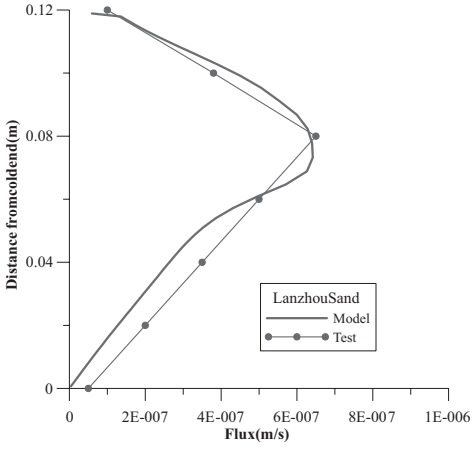

Figure 8. Comparison of flow rates for model and test data for Lanzhou sand sample.

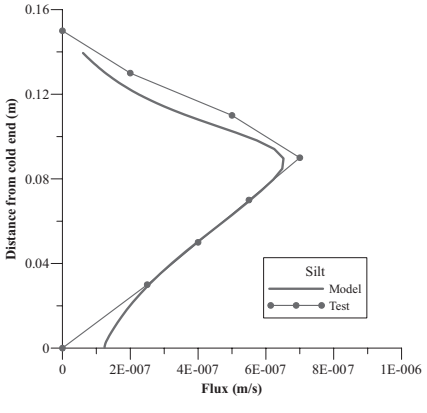

Figure 9. Comparison of flow rates for model and test data for silt sample.

5 CONCLUSIONS

This paper analyses the flow of unfrozen water in frozen soils. The partial liquid saturation in frozen soils can be expressed in term of cryogenic suction. The movement of liquid water in frozen soils can be modeled by a generalized Darcy law which depends on the intrinsic permeability and a relative permeability. The transfer of liquid water is driven by the gradient of cryogenic suction. Already published experiments on frozen samples have been modeled using the concepts explained above. To that end, a formal coupled thermo-hydraulic framework based on balance equations has been used in this work. The comparisons between models result and experimental observation shows that the proposed approach captures the main tendencies observed in the experimental campaign

REFERENCES

Beskow, G. (1935). "Soil Freezing and Frost Heaving with Special Reference to Roads and Railroads." The Swedish Geological Society.

Everett, D. (1961). "The thermodynamics of frost damage to porous solids." Trans. Faraday Soc., 57(0), 1541–1551.

Harlan, R. (1973). "Analysis of coupled heat-fluid transport in partially frozen soil." Water Resources Research, 9(5), 1314–1323.

Konrad, J.M. and Morgenstern, N.R. (1981). "The segregation potential of a freezing soil." Canadian Geotechnical Journal, 18(4), 482–491.

Miller, R. "Frost heaving in non-colloidal soils." 708–713.

Nishimura, S., Gens, A., Olivella, S. and Jardine, R. (2009). "THM-coupled finite element analysis of frozen soil: formulation and application." Geotechnique, 59(3), 159–171.

Olivella, S., Gens, A., Carrera, J. and Alonso, E. (1996). «Numerical formulation for a simulator (CODE_ BRIGHT) for the coupled analysis of saline media.» Engineering computations, 13(7), 87–112.

Taber, S. (1929). «Frost heaving.» The Journal of Geology, 428–461.

Tice, A., Black, P. and Berg, R. (1988). «Unfrozen water contents of undisturbed and remolded Alaskan silt as determined by nuclear magnetic resonance.» Army Cold Regions Research and Engineering Lab., Hanover, NH (USA).

Thomas, H., Cleall, P., Li, Y., Harris, C. and Kern-Luetschg, M. (2009). «Modelling of cryogenic processes in permafrost and seasonally frozen soils.» Geotechnique, 59(3), 173–184.

Xu, X., Wang, J., Zhang, L., Deng Y. (1999), «Mechanisms of Frost Heave and Salt Expansion» of Soils» Science Press.

This page intentionally left blank

Advances in Unsaturated Soils – Caicedo et al. (eds)
© 2013 Taylor & Francis Group, London, ISBN 978-0-415-62095-6

Probabilistic analyses of slope stability under infiltration conditions

I.F. Otálvaro
Pontificia Universidad Javeriana Seccional Cali, Cali, Colombia

M.P. Cordão-Neto
Universidade de Brasília, Brasília, Brasil

ABSTRACT: One of the most important causes of landslides in tropical zone is infiltration due to rainfall. In this case, slope stability analyses are usually done by deterministic methods. Nowadays, papers and reports which combine Limited Equilibrium Method (LEM) and Finite Element Method (FEM) are more common. In this paper, FEM is used to analyze seepage problem and LEM is used to determine safety factor. In addition, associating probabilistic analyses to LEM and FEM can improve the results and lead to a better understanding of landslides induced by rainfall. Thus, the First Order Second Moment (FOSM) method is used to quantify the influence of mechanical and hydraulic parameters in safety factor. Furthermore, the porewater pressure field is determined by SEEP/W (Geo-slope International, 2004a) and used as input in LEM analyses. Results show that the influence of each parameter in safety factor changes with time during the infiltration process.

1 INTRODUCTION

Several natural disasters associated with climate change, such as floods and landslides, happen in Latin American cities. Landslides are induced by different causes, including heavy rainfall or long rain seasons. In the latter, a better understanding about how rainfall, infiltration and landslides are related is required.

Geotechnical tools used in landslides analyses were improved in the last decades. Constitutive and numerical models are now able to analyze different kind of boundary problems. In addition, laboratory techniques are cabled to characterize hydraulic and mechanical behavior of soils. However, current knowledge and new techniques are not applied very often on landslide warning systems, for example.

Thus, in this paper, a slope stability analyze of hypothetical example is presented. Heavy rainfall is applied as boundary condition and it triggers a failure mechanism.

Two commercial softwares are used to determining the porewater pressure field and safety factor. Furthermore, a probabilistic method is used to quantify the influence of hydraulic and mechanical parameters in safety factor and also include a second index of the safety factor as a criterion for decision. Thus, the safety factor and reliability index of that analysis can be incorporated in the planning of landslide warning systems.

2 PROBABILISTIC METHOD

Uncertainty is always present in geotechnical analysis. Natural variability of the soil or limited knowledge of its behavior is reflected in the constitutive models used to their representation. According to Mašín (2009), these uncertainties are in geotechnical engineering commonly accounted for using deterministic concepts, such as scaling the uncertain values of material parameters to calculate different safety factors. However, this approach giving a false security in some cases because it ignores the uncertainty of the variables involved. At present, different probabilistic methods to evaluate the effects of variability are performed.

Probabilistic methods are normally used to evaluate statistical distribution of a performance function $Y = g(X_1, X_2, \ldots, X_n)$ based on known statistical features of input variables Xi. Due to its complexity, the probabilistic methods can be classified into three categories: methods which do not consider spatial randomness of input variables, methods which consider spatial variability of input variables and hybrid methods. Methods which neglect spatial variability are commonly used in stability analysis. The most popular are the Monte Carlo method (MCM), the First Order Second Moment method (FOSM) and the Point Estimate method (PEM).

Simulations using MCM are employed to solve problems by generating suitable random numbers

(or pseudo-random numbers), evaluating the dependent variable for a large number of possibilities. The MCM involves and defines the variables which generate uncertainty and probabilistic distribution function (pdf). Also, it determines the value of this function using variable values randomly obtained considering the pdf. This is repeated until there is sufficient data to assemble the probabilistic distribution function. The number of required trials for Monte Carlo method depends on the confidence level of the solutions, as well as the number of considered variables (Harr, 1987).

Rosenblueth (1975, 1981) proposed the PEM method to provide approximation of the low-order moments for the dependent variables starting from the low-order moments of the independent variable x. In the PEM method, all possible combinations for two-point estimate for each independent variable are made.

The FOSM method is an approximate approach based on Taylor's series expansion of the performance function $g(X_1, X_2, \ldots, X_n)$ around its mean value. The FOSM method is described in more detail below.

2.1 *First-order second-moment (FOSM) method*

The FOSM method is an approximate approach based on Taylor's series expansion of function $g(X_1, X_2, \ldots, X_n)$. g is function of a number of input variables X_n which represent uncertainty parameters. For uncorrelated input variables, the mean and variance of the function are given by Equations (1) and (2), respectively:

$$E[Y] \cong g\left(E[X_1], E[X_2], \ldots, E[X_n]\right) \tag{1}$$

$$\sigma^2[Y] \cong \sum_{1}^{n}\left(\frac{\partial g}{\partial X_i}\right)^2 \cdot \sigma^2[X_i] \tag{2}$$

where $E[-]$ = mean; $\sigma^2[-]$ = variance. Equation (2) requires the values of some partial derivatives. For most geotechnical models, the analytical evaluation of the derivatives is complex. Thus, Finite Difference Method (FDM) is used to calculate that partial derivatives and any of the following forms (forward, backward or central differences) can be used in this:

$$\frac{\partial g^F}{\partial X_i} \approx \frac{g(E[Xi] + \Delta Xi) - g(E[Xi])}{\Delta Xi} \tag{3}$$

$$\frac{\partial g^B}{\partial X_i} \approx \frac{g(E[Xi]) - g(E[Xi] - \Delta Xi)}{\Delta Xi} \tag{4}$$

$$\frac{\partial g^C}{\partial X_i} \approx \frac{g(E[Xi] + \Delta X) - g(E[Xi] - \Delta Xi)}{2\Delta Xi} \tag{5}$$

where ΔXi = increment. The derivative at a point is more precisely evaluated using very small increments. According to Wolff (1994), evaluating the derivative in a range of plus and minus one standard deviation may capture better the nonlinear behavior of the function in a range of likely values. However, this increase may be excessive in some cases. The increments and decrements the variable should be small, this ensures adequate accuracy.

2.2 *Reliability index*

The most effective application of probability theory to the analysis of slope stability has stated the uncertainties as a reliability index (Christian et al., 1994), which is defined as:

$$\beta = \frac{E[Y] - 1}{\sigma^2[Y]} \tag{6}$$

where β = reliability index. The reliability index describes safety by the number of standard deviations separating the best estimate of $E[Y]$ from its defined failure value of 1.0. Also, it can be considered as a way of normalizing the safety factor with respect to its standard deviation. The definition does not require the probability distribution of function $g(X_1, X_2, \ldots, X_n)$ to be known, but there is a tacit assumption that function $g(X_1, X_2, \ldots, X_n)$ is distributed in some way that can be described meaningfully by an expected value and standard deviation. When the shape of the probability distribution of the safety factor is known, the reliability index can be related to the probability of failure.

2.3 *Steps in reliability analysis*

In this paper, Baecher & Christian (2003) methodology was adopted. The steps for performing this analysis are:

- *Establish an analytical model*;
- *Estimate statistical descriptions of the parameters. The parameters are described by their mean values and variances*;
- *Calculate statistical moments of the performance function* (*Eqs. 1 and 2*);
- *Calculate the reliability index*.

3 STABILITY ANALYSIS

The safety factor of a hypothetical tropical soil slope subjected to heavy rainfall conditions was

analyzed for a period of 48 hours. In order to determine the slope stability over time, the porewater pressure field is analyzed by SEEP/W (GEO-SLOPE International, 2004a). Then, the safety factor is calculated with Limit Equilibrium Method using SLOPE/W (GEO-SLOPE International, 2004b), which allows the consideration of the porewater pressure values obtained with SEEP/W.

The boundary conditions determination for the flux problem were based on information from Terlien (1998), who has shown that triggering mechanism of the landslides which occurred in Manizales, Colombia, corresponded to a rainfall of 70 mm per day. Furthermore, Gitirana Jr. et al. (2005) explained that if infiltration is smaller that saturated permeability then all rainfall will infiltrate. Hence, during the analysis, the infiltration rate was kept constant and equal to 70 mm/day applied over the surface (toe, crest and slope). In order to determine the embankment safety factor for each time step, the porewater pressure distribution was determined for different instants (t = 0, 8, 16, 24, 36 and 48 hours).

3.1 *Initial boundary conditions and geometry*

Figure 1 presents geometry, boundary conditions and initial conditions of the slope stability. The slope inclination is 1.5H:1.0V and it is 10 m high. The initial ground water table was obtained from a steady flow analysis. The initial porewater pressure distribution was determined using hypothesis that an existing of water table as show in Fig. 1.

The maximum initial suction was restricted to 50 kPa from the equilibrium condition.

3.2 *Soil properties*

The mean values of the soil given in Table 1 correspond to data obtained in the laboratory by Oliveira (2004) from a tropical soil compacted in normal Proctor optimum water content. The shear strength was obtained by stress controlled constant water triaxial tests by measuring suction with a high capacity tensiometer. The "Three-Sigma rule" was used to determine the saturated and unsaturated shear strength variability. That rule can be used to estimate a value of standard deviation by first estimating the highest and the lowest conceivable values of the parameter and then dividing the difference between them by six (Duncan, 2000).

Figure 2 presents the soil water retention curve (WRC) and the hydraulic conductivity functions. The unimodal WRC presented on Figure 2 is defined by a closed van Genutchten form equation (van Genutchten, 1980). The hydraulic conductivity function was based on the WRC, using van Genutchten (1980) Mualem's model. The saturated hydraulic conductivity value is 2.24 × 10–5 m/s.

The analysis assumed that the independent variables are not correlated. This fact increases the variance in a small amount for the FOSM method, which is considered insignificant for the outlined goals in this article.

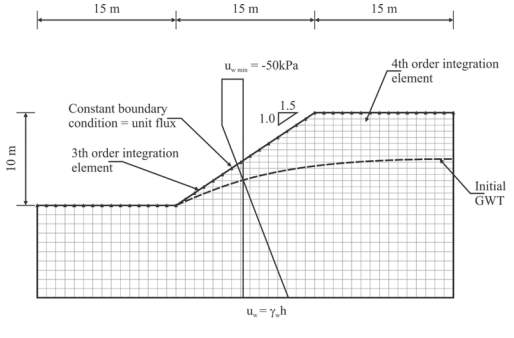

Figure 1. Problem geometry, boundary conditions, and initial values.

Table 1. Values of parameters used in analysis.

Parameter	Mean	COV (%)
Unit weight of soil	18.1 kN/m^3	4.2
Effective cohesion	12 kPa	20
Effective angle of internal friction	30°	6
Saturated water conductivity	2.24E-5 m/s	90
Air entry value	8 kPa	30
ϕb*	25°	15

* Angle indicating the rate of increase of shear strength relative to increase matric suction.

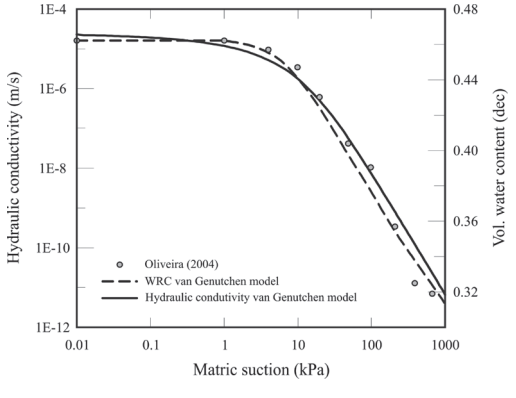

Figure 2. Soil water retention curve and hydraulic conductivity functions for a tropical compacted soil.

4 RESULTS

The water table rise produces an increase in porewater pressure and a decrease in shear strength within the slope. Figure 3 shows safety factor of evolution and the boundary porewater pressures values with the rain time step. The maximum suction after 48 hours is a 31 kPa. The changes in the porewater pressure field between initial and final time steps are similar to those presented by Evans & Lam (2002).

The variance of the safety factor was calculated using the three definitions of finite differences presented (Eq. 2, 3 e 4) and the results are shown in Fig. 4. The most significant changes in porewater pressure values were recorded after 8 hours and they reflect on the reliability index of the safety factor. The technique was used to determine the derivatives required in Eq. (2) have significant influence until 16 hours after the beginning of rain.

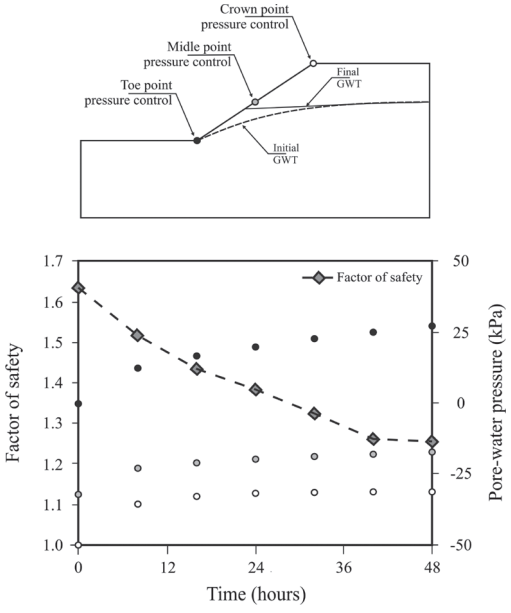

Figure 3. Factor of safety and boundary pressure evolution with the rain time.

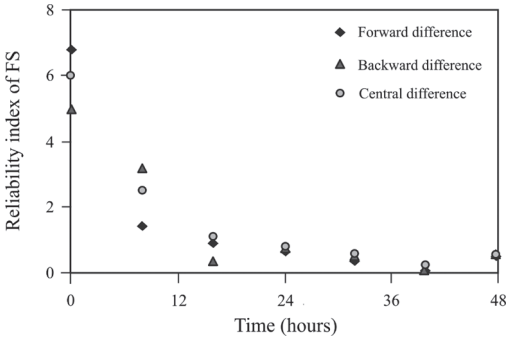

Figure 4. Reliability index of the factor of safety evolution with the rain time.

The Figure 4 shows that using the central difference reduces bias. For this reason, the central difference is best to assess the problem. Wolff (1994) recommends evaluating the derivative over a range of plus and minus one standard deviation may better capture some of the nonlinear behavior. However, the increment used was lower than the standard deviation, and equal to 1% of the mean value. Otálvaro et al. (2011) verified the approximation of the derivative varying ΔXi from 0.001% to 10% of the mean, discovering that the variance is stable for values less than 1%.

The variance of the dependent variable is obtained from the sum of n terms in the Eq. (2). With the dependent variable variance value is possible to calculate the contribution of each independent variable as:

$$Cont_j = \left(\frac{\partial g}{\partial X_j}\right)^2 \sigma^2\left[X_j\right] \Big/ \sum_1^n \left(\frac{\partial g}{\partial X_i}\right)^2 \cdot \sigma^2\left[X_i\right] \quad (7)$$

Where $Cont_j$ = contribution of the variable j. The influence of each parameter in safety factor variance was calculated using Equation (7) and results are shown in Figure 5.

In the first time step, the effective angle of internal friction and effective cohesion control the variance of the safety factor. After the infiltration process starts, variance is controlled by saturated water permeability and air-entry value. Similar results have been found by Sivakumar-Babu & Murthy (2005).

5 CONCLUSIONS

The slope stability analysis using a non-coupled solution shows that the variance on safety factor is affected by the hydraulic parameters.

The methodology used in this paper incorporating First Order Second Moment in the non-coupled slope stability analysis can be easily used to estimate the reliability of slopes under rainfall conditions. The results of these analyses can help defining thresholds for warning systems.

The derivative required in First Order Second Moment method can be calculated with the central difference approximation, as suggested by Wolff (1994), reducing the independent variable increment.

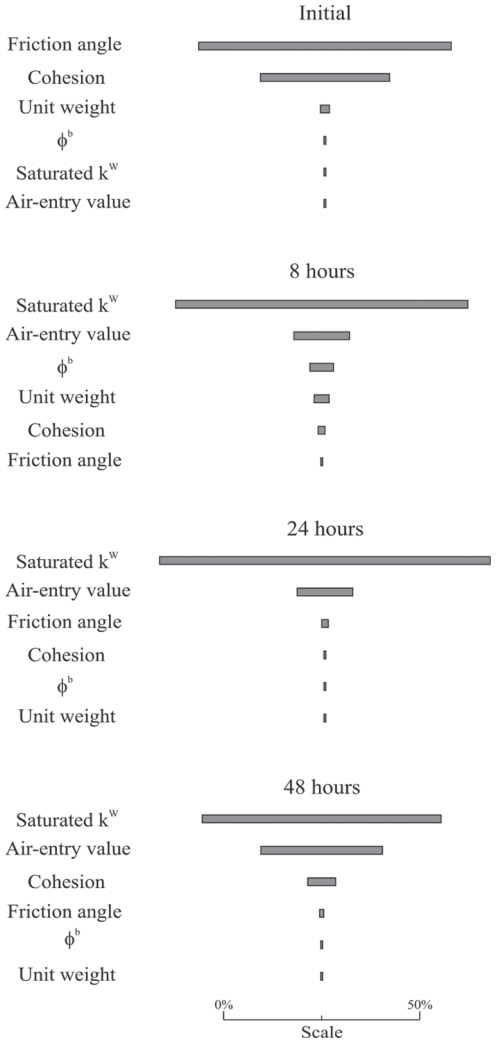

Figure 5. Variable's contribution on the variance of the factor safety.

Further research can be made related to topics of this paper. It is necessary to increase data for hydraulic conductivity and soil water retention curve statistical analysis. Also, the threshold approach for warning systems should be rethought, considering phenomena such as infiltration, not only the direct correlation with rainfall. It is necessary to incorporate the tools developed in the unsaturated soil mechanics in daily practice.

ACKNOWLEDGEMENTS

The authors would like to thank of the "Conselho Nacional de Desenvolvimento Científico e Tecnológico" CNPq of Brazil for providing the financial support for this research.

REFERENCES

Baecher, G.B. & Christian, J.T. 2003.*Reliability and Statistics in Geotechnical Engineering*. London and New York. John Wiley and Sons.

Christian, J.T., Ladd, C.C. & Baecher, G.B. 1994. Reliability applied to slope stability analysis. *Journal of Geotechnical Engineering* 120(12): 2180–2207.

Duncan, J.M. 2000. Factors of safety and reliability in geotechnical engineering. *Journal of Geotechnical and Geoenvironmental Engineering* 130(10): 985–1003.

Evans, N.C. & Lam, J.S. 2002. *Soil moisture conditions in vegetated cut slopes and possible implications for stability. Geo Report No. 140*. Hong Kong. Geotechnical Engineering Office Civil Engineering Department The Government of the Hong Kong Special Administrative Region.

GEO-SLOPE International. 2004a. Seepage modeling with SEEP/W. John Krahn Editor. *An engineering methodology*.

GEO-SLOPE International. 2004b. Stability modeling with SLOPE/W. John Krahn Editor. *An engineering methodology*.

Gitirana, G. Jr., Fredlund, M.D. & Fredlund, D.G. 2005. Infiltration-runoff Boundary Conditions in Seepage Analysis. *Proceedings of the 58th Canadian Geotechnical Conference*. Saskatoon, Canada.

Harr, M.E. 1987.*Reliability-Based Design in Civil Engineering*. New York. McGraw-Hill Book Company.

Mašín, R.S. 2009. Comparison of different probabilistic methods for predicting stability of a slope in spatially variable c–ϕ soil. *Computers and Geotechnics* 37(1–2): 132–140.

Oliveira, O.M. 2004. *Unsaturated shear strength study on a compacted residual soil*. Ph.D. Thesis. Engenerring School São Paulo University. São Paulo.

Otálvaro, I.F. Cordão-Neto, M.P. & Medero G.M. 2011. Assessment of volumetric collapse using probabilistic approach. In Alonso & Gens (eds). *Unsaturated Soils*. London. Taylor & Francis Group.

Rosenblueth, E. 1975. Point estimates for probability moments. *Proceedings National Academy of Science* (10): 3812–3814.

Rosenblueth, E. 1981. Two-point estimates in probabilities. *Applied Mathematical Modelling* 5(2): 329–335.

Sivakumar Babu, G.L. & Murthy, D.S.N. 2005. Reliability Analysis of Unsaturated Soil Slopes. *Journal of Geotechnical and Geoenvironmental Engineering* 131(11): 1423–1428.

Terlien, M.T.J. 1998. The determination of statistical and deterministic hydrological landslide-triggering thresholds. *Environmental Geology* 35 (2–3): 124–130.

van Genuchten, M. Th. 1980. A closed-form equation for predicting the hydraulic conductivity of unsaturated soils. *Soil Science Society American Journal* 44(5): 892–898.

Wolff, T.F. 1994. *Evaluating the reliability of existing levees, Technical report*. US Army Engineer Waterways Experiment Station, Geotechnical Laboratory.

This page intentionally left blank

Advances in Unsaturated Soils – Caicedo et al. (eds)
© 2013 Taylor & Francis Group, London, ISBN 978-0-415-62095-6

Modeling gas hydrate bearing sediments using a coupled approach

M. Sanchez & A. Shastri
Texas A&M University, College Station, Texas, USA

J.C. Santamarina
Georgia Institute of Technology, Atlanta, Georgia, USA

ABSTRACT: Gas hydrates are crystalline clathrate compounds made of water and a low molecular gas like methane. Gas hydrates are generally present in oil-producing areas and in permafrost regions. Methane hydrate deposits can lead to large-scale submarine slope failures, blowouts, platform foundation failures, and borehole instability. Gas hydrates constitute also an attractive source of energy as they are estimated to contain very large reserves of methane. Hydrate formation, dissociation and methane production from hydrate bearing sediments are coupled Thermo-Hydro-Mechanical (THM) processes that involve, amongst other, exothermic formation and endothermic dissociation of hydrate and ice phases, mixed fluid flow and large changes in fluid pressure. A comprehensive THM formulation is briefly presented here. Momentum balance, mass balance and energy balance equations take into consideration the interaction among all phases (i.e., solid, liquid, gas, hydrates and ice) and mechanical equilibrium. Constitutive equations describe the intrinsic THM behavior of the sediment. Simulation results conducted for hydrate bearing sediments subjected to boundary conditions highlight the complex interaction among THM processes in hydrate bearing sediments.

1 INTRODUCTION

Gas hydrates are solid compounds made of water clustered around low molecular weight gases (e.g., methane, ethane, hydrogen sulphide and carbon dioxide). Stability and behavior of Hydrate Bearing Sediments (HBS) are strongly dependent on thermo-hydro-mechanical (THM) actions affecting the gas hydrate compound. Methane hydrates form under certain pressure and temperature conditions typically found in submarine sediments and permafrost. Their distribution is typically correlated with the presence of oil reservoirs and thermogenic gas.

Methane hydrates are foreseen as a potential energy resource as large reserves are estimated worldwide (e.g., Sloan, 1998; Rutqvist and Moridis, 2007). Unstable hydrate dissociation is seen to cause borehole instability, blowouts, foundation failures, and trigger large-scale submarine slope failures (e.g., Kayen & Lee, 1991; Jamaluddin et al., 1991; Briaud and Chaouch, 1997; Chatti et al., 2005). The release of methane would further increase greenhouse effects and contribute to global warming (e.g., Dickens et al., 1997).

Therefore a thorough understanding of the behavior of HBS and its related process is much required. The testing of natural HBS is found to be challenging owing to the pressure and temperature condition that they exist in. Experimental studies are further hindered due to the low solubility of methane in water when preparing artificial samples. The emphasis in such a situation has emphasizes the role of numerical investigations.

The behavior of HBS is complex in nature as disassociation may take place due to an increase in temperature; a decrease in fluid pressure; changes in the fluid chemistry, or a combination of them. The dissociation causes important changes on the mass transport of fluids and fluid pressures. Changes in fluid pressures will alter the effective stress, affecting in turn the stiffness, strength and dilatancy of the sediment. It is evident that the behavior of HBS is controlled by strong THM coupled processes.

Partial formulations have previously been developed to understand hydrate formation and dissociation within well-defined boundary conditions (Rempel and Buffett 1997, 1998; Xu and Ruppel 1999; Davie and Buffett, 2001; Ahmadi et al., 2004; Nazridoust and Ahmadi 2007).

The responses of the soil sediments are either disregard or handled using simplified assumptions (e.g., non-deformable rigid porous medium is assumed in Nazridoust and Ahmadi 2007). Rutqvist and Moridis (2007) and Rutqvist (2011) presented a more general THMC approach by linking (sequentially) a geomechanical code (FALC^{3D})

with a multiphase fluid and heat transport simulator TOUGHT. However the formulation was not truly coupled and solved the sediment and the hydrate state variables separately.

The THM formulation proposed herein is fully coupled. In term of hydrate dissociation, it considers that dissociation can place very fast (i.e., local equilibrium is assumed), or it can develop in time (through a kinematic law). The dependence of effective stress, stiffness, strength, conduction properties and volume change on the hydrate saturation are also implemented in the proposed framework.

A brief description of the THM formulation is presented in the next section. The algorithm is tested and demonstrated using well-constrained elemental cases. Simulation of gas production in-situ by depressurization at the borehole is performed here. Code validation against a database of reported cases and the analysis of various potential field conditions are reported elsewhere (e.g., Sanchez et al., 2012 Shastri, 2013).

2 THEORETICAL FRAMEWORK

The THM phenomena that take place in hydrate-bearing sediments include the main following phenomena:

1. heat transport through conduction, liquid and gas phase advection,
2. heat of formation-dissociation,
3. water flux as liquid phase,
4. methane flux in gas phase and as dissolved methane (diffusion in liquid phase),
5. heat of ice formation/thaw,
6. fluid transport of chemical species,
7. mechanical behavior; effective stress and hydrate-concentration dependent sediment behavior. The formulation comprised of balance equations, constitutive equations, equilibrium restrictions, and kinetic reactions. Those equations have been implemented in CODE-BRIGHT. The main equations are presented in the subsequent sections.

2.1 *Phases and species—mass densities*

The pores in the granular skeleton of the hydrate bearing sediments are filled with gas, hydrate, water or ice (Figure 1a). The three main species mineral, water, and methane are found in five phases: solid mineral particles, liquid, gas, hydrates and ice as shown in the phase diagram Figure 1b.

The liquid phase is made of water and dissolved gas. The solubility of methane in water [mol/m^3] increases with pressure and decreases with

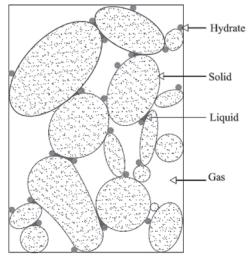

Figure 1a. Granular structure of HBS.

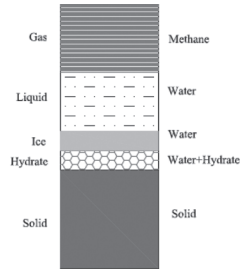

Figure 1b. Phase diagram of HBS.

temperature and salt concentration. In the absence of hydrates and opposite effect is observed (i.e., an increase in solubility with increase in temperature and decrease in pressure). The implemented formulation is able to simulate hydrate formation from a dissolved phase. The density of the liquid ρ_ℓ depends on temperature T [°K] and pressure P_ℓ [MPa]. The asymptotic solution for small volumetric changes is:

$$\rho_\ell = \rho_{\ell o}\left(1+\frac{P_\ell}{B_\ell}\right)\left[1-\beta_{T\ell}\left(\frac{T-277^\circ K}{5.6}\right)^2\right] \quad (1)$$

where, $\rho_{\ell o} = 0.9998$ g/m^3 is the mass density of water at atmospheric pressure T is temperature in °K and $B_\ell = 2000$ MPa is the maximum bulk stiffness of water (at 277 °K), and $\beta_{T\ell} = 0.0002$ °K^{-1} is the thermal expansion coefficient. Corrections for salt concentration are disregarded as a first approximation. Pure methane gas constitutes the gas phase. The contribution of water vapor in the gas phase to the mass density of the gas phase and to short-duration mass transport processes is disregarded as its contribution is seen to be minimal. The mass density of the gas phase is pressure P_g [MPa] and temperature T [°K] dependent and it can be estimated using the ideal gas law modified for methane gas.

$$\rho_g = \frac{M_m P_g}{RT}\left[1176+12.7\frac{P_g}{1MPa}-0.45\left(\frac{P_g}{1MPa}\right)^2\right] \quad (2)$$

where, the gas constant R = 8.314 J/(molºK) and the molecular mass of methane $M_m = 16.042$ g/mol (example: $\rho_g = 86$ g/m^3 at T = 280ºK and $P_g = 10$ MPa).

The hydrate phase is made of water and methane. The mass fraction of water in hydrate $\alpha = m_w/m_h$ depends on the hydration number χ for methane hydrates. The ice transformation may take

place during fast depressurization. The densities of the hydrate, the ice and the mineral phases are assumed constant.

2.2 *Volumetric relations*

The total volume V_{total} is the sum of the partial volume of each β-phase V_β, where the subindex β is related to the solid 's', liquid 'ℓ', gas 'g', hydrate 'h' and ice 'I' phases. Assuming that the solid mineral is a non-reactive phase, the total porosity is defined as the ratio of the volume of voids $V_v = 1 - V_s$ to the total volume V_{total},

$$\phi = \frac{V_v}{V_{total}} = \frac{V_g + V_\ell + V_h + V_i}{V_{total}} \tag{3}$$

The volume of voids V_v is occupied by the liquid, gas, hydrate and ice phases; the associated volume fractions are $S_\beta = V_\beta / V_v$ and the following volumetric restriction applies

$$S_\ell + S_g + S_h + S_i = 1 \tag{4}$$

Balance equations apply to mass of water, methane, mineral, internal and linear momentum. As an example, the water mass balance equation of methane is presented as follows:

$$\frac{\partial}{\partial t}\left\{\left[\rho_g S_g + (1-\alpha)\rho_h S_h\right]\phi\right\} + \nabla.\left[\rho_g \mathbf{q}_g + \rho_g S_g \phi \mathbf{v} + (1-\alpha)\rho_h S_h \phi \mathbf{v}\right] = f^m \tag{5}$$

where, P_g and P_h are the densities of the methane gas and hydrates, S_g and S_h are the gas and hydrate concentrations, q_g is the rate of flow of methane, ϕ is the porosity and α is the mass fraction of water in hydrate.

Constitutive equations and equilibrium restrictions relate the main unknowns (i.e., **u**, P_l; P_g, P_h T) with the dependent variables (i.e., stresses; S_l; S_g; S_h fluxes). For example, the retention curve dictates the relationship between the interfacial tension sustained by the difference in liquid and gas pressures; and the effective degree of liquid saturation S_ℓ^*, which is given by:

$$S_\ell^* = \frac{S_\ell}{S_\ell + S_g} = \left[1 + \left(\frac{P_c}{P_o}\right)^{\frac{1}{1-\lambda}}\right]^{-\lambda} \tag{6}$$

where, λ and P_0 are model parameters related to the pore structure of the sediment. Due to space limitations, the other constitutive equations are not presented in this paper. The explanation of mass balance of the constituents, energy balance and constitutive relations are detailed in Sanchez et al. (2012).

The fluid pressure and the temperature control the reaction kinetics of the transformation between the water, hydrates and ice phases. Four regions appear for gas-water systems when the hydrate stability and the ice-water boundaries are superimposed on the pressure-temperature PT-space, as shown in Figure 2. The presence of free gas, water, ice and hydrate in each quadrant depends on the relative mass of water and gas, and the PT trajectory.

3 NUMERICAL SIMULATIONS

The mathematical formulation has been implemented in the finite element computer program CODE-BRIGHT (Olivella et al., 1996). It has been previously been used to numerically solve THCM problems in porous media. Details related to the code can be found elsewhere (e.g., Olivella et al., 1996, Gens et al., 2009). The main aspects can be summarized as follows:

1. The state variables are: solid velocity, **u** (one, two or three spatial directions); liquid pressure P_l, gas pressure P_g temperature T and chemical species concentration.
2. Small strains and small strain rates are assumed for solid deformation.
3. Thermal equilibrium between phases in a given element is assumed.
4. All constitutive equations are modified and new equations are added to properly accommodate for the behavior of hydrate bearing sediments and all phases involved.

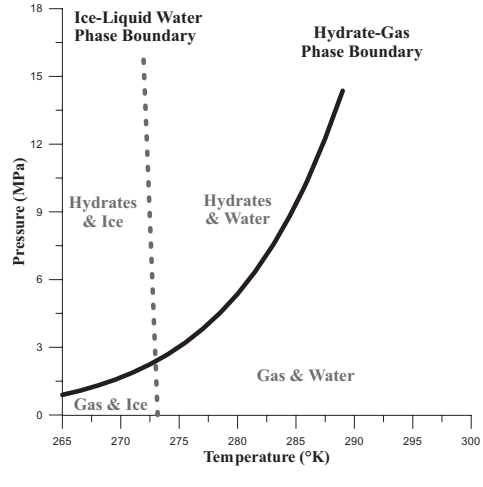

Figure 2. Phase boundaries in for water-gas mixtures in the pressure-temperature space.

4 MODELING RESULTS

The formulation has been extensively tested for a wide range of field conditions. A critical component of a THM formulation for HBS is to model properly the possible phase changes that may occur under different field/laboratory conditions illustrated in Figure 2. To show the performance of the algorithm a simplified case of dissociation induced through depressurization is presented here.

The simulation would be a simplified model for studying production of methane gas in HBS through the process of depressurization. The mesh generated for the simulation is shown in Figure 3.

The hydrate dissociation is induced following a stress path characterized by an isothermal depressurizing (Figure 4). The test initial conditions are identified as '0' in Figure 4, as follows:

T = 279.1 ˚K;

Pc = 0.018 MPa (i.e., P_l = 12 MPa, P_g = 12.01 MPa);

$S_l = S_g = 0.5$.

The initial hydrate concentration is set as $S_h = 0.2$.

As expected, phase changes for the hydrate (i.e., dissociation) starts when the stress path touches the phase boundary (at point '1' in Figure 4). The further drop in the pressure results in complete dissociation gas hydrate . The variation of the hydrate concentration and the system pressure for each step in the sample is shown in figure 5.

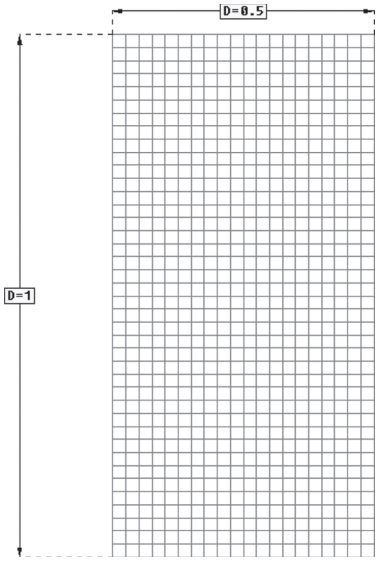

Figure 3. Finite element mesh.

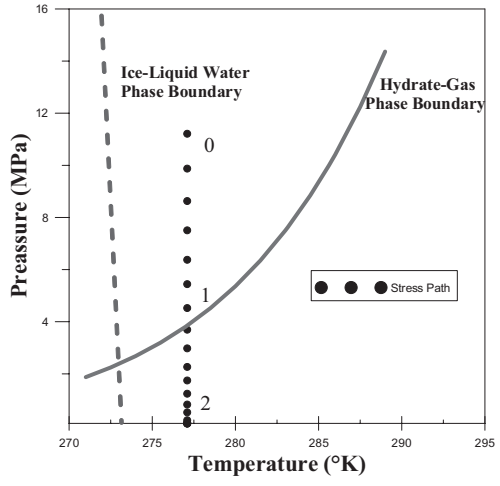

Figure 4. Depressurizing stress path.

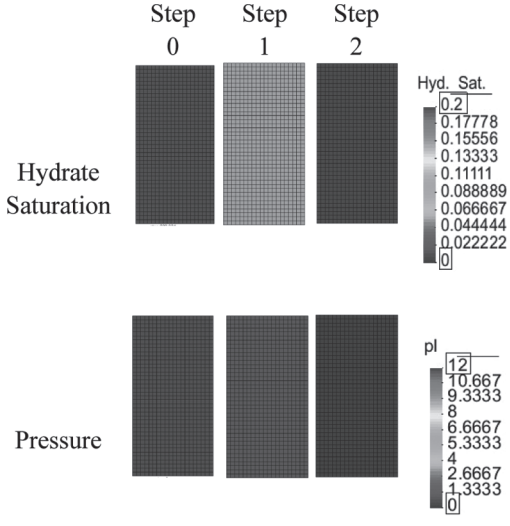

Figure 5. Variation of hydrate concentration with pressure of the system.

The formulation is now tested for hydrate dissociation with an increase in temperature. The same initial conditions adopted for the depressurization is now used for the process of isobaric heating. The stress path of the sample is shown in figure 5. The initial conditions are identified as '0' in Figure 6. The temperature of the sample is now increased until it reaches step 1 (indicated by '1' in Figure 6), where hydrate dissociation begins. The test is concluded with all the hydrate is seen to be dissociated (at '2' in Figure 6).

The variation of the hydrate concentration is shown alongside with the variation in temperature

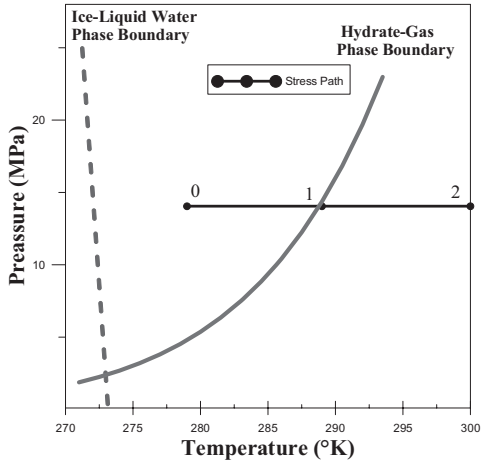

Figure 6. Heating stress path.

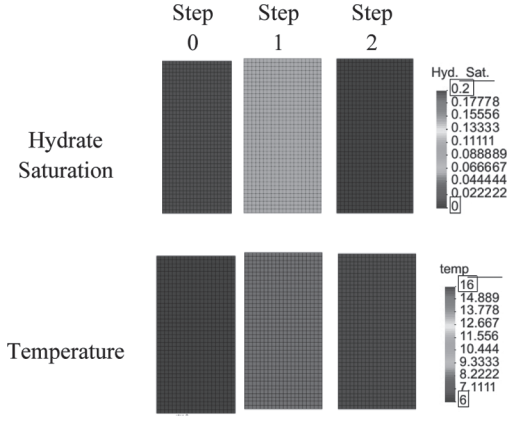

Figure 7. Variation of hydrate concentration with temperature of the system.

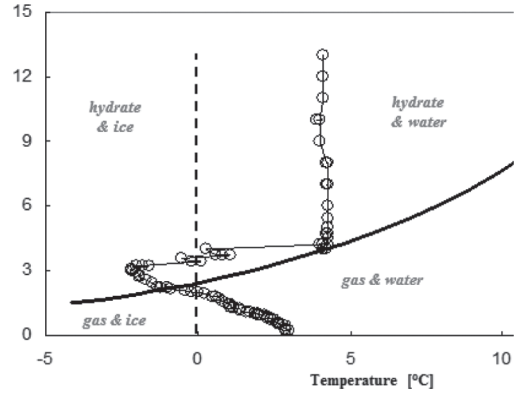

Figure 8. Experimental data was gathered during the depressurization of a pressure core gathered from the Krishna-Godavari Basin (reported in Yun et al., 2010).

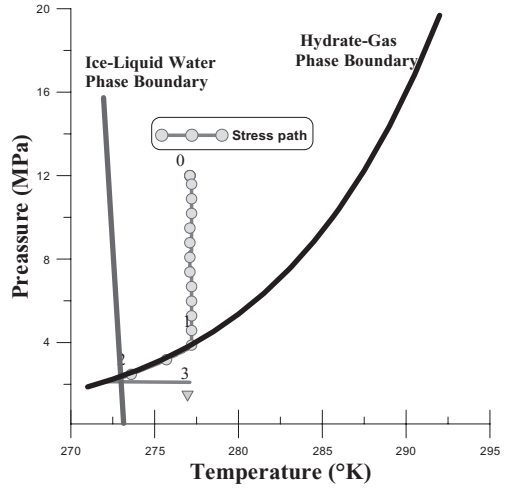

Figure 9. Modeling the depressurization test at point level following the stress path reported in Yun et al. (2010).

(Figure 7). It can be seen that dissociation starts at 16° C (289 °K). As expected The hydrate is seen to disassociate completely beyond that temperature.

The last case study is associated with the analysis of a venting (depressurization) experiment performed on a pressurized core recovered from hydrate bearing sediments in the Krishna-Godavari Basin India. The core was depressurized while measuring the internal temperature in the sediment at the center of the core (Yun et al., 2010). The measured PT evolution is presented in Figure 5. The endothermic dissociation that takes place during depressurization cools down the sample (as recorded by thermocouples, Fig. 8b). During hydrate dissociation the stress path moves on the phase boundary towards the water-to-ice transformation line, reaching freezing temperatures and leading to ice formation. Many unknowns restrict careful modeling, such as internal fluid pressure, gas pressure, temperature and strains along the core length. Instead, the intent is to demonstrate the formation of secondary ice and to anticipate internal parameters based on constitutive data reported in Yun et al. (2010). Figure 9 presents the main model results obtained from an analysis at point level. The model is able to describe very well the main patterns observed in the experiment. Note that the T measured during the test is punctual and the recovering of the temperature observed after touching the ice-water face boundary is due to heat transfer from the

surroundings. Noticeably, this situation is not reproduced by simulation 'at point level', the solution of a boundary value problem will make that possible. The model predicts the formation of ice during dissociation at freezing temperature

5 CONCLUSIONS

The proper modeling of hydrate bearing sediments is a relevant aspect as hydrate behavior may affect foundation of off-shore platforms, borehole stability and submarine slopes. Hydrates has also became in a viable source of energy. Various thermal, mechanical and hydraulic strongly coupled processes affect the behavior of HBS and its modeling would require a formal THMC formulation. Such a formulation has been briefly presented here and implementation into the finite element program CODE_BRIGHT. The simple stress paths presented in this paper show that the model response is the expected one for the simulated conditions. The code has ben also used to model an actual depressurization test under controlled conditions. The main patterns of behavior have been correctly predicted by the model.

REFERENCES

Ahmadi, G., Ji, C. and Smith, D.H. (2004). "Numerical solution for natural gas production from methane hydrate dissociation." Journal of petroleum science and engineering, 41(4), 269–285.

Briaud, J.L. and Chaouch, A. (1997). "Hydrate melting in soil around hot conductor." Journal of geotechnical and geoenvironmental engineering, 123(7), 645–653.

Chatti, I., Delahaye, A., Fournaison, L. and Petitet, J-P. (2005). "Benefits and drawbacks of clathrate hydrates: a review of their areas of interest." Energy conversion and management; 46: 1333–1343.

Davie, M.K. and Buffett, B.A. (2001). "A numerical model for the formation of gas hydrate below the seafloor." Journal of Geophysical Research, 106(B1), 497–514.

Dickens, G.R., Paull, C.K. and Wallace, P. (1997). "Direct measurement of in situ methane quantities in a large gas-hydrate reservoir." Nature, 385, 426–428.

Jamaluddin, A., Kalogerakis, N. and Bishnoi, P. (1991). "Hydrate plugging problems in undersea natural gas pipelines under shutdown conditions." Journal of Petroleum Science and Engineering; 5: 323–335.

Kayen, R.E. and Lee, H.J. (1991). "Pleistocene slope instability of gas hydrate laden sediment on the Beaufort sea margin." Marine Georesources & Geotechnology, 10(1–2), 125–141.

Nazridoust, K. and Ahmadi, G. (2007). "Computational modeling of methane hydrate dissociation in a sandstone core." Chemical engineering science, 62(22), 6155–6177.

Olivella, S., Carrera, J., Gens, A. and Alonso, E.E. (1994). "Non-isothermal multiphase flow of brine and gas through saline media." Transport in porous media, 15, pp. 271–293.

Olivella, S., Gens, A., Carrera, J. and Alonso, E.E. (1996). "Numerical formulation for a simulator (CODE-BRIGHT) for the coupled analysis of saline media." Engineering Computations; (13)7: 87–112.

Rempel, A. and Buffett, B. (1997). "Formation and accumulation of gas hydrate in porous media." Journal of Geophysical Research, 102, 10–10.

Rutqvist, J. and Moridis, G. (2007). "Numerical studies of geomechanical stability of hydrate-bearing sediments." Offshore Technological Conference, Houston, U.S.A.; 30/04–3/05 2007. OTC 18860.

Rutqvist, J. (2011). "Status of the TOUGH-FLAC simulator and recent applications related to coupled fluid flow and crustal deformations." Computers & Geosciences, 37(6), 739–750.

Sánchez, M., Santamarina, C. and Shastri, A. (2012). "Coupled THM Analysis of Gas Hydrate Bearing Sediments" under review.

Shastri, A. (2013) "Coupled Thermo-Hydro-Mechanical and Geochemical Modeling in Porous Media Ph.D Thesis.

Sloan, E.D. (1998). "Clathrate Hydrates of Natural Gases." 2nd Ed. Marcel Dekker, Inc, New York.

Xu, W. and Ruppel, C. (1999). "Predicting the occurrence, distribution and evolution of methane gas hydrate in porous marine sediments." Journal of Geophysical Research, 104(B3), 5081–5095.

Yun, T.S., Fratta, D. and Santamarina, J.C. (2010). "Hydrate-Bearing Sediments from the Krishna–Godavari Basin: Physical Characterization, Pressure Core Testing and Scaled Production Monitoring." Energy & Fuels.

Advances in Unsaturated Soils – Caicedo et al. (eds)
© 2013 Taylor & Francis Group, London, ISBN 978-0-415-62095-6

Effect of soil replacement option on surface deflections for expansive clay profiles

A. Bharadwaj, S.L. Houston, W.N. Houston & B. Welfert
Arizona State University, Tempe, AZ, USA

K.D. Walsh
San Diego State University, San Diego, CA, USA

ABSTRACT: In this paper the results of a stress-deformation parametric analysis are presented to show the effect of an artificial non-expansive replacement layer over an intact expansive soil on the heave at the surface. Finite element code SV Flux and SV Solid are used to perform the stress-deformation analysis. Climatic boundary conditions for a semi arid region are used. Significant decreases in the heave amount were noted, depending on the thickness and soil type of the replacement soil.

1 INTRODUCTION

Expansive soils are associated with shrink and swell behavior and may cause serious damage to structures. Residential foundations such as slab-on ground are generally built on unsaturated soils including expansive soils and are subject to deformations associated with changes in matric suction/moisture content in the soil. The problem of expansive soils is more pronounced in arid regions where changes in soil suction as a result of development can be much greater than in humid regions. Expansive soils are also called moisture sensitive soils because when subjected to wetting, they undergo substantial volume changes associated with the swelling process.

Various methods are available and practiced to reduce swelling in soils at the ground surface to prevent the damage caused to structures. Mitigation measures may be broadly defined as any actions or designs that lessen or solve moisture sensitive soil problems (Houston et al., 2001).

Among the various techniques for expansive soil mitigation, the removal and replacement technique (remove-and-replace) is very popular for lightly loaded structures and shallow foundations. The heave reducing effect of replacement of expansive soil with a non expansive layer has been studied by various authors (Katti 1979, Walsh et al., 2009, Murthy & Praveen 2008) in the past. A large volume of intact soil when replaced with non expansive soil can attenuate the surface heave feature. The mechanisms for reduction of heave are: (1) removal of expansive soil with non-expansive soil results in a zone of no-heave where the expansive soils are replaced, thereby reducing surface heave, (2) the replacement soil may change the degree and depth of wetting in the native expansive clay profile by increasing, decreasing, or having only minimal effect on the amount of surface and near-surface water that infiltrates into the soil, (3) the placement of a non-expansive soil layer pushes the seat of movement deeper into the profile, thereby reducing the differential movements at the ground surface, and (4) the non-expansive soil layer may provide increased confinement for any expansive soil that does get wet, thereby reducing volume change.

In general, the non-expansive soil layer could have a saturated hydraulic conductivity the same as, higher than, or lower than the underlying expansive soil. As a part of an on-going study at Arizona State University, the full range of hydraulic properties of the replacement layer is being evaluated. In this paper, preliminary findings are presented for the case of remove-and-replace mitigation where the replacement layer has a higher hydraulic conductivity than the underlying clay. This represents, for example replacement of expansive soil with a non-expansive granular fill.

2 ANALYSIS OF SLAB-ON-GROUND FOUNDATION ON EXPANSIVE CLAY PROFILE WITH REMOVE-AND-REPLACEMENT MITIGATION

The problem that was analyzed is described schematically in figure 1. In these analyses the problem is analyzed as a two-dimensional (2D)

problem for both fluid flow and deformation. The soil properties of clay typical of highly plastic clays in the Phoenix, Arizona, region were used. The clay is classified as CH, has a LL of 85 and a PI of 53 and a swell pressure of 700 kPa.

The basic soil properties of the expansive clay are tabulated below in Table 1. In the simulation performed, roof runoff from the residential house falls directly on the edge of the foundation of the house. A pond of 150 mm (6 inches) depth is allowed to occur a during rain event, and any additional roof runoff is allowed to runoff of the site. The surface flux conditions outside of the region of ponding correspond to natural climatic conditions. The surface flux simulates desert landscaping conditions with some degree of ponding of rain water next to the structure. This has been observed to be a fairly common condition for residential structures in the Phoenix, AZ area (Dye 2008). The concentration of water next to the structure can cause differential heave which can damage the structure.

The position of the domain boundaries (depth and width of the modeled soil profile) was determined iteratively by moving the boundaries for various SV Flux runs until position of boundaries had negligible effect on pore pressure and saturation variations in the vicinity of the slab-on-ground region. A separate analysis was performed to determine the optimum grid size (dx) and time step (dt) to obtain numerically stable results for this problem. A smaller dx was chosen for the upper layers since changes in soil moisture content are concentrated in the upper region of the profile. Deep down in the profile a larger grid size was used. The dx used for the expansive clay profile was 0.5 m globally. For the replaced soil profile a dx of 0.25 m was applied at the top (near surface) and the rest is kept at 0.5 m. These are preliminary runs and more investigation is ongoing with even smaller grid size. The maximum time increment (dt) used for the analyses was 0.5 days.

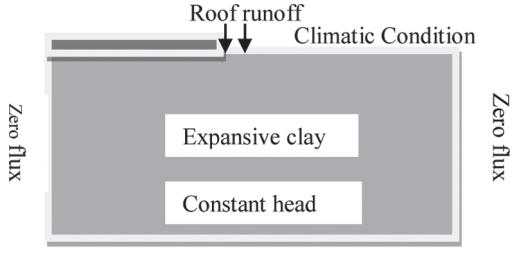

Figure 1. Schematics of the example problem.

Table 1. Soil properties for expansive and replacement soil.

Soil property	Higher K_{sat}	Expansive clay
Dry density	1770 kg/m^3	1360 kg/m^3
Total unit weight	20.6 kN/m^3	18.41 kN/m^3
Sat. VWC	0.33	0.512
K_{sat}	7.2×10^{-2} m/day	2.09×10^{-4} m/day
Gs	2.64	2.8

3 PROBLEM SET-UP

Seepage deformation analyses can be performed using either a coupled or uncoupled approach. For these analyses an uncoupled approach was used wherein unsaturated flow was modeled separately from stress-deformation (heave) analyses. The results from the SV Flux flow analyses were used as input to the heave analyses performed using SV Solid. Initial (preconstruction) soil suction profiles were determined through a simulated 30 yr period of application of a surface flux condition corresponding to Phoenix, AZ, climatic conditions as determined by Dye (2008). A steady state run was done to obtain the initial condition for stress-deformation analyses. Once the initial suction profile was determined for the natural expansive clay profile, a replacement layer of a certain depth (Figure 2) is placed, and surface flux conditions associated with the roof runoff condition are applied. After several years of simulation of ponding of roof runoff next to the structure, the final (post construction) suction profile is obtained. The initial (preconstruction) and final (post construction) soil suction profiles are used as input into the stress-deformation analyses performed using SV Solid. Three different depths of top native expansive clay are removed and replaced with non expansive soil having a hydraulic conductivity two orders of magnitude higher than the native clay.

The different replacement depths are shown in Figure 2.

A mixed formulation (Celia 1990) of the seepage equation was used for the SV Flux analyses:

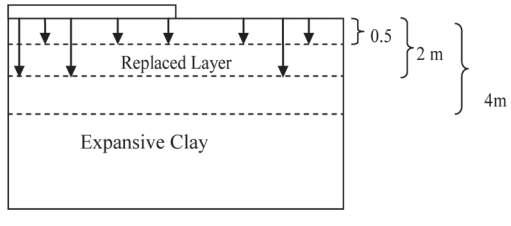

Figure 2. Replaced soil profile.

$$\frac{\partial}{\partial x}\left[\left(k_x^w(\theta)+k^{vd}(\theta)\right)\frac{\partial h}{\partial x}\right] + \frac{\partial}{\partial y}\left[\left(k_y^w(\theta)+k^{vd}(\theta)\right)\frac{\partial h}{\partial y}-k^{vd}(\theta)\right]=\frac{\partial \theta}{\partial t} \quad (1)$$

The SWCC for the soil in this problem is defined by using the Fredlund and Xing fit (1994) which is given by the equation below:

$$\theta_w=\theta_s C(\psi)\left[\frac{1}{\ln\left(e+\left(\frac{\psi}{a}\right)^n\right)}\right]^m \quad (2)$$

$$C(\psi)=1-\frac{\ln\left(1+\frac{\psi}{h_r}\right)}{\ln\left(1+\frac{1000000}{h_r}\right)} \quad (3)$$

where θ_w = volumetric water content at soil suction Ψ; θ_s = saturated volumetric water content; a = a material parameter which is primarily a function of air entry value of the soil in kPa; n = a material parameter which is primarily a function of rate of water extraction from the soil once the air entry value has been exceeded; m = a material parameter which is primarily a function of the residual water content; h_r = suction at which residual water content occurs, kPa; Ψ = soil suction.

The SWCC curves for the native soil and replacement soil are shown in Figure 3.

A Leong and Rahardjo fit (1997) is used to describe the unsaturated hydraulic conductivity for this problem. The hydraulic conductivity curves (Fig. 4) show a cross-over effect (Shackelford & Nelson 1996).

$$k_{(\psi)}=k_s\left[\ln\left(e+\left(\frac{\psi}{a}\right)^n\right)\right]^{-pm} \quad (4)$$

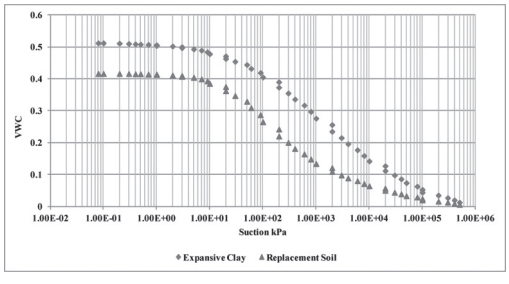

Figure 3. SWCC for expansive and replacement soil.

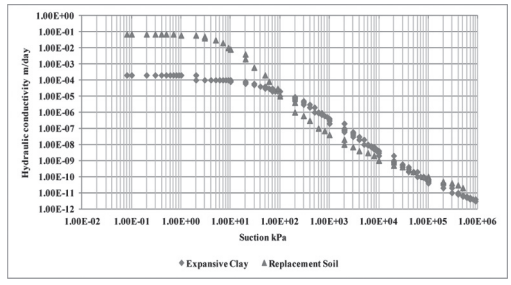

Figure 4. K_{unsat} curves for expansive and replacement soil.

where n = controls the slope at the inflection point; m = residual water content in the soil; p = different constant soil parameters; K_s = saturated hydraulic conductivity.

Wilson's limiting equation (1997) was used to obtain the actual evaporation. In order to avoid instability due to high spikes in evaporation from occurring, a gradient limit was applied.

$$AE=PE\left[\frac{u_v^{soil}-u_v^{air}}{u_{vo}^{soil}-u_v^{air}}\right] \quad (5)$$

where u_v^{soil} is the actual vapor pressure at the soil surface, kPa; u_{vo}^{soil} is the saturated vapor pressure in the soil at the ground surface, kPa; u_v^{air} is the vapor pressure in the air above the soil surface, kPa.

4 HEAVE ANALYSES

The soil heave was modeled using a suction volume change index. The equation showing the relationship between volumetric heave and the suction volume change index follows (Fredlund & Rahardjo 1993).

$$\partial\varepsilon_v=m_1^s d\left(\sigma_{mean}-u_a\right)+m_2^s d\left(u_a-u_w\right) \quad (6)$$

where σ_{mean} is the mean net normal stress $(\sigma_1+\sigma_2+\sigma_3)/3$; (u_a-u_w) is the matric suction; m_1^s, m_2^s are volume change coefficients with respect to change in net normal stress and matric suction respectively. Similarly, the volume change can be obtained by associating the volume change indices with void ratio surface for different loading conditions, given by (Fredlund & Rahardjo 1993).

$$de=C_s d\log\left(\sigma-u_a\right)+C_m d\log\left(u_a-u_w\right) \quad (7)$$

The matric suction volume change index was input as a function of depth. As can be seen from Figure 5 where C_m (Volume change index

Table 2. Swelling soil properties for expansive and replacement soil.

Soil	Poisson's ratio	C_s	e_0
Higher K_{sat}	0.35	0.05	0.99
Expansive clay	0.35	0.3	0.5

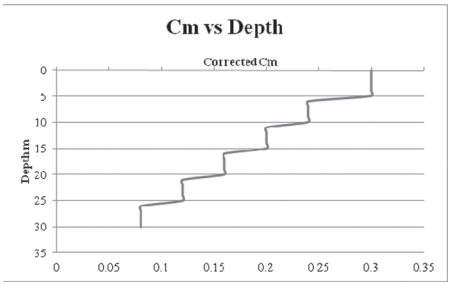

Figure 5. Variation of C_m with depth for the natural expansive clay profile.

with respect to matric suction) goes down with depth. This reduction in C_m with depth is due to reduced expansion potential as the confining stress approaches the swell pressure of the clay.

For the upper layer (low confinement), the swelling index for the expansive clay is 0.13 and the swelling index for the replacement layer is 0.05 (negligible since non expansive). A value of 0 can not be used due to numerical instability in the results.

For a 2D plane strain loading, the governing deformation Equations 8 and 9 are given by Hung & Fredlund (2000). These PDE's are solved in SV Solid to obtain the final deformations in a stress deformation analyses.

$$\frac{\partial}{\partial x}\left(c_{11}\frac{\partial u}{\partial x}+c_{12}\frac{\partial v}{\partial y}\right)+c_{33}\frac{\partial}{\partial y}\left(\frac{\partial u}{\partial y}+\frac{\partial v}{\partial x}\right) -d_s\frac{\partial\left(u_a-u_w\right)}{\partial x}+b_x=0 \tag{8}$$

$$c_{33}\frac{\partial}{\partial x}\left(\frac{\partial u}{\partial y}+\frac{\partial v}{\partial x}\right)+\frac{\partial}{\partial y}\left(c_{12}\frac{\partial u}{\partial x}+c_{22}\frac{\partial v}{\partial y}\right) -d_s\frac{\partial\left(u_a-u_w\right)}{\partial x}+b_x=0 \tag{9}$$

where bx and by are body forces in the x- and y-directions respectively.

$$c_{11}=c_{22}=\frac{(1-\mu)E}{(1+\mu)(1-2\mu)} \tag{10}$$

$$c_{12}=\frac{\mu E}{(1+\mu)(1-2\mu)} \tag{11}$$

$$c_{33}=\frac{E}{2(1+\mu)} \tag{12}$$

$$d_s=\frac{E}{(1-2\mu)H} \tag{13}$$

where E is the elasticity parameter for the soil structure with respect to a change in net normal stress; H is an elasticity parameter for the soil structure with respect to a change in matric suction; and μ is the Poisson's ratio for the soil structure.

5 RESULTS

The pore pressure (Figure 6) and saturation (Figure 7) results show that in arid regions the soil remains on the dry side even after a wetting event. The higher conductivity replacement layer retard water infiltration by storing it during wetting and evaporating it during drying event.

6 CONCLUSIONS

It is evident from the displacement plots that there is a substantial decrease in heave at the surface (Figure 8) with increases in the thickness of the upper portion of the soil profile replaced with a

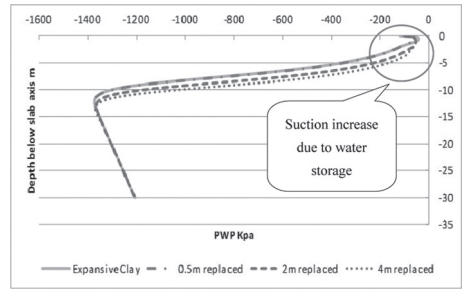

Figure 6. Pore pressure variation below slab edge.

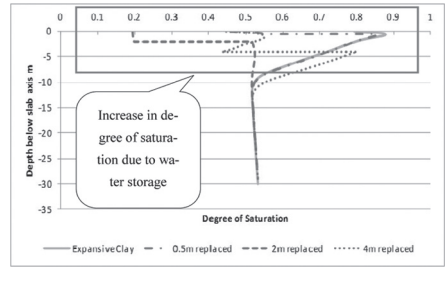

Figure 7. Saturation variation below slab edge.

higher conductivity, less expansive soil. There is a significant reduction in the heave occurring on the ground and at the surface right next to the slab edge (Figure 9) with increasing thickness of the replacement layer. This can lead to reduced differential movement and therefore less cracking and damage to the foundations of the structure. The higher conductivity layer at the top of the natural expansive clay is behaving like a sponge, due to its relatively high storage capacity, to hold onto water applied during rainfall events until it can be evaporated out from the replacement layer. The "sponge effect" of the non expansive layer traps the water while it is infiltrating and stores it for future evaporation during long non-rain periods. The function of the replacement layer can be compared to evapotranspirative (ET) covers used for landfills. The purpose of putting covers on landfills is to keep off water from infiltrating so that there is minimal leachate generation. The same principle applies to this case. The swelling is reduced in expansive soils because the surface layer can act to resist deep movement of water into the underlying clay profile for certain conditions of storage capacity, conductivity of replacement layer, and surface flux conditions.

In the case of arid and semi-arid climates, ET covers are superior to other cover systems. The typical thickness of ET covers used for landfill is 1.2 m to 1.8 m. Typical values of saturated hydraulic conductivity for the storage layer of an ET cover are 1×10^{-4} and 1×10^{-5} cm/s (Kavazanjian Jr 2001). Sandy silt and silty sand have been found to be optimal soils for ET covers. Clayey soil however, does not give up water easily but it is also difficult for water to get into the tiny pores of clay material. Studies at Yucaipa landfill and Gaffey street landfill have shown that ET covers perform better than prescriptive covers for landfills (Evans et al., 2000).

The higher conductivity replacement appears to be a good option to reduce heave in arid regions. As mentioned before that this is an ongoing project, further cases are being studied. A comparative study is being done with different types of replacement soil options to obtain the optimal soil type. The best choice for replacement materials is expected to be site-specific, and dependent on climatic and irrigation conditions, as a minimum.

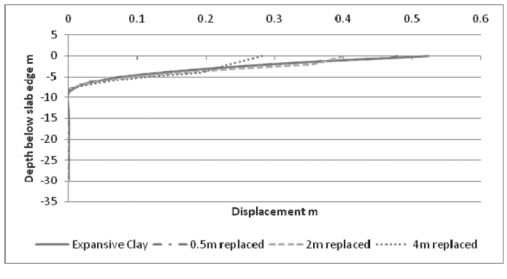

Figure 8. Displacement below slab edge.

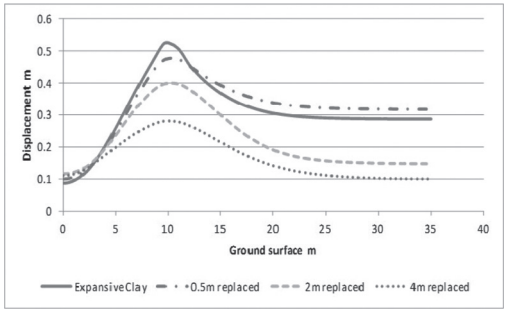

Figure 9. Heave at ground surface.

ACKNOWLEDGEMENT

This study was supported, in part, by the National Science Foundation (NSF) under grant number CMMI-0825089. The opinions, conclusions, and interpretations expressed in this paper are those of the authors, and not necessarily of NSF.

REFERENCES

Celia, M.A. & Bouloutas, E.T. 1990. A General Mass-Conservative Numerical Solution for the Unsaturated Flow Equation. *Water Resources Research* Vol. 26(7): 1483–1496.

Dye, H. Moisture Movement through Expansive Soil and Impact on Performance of Residential Structures, PhD Dissertation, Arizona State University, 2008.

Evans, T.M., Meyers, D.K., Gharios, K.M., Hadj-Hamou, H. & Kavazanjian, Jr, E. The use of a capillary barrier final cover for reclamation of a closed municipal solid waste landfill. *Proceedings of the 3rd annual arid climate symposium, SWANA, New Mexico Chapter, 12–14 April 2000* Albuquerque.

Fredlund, D.G. & Xing, A. (1994). Equations for the soil-water characteristics curve, *Canadian Geotechnical Journal* 31(3): 521–532.

Houston, S.L., Houston, W.N., Zapata, C.E. & Lawrence, C. 2001. Geotechnical engineering practice for collapsible soils, Department of Civil and Environmental Engineering, Arizona State University, Tempe, Arizona, 85287–5306.

Katti, R.K. 1979. Search for solutions to problems in black cotton soils. *First Indian Geotechnical Society Annual Lecture, Indian Geotechnical Journal* 9–1: 1–88.

Kavazanjian, Jr, K. Design and Performance of evapotranspirative cover systems for arid region landfills. *36th Annual Western States Engineering Geology and*

Geotechnical Engineering Symposium, 28–30 March 2001 pp. 11–26l, University of Nevada, Las Vegas: Nevada.

Leong, E.C. & Rahardjo, H. 1997. Permeability Functions for unsaturated soils. *Journal of Geotechnical and Geoenvironmental Engineering. ASCE* 1118–1126.

Murthy, V.R. & Praveen, G.V. 2008. Use of chemically stabilized soil as cushion material below light weight structures founded on expansive soil. *Journal of materials in civil and materials, ASCE*, May, Vol. ASCE 0899-1561 (2008) 20: 5(392).

Shackelford, C.D. & Chiu, T.F. The influence of the capillary barrier effect on the use of sand underdrains in waste disposal practice. R.N. Young and H.R. Thomas, Thomas Telford (ed.), *Geoenvironmental engineering, contaminated ground: Fate of pollutants and remediation* 357–364. London.

SoilVision Systems Ltd. 2008. SVFlux User's Manual. SoilVision Systems Ltd., Saskatoon: SK.

Vu, H.Q. & Fredlund, D.G. 2000. Implementation of soil Property Functions in Volume Change Analysis in Unsaturated Soils.

Walsh, K.D., Houston, S.L. & Harraz, A.M. Finite Element Evalustion of Deep-Seated Swell. *Proceedings, 4th Asia-Pacific Conference on Unsaturated Soils*, *Nov. 2009* 23–25. Newcastle: Australia.

Wilson, G.W., Fredlund, D.G. & Barbour, S.L. 1997. The effect of soil suction on evaporative fluxes from soil surfaces, *Canadian Geotechnical Journal* 34(4): 145–155.

Geotechnical problems and soil atmosphere interaction

This page intentionally left blank

Advances in Unsaturated Soils – Caicedo et al. (eds)
© 2013 Taylor & Francis Group, London, ISBN 978-0-415-62095-6

Capillary barrier dissipation by new wicking geotextile

M. Azevedo & J.G. Zornberg
The University of Texas at Austin, Austin, TX, USA

ABSTRACT: A capillary barrier will form and restrict water flow when two porous materials with differing porous structures (e.g., a geotextile overlain by a fine-grained soil) are in contact with one another. This can be problematic as the capillary barrier may cause undesirable moisture build-up in the overlying soil. A new geotextile has been manufactured to help dissipate a barrier by "wicking" or laterally draining moisture away from the soil. Research at The University of Texas at Austin investigated the unsaturated properties of various versions of this wicking geotextile, under both woven and non-woven configurations. The testing program includes small soil column infiltration tests with moisture monitored by time domain reflectometers. Also, modified hanging column tests were conducted to define the hydraulic properties of the geotextile. Test results illustrate advantages in lateral drainage of the wicking geotextile when compared to regular geotextiles.

1 INTRODUCTION

In unsaturated conditions, a capillary break can form and restrict water flow when two porous materials with differing hydraulic conductivities are in contact with one another (e.g., a fine-grained soil overlying a coarse-grained soil). Due to the relatively large opening sizes of geotextiles, a geotextile acts similarly to a coarse-grained soil. Capillary breaks will increase the moisture storage in the overlying soil by forming a barrier at the interface of the materials. The cause of the capillary barrier is a difference in hydraulic conductivity between the large pores of a coarse-grained material and the small pores of the overlying fine-grained soil. This difference means that the small pores will restrict water from entering the larger pores. At a certain suction level, termed the breakthrough suction, the hydraulic conductivity of the two materials will be equal to one another and the barrier will fade away. Until there is enough moisture to break into the larger pores, moisture buildup will occur in the fine-grained soil (Zornberg et al., 2010).

The phenomenon of capillary barriers in unsaturated soils has gained increasing attention in recent years. A common application that takes advantage of capillary barriers is evapotranspirative covers for landfills. Alternative covers make use of the fact that moisture will accumulate in the soil cover, minimizing percolation into the waste. The moisture will then dissipate over the dry season due to evapotranspiration. Another beneficial application for capillary barriers is for agriculture. The barrier can be engineered to provide additional moisture to the root zone of crops.

While there are several other applications which may benefit from the development of capillary barriers, there are also many applications where an increase in moisture storage from a capillary barrier can be detrimental. For example, for the case of a geotextile reinforced slope, not accounting for moisture accumulation due to the formation of a capillary barrier at the soil-geotextile interface could be detrimental to its stability. Accordingly, a geotextile has been developed with the objective of minimizing the effect of a capillary barrier by using special wicking fibers. The wicking fibers allow the geotextile to reduce the effect of a capillary barrier through mechanisms such as enhanced lateral drainage.

This geotextile has the potential to perform the functions of separation, filtration, protection, reinforcement, and drainage. These multiple functions achieved by a single geosynthetic product could lead to significant cost savings compared to the use of separate products that perform equivalent functions.

1.1 *Wicking fiber*

The wicking fiber is a nylon fiber with a unique cross-section. The fiber cross-section is deep grooved (4DG) allowing for water to be carried by channels along the longitudinal axis of the nylon fiber. A picture of the cross section of the fiber can be seen in Figure 1.

The nylon fabric is both hydrophilic and hygroscopic. That is, the nylon will pull water from the surrounding soil as well as provide a conduit for the moisture along its channels. Nylon would

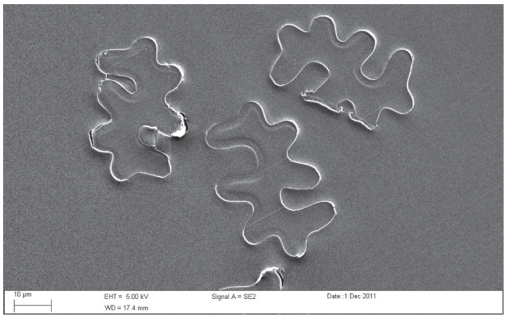

Figure 1. Typical 4DG wicking fiber cross-section.

typically provide these two functions, but an additive enhances them. The additive is not a coating that may diminish with time, but an additive to the nylon formula. The channels will provide some moisture storage as well, but since the channels are not large, their main function is to transport any absorbed water laterally. The channel width between the grooves is approximately 8 µm to prevent clogging from larger particles.

1.2 *Geotextiles*

A total of five different geotextiles were included in the testing program. A brief description of these geotextiles is summarized in Table 1. Each geotextile has been named GT1 through GT5.

GT1 is the control geotextile since it does not have any quantity of wicking fiber. It is commercialized as Mirafi 180 N and is a nonwoven fabric made of standard polypropylene (PP).

All other geotextiles in this study have some amount of wicking fiber. GT2 is commercialized as Mirafi H2Ri and is a woven geotextile composed of standard PP and nylon wicking fiber. The nylon fibers are bundled into strands of approximately 200 fibers. The PP is hydrophobic so it will not absorb water. Instead, the pattern of the weave and the PP itself will help guide the water laterally along with the nylon fibers.

The third geotextile in the study, GT3, is a nonwoven blend of fibers composed of 50% 4DG nylon wicking fibers and 50% standard PP fibers. Similarly, GT4 is a nonwoven blend composed of 50% 4DG nylon wicking fibers and 50% hydrophilic PP fibers. To make the PP hydrophilic, an additive was added to the formula for standard PP. Ideally, the hydrophilic PP will help distribute water to the wicking fibers and increase water movement speed.

The last geotextile in the testing program, GT5, is a nonwoven composed of 100% 4DG nylon wicking fibers. Unfortunately, a woven geotextile made of 100% 4DG nylon wicking fibers could not be created due to challenges in its manufacturing process.

Table 1. List of geotextiles for testing program.

Name	Geotextile description
GT1	Non-woven PP (Mirafi 180 N)
GT2	Woven wicking (Mirafi H2Ri)
GT3	NW 50/50 4DG wicking/PP
GT4	NW 50/50 4DG wicking/Hydrophilic
GT5	NW 100% 4DG wicking

It should be noted that none of the five geotextiles tested in this study had any coating applied to them. While coatings were considered and could provide some benefits to lateral drainage, their use adds a new variable with possible changes with time. Therefore, only additives that were directly included in a polymer's composition were used in this study.

2 WATER RETENTION CURVES (WRC)

A typical WRC for geotextiles is shown in Figure 2 (Bouazza et al., 2006). The WRC shows how the volumetric water content for a material changes with increasing or decreasing suction. The desorption curve (drying path) starts with an initially saturated sample and then increasing suction is applied until the sample reaches residual moisture conditions (going from left to right on the WRC). The initial saturated volumetric water content is the same as the porosity since all the air in the sample has been replaced by water. The final residual water content is due to a small amount of water trapped in the soil pores with no pathway to escape. The air entry value is the value at which the sample first starts to no longer be saturated. The adsorption curve (wetting path) starts out with an initially dry sample and then decreasing suction is applied until the sample becomes saturated (going from right to left on the WRC).

For a geotextile WRC, there is a pronounced hysteresis between wetting and drying paths. An explanation for this hysteresis is that air becomes entrapped in the larger pores, which prevents the geotextile from becoming saturated. The hysteresis for soil WRC is not as prevalent as for geotextiles. Furthermore, geotextile wetting curves obtained via different methods such as hanging column and capillary rise show varying amounts of hysteresis (Krisdani et al., 2006).

Figure 3 shows how the WRC varies for different types of soils (Fredlund et al., 1994). The soils with smaller pore sizes have higher capillary forces and need higher suction to remove water. For coarse-grained soils, the volumetric water content

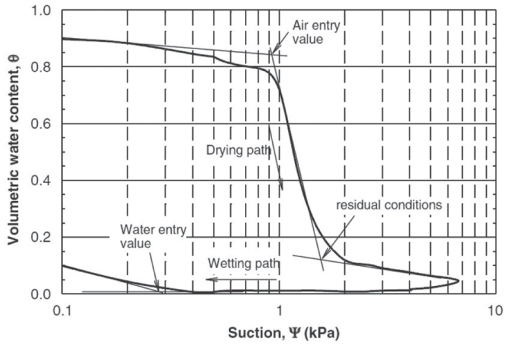

Figure 2. Typical geotextile WRC (Bouazza et al., 2006).

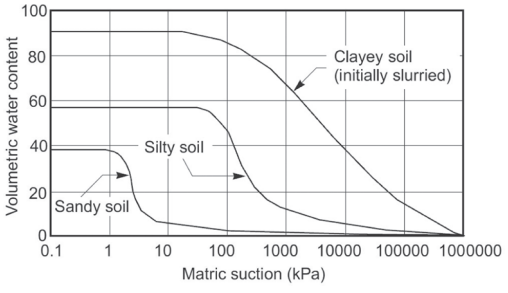

Figure 3. Typical WRCs for different soil types (Fredlund et al., 1994).

decreases sharply over a narrow range of suction. For fine-grained soils, the volumetric water content decreases slowly over a large range of suction. This behavior is explained by the pore size distribution of the soils (McCartney et al., 2005). Coarse-grained soils generally have a uniform pore size, while finer grained soils have a larger distribution of smaller pores. A WRC for a geotextile is similar to that of a coarse-grained soil. Since a geotextile has uniform and comparatively large pores, the WRC shows a steep drying path. The main difference between a soil and geotextile WRC is the wetting path.

2.1 *Modified hanging column test*

The hanging column test commonly used for soils can be modified for geotextiles as shown in the setup by Stormont et al. (1997) in Figure 4. The entire system is sealed to the environment to prevent moisture losses from evaporation. A geotextile specimen is placed into contact with a saturated porous ceramic plate in a Buchner funnel. A seating load is placed on top of the geotextile specimen so that the geotextile remains in contact with the ceramic plate throughout the test. The funnel can be raised or lowered and the head difference between the bottom of the geotextile and the surface of the water reservoir is the applied suction. By raising the funnel to various heights and weighing the geotextile specimen after waiting 24–48 hours at each stage to reach equilibrium, the entire WRC for the geotextile may be obtained.

2.2 *WRC of the wicking geotextile*

The modified hanging column setup in Figure 4 was used to obtain the WRC for the woven wicking geotextile (GT2). Both the drying and wetting curves can be seen in Figure 5. The van Genuchten function was used to fit a curve through the data for the drying path. From the WRC, it is observed that GT2 has a comparatively low porosity, of around 0.2. Also, the volumetric water content does not decrease sharply over a narrow suction range like a regular geotextile. Instead, the water content decreases gradually like a fine-grained soil. However, the WRC is still in a low suction range, which corresponds to a coarse-grained soil.

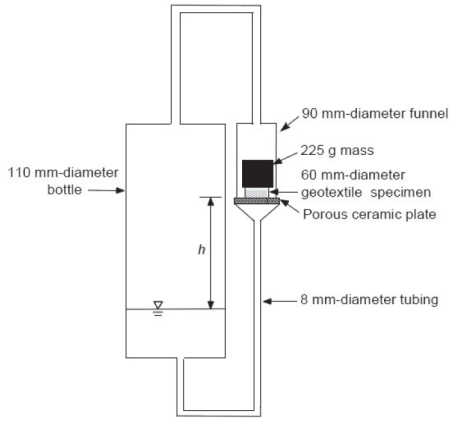

Figure 4. Setup of a modified hanging column test for geotextiles (Stormont et al., 1997).

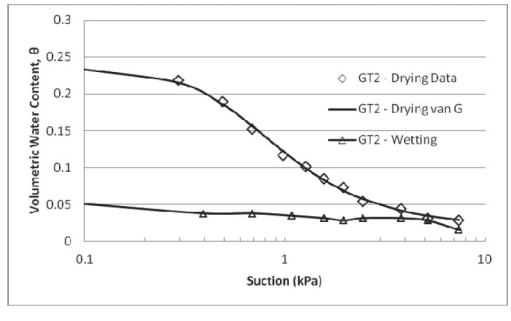

Figure 5. Water retention curve for GT2.

For example, in Figure 3, the suction range for a silty soil goes up to 1,000 kPa. For the sandy soil, the suction range only goes up to 10 kPa, just like for GT2.

Another observation from the wetting curve portion of the WRC is that the wicking geotextile barely absorbed moisture upon wetting. This may just be for the same reasons as other geotextiles which also have minimal absorption upon wetting. It can be noted that this hysteresis may be the result of the wicking fibers not being in contact with the porous stone as shown in Figure 6. The wicking geotextile is composed of black PP fibers and white nylon fibers. Because the geotextile is woven, the surface of the geotextile is uneven and while the PP fibers contact the porous stone, the nylon fibers do not. Since the PP does not absorb moisture and the wicking geotextile depends on the nylon fibers for its moisture capacity, this lack of contact may be why so little water is absorbed during wetting. This may not be an issue in actual soil because the soil should fill in all the pore spaces between the PP fibers.

2.3 *Comparison of mirafi wicking geotextile WRC to other materials*

The WRC of the nonwoven geotextile GT1 is shown in Figure 7. The nonwoven blends of wicking fiber GT3 and GT4 had a WRC very similar to that of GT1. The nonwoven geotextiles behave as expected, with a sharp decrease in water content over a very narrow suction range. The drying curves for the nonwoven geotextiles cover a wider range of moisture content, which differs from the drying curves from GT2. This is expected however, since the nonwoven geotextiles are thicker than GT2 and have more moisture storage capacity. The important difference in the curves of GT1 and GT2 is the water entry suction on the wetting curve. GT2 has a water entry value of 5 kPa while GT1 has a water entry value of 0.2 kPa. This means that GT2 will start absorbing water faster than GT1 and possibly be able to minimize the moisture buildup from a capillary barrier.

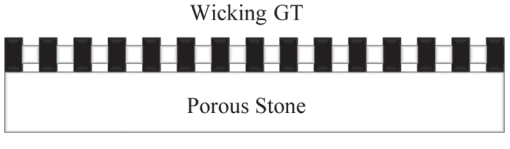

Figure 6. Diagram of GT2 over porous stone.

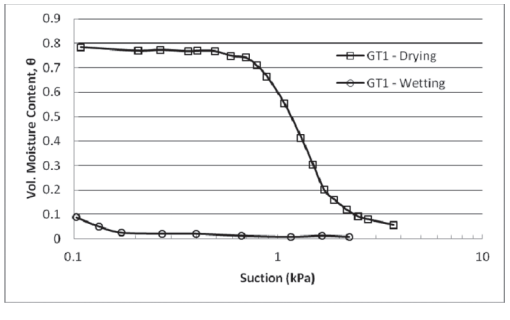

Figure 7. Water retention curve for GT1.

3 SMALL SOIL COLUMN CAPILLARY BARRIER MODEL

The experimental setup to monitor the formation of a capillary barrier is shown in Figure 8. The setup consists of a 19.7 cm diameter column with 15 cm of clay compacted in five lifts of 3 cm. The column is instrumented with three time domain reflectometer (TDR) probes to monitor water content. Flow is supplied to the column from above with a low flow pump at a constant rate of 0.38 mL/min. The flow is evenly distributed with a large filter paper at the top of the soil column. Beneath the soil is a geotextile underlain by 2 cm of clean gravel. The geotextile extends 3 cm from the edge of the column to allow for lateral drainage. There is a base plate underneath the gravel with an array of holes drilled into it to allow water to drain from the column. The water drains into a tipping bucket connected to the bottom of the column which is used to indicate when water has penetrated into the gravel layer.

All column tests used the same clay soil at a relative compaction level of 80%, which corresponds to a porosity (i.e., saturated volumetric moisture

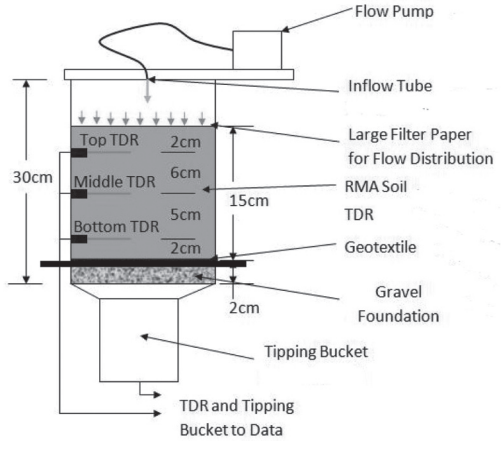

Figure 8. Setup for small soil capillary barrier model (Pickles 2009).

content) of 0.46. Also, all tests had a target initial volumetric water content of 0.15.

The geotextile and the gravel cause the development of a capillary barrier, creating moisture buildup in the column. Moisture keeps building up above the geotextile until a certain point, at which point breakthrough is achieved and there is finally flow through the geotextile into the gravel layer. At this point, there will be minimal storage in the gravel layer before the tipping bucket detects that breakthrough has occurred.

3.1 *Moisture data*

The capillary barrier formation is observed with the TDRs that are installed throughout the soil column. Figure 9 shows an example of volumetric water content with time as measured by the TDRs. Initially, the entire column is at a volumetric moisture content of 0.15. After the pump is turned on, the top TDR sees a jump in water content as it does not take long for the wetting front to reach the top probe. The moisture content for the top TDR remains constant at about 0.25 as the moisture front progresses downward into the column. The other two TDRs see similar jumps in water content as the moisture front reaches their location. If there were no gravel layer or geotextile, then the moisture content would remain at 0.25 for all three TDRs after the passing of the moisture front. However, since there is a gravel layer, a capillary barrier develops at around 2,000 minutes and this is observed in Figure 9. Once the wetting front reaches the geotextile, the wetting front is impeded and moisture increases up the column. The moisture buildup is greatest in the bottom TDR and least in the top TDR since it takes longer for the wetting front to travel back to the top of the column.

Moisture buildup continues until breakthrough suction is reached. The water content recorded by the TDRs remains constant for the entire column after breakthrough has occurred. If the column did not allow for drainage, then water would immediately flow into the gravel layer upon breakthrough and would be detected by the tipping bucket. This is indicated by the dotted line in Figure 9. However, since the setup allows for drainage, some of the moisture buildup is diverted laterally by the geotextile upon breakthrough and does not immediately flow into the gravel layer. Eventually, however, there will be some moisture that makes it through the geotextile and breakthrough will be detected by the tipping bucket. This delayed breakthrough is indicated by the dashed line in Figure 9.

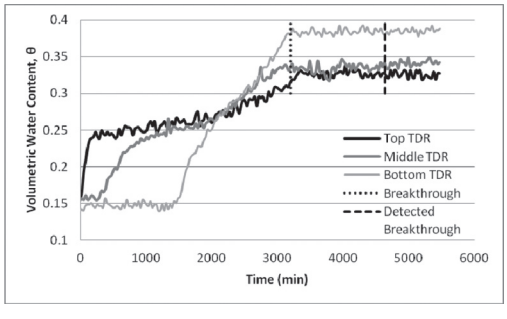

Figure 9. Example water content data from TDRs.

3.2 *Test results*

A series of small soil column tests were conducted using the five geotextiles listed in Table 1. The goal of testing was to see which geotextile performed the best in terms of lateral drainage as well as possibly minimizing the capillary barrier. All geotextiles were unable to reduce the amount of moisture buildup from the capillary barrier. This is somewhat expected because even though there is a difference in the barrier formed for the various geotextiles, there is still the common gravel layer for every test. This gravel layer forms a second capillary barrier which also needs to be overcome before water can flow into the gravel layer.

In order to quantify the effect of lateral drainage, the percolation rate through the geotextile was calculated. This value was chosen instead of the actual amount of percolation since some tests lasted longer than others and, therefore, were exposed to more flow. The percolation reported here is only the flow that makes it through the base of the column. The idea is that if a geotextile has significant lateral drainage, then most of the moisture buildup will escape through the sides of the column and only a small amount will be left to reach the bottom of the column. Therefore, the smaller the percolation rate, the better the lateral drainage provided by the geotextile.

To calculate the percolation rate, it was first necessary to calculate the time that the geotextile was exposed to flow by subtracting the time it took to reach breakthrough from the total amount of time that the pump was supplying water to the column. To calculate the total outflow at the bottom of the column, the number of tips were multiplied by the volume per tip. The tipping buckets used in this setup have a volume of 8.24 mL per tip. Finally, the percolation rate through the geotextile was calculated by dividing the two previous results. A summary of these calculations can be seen in Table 2.

The percolation rate data in Table 2 provides a comparative assessment of the geotextiles that perform better in terms of lateral drainage. It is

Table 2. Percolation rate calculations.

Test value	Test 1	Test 2	Test 3	Test 4	Test 5
Geotextile	GT1	GT2	GT3	GT4	GT5
Time to brkth.*	3,575	4,640	4,487	4,951	11,622
Total test time*	5,896	5,481	6,665	5,472	12,740
Δ ($T_{bkth} - T_{total}$)*	2,321	841	2,178	521	1,118
Number of tips	79	2	8	7	2
Apprx. outflow†	651	16	66	58	16
Percolation rate‡	0.280	0.020	0.030	0.111	0.015

* minutes † mL ‡ mL/min.

clear that the control, regular nonwoven GT1 performs the worst, as expected. With an inflow rate of 0.38 mL/min, GT1 only minimally reduces the rate that makes it though the geotextile to 0.28 mL/min. Therefore, 74% of the applied flow reaches the gravel layer. The nonwoven 50/50 blend of hydrophilic PP and 4DG wicking fiber (GT4) performed better than GT1, but 29% of the inflow still made it to the gravel layer instead of being redirected laterally. On the other hand, GT2, GT3, and GT5 all performed comparatively much better. The percolation in columns using these geotextiles is reduced to approximately 0.02 mL/min, or an order of magnitude difference from GT1. Only 5% of the inflow makes it into the gravel layer, indicating that these three combinations of wicking fiber create a geotextile that has very good lateral drainage capabilities.

3.3 *Dissipation of capillary barrier*

While a capillary barrier still developed with each of the geotextiles, the lateral drainage function provided by the wicking fibers was able to dissipate the capillary barrier after it formed. Figure 10 shows the dissipation of the capillary barrier by GT5. For that test, the pump was shut off about a day after breakthrough was detected. Up until this point, the moisture in the column had been constant for multiple days after the initial breakthrough (not the detected breakthrough). As soon as the pump was turned off, the geotextile kept laterally wicking away water from the soil immediately above it. This corresponded to a drop in moisture content in the top TDR of the column. Without a continuous supply, the wetting front continued downward until it reached the geotextile where it drained laterally. Eventually, the geotextile was able to reduce the moisture buildup from the capillary barrier in the middle and bottom of the column as well.

The GT5 geotextile saw the greatest moisture buildup dissipation, which can be expected as it has the greatest amount of wicking fibers. Both GT2 and GT3 were able to dissipate moisture as well,

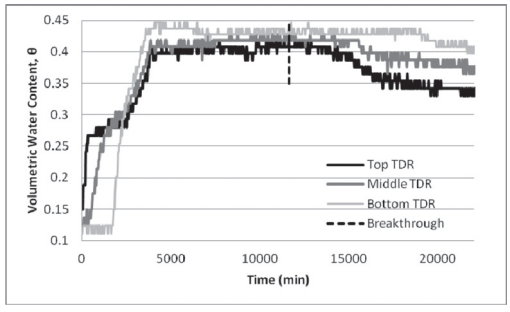

Figure 10. Dissipation of capillary barrier by GT5.

but to a lesser extent than GT5. Those geotextiles saw a decrease in moisture content near the top of the column, but not so much at the bottom of the column.

It is important to note that the decrease in moisture content in the column once the water supply is removed is not attributed to a drying front from evaporation. Tests run with geotextiles with no wicking fibers maintained constant water contents for days after removing the water supply. Only after a few days did the water content near the top of the column begin to slightly decrease. Tests were conducted indoors at room temperature and a low relative humidity of approximately 30%.

4 CONCLUSIONS

Results from infiltration column tests that allow for lateral drainage have shown that various woven and nonwoven configurations of geotextiles with 4DG nylon wicking fiber reduce the moisture buildup formed by a capillary barrier. The moisture dissipation is a direct result of the lateral drainage capabilities of the wicking fiber. Besides drainage, this geotextile has the potential to perform the functions of separation, filtration, protection, and reinforcement. This could lead to an all in one geosynthetic product with significant cost savings. Overall, these features are expected to help prevent common geotechnical problems associated with the use of geotextiles in unsaturated soils.

Ongoing tests are focusing on the conclusion from the WRC for the wicking geotextile which found that the wicking geotextile could minimize moisture buildup from a capillary barrier. New blends of nonwoven fibers will be tested in the same small soil column setup, but no lateral drainage will be allowed. Also, the gravel layer will be replaced with a layer of the same clay that makes up the rest of the column. Therefore, any moisture accumulation will solely be attributed to a capillary barrier from a geotextile and not the gravel

layer since it is not present. Hopefully, one of the nonwoven blends will allow for complete passage of water into the base layer, with no additional moisture buildup. Thus creating a geotextile that does not form a capillary barrier.

REFERENCES

Bouazza, A., Freund, M. & Nahlawi, H. 2006. Water retention of nonwoven polyester geotextiles. *Polymer Testing*, 25 (8), 1038–1043.

Fredlund, D.G. & Xing, A. 1994. Equations for the soil-water characteristic curve. *Canadian Geotechnical Journal*, 31 (4), 521–532.

Krisdani, H., Rahardjo, H. & Leong, E.C. 2006. *Experimental study of 1-D capillary barrier model using geosynthetic material as the coarse-grained layer*. In: *Proceedings of the 4th International Conference on Unsaturated Soils, UNSAT 2006*, Vol. 2 (pp. 1683–1694). Carefree, Arizona: ASCE.

McCartney, J.S., Kuhn, J.A. & Zornberg, J.G. 2005. Geosynthetic drainage layers in contact with unsaturated soils. In: *Proceedings of the 16th International Conference on Soil Mechanics and Geotechnical Engineering (16ICSMGE)* (pp. 2301–2305). Osaka, Japan: Millpress.

Pickles, C.B. 2009. *Hydraulic classification of unsaturated nonwoven geotextiles for use in soil structures. Master's thesis*. The University of Texas at Austin, Austin, TX.

Stormont, J.C., Henry, K. & Evans, T. 1997. Water retention functions of four nonwoven polypropylene geotextiles. *Geosynthetics International*, 4 (6), 661–672.

Zornberg, J.G., Bouazza, A. & McCartney, J.S. 2010. Geosynthetic capillary barriers: Current state of knowledge. *Geosynthetics International*, 17 (5), 273–300.

This page intentionally left blank

Advances in Unsaturated Soils – Caicedo et al. (eds)
© 2013 Taylor & Francis Group, London, ISBN 978-0-415-62095-6

Suction stress influence on strength parameters used in geotechnical engineering

R. Baltodano-Goulding
LANAMME-University of Costa Rica, San Pedro, San Jose, Costa Rica
Costa Rica Institute of Technology, Cartago, Cartago, Costa Rica

ABSTRACT: A series of shear strength tests using identical specimens but at different degrees of saturation were performed. Since the specimens were identical the most important variable affecting the shear strength and undrained strength parameters is the change in suction stress that modifies the state of effective stress, thus affecting soil behavior. Laboratory results demonstrated that this change in degrees of saturation has an effect on certain types of soil that can be significant for design. Three types of geotechnical engineering projects were analyzed: spread footing design, earth retaining structures design, and slope stability analysis. Changes in dimensions and safety factors of shallow foundation can be seen from a change in suction stress. Earth retaining structures performance and slope stability was also analyzed for the changes observed. Finally, a comparison between safety factors and its relationship to uncertainty in geotechnical engineering design at different degrees of saturation was performed.

1 INTRODUCTION

A series of shear strength tests were performed on six different types of soils at controlled densities and degrees of saturation. Testing included fully-saturated triaxial and unconfined compression tests at different degrees of saturation. Since the specimens were prepared at the same densities, and using the same soil type, the most important variable affecting the shear strength of these soils and in its undrained strength parameters, is the change in suction stress. Baltodano-Goulding (2006) performed direct shear testing and tensile strength testing on unsaturated F-40, F-55, and F-75 Ottawa Sand with three different particle sizes to isolate the effects of changes in the degree of saturation on the shear strength on those types of soils. It was concluded that for this particular kind of soil the effect of the changes in matric suction resulting from varying the degree of saturation were minimal. So it could be inferred that for similar granular soils changes in shear strength parameter related to water content might be minimal too, due to the small ranges of matric suction that these soils can developed.

However, for cohesive soils, where forces other than capillary forces act, these changes could become more critical in the shear strength parameters obtained. It is for this reason that it was decided to investigate the changes that varying the degree of saturation on several type of cohesive soils from different parts of Costa Rica, Central America could produce on the undrained shear strength parameters normally used for geotechnical design.

Since many factors can affect the shear strength parameters of cohesive soil it is imperative that the soil specimen densities be controlled in order to isolate the influence of water content. If certain void ratio remains constant for all specimens tested the only variable affecting the shear strength is the suction stress. Compacted specimens with fixed values of void ratio but different water content percentages were used to analyze the influence of degree of saturation on the soil behavior. It is worth mentioning that if the specimens are compacted at the same void ratios but with different water contents not only the degree of saturation is a variable but also the internal structure of the soil which is dependent on the amount of water use for compaction. These changes in structures can also affect the shear strength of the soil, but they can be considered also a consequence of the changes in the suction stress. According to Mitchell (1997), soil structure can be defined as the combined effect of fabric, composition, and interparticle forces. Nevertheless, Mitchell (1997) mentioned that the mechanical properties of soils are influenced by the soil type, the structure type, and the stresses, and soil structure and interparticle forces are included in our definition of suction stress. On the other hand, the resulting fabric, after the compaction process is done, will be affected by the energy of compaction and the degree of saturation, but

since the specimens were prepared at the same void ratio those changes in fabric are due to the change in degree of saturation, so it is also captured in our definition of suction stress.

While considering the effective stress in unsaturated soils, the macroscopic stresses such as total stresses, pore water pressure, and pore air pressure, must be considered. However, the microscopic stresses such as physical-chemical forces among the particles, and capillary forces must also be considered (Baltodano-Goulding 2007). According to Lu & Likos (2006), the effective stress in unsaturated soils can be expressed in a general macroscopic equation capturing all the microscopic effects in one term called suction stress, i.e. the microscopic forces contributing to the state of effective stress of the soil such as physical-chemical forces at the saturated state, changes on those forces due to desaturation of the soil, capillary forces, and matric suction effects, can be combined in a macroscopic terms called suction stress. This term will allow us to attribute all changes in shear strength for typical soils, when the degree of saturation is a variable, to the suction stress.

In order to evaluate if the expected changes in shear strength parameters could have a significant effect on the level of safety or could be used to optimize the design process of geotechnical structures, it was decided to perform simple design calculations of shallow foundations, retaining walls, and slope stability analysis.

2 MATERIALS AND METHODS

Soils used for this research were obtained from the sites listed on Table 1. All of these soils are located within the Central Valley in Costa Rica, Central America. Laboratory testing included water content, Atterberg limits, grain size distribution, standard Proctor, UU triaxial tests, and unconfined compression tests. Preparation of the soil specimens included sieving through the # 4 sieve in order to create a particular type of soil that can be classified as a fine grain size soil plastic or non-plastic.

Table 1. Soil specimen properties.

Soil	Classification (USCS)	Atterberg limits		Standard Proctor results	
		LL	PI	Dry unit weight (kPa)	Optimum water content (%)
1	MH	55	22	15.3	23.5%
2	CL	38	15	16.8	19.5%
3	SC	28	9	20.8	12%
4	SC	40	15	16.9	16%
5	SC	47	18	15.5	21%
6	SM	26	NP	19.6	11%
7	CL	36	8	12.7	28%
8	ML	40	NP	10.8	37%

Compacted specimens were prepared using Ladd (1978) undercompaction method. This method allows achieving homogeneous specimens and reproducible densities.

Once the laboratory testing was finished and undrained shear strength values were obtained, design of square footings for an allowable pressure of 35 kN, cantilever, gravity, and tie-back retaining walls, and slope stability analysis for a 2.5:1, 15 meter-high slope with a 150 kPa distributed surcharge load, were performed at different degrees of saturation.

Square footing design was calculated using Terzaghi´s bearing capacity equation for square footing using a bearing capacity factor (*Nc*) of 5.74. First shallow foundations were design with a fix allowable pressure and a factor of safety of 3.0 for each value of undrained shear strength determined, for each type of soil at the different degrees of saturation producing different foundation widths.

Lateral earth pressures were calculated using Rankine´s and Coulomb´s theory. On the other hand, tie-back walls were design using the SNAILwin version 3.10 software from the California Department of Transportation.

Slope stability analyses were performed using a limit equilibrium approach (method of slices). Three methods were used to estimate the factor of safety: Fellenius, simplified Bishop, and simplified Janbu. In addition, a seismic coefficient of 0.25 was used during the analysis, which is appropriate for the Central Valley zone in Costa Rica. Analyses were made using the SLIDE 5.0 software from Rockscience Inc.

Then retaining walls were design with fix dimensions producing different factors of safety for each value of undrained shear strength determined, for each type of soil at the different degrees of saturation. Wall dimensions were varied in order to maintain a factor of safety of 1.5 for sliding and overturning, and of 3.0 for bearing capacity.

Finally slope stability analyses were performed with a fix height and surcharge producing different factors of safety for each value of undrained shear strength and total unit weight determined. All analyses and designs done for this work are for short-term conditions.

The applicability of determining shear strength changes with saturation greatly depends on either assuring that a particular saturation condition will be maintained in the field or that a good understanding of the soil conditions is achieved,

before design and construction of the geotechnical structure. Since the degree of saturation is affected by precipitation, infiltration, evapotranspiration, and soil characteristics such as soil type, structure and state of effective stress, to ensure that saturation will remain constant throughout time is very difficult, even if an efficient drainage system is constructed. Therefore, it is probably better to focus on achieving a better understanding of soil conditions. For instance, if an unconfined compression test is used to design shallow foundations or retaining walls, and the degree of saturation of the sample is less than the maximum probable degree of saturation, unsafe conditions could be developed. On the other hand, if a design suction value (Fredlund & Rahardjo 1993) is determined, it might be possible to design for that condition instead of for a fully saturated condition and optimized our designs. Also the need for a probabilistic geotechnical design might be necessary.

3 RESULTS

Undrained shear strength were determined from unconfined compression tests using specimens at approximately the same density and varying degrees of saturation. Results for all type of soil tested and one of the two void ratios used are shown in Table 2.

3.1 *Shallow foundation design results*

Considering that a change in the degree of saturation produced a chance in unconfined compression values, shallow foundations were designed for the different types of soil, degrees of saturation and void ratios. Table 3 shows results obtained for soil 4 and 6 considering change in dimensions and cost associated to this change. It was observed that for increasing degree of saturation, on the same soil at the same density, a reduction in the design safety factor could be produced generating and unsafe condition, if a redesigning of the footing is not performed.

3.2 *Earth retaining wall design*

Earth retaining walls were also designed for the different types of soil, degrees of saturation and void ratios. It was observed that the factors of safety for overturning, sliding, and bearing capacity have a tendency to decrease as the degree of saturation increases.

Using results obtained for soil 3 the factors of safety were evaluated for an 8-meter tall wall. Tiebacks with 10 degree inclinations from the horizontal plane and 400 kN tensile strength, located every 2 meters horizontally and every 2 meters vertically were used. The results obtained showed a reduction in the factor of safety as the degree of saturation increased. The results obtained using the SNAILwin version 3.10 software developed by

Table 2. Undrained shear strength testing results.

Soil	Void ratio	Degree of saturation (%)	Total unit weight (kN/m^3)	Undrained shear strength (kPa)
1	0.89	48	16.2	31
		58	16.7	121
		68	17.2	99
		81	17.8	104
		90	18.2	79
2	0.58	48	18.5	237
		58	18.9	213
		70	19.3	200
		80	19.6	160
		96	20.2	115
3	0.50	50	19.3	45
		68	19.9	27
		79	20.2	11
		82	20.3	7
4	0.70	56	17.8	75
		60	18.0	65
		74	18.6	49
		80	18.8	25
		84	19.0	15
5	0.53	33	18.4	13
		44	18.8	17
		45	18.8	27
		53	19.1	31
		57	19.2	35
6	1.10	39	14.6	85
		45	14.9	102
		64	15.9	100
		65	16.0	97
		71	16.3	120
7	1.0	21	13.4	86
		33	14.4	177
		35	14.4	30
		36	15.2	68
		36	14.8	148
		42	15.1	45
		43	15.1	96
		44	15.0	87
		46	15.1	27
8	1.10	39	13.5	126
		40	13.8	95
		46	13.7	97
		48	13.7	61
		56	14.0	154
		58	14.1	81
		60	14.1	18
		63	14.5	127

Table 3. Saturation influence on shallow foundation dimensions for soil 4 and 5. Gomez & Baltodano-Goulding (2009).

Soil	Void ratio	Degree of saturation (%)	Foundation width (m)
4	0.70	56	0.87
		60	0.93
		74	1.07
		80	1.50
		84	1.95
5	0.87	33	0.76
		44	0.78
		45	0.69
		53	0.67
		57	0.73

Table 4. Tie-back wall factors of safety for soil 3 at different degrees of saturation and void ratios.

Void ratio	Degree of saturation (%)	Undrained shear strength (kPa)	Factor of safety
0.35	51	195	5.7
	64	155	4.1
	70	87	2.4
	84	90	2.5
	94	35	0.9
0.50	50	45	1.3
	68	27	0.8
	79	11	0.3
	82	7	0.2

the California Department of Transportation are summarized in table 4.

As shown in table 4, if a particular factor of safety needs to be maintained the reinforcement pattern will have to be changed according to the degree of saturation, thus affecting the design.

3.3 *Slope stability analysis results*

Finally, it was observed that the factors of safety for the slope stability analyses performed have a tendency to decrease as the degree of saturation increases. Table 5 shows the factors of safety as a function of degree of saturation for soil 1 and 2 using SLIDE 5.0 from Rockscience Inc.

4 CONCLUSIONS

It was determined that for a change in degree of saturation, the shear strength of the soil investigated can be affected due to a close relationship among the degree of saturation and the suction stress.

Table 5. Slope stability results for soil 1 and soil 2.

Soil	Void ratio	Degree of saturation (%)	Bishop simplified factor of safety	Janbu simplified factor of safety
1	0.89	48	0.3	0.4
		58	1.3	1.4
		68	1.1	1.1
		81	1.1	1.2
		90	0.8	0.9
	0.70	53	1.2	1.3
		67	1.9	2.0
		77	2.2	2.3
		89	1.8	1.8
2	0.58	48	2.5	2.6
		58	2.2	2.3
		70	2.0	2.1
		80	1.6	1.7
		96	1.1	1.2
	0.50	57	4.9	5.1
		70	4.0	4.1
		76	2.7	2.8
		85	2.6	2.6

It was also observed that a suction stress decrease can produce a decrease in undrained shear strength, thus affecting geotechnical engineering designs. However, it is important to mention that due to the double peak behavior that these soils exhibit, there are portion of the suction stress vs. shear strength curve that will produce an increase in shear strength for an increase in degree of saturation, even though the overall tendency is to have a decrease in shear strength as the degree of saturation increases. This behavior is more common in granular soils, as mentioned by Baltodano-Goulding (2006), than in fine grain soils where the saturation mechanisms are more complex; however, it was observed as part of this research, in fine soils too. This observed reduction in shear strength, as the degree of saturation increases in the capillary regime and decreases in the funicular regime, could produce and unsafe condition, if this reduction is not analyzed or considered during the design stage.

The observed variations in level of safety for the geotechnical structures analyzed suggests that probabilistic design procedures that somehow account for the uncertainty of shear strength parameters related to changes in the degree of saturation could be a good tools in dealing with this problem. The author is currently involve in a research project

which pretends reduce the uncertainty of soils by considering changes in water content.

REFERENCES

Baltodano-Goulding, R. (2006). "Tensile Strength, Shear Strength, and Effective Stress for Unsaturated Sand" Doctoral Dissertation. University of Missouri-Columbia.

Baltodano-Goulding, R. (2007). "Suction Stress Characteristic Curve for Unsaturated Ottawa Sand" 60th Canadian Geotechnical Conference/8th Joint CGS/IAH Conference. October 21 to 24, 2007. Ottawa, Ontario, Canada.

California Department of Transportation. SNAIL win version 3.10 software. Soil Reinforcement Program. Sacramento, California.

Fredlund, D.G. & Rahardjo, H. (1993). "Soil Mechanics for Unsaturated Soil". Wiley & Sons Inc. New York.

Gomez, C. & Baltodano-Goulding, R. (2009). "Suction Stress Effect on the bearing capacity of Shallow Foundations" III South American Young Geotechnical Engineers Conference, March 30 to April 1 2009. Cordoba, Argentina.

Ladd, R.S. (1978). "Preparing Test Specimens using Undercompaction". Geotechnical Testing Journal, pp. 16–23. GTJDJ. March 1978.

Lu, N. & Likos, W. (2006). "Soil Suction Characteristic Curve". Journal of Geotechnical and Geoenvironmental Engineering. February 2006 pp. 131–142.

Mitchell, J.K. (1993). "Fundamentals of Soil Behavior". John Wiley & Sons, Inc. New York.

Rockscience Inc. SLIDE version 5.0 software. Toronto, Ontario, Canada.

This page intentionally left blank

Advances in Unsaturated Soils – Caicedo et al. (eds)
© 2013 Taylor & Francis Group, London, ISBN 978-0-415-62095-6

Quantification and modeling of water flow in sandy soils in Northeast Thailand

S. Seltacho
Land Development Department, Khon Kaen, Thailand

V. Sriboonlue
Khon Kaen University, Khon Kaen, Thailand

N. Suwanang & W. Wiriyakitnateekul
Land Development Department, Bangkok, Thailand

C. Hammecker
Institut de Recherche pour le Développement UMR 210 - LDD, Bangkok, Thailand

ABSTRACT: Northeast Thailand is characterized by an undulating landscape that has undergone important land use changes during these last decades. After massive land clearing of the uplands, the global water balance has been modified, as illustrated by a general upraise of a deep water-table. Recently rubber trees have been planted widely in the uplands to replace cash crops introduced after deforestation. In order to evaluate the environmental incidence of this new land use, an experimental site has been installed in a mini watershed near Khonkaen. These studies focused especially on the quantification and modeling of soil water flow and on the evaluation of the sustainability of this cropping system. At the present stage of development the young trees' water uptake is not affecting significantly water balance. However modeling predicted that the water resources won't be sufficient for the trees once mature with the present planting density.

1 INTRODUCTION

The North East of Thailand (Isaan) is the poorest and most populated region of the country, relying mainly on agricultural production for its economical development. It is characterized by an undulating landscape with paddy fields located in the lowlands and the uplands were traditionally covered by original *Dipterocarpus* forest. However development of cash crops (sugar cane, cassava,..) has led to intensive land clearing during these last 50 years in the uplands (Wil1iamson et al., 1989). The replacement of trees by annual crops has increased runoff, soil erosion and has drastically modified the water balance at a regional scale, with a general upraise of a deep groundwater. Evapotranspiration in the recharge areas decreased notably when shifting from forest to annual crops, and therefore the rainfall contributed to the recharge of a groundwater leaching Eocene salt deposits. one of the off-site effect of the upraise of the saline groundwater was soil salinization in the low lands.

Rubber tree (*Hevea brasiliensis*) originally found in the Amazon rainforest has been exploited since the end of 19th century for it's sap (latex) and has become a major economic crop. This plant has been spread extensively over many tropical regions in the world, especially in South-East Asia and Africa. Nowadays most of rubber tree plantations are located in South-East Asia and particularly in Thailand which is the world's first natural rubber producer and exporter. Traditionally rubber production is located in the south of Thailand where the climatic and edaphic conditions are optimal. However in order to face the increasing demand for natural rubber, and to help small holders to increase their incomes, Thai government promoted the development of rubber tree plantations in the uplands of North-East Thailand. Despite adverse environmental conditions in this region due to insufficient rainfall (less than 1300 mm/year instead of 1500 mm/year usually recommended) as well as soil unfertility, local farmers have widely planted rubber trees in the area without considering the climatic and edaphic specificity of the region. In order to quantify the effect of rubber tree plantation on the region's water resources, and to evaluate the sustainability of this activity, a mini

watershed in the region of Khon Kaen has been selected to monitor the different components of the water balance along a toposequence. A special focus will be put on the evolution of the groundwater level, in order to test the possibility to draw it down to its original depth. Time necessary to measure actual changes in the water balance is generally long, therefore numerical simulation will be used to quantify and forecast these processes and test alternative situations.

2 MATERIAL AND METHODS

2.1 *Location and soil description*

The experiments were conducted along a toposequence in a mini watershed of 2 km^2 located near Ban Non Tun, 19 km southwest of Khon Kaen (16º, 19' 55"N, 102º 44' 36"E). In this area most of the surface (100 ha) is covered with young rubber trees, ruzi grass (*Bracharia Ruziziensis*) on the slopes and paddy fields are in the low land. The soil description revealed a general shallow soil profile ranging from 0.9 m in the upper part of the toposequence to 2.7 m downslope, in the waterway. The soil is composed of a sandy layer of 0.7 m to 2.2 m overlying a denser clayey layer in contact with the bed rock which is composed of weathered and fractured sandstone (Figure 1).

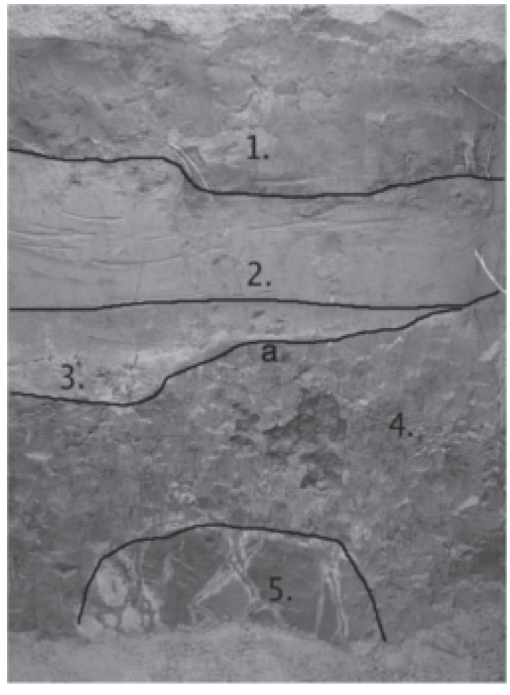

Figure 1. Soil profile with sandy layers (1, 2 and 3) on the top, and clayey layer (4) overlying the bedrock (5).

2.2 *Soil physical properties*

Water flow in soil is governed by the unsaturated soil properties, namely their hydraulic conductivity and water retention curves. As these parameters are often tedious and expensive to measure, the Beerkan method (Braud et al., 2005, Haverkamp et al., 1994, Lassabatere et al., 2006) had been chosen. This method is based on derivation of the retention curve from particle size distribution and hydraulic conductivity from a simple single ring infiltration experiment. This method has been shown to provide good estimation of the unsaturated soil properties and to be robust (Lassabatere et al., 2006, Mubarak et al., 2009).

2.3 *Water flow quantification*

Fine quantification of water balance in the soil-plant-atmosphere system at the experimental plantation in Ban Noon Tun was achieved through the installation of specific equipment. It is composed of a succession of three monitoring stations recording the changes in soil water content (capacitive soil moisture probes), the matrix potential (tensiometers) at different depths (0.10, 0.25, 0.45, 0.60 and 1.10 m), the level of the water-table (piezometers), meteorological data (temperature, relative humidity, wind speed, global radiation) and the flow rate of sap (heat dissipation probes).

2.4 *Modelling*

2D soil water flow modelling along the toposequence has been performed with the HYDRUS2D software that allows simulation of water flow, heat transfer and solute transport in variably saturated porous media. The 2D form of Richards equation is solved numerically with the finite element method. The domain represents a 2D section along the toposequence, the horizontal distance is 360 m and the vertical distance is 20 m upslope and 11 m downslope (Figure 2). The upper boundary conditions were set to atmospheric conditions with experimental meteorological data and sap flow measurements (rainfall, evaporation and transpiration). Lower boundary condition was set to variable pressure head corresponding to measured piezometric head, while lateral boundary conditions were set to zero flux. The root uptake procedure was computed with the model of Fedes and parameters from litterature (Vijayakumar et al., 1998). The root density was set to 0.5 from the soil surface until a depth of 80, 100, and 150 cm respectively in upslope, midslope, and downslope

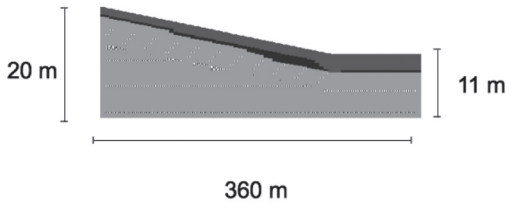

Figure 2. Geometry of the domain for modelling with HYDRUS2D.

position. The unsaturated soil parameters obtained with Beerkan method were used as first guess for the calibration procedure, using data from 13 May 2007 to 31 December 2007. The goodness of fit for the various simulations was quantified using the RMSE values, calculated with moisture contents for the entire simulation period.

$$RMSE_{\theta(t)} = \sqrt{\frac{1}{L}\sum_{i=1}^{L}(\theta - \overline{\theta}_i)^2} \quad (1)$$

where L is the number of measured and computed values of soil moisture, respectively θ and $\overline{\theta}$.

These parameters were then validated during a simulation period of one year in 2008, taking into account the corresponding daily boundary conditions.

In order to simulate the influence of different planting density, reduction coefficients were applied to the transpiration rates for different simulations. When this study took place the trees were still juvenile with girths of 15 cm, whereas mature trees in plantations usually reach 50 cm in girth. Therefore the situation with mature trees was also simulated, considering proportionality between the trunk surface areas (respectively 18 and 200 cm^2), corresponding to values found for mature trees in this area (Isarangkool Na Ayutthaya et al., 2011). The spacing of the trees was simulated with reduction coefficients of 0.8 and 0.5.

3 RESULTS

3.1 *Field measurements*

The continuous monitoring of soil water content and soil matric potential at different depths in the soil profile, in different positions along the toposequence showed that during the rainy season a perched water-table appeared on top of the clayey layer. This temporary water-table disappeared rapidly after the rainy season until the next rainy season. Water barely infiltrated into the clayey layer and the bedrock underneath.

Due to some technical problems, sap flow measurement were not available over the entire period of monitoring. Therefore the missing transpiration data were computed from the empirical relationship between ETo and the measured sapflow values (Figure 3). ETo was calculated from meteorological data with Penman-Monteith equation (Allen et al., 1998) and represents the evapotranspiration rate from a reference surface, not short of water, generally turf grass growing under optimal agronomic conditions. This empirical model was validated by other authors, studying the same clone in the same area (Isarangkool Na Ayutthaya et al., 2011). These results showed that the tree transpiration values were extremely low (0.1 to 0.2 mm/d) mainly because of the small diameter of the trees. The quantification of the water flow during the rainy season of the soil-plant-atmosphere system showed that 44% of the rainfall was taken up by the trees and superficial runoff represented 10%. Storage in the soil and vertical leaching represented respectively 2% and 4%. Hypodermic lateral water flow along the slope was found to be very important as it corresponded to 40% of the rainfall (Figure 4).

3.2 *Modelling*

The calibration procedure was achieved both with the inverse modelling facility of HYDRUS2D and manual fine tuning. The parameters for van Genuchten model of retention curve and hydraulic properties are reported in table 1. Their values were satisfactory in the modeling procedure for the description of the soil water flow along

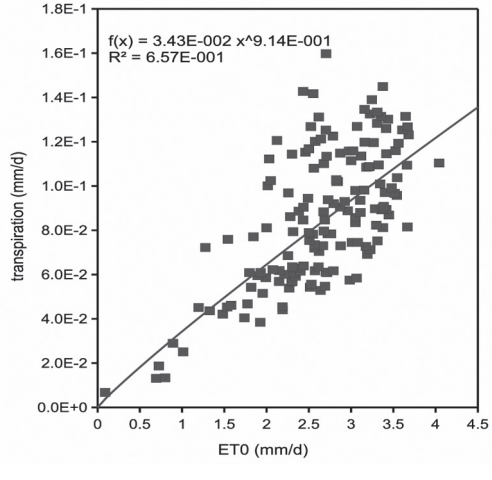

Figure 3. Relationship between measured ETo and transpiration derived from sap flow.

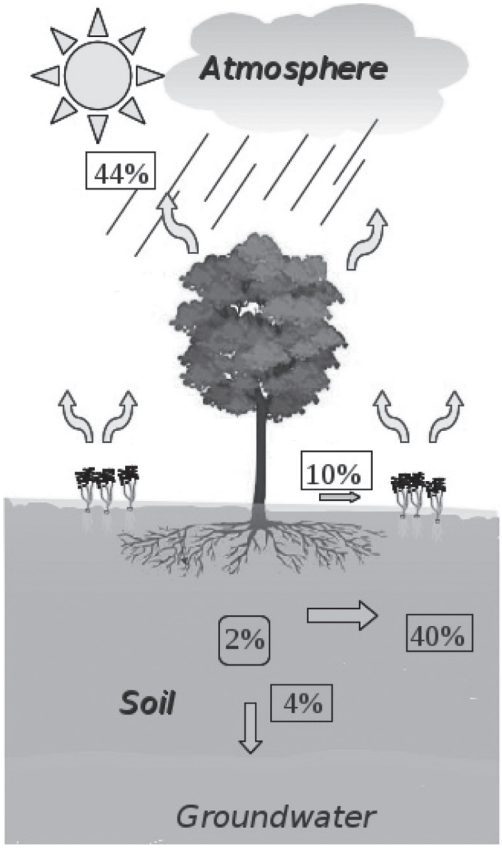

Figure 4. Distribution of rainfall water in the different compartments.

Table 1. Unsaturated soil characteristics for the three main soil layers.

	θ_r	θ_s	α m^{-1} ($\times 10^2$)	n	K_s $m \cdot s^{-1}$ ($\times 10^{-7}$)
Sandy	0.01	0.40	0.018	1.8	72
Clayey	0.01	0.38	0.047	1.51	0.0116
Bedrock	0.05	0.34	0.013	1.30	5.8

the toposequence for the following period of monitoring. The model computed the evolution of water content and RMSE was 0.054, 0.039, 0.043 respectively in the upslope, mid-slode and downslope position. Results for long term modelling showed that during the rainy season the sandy layers along the toposequence saturated until building up a perched water table. On the other hand, infiltration was extremely limited throughout the clayey layer and the water content of the underlying bedrock remained constant. The perched water table flowed down the slope and fed the deep groundwater at the bottom of the slope where the clayey layer was interrupted (Figure 5). In order to evaluate the availability of water resources necessary to meet plant requirements, the potential root uptake depending on climatic conditions and the computed actual root water uptake, taking into account the availability of water in soil, were compared (Figure 6). Despite the soil being sometimes saturated during the rainy season, the actual root water uptake was less than the climatic demands.

Results show that the difference between potential and actual root uptake diminished when the reduction coefficient decreases from 1 to 0.8 and 0.5. For the case of mature trees with 10 fold tanspiration rate the difference was extremely important. For the situations with coefficients 1, 0.8 and 0.5 the actual root water uptake represented around 50% of the potential root water uptake. On the other hand with the mature tree situation, the

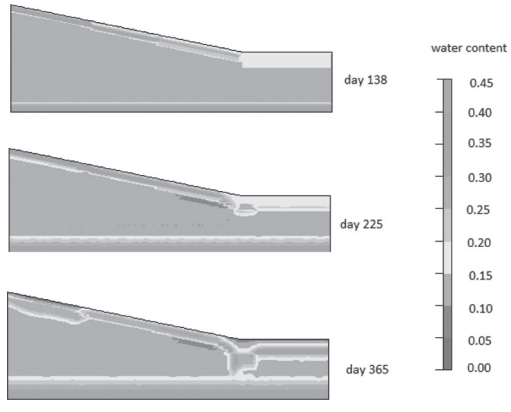

Figure 5. Simulated soil water content along the toposequence.

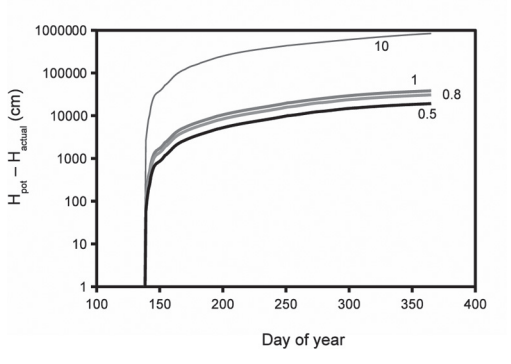

Figure 6. Simulated difference between the potential and the actual root water uptake for different coefficients applied to transpiration rate.

actual root water uptake represented less than 0.1% of the potential water uptake, witnessing clearly that the water resources are insufficient to meet the requirements for mature trees.

4 DISCUSSION

The measurements of the water flow in soil, soil surface, in groundwater and the sap flow in the tree trunk showed that during one year, water from rainfall is not allocated very efficiently to the plant requirements. Half of the rainfall was wasted with lateral hypodermic flow and surface runoff because of the pedological features of this soil which is shallow and limited by an impervious clayey layer. Only 2% of the total rainfall was stored in the soil. Numerical simulation of water flow during the same period confirmed this fact and showed that the perched water table mainly flowed down laterally. Downslope where the clayey layer is interrupted probably because of a deeper position of the bedrock, water accumulated in the soil and finally fed the deeper groundwater. The temporary perched water table connected to the deep groundwater exclusively by leaks throughout the clayey layer in the waterway.

A consequence of this lateral loss of water resources for the crops was illustrated by the important difference between the potential uptake by the roots and the actual uptake computed by the model. Considering the limited resources of water for the development of this crop, simulation about the reduction of planting density were performed and showed slight improvement when compared to the situation with young trees. The difference was therefore drastic when compared to the theoretical situation of mature trees where the transpiration would be tenfold. It appeared clearly that in this situation the water resources were insufficient to meet the requirements and therefore jeopardized the development of Rubber tree in this area.

5 CONCLUSIONS

In this study where the complete water budget along a toposeqeunce in a rubber tree plantation was measured and simulated with HYDRUS2D it was shown that combination of climatic and pedological conditions were adverse for the development of the young rubbber trees as half of the rainfall was dedicated to lateral hypodermic flow and superficial runoff, and that only a very little part was stored in the soil for the rainy season. When extrapolated to the water requirements of mature trees, numerical simulation showed clearly that the pedo-hydric conditions of this area were not suitable for the development of the trees at the present planting density.

REFERENCES

Allen, R.G., Pereira, L.S., Raes, D. and Smith, M. (1998). Crop evapotranspiration—Guidelines for computing crop water requirements. Number 56 in FAO Irrigation and Drainage Paper. FAO, Rome.

Braud, I., De Condappa, D., Soria, J.M. Haverkamp, R. Angulo-Jaramillo, R., Galle, S. and Vauclin, M. (2005). Use of scaled forms of the infiltration equation for the estimation of unsaturated soil hydraulic properties (the beerkan method). European Journal of Soil Science 56(3), 361–374.

Haverkamp, R., Ross, P.J., Smettem, K.R.J. and Parlange, J.Y. (1994). Three-dimensional analysis of infiltration from the disc infiltrometer: 2. physically based infiltration equation. Water Resour. Res. 30(11), 2931–2935.

Isarangkool Na Ayutthaya, S., Do, F.C., Pannangpetch, K., Junjittakarn, J., Maeght, J.-L., Rocheteau, A. and Cochard, H. (2011). Water loss regulation in mature hevea brasiliensis: effects of intermittent drought in the rainy season and hydraulic regulation. Tree Physiology 31(7), 751–762.

Lassabatere, L., Angulo-Jaramillo, R., Soria Ugalde, J.M., Cuenca, R., Braud, I. and Haverkamp, R. (2006, February). Beerkan estimation of soil transfer parameters through infiltration experiments–best. Soil Sci Soc Am J 70(2), 521–532.

Mubarak, I., Mailhol, J.C., Angulo-Jaramillo, R., Bouarfa, S. and Ruelle, P. (2009, November). Effect of temporal variability in soil hydraulic properties on simulated water transfer under high-frequency drip irrigation. Agricultural Water Management 96(11), 1547–1559.

Vijayakumar, K., Dey, S., Chandrasekhar, T., Devakumar, A., Mohankrishna, T., Sanjeeva Rao, P. and Sethuraj, M. (1998, January). Irrigation requirement of rubber trees (hevea brasiliensis) in the subhumid tropics. Agricultural Water Management 35(3), 245–259.

Williamson, D.R., Peck, A., Turner, J. and Arunin, S. (1989, May). Groundwater hydrology and salinity in a valley in northeast thailand. IAHS Publication 185, 147–154.

This page intentionally left blank

Advances in Unsaturated Soils – Caicedo et al. (eds)
© 2013 Taylor & Francis Group, London, ISBN 978-0-415-62095-6

A rainfall threshold for the occurrence of landslides in manmade slopes in residual soils in the northwest of Colombia

C.H. Hidalgo
University of Medellin, Medellin, Colombia

A.P. de Assis
University of Brasilia, Brasilia, Brazil

ABSTRACT: The purpose of this paper was to determine a rainfall threshold to estimate the probability of occurrence of landslides in roadway slopes. The analysis was performed for a roadway slopes excavated in residual soils derived from igneous intrusive rocks from the stock of Altavista, Medellin, Colombia. The threshold were raised in terms of total rainfall accumulated for short term of 1, 3 and 5 days and precedent moisture in soil due to long term rainfall of 15, 30 and 60 days. Rainfall data and landslides recorded for a period of four years were used to determine the thresholds. The thresholds found show that for slopes excavated in these soils the amount of rainfall that triggers the landslide is about 50% of the rainfall that causes landslides in natural slopes in the same area.

1 INTRODUCTION

Landslides represent one of the greatest geotechnical problems in countries like Colombia. On roads in the Andean zone, the problem of landslides results particularly significant due to the injuries and deaths of people, as well as its effects on mobility and economical loses. Between 2010 and 2011 in 15 departments of Colombia, the landslides on roads caused several deaths and injuries while more than USD500 was invested on road restoration. However, real direct and indirect economic losses are unquantifiable due to lack of information. In general, the rainfall causes the majority of these landslides, but the relationship between the process of mass movements and rainfall is still poorly understood and there are no models to assess this problem in practice.

This work presents a simple statistical relationship between landslides and accumulated rainfall on slopes of roadways in residual soils of Altavista stock in Antioquia, Colombia.

2 RAINFALL THRESHOLDS

The hydro-mechanical and hydraulic conditions of the terrain and the state of saturation of the soil are determinant on the conditions of stability of slopes. The rainfalls have a double effect: reduce the soil cohesion and increase the pore pressure. This influence of the rainfall on slope stability depends of the duration and intensity of the rainfall.

Attempts have been made to develop coupled models to simulate the effects of the precipitation on the slope stability (Rahardjo et al., 2001, Gitirana, 2005 Karam, 2005, Godt et al., 2008, Salciarini et al., 2008, Cascini et al., 2010, Conte & Troncone, 2012), these authors have used models that consider the gradual advance of the wet front and the reduction of suction and shear strength of the soils. These methods are still based on major simplifications and the input parameters are difficult and expensive for common cases. Consequently, these methods are still recommended only for preliminary assessments and for when there is a good amount of measurements of the involved parameters (Conte & Troncone, 2012). Due to the complexity of relationship rainfall-infiltration-landslides, in general the evaluation of the process of landslides triggered by rainfall is still based on empirical methods.

In researches conducted in different parts of the world it has been shown that the relationship between rainfall and landslides is highly influenced by conditions of preceding rainfall or rain accumulated on the ground before the triggering event (Chen & Lee, 2004, Ko, 2005, Rahardjo et al., 2001, Rahardjo et al., 2005, Rahimi et al., 2010, Brunetti et al., 2010, Zêzere et al., 2005, Jaiswal and Van Westen, 2009 and 2010, Echeverri & Valencia, 2004, Moreno et al., 2006, Aristizabal et al., 2010, Hidalgo and Assis, 2011). In general these studies have identified thresholds with precedent rainfall of 15, 30, 60 and 90 days, and different durations of triggering events as 1, 3 or 5 days. In some

studies it has been considered the rainfall intensity in the establishment of thresholds.

In residual soils, studies have shown that in slopes in well-drained soils (permeability coefficient of saturated soil ks ≥ 10^{-4} m/s) the stability is more affected by high intensity rainfall. In these cases the rainfall represents only a fraction of the permeability coefficient of the saturated soil. Furthermore, they determined that poorly-drained slopes (ks ≤ 10^{-6} m/s) are more affected by rainfall in which the intensity equals ks, rainfalls of high intensity but low duration have the greatest influence on stability (Rahardjo et al., 2007, Rahimi et al., 2010).

The triggering effect of rainfall on landslides can be estimated using thresholds of failure. These thresholds represent a relationship between the amount of rain accumulated before and during the event of a landslide that are established statistically. There are several studies that use the accumulated precipitation during the 3 days preceding the event, called antecedent rain and rainfall accumulated during the 15 days preceding the earlier called precedent rainfall (Echeverri & Valencia, 2004). These authors studied the relationship between rainfall and landslides in natural slopes of La Iguana river basin in the city of Medellin, Colombia, in the period 1980–2001 with 40 records of landslides and rainfall data of the meteorological station "San Cristobal" of the de Medellin public services company. For this zone was determined a threshold for a hazard landslide for precedent rainfall of 15 days (R_{15}) and a 3-day antecedent rainfall (R_3) and proposed a threshold that was exceeded by 95% of data processed by them according to the equation:

$$A = R_3 - 60 + 0.55R_{15} \tag{1}$$

where: A is the hazard of landslide triggered by rainfall, R_3 is the 3 day antecedent rainfall and R_{15} is the accumulated precipitation of the 15 days preceding the R_3.

Later, Moreno et al. (2006) studied the relationship between rainfall and landslides in the department of Antioquia, Colombia for the time period 1974–1998. With a total of 283 landslides have determined a threshold according to the equation:

$$R_3 = 75 - 0.5R_{15} \tag{2}$$

where R_3 is the 3 day antecedent rainfall and R_{15} is the accumulated precipitation of the 15 days preceding the R_3.

There is some similarity between these two equations, the fact results logical when it is considered that La Iguana river basin is located in the department of Antioquia. The differences between the two equations are associated with the differences in the periods of time analyzed and geological and human constraints. The human intervention may be more substantial in the Iguana basin due to its proximity to hard urbanized areas of the city of Medellín.

The threshold proposed by Moreno et al. (2006), which is presented in equation 2, was adopted by the early warning system of the Aburrá Valley, Colombia-SIATA (Aristizabal et al., 2010).

Also for the Aburrá Valley has been identified as the most important constraint for the occurrence of landslides are the seasonal rainfall, the long-term accumulative rainfall of around 60 mm in 30, 160 mm in 60 days, and 200 mm for 90 days (Aristizabal et al., 2011), the last two quantities are called antecedent accumulative rainfall (LAA).

Jaiswal & Van Westen (2009 and 2010) conducted research in which empirical thresholds were used to estimate the probability of failure in slopes of roadways of southern India. Using the Poisson distribution with the estimated rate λ represents the average number of events occurring in a unit of time or space. The expression for the Poisson distribution is:

$$P(X \le x) = \sum_{n=0}^{x} \frac{\lambda^n}{n!} e^{-\lambda} \tag{3}$$

where x and n are positive integers and λ is a parameter that denotes the average number of events (X) occurring at time t, which can be estimated as:

$$\hat{\lambda} = \frac{X}{t} \tag{4}$$

Hidalgo and Assis (2010 and 2011) combined these empirical relationships to assess risk for landslides on a roadway with rainfall data recorded on days when there were landslides and without considering the probability of exceedance of the threshold. The thresholds obtained in these studies shows a relationship between rainfall of 15 and 5 days.

3 RAINFALL THRESHOLDS DETERMINATION

As a study case, it was considered a section of a highway in the eastern sector of the roadway named Aburrá Cauca Conection in the department of Antioquia, Colombia, between the bridge over the river La Iguana and the eastern portal of the tunnel Fernando Gomez Martinez, abscissa km 4+000 to km 9+100.

The area where the roadway is located is characterized by a geology compounded by igneous intrusive rocks of the Altavista stock. These rocks produce layers of residual soils with thicknesses up to 50 m. The more superficial soils are characterized by low plasticity and low cohesion as may be seen in Table 1. The results presented in this table were determined with more than 30 determinations.

Since the beginning of operation of the road and for 4 years, this section of the roadway had 168 landslides which are associated with precipitation. In general the landslides occurred when there were large amount of accumulated precipitation as seen in Figures 1 and 2 which show the data of the climatological station of San Cristobal and records of landslides respectively.

Table 1. Soils characteristics in the area.

Property	Mean	Standard deviation	CV (%)
Dry unit weight (kN/m^3)	11.3	1.2	11
Wet unit weight (kN/m^3)	15.9	1.4	9
Unsaturated cohesion (kPa)	36.8	21.0	57
Effective cohesion (kPa)	7.3	7.6	103
Unsaturated friction angle (º)	31	6.9	22
Effective friction angle (º)	37.1	4.8	13
Liquid limit (%)	51.6	17.9	0.3
Plasticity limit (%)o	37.2	10.2	0.3
Plasticity index (%)	14.4	12.7	0.9

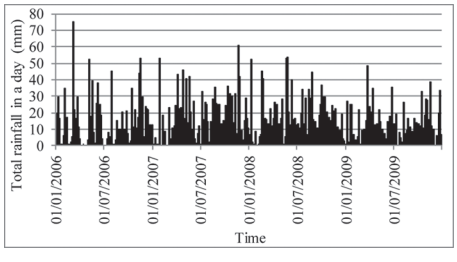

Figure 1. Accumulated daily rainfall by San Cristobal meteorological station (Hidalgo and Assis 2011).

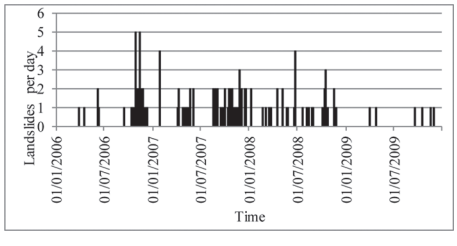

Figure 2. Data of landslides occurrence in the roadway (Hidalgo y Assis 2011).

Rainfall thresholds were established from daily accumulative rainfall antecedent and precedent to the landslide, assessing the accumulative effects of rainfall by 15, 30 and 60 days. In Figure 3 are shown the combinations for rainfall of 5 and 15 days are showed.

For the purpose of this work the precipitation or rainfall antecedent (PA) for the short-term accumulated precipitation, or precipitation in the days immediately to the landslide and the precipitation of long term (PP). PP is determined as the total rainfall accumulated in the days before the PA. To establish thresholds, for each day in which there were landslides there were determined antecedent rainfall accumulated of 1, 3 and 5 days prior to landslides and 15, 30 and 60 days preceding the former days, this means that these were generally considered rainy periods between 1 and 65 days, the data was plot as illustrated in Figure 3. The proposed thresholds were determined considering that landslides arise when antecedent rainfall and preceding rainfall reach their main value. It was evaluated the different possible combinations finding the thresholds defined by an equation of the form:

$$PA_j = a - bPP_{ji} \tag{5}$$

where PA_j is the accumulated precipitation of j days antecedent to the landslides, j = 1, 3 and 5, PP_i is the accumulated precipitation of *i* days before i = 15, 30 and 60 days.

In Tables 2 and 3 are presented the statistics of each parameter considered in the evaluation

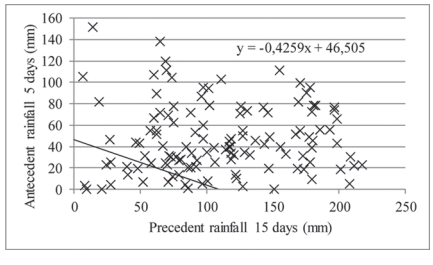

Figure 3. Combinations of total accumulated rainfall of 5 and 15 days, for days with landslides.

Table 2. Antecedent rainfall.

	San cristobal station		
	PA_5	PA_3	PA_1
Mean	46.5	32.4	14.0
Standard deviation	32.4	25.3	13.9
CV	0.7	0.8	1.0

Table 3. Precedent rainfall.

Station	j	i	Mean PP	Standard deviation PP	CV of PP
San cristobal	1	15	78.1	51.6	0.7
		30	164.9	90.2	0.5
		60	268.2	157.1	0.6
	3	15	109.6	54.4	0.5
		30	214.5	75.9	0.4
		60	401.8	122.5	0.3
	5	15	109.2	54.5	0.5
		30	239.2	79.6	0.3
		60	393	121.5	0.3

Table 4. Parameters of failure thresholds.

Station	j	i	a	b	N	PE
San cristobal	1	15	14.02	0.179	98	80.9
		30	14.02	0.085	102	84.3
		60	14.02	0.052	100	82.4
	3	15	32.36	0.295	105	86.8
		30	32.36	0.151	110	90.9
		60	32.36	0.081	110	90.9
	5	15	46.51	0.425	106	87.6
		30	46.51	0.194	114	94.2
		60	46.51	0.118	112	92.6

using different combinations with Equation 5. The parameters used were the antecedent precipitation of 1 day (PA_1), antecedent rain 3 days (PA_3), 5-day antecedent rainfall (PA_5), accumulated precipitation of the 15 days preceding the 1, 3 and 5 days ($PP_{1/15}$, $PP_{3/15}$, $PP_{5/15}$) accumulated precipitation from the previous 30 days 1, 3 and 5 days ($PP_{1/30}$, $PP_{3/30}$, $PP_{5/30}$) and cumulative rainfall 60 days preceding the 1, 3 and 5 days ($PP_{1/60}$, $PP_{3/60}$, $PP_{5/60}$). In Table 4 the coefficients *a* and *b* are presented for each combination, the number of days that the threshold has been exceeded (*N*) and had landslides and the probability of the threshold being exceeded during these days (PE).

For rainstorms of short duration, in this case events of 1 day of duration, is observed that the values of the intercept of the threshold is 14.02 mm and that the threshold has been exceeded between 80.9 and 84.3% of the days with landslides.

This implies that when the moisture is high, long-term accumulative rainfall 15, 30 or 60 days with values between 78.1 mm and 268.2 mm short rains, and low intensity rainfalls in the order of 3.11 mm to 2.14 mm can cause landslides. For preceding rainfall of 30 days the threshold presents an exceedance rate of at least 84.9, and exceedance rates greater than 76% in the case of 15 and 60 days. In this work is proposed for short duration storms a threshold based on precipitation preceding 30 days with the following equation:

$$PA_1 = 14 - (0.1)PP_{30} \quad (6)$$

where PA_1 is the accumulated precipitation of the day before to the event and PP_{30} is the rainfall accumulated in the previous 30 days.

Regarding the antecedents rainfall, it can be identified that the 5 day accumulated rainfall presents a smaller dispersion around the mean, given in terms of the coefficient of variation is 0.70. However for 1 and 3 days these values are 0.8 and 1.0.

The precedent rainfall also exhibit a similar trend and the dispersion decreases when higher is the number of days considered. For 60 days the coefficients of variation obtained are between 0.3 and 0.6, but for 15 and 30 days the coefficient of variation of 0.5–0.7 and 0.3–0.5 are obtained. Although the rain accumulated for 60 days presents the minimum variations in absolute terms, for practical purposes the observed variations in the order of 0.1 with respect to rainfall of 15 and 30 days, resulting insignificant.

For rainstorms of longer duration, in this case events of 5 hours duration is observed that values of the intercept of the threshold varies between 46.24 mm and 46.51 mm, and that the threshold has been exceeded between 86.0 and 94.2% of the days that were landslides.

This implies that when the moisture is high, for long-term cumulative rainfall 15, 30 or 60 days with values between 78.1 mm and 401.8 mm and for five days landslides can be caused by accumulative rainfall of the order of 46 mm with an exceedance rate of at least 87%. The thresholds for precedent rainfall of 30 days, they have observed exceedance rates greater than in the cases of 15 and 60 days. Considering that accumulated rainfall for 15 and 30 days are simpler to obtain, thresholds based on rainstorms of 5 days duration and previous precipitation of 30 and 15 days are proposed:

$$PA_5 = 46 - 0.42PP_{15} \quad (7)$$
$$PA_5 = 46 - 0.19PP_{30} \quad (8)$$

comparing the thresholds obtained in this study with those proposed for the slopes in the study area, Equations 1 and 2, which were developed with 3 days antecedent rainfall and rainfall precedent 15 days, it can be observed that the threshold of equations 1 and 2 present values of the rainfall intercept of 60 mm and 75 mm, considerably higher than those obtained in this work for the same combination that are of the order of 30 mm. The intercept of the precedent precipitation is equal in

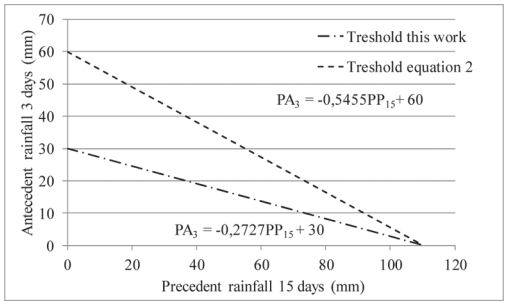

Figure 4. Comparison between the treshold for PA_3 and PP_{15}.

both cases the order of 110 mm. This relationship, shown in Figure 4, indicates a lower susceptibility of the slopes evaluated in this study.

This significant difference is due to anthropogenic impact by roadway construction since the landslides considered in this study are all located along the roadway slopes excavation. The anthropic effect tends to increase the likelihood of failure since it translate the threshold of failure to smaller values of rainfall background with a differences in the order of 30 mm, therefore, natural slopes which have low susceptibility to landslides, when affected by man activities can spend an unstable situation critical.

This also explains why most landslides in Aburrá Valley, Colombia, occur in highly intervened areas, but areas with similar topographical, geological and climatic features, but with less human intervention, have less landslides. It may then be proposed a threshold that allows considering the anthropic effect on areas with high anthropogenic interventions for this region of Antioquia, which is given as:

$$PA_3 = 30 - 0.1PP_{15} \quad (9)$$

4 CONCLUSION

The threshold for manmade slopes in residual soils when compared with thresholds of natural slopes, shows that these are more likely than this slopes fail.

The slopes in the residual soils of Altavista stock are likely to present landslides with combinations of rainfall that have high probability of occurrence. Therefore, these slopes should be designed for critical conditions of saturation or ensure excellent drainage conditions.

Still, further research is required to understand the relationships between rainfall and landslides in slopes, because still there are cases where landslides has occurred with rainfall below the threshold and many instances in which when the threshold was exceeded there are not recorded landslides.

REFERENCES

Aristizábal, E, Gamboa, M. & Leoz, F. 2010. early warning system for rainfall-induced landslides in the Aburrá Valley, Colombia. Revista EIA, No. 13: 155–169, Julio 2010. (In spanish)

Aristizábal, E., González, T., Montoya, J.D., Vélez, J.I., Martínez, H. & Guerra, A. 2011. Analysis of empirical rainfall thresholds for the prognosis of landslides in the Aburrá Valley, Colombia. Revista EIA, No. 15: 95–111. (In spanish)

Brunetti, M.T., Peruccacci, S., Rossi, M., Luciani, S., Valigi, D. & Guzzetti, F. 2010. Rainfall thresholds for the possible occurrence of landslides in Italy. Nat. Hazards Earth Syst. Sci., 10, 447–458.

Cascini, L., Cuomo, S. Pastor, M. & Sorbino, G. 2010. Modelling of rainfall-Induced shallow landslides of the flow-type. Journal of Geotechnical and Geoenvironmental Engineering, Vol. 136, No. 1: 85–98.

Chen, H. & Lee, C. 2004. Geohazards of slope mass movement and its prevention in Hong Kong. Engineering Geology 76: 3–25.

Conte, E. & Troncone, A. 2012. A method for the analysis of soil slips triggered by rainfall. Geotechnique 62, No. 3, 187–192.

Echeverri, O.Y Valencia, Y. 2004. Analysis of landslides in the basin of the Iguana river from Medellin city based on rainfall-slope-geological formation interaction. Dyna, 71 No. 142: 33–45. (In spanish)

Gitirana, J.F.N. 2005. Weather-Related Geo-Hazard Assessment Model For Railway Embankment Stability. Ph.D. Thesis, University of Saskatchewan, Saskatoon, Saskatchewan, Canada, 411 p.

Godt, J.W., Baum, R.L., Savage, W.Z., Salciarini, D., Schulz, W.H. & Harp, E.L. 2008. Transient deterministic shallow landslide modeling: Requirements for susceptibility and hazard assessments in a GIS framework. Engineering Geology 102: 214–226.

Hidalgo, C. & Assis, A. 2011a. Quantitative risk assessment for landslides triggered by rainfall on a highway in northwestern Colombia. Proceedings of the XII Panamerican Geotechnical Conference, Toronto, Ontario, Canada. (In spanish)

Jaiswal, P. & Van Westen, C.J. 2009b. Estimating temporal probability for landslide initiation along transportation routes based on rainfall thresholds. Engineering Geology 116: 236–250. Geomorphology 112: 96–105.

Jaiswal, P., Van Westen, C.J. & Jetten, V. 2010. Quantitative landslide hazard assessment along a transportation corridor in southern India. Engineering Geology 116: 236–250.

Ko, F.W.Y. 2005. Correlation Between Rainfall And Natural Terrain Landslide Occurrence In Hong Kong. Geotechnical Engineering Office, Hong Kong, Geo Report No. 168: 77 p.

Moreno, H.A., Vélez, M.A., Montoya, J.D. & Rhenals, R.L. 2006. Rainfall and landslides in Antioquia: analysis of its occurrence in interannual,

intraannual and daily scales. Revista EIA, No 5: 59–69, Medellín (In spanish).
Rahardjo, H., Hong, T.H., Rezaur, R.B. & Leong, E.C. 2007. Factors controlling instability of homogeneous soil slopes under rainfall. Journal of Geotechnical and Geoenvironmental Engineering, Vol. 133, No. 12: 1532–1543.
Rahardjo, H., Lee, T.T., Leong, E.C. & Rezaur, R.B. 2005. Response of a residual soil slope to rainfall. Canadian Getechnical Journal vol 42: 340–351.
Rahardjo, H., Li, X.W., Toll, D.G. & Leong, E.C. 2001. The effect of antecedent rainfall on slope stability. Geotechnical and Geological Engineering 19: 371–399.
Rahimi, A., Rahardjo, H. & Leong, E.C. 2010. Effect of hydraulic properties of soil on rainfall-induced slope failure. Engineering Geology 114: 135–143.
Salciarini, D., Godt, J.W., Savage, W.Z., Baum R.L. & Conversini, P. 2008. Modeling landslide recurrence in Seattle, Washington, USA. Engineering Geology 102: 227–237.
Zêrere, J.L., Trigo, R.M.Y. & Trig, I.F. 2005. Shallow and deep landslides induced by rainfall in the Lisbon region (Portugal): assessment of relationships with the North Atlantic Oscillation. Natural hazards and Earth Systems Sciences 5: 331–344.

Advances in Unsaturated Soils – Caicedo et al. (eds)
© 2013 Taylor & Francis Group, London, ISBN 978-0-415-62095-6

Use of artificial intelligence in Soil compaction modeling

E.L. Pérez González
Universidad Nacional Experimental Francisco de Miranda, Coro, State of Falcón, Venezuela

ABSTRACT: Soil modeling process requires a large amount of high quality experimental data. However, products of these processes fail to be satisfactory in most cases. This is due primarily to non-linear behavior that correlates different variables to be considered. This article presents a methodology to train surrogate models based on Support Vector Machines (SVM) using limited experimental data. Polynomial, Gaussian, and exponential radial basis function kernels were used for modeling. It has been proved that assembling the best models in a new one can surpass some of these individually. Several indicators were used to measure the model performance. An absolute relative error of 16% was reported during the use of the best ones. SVM offers a simple and reliable way in modeling the behavior of soils and can greatly enhance the capacity in soil mechanics laboratories in Latin America.

1 INTRODUCTION

The surrogate-based modeling approach is becoming popular and has demonstrated to be useful in the analysis and optimization of computationally expensive simulation-based modeling, for example, the aerospace (Li & Padula 2004, Queipo et al., 2005), automobile (Kurtaran et al., 2002), and Oil industries (Queipo et al., 2002a, b). Surrogate-based modeling makes reference to the idea of constructing an alternative fast model (surrogate) from numerical simulation data and using it for analysis and optimization purposes.

The rapid development of computer hardware and software has inspired to new approaches to data and analysis processing. These new approaches attempt to imitate the human brain and perception by building intelligent systems that can learn automatically from previous experiences. These approaches do not also depend on *a priori* assumptions such as the "well-behaved" statistical distribution of random processes required in most of statistical analysis (Jain & Dubes 1988, Haykin 1999). A collection of these new approaches is referred to as artificial intelligence (AI) and has been applied to modeling different civil engineering systems in the last decade (Dibike et al., 2001, Lizarazo & Gomez 2007, Zeghal 2008, Kasthurirangan et al., 2011).

Kernel-based methods (Girosi 1998, Müller et al., 2001) provide the flexibility of generating models under alternative loss functions and, in particular, support vector machine (SVM) developed by Vapnik (1995) at AT&T Laboratories in the mid-1990s. For a discussion of SVM applications in engineering, see Clarke et al. (2005) and references therein.

SVM power dwells upon several fronts, such as: (1) robustness and sparseness of solution; the goodness of the adjustment is measured not by the usual quadratic loss function (mean square error) but by a different loss function (ε-insensitive) similar to those used in robust statistics (e.g., a way of dealing with deviations from idealized assumptions) and a (2) flexible and mathematically sound approach; non-linear regression models (e.g., polynomials, Gaussian radial basis functions, splines, etc.) can be constructed as linear models by mapping the input data into a so-called feature space, namely, a reproducing kernel Hilbert space (Wahba 2000). The linear models (a single framework) are formulated in terms of dot products in a feature space which can be efficiently calculated using special functions (kernels) associated with non-linear regression models of interest, evaluated in the original space (kernel trick). This framework can also be used with quadratic loss functions, which makes it an ideal setting for ensembles of surrogate-based analysis and optimization.

This article provides a general approach, with a reasonable computational cost toward the optimal selection of SVM compacted soil modeling behavior. This technology can improve the analysis of results in soil mechanics laboratories.

2 DEFINING A PROBLEM

Given a training sample $E = ((x_h, y_h): 1 \le h \le n)$ defined in $D \subset Rq$ (empirical results), and l kernel-based surrogate models M_i, $1 \le i \le l$ constructed from sample E, select a set of m surrogate models and build a weighted average model:

$$w_{avg} = \sum_{i=1}^{m} \beta_i(x) M_i(x) \quad (1)$$

Given that the weighted average model surpasses as many individual surrogates as possible in the equation above, $\beta_i(x)$ represents the weight of model $M_i(x)$ at location x, the performance measures are: mean square error (*mse*), standard deviation (*std*), and maximum absolute error (*mae*), the following equations are used:

$$mse = \frac{\sum_{h=1}^{n} \left(y_h - M(x_h)\right)^2}{n} \quad (2)$$

$$std = \sqrt{\frac{\sum_{h=1}^{n} \left(y_h - M(x_h)\right)}{n-1}} \quad (3)$$

$$mae = \max\left|y_h - M(x_h)\right| \quad (4)$$

3 SOLUTION METHODOLOGY

The following steps are included:

a. The model input and output values are normalized to scale [–1, 1].
b. For each of the SVM models differing in kernel and loss function, a set of parameters are specified, namely, C (regularization parameter) and ε (size of insensitive zone); the kernels in SVM models are described, for example, as Gaussian with width *h* or polynomial with degree *p*. The parameters C and ε were identified using cross-validation (k-fold strategy) that they minimize the mean absolute value of errors. Specifically, after dividing the data into n/k clusters, each fold is constructed using an element from each of the clusters so it is a representative sample of the model of interest.
c. Select the best *m* models among the set of non-dominated models. The selection criteria are the mean square cross-validation errors, and non-dominated models make reference to models that provide the lowest error prediction in at least one point in the training data.
d. Using the best of the *m* models specified in the previous step, partial data shall be used from the validation tests to predict the expected results in the "untested" spectra. Later, results shall be compared with real values.

4 OVERVIEW

One of the broadest subfield in AI is the Machine learning (ML) focusing on the development of data modeling techniques and algorithms that learn from data. SVM is one of the ML techniques derived from statistical learning theory by Vapnik and Chervonenkis (1964). The foundations of SVM were developed by Vapnik (1995) at AT&T Bell Laboratories and SVM is recognized as an attractive and promising tool to solve classification and regression related problems (Gunn, 1998).

Initial work on SVM as a classifier is focused on optical character recognition and object recognition tasks (Smola & Scholkopf 2004). SVM has also provided excellent performances in regression and time-series prediction applications (Smola & Scholkopf 2004).

Comprehensive tutorials on SVM for regression are available in many sources (Gunn 1998, Cristianini & Shawe-Taylor 2000, Herbrich 2002; Scholkopf & Smola 2002, Smola & Scholkopf 2004).

4.1 *SVM- regression theory*

Training data is given as $\{(x_1,y_1), \ldots, (x_n,y_n)\} \subset X$, where X denotes the space of the training data patterns (e.g., $X = R^d$). The goal of SVM is finding a function f minimizing the expected risk (Vapnik 1982)

$$R[f] = \int L[x, y, f(x)] dP(x, y) \quad (5)$$

where R[*f*] = risk functional; x = input vector; y = output vector; $L[x, y, f(x)]$ denotes a loss function determining how we shall penalize the estimation errors based on the empirical data X; and $P(x,y)$ denotes distribution. Given that we do not know the distribution $P(x,y)$, we can only use X for estimating a function f that minimizes R[*f*].

Based on risk functional conditions, the SVM algorithm aims to find a function $f(x)$ that has at least ε deviation from the current obtained targets y_i for all the training data, and at the same time is as flat as possible (Smola & Scholkopf 2004). In other words, errors under the precision parameter ε are accepted and errors above than ε are not accepted. The case of linear functions f for given training data can be represented by the following equation:

$$f(x) = \langle w, x \rangle + b \quad (6)$$

where $w \in X$ and $b \in R$; $\langle w, x \rangle$ denotes the dot product in X; and the vector w = normal vector; The parameter $b/|w|$ determines the offset of the system from the origin along the normal vector w. The optimal regression function is given by the minimum of the following function Φ:

$$\Phi(w, \xi) = \frac{1}{2}\|w\|^2 + C\sum_{i=1}^{n}(\xi_i + \xi_i^*) \quad (7)$$

where C = pre-specified SVM tolerance parameter and ξ_i and ξ_i^* = slack variables determining the

degree from which data points shall be penalized if the error is larger than the precision parameter ε. A loss function can be introduced to function Φ to penalize estimation errors. This step is called "soft margin loss setting" (Scholkopf & Smola 2002). Some loss functions commonly used include ε-insensitive, Laplacian, Gaussian, Huber's robust loss, polynomial, and piecewise polynomial. Detailed description of these loss functions and the corresponding density models are provided in Smola and Scholkopf (2004).

The loss function is mostly referred to the ε-insensitive because it can produce sparseness in the support vectors. Figure 1 illustrates ε-insensitive loss function setting to given data in SVM also represented by the following equation:

$$L_\varepsilon = \begin{cases} 0 & if \quad |f(x)-y| < \varepsilon \\ |f(x)-y| - \varepsilon & otherwise \end{cases} \tag{8}$$

The minimum of the functional Φ problem can be considered as a quadratic programming (QP) problem. Using the Lagrange theory of quadratic programming, the w and b of regression function given by Equation 6 are obtained using the following:

$$w = \sum_{i=1}^{n} \left(\alpha_i - \alpha_i^*\right) x_i \tag{9}$$

Thus,

$$f(x) = \sum_{i=1}^{n} \left[(\alpha_i - \alpha_i^*) \langle x_i, x \rangle \right] + b \tag{10}$$

$$b = \frac{1}{n} \sum_{i=1}^{n} \left(y_i - \sum_{j=1}^{n} \left(\alpha_j - \alpha_j^*\right) \langle x_i, x_j \rangle \right) \tag{11}$$

Based on the Karush-Kuhn-Tucker conditions demanding that the product among the dual variables and constraints should vanish for optimality, the coefficients α_i and α_i^* of the data points inside ε bound of the function f are zero and the coefficient $(\alpha_i - \alpha_i^*)$ of the data points lying on or outside the ε bound have no-zero value. The support vectors are referred to data points with non-vanishing coefficients (see Fig. 1). According to Equation 9, it is evident that support vectors are only used in determining the decision function since the coefficient $(\alpha_i - \alpha_i^*)$ of other data points are all equal to zero.

In case of nonlinear regression, instead of trying to adjust a nonlinear model, the training patterns x_i are pre-processed into a high-dimensional feature space R^D by mapping ϕ: $R^d \rightarrow R^D$. Therefore, the dot product $\langle x_i, x_j \rangle$ in R^d for the linear case is equivalent to $\langle \phi(x_i), \phi(x_j) \rangle$ in R^D for the nonlinear case. The SVM training algorithm would only depend on the data through dot products in R^D. If the

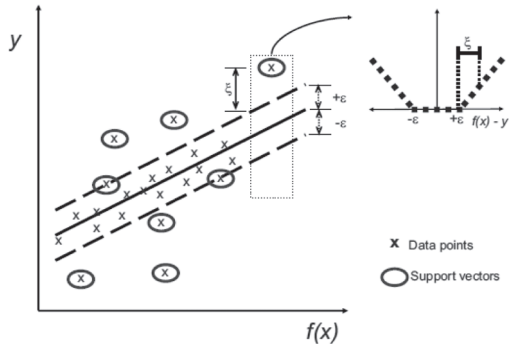

Figure 1. ε-insensitive loss function setting for SVM in regression.

dot product in the feature space R^D is expressed by following the equation called Kernel function, one would only need to use K in the SVM training algorithm without treating the feature space explicitly to obtain $\phi(x_i)$

$$K(x_i, x_j) = \langle \phi(x_i), \phi(x_i) \rangle \tag{12}$$

Typical Kernel functions described in Gunn (1998) include polynomial, Gaussian radial basis function, exponential radial basis function, multilayer perceptron, and so on. In this way, a nonlinear model in the original space can be transformed to the linear model in the new space. The regressions function for linear case as shown in Equation 10 and 11, can be transformed to the one for nonlinear case with Kernel function as follows:

$$f(x) = \sum_{i=1}^{n} \left[(\alpha_i - \alpha_i^*) K(x_i, x) \right] + b \tag{13}$$

$$b = \frac{1}{n} \sum_{i=1}^{n} \left(y_i - \sum_{j=1}^{n} \left(\alpha_j - \alpha_j^*\right) K(x_i, x) \right) \tag{14}$$

5 CASE STUDIES

5.1 *General considerations*

CBR (ASTM D1883), a semi-empirical test to estimate soil strength, is widely used in Latin American countries and worldwide for both soil-material characterization and pavement design (Sanchez-Leal, 2002). This is a low-cost and easy procedure test, but has several restrictions that make difficult interpreting the results under the unsaturated soil mechanics approach.

A framework of interpretation composed by contours graphs for CBR and concepts of Unsaturated Soil Mechanics was established by Sanchez-Leal (2002), later adopted by the Venezuelan specifications for design and quality

control of compacted soil (Fondonorma 2009). This framework proposes the use of a factorial experiment design to study the strength resulting from the relationship between soil suction, indirectly qualified by soil's water content (or saturation degree) and the energy of compaction, which affected the shape of the soil-water characteristic curve (SWCC), all this based on the ASTM D1883 variant 7.2, "Bearing Ratio for a range of Water content", this analysis framework is known as *strength maps*.

The strength maps framework was used to test SVM modeling for compacted soils. The solution methodology presented in section 3 is used to train a model that can predict the form of the strength maps for several types of soils. Empirical data was used to train the SVM-model. In table 1, the area presented the statistical description for input and output parameters. Soils used in the study were predominantly SM, GM and GC, according to Unified Soil Classification System (ASTM D2787), these are sands and/or gravel with more than 12% of silts or clays.

Maximum and minimum CBR can be related to a continuous quantitative scale by means of characteristics factors, F_p and F_{np} (Sanchez-Leal 2000). Fp is defined as the linear combination of both plasticity and gradation, as in equation 15, and related to soil classification in table 2.

$$F_p = \left(1 + w_L\right)\frac{F}{1+G} \tag{15}$$

where w_L is Liquid limit, F is finer content, or passing sieve #200 (0.075 mm), G is Gravel content, or coarser than sieve #4 (4.75 mm), all in decimal. These same parameters were selected to train the SVM-model.

Soil has variations in its resistance in connection to the suction changes in the mass of soil (Vanapalli et al., 1996). Traditional ASTM D1883 test is executed with non-controlled suction condition; however, the degree of saturation was taken as an indirect measure for the suction value, considering the suction as inversely proportional to the saturation degree of soil.

Table 1. Definition and ranges of values for input and output parameters used in SVM model development.

	Range			
Parameter	Min	Max	Mean	Std. dev.
Gravel (%)	12.7	79.1	33.6	19.6
Sand (%)	2.4	48.3	33.6	15.8
Fines (%)	14.5	49.9	32.8	13.3
ω_L (%)	22.0	38.2	31.1	6.8
Ip (%)	0.7	26.1	6.7	7.3
Moisture (%)	4.3	20.2	10.9	4.4
Saturation (%)	39.5	93.1	70.1	14.8
Specific gravity	2.4	3.0	2.6	0.2
Dry density (kN/m^3)	14.71	21.94	18.72	1.39
CBR (%)	1.9	36.6	11.8	9.5

Table 2. Fp related to soil classification (Sanchez-Leal, 2002).

F_p range	Soil classification
0.0–0.2	Silty and clayey gravels
0.2–0.5	Silty and clayey sand with gravels
0.5–0.7	Silty and clayely sands
0.7–1.4	Sandy and silty lean clays
> 1.4	Fat clays

The data used in this study were performed in the soil mechanics laboratory of Universidad Nacional Experimental Francisco de Miranda (UNEFM) in Coro, state of Falcón, Venezuela. 60 points of the CBR test used in this study, 80% (48) of these points were taken for model construction, using cross validation, and the rest of these (12) were used for testing.

The data was analyzed with and without noise. The data with noise consider two noise levels ($\alpha_1 = 0.05$, $\alpha_2 = 0.1$) and a uniform noise distribution U, as specified by the following expression:

$$F_k\left(1 + \alpha\left(U - \frac{1}{2}\right)\right) \tag{16}$$

Noise is added to the experimental data to emulate the variations present in materials, sampling and test method.

Models under consideration with ε-insensitive loss functions and kernels for Polynomial, Gaussian radial basis functions, and Exponential radial basis functions are specified in Table 3.

The ε and C values under consideration are 0.5 C_{cm}, 1.0 C_{cm}, and 1.5 C_{cm}, respectively; the h values are set equal to h_{cm}^{inf}, h_{cm}^{med} and h_{cm}^{sup}, with C_{cm} and h_{cm} reference values as proposed by Cherkassky and Ma (2004). The kernel-based regression problems are solved using the Matlab support vector machines (SVM) toolbox (Gunn 1998).

5.2 *SVM models prediction accuracy*

Parameters are shown in Table 4, mean square error, standard deviations and maximal absolute error of the best and worst models with kernel used. Considering these results, is deducted that the polynomial kernel is the best to predict CBR-values in compacted soils.

The ensemble of the surrogate models was performed as proposed by Goel et al. (2007), where

Table 3. Kernel functions associated with a variety of modeling schemes.

Kernel	Parametrization
Polynomial order *d*	$k(x,x') = [(x,x')' + c]^d \; d \in N, c \geq 0$
RBF	$k(x,x') = \exp(-abs(x-x')^2/2h^2) \; h \geq 0$
ERBF	$k(x,x') = \exp(-abs(x-x')/2h^2) \; h \geq 0$

Table 4. Performance of SVM models with different Kernels.

	Kernel	h	C_i	ε_i	MSE	STD	MAE
Best	Poly	3.0	63.52	5.72	27.67	5.47	9.69
	RBF	0.2	63.52	5.72	42.89	6.33	15.09
	ERBF	0.5	21.17	5.72	49.87	4.88	15.44
Worst	Poly	3.0	63.52	17.15	83.01	7.05	16.54
	RBF	0.5	42.35	11.43	103.18	6.94	16.31
	ERBF	0.2	63.52	17.15	135.64	7.86	28.09

weights are a function of relative magnitude of (global data-based) errors. The associated weight with *i*th surrogate is given as:

$$w_i = \frac{\sum_{j=1, j\neq i}^{N_{SM}} E_j}{(N_{SM}-1)\sum_{j=1}^{N_{SM}} E_j} \tag{17}$$

where E_j is the global data-based error measure for the *j*th surrogate model, and N_{SM} is the number of surrogate models. Table 5 shows the weighted vectors for the surrogate models studied, and the performance result of the ensemble of models.

The SVM-ensemble model was used to predict the response expected from soil, and a strength map was built with this information. A soil with 28.3% of Gravel, 48.3% of sand, 23.3% of Fines, w_L of 22.2%, and Specific Gravity of 2.54. The F_p calculated was 0.2216 corresponding to a "Silty and clayey sand with gravels". Dry density and Degree of saturation were evaluated using the same values obtained in laboratory (lab condition). Figure 2 shows the lab measures strength map. Figure 3 shows the strength map built with the predicted values of the SVM-ensemble model.

Results of the SVM-prediction are shown in Table 6, compared with the real laboratory results. Absolute relative error (ARE) was calculated using the following expression:

$$ARE = \frac{|x_R - x_P|}{x_R} \times 100\% \tag{18}$$

where x_R is the real laboratory value and x_P is the predicted value. A mean ARE value of 16% was reported.

Table 5. Weighted and performance of ensemble SVM model.

Weighted			Performance		
Poly	RBF	ERBF	MSE	STD	MAE
0.3851	0.3129	0.2930	25.79	5.52	11.98

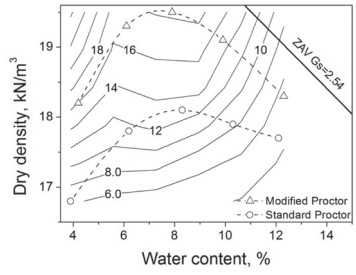

Figure 2. Strength map with CBR laboratory measures.

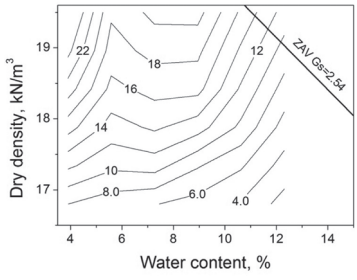

Figure 3. Strength map with SVM-ensemble CBR prediction.

Table 6. ARE between real lab measure and SVM-prediction.

DSW (kN/m³)	Moisture (%)	CBR (%) *Lab*	CBR (%) *SVM*	ARE (%)
18.2	4.2	15.9	18.3	15%
19.3	6.1	16.3	17.6	8%
19.5	7.9	18.9	21.7	15%
19.1	9.9	15.1	16.3	8%
18.3	12.3	5.4	6.8	26%
16.8	3.9	6.3	8.0	27%
17.8	6.2	11.1	12.8	15%
18.1	8.3	14.8	16.7	13%
17.9	10.3	8.5	10.5	24%
17.7	12.1	4.6	5.0	9%

6 CONCLUSIONS

This study has proposed using a SVM model to predict the strength behavior of compacted soils. The study was limited to the analysis of CBR prediction (ASTM D1883). A comprehensive parametric

analysis was conducted to determine optimal selection of the three controlling parameters (C, ε, and *h*) for the SVM-based predictive CBR models. A SVM ensemble model was developed using three different Kernels (e.g., poly, RBF, ERBF). The ensemble model shows a higher performance in comparison with the individual SVM-models.

SVM can provide a reliable method for the analysis of laboratory results, and is able to extend our range of information at low cost. SVM requires only three controlling parameters C, ε, and *h* with little dependency on the magnitude of training data required. These advantages of SVM can make a promising alternative considering the availability of limited and non-representative data frequently found in construction materials characterization.

The results of this study demonstrate the feasibility of using SVM in compacted soils modeling, while this research was limited to CBR test, the author encourages the readers to use the same solution methodology proposed in this article to generate their own models of various features of interest in compacted soils.

REFERENCES

ASTM D1883 (2007). Standard Test Method for CBR (California Bearing Ratio) of Laboratory-Compacted Soils. *Annual book of ASTM Standards: Vol. 04.08*.

ASTM D2487 (2011). Standard Practice for Classification of Soils for Engineering Purposes (Unified Soil Classification System). *Annual book of ASTM Standards: Vol. 04.08*.

Clarke, S.M., Griebsch, J.H. and Simpson, T. (2005). Analysis of support vector regression for approximation of complex engineering analyses. *ASME J Mech Des 127(6)*: 1077–1087.

Cherkassky, V. and Ma, Y. (2004). Practical selection of SVM parameters and noise estimation for SVM regression. *Neural Netw 17*(*1*): 113–126.

Cristianini, N. and Shawe-Taylor, J. (2000). An introduction to support vector machines, *Cambridge University Press, Cambridge, U.K.*

Dibike, Y.B., Velickov, S., Solomatine, D. and Abbot, M.B. (2001). Model induction with support vector machines: Introduction and applications. *J. Comput. Civ. Eng.*, 208–216.

Fondonorma, (2009). NTF 2000-1-2009: Carreteras, autopistas y vias urbanas. Especificaciones y mediciones. *Fondonorma CT3 Obras civiles. Caracas, Venezuela.*

Girosi, F. (1998). An equivalence between sparse approximation and support vector machines. *Technical Report AIM-1606, Artificial Intelligence Laboratory, Massachusetts Institute of Technology (MIT), Cambridge*.

Goel, T., Haftka, R., Shyy, W. and Queipo, N. (2007). Ensemble of surrogates. *Struct Multidisc Optim (2007) 33*: 199–216.

Gunn, S.R. (1998). Support vector machines for classification and regression. *Technical Rep.*, Image Speech and Intelligent Systems Research Group, Univ. of Southampton, Southampton, U.K.

Haykin, S. (1999). Neural networks: A comprehensive foundation. *Prentice-Hall, Englewood Cliffs, N.J.*

Herbrich, R. (2002). Learning kernel classifiers: Theory and algorithms, *MIT Press, Cambridge, Mass.*

Jain, A.K. and Dubes, R.C. (1988). Algorithms for clustering data. *Prentice-Hall, Englewood Cliffs, N.J*.

Kasthurirangan, G. and Sunghwan, K. (2011). Support vector machines approach to HMA stiffness prediction. *Journal of engineering mechanics—ASCE.* 138–146.

Kurtaran, H., Eskandarian, A., Marzougui, D. and Bedewi, N.E. (2002). Crashworthiness design optimization using successive response surface approximations. *Comput Mech 29*: 409–421.

Li, W. and Padula, S. (2004). Approximation methods for conceptual design of complex systems. *In: Schumaker L, Chui C, Neaumtu M (eds) Eleventh international conference on approximation theory, May 2004*.

Lizarazo, J.M. and Gomez, J.G. (2007). Desarrollo de un modelo de redes neuronales artificiales para predecir la resistencia a la compresión y resistividad eléctrica del concreto. *Ingenieria e Investigacion. U. N. de Colombia. 27*: 11–18.

Müller, K., Mika, S., Rätsch, G., Tsuda, K. and Schölkopf, B. (2001). An introduction to kernel-based learning algorithms. *IEEE Trans Neural Netw 12*(*2*): 181–201.

Queipo, N.V., Goicochea, J. and Pintos S (2002) Surrogate modeling based optimization of SAGD processes. *J Pet Sci Eng 35* (*1–2*): 83–93.

Queipo, N.V., Haftka, R., Shyy, W., Goel, T., Vaidyanathan, R. and Kevin Tucker, P. (2005). Surrogate-based analysis and optimization. *J Progress Aerospace Sci 41:* 1–28.

Queipo, N.V., Verde, A., Canelón, J. and Pintos, S. (2002). Efficient global optimization of hydraulic fracturing designs. *J Pet Sci Eng 35* (*3–4*): 151–166.

Sanchez-Leal, F.J. (2002). Interpretation of CBR-test results under shear strength concept of unsaturated soil mechanics. *Proceedings of the third international conference on unsaturated soils, UNSAT 2002.* 663–668.

Sanchez-Leal, F.J. (2000). Prediccion de los parámetros de resistencia del material de suelo. *2do Congreso Venezolano del Asfalto, Maracaibo, Venezuela.*

Schölkopf, B. and Smola, A.J. (2002). Learning with kernels. *MIT Press, Cambridge, MA*.

Smola, A. and Scholkopf, B. (2004). A tutorial on support vector regression. *Stat. Comput.*, 14, 199–222.

Vanapalli, S.K., Fredlund, D.G., Pufahl, D.E. and Clifton, A.W. (1996) Model for the prediction of shear strength with respect to soil suction. *Can. Geotech. J. 33*: 379–392.

Vapnik, V. (1982). Estimation of dependences based on empirical data, *Springer, Berlin*.

Vapnik, V. (1995). The nature of statistical learning theory, *Springer, New York*.

Vapnik, V. and Chervonenkis, A. (1964). A note on one class of perceptrons. *Automation and Remote Control*, 25(1).

Wahba, G. (2000). An introduction to model building with reproducing kernel Hilbert spaces. *Technical Report 1020, University of Wisconsin-Madison Statistics Department.*

Zeghal, M. (2008). Visco-elastic portrayal of bituminous materials: artificial neural network approach. *GeoCongress, New Orleans, USA, March 9–12, 2008, pp.* 1–8.

New theories and testing techniques related with Unsaturated Soil Mechanics have proven to be valuable tools to study a broad spectrum of geo-materials which includes rocks, rock fills, frozen soils and domiciliary solid wastes. These new theories and testing techniques have permitted the analysis of several traditional problems from a new perspective (e.g., swelling or collapsible soils and compacted soils or pavements materials), and they have also shown their efficiency to study new energy-related problems like CO_2 sequestration and nuclear waste disposal.

Advances in Unsaturated Soils is a collection of papers from the 1st Pan-American Conference on Unsaturated Soils organized in Cartagena de Indias, Colombia, in February 2013. The volume includes 76 research papers coming for all over the world, as well as 7 keynotes papers by well known international researchers. The contributions present a variety of topics including:

- Advances in testing techniques
- Unsaturated soil behavior
- Constitutive modeling and microstructure
- Numerical modeling
- Geotechnical problems

Advances in Unsaturated Soils is expected to become a useful reference to academics and professionals involved in Unsaturated Soil Mechanics.

ISBN 978-0-415-62095-6

9 780415 620956

CRC Press
Taylor & Francis Group
an informa business
www.crcpress.com

6000 Broken Sound Parkway, NW
Suite 300, Boca Raton, FL 33487
Schipholweg 107C
2316 XC Leiden, NL
2 Park Square, Milton Park
Abingdon, Oxon OX14 4RN, UK